

SYNTHETIC METHODS TO CONTROL ALUMINUM PROXIMITY  
IN CHABAZITE ZEOLITES AND CONSEQUENCES FOR  
ACID AND REDOX CATALYSIS

A Dissertation

Submitted to the Faculty

of

Purdue University

by

John R. Di Iorio

In Partial Fulfillment of the

Requirements for the Degree

of

Doctor of Philosophy

December 2018

Purdue University

West Lafayette, Indiana



**THE PURDUE UNIVERSITY GRADUATE SCHOOL**  
**STATEMENT OF DISSERTATION APPROVAL**

Dr. Rajamani Gounder, Chair

Davidson School of Chemical Engineering

Dr. Fabio H. Ribeiro

Davidson School of Chemical Engineering

Dr. Jeffrey Greeley

Davidson School of Chemical Engineering

Dr. Jeffrey T. Miller

Davidson School of Chemical Engineering

Dr. Corey Thompson

Department of Chemistry

**Approved by:**

Dr. John Morgan

Head of the School Graduate Program

To my family. Whose endless support, optimism, and sacrifices have enabled this  
opportunity and shaped who I am today.



## ACKNOWLEDGMENTS

To Raj Gounder, whose mentorship, patience, and wisdom has been invaluable and has given me the confidence to push myself beyond what I once thought was achievable. Your passion for research and learning has provided an exceptional example and has influenced the way that I think as a teacher, scientist, and mentor. Thank you for all of the encouragement and feedback, especially when my writing is less than acceptable, that you have given me over these 5 years. This has been an experience that I will be forever grateful to have been a part of. Specific acknowledgments for technical contributions are made within each chapter. Here, I would like to acknowledge all those who have helped shape my experience at Purdue and in life. Yury Zvinevich, whose advice and friendship has allowed me to learn at the hands of a instrumentation wizard and taught me how irreplaceable hands-on experience can be. Thank you for everything you have helped me with and for everything that you do for the catalysis research groups. This place would not be the same without you. To all the elder members of the Fabio research group, including Drs. Mike Detweiler, Atish Parekh, Kaiwalya Sabnis, Paul Dietrich, John Degenstein, and Zhenglong Li. Thank you for your mentorship and friendship. To Dr. Jamie Harris, Dr. Sydney Hollingshead, Dr. Vishrut Garg, and soon-to-be-Dr. Michael Cordon. I will always cherish your friendship and I am glad to have been able to cross paths with you. To Austin Tackaberry, Daniel Gonzalez, Sawyer Morgan, Ricardo Cogua, and Chris Ioeger who worked with me as undergrad researchers. Thank you for your hard work and willingness to learn. To all of the members of the Gounder and Ribeiro Research groups, thank you for all of your feedback and discussions. It has been a privilege to work with such great people and researchers. I would like to acknowledge my family, who this dissertation is dedicated to. Thank you for all of your support and

encouragement over the past 27+ years. I owe everything that I have accomplished to you. Finally, I want to thank Ana Steen for always reminding me that, whether you were aware of it or not, this journey isn't about content or composition, but in the pleasure of living. And that happiness isn't about freezing and clinging to each momentary pleasure, but in ensuring that one's life produces many future moments to anticipate. Thank you for everything.

## TABLE OF CONTENTS

|  | Page  |
|--|-------|
| LIST OF TABLES . . . . .   | xvi   |
| LIST OF FIGURES . . . . .  | xxiii |
| ABSTRACT . . . . .   | lvii  |
| 1 INTRODUCTION . . . . .   | 1     |
| 2 THE DYNAMIC NATURE OF BRØNSTED ACID SITES IN CU-ZEOLITES<br>DURING NOX SELECTIVE CATALYTIC REDUCTION: QUANTIFICA-<br>TION BY GAS-PHASE AMMONIA TITRATION . . . . . | 11    |
| 2.1 Introduction . . . . .   | 11    |
| 2.2 Experimental Methods . . . . .   | 13    |
| 2.2.1 Catalyst Synthesis and Preparation . . . . .   | 13    |
| 2.2.2 Characterization of Catalyst Structure and Composition . . . . .   | 15    |
| 2.2.3 Titration of Brønsted Acid Sites using Amines . . . . .  | 15    |
| 2.3 Results and Discussion . . . . .   | 18    |
| 2.3.1 NH <sub>3</sub> Titration of Brønsted Acid Sites in H-Zeolites after Ox-<br>idative Treatments . . . . .   | 18    |
| 2.3.2 NH <sub>3</sub> Titration of Brønsted Acid Sites in Cu-Zeolites after Ox-<br>idative Treatments . . . . .  | 22    |
| 2.3.3 NH <sub>3</sub> Titration of Brønsted Acid Sites in Cu-Zeolites after Re-<br>ductive Treatments . . . . .  | 23    |
| 2.4 Conclusions . . . . .  | 26    |
| 2.5 Acknowledgements . . . . .   | 27    |
| 2.6 Figures and Tables . . . . .   | 28    |
| 2.7 Supporting Information . . . . .   | 29    |
| 2.7.1 Atomic Absorption Spectroscopy of Catalyst Samples. . . . .  | 29    |
| 2.7.2 X-Ray Diffraction Characterization of Catalyst Samples. . . . .  | 30    |
| 2.7.3 N <sub>2</sub> Adsorption Isotherms of Catalyst Samples. . . . .   | 32    |
| 2.7.4 <sup>27</sup> Al Magic Angle Spinning Nuclear Magnetic Resonance ( <sup>27</sup> Al<br>MAS NMR) on H-ZSM-5 and H-SSZ-13 zeolites. . . . .                      | 35    |
| 2.7.5 Comparison of NH <sub>3</sub> and n-propylamine titrations on ZSM-5 and<br>SSZ-13 . . . . .  | 38    |
| 2.7.6 NH <sub>3</sub> TPD profiles after saturation at 323 K . . . . .   | 39    |
| 2.7.7 <i>n</i> -Propylamine titrations of ZSM-5 and SSZ-13 zeolites . . . . .  | 40    |
| 2.7.8 Ambient UV-Visible Spectroscopy of Cu-SSZ-13 . . . . .   | 42    |

|        |  |     |
|--------|--|-----|
| 3      | CONTROLLING THE ISOLATION AND PAIRING OF ALUMINUM IN CHABAZITE ZEOLITES USING MIXTURES OF ORGANIC AND IN-ORGANIC STRUCTURE-DIRECTING AGENTS . . . . .                    | 45  |
| 3.1    | Introduction . . . . .   | 45  |
| 3.2    | Experimental Methods . . . . .   | 49  |
| 3.2.1  | Synthesis of SSZ-13 zeolites . . . . .   | 49  |
| 3.2.2  | Preparation of H-form and partially cation-exchanged zeolites . . . . .  | 50  |
| 3.2.3  | Zeolite Characterization . . . . .   | 52  |
| 3.3    | Results and Discussion . . . . .   | 55  |
| 3.3.1  | Quantification of isolated and paired Al in SSZ-13 zeolites . . . . .  | 55  |
| 3.3.2  | Distribution of Al atoms in SSZ-13 zeolites synthesized using only N,N,N-trimethyl-1-adamantylammonium cations . . . . .   | 58  |
| 3.3.3  | Effect of synthesis gel cationic charge density on the arrangement of Al in SSZ-13 zeolites . . . . .  | 61  |
| 3.3.4  | Proposed role of synthesis gel cationic charge density on framework Al distribution in SSZ-13 zeolites . . . . .   | 63  |
| 3.4    | Conclusions . . . . .  | 64  |
| 3.5    | Acknowledgements . . . . .   | 66  |
| 3.6    | Figures and Tables . . . . .   | 67  |
| 3.7    | Supporting Information . . . . .   | 78  |
| 3.7.1  | Synthesis of SSZ-13(5) Zeolites . . . . .  | 78  |
| 3.7.2  | Synthesis of SSZ-13(15, 1) and SSZ-13(25, 1) Zeolites . . . . .  | 78  |
| 3.7.3  | Synthesis of Pure-silica Chabazite (Si-CHA). . . . .   | 79  |
| 3.7.4  | Synthesis and Characterization of SSZ-13 Zeolites without Na <sup>+</sup> . . . . .  | 80  |
| 3.7.5  | Synthesis of SSZ-13 Zeolites at Constant Na <sup>+</sup> /TMAda <sup>+</sup> and Varied Si/Al Ratio . . . . .  | 80  |
| 3.7.6  | Synthesis of SSZ-13 Zeolites at Si/Al = 15 and 25 at Constant (Na <sup>+</sup> +TMAda <sup>+</sup> )/Al with Varying Na <sup>+</sup> /TMAda <sup>+</sup> Ratio . . . . . | 81  |
| 3.7.7  | Synthesis of SSZ-13 Zeolites at Si/Al = 15 with Varying (Na <sup>+</sup> + TMAda <sup>+</sup> ) / Al and Varying Na <sup>+</sup> /TMAda <sup>+</sup> . . . . .           | 82  |
| 3.7.8  | Powder X-Ray Diffraction Patterns of SSZ-13 Zeolites . . . . .   | 84  |
| 3.7.9  | Ar Adsorption Isotherms of Catalyst Samples . . . . .  | 91  |
| 3.7.10 | Thermogravimetric Analysis (TGA) to Measure the Organic Content of As-Synthesized Zeolites . . . . .   | 95  |
| 3.7.11 | <sup>27</sup> Al Magic Angle Spinning Nuclear Magnetic Resonance ( <sup>27</sup> Al MAS NMR) . . . . .   | 95  |
| 3.7.12 | Copper Cation Speciation in SSZ-13 Zeolites . . . . .  | 98  |
| 3.7.13 | Statistical Estimates of Paired Aluminum in CHA Zeolites . . . . .   | 100 |
| 3.7.14 | Derivation of Cobalt Ion-Exchange Isotherm . . . . .   | 100 |
| 3.7.15 | UV-Vis Spectroscopy of Co-SSZ-13(15, 1) . . . . .  | 104 |
| 3.7.16 | Sodium Cation Exchange Procedure and Derivation of Ion-Exchange Isotherm . . . . .   | 104 |

|   | Page |
|---|------|
| 3.7.17 Characterization Data for SSZ-13(15) with Varying ( $\text{Na}^+$ + $\text{TMAda}^+$ ) / Al (Total Charge) and Constant $\text{Na}^+$ / $\text{TMAda}^+$ Ratios (Charge Density) . . . . . | 106  |
| 3.7.18 Characterization Data for SSZ-13(15) with Varying ( $\text{Na}^+$ + $\text{TMAda}^+$ ) / Al (Total Charge) and Varying $\text{Na}^+$ / $\text{TMAda}^+$ Ratios (Charge Density) . . . . .  | 107  |
| 3.7.19 Characterization Data for SSZ-13(25) with Constant ( $\text{Na}^+$ + $\text{TMAda}^+$ ) / Al (Total Charge) and Varying $\text{Na}^+$ / $\text{TMAda}^+$ Ratios (Charge Density) . . . . . | 109  |
| 4 COOPERATION AND COMPETITION BETWEEN ORGANIC AND IN-ORGANIC STRUCTURE DIRECTING AGENTS INFLUENCES THE ALUMINUM ARRANGEMENT IN CHA ZEOLITES . . . . .   | 111  |
| 4.1 Introduction . . . . .  | 111  |
| 4.2 Results and Discussion . . . . .  | 113  |
| 4.3 Supporting Information . . . . .  | 126  |
| 5 STRUCTURAL AND KINETIC CHANGES TO SMALL-PORE CU-ZEOLITES AFTER HYDROTHERMAL AGING TREATMENTS AND SELECTIVE CATALYTIC REDUCTION OF NOX WITH AMMONIA . . . . .                                    | 139  |
| 5.1 Introduction . . . . .  | 139  |
| 5.2 Experimental Methods . . . . .  | 142  |
| 5.2.1 Catalyst synthesis and treatment . . . . .  | 142  |
| 5.2.2 Catalyst structural characterization . . . . .  | 144  |
| 5.2.3 Brønsted acid site quantification using $\text{NH}_3$ titration methods . . . . .   | 145  |
| 5.2.4 Kinetic measurements of standard SCR turnover rates . . . . .   | 146  |
| 5.3 Results and Discussion . . . . .  | 147  |
| 5.3.1 Structural features of CHA, AEI and RTH topologies . . . . .  | 147  |
| 5.3.2 Synthesis and characterization of H-form and Cu-form zeolites before hydrothermal aging . . . . .   | 148  |
| 5.3.3 Standard SCR kinetics of Cu-zeolites before hydrothermal aging . . . . .  | 149  |
| 5.3.4 Characterization of Cu-form zeolites before and after hydrothermal aging . . . . .  | 151  |
| 5.3.5 Standard SCR kinetics of Cu-form zeolites before and after hydrothermal aging . . . . .   | 153  |
| 5.3.6 Characterization of Cu-form zeolites before and after hydrothermal aging, and after exposure to NOx SCR . . . . .   | 154  |
| 5.4 Conclusions . . . . .   | 155  |
| 5.5 Acknowledgements . . . . .  | 157  |
| 5.6 Figures and Tables . . . . .  | 158  |
| 5.7 Supporting Information . . . . .  | 166  |
| 5.7.1 Powder X-ray diffraction patterns on H- and Cu-zeolites . . . . .   | 166  |
| 5.7.2 Argon adsorption isotherms on H- and Cu-zeolites . . . . .  | 167  |

|  | Page |
|--|------|
| 5.7.3 $^{27}\text{Al}$ MAS NMR spectra on H- and Cu-zeolites . . . . .   | 167  |
| 5.7.4 IR Spectra of H-RTH Before and After $\text{NH}_3$ Exposure . . . . .  | 172  |
| 5.7.5 $\text{NH}_3$ TPD on Cu-zeolites . . . . .   | 172  |
| 6 CATALYSIS IN A CAGE: CONDITION-DEPENDENT SPECIATION AND<br>DYNAMICS OF EXCHANGED CU CATIONS IN SSZ-13 ZEOLITES . . | 177  |
| 6.1 Introduction . . . . .   | 177  |
| 6.2 Results and Discussion . . . . .   | 181  |
| 6.2.1 Cu Cation Speciation in Cu-SSZ-13. . . . .   | 181  |
| 6.2.2 Copper Cation Structure under <i>ex situ</i> Conditions. . . . .   | 188  |
| 6.2.3 Copper Speciation at SCR Conditions. . . . .   | 192  |
| 6.2.4 SCR Mechansim . . . . .  | 198  |
| 6.2.5 SCR Rates on Other Cu-Zeolites. . . . .  | 200  |
| 6.3 Discussion . . . . .   | 201  |
| 6.3.1 Al Distribution and Cu Speciation <i>ex situ</i> . . . . .   | 201  |
| 6.3.2 Cu Speciation <i>in situ</i> . . . . .   | 202  |
| 6.3.3 Mechanistic Implications for SCR. . . . .  | 204  |
| 6.3.4 Implications for Partial Methane Oxidation. . . . .  | 206  |
| 6.4 Conclusions . . . . .  | 206  |
| 6.5 Experimental Methods . . . . .   | 208  |
| 6.5.1 DFT and AIMD Details . . . . .   | 208  |
| 6.5.2 Ab Initio Free Energies . . . . .  | 209  |
| 6.5.3 Zeolite Synthesis and Characterization. . . . .  | 210  |
| 6.5.4 $\text{NH}_3$ Temperature-Programmed Desorption. . . . .   | 211  |
| 6.5.5 Kinetics . . . . .   | 212  |
| 6.5.6 Spectroscopic Methods (XAS, FTIR). . . . .   | 212  |
| 6.6 Acknowledgements . . . . .   | 213  |
| 6.7 Figures and Tables . . . . .   | 215  |
| 6.8 Supporting Information . . . . .   | 232  |
| 6.8.1 HSE06-TSvdw Values for Phase Diagram Species . . . . .   | 232  |
| 6.8.2 $\text{H}_2\text{O}$ Pressure Phase Diagrams . . . . .   | 232  |
| 6.8.3 $\text{Z}_2\text{Cu}$ vs $\text{ZCuOH}$ Exchange Energetics . . . . .  | 235  |
| 6.8.4 XRD Patterns . . . . .   | 236  |
| 6.8.5 Atomic absorption spectroscopy . . . . .   | 237  |
| 6.8.6 FTIR Details . . . . .   | 237  |
| 6.8.7 Si:Al 5 repeat synthesis with H:Al ratios between 0.45-0.85 . .  | 240  |
| 6.8.8 Si:Al=5 Cu:Al=0.02 Data . . . . .  | 241  |
| 6.8.9 XAS Details . . . . .  | 242  |
| 6.8.10 Mobility Calculation Details . . . . .  | 243  |
| 6.8.11 XANES Fitting Details . . . . .   | 244  |
| 6.8.12 $\text{Z}_2\text{Cu}$ Modes . . . . .   | 244  |
| 6.8.13 RDF Calculations . . . . .  | 246  |
| 6.8.14 XANES Reversibility Data . . . . .  | 256  |

|   | Page    |
|---|---------|
| 6.8.15 Four site Adsorbate Binding Energies . . . . .   | 259     |
| 6.8.16 NH <sub>3</sub> phase diagram results at experimental SCR conditions . .   | 259     |
| 6.8.17 Cu diammine diffusion CI-NEB . . . . .   | 259     |
| 6.8.18 <i>operando</i> XAS . . . . .  | 259     |
| 6.8.19 NO+NH <sub>3</sub> NEBS . . . . .  | 261     |
| 6.8.20 Disappearance of Proximal Sites Upon reoxidation . . . . .   | 262     |
| 6.8.21 Mechanism energies . . . . .   | 265     |
| 6.8.22 Kinetic Data for BEA and ZSM-5 . . . . .   | 265     |
| 6.8.23 Z <sub>2</sub> Cu 200 C vs 400 C EXAFS comparison . . . . .  | 265     |
| 6.8.24 200 C XANES, ZCuOH, NO only . . . . .  | 266     |
| 6.8.25 Synthesis details . . . . .  | 266     |
| 6.8.26 Micropore volume . . . . .   | 268     |
| 6.8.27 <sup>27</sup> Al NMR . . . . .   | 270     |
| 6.8.28 NH <sub>3</sub> TPD . . . . .  | 272     |
| <br>7 DYNAMIC MULTINUCLEAR SITES FORMED BY MOBILIZED COP-<br>PER IONS IN NOX SELECTIVE CATALYTIC REDUCTION . . . . .  | <br>275 |
| 7.1 Introduction . . . . .  | 275     |
| 7.2 Turnover rates depend on the spatial density of single Cu sites . . . .   | 276     |
| 7.3 Cu <sup>I</sup> site density requirements differ for oxidation with O <sub>2</sub> and NO <sub>2</sub> .  | 279     |
| 7.4 Solvation by ammonia confers mobility to single Cu ions . . . . .   | 282     |
| 7.5 Outlook . . . . .   | 285     |
| 7.6 Acknowledgements . . . . .  | 286     |
| 7.7 Figures and Tables . . . . .  | 288     |
| 7.8 Supporting Information . . . . .  | 294     |
| 7.8.1 Synthesis Methods and Characterization . . . . .  | 294     |
| 7.8.2 SCR Kinetics . . . . .  | 298     |
| 7.8.3 X-Ray Absorption Spectroscopy . . . . .   | 300     |
| 7.8.4 Kinetic models for the transient oxidation experiments . . . .  | 304     |
| 7.8.5 DFT Methods . . . . .   | 306     |
| 7.8.6 NO titrations to probe reaction stoichiometry . . . . .   | 307     |
| 7.8.7 Random Distribution of Cu per Cage . . . . .  | 309     |
| 7.8.8 Metadynamics . . . . .  | 309     |
| 7.8.9 Electrostatics . . . . .  | 311     |
| 7.8.10 Stochastic Simulation . . . . .  | 312     |
| <br>8 INTRODUCING CATALYTIC DIVERSITY INTO SINGLE-SITE CHABAZITE<br>ZEOLITES OF FIXED COMPOSITION VIA SYNTHETIC CONTROL<br>OF ACTIVE SITE PROXIMITY . . . . . | <br>341 |
| 8.1 Introduction . . . . .  | 341     |
| 8.2 Results and Discussion . . . . .  | 343     |
| 8.2.1 Synthesis of CHA zeolites with different Al arrangements. . . .   | 343     |

|   | Page |
|---|------|
| 8.2.2 Methanol dehydration to dimethyl ether: a Brønsted acid probe reaction. . . . .   | 347  |
| 8.2.3 Methanol dehydration catalysis on CHA zeolites containing only isolated H <sup>+</sup> sites. . . . .                                   | 349  |
| 8.2.4 Methanol dehydration catalysis on H-CHA zeolites containing paired protons. . . . .   | 352  |
| 8.3 Conclusions . . . . .   | 354  |
| 8.4 Experimental Methods . . . . .  | 356  |
| 8.4.1 Synthesis and preparation of MFI and CHA zeolites. . . . .  | 356  |
| 8.4.2 Characterization of CHA and MFI zeolites. . . . .   | 359  |
| 8.4.3 Measurement of methanol dehydration rates and titration of Brønsted acid sites during catalysis. . . . .                                | 360  |
| 8.4.4 Measurement of <i>in situ</i> IR spectra on CHA and MFI zeolites. . . . .   | 362  |
| 8.5 Acknowledgements . . . . .  | 363  |
| 8.6 Figures and Tables . . . . .  | 365  |
| 8.7 Supporting Information . . . . .  | 375  |
| 8.7.1 Synthesis and ion-exchange of CHA and MFI zeolites . . . . .  | 375  |
| 8.7.2 Characterization of CHA and MFI zeolites . . . . .  | 376  |
| 8.7.3 Methanol dehydration catalysis . . . . .  | 407  |
| 8.7.4 IR spectra under steady methanol dehydration . . . . .  | 429  |
| 8.7.5 Evaluation of mass transfer in CHA zeolites . . . . .   | 431  |
| 8.7.6 Origin of kinetic inhibition in CHA zeolites . . . . .  | 445  |
| REFERENCES . . . . .  | 451  |
| A A BRIEF REVIEW OF THE LITERATURE PERTAINING TO THE ROLE OF PAIRED AL SITES IN CHA FOR VARIOUS APPLICATIONS . . . . .                        | 505  |
| A.1 Introduction . . . . .  | 505  |
| A.2 Acid strength [477] . . . . .   | 506  |
| A.3 Characterization of Al arrangement [480] . . . . .  | 506  |
| A.4 CO <sub>2</sub> Adsorption [217, 481] . . . . .   | 507  |
| A.5 MTO [216, 484] . . . . .  | 508  |
| A.6 Hydrothermal Stability and Sulfur Poisoning During NO <sub>x</sub> SCR [239, 489] 509   |      |
| A.7 Partial methane oxidation to methanol [219, 490–493] . . . . .  | 510  |
| B CATALYSIS SCIENCE OF NO <sub>x</sub> SELECTIVE CATALYTIC REDUCTION WITH AMMONIA OVER CU-SSZ-13 AND CU-SAPO-34 . . . . .                     | 511  |
| C EFFECTS OF ACID SITE PROXIMITY AND CONFINEMENT IN ZEOLITES ON PREVALENT REACTION MECHANISMS DURING METHANOL DEHYDRATION CATALYSIS . . . . . | 513  |
| C.1 Inhibition of methanol dehydration rates in CHA zeolites . . . . .  | 513  |
| C.1.1 Estimation of methanol activity coefficients . . . . .  | 515  |
| C.1.2 Inhibition in small-pore zeolites . . . . .   | 521  |



|   | Page |
|---|------|
| C.1.3 Methanol dehydration rates at elevated temperatures . . . . .   | 522  |
| C.1.4 Methanol adsorption isotherms . . . . .   | 524  |
| C.1.5 Inhibition at low temperatures (323 K) . . . . .  | 526  |
| C.1.6 Steady-state isotopic transient kinetic analysis of methanol de-<br>hydration in CHA . . . . .  | 527  |
| C.2 Interpretation of methanol dehydration activation parameters . . . . .  | 531  |
| C.2.1 Comparison of isolated protons in CHA and MFI . . . . .   | 532  |
| C.2.2 Comparison of isolated and paired protons in CHA . . . . .  | 535  |
| C.3 Effect of paired protons in other zeolite frameworks . . . . .  | 538  |
| D SOLID-STATE NMR STRUCTURAL CHARACTERIZATION OF INOR-<br>GANIC AND ORGANIC STRUCTURE DIRECTING AGENTS WITH<br>FRAMEWORK AL ATOMS IN CHABAZITE ZEOLITES . . . . . | 541  |
| D.1 Introduction . . . . .  | 541  |
| D.2 Sample Preparation . . . . .  | 542  |
| D.2.1 Synthesis of CHA with different fractions of paired Al sites . .  | 542  |
| D.2.2 Synthesis of N,N,N-trimethyl-d <sub>9</sub> -1-adamantylammonium hydrox-<br>ide . . . . .   | 542  |
| D.2.3 Synthesis of CHA zeolites with TMAda-d <sub>9</sub> . . . . .   | 543  |
| D.3 Results and Discussion . . . . .  | 544  |
| E TITRATION AND QUANTIFICATION OF OPEN AND CLOSED LEWIS<br>ACID SITES IN TIN-BETA ZEOLITES THAT CATALYZE GLUCOSE<br>ISOMERIZATION . . . . .                       | 559  |
| E.1 Introduction . . . . .  | 559  |
| E.2 Experimental Methods . . . . .  | 563  |
| E.2.1 Catalyst Synthesis . . . . .  | 563  |
| E.2.2 Catalyst Characterization . . . . .   | 565  |
| E.2.3 Temperature Programmed Desorption . . . . .   | 567  |
| E.2.4 Infrared Spectroscopy and Determination of Integrated Molar<br>Extinction Coefficients . . . . .  | 568  |
| E.2.5 Kinetic and Isotopic Tracer Studies of Glucose Reactions with<br>Sn-Beta . . . . .  | 570  |
| E.3 Results and Discussion . . . . .  | 572  |
| E.3.1 Structural Characterization of Stannosilicates . . . . .  | 572  |
| E.3.2 Quantification of Lewis acid sites: IR studies with pyridine .  | 575  |
| E.3.3 Quantification of Lewis acid sites: TPD studies with n-propylamine<br>and ammonia . . . . .   | 576  |
| E.3.4 Quantification of open and closed Lewis acid sites: IR studies<br>with deuterated acetonitrile . . . . .  | 578  |
| E.3.5 Glucose isomerization rate constants on hydrophobic and hy-<br>drophilic Sn-Beta zeolites . . . . .   | 581  |
| E.4 Conclusions . . . . .   | 585  |

|  | Page |
|--|------|
| E.5 Acknowledgements . . . . .   | 586  |
| E.6 Figures and Tables . . . . .   | 588  |
| E.7 Supporting Information . . . . .   | 603  |
| E.7.1 X-ray diffractograms of stannosilicate samples. . . . .  | 603  |
| E.7.2 N <sub>2</sub> and H <sub>2</sub> O adsorption isotherms of zeolite samples. . . . .   | 604  |
| E.7.3 Diffuse-reflectance UV-Visible spectra of zeolite samples. . . . .   | 607  |
| E.7.4 <sup>1</sup> H NMR spectra of sugars after reaction of glucose-D2 with<br>zeolite samples in water. . . . .                    | 614  |
| E.7.5 Determination of integrated molar extinction coefficients for<br>pyridine on H-Y zeolite. . . . .                              | 617  |
| E.7.6 Pyridine titration and infrared spectroscopy of zeolite samples. . . . .   | 619  |
| E.7.7 n-Propylamine temperature programmed desorption (TPD) ex-<br>periments on zeolites. . . . .                                    | 621  |
| E.7.8 Ammonia temperature programmed desorption experiments on<br>zeolite samples. . . . .   | 627  |
| E.7.9 Deuterated acetonitrile titration and infrared spectroscopy of<br>zeolites. . . . .  | 629  |
| E.7.10 Kinetic measurements of glucose isomerization on zeolite samples. . . . .   | 647  |
| F MOLECULAR STRUCTURE AND CONFINING ENVIRONMENT OF<br>TIN SITES IN SINGLE-SITE ZEOLITES . . . . .                                    | 659  |
| F.1 Introduction . . . . .   | 659  |
| F.2 Results and Discussion . . . . .   | 661  |
| F.2.1 Synthesis of Sn-CHA and Bulk Structural Characterization of<br>Stannosilicates . . . . .                                       | 661  |
| F.2.2 Quantifying Lewis acidic Sn sites using d <sub>3</sub> -acetonitrile and pyri-<br>dine titration and IR spectroscopy . . . . . | 663  |
| F.2.3 Catalytic interrogation of the confining environment around Sn<br>sites in Sn-CHA . . . . .                                    | 666  |
| F.2.4 Probing local Sn structure using <sup>119</sup> Sn DNP NMR spectroscopy . . . . .  | 669  |
| F.2.5 DFT calculations of <sup>119</sup> Sn DNP NMR chemical shifts, spans,<br>and CSA parameters . . . . .                          | 672  |
| F.3 Conclusions . . . . .  | 674  |
| F.4 Acknowledgements . . . . .   | 676  |
| F.5 Figures and Tables . . . . .   | 677  |
| F.6 Supporting Information . . . . .   | 687  |
| F.6.1 Statement of author contributions . . . . .  | 687  |
| F.6.2 Experimental and theoretical methods . . . . .   | 687  |
| F.6.3 X-ray diffraction patterns . . . . .   | 698  |
| F.6.4 Adsorption isotherms and pore size distributions . . . . .   | 699  |
| F.6.5 Diffuse reflectance UV-visible spectra and Tauc plots . . . . .  | 702  |
| F.6.6 Thermogravimetric analysis . . . . .   | 705  |
| F.6.7 X-ray absorption spectroscopy . . . . .  | 708  |

|   | Page |
|---|------|
| F.6.8 Supplementary infrared spectra . . . . .  | 712  |
| F.6.9 Ammonia temperature programmed desorption . . . . .   | 714  |
| F.6.10 Intermolecular MPVO reactions . . . . .  | 715  |
| F.6.11 Additional details for $^{119}\text{Sn}$ , and $^{29}\text{Si}$ NMR spectra for Sn-CHA-F722  |      |
| F.6.12 2D $^{119}\text{Sn}$ and 2D $^{15}\text{N}$ CPMAT spectra of pyridine saturated Sn-<br>CHA-F-70 and $^{15}\text{N}$ NMR spectra of pyridine saturated Si-CHA-F.729 |      |
| F.6.13 DFT Calculations . . . . .   | 733  |
| VITA . . . . .  | 735  |

## LIST OF TABLES

| Table  | Page |
|--|------|
| 2.1 Number of $H^+$ sites (per $Al_{tot}$ ) measured from $NH_3$ titration of H-zeolites and Cu-zeolites after oxidative treatments, including data originally reported by Bates et al. [78]. . . . .  | 31   |
| 2.2 Number of $H^+$ sites measured using gaseous $NH_3$ titration of Cu-SSZ-13 after oxidative treatments ( $H^+_{ox}$ ) and reductive treatments in flowing NO and $NH_3$ at 473 K for 2 hours ( $H^+_{red}$ ). Data adapted from Paolucci et al. [85]. | 31   |
| 2.3 Elemental composition, and $N_2$ -derived BET surface areas and micropore volumes for all zeolite samples in this study [78]. . . . .  | 36   |
| 2.4 $^{27}Al$ MAS NMR quantification results for H and $NH_4$ -form of the ZSM-5 ( $Si/Al_{tot} = 17, 30, 43$ , and $89$ ) and SSZ-13 ( $Si/Al_{tot} = 4.5$ ) samples [78]. . . . .  | 39   |
| 2.5 Comparison of the $H^+/Al_{tot}$ ratios for zeolite samples measured by $NH_3$ and n-propylamine (NPA). . . . .  | 40   |
| 2.6 Number of $H^+$ sites measured from the $NH_3$ and $C_3H_6$ desorbed after n-propylamine decomposition on H- and Cu-form zeolites. Data originally reported by Bates et al. [78]. . . . .  | 43   |
| 3.1 Characterization data for all $Na^+$ -free SSZ-13 samples at different Si/Al ratios. . . . .   | 77   |
| 3.2 Characterization data for SSZ-13(15) and MOR samples synthesized with constant synthesis solution Si/Al, constant hydroxide concentration, and varying $Na^+/TMAda^+$ . . . . .  | 77   |
| 3.3 Calculation of the number of $TMAda^+$ per cage for SSZ-13(X,0) and SSZ-13(15,X) with maintaining a constant $(Na^+ + TMAda^+)/Al$ ratio. . . . .  | 95   |
| 3.4 Cu/Al, saturation Co/Al, predicted $M^{2+}/Al$ , and residual $H^+/Al$ on H-SSZ-13(5), H-SSZ-13(15, 1), and H-SSZ-13(25, 1). . . . .   | 98   |
| 3.5 Characterization for SSZ-13 samples synthesized at a constant $Na^+/TMAda^+ = 0.67$ and varying Si/Al. . . . .   | 106  |
| 3.6 Characterization data for SSZ-13(15) and MOR samples synthesized with constant synthesis solution Si/Al and varying total solution charge and $Na^+/TMAda^+$ . . . . .   | 107  |

| Table  | Page |
|--|------|
| 3.7 Characterization data for SSZ-13(15) and MOR samples synthesized with constant synthesis solution Si/Al and varying total solution charge and $\text{Na}^+/\text{TMAda}^+$ . . . . .   | 109  |
| 4.1 Elemental analysis of CHA synthesized with $\text{K}^+/\text{TMAda}^+ = 1\text{-}20$ measured by AAS and EDX. . . . .  | 117  |
| 4.2 Total $\text{K}^+$ and $\text{TMAda}^+$ content per Al, total cationic charge of the crystalline zeolite product ( $(\text{K}^+ + \text{TMAda}^+)/\text{Al}$ ), $\text{H}^+/\text{Al}$ , and estimated number of lattice defects on CHA zeolites synthesized with $\text{K}^+/\text{TMAda}^+ = 1\text{-}20$ . . . . .  | 119  |
| 4.3 Phase analysis of CHA synthesized with $\text{K}^+/\text{TMAda}^+ = 2, 10, \text{ and } 20$ using refinement of powder XRD data. . . . .   | 132  |
| 4.4 $\text{H}^+/\text{Al}$ before Cu-exchange, Cu/Al, $\text{H}^+/\text{Al}$ after Cu-exchange, standard $\text{NH}_3\text{-SCR}$ rates (473 K, per Cu), NO, $\text{O}_2$ , and $\text{NH}_3$ reaction orders, and apparent activation energies on Cu-CHA zeolites synthesized without alkali, or with $\text{Na}^+/\text{TMAda}^+ = 1$ , $\text{K}^+/\text{TMAda}^+ = 2$ , and $\text{K}^+/\text{TMAda}^+ = 15$ . . . . . | 137  |
| 5.1 Structural properties of the 8-MR molecular sieve frameworks in this study (CHA, AEI, RTH). . . . .  | 158  |
| 5.2 Site and structural properties of H-form and Cu-form zeolites prior to hydrothermal aging . . . . .  | 158  |
| 5.3 Site and structural properties of H-form zeolites, and of Cu-exchanged zeolites before and after hydrothermal aging, and before and after exposure to standard SCR gases. Standard SCR rates (473 K), apparent activation energies, and apparent reaction orders for Cu-form zeolites before and after hydrothermal aging treatments. . . . .  | 159  |
| 6.1 $\text{H}_2\text{O}$ Adsorption Energies ( $\Delta E_{\text{ads}}$ ) on Cu Sites Computed Using HSE06-TSvdw <sup>a</sup> . . . . .   | 215  |
| 6.2 Comparison of AIMD (Left) and EXAFS (Right) Characterization of 2Al and 1Al Sites, Including Cu-X (X = O, N) Coordination Number (CN), Average Cu-X Distances, and Whether Second-Shell Features Appear. . .   | 222  |
| 6.3 Characterization of 2Al and 1Al Cu-SSZ-13 Catalysts during Low-Temperature (473 K) Standard SCR: XANES $\text{Cu}^{\text{I}}/\text{Cu}^{\text{II}}$ Fraction, SCR Rates (per Cu and mol NO) in the <i>operando</i> Reactor/Plug-Flow Reactor, Apparent Activation Energies, and Apparent NO, $\text{O}_2$ , and $\text{NH}_3$ Orders. . . . .  | 224  |
| 6.4 HSE06-TSvdw-Computed Sequential $\text{NH}_3$ Adsorption Structures and Energies <sup>a</sup> . . . . .  | 226  |

| Table   | Page |
|---|------|
| 6.5 Calculated total energies ( $\text{kJ mol}^{-1}$ ), ZPE's of adsorbed species, and normalized Bader charges for the 2Al system. . . . .   | 233  |
| 6.6 Calculated total energies ( $\text{kJ mol}^{-1}$ ), ZPE's of adsorbed species, and normalized Bader charges for the 1Al system. . . . .   | 234  |
| 6.7 AAS obtained Si:Al and Cu:Al values on all zeolite samples. . . . .   | 238  |
| 6.8 AAS obtained Si:Al and Co:Al values after Co saturation. . . . .  | 239  |
| 6.9 Summary of Cu-O coordination in para $\text{Z}_2\text{Cu}$ and relative energies for the three modes. . . . .   | 246  |
| 6.10 Binding energies ( $\text{kJ mol}^{-1}$ ) for one of each of the SCR gas species on the four different adsorption site models. . . . .   | 257  |
| 6.11 Full free energies of formation at SCR conditions for all $\text{NH}_3$ 2Al and 1Al phase diagram species. . . . .   | 258  |
| 6.12 Mechanism Energies. . . . .  | 263  |
| 6.13 Rates, apparent orders, and apparent activation energies on BEA and ZSM-5 samples (only the rate was measured on the 3.3 Cu wt% BEA sample). . . . .   | 264  |
| 6.14 Micropore volumes for H-SSZ-13, H-BEA, and H-ZSM-5. . . . .  | 269  |
| 6.15 Fraction of extra-framework Al estimated from $^{27}\text{Al}$ NMR. . . . .  | 271  |
| 7.1 Bulk elemental analysis and fraction of isolated $\text{Cu}^{\text{II}}$ and $\text{Cu}^{\text{II}}(\text{OH})$ sites on a series of Cu-exchanged SSZ-13 samples with varying Si/Al (4.5-25) and Cu/Al (0.03-0.59); arranged by increasing Cu/Al for a fixed Si/Al ratio.332                      |      |
| 7.2 A series of Cu-exchanged SSZ-13 samples with varying Si/Al (4.5-25) and Cu/Al (0.03-0.44) (X = Mean Cu-Cu distance in A, rounded down, labels (a-h) correspond to those in Figure 7.2); arranged by increasing Cu/Al for a fixed Si/Al ratio. . . . .   | 333  |
| 7.3 Standard SCR kinetic parameters measured on a series of Cu-exchanged SSZ-13 samples with Si/Al = 15 and Cu/Al varying from 0.03-0.44; arranged by increasing Cu/Al. (X = Mean Cu-Cu distance in A, rounded down, labels (a, f, and g) correspond to those in Figure 7.2). . . . .                 | 334  |
| 7.4 Operando steady state $\text{Cu}^{\text{I}}$ fraction for a series of Cu-SSZ-13 samples with varying Cu density from 0.07-0.57 atom $(10^3\text{A}^3)^{-1}$ . Feed conditions: 300 ppm NO, 300 ppm $\text{NH}_3$ , 10% $\text{O}_2$ , 5% $\text{CO}_2$ , 2% $\text{H}_2\text{O}$ , 473 K. . . . . | 335  |

| Table  | Page |
|--|------|
| 7.5 Operando steady state $\text{Cu}^I$ fraction for a series of Cu-SSZ-13 samples with varying Cu density from 0.07-0.57 atom $(10^3\text{A}^3)^{-1}$ . Feed conditions: 300 ppm NO, 300 ppm $\text{NH}_3$ , 10% $\text{O}_2$ , 5% $\text{CO}_2$ , 2% $\text{H}_2\text{O}$ , 473 K. . . . .   | 336  |
| 7.6 Fitted $\text{Cu}^I$ fraction before and after oxidation with 10% $\text{O}_2$ at 473 K starting from $\text{Cu}^I(\text{NH}_3)_2$ for Cu-CHA-20, Cu-CHA-15 and Cu-CHA-29. .   | 337  |
| 7.7 Fitted $\text{Cu}^I$ fraction before and after repeated subsequent oxidation with 10% $\text{O}_2$ at 473 K starting from $\text{Cu}^I(\text{NH}_3)_2$ in each cycle for Cu-CHA-29.  | 337  |
| 7.8 Fitted $\text{Cu}^I$ fraction before and after oxidation with 100 ppm $\text{NO}_2$ at 473 K starting from $\text{Cu}^I(\text{NH}_3)_2$ for Cu-CHA-20, Cu-CHA-15 and Cu-CHA-29.  | 338  |
| 7.9 PBE+D2 DFT computed reaction energies (column 2), total energy differences along the reaction coordinate (column 3), and normalized Bader charge [79] derived Cu oxidation states for the product in each step (column 4) for all results reported in Figure 7.4. . . . .  | 338  |
| 7.10 Computed PBE+D2 and HSE06+TSvdw reaction energies for $\text{O}_2$ and $\text{NO}_2$ adsorption on a $\text{Cu}^I(\text{NH}_3)_2$ monomer. Rows 1 and 2 reference the two different (A, B) $\text{O}_2$ adsorption configurations in Figure 7.21. Columns 3 and 5 report the normalized Bader charge [79] derived Cu oxidation state. | 339  |
| 7.11 Metadynamics parameters. . . . .  | 339  |
| 8.1 Characterization Data and Methanol Dehydration Rate Constants for CHA Zeolites Synthesized at Different Compositions and with Different Fractions of Paired Al Sites in $\text{OH}^-$ and $\text{F}^-$ Media. . . . .  | 364  |
| 8.2 Weights (in grams) of synthesis reagents used in the crystallization of CHA zeolites with different Al precursors and equimolar amounts of $\text{Na}^+$ and $\text{TMAda}^+$ in $\text{OH}^-$ media. . . . .  | 375  |
| 8.3 Characterization data of CHA zeolites synthesized using $\text{Al}(\text{OH})_3$ as the aluminum source, without $\text{Na}^+$ in $\text{OH}^-$ and $\text{F}^-$ media. . . . .  | 377  |
| 8.4 Characterization of CHA zeolites synthesized with various Al precursors with equimolar $\text{Na}^+$ and $\text{TMAda}^+$ in $\text{OH}^-$ media. . . . .  | 378  |
| 8.5 Characterization of CHA zeolites synthesized using $\text{Al}(\text{OH})_3$ and equimolar $\text{Na}^+$ and $\text{TMAda}^+$ in $\text{OH}^-$ media. Also included is CHA-OH(16,6%) zeolite, which was synthesized using $\text{TMAda}^+$ and hexyldecyltrimethylammonium bromide (CTAB) in $\text{OH}^-$ media. . . . .               | 378  |
| 8.6 Characterization of commercial MFI zeolites ( $\text{Si}/\text{Al} = 30\text{-}43$ ). . . . .  | 379  |

| Table  | Page |
|--|------|
| 8.7 Crystallite diameters ( $\mu\text{m}$ ) of CHA zeolites with different fractions of paired Al (Table 8.1, main text) estimated from DLS and SEM micrographs. . . . .   | 398  |
| 8.8 Fraction of framework Al atoms ( $\text{Al}_f/\text{Al}_{\text{tot}}$ ) from $^{27}\text{Al}$ NMR and $\text{H}^+/\text{Al}_f$ for each CHA zeolites synthesized without $\text{Na}^+$ in $\text{OH}^-$ and $\text{F}^-$ media. .  | 400  |
| 8.9 Fraction of framework Al atoms ( $\text{Al}_f/\text{Al}_{\text{tot}}$ ) from $^{27}\text{Al}$ NMR and $\text{H}^+/\text{Al}_f$ for each CHA zeolite synthesized with various Al precursors and equimolar amounts of $\text{Na}^+$ and $\text{TMAda}^+$ in $\text{OH}^-$ media. . . . . | 402  |
| 8.10 Fraction of framework Al atoms ( $\text{Al}_f/\text{Al}_{\text{tot}}$ ) from $^{27}\text{Al}$ NMR and $\text{H}^+/\text{Al}_f$ for different CHA zeolites synthesized with equimolar amounts of $\text{Na}^+$ and $\text{TMAda}^+$ in $\text{OH}^-$ media. . . . .                    | 403  |
| 8.11 Titration of residual $\text{H}^+$ sites on CHA-OH(16,24%), CHA-OH(14,0%), CHA-F(17,0%), and CHA-F(18,0%) after $\text{Cu}^{2+}$ ion-exchange. . . . .  | 406  |
| 8.12 Conversions and rates of DME formation (per gram) for various control materials measured at 433 K and 3.5 kPa $\text{CH}_3\text{OH}$ . . . . .  | 414  |
| 8.13 Activation parameters for associative rate first and zero order rate constants (per $\text{H}^+$ ) on H-MFI(43) and an H-MFI ( $\text{Si}/\text{Al} = 30$ ) reported by Jones et al [451]. . . . .  | 420  |
| C.1 Activation enthalpies, entropies, and free energies for first- and zero-order rate constants (415 K) at isolated and paired protons in CHA. . . . .  | 534  |
| D.1 $\text{Si}/\text{Al}$ , $\text{H}^+/\text{Al}$ , $\text{Co}/\text{Al}$ , $\text{Na}^+/\text{Al}$ , and $\text{TMAda}^+/\text{Al}$ data of CHA zeolites synthesized with different fractions of paired Al sites. . . . .  | 542  |
| D.2 Quadrupolar coupling constants ( $C_Q$ ), asymmetry parameters ( $\eta_Q$ ), and isotropic chemical shifts ( $\delta_{\text{iso}}$ ) for the two distinct sites observed on Samples C and D from 3Q $^{27}\text{Al}$ SS MAS NMR spectra (Figure D.6). . . . .                          | 549  |
| E.1 Site and structural characterization data for the samples in this study. .   | 599  |
| E.2 Integrated molar extinction coefficients ( $\mathcal{E}$ ) for infrared peaks for pyridine and deuterated acetonitrile adsorbed to different sites on Sn-Beta and H-Y zeolites, determined assuming equimolar titrant binding to each type of site.                                    | 601  |
| E.3 Fraction of Lewis acidic Sn sites (per mol Sn) on each sample counted with different base titrants. Binding stoichiometries of 1 per site for each titrant.  | 602  |



| Table  | Page |
|--|------|
| E.4 Edge energies for all samples determined from x-intercepts of linear portions of Tauc plots (Figs. E.19 and E.20) DRUV band centers at maximum F(R) intensity are reported for spectra collected after dehydration treatments (Figs. E.17 and E.18), and parenthetical values are for second band observed in some DRUV spectra. . . . . | 609  |
| E.5 Molecules of NPA desorbed per Sn after saturation with 1000 ppm NPA for 4 h at 323 K followed by purging for 4 h and 8 h. . . . .  | 623  |
| E.6 Moles of NPA desorbed per g zeolite after saturation with 1000 ppm NPA for 4 h at 323 K followed by purging for 8 h. . . . .   | 624  |
| E.7 Molecules of NH <sub>3</sub> desorbed (per Sn) after saturation with 500 ppm NH <sub>3</sub> for 5 h at 323 K, followed by purging for 8 h. . . . .  | 628  |
| E.8 Moles of NH <sub>3</sub> desorbed (per g) after saturation with 500 ppm NH <sub>3</sub> for 5 h at 323 K followed by purging for 8 h. . . . .  | 629  |
| E.9 Peak areas at saturation for the 2316 cm <sup>-1</sup> , 2308 cm <sup>-1</sup> , 2287 cm <sup>-1</sup> , 2275 cm <sup>-1</sup> and 2265 cm <sup>-1</sup> peaks for all Sn samples in this study. . . . .   | 646  |
| E.10 Site and structural characterization data for the samples in this study. .  | 657  |
| F.1 Site and structural characterization data for the samples in this study. .   | 682  |
| F.2 Lewis acid site and silanol group concentrations determined using pyridine and acetonitrile IR and ammonia TPD for the samples in this study.. .   | 683  |
| F.3 Intramolecular and intermolecular MPVO reaction rates measured on the samples in this study. . . . .   | 684  |
| F.4 Chemical shift anisotropy (CSA) parameters for the two different Sn sites identified in the hydrated and dehydrated states of Sn-CHA-F-70. . . . .   | 685  |
| F.5 Chemical shift anisotropy (CSA) parameters for the two different Sn sites identified in the hydrated and dehydrated states of Sn-CHA-F-70. . . . .   | 686  |
| F.6 Summary of XAS studies on stannosilicate materials. . . . .  | 711  |
| F.7 Reaction rates over Sn-CHA-F-60, Sn-Beta-F-116, Si-CHA-F, and Sn-xerogel, for the intermolecular MPVO reaction of ethanol and acetone. .   | 718  |
| F.8 Control experiments performed using Sn-CHA-F-60, Sn-Beta, Si-CHA-F, and Sn-xerogel, as well as those performed in empty reactors. . . . .  | 719  |
| F.9 Reaction rates over Sn-CHA-F-60, Sn-Beta-F-116, Si-CHA-F, and Sn-xerogel, for the intermolecular MPVO reaction of ethanol and acetone. .   | 723  |

| Table  | Page |
|--|------|
| F.10 NMR CSA parameters calculated from DFT for hydrated (two water molecules bound to each Sn site, two second shell waters, and implicit water) and dehydrated Sn-CHA. . . . .   | 733  |
| F.11 NMR CSA parameters calculated with DFT for pyridine saturated Sn-CHA-F and Si-CHA-F. . . . .  | 733  |
| F.12 DFT calculated pyridine adsorption free energies (calculated at 298 K) with respect to each site and the corresponding isolated pyridine molecules ( $\Delta G$ , kcal mol <sup>-1</sup> ). The optimized structures were calculated at the lower level of theory described in the computational details section (Section F.6.2). The energies correspond to single-point calculations performed with the M06, and Sn was described by the LanL2DZ effective core pseudopotential (ECP) augmented with a d polarization function; the rest of atoms directly were described by a 6-311+G(d, p) basis set. The thermal correction terms were included and taken from the calculations at the lower level of theory described in the computational details section (Section F.6.2). . . . . | 734  |

## LIST OF FIGURES

| Figure   | Page |
|--|------|
| 1.1 Different arrangements of Al atoms between (a) isolated and (b, c) paired configurations in a 6-MR. . . . .  | 3    |
| 2.1 Isolated $\text{Cu}^{2+}$ ions in SSZ-13 ( $\text{Si}/\text{Al}_{\text{tot}} = 4.5$ ) that balance two framework Al atoms reduce in flowing NO and $\text{NH}_3$ (473 K) to form a proximal $\text{Cu}^+$ and $\text{H}^+$ site pair [85]. . . . .   | 28   |
| 2.2 $\text{NH}_3$ desorption rates during TPD of H-ZSM-5 ( $\text{Si}/\text{Al}_{\text{tot}} = 12.5$ ) after gas-phase $\text{NH}_3$ adsorption at 433 K without purging or washing (light trace), and with purging in flowing wet helium at 433 K (dark trace). . . . .   | 28   |
| 2.3 (a) $\text{NH}_3$ saturation at 433 K leads to adsorption on Brønsted and Lewis acid sites, and physisorption near pore walls, but (b) purging in wet helium at 433 K (8 h) desorbs $\text{NH}_3$ at non-protonic sites and enables quantification of Brønsted acid sites via (c) TPD to 873 K [78]. . . . .   | 29   |
| 2.4 $\text{NH}_3$ desorption rates during TPD of H-ZSM-5 with $\text{Si}/\text{Al}_{\text{tot}}$ of (a) 17, (b) 30, (c) 43, and (d) 89 for gas-phase $\text{NH}_3$ adsorption at 323 K with water wash (light grey trace), gas-phase $\text{NH}_3$ adsorption at 433 K with wet helium purge (black trace), and aqueous $\text{NH}_4\text{NO}_3$ ion exchange (grey trace) [78]. Quantification of the total number of $\text{H}^+$ for each sample can be found in Table 2.1. . . . .                                   | 30   |
| 2.5 Number of $\text{H}^+$ sites titrated by gas phase $\text{NH}_3$ at 433 K followed by purging in He and n-propylamine (NPA) for Cu (open) and H-form (solid) zeolites. The dashed line corresponds to the parity line. Data given Table 2.6 of the Supporting Information. . . . .   | 32   |
| 2.6 Number of residual $\text{H}^+$ sites, relative to the number on the parent H-SSZ-13 ( $\text{H}^+_{\text{parent}}$ ), measured by $\text{NH}_3$ titration on oxidized forms of Cu-SSZ-13 samples of varying total Cu content (per $\text{H}^+_{\text{parent}}$ ). The dashed lines with slopes (m) of -2, -1, and 0 represent Cu exchange stoichiometries of 2, 1, or 0 $\text{H}^+$ sites, respectively. Error bars correspond to 90% confidence intervals [78]. Tabulated data can be found in Table 2.2. . . . . | 33   |
| 2.7 $\text{NH}_3$ desorption rates during TPD of Cu-SSZ-13 ( $\text{Si}/\text{Al}_{\text{tot}} = 4.5$ ) (a) $\text{Cu}/\text{Al}_{\text{tot}} = 0.12$ and (b) $\text{Cu}/\text{Al}_{\text{tot}} = 0.20$ before (dark trace) and after (light trace) reduction in flowing NO and $\text{NH}_3$ at 473 K (Figure 2.1) [85]. . . . .  | 34   |

| Figure   | Page |
|--|------|
| 2.8 The number of extra $H^+$ sites ( $H^+_{red} - H^+_{ox}$ per $Cu_{tot}$ ) formed after reduction of Cu-SSZ-13 ( $Si/Al_{tot} = 4.5$ , $Cu/Al_{tot} = 0.12$ and $0.20$ ) in NO and $NH_3$ at 473 K, as a function of Cu+ content (per $Cu_{tot}$ ). The dashed line represents the parity line, expected if one additional $H^+$ site were formed per Cu+ (Scheme 1). Data adapted from Paolucci et al. [85]. . . . . | 35   |
| 2.9 X-Ray diffraction patterns for (a) H-SSZ-13 ( $Si/Al_{tot} = 4.5$ ) and H-ZSM-5 with $Si/Al_{tot}$ of (b) 12.5, (c) 17, (d) 30, (e) 43, and (f) 89. . . . .  | 37   |
| 2.10 $^{27}Al$ MAS NMR spectra for all H-ZSM-5 (dashed line) and $NH_4$ -ZSM-5 (solid line) samples with $Si/Al_{tot} =$ (a) 17, (b) 30, (c) 43, and (d) 89 [78]. . . . .  | 38   |
| 2.11 $^{27}Al$ MAS NMR spectra for H-SSZ-13 (dashed line) and $NH_4$ -ZSM-5 (solid line) samples with $Si/Al_{tot} = 4.5$ [78]. . . . .  | 39   |
| 2.12 $NH_3$ desorption rates during TPD of (a) H-ZSM-5 ( $Si/Al_{tot} = 43$ ) and (b) H-SSZ-13 ( $Si/Al_{tot} = 4.5$ ) after gas phase saturation with $NH_3$ at 323 K . . . . .   | 41   |
| 2.13 n-Propylamine decomposes only on Brønsted acid sites to form $NH_3$ and $C_3H_6$ [117]. . . . .   | 41   |
| 2.14 Desorption rates of reactive n-propylamine decomposition products $NH_3$ (dark trace) and $C_3H_6$ (light trace) during TPD of H-ZSM-5 ( $Si/Al_{tot} = 17$ ) [78]. . . . .   | 42   |
| 2.15 Integrated area of the hydrated $Cu^{2+}$ d-d transition absorbance band (centered at $12,500\text{ cm}^{-1}$ ) measured by UV-Vis spectroscopy as a function of total Cu content ( $Cu/Al_{tot}$ ). The dashed line represents the best fit for a linear trendline through the origin. . . . .   | 44   |
| 3.1 Different arrangements of Al atoms between (a) isolated and (b, c) paired configurations in a 6-MR. . . . .  | 67   |
| 3.2 Proposed organization of Si and Al atoms in the CHA crystallization medium to form (a) isolated Al in the presence of $TMAda^+$ , or (b) paired Al in the presence of $TMAda^+$ and $Na^+$ . . . . .   | 67   |
| 3.3 (a) $Co^{2+}$ and (b) $Na^+$ ion-exchange isotherms measured on SSZ-13(15,0) (circles) and SSZ-13(15,1) (squares); solid lines represent least-squares regression of data to Langmuirian isotherms. . . . .  | 68   |
| 3.4 The number of residual $H^+$ sites measured by $NH_3$ titration on Co-SSZ-13(15, 1) samples of increasing Co content. The two dashed lines correspond to slopes of -2 and -1, reflecting exchange of only divalent or monovalent species, respectively. . . . .  | 69   |

| Figure  | Page |
|---|------|
| 3.5 Diffuse reflectance UV-Visible absorption spectra of Co-SSZ-13(15,1) samples with increasing $\text{Co}^{2+}$ content ( $\text{Co}/\text{Al} = 0.021, 0.027, 0.041, 0.084, 0.080$ from light to dark); inset shows integrated areas for $\text{Co}^{2+}$ d-d transitions (ca. $19,000 \text{ cm}^{-1}$ ) as a function of Co content. . . . .   | 70   |
| 3.6 $\text{Co}^{2+}$ (squares) and $\text{Cu}^{2+}$ (closed circles) saturation values on SSZ-13(5), SSZ-13(15, 1), and SSZ-13(25, 1) plotted against the maximum $\text{M}^{2+}/\text{Al}$ predicted for a random Al distribution. $\text{Cu}^{2+}$ saturation values (open circles) on SSZ-13 ( $\text{Si}/\text{Al} = 4-45$ ) prepared from equimolar $\text{Na}^+$ and $\text{TMAda}^+$ mixtures reported by Deimund et al [158]. The dashed line represents a parity line. . . . . | 71   |
| 3.7 $^{29}\text{Si}$ MAS NMR (solid traces) and $^1\text{H}$ - $^{29}\text{Si}$ CP MAS NMR (dashed traces) of a) H-SSZ-13(15, 0) and b) H-SSZ-13(15, 1). . . . .  | 72   |
| 3.8 Number of residual $\text{H}^+$ sites on SSZ-13(15, 1) after increasing extents of $\text{Cu}^{2+}$ exchange (circles) and after $\text{Co}^{2+}$ saturation (squares), and on SSZ-13(15, 0) after $\text{Cu}^{2+}$ exchange (diamond). The two dashed lines correspond to slopes of -2 and -1, reflecting exchange of only isolated $\text{Cu}^{2+}$ or $[\text{CuOH}]^+$ , respectively. . . . .  | 73   |
| 3.9 Fraction of Al in paired configurations, measured by $\text{Co}^{2+}$ titration, in SSZ-13 zeolites ( $\text{Si}/\text{Al} = 15$ ) as a function of the $\text{Na}^+/\text{TMAda}^+$ ratio (i.e., cationic charge density) in crystallization media containing fixed total cationic charge. Dashed lines bound a region where a mixed CHA/MOR phase is observed. . . . .  | 74   |
| 3.10 Fraction of Al in paired configurations, measured by titration with $\text{Co}^{2+}$ , in SSZ-13 zeolites ( $\text{Si}/\text{Al} = 15$ ) as a function of the cationic charge density with constant cationic charge (squares) and with cationic charge (open circles). Dashed lines bound a region where a mixed CHA/MOR phase is observed. . . . .  | 75   |
| 3.11 Fraction of Al in paired configurations, measured by $\text{Co}^{2+}$ titration, in SSZ-13 zeolites ( $\text{Si}/\text{Al} = 15$ ) as a function of the solid $\text{Na}^+$ content for samples synthesized from solutions containing $0 < \text{Na}^+/\text{TMAda}^+ < 1$ (solid circles) and $1 < \text{Na}^+/\text{TMAda}^+ < 2$ (open circles). The dashed line corresponds to a slope of two. . . . .   | 76   |
| 3.12 Powder X-ray diffraction patterns for a) SSZ-13(5), b) SSZ-13(15, 1) and, c) SSZ-13(25, 1). . . . .  | 84   |
| 3.13 Powder X-ray diffraction patterns for a) SSZ-13(10, 0), b) SSZ-13(15, 0), c) SSZ-13(20, 0), d) SSZ-13(25, 0), e) SSZ-13(30, 0), f) SSZ-13(60, 0), and g) Si-CHA samples synthesized in the absence of $\text{Na}^+$ at varying $\text{Si}/\text{Al}$ ratios. . . . .   | 85   |

| Figure   | Page |
|--|------|
| 3.14 Powder X-ray diffraction patterns for six independent syntheses of SSZ-13(15, 0). . . . .   | 86   |
| 3.15 Powder X-ray diffraction patterns for a) SSZ-13(5, 0.67), b) SSZ-13(10, 0.67), c) SSZ-13(15, 0.67), d) SSZ-13(25, 0.67), e) SSZ-13(50, 0.67), f) SSZ-13(100, 0.67), and g) SSZ-13(200, 0.67) samples synthesized with constant $\text{Na}^+/\text{TMAda}^+ = 0.67$ and varying Si/Al ratios. . . . .  | 87   |
| 3.16 Powder X-ray diffraction patterns for a) SSZ-13(15, 0), b) SSZ-13(15, 0.25), c) SSZ-13(15, 0.50), d) SSZ-13(15, 0.67), e) SSZ-13(15, 1.00), f) SSZ-13(15, 1.50), g) SSZ-13(15, 2.00), h) MOR(15, 2.50), and i) MOR(15, 3.00) samples synthesized with constant solution $\text{Si}/\text{Al} = 15$ , $(\text{Na}^+ + \text{TMAda}^+)/\text{Al}$ (total charge), and varying $\text{Na}^+/\text{TMAda}^+$ ratios (charge density). . . . . | 88   |
| 3.17 Powder X-ray diffraction patterns for a) SSZ-13(25, 0), b) SSZ-13(25, 0.50), c) SSZ-13(25, 0.67), d) SSZ-13(25, 1.00), and e) SSZ-13(25, 2.00) samples synthesized with constant solution $\text{Si}/\text{Al} = 25$ and $(\text{Na}^+ + \text{TMAda}^+)/\text{Al}$ (total charge), and varying $\text{Na}^+/\text{TMAda}^+$ ratios (charge density). . . . .   | 89   |
| 3.18 Powder X-ray diffraction patterns for a) SSZ-13(15, 0), b) SSZ-13(15, 0.35), c) SSZ-13(15, 0.70), d) SSZ-13(15, 0.93), e) SSZ-13(15, 1.38), f) SSZ-13(15, 2.09), g) MOR(15, 3.45), h) MOR(15, 4.16, and i) MOR(15, 5.55) samples synthesized with constant solution $\text{Si}/\text{Al} = 15$ and varying $(\text{Na}^+ + \text{TMAda}^+)/\text{Al}$ (total charge) and $\text{Na}^+/\text{TMAda}^+$ ratios (charge density). . . . .    | 90   |
| 3.19 Ar adsorption isotherms at measured at 87 K on a) SSZ-13(5), b) SSZ-13(15, 1), and c) SSZ-13(25, 1). . . . .  | 91   |
| 3.20 Ar adsorption isotherms at measured at 87 K on a) SSZ-13(15, 0), b) SSZ-13(20, 0), c) SSZ-13(25, 0), d) SSZ-13(30, 0), and e) Si-CHA. . . . .   | 92   |
| 3.21 Ar adsorption isotherms at measured at 87 K on a) H-SSZ-13(15, 0), b) H-SSZ-13(15, 0.25), c) H-SSZ-13(15, 0.50), d) H-SSZ-13(15, 0.67), e) H-SSZ-13(15, 1.00), f) H-SSZ-13(15, 1.50), and g) H-SSZ-13(15, 2.00). . . . .  | 93   |
| 3.22 Ar adsorption isotherms at measured at 87 K on a) H-SSZ-13(25, 0), b) H-SSZ-13(25, 0.25), c) H-SSZ-13(25, 0.50), d) H-SSZ-13(25, 1.00), and e) H-SSZ-13(25, 2.00). . . . .  | 94   |
| 3.23 $^{27}\text{Al}$ MAS NMR spectra for a) H-SSZ-13(15, 0), b) H-SSZ-13(20, 0), c) H-SSZ-13(25, 0), and d) H-SSZ-13(30, 0). . . . .  | 96   |
| 3.24 $^{27}\text{Al}$ MAS NMR spectra for a) H-SSZ-13(15, 0), b) H-SSZ-13(15, 0.25), c) H-SSZ-13(15, 0.50), d) H-SSZ-13(15, 0.67), e) H-SSZ-13(15, 1.00), f) H-SSZ-13(15, 1.50), and g) H-SSZ-13(15, 2.00). . . . .  | 97   |

| Figure  | Page |
|---|------|
| 3.25 Number of residual $H^+$ sites, normalized to the parent $H^+/Al$ for each sample, after $Cu^{2+}$ exchange (circles) as a function of the $Cu/Al$ ratio, after $Co^{2+}$ saturation (squares) on H-SSZ-13(5) (black), H-SSZ-13(15, 1) (dark grey), and H-SSZ-13(25, 1) (grey). Dashed lines indicate predictions from statistical calculations of random Al distributions and the sequential exchange of $Cu^{2+}$ at paired Al sites (2 Al in 6-MR) followed by exchange of $[CuOH]^+$ at isolated Al sites. . . . . | 99   |
| 3.26 Statistical calculations for the random distribution of Al in CHA at varying Si/Al ratios, obeying Lowenstein's Rule [37]. The circles denote SSZ-13 materials synthesized at Si/Al = 5, 15, and 25 and correspond to theoretical $M^{2+}/Al = 0.22, 0.09$ , and $0.05$ , respectively. . . . .  | 100  |
| 3.27 Ambient UV-Vis spectra of Co-SSZ-13(15, 1) with Co/Al values of 0.021 (faint grey trace), 0.022 (light grey trace), 0.047 (grey trace), 0.08 (dark grey trace), and 0.084 (black trace). . . . .   | 104  |
| 3.28 Si/Al ratio as a function of $Na^+/TMAda^+$ ratio for SSZ-13(15) samples synthesized with (squares) and without (circles) a constant $(Na^+ + TMAda^+) / Al$ ratio. The dashed line is a linear fit to the samples synthesized without constant $(Na^+ + TMAda^+) / Al$ (circles). . . . .   | 108  |
| 3.29 Fraction of paired Al atoms measured by titration with $Co^{2+}$ as a function of the synthesis solution charge density on SSZ-13(25) synthesized with constant total solution charge. . . . .   | 110  |
| 4.1 Fraction of Al in pairs, measured by $Co^{2+}$ exchange, as a function of the number of Al in pairs predicted for a random Al distribution subject Lowenstein's Rule. Samples are synthesized with $Al(OH)_3$ and $Na^+/TMAda^+ = 0-2$ in $OH^-$ media (orange) and $Na^+/TMAda^+ = 0$ in $F^-$ media (blue) or with $Al(O-i-Pr)_3$ with $Na^+/TMAda^+ = 1$ (green squares) and $Na^+/TMAda^+ = 0$ (green circle). . . . .  | 114  |
| 4.2 X-ray diffraction patterns (left) and SEM micrographs (right) taken at 1300x magnification of CHA synthesized with $K^+/TMAda^+$ ratios of (a) 1, (b) 2, (c) 3, (d) 4, (e) 5, (f) 10, (g) 15, and (h) 20. Scale bar in SEM images in $50 \mu m$ . . . . .   | 116  |

| Figure  | Page |
|---|------|
| 4.3 (a) Number of TMAda <sup>+</sup> per CHA cage (squares), measured by TGA, and amount of Na <sup>+</sup> retained per CHA cage (circles), measured by AAS, as a function of the Na <sup>+</sup> /TMAda <sup>+</sup> ratio in the synthesis media. (b) Number of TMAda <sup>+</sup> per CHA cage (squares and amount of K <sup>+</sup> retained per CHA cage (circles) as a function of the K <sup>+</sup> /TMAda <sup>+</sup> ratio in the synthesis media. (c) Number of TMAda <sup>+</sup> per CHA cage as a function of the amount of K <sup>+</sup> (squares) or Na <sup>+</sup> (circles) retained on the crystalline CHA product. Dashed (slope ca. 1/3) and dotted (slope ca. 0) lines are regressions to K <sup>+</sup> (squares) and Na <sup>+</sup> (circles) data sets, respectively. . . . . | 118  |
| 4.4 (a) Snapshot of a single TMAda <sup>+</sup> molecule (brown: C, blue: N, white: H) within the CHA cage. The numbers 1-6 correspond to the 6 unique Al sites, relative to the N atom of TMAda <sup>+</sup> , and the corresponding colors (1: green, 2: grey, 3: orange, 4: light blue, 5: purple, 6: red) represent equivalent sites. (b) DFT energies, relative to Al position 1, of TMAda <sup>+</sup> confined with the CHA cage for the six different single Al sites in the 1x1x1 (black) and 1x1x2 (red) supercells. Inset snapshots show the relaxed structures for each Al position. . . . .  | 121  |
| 4.5 DFT energies as a function of the Al-Al distance when two TMAda <sup>+</sup> molecules are located in adjacent cages in CHA. Three unique TMAda-TMAda orientations were investigated at each Al-Al distance (Supp. Info.).  | 122  |
| 4.6 (a) Snapshot of the most stable configuration of Na <sup>+</sup> (black) in the presence of a TMAda <sup>+</sup> molecule in an adjacent cage with 2 framework Al atoms (green). Yellow: Si, green: Al, red: O, dark grey: C, blue: N, white: H, black: Na. (b) DFT energies as a function of the Al-Al distance when one Na <sup>+</sup> and one TMAda <sup>+</sup> molecule are located in adjacent cages in CHA. . . . .   | 124  |
| 4.7 X-Ray diffraction patterns of CHA synthesized using Al(O-i-Pr) <sub>3</sub> at Si/Al = 15 and (a) Na <sup>+</sup> /TMAda <sup>+</sup> = 0 and (b)-(d) Na <sup>+</sup> /TMAda <sup>+</sup> = 1. . . . .  | 126  |
| 4.8 X-Ray diffraction patterns of zeolites synthesized with K <sup>+</sup> /TMAda <sup>+</sup> of (a) 30, (b) 50, (c) 100, and (d) ∞. A commercial MFI zeolite (Si/Al = 43) is shown in (e). . . . .  | 127  |
| 4.9 SEM micrographs of CHA synthesized with K <sup>+</sup> /TMAda <sup>+</sup> = 1 taken at (a) 1300x and (b) 5000x magnification. . . . .  | 128  |
| 4.10 SEM micrographs of CHA synthesized with K <sup>+</sup> /TMAda <sup>+</sup> = 2 taken at (a) 1250x and (b) 4800x magnification. . . . .   | 128  |
| 4.11 SEM micrographs of CHA synthesized with K <sup>+</sup> /TMAda <sup>+</sup> = 3 taken at (a) 1250x and (b) 5000x magnification. . . . .   | 129  |



| Figure  | Page |
|---|------|
| 4.12 SEM micrographs of CHA synthesized with $K^+/TMAda^+ = 4$ taken at (a) 1250x and (b) 5000x magnification. . . . .  | 129  |
| 4.13 SEM micrographs of CHA synthesized with $K^+/TMAda^+ = 5$ taken at (a) 1250x and (b) 5000x magnification. . . . .  | 130  |
| 4.14 SEM micrographs of CHA synthesized with $K^+/TMAda^+ = 10$ taken at (a) 1400x and (b) 5900x magnification. . . . .   | 130  |
| 4.15 SEM micrographs of CHA synthesized with $K^+/TMAda^+ = 15$ taken at (a) 1300x and (b) 5100x magnification. . . . .   | 131  |
| 4.16 SEM micrographs of CHA synthesized with $K^+/TMAda^+ = 20$ taken at (a) 1700x and (b) 4900x magnification. . . . .   | 131  |
| 4.17 EDX elemental analysis of the two distinct high-silica (1) and low-silica (2) phases observed for CHA synthesized with $K^+/TMAda^+ = 20$ . . . . .  | 132  |
| 4.18 Ar adsorption (closed circles) and desorption (open circles) isotherms (87 K) on CHA synthesized with $K^+/TMAda^+ = 2$ . . . . .  | 133  |
| 4.19 Ar adsorption (closed circles) and desorption (open circles) isotherms (87 K) on CHA synthesized with $K^+/TMAda^+ = 15$ . . . . .   | 134  |
| 4.20 Charge distribution and partial charges of a TMAda molecule confined within the CHA unit cell after substitution of a single framework Al atom. . . . .  | 135  |
| 4.21 TMAda occluded within a 1x1x1 36 T-atom supercell (left) and 1x1x2 72 T-atom supercell (right) containing 1 Al atom per unit cell. Brown: Si, light grey: Al, red: O, dark grey: C, blue: N, white: H. . . . .                       | 135  |
| 4.22 DFT energies, relative to Al position 1, of TMAda confined with the CHA cage for the six different single Al sites in the 1x1x2 supercell using the PBE (black) and PBE-D3 (red) functional. . . . .                                 | 136  |
| 4.23 Descriptor model regressed to DFT calculated energies using three descriptors for 1) the Al-Al distance, 2) the distances between N-Al centers, and 3) the N-N distance. . . . .   | 136  |
| 5.1 $^{27}Al$ MAS NMR spectra of hydrated fresh (solid) and aged (dashed) Cu-form of RTH, CHA and AEI zeolites. . . . .   | 160  |
| 5.2 $NH_3$ desorption rates as a function of temperature on H-form (solid) and fresh Cu-form (dashed) on AEI, CHA, and RTH zeolites. . . . .  | 161  |
| 5.3 UV-vis spectra on hydrated fresh Cu-form before SCR (solid), aged Cu-form before SCR (dashed), and aged after SCR (dotted) on RTH, CHA and AEI zeolites. Spectra are offset for clarity (CHA: by 0.4 a.u., RTH: by 0.8 a.u.). . . . . | 162  |

| Figure  | Page |
|---|------|
| 5.4 Dependence of standard SCR turnover rates (per Cu) on temperature for fresh (circles) and aged (squares) Cu-form AEI (hollow), CHA (cross hatched), and RTH (filled circles) zeolites. . . . .  | 163  |
| 5.5 Powder XRD patterns of fresh Cu-form before SCR (dark), aged Cu-form before SCR (medium), and aged Cu-form after SCR (light) on AEI, CHA, and RTH zeolites. Diffraction patterns are normalized so that the maximum peak intensity in each pattern is unity, and offset for clarity. . . . .  | 164  |
| 5.6 Ar adsorption isotherms (87 K) on fresh Cu-form before SCR (circles), aged Cu-form before SCR (triangles), aged Cu-form after SCR (squares) on AEI, CHA, and RTH zeolites. Isotherms are vertically offset for clarity (CHA: $160 \text{ cm}^3 \text{ g}^{-1}$ , RTH: by $320 \text{ cm}^3 \text{ g}^{-1}$ ). . . . .                         | 165  |
| 5.7 XRD patterns of H-form (dark) and Cu-form (light) AEI, CHA, and RTH zeolites. Diffraction patterns are normalized so that the maximum peak intensity in each pattern is unity. . . . .  | 166  |
| 5.8 Ar adsorption isotherms (87 K) on H-form (filled) and Cu-form (open) RTH, CHA, and AEI zeolites. Adsorption isotherms are vertically offset (CHA: $160 \text{ cm}^3 \text{ g}^{-1}$ , RTH: $320 \text{ cm}^3 \text{ g}^{-1}$ ) for clarity. . . . .   | 167  |
| 5.9 $^{27}\text{Al}$ MAS NMR spectra of H-AEI and Cu-AEI. . . . .   | 169  |
| 5.10 $^{27}\text{Al}$ MAS NMR spectra of H-CHA and Cu-CHA. . . . .  | 170  |
| 5.11 $^{27}\text{Al}$ MAS NMR spectra of H-RTH and Cu-RTH. . . . .  | 171  |
| 5.12 $\text{NH}_3$ desorption rates as a function of temperature on fresh Cu-form after SCR (solid), aged Cu-form before SCR (dashed) and aged Cu-form after SCR (dotted) on CHA, RTH, and AEI zeolites. . . . .  | 172  |
| 5.13 IR spectra (OH stretching region: $3400\text{-}3900 \text{ cm}^{-1}$ ) of H-RTH at 433 K before (dark) and after (light) $\text{NH}_3$ saturation. . . . .   | 174  |
| 5.14 IR spectra (OH stretching region: $1300\text{-}2500 \text{ cm}^{-1}$ ) of H-RTH at 433 K before (dark) and after (light) $\text{NH}_3$ saturation. . . . .   | 175  |
| 6.1 (left) Side view of the chabazite cage. (right) HSE06-optimized structures of (A,B) dehydrated oxidized and reduced Cu sites and (C) hydrated oxidized sites. Label indicates location of Cu ion within the chabazite cage. . . . .   | 215  |
| 6.2 Formation free energies ( $\Delta G_{\text{form}}$ ) $\text{CuH}_x\text{O}_y$ species at (left) 298 K, 2% $\text{H}_2\text{O}$ , 20% $\text{O}_2$ , and at (right) 673 K, 2% $\text{H}_2\text{O}$ , 20% $\text{O}_2$ on the 2Al ( $\text{Z}_2\text{Cu}$ ) and 1Al ( $\text{ZCu}$ ) sites. Common energy reference set through eq 6.6. . . . . | 216  |

| Figure   | Page |
|--|------|
| 6.3 <i>ex situ</i> Cu speciation phase diagrams based on HSE06-TSvdw calculations on 1Al (left) and 2Al (right) Cu exchange sites. Regions indicate site composition that minimizes free energy at 2% H <sub>2</sub> O and given T and PO <sub>2</sub> . Labeled on the phase diagram and illustrated below are minimum free energy species at (1) ambient (298 K, 20% O <sub>2</sub> ), (2) oxidizing (673 K, 20% O <sub>2</sub> ), and (3) inert (673 K, 10 <sup>-6</sup> atm O <sub>2</sub> in He). . . . .   | 217  |
| 6.4 Predicted Cu site compositional phase diagram versus Si:Al and Cu:Al ratios. Color scale indicates predicted fraction of CuOH. White line demarcates transition from [Z <sub>2</sub> Cu]-only region to mixed [Z <sub>2</sub> Cu]/[ZCuOH] region. White circles indicated compositions of synthesized Cu-SSZ-13 samples. . . . .   | 218  |
| 6.5 Residual H <sup>+</sup> sites per parent sample H <sup>+</sup> from NH <sub>3</sub> titrations on oxidized M-SSZ-13 samples versus extent of M/Al exchange for Si:Al = 5 (blue), 15 (green), and 25 (orange). Open and filled symbols denote Cu <sup>2+</sup> and saturated Co <sup>2+</sup> exchange, respectively. Dashed lines are model predictions.   | 219  |
| 6.6 FTIR spectra of oxidized Cu-SSZ-13 samples (Cu:Al = 0-0.44, Si:Al = 15). Inset: Integrated 3660 cm <sup>-1</sup> CuO-H area as a function of Cu:Al ratio.  | 220  |
| 6.7 Left: XANES spectra collected on the 1Al (teal dashes) and 2Al (black lines) Cu-SSZ-13 samples under treatment in 2% H <sub>2</sub> O, 20% O <sub>2</sub> at 298 K. Middle: EXAFS spectra under the same conditions. Right: 298 K AIMD RDFs and integrated RDFs (inset). . . . .   | 220  |
| 6.8 Cu positions (gray balls) visited during 90 ps of NVT AIMD at 298 K. Fixed zeolite framework shown for ease of visualization; framework was unconstrained during dynamics. Inset illustrates discretization used to compute relative Cu mobilities. . . . .  | 221  |
| 6.9 Left: XANES spectra collected on the 1Al (top) and 2Al (bottom) samples after treatment in 20% O <sub>2</sub> at 673 K (solid blue lines), He at 673 K (dashed teal lines), and in 3% H <sub>2</sub> at 523 K (dot-dash red lines). Middle: Corresponding EXAFS spectra. Right: AIMD Cu-Si/O/Al RDFs for ZCuOH and ZCu (top) and Z <sub>2</sub> Cu (bottom). Insets show integrated RDFs. . . . .  | 223  |
| 6.10 Left: XANES spectra of the 1 Al (top) and 2Al (bottom) Cu-SSZ-13 samples under treatment in 2% H <sub>2</sub> O, 10% O <sub>2</sub> , 300 ppm of NH <sub>3</sub> at 473 K (O <sub>2</sub> + NH <sub>3</sub> , blue traces), 2% H <sub>2</sub> O and 300 ppm of NO/NH <sub>3</sub> at 473 K (NO + NH <sub>3</sub> , red lines), and in 2% H <sub>2</sub> O, 10% O <sub>2</sub> , 300 ppm of NO/NH <sub>3</sub> at 473 K (black traces). Middle: EXAFS collected under same conditions. Right: AIMD Cu-Si/O/Al RDFs for the most stable Cu <sup>I</sup> (red lines) and Cu <sup>II</sup> (blue traces) species on the 1 and 2Al sites in the presence of NH <sub>3</sub> . Insets: Integrated RDFs. . . . . | 224  |

| Figure  | Page |
|---|------|
| 6.11 Parity plot of HSE06-TSvdw-computed binding energies of gaseous species relevant to SCR on 2Al oxidized ( $Z_2Cu$ , blue) and reduced ( $ZNH_4/ZCu$ , red) versus corresponding oxidized ( $ZCuOH$ , blue) and reduced ( $ZCu$ , red) 1Al sites. . . . .   | 225  |
| 6.12 Phase diagrams for 1Al (left) and 2Al (right) sites with varying T and $P_{O_2}$ at 300 ppm of $NH_3$ and 2% $H_2O$ . Relative rankings for all species $\Delta G_{form} < 0$ at 473 K and 10% $O_2$ (chrome spheres on the phase diagrams) are given to the right of each phase diagram. The structures shown on the bottom are the most stable $Cu^I$ (red) and $Cu^{II}$ (golden) under these conditions. . . . . | 227  |
| 6.13 Cu positions (gray balls) sampled inside the zeolite cage during 90 ps of equilibrated NVT AIMD at 473 K for the most stable $NH_3$ solvated $Cu^I$ and $Cu^{II}$ species. . . . .   | 228  |
| 6.14 HSE06 CI-NEB calculated activation ( $E_a$ ) and reaction energies for NO-assisted reduction of $NH_3$ solvated $Cu^{II}$ 1Al (black) and 2Al (green) sites. Transition state structures are shown boxed. For ease of visualization, most of the zeolite framework is hidden. . . . .  | 229  |
| 6.15 Number of extra $H^+$ sites (per Al) formed after reduction of $Cu^{II}$ to $Cu^I$ in flowing NO and $NH_3$ (473 K) as measured by $NH_3$ titration and TPD. Dashed lines represent the predicted number of $H^+$ formed on the basis of the assumption that reduction of only $Cu^{II}$ at 2Al sites forms a $Cu^I/H^+$ site pair. . . . .  | 230  |
| 6.16 (Left) Proposed parallel standard SCR cycles for $NH_3$ -solvated Cu ions near 1Al (black) or 2Al (green). (Right) HSE06-TSvdw computed reaction energies along each step of the proposed cycles. 1-5 correspond to the intermediates in the left panel. Listed are the molecules consumed (+) and generated (-) between each intermediate. . . . .  | 231  |
| 6.17 Standard SCR rates per g catalyst at 473 K on Cu-exchanged SSZ-13, ZSM-5, and BEA versus Cu weight percent. . . . .  | 231  |
| 6.18 $H_2O$ partial pressure phase diagrams at fixed $O_2$ pressures. . . . .   | 232  |
| 6.19 $Z_2CuH_2O$ vs. $ZH/ZCuOH$ energetics in a single supercell. . . . .   | 235  |
| 6.20 $Z_2CuH_2O$ vs. $ZH/ZCuOH$ energetics in a 2x1x1 supercell. . . . .  | 235  |
| 6.21 $Z_2CuH_2O/ZCuOH$ vs. $ZH/ZCuOHx2$ energetics in a 2x1x1 supercell. . .  | 236  |
| 6.22 XRD spectra on the H-form of the Si:Al 5, 15, and 25 samples. . . . .  | 236  |
| 6.23 XRD spectra on the H-form of BEA and ZSM-5 samples. . . . .  | 237  |

| Figure   | Page |
|--|------|
| 6.24 (left) XRD spectra for Si:Al 5 samples with H:Al ranging from 0.85(A) to 0.65(B) to 0.45(C) (right) NH <sub>3</sub> TPDs following a purge of physisorbed NH <sub>3</sub> to determine the number of H:Al. . . . .  | 240  |
| 6.25 Residual H <sup>+</sup> sites per parent sample H <sup>+</sup> from NH <sub>3</sub> titrations on oxidized M-SSZ-13 samples vs. extent of M/Al exchange for Si:Al = 5 at a pH=5 (black shapes) and no pH control (green shapes). Open and filled symbols denote Cu <sup>2+</sup> and saturated Co <sup>2+</sup> exchange, respectively. Dashed lines are model predictions. . . . . | 241  |
| 6.26 Ring structures surrounding the 6MR, shown in perspective view for clarity. 4MR and 8MR alternates around the 6MR. . . . .  | 245  |
| 6.27 Pictures of Z <sub>2</sub> Cu modes. . . . .  | 246  |
| 6.28 RDF of Cu-x (x=Si,Al,O) in [Z <sub>2</sub> Cu <sup>II</sup> ]. . . . .  | 247  |
| 6.29 RDF of Cu-x (x=Si,Al,O) in [ZCu <sup>I</sup> ]. . . . .   | 248  |
| 6.30 RDF of Cu-x (x=Si,Al,O) in [ZCu <sup>II</sup> OH]. . . . .  | 249  |
| 6.31 RDF of Cu-x (x=Si,Al,O) in Z <sub>2</sub> [Cu <sup>II</sup> (H <sub>2</sub> O) <sub>4</sub> ](H <sub>2</sub> O) <sub>2</sub> . . . . .  | 250  |
| 6.32 RDF of Cu-x (x=Si,Al,O) in Z <sub>2</sub> [Cu <sup>II</sup> (H <sub>2</sub> O) <sub>3</sub> ](H <sub>2</sub> O) <sub>3</sub> . . . . .  | 251  |
| 6.33 RDF of Cu-x (x=Si,Al,O,N) in Z[Cu <sup>I</sup> (NH <sub>3</sub> ) <sub>2</sub> ]. . . . .   | 252  |
| 6.34 RDF of Cu-x (x=Si,Al,O,N) in Z[Cu <sup>I</sup> (NH <sub>3</sub> ) <sub>2</sub> ]/[ZNH <sub>4</sub> ]. . . . .   | 253  |
| 6.35 RDF of Cu-x (x=Si,Al,O,N) in Z <sub>2</sub> [Cu <sup>II</sup> (NH <sub>3</sub> ) <sub>4</sub> ]. . . . .  | 254  |
| 6.36 RDF of Cu-x (x=Si,Al,O,N) in Z[Cu <sup>II</sup> (OH)(NH <sub>3</sub> ) <sub>3</sub> ]. . . . .  | 255  |
| 6.37 XANES spectra collected after exposing Si:Al 4.5 Cu:Al 0.08 (2Al) and Si:Al 15 Cu:Al 0.44 (1Al) to O <sub>2</sub> balance He at 673 K following pretreatment in He at 673 K. . . . .  | 256  |
| 6.38 CI-NEB for Cu diammine to transverse the 8MR. . . . .   | 259  |
| 6.39 EXAFS spectrum collected at 473 K, 2% H <sub>2</sub> O, 300 ppm NH <sub>3</sub> , 10% O <sub>2</sub> , 300 ppm NO, on a Cu:Al = 0.41, Si:Al = 25 sample. Rate per gram catalyst is 81x10 <sup>-8</sup> . . . . .  | 260  |
| 6.40 XANES spectra collected after exposing Si:Al = 4.5, Cu:Al = 0.08 (2Al) and Si:Al = 15, Cu:Al = 0.44 (1Al) to O <sub>2</sub> balance He at 673 K following pretreatment in He at 673 K. . . . .  | 261  |
| 6.41 Titration of residual Brønsted sites on a Si:Al=5 Cu:Al=0.21 SSZ-13 sample, before reduction in NO+NH <sub>3</sub> , after reduction, and after reduction followed by oxidation. . . . .  | 262  |

| Figure  | Page |
|---|------|
| 6.42 EXAFS spectra collected after exposing Si:Al 4.5 Cu:Al 0.08 (2Al) to either NO+NH <sub>3</sub> (red) or O <sub>2</sub> +NH <sub>3</sub> (orange), at (left) 200 C, and (right) 400 C.  | 265  |
| 6.43 XANES spectra collected after exposing Si:Al 15 Cu:Al 0.44 to 300 ppm NO and balance He at 200 C until steady-state. . . . .   | 266  |
| 6.44 Micropore Ar adsorption isotherms on H-SSZ-13 5, 15, and 25 samples. .   | 269  |
| 6.45 Micropore N <sub>2</sub> adsorption isotherms on H-BEA and H-ZSM-5. . . . .  | 270  |
| 6.46 <sup>27</sup> Al NMR spectra for SSZ-13 at Si:Al 5, 15, 25. . . . .  | 272  |
| 7.1 <b>Cu-density dependence of SCR rates.</b> (A) The CHA cage [1] and schematic representation of the Cu ion densities per CHA cage in samples a and g. (B) Standard NO <sub>x</sub> SCR rates (per volume catalyst; 473 K; measured in a differential reactor by using a gas mixture representative of practical low-temperature application, including 2.5% H <sub>2</sub> O; details in Supp. Info. section 7.8.2) and apparent O <sub>2</sub> orders measured on Cu-CHA-X samples (Si/Al = 15, table 7.3) of increasing Cu ion density. Colored line is a visual guide; regression fits to the quadratic ( $R^2 = 0.99$ ) and linear ( $R^2 = 0.99$ ) kinetic regimes are detailed in Supp. Info. section 7.8.2. . . . .  | 288  |
| 7.2 <b>Cu-density dependence of <i>operando</i> Cu oxidation state.</b> The dependence of Cu <sup>I</sup> fraction on Cu ion volumetric density during steady-state standard SCR at 473 K was measured by XANES (details in Supp. Info. section 7.8.3). Data points include samples a, f, and g shown in Fig. 7.1 (Si/Al = 15, filled squares), samples at Si/Al = 4.5 and Si/Al = 25 (open squares), and comparable literature data [open circle Ref [360], Si/Al = 16; open triangle Ref [41], Si/Al = 4.5]. Inset shows NH <sub>3</sub> -solvated, isolated Cu <sup>I</sup> and Cu <sup>II</sup> species previously observed and computed [79] to be present during standard SCR at 473 K. Gray, Cu; green, Al; yellow, Si; red, O; blue, N; and white, H. The colored arrow is a visual guide; error bars represent the absolute 5% uncertainty from linear combination XANES fitting (details in Supp. Info. section 7.8.3). . . . . | 289  |

- 7.3 Kinetics of Cu<sup>I</sup> oxidation by O<sub>2</sub>.** (A) Temporal evolution of the XANES-measured Cu<sup>I</sup> fraction is plotted for the Cu-CHA-29 (a, red), Cu-CHA-20 (c, blue), and Cu-CHA-15 (h, black) samples during transient oxidation in 10% O<sub>2</sub> at 473 K. Least-squares fit to Eq. 7.2 is shown by solid lines, and predicted recalcitrant Cu<sup>I</sup> fractions are shown as horizontal bars. [Cu<sup>I</sup>]<sub>∞</sub> was set by forcing the fit through the last (longest time) data point; [Cu<sup>I</sup>](0)/[Cu<sup>I</sup>]<sub>0</sub> was set to 1 (full details in Supp. Info. section 7.8.4). The Cu<sup>I</sup> fractions reported contain an absolute 5% error from linear combination XANES fits (details in Supp. Info. section 7.8.3). Inset, the Fourier transform of the k<sup>2</sup>-weighted EXAFS signal (FT[k<sup>2</sup>χ(k)]) in R-space (R) of Cu-CHA-15 collected before O<sub>2</sub> exposure and after the transient experiment. (B) Snapshots taken from simulated initial (time = 0) and final (time → ∞) Cu<sup>I</sup> spatial distributions corresponding to the three samples (a, c, and h) in (A). Cu<sup>I</sup> volumetric footprints are denoted by 9 Å-radius green spheres. Simulation results include decomposition of unoxidized Cu<sup>I</sup> fraction into physically isolated (Iso) and functionally isolated (MC) components. . . . . 290
- 7.4 Simulation of O<sub>2</sub> adsorption and oxidation of two Cu<sup>I</sup>(NH<sub>3</sub>)<sub>2</sub> equivalents.** DFT-computed energy landscape is shown for the diffusion of Cu<sup>I</sup>(NH<sub>3</sub>)<sub>2</sub> through an 8-MR CHA window into an adjacent cage and subsequent bimolecular reaction with O<sub>2</sub>. All minima and transition states were computed here, except C to D, which is taken from [423]. Gray, Cu; green, Al; red, O; blue, N; and white, H. . . . . 291
- 7.5 Simulated Cu<sup>I</sup>(NH<sub>3</sub>)<sub>2</sub> diffusion up to 11 Å from charge-compensating Al.** On left, the metadynamics-computed free energy at 473 K of Cu<sup>I</sup>(NH<sub>3</sub>)<sub>2</sub> in the 72-T site CHA supercell versus Cu-Al distance. The red line is the energy profile predicted from a point-charge electrostatic model, described in Supp. Info. section 7.8.9. Labeled are reactant state (1) [Cu<sup>I</sup>(NH<sub>3</sub>)<sub>2</sub> in the same cage as Al], transition state (2) [Cu<sup>I</sup>(NH<sub>3</sub>)<sub>2</sub> diffusion through 8-MR], and product state (3) [Cu<sup>I</sup>(NH<sub>3</sub>)<sub>2</sub> in the neighboring cage without Al]. Corresponding representative Cu<sup>I</sup>(NH<sub>3</sub>)<sub>2</sub> configurations from the trajectories are shown on the right. Gray, Cu; green, Al; blue, N; and white, H. . . . . 292
- 7.6 Proposed low-temperature SCR catalytic cycle.** Reduction steps proceed on site-isolated Cu<sup>II</sup> ions residing near one (left-hand cycle) or two (right-hand cycle) framework Al centers with constrained diffusion of Cu<sup>I</sup> ions into single cages and oxidation by O<sub>2</sub> (inner step). NH<sub>4</sub><sup>+</sup> is formed and consumed in the right-hand cycle to maintain stoichiometry and charge balance. Gray, Cu; yellow, Si; red, O; blue, N; and white, H. . . . . 293

| Figure   | Page |
|--|------|
| 7.7 72-T site supercell for metadynamics simulation. Color code for different elements in superimposed figure: gray=Cu, green=Al, yellow=Si, red=O, blue=N and white=H. . . . .  | 310  |
| 7.8 X-Ray diffraction patterns of H-SSZ-13 zeolites with Si/Al = 4.5 (blue), Si/Al = 15 (red), and Si/Al = 25 (black), measured using a Cu K $\alpha$ source ( $\lambda$ = 0.154 nm). Diffraction patterns are vertically offset for clarity. Cu-exchanged forms of these materials show equivalent XRD patterns [450].  | 314  |
| 7.9 Ar adsorption isotherms on H-SSZ-13 with Si/Al = 4.5 (blue), Si/Al = 15 (red), and Si/Al = 25 (black). Isotherms are vertically offset for clarity (Si/Al=15: by 200 cm <sup>3</sup> g <sup>-1</sup> , Si/Al=25: by 400 cm <sup>3</sup> g <sup>-1</sup> ). Cu-exchanged forms of these materials show similar adsorption isotherms, with slight decreases in micropore volumes caused by the presence of Cu [450]. . . . | 315  |
| 7.10 XANES spectra for Cu-CHA-20 (red) and Cu-CHA-29 (green) at ambient conditions, and for bulk Cu <sup>II</sup> O (pink). . . . .  | 316  |
| 7.11 UV-Vis spectra for Cu-CHA-15 (blue), Cu-CHA-20 (black), and Cu-CHA-29 samples (red) recorded at ambient conditions. . . . .   | 317  |
| 7.12 Operando XANES spectra of Cu-CHA-15 (red) and Cu-CHA-29 (dark blue) during steady-state standard SCR (300 ppm NO, 300 ppm NH <sub>3</sub> , 10% O <sub>2</sub> , 2% H <sub>2</sub> O, 5% CO <sub>2</sub> , 463-473 K). Reference spectra for aqueous Cu <sup>I</sup> (NH <sub>3</sub> ) <sub>2</sub> (grey), isolated Cu <sup>I</sup> [79] (pink) and isolated Cu <sup>II</sup> (light blue) sites [79]. . . . .        | 318  |
| 7.13 XANES spectra collected during transient oxidation of the reduced forms of Cu-CHA-29 sample with 10% O <sub>2</sub> (top) and 100 ppm NO <sub>2</sub> (bottom), as a function of time (labeled in figure). . . . .  | 319  |
| 7.14 XANES spectra during transient oxidation of the reduced forms of Cu-CHA-20 sample with 10% O <sub>2</sub> (top) and 100 ppm NO <sub>2</sub> (bottom), as a function of time (labeled in figure). . . . .  | 320  |
| 7.15 XANES spectra during transient oxidation of the reduced forms of Cu-CHA-15 sample with 10% O <sub>2</sub> (top) and 100 ppm NO <sub>2</sub> (bottom), as a function of time (labeled in figure). . . . .  | 321  |
| 7.16 The k <sup>2</sup> weighted Fourier transform (moduli and imaginary parts of FT on top left and top right, respectively) and raw EXAFS spectra (bottom) collected before (black) and after (red) oxidation with 10% O <sub>2</sub> at 473 K, starting from the reduced Cu(I)(NH <sub>3</sub> ) <sub>2</sub> state of Cu-CHA-29. . . . .   | 322  |



| Figure  | Page |
|---|------|
| 7.17 The $k^2$ weighted Fourier transform (moduli and imaginary parts of FT on top left and top right, respectively) and raw EXAFS spectra (bottom) collected before (black) and after (red) oxidation with 10% $O_2$ at 473 K, starting from the reduced $Cu(I)(NH_3)_2$ state of Cu-CHA-20. . . . .   | 323  |
| 7.18 The $k^2$ weighted Fourier transform (moduli and imaginary parts of FT on top left and top right, respectively) and raw EXAFS spectra (bottom) collected before (black) and after (red) oxidation with 10% $O_2$ at 473 K, starting from the reduced $Cu(I)(NH_3)_2$ state of Cu-CHA-15. . . . .   | 324  |
| 7.19 NO concentrations measured in the reactor effluent during five step-wise treatments of Cu-CHA-15, in order to quantify NO consumption (per Cu) in treatment steps 2, 4, and 5 above, which correspond to different steps in the proposed standard SCR cycle (Figure 6). Red and blue traces indicate experiments with the blank reactor and catalyst-loaded reactor, respectively.                       | 325  |
| 7.20 Temporal evolution of the XANES-measured $Cu^I$ fraction in Cu-CHA-29 (A, red), Cu-CHA-20 (C, blue), and Cu-CHA-15 (H, black) during transient oxidation in 100 ppm $NO_2$ at 473 K. Least-squares fit to Eq. 7.15 is shown by solid lines. . . . .  | 325  |
| 7.21 Structures for $O_2$ configuration (A), $O_2$ configuration (B) and $NO_2$ (C) adsorbed on a single $Cu^I(NH_3)_2$ . Calculations were performed in the CHA supercell described in 7.8.5, and the framework removed from this figure for clarity. . . . .  | 326  |
| 7.22 The fraction of lone Cu within zeolite cages randomly dispersed on the zeolite framework unable to oxidize compared with experimental measurements. . . . .  | 326  |
| 7.23 Fraction of unoxidizable $Cu^I$ as a function of Cu density from simulation. Splines were drawn through the discrete simulations at each density to yield continuous curves in the figure. 9 A (bold red line) represents the metadynamics-predicted maximum Cu diffusion distance. Black data points are experimental observations from Figure 7.3. . . . .   | 327  |
| 7.24 Phase diagrams for 2Al (“Z <sub>2</sub> ”) exchanged Cu sites with varying $P_{NH_3}$ and $P_{H_2O}$ at 473 K and 10% $O_2$ . The chrome sphere demarcates $NH_3$ and $H_2O$ pressures equivalent to those used in the kinetic experiments reported in figure 7.1 and figure 7.2. All DFT-computed structures, energies, and methods used to generate this diagram can be found in Paolucci et al. [79]. | 328  |

| Figure   | Page |
|--|------|
| 7.25 Phase diagrams for 1Al (“Z”) exchanged Cu sites with varying $P_{NH_3}$ and $P_{H_2O}$ at 473 K and 10% $O_2$ . The chrome sphere demarcates $NH_3$ and $H_2O$ pressures equivalent to those used in the kinetic experiments reported in figure 7.1 and figure 7.2. All DFT-computed structures, energies, and methods used to generate this diagram can be found in Paolucci et al. [79].  | 329  |
| 7.26 Dependence of SCR turnover rates (300 ppm NO, 300 ppm $NH_3$ , 10% $O_2$ , 7% $CO_2$ , 200-120000 ppm $H_2O$ and balance $N_2$ at 473 K) on $H_2O$ pressure on Cu-CHA-19. Line denotes regression of power rate law to measured rate data, with a best-fit slope of 0.03, corresponding to the apparent $H_2O$ reaction order. . . . .  | 330  |
| 7.27 Standard SCR rates (300 ppm NO, 300 ppm $NH_3$ , 10% $O_2$ , 7% $CO_2$ , 3% $H_2O$ and balance $N_2$ ) measured in the temperature range of 450-480 K on Cu-CHA-19 in the laboratory differential PFR (red squares) and in the <i>operando</i> XAS reactor (black triangle). Line denotes regression of an Arrhenius rate equation to the lab PFR rate data. . . . .  | 331  |
| 8.1 Schematic Representation of the Organization of Si and Al Atoms in the Crystallizing Polyanionic CHA Framework To Form (a) Isolated Al with Only $TMAda^+$ or (b) Paired Al in the Presence of $TMAda^+$ and $Na^+$ (adapted from Di Iorio et al [42]). . . . .  | 365  |
| 8.2 Fraction of Al in pairs as a function of $Na^+$ retained on CHA products of fixed composition ( $Si/Al_f = 14-18$ ) crystallized in $OH^-$ (squares) media with $Na^+/TMAda^+ \leq 1$ (filled), $Na^+/TMAda^+ > 1$ (open), and $F^-$ (open circle) media using $Al(OH)_3$ and $Al(O-i-Pr)_3$ (diamond) as aluminum sources. The dashed line represents the parity line (slope = 2) expected if each $Na^+$ cation formed a paired Al site. Eight independent CHA samples crystallized using only $TMAda^+$ are plotted at the origin. .          | 366  |
| 8.3 Elementary Steps in the Associative Methanol Dehydration Pathway (adapted from Carr et al [82]. . . . .  | 367  |
| 8.4 Elementary Steps in the Dissociative Methanol Dehydration Pathway (adapted from Carr et al [82]. . . . .   | 368  |
| 8.5 First-order (closed) and zero-order (open) associative methanol dehydration rate constants (per $H^+$ ) as a function of $H^+$ density (per unit cell) on H-zeolites. Data shown for H-CHA samples crystallized in $OH^-$ and $F^-$ media ( $Si/Al = 14-18$ ) to contain only isolated protons at 415 K, (squares), for commercial H-MFI samples ( $Si/Al = 17-43$ , Zeolyst) at 415 K (circles), and for H-MFI samples ( $Si/Al = 17-120$ , inclusive of commercial Zeolyst samples) reported by Jones et al. [83] at 433 K (diamonds). . . . . | 369  |

| Figure  | Page |
|---|------|
| 8.6 Dependence of the intraparticle effectiveness factor on the Thiele modulus for methanol dehydration on H-CHA zeolites with Si/Al <sub>f</sub> = 14-18 with 0% (circles), 18-30% (triangles), and 44% (diamond) paired Al. Data also shown for H-CHA with Si/Al <sub>f</sub> = 27 (square), and H-CHA synthesized with CTAB (cross). Dashed line is the effectiveness factor predicted for a first-order reaction in a spherical pellet (Section 8.7.5, Supporting Information). | 370  |
| 8.7 DME formation rates (per H <sup>+</sup> , 415 K) as a function of methanol pressure on (a) linear and (b) logarithmic axes (for clarity) for H-CHA with 0% (circles), 18% (diamonds), 30% (triangles), and 44% (squares) paired Al. Dashed lines represent best fits of the methanol dehydration rate expression (eq 8.3) regressed to the data. . . . .  | 371  |
| 8.8 <i>in situ</i> IR spectra of (a) H-CHA (Si/Al <sub>f</sub> = 14) containing only isolated protons and (b) H-MFI (Si/Al = 43, Zeolyst) under 0.77 kPa CH <sub>3</sub> OH at 415 K. Vertical dashed lines indicate the location of surface (1457 cm <sup>-1</sup> ) and (c) gas-phase (1454 cm <sup>-1</sup> ) methoxy deformation modes. . . . .   | 372  |
| 8.9 First-order (squares) and zero-order (circles) rate constants (415 K, per H <sup>+</sup> ) on CHA zeolites (Si/Al <sub>f</sub> = 14-18) as a function of the fraction of Al in pairs. Dashed lines are linear regressions to the data points (solid). Extrapolated dehydration rate constants for paired protons are shown as open symbols. . . . .   | 373  |
| 8.10 <i>in situ</i> IR spectra of H-CHA (Si/Al <sub>f</sub> = 14-17) containing 0-44% paired Al (light to dark) under 0.77 kPa CH <sub>3</sub> OH (415 K). Dashed lines indicate the location of surface (1457 cm <sup>-1</sup> ) and gas-phase (1454 cm <sup>-1</sup> ; dash-dotted spectrum) methoxy deformation modes. The inset shows the integrated area of the surface methoxy peak as a function of the fraction of Al in pairs.   | 374  |
| 8.11 XRD patterns of a) CHA-F(18,0%), b) CHA-F(17,0%), c) CHA-OH(27,0%), d) CHA-OH(14,0%), and e) CHA-OH(17,0%) zeolites synthesized without Na <sup>+</sup> . . . . .  | 381  |
| 8.12 XRD patterns of CHA zeolites synthesized with a) AlCl <sub>3</sub> , b) NaAlO <sub>2</sub> , c) Al(O-i-Pr) <sub>3</sub> , d) Al <sub>2</sub> O <sub>3</sub> , e) Al(NO <sub>3</sub> ) <sub>3</sub> , and f) Al(OH) <sub>3</sub> and equimolar Na <sup>+</sup> and TMAda <sup>+</sup> in OH <sup>-</sup> media. . . . .   | 382  |
| 8.13 XRD patterns of a) CHA-OH(17,30%), b) CHA-OH(16,24%), and c) CHA-OH(15,18%) zeolites synthesized with Al(OH) <sub>3</sub> and equimolar Na <sup>+</sup> and TMAda <sup>+</sup> in OH <sup>-</sup> media. . . . .   | 383  |
| 8.14 XRD patterns of Na <sup>+</sup> -free CHA-OH(16,6%) zeolite synthesized with Al(OH) <sub>3</sub> , TMAda <sup>+</sup> , and CTAB in OH <sup>-</sup> media. . . . .   | 384  |
| 8.15 XRD pattern of Si-CHA synthesized with TMAda <sup>+</sup> in F <sup>-</sup> media. . . . .   | 384  |

| Figure  | Page |
|---|------|
| 8.16 XRD patterns of a) H-MFI(30) and b) H-MFI(43) zeolites. . . . .  | 385  |
| 8.17 Ar adsorption isotherms (87 K) on a) CHA-F(18,0%), b) CHA-F(14,0%),<br>c) CHA-OH(27,0%), d) CHA-OH(17,0%), and e) CHA-OH(18,0%) zeolites<br>synthesized without $\text{Na}^+$ using $\text{OH}^-$ and $\text{F}^-$ anions. . . . .   | 386  |
| 8.18 Ar adsorption isotherms (87 K) on CHA zeolites synthesized with a) $\text{AlCl}_3$ ,<br>b) $\text{NaAlO}_2$ , c) $\text{Al}(\text{O-i-Pr})_3$ , d) $\text{Al}_2\text{O}_3$ , e) $\text{Al}(\text{NO}_3)_3$ , and f) $\text{Al}(\text{OH})_3$ and<br>equimolar $\text{Na}^+$ and $\text{TMAda}^+$ in $\text{OH}^-$ media. . . . .   | 387  |
| 8.19 Ar adsorption isotherms (87 K) on a) CHA-OH(17,30%), b) CHA-OH(16,24%),<br>and c) CHA-OH(15,18%) zeolites synthesized with $\text{Al}(\text{OH})_3$ and equimolar<br>$\text{Na}^+$ and $\text{TMAda}^+$ in $\text{OH}^-$ media. . . . .  | 388  |
| 8.20 Ar adsorption isotherms (87 K) on $\text{Na}^+$ -free CHA-OH(16,6%) zeolite syn-<br>thesized with $\text{Al}(\text{OH})_3$ , $\text{TMAda}^+$ , and CTAB in $\text{OH}^-$ media. . . . .   | 389  |
| 8.21 Ar adsorption isotherms (87 K) on Si-CHA zeolite synthesized with $\text{TMAda}^+$<br>in $\text{F}^-$ media. . . . .   | 390  |
| 8.22 $\text{N}_2$ adsorption isotherms (77 K) on a) H-MFI(30) and b) H-MFI(43) zeolites.  | 391  |
| 8.23 SEM image of the bulk sample of CHA-OH(14,0%). . . . .   | 393  |
| 8.24 SEM image of the bulk sample of CHA-OH(17,0%). . . . .   | 394  |
| 8.25 SEM image of the bulk sample of CHA-OH(27,0%). . . . .   | 394  |
| 8.26 SEM image of the bulk sample of CHA-F(18,0%). . . . .  | 395  |
| 8.27 SEM image of the bulk sample of CHA-OH(15,18%). . . . .  | 395  |
| 8.28 SEM image of the bulk sample of CHA-OH(16,24%). . . . .  | 396  |
| 8.29 SEM image of the bulk sample of CHA-OH(17,30%). . . . .  | 396  |
| 8.30 SEM image of the bulk sample of CHA-OH(14,44%). . . . .  | 397  |
| 8.31 SEM image of the bulk sample of CHA-OH(16,6%). . . . .   | 397  |
| 8.32 $^{27}\text{Al}$ MAS NMR spectra of a) CHA-F (18,0%), b) CHA-F (17,0%), c)<br>CHA-OH (27,0%), d) CHA-OH (14,0%), and e) CHA-OH (17,0%) zeolites<br>synthesized without $\text{Na}^+$ using $\text{OH}^-$ and $\text{F}^-$ anions. . . . .  | 400  |
| 8.33 $^{27}\text{Al}$ MAS NMR spectra of CHA zeolites synthesized with a) $\text{AlCl}_3$ , b)<br>$\text{NaAlO}_2$ , c) $\text{Al}(\text{O-i-Pr})_3$ , d) $\text{Al}_2\text{O}_3$ , e) $\text{Al}(\text{NO}_3)_3$ , and f) $\text{Al}(\text{OH})_3$ and<br>equimolar $\text{Na}^+$ and $\text{TMAda}^+$ in $\text{OH}^-$ media. . . . . | 401  |
| 8.34 $^{27}\text{Al}$ MAS NMR spectra of a) CHA-OH(17,30%), b) CHA-OH(16,24%),<br>and c) CHA-OH(15,18%) zeolites synthesized with $\text{Al}(\text{OH})_3$ and equimolar<br>$\text{Na}^+$ and $\text{TMAda}^+$ in $\text{OH}^-$ media. . . . .  | 403  |

| Figure  | Page |
|---|------|
| 8.35 Amount of exchanged $\text{Co}^{2+}$ retained on H-CHA-F(18,0%) as a function of the $\text{Co}^{2+}$ concentration in solution at equilibrium. . . . .  | 405  |
| 8.36 Amount of $\text{Co}^{2+}$ retained on H-CHA-F(18,0%) as a function of successive $\text{Co}^{2+}$ titrations with a 0.5M $\text{Co}(\text{NO}_3)_2$ solution. . . . .   | 406  |
| 8.37 The number of residual $\text{H}^+$ sites (per $\text{H}^+$ site on the H-form parent zeolite) as a function of the Cu-loading (per $\text{H}^+$ site on the H-form parent zeolite) for CHA-OH(16,24%) (circle), CHA-OH(14,0%) (square), CHA-F(17,0%) (diamond), and CHA-F(18,0%) (triangle) zeolites. Dashed lines represent the expected exchange stoichiometry for exclusively $\text{Cu}^{2+}$ ( $m = -2$ ) or $[\text{CuOH}]^+$ ( $m = -1$ ). . . . . | 407  |
| 8.38 Methanol dehydration rates (per $\text{H}^+$ , 415 K) on H-CHA-OH(14,0%) zeolites as a function of time-on-stream under 2.5 kPa $\text{CH}_3\text{OH}$ . . . . .   | 415  |
| 8.39 Methanol dehydration rates (per $\text{H}^+$ ) on H-MFI(30) (squares) and H-MFI(43) (circles) at 433 K and on H-MFI(30) (diamonds) and H-MFI(43) (crosses) at 415 K. Triangle data points are methanol dehydration rates on H-MFI ( $\text{Si}/\text{Al} = 30$ ) at 433 K reported by Jones et al [83]. Dashed lines are regressions of the data to the associative pathway (Eq. 8.16). . .  | 417  |
| 8.40 Methanol dehydration rates (per gram, 433 K) on H-MFI(43) zeolites as a function of cumulative moles of pyridine dosed. The dashed line is a linear regression to the data (last three points omitted). . . . .  | 418  |
| 8.41 Associative rate first (squares) and zero (circles) order rate constants (per $\text{H}^+$ ) on H-MFI(43) measured as a function of temperature (405-433 K). .   | 420  |
| 8.42 Methanol dehydration rates (per $\text{H}^+$ , 415 K) on H-CHA-OH(16,0%) as a function of methanol partial pressure. Dashed line is a regression to the generalized rate expression (Eq. 8.38). . . . .  | 421  |
| 8.43 Methanol dehydration rates (per $\text{H}^+$ , 415 K) on H-CHA-OH(26,0%) as a function of methanol partial pressure. Dashed line is a regression to the generalized rate expression (Eq. 8.38). . . . .  | 422  |
| 8.44 Methanol dehydration rates (per $\text{H}^+$ , 415 K) on H-CHA-F(17,0%) as a function of methanol partial pressure. Dashed line is a regression to the generalized rate expression (Eq. 8.38). . . . .   | 423  |
| 8.45 Methanol dehydration rates (per $\text{H}^+$ , 415 K) on H-CHA-OH(16,6%) as a function of methanol partial pressure. Dashed line is a regression to the generalized rate expression (Eq. 8.38). . . . .  | 424  |

| Figure   | Page |
|--|------|
| 8.46 Methanol dehydration rates (per $\text{H}^+$ , 415 K) on H-MFI(17) as a function of methanol partial pressure. Dashed line is a regression to the associative rate expression (Eq. 8.16). . . . .   | 425  |
| 8.47 Methanol dehydration rates (per $\text{H}^+$ , 415 K) on H-MFI(30) as a function of methanol partial pressure. Dashed line is a regression to the associative rate expression (Eq. 8.16). . . . .   | 426  |
| 8.48 Methanol dehydration rates (per $\text{H}^+$ , 415 K) on H-MFI(43) as a function of methanol partial pressure. Dashed line is a regression to the associative rate expression (Eq. 8.16). . . . .   | 427  |
| 8.49 Associative first order rate constants (per $\text{H}^+$ , 433 K) as a function of pore diameter in MFI, MTT, MTW, MOR, SFH, BEA, and FAU zeolites. Dashed line is an exponential regression to the data. All data is reproduced from Jones et al [22]. . . . .                         | 428  |
| 8.50 IR spectra of H-CHA-OH(14,0%) under 0 kPa $\text{CH}_3\text{OH}$ (bold) and 0.15, 0.77, 1.5, 3.0, 5.9, 13.5, and 22 kPa $\text{CH}_3\text{OH}$ (thin) at 415 K. . . . .   | 429  |
| 8.51 IR spectra of H-CHA-OH(14,44%) under 0 kPa $\text{CH}_3\text{OH}$ (bold) and 0.15, 0.77, 1.5, 3.0, 5.9, 13.5, and 22 kPa $\text{CH}_3\text{OH}$ (thin) at 415 K. . . . .  | 430  |
| 8.52 IR spectra of H-MFI(43) under 0 kPa $\text{CH}_3\text{OH}$ (bold) and 0.15, 0.77, 1.5, 3.0, 5.9, 13.5, and 22 kPa $\text{CH}_3\text{OH}$ (thin) at 415 K. . . . .   | 430  |
| 8.53 Methanol dehydration rates (squares; per $\text{H}^+$ , 415 K, 1 kPa $\text{CH}_3\text{OH}$ ) and conversion (circles) on H-CHA-OH(14,0%) as a function of residence time. Dashed lines represent a linear regression to conversion data and the average rate of DME formation. . . . . | 432  |
| 8.54 Methanol partial pressures in H-CHA-OH(14,0%) as a function of particle radius, where zero is the crystal center, for bulk $\text{CH}_3\text{OH}$ pressures of 0.05, 0.1, 0.2, 0.4, 0.8, 1.6, 3.2, 6.4, 12.8, 25.6, and 51.2 kPa at 415 K. . . . .                                      | 435  |
| 8.55 Methanol partial pressures in H-CHA-OH(17,0%) as a function of particle radius, where zero is the crystal center, for bulk $\text{CH}_3\text{OH}$ pressures of 0.05, 0.1, 0.2, 0.4, 0.8, 1.6, 3.2, 6.4, 12.8, 25.6, and 51.2 kPa at 415 K. . . . .                                      | 436  |
| 8.56 Methanol partial pressures in H-CHA-F(18,0%) as a function of particle radius, where zero is the crystal center, for bulk $\text{CH}_3\text{OH}$ pressures of 0.05, 0.1, 0.2, 0.4, 0.8, 1.6, 3.2, 6.4, 12.8, 25.6, and 51.2 kPa at 415 K. . . . .                                       | 437  |
| 8.57 Methanol partial pressures in H-CHA-OH(27,0%) as a function of particle radius, where zero is the crystal center, for bulk $\text{CH}_3\text{OH}$ pressures of 0.05, 0.1, 0.2, 0.4, 0.8, 1.6, 3.2, 6.4, 12.8, 25.6, and 51.2 kPa at 415 K. . . . .                                      | 438  |

| Figure   | Page |
|--|------|
| 8.58 Methanol partial pressures in H-CHA-OH(16,6%) as a function of particle radius, where zero is the crystal center, for bulk CH <sub>3</sub> OH pressures of 0.05, 0.1, 0.2, 0.4, 0.8, 1.6, 3.2, 6.4, 12.8, 25.6, and 51.2 kPa at 415 K. . . . .  | 439  |
| 8.59 Methanol partial pressures in H-CHA-OH(15,18%) as a function of particle radius, where zero is the crystal center, for bulk CH <sub>3</sub> OH pressures of 0.05, 0.1, 0.2, 0.4, 0.8, 1.6, 3.2, 6.4, 12.8, 25.6, and 51.2 kPa at 415 K. . . . .   | 440  |
| 8.60 Methanol partial pressures in H-CHA-OH(16,24%) as a function of particle radius, where zero is the crystal center, for bulk CH <sub>3</sub> OH pressures of 0.05, 0.1, 0.2, 0.4, 0.8, 1.6, 3.2, 6.4, 12.8, 25.6, and 51.2 kPa at 415 K. . . . .   | 441  |
| 8.61 Methanol partial pressures in H-CHA-OH(17,30%) as a function of particle radius, where zero is the crystal center, for bulk CH <sub>3</sub> OH pressures of 0.05, 0.1, 0.2, 0.4, 0.8, 1.6, 3.2, 6.4, 12.8, 25.6, and 51.2 kPa at 415 K. . . . .   | 442  |
| 8.62 Methanol partial pressures in H-CHA-OH(14,44%) as a function of particle radius, where zero is the crystal center, for bulk CH <sub>3</sub> OH pressures of 0.05, 0.1, 0.2, 0.4, 0.8, 1.6, 3.2, 6.4, 12.8, 25.6, and 51.2 kPa at 415 K. . . . .   | 443  |
| 8.63 Methanol dehydration rates (per H <sup>+</sup> , 415 K) on H-CHA-OH(14,0%) as a function of water pressure at 0.05 (circles), 2.5 (triangle), and 50 (squares) kPa CH <sub>3</sub> OH. Open points from steady state rates (415 K), without co-feeding H <sub>2</sub> O, and water pressures are from product formation. Labels indicate the water order under each set of conditions. Dashed lines are power law regressions to the data. . . . .  | 447  |
| 8.64 Methanol dehydration rates (per H <sup>+</sup> , 415 K) on H-CHA-OH(14,44%) as a function of water pressure at 0.05 (circles), 2.5 (triangle), and 50 (squares) kPa CH <sub>3</sub> OH. Open points from steady state rates (415 K), without co-feeding H <sub>2</sub> O, and water pressures are from product formation. Labels indicate the water order under each set of conditions. Dashed lines are power law regressions to the data. . . . . | 448  |
| 8.65 Methanol dehydration rates (per H <sup>+</sup> , 415 K) on H-AEI zeolite as a function of methanol partial pressure. Dashed line is a regression to the generalized rate expression (Eq. 8.38). . . . .   | 450  |
| C.1 DFT calculated structures of intermediates and transition states for the associative (inner circle) and dissociative (outer circle) mechanisms. . . .  | 514  |
| C.2 Methanol activity coefficient as a function of intrapore concentration on H-CHA (Si/Al = 15, 0% paired Al) at 293 K (black) and 308 K (grey), and extrapolated to 415 K (dashed), and on H-MFI (Si/Al = 43) at 293 K (yellow). . . . .   | 516  |

| Figure  | Page |
|---|------|
| C.3 Log-log analysis of the DME formation rate (per $\text{H}^+$ ) as a function of methanol pressure (0.01-50 kPa) on H-CHA (Si/Al = 15, 0% paired Al) at 383 K (yellow), 403 K (orange), and 415 K (blue). Dashed lines are best-fit lines to extract reaction orders at low methanol pressures and corresponding reaction orders (i.e., slopes) are provided. . . . .  | 520  |
| C.4 DME formation rates (per total $\text{H}^+$ ) measured at 415 K as a function of methanol partial pressure on a representative H-form CHA (green), LTA (orange), LEV (blue), and AEI (red) catalyst. . . . .  | 522  |
| C.5 (a) DME formation rates (per $\text{H}^+$ ) measured at 415 K (blue), 433 K (green), 450 K (orange), and 473 K (red) and (b) first- (blue) and zero-order (red) rate constants (per $\text{H}^+$ ) measured as a function of temperature (415-473 K) on a CHA zeolite containing 24% of Al in pairs. . . . .  | 523  |
| C.6 IR spectra of H-CHA (0% paired Al, Si/Al = 15) under 10 kPa $\text{CH}_3\text{OH}$ measured at 343 K (orange), 353 K (grey), 373 K (yellow), 415 K (light blue), 433 K (green), and 473 K (dark blue). Inset shows the intensity of the bands representative of methanol clusters (ca. $3350\text{ cm}^{-1}$ ; red) and protonated methanol dimers (ca. $2620\text{ cm}^{-1}$ ; blue) as a function of temperature. . . . . | 524  |
| C.7 Methanol dehydration rates (415 K, per proton) normalized to the maximum rate of H-CHA with 0% (solid) and 44% paired Al (dashed) and differential methanol adsorption data measured at 293 K on H-CHA with 0% (circles) and 44% paired Al (squares) as a function of the gas-phase methanol free-energy. . . . .   | 525  |
| C.8 Infrared spectra measured at 293 K on H-CHA with 0% paired Al as a function of methanol dosing (0.01-3 $\text{CH}_3\text{OH}/\text{H}^+$ ). . . . .   | 526  |
| C.9 DME formation rates as a function of methanol pressure measured at 323 K and a total flow rate of $25\text{ cm}^3\text{ min}^{-1}$ (blue) and $100\text{ cm}^3\text{ min}^{-1}$ (50 kPa; red). Dashed line is a fit of the associative dehydration rate law, without inhibition, from Carr et al. [82] to rates measured below 10 kPa. . . . .  | 527  |
| C.10 DME formation rates (per $\text{H}^+$ ) measured at 415 K as a function of pressure on a CHA zeolite with 0% paired Al on the SSITKA IR/MS (blue) and PFR (red) [214]. . . . .   | 528  |
| C.11 Steady-state isotopic switch from 12 kPa unlabeled $\text{CH}_3\text{OH}$ to 12 kPa $^{13}\text{CH}_3\text{OH}$ (blue). The $^{13}\text{C}$ -DME response is shown in red. Ar (black) and Kr (grey) inert tracers are provided to show gas holdup. . . . .   | 529  |



| Figure  | Page |
|---|------|
| C.12 (a) $N_{DME}$ (per $H^+$ ) and (b) the intrinsic turnover frequency (per $H^+$ ) measured as a function of methanol pressure (0.1-25 kPa) at 415 K on CHA zeolites containing 0% (blue) and 30% (red) paired Al. . . . .   | 530  |
| C.13 DFT calculated free energies (433 K, 1 bar) for the associative (dashed) and dissociative (solid) methanol dehydration mechanisms on isolated protons in CHA. . . . .  | 533  |
| C.14 Structure of the methoxy transition state at a paired proton in CHA. Values represent the distance between adjacent nuclei (green connectors) in pm. . . . .   | 537  |
| C.15 DFT calculated free energies (433 K, 1 bar) for the associative (dashed) and dissociative (solid) methanol dehydration mechanisms on isolated (black) and paired (blue) protons in CHA. . . . .  | 538  |
| C.16 IR spectra of CHA containing 0% (light green) and 44% (dark green) paired Al, LEV (blue; Si/Al = 17, 12% paired Al), AEI (red; Si/Al = 16, 32% paired Al), AFX (yellow; Si/Al = 9, 34% paired Al), and RTH (grey; Si/Al = 15, 16% paired Al) under 0.77 kPa $CH_3OH$ at 415 K. . . . . | 539  |
| D.1 $^{27}Al$ SS MAS NMR spectra of Samples A (black), B (red), C (blue), and D (purple) over the whole range measured (a) and focused on the tetrahedral Al resonance (b). . . . .   | 545  |
| D.2 $^{29}Si$ SS MAS NMR spectra of Samples A (black), B (red), C (blue), and D (purple). . . . .   | 546  |
| D.3 $^{13}C$ NMR spectra of TMAda+-d <sub>9</sub> dissolved in D <sub>2</sub> O with an absent NMR line for methyl C ( $\delta = 48$ ppm). Inset shows the assignment of the different expected chemical shifts for TMAda+. . . . .   | 547  |
| D.4 $^{29}Si$ (upper) and $^{27}Al$ (lower) MAS DNP NMR spectra of Samples A (a) and C (b) without (black) and with (red) microwave-excitation. . . . .   | 547  |
| D.5 $^{27}Al\{^{29}Si\}$ J-based INEPT MAS NMR spectrum of Sample A. . . . .  | 548  |
| D.6 3Q $^{27}Al$ SS MAS NMR spectra of Samples C (a) and D (b) and two distinct sites for Samples C ((i) and (ii)) and D ((iii) and (iv)). . . . .  | 549  |
| D.7 $^{27}Al$ - $^{27}Al$ SQ-DQ MAS NMR cross-correlation peaks of Samples A (black), B (red), C (blue), and D (purple). Dashed lines represent the magnitude of each cross-correlation peak for the corresponding samples (same color identities). . . . .                                 | 550  |
| D.8 $^{13}C$ SS MAS NMR spectra of as-synthesized CHA Samples A (black), B (red), C (blue), and D (purple). Inset shows the assignment of the five $^{13}C$ NMR lines to the five unique C atoms of the TMAda+ molecule. . .  | 551  |

| Figure   | Page |
|--|------|
| D.9 $^1\text{H}$ SS MAS NMR spectra of as-synthesized CHA Samples A (black), B (red), C (blue), and D (purple). Inset shows the assignment of the four unique H atoms of the TMAda+ molecule. . . . .  | 552  |
| D.10 $^1\text{H}$ - $^{13}\text{C}$ HETCOR SS MAS NMR spectra of as-synthesized Sample B measured at 100 K. . . . .  | 553  |
| D.11 Variable-temperature $^1\text{H}$ SS MAS NMR spectra of Sample measured at 293 K (black) and 100 K (red). Black arrow is included to emphasize the broadening of the methyl $^1\text{H}$ NMR line. Inset shows the $\text{C}_3$ -axis of rotation of the TMAda+ molecule. . . . .   | 554  |
| D.12 $^1\text{H}\{^{27}\text{Al}\}$ REDOR MAS NMR spectra (a) without ( $\text{S}_0$ ) and with (S) $^{27}\text{Al}$ dipolar dephasing of $^1\text{H}$ spectra. (b) Shows the difference in dipolar dephasing of each unique proton in TMAda+ as a function of dephasing time. . . . .   | 555  |
| D.13 $^{23}\text{Na}$ MAS NMR of Samples A (black), B (red), and C (blue) before (a) and after (b) removal of TMAda+. . . . .  | 555  |
| D.14 $^{23}\text{Na}$ 3Q MAS NMR of Samples A (a) and C (b). . . . .   | 556  |
| D.15 Variable-temperature $^{23}\text{Na}$ MAS NMR spectra taken at 293 K (black) and 100 K (red). . . . .   | 556  |
| D.16 $^1\text{H}\{^{23}\text{Na}\}$ REDOR MAS NMR spectra (a) without ( $\text{S}_0$ , black) and with (S, red) $^{23}\text{Na}$ dipolar dephasing of $^1\text{H}$ spectra measured at 100 K. (b) Shows the difference in dipolar dephasing of methyl protons in TMAda+ with $^{23}\text{Na}$ as a function of dephasing time. . . . .                                   | 557  |
| E.1 Adsorption of $\text{CD}_3\text{CN}$ on different sites in stannosilicates and corresponding $\nu(\text{C}\equiv\text{N})$ infrared vibrational frequencies. . . . .   | 588  |
| E.2 Plausible reaction mechanism for glucose-fructose isomerization on open Sn sites in Sn-Beta involving kinetically-relevant 1,2-intramolecular hydride shift (Step 2). For clarity, kinetically-irrelevant steps are lumped as quasi-equilibrated reactions (Steps 1, 3-5). . . . .   | 588  |
| E.3 Diffuse reflectance UV-Vis spectra in Kubelka-Munk units (normalized to the maximum $F(R)$ intensity within each series) for (a) Sn-Beta-F-170, (b) Sn-Beta-OH-200, and (c) $\text{SnO}_2/\text{Si-Beta}$ collected under ambient conditions (thin solid line), after dehydration at 523 K (thick solid line), and after rehydration at 303 K (dashed line). . . . . | 589  |

| Figure   | Page |
|--|------|
| E.4 IR spectra measured at low pyridine coverage (0.09-0.20 pyridine/Sn) and saturated spectra (thick lines) for (a) Sn-Beta-F-100, (b) Sn-Beta-F-140, and (c) Sn-Beta-OH-170. Dashed reference lines shown for Lewis acid sites ( $1615\text{ cm}^{-1}$ , $1450\text{ cm}^{-1}$ ), Lewis or Brønsted acid sites ( $1575\text{ cm}^{-1}$ , $1490\text{ cm}^{-1}$ ), Brønsted acid sites ( $1550\text{ cm}^{-1}$ ), and gas-phase pyridine ( $1595\text{ cm}^{-1}$ ). . . . .   | 590  |
| E.5 Determination of the integrated molar extinction coefficient for pyridine adsorbed on Lewis acid sites ( $1450\text{ cm}^{-1}$ ) on Sn-Beta-OH-170 (black squares), Sn-Beta-F-140 (open triangles), Sn-Beta-F-100 (black circles), from IR peak areas corresponding to pyridine/Sn coverages between 0.04-0.66. . . . .  | 591  |
| E.6 Titrant molar uptakes (per Sn) compared to pyridine molar uptakes (per Sn) at saturation of Sn-Beta samples with (a) n-propylamine (NPA, black squares), (b) ammonia ( $\text{NH}_3$ , open triangles), and (c) $\text{CD}_3\text{CN}$ (black circles were included and $\circ$ were not included in fitting of $\mathcal{E}$ values). Parity lines shown as dashed lines. NPA titration data not shown for samples denoted with an asterisk in Table 3E.3, for which TPD quantification includes binding to residual defect sites. . . . .  | 592  |
| E.7 FTIR difference spectra of Sn-Beta-F-105 (relative to the vacant surface) (a) with increasing $\text{CD}_3\text{CN}$ increasing coverage and (b) at a coverage of $0.65\text{ CD}_3\text{CN/Sn}$ with deconvolution into component peaks. Dashed reference lines shown for open Sn sites ( $2316\text{ cm}^{-1}$ ), closed Sn sites ( $2308\text{ cm}^{-1}$ ), $(\text{SiO})_2\text{Sn}(\text{OH})_2$ sites ( <i>speculative assignment</i> , $2287\text{ cm}^{-1}$ ), silanol groups ( $2275\text{ cm}^{-1}$ ), and gas-phase $\text{CD}_3\text{CN}$ ( $2265\text{ cm}^{-1}$ ). . . . . | 593  |
| E.8 Evolution of IR peak areas for $2316\text{ cm}^{-1}$ (black triangles), $2308\text{ cm}^{-1}$ (diamonds), $2287\text{ cm}^{-1}$ (black circles), and $2275\text{ cm}^{-1}$ ( $\circ$ ) peaks with increasing $\text{CD}_3\text{CN}$ coverage on Sn-Beta-F-105. . . . .   | 594  |
| E.9 Moles of $\text{CD}_3\text{CN}$ adsorbed on open Sn sites (diamonds) and closed Sn sites (black triangles) on Sn-Beta-F-105, together with the ratio of open-to-closed Sn sites titrated (black circles), as a function of $\text{CD}_3\text{CN}$ coverage. . . . .  | 595  |
| E.10 Dependence of initial glucose-fructose isomerization turnover rate (per total Sn, $373\text{ K}$ ) for Sn-Beta-F-220 on the initial aqueous-phase glucose concentration (1-10% (w/w)). . . . .  | 596  |
| E.11 Dependence of initial glucose-fructose isomerization turnover rates (per total Sn, $373\text{ K}$ , 1% (w/w) glucose) on pyridine coverage from titration before reaction on (a) Sn-Beta-F-110 and (b) Sn-Beta-F-170. The fraction of Sn open sites counted <i>ex situ</i> by $\text{CD}_3\text{CN}$ are shown as open diamonds along the x-axes. . . . .   | 597  |

| Figure   | Page |
|--|------|
| E.12 First-order glucose-fructose isomerization rate constant (per open Sn site, 373 K) in water for hydrophobic Sn-Beta-F (black circles) and hydrophilic Sn-Beta-OH ( $\circ$ ) samples as a function of Sn/Si ratio. Dashed lines indicate the averaged turnover rate within each series. . . . .   | 598  |
| E.13 Powder XRD patterns of the stannosilicate samples in this study. Patterns for Sn-Beta-OH-170 and Sn-Beta-OH-200 multiplied by $10\times$ , and Sn-xerogel multiplied by $5\times$ , for clarity. . . . .  | 603  |
| E.14 $N_2$ adsorption isotherms (77 K) for all samples used in this study. Isotherms offset by $200\text{ cm}^3\text{ g}^{-1}$ for clarity. . . . .  | 605  |
| E.15 $H_2O$ adsorption isotherms (293 K) for Sn-Beta-F samples used in this study. Isotherms offset by $100\text{ cm}^3\text{ g}^{-1}$ for clarity. . . . .  | 606  |
| E.16 $H_2O$ adsorption isotherms (293 K) for Sn-Beta-OH samples, $SnO_2/Si$ -Beta-F, and Sn-xerogel used in this study. Isotherms offset by $300\text{ cm}^3\text{ g}^{-1}$ for clarity. . . . .   | 607  |
| E.17 DRUV spectra for Sn-zeolite samples collected after dehydration treatments (523 K). Spectra normalized to $F(R)$ at the peak maximum and artificially offset for clarity. . . . .   | 610  |
| E.18 DRUV spectra for Sn-zeolite samples collected after dehydration treatments (523 K). Spectra normalized to $F(R)$ at the peak maximum and artificially offset for clarity. . . . .   | 611  |
| E.19 Tauc plots for Sn-zeolite samples from DRUV spectra collected after dehydration treatments (523 K). . . . .   | 612  |
| E.20 Tauc plots for Sn-zeolite samples from DRUV spectra collected after dehydration treatments (523 K). Inset shows low-energy region for Sn-Beta-OH-200 that gives rise to the edge energy reported in Table E.1. . . . .  | 613  |
| E.21 $^1H$ NMR spectra for glucose recovered after glucose isomerization catalysis with the Sn-Beta samples tested in this study. The resonating multiplet centered around $\delta = 4.7$ ppm corresponds to residual water present after freeze drying the monosaccharide products . . . . .  | 615  |
| E.22 $^1H$ NMR spectra for the fructose recovered after glucose isomerization catalysis with the Sn-Beta samples tested in this study. A small resonance at $\delta=3.47$ ppm (denoted with an asterisk) is present in fructose products on Sn-Beta-OH-170 and Sn-Beta-OH-200, indicating a small contribution of the enolate mechanism by hydroxyl ions that becomes detectable at the longer reaction times ( $>4$ h) used to attain higher glucose conversion on these samples. . . . . | 616  |

| Figure  | Page |
|---|------|
| E.23 IR spectra after progressive titration of pyridine on H-Y (Si/Al=2.6, Zeolyst) at 423 K (pyridine/Al = 0.005-0.040). Dashed lines at 1630 $\text{cm}^{-1}$ (protonated pyridine), 1545 $\text{cm}^{-1}$ (protonated pyridine), and 1490 $\text{cm}^{-1}$ (protonated pyridine or pyridine bound to Lewis acidic Al sites). . . . .   | 618  |
| E.24 Integrated area of 1545 $\text{cm}^{-1}$ IR peak multiplied by wafer cross-sectional area plotted against the amount of pyridine adsorbed on H-Y (Si/Al=2.6, Zeolyst) at 423 K. . . . .  | 619  |
| E.25 IR spectra after progressive titration of pyridine on high temperature-treated H-Y (Si/Al=2.6, Zeolyst) at 423 K (pyridine/Al = 0.012-0.13). Dashed lines shown at 1630 $\text{cm}^{-1}$ (protonated pyridine), 1615 $\text{cm}^{-1}$ (pyridine bound to Lewis acidic Al sites), 1545 $\text{cm}^{-1}$ (protonated pyridine), 1490 $\text{cm}^{-1}$ (protonated pyridine or pyridine bound to Lewis acidic Al sites), and 1455 $\text{cm}^{-1}$ (pyridine bound to Lewis acidic Al sites). . . . .   | 620  |
| E.26 IR difference spectra for pyridine saturated Sn-Beta samples after evacuation at 423 K for 900 s for (a) Sn-Beta-F-100, (b) Sn-Beta-F-105, (c) Sn-Beta-F-110, (d) Sn-Beta-F-140, (e) Sn-Beta-F-170, (f) Sn-Beta-F-220, (g) Sn-Beta-OH-170, (h) Sn-Beta-OH-200, (i) $\text{SnO}_2/\text{Si-Beta}$ , and (j) Sn-xerogel. All spectra normalized to the overtone and combination modes of Si-O-Si stretches (1750-2100 $\text{cm}^{-1}$ ) and to the maximum peak intensity for clarity. Dashed lines shown at 1610 $\text{cm}^{-1}$ (pyridine bound to Lewis acidic Sn sites), 1540 $\text{cm}^{-1}$ (protonated pyridine), 1490 $\text{cm}^{-1}$ (protonated pyridine or pyridine bound to Lewis acidic Sn sites), and 1450 $\text{cm}^{-1}$ (pyridine bound to Lewis acidic Sn sites). . . . . | 622  |
| E.27 IR spectra for pyridine-saturated Sn-Beta-F-100 during exposure to dynamic vacuum at 423 K for 0 s, 300 s, and 900 s (thin to thick traces) after saturation with pyridine. Dashed lines shown at 1610 $\text{cm}^{-1}$ (pyridine bound to Lewis acidic Sn sites), 1545 $\text{cm}^{-1}$ (protonated pyridine), 1490 $\text{cm}^{-1}$ (protonated pyridine or pyridine bound to Lewis acidic Sn sites), and 1450 $\text{cm}^{-1}$ (pyridine bound to Lewis acidic Sn sites). . . . .   | 623  |
| E.28 Integrated area of the IR peak at 1450 $\text{cm}^{-1}$ as a function of time exposed to dynamic vacuum at 423 K for pyridine-saturated Sn-Beta-F-100. Dashed line at 900 seconds added for reference. . . . .   | 624  |
| E.29 NPA ( $m/z = 59$ ) response factor calibration curve of the mass spectrometer area ratio of NPA/Ar as a function of the molar ratio of NPA/Ar. .   | 625  |

| Figure  | Page |
|---|------|
| E.30 NPA TPD profiles after saturation with 1000 ppm NPA for 4 h at 323 K followed by purging for 4 h (grey trace) and 8 h (black trace) at 338 K in $25 \text{ cm}^3 \text{ s}^{-1} \text{ g}^{-1}$ UHP He on (a) Sn-Beta-F-100, (b) Sn-Beta-F-105, (c) Sn-Beta-F-110, (d) Sn-Beta-F-140, (e) Sn-Beta-F-170, (f) Sn-Beta-F-220, and (g) Sn-Beta-OH-170 and (h) Sn-Beta-OH-200. . . . .   | 626  |
| E.31 NPA TPD profiles on (a) Sn-Beta-F-140 and (b) Sn-Beta-F-170 after saturation in 1000 ppm NPA for 4 h followed by purging at 338 K in $25 \text{ cm}^3 \text{ s}^{-1} \text{ g}^{-1}$ He for 4 h (dark grey trace), 8 h (grey trace), 12 h (light grey trace), and 16 h (faint grey trace). A purge performed at 323 K for 8 h in $25 \text{ cm}^3 \text{ s}^{-1} \text{ g}^{-1}$ He is used to represent a 0 h purge at 338 K (black trace). . . . . | 631  |
| E.32 Molecules of NPA desorbed per molecule of Sn as a function of the purge length on (a) Sn-Beta-F-140 and (b) Sn-Beta-F-170 after saturation in 1000 ppm NPA for 4 h followed by purging at 338 K in $25 \text{ cm}^3 \text{ s}^{-1} \text{ g}^{-1}$ He. A purge performed at 323 K for 8 h in $25 \text{ cm}^3 \text{ s}^{-1} \text{ g}^{-1}$ He is used as a representation for a 0 h purge at 338 K. . . . .  | 632  |
| E.33 NPA desorption rate on (a) Sn-Beta-F-140 and (b) Sn-Beta-OH-170 after saturation in 1000 ppm NPA for 4 h (grey trace) and 16 h (black trace) followed by an 8 h purge at 338 K in $25 \text{ cm}^3 \text{ s}^{-1} \text{ g}^{-1}$ He. . . . .  | 633  |
| E.34 $\text{NH}_3$ ( $m/z = 17$ ) calibration curve of the mass spectrometer area ratio of $\text{NH}_3/\text{Ar}$ as a function of the molar ratio of $\text{NH}_3/\text{Ar}$ . . . . .  | 634  |
| E.35 $\text{NH}_3$ TPD profiles after saturation in $75 \text{ cm}^3 \text{ s}^{-1} \text{ g}^{-1}$ 500 ppm $\text{NH}_3/\text{He}$ at 323 K for 5 h followed by purging in dry He ( $25 \text{ cm}^3 \text{ s}^{-1} \text{ g}^{-1}$ ) at 331 K for 8 h on (a) Sn-Beta-F-100, (b) Sn-Beta-F-105, (c) Sn-Beta-F-110 (d) Sn-Beta-F-140, (e) Sn-Beta-F-170, (f) Sn-Beta-F-200, (g) Sn-BEA-OH-170, (h) Sn-Beta-OH-200. . . . .                                | 635  |
| E.36 $\text{NH}_3$ TPD profiles after saturation of Sn-Beta-F-100 for 5 h in $75 \text{ cm}^3 \text{ s}^{-1} \text{ g}^{-1}$ 500 ppm $\text{NH}_3/\text{He}$ at 323 K followed by purging in dry He ( $25 \text{ cm}^3 \text{ s}^{-1} \text{ g}^{-1}$ ) at 331 K for 0 h (black trace), 4 h (dark grey trace), 8 h (grey trace), and 12 h (light grey trace). . . . .   | 636  |
| E.37 $\text{NH}_3$ TPD profiles after saturation of Sn-Beta-F-100 for 5 h (black trace) or 16 h (grey trace) in $75 \text{ cm}^3 \text{ s}^{-1} \text{ g}^{-1}$ 500 ppm $\text{NH}_3/\text{He}$ at 323 K followed by purging in dry He ( $25 \text{ cm}^3 \text{ s}^{-1} \text{ g}^{-1}$ ) at 331 K for 8 h. . . . .  | 637  |
| E.38 IR peak areas for Sn-BEA-F-100 after saturation and exposure to dynamic vacuum for open Sn sites (squares) and closed Sn sites (diamonds) as a function of time exposed to dynamic vacuum. . . . .   | 638  |
| E.39 IR peak areas for Sn-BEA-F-140 after saturation for open Sn sites (squares) and closed Sn sites (diamonds) as a function of moles adsorbed at saturation. . . . .  | 639  |

| Figure  | Page |
|---|------|
| E.40 2275 $\text{cm}^{-1}$ peak area versus perturbed OH peak area (3000-3600 $\text{cm}^{-1}$ . .  | 642  |
| E.41 2275 $\text{cm}^{-1}$ band area versus negative SiOH band area (ca. 3740 $\text{cm}^{-1}$ ). .   | 643  |
| E.42 FTIR spectra of a dealuminated Beta zeolite after sequential doses of $\text{CD}_3\text{CN}$ . Dashed lines shown at 2316 $\text{cm}^{-1}$ , 2308 $\text{cm}^{-1}$ , 2287 $\text{cm}^{-1}$ , 2275 $\text{cm}^{-1}$ , and 2265 $\text{cm}^{-1}$ . . . . .   | 644  |
| E.43 IR band area for the 2275 $\text{cm}^{-1}$ peak on dealuminated Beta as a function of moles $\text{CD}_3\text{CN}$ adsorbed. The slope of this line is the $\mathcal{E}$ value estimated for the 2275 $\text{cm}^{-1}$ site. . . . .   | 645  |
| E.44 IR spectra of $\text{CD}_3\text{CN}$ three sequential doses (0.05 mol $\text{CD}_3\text{CN}/\text{Sn}$ per dose) on Sn-xerogel. Dashed lines shown at 2316 $\text{cm}^{-1}$ , 2308 $\text{cm}^{-1}$ , 2287 $\text{cm}^{-1}$ , and 2275 $\text{cm}^{-1}$ . . . . .  | 646  |
| E.45 IR spectra of $\text{CD}_3\text{CN}$ dosed on Sn-xerogel to saturation. Dashed lines shown at 2316 $\text{cm}^{-1}$ , 2308 $\text{cm}^{-1}$ , 2287 $\text{cm}^{-1}$ , and 2275 $\text{cm}^{-1}$ . . . . .  | 647  |
| E.46 IR difference spectra at $\text{CD}_3\text{CN}$ saturation coverages (relative to the $\text{CD}_3\text{CN}$ -free wafers and normalized to the maximum intensity of each spectra for clarity). (a) Spectra for (i) Sn-Beta-F-100, (ii) Sn-Beta-F-105, (iii) Sn-Beta-F-110, (iv) Sn-Beta-F-140, (v) Sn-Beta-F-170, (vi) Sn-Beta-F-220. (b) Spectra for (i) Sn-Beta-OH-170, (ii) Sn-Beta-OH-200, (iii) $\text{SnO}_2/\text{Si-Beta}$ , (iv) Sn-xerogel. Dashed lines shown at 2316 $\text{cm}^{-1}$ , 2308 $\text{cm}^{-1}$ , 2287 $\text{cm}^{-1}$ , 2275 $\text{cm}^{-1}$ and 2265 $\text{cm}^{-1}$ . . . . . | 648  |
| E.47 Initial glucose isomerization rates (373 K, normalized to untitrated samples) as a function of pre-adsorbed pyridine (a) per gram, (b) per micropore volume, and (c) per external surface area for Sn-Beta-F-110 (closed circles) and Sn-Beta-F-170 (open circles). . . . .  | 652  |
| E.48 Scanning electron microscope images of Sn-Beta-F-110 and Sn-Beta-F-170.  | 653  |
| E.49 Molar water uptake measured at $P/P_0=0.2$ , after subtracting the contribution from (a) total Sn (estimated by AAS) or (b) Lewis acidic Sn assuming 2:1 $\text{H}_2\text{O}:\text{Sn}$ binding stoichiometry, plotted as a function of the silanol content. . . . .   | 655  |
| E.50 Rate constants per open Sn sites for all Sn-Beta-F samples as a function of the silanol content measured using the $\mathcal{E}$ value for the peak for $\text{CD}_3\text{CN}$ bound to silanol sites centered at 2275 $\text{cm}^{-1}$ . Trendlines show correlation of rate constant with $1/(\text{mol SiOH g}^{-1})$ (dashed line) and $1/(\text{mol SiOH g}^{-1})^2$ (solid line) determined by linear regression. . . . .  | 656  |

| Figure  | Page |
|---|------|
| F.1 Depictions of (a) framework Sn structures (closed, hydrolyzed-open, and defect) that may be present in Sn zeolites, and (b) the proposed molecular structures of Sn sites under dehydrated and hydrated conditions. . . . .   | 677  |
| F.2 (a) IR difference spectra (relative to zero coverage) of Sn-CHA-F-70 upon sequential dosing of CD <sub>3</sub> CN to saturation coverages. Vertical dashed lines are shown for open (2316 cm <sup>-1</sup> ) and closed (2308 cm <sup>-1</sup> ) Sn sites. (b) IR spectra of CD <sub>3</sub> CN-saturated Sn-CHA-F-60, with thin dotted curve representing the sum of the component peaks, shown as thin solid lines for CD <sub>3</sub> CN bound to open (2316 cm <sup>-1</sup> ) and closed Sn sites (2308 cm <sup>-1</sup> ), Sn sites within high defect surfaces (2287 cm <sup>-1</sup> ), hydrogen bound to SiOH groups (2275 cm <sup>-1</sup> ), and gas phase or physisorbed CD <sub>3</sub> CN (2265 cm <sup>-1</sup> ). . . . . | 678  |
| F.3 (a) 2D <sup>119</sup> Sn CPMAT spectrum of hydrated Sn-CHA-F-70 and (b) extracted 1D <sup>119</sup> Sn NMR spectrum for Sn-CHA-F-70 (blue trace) fit with two sets of CSA parameters (light blue and green traces) and their combination (red trace) resulting in better description of the experimental spectrum. The spectrum was acquired on Bruker 600 MHz (14.1 T) DNP NMR spectrometer. MAS = 4 kHz; CP contact time = 1.5 ms; recycle delay = 3.5 s; 256 scans per <i>t</i> <sub>1</sub> increment, and 85 <i>t</i> <sub>1</sub> increments were acquired. The CSA fit was done using solid lineshape feature in Bruker's Topspin program. . . . .   | 679  |
| F.4 (a) 2D <sup>15</sup> N{ <sup>1</sup> H} CPMAT NMR spectrum and (b) extracted 1D <sup>15</sup> N NMR spectra and corresponding CSA fit for pyridine-saturated Sn-CHA-F-70. The spectrum was acquired on Bruker 600 MHz (14.1 T) DNP NMR spectrometer. MAS= 4 kHz; CP contact time= 8.0 ms; recycle delay = 4.5 s; 112 scans per <i>t</i> <sub>1</sub> increment, and 112 <i>t</i> <sub>1</sub> increments were acquired. The CSA fit was performed using the solid lineshape feature in Bruker's Topspin program. . . . .  | 680  |
| F.5 DFT optimized structures for (a) hydrated closed Sn sites, defect-open Sn sites, and hydrolyzed-open Sn sites, for dehydrated closed Sn sites, defect Sn sites, and hydrolyzed-open Sn sites, and (b) for pyridine saturated closed Sn, and defect Sn sites. Calculated isotropic chemical shifts ( $\delta_{iso}$ ), span ( $\Omega$ ), and skew ( $\kappa$ ) are shown for each site. Details of DFT calculations are in Section F.6.13. . . . .  | 681  |
| F.6 XRD patterns for (a) Si-CHA-F (b) Sn-CHA-F-60 (c) Sn-CHA-F-70 (d) Sn-Beta-F-116 and (e) Sn-xerogel. Patterns are normalized to their maximum intensity and offset vertically for clarity. . . . .   | 698  |



| Figure   | Page |
|--|------|
| F.7 (a) Ar adsorption isotherms for Si-CHA-F (circles) Sn-CHA-F-60 (diamonds), Sn-CHA-F-70 (triangles) and N <sub>2</sub> adsorption for Sn-Beta-F-116 (squares). Micropore volumes are reported in Table F.1. (b) water adsorption isotherms on Sn-CHA-F-60 (squares), Sn-CHA-F-70 (triangles), Sn-Beta-F-116 (diamonds), and Si-CHA (circles). . . . . | 699  |
| F.8 Pore size distribution of (a) Sn-CHA-F-60 and (b) Sn-CHA-F-70 from NLDT analysis of Ar adsorption isotherm (87 K). Solid lines included to guide the eye. . . . .  | 700  |
| F.9 Pore size distribution of (a) Si-CHA-F and (b) Sn-xerogel from NLDT analysis of Ar adsorption isotherm (87 K). Solid lines included to guide the eye. . . . .  | 701  |
| F.10 DRUV spectra in Kubelka-Munk units (normalized to the maximum F(R) intensity) for (a) Sn-CHA-F-60 (b) Sn-CHA-F-70, (c) Sn-Beta-F-116, and (d) Sn-xerogel collected (i) under ambient conditions (thin solid line), (ii) after dehydration at 523 K (thick solid line), and (iii) after rehydration at 303 K (dashed line). . . . .                  | 702  |
| F.11 DRUV spectra for Sn-CHA-70 after dehydration in flowing He at 523 K (dotted line) and 623 K (solid line). . . . .   | 703  |
| F.12 Tauc plots for the samples in this study. . . . .   | 704  |
| F.13 (a) TGA profile for Sn-CHA-70 and (b) moles of water desorbed (per g zeolite) above 623 K (solid line) compared to the moles of Sn present in Sn-CHA-F-70 (dotted line). . . . .  | 706  |
| F.14 (a) Fractional mass lost and (b) heat flow (per g zeolite) as functions of temperature for (i) Sn-CHA-F-70 (ii) Si-CHA-F and (iii) Sn-Beta-F-116. . . . .   | 707  |
| F.15 IR difference spectra (relative to zero coverage) of (a) Si-CHA-F and (b) Sn-Beta-F-116 upon sequential dosing of CD <sub>3</sub> CN to saturation coverages; dashed lines are shown at 2316 cm <sup>-1</sup> and 2308 cm <sup>-1</sup> for open and closed Sn sites, respectively. . . . .   | 712  |
| F.16 IR difference spectra (relative to zero coverage) for (a) Sn-CHA-F-60 and (b) Sn-CHA-F-70 saturated with pyridine and then exposed to dynamic vacuum (10 <sup>-1</sup> Torr, 900 s). Spectra are offset vertically for clarity. . . . .   | 713  |
| F.17 Temperature programmed desorption profile for NH <sub>3</sub> -saturated (a) Sn-CHA-F-60 and (b) Sn-CHA-F-70. . . . .   | 714  |

| Figure   | Page |
|--|------|
| F.18 (a) Transient reaction profile for the reaction of ethanol and propionaldehyde over Sn-CHA (333K, 0.6 M propionaldehyde diluted in ethanol solvent). Linear fit to first four data points (dotted line) demonstrates that determination of initial rate by extrapolation to initial time is accurate for data within the first 3600s of reaction time. (b) Propionaldehyde conversion (circles), ethanol conversion (triangles), and C <sub>3</sub> mass balance ((propionaldehyde + n-propanol + 1,1-diethoxy propane)/(moles propionaldehyde converted)) (squares) as a function of time. . . . .   | 717  |
| F.19 Equilibrium conversion of (a) acetone as a function of initial ethanol:acetone ratio (diamonds, 333 K; circles, 313 K) and (b) propionaldehyde as a function of initial ethanol:propionaldehyde ratio (333 K). Determined using AIChE DIPPR database [662]. . . . .   | 718  |
| F.20 m/z spectra for n-propanol formed over Sn-CHA-F-60 from reactions in (a) C <sub>2</sub> D <sub>5</sub> OH and (b) C <sub>2</sub> H <sub>5</sub> OH solvent. . . . .   | 720  |
| F.21 m/z spectra for n-propanol formed over Sn-Beta-F-116 from reaction of C <sub>2</sub> D <sub>5</sub> OH and propionaldehyde in C <sub>2</sub> D <sub>5</sub> OH solvent. . . . .   | 721  |
| F.22 (a) 1D <sup>119</sup> Sn DNP enhanced CP spin-echo MAS spectrum for hydrated Sn-CHA-F-70 (MAS = 4 kHz, CP contact time = 1.5 ms, recycle delay = 3.5 s, 512 scans). (b) Reconstructed 1D <sup>119</sup> Sn DNP enhanced CP-CPMG spectrum for dehydrated Sn-CHA-F-70 after dehydration under vacuum (1*10 <sup>-4</sup> Torr) at 773 K (MAS = 10 kHz, CP contact time = 1.5 ms, recycle delay = 3.0 s, 24636 scans). 20 echoes were acquired, and 17 echoes were used to reconstruct the full-echo spectrum. Both were measured on a Bruker 600 MHz (14.1 T) DNP spectrometer. (c) extracted 1D <sup>119</sup> Sn NMR spectrum for Sn-CHA-F-70 (blue trace) fit with one set of CSA parameters (red trace). The spectrum was acquired on Bruker 600 MHz (14.1 T) DNP NMR spectrometer. MAS= 4 kHz; CP contact time= 1.5 ms; recycle delay = 3.5 s; 256 scans per <i>t1</i> increment, and 85 <i>t1</i> increments were acquired. The CSA fit was done using solid lineshape feature in Bruker's Topspin program2D. . . . . | 722  |

| Figure  | Page |
|---|------|
| F.23 (a) 1D DNP-enhanced reconstructed CP-CPMG spectrum of hydrated Sn-xerogel. MAS = 10 kHz. Number of scans = 512. Recycle delay = 3.9 s. 20 echoes were collected, and 19 echoes were used to reconstruct the single full-echo spectrum. (b) 2D DNP-enhanced CPMAT spectrum of hydrated Sn-xerogel. MAS = 4 kHz. Recycle delay = 3.9 s. Number of scans = 224 per $t1$ increment. 91 $t1$ increments were collected and used. Both spectra were measured on Bruker 600 MHz (14.1 T) DNP spectrometer. (c) The sum of the positive projection of the $f1$ (isotropic) dimension of the 2D CPMAT spectrum (blue trace), and the corresponding peak deconvolution (red trace) using the solid lineshape feature implemented in Bruker Topspin software. . . . . | 724  |
| F.24 (a) 2D DNP enhanced CPMAT spectrum of dehydrated Sn-CHA-F-70, measured on Bruker 400 MHz (9.4 T) DNP spectrometer. MAS = 5 kHz. Recycle delay = 6.2 s. CP contact time = 4.0 ms. 896 scans were acquired for each $t1$ increment, and 16 $t1$ increments were collected. (b) 1D DNP enhanced CP-Total Sideband Suppression (CP-TOSS) spectrum of dehydrated Sn-CHA-F-70, measured on Bruker 400 MHz (9.4 T) DNP spectrometer, and the corresponding fit of isotropic sites (-437 and -480 ppm). (c) Fit values of CSA parameters of the isotropic site extracted at -437 ppm on the isotropic dimension of the 2D CPMAT spectrum for dehydrated Sn-CHA-F-70. CSA fit was done using the solid lineshape feature in Bruker Topspin software . . . . .       | 725  |
| F.25 $^{29}\text{Si}$ DNP enhanced CPMAS NMR spectra for hydrated Sn-CHA-F-70, measured on Bruker 600 MHz (14.1 T) DNP spectrometer. The corresponding peak deconvolution (envelope: red trace) using solid lineshape feature implemented in Bruker Topspin software. . . . .   | 726  |
| F.26 $^{29}\text{Si}$ DNP enhanced CPMAS NMR spectra for hydrated Sn-CHA-F-70 with varying CP contact time, measured on Bruker 600 MHz (14.1) DNP spectrometer. MAS = 10kHz. Recycle delay = 5 s. 32 to 128 scans were acquired to have spectra with a high signal-to-noise ratio. . . . .  | 727  |
| F.27 $^{29}\text{Si}$ NMR direct-excitation spectra for hydrated Sn-CHA-F-60 measured on 700 MHz (16.4 T) NMR spectrometer. The experimental spectrum (blue trace) was fit (red trace) with the solid lineshape feature in Bruker Topspin software. MAS = 10 kHz. Number of scans = 40. Recycle delay = 3600 s to make sure of full relaxation of NMR signals. The ratio of two sites ( $Q_4$ vs. $Q_3$ ) was estimated by integrating the area of each peak. . .   | 728  |

| Figure   | Page |
|--|------|
| F.28 1D $^{119}\text{Sn}$ DNP enhanced reconstructed CP-CPMG spectrum for pyridine saturated, dehydrated (a) Sn-CHA-F-70 and (b) Sn-xerogel. MAS= 10 kHz. Recycle delay= (a) 3.0 s and (b) 6.2 s. CP contact time= (a) 4.0 ms and (b) 1.5 ms. (a) 520 and (b) 1024 scans were acquired. 20 echoes were acquired, and (a) 19 echoes and (b) 6 echoes were used to reconstruct the single full-echo spectra. Both spectra were acquired on Bruker 600 MHz (14.1 T) DNP NMR spectrometer. . . . .   | 729  |
| F.29 (a) 2D $^{119}\text{Sn}$ CPMAT NMR spectra for pyridine-saturated Sn-CHA-F-70 and (b) extracted 1D $^{119}\text{Sn}$ NMR spectra for pyridine-saturated Sn-CHA-F-70 for the two resonances observed in the isotropic dimension. The spectrum was acquired on Bruker 600 MHz (14.1 T) DNP NMR spectrometer. MAS= 6 kHz; CP contact time= 4.0 ms; recycle delay = 3.0 s; 448 scans per $t1$ increment, and 107 $t1$ increments were acquired. The CSA fit was done using the solid lineshape feature in Bruker's Topspin program. . . . . | 730  |
| F.30 1D $^{15}\text{N}$ NMR spectra for pyridine saturated, dehydrated Sn-CHA-F-70 (dotted lines are shown at 289 ppm and 262 ppm for pyridine hydrogen bound to SiOH groups and pyridine bound to Lewis acidic Sn sites, respectively). The spectrum was acquired on Bruker 600 MHz (14.1 T) DNP NMR spectrometer. MAS= 10 kHz; CP contact time= 8.0 ms; recycle delay = 4.5 s; 512 scans were acquired. . . . .  | 731  |
| F.31 DNP-enhanced $^{15}\text{N}$ CPMAS spectrum of $^{15}\text{N}$ pyridine treated dehydrated Sn-xerogel (MAS = 11.5 kHz, Recycle delay = 6.8 s, number of scans = 64). The spectrum was acquired on Bruker 600 MHz (14.1 T) DNP NMR spectrometer. . . . .   | 732  |
| F.32 DNP-enhanced $^{15}\text{N}$ CPMAS spectrum of $^{15}\text{N}$ pyridine treated dehydrated Si-CHA-F. The spectrum was acquired on Bruker 600 MHz (14.1 T) DNP NMR spectrometer. MAS= 10 kHz; CP contact time= 8.0 ms; recycle delay = 6.0 s; 7136 scans were acquired. . . . .  | 732  |
| F.33 DFT optimized (B3LYP-D3) structures for pyridine saturated (a) closed Sn with 2 bound pyridine and (b) defect Sn sites with one bound pyridine. Atoms that were not bound directly to Sn were treated with the 6-31G(d,p) basis set (Si: yellow, O: red, C: gray, H: white)), while O and N atoms bonded to Sn were treated with the 6-31+G(d) basis set (N: green, O: red) and Sn (blue) was treated with the LanL2DZ effective core pseudopotential augmented with a d polarization function. . . . .                                 | 734  |

## ABSTRACT

Di Iorio, John R. PhD, Purdue University, December 2018. Synthetic Methods to Control Aluminum Proximity in Chabazite Zeolites and Consequences for Acid and Redox Catalysis. Major Professor: Rajamani Gounder.

Zeolites contain distinct Brønsted acid site ( $H^+$ ) ensembles that arise from differences in the arrangement of framework Al atoms ( $Al-O(-Si-O)_x-Al$ ) between isolated ( $x \geq 3$ ) and paired ( $x=1,2$ ) configurations, the latter defined by their ability to exchange certain divalent cations (e.g.,  $Cu^{2+}$ ,  $Co^{2+}$ ). Manipulation of the synthesis conditions used to prepare MFI zeolites has been proposed to influence the proximity of framework Al atoms, but in a manner that is neither determined randomly nor by any simple predictive rules. Moreover, the effects of proton proximity have been studied for hydrocarbon catalysis in MFI zeolites, but interpretations of catalytic phenomena are convoluted by effects of the distribution of framework Al atoms among different crystallographic tetrahedral sites (T-sites) and diverse pore environments (i.e., confining environments) present in MFI. This work instead focuses on the chabazite (CHA) framework, which contains a single crystallographically-distinct lattice tetrahedral site (T-site) that allows clarifying how synthesis conditions influence Al proximity, and in turn, how  $H^+$  site proximity influences catalysis independent of T-site location.

Selective quantification of the number and type of  $H^+$  site ensembles present in a given zeolite allows for more rigorous normalization of reaction rates by the number of active sites, but also for probing the number and identity of active sites on bi-functional catalysts that contain mixtures of Brønsted and Lewis acid sites. Gaseous  $NH_3$  titrations can be used to count the total number of protons on small-pore CHA zeolites, which are inaccessible to larger amine titrants (e.g., pyridine, alkylamines),

and can be used to quantify the exchange stoichiometry of extraframework metal cations (e.g.,  $\text{Cu}^{2+}$ ,  $[\text{CuOH}]^+$ ) that are stabilized at different framework Al arrangements. Additionally, paired Al sites in CHA zeolites can be titrated selectively by divalent  $\text{Co}^{2+}$  cations, whose sole presence is validated by measuring UV-Visible spectra, counting residual protons after  $\text{Co}^{2+}$  exchange, and titration of paired Al with other divalent cations (e.g.,  $\text{Cu}^{2+}$ ). These different titration procedures enabled reliable and reproducible quantification of different Al arrangements, and recognition of the effects of different synthetic methods on the resulting arrangement of framework Al atoms in CHA zeolites.

Upon the advent of this suite of characterization and titration tools, different synthetic methods were developed to crystallize CHA zeolites at constant composition (e.g.,  $\text{Si}/\text{Al} = 15$ ) but with systematic variation in their paired Al content. The substitution of N,N,N-trimethyl-1-adamantylammonium ( $\text{TMAda}^+$ ) cations for  $\text{Na}^+$  in the synthesis media ( $\text{Na}^+/\text{TMAda}^+ < 2$ ), while holding all other synthetic variables constant, resulted in CHA zeolites of similar composition ( $\text{Si}/\text{Al} = 15$ ) and organic content (ca. 1  $\text{TMAda}^+$  per cage), but with percentages of paired Al (0-44%) that increased with the total amount of sodium retained on the zeolite product. This result suggests that sodium atoms are occluded near the ammonium group of  $\text{TMAda}^+$  leading to the formation of a paired Al site. Replacement of  $\text{Na}^+$  by  $\text{K}^+$  in the synthesis media allowed for the crystallization of CHA ( $\text{Si}/\text{Al} = 15$ ) at much higher ratios of alkali to  $\text{TMAda}^+$  ( $\text{K}^+/\text{TMAda}^+ < 20$ ), likely due to the suppression of alternate crystalline phases by  $\text{K}^+$ . Incorporation of  $\text{K}^+$  during crystallization of CHA did not correlate with the formation of paired Al sites, but instead resulted in the displacement of one  $\text{TMAda}^+$  molecule by two  $\text{K}^+$  cations, which likely assist in the stabilization of the CHA framework at low  $\text{TMAda}^+$  concentrations. Ab initio molecular dynamics simulations were used to assess the stability of various Al-Al arrangements in the presence of different combinations of  $\text{Na}^+$ ,  $\text{K}^+$ , and  $\text{TMAda}^+$  cations, and provide thermodynamic insight into electrostatic interactions between  $\text{Na}^+$  and  $\text{TMAda}^+$  cations that stabilize paired Al sites in CHA.

Using these synthetic procedures to prepare CHA zeolites of similar composition, but with varied arrangements of framework Al, the catalytic consequences of framework Al arrangement were investigated using acid and redox catalysis. The low-temperature (473 K) selective catalytic reduction of NO<sub>x</sub> with NH<sub>3</sub> (NH<sub>3</sub>-SCR) was investigated over Cu-exchanged CHA zeolites containing various Al arrangements. Cu cations exchange as both divalent Cu<sup>2+</sup> and monovalent [CuOH]<sup>+</sup> complexes, which exchange at paired and isolated Al sites, respectively, and turnover with similar SCR rates (473 K). In situ and operando X-ray absorption spectroscopy (XAS) were used to monitor the oxidation state and coordination environment of Cu as a function of time and environmental conditions. Rationalization of these experimental observations by first-principles thermodynamics and ab initio molecular dynamics simulations revealed that both Cu<sup>2+</sup> and [CuOH]<sup>+</sup> complexes are solvated by NH<sub>3</sub> and undergo reduction to Cu<sup>+</sup> upon oxidation of NO with NH<sub>3</sub>. Cu<sup>+</sup> cations become mobilized by coordination with NH<sub>3</sub> under reaction conditions (473 K, equimolar NO and NH<sub>3</sub> feed), and activate O<sub>2</sub> through a dicopper complex formed dynamically during reaction. These results implicate the spatial density of nominally site-isolated Cu cations and, in turn, the arrangement of anionic framework Al atoms that anchor such cationic Cu complexes, influence the kinetics of O<sub>2</sub> activation in selective oxidation reactions, manifested as SCR rates (per 1000 A<sup>3</sup>) that depend quadratically on Cu density (per 1000 A<sup>3</sup>) and become rate-limiting processes in practice at low temperatures.

Furthermore, first-order and zero-order rate constants (415 K, per H<sup>+</sup>) of methanol dehydration, a probe reaction of acid strength and confinement effects in solid Brønsted acids, are nearly one order of magnitude larger on paired than on isolated protons in CHA zeolites, reflecting differences in prevalent mechanisms and apparent enthalpic and entropic barriers at these different active site ensembles. Yet, these differences in rate constants and activation parameters at isolated and paired protons do not persist within larger pore zeolites (e.g., MFI). In situ IR spectra measured during steady-state methanol dehydration catalysis (415 K, 0.05-22 kPa CH<sub>3</sub>OH)

reveal that surface methoxy species are present in CHA zeolites containing paired protons, but not in CHA zeolites containing only isolated protons or MFI zeolites, providing evidence that sequential dehydration pathways via methoxy intermediates become accessible on paired protons in CHA. Density functional theory is used to provide atomistic detail of confined intermediates and transition states at isolated and paired protons in CHA and MFI zeolites, indicating that paired protons in CHA preferentially stabilize dehydration transition states that are partially-confined within the 8-membered ring (8-MR) of CHA. These findings provide evidence that catalytic diversity for the same stoichiometric reaction among zeolites of fixed structure and composition, even for frameworks containing a single T-site, can be introduced deliberately through synthetic control of the atomic arrangement of matter.



## 1. INTRODUCTION

Zeolites are crystalline, microporous frameworks (pore diameter:  $<2$  nm) constructed from tetrahedrally-coordinated  $\text{Si}^{4+}$  heteroatoms (T-atom) connected by bridging  $\text{O}_2^-$  atoms (chemical formula:  $\text{SiO}_2$ ). Differences in the coordination environment around a given T-atom yields a symmetry-distinct tetrahedral site (T-site), whose connectivity to adjacent T-sites (either of similar or distinct symmetry) allows for a diversity of crystallographically-unique frameworks ( $>230$  discovered structures [1];  $>10^6$  predicted frameworks [2, 3]). Isomorphous substitution of  $\text{Al}^{3+}$  for  $\text{Si}^{4+}$  results in the formation of framework anionic charges (i.e.,  $\text{AlO}_2^-$ ) that require charge-balancing by extraframework cations (e.g.,  $\text{Na}^+$ ), whose identity can be tuned for various applications [4–7], and leads to the formation of Bronsted acid sites ( $\text{H}^+$ ) when extraframework protons charge-balance lattice anionic charges. Aluminosilicate zeolites are widely used as solid acid catalysts in the petrochemical industry [8, 9], because of the diverse structure of their microporous channels, which are of molecular dimension ( $<2$  nm) and can regulate reactivity and selectivity based on the size and structure of reactants, products, or transition states [10–13].

Early investigations of the identity of the active site in aluminosilicate zeolites reported that hexane cracking rates (per g, 811 K) increased linearly with total Al density (per g) in MFI zeolites [14]. These results suggested that all  $\text{H}^+$  sites are catalytically-equivalent in MFI and that rates of hexane cracking (811 K) are independent of composition ( $\text{Si}/\text{Al} = 10\text{--}10000$ ) and topographic location, as would be expected for a single-site catalyst [15]. More recently, catalytic turnover rates of hydrocarbon reactions have been recognized to depend on the location of  $\text{H}^+$  sites within MOR zeolites, despite equivalent acid strength as described rigorously by deprotonation energy (DPE) [16], because the size and shape of microporous voids that

stabilize confined intermediates and transition states through van der Waals interactions [17–22]. Deconvolution of the catalytic behavior of zeolites containing active sites located within voids of different size requires preferential titration of protons in certain ring sizes or acquisition of zeolites of different provenance [21, 23]. These observations suggest that the catalytic behavior of zeolite catalysts strongly depends on the synthetic conditions used to prepare such frameworks.

Synthetic control of the location of Al atoms within a given zeolite is still an emerging area of research, but has been demonstrated in ferrierite zeolites (FER) synthesized in the presence of multiple organic structure directing agents (SDAs) of different size [24–28] and in MFI zeolites when synthesized using mixtures of organic and inorganic SDAs [29–32]. Turnover rates in zeolite catalysis, however, may still be further convoluted by the proximity of  $H^+$  sites, which is regulated by the proximity of framework Al atoms. Distinct Brønsted acid site configurations within a given zeolite arise from different arrangements ( $Al-O(-Si-O)_x-Al$ ) of framework Al atoms between isolated ( $x \geq 3$ ) or paired configurations ( $x = 1, 2$ ; Figure 1.1), where the latter are defined by their ability to ion-exchange divalent cations. One example, is in Cu-exchanged zeolites utilized for the selective catalytic reduction (SCR) of  $NO_x$  with  $NH_3$  where  $Cu^{2+}$  cations exchange non-selectively as monovalent  $[CuOH]^+$  complexes at isolated Al and as divalent  $Cu^{2+}$  cations at paired Al in both MFI [33] and chabazite (CHA) [34–42] zeolites. Thus, synthetic methods to control the proximity of framework Al atoms can open new opportunities to introduce structural and catalytic diversity in a given zeolite with fixed elemental composition, but require methods for quantification of the distribution of Al atoms in the zeolite framework.

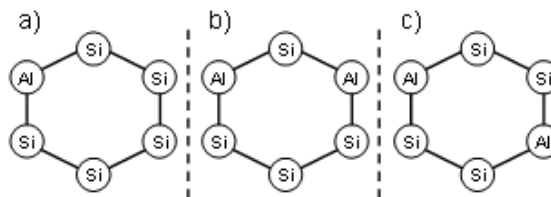


Figure 1.1. Different arrangements of Al atoms between (a) isolated and (b, c) paired configurations in a 6-MR.

Solid-state magic-angle spinning nuclear magnetic resonance (SS MAS NMR) has been used to resolve the connectivity of Si nuclei within different zeolite frameworks [43–47], yet  $^{29}\text{Si}$  MAS NMR is incapable of resolving if neighboring Al atoms are positioned in the same ring or channel, or are facing different channels, as both configurations give rise to identical NMR lines [48]. Multiple quantum (MQ)  $^{27}\text{Al}$  MAS NMR techniques can resolve interactions between adjacent Al nuclei ( $<5$  nm) [49–52], but are unable to resolve Al pairing within zeolites due to a lack of correlation between the isotropic chemical shift and T-site local environment (T-O-T angle) in silica-rich zeolites [53, 54]. Moreover, assignment of T-site specific chemical shifts requires the use of quantum chemical/molecular mechanics simulations to predict stable structures for specific local geometries that give rise to experimentally observed chemical shifts [55–58]. The direct quantification of paired Al sites in pentasil zeolites (MOR, BEA, MFI, FER) has been studied via ion-exchange with divalent  $\text{Co}^{2+}$  cations, as a chemical titrant [48, 59–70, 70–74]. Yet, clear evidence for a single ion-exchange procedure that leads to the exchange of exclusively divalent  $\text{Co}^{2+}$  cations is convoluted amongst multiple reports [48, 59–70, 70–74] and is often conflicting [48, 60]. Methods for the selective exchange of solely divalent  $\text{Co}^{2+}$  cations are still inconclusive, but more rigorous development of these procedures can lead to techniques that allow for direct chemical titration of paired Al sites in zeolites.

Despite the lack of a definitive method to quantify the arrangement of Al atoms in zeolites, the effects of proton proximity on catalysis have been studied in MFI zeolites

through variation in bulk Al concentration (Si/Al) [61, 75, 76]. Turnover rates (per  $\text{H}^+$ ) of hydrocarbon cracking generally increased with total Al content [61, 75], but changes in the bulk composition only influence Al proximity on average. Recently, modification of the  $\text{Na}^+$  cation concentration in the synthesis of MFI zeolites led to changes in the number of paired Al sites [74], as measured by saturation with ion-exchanged  $\text{Co}^{2+}$  cations [48, 48, 65, 68, 70, 73, 74], but the influence of anionic charged species ( $\text{OH}^-$ ,  $\text{Cl}^-$ ,  $\text{NO}_3^-$ ) and different sources of Si and Al precursors, which was not controlled for, were also shown to modify the Al isolation, but often with changes in bulk Al concentration [48, 65, 74]. As a result, the routes used to synthesize MFI zeolites can influence the arrangement of framework Al atoms, but in a manner that is neither random nor defined by any deterministic rules. Moreover, the structure of a paired Al site in MFI, is ill-defined, as MFI contains three distinct 6-membered rings that can exchange divalent  $\text{Co}^{2+}$  cations. Thus, while paired  $\text{H}^+$  sites in MFI (Si/Al = 13-140) have been proposed to increase alkene oligomerization [77] and alkane cracking [75] turnover rates, concomitant changes in the distribution of Al among different void environments (i.e., straight and sinusoidal channels, and intersections) [61] have prevented unambiguous kinetic assessments of proton proximity effects in zeolites.

In this work, we focus on the CHA framework, which is constructed from the translation of double six-membered ring (6-MR) hexagonal prisms in a AABBC stacking sequence to form larger CHA cages (0.72 x 0.72 x 1.2 nm), whose access is regulated by 8-MR windows (ca. 0.38 nm). As a result, the CHA framework contains a single crystallographically-distinct T-site, which simplifies interpretation of structural characterization data and thus allows clarifying how different synthetic procedures influence Al pairing independent of T-site and, in turn, how Al arrangement influences redox catalysis at extraframework Lewis acid sites and Brønsted acid catalysis. Moreover, the high-symmetry of the CHA framework acts as a well-defined model system to facilitate the integration of theoretical and experimental assessments of catalytic active sites and reaction mechanisms in zeolites.

The quantification of  $H^+$  sites in CHA zeolites requires judicious choices of the titrants used because 8-MR windows (0.38 nm) limit transport through the framework and prevent typically used bulky titrants (e.g., alkylamines, pyridine) from accessing all  $H^+$  sites in CHA [49, 78]. Furthermore, titration of the number of  $H^+$  sites that remain after ion-exchange with redox-active metals (e.g.,  $Cu^{2+}$ ) cannot be performed using aqueous phase procedures involving small monovalent cations (e.g.,  $Na^+$  or  $NH_4^+$ ) because these titrants will also displace extraframework  $Cu^{2+}$  cations. Chapter 2 discusses titration methods using gaseous  $NH_3$  that selectively titrate  $H^+$  sites in metal-exchanged zeolites when Lewis acid-bound and physisorbed  $NH_3$  are removed after  $NH_3$  saturation steps, such as by flushing in wet helium at 433 K. IR spectra indicate that these  $NH_3$  saturation and purging steps led to the complete disappearance of Bronsted acidic OH stretching modes in small-pore CHA zeolites, contrasting the inability of larger amine titrants (e.g., n-propylamine) to access the same number of  $H^+$  sites in CHA ( $<0.25$ ).  $NH_3$  titration of residual  $H^+$  sites remaining after  $Cu^{2+}$  ion-exchange in low-silica CHA zeolites ( $Si/Al = 4.5$ ,  $Cu/Al < 0.20$ ) reveals that 2  $H^+$  are removed per Cu after oxidative treatments, but only 1  $H^+$  is removed per Cu after reduction of  $Cu^{2+}$  by NO and  $NH_3$  (473 K), indicating that a  $Cu^+/H^+$  pair forms during the NO and  $NH_3$  assisted reduction of  $Cu^{2+}$  cations. These titration procedures probe the dynamic role of  $Cu^{2+}$  active sites during the selective catalytic reduction of NO with  $NH_3$  and can be used to elucidate exchange stoichiometries of extraframework cations, which is sensitive to the underlying Al arrangement in small-pore CHA zeolites.

CHA zeolites prepared with different amounts of framework Al ( $Si/Al = 5-25$ ) contain different fractions of paired Al sites because changes to the bulk Al content, on average, change the total number of paired Al sites. Titration of residual  $H^+$  sites remaining after Cu exchange of CHA zeolites ( $Si/Al = 5-25$ ) indicated that Cu preferentially exchanges first as divalent  $Cu^{2+}$  at paired Al sites (2  $H^+$  removed per Cu) and then as monovalent  $[CuOH]^+$  at isolated Al sites, consistent with density functional theory (DFT) calculations that predict larger adsorption energies for  $Cu^{2+}$  at

paired Al than for  $[\text{CuOH}]^+$  at isolated (dehydrated,  $\text{Cu}^{2+}$ :  $-70 \text{ kJ mol}^{-1}$ ;  $[\text{CuOH}]^+$ :  $-10 \text{ kJ mol}^{-1}$ ) [79]. CHA zeolites ( $\text{Si}/\text{Al} = 5\text{-}25$ ) were also equilibrated with aqueous  $\text{Co}^{2+}$  ion-exchange solutions, in order to corroborate the total number of paired Al sites measured from Cu-exchange. In contrast with Cu exchange, Co exchanged predominately as divalent  $\text{Co}^{2+}$  cations, evident in the replacement of two  $\text{H}^+$  sites per exchanged Co, independent of Co content. Saturation  $\text{Co}^{2+}/\text{Al}$  and  $\text{Cu}^{2+}/\text{Al}$  uptakes were identical on all CHA zeolites ( $\text{Si}/\text{Al} = 5\text{-}25$ ), indicating that  $\text{Co}^{2+}$  cations selectively titrate paired Al in CHA zeolites, and that such protocols can be used to quantify paired Al sites given additional validation of exchange procedures using titration and spectroscopic methods to verify the sole presence of  $\text{Co}^{2+}$  cations.

This suite of titration procedures was used to investigate synthetic methods to prepare CHA at fixed composition, but with different fraction of paired Al sites, as discussed in Chapter 3. CHA zeolites ( $\text{Si}/\text{Al} = 15\text{-}30$ ) crystallized using only N,N,N-trimethyl-1-admantylammonium cations ( $\text{TMAda}^+$ ) contained predominantly isolated framework Al, evident in their inability to exchange divalent cations. Fractional replacement of  $\text{TMAda}^+$  for  $\text{Na}^+$  in CHA crystallization media ( $\text{Na}^+/\text{TMAda}^+ < 2$ ), with all other synthesis variables held constant, crystallized CHA zeolites of similar composition ( $\text{Si}/\text{Al}=15$ ), but with a total number of Al pairs that increased as the amount of  $\text{Na}^+$  occluded on the crystalline product increased. These results suggest that the relative ratio of bulky organic (e.g.,  $\text{TMAda}^+$ ) and small inorganic (e.g.,  $\text{Na}^+$ ) cations in the synthesis media, which determines its cationic charge density, influences the formation of paired Al sites in CHA zeolites.  $\text{Na}^+$  concentrations exceeding  $\text{Na}^+/\text{TMAda}^+$  of 2 resulted in a phase transformation to MOR, likely caused by the need to crystallize higher T-atom density frameworks to satisfy electrostatic constraints imposed by the charge density of the synthesis media. These observations extend concepts of charge density mismatch theory, which have previously led to preparation of new synthetic frameworks and compositions, to influence the arrangement of framework Al atoms in a given zeolite at fixed composition and provide new routes to introduce structural and catalytic diversity in zeolites.

Interactions between organic and inorganic SDAs were further probed in Chapter 4 using  $K^+$  cations instead of  $Na^+$  during the synthesis of CHA zeolites with  $TMAda^+$ . CHA zeolites ( $Si/Al = 15$ ) crystallized across a much wider range of  $K^+/TMAda^+$  ratios ( $<20$ ) than when  $Na^+$  was used as the inorganic SDA ( $Na^+/TMAda^+ < 2$ ). These results highlight the ability of different alkali cations to act as structure-directing agents [80] and likely reflect the limited role that  $K^+$  has as a structure-directing agent, which instead aids in the crystallization of CHA by preventing the formation of other undesired phases, as has been previously suggested for the synthesis of IFR zeolites [81]. SEM micrographs reveal the formation of a secondary phase at  $K^+/TMAda^+ > 10$ , which contains a higher concentration of both  $K^+$  and Al (from EDS mapping) than the bulk average measured by atomic absorption spectroscopy, suggesting the formation of a K-rich CHA phase, which appears to sequester excess  $K^+$  at high  $K^+/TMAda^+$  ratios. Unlike CHA synthesized using mixtures of  $Na^+$  and  $TMAda^+$ , the number of  $TMAda^+$  molecules per cage decreases as the amount of occluded  $K^+$  increases, which is not accompanied by a subsequent increase in the number of paired Al sites. These results suggest that the role of  $K^+$  during crystallization of CHA zeolites is markedly different than that of  $Na^+$ . Ab initio molecular dynamics simulations reveal that electrostatic interactions between the quaternary N-atom of  $TMAda^+$  and the anionic Al center favor the formation of isolated Al sites (i.e., sites that are not exchangeable by  $Co^{2+}$ ), but that introduction of  $Na^+$  alters the free energy landscape to favor the formation of paired Al. While these observations do not directly describe the incorporation of Al during crystallization, which is often a kinetically-controlled process, they do provide evidence that different alkali cations can influence the stability of different Al-Al arrangements in CHA zeolites during crystallization, and that experimentally-guided calculations can be used to predict material properties of different synthesis routes.

Predictable synthetic control of the arrangement of framework Al atoms in zeolites at fixed composition enables routes to prepare zeolites with tunable catalytic and structural properties, while maintaining a constant density of active sites. Cu-

exchanged zeolites are widely used for the selective catalytic reduction of NO<sub>x</sub> with NH<sub>3</sub>, but suffer from deactivation due to exposure to water vapor (up to 10 wt%) at high-temperatures (up to 1073 K) in automotive applications. Chapter 5 investigates the deactivation of three different small-pore cage-based zeolite frameworks (AEI, CHA, RTH) after hydrothermal aging, in order to study the effect of zeolite topology on the structural and kinetic changes that occur to Cu-zeolites used in NO<sub>x</sub> abatement. Rates of NO<sub>x</sub> SCR (473 K, per Cu) on Cu-exchanged AEI and CHA zeolites, which are constructed from double six-membered ring building units, decrease to a similar extent after hydrothermal aging, suggesting a similar resistance to deactivation in both these frameworks. Cu-RTH, which is a small-pore pentasil framework with a pseudo-1D connectivity, essentially deactivates completely after hydrothermal aging. These findings highlight the beneficial properties conferred by double six-membered ring (D6R) composite building units and demonstrate that both exposure to hydrothermal aging conditions and subsequent exposure to SCR reactants at low temperatures are responsible for deleterious structural changes to Cu sites. These results further indicate that the predictions of active site stability cannot be inferred solely from assessments of framework structural integrity, but also require detailed kinetic characterization of Cu active sites after hydrothermally aged zeolites are exposed to low temperature SCR reaction conditions.

The nature of the Cu active sites formed in Cu-CHA zeolites and their involvement in the NO<sub>x</sub> SCR mechanism are described in Chapter 6 and 7. The presence of Cu<sup>2+</sup> and [CuOH]<sup>+</sup> cations is elucidated using ex situ IR and X-ray absorption spectroscopies and titration with gas-phase NH<sub>3</sub> after both oxidative and reductive treatments. Cooperative use of in operando and in situ X-ray absorption spectroscopy and ab initio calculations reveal that both Cu<sup>2+</sup> and [CuOH]<sup>+</sup> become solvated by NH<sub>3</sub> to form mobilized active sites that turnover with indistinguishable rates (473 K, per Cu), which do not vary with Cu density at high Cu loadings. At low Cu content, however, SCR rates (473 K, per Cu; equimolar NO and NH<sub>3</sub>) increase linearly with Cu content. This dependence on the Cu volumetric density is inconsistent with



the single-site kinetic behavior observed at high Cu densities because mobilized Cu ions traverse zeolite pores to form transient Cu-dimers that mediate  $O_2$  activation, a critical step in the low-temperature SCR mechanism. Electrostatic tethering of cationic Cu complexes at anionic framework aluminum centers defines the space that each Cu cation can sample and, thus, its capacity to activate  $O_2$ . This dynamic and reversible formation of multinuclear Cu sites from mobilized single atoms represents a distinct phenomenon that falls outside the conventional boundaries of a heterogeneous or homogeneous catalyst. Moreover, these results underscore the necessity to experimentally and computationally probe the active site under working conditions that correspond to catalytic turnover.

Finally, Chapter 8 discusses the effect of the Al arrangement in CHA on acid catalysis using the dehydration of methanol to dimethyl ether (DME), a reaction sensitive to both differences in acid strength and confinement effects in zeolites [82,83]. DME formation rates (415 K, per  $H^+$ ) on CHA zeolites increase linearly at low methanol pressures, but decrease at high methanol pressures suggesting that DME formation is inhibited by adsorbed methanol at high pressures. This behavior contrasts that of larger pore zeolites (e.g., MFI) and unconfined acid sites (e.g., polyoxometalates) characterized by a kinetic regime that is zero-order at high  $CH_3OH$  pressures. DME formation rates (415 K, per  $H^+$ ) on CHA zeolites increased systematically with the fraction of paired  $H^+$  sites and turnover rates were ca. 10x higher on paired than on isolated  $H^+$  sites. Indicating that paired protons in CHA stabilize intermediates and transition states more effectively than isolated protons or provide access to dehydration pathways inaccessible to isolated protons. In situ IR spectra collected in the first-order kinetic regime (415 K,  $<1.5$  kPa  $CH_3OH$ ) provide evidence of surface methoxy ( $1457\text{ cm}^{-1}$ ) formation on CHA containing paired Al sites, in amounts that increased with paired acid site content in CHA. Methoxy species were not detected at similar  $CH_3OH$  pressures for CHA zeolites containing only isolated protons, or in MFI zeolites. This suggests that paired protons in CHA form DME through a dissociative pathway, in which  $CH_3OH$  monomers dehydrate to form methoxy species

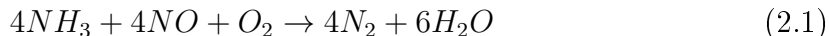
that react with a second methanol to form DME. This differs from the prevalent pathway on supported Keggin polyoxometalate clusters and on larger pore zeolites, which involves an associative pathway and direct DME elimination from co-adsorbed  $\text{CH}_3\text{OH}$  dimers at  $\text{H}^+$  sites. These findings highlight the catalytic diversity of paired and isolated Brønsted acid site ensembles for methanol conversion catalysis, even within single T-site frameworks (e.g., CHA), caused by differences in the stabilities of reactive intermediates and transition states, which can alter the prevalent reaction mechanism.

## 2. THE DYNAMIC NATURE OF BRØNSTED ACID SITES IN CU-ZEOLITES DURING NOX SELECTIVE CATALYTIC REDUCTION: QUANTIFICATION BY GAS-PHASE AMMONIA TITRATION

### 2.1 Introduction

Redox-active metal centers can be isolated in extraframework locations, via ion-exchange of Brønsted acid sites ( $H^+$ ) present at oxygen atoms that bridge Si and Al atoms in aluminosilicate (zeolite;  $Al^{3+}$  substituted for  $Si^{4+}$ ) and in silicoaluminophosphate (SAPO;  $Si^{4+}$  substituted for  $P^{5+}$ ) frameworks. This underlying concept describes the behavior of high aluminum ( $Si/Al_{tot} = 4.5$ ) SSZ-13 zeolites containing isolated extraframework  $Cu^{2+}$  cations [35,84], which undergo redox cycling ( $Cu^{2+}/Cu^+$ ) during the selective catalytic reduction (SCR) of NOx ( $x = 1, 2$ ) compounds with  $NH_3$  [85–87].

Cu-exchanged SSZ-13 [88,89] and SAPO-34 [90] of the chabazite (CHA) topology, as well as other redox-active metal-exchanged molecular sieves [91–93], have been investigated for NOx emission control strategies in mobile sources because they catalyze SCR reactions, which under standard conditions (equimolar NO and  $NH_3$  feed) occurs by the stoichiometric reaction:



Most mechanistic proposals for standard SCR on Cu-zeolites [37, 94, 95], Fe-zeolites [96–100], and VOx-TiO2 [101, 102] implicate a bifunctional mechanism with steps involving reactions of NO with Lewis acid-bound  $NH_3$  intermediates, with Brønsted acid-bound  $NH_4^+$  intermediates, or with their derivatives, including our most recent mechanistic proposal for low temperature (473 K) standard SCR on high aluminum Cu-SSZ-13 zeolites [85]. We have used *operando* X-ray absorption spectroscopy (XAS) and ambient UV-Visible spectroscopy to show that the initial

exchange of  $\text{Cu}(\text{NO}_3)_2$  onto  $\text{H}^+$  sites balancing framework Al atoms ( $\text{Al}_f$ ) in Cu-SSZ-13 ( $\text{Si}/\text{Al}_f = 5.3$ ,  $\text{Cu}/\text{Al}_{\text{tot}} = 0.020$ ) formed predominantly isolated  $\text{Cu}^{2+}$  ions [37,78]. The formation of predominantly isolated  $\text{Cu}^{2+}$  sites up to a  $\text{Cu}/\text{Al}_{\text{tot}}$  value of 0.20 was consistent with a statistical simulation of a random Al siting in the CHA framework, which predicted that the fraction of Al present in a configuration with two Al atoms in a double six-membered ring (6-MR) was 0.22 (for  $\text{Si}/\text{Al}_f = 5.3$ ), and with density functional theory (DFT) calculations, which indicated that  $\text{Cu}^{2+}$  sites were most stable when exchanged at two  $\text{Al}_f$  atoms sited in a double 6-MR [37]. Differential standard SCR rates (per g, 473 K) increased linearly with isolated  $\text{Cu}^{2+}$  density (per g) on Cu-SSZ-13, yet were undetectable on H-SSZ-13 and were independent of the number of *residual*  $\text{H}^+$  sites (per g) remaining after  $\text{Cu}^{2+}$  exchange on Cu-SSZ-13 [37,78]. Brandenberger et al. [103] reported similar rates of standard SCR (per g, 473–573 K) on Fe-ZSM-5 monoliths after residual  $\text{H}^+$  sites were removed by silanization, and Gao et al. [104] reported similar NOx conversion (423–473 K) during standard SCR on Cu-SSZ-13 samples after residual  $\text{H}^+$  sites were partially exchanged with  $\text{Na}^+$ .

At first glance, this kinetic behavior implies that isolated  $\text{Cu}^{2+}$  sites, but not  $\text{H}^+$  sites, are required to catalyze NOx SCR with  $\text{NH}_3$  on Cu-SSZ-13. We have recently provided experimental and theoretical evidence, however, indicating that isolated  $\text{Cu}^{2+}$  ions balanced by two  $\text{Al}_f$  atoms are reduced by NO and  $\text{NH}_3$  (473 K) to form a  $\text{Cu}^+$  and  $\text{H}^+$  pair during the SCR redox cycle [85] (Fig. 2.1). The additional  $\text{H}^+$  sites generated from the standard SCR reduction half-cycle have been quantified by adsorbed  $\text{NH}_4^+$  species that react stoichiometrically with NO after gaseous  $\text{NH}_3$  is removed from standard SCR feeds [37], and by  $\text{NH}_3$  titrants exposed to Cu-SSZ-13 samples after reduction treatments in flowing NO and  $\text{NH}_3$  [85]. These  $\text{H}^+$  sites are formed *proximal* to  $\text{Cu}^+$  sites and bind  $\text{NH}_4^+$  intermediates that are kinetically-relevant in the standard SCR oxidation half-cycle. Although residual  $\text{H}^+$  sites on Cu-SSZ-13 do not influence differential SCR turnover rates (per g, 473 K) that show essentially zero-order dependences (between -0.2 and 0.1) on  $\text{NH}_3$  pressure [37],

such sites can bind and release  $\text{NH}_3$  during actual SCR operation and may become kinetically-relevant in a regime where rates become limited by  $\text{NH}_4^+$  surface coverages. The differential standard SCR turnover rates (per g, 473 K) measured previously on Cu-SSZ-13, which show different dependences on the number of *residual* and *proximal*  $\text{H}^+$  sites, provide insight into the different types and mechanistic roles of  $\text{H}^+$  sites present on Cu-SSZ-13 during standard SCR redox cycles.

Here, we review methods we have developed recently to quantify, by direct chemical titration, Brønsted acid sites present on small-pore Cu-SSZ-13 zeolites after exposure to oxidation [78] and reduction [85] treatments that are representative of the prevailing gaseous environments during standard SCR oxidation and reduction half-cycles. These methods titrate  $\text{H}^+$  sites using gaseous ammonia, which can access all void spaces in small-pore (8-MR) CHA zeolites [78] and which is the co-reductant in standard SCR. Although gaseous  $\text{NH}_3$  binds non-selectively to Brønsted acid sites, to Lewis acid sites (partial or extra-framework Al, extra-framework  $\text{Cu}^{2+}$  or  $\text{Cu}^+$ ), and on siliceous pore walls [78,105,106], we demonstrate how  $\text{NH}_3$  bound at non-protonic sites can be purged prior to temperature programmed-desorption (TPD) to enable straightforward quantification of the number of  $\text{H}^+$  sites [78]. We also discuss how gaseous  $\text{NH}_3$  titration of  $\text{H}^+$  sites provides an *in situ* method to probe structural changes to active sites in Cu-SSZ-13 after standard SCR oxidation and reduction half-cycles [85], which are reminiscent of previously reported structural changes to active  $\text{VO}_x$ - $\text{TiO}_2$  oxide surfaces during SCR redox cycles [101,107,108].

## 2.2 Experimental Methods

### 2.2.1 Catalyst Synthesis and Preparation

$\text{NH}_4$ -ZSM-5 samples of varying Al content were obtained from Zeolyst, corresponding to product numbers CBV2314 ( $\text{Si}/\text{Al}_{\text{tot}} = 12.5$ ), CBV3024E ( $\text{Si}/\text{Al}_{\text{tot}} = 17.3$ ), CBV5524G ( $\text{Si}/\text{Al}_{\text{tot}} = 30.6$ ), CBV8014 ( $\text{Si}/\text{Al}_{\text{tot}} = 43$ ) and CBV1502 ( $\text{Si}/\text{Al}_{\text{tot}} = 89$ ).  $\text{NH}_4$ -form ZSM-5 catalysts were converted to their H-form by treatment in

flowing dry air ( $100 \text{ cm}^3 \text{ min}^{-1} \text{ g cat}^{-1}$ , 99.999% UHP, Indiana Oxygen) at 773 K ( $0.0167 \text{ K s}^{-1}$ ) for 4 h.

Na-SSZ-13 zeolites were synthesized by a method reported by Zones [109]. 24.10 g of sodium silicate ( $\text{Na}_2\text{O}$  10.6 wt%,  $\text{SiO}_2$  26.5 wt%, Sigma-Aldrich) and 3.14 g of a 1.0 M sodium hydroxide solution (NaOH: 98 wt%, Alfa Aesar) were added to 4.82 g of deionized water (18.2 M $\Omega$ ) in a perfluoroalkoxy alkane (PFA) plastic vessel (Saville Corp.) and homogenized for 15 minutes under ambient conditions. 0.37 g of  $\text{NH}_4\text{-Y}$  (Zeolyst CBV300, Si/Al = 2.6) were added and the mixture was stirred for 30 minutes under ambient conditions. 1.58 g of N,N,N-trimethyl-1-adamantylammonium hydroxide (TMAdaOH, 25 wt%, Sachem), which is the structure directing agent for SSZ-13, were then added and the mixture was homogenized for 30 minutes under ambient conditions. The synthesis gel was then loaded into a  $45 \text{ cm}^3$  Teflon-lined stainless steel autoclave and heated under rotation at 413 K for 6 days at 60 RPM.

The crystalline solids were thoroughly washed with deionized water and acetone (99.9 wt%, Sigma Aldrich) in alternating steps ( $30 \text{ cm}^3$  solvent per g solids) until the pH of the supernatant remained constant between washes. Solids were recovered using centrifugation, dried at 373 K for 24 h, and then treated in flowing dry air ( $100 \text{ cm}^3 \text{ min}^{-1} \text{ g cat}^{-1}$ , 99.999% UHP, Indiana Oxygen) at 853 K ( $0.0167 \text{ K s}^{-1}$ ) for 10 h. Na-zeolites were converted to their  $\text{NH}_4$ -form by ion-exchange with a 0.1 M aqueous  $\text{NH}_4\text{NO}_3$  (99.9%, Sigma Aldrich) solution ( $100 \text{ g}$  solution per g solids) for 10 h at 353 K and 300 RPM, followed by thorough washing with deionized water and recovery via centrifugation.  $\text{NH}_4$ -zeolites were converted to their H-form by treatment in flowing dry air ( $100 \text{ cm}^3 \text{ min}^{-1} \text{ g cat}^{-1}$ , 99.999% UHP, Indiana Oxygen) at 773 K ( $0.0167 \text{ K s}^{-1}$ ) for 4 h.

Cu-exchanged ZSM-5 and SSZ-13 zeolites were obtained via ion-exchange of H-form zeolites with aqueous  $\text{Cu}(\text{NO}_3)_2$  (0.01M - 0.1M, 99.999% metals basis, Sigma-Aldrich) solutions for 4 h at 300 RPM under ambient conditions ( $100 \text{ g}$  solution per g solids) [78]. The pH was maintained at ca. 5 through dropwise addition of a 1.0 M

$\text{NH}_4\text{OH}$  (Sigma Aldrich) solution. The solids were thoroughly washed with deionized water, until the pH was constant between washes, and recovered via centrifugation.

### 2.2.2 Characterization of Catalyst Structure and Composition

The total Si, Al, and Cu content of each sample were determined using atomic absorption spectroscopy (AAS) on a Perkin Elmer AAnalyst 300 Atomic Absorption Spectrometer (experimental details in Section 2.7.1, data in Table 2.3 of the Supporting Information). The MFI and CHA framework topologies of ZSM-5 and SSZ-13 zeolites, respectively, were confirmed using powder X-ray diffraction (XRD) patterns collected on a Rigaku SmartLab X-ray diffractometer (experimental details in Section 2.7.2, powder XRD patterns in Fig. 2.9 of the Supporting Information). The micropore volumes of each sample were determined from  $\text{N}_2$  adsorption isotherms measured at 77 K using a Micromeritics ASAP 2020 Surface Area and Porosity Analyzer, and were in reasonable agreement with the values expected for MFI and CHA frameworks (experimental details and discussion in Section 2.7.3, data in Table 2.3 of the Supporting Information).  $^{27}\text{Al}$  magic angle spinning nuclear magnetic resonance (MAS NMR) spectra of ZSM-5 samples were collected using a Bruker Avance 500 MHz spectrometer in a wide-bore 11.7 Tesla magnet (Caltech Solid-State NMR Facility), and of SSZ-13 samples were collected using a Chemagnetics CMX400 400 MHz spectrometer in a wide-bore 9.4 Tesla magnet (Purdue Interdepartmental NMR Facility), as described elsewhere [78]. The  $^{27}\text{Al}$  MAS NMR spectra of ZSM-5 and SSZ-13 samples are shown respectively in Figures 2.10 and 2.11, and the fraction of Al present in each sample is listed in Table 2.4 (additional details in Section 2.7.4 of the Supporting Information).

### 2.2.3 Titration of Brønsted Acid Sites using Amines

The number of  $\text{H}^+$  sites on each H-form and Cu-exchanged ZSM-5 and SSZ-13 sample after oxidative treatments in flowing air (773 K) was measured using a titration

procedure intended to saturate zeolite samples with gaseous  $\text{NH}_3$  prior to purging all  $\text{NH}_3$  species bound to non-protonic sites. This procedure involved saturating zeolite samples (0.03-0.05 g) in flowing gaseous  $\text{NH}_3$  (3%  $\text{NH}_3$  in Ar, Praxair) diluted to 500 ppm with ultrahigh purity He (UHP, 99.999%, Indiana Oxygen) at 433 K for 2 h and a total flow rate of  $350 \text{ cm}^3 \text{ min}^{-1}$ . Subsequently,  $\text{NH}_3$ -saturated samples were purged in flowing UHP helium ( $350 \text{ cm}^3 \text{ min}^{-1}$ ) containing moisture (up to 3%  $\text{H}_2\text{O}$ , hereafter referred to as “wet helium”) at 433 K for 8 h prior to temperature programmed desorption (TPD) experiments. Deionized water was introduced into the flowing helium stream using a heated shell-type humidifier (Perma Pure MH-Series) in which the diffusion of water across a Nafion membrane was controlled by temperature.  $\text{NH}_3$  titration experiments were also performed on an H-ZSM-5 and a Cu-ZSM-5 sample in which the wet helium purge step at 433 K was not performed prior to TPD, in order to demonstrate the effect of this purge step.

TPD experiments were performed using a Micromeritics Autochem II 2920 Chemisorption analyzer equipped with an Agilent 5975C mass selective detector (MSD) to identify the gaseous species evolved from the catalyst samples. Catalyst samples were supported between two quartz wool plugs inside a U-shaped quartz cell held within a clam-shell furnace, held in  $50 \text{ cm}^3 \text{ min}^{-1}$  flowing UHP helium (99.999%, Indiana Oxygen) at ambient temperature for 1 h, and heated to 873 K ( $0.167 \text{ K s}^{-1}$ ). The effluent stream from the quartz cell was sent via heated transfer lines held at 383 K to the MSD. The MSD  $m/z = 17$  signal for  $\text{NH}_3$  was calibrated by performing  $\text{NH}_3$  TPD experiments with four  $\text{NH}_4$ -ZSM-5 zeolites of varying Si/Al ratio (Si/Al = 17-89, Zeolyst), whose  $\text{NH}_3$  content was measured in independent TPD experiments performed in a gas-phase plug-flow reactor connected to a MKS Multigas 2030 gas-phase FT-IR spectrometer with on-board  $\text{NH}_3$  calibrations. After each TPD experiment, a  $0.5 \text{ cm}^3$  sample loop was filled with argon (UHP, 99.999%, Indiana Oxygen) and injected into  $50 \text{ cm}^3 \text{ min}^{-1}$  flowing UHP helium that was sent to the MSD as a reference standard to correct for instrument drift between TPD experiments. The total  $\text{NH}_3$  desorbed was quantified from the  $m/z = 17$  MSD signal



after subtraction of the contributing fragments of water ( $m/z = 17$ ), which appears in constant proportion to the  $m/z = 18$  MSD signal for its parent ion.

Each H-form and Cu-form ZSM-5 and SSZ-13 sample was also titrated, after oxidative treatments in flowing air (773 K), with *n*-propylamine (NPA) at 323 K, followed with a helium purge and subsequent TPD. On H-ZSM-5 zeolites, two other independent  $\text{NH}_3$  titration methods were used to measure the number of  $\text{H}^+$  sites, which involved either gaseous saturation with  $\text{NH}_3$  at 323 K followed with a helium purge and washing in deionized water, or an aqueous-phase exchange using  $\text{NH}_4\text{NO}_3$  followed by washing with deionized water. Detailed procedures on these  $\text{NH}_3$  and NPA titration methods are reported elsewhere [78].

Titration of  $\text{H}^+$  sites on Cu-SSZ-13 samples after oxidative treatment in flowing air (773 K), followed by reductive treatments that have been observed to cause  $\text{Cu}^{2+}$  to  $\text{Cu}^+$  reduction in independent *operando* XAS experiments, were performed as originally described elsewhere [85]. After oxidative treatments, Cu-SSZ-13 samples were held under flowing NO (500 ppm) and  $\text{NH}_3$  (500 ppm) in balance UHP helium (99.999%, Indiana Oxygen) at a total flow rate of  $350 \text{ cm}^3 \text{ min}^{-1}$  at 473 K for 2 h. *Operando* XAS experiments indicated that these conditions were sufficient to reduce  $\text{Cu}^{2+}$  cations predominantly to the  $\text{Cu}^+$  oxidation state [85]. The temperature was then lowered to 423 K in the same gaseous mixture, followed by replacement of the 500 ppm NO and 500 ppm  $\text{NH}_3$  mixture with a gaseous stream containing 500 ppm of  $\text{NH}_3$  (balance He) at same total gas flow rate ( $350 \text{ cm}^3 \text{ min}^{-1}$ ) for 2 h. Finally,  $\text{NH}_3$  was removed from the gaseous stream, the catalyst was held in flowing wet helium ( $350 \text{ cm}^3 \text{ min}^{-1}$ ) for 8 h, and followed by a TPD in flowing helium ( $350 \text{ cm}^3 \text{ min}^{-1}$ ) to 823 K.

## 2.3 Results and Discussion

### 2.3.1 $\text{NH}_3$ Titration of Brønsted Acid Sites in H-Zeolites after Oxidative Treatments

Ammonia adsorbs onto both Brønsted and Lewis acid sites in zeolites [105, 110, 111], but infrared (IR) spectra can be used to distinguish  $\text{NH}_4^+$  species formed upon protonation by  $\text{H}^+$  sites (ca.  $1425\text{ cm}^{-1}$ ) from  $\text{NH}_3$  species bound to Lewis acid sites (ca.  $1625\text{ cm}^{-1}$ ), and to quantify their molar concentrations upon converting integrated absorbances using molar extinction coefficients (H-MOR:  $\epsilon(\text{NH}_4^+)$ , ca.  $1450\text{ cm}^{-1} = 0.147\text{ cm}^2\text{ }\mu\text{mol}^{-1}$ ;  $\epsilon(\text{NH}_3)$ , ca.  $1620\text{ cm}^{-1} = 0.022\text{ cm}^2\text{ }\mu\text{mol}^{-1}$  [112]). Ammonia desorption from Brønsted acid sites tends to give rise to the highest temperature desorption peaks (600-700 K) in temperature-programmed desorption (TPD) experiments (Fig. 2.12, Supporting Information) [105, 106, 113], although desorption from non-protonic binding sites can occur in this temperature range under certain experimental conditions, complicating efforts to deconvolute TPD profiles and determine the contributions solely from  $\text{NH}_4^+$  species [114]. The number of  $\text{NH}_4^+$  species can be estimated unambiguously, however, by first desorbing  $\text{NH}_3$  species bound to non-protonic sites prior to performing TPD experiments. Woolery et al. showed that saturation of H-ZSM-5 with gaseous  $\text{NH}_3$  followed by purging in flowing dry helium at 398 K evolved Lewis acid-bound  $\text{NH}_3$  at lower temperatures (ca. 500 K) than  $\text{NH}_4^+$  species (ca. 633 K) during a subsequent TPD, but that purging  $\text{NH}_3$ -saturated samples instead in flowing wet helium at 398 K led only to the desorption of  $\text{NH}_4^+$  species in the TPD experiment [105]. This and other studies show that  $\text{NH}_3$  has the potential to titrate different types of acid sites on zeolites, but that refinement of titration methods to selectively target Brønsted acid sites in the presence of Lewis acid sites, present as partial- or fully-extraframework Al species [105] or as extraframework metal cations (e.g.,  $\text{Cu}^{2+}$ ) [78], would enable quantifying  $\text{H}^+$  sites from a straightforward TPD experiment, precluding efforts to deconvolute TPD profiles with multiple desorption features or to collect and interpret IR spectra.

The saturation of H-ZSM-5 ( $\text{Si}/\text{Al}_{\text{tot}} = 17$ ) with gaseous  $\text{NH}_3$  at 323 K, followed by TPD, evolved  $\text{NH}_3$  bound to Lewis acidic Al sites at lower temperatures (ca. 433 K, Figure 2.12, Supporting Information) than  $\text{NH}_4^+$  bound to  $\text{H}^+$  sites (ca. 600 K, Figure 2.12) [78], consistent with previous reports [105]. We hypothesized that removing  $\text{NH}_3$  from the flowing gas stream after saturation, for long enough times and at a temperature near the maximum desorption rate of the low temperature desorption feature (433 K), would result in the desorption of all  $\text{NH}_3$  species bound to non-protonic sites. The  $\text{NH}_3$  TPD profiles measured after saturation of H-ZSM-5 with gaseous  $\text{NH}_3$  at 433 K, with and without subsequent purging in flowing helium that contained traces of moisture, are shown in Figure 2.2. Both low and high temperature  $\text{NH}_3$  desorption features are present in  $\text{NH}_3$ -TPD profiles measured when purging in flowing wet helium does not occur (Fig. 2.2, light trace), while purging in flowing wet helium (433 K, 8 h) results in the evolution of only the high temperature  $\text{NH}_4^+$  desorption feature (Fig. 2.2, dark trace) [78]. The treatment of  $\text{NH}_3$ -saturated zeolites in flowing wet helium at temperatures corresponding to detectable desorption rates of  $\text{NH}_3$  bound Lewis acid sites (433 K) agrees with the previous reports by Woolery et al. [105].

These findings indicate that Brønsted acid sites on H-form zeolites can be selectively titrated using gaseous  $\text{NH}_3$ , as long as post-saturation purging procedures are sufficient to remove physically adsorbed and Lewis acid-bound  $\text{NH}_3$  species (Figure 2.3). The  $\text{NH}_3$  TPD profiles of four H-ZSM-5 zeolites of different Al content, after saturation with gaseous  $\text{NH}_3$  at 433 K and purging in flowing wet helium (433 K, 8 h), are shown in Figure 2.4 (dark trace) together with  $\text{NH}_3$  TPD profiles measured after two independent  $\text{NH}_3$  saturation treatments intended to selectively retain  $\text{NH}_4^+$  species [78]. One treatment involved aqueous-phase  $\text{NH}_4^+$  ion-exchange of H-ZSM-5, which occurs only at  $\text{H}^+$  sites and not at Lewis acidic Al sites [105], followed by washing in liquid water before measuring  $\text{NH}_3$  TPD profiles (Fig. 2.4, grey traces). The other treatment involved gas-phase  $\text{NH}_3$  saturation at 323 K, followed by washing in liquid water to remove  $\text{NH}_3$  bound to Lewis acidic Al species [78], prior to mea-

surement of  $\text{NH}_3$  TPD profiles (Fig. 2.4, light grey traces). The  $\text{NH}_3$  TPD profiles measured after each of the three  $\text{NH}_3$  titration methods are virtually indistinguishable (Fig. 2.4), and the amounts of  $\text{NH}_3$  quantified from these profiles are similar within experimental error (Table 2.1), providing further evidence that gaseous  $\text{NH}_3$  saturation (433 K) followed by purging in wet helium (433 K, 8 h) indeed selectively titrated  $\text{H}^+$  sites on H-ZSM-5.

*n*-Propylamine (NPA) titrants, which adsorb onto both Brønsted and Lewis acid sites but decomposes via Hoffman-type elimination reactions only on  $\text{H}^+$  sites to form  $\text{NH}_3$  and  $\text{C}_3\text{H}_6$  (Scheme 2.13, Section 2.7.6 of the Supporting Information) [114–117], also corroborate the findings of  $\text{NH}_3$  titrations on H-ZSM-5. The  $\text{NH}_3$  and  $\text{C}_3\text{H}_6$  TPD profiles for a representative H-ZSM-5 sample are shown in Figure 2.14 of the Supporting Information, with quantification provided in Table 2.6 of the Supporting Information. The numbers of  $\text{H}^+$  sites on H-ZSM-5 samples measured from  $\text{NH}_3$  titrations were equivalent, within experimental error, to the numbers measured by reactive NPA decomposition (Table 2.1, Fig. 2.5). On H-ZSM-5 zeolites,  $\text{H}^+/\text{Al}_{\text{tot}}$  values ranged from 0.68–1.02, yet varied non-monotonically with  $\text{Si}/\text{Al}_{\text{tot}}$  ratio (Table 2.1), indicating that the number of  $\text{H}^+$  sites was not necessarily equal to the number of total Al atoms on these samples [78]. The fraction of framework Al ( $\text{Al}_f$ ) atoms estimated from tetrahedral NMR line intensities in  $^{27}\text{Al}$  MAS NMR spectra (Fig. 2.10, Supporting Information), which are often treated as structural surrogates for Brønsted acid sites in zeolites, ranged from 0.93–1.00 (Table 2.1) [78]. Thus, even after correcting for  $\text{Al}_f$  content, NPA and  $\text{NH}_3$  titrations estimated sub-stoichiometric  $\text{H}^+/\text{Al}_f$  ratios of 0.77 and 0.75 on H-ZSM-5 samples with  $\text{Si}/\text{Al}_{\text{tot}}$  ratios of 17 and 89, respectively (Table 2.1). These data provide yet another demonstration that framework Al atoms can overestimate the number of  $\text{H}^+$  sites in zeolites [118,119], especially when measured under *ex situ* conditions and after hydration treatments intended to sharpen  $^{27}\text{Al}$  MAS NMR lines, because exposure to water causes structural changes to Al atoms that are partially-coordinated to aluminosilicate frameworks [120–125] and their detection as tetrahedral Al species. Yet, Al atoms partially-coordinated

within zeolite frameworks, which are formed via Al-O hydrolysis during combustion of organic structure directing agents in oxidative treatments, behave as Lewis acid sites that bind  $\text{NH}_3$  [105] and therefore are not detected using titration methods that solely count  $\text{NH}_4^+$  species. As a result, methods that use chemical titrants to directly count  $\text{H}^+$  sites on zeolites, instead of those that estimate the number of structural surrogates for such sites ( $\text{Al}_f$  atoms) under *ex situ* conditions, are required to accurately quantify Brønsted acid sites and, in turn, determine their effects on catalytic reactivity.

The numbers of  $\text{H}^+$  sites estimated by  $\text{NH}_3$  and *n*-propylamine titrations on small-pore H-SSZ-13 zeolites ( $\text{Si}/\text{Al}_{\text{tot}} = 4.5$ ) are also listed in Table 2.1 and plotted in Figure 2.5. *n*-Propylamine titrations (323 K, 2 h) provided  $\text{H}^+/\text{Al}_{\text{tot}}$  values of 0.16, in contrast to the much higher  $\text{H}^+/\text{Al}_{\text{tot}}$  values measured on medium-pore H-ZSM-5 (0.69-1.01, Table 2.1) using equivalent titration procedures. The incomplete titration of  $\text{H}^+$  sites in small-pore 8-MR CHA zeolites (ca. 0.39 nm diameter [126]), but not in medium-pore 10-MR MFI zeolites (ca. 0.51 nm in diameter [127]), likely reflects the restricted diffusion of *n*-propylamine (ca 0.53 nm in diameter [78]) through spatially-constrained 8-MR limiting apertures. Increasing the *n*-propylamine saturation time from 2 to 4 hours at 323 K led to only a small increase in the total number of  $\text{H}^+$  sites titrated in H-SSZ-13 (0.16 to 0.18  $\text{H}^+/\text{Al}_{\text{tot}}$ , respectively) [78], although higher adsorption temperatures may further increase the number of  $\text{H}^+$  sites titrated. The adsorption of *n*-propylamine at each  $\text{H}^+$  site in H-SSZ-13 ( $\text{Si}/\text{AlAl}_{\text{tot}} = 4.5$ ) may also become sterically hindered by titrants adsorbed at nearby sites, as reported previously using amine titrants of varying size in H-ZSM-5 [128]. These data highlight the vigilance required when adapting titration methods to porous materials of different topology, and the requirement to use  $\text{NH}_3$  titrants to accurately quantify  $\text{H}^+$  sites confined within microporous solids whose limiting apertures may restrict access to larger titrants.

### 2.3.2 $\text{NH}_3$ Titration of Brønsted Acid Sites in Cu-Zeolites after Oxidative Treatments

Among the methods reviewed in Section 2.3.1, gas-phase  $\text{NH}_3$  titration methods are preferred to count  $\text{H}^+$  sites on partially metal-exchanged zeolites, because liquid-phase washing or ion-exchange procedures may change the structure or distribution of extraframework metal cations. The treatment of Cu-ZSM-5 zeolites in flowing air (773 K), followed by gaseous  $\text{NH}_3$  adsorption and subsequent purging in flowing wet helium (433 K), led to the evolution of similar amounts of  $\text{NH}_3$  in TPD experiments as did reactive n-propylamine decomposition (Table 2.1, Fig. 2.5) [78]. As observed for H-ZSM-5 (Fig. 2.2), the saturation of Cu-ZSM-5 with  $\text{NH}_3$  at 433 K retained  $\text{NH}_3$  bound at Lewis acidic Cu and Al species if purging in flowing wet helium (433 K) was not performed. These findings, taken together, indicate that gaseous  $\text{NH}_3$  saturation followed by steps that purge  $\text{NH}_3$  bound to non-protonic sites leads to the retention of  $\text{NH}_4^+$  species only at  $\text{H}^+$  sites in partially-Cu-exchanged zeolites. They demonstrate how  $\text{NH}_3$  can be used to selectively titrate  $\text{H}^+$  sites in the presence of Lewis acidic Cu cations on zeolites, extending the findings of Woolery et al. for methods that selectively adsorb  $\text{NH}_3$  onto  $\text{H}^+$  sites in the presence of Lewis acidic Al species in H-ZSM-5 [105].

In a previous set of studies [37, 78, 129], we have discussed the preparation and characterization of a series of Cu-SSZ-13 samples ( $\text{Si}/\text{Al}_{\text{tot}} = 4.5$ ,  $\text{Cu}/\text{Al}_{\text{tot}} = 0\text{-}0.20$ ) containing predominantly isolated  $\text{Cu}^{2+}$  species after oxidation in flowing air at 773 K and cooling to ambient temperatures. These samples give rise to ambient UV-Visible spectra that show absorption bands for d-d transitions in hydrated  $\text{Cu}^{2+}$  ions centered at  $12,500\text{ cm}^{-1}$ , whose integrated areas increase linearly with Cu content (Fig. 2.15, Supporting Information), and to ambient X-ray absorption spectra that are indistinguishable from a hexacoordinated hydrated  $\text{Cu}^{2+}$  reference (aqueous  $\text{Cu}(\text{NO}_3)_2$ ) and that do not show detectable CuO or  $\text{Cu}^+$  signatures. The number of residual  $\text{H}^+$  sites counted by gaseous  $\text{NH}_3$  titration on these oxidized Cu-SSZ-13 samples decreased with increasing  $\text{Cu}^{2+}$  content, with the stoichiometry expected from the replacement

of two  $\text{H}^+$  sites for each  $\text{Cu}^{2+}$  cation (Fig. 2.6), but not with any other exchange stoichiometries (0 or 1  $\text{H}^+$  site exchanged per Cu) [78]. We note that the SSZ-13 sample with lowest Cu content studied ( $\text{Cu}/\text{Al}_{\text{tot}} = 0.02$ ) appears to be an outlier and contains fewer residual  $\text{H}^+$  sites than expected, and that SSZ-13 samples with Cu contents higher than  $\text{Cu}/\text{Al}_{\text{tot}} > 0.20$  deviate from the 2:1  $\text{H}^+:\text{Cu}^{2+}$  exchange stoichiometry because of the formation of copper-oxo ( $\text{Cu}_x\text{O}_y$ ) clusters, which are detectable in *ex situ* XAS and UV-Visible spectra [37,129]. *In situ* infrared experiments performed under flowing  $\text{NH}_3$  on the parent H-SSZ-13 zeolite showed the complete disappearance of Brønsted acidic OH bands and the concomitant appearance of an  $\text{NH}_4^+$  infrared band at  $1425\text{ cm}^{-1}$  [78]. These findings indicate that  $\text{NH}_3$  (at 433 K) can access all  $\text{H}^+$  sites in SSZ-13, unlike n-propylamine titrants (323 K) that measure only a small fraction ( $<0.25$ ) of all  $\text{H}^+$  sites present on H-SSZ-13 and Cu-SSZ-13 zeolites (Fig. 2.5). As we discuss next, the ability to access all  $\text{H}^+$  sites present on Cu-exchanged SSZ-13 zeolites using gaseous  $\text{NH}_3$  titrants enables quantifying the number of  $\text{H}^+$  sites present under gaseous environments that resemble those present during reduction half-cycles in standard SCR, providing additional insight into the active site structures present during standard SCR redox cycles.

### 2.3.3 $\text{NH}_3$ Titration of Brønsted Acid Sites in Cu-Zeolites after Reductive Treatments

Although initially-exchanged copper species are present on Cu-SSZ-13 ( $\text{Si}/\text{Al}_{\text{tot}} = 4.5$ ,  $\text{Cu}/\text{Al}_{\text{tot}} = 0\text{-}0.20$ ) as isolated  $\text{Cu}^{2+}$  ions after ion-exchange and oxidative treatments in air [78], *operando* X-ray absorption spectroscopy experiments indicate that both  $\text{Cu}^{2+}$  and  $\text{Cu}^+$  ions are present during standard SCR catalytic turnovers (473 K) [85,86,130]. Furthermore, transient X-ray absorption spectra collected after  $\text{O}_2$  is removed from standard SCR gas mixtures demonstrate that the concurrent presence of NO and  $\text{NH}_3$  at 473 K leads to near complete reduction of  $\text{Cu}^{2+}$  to  $\text{Cu}^+$  [85]. Specifically, after two Cu-SSZ-13 samples ( $\text{Si}/\text{Al}_{\text{tot}} = 4.5$ ,  $\text{Cu}/\text{Al}_{\text{tot}} = 0.12$  and 0.20) were exposed to 500 ppm of NO and 500 ppm  $\text{NH}_3$  at 473 K for 2 hours,

XAS spectra indicated that the fractions of Cu present as  $\text{Cu}^+$  cations were 0.75 and 0.95, respectively (Table 2.2). Density functional theory calculations performed on an isolated  $\text{Cu}^{2+}$  cation balancing two  $\text{Al}_f$  atoms in a double 6-MR of SSZ-13 have identified a plausible standard SCR mechanism involving a  $\text{Cu}^{2+}/\text{Cu}^+$  redox cycle [85], in which  $\text{Cu}^{2+}$  reduction proceeds via NO-assisted cleavage of N-H bonds in  $\text{Cu}^{2+}$ -bound  $\text{NH}_3$  species to form a  $\text{Cu}^+$  ion and a proximal  $\text{H}^+$  site (Figure 2.1) [85].

Thus, we hypothesized that reducing Cu-SSZ-13 zeolites ( $\text{Si}/\text{Al}_{\text{tot}} = 4.5$ ,  $\text{Cu}/\text{Al}_{\text{tot}} = 0\text{-}0.20$ ) in flowing NO and  $\text{NH}_3$  at 473 K, followed by cooling to 423 K and removing NO from the flowing gaseous  $\text{NH}_3$  stream, and finally followed by flushing in flowing wet helium, should lead to  $\text{NH}_4^+$ -saturated surfaces with one additional  $\text{NH}_4^+$  species for each  $\text{Cu}^+$  and  $\text{H}^+$  site pair generated. The  $\text{NH}_3$  TPD profiles of two Cu-SSZ-13 samples ( $\text{Si}/\text{Al}_{\text{tot}} = 4.5$ ,  $\text{Cu}/\text{Al}_{\text{tot}} = 0.12$  and  $0.20$ ) measured after this reductive treatment are shown in Figure 2.7 (light traces), together with TPD profiles measured after  $\text{NH}_3$  saturation was performed on these samples after oxidative treatments (dark traces). The  $\text{NH}_4^+$  species that desorb from oxidized forms of Cu-SSZ-13 reflect those bound to *residual*  $\text{H}^+$  sites after  $\text{Cu}^{2+}$  exchange (Figure 2.3) [78], while those that desorb from reduced forms of Cu-SSZ-13 also reflect additional  $\text{NH}_4^+$  species at new proton sites formed upon  $\text{Cu}^{2+}$  reduction (Figure 2.1). Quantification of these TPD profiles gave  $\text{H}^+/\text{Al}_{\text{tot}}$  values that were higher on the reduced forms of Cu-SSZ-13 by 0.09 and 0.21 for the  $\text{Cu}/\text{Al}_{\text{tot}} = 0.12$  and  $0.20$  samples, respectively (Table 2.2). The numbers of additional  $\text{H}^+$  sites (per  $\text{Cu}_{\text{tot}}$ ) measured on the reduced Cu-SSZ-13 samples were in stoichiometric agreement with their respective  $\text{Cu}^+/\text{Cu}_{\text{tot}}$  fractions (Fig. 2.8), which were estimated using XAS-derived  $\text{Cu}^+$  and  $\text{Cu}^{2+}$  distributions after reduction in NO and  $\text{NH}_3$  at 473 K for 2 hours [85]. The detection of additional  $\text{H}^+$  sites on Cu-SSZ-13 samples prepared to contain predominantly  $\text{Cu}^{2+}$  cations after ion-exchange and oxidative treatments, but then treated under flowing NO and  $\text{NH}_3$  at pressures (500 ppm each) and temperatures (473 K) typical of standard SCR that cause  $\text{Cu}^{2+}$  reduction to  $\text{Cu}^+$ , is possible only using a gaseous titrant that can be



introduced *in situ* and that can access all microporous void spaces within small-pore (8-MR) CHA zeolites.

The generation of one additional  $\text{H}^+$  site per  $\text{Cu}^+$  cation (Table 2.2, Fig. 2.8) is consistent with a standard SCR redox mechanism on isolated  $\text{Cu}^{2+}$  sites that balance two  $\text{Al}_f$  atoms in SSZ-13 [85], in which  $\text{Cu}^{2+}$  sites are reduced by NO and  $\text{NH}_3$  to form a  $\text{Cu}^+$  cation at one  $\text{Al}_f$  atom and a proximal  $\text{H}^+$  site at the other  $\text{Al}_f$  atom (Figure 2.1). This SCR mechanistic proposal involving two types of Brønsted acid sites, those that remain after  $\text{Cu}^{2+}$  ion exchange (residual  $\text{H}^+$  sites) and those generated *in situ* during the  $\text{Cu}^{2+}/\text{Cu}^+$  redox cycle (proximal  $\text{H}^+$  sites), is also consistent with observations reported previously regarding the mechanistic roles of  $\text{H}^+$  sites during standard SCR that seem contradictory, at first glance. Standard SCR turnover rates on Cu-SSZ-13 (per g, 473 K), when measured in a kinetic regime with a zero-order dependence on  $\text{NH}_3$  pressure, depend linearly on the number of  $\text{Cu}^{2+}$  sites (per g) and, in turn, the number of *proximal*  $\text{H}^+$  sites (per g) generated during reduction half-cycles [37, 78]. These standard SCR turnover rates are independent of the number of residual  $\text{H}^+$  sites (per g), which can bind and release  $\text{NH}_3$  during SCR catalysis, the dynamic behavior of which must be understood to accurately model and control practical SCR systems during transient operation [131–134]. Yet, *residual*  $\text{H}^+$  sites are kinetically-irrelevant under conditions commensurate with near-saturation  $\text{NH}_4^+$  coverages and zero-order dependences on  $\text{NH}_3$  pressure. Standard SCR rates on mixed  $\text{VO}_x$ - $\text{TiO}_2$  catalysts (per g, 523–573 K) have been reported to depend linearly on the concentration of  $\text{NH}_4^+$  surface intermediates measured by *in situ* infrared spectroscopy, which were found in proportion to the number of Brønsted acidic OH groups formed upon reduction of  $\text{V}^{5+}=\text{O}$  centers to  $\text{V}^{4+}$ -OH sites [101, 107, 108, 135]. These additional Brønsted acidic OH groups generated during standard SCR redox cycles have now been experimentally detected and measured directly on both mixed  $\text{VO}_x$ - $\text{TiO}_2$  oxides [101, 135] and Cu-SSZ-13 zeolites [85], and appear to be catalytically-relevant because their density (per g) is proportional to standard SCR rates (per g).

## 2.4 Conclusions

The saturation of H-form and partially Cu-exchanged ZSM-5 and SSZ-13 zeolites with gaseous  $\text{NH}_3$  at 433 K, followed by purging treatments that remove  $\text{NH}_3$  species bound at non-protonic sites, enables the selective titration and quantification of Brønsted acidic OH groups in a subsequent TPD experiment. On ZSM-5 zeolites, this gaseous  $\text{NH}_3$  titration method gives quantitative agreement with independent techniques that selectively ion-exchange  $\text{NH}_4^+$  at  $\text{H}^+$  sites, selectively adsorb  $\text{NH}_3$  at  $\text{H}^+$  sites by using water to remove  $\text{NH}_3$  bound to Lewis acid sites, or selectively react n-propylamine with  $\text{H}^+$  sites. Reactive n-propylamine decomposition, however, does not provide accurate measurements of  $\text{H}^+$  sites located within small-pore (8-MR) SSZ-13 zeolites at conditions that otherwise may accurately count  $\text{H}^+$  sites located within medium-pore (10-MR) ZSM-5 zeolites. For small-pore molecular sieves, gaseous  $\text{NH}_3$  titrants provide the most accurate estimate of  $\text{H}^+$  sites, and the most relevant estimate of the number of  $\text{H}^+$  sites that may participate in  $\text{NO}_x$  selective catalytic reduction (SCR) reactions using  $\text{NH}_3$  as the co-reductant.

Gaseous  $\text{NH}_3$  titration of residual  $\text{H}^+$  sites in a series of Cu-exchanged, high aluminum SSZ-13 zeolites ( $\text{Si}/\text{Al}_{\text{tot}} = 4.5$ ,  $\text{Cu}/\text{Al}_{\text{tot}} = 0\text{-}0.20$ ) after oxidative treatments indicated that copper cations initially exchange as  $\text{Cu}_{2+}$  species that replace two  $\text{H}^+$  sites, most likely sited at double 6-MR structures that contain two framework Al atoms. After reduction of these Cu-SSZ-13 samples in flowing NO and  $\text{NH}_3$  at 473 K,  $\text{NH}_3$  titrants detected additional  $\text{H}^+$  sites formed in equimolar amounts with respect to the number of Cu+ ions formed via  $\text{Cu}_{2+}$  reduction, consistent with our recent mechanistic proposal for standard SCR redox cycles on isolated  $\text{Cu}_{2+}$  cations that balance two framework Al atoms in Cu-SSZ-13 [85]. The use of gaseous  $\text{NH}_3$  as a selective titrant for  $\text{H}^+$  sites on partially metal-exchanged, small-pore zeolites has enabled accurately quantifying different numbers of  $\text{H}^+$  sites after oxidative and reductive treatments. It has provided new insights into the origin of the different types of  $\text{H}^+$  sites present under gaseous environments that prevail during oxidation

and reduction half-cycles of standard SCR on Cu-SSZ-13, the mechanistic roles of these  $H^+$  sites in standard SCR catalytic redox cycles, and the structural changes to active sites on Cu-SSZ-13 during SCR cycles and their resemblance to structural changes observed previously on mixed  $VO_x$ - $TiO_2$  oxides. We expect that this gaseous  $NH_3$  titration method can be extended and adapted to interrogate the surfaces of microporous solids containing redox-active metal centers and of reducible oxides of varying composition and structure, and their dynamic nature before and after reaction or under various gas environments, in order to provide useful insights into the mechanistic details of, and active site structures during, catalytic redox cycles.

## 2.5 Acknowledgements

We acknowledge the financial support provided by the National Science Foundation GOALI program under award number 1258715-CBET. RG also acknowledges financial support from a Ralph E. Powe Junior Faculty Enhancement Award from the Oak Ridge Associated Universities, and from a Purdue Research Foundation Summer Faculty Grant. Support for JTM was provided under the auspices of the U.S. DOE, Office of Basic Energy Sciences, Division of Chemical Sciences, Geosciences, and Biosciences under contract number DE-AC0-06CH11357. We would like to thank Sachem, Inc. for their donation of the structure-directing agent used to synthesize SSZ-13, Dr. Yury Zvinevich for assistance constructing a custom-built acid site titration unit, Austin Tackaberry for assistance with SSZ-13 sample preparation, and Arthur Shih and Jonatan Albarracin-Caballero for assistance with some of the  $NH_3$  TPD experiments. Finally, we would like to thank Professor Mark E. Davis for continuing to lead by example and inspire his current and former colleagues to pursue creative research problems in catalysis.

Additionally, I acknowledge Springer for granting permission to reproduce this chapter of my thesis. Reprinted by permission from: Springer Topics in Catalysis, 2015, 58, 424-434, [COPYRIGHT] 2015. The full article can be accessed here: [dx.doi.org/10.1007/s11244-015-0387-8](https://doi.org/10.1007/s11244-015-0387-8).

## 2.6 Figures and Tables

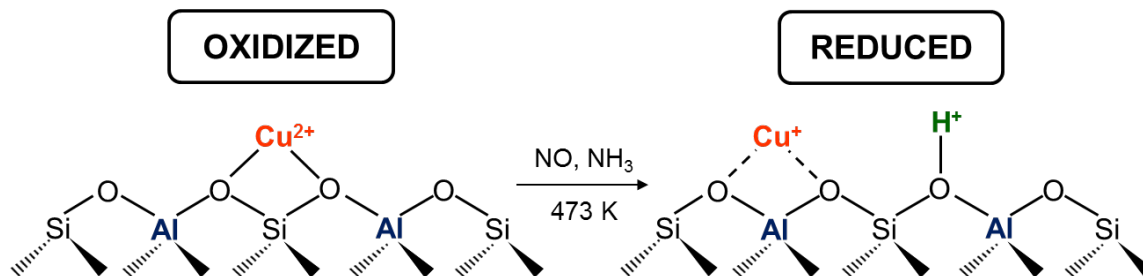


Figure 2.1. Isolated  $\text{Cu}^{2+}$  ions in SSZ-13 ( $\text{Si}/\text{Al}_{\text{tot}} = 4.5$ ) that balance two framework Al atoms reduce in flowing NO and  $\text{NH}_3$  (473 K) to form a proximal  $\text{Cu}^+$  and  $\text{H}^+$  site pair [85].

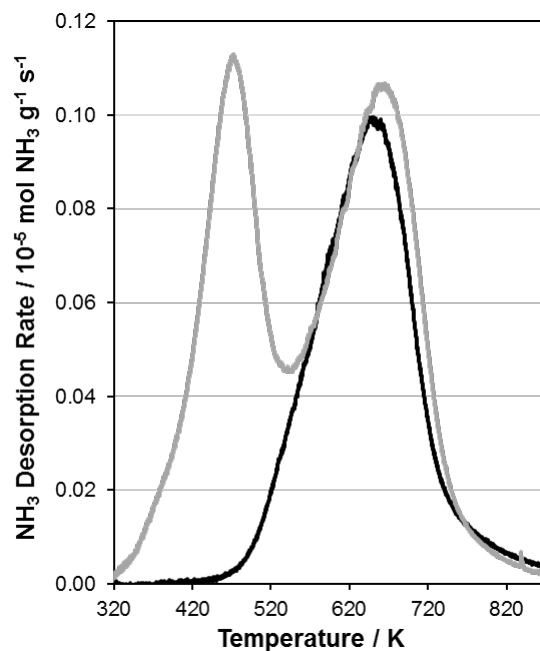


Figure 2.2.  $\text{NH}_3$  desorption rates during TPD of H-ZSM-5 ( $\text{Si}/\text{Al}_{\text{tot}} = 12.5$ ) after gas-phase  $\text{NH}_3$  adsorption at 433 K without purging or washing (light trace), and with purging in flowing wet helium at 433 K (dark trace).

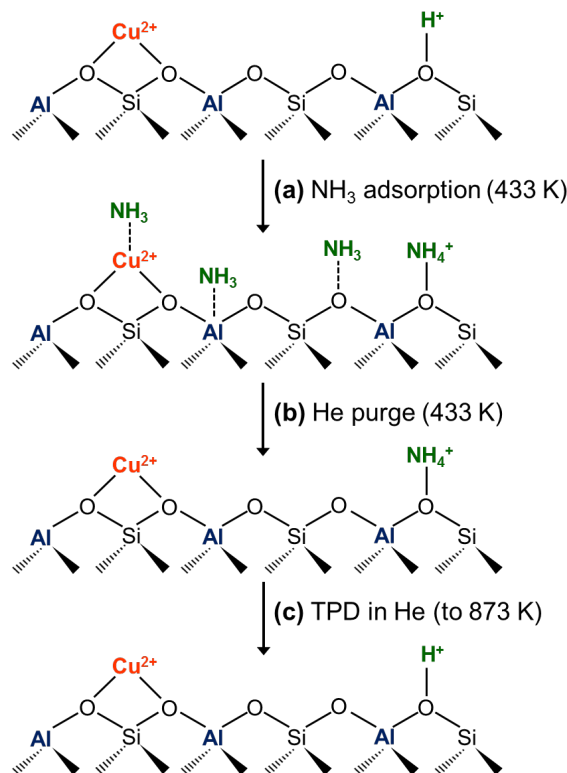


Figure 2.3. (a)  $\text{NH}_3$  saturation at 433 K leads to adsorption on Brønsted and Lewis acid sites, and physisorption near pore walls, but (b) purging in wet helium at 433 K (8 h) desorbs  $\text{NH}_3$  at non-protonic sites and enables quantification of Brønsted acid sites via (c) TPD to 873 K [78].

## 2.7 Supporting Information

### 2.7.1 Atomic Absorption Spectroscopy of Catalyst Samples.

The total Si, Al, and Cu contents of each sample were determined using atomic absorption spectroscopy (AAS) on a Perkin Elmer AAnalyst 300 Atomic Absorption Spectrometer. Typically, 0.02 g of zeolite were dissolved in 2 g of hydrofluoric acid (48 wt%, Alfa Aesar) and the solution was allowed to sit overnight, prior to dilution with 60 g of deionized water. Absorbances were measured using radiation sources at wavelengths of 251.6 nm, 309.3 nm, and 324.8 nm for Si, Al, and Cu, respectively, in an acetylene/nitrous oxide flame. Elemental compositions were determined from

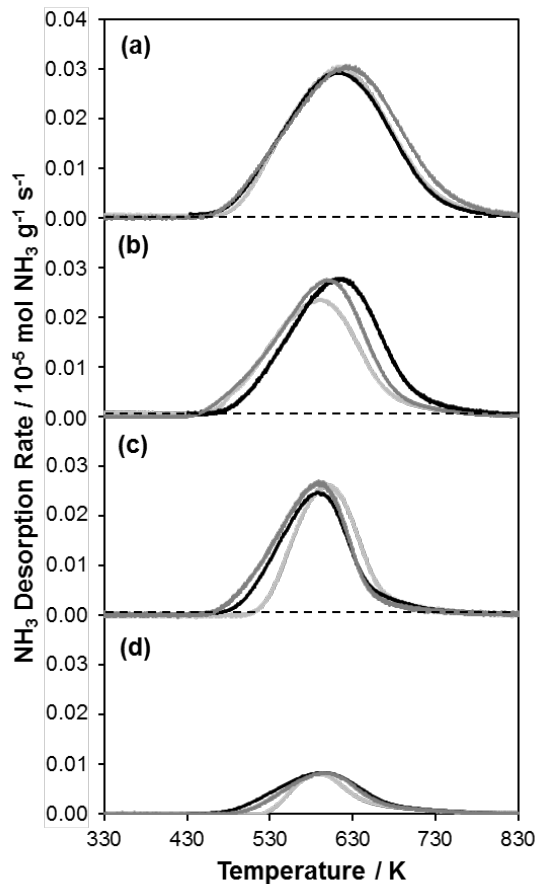


Figure 2.4.  $\text{NH}_3$  desorption rates during TPD of H-ZSM-5 with  $\text{Si}/\text{Al}_{\text{tot}}$  of (a) 17, (b) 30, (c) 43, and (d) 89 for gas-phase  $\text{NH}_3$  adsorption at 323 K with water wash (light grey trace), gas-phase  $\text{NH}_3$  adsorption at 433 K with wet helium purge (black trace), and aqueous  $\text{NH}_4\text{NO}_3$  ion exchange (grey trace) [78]. Quantification of the total number of  $\text{H}^+$  for each sample can be found in Table 2.1.

calibration curves derived from known standard solutions, and are listed for each sample in Table 2.3.

### 2.7.2 X-Ray Diffraction Characterization of Catalyst Samples.

Zeolite framework topologies were determined from powder X-ray diffraction - (XRD) patterns measured on a Rigaku SmartLab X-ray diffractometer with a  $\text{Cu K}\alpha$

Table 2.1.

Number of  $H^+$  sites (per  $Al_{tot}$ ) measured from  $NH_3$  titration of H-zeolites and Cu-zeolites after oxidative treatments, including data originally reported by Bates et al. [78].

| Zeolite   | Si/ $Al_{tot}$ | Cu/ $Al_{tot}$ | $H^+/Al_{tot}$            |                        |                                | $Al_i/Al_{tot}^a$ | $H^+/Al_i^b$ | $H^+_{NPA}/H^+_{NH_3}^c$ |
|-----------|----------------|----------------|---------------------------|------------------------|--------------------------------|-------------------|--------------|--------------------------|
|           |                |                | $NH_3$<br>(433 K,<br>gas) | $NH_3$<br>(323 K, gas) | $NH_3$<br>(323 K, $NH_4NO_3$ ) |                   |              |                          |
| H-ZSM-5   | 17             | -              | 0.75                      | 0.76                   | 0.77                           | 0.99              | 0.76         | 1.04                     |
|           | 30             | -              | 1.02                      | 0.90                   | 0.96                           | 1.00              | 1.02         | 0.97                     |
|           | 43             | -              | 0.94                      | 0.93                   | 0.98                           | 0.94              | 1.00         | 1.06                     |
|           | 89             | -              | 0.68                      | 0.68                   | 0.74                           | 0.93              | 0.73         | 1.01                     |
| Cu-ZSM-5  | 17             | 0.15           | 0.35                      | -                      | -                              |                   | 0.35         | 1.22                     |
|           | 17             | 0.20           | 0.34                      | -                      | -                              |                   | 0.34         | 0.93                     |
|           | 17             | 0.27           | 0.38                      | -                      | -                              |                   | 0.38         | 0.88                     |
| H-SSZ-13  | 4.5            | -              | 0.65                      | -                      | -                              | 0.85              | 0.76         | 0.26                     |
| Cu-SSZ-13 | 4.5            | 0.02           | 0.45                      | -                      | -                              |                   | 0.53         | 0.14                     |
|           | 4.5            | 0.04           | 0.60                      | -                      | -                              |                   | 0.71         | 0.12                     |
|           | 4.5            | 0.09           | 0.43                      | -                      | -                              |                   | 0.51         | 0.09                     |
|           | 4.5            | 0.12           | 0.37                      | -                      | -                              |                   | 0.44         | n.m.*                    |
|           | 4.5            | 0.16           | 0.32                      | -                      | -                              |                   | 0.38         | 0.13                     |
|           | 4.5            | 0.20           | 0.31                      | -                      | -                              |                   | 0.36         | 0.07                     |
|           | 4.5            | 0.35           | 0.24                      | -                      | -                              |                   | 0.28         | 0.00                     |

<sup>a</sup>  $Al_i/Al_{tot}$  values determined from  $^{27}Al$  MAS NMR and listed in Table S.2 (Supporting Information).

<sup>b</sup>  $H^+$  counts from gaseous  $NH_3$  titrations at 433 K.

<sup>c</sup> Calculated using  $H^+$  counts from gaseous  $NH_3$  titrations at 433 K, and  $H^+_{NPA}$  values listed in Table S.3 (Supporting Information).

\*n.m., not measured.

Table 2.2.

Number of  $H^+$  sites measured using gaseous  $NH_3$  titration of Cu-SSZ-13 after oxidative treatments ( $H^+_{ox}$ ) and reductive treatments in flowing NO and  $NH_3$  at 473 K for 2 hours ( $H^+_{red}$ ). Data adapted from Paolucci et al. [85].

| Zeolite   | Si/ $Al_{tot}$ | Cu/ $Al_{tot}$ | $Cu^+/Cu_{tot}^a$ | $Cu^+/Al_{tot}$ | $H^+/Al_{tot}$ |             |                        | $(H^+_{red} - H^+_{ox})/Cu^+$ |
|-----------|----------------|----------------|-------------------|-----------------|----------------|-------------|------------------------|-------------------------------|
|           |                |                |                   |                 | $H^+_{ox}$     | $H^+_{red}$ | $H^+_{red} - H^+_{ox}$ |                               |
| Cu-SSZ-13 | 4.5            | 0.12           | 0.75              | 0.09            | 0.37           | 0.46        | 0.09                   | 1.00                          |
|           | 4.5            | 0.20           | 0.95              | 0.19            | 0.32           | 0.53        | 0.21                   | 1.05                          |

<sup>a</sup> Fraction of total Cu present as  $Cu^+$  in after reduction in NO and  $NH_3$  determined by *operando* XAS [8].

radiation source operated at 1.76 kW. Typically, 0.01 g of zeolite powder were loaded onto a zero background, low dead volume sample holder (Rigaku) and the diffraction pattern was measured from 4–40 degrees  $2\theta$  at a scan rate of 2.4 degrees  $min^{-1}$ . The resulting powder XRD patterns are shown in Figure 2.9, and were compared

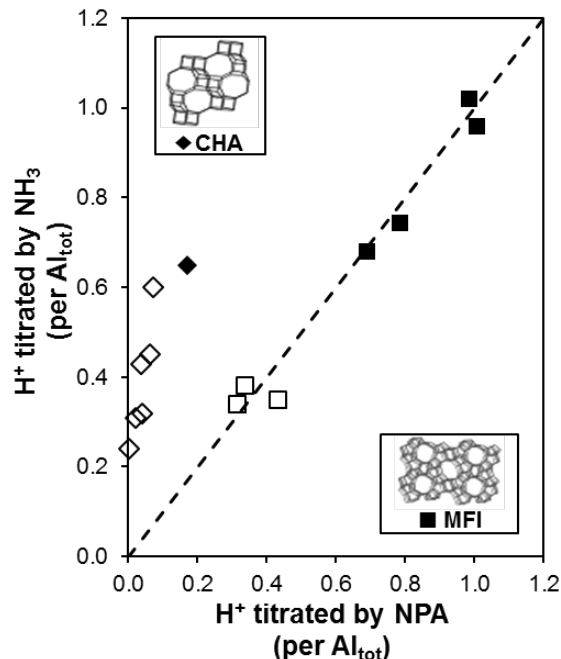


Figure 2.5. Number of H<sup>+</sup> sites titrated by gas phase NH<sub>3</sub> at 433 K followed by purging in He and n-propylamine (NPA) for Cu (open) and H-form (solid) zeolites. The dashed line corresponds to the parity line. Data given Table 2.6 of the Supporting Information.

to a known reference material and to diffraction patterns for MFI (H-ZSM-5) and CHA (H-SSZ-13) reported in the International Zeolite Association (IZA) structure database [1].

### 2.7.3 N<sub>2</sub> Adsorption Isotherms of Catalyst Samples.

Micropore volumes were determined from N<sub>2</sub> adsorption isotherms measured at 77 K on a Micromeritics ASAP 2020 Surface Area and Porosity Analyzer. Samples were first pelleted and sieved to retain particles between 180-250  $\mu\text{m}$  in diameter, degassed by heating 0.03–0.05 g of sample to 393 K (0.167 K s<sup>-1</sup>) under high vacuum ( 5  $\mu\text{mHg}$ ) for 2 h, and then further heated to 623 K (0.167 K s<sup>-1</sup>) under high vacuum ( 5  $\mu\text{mHg}$ ) for 8 h. Extrapolation of the linear volumetric uptake during



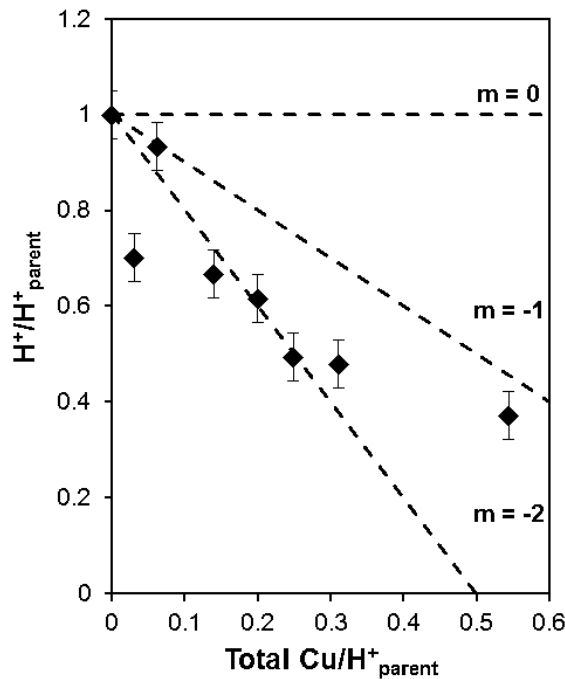


Figure 2.6. Number of residual  $\text{H}^+$  sites, relative to the number on the parent H-SSZ-13 ( $\text{H}^+_{\text{parent}}$ ), measured by  $\text{NH}_3$  titration on oxidized forms of Cu-SSZ-13 samples of varying total Cu content (per  $\text{H}^+_{\text{parent}}$ ). The dashed lines with slopes ( $m$ ) of -2, -1, and 0 represent Cu exchange stoichiometries of 2, 1, or 0  $\text{H}^+$  sites, respectively. Error bars correspond to 90% confidence intervals [78]. Tabulated data can be found in Table 2.2.

mesopore filling (0.08–0.30  $P/P_0$ ) to zero relative pressure gave an estimate for the volume of adsorbed gas in micropores ( $\text{cm}^3 \text{ g cat}^{-1}$  at STP). These estimates agreed with the micropore volume determined by analyzing the semi-log derivative plot of the adsorption isotherm,  $\partial(V_{\text{ads}})/\partial(\ln(P/P_0))$  vs.  $\ln(P/P_0)$ . This analysis requires identifying the first maximum of  $\partial(V_{\text{ads}})/\partial(\ln(P/P_0))$ , which corresponds to the relative pressure at which the micropore filling transition occurs, and then identifying the subsequent minimum that corresponds to the end of micropore filling [136, 137]. Micropore volumes were obtained by converting adsorbed gas volumes (at STP) to liquid volumes assuming the liquid density of  $\text{N}_2$  at 77 K, and are listed in

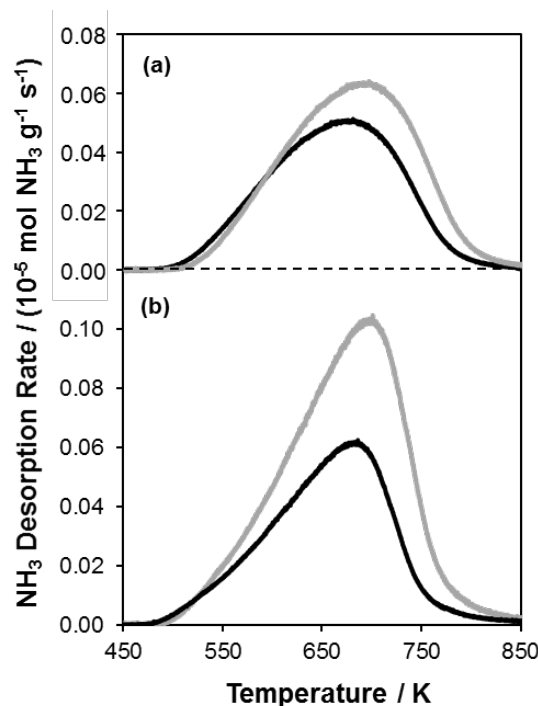


Figure 2.7.  $\text{NH}_3$  desorption rates during TPD of Cu-SSZ-13 ( $\text{Si}/\text{Al}_{\text{tot}} = 4.5$ ) (a)  $\text{Cu}/\text{Al}_{\text{tot}} = 0.12$  and (b)  $\text{Cu}/\text{Al}_{\text{tot}} = 0.20$  before (dark trace) and after (light trace) reduction in flowing NO and  $\text{NH}_3$  at 473 K (Figure 2.1) [85].

Table 2.3 along with BET surface areas. The H-ZSM-5 samples with  $\text{Si}/\text{Al}_{\text{tot}} = 12.5$ , 17, 30, and 43 had micropore volumes between  $0.13\text{--}0.17\text{ cm}^3\text{ g}^{-1}$ . The H-ZSM-5 with  $\text{Si}/\text{Al}_{\text{tot}} = 89$ , however, exhibited an abnormally low micropore volume of  $0.06\text{ cm}^3\text{ g}^{-1}$ , despite the similar XRD patterns among all ZSM-5 samples. Cu-ZSM-5 samples ( $\text{Si}/\text{Al}_{\text{tot}} = 17$ ,  $\text{Cu}/\text{Al}_{\text{tot}} = 0\text{--}0.27$ ) gave micropore volumes between  $0.14\text{--}0.15\text{ cm}^3\text{ g}^{-1}$ . The H-SSZ-13 ( $\text{Si}/\text{Al}_{\text{tot}} = 4.5$ ) sample had a micropore volume of  $0.26\text{ cm}^3\text{ g}^{-1}$  and the Cu-SSZ-13 ( $\text{Si}/\text{Al}_{\text{tot}} = 4.5$ ,  $\text{Cu}/\text{Al}_{\text{tot}} = 0\text{--}0.35$ ) samples gave micropore volumes between  $0.20\text{--}0.24\text{ cm}^3\text{ g}^{-1}$ .

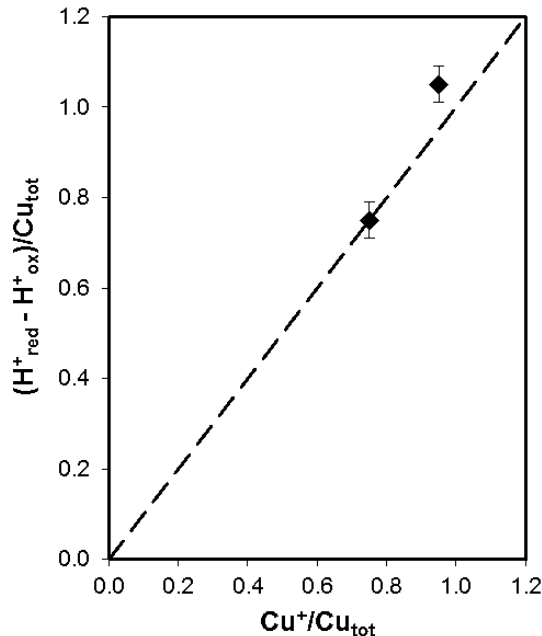


Figure 2.8. The number of extra  $\text{H}^+$  sites ( $\text{H}^+_{\text{red}} - \text{H}^+_{\text{ox}}$  per  $\text{Cu}_{\text{tot}}$ ) formed after reduction of Cu-SSZ-13 ( $\text{Si}/\text{Al}_{\text{tot}} = 4.5$ ,  $\text{Cu}/\text{Al}_{\text{tot}} = 0.12$  and  $0.20$ ) in NO and  $\text{NH}_3$  at 473 K, as a function of  $\text{Cu}^+$  content (per  $\text{Cu}_{\text{tot}}$ ). The dashed line represents the parity line, expected if one additional  $\text{H}^+$  site were formed per  $\text{Cu}^+$  (Scheme 1). Data adapted from Paolucci et al. [85].

#### 2.7.4 $^{27}\text{Al}$ Magic Angle Spinning Nuclear Magnetic Resonance ( $^{27}\text{Al}$ MAS NMR) on H-ZSM-5 and H-SSZ-13 zeolites.

$^{27}\text{Al}$  MAS NMR spectra were recorded on  $\text{NH}_4$ -ZSM-5, H-ZSM-5,  $\text{NH}_4$ -SSZ-13, and H-SSZ-13 to estimate the fraction of framework ( $\text{Al}_f$ ) and extraframework Al ( $\text{Al}_{\text{ex}}$ ) species present in each material. Spectra of H-ZSM-5 samples were collected using a Bruker Avance 500 MHz spectrometer in a wide-bore 11.7 Tesla magnet (Caltech Solid-State NMR Facility), and of H-SSZ-13 were collected using a Chemagnetics CMX400 400 MHz spectrometer in a wide-bore 9.4 Tesla magnet (Purdue Interdepartmental NMR Facility), as described elsewhere [78]. Briefly, spectra were acquired at ambient conditions from 456 scans with  $12.5 \mu\text{s}$  pulses and a 2 s delay and were measured at 104.24 MHz and a MAS rate of 5 kHz. Zeolite samples were hydrated

Table 2.3.  
Elemental composition, and N<sub>2</sub>-derived BET surface areas and micropore volumes for all zeolite samples in this study [78].

| Zeolite   | Si/Al <sub>tot</sub> <sup>a</sup> | Cu/Al <sub>tot</sub> <sup>a</sup> | Zeolyst Call Number | Measured BET Surface Area (m <sup>2</sup> g <sup>-1</sup> ) <sup>b</sup> | t-plot micropore volume (cm <sup>3</sup> g <sup>-1</sup> ) <sup>b</sup> |
|-----------|-----------------------------------|-----------------------------------|---------------------|--|---|
| H-ZSM-5   | 12.5                              | 0                                 | CBV 2314            | 325  | 0.15  |
|           | 17                                | 0                                 | CBV 3024E           | 498  | 0.15  |
|           | 30                                | 0                                 | CBV 5524G           | 519  | 0.17  |
|           | 43                                | 0                                 | CBV 8014            | 425  | 0.13  |
|           | 89                                | 0                                 | CBV 1502            | 400  | 0.06  |
| H-SSZ-13  | 4.5                               | 0                                 | -                   | 597  | 0.26  |
| Cu-ZSM-5  | 17                                | 0.15                              | CBV 3024E           | 441  | 0.14  |
|           | 17                                | 0.20                              | CBV 3024E           | 467  | 0.15  |
|           | 17                                | 0.27                              | CBV 3024E           | 453  | 0.14  |
| Cu-SSZ-13 | 4.3                               | 0.02                              | -                   | 508  | 0.22  |
|           | 4.3                               | 0.04                              | -                   | 568  | 0.24  |
|           | 4.5                               | 0.09                              | -                   | 544  | 0.23  |
|           | 4.5                               | 0.16                              | -                   | 464  | 0.20  |
|           | 4.5                               | 0.20                              | -                   | 525  | 0.23  |
|           | 4.5                               | 0.35                              | -                   | 496  | 0.24  |

<sup>a</sup> Measured Si/Al<sub>tot</sub> and Cu/Al<sub>tot</sub> ratios were determined from atomic absorption spectroscopy.

<sup>b</sup> The 90% confidence intervals for surface area and micropore volumes are  $\pm 51$  m<sup>2</sup> g<sup>-1</sup> and  $\pm 0.01$  cm<sup>3</sup> g<sup>-1</sup>, respectively.

by holding for >48 h in a desiccator containing a saturated potassium chloride (KCl) solution prior to packing in a 4mm ZrO<sub>2</sub> rotor. All <sup>27</sup>Al MAS NMR spectra are referenced to an aqueous 1.0M Al(NO<sub>3</sub>)<sub>3</sub> solution.

The <sup>27</sup>Al MAS NMR spectra for the ZSM-5 samples are shown in Figure 2.10 and the spectra for SSZ-13 are shown in Figure 2.11.

Tetrahedrally-coordinated Al atoms were characterized by a line centered around 55 ppm (52 ppm for ZSM-5 and 58 ppm for SSZ-13), with a small shoulder representative of pentacoordinated Al [118,138,139]. The relative intensity of the resonance at 52 ppm in H-ZSM-5 increased with increasing Al content (Fig. 2.10). Octahedrally-coordinated Al atoms were characterized by a line centered at 0 ppm. The sum of

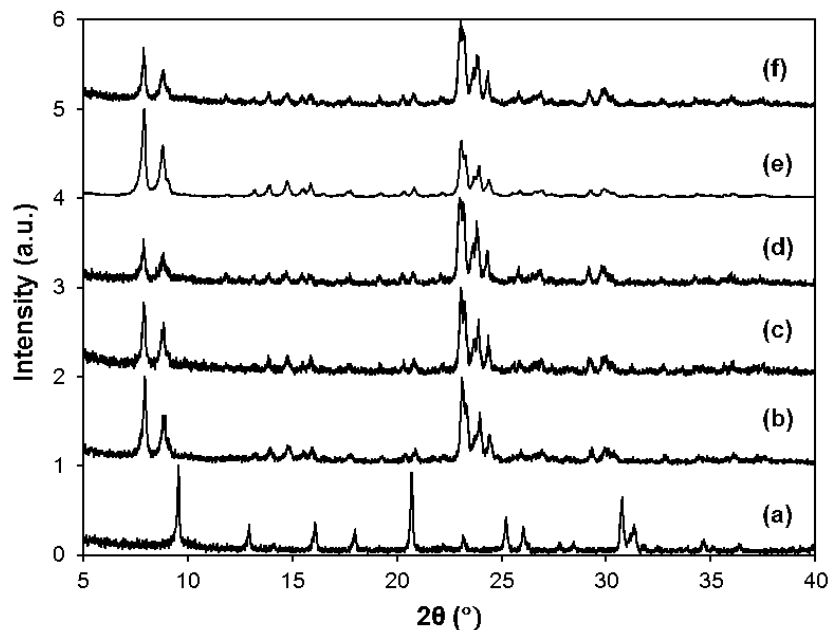


Figure 2.9. X-Ray diffraction patterns for (a) H-SSZ-13 ( $\text{Si}/\text{Al}_{\text{tot}} = 4.5$ ) and H-ZSM-5 with  $\text{Si}/\text{Al}_{\text{tot}}$  of (b) 12.5, (c) 17, (d) 30, (e) 43, and (f) 89.

the tetrahedral and pentacoordinated Al were taken to reflect the total amount of  $\text{Al}_f$  species present, while the octahedrally-coordinated Al atoms were taken to reflect  $\text{Al}_{\text{ex}}$  species. The fraction of Al present in tetrahedral coordination was estimated from the ratio of integrated areas for the 55 ppm line to the total Al area, and is listed for each sample in Table 2.4.

Small amounts of  $\text{Al}_{\text{ex}}$  species were observed in NMR spectra for H-ZSM-5 with  $\text{Si}/\text{Al}_{\text{tot}} = 43$  and 89, 6% and 7%, respectively, and the H-ZSM-5 with  $\text{Si}/\text{Al}_{\text{tot}} = 17$ , and 30 showed  $\text{Al}_{\text{ex}}$  content of less than 2% (Fig. 2.10). The NMR spectra of H-SSZ-13 showed a larger  $\text{Al}_{\text{ex}}$  contribution of 15% (Fig. 2.11). All  $\text{NH}_4$ -ZSM-5 and  $\text{NH}_4$ -SSZ-13 showed  $\text{Al}_{\text{ex}}$  content of less than 2%. A small increase in the amount of  $\text{Al}_{\text{ex}}$  was observed in the H-form relative to the  $\text{NH}_4$ -form zeolite, which can be attributed to either irreversible removal of  $\text{Al}_f$  species from the lattice to form  $\text{Al}_{\text{ex}}$  or

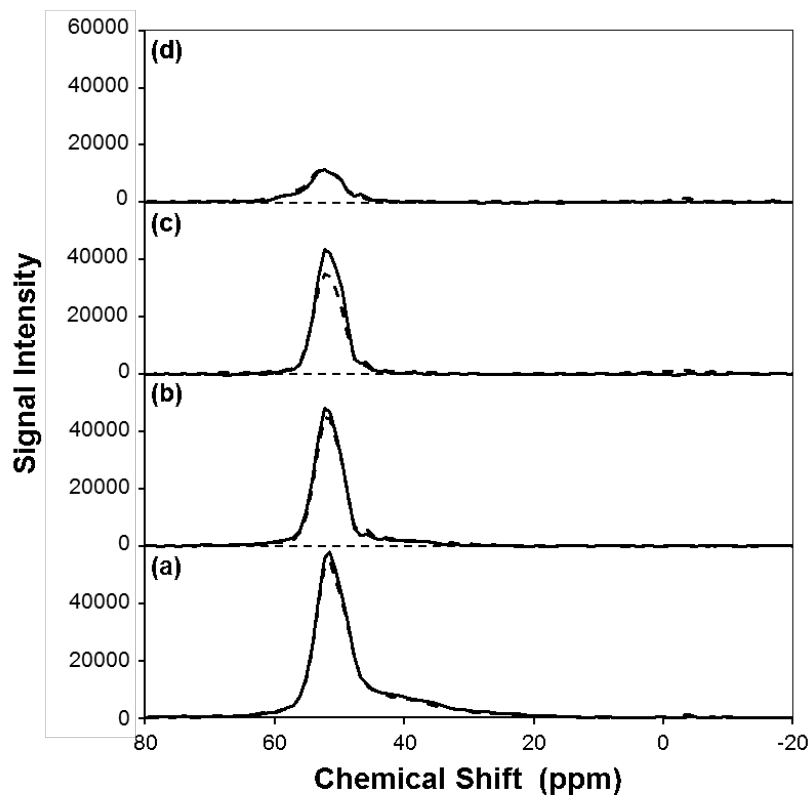


Figure 2.10.  $^{27}\text{Al}$  MAS NMR spectra for all H-ZSM-5 (dashed line) and  $\text{NH}_4$ -ZSM-5 (solid line) samples with  $\text{Si}/\text{Al}_{\text{tot}} =$  (a) 17, (b) 30, (c) 43, and (d) 89 [78].

to the reversible change between tetrahedral ( $\text{Al}_f$ ) and octahedral ( $\text{Al}_{\text{ex}}$ ) coordination depending on the surrounding conditions [118, 121, 122].

### 2.7.5 Comparison of $\text{NH}_3$ and n-propylamine titrations on ZSM-5 and SSZ-13

The number of  $\text{H}^+$  sites measured by  $\text{NH}_3$  titrations at 433 K, followed by purging in flowing helium, and measured by n-propylamine (Table 2.6, Section 2.7.7) are listed in Table 2.5, and are plotted in Figure 2.5 of the main text.

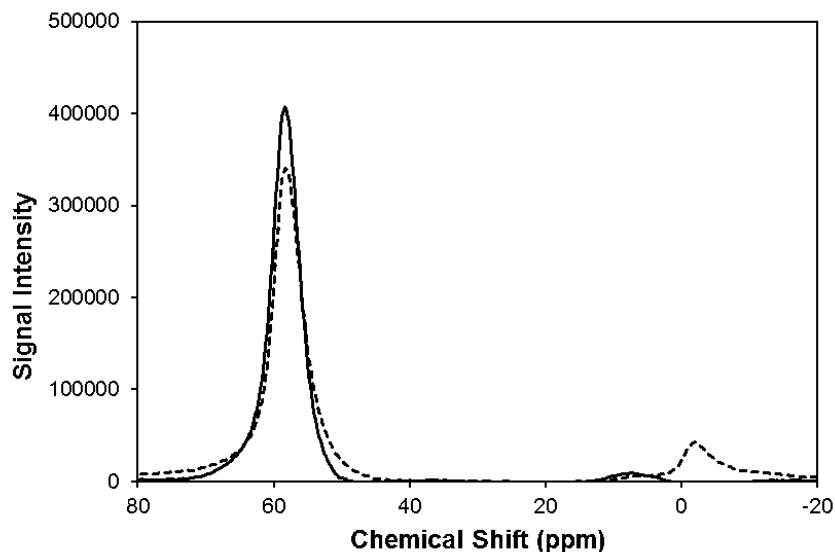


Figure 2.11.  $^{27}\text{Al}$  MAS NMR spectra for H-SSZ-13 (dashed line) and  $\text{NH}_4$ -ZSM-5 (solid line) samples with  $\text{Si}/\text{Al}_{\text{tot}} = 4.5$  [78].

Table 2.4.

$^{27}\text{Al}$  MAS NMR quantification results for H and  $\text{NH}_4$ -form of the ZSM-5 ( $\text{Si}/\text{Al}_{\text{tot}} = 17, 30, 43$ , and 89) and SSZ-13 ( $\text{Si}/\text{Al}_{\text{tot}} = 4.5$ ) samples [78].

| Zeolite       | Zeolyst Call Number | $\text{Si}/\text{Al}_{\text{tot}}^{\text{a}}$ | $\text{Al}_{\text{t}}/\text{Al}_{\text{tot}}$ for $\text{NH}_4$ -form <sup>b</sup> | $\text{Al}_{\text{ex}}/\text{Al}_{\text{tot}}$ for $\text{NH}_4$ -form | $\text{Al}_{\text{t}}/\text{Al}_{\text{tot}}$ for H-form <sup>b</sup> | $\text{Al}_{\text{ex}}/\text{Al}_{\text{tot}}$ for H-form |
|---------------|---------------------|---|--|--|---|---|
| <b>ZSM-5</b>  | CBV 3024E           | 17  | 1.0  | 0  | 0.99  | 0.01  |
|               | CBV 5524G           | 30  | 1.0  | 0  | 1.00  | 0.00  |
|               | CBV 8014            | 43  | 1.0  | 0  | 0.94  | 0.06  |
|               | CBV 1502            | 89  | 0.98   | 0.02   | 0.93  | 0.07  |
| <b>SSZ-13</b> | -                   | 4.5   | 0.99   | 0.01   | 0.85  | 0.15  |

<sup>a</sup> Measured  $\text{Si}/\text{Al}_{\text{tot}}$  ratios were determined from atomic absorption spectroscopy.

<sup>b</sup>  $\text{Al}_{\text{t}}$  contains the sum of areas for the tetrahedral and pentacoordinated Al species.

## 2.7.6 $\text{NH}_3$ TPD profiles after saturation at 323 K

The  $\text{NH}_3$  TPD profiles for H-ZSM-5 ( $\text{Si}/\text{Al}_{\text{tot}} = 17$ ) and H-SSZ-13 ( $\text{Si}/\text{Al}_{\text{tot}} = 4.5$ ) are shown in Figure 2.12, after the samples were saturated with gas-phase  $\text{NH}_3$

Table 2.5.

Comparison of the  $H^+/Al_{tot}$  ratios for zeolite samples measured by  $NH_3$  and *n*-propylamine (NPA).

| Zeolite                       | Si/ $Al_{tot}$ | Cu/ $Al_{tot}$ | $H^+/Al_{tot}$           |                      |                      |
|-------------------------------|----------------|----------------|--------------------------|----------------------|----------------------|
|                               |                |                | $NH_3^a$<br>(433 K, gas) | NPA<br>(323 K, avg.) | $H^{+NH_3}/H^{+NPA}$ |
| <b>H-ZSM-5<br/>(Zeolyst)</b>  | 17             | -              | 0.75                     | 0.79                 | 0.99                 |
|                               | 30             | -              | 1.02                     | 0.99                 | 1.00                 |
|                               | 43             | -              | 0.96                     | 1.01                 | 0.94                 |
|                               | 89             | -              | 0.68                     | 0.69                 | 0.93                 |
| <b>H-SSZ-13</b>               | 4.5            | -              | 0.65                     | 0.17                 | 3.82                 |
| <b>Cu-ZSM-5<br/>(Zeolyst)</b> | 17             | 0.15           | 0.35                     | 0.43                 | 0.81                 |
|                               | 17             | 0.20           | 0.34                     | 0.32                 | 1.08                 |
|                               | 17             | 0.27           | 0.38                     | 0.34                 | 1.13                 |
| <b>Cu-SSZ-13</b>              | 4.5            | 0.02           | 0.45                     | 0.06                 | 7.32                 |
|                               | 4.5            | 0.04           | 0.60                     | 0.07                 | 8.44                 |
|                               | 4.5            | 0.09           | 0.43                     | 0.04                 | 11.27                |
|                               | 4.5            | 0.16           | 0.32                     | 0.04                 | 7.95                 |
|                               | 4.5            | 0.20           | 0.31                     | 0.02                 | 15.31                |
|                               | 4.5            | 0.35           | 0.24                     | 0.002                | 164.92               |

<sup>a</sup>  $NH_3$  saturation performed at 433 K with He purge.

<sup>b</sup> *n*-Propylamine  $H^+/Al_{tot}$  is the average of the  $H^+/Al_{tot}$  determined from the decomposition products ( $NH_3$  and  $C_3H_6$ ) [2].

at 323 K. The low temperature peak centered at ca. 433 K corresponded to weakly-bound and Lewis acid-bound  $NH_3$ , while the high temperature peak at ca. 600 K corresponded to  $NH_4^+$  bound to  $H^+$  sites [78].

#### 2.7.7 *n*-Propylamine titrations of ZSM-5 and SSZ-13 zeolites

Alkylamine titrants of varying alkyl chain length ( $C_1$ - $C_4$ ) are often chosen to count  $H^+$  sites on solid acids, because although they adsorb onto both Brønsted and Lewis acid sites, they decompose via Hoffman-type elimination reactions only on  $H^+$  sites to form  $NH_3$  and the corresponding alkene (Scheme 2.13) [114–117].

The adsorption of *n*-propylamine (ca. 0.53 nm in diameter [78]) on medium-pore H-ZSM-5 and Cu-ZSM-5 zeolites (ca. 0.51 nm in diameter [127]) led to the evolution



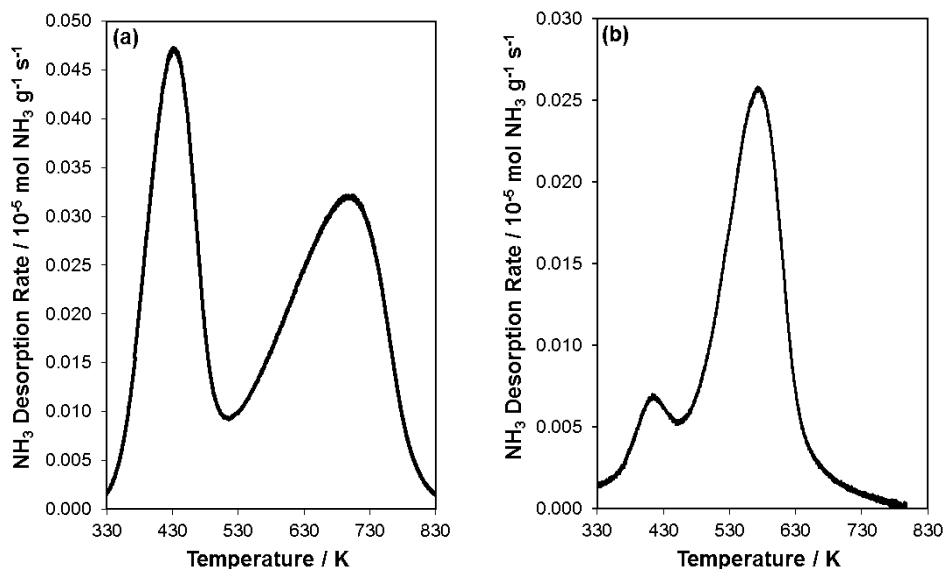


Figure 2.12.  $\text{NH}_3$  desorption rates during TPD of (a) H-ZSM-5 ( $\text{Si}/\text{Al}_{\text{tot}} = 43$ ) and (b) H-SSZ-13 ( $\text{Si}/\text{Al}_{\text{tot}} = 4.5$ ) after gas phase saturation with  $\text{NH}_3$  at 323 K

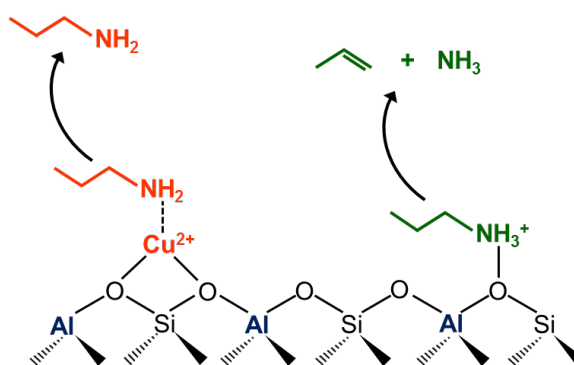


Figure 2.13. n-Propylamine decomposes only on Brønsted acid sites to form  $\text{NH}_3$  and  $\text{C}_3\text{H}_6$  [117].

of equimolar amounts of  $\text{NH}_3$  and  $\text{C}_3\text{H}_6$  during a subsequent TPD (Figure 2.13), Table 2.6), as expected from the reactive decomposition of n-propylammonium ions at  $\text{H}^+$  sites. The numbers of  $\text{NH}_3$  and  $\text{C}_3\text{H}_6$  species (per  $\text{Al}_{\text{tot}}$ ) evolved via reactive n-propylamine decomposition on H-ZSM-5 zeolites of varying Al content ( $\text{Si}/\text{Al}_{\text{tot}} =$

17-89), and on Cu-ZSM-5 zeolites of varying Cu content ( $\text{Si}/\text{Al}_{\text{tot}}=17$   $\text{Cu}/\text{Al}_{\text{tot}}=0$ -0.27) are listed in Table 2.6 [78]. For the samples with  $\text{Cu}/\text{Al}_{\text{tot}} = 0.15$  and 0.20, reactive n-propylamine decomposition detects two fewer residual  $\text{H}^+$  sites per Cu (Table 2.6), consistent with the exchange of each  $\text{Cu}^{2+}$  cation for two  $\text{H}^+$  sites. The number of residual  $\text{H}^+$  sites is similar for the samples with  $\text{Cu}/\text{Al}_{\text{tot}} = 0.20$  and 0.27 (Table 2.6), indicating that different Cu species may be present on the  $\text{Cu}/\text{Al}_{\text{tot}} = 0.27$  sample.

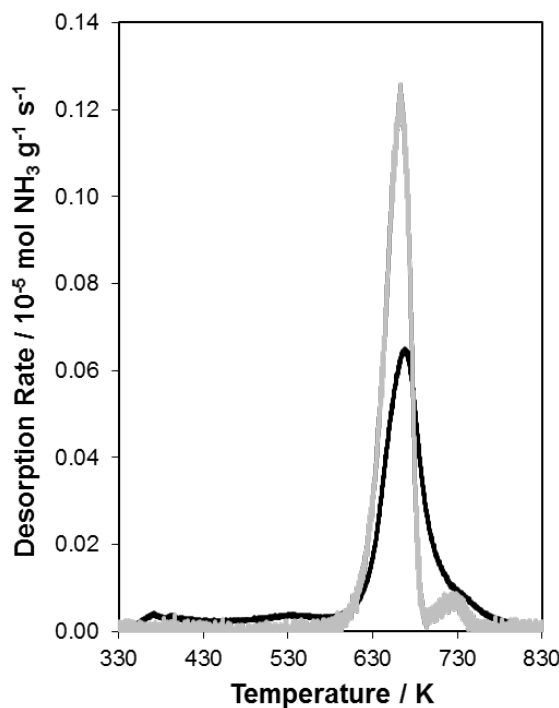


Figure 2.14. Desorption rates of reactive n-propylamine decomposition products  $\text{NH}_3$  (dark trace) and  $\text{C}_3\text{H}_6$  (light trace) during TPD of H-ZSM-5 ( $\text{Si}/\text{Al}_{\text{tot}} = 17$ ) [78].

### 2.7.8 Ambient UV-Visible Spectroscopy of Cu-SSZ-13

Ambient UV-Visible-Near Infrared (UV-Vis-NIR) spectra measured using a diffuse reflectance technique were collected on a Varian UV-Vis-NIR spectrophotome-

Table 2.6.

Number of  $H^+$  sites measured from the  $NH_3$  and  $C_3H_6$  desorbed after n-propylamine decomposition on H- and Cu-form zeolites. Data originally reported by Bates et al. [78].

| Zeolite   | Si/Al <sub>tot</sub> | Cu/Al <sub>tot</sub> | H <sup>+</sup> /Al <sub>tot</sub> |  | Al <sub>f</sub> /Al <sub>tot</sub> <sup>a</sup> | H <sup>+</sup> /Al <sub>f</sub> <sup>b</sup> |
|-----------|----------------------|----------------------|-----------------------------------|--|---|--|
|           |                      |                      | NPA<br>(323 K, NH <sub>3</sub> )  | NPA<br>(323 K, C <sub>3</sub> H <sub>6</sub> ) |   |  |
| H-ZSM-5   | 17                   | -                    | 0.80                              | 0.77   | 0.99  | 0.79   |
|           | 30                   | -                    | 0.98                              | 0.99   | 1.00  | 0.99   |
|           | 43                   | -                    | 1.06                              | 0.95   | 0.94  | 1.06   |
|           | 89                   | -                    | 0.71                              | 0.67   | 0.93  | 0.74   |
| Cu-ZSM-5  | 17                   | 0.15                 | 0.40                              | 0.46   |   | 0.43   |
|           | 17                   | 0.20                 | 0.33                              | 0.30   | 0.99  | 0.32   |
|           | 17                   | 0.27                 | 0.35                              | 0.32   |   | 0.34   |
| H-SSZ-13  | 4.5                  | -                    | 0.16                              | 0.18   | 0.85  | 0.20   |
| Cu-SSZ-13 | 4.5                  | 0.02                 | 0.06                              | 0.06   |   | 0.07   |
|           | 4.5                  | 0.04                 | 0.08                              | 0.08   |   | 0.09   |
|           | 4.5                  | 0.09                 | 0.04                              | 0.03   |   | 0.04   |
|           | 4.5                  | 0.16                 | 0.05                              | 0.03   | 0.85  | 0.05   |
|           | 4.5                  | 0.20                 | 0.02                              | 0.02   |   | 0.02   |
|           | 4.5                  | 0.35                 | 0.00                              | 0.00   |   | 0.00   |

<sup>a</sup> Al<sub>f</sub>/Al<sub>tot</sub> values determined from <sup>27</sup>Al MAS NMR and details can be found in Table S2 (Supporting Information).

<sup>b</sup> H<sup>+</sup>/Al<sub>f</sub> is the average of the H<sup>+</sup>/Al<sub>f</sub> counts from NH<sub>3</sub> and C<sub>3</sub>H<sub>6</sub> desorption.

ter (Cary 5000) equipped with a Harrick-Scientific Praying-Mantis diffuse reflectance accessory (DRA). Barium sulfate (BaSO<sub>4</sub>, 98 wt%, Sigma Aldrich) was used as a reference material when collecting background scans. This material was sieved to a particle size of 125–250  $\mu m$  before taking the background scan. UV-Vis spectra were collected from 7000–50,000  $cm^{-1}$  at a scan speed of 2000  $cm^{-1} min^{-1}$ . Cu-SSZ-13 samples were pretreated in 10% O<sub>2</sub>/N<sub>2</sub> at 798 K elsewhere and subsequently exposed to ambient conditions. This was done to ensure that these samples were hydrated. Approximately 0.1 g of each sample was placed in the sample cup and spectral measurements were taken. The peak observed at 12,500  $cm^{-1}$  is the contribution from the d–d transition of hydrated isolated Cu<sup>2+</sup> ions [36, 129]. The peaks between 30,000–50,000  $cm^{-1}$  have been assigned to a convolution of different oxygen to Cu<sup>2+</sup> charge transfer and bare zeolite absorption edge [36, 129]. The integrated spectra of the band at 12,500  $cm^{-1}$  can be found below in Figure 2.15. A linear increase in the integrated

absorbance band area centered around  $12,500\text{ cm}^{-1}$  was observed for increasing total Cu content ( $\text{Cu}/\text{Al}_{\text{tot}}$ ) and is demonstrated by a best fit trendline passing through the origin.

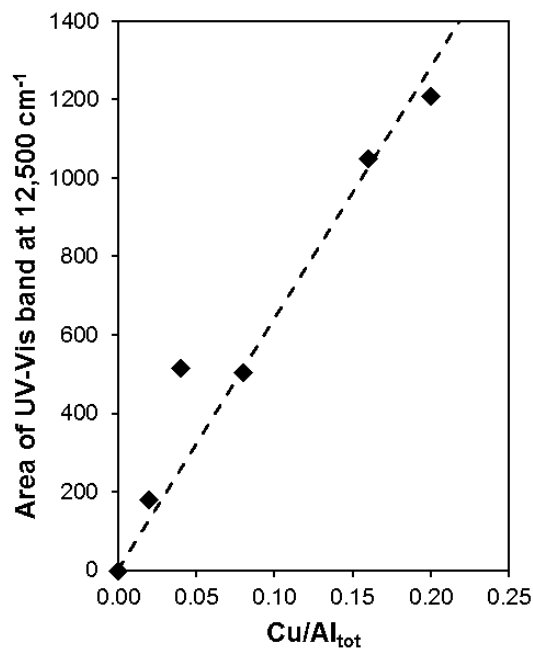


Figure 2.15. Integrated area of the hydrated  $\text{Cu}^{2+}$  d-d transition absorbance band (centered at  $12,500\text{ cm}^{-1}$ ) measured by UV-Vis spectroscopy as a function of total Cu content ( $\text{Cu}/\text{Al}_{\text{tot}}$ ). The dashed line represents the best fit for a linear trendline through the origin.

### 3. CONTROLLING THE ISOLATION AND PAIRING OF ALUMINUM IN CHABAZITE ZEOLITES USING MIXTURES OF ORGANIC AND INORGANIC STRUCTURE-DIRECTING AGENTS

#### 3.1 Introduction

Brønsted acidic zeolites are silica-based molecular sieve frameworks that contain a fraction of their silicon atoms substituted with aluminum atoms, which generate anionic charges balanced by protons that differ in local micropore environment among known zeolite topologies and in density with changes in bulk elemental composition (Si/Al ratio). Even a given zeolite at fixed composition, however, contains structural and catalytic diversity conferred by the arrangement and distribution of its framework Al atoms. One type of Al arrangement describes the location of Al atoms among different pores of a given zeolite, as in the case of ferrierite (FER) zeolites (Si/Al = 10-20) that can be synthesized with mixtures of organic structure directing agents (SDAs) that differ in size and direct the siting of framework Al atoms in either 8-membered ring (8-MR) or 10-MR locations [140–142]. Similarly, MFI zeolites synthesized in the presence of only tetrapropylammonium ( $\text{TPA}^+$ ) cations contain higher fractions of Al atoms located in 10-MR channel intersections, within which  $\text{TPA}^+$  cations remain occluded in crystalline products, than MFI zeolites synthesized with mixtures of organic  $\text{TPA}^+$  and inorganic alkali ( $\text{Na}^+$ ) cations, which reside within straight and sinusoidal 10-MR channels [32]. The distribution of Al among different voids of a given zeolite influences catalytic reactivity, in spite of the similar acid strength of attendant protons [16], because reactive intermediates and transition states stabilized at such protons interact with surrounding oxide cavities by van der Waals forces whose strength depends on the geometry of the confining environment [21, 143, 144]. This Al distribution also influences the structural stability of a given zeolite, as in

the case of BEA zeolites whose Al atoms in different tetrahedral sites (T-sites), quantified by fitting Al K-edge extended X-ray absorption fine-structure (EXAFS) and  $^{27}\text{Al}$  MAS NMR spectra to those derived from DFT-based molecular dynamics simulations, showed different susceptibility to steam dealumination after hot liquid water treatments (433-573 K, 24 h) [145–147].

Another type of Al arrangement describes the proximity of Al atoms within the framework, ranging from the limit of Al site isolation ( $\text{Al-O}(-\text{Si-O})_x\text{-Al}$ ,  $x \geq 3$ ) to higher densities of proximal or “paired” Al atoms, which are defined here as two Al atoms separated by either one or two Si atoms in a 6-MR ( $\text{Al-O}(-\text{Si-O})_x\text{-Al}$ ,  $x = 1, 2$ ; Figure 3.1) because both configurations in chabazite (CHA) zeolites exchange divalent cations with similar energies (within 20 kJ/mol for  $\text{Cu}^{2+}$  according to DFT) [37,148]. Steam dealumination of faujasite (FAU) zeolites preferentially removes Al atoms in next-nearest neighbor configurations, identified by  $\text{Q}_2$  sites ( $(\text{Si-O})_2\text{-Si}(\text{O-Al})_2$ :  $\delta = -95$  ppm) in  $^{29}\text{Si}$  MAS NMR spectra, to form “ultra-stable” Y (USY) zeolites that contain predominantly isolated Al atoms that are less susceptible to further structural changes [149–151]. Isolated Al atoms among different T-sites and zeolite topologies in periodic DFT models generate protons of equivalent ensemble-averaged deprotonation energy (DPE) [16], a rigorous and probe-independent measure of Brønsted acid strength that influences reactivity in acid catalysis [152–155], while paired Al atoms generate weaker protons with higher DPE values (by 11-108 kJ  $\text{mol}^{-1}$ ) according to quantum chemical calculations on embedded cluster models [156]. Higher fractions of isolated Al atoms in CHA zeolites, achieved by increasing the bulk Si/Al ratio from 2 to 70, correlate with longer time-on-stream stabilities and lesser amounts of coke formed during methanol-to-olefins (MTO) catalysis (548-673 K) [157,158]. These findings indicate that synthetic methods that control the isolation and pairing of framework Al atoms in zeolites would provide new opportunities to introduce structural and catalytic diversity in a given zeolite at fixed composition.

The collective work of Dedecek and co-workers has provided evidence that different procedures used to synthesize MFI and other zeolites lead to different fractions of

paired Al atoms, quantified by  $\text{Co}^{2+}$  titration, and has concluded that Al siting in zeolites is not determined randomly but also is not controlled by simple rules [48]. MFI zeolites synthesized with  $\text{TPA}^+$  cations as the organic SDA and different Al sources ( $\text{AlCl}_3$ ,  $\text{Al}(\text{NO}_3)_3$ ,  $\text{Al}_2\text{O}_3$ , Al-tri-*sec*-butoxide) contained similar Si/Al ratios (28-29) but varying fractions of paired Al (0.07-0.33), while MFI zeolites synthesized with  $\text{Al}(\text{OH})_3$  or metallic Al sources contained higher fractions of paired Al ( $>0.50$ ) but also higher Si/Al ratios (34-60) [74]. In contrast, MFI zeolites synthesized with only  $\text{TPA}^+$  and different Si sources (tetraethoxy orthosilicate, fumed silica, colloidal silica, sodium silicate) contained similar paired Al fractions (0.06-0.12) and similar Si/Al ratios (23-25) [65]. The addition of  $\text{Na}^+$  (via  $\text{NaCl}$ ) to  $\text{TPA}^+$ -containing synthesis gels crystallized MFI zeolites (Si/Al = 22) with lower paired Al fractions (0.15) than those crystallized with  $\text{TPA}^+$  alone (0.40), but only to a point, beyond which increasing  $\text{Na}^+$  concentrations did not influence the crystalline products formed [159]. The use of Na sources with different counteranions ( $\text{OH}^-$ ,  $\text{Cl}^-$ ,  $\text{PO}_4^{3-}$ ; fixed Na/Al = 3.3) crystallized MFI zeolites (Si/Al = 21-29) with paired Al fractions that varied with counteranion identity (0.06, 0.14, 0.24, respectively) and were invariant with  $\text{Na}^+$  content (Na/Al = 3.3-9.9) when  $\text{Cl}^-$  and  $\text{PO}_4^{3-}$  were present (0.14-0.18 and 0.22-0.26, respectively), but increased with  $\text{Na}^+$  content (0.06-0.58) when  $\text{OH}^-$  was present [74]. Taken together, these findings suggest that the isolated and paired Al distribution in MFI zeolites can *sometimes* be influenced by changing the concentrations and identities of certain reactant precursors, but without predictable or systematic trends with a single synthesis parameter and, in certain cases, also with changes to zeolite bulk composition (Si/Al = 20-60).

Here, we focus on the synthesis of CHA zeolites (SSZ-13) [109], which are used commercially in their H-form to catalyze MTO [160,161] and after Cu- or Fe-exchange to catalyze  $\text{NO}_x$  ( $x = 1, 2$ ) selective catalytic reduction (SCR) with ammonia in mobile-source pollution abatement [88,90]. CHA zeolites contain one unique T-site and double 6-membered ring (6-MR) building units that interconnect to form 8-MR windows (0.38 nm diam.), which limit transport into larger cages (0.82 nm diam.,

18 T-atoms per cage). They are commonly synthesized in the presence of N,N,N-trimethyl-1-adamantylammonium cations (TMAda<sup>+</sup>), which become occluded within CHA cages during crystallization [162], although other organic SDAs (tetraethylammonium hydroxide, benzyltrimethylammonium hydroxide) have also been reported [163–165]. Methods to synthesize low-silica SSZ-13 zeolites (Si/Al < 7) involve using low-silica FAU zeolites (Si/Al < 5) as the Al source in the presence of TMAda<sup>+</sup> [162], or using amorphous aluminosilicate [166] and FAU precursors [167] in organic-free media. Methods to synthesize high-silica SSZ-13 zeolites of varying Si/Al ratio (Si/Al > 10) involve preparing precursor solutions in hydroxide media with equimolar amounts of Na<sup>+</sup> and TMAda<sup>+</sup> cations with varying Al content [84, 109, 158], or in fluoride media using only TMAda<sup>+</sup> [168]. Mechanistic insights and conclusions regarding the consequences of synthesis methods on the siting of Al atoms in CHA zeolites have not been made previously, but different preparation routes are expected to influence the Al distribution as has been previously suggested for CHA zeolites [169] and demonstrated for MFI zeolites [65, 74, 159].

Here, we report methods for the systematic control of Al isolation in SSZ-13 zeolites, at constant Si/Al ratio, by systematically changing the Na<sup>+</sup>/TMAda<sup>+</sup> ratio in the synthesis solution. We provide evidence that SSZ-13 crystallized in hydroxide media with only TMAda<sup>+</sup> cations contain exclusively isolated framework Al atoms, and that the number of paired Al atoms increases linearly with the number of Na<sup>+</sup> cations retained within final crystalline products. During these syntheses, the total hydroxide concentration (OH<sup>−</sup>/Al), Si/Al ratio, total cationic charge ((Na<sup>+</sup> + TMAda<sup>+</sup>)/Al), total water content, reagent precursor sources, and synthesis conditions are held constant. This carefully regulated and systematic synthesis approach enables us to isolate the consequences of using organic and inorganic SDA mixtures on the formation of paired Al atoms in SSZ-13 at fixed Si/Al ratio, and to identify a clear, predictive and single-valued synthesis-structure relation between the fraction of paired Al in SSZ-13 zeolites and the Na<sup>+</sup>/TMAda<sup>+</sup> ratio in the hydroxide media used to crystallize them.



## 3.2 Experimental Methods

### 3.2.1 Synthesis of SSZ-13 zeolites

High-aluminum Na-SSZ-13 zeolites ( $\text{Si}/\text{Al} = 5$ ) were synthesized using a recipe adapted from the procedure described by Fickel et al. [34], which is a modified version of the original synthesis reported by Zones [162] and can be found in Section 3.7.1 of the Supporting Information. SSZ-13 zeolites of  $\text{Si}/\text{Al} = 15$  and 25 were synthesized following an adapted procedure described by Deka et al. [84], which is a modified version of the original synthesis reported by Zones [109], and can be found in Section 3.7.2 of the Supporting Information. Pure-silica chabazite was synthesized following the procedure reported by Diaz-Cabanas et al. [170] and is described in Section 3.7.3 of the Supporting Information.

Synthesis of  $\text{Na}^+$ -free SSZ-13 zeolites ( $\text{Si}/\text{Al} = 10, 15, 20, 25, 30, 60$ ) was attempted in hydroxide media from precursor solutions containing molar ratios of 1  $\text{SiO}_2$ / X  $\text{Al}_2\text{O}_3$ / 0.5 TMAdaOH/ 44  $\text{H}_2\text{O}$ , where X was varied between 0.067-0.20 (full synthesis procedures in Section 3.7.4, Supp. Info.). In a typical synthesis experiment, an aqueous TMAdaOH solution (25 wt% Sachem) was added to deionized water (18.2 M $\Omega$ ) in a perfluoroalkoxy alkane (PFA) container (Saville Corp.) and stirred for 15 minutes under ambient conditions. Next,  $\text{Al}(\text{OH})_3$  (98 wt%, SPI Pharma) was added to the TMAdaOH solution and the mixture was homogenized for 15 minutes under ambient conditions. Then, colloidal silica (Ludox HS40, 40 wt%, Sigma Aldrich) was added to the mixture and the contents were stirred for 2 h at ambient conditions until a homogeneous solution was obtained. The synthesis solution was then transferred to a 45 ml Teflon-lined stainless steel autoclave (Parr Instruments) and heated in a forced convection oven (Yamato DKN-402C) at 433 K and rotated at 40 RPM for 6 days.

SSZ-13 zeolites were synthesized in hydroxide media from precursor solutions that contained a constant  $\text{Na}^+/\text{TMAda}^+$  ratio of 0.67 but with varying  $\text{Si}/\text{Al}$  ratios (10-200), in which precursor solutions contained molar ratios of 1  $\text{SiO}_2$ / X

$\text{Al}_2\text{O}_3$ / 0.3 TMAdaOH/ 0.2 NaOH/ 44  $\text{H}_2\text{O}$  (full synthesis procedures in Section 3.7.5, Supp. Info.). SSZ-13 zeolites were synthesized at Si/Al ratios of 15 and 25 with varying charge density ( $\text{Na}^+/\text{TMAda}^+ = 0\text{-}3$ ), but with constant total charge ( $(\text{Na}^+ + \text{TMAda}^+)/\text{Al} = 7.5$ ), in which precursor solutions contained molar ratios of 1  $\text{SiO}_2$ / Y  $\text{Al}_2\text{O}_3$ / X TMAdaOH/  $(0.5 - X)$  NaOH/ 44  $\text{H}_2\text{O}$  (full synthesis procedures in Section 3.7.6, Supp. Info.). SSZ-13 zeolites were synthesized at a solution Si/Al ratio of 15 with varying charge density ( $\text{Na}^+/\text{TMAda}^+ = 0\text{-}5.6$ ) and varying total cationic charge ( $(\text{Na}^+ + \text{TMAda}^+)/\text{Al} = 5.4\text{-}7.1$ ) (full synthesis procedures in Section 3.7.7, Supp. Info.). The preparation and crystallization procedures for  $\text{Na}^+$ -containing zeolites occurred as described for  $\text{Na}^+$ -free zeolites, in which the Al addition and homogenization step was followed by addition of  $\text{Na}^+$  via a 5M sodium hydroxide solution (NaOH: 16.7 wt% NaOH in deionized water; NaOH 98 wt% Alfa Aesar) and homogenization for 15 minutes under ambient conditions.

### 3.2.2 Preparation of H-form and partially cation-exchanged zeolites

Solids were recovered from autoclaves after their allotted crystallization time and washed thoroughly with deionized water (18.2 M $\Omega$ ) and acetone (99.9 wt%, Sigma Aldrich) in alternating steps (70  $\text{cm}^3$  solvent per g solids) until the pH of the supernatant remained constant between washes, followed by a final water wash to remove residual acetone. Solids then were recovered via centrifugation, dried at 373 K under stagnant air for 24 h, and then treated in flowing dry air (1.67  $\text{cm}^3 \text{ s}^{-1} \text{ g}_{\text{cat}}^{-1}$ , 99.999 % UHP, Indiana Oxygen) at 853 K (0.0167 K  $\text{s}^{-1}$ ) for 10 h. The residual  $\text{Na}^+$  content was removed by converting to the  $\text{NH}_4$ -form via aqueous phase ion-exchange using 150  $\text{cm}^3$  of a 1.0M  $\text{NH}_4\text{NO}_3$  solution (8.0 wt% in  $\text{H}_2\text{O}$ ; 99.9 wt%, Sigma Aldrich) per g solids for 24 h at ambient conditions, followed by washing the solids four times with deionized water (70  $\text{cm}^3$  per g solids).  $\text{NH}_4$ -form zeolites were recovered using centrifugation, dried at 373 K under stagnant air for 24 h, and then converted to their H-form by treatment in flowing dry air (1.67  $\text{cm}^3 \text{ s}^{-1} \text{ g}_{\text{cat}}^{-1}$ , 99.999% UHP, Indiana Oxygen) at 773 K (0.0167 K  $\text{s}^{-1}$ ) for 4 h.

H-SSZ-13 zeolites were converted to their  $\text{Cu}^{2+}$  form by ion-exchange using aqueous  $\text{Cu}(\text{NO}_3)_2$  solutions with molarities ranging between 0.001 M-0.25 M (0.02-3.75 wt%  $\text{Cu}(\text{NO}_3)_2$ ; 99 wt%, Sigma Aldrich) for 4 h at ambient conditions under stirring. The pH of the exchange solution was controlled to 5 through dropwise addition of 0.1 M  $\text{NH}_4\text{OH}$  (ca. pH = 11; Sigma Aldrich). After  $\text{Cu}^{2+}$  exchange, samples were washed four times with deionized water until the pH was constant between washes, recovered via centrifugation, and then dried at 373 K under stagnant air for 24 h. Cu-zeolites were then treated in flowing dry air ( $1.67 \text{ cm}^3 \text{ s}^{-1} \text{ g}_{\text{cat}}^{-1}$ , 99.999% UHP, Indiana Oxygen) at 773 K ( $0.0167 \text{ K s}^{-1}$ ) for 4 h.

H-SSZ-13 zeolites were converted to their  $\text{Co}^{2+}$  form by an aqueous ion-exchange using  $150 \text{ cm}^3$  of a 0.25 M  $\text{Co}(\text{NO}_3)_2$  (4.6 wt%  $\text{Co}(\text{NO}_3)_2$ ; 99 wt%, Sigma Aldrich) solution per g zeolite for 4 h at ambient conditions under stirring. The pH of the exchange solution was not controlled and reached a final value of ca. 3.3 after 4 h. After the exchange the samples were washed four times with deionized water ( $70 \text{ cm}^3$  per g solids), recovered using centrifugation, and dried at 373 K under stagnant air for 24 h. Co-SSZ-13 materials were then treated in flowing dry air ( $1.67 \text{ cm}^3 \text{ s}^{-1} \text{ g}_{\text{cat}}^{-1}$ , 99.999% UHP, Indiana Oxygen) at 773 K ( $0.0167 \text{ K s}^{-1}$ ) for 4 h. A subsequent  $\text{Co}^{2+}$  ion exchange was performed using a 0.5M  $\text{Co}(\text{NO}_3)_2$  solution (9.2 wt%  $\text{Co}(\text{NO}_3)_2$ ) to verify that each sample was saturated with  $\text{Co}^{2+}$  after exchanges performed with 0.25 M solutions.

H-SSZ-13 zeolites were converted to their  $\text{Na}^+$  form using  $150 \text{ cm}^3$  of an aqueous NaCl (99 wt%, Sigma Aldrich) solution per g zeolite with molarities ranging from 0.01-2.0 M (0.06-11.7 wt% NaCl in deionized water) for 24 h at ambient conditions. The pH of the  $\text{Na}^+$  exchanges was not controlled and reached a final value of ca. 3.2 after 24 h.  $\text{Na}^+$  exchanged samples were washed four times with deionized water ( $70 \text{ cm}^3$  per g solids), recovered using centrifugation, and dried at 373 K under stagnant air for 24 h. Na-SSZ-13 materials were then treated in flowing dry air ( $1.67 \text{ cm}^3 \text{ s}^{-1} \text{ g}_{\text{cat}}^{-1}$ , 99.999% UHP, Indiana Oxygen) at 773 K ( $0.0167 \text{ K s}^{-1}$ ) for 4 h.

### 3.2.3 Zeolite Characterization

Zeolite topologies were determined from powder X-ray diffraction (XRD) patterns measured on a Rigaku SmartLab X-ray diffractometer with a Cu K $\alpha$  radiation source ( $\lambda=0.154$  nm) operated at 1.76 kW. Typically, 0.50 g of zeolite powder were loaded onto a high volume sample holder (Rigaku) and the diffraction pattern was measured from 4–40°  $2\theta$  at a scan rate of 0.04° s<sup>-1</sup>. Powder XRD patterns for all synthesized materials were compared to a known reference material and to diffraction patterns for CHA (SSZ-13) and MOR reported in the International Zeolite Association (IZA) structure database [1]. All XRD patterns are normalized such that the maximum peak intensity in each pattern is set to unity, and are shown in Section 3.7.8 of the Supporting Information.

Zeolite micropore volumes were determined from Ar adsorption isotherms measured on H-SSZ-13 samples held at 87 K in a liquid Ar bath using a Micromeritics ASAP 2020 Surface Area and Porosity Analyzer. Micropore volumes were obtained by converting adsorbed gas volumes (cm<sup>3</sup> g<sub>cat</sub><sup>-1</sup> at STP) to liquid volumes using a density conversion factor assuming the liquid density of Ar at 87 K. Samples were pelleted and sieved to a nominal diameter between 180–250  $\mu$ m before degassing by heating 0.03–0.05 g of sieved sample to 393 K (0.167 K s<sup>-1</sup>) under high vacuum (ca. 5  $\mu$ mHg) for 2 h, and then further heating to 623 K (0.167 K s<sup>-1</sup>) under high vacuum (5  $\mu$ mHg) and holding for 9 h. Micropore volumes (cm<sup>3</sup> g<sub>cat</sub><sup>-1</sup> at STP) were estimated from extrapolation of the linear volumetric uptake during the beginning of mesopore filling (0.08–0.30 P/P<sub>0</sub>) to zero relative pressure, which agreed with micropore volumes estimated from analyzing the semi-log derivative plot of the adsorption isotherm ( $\partial(V_{\text{ads}})/\partial(\ln(P/P_0))$  vs.  $\ln(P/P_0)$ ). All Ar adsorption isotherms are shown in Section 3.7.9 of the Supporting Information.

Atomic absorption spectroscopy (AAS) was used to determine the total Si, Al, Na, Cu, and Co content of each sample using a Perkin Elmer AAnalyst 300 Atomic Absorption Spectrometer. Samples were prepared for AAS measurements by dissolv-

ing 0.02 g of zeolite in 3 g of hydrofluoric acid (48 wt%, Sigma Aldrich), letting the solution sit overnight, and then diluting with 60 g of deionized water (18.2 M $\Omega$ ). *Caution: when working with HF acid, use appropriate personal protective equipment, ventilation, and other safety measures.* Absorbances were measured using radiation sources at wavelengths of 251.6 nm and 309.3 nm for Si and Al, respectively, in a reducing acetylene/nitrous oxide flame and at wavelengths of 589.0 nm, 324.8 nm, and 240.7 nm for Na, Cu, and Co, respectively, in an oxidizing acetylene/air flame. Elemental compositions were determined from calibration curves derived from known standard solutions.

Thermogravimetric analysis (TGA) experiments were performed on a TA Instruments SDT Q600 thermogravimetric analyzer and differential scanning calorimeter (TGA-DSC) by heating 0.02 g of as-synthesized SSZ-13 in 83.3 cm<sup>3</sup> s<sup>-1</sup> g<sub>cat</sub><sup>-1</sup> dry air (UHP, 99.999%, Indiana Oxygen) to 523 K (0.167 K s<sup>-1</sup>) and holding for 0.5 h to remove physisorbed water before further heating to 1073 K (0.167 K s<sup>-1</sup>). Combustion of the organic structure directing agent was characterized by a sharp exothermic heat flow centered around 773 K, which was accompanied by a sharp decrease in mass. All SSZ-13 samples exhibited a weight loss of about 20 wt% associated with combustion of TMAda<sup>+</sup>, corresponding to one TMAda<sup>+</sup> molecule per CHA cage (Table 3.3, Section 3.7.10 in Supp. Info.), consistent with reported organic weight loss of TMAda<sup>+</sup> synthesized SSZ-13 [158, 162].

<sup>27</sup>Al magic angle spinning nuclear magnetic resonance (MAS NMR) spectra were recorded on H-SSZ-13 zeolite samples to quantify their fraction of framework and extraframework Al. NMR spectra of H-SSZ-13 were collected using a Chemmagetics CMX-Infinity 400 spectrometer in a wide-bore 9.4 Tesla magnet (Purdue Interdepartmental NMR Facility) and were acquired at ambient conditions using a 2.3  $\mu$ s pulse (equivalent to ca. 30 degrees), an acquisition time of 12.8ms and a relaxation delay of 1s and were measured at 104.24 MHz and a MAS rate of 5 kHz. <sup>1</sup>H decoupling was used during acquisition, employing two-pulse phase modulation (TPPM) scheme. Zeolite samples were hydrated by holding for >48 h in a desiccator containing a sat-

urated potassium chloride (KCl) solution prior to packing in a 4mm ZrO<sub>2</sub> rotor. All <sup>27</sup>Al MAS NMR spectra are referenced to a static sample of AlCl<sub>3</sub> dissolved in D<sub>2</sub>O (0 ppm <sup>27</sup>Al line) and are shown in Section 3.7.11 of the Supporting Information.

<sup>29</sup>Si MAS NMR spectra were recorded on H-SSZ-13 samples to characterize their coordination of Si atoms. Spectra of H-SSZ-13 were collected using a Chemagnetics CMX-Infinity 400 spectrometer in a wide-bore 9.4 Tesla magnet (Purdue Interdepartmental NMR Facility) operated at 79.6 MHz and equipped with a 5mm H-X-Y MAS probe. Zeolite samples were packed in 5mm ZrO<sub>2</sub> rotors and spun with a MAS rate of 5.6 kHz at room temperature. Single-pulse spectra were obtained using a <sup>29</sup>Si pulse of 5μs (ca. 90 degrees) and CP spectra used a <sup>1</sup>H 90-degree pulse of 5μs and a contact time of 2ms. Both types of spectra were collected with a relaxation delay of 60s and an acquisition time of 20.5ms were used, along with <sup>1</sup>H decoupling during acquisition using the TPPM modulation scheme. Zeolite samples were hydrated by holding for >48 h in a desiccator containing a saturated potassium chloride (KCl) solution prior to packing in a 5mm ZrO<sub>2</sub> rotor. All <sup>29</sup>Si MAS NMR spectra are referenced to a solid sodium salt of 4,4-dimethyl-4-silapentane-1-sulfonic acid (DSS) with the <sup>29</sup>Si line referenced to 0 ppm.

The number of H<sup>+</sup> sites on H-form zeolites was quantified by temperature programmed desorption (TPD) of samples after liquid-phase ion-exchange with NH<sub>4</sub><sup>+</sup> cations, while the number of residual H<sup>+</sup> sites on metal-exchanged zeolites (Cu- and Co-SSZ-13) was quantified by TPD of samples saturated with gas-phase NH<sub>3</sub> after performing purging treatments that remove all non-Brønsted bound NH<sub>3</sub> from the samples, as reported in detail elsewhere [78,171]. TPD experiments were performed using a Micromeritics Autochem II 2920 Chemisorption analyzer connected to an Agilent 5973N mass selective detector (MSD).

UV-Visible spectroscopy (UV-Vis) was used to determine the oxidation state of Co<sup>2+</sup> ions and to detect the presence of Co-oxides on Co-SSZ-13(15, 1) after exchange with Co(NO<sub>3</sub>)<sub>2</sub> solutions of varying molarity. Diffuse reflectance UV-Vis spectra were recorded under ambient conditions using a Varian Cary 5000 UV-Vis-NIR Spectropho-

tometer attached with a Harrick Scientific Praying Mantis diffuse reflectance accessory. Baseline spectra were recorded for every sample using barium sulfate ( $\text{BaSO}_4$ ; 98 wt%, Sigma Aldrich) as a 100% reflectance reference material and also on H-SSZ-13(15, 1), which is subtracted from the Co-SSZ-13(15, 1) spectra. Spectra were recorded from 12,500-50,000  $\text{cm}^{-1}$  at a scan rate of 167  $\text{cm}^{-1} \text{ s}^{-1}$ . Typically, 0.10-0.15 g of Co-SSZ-13 samples were loaded into a sample cup and pressed with a clean microscope slide until the surface was uniform.

### 3.3 Results and Discussion

#### 3.3.1 Quantification of isolated and paired Al in SSZ-13 zeolites

Methods were first developed to quantify the number of protons that compensate isolated and paired Al sites in H-SSZ-13 zeolites of different elemental composition. Each high-silica ( $\text{Si}/\text{Al} > 10$ ) sample is denoted as H-SSZ-13(X,Y), where X and Y are the Si/Al ratio and the  $\text{Na}^+/\text{TMAda}^+$  ratio in the synthesis gel. High-silica SSZ-13 zeolites ( $\text{Si}/\text{Al} = 15, 25$ ) were crystallized from precursor solutions containing equimolar amounts of  $\text{Na}^+$  and  $\text{TMAda}^+$  cations but different Al contents [84, 109], and one low-silica SSZ-13 zeolite ( $\text{Si}/\text{Al} = 5$ ) was prepared using  $\text{TMAda}^+$  cations and low-silica FAU zeolites as the Al source [34, 162]. H-SSZ-13(5), H-SSZ-13(15, 1), and H-SSZ-13(25, 1) showed XRD patterns consistent with phase-pure CHA (Fig. 3.12, Supp. Info.). Micropore volumes were consistent with the CHA topology for H-SSZ-13(15, 1) and H-SSZ-13(25, 1) zeolites (0.18-0.19  $\text{cm}^3 \text{ g}^{-1}$ , Ar adsorption isotherms in Fig. 3.19, Supp. Info.), but slightly lower for H-SSZ-13(5) zeolites made via FAU-to-CHA transformation (0.16  $\text{cm}^3 \text{ g}^{-1}$ ) [158] that are also characterized by  $\text{H}^+/\text{Al}$  ratios (0.65 by  $\text{NH}_3$  TPD) and framework Al contents ( $\text{Al}_f/\text{Al}_{\text{tot}} = 0.85$  by  $^{27}\text{Al}$  MAS NMR) lower than expected for phase-pure CHA [78].

H-SSZ-13(5), H-SSZ-13(15,1) and H-SSZ-13(25,1) samples were equilibrated with aqueous  $\text{Cu}(\text{NO}_3)_2$  solutions of increasing molarity to obtain partially Cu-exchanged zeolites, with solid Cu/Al ratios measured by atomic absorption spectroscopy (AAS).

The numbers of residual  $\text{H}^+$  sites on H-form and Cu-exchanged zeolites were measured by  $\text{NH}_3$  temperature-programmed desorption after  $\text{NH}_3$ -saturated samples were held in flowing wet helium (3%  $\text{H}_2\text{O}$ , 433 K) to remove Cu-bound  $\text{NH}_3$  and retain only  $\text{NH}_4^+$  species [78,171]. Cu exchanged predominantly as isolated  $\text{Cu}^{2+}$  cations for two  $\text{H}^+$  sites until Cu/Al ratios of 0.21, 0.09 and 0.05 on H-SSZ-13(5), H-SSZ-13(15,1) and H-SSZ-13(25,1), respectively, and then as isolated  $[\text{CuOH}]^+$  complexes for one  $\text{H}^+$  site (Table 3.4, Fig. 3.25, Supp. Info.), consistent with DFT calculations and variable temperature-programmed XRD analysis indicating that a  $\text{Cu}^{2+}$  cation exchanged at 2 Al atoms in a 6-MR is the most stable Cu exchange site in CHA zeolites [34, 37]. The transition from  $\text{Cu}^{2+}$  to  $[\text{CuOH}]^+$  agrees quantitatively with statistical estimates of the number of paired Al atoms in a 6-MR of CHA based on a random Al distribution obeying Löwenstein’s rule (Fig. 3.26, Supp. Info.) [129]. These findings also agree with recent observations that SSZ-13 zeolites crystallized from synthesis gels containing equimolar amounts of  $\text{Na}^+$  and  $\text{TMAda}^+$  ( $\text{Si}/\text{Al} = 4\text{-}55$ ) exchanged an equivalent number of  $\text{Cu}^{2+}$  cations as the number of paired Al predicted for a random Al distribution [158]. Taken together, these data suggest that the  $\text{Cu}^{2+}$  saturation capacity provides a direct measurement of the number of paired Al, and that synthesis gels containing equimolar amounts of  $\text{Na}^+$  and  $\text{TMAda}^+$  but varying Al content crystallize SSZ-13(X,1) zeolites with their framework Al atoms distributed randomly, subject to Löwenstein’s rule.

H-SSZ-13 samples were also equilibrated with aqueous  $\text{Co}(\text{NO}_3)_2$  solutions of increasing molarity to obtain partially Co-exchanged zeolites and measure ion-exchange isotherms (derivation in Section 3.7.14, Supp. Info.), in order to corroborate the findings from Cu-exchange, considering previous evidence for the non-random ordering of Al atoms in certain CHA zeolites [172,173]. In contrast with Cu exchange, Co exchanged exclusively as isolated  $\text{Co}^{2+}$  cations with Langmuirian adsorption behavior until saturation, as shown for H-SSZ-13(15,1) in Fig. 3.3, evident in the replacement of two  $\text{H}^+$  sites per exchanged Co cation (Fig. 3.4). Diffuse reflectance UV-Vis (DRUV) spectra recorded under ambient conditions on Co-SSZ-13(15, 1) zeolites with varying



Co content ( $\text{Co}/\text{Al} = 0.02\text{--}0.08$ ) are shown for the d-d transition region ( $12,500\text{--}28,500\text{ cm}^{-1}$ ) in Figure 3.5 (full spectra in Fig. 3.7.16, Supp. Info.). Increasing Co content in Co-SSZ-13(15, 1) resulted in a linear increase in the area of DRUV absorption bands for d-d electronic transitions of isolated, octahedrally-coordinated hydrated  $\text{Co}^{2+}$  cations ( $19,000\text{ cm}^{-1}$ , Fig. 3.5 inset), which are observed at similar energies for electronic transitions of isolated, tetrahedrally-coordinated  $\text{Co}^{2+}$  cations located near 6-MRs of dehydrated FAU zeolites [174–178]. Absorption bands in a region reflecting charge transfer transitions in Co oxides ( $25,000\text{--}33,000\text{ cm}^{-1}$  [175, 177]) do not appear in the spectra of any Co-SSZ-13(15, 1) sample except that containing  $\text{Co}/\text{Al} = 0.08$ , where a small feature centered  $26,500\text{ cm}^{-1}$  is detectable but likely reflects trigonally-coordinated  $\text{Co}^{2+}$  within a 6-MR, which exhibits an additional higher energy d-d transition ( $24,000\text{--}27,000\text{ cm}^{-1}$ ) in FAU and LTA zeolites [176, 177, 179, 180].

Saturation  $\text{Co}^{2+}/\text{Al}$  and  $\text{Cu}^{2+}/\text{Al}$  uptakes were identical on all three H-SSZ-13 samples (Fig. 3.6), and also identical to the fraction of Al pairs predicted at these Si/Al ratios if framework Al atoms were distributed randomly subject to Löwenstein’s rule (Section 3.7.13, Supp. Info.) [37]. We conclude that  $\text{Co}^{2+}$  cations selectively titrate paired Al in CHA zeolites [159] and that the number of Al atoms in a paired configuration can be quantified from twice the saturation  $\text{Co}^{2+}$  exchange capacity, as long as spectroscopic and titration evidence verifies the sole presence of  $\text{Co}^{2+}$  cations. The saturation  $\text{Co}^{2+}$  exchange capacity is a direct and functional descriptor of the number of framework Al sites that can stabilize an extraframework divalent charge (i.e., paired Al), which is different than the number of proximal Al sites detected by Al characterization methods such as NMR, because Al atoms may be separated by two Si T-atoms ( $\text{Al-O-(Si-O)}_2\text{-Al}$ ) but generate  $\text{H}^+$  sites within different pores [48]. We also conclude that synthesis solutions containing equimolar amounts of  $\text{Na}^+$  and  $\text{TMAda}^+$  crystallized SSZ-13 zeolites with randomly distributed framework Al atoms at different compositions, which was unexpected considering the non-random siting of Al atoms reported for CHA [172, 173] and other zeolites [150, 181–185].

### 3.3.2 Distribution of Al atoms in SSZ-13 zeolites synthesized using only N,N,N-trimethyl-1-adamantylammonium cations

High-silica SSZ-13 zeolites (Si/Al = 15, 25) crystallized from solutions comprising equimolar amounts of Na<sup>+</sup> and TMAda<sup>+</sup> contained a detectable fraction of paired Al atoms, as quantified by their saturation uptakes of divalent cations. The maximum density of framework Al atoms beyond which the incorporation of additional Al causes unavoidable formation of next-nearest-neighbor Al arrangements (Al-O-Si-O-Al) can be calculated from the topological density of zeolite frameworks [186,187] and occurs for CHA at a Si/Al ratio of 7 [186], suggesting that SSZ-13 with Si/Al >7 can be prepared, in theory, to contain exclusively isolated Al atoms. Each TMAda<sup>+</sup> cation contains a large hydrophobic adamantyl moiety (0.7 nm diam.) covalently bound to a singly-charged quaternary ammonium center and occupies the void space within one CHA cage (12 T-atoms) [162]. Thus, we hypothesized that SSZ-13 crystallized solely in the presence of TMAda<sup>+</sup>, based on steric constraints, should result in the isolation of one Al atom per CHA cage (Si/Al = 11, defect-free).

The hydroxide-mediated crystallization of SSZ-13 using only TMAda<sup>+</sup>, in the absence of alkali, was attempted at different synthesis solution Si/Al ratios (10-60) with all other synthesis parameters held constant. Precursor solutions containing Si/Al ratios of 15 (repeated a total of 6x), 20, 25 and 30 were able to crystallize phase-pure CHA zeolites (XRD patterns in Fig. 3.13, Ar adsorption isotherms in Fig. 3.20, Supp. Info) with solid Si/Al ratios between 15-26. All crystalline samples contained undetectable amounts of extraframework Al by <sup>27</sup>Al NMR (spectra in Section 3.7.11, Supp. Info.) and H<sup>+</sup>/Al ratios measured by NH<sub>3</sub> titration between 0.94-0.98 (Table 3.1), reflecting the nearly complete incorporation of Al atoms within the CHA framework. The Co<sup>2+</sup> exchange isotherm measured on SSZ-13 (15,1) shows Langmuirian adsorption behavior to saturation at Co/Al = 0.09, while SSZ-13(15,0) showed negligible Co<sup>2+</sup> exchange even at >10x higher aqueous-phase [Co<sup>2+</sup>]/[H<sup>+</sup>]<sup>2</sup> ratios (Fig. 3.3). In sharp contrast, Na<sup>+</sup> exchange isotherms (Fig. 3.3) on SSZ-13(15,0) and SSZ-13(15,1) reached saturation at Na/Al = 0.91 and 1.02, respectively (isotherm

derivation in Section 3.7.16, Supp. Info.). These data suggest that all Al atoms are completely isolated in SSZ-13 zeolites synthesized with only TMAda<sup>+</sup> cations, consistent with the occlusion of 1 TMAda<sup>+</sup> molecule per CHA cage, as inferred from thermogravimetric analysis (Table 3.1), that directs the siting of 1 Al atom per CHA cage.

<sup>29</sup>Si MAS NMR spectra (Fig. 3.7, solid traces) of SSZ-13(15,0) and SSZ-13(15,1) appear indistinguishable and show high occupancies of both Q<sub>4</sub> sites (Si-(O-Si)<sub>4</sub>:  $\delta = -111$  ppm) and Q<sub>3</sub> sites ((Si-O)<sub>3</sub>-Si-(O-Al):  $\delta = -105$  ppm), along with a third feature ca. -101 ppm that reflects either Q<sub>2</sub> sites ((Si-O)<sub>2</sub>-Si-(O-Al)<sub>2</sub>) or silanol groups (Si(OSi)<sub>3</sub>OH) [55, 168]. <sup>1</sup>H-<sup>29</sup>Si CP MAS NMR spectra (Fig. 3.7, dashed traces) showed a distinct resonance ca. -101 ppm, suggesting that silanol groups, but not Q<sub>2</sub> sites, are also present on these samples. These data suggest that Al-(O-Si)<sub>2</sub>-O-Al linkages are formed preferentially over Al-O-Si-O-Al linkages (<sup>29</sup>Si Q<sub>2</sub> sites) in SSZ-13(15,1), as has also been observed in FAU zeolites [188, 189], but that not even Al-(O-Si)<sub>2</sub>-O-Al linkages are formed in SSZ-13(15,0) zeolites, which are unable to exchange Co<sup>2+</sup> cations (Fig. 3.3).

Attempts to crystallize SSZ-13 zeolites with Si/Al >30 in hydroxide media with only TMAda<sup>+</sup> resulted in amorphous phases, apparently because crystallization was frustrated by the requirement to form anionic framework vacancy defects to balance excess cationic charges in occluded TMAda<sup>+</sup> cations that did not balance framework Al (Table 3.3). These observations are consistent with the ability of SSZ-13 to crystallize with low Al densities (Si/Al >60) and in a purely siliceous form (Si/Al =  $\infty$ ) in the presence of fluoride anions (Section 3.7.3, Supp. Info.) [190], which remain occluded within crystalline solids to balance excess cationic charges introduced by TMAda<sup>+</sup> cations. SSZ-13 synthesis solutions with Si/Al <15 also formed amorphous phases when only TMAda<sup>+</sup> was present, yet formed phase-pure SSZ-13 (Si/Al = 9) when additional Na<sup>+</sup> cations were added to these solutions (Fig. 3.15, Table 3.5, Supp. Info.), indicating that such high concentrations of AlO<sub>4</sub><sup>-</sup> tetrahedra led to anionic charge densities higher than TMAda<sup>+</sup> cations alone were capable

of stabilizing. These observations are consistent with charge density mismatch theory [191–196], which proposes that the crystallization of aluminosilicate synthesis solutions with a high density of anionic charge (i.e. low Si/Al ratios, high concentrations of  $\text{AlO}_4^-$  tetrahedra) becomes inhibited in the presence of SDAs with low cationic charge density (e.g., bulky organics) [193, 194], and that the addition of small amounts of cations with higher charge density (e.g.  $\text{Na}^+$ ) can help overcome this barrier to crystallization [192]. Although previous work has shown that charge density mismatch approaches can be used to crystallize zeolites of new topology (e.g., UFI [196]) or known zeolites at compositions that were previously inaccessible (e.g., BPH and LTA with Si/Al >1, and ERI with Si/Al >5 [195–197]), the demonstration herein illustrates that these approaches can control the arrangement of isolated and paired Al atoms in a given zeolite at fixed composition.

None of the SSZ-13(X,0) zeolites were able to exchange detectable amounts of  $\text{Co}^{2+}$  (Table 3.1), demonstrating that SSZ-13 crystallized solely in the presence of  $\text{TMAda}^+$  contains only isolated framework Al (1 Al per 6-MR). All SSZ-13(X,0) samples contained one 1  $\text{TMAda}^+$  molecule per CHA cage (Table 3.3), as expected during the formation of CHA crystallites [158, 162]. Furthermore, Cu exchanged onto SSZ-13(15,0) solely as  $[\text{CuOH}]^+$  species ( $\text{Cu}/\text{Al} = 0.24$ , residual  $\text{H}^+/\text{Al} = 0.76$ , Figure 3.8) as expected if every framework Al atom were isolated, in sharp contrast to the sequential exchange of  $\text{Cu}^{2+}$  at paired Al and  $[\text{CuOH}]^+$  at isolated Al on SSZ-13(15,1) (Fig. 3.8 and Fig. 3.25, Supp. Info). These findings also agree with recent reports of the predominance of monovalent  $[\text{CuOH}]^+$  species in high-silica Cu-SSZ-13 zeolites ( $\text{Si}/\text{Al} = 14$ ,  $\text{Cu}/\text{Al} = 0.44$ ) [36, 38, 39, 41] synthesized using only  $\text{TMAda}^+$  cations in fluoride media [168], as would be expected from the incorporation of isolated Al atoms by  $\text{TMAda}^+$  cations. The different  $\text{Na}^+/\text{TMAda}^+$  ratios used to synthesize H-SSZ-13(15,0) and H-SSZ-13(15,1) resulted in zeolites with identical bulk compositions ( $\text{Si}/\text{Al} = 15$ ,  $\text{H}^+/\text{Al} = 0.98$ ), but dramatic differences in their distributions of isolated and paired framework Al sites, suggesting that the use of monovalent SDAs of different size and cationic charge density directly influenced the arrangement and distribution

of the framework Al atoms. These findings extend the concepts of charge density mismatch in zeolite crystallization and demonstrate that using organic and inorganic SDA mixtures opens routes to systematically control the arrangement of matter in zeolites at fixed composition of matter.

### 3.3.3 Effect of synthesis gel cationic charge density on the arrangement of Al in SSZ-13 zeolites

The synthesis solutions used to crystallize SSZ-13(15,0) and SSZ-13(15,1) contained constant total cationic charge  $((\text{Na}^+ + \text{TMAda}^+)/\text{Al})$  but different cationic charge densities, as a result of different ratios of two monovalent cations ( $\text{Na}^+/\text{TMA-da}^+$ ) with different molecular volumes. Thus, we next focused on systematically varying the molar ratio of  $\text{Na}^+/\text{TMAda}^+$  (i.e., cationic charge density) between 0-3 at a fixed synthesis solution composition ( $\text{Si}/\text{Al} = 15$ ), fixed total cationic charge  $((\text{Na}^+ + \text{TMAda}^+)/\text{Al} = 7.5)$  and fixed total hydroxide concentration ( $\text{OH}^-/\text{Al} = 7.5$ ). Precursor solutions with constant total cationic charge and  $\text{Si}/\text{Al}$  ratio (15) crystallized phase-pure CHA zeolites with  $\text{Si}/\text{Al} = 15$  (Table 3.2), whose occluded  $\text{TMAda}^+$  content was measured by TGA (1  $\text{TMAda}^+$  per cage, Table 3.3, Supp. Info.) and  $\text{Na}^+$  content was measured by AAS. The  $(\text{TMAda}^+ + \text{Na}^+)/\text{Al}$  ratio on each SSZ-13(15,X) sample was near unity (Table 3.2), indicating that every framework Al atom was charge-balanced by either a  $\text{TMAda}^+$  or  $\text{Na}^+$  cation. Precursor solutions with increasing  $\text{Na}^+/\text{TMAda}^+$  ratio (0 to 1) crystallized SSZ-13(15,X) zeolites that showed a linear increase in saturation  $\text{Co}^{2+}$  uptakes between  $\text{Co}/\text{Al}$  values of 0 and 0.08 (Fig. 3.9), which range from the limit of Al isolation ( $\text{Co}/\text{Al} = 0$ ) to that predicted for a random Al distribution ( $\text{Co}/\text{Al} = 0.09$ ) [37]. As  $\text{Na}^+/\text{TMAda}^+$  ratios increased from 1 to 2, saturation  $\text{Co}^{2+}$  uptakes decreased toward zero (Fig. 3.9), while  $\text{Na}^+/\text{TMAda}^+$  ratios  $>2$  caused a phase transition toward formation of mordenite (MOR) zeolites (XRD patterns in Fig. 3.16, Supp. Info.).

A second set of synthesis experiments with varying total cationic charge of the precursor solution (i.e.,  $(\text{Na}^+ + \text{TMAda}^+)/\text{Al}$ ) at constant  $\text{Si}/\text{Al} = 15$  (Table 3.6, Sec-

tion 3.7.18, Supp. Info.) was used to probe the influence of total cationic charge on Al siting. SSZ-13 crystallized with solid Si/Al ratios that systematically decreased from 18 to 12 with increasing total cationic charge (Fig. 3.28), yet the fraction of paired Al depended only on the cationic charge density determined by the  $\text{Na}^+/\text{TMAda}^+$  ratio in the precursor solution (Fig. 3.10). SSZ-13 zeolites crystallized from solutions with varying total charge had varying compositions ( $\text{Si}/\text{Al} = 18\text{-}12$ ), while SSZ-13 synthesized with constant total charge had similar compositions ( $\text{Si}/\text{Al} = 15$ ) (Fig. 3.9). The decrease in the Si/Al ratio in the final crystalline SSZ-13 product suggests that the solid Al content is controlled by the total cationic charge in the synthesis solution, independent of the charge density, and depends on the ratio of cations to anionic  $\text{AlO}_4^-$  tetrahedra (i.e.  $(\text{Na}^+ + \text{TMAda}^+)/\text{Al}$ ). Furthermore, both sets of SSZ-13(15) zeolites undergo a phase transformation to MOR at the same  $\text{Na}^+/\text{TMAda}^+$  ratio ( $>2$ ), irrespective of the Si/Al ratio or total cationic charge (Fig. 3.10), suggesting that this phase transformation is governed by thermodynamic driving forces in order satisfy electrostatic constraints imposed by the charge density of the synthesis solution.

An analogous set of experiments performed at a constant synthesis solution Si/Al ratio of 25 and constant  $(\text{Na}^+ + \text{TMAda}^+)/\text{Al}$  ratio (Table 3.7, Section 3.7.19, Supp. Info.), but with varying cationic charge density ( $\text{Na}^+/\text{TMAda}^+$ ), were also performed. The number of paired Al sites, measured by  $\text{Co}^{2+}$  titration, increased from the limit of Al site isolation ( $\text{Co}/\text{Al} = 0$ ) in SSZ-13(25, 0) to the value predicted ( $\text{Co}/\text{Al} = 0.04$ ) for a random Al distribution in SSZ-13 (25, 1), and then decreases with as the  $\text{Na}^+/\text{TMAda}^+$  content increases beyond unity (Fig. 3.29). These findings are analogous to the dependence of paired Al content on cationic charge density for SSZ-13(15, X) zeolites synthesized at constant total cationic charge. These data provide further evidence that the cationic charge density in the crystallization medium, varied here through the  $\text{Na}^+/\text{TMAda}^+$  ratio, influences the siting of Al in isolated or paired framework locations in SSZ-13 zeolites.

### 3.3.4 Proposed role of synthesis gel cationic charge density on framework Al distribution in SSZ-13 zeolites

SSZ-13 zeolites contained predominantly isolated framework Al atoms when crystallized in the presence of only TMAda<sup>+</sup> cations (1 per CHA cage; Table 3.3, Supp. Info.), as expected if each framework Al and attendant anionic charge were positioned near their cationic quaternary ammonium centers and if non-polar siloxane portions of the zeolite framework were organized around their hydrophobic and non-polar adamantyl groups (Scheme 3.2). Interestingly, SSZ-13 zeolites (Si/Al = 15) crystallized from precursor media with Na<sup>+</sup> cations also present (Na<sup>+</sup>/TMAda<sup>+</sup> <2) contained a number of paired Al atoms that was similar to the Na<sup>+</sup> content of the crystalline solid (Fig. 3.11). We surmise this phenomenon reflects the positioning of a second framework Al atom compensated by a Na<sup>+</sup> cation (which is sited within a 6-MR) proximal to an Al atom compensating the cationic portion of a TMAda<sup>+</sup> cation (which is occluded within the CHA cage), in order to avoid disruption of non-polar contacts between the siloxane framework and the adamantyl group of TMAda<sup>+</sup> (Scheme 3.2). Although zeolite crystallization predominantly occurs by a series of kinetically-controlled processes [198–200], this hypothesis suggests that the incorporation of Al atoms into the oxide framework during crystallization can be directed via electrostatic forces and influenced by thermodynamic considerations.

The amount of Na<sup>+</sup> incorporated into SSZ-13 zeolites (Si/Al = 15) increases with precursor solution Na<sup>+</sup>/TMAda<sup>+</sup> ratios between 0 and 1, and then decreases as Na<sup>+</sup>/TMAda<sup>+</sup> ratios increase further between 1 and 2 (Table 3.2), beyond which additional Na<sup>+</sup> causes a phase transformation to MOR (Fig. 3.9). These phenomena appear to reflect the partitioning of Na<sup>+</sup> cations within a separate amorphous phase that does not crystallize CHA, but which eventually (at Na<sup>+</sup>/TMAda<sup>+</sup> >2) crystallizes MOR (Fig. 3.9), a commonly observed competition between organic and alkali cations present in zeolite synthesis solutions [80]. We note that different Na<sup>+</sup> concentrations in crystallization media of pentasil zeolites (e.g., MFI) have been observed to influence the paired Al density measured by Co<sup>2+</sup> titration [74], but in a non-

systematic and uncontrolled manner, either because other synthesis parameters (e.g., counteranions, Si and Al precursors used) were not controlled for, or because  $\text{Na}^+$  and tetrapropylammonium ( $\text{TPA}^+$ ) mixtures used to crystallize MFI zeolites do not function mechanistically as the  $\text{Na}^+$  and  $\text{TMAda}^+$  mixtures used here to crystallize CHA zeolites.

### 3.4 Conclusions

Titration procedures to quantify the number of paired Al sites in SSZ-13 zeolites ( $\text{Si}/\text{Al} = 5, 15, 25$ ) using divalent  $\text{Co}^{2+}$  were developed by measurement of ion-exchange isotherms on samples synthesized using an equimolar amount of  $\text{Na}^+$  and  $\text{TMAda}^+$ . The sole presence of isolated  $\text{Co}^{2+}$  cations on samples exposed to ambient conditions was verified by diffuse-reflectance UV-Visible spectra, which showed bands for d-d transition at  $19,000\text{ cm}^{-1}$  characteristic of hydrated  $\text{Co}^{2+}$  cations and whose integrated area increased linearly with increasing Co content. Furthermore, each exchanged  $\text{Co}^{2+}$  cation replaced two  $\text{H}^+$  sites, quantified by selective titration of residual  $\text{H}^+$  sites in Co-exchanged SSZ-13 zeolites using gaseous  $\text{NH}_3$  saturation and purge procedures developed to retain only  $\text{NH}_4^+$  species [171]. The number of paired Al sites on SSZ-13 zeolites was also determined by counting residual  $\text{H}^+$  sites after different extents of Cu cation exchange, which occurs sequentially as isolated  $\text{Cu}^{2+}$  cations at paired Al sites and then as  $[\text{CuOH}]^+$  species at isolated Al sites. On SSZ-13 samples crystallized using equimolar ratios of  $\text{Na}^+$  and  $\text{TMAda}^+$ , saturation  $\text{Cu}^{2+}$  uptakes agreed quantitatively with saturation  $\text{Co}^{2+}$  uptakes and the predicted number of Al pairs for a random Al distribution obeying Löwenstein’s rule. These spectroscopic and titration data provide the requisite evidence to confirm the sole presence of  $\text{Co}^{2+}$  cations at coverages that saturate paired Al sites, which cannot be assumed or asserted based solely on the adoption of  $\text{Co}^{2+}$  ion-exchange protocols reported previously.

SSZ-13 zeolites ( $\text{Si}/\text{Al} = 15\text{-}30$ ) synthesized solely in the presence of  $\text{TMAda}^+$  cations did not contain any paired Al sites, evident in their inability to exchange



$\text{Co}^{2+}$  or  $\text{Cu}^{2+}$  cations, indicating the complete isolation of framework Al atoms. SSZ-13 zeolites synthesized at fixed Si/Al ratio (15 or 25) with varying ratios of  $\text{Na}^+$  and  $\text{TMAda}^+$  cations in the synthesis solution, while all other synthesis parameters were held constant, contained a number of paired Al sites that increased linearly with solution  $\text{Na}^+/\text{TMAda}^+$  ratio (0-1) and reached a maximum value at  $\text{Na}^+/\text{TMAda}^+ = 1$ . The number of Al pairs in SSZ-13 decreased as the  $\text{Na}^+/\text{TMAda}^+$  ratio increased from 1-2, beyond which a phase transformation to MOR occurred. The number of paired Al correlated linearly with the retained  $\text{Na}^+$  content in crystalline SSZ-13 products, suggesting that  $\text{Na}^+$  cations are sited proximal to cationic quaternary-ammonium centers of  $\text{TMAda}^+$  so as to induce Al pairing and avoid disruption of non-polar contacts between siloxane bonds and the hydrophobic adamantyl group of  $\text{TMAda}^+$ . The distribution of isolated and paired Al sites in SSZ-13 can be systematically controlled by varying the  $\text{Na}^+/\text{TMAda}^+$  ratio, a surrogate for the synthesis gel cationic charge density.

The findings reported herein demonstrate that the cationic charge density of the crystallization medium, determined by the amounts of organic and inorganic structure directing agents present, influences the anionic charge density in the zeolite lattice, determined by the distribution of framework Al atoms. We expect that the approach described herein, to control the isolation and pairing of Al atoms by manipulating the cationic charge density in the crystallization medium, can be adapted to control the arrangement of Al atoms at fixed elemental composition (Si/Al) in other zeolite topologies that utilize mixtures of organic and inorganic structure directing agents. The arrangement of framework Al atoms influences the hydrothermal stability of a given zeolite and also controls the speciation of extraframework cations that behave as catalytic active sites, as in the case of monovalent  $[\text{CuOH}]^+$  complexes exchanged at isolated Al and divalent  $\text{Cu}^{2+}$  cations exchanged at paired Al in CHA zeolites for NOx SCR with  $\text{NH}_3$  in automotive emission control. Therefore, the ability to systematically control the arrangement of isolated and paired Al in zeolites promises to expand their structural and catalytic diversity in a manner that has remained

dormant and inaccessible to date, and provides access to one of the few opportunities to do so for a given zeolite at fixed composition.

### 3.5 Acknowledgements

We acknowledge the financial support from the National Science Foundation GOALI program under award number 1258715-CBET. We thank Sachem, Inc. for providing the organic structure-directing agent used to synthesize SSZ-13, Ishant Khurana (Purdue) for assistance with ammonia titration experiments, and Dr. John Harwood (Purdue Interdepartmental NMR Facility) for assistance collecting NMR spectra. We also thank Prof. Jeffrey T. Miller (Purdue), Prof. Fabio H. Ribeiro (Purdue), Prof. William F. Schneider (Notre Dame) and Christopher Paolucci (Notre Dame) for helpful technical discussions.

Additionally, I acknowledge the American Chemical Society for granting permission to reproduce this chapter of my thesis. Adapted with permissions from Chemistry of Materials, 2016, 28, 2236-2247. Copyright (2016) American Chemical Society. The full article can be accessed here: [dx.doi.org/10.1021/acs.chemmater.6b00181](https://doi.org/10.1021/acs.chemmater.6b00181).

## 3.6 Figures and Tables

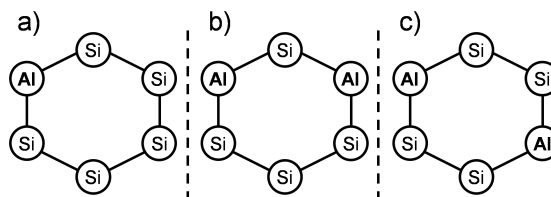


Figure 3.1. Different arrangements of Al atoms between (a) isolated and (b, c) paired configurations in a 6-MR.

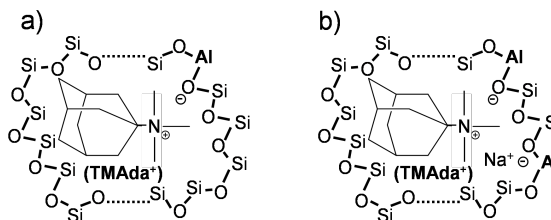


Figure 3.2. Proposed organization of Si and Al atoms in the CHA crystallization medium to form (a) isolated Al in the presence of TMAda<sup>+</sup>, or (b) paired Al in the presence of TMAda<sup>+</sup> and Na<sup>+</sup>.

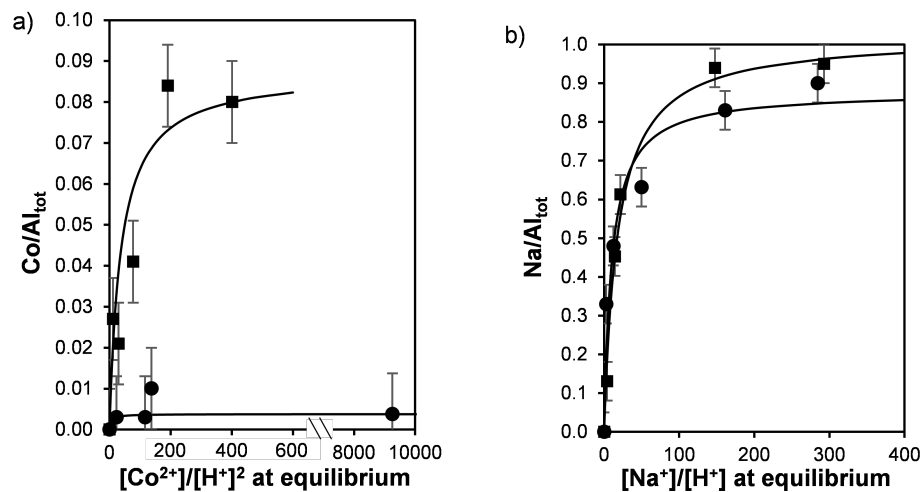


Figure 3.3. (a)  $\text{Co}^{2+}$  and (b)  $\text{Na}^+$  ion-exchange isotherms measured on SSZ-13(15,0) (circles) and SSZ-13(15,1) (squares); solid lines represent least-squares regression of data to Langmuirian isotherms.

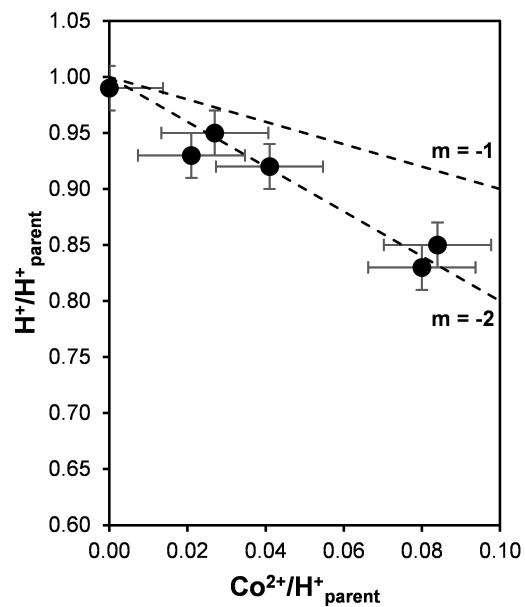


Figure 3.4. The number of residual  $\text{H}^+$  sites measured by  $\text{NH}_3$  titration on Co-SSZ-13(15, 1) samples of increasing Co content. The two dashed lines correspond to slopes of -2 and -1, reflecting exchange of only divalent or monovalent species, respectively.

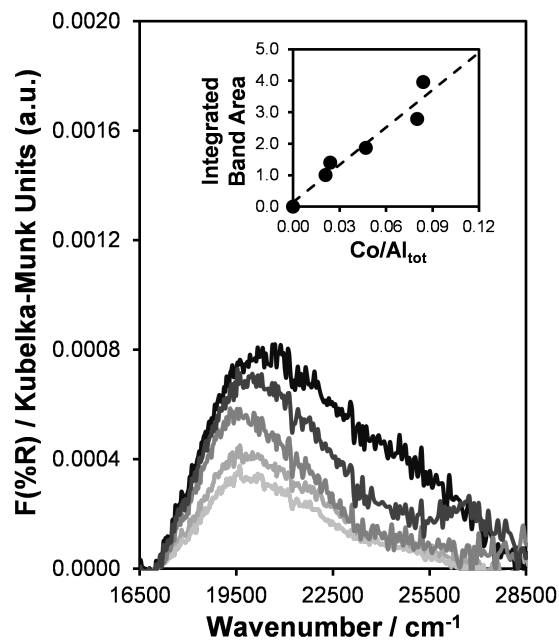


Figure 3.5. Diffuse reflectance UV-Visible absorption spectra of Co-SSZ-13(15,1) samples with increasing  $\text{Co}^{2+}$  content ( $\text{Co}/\text{Al} = 0.021, 0.027, 0.041, 0.084, 0.080$  from light to dark); inset shows integrated areas for  $\text{Co}^{2+}$  d-d transitions (ca.  $19,000 \text{ cm}^{-1}$ ) as a function of Co content.

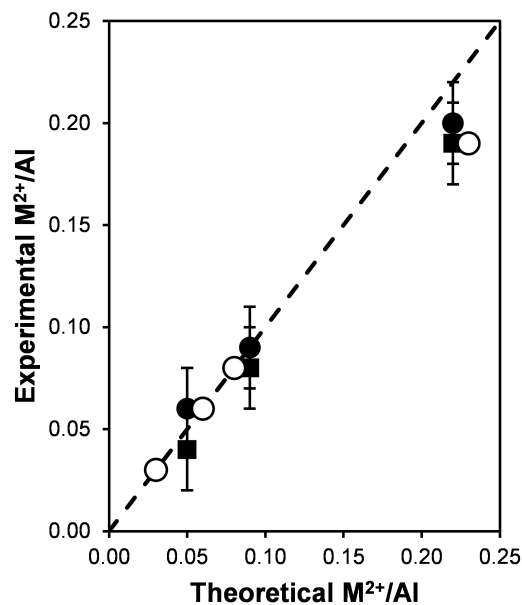


Figure 3.6.  $Co^{2+}$  (squares) and  $Cu^{2+}$  (closed circles) saturation values on SSZ-13(5), SSZ-13(15, 1), and SSZ-13(25, 1) plotted against the maximum  $M^{2+}/Al$  predicted for a random Al distribution.  $Cu^{2+}$  saturation values (open circles) on SSZ-13 ( $Si/Al = 4-45$ ) prepared from equimolar  $Na^+$  and  $TMAda^+$  mixtures reported by Deimund et al [158]. The dashed line represents a parity line.

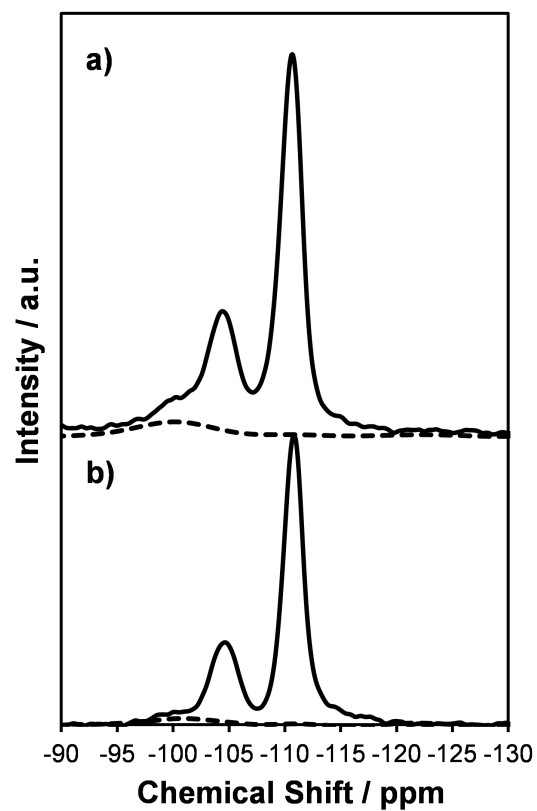


Figure 3.7.  $^{29}\text{Si}$  MAS NMR (solid traces) and  $^1\text{H}$ - $^{29}\text{Si}$  CP MAS NMR (dashed traces) of a) H-SSZ-13(15, 0) and b) H-SSZ-13(15, 1).



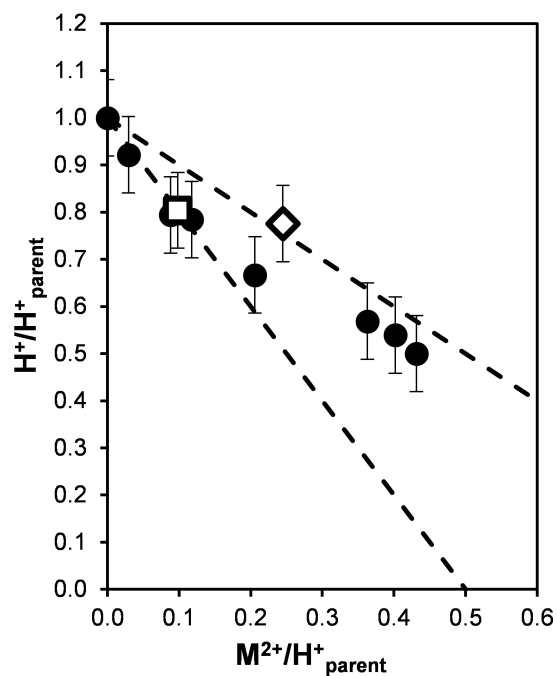


Figure 3.8. Number of residual  $H^+$  sites on SSZ-13(15, 1) after increasing extents of  $Cu^{2+}$  exchange (circles) and after  $Co^{2+}$  saturation (squares), and on SSZ-13(15, 0) after  $Cu^{2+}$  exchange (diamond). The two dashed lines correspond to slopes of -2 and -1, reflecting exchange of only isolated  $Cu^{2+}$  or  $[CuOH]^+$ , respectively.

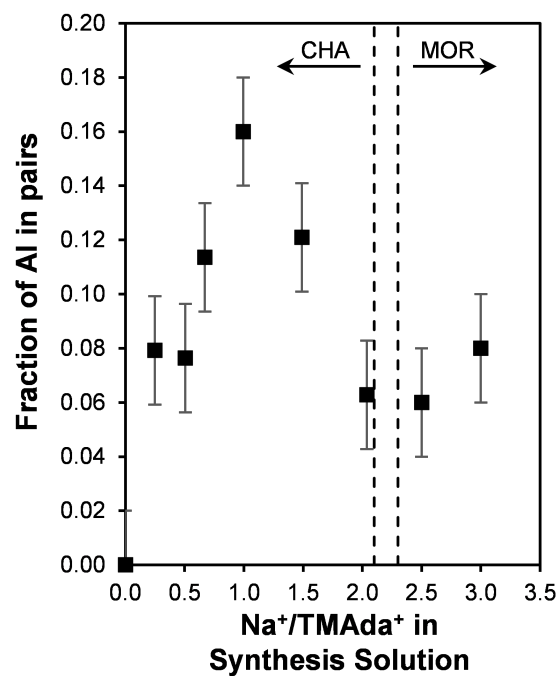


Figure 3.9. Fraction of Al in paired configurations, measured by  $\text{Co}^{2+}$  titration, in SSZ-13 zeolites ( $\text{Si}/\text{Al} = 15$ ) as a function of the  $\text{Na}^+/\text{TMAda}^+$  ratio (i.e., cationic charge density) in crystallization media containing fixed total cationic charge. Dashed lines bound a region where a mixed CHA/MOR phase is observed.

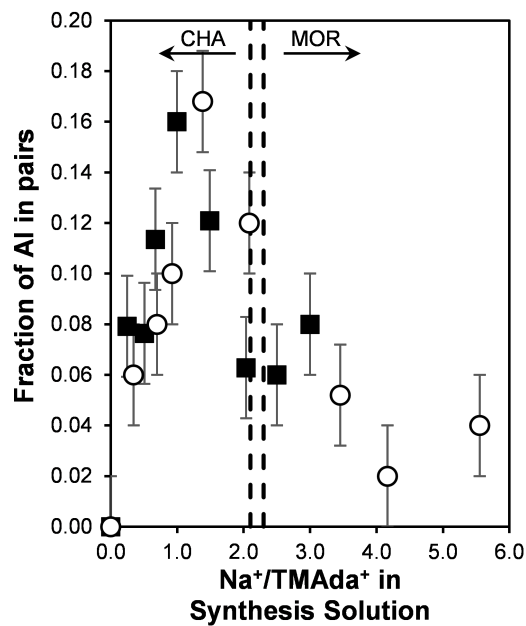


Figure 3.10. Fraction of Al in paired configurations, measured by titration with  $\text{Co}^{2+}$ , in SSZ-13 zeolites ( $\text{Si}/\text{Al} = 15$ ) as a function of the cationic charge density with constant cationic charge (squares) and with cationic charge (open circles). Dashed lines bound a region where a mixed CHA/MOR phase is observed.

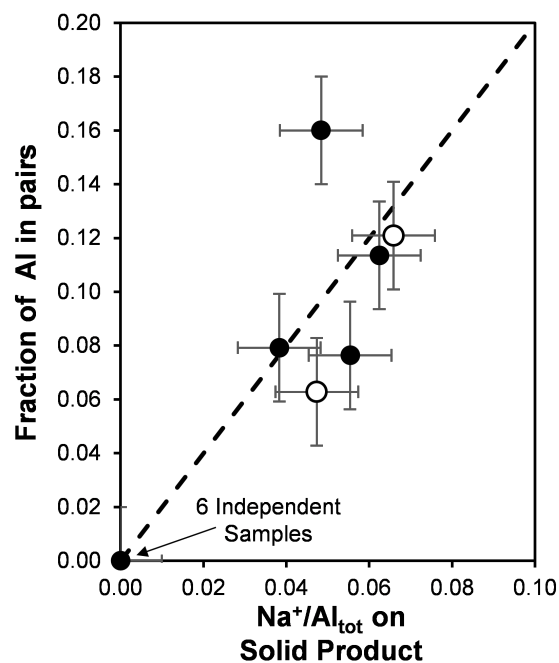


Figure 3.11. Fraction of Al in paired configurations, measured by Co<sup>2+</sup> titration, in SSZ-13 zeolites (Si/Al = 15) as a function of the solid Na<sup>+</sup> content for samples synthesized from solutions containing  $0 < \text{Na}^+/\text{TMAda}^+ < 1$  (solid circles) and  $1 < \text{Na}^+/\text{TMAda}^+ < 2$  (open circles). The dashed line corresponds to a slope of two.

Table 3.1.  
Characterization data for all Na<sup>+</sup>-free SSZ-13 samples at different Si/Al ratios.

Table 1. Characterization Data for All Na<sup>+</sup>-Free SSZ-13 Samples at Different Si/Al Ratios

| sample                       | Si/Al (gel) | Si/Al (solid)          | Al <sub>l</sub> /Al <sub>tot</sub> | TMAda <sup>+</sup> /Al | H <sup>+</sup> /Al | Co/Al <sup>d</sup> |
|------------------------------|-------------|------------------------|------------------------------------|------------------------|--------------------|--------------------|
| SSZ-13(10, 0)                | 10          | amorphous <sup>b</sup> | -                                  | -                      | -                  | -                  |
| SSZ-13(15, 0)                | 15          | 14.5                   | 1.00                               | 1.08                   | 0.98 <sup>c</sup>  | 0.00               |
| SSZ-13(20, 0)                | 20          | 17.5                   | 0.97                               | 1.00                   | 0.94               | 0.00               |
| SSZ-13(25, 0)                | 25          | 24.6                   | 0.95                               | 1.44                   | 0.96               | 0.00               |
| SSZ-13(30, 0)                | 30          | 26.1                   | 0.96                               | 1.66                   | 0.97               | 0.00               |
| SSZ-13(60, 0)                | 60          | amorphous <sup>b</sup> | -                                  | -                      | -                  | -                  |
| SSZ-13(15, 0)-2 <sup>a</sup> | 15          | 16.1                   | -                                  | -                      | 0.96               | 0.00               |
| SSZ-13(15, 0)-3 <sup>a</sup> | 15          | 13.8                   | -                                  | -                      | 0.95               | 0.01               |
| SSZ-13(15, 0)-4 <sup>a</sup> | 15          | 17.0                   | -                                  | -                      | 0.98               | 0.00               |
| SSZ-13(15, 0)-5 <sup>a</sup> | 15          | 15.2                   | -                                  | -                      | 1.02               | 0.00               |
| SSZ-13(15, 0)-6 <sup>a</sup> | 15          | 14.3                   | -                                  | -                      | 0.95               | 0.01               |

<sup>a</sup>Repeated synthesis of SSZ-13(15, 0). <sup>b</sup>Determined to be an amorphous material from XRD (Figure S.2) and no further characterization was performed. <sup>c</sup>In agreement with saturation Na/Al value of 0.91 determined from Na-exchange isotherm. <sup>d</sup>Saturation Co/Al value determined from Co-exchange with a 0.25 M Co(NO<sub>3</sub>)<sub>2</sub> solution.

Table 3.2.  
Characterization data for SSZ-13(15) and MOR samples synthesized with constant synthesis solution Si/Al, constant hydroxide concentration, and varying Na<sup>+</sup>/TMAda<sup>+</sup>.

| sample           | Si/Al | micropore volume (cm <sup>3</sup> g <sup>-1</sup> ) | H <sup>+</sup> /Al | Na <sup>+</sup> /Al | TMAda <sup>+</sup> /Al | (Na <sup>+</sup> + TMAda <sup>+</sup> )/Al | Co/Al |
|------------------|-------|---|--------------------|---------------------|------------------------|--|-------|
| SSZ-13(15, 0)    | 14.5  | 0.21  | 0.98               | 0.00                | 1.08                   | 1.08                                       | 0.00  |
| SSZ-13(15, 0.25) | 13.5  | 0.20  | 0.92               | 0.04                | 0.93                   | 0.97                                       | 0.04  |
| SSZ-13(15, 0.50) | 14.7  | 0.17  | 1.02               | 0.06                | 0.97                   | 1.03                                       | 0.04  |
| SSZ-13(15, 0.67) | 15.0  | 0.16  | 0.98               | 0.06                | 0.93                   | 0.99                                       | 0.06  |
| SSZ-13(15, 1.00) | 14.8  | 0.19  | 0.99               | 0.05                | 1.04                   | 1.09                                       | 0.08  |
| SSZ-13(15, 1.50) | 15.2  | 0.19  | 1.03               | 0.07                | 1.05                   | 1.12                                       | 0.06  |
| SSZ-13(15, 2.00) | 13.5  | 0.17  | 1.06               | 0.05                | 0.89                   | 0.94                                       | 0.03  |
| MOR(15, 2.50)    | 10.5  | -   | -                  | 0.08                | -                      | -  | 0.02  |
| MOR(15, 3.00)    | 11.9  | -   | -                  | 0.09                | -                      | -  | 0.01  |

### 3.7 Supporting Information

#### 3.7.1 Synthesis of SSZ-13(5) Zeolites

The synthesis recipe for SSZ-13(5) was adapted from the procedure described by Fickel et al. [34], which is a modified version of the original synthesis reported by Zones [162]. A synthesis molar ratio of 1  $\text{SiO}_2$ / 0.031  $\text{Al}_2\text{O}_3$ / 0.017 TMAdaOH/ 0.770  $\text{Na}_2\text{O}$ / 12.1  $\text{H}_2\text{O}$  was used. A typical synthesis involved adding 3.14 g of a 1M NaOH solution (3.3 wt% NaOH, Alfa Aesar) to 4.82 g of deionized water (18.2 M $\Omega$ ) in a PFA jar and stirring the solution for 15 minutes at ambient conditions. 24.10 g of sodium silicate (10.6 wt%  $\text{Na}_2\text{O}$ , 25.6 wt%  $\text{SiO}_2$ ; Sigma Aldrich) was added and homogenized for 15 minutes under ambient conditions. 0.37 g of  $\text{NH}_4$ -Y zeolite (Zeolyst CBV300, Si/Al = 2.6) were added and the mixture was homogenized for 30 minutes under ambient conditions. 1.58 g of a 1M TMAdaOH solution (25 wt% Sachem) was then added to the mixture and stirred for 30 minutes under ambient conditions. All synthesis reagents were used without further purification. The synthesis solution was then transferred to a 45 ml Teflon-lined stainless steel autoclave (Parr Instruments) and placed in a forced convection oven (Yamato DKN-402C) at 413 K and rotated at 60 RPM for 6 days.

#### 3.7.2 Synthesis of SSZ-13(15, 1) and SSZ-13(25, 1) Zeolites

The synthesis recipe for SSZ-13(15, 1) and SSZ(25, 1) zeolites was adapted from the procedure described by Deka et al. [84], which is a modified version of the original synthesis reported by Zones [109]. A synthesis molar ratio of 1  $\text{SiO}_2$ / X  $\text{Al}_2\text{O}_3$ / 0.25 TMAdaOH/ 0.125  $\text{Na}_2\text{O}$ / 44  $\text{H}_2\text{O}$  was used, where X = 0.033 or 0.020 for Si/Al = 15 and 25, respectively. A typical synthesis involved adding 4.432 g of an aqueous TMAdaOH solution (25 wt%, Sachem) to 10.365 g of deionized  $\text{H}_2\text{O}$  (18.2 M $\Omega$ ) to a perfluoroalkoxy alkane (PFA) jar and stirring the solution under ambient conditions for 15 minutes. Next, 0.109 or 0.065 g (for Si/Al = 15 or 25) of  $\text{Al}(\text{OH})_3$  (98 wt%, SPI Pharma) and 1.258 g of a 5M sodium hydroxide solution (NaOH: 16.7 wt% NaOH

in deionized water; NaOH pellets 98 wt%, Alfa Aesar) was added to the aqueous TMAdaOH solution and the mixture was stirred under ambient conditions for 15 minutes to homogenize the contents. Finally, 3.150 g of colloidal silica (Ludox AS40, 40 wt% SiO<sub>2</sub>, Sigma Aldrich) was added to the mixture and stirred for 2 h under ambient conditions. All synthesis reagents were used without further purification. The synthesis solution was then transferred to a 45 ml Teflon-lined stainless steel autoclave (Parr Instruments) and placed in a forced convection oven (Yamato DKN-402C) at 433 K and rotated at 40 RPM for 6 days.

### 3.7.3 Synthesis of Pure-silica Chabazite (Si-CHA).

Pure SiO<sub>2</sub> chabazite was synthesized following the procedure reported by Díaz-Cabañas et al. [170] using a synthesis solution molar ratio of 1 SiO<sub>2</sub>/ 0.5 TMAdaOH/ 0.5 HF/ 3 H<sub>2</sub>O. In a typical synthesis 13 g of tetraethylorthosilicate (TEOS; 98 wt%, Sigma Aldrich) were added to a PFA jar containing 25.849 g of a 1M TMAdaOH solution (25 wt%, Sachem) and stirred under ambient conditions. Ethanol, formed from the hydrolysis of TEOS, and excess water were then evaporated to reach the target molar ratios by placing the TEOS and TMAdaOH solution under flowing air while stirring at ambient conditions. During the evaporation process, once the solution mass came within 5 g of the desired final mass, an additional 10 g of water were added to ensure complete hydrolysis of TEOS and to allow additional time to completely evaporate the ethanol. This rehydration process was performed twice during the evaporation step. As the synthesis solution neared the desired H<sub>2</sub>O/SiO<sub>2</sub> ratio of 3, the solution began to solidify and had to be stirred by hand for three additional hours in order to complete the water evaporation process. Once the synthesis solution had reached the desired H<sub>2</sub>O/SiO<sub>2</sub> ratio, 1.275 g of concentrated hydrofluoric acid (HF; 48 wt%, Sigma Aldrich) was added dropwise to the synthesis and homogenized for 15 minutes. ***Caution: when working with hydrofluoric acid use appropriate personal protective equipment, ventilation, and other safety measures.*** Upon addition of HF to the solidified synthesis solution, the solution immediately

became a thick paste that became more solution-like under stirring. The solution was then left to sit uncovered under ambient conditions for 30 minutes to allow for any residual HF to evaporate before transferring the solution to a 45 ml Teflon-lined stainless steel autoclave (Parr Instruments) and heated in a forced convection oven (Yamato DKN-402C) at 423 K under rotation at 40 RPM for 40 h. All synthesis reagents were used without further purification.

### 3.7.4 Synthesis and Characterization of SSZ-13 Zeolites without $\text{Na}^+$

For the synthesis of  $\text{Na}^+$ -free SSZ-13 zeolites in hydroxide media, a molar ratio of  $1 \text{ SiO}_2 / X \text{ Al}_2\text{O}_3 / 0.5 \text{ TMAdaOH} / 44 \text{ H}_2\text{O}$  was used, where  $X = 0.050, 0.033, 0.025, 0.02, 0.017, \text{ or } 0.008$  for  $\text{Si}/\text{Al} = 10, 15, 20, 25, 30$  and  $60$ , respectively. In a typical synthesis  $14.071 \text{ g}$  of a TMAdaOH solution (25 wt% Sachem) were added to  $12.841 \text{ g}$  of deionized water ( $18.2 \text{ M}\Omega$ ) in a PFA jar and stirred for 15 minutes under ambient conditions. Next  $0.260, 0.173, 0.130, 0.104, 0.087, \text{ or } 0.044 \text{ g}$  ( $\text{Si}/\text{Al} = 10, 15, 20, 25, 30, \text{ and } 60$ , respectively) of  $\text{Al}(\text{OH})_3$  (98 wt%, SPI Pharma) were added to the TMAdaOH solution and the mixture was homogenized for 15 minutes under ambient conditions. Then  $5 \text{ g}$  of colloidal silica (Ludox HS40, 40 wt%, Sigma Aldrich) were added to the mixture and the contents were stirred for 2 h at ambient conditions until a homogeneous solution was obtained. All synthesis reagents were used without further purification. The synthesis solution was then transferred to a 45 ml Teflon-lined stainless steel autoclave (Parr Instruments) and heated in a forced convection oven (Yamato DKN-402C) at 433 K and rotated at 40 RPM for 6 days.

### 3.7.5 Synthesis of SSZ-13 Zeolites at Constant $\text{Na}^+/\text{TMAda}^+$ and Varied $\text{Si}/\text{Al}$ Ratio

SSZ-13 zeolites were synthesized at a constant  $\text{Na}^+/\text{TMAda}^+$  ratio of  $2/3$  and with gel  $\text{Si}/\text{Al}$  ratios ranging from 10-200 in hydroxide media. A synthesis gel molar ratio of  $1 \text{ SiO}_2 / X \text{ Al}_2\text{O}_3 / 0.3 \text{ TMAdaOH} / 0.2 \text{ NaOH} / 44 \text{ H}_2\text{O}$  was used, where  $X = 0.100, 0.050, 0.033, 0.020, 0.010, 0.005, \text{ and } 0.0025$ , for  $\text{Si}/\text{Al}$  ratios of 5, 10, 15, 25,



50, 100, and 200, respectively. In a typical synthesis 8.443 g of a TMAdaOH solution (25 wt% Sachem) were added to 15.698 g of deionized water (18.2 MΩ) in a PFA jar and stirred for 15 minutes under ambient conditions. Next 0.519, 0.260, 0.173, 0.104, 0.052, 0.026, or 0.013 g ( $\text{Si}/\text{Al} = 5, 10, 15, 25, 50, 100, \text{ and } 200$ , respectively) of  $\text{Al}(\text{OH})_3$  (98 wt%, SPI Pharma) were added to the TMAdaOH solution and the mixture was homogenized for 15 minutes under ambient conditions. Then 5 g of colloidal silica (Ludox HS40, 40 wt%, Sigma Aldrich) were added to the mixture and the contents were stirred for 2 h at ambient conditions. All synthesis reagents were used without further purification. The synthesis gel was then transferred to a 45 ml Teflon-lined stainless steel autoclave (Parr Instruments) and heated in a forced convection oven (Yamato DKN-402C) at 433 K and rotated at 40 RPM for 6 days.

### 3.7.6 Synthesis of SSZ-13 Zeolites at $\text{Si}/\text{Al} = 15$ and 25 at Constant $(\text{Na}^+ + \text{TMAda}^+)/\text{Al}$ with Varying $\text{Na}^+/\text{TMAda}^+$ Ratio

The synthesis of SSZ-13 zeolites in synthesis solutions with varying charge density, but with constant total charge, was performed at a  $\text{Si}/\text{Al} = 15$  and 25 at a constant ratio of  $(\text{Na}^+ + \text{TMAda}^+)/\text{Al} = 7.5$  while letting the  $\text{Na}^+/\text{TMAda}^+$  ratio vary from 0 to 3. A synthesis solution molar ratio of  $1 \text{ SiO}_2 / Y \text{ Al}_2\text{O}_3 / X \text{ TMAdaOH} / (0.5 - X) \text{ NaOH} / 44 \text{ H}_2\text{O}$  was used, where  $X = 0.50, 0.40, 0.33, 0.30, 0.25, 0.20, 0.17, 0.14, \text{ and } 0.125$ , for  $\text{Na}^+/\text{TMAda}^+$  ratios of 0,  $1/4$ ,  $1/2$ ,  $2/3$ , 1,  $3/2$ , 2, 2.5, and 3, respectively, and  $Y = 0.033$  and 0.025 for  $\text{Si}/\text{Al} = 15$  and 25, respectively. In a typical synthesis 14.071, 11.257, 9.381, 8.443, 7.036, 5.628, 4.690, 4.020, or 3.518 g ( $\text{Na}^+/\text{TMAda}^+ = 0, 1/4, 1/2, 2/3, 1, 3/2, 2, 2.5, \text{ and } 3$ , respectively) of a TMAdaOH solution (25 wt% Sachem) were added to 12.841, 14.269, 15.222, 15.698, 16.412, 17.127, 17.603, 17.943, or 18.198 g ( $\text{Na}^+/\text{TMAda}^+ = 0, 1/4, 1/2, 2/3, 1, 3/2, 2, 2.5, \text{ and } 3$ , respectively) of deionized water (18.2 MΩ) in a PFA jar and stirred for 15 minutes under ambient conditions. Next 0.173 or 0.104 g ( $\text{Si}/\text{Al} = 15$  or 25, respectively) of  $\text{Al}(\text{OH})_3$  (98 wt%, SPI Pharma) were added to the TMAdaOH solution and then 0, 0.815, 1.359, 1.630, 2.038, 2.446, 2.717, 2.911, or 3.057 g ( $\text{Na}^+/\text{TMAda}^+ = 0, 1/4, 1/2, 2/3, 1,$

3/2, 2, 2.5, and 3, respectively) of a 5M sodium hydroxide solution (NaOH: 16.7 wt% NaOH in deionized water; NaOH 98 wt% Alfa Aesar) were added and the mixture was homogenized for 15 minutes under ambient conditions. Then 5 g of colloidal silica (Ludox HS40, 40 wt%, Sigma Aldrich) were added to the mixture and the contents were stirred for 2 h at ambient conditions. All synthesis reagents were used without further purification. The synthesis solution was then transferred to a 45 ml Teflon-lined stainless steel autoclave (Parr Instruments) and heated in a forced convection oven (Yamato DKN-402C) at 433 K and rotated at 40 RPM for 6 days.

### 3.7.7 Synthesis of SSZ-13 Zeolites at Si/Al = 15 with Varying ( $\text{Na}^+ + \text{TMAda}^+$ ) / Al and Varying $\text{Na}^+/\text{TMAda}^+$

Synthesis of SSZ-13 zeolites with varying total charge and charge density were performed at a solution Si/Al ratio of 15 while varying the  $\text{Na}^+/\text{TMAda}^+$  (charge density) from 0 to 5.6 and  $(\text{Na}^+ + \text{TMAda}^+)/\text{Al}$  (total charge) from 5.4 to 7.1. A synthesis solution molar ratio of 1  $\text{SiO}_2$ / 0.033  $\text{Al}_2\text{O}_3$ / X  $\text{TMAdaOH}$ / (0.5 - X)  $\text{NaOH}$ / 44  $\text{H}_2\text{O}$  was used, where X = 0.50, 0.37, 0.29, 0.26, 0.21, 0.16, 0.11, 0.097, and 0.076, for  $\text{Na}^+/\text{TMAda}^+$  ratios of 0, 0.35, 0.70, 0.93, 1.38, 2.09, 3.45, 4.16, and 5.55, respectively. In a typical synthesis 8.443, 6.254, 4.966, 4.374, 3.547, 2.732, 1.897, 1.636, or 1.289 g ( $\text{Na}^+/\text{TMAda}^+ = 0, 0.35, 0.70, 0.93, 1.38, 2.09, 3.45, 4.16, \text{ and } 5.55$ , respectively) of a  $\text{TMAdaOH}$  solution (25 wt% Sachem) were added to 7.704, 8.816, 9.469, 9.770, 10.190, 10.603, 11.027, 11.160, or 11.336 g ( $\text{Na}^+/\text{TMAda}^+ = 0, 0.35, 0.70, 0.93, 1.38, 2.09, 3.45, 4.16, \text{ and } 5.55$ , respectively) of deionized water (18.2 M $\Omega$ ) in a PFA jar and stirred for 15 minutes under ambient conditions. Next 0.104 g of  $\text{Al}(\text{OH})_3$  (98 wt%, SPI Pharma) were added to the  $\text{TMAdaOH}$  solution and then 0, 0.634, 1.007, 1.178, 1.418, 1.654, 1.896, 1.972, or 2.072 g ( $\text{Na}^+/\text{TMAda}^+ = 0, 0.35, 0.70, 0.93, 1.38, 2.09, 3.45, 4.16, \text{ and } 5.55$ , respectively) of a 5M sodium hydroxide solution (NaOH: 16.7 wt% NaOH in deionized water; NaOH 98 wt% Alfa Aesar) were added and the mixture was homogenized for 15 minutes under ambient conditions. Then 3 g of colloidal silica (Ludox HS40, 40 wt%, Sigma Aldrich) were added to the

mixture and the contents were stirred for 2 h at ambient conditions. All synthesis reagents were used without further purification. The synthesis solution was then transferred to a 23 ml Teflon-lined stainless steel autoclave (Parr Instruments) and heated in a forced convection oven (Yamato DKN-402C) at 433 K and rotated at 40 RPM for 6 days.

## 3.7.8 Powder X-Ray Diffraction Patterns of SSZ-13 Zeolites

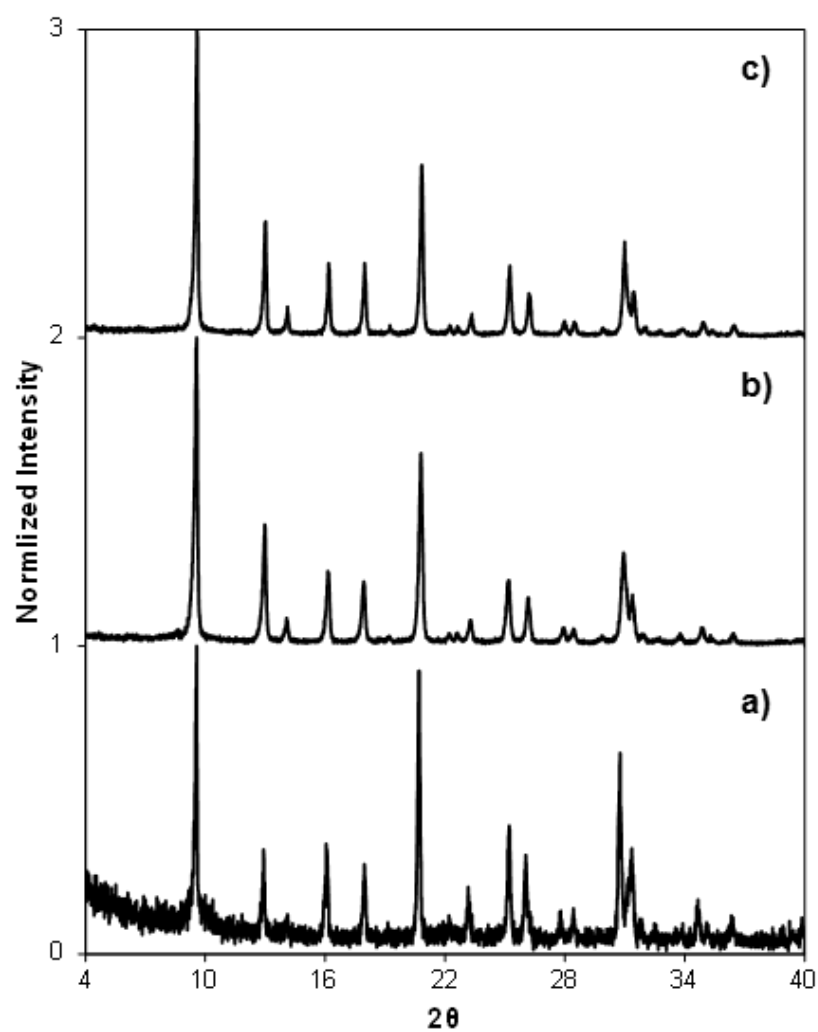


Figure 3.12. Powder X-ray diffraction patterns for a) SSZ-13(5), b) SSZ-13(15, 1) and, c) SSZ-13(25, 1).

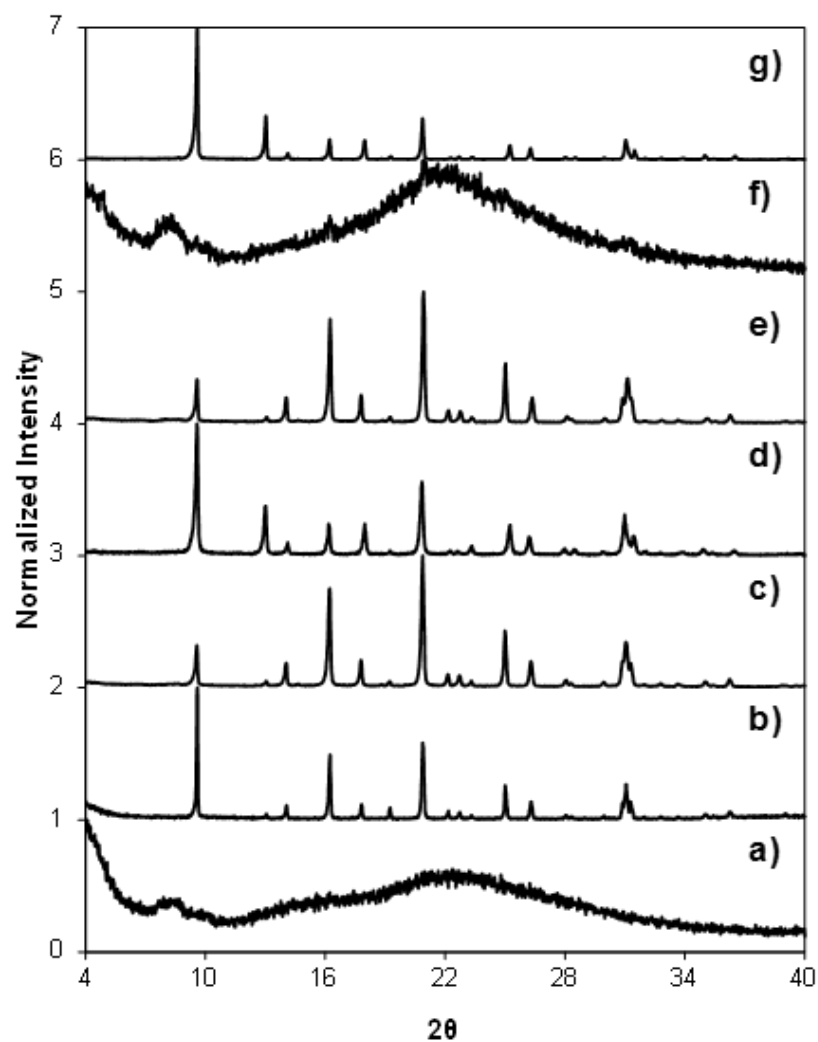


Figure 3.13. Powder X-ray diffraction patterns for a) SSZ-13(10, 0), b) SSZ-13(15, 0), c) SSZ-13(20, 0), d) SSZ-13(25, 0), e) SSZ-13(30, 0), f) SSZ-13(60, 0), and g) Si-CHA samples synthesized in the absence of Na<sup>+</sup> at varying Si/Al ratios.

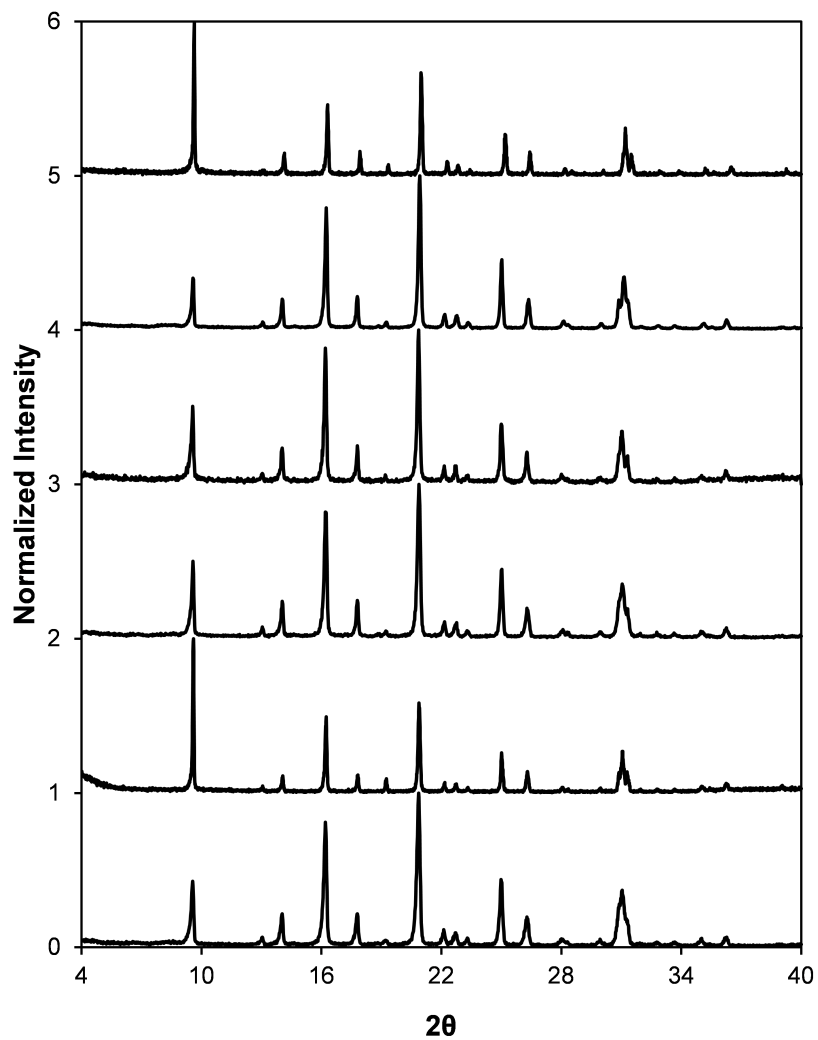


Figure 3.14. Powder X-ray diffraction patterns for six independent syntheses of SSZ-13(15, 0).

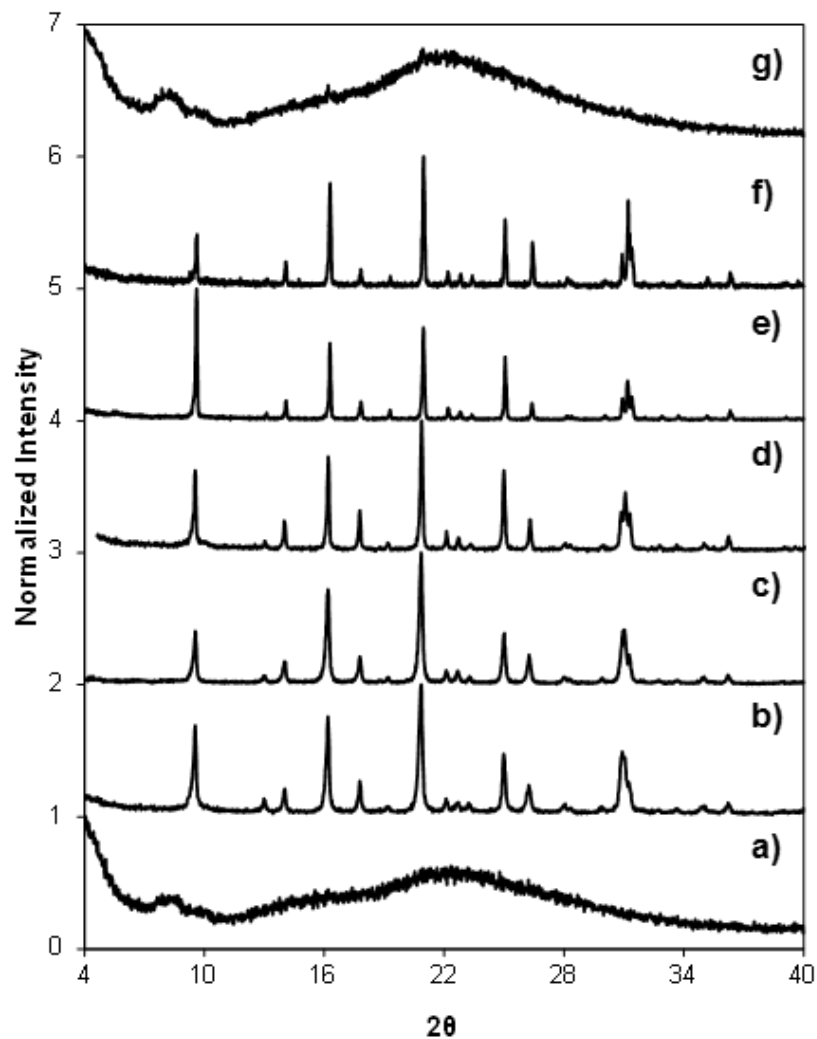


Figure 3.15. Powder X-ray diffraction patterns for a) SSZ-13(5, 0.67), b) SSZ-13(10, 0.67), c) SSZ-13(15, 0.67), d) SSZ-13(25, 0.67), e) SSZ-13(50, 0.67), f) SSZ-13(100, 0.67), and g) SSZ-13(200, 0.67) samples synthesized with constant  $\text{Na}^+/\text{TMAda}^+ = 0.67$  and varying Si/Al ratios.

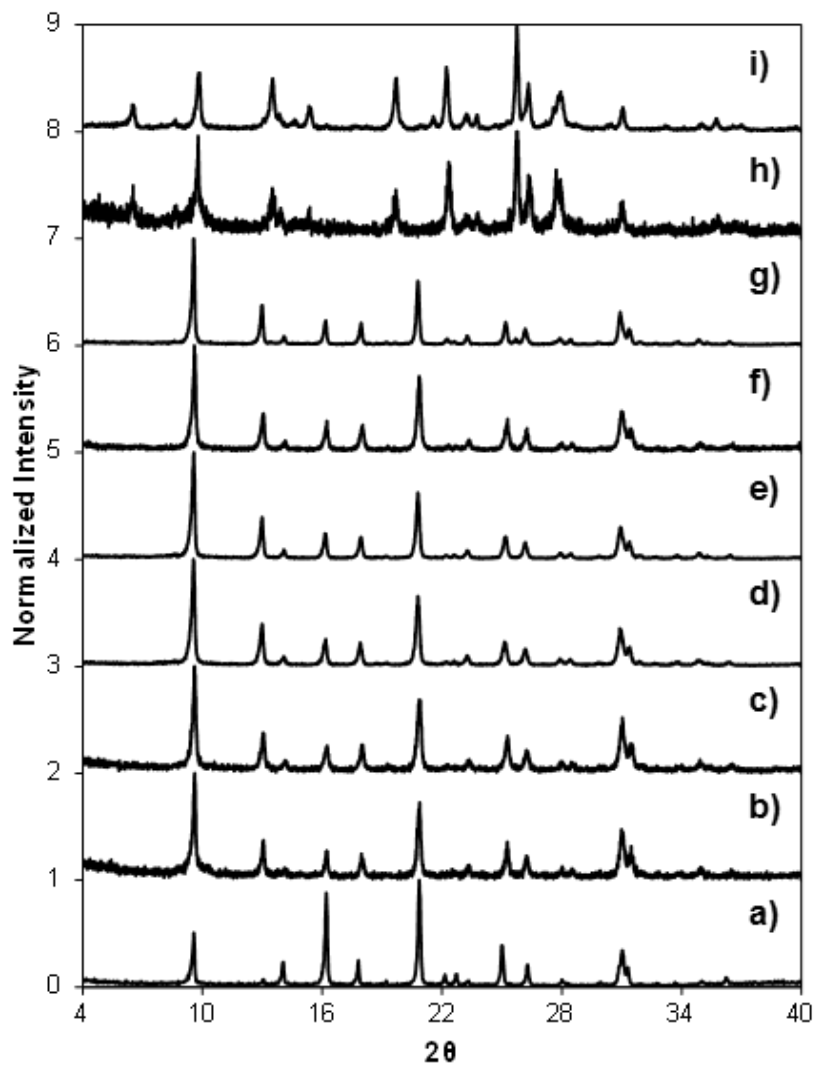


Figure 3.16. Powder X-ray diffraction patterns for a) SSZ-13(15, 0), b) SSZ-13(15, 0.25), c) SSZ-13(15, 0.50), d) SSZ-13(15, 0.67), e) SSZ-13(15, 1.00), f) SSZ-13(15, 1.50), g) SSZ-13(15, 2.00), h) MOR(15, 2.50), and i) MOR(15, 3.00) samples synthesized with constant solution Si/Al = 15,  $(\text{Na}^+ + \text{TMAda}^+)/\text{Al}$  (total charge), and varying  $\text{Na}^+/\text{TMAda}^+$  ratios (charge density).



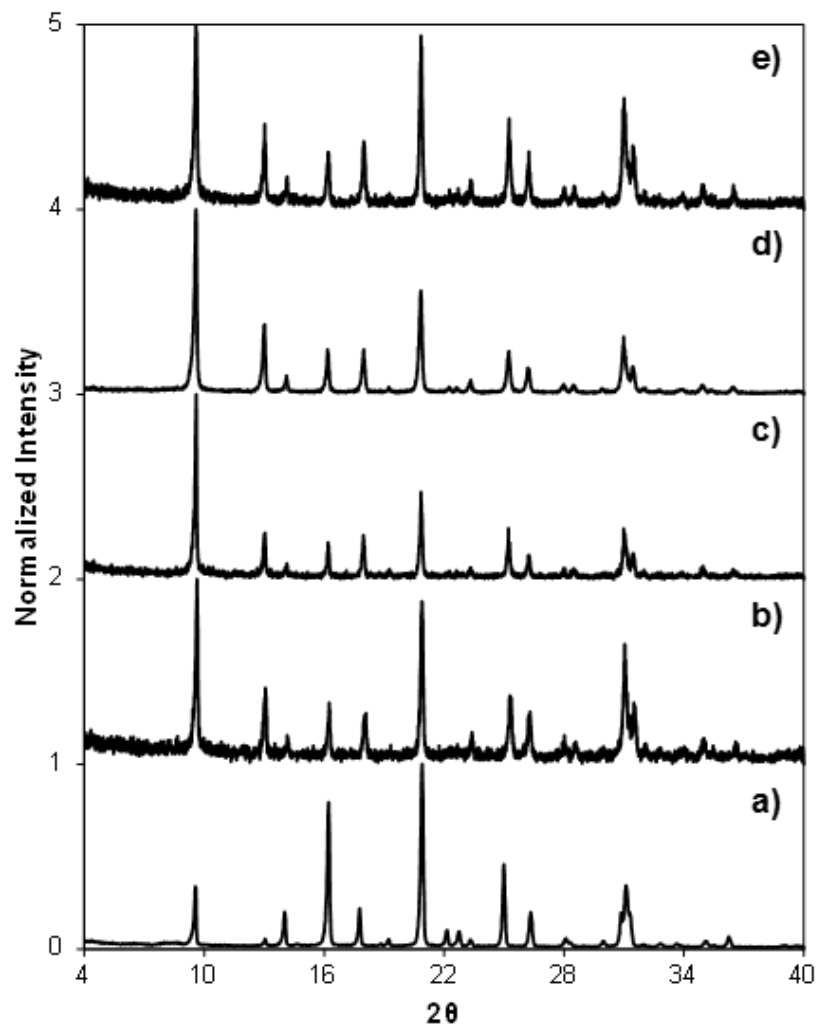


Figure 3.17. Powder X-ray diffraction patterns for a) SSZ-13(25, 0), b) SSZ-13(25, 0.50), c) SSZ-13(25, 0.67), d) SSZ-13(25, 1.00), and e) SSZ-13(25, 2.00) samples synthesized with constant solution  $\text{Si}/\text{Al} = 25$  and  $(\text{Na}^+ + \text{TMAda}^+) / \text{Al}$  (total charge), and varying  $\text{Na}^+/\text{TMAda}^+$  ratios (charge density).

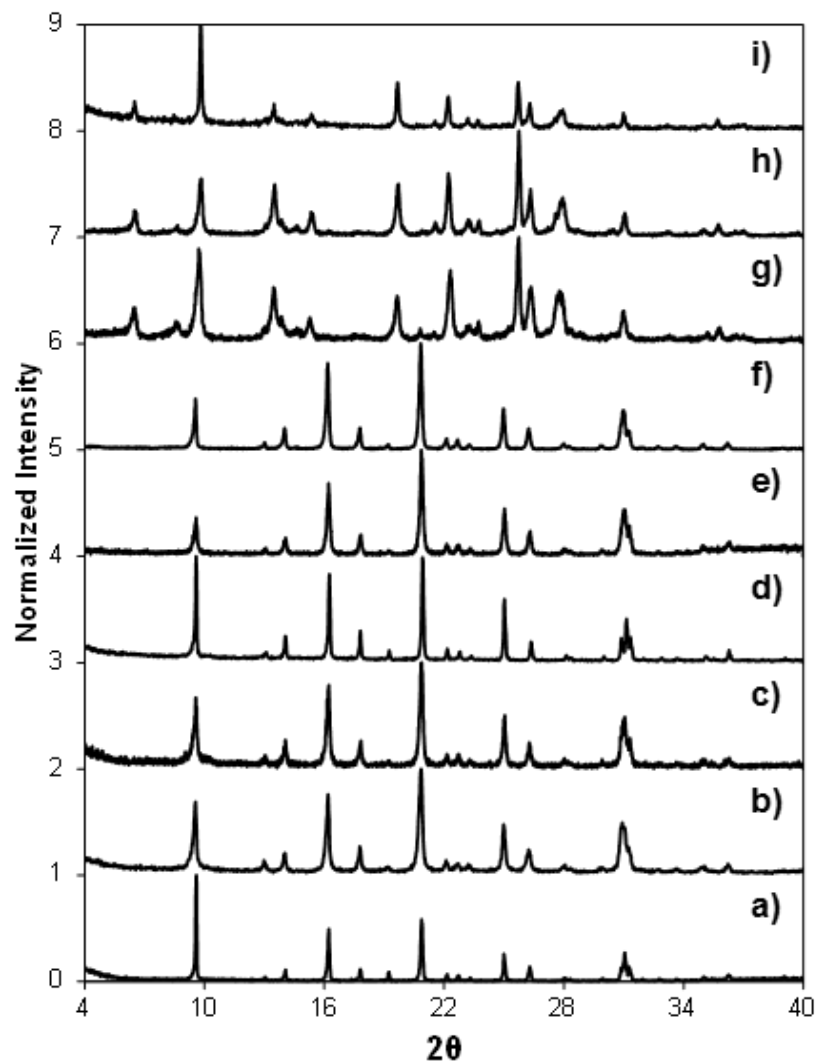


Figure 3.18. Powder X-ray diffraction patterns for a) SSZ-13(15, 0), b) SSZ-13(15, 0.35), c) SSZ-13(15, 0.70), d) SSZ-13(15, 0.93), e) SSZ-13(15, 1.38), f) SSZ-13(15, 2.09), g) MOR(15, 3.45), h) MOR(15, 4.16, and i) MOR(15, 5.55) samples synthesized with constant solution Si/Al = 15 and varying  $(\text{Na}^+ + \text{TMAda}^+)/\text{Al}$  (total charge) and  $\text{Na}^+/\text{TMAda}^+$  ratios (charge density).

## 3.7.9 Ar Adsorption Isotherms of Catalyst Samples

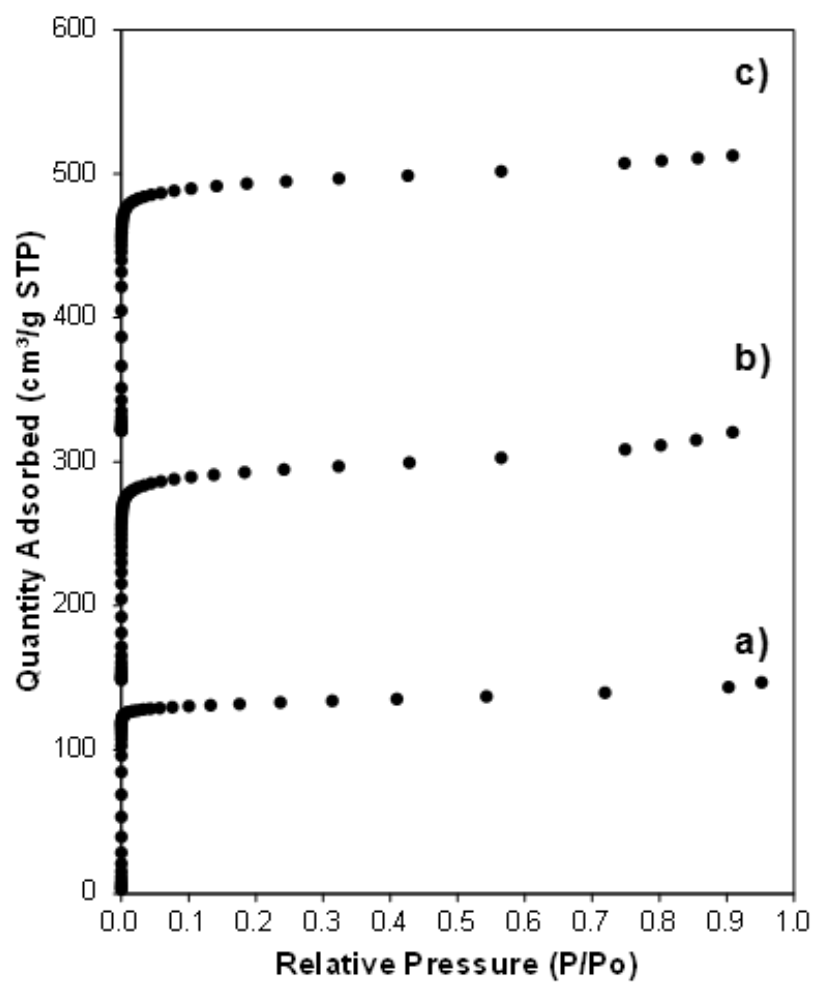


Figure 3.19. Ar adsorption isotherms at measured at 87 K on a) SSZ-13(5), b) SSZ-13(15, 1), and c) SSZ-13(25, 1).

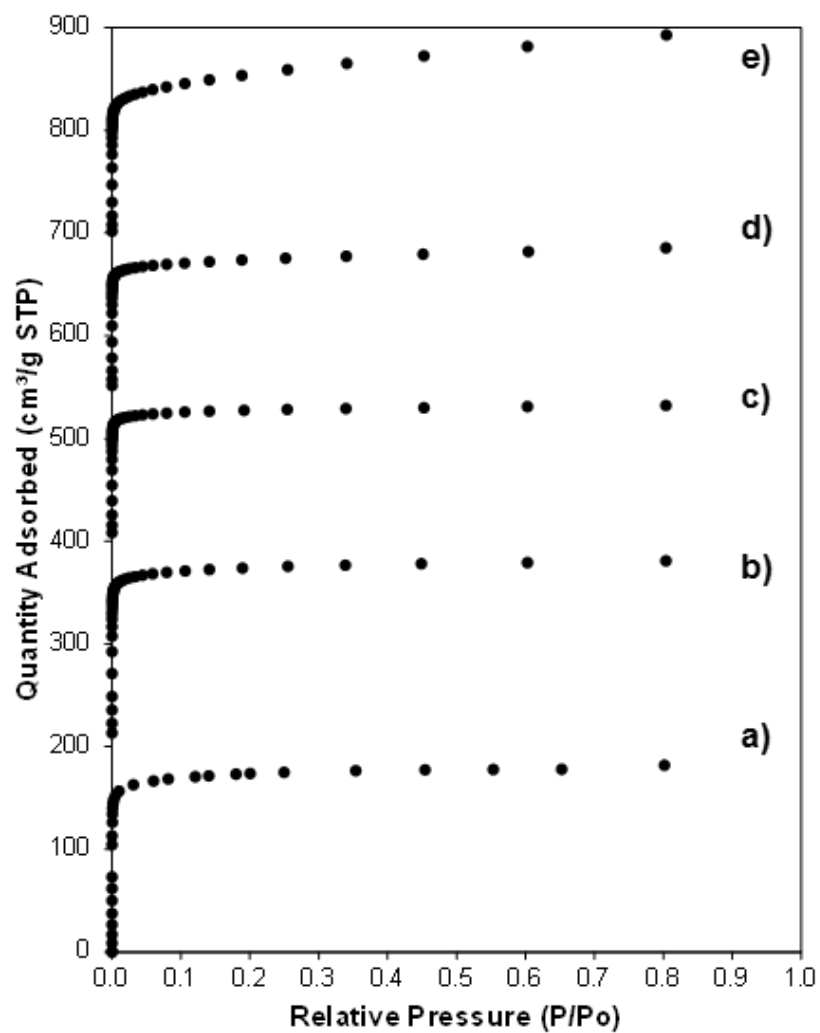


Figure 3.20. Ar adsorption isotherms at measured at 87 K on a) SSZ-13(15, 0), b) SSZ-13(20, 0), c) SSZ-13(25, 0), d) SSZ-13(30, 0), and e) Si-CHA.

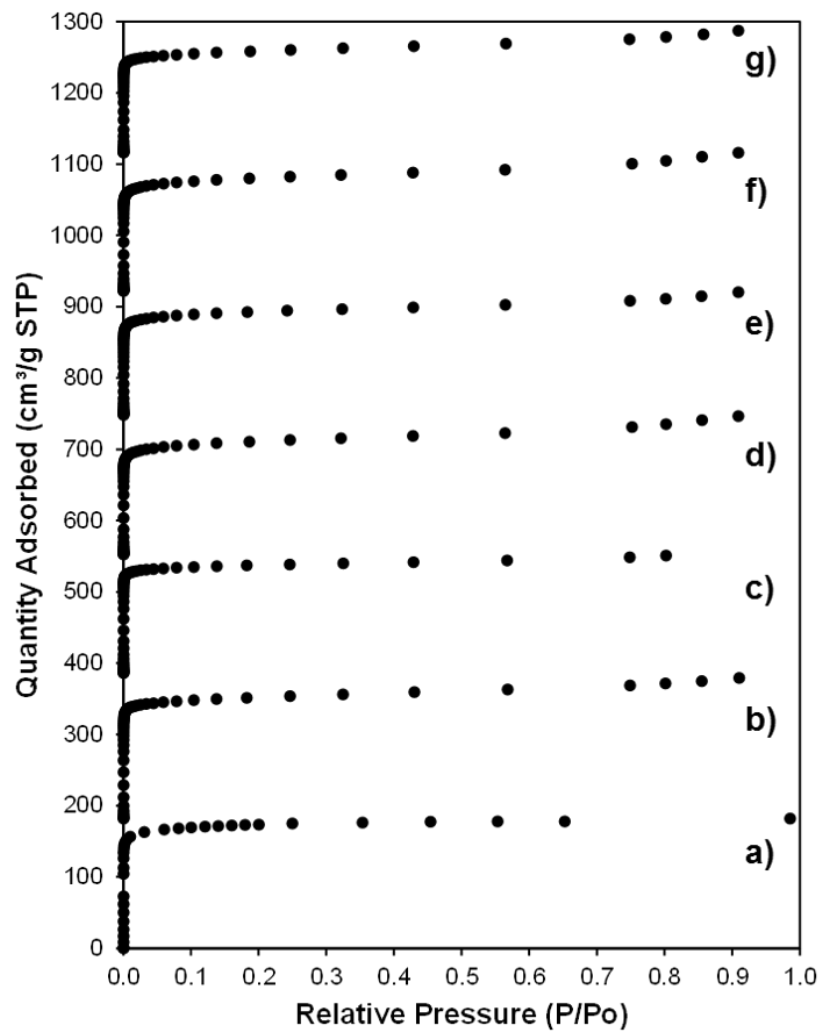


Figure 3.21. Ar adsorption isotherms at measured at 87 K on a) H-SSZ-13(15, 0), b) H-SSZ-13(15, 0.25), c) H-SSZ-13(15, 0.50), d) H-SSZ-13(15, 0.67), e) H-SSZ-13(15, 1.00), f) H-SSZ-13(15, 1.50), and g) H-SSZ-13(15, 2.00).

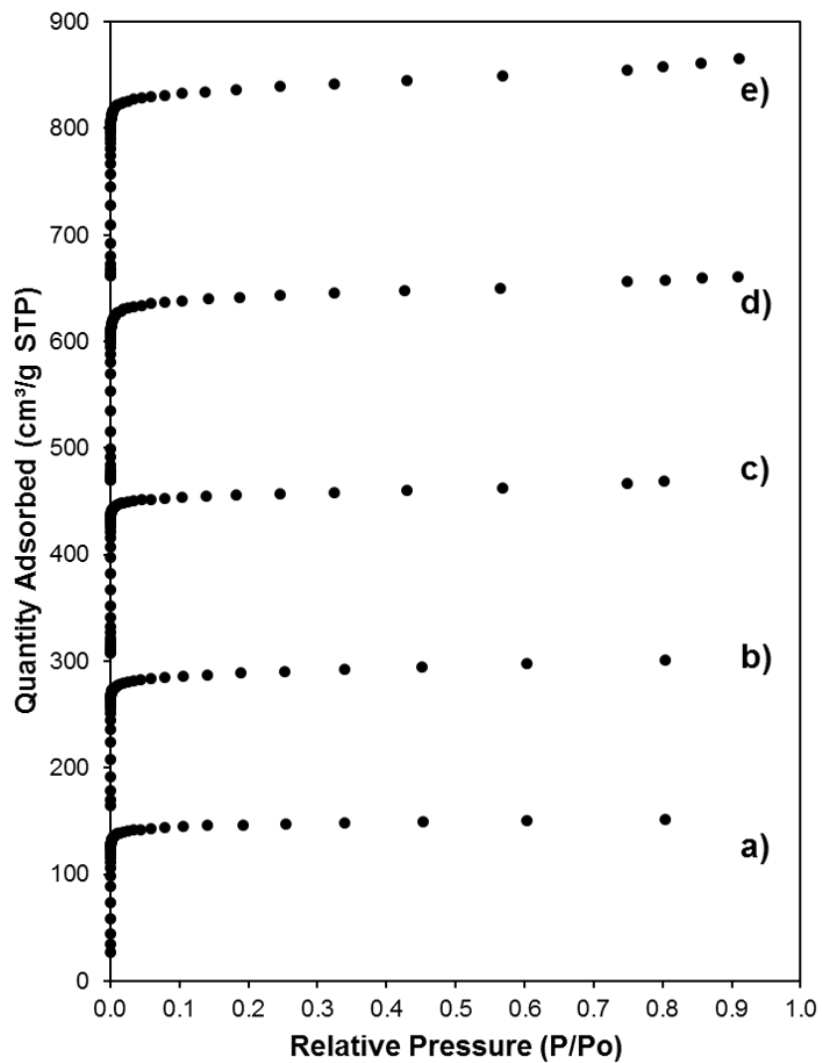


Figure 3.22. Ar adsorption isotherms at measured at 87 K on a) H-SSZ-13(25, 0), b) H-SSZ-13(25, 0.25), c) H-SSZ-13(25, 0.50), d) H-SSZ-13(25, 1.00), and e) H-SSZ-13(25, 2.00).

### 3.7.10 Thermogravimetric Analysis (TGA) to Measure the Organic Content of As-Synthesized Zeolites

Table 3.3.

Calculation of the number of TMAda<sup>+</sup> per cage for SSZ-13(X,0) and SSZ-13(15,X) with maintaining a constant (Na<sup>+</sup>+TMAda<sup>+</sup>)/Al ratio.

| Sample ID        | Si/Al | TMAda <sup>+</sup> /Al | TMAda <sup>+</sup> /Cage |
|------------------|-------|------------------------|--------------------------|
| SSZ-13(15, 0)    | 14.5  | 1.08                   | 1.25                     |
| SSZ-13(20, 0)    | 17.5  | 1.00                   | 0.97                     |
| SSZ-13(25, 0)    | 24.6  | 1.44                   | 1.01                     |
| SSZ-13(30, 0)    | 26.1  | 1.66                   | 1.10                     |
| SSZ-13(15, 0.25) | 13.5  | 0.93                   | 1.15                     |
| SSZ-13(15, 0.50) | 14.7  | 0.97                   | 1.11                     |
| SSZ-13(15, 0.67) | 15.0  | 0.93                   | 1.04                     |
| SSZ-13(15, 1.00) | 14.8  | 1.04                   | 1.18                     |
| SSZ-13(15, 1.50) | 15.2  | 1.05                   | 1.17                     |
| SSZ-13(15, 2.00) | 13.5  | 0.89                   | 1.10                     |

### 3.7.11 <sup>27</sup>Al Magic Angle Spinning Nuclear Magnetic Resonance (<sup>27</sup>Al MAS NMR)

The <sup>27</sup>Al MAS NMR spectra for SSZ-13 samples synthesized without Na<sup>+</sup> are shown in Figure 3.23 and those synthesized at constant Si/Al = 15, (Na<sup>+</sup>+TMAda<sup>+</sup>)/Al, and varying Na<sup>+</sup>/TMAda<sup>+</sup> are shown in Figure 3.24. Tetrahedrally-coordinated Al atoms were characterized by a resonance centered around 60 ppm. There was no shoulder present at about 48 ppm, representative of pentacoordinated Al, and a minimal (0-5%) amount of octahedral Al present at about 0 ppm [118, 138, 139]. Spectra were recorded with different sample masses so a quantitative comparison of the line intensities between different samples is not possible because the intensity is a function of the total Al content in the rotor, therefore the intensity of each H-SSZ-13 spectra was normalized by the maximum intensity in each spectrum to allow for qualitative comparison of the different H-SSZ-13 samples.

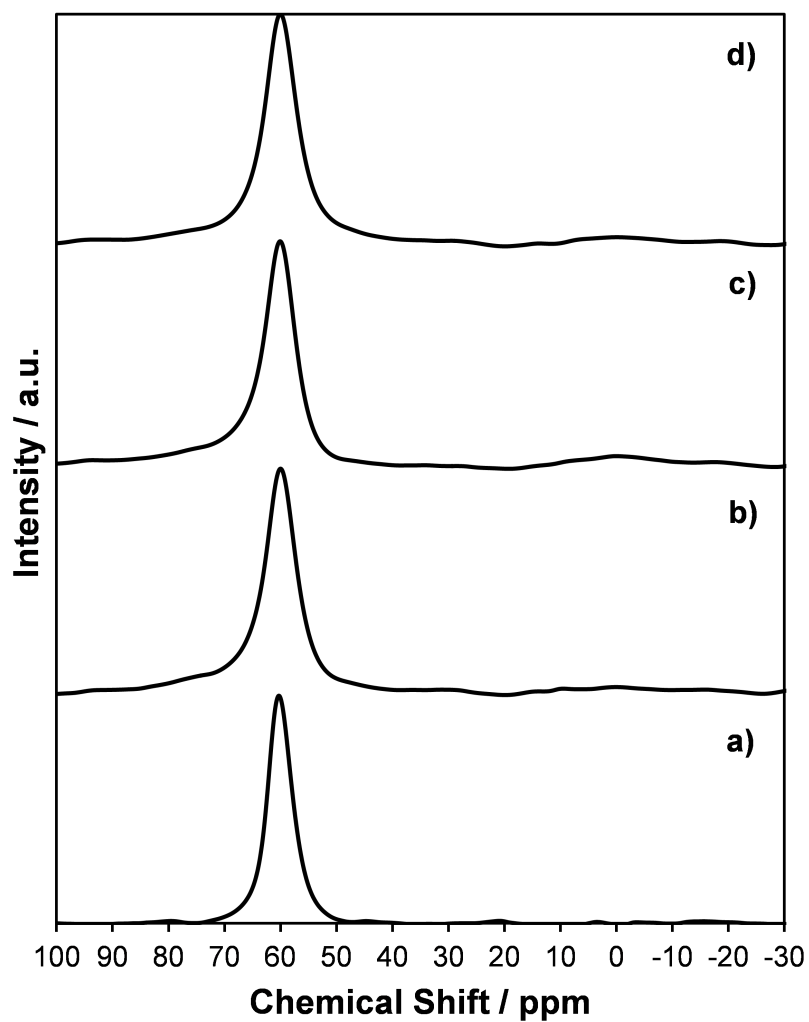


Figure 3.23.  $^{27}\text{Al}$  MAS NMR spectra for a) H-SSZ-13(15, 0), b) H-SSZ-13(20, 0), c) H-SSZ-13(25, 0), and d) H-SSZ-13(30, 0).



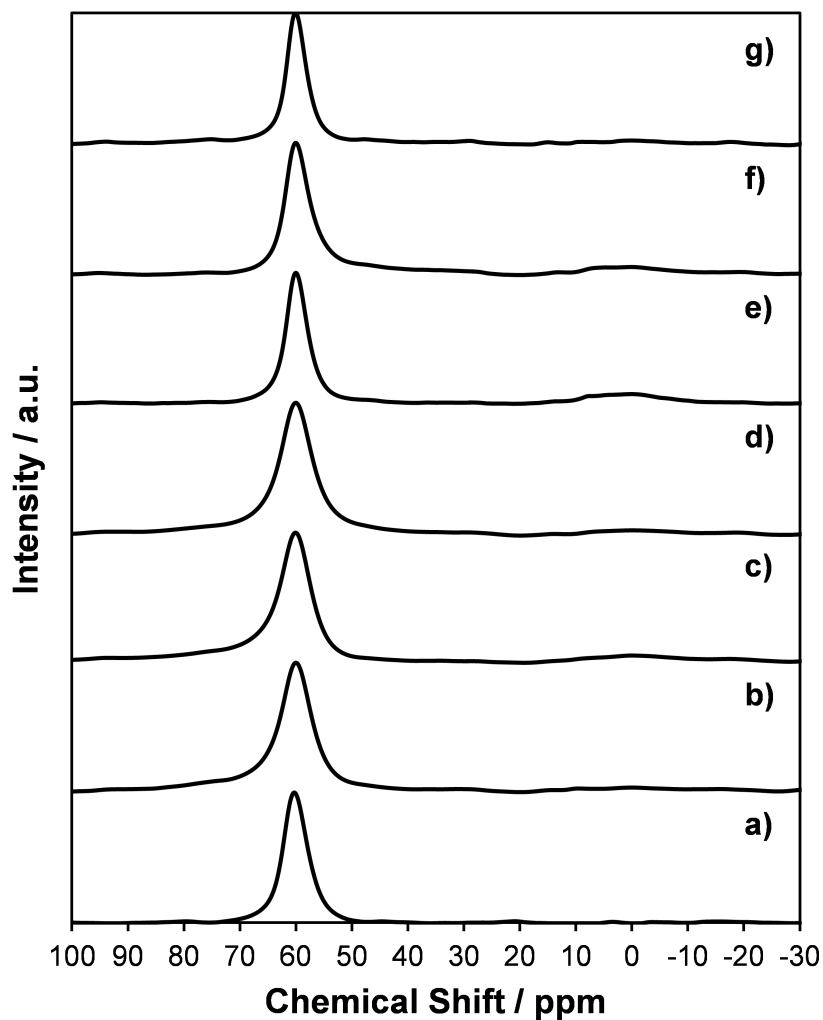


Figure 3.24.  $^{27}\text{Al}$  MAS NMR spectra for a) H-SSZ-13(15, 0), b) H-SSZ-13(15, 0.25), c) H-SSZ-13(15, 0.50), d) H-SSZ-13(15, 0.67), e) H-SSZ-13(15, 1.00), f) H-SSZ-13(15, 1.50), and g) H-SSZ-13(15, 2.00).

## 3.7.12 Copper Cation Speciation in SSZ-13 Zeolites

Table 3.4.  
Cu/Al, saturation Co/Al, predicted  $M^{2+}/Al$ , and residual  $H^+/Al$  on H-SSZ-13(5), H-SSZ-13(15, 1), and H-SSZ-13(25, 1).

| Sample        | Si/Al | Micropore<br>Volume<br>( $cm^3 g_{cat}^{-1}$ ) | $H^+/Al^a$ | Co/Al | $H^+/Al^b$ | Predicted<br>$M^{2+}/Al$ | Cu/Al | $H^+/Al^c$ |
|---------------|-------|--|------------|-------|------------|--------------------------|-------|------------|
| SSZ-13(5)     | 4.5   | 0.16   | 0.65       | 0.19  | 0.28       | 0.22                     | 0.00  | 0.65       |
|               |       |  |            |       |            |                          | 0.02  | 0.45       |
|               |       |  |            |       |            |                          | 0.04  | 0.60       |
|               |       |  |            |       |            |                          | 0.09  | 0.43       |
|               |       |  |            |       |            |                          | 0.12  | 0.37       |
|               |       |  |            |       |            |                          | 0.16  | 0.32       |
|               |       |  |            |       |            |                          | 0.20  | 0.31       |
| SSZ-13(15, 1) | 14.8  | 0.19   | 1.02       | 0.08  | 0.82       | 0.09                     | 0.00  | 1.02       |
|               |       |  |            |       |            |                          | 0.03  | 0.94       |
|               |       |  |            |       |            |                          | 0.09  | 0.81       |
|               |       |  |            |       |            |                          | 0.12  | 0.79       |
|               |       |  |            |       |            |                          | 0.21  | 0.68       |
|               |       |  |            |       |            |                          | 0.37  | 0.58       |
|               |       |  |            |       |            |                          | 0.41  | 0.55       |
| SSZ-13(25, 1) | 24.1  | 0.18   | 0.98       | 0.04  | 0.88       | 0.05                     | 0.44  | 0.51       |
|               |       |  |            |       |            |                          | 0.00  | 0.96       |
|               |       |  |            |       |            |                          | 0.06  | 0.86       |
|               |       |  |            |       |            |                          | 0.21  | 0.74       |
|               |       |  |            |       |            |                          | 0.37  | 0.58       |
|               |       |  |            |       |            |                          | 0.41  | 0.54       |

<sup>a</sup>  $H^+/Al$  measured on the parent H-SSZ-13 sample

<sup>b</sup>  $H^+/Al$  measured after saturation with  $Co^{2+}$

<sup>c</sup>  $H^+/Al$  measured after ion-exchange with  $Cu^{2+}$

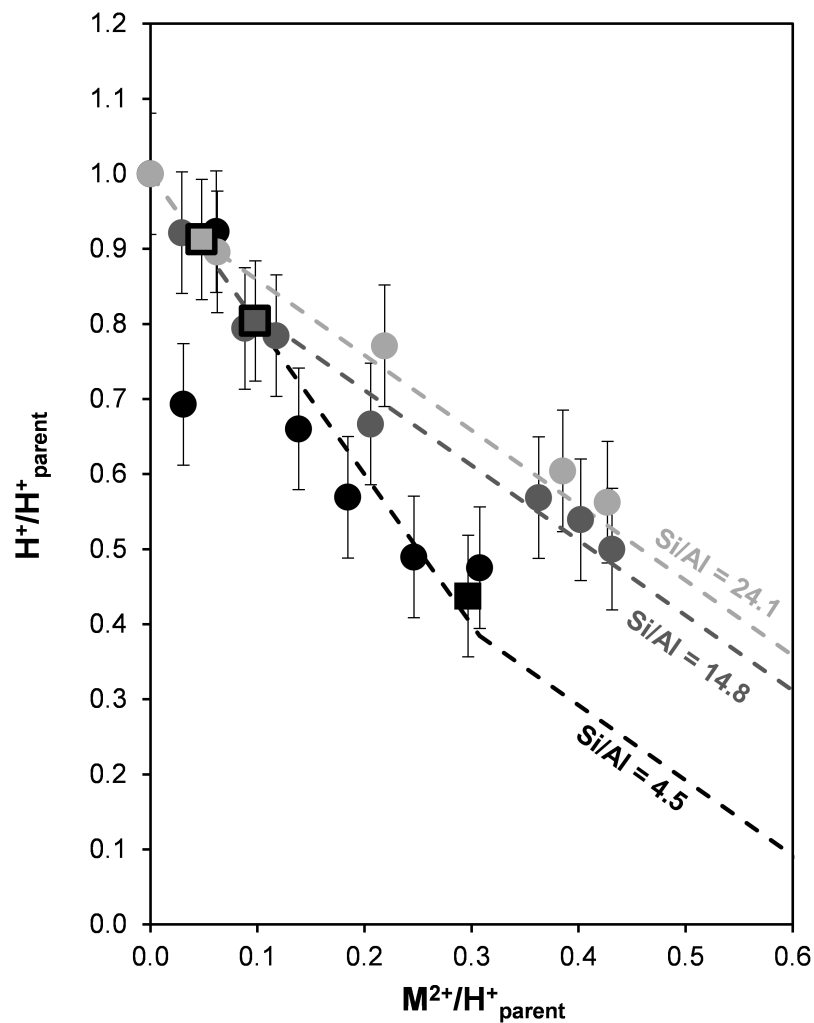


Figure 3.25. Number of residual  $H^+$  sites, normalized to the parent  $H^+/Al$  for each sample, after  $Cu^{2+}$  exchange (circles) as a function of the  $Cu/Al$  ratio, after  $Co^{2+}$  saturation (squares) on H-SSZ-13(5) (black), H-SSZ-13(15, 1) (dark grey), and H-SSZ-13(25, 1) (grey). Dashed lines indicate predictions from statistical calculations of random Al distributions and the sequential exchange of  $Cu^{2+}$  at paired Al sites (2 Al in 6-MR) followed by exchange of  $[CuOH]^+$  at isolated Al sites.

### 3.7.13 Statistical Estimates of Paired Aluminum in CHA Zeolites

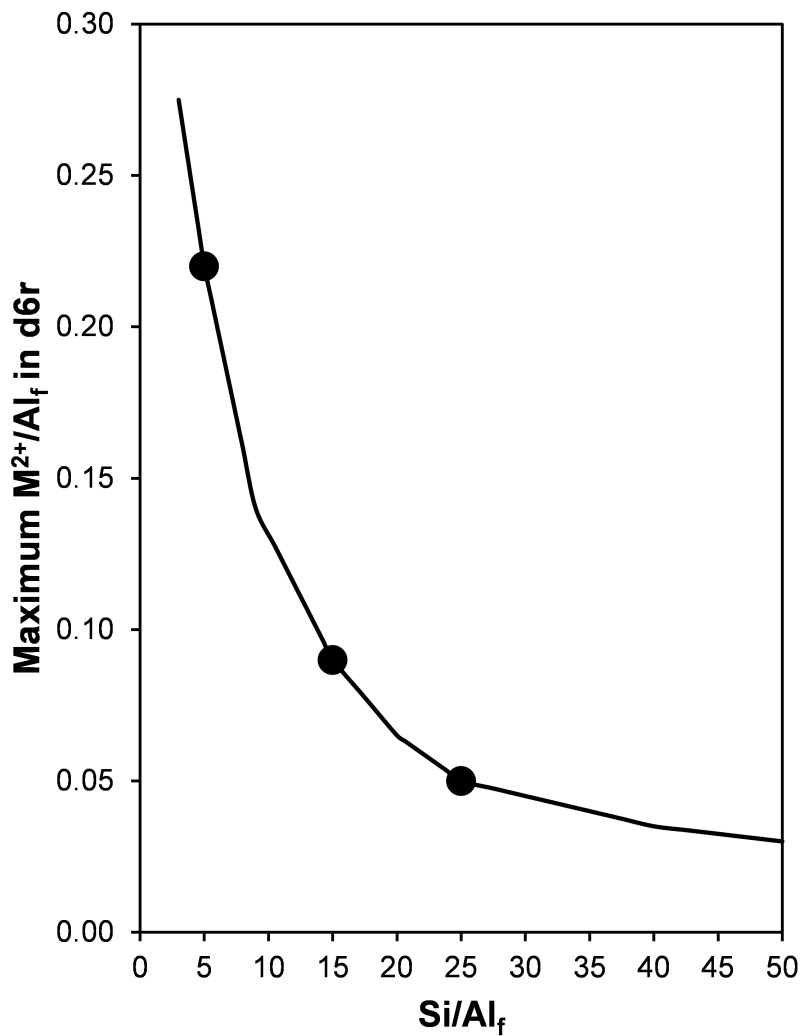


Figure 3.26. Statistical calculations for the random distribution of Al in CHA at varying Si/Al ratios, obeying Lowenstein's Rule [37]. The circles denote SSZ-13 materials synthesized at Si/Al = 5, 15, and 25 and correspond to theoretical  $M^{2+}/Al = 0.22$ , 0.09, and 0.05, respectively.

### 3.7.14 Derivation of Cobalt Ion-Exchange Isotherm

In order to demonstrate complete saturation of H-SSZ-13 samples with  $Co^{2+}$ , an ion-exchange isotherm was measured on both H-SSZ-13(15, 0) and H-SSZ-13(15, 1)

using  $\text{Co}(\text{NO}_3)_2$  molarities ranging from 0.005-0.5 M and the procedure described previously in the main text. The Langmuirian ion-exchange isotherm was derived by first assuming that the total Al atoms on a given sample ( $\text{Al}_{\text{tot}}$ ) are equal to the number of Al atoms that cannot exchange a cation ( $\text{Al}_{\text{non,exch}}$ ) and the number of Al atoms that can be ion-exchanged ( $\text{Al}_{\text{exch}}$ ):

$$\text{Al}_{\text{tot}} = \text{Al}_{\text{non,exch}} + \text{Al}_{\text{exch}} \quad (3.1)$$

The number of  $\text{Al}_{\text{exch}}$  atoms is equal to the sum of the number of isolated Al sites, which can exchange a monovalent cation ( $\text{Al}_{\text{iso}}^{\text{tot}}$ ), and twice the number of paired Al sites, which can exchange a divalent cation ( $\text{Al}_{\text{pair}}^{\text{tot}}$ ):

$$\text{Al}_{\text{exch}} = \text{Al}_{\text{iso}}^{\text{tot}} + 2\text{Al}_{\text{pair}}^{\text{tot}} \quad (3.2)$$

A mole balance on each of the  $\text{Al}_{\text{iso}}^{\text{tot}}$  and  $\text{Al}_{\text{pair}}^{\text{tot}}$  terms describes the types of cations they can exchange:

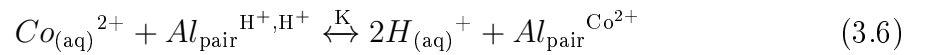
$$\text{Al}_{\text{iso}}^{\text{tot}} = \text{Al}_{\text{iso}}^{\text{H}^+} \quad (3.3)$$

$$\text{Al}_{\text{pair}}^{\text{tot}} = \text{Al}_{\text{pair}}^{\text{H}^+, \text{H}^+} + \text{Al}_{\text{pair}}^{\text{Co}^{2+}} \quad (3.4)$$

where  $\text{Al}_{\text{iso}}^{\text{H}^+}$  are isolated Al sites charge-balanced by a single  $\text{H}^+$ ,  $\text{Al}_{\text{pair}}^{\text{H}^+, \text{H}^+}$  are paired Al sites charge-balanced by two  $\text{H}^+$  sites, and  $\text{Al}_{\text{pair}}^{\text{Co}^{2+}}$  are paired Al sites charge-balanced by a  $\text{Co}^{2+}$  ion. In this derivation, isolated  $\text{Co}^{2+}$  cations are assumed to be the only Co species present and can only be exchanged at a paired Al site, while  $\text{H}^+$  are the only monovalent cations present and can exchange at both isolated and paired Al sites. Substituting Eq. 3.2-3.4 into Eq. 3.1 results in a site balance equation relating  $\text{Al}_{\text{tot}}$  to the number of Al sites occupied by different cations:

$$\text{Al}_{\text{tot}} = \text{Al}_{\text{non,exch}} + \text{Al}_{\text{iso}}^{\text{H}^+} + 2(\text{Al}_{\text{pair}}^{\text{H}^+, \text{H}^+} + \text{Al}_{\text{pair}}^{\text{Co}^{2+}}) \quad (3.5)$$

The exchange of aqueous  $\text{Co}^{2+}$  ions  $\text{Co}_{(\text{aq})}^{2+}$  onto paired Al sites occupied by two protons ( $\text{Al}_{\text{pair}}^{\text{H}^+, \text{H}^+}$ ) to form aqueous  $\text{H}^+$  ( $\text{H}_{(\text{aq})}^+$ ) and paired Al sites occupied by  $\text{Co}^{2+}$  ( $\text{Al}_{\text{pair}}^{\text{Co}^{2+}}$ ) is given by the following equilibrium reaction:



where  $K$  is the equilibrium constant and is defined in terms of the following concentrations as:

$$K = \frac{[H_{(aq)}^+]^2 [Al_{pair}^{Co^{2+}}]}{[Co_{(aq)}^{2+}] [Al_{pair}^{H^+, H^+}]} \left( \frac{1}{C^0} \right) \quad (3.7)$$

where  $C^0$  is the standard state reference concentration of 1 M.

Dividing Eq. 3.5 by  $Al_{tot}$  yields a site balance equation expressed in terms of the fractional coverages ( $\theta$ ) for each species:

$$1 = \frac{Al_{non,exch}}{Al_{tot}} + \theta_{iso}^{H^+} + 2(\theta_{pair}^{H^+, H^+} + \theta_{pair}^{Co^{2+}}) \quad (3.8)$$

where  $\theta_{iso}^{H^+}$  is the coverage of  $Al_{iso}^{H^+}$  species,  $\theta_{pair}^{H^+, H^+}$  is the coverage of  $Al_{pair}^{H^+, H^+}$  species, and  $\theta_{pair}^{Co^{2+}}$  is the coverage of  $Al_{pair}^{Co^{2+}}$  and each coverage term is defined as follows:

$$\theta_{iso}^{H^+} = \frac{Al_{iso}^{H^+}}{Al_{tot}} \quad (3.9)$$

$$\theta_{pair}^{H^+, H^+} = \frac{Al_{pair}^{H^+, H^+}}{Al_{tot}} \quad (3.10)$$

$$\theta_{pair}^{Co^{2+}} = \frac{Al_{pair}^{Co^{2+}}}{Al_{tot}} \quad (3.11)$$

Dividing Eq. 3.1 by  $Al_{tot}$  also results in an expression for the fraction of  $Al_{exch}$  ( $\frac{Al_{exch}}{Al_{tot}}$ ) in terms of the fraction of  $Al_{non,exch}$  ( $\frac{Al_{non,exch}}{Al_{tot}}$ ):

$$\frac{Al_{exch}}{Al_{tot}} = 1 - \frac{Al_{non,exch}}{Al_{tot}} \quad (3.12)$$

Substituting Eq. 3.12 into Eq. 3.8 results in the following equation that describes the  $\frac{Al_{exch}}{Al_{tot}}$  in terms of the fractional coverages of each species:

$$\frac{Al_{exch}}{Al_{tot}} = \theta_{iso}^{H^+} + 2(\theta_{pair}^{H^+, H^+} + \theta_{pair}^{Co^{2+}}) \quad (3.13)$$

where  $2(\theta_{pair}^{H^+, H^+} + \theta_{pair}^{Co^{2+}})$  is equal to the fraction of  $Al_{pair}$  present ( $\frac{Al_{pair}}{Al_{tot}}$ ).

The equilibrium constant,  $K$  (Eq. 3.7), can be rewritten in terms of coverages to derive an expression for  $\theta_{pair}^{H^+, H^+}$ :

$$\theta_{pair}^{H^+, H^+} = \frac{[H_{(aq)}^+]^2 \theta_{pair}^{Co^{2+}}}{K [Co_{(aq)}^{2+}]} \quad (3.14)$$

Eq. 3.14 can then be substituted into Eq. 3.13 to obtain an expression in terms of quantities that can be measured experimentally:

$$\frac{Al_{\text{exch}}}{Al_{\text{tot}}} = \theta_{\text{iso}}^{\text{H}^+} + 2\left(\frac{[H_{(\text{aq})}^+]^2 \theta_{\text{pair}}^{\text{Co}^{2+}}}{K[Co_{(\text{aq})}^{2+}]} + \theta_{\text{pair}}^{\text{Co}^{2+}}\right) \quad (3.15)$$

Eq. 3.15 can be rearranged to solve for  $\theta_{\text{pair}}^{\text{Co}^{2+}}$ , which is a mathematical representation of the  $\text{Co}^{2+}$  exchange isotherm:

$$\theta_{\text{pair}}^{\text{Co}^{2+}} = \left(\frac{1}{2}\right)\left(\frac{Al_{\text{exch}}}{Al_{\text{tot}}} - \theta_{\text{iso}}^{\text{H}^+}\right)\left(\frac{K[Co_{(\text{aq})}^{2+}]/[H_{(\text{aq})}^+]^2}{1 + K[Co_{(\text{aq})}^{2+}]/[H_{(\text{aq})}^+]^2}\right) \quad (3.16)$$

where the term  $[Co_{(\text{aq})}^{2+}]/[H_{(\text{aq})}^+]^2$  represents the ratio of  $\text{Co}_{(\text{aq})}^{2+}$  and  $\text{H}_{(\text{aq})}^+$  in the exchange solution at equilibrium, and where the term  $\left(\frac{1}{2}\right)\left(\frac{Al_{\text{exch}}}{Al_{\text{tot}}} - \theta_{\text{iso}}^{\text{H}^+}\right)$  is equal to  $\frac{Al_{\text{pair}}}{Al_{\text{tot}}}$  from Eq. 3.13 and represents the saturation limit of the  $\text{Co}^{2+}$  exchange isotherm. This allows Eq. 3.16 to be rewritten as:

$$\theta_{\text{pair}}^{\text{Co}^{2+}} = \frac{Al_{\text{pair}}}{Al_{\text{tot}}}\left(\frac{K[Co_{(\text{aq})}^{2+}]/[H_{(\text{aq})}^+]^2}{1 + K[Co_{(\text{aq})}^{2+}]/[H_{(\text{aq})}^+]^2}\right) \quad (3.17)$$

Eq. 3.17 can be regressed to the experimental data to estimate K and  $\frac{Al_{\text{pair}}}{Al_{\text{tot}}}$ . The isotherms fit to the experimental data on both H-SSZ-13(15, 1) and H-SSZ-13(15, 0) are shown in Figure 3.3 of the main text. For H-SSZ-13(15, 1) the value of the equilibrium constant, K, was 0.027 and the value of  $\frac{Al_{\text{pair}}}{Al_{\text{tot}}}$  was 0.087, which is the predicted maximum number of sites capable of exchanging a divalent cation (e.g.,  $\text{Co}^{2+}$ ). For H-SSZ-13(15, 0), K was 0.016 and  $\frac{Al_{\text{pair}}}{Al_{\text{tot}}}$  was 0.003.

### 3.7.15 UV-Vis Spectroscopy of Co-SSZ-13(15, 1)

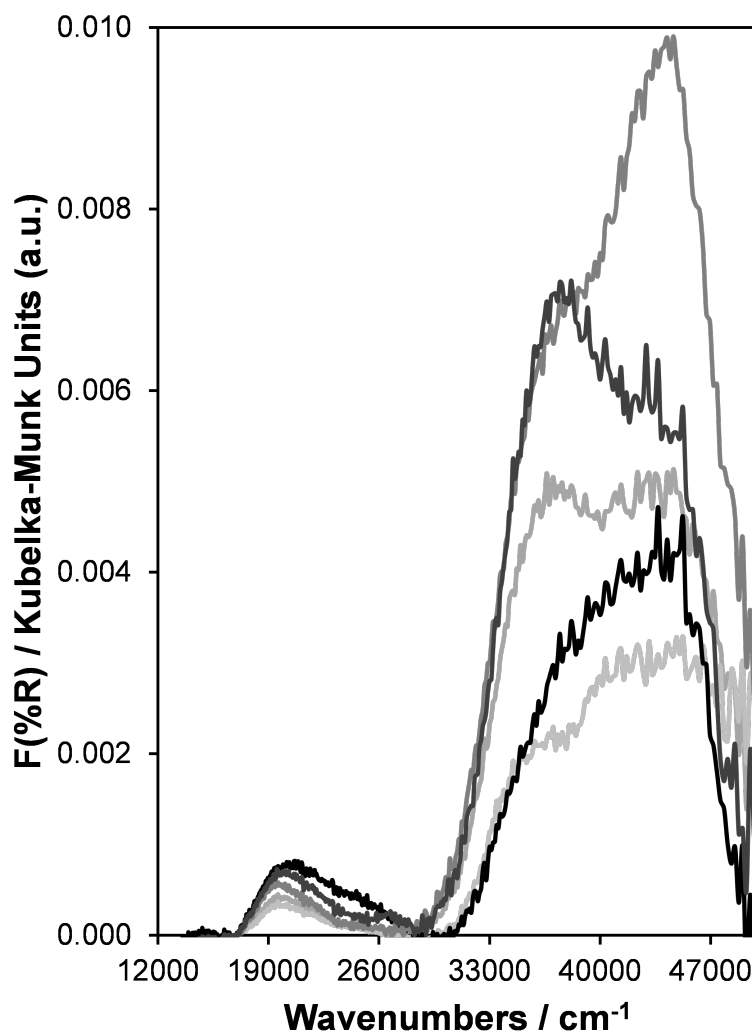


Figure 3.27. Ambient UV-Vis spectra of Co-SSZ-13(15, 1) with Co/Al values of 0.021 (faint grey trace), 0.022 (light grey trace), 0.047 (grey trace), 0.08 (dark grey trace), and 0.084 (black trace).

### 3.7.16 Sodium Cation Exchange Procedure and Derivation of Ion-Exchange Isotherm

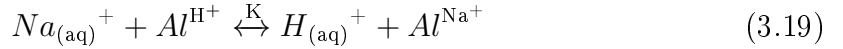
A Langmuirian isotherm model for  $\text{Na}^+$  exchange was derived starting from Eq. 3.1, but using only a single adsorption site to describe the  $\text{Al}_{\text{exch}}$  since a monovalent



cation cannot distinguish between isolated and paired Al sites. Therefore,  $Al_{\text{exch}}$  can be described by the sum of the total number of Al exchange sites with a  $H^+$  and with a  $Na^+$  present:

$$Al_{\text{exch}} = Al^{H^+} + Al^{Na^+} \quad (3.18)$$

The equilibrium reaction of aqueous  $Na^+$  ions ( $Na_{(aq)}^+$ ) with proton-occupied Al exchange sites ( $Al^{H^+}$ ) to form aqueous  $H^+$  ( $H_{(aq)}^+$ ) and sodium-occupied Al sites ( $Al^{Na^+}$ ) is given by:



where  $K$  is the equilibrium constant defined in terms of concentrations as:

$$K = \frac{[H_{(aq)}^+][Al^{Na^+}]}{[Na_{(aq)}^+][Al^{H^+}]} \quad (3.20)$$

Substituting Eq. 3.18 into Eq. 3.1 and dividing by  $Al_{\text{tot}}$  provides an expression in terms of the fractional coverages ( $\theta$ ) of each species:

$$1 = \frac{Al_{\text{non,exch}}}{Al_{\text{tot}}} + \theta^{H^+} + \theta^{Na^+} \quad (3.21)$$

where  $\theta^{H^+}$  is the coverage of  $Al^{H^+}$  and  $\theta^{Na^+}$  is the coverage of  $Al^{Na^+}$  defined as follows:

$$\theta^{H^+} = \frac{Al^{H^+}}{Al_{\text{tot}}} \quad (3.22)$$

$$\theta^{Na^+} = \frac{Al^{Na^+}}{Al_{\text{tot}}} \quad (3.23)$$

Substituting Eq. 3.12 into Eq. 3.21 results in an equation that describes  $\frac{Al_{\text{non,exch}}}{Al_{\text{tot}}}$  in terms of the fractional coverage of  $H^+$  and  $Na^+$ :

$$\frac{Al_{\text{non,exch}}}{Al_{\text{tot}}} = \theta^{H^+} + \theta^{Na^+} \quad (3.24)$$

The equilibrium constant,  $K$  (Eq. 3.20), can be rewritten in terms of coverages to obtain an explicit expression for  $\theta^{H^+}$ :

$$\theta^{H^+} = \frac{[H_{(aq)}^+]\theta^{Na^+}}{K[Na_{(aq)}^+]} \quad (3.25)$$

Eq. 3.25 can be substituted into Eq. 3.24 to obtain an expression in terms of quantities that can be measured experimentally:

$$\frac{Al_{\text{non,exch}}}{Al_{\text{tot}}} = \theta^{Na^+} \left( 1 + \frac{[H_{(aq)}^+]}{K[Na_{(aq)}^+]} \right) \quad (3.26)$$

Eq. 3.26 can be rearranged to obtain an expression for  $\theta^{\text{Na}^+}$ , which is the  $\text{Na}^+$  exchange isotherm:

$$\theta^{\text{Na}^+} = \frac{Al_{\text{exch}}}{Al_{\text{tot}}} \left( \frac{K[Na_{(\text{aq})}^+]/[H_{(\text{aq})}^+]}{1 + K[Na_{(\text{aq})}^+]/[H_{(\text{aq})}^+]} \right) \quad (3.27)$$

The term  $[Na_{(\text{aq})}^+]/[H_{(\text{aq})}^+]$  represents the ratio of  $\text{Na}_{(\text{aq})}^+$  and  $\text{H}_{(\text{aq})}^+$  ions in the exchange solution at equilibrium. Eq. 3.27 can be regressed to the experimental data to estimate  $K$  and  $\frac{Al_{\text{exch}}}{Al_{\text{tot}}}$ . The isotherm fit to the experimental data is shown in Figure 3.3 of the main text. For H-SSZ-13(15, 0) the value of the equilibrium constant,  $K$ , was 0.055 and the value of  $\frac{Al_{\text{exch}}}{Al_{\text{tot}}}$  was 1.02. For H-SSZ-13(15, 1),  $K$  was 0.14 and the value of  $\frac{Al_{\text{exch}}}{Al_{\text{tot}}}$  was 0.91, which is in agreement with the experimental results for the  $\text{H}^+/\text{Al}$  determined from  $\text{NH}_3$  TPD (Table 3.2 in main text).

### 3.7.17 Characterization Data for SSZ-13(15) with Varying $(\text{Na}^+ + \text{TMAda}^+) / \text{Al}$ (Total Charge) and Constant $\text{Na}^+/\text{TMAda}^+$ Ratios (Charge Density)

Table 3.5.

Characterization for SSZ-13 samples synthesized at a constant  $\text{Na}^+/\text{TMA-da}^+ = 0.67$  and varying  $\text{Si}/\text{Al}$ .

| Sample            | Si/Al | Micropore<br>Volume<br>( $\text{cm}^3 \text{g}^{-1}$ ) | $\text{H}^+/\text{Al}$ | $\text{Na}^+/\text{Al}$ | $\text{TMAda}^+/\text{Al}$ | $(\text{Na}^+ + \text{TMAda}^+)/\text{Al}$ | Co/Al |
|-------------------|-------|--|------------------------|-------------------------|----------------------------|--|-------|
| SSZ-13(10, 0.67)  | 10.0  | -  | 0.83                   | 0.11                    | -                          | -  | 0.07  |
| SSZ-13(15, 0.67)  | 15.0  | 0.16   | 0.98                   | 0.06                    | 0.93                       | 0.99                                       | 0.06  |
| SSZ-13(25, 0.67)  | 21.1  | -  | -                      | 0.08                    | -                          | -  | 0.03  |
| SSZ-13(50, 0.67)  | 36.2  | -  | -                      | 0.01                    | -                          | -  | 0.01  |
| SSZ-13(100, 0.67) | 65.0  | -  | -                      | 0.04                    | -                          | -  | 0.01  |

3.7.18 Characterization Data for SSZ-13(15) with Varying ( $\text{Na}^+ + \text{TMAda}^+$ ) / Al (Total Charge) and Varying  $\text{Na}^+/\text{TMAda}^+$  Ratios (Charge Density)

Table 3.6.

Characterization data for SSZ-13(15) and MOR samples synthesized with constant synthesis solution Si/Al and varying total solution charge and  $\text{Na}^+/\text{TMAda}^+$ .

| Sample           | Si/Al | Micropore<br>Volume<br>( $\text{cm}^3 \text{g}^{-1}$ ) | $\text{H}^+/\text{Al}$ | $\text{Na}^+/\text{Al}$ | $\text{TMAda}^+/\text{Al}$ | $(\text{Na}^+ + \text{TMAda}^+)/\text{Al}$ | Co/Al |
|------------------|-------|--|------------------------|-------------------------|----------------------------|--|-------|
| SSZ-13(15, 0)    | 17.5  | 0.20   | 0.91                   | 0.01                    | 1.20                       | 1.21                                       | 0.00  |
| SSZ-13(15, 0.35) | 17.0  | -  | -                      | 0.01                    | 1.06                       | 1.07                                       | 0.03  |
| SSZ-13(15, 0.70) | 15.5  | 0.18   | -                      | 0.04                    | 0.89                       | 0.93                                       | 0.04  |
| SSZ-13(15, 0.93) | 15.1  | 0.16   | -                      | 0.05                    | 0.94                       | 0.99                                       | 0.06  |
| SSZ-13(15, 1.38) | 13.3  | -  | 0.96                   | 0.04                    | 0.92                       | 0.96                                       | 0.08  |
| SSZ-13(15, 2.09) | 11.6  | -  | -                      | 0.02                    | 1.01                       | 1.03                                       | 0.06  |
| MOR(15, 3.45)    | 11.9  | -  | -                      | 0.08                    | -                          | -  | 0.03  |
| MOR(15, 4.16)    | 11.9  | -  | -                      | 0.09                    | -                          | -  | 0.01  |
| MOR(15, 5.55)    | 9.9   | -  | 0.94                   | 0.10                    | -                          | -  | 0.02  |

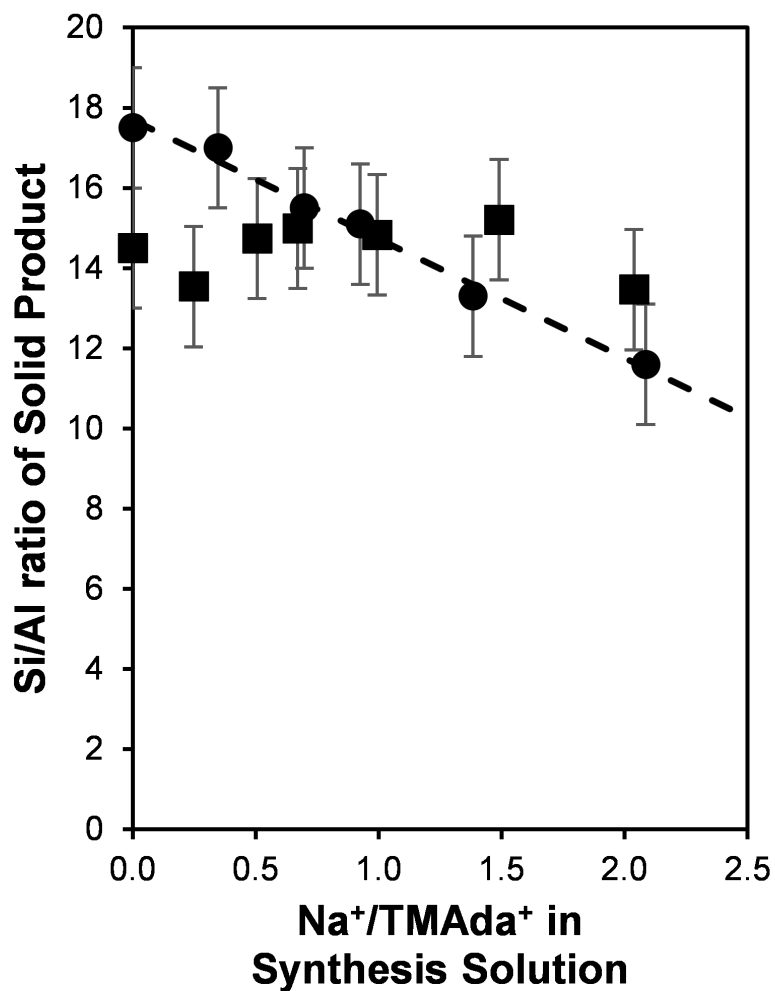


Figure 3.28. Si/Al ratio as a function of Na<sup>+</sup>/TMAda<sup>+</sup> ratio for SSZ-13(15) samples synthesized with (squares) and without (circles) a constant (Na<sup>+</sup> + TMAda<sup>+</sup>) / Al ratio. The dashed line is a linear fit to the samples synthesized without constant (Na<sup>+</sup>+TMAda<sup>+</sup>)/Al (circles).

3.7.19 Characterization Data for SSZ-13(25) with Constant ( $\text{Na}^+ + \text{TMAda}^+$ ) / Al (Total Charge) and Varying  $\text{Na}^+/\text{TMAda}^+$  Ratios (Charge Density)

Table 3.7.

Characterization data for SSZ-13(15) and MOR samples synthesized with constant synthesis solution Si/Al and varying total solution charge and  $\text{Na}^+/\text{TMAda}^+$ .

| Sample           | Si/Al | Micropore<br>Volume<br>( $\text{cm}^3 \text{g}^{-1}$ ) | $\text{H}^+/\text{Al}$ | $\text{Na}^+/\text{Al}$ | $\text{TMAda}^+/\text{Al}$ | $(\text{Na}^+ + \text{TMAda}^+)/\text{Al}$ | Co/Al |
|------------------|-------|--|------------------------|-------------------------|----------------------------|--|-------|
| SSZ-13(25, 0.25) | 25.3  | 0.19   | -                      | 0.05                    | 1.04                       | 1.09                                       | 0.03  |
| SSZ-13(25, 0.50) | 24.7  | 0.19   | -                      | 0.11                    | 0.96                       | 1.07                                       | 0.03  |
| SSZ-13(25, 1.00) | 24.1  | 0.20   | 1.02                   | 0.06                    | 1.01                       | 1.07                                       | 0.04  |
| SSZ-13(25, 2.00) | 26.1  | 0.20   | -                      | 0.05                    | 0.94                       | 0.99                                       | 0.02  |

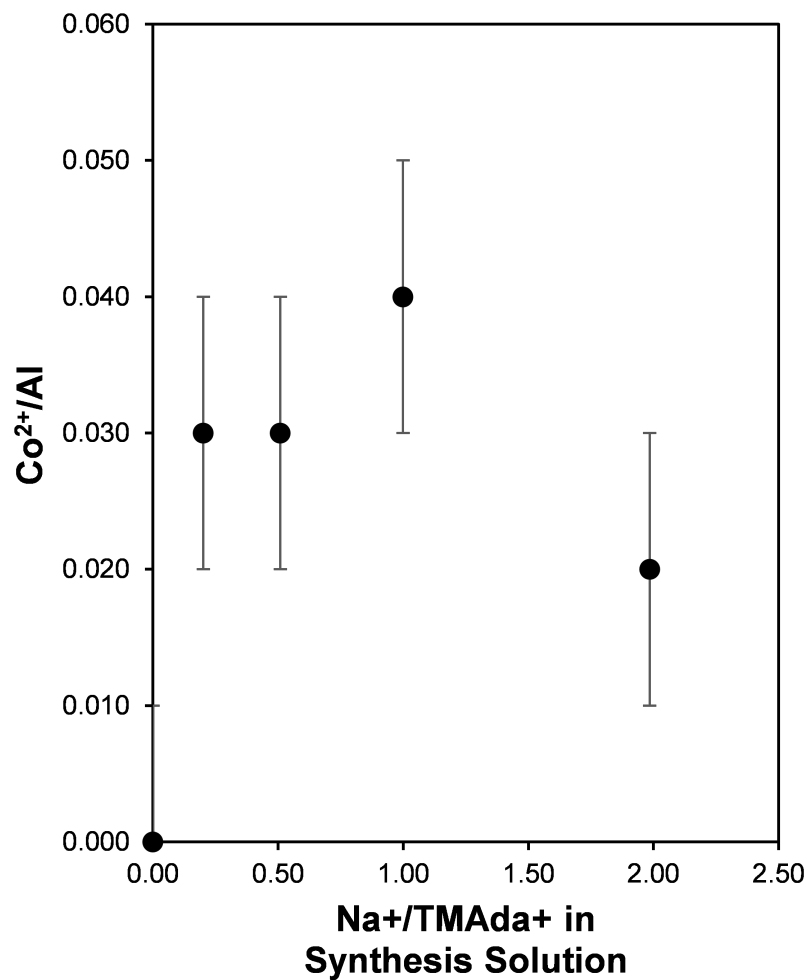


Figure 3.29. Fraction of paired Al atoms measured by titration with  $\text{Co}^{2+}$  as a function of the synthesis solution charge density on SSZ-13(25) synthesized with constant total solution charge.

## 4. COOPERATION AND COMPETITION BETWEEN ORGANIC AND INORGANIC STRUCTURE DIRECTING AGENTS INFLUENCES THE ALUMINUM ARRANGEMENT IN CHA ZEOLITES

### 4.1 Introduction

Zeolite materials provide a convenient platform for tailored materials design efforts because of their well-defined crystalline frameworks, which facilitate connecting data and insights from experimental and theoretical assessments of catalyst structure and function [201]. Monte-Carlo simulations of silica polymerization have shown that both the volume occupied by organic structure-directing agents (SDA) and the attractive forces between the SDA and lattice oxygen atoms are important for stabilizing microporous voids during crystallization from monomeric silica precursors [202–204]. *In silico* design of SDAs have generated libraries of different organic molecules that could lead to more efficient synthesis routes to prepare known zeolites, or the discovery of new synthetic zeolites that have only been predicted to be stable by theory [205–207]. Such theory-guided materials discovery approaches have recently been used to synthesize new organic SDAs for the AEI [208], SFW [209], and STW [210] zeolite frameworks, as well as to synthesize the first chiral zeolite framework [207, 211]. Computational methods can also be used to design organic SDAs that mimic transition state structures of a specific reaction, in order to guide synthesis of a zeolite framework that may benefit a desired chemical transformation [212].

The catalytic properties of zeolites are not only defined by their framework connectivity, but also by the microscopic atomic arrangement of framework Al atoms that generate catalytic active sites. In the case of chabazite (CHA) zeolites, which are high-symmetry frameworks comprised of a single unique tetrahedral-site (T-site), distinct arrangements of framework Al (i.e.,  $\text{Al-O}(\text{-Si-O})_x\text{-Al}$ ) between isolated ( $x \geq 3$ ) or

paired ( $x = 1, 2$ ) configurations have been characterized, the latter by exchange of divalent  $\text{Co}^{2+}$  and  $\text{Cu}^{2+}$  cations [42,48,79,213]. These different framework Al ensembles in CHA have been linked to differences in turnover rates for methanol dehydration to dimethyl ether (per total  $\text{H}^+$ , 415 K) [214], time-on-stream stability for methanol-to-olefins catalysis (623 K) [158, 215, 216],  $\text{CO}_2$  adsorption equilibrium constants [217], and the speciation of extraframework cationic Cu complexes [34–36,38–42,78,79,218] that mediate partial methane oxidation (PMO) to methanol [219–221] and selective catalytic reduction (SCR) of  $\text{NO}_x$  with  $\text{NH}_3$  [222]. Thus, synthetic protocols that purposefully influence the arrangement of heteroatoms substituted in zeolite frameworks, and theoretical models of SDA-framework interactions that can aid in development of such protocols, would provide avenues to prepare zeolites with tailored catalytic and adsorption properties.

Cationic SDA molecules facilitate the substitution of solubilized anionic  $\text{AlO}_2^-$  for framework  $\text{SiO}_2$  species during crystallization [223, 224] and have been proposed to influence the siting of Al at specific T-site locations based on the proximity of the charged portion of the SDA and the anionic lattice Al site [32, 56, 57, 141, 223, 225]. The effects of mixtures of cationic organic and inorganic SDAs on the energetics of Al siting, however, are not as well understood. Crystallization of high-silica ( $\text{Si}/\text{Al} > 7$ ) zeolites typically relies on the presence of organic SDA molecules in order to balance the anionic lattice charges via electrostatic interactions and to stabilize the siliceous portions of the zeolite lattice via dispersive interactions [80, 198, 202, 226], which can be tailored to selectively guide crystallization towards the desired crystal phase [205]. Incorporation of alkali cations during zeolite crystallization has been used to control crystal morphology of MFI [227], spatially bias Al incorporation in FAU [228], and to influence the arrangement of Al sites in MFI zeolites among differently sized voids (straight and sinusoidal channels and their intersections) [29–32] and between isolated and paired configurations [48, 74]. Previously, we have reported that CHA zeolites ( $\text{Si}/\text{Al} = 15$ ) crystallized from synthesis media containing only low charge-density organic N,N,N-trimethyl-1-adamantylammonium cations ( $\text{TMAda}^+$ )

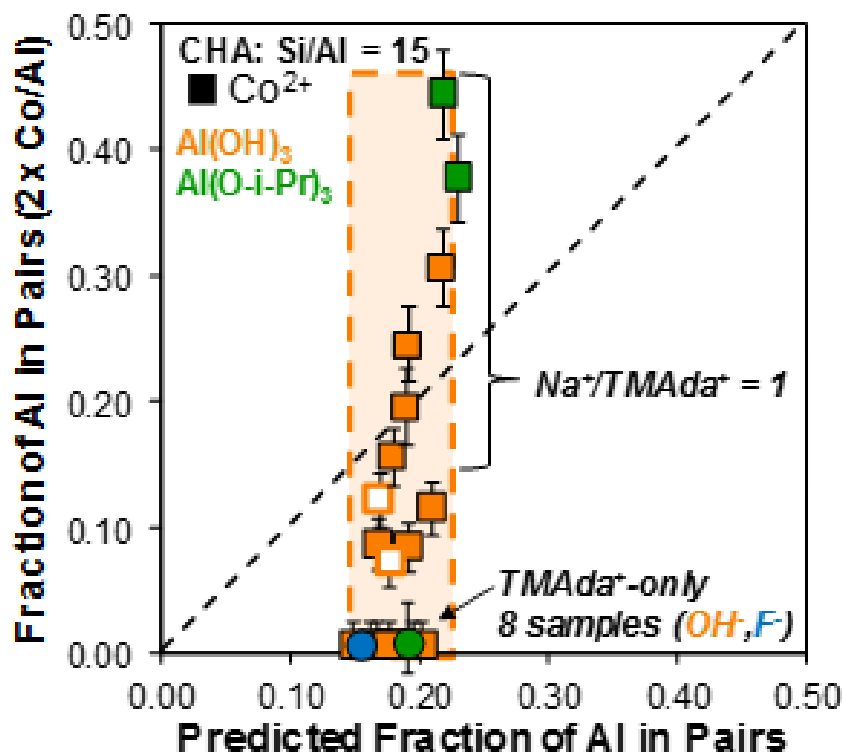


as the structure-directing agent (SDA) contain predominantly isolated Al sites [42], because adamantyl groups (ca. 0.7 nm diam.) appear to impose steric constraints that limit the occupation of each CHA cage (ca. 0.7 nm diam.) to only one TMAda<sup>+</sup> molecule [162]. The partial substitution of Na<sup>+</sup> for TMAda<sup>+</sup> in CHA synthesis media ( $0 < \text{Na}^+/\text{TMAda}^+ < 2$ ), while holding all other synthesis variables constant, crystallizes CHA zeolites (Si/Al = 15) that contain one TMAda<sup>+</sup> molecule per CHA cage, but varying amounts of Na<sup>+</sup> that correlates with the total number of paired Al sites as measured by saturation levels of Co<sup>2+</sup> ion-exchange [42, 214]. Increasing the Na<sup>+</sup>/TMAda<sup>+</sup> above 2 resulted in a phase transformation to MOR, likely reflecting a preference to form a higher density framework to satisfy electrostatic constraints imposed by the charge density of the synthesis media [42, 193, 196, 229].

## 4.2 Results and Discussion

We recently reported that the choice of the Al precursor used during CHA crystallization also appears to influence the formation of paired Al sites [214]. Here, two additional CHA zeolites were synthesized using aluminum isopropoxide (Al(O-*i*-Pr)<sub>3</sub>) and equimolar amounts of Na<sup>+</sup> and TMAda<sup>+</sup>, which indicate that using Al(O-*i*-Pr)<sub>3</sub> as the Al precursor results in CHA zeolites that contain nearly 40% of their Al atoms in paired arrangements (Figure 4.1, details in Supp. Info.), which is nearly twice the number that would be expected for a statistically random Al distribution in CHA zeolites of this composition (Si/Al = 15) [79, 129].

Figure 4.1. Fraction of Al in pairs, measured by  $\text{Co}^{2+}$  exchange, as a function of the number of Al in pairs predicted for a random Al distribution subject Lowenstein's Rule. Samples are synthesized with  $\text{Al}(\text{OH})_3$  and  $\text{Na}^+/\text{TMAda}^+ = 0-2$  in  $\text{OH}^-$  media (orange) and  $\text{Na}^+/\text{TMAda}^+ = 0$  in  $\text{F}^-$  media (blue) or with  $\text{Al}(\text{O-i-Pr})_3$  with  $\text{Na}^+/\text{TMAda}^+ = 1$  (green squares) and  $\text{Na}^+/\text{TMAda}^+ = 0$  (green circle).



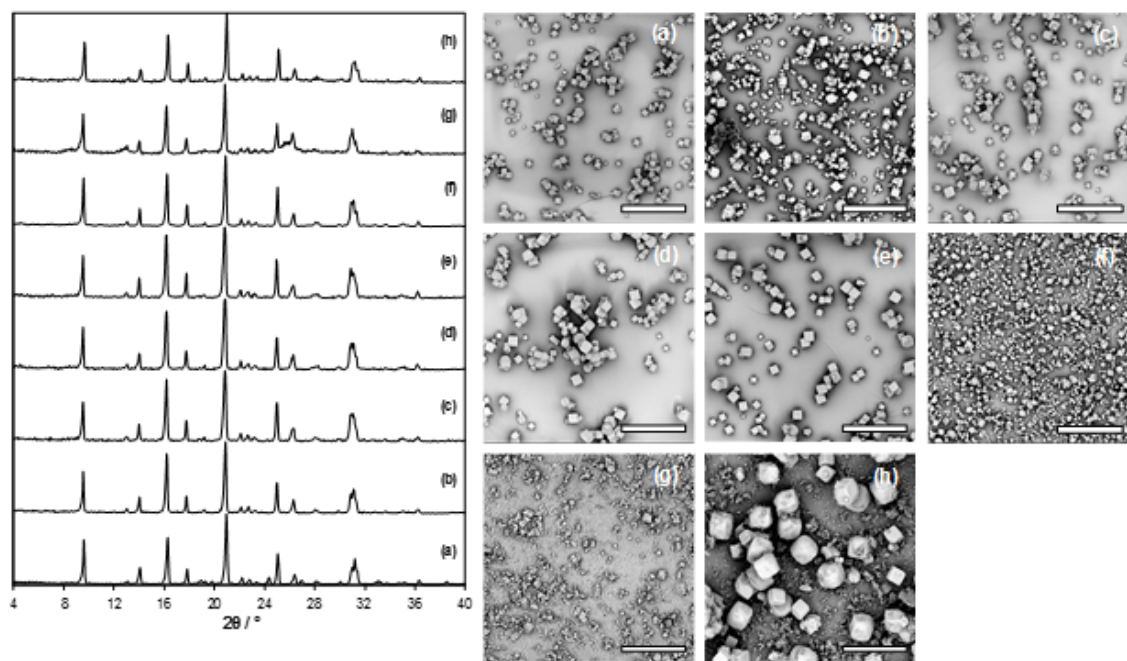
CHA zeolites crystallized in synthesis media containing only  $\text{TMAda}^+$  as the SDA, but in the presence of  $\text{Al}(\text{O-i-Pr})_3$ , do not contain paired Al sites (Figure 4.1, details in Supp. Info.), consistent with previous observations of CHA synthesized using only  $\text{TMAda}^+$  and aluminum hydroxide ( $\text{Al}(\text{OH})_3$ ) as the Al source [42]. Thus, the presence of  $\text{Na}^+$  in CHA synthesis media leads to the formation of paired Al sites regardless of Al precursor ( $\text{Co}/\text{Al} < 0.01$  when  $\text{Na}^+/\text{TMAda}^+ = 0$  for  $\text{Al}(\text{OH})_3$  or  $\text{Al}(\text{O-i-Pr})_3$ ) or mineralizing agent (e.g.,  $\text{OH}^-$  or  $\text{F}^-$ ) [214], suggesting that the structure of the cations used to facilitate zeolite crystallization predominantly affects Al siting. Taken together, these results suggest cooperative interactions between organic  $\text{TMAda}^+$

molecules and inorganic alkali cations (e.g.,  $\text{Na}^+$ ) guide the formation of paired Al sites during CHA crystallization.

Here, we further probe this hypothesis by utilizing  $\text{K}^+$ , instead of  $\text{Na}^+$ , as the alkali SDA cation together with  $\text{TMAda}^+$  during CHA synthesis.  $\text{K}^+$  suppresses the formation of certain crystal phases (e.g., BEA [81], MFI [230]), and also enables the crystallization of low-silica CHA ( $\text{Si}/\text{Al} < 5$ ) from FAU precursors in the absence of organic SDAs [231–234], a transformation that is inaccessible using only  $\text{Na}^+$  without using high concentrations of seed crystals (ca. 10  $\text{SiO}_2$  wt% seed) [167]. These observations suggest that  $\text{K}^+$  can guide crystallization towards the CHA framework, with different consequences than  $\text{Na}^+$  regarding their role in directing Al incorporation. The influence of  $\text{K}^+$  on the arrangement of Al in high-silica CHA ( $\text{Si}/\text{Al} = 15$ ) crystallized in the presence of  $\text{TMAda}^+$  was investigated using previously reported synthesis procedures to prepare CHA with varying  $\text{Na}^+/\text{TMAda}^+$  ratios [42], but by substituting KOH for NaOH in the synthesis solution (details in Supp. Info.).

Synthesis media containing  $\text{K}^+/\text{TMAda}^+ \geq 20$  resulted in CHA zeolites without detectable phase impurities from X-ray diffraction data (Figure 4.2), but increasing the  $\text{K}^+/\text{TMAda}^+$  beyond 20 resulted in the formation of MFI ( $\text{K}^+/\text{TMAda}^+$  up to  $\infty$ ; Supp. Info.). This reflects the role of  $\text{TMAda}^+$  to assist in directing toward the CHA phase, and that  $\text{K}^+$  alone is unable to crystallize CHA under the synthesis conditions reported here. The use of  $\text{K}^+$  enables CHA to crystallize from solutions containing much higher alkali/ $\text{TMAda}^+$  ratios than when  $\text{Na}^+$  is used as the alkali source (MOR was observed at  $\text{Na}/\text{TMAda} > 2$ ) [42]. These results highlight the capacity of different alkali cations to act as co-SDAs [80] with  $\text{TMAda}^+$ , and appear to reflect the tendency of  $\text{K}^+$  to suppress the formation of other undesired phases, as previously suggested for the synthesis of IFR zeolites from mixtures of  $\text{K}^+$  and benzyl mono- and di-azabicyclo complexes [81].

Figure 4.2. X-ray diffraction patterns (left) and SEM micrographs (right) taken at 1300x magnification of CHA synthesized with  $K^+/TMAda^+$  ratios of (a) 1, (b) 2, (c) 3, (d) 4, (e) 5, (f) 10, (g) 15, and (h) 20. Scale bar in SEM images in  $50\ \mu m$ .



SEM micrographs of CHA zeolites (Figure 4.2) synthesized with  $K^+/TMAda^+ < 10$  are comprised of cubic crystals ranging in size from  $4\text{--}8\ \mu m$  and are of similar composition (Table 4.1). CHA synthesized with  $K^+/TMAda^+ > 10$ , however, are comprised of a mixture of two distinct crystalline CHA phases that differ markedly in size and composition (Table 4.1), indicating that a low-silica K-rich CHA phase ( $Si/Al < 7$ ,  $K^+/Al > 1.5$ ) begins to form in parallel to the high-silica CHA phase that are dominant crystal products from synthesis solutions containing  $K^+/TMAda^+ < 10$  ( $Si/Al > 10$ ,  $K^+/Al < 0.70$ ). This is consistent with refinement of X-ray diffraction (XRD) data indicating that CHA synthesized with  $K^+/TMAda^+ < 10$  are nearly phase-pure high-silica CHA (Supp. Info.), but that only 67% of  $K^+/TMAda^+ = 20$  is comprised of high-silica CHA. Elemental analysis of these two distinct CHA

phases by EDX show that the high-silica CHA phase (Supp. Info.) has an elemental composition similar to other CHA samples synthesized with  $K^+/TMAda^+ < 10$  (Table 4.1).

Table 4.1.  
Elemental analysis of CHA synthesized with  $K^+/TMAda^+ = 1-20$  measured by AAS and EDX.

| AAS               |       |          |                        | SEM/EDX      |                    |                        |              |                    |
|-------------------|-------|----------|------------------------|--------------|--------------------|------------------------|--------------|--------------------|
| $K^+/TMAda^+{}^a$ | Si/Al | $K^+/Al$ | Si/Al (1) <sup>b</sup> | $K^+/Al$ (1) | Size (1) / $\mu m$ | Si/Al (2) <sup>c</sup> | $K^+/Al$ (2) | Size (2) / $\mu m$ |
| 1                 | 15    | 0.37     | 12                     | 0.68         | 3-5                | -                      | -            | -                  |
| 2                 | 16    | 0.51     | 14                     | 0.50         | 3-6                | -                      | -            | -                  |
| 3                 | 14    | 0.53     | -                      | -            | 4-8                | -                      | -            | -                  |
| 4                 | 13    | 0.56     | -                      | -            | 4-8                | -                      | -            | -                  |
| 5                 | 11    | 0.43     | 10                     | 0.52         | 4-8                | -                      | -            | -                  |
| 10                | 11    | 0.71     | 11                     | 0.56         | 2-5                | -                      | -            | <0.5               |
| 15                | 10    | 1.43     | 12.1                   | 0.71         | 2-4                | 6.8                    | 1.5          | <0.5               |
| 20                | 10    | 1.21     | 10.2                   | 0.60         | 10-15              | 7.5                    | 1.6          | <0.5               |

<sup>a</sup>  $K^+/TMAda^+$  ratio in the synthesis solution.  
<sup>b</sup> (1) represents the primary CHA crystal phase (large cubes)  
<sup>c</sup> (2) represents the secondary CHA crystal phase (small rods/platelets)

CHA zeolites crystallized from mixtures of  $Na^+$  and  $TMAda^+$  contain one  $TMAda^+$  per cage (ca. 20-22 wt% organic) [42,158,162], independent of the amount of residual  $Na^+$  retained within crystalline products (Figure 4.3) [42,214], yet those crystallized from mixtures of  $K^+$  and  $TMAda^+$  showed that the occupancy of  $TMAda^+$  per CHA cage systematically decreased as the amount of  $K^+$  retained on crystalline CHA product increased (Figure 4.3, Table 4.1). The negative correlation observed between  $TMAda^+$  and  $K^+$  in the crystalline CHA products suggests that three  $K^+$  cations displace a single  $TMAda^+$  from the CHA cage and that  $K^+$  assists in the stabilization of the CHA framework up to a limit of approximately 2  $TMAda^+$  per unit cell (Figure

4.3). While the total Al content does increase with increasing  $K^+$  content (Table 4.1), the presence of excess cationic charge, relative to the anionic charge of the framework (e.g.,  $(K^+ + TMAda^+)/Al > 1$ ; Table 4.2), suggests that the formation of anionic lattice defects is required to compensate the excess extraframework charge in CHA synthesized using  $K^+$  cations (Table 4.2) [225]. Titration of protons by aqueous  $NH_4^+$  ion-exchange show that CHA zeolites synthesized with  $K^+/TMAda^+ < 10$  contain nearly all of their Al in framework positions, but that further increasing the  $K^+/TMAda^+$  ratio leads to higher fractions of Al that are inaccessible to hydrated  $NH_4^+$  cations, possibly reflecting pore-blockage in CHA synthesized with  $K^+/TMAda^+ > 10$  (Supp. Info.) or the formation of extraframework Al sites (Table 4.2).

Figure 4.3. (a) Number of  $TMAda^+$  per CHA cage (squares), measured by TGA, and amount of  $Na^+$  retained per CHA cage (circles), measured by AAS, as a function of the  $Na^+/TMAda^+$  ratio in the synthesis media. (b) Number of  $TMAda^+$  per CHA cage (squares) and amount of  $K^+$  retained per CHA cage (circles) as a function of the  $K^+/TMAda^+$  ratio in the synthesis media. (c) Number of  $TMAda^+$  per CHA cage as a function of the amount of  $K^+$  (squares) or  $Na^+$  (circles) retained on the crystalline CHA product. Dashed (slope ca. 1/3) and dotted (slope ca. 0) lines are regressions to  $K^+$  (squares) and  $Na^+$  (circles) data sets, respectively.

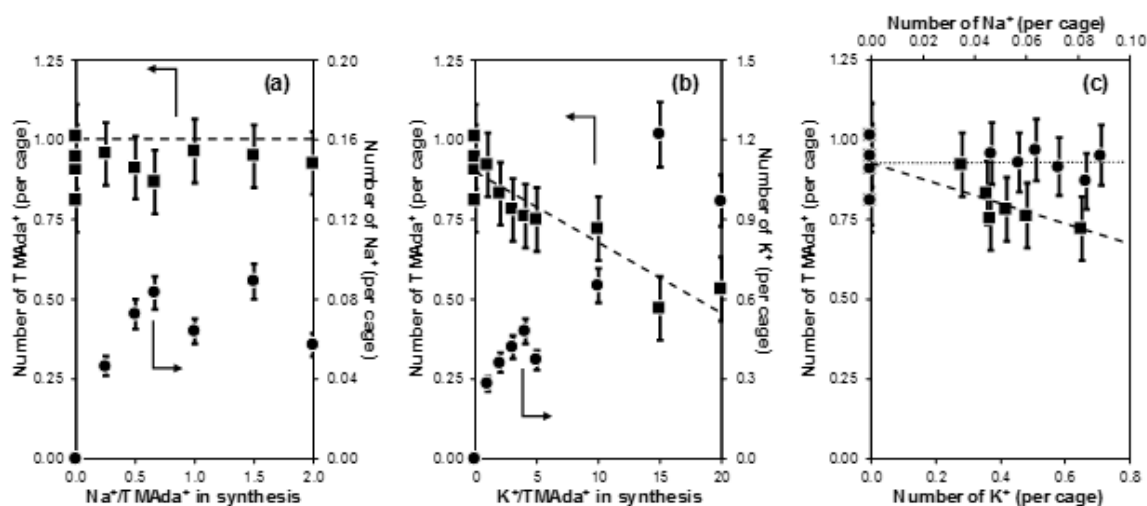


Table 4.2.

Total  $K^+$  and  $TMAda^+$  content per Al, total cationic charge of the crystalline zeolite product ( $(K^+ + TMAda^+)/Al$ ),  $H^+/Al$ , and estimated number of lattice defects on CHA zeolites synthesized with  $K^+/TMAda^+ = 1-20$ .

| $K^+/TMAda^+$ <sup>a</sup> | Si/Al | $K^+/Al$ | $TMAda^+/Al$ | $(K^+ + TMAda^+)/Al$ | $H^+/Al$ <sup>b</sup> | Co/Al | Defects per unit cell <sup>c</sup> |
|----------------------------|-------|----------|--------------|----------------------|-----------------------|-------|------------------------------------|
| 1                          | 15    | 0.37     | 1.23         | 1.60                 | 0.98                  | 0.05  | 1.35                               |
| 2                          | 16    | 0.51     | 1.18         | 1.69                 | 1.01                  | 0.03  | 1.46                               |
| 3                          | 14    | 0.53     | 0.98         | 1.50                 | 1.05                  | 0.01  | 1.20                               |
| 4                          | 13    | 0.56     | 0.89         | 1.45                 | 1.00                  | <0.01 | 1.15                               |
| 5                          | 11    | 0.43     | 0.88         | 1.31                 | 0.96                  | 0.01  | 0.36                               |
| 10                         | 11    | 0.71     | 0.78         | 1.49                 | 1.02                  | 0.01  | 1.11                               |
| 15                         | 10    | 1.43     | 0.55         | 1.97                 | 0.82                  | <0.01 | 1.80                               |
| 20                         | 10    | 1.21     | 0.66         | 1.88                 | 0.41                  | 0.01  | 1.23                               |

<sup>a</sup>  $K^+/TMAda^+$  ratio in the synthesis media.  
<sup>b</sup>  $H^+/Al$  measured by  $NH_3$  TPD.  
<sup>c</sup> Number of defects per unit cell estimated from a charge balance on the as-synthesized zeolite:  $[K^+ + TMAda^+] - AlO_2^-$

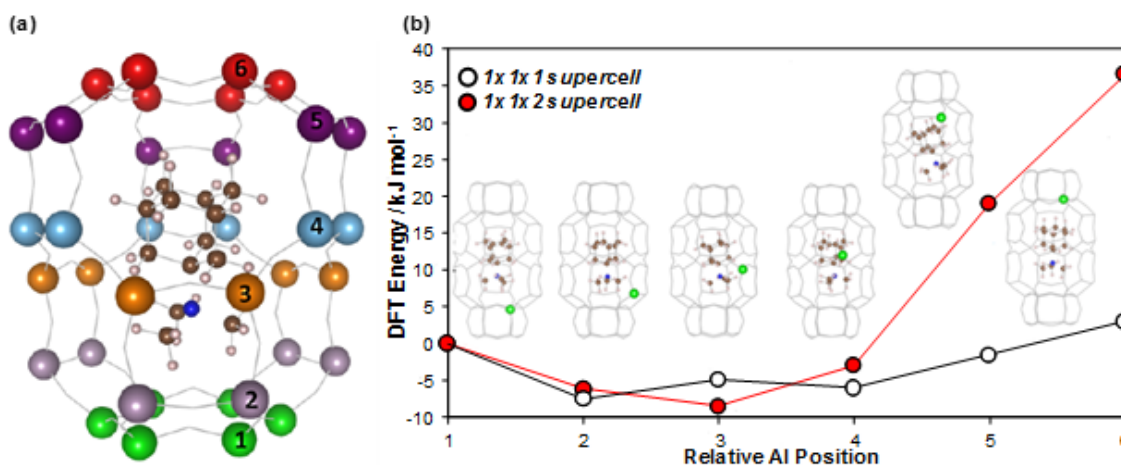
We previously observed that the number of paired Al sites, quantified by  $Co^{2+}$  titration, in CHA synthesized with  $Na^+$  increased as the total amount of  $Na^+$  retained on the crystalline product increased [42, 214]. Here, we observe contrasting behavior for CHA zeolites synthesized with  $K^+$ , where the total amount of  $K^+$  retained after crystallization does not correlate with the number of Al pairs (Table 24.2). At low  $K^+/TMAda^+$  ratios in the synthesis media ( $K^+/TMAda^+ < 2$ ), the occlusion of  $K^+$  resulted in the formation of paired Al sites, but in lower amounts ( $Co/Al = 0.05$ ) to what has been previously reported for CHA synthesized with mixtures of  $Na^+$  and  $TMAda^+$  ( $Co/Al = 0.10$ ) [42, 214]. As the  $K^+/TMAda^+$  ratio in the synthesis solution increased, the ratio of  $K^+$  to  $TMAda^+$  in the crystalline product systematically increased (Figure 4.3), suggesting that  $K^+$  competes with  $TMAda^+$  for similar voids

in CHA and favors the formation of isolated Al sites. This behavior is markedly different than that of  $\text{Na}^+$ , which reflects the occlusion of  $\text{Na}^+$  within void spaces that are unoccupied by  $\text{TMAda}^+$  so as to stabilize the two anionic charges in a paired Al configuration. These results reflect the preference of extraframework cationic SDAs to stabilize different Al arrangements during CHA crystallization, consistent with prior findings that extraframework  $\text{Cu}^{2+}$  and  $\text{H}^+$  cations preferentially stabilize different Al arrangements in CHA [213].

Building on this prior work, the interactions between different framework Al arrangements and various cation arrangements ( $\text{Na}^+$ ,  $\text{K}^+$ , and  $\text{TMAda}^+$ ) were investigated using ab initio molecular dynamics. Ab initio molecular dynamics (AIMD) simulations (433 K, PBE-D3, 20 ps sampling interval; details in Supp. Info.) show that the  $\text{TMAda}^+$  molecule is preferentially oriented along the c-axis of the CHA cage and is free to rotate along this axis (Figure 4.4), and reorientation orthogonal to the c-axis is unfavorable due to steric constraints (movie and energetics in Supp. Info.). Substitution of a single Al atom into the CHA unit cell (1x1x2 supercell, 72 T-atoms) results in a fully separated ion-pair (Supp. Info.), where  $\text{TMAda}^+$  loses a full electron (net charge: +1) to the framework that is localized at the Al center (net charge: -1). Placement of the Al atom at positions 1-4, which are located at a similar distance to the nitrogen atom of the  $\text{TMAda}^+$  molecule (Figure 4.4), are similar in energy. Sites 5 and 6, however, show a strong dependence on unit cell size, reflecting interaction of the Al site with a second  $\text{TMAda}^+$  residing in a neighboring unit cell across the periodic boundary (Figure 4.4). Additionally, the DFT energies of each configuration are independent of van der Waals forces (Supp. Info.), indicating that the stabilization of a single Al atom by one  $\text{TMAda}^+$  molecule is governed by electrostatic forces and only depends on the distance between the two ions.



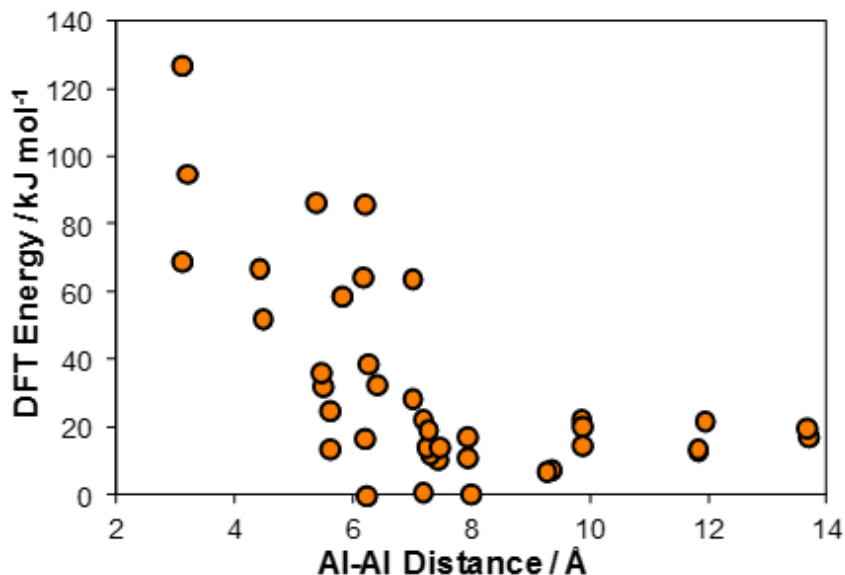
Figure 4.4. (a) Snapshot of a single TMAda<sup>+</sup> molecule (brown: C, blue: N, white: H) within the CHA cage. The numbers 1-6 correspond to the 6 unique Al sites, relative to the N atom of TMAda<sup>+</sup>, and the corresponding colors (1: green, 2: grey, 3: orange, 4: light blue, 5: purple, 6: red) represent equivalent sites. (b) DFT energies, relative to Al position 1, of TMAda<sup>+</sup> confined with the CHA cage for the six different single Al sites in the 1x1x1 (black) and 1x1x2 (red) supercells. Inset snapshots show the relaxed structures for each Al position.



In order to understand the interactions between TMAda<sup>+</sup> molecules confined in adjacent CHA cages, further AIMD simulations were performed to investigate the stability of different two Al configurations when two TMAda<sup>+</sup> molecules are confined in neighboring cages. The stability of different Al-Al arrangements in the two TMAda<sup>+</sup> system is also governed by electrostatic interactions, where repulsive forces between similar charges dominate at short Al-Al distances, while attractive forces between the cationic quaternary N center in the SDA and the anionic framework Al dominate at large Al-Al distances (Supp. Info.). Decomposition of these observations into descriptors of the different charge-center interactions (N-N, N-Al, or Al-Al interactions) reveal that the minimum energy of the two TMAda<sup>+</sup> case is achieved when the Al-Al distance is large, but each Al atom is located close to the N atom of its corresponding TMAda<sup>+</sup> cation (Supp. Info.). These results show that Al atoms separated by either

zero (Lowenstein's Rule) [235] or one Si neighbor are energetically unfavorable (Supp. Info.), but that TMAda<sup>+</sup> alone does not provide any particular preference for placing Al atoms into specific arrangements, and generally favors increased dispersion of Al throughout the lattice (Figure 4.5). These computational results are consistent with experimental observations that CHA zeolites synthesized using only TMAda<sup>+</sup> contain predominantly isolated Al sites, and provide a methodology to probe the interactions between different types of extraframework cations and the stability of different Al-Al arrangements in CHA zeolites.

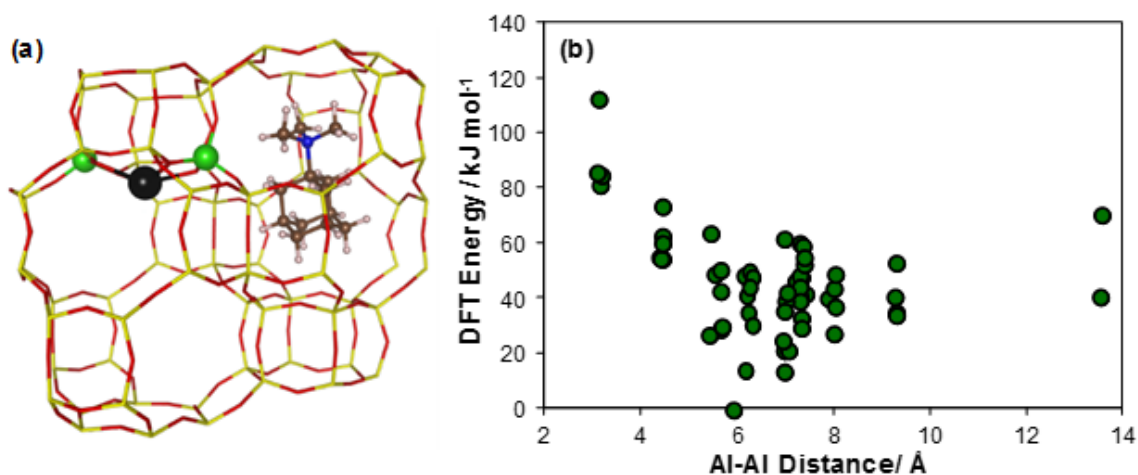
Figure 4.5. DFT energies as a function of the Al-Al distance when two TMAda<sup>+</sup> molecules are located in adjacent cages in CHA. Three unique TMAda-TMAda orientations were investigated at each Al-Al distance (Supp. Info.).



DFT energies indicate that Na<sup>+</sup> cations preferentially occupy the six-membered ring of CHA in the presence of TMAda<sup>+</sup> in an adjacent cage (Figure 4.6). As was observed for the case with two TMAda<sup>+</sup> cations in adjacent cages, the stability of different Al-Al arrangements depends on both the Al-Al distance and the location of the Na<sup>+</sup> and TMAda<sup>+</sup> cations. As observed in the two TMAda<sup>+</sup> case, Al atoms sepa-

rated by either one or two Si neighbors are the highest energy arrangements indicating that Lowenstein's Rule is still obeyed in the presence of  $\text{TMAda}^+$  and  $\text{Na}^+$ . These observations complement previous reports that Al-Al nearest neighbors are the most stable 2 Al arrangements when protons compensate lattice Al sites, and underscore the necessity for models that reflect realistic operating conditions [79, 213]. Unlike the  $\text{TMAda}^+$ -only case, which did not show a strong preference to any specific Al-Al arrangement (Figure 4.5),  $\text{Na}^+$  cations appear to favor the incorporation of two Al atoms in the same 6-MR when  $\text{TMAda}^+$  is located in an adjacent cage (Figure 4.6). This preference for  $\text{Na}^+$  incorporation to form a paired Al site is consistent with experimental observations that  $\text{Na}^+$  occluded during CHA crystallizations promotes the formation of paired Al sites [42]. While these observations do not directly describe the incorporation of Al during crystallization, which is often kinetically-limited [198] and sensitive to solvent effects [236] and significant long-range electrostatic interactions between extraframework cations residing in adjacent cages, they do provide evidence that different cations can alter the stability of different Al-Al arrangements in CHA zeolites.

Figure 4.6. (a) Snapshot of the most stable configuration of  $\text{Na}^+$  (black) in the presence of a  $\text{TMAda}^+$  molecule in an adjacent cage with 2 framework Al atoms (green). Yellow: Si, green: Al, red: O, dark grey: C, blue: N, white: H, black: Na. (b) DFT energies as a function of the Al-Al distance when one  $\text{Na}^+$  and one  $\text{TMAda}^+$  molecule are located in adjacent cages in CHA.



Finally, we compared the performance of Cu-exchanged CHA zeolites prepared using mixtures of  $\text{TMAda}^+$  and  $\text{Na}^+$  or  $\text{TMAda}^+$  and  $\text{K}^+$  as co-SDAs (synthesis and characterization details in SI) for the selective catalytic reduction (SCR) of  $\text{NO}_x$  with  $\text{NH}_3$ . Turnover rates of  $\text{NO}_x$  SCR (per Cu, 473 K) depend on the spatial density of nominally site-isolated Cu cations (Cu per 1000  $\text{\AA}^3$ ) and, in turn, the arrangement of anionic framework Al atoms that anchor such cationic Cu complexes. This reflects  $\text{O}_2$  oxidation steps involving two  $[\text{Cu}(\text{NH}_3)_2]^+$  complexes, which are electrostatically-tethered at anionic framework Al sites with localized mobility [237], that becomes the rate-limiting process at low temperatures. The stability of Cu-CHA zeolites also depends on the distribution of  $\text{Cu}^{2+}$  and  $[\text{CuOH}]^+$  complexes, which respectively exchange at paired and isolated Al sites, because they show differences in their resistance to deactivation by sulfur poisoning [238, 239] and hydrothermal aging [240]. Cu-exchanged CHA zeolites synthesized using  $\text{TMAda}^+$  with either  $\text{Na}^+$

or  $K^+$  as the alkali co-SDA (prior to hydrothermal aging) showed similar  $NO_x$  SCR rates (per Cu, 473 K), apparent reactant orders, and activation energies (Supp. Info.), which are consistent with previously reported SCR rates (473 K, per Cu) on Cu-CHA with similar Cu densities (Cu per 1000  $\text{\AA}^3$ ) [237]. Cu-CHA synthesized using  $Na^+$  or  $K^+/TMAda^+ < 10$  deactivate to similar extents after hydrothermal aging (10 vol%  $H_2O$ , 1073 K, 16 h), suggesting that the stability of the CHA framework with similar Al arrangements and total Al incorporation ( $H^+/Al > 0.90$ ) is not influenced by the synthesis procedure. Cu-CHA synthesized with  $K^+/TMAda^+ = 15$  exhibits more severe deactivation after hydrothermal aging (Supp. Info.), likely reflecting the highly defective nature of CHA zeolites prepared with  $K^+/TMAda^+ > 10$ , which contain  $H^+/Al$  counts lower than unity and micropore volumes that deviate significantly from CHA prepared with low alkali/ $TMAda^+$  ratios or in alkali-free crystallization media (Supp. Info.).

These results highlight how CHA zeolites with similar microscopic arrangements of framework Al atoms can be prepared from synthetic protocols that use different alkali cations together with organic  $TMAda^+$ , which modifies the dominant SDA-framework interactions that influence Al siting.  $Na^+$  preferentially occupies 6-MR voids in CHA and stabilizes paired Al sites in the presence of  $TMAda^+$ , which are occluded within larger CHA cages, suggesting cooperative interactions that stabilize regions of locally higher anionic charge densities (i.e., paired Al) than can be stabilized with  $TMAda^+$  alone.  $K^+$  cations compete with  $TMAda^+$  for occupancy within CHA cages and eventually cause the displacement of  $TMAda^+$  at high  $K^+$  concentrations ( $K^+/TMAda^+ > 2$ ), which assists in stabilizing the CHA framework at higher alkali concentrations in the synthesis media ( $K^+/TMAda^+$  up to 20) than possible with  $Na^+$  (MOR formed at  $Na^+/TMAda^+ > 2$ ). These observations likely reflect the different roles that cationic SDAs play in stabilizing zeolite frameworks that contain high anionic charge densities [192, 229].  $K^+$  cations favor the formation of isolated Al sites, a consequence of their competition with  $TMAda^+$  for occupancy within large CHA cages, in contrast to  $Na^+$  that does not compete with  $TMAda^+$  and

causes the formation of paired Al sites. The theoretical models used here describe interactions of cationic SDAs with the anionic zeolite lattice and can be used to aid in the design of experimental synthesis approaches to purposefully guide the incorporation of framework heteroatoms during zeolite crystallization. These findings provide a methodology to probe cooperative and competitive interactions of mixtures of organic and inorganic SDAs during zeolite crystallization, and provide opportunities to design zeolitic materials with tailored adsorption and catalytic function.

### 4.3 Supporting Information

Figure 4.7. X-Ray diffraction patterns of CHA synthesized using  $\text{Al}(\text{O-i-Pr})_3$  at  $\text{Si}/\text{Al} = 15$  and (a)  $\text{Na}^+/\text{TMAda}^+ = 0$  and (b)-(d)  $\text{Na}^+/\text{TMAda}^+ = 1$ .

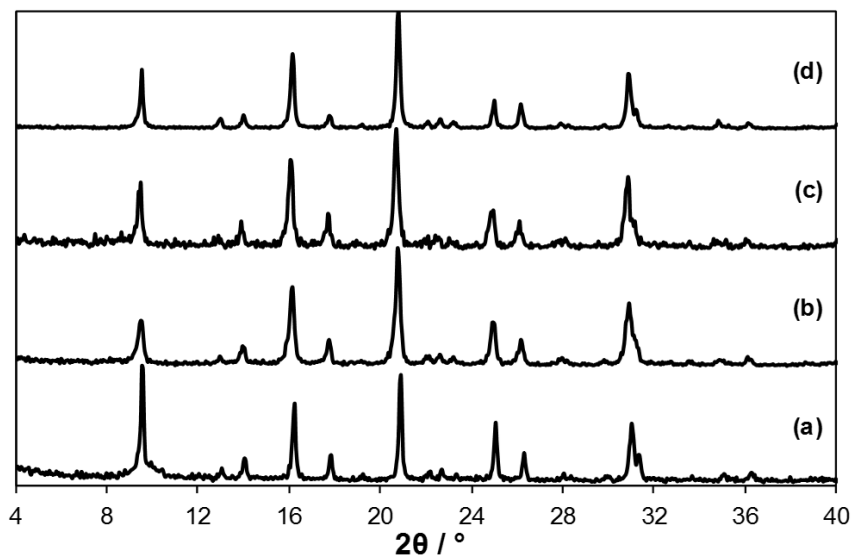
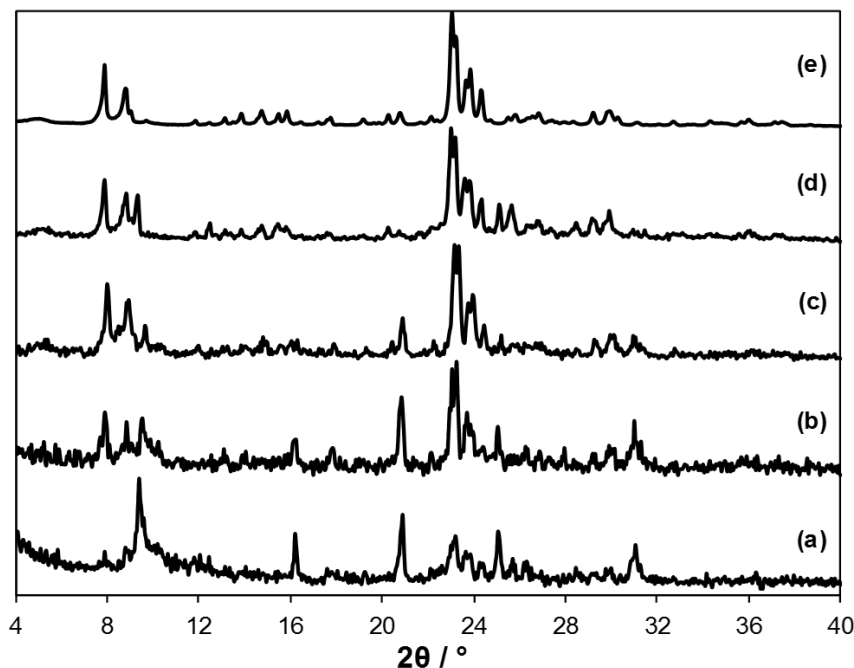


Figure 4.8. X-Ray diffraction patterns of zeolites synthesized with  $K^+/TMAda^+$  of (a) 30, (b) 50, (c) 100, and (d)  $\infty$ . A commercial MFI zeolite (Si/Al = 43) is shown in (e).



Nearly all CHA zeolites synthesized using  $K^+$  contain visible defects (Figures 4.9-4.16, Supp. Info.) that appear to be the formation of large mesopores, which are not observed in CHA synthesized without alkali ( $TMAda^+$ -only) or with mixtures of  $Na^+$  and  $TMAda^+$  [214]. Ar adsorption-desorption isotherms reveal that CHA synthesized with  $K^+/TMAda^+ = 2$  has a micropore volume similar to CHA synthesized with different mixtures of  $TMAda^+$  and  $Na^+$  ( $0.19 \text{ cm}^3 \text{ g}^{-1}$ ) [42,158], and does not contain mesopores, evidenced by the lack of desorption hysteresis (Figure 4.18) [241,242]. Meanwhile, CHA synthesized with  $K^+/TMAda^+ = 15$  has an Ar micropore volume significantly lower than expected for CHA ( $0.06 \text{ cm}^3 \text{ g}^{-1}$ ) and displays Type-H4 desorption hysteresis (step-down at  $P/P_0$  ca. 0.4; Figure 4.19) indicating the presence of disordered mesopores [241,242] possibly formed by defects caused by excessive cation charge density or from adsorption within the secondary phase. This set of data suggests that the role of  $K^+$  during crystallization of CHA zeolites is different than that

of  $\text{Na}^+$ , whose occlusion during crystallization does not displace  $\text{TMAda}^+$  (Figure 4.3, main text) [42], and will likely be reflected in the Al arrangement of the crystalline product.

Figure 4.9. SEM micrographs of CHA synthesized with  $\text{K}^+/\text{TMAda}^+ = 1$  taken at (a) 1300x and (b) 5000x magnification.

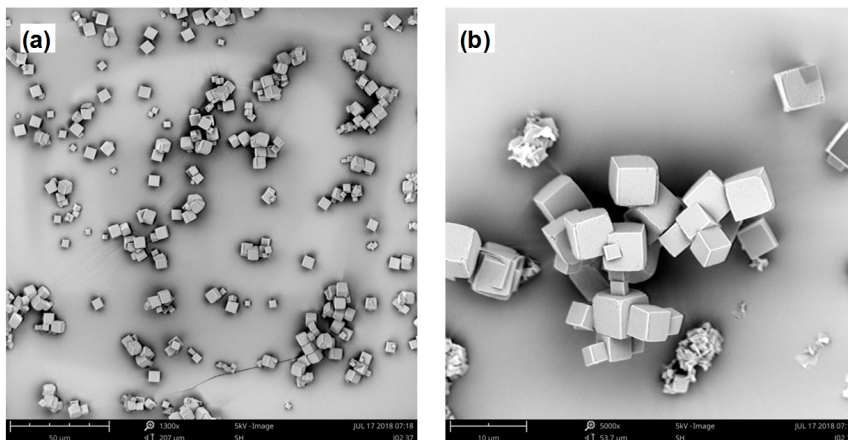


Figure 4.10. SEM micrographs of CHA synthesized with  $\text{K}^+/\text{TMAda}^+ = 2$  taken at (a) 1250x and (b) 4800x magnification.

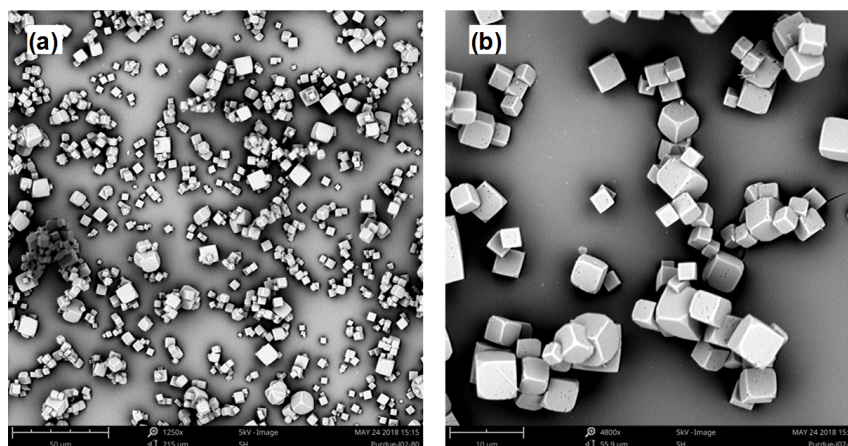




Figure 4.11. SEM micrographs of CHA synthesized with  $K^+/TMAda^+ = 3$  taken at (a) 1250x and (b) 5000x magnification.

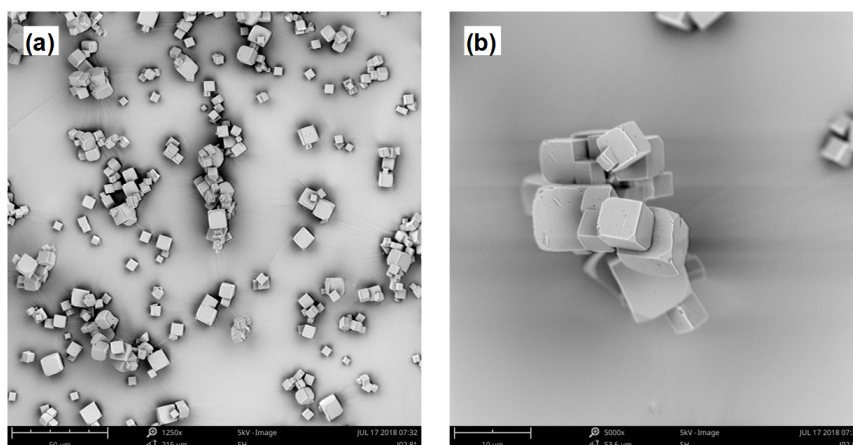


Figure 4.12. SEM micrographs of CHA synthesized with  $K^+/TMAda^+ = 4$  taken at (a) 1250x and (b) 5000x magnification.

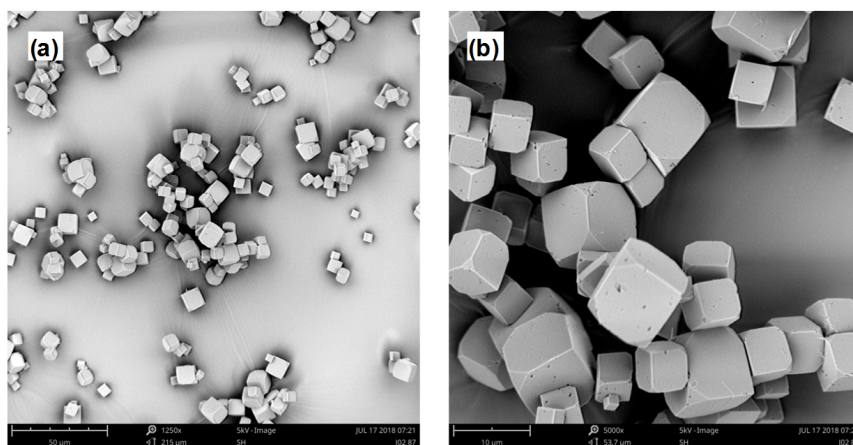


Figure 4.13. SEM micrographs of CHA synthesized with  $K^+/TMAda^+ = 5$  taken at (a) 1250x and (b) 5000x magnification.

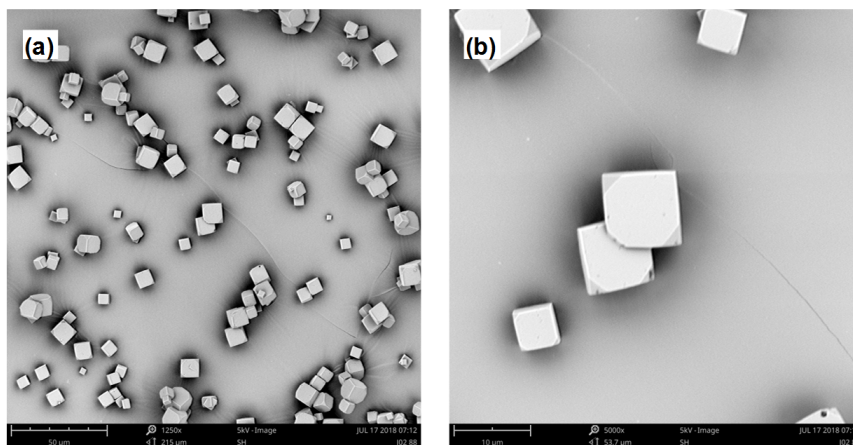


Figure 4.14. SEM micrographs of CHA synthesized with  $K^+/TMAda^+ = 10$  taken at (a) 1400x and (b) 5900x magnification.

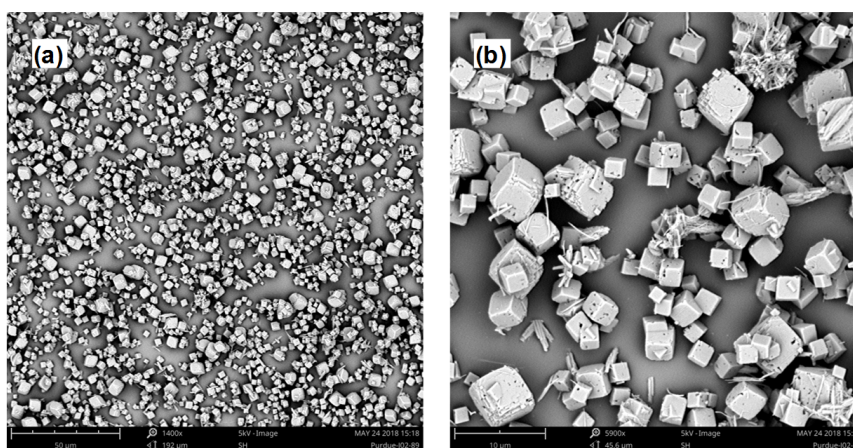


Figure 4.15. SEM micrographs of CHA synthesized with  $K^+/TMAda^+ = 15$  taken at (a) 1300x and (b) 5100x magnification.

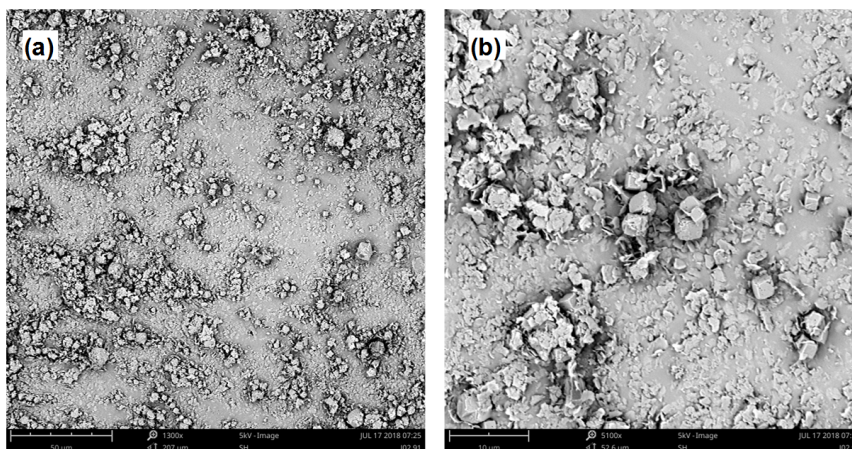


Figure 4.16. SEM micrographs of CHA synthesized with  $K^+/TMAda^+ = 20$  taken at (a) 1700x and (b) 4900x magnification.

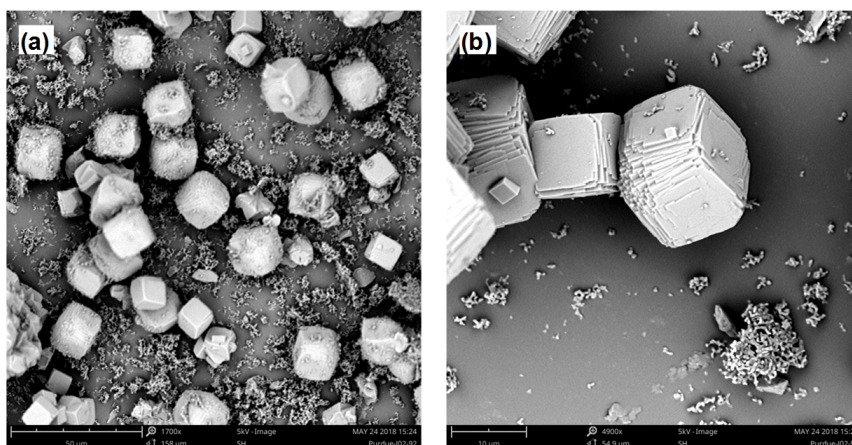


Table 4.3.

Phase analysis of CHA synthesized with  $K^+/TMAda^+ = 2, 10, \text{ and } 20$  using refinement of powder XRD data.

| $K^+/TMAda^+$ <sup>a</sup> | $a_0 / \text{\AA}$ | $c_0 / \text{\AA}$ | Unit Cell<br>Volume <sup>b</sup> / $\text{\AA}^3$ | % High<br>silica CHA <sup>c</sup> |
|----------------------------|--------------------|--------------------|---|-----------------------------------|
| 2                          | 13.584             | 14.795             | 2364  | 88                                |
| 10                         | 13.595             | 14.811             | 2371  | 91                                |
| 20                         | 13.580             | 14.805             | 2365  | 67                                |

<sup>a</sup>  $K^+/TMAda^+$  ratio in the synthesis solution.

<sup>b</sup> Unit cell volume calculated for a trigonal unit cell of space group R-3m with  $a_0=b_0 \neq c_0$ , and  $\alpha=\beta=90^\circ$ ,  $\gamma=120^\circ$ .

<sup>c</sup> Percent determined from a two-component fitting of XRD data into a high-silica and low-silica phase.

Figure 4.17. EDX elemental analysis of the two distinct high-silica (1) and low-silica (2) phases observed for CHA synthesized with  $K^+/TMAda^+ = 20$ .

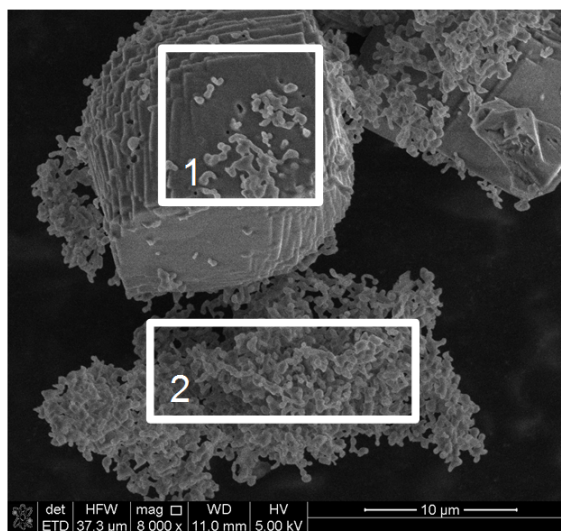


Figure 4.18. Ar adsorption (closed circles) and desorption (open circles) isotherms (87 K) on CHA synthesized with  $K^+/TMAda^+ = 2$ .

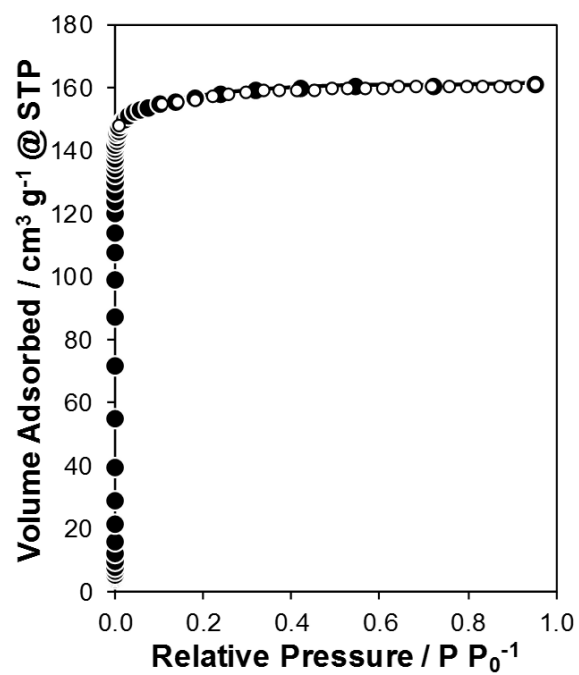


Figure 4.19. Ar adsorption (closed circles) and desorption (open circles) isotherms (87 K) on CHA synthesized with  $K^+/TMAda^+ = 15$ .

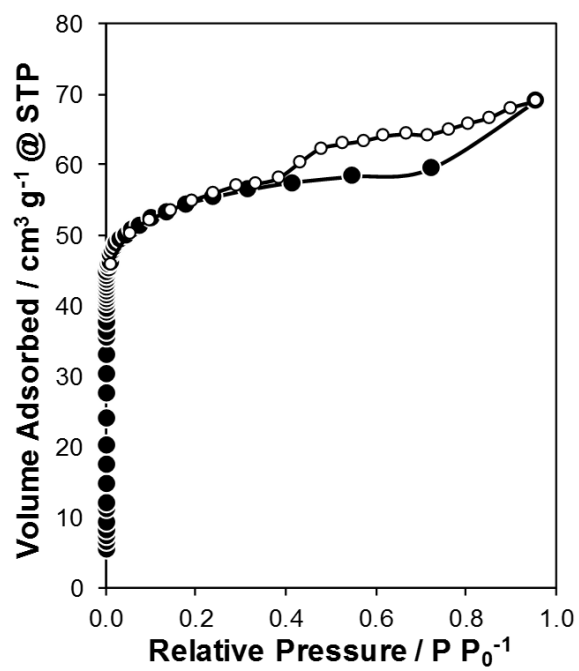




Figure 4.20. Charge distribution and partial charges of a TMAda molecule confined within the CHA unit cell after substitution of a single framework Al atom.

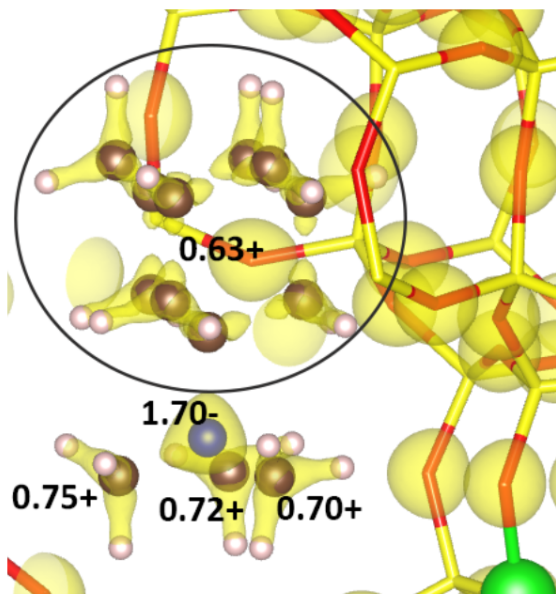


Figure 4.21. TMAda occluded within a 1x1x1 36 T-atom supercell (left) and 1x1x2 72 T-atom supercell (right) containing 1 Al atom per unit cell. Brown: Si, light grey: Al, red: O, dark grey: C, blue: N, white: H.

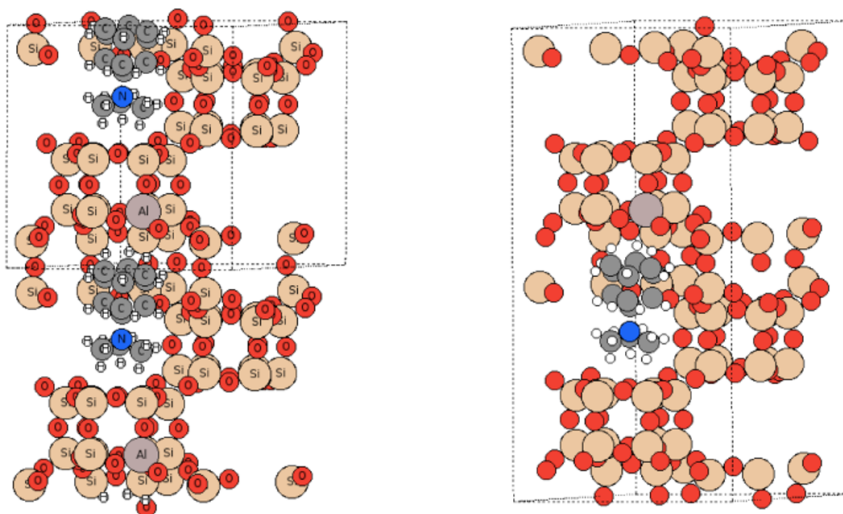


Figure 4.22. DFT energies, relative to Al position 1, of TMAda confined with the CHA cage for the six different single Al sites in the 1x1x2 super-cell using the PBE (black) and PBE-D3 (red) functional.

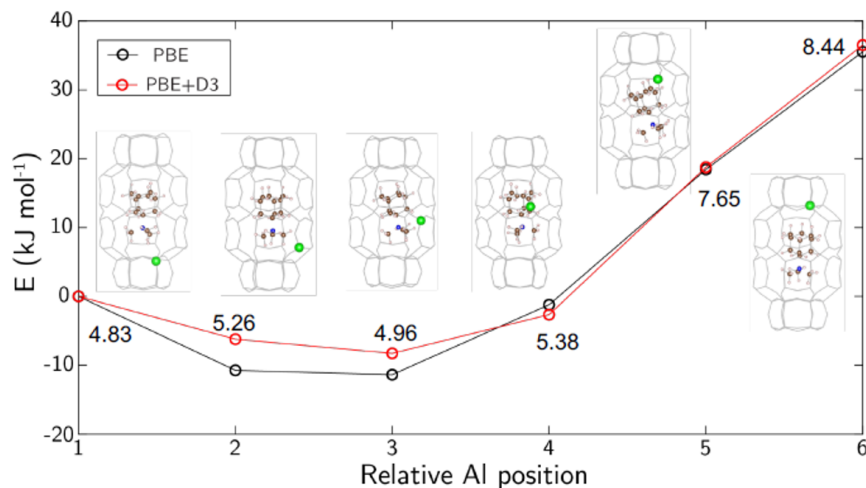


Figure 4.23. Descriptor model regressed to DFT calculated energies using three descriptors for 1) the Al-Al distance, 2) the distances between N-Al centers, and 3) the N-N distance.

• Electrostatic descriptors:

1.  $1/d_{\text{Al-Al}}$
2.  $1/d_{\text{Al1-N1}} + 1/d_{\text{Al1-N2}} + 1/d_{\text{Al2-N1}} + 1/d_{\text{Al2-N2}}$
3.  $1/d_{\text{N1-N2}}$

| Descriptor | Coefficient ( $\text{\AA}^2 \text{ eV}$ ) |
|------------|---|
| 1          | 5.35                                      |
| 2          | -3.50                                     |
| 3          | 0.89                                      |

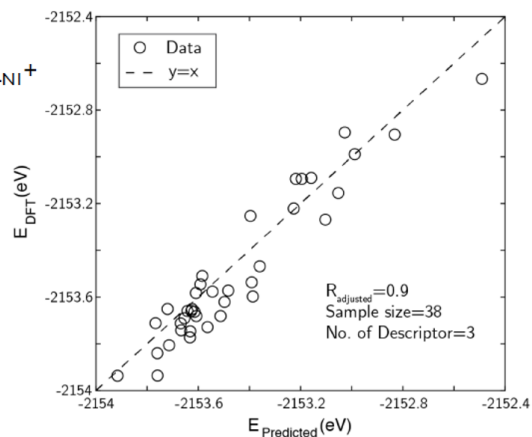




Table 4.4.

H<sup>+</sup>/Al before Cu-exchange, Cu/Al, H<sup>+</sup>/Al after Cu-exchange, standard NH<sub>3</sub>-SCR rates (473 K, per Cu), NO, O<sub>2</sub>, and NH<sub>3</sub> reaction orders, and apparent activation energies on Cu-CHA zeolites synthesized without alkali, or with Na<sup>+</sup>/TMAda<sup>+</sup> = 1, K<sup>+</sup>/TMAda<sup>+</sup> = 2, and K<sup>+</sup>/TMAda<sup>+</sup> = 15.

| Sample                                  |       | H <sup>+</sup> /Al <sup>a</sup> | Cu/Al | H <sup>+</sup> /Al <sup>b</sup> | SCR Rate <sup>c</sup> | NO Order | O <sub>2</sub> Order | NH <sub>3</sub> Order | E <sub>app</sub> <sup>d</sup> |
|---|-------|---------------------------------|-------|---------------------------------|-----------------------|----------|----------------------|-----------------------|-------------------------------|
| Alkali-Free                             | Fresh | 0.96                            | 0.28  | 0.67                            | 8.5                   | 0.7      | 0.4                  | -0.3                  | 67                            |
|   | Aged  |                                 |       | 0.31                            | 5.5                   | 0.9      | 0.3                  | -0.1                  | 59                            |
| Na <sup>+</sup> /TMAda <sup>+</sup> = 1 | Fresh | 1.02                            | 0.24  | 0.67                            | 7.2                   | 0.7      | 0.3                  | -0.2                  | 61                            |
|   | Aged  |                                 |       | 0.36                            | 5.7                   | 0.8      | 0.3                  | -0.1                  | 56                            |
| K <sup>+</sup> /TMAda <sup>+</sup> = 2  | Fresh | 1.01                            | 0.22  | 0.50                            | 10.4                  | 0.7      | 0.4                  | -0.3                  | 54                            |
|   | Aged  |                                 |       | 0.01                            | 4.2                   | 0.6      | 0.6                  | 0.0                   | 49                            |
| K <sup>+</sup> /TMAda <sup>+</sup> = 15 | Fresh | 0.82                            | 0.27  | 0.40                            | 5.0                   | 0.7      | 0.4                  | -0.2                  | 57                            |
|   | Aged  |                                 |       | 0.01                            | 2.9                   | 0.7      | 0.3                  | 0.0                   | 38                            |

<sup>a</sup> H<sup>+</sup>/Al measured on the parent H-form zeolite

<sup>b</sup> H<sup>+</sup>/Al measured on the Cu-form before (fresh) and after (aged) hydrothermal aging

<sup>c</sup> SCR rates measured at 473 K. 10<sup>-3</sup> mol NO (mol Cu s)<sup>-1</sup>

<sup>d</sup> Apparent activation energy in units of kJ mol<sup>-1</sup>



## 5. STRUCTURAL AND KINETIC CHANGES TO SMALL-PORE CU-ZEOLITES AFTER HYDROTHERMAL AGING TREATMENTS AND SELECTIVE CATALYTIC REDUCTION OF NO<sub>x</sub> WITH AMMONIA

### 5.1 Introduction

Leading emissions control strategies for the abatement of hazardous nitrogen oxide pollutants (NO<sub>x</sub>,  $x = 1, 2$ ) in lean burn and diesel engine exhaust involve their selective catalytic reduction (SCR) with ammonia, which is generated from the decomposition of urea stored in an on-board tank. Cu- and Fe-exchanged molecular sieves used to practice automotive SCR aftertreatment [92, 243–247] are required to retain sufficient SCR performance after excursions to high temperatures ( $>923$  K) in the presence of steam (ca. 7% H<sub>2</sub>O (v/v)) [35, 89, 133, 248], conditions experienced during regeneration of particulate filters. The structural integrity of molecular sieve frameworks with medium pores (e.g., MFI [93, 97, 249–252], FER [97]; ca. 0.5 nm diam.) and large pores (e.g., BEA [93, 250, 253, 254], FAU [93];  $>0.6$  nm diam.) becomes compromised during hydrothermal aging [93, 97, 249–254]; moreover, active sites within such frameworks can be poisoned chemically by residual hydrocarbons in exhaust streams. These deactivation issues are mitigated within small-pore, eight-membered ring (8-MR;  $<0.4$  nm diam.) frameworks, which led to the advent of the aluminosilicate (SSZ-13) and silicoaluminophosphate (SAPO-34) compositions of the chabazite (CHA) topology [88, 93, 255], as commercially used NO<sub>x</sub> SCR catalysts. Other small-pore molecular sieves with three-dimensional (e.g., AFX [250], AEI [256], KFI [250], SAV [257], SFW [209, 258]) and two-dimensional (e.g., LEV [250], DDR [250], RTH [259]) pore connectivity have been considered as alternatives to CHA molecular sieves, based on observations that small-pore frameworks retain their structural integrity after exposure to hydrothermal aging conditions.

Hydrothermal aging of zeolites leads to the removal of aluminum atoms from framework locations [250, 260–262], which stabilize redox-active, extraframework Cu cations and ammonium species during SCR catalysis. Framework dealumination generally leads to sintering of extraframework alumina and mixed oxide domains with concomitant losses in microporous structure [263–265] that may restrict molecular traffic to active sites. The effects of hydrothermal aging treatments on dealumination have been assessed by changes in Al coordination using solid-state  $^{27}\text{Al}$  magic angle spinning nuclear magnetic resonance (MAS NMR), and in long-range crystalline structure using X-ray diffraction (XRD) and micropore volume measurements [93, 266–269]. Structural changes upon dealumination are more severe in Cu-exchanged medium pore and large-pore zeolites (e.g., Cu-MFI, Cu-BEA) than in small-pore zeolites (e.g., Cu-CHA, Cu-AEI) [93, 253, 270], which are more recalcitrant to hydrothermal deactivation. Aluminum hydroxide species ( $\text{Al}(\text{OH})_3$ ; ca. 0.5 nm in diam.) formed upon dealumination at high temperatures are thought to be unable to diffuse through 8-MR windows in CHA [250] and AEI [270] (ca. 0.38 nm in diam.), which prevents the formation of larger extraframework alumina aggregates and allows for reincorporation of monomeric Al species within framework vacancy positions at low temperatures. Dealumination upon hydrothermal aging is also suppressed by the presence of extraframework cations (e.g., Cu, Na, Li, Mg) [270–272], which remove Brønsted acid sites that are vulnerable locations for hydrolysis of framework bonds [273–275]. Consequently, the ability of a zeolite framework to resist dealumination and retain its structural integrity upon hydrothermal aging has been used to identify promising candidates for practical NO<sub>x</sub> SCR catalysis.

Deactivation caused by hydrothermal aging of molecular sieves may also reflect changes to the structure and location of extraframework Cu cations, such as their aggregation into larger Cu oxide species ( $\text{Cu}_x\text{O}_y$ ), because the former isolated cations have been implicated as active sites for low temperature (473 K) SCR catalysis [40, 41, 79] while the latter oxide clusters are unreactive [78]. The disappearance of isolated  $\text{Cu}^{2+}$  cations upon hydrothermal aging of Cu-SSZ-13 has been inferred from

the attenuation of absorption features characteristic of framework (T–O–T) vibrations ( $900$  and  $940\text{ cm}^{-1}$ ) perturbed by ion-exchanged Cu species in diffuse-reflectance infrared (DRIFTS) spectra, from decreases in the amount of  $\text{NH}_3$  desorbed from Lewis acidic Cu cations (ca.  $553\text{ K}$ ) in TPD experiments, 32 and from decreases in electron paramagnetic resonance (EPR) signals for isolated  $\text{Cu}^{2+}$  cations [267]. The aggregation of isolated  $\text{Cu}^{2+}$  cations into larger  $\text{Cu}_x\text{O}_y$  domains upon hydrothermal aging has been detected by electron microscopy (TEM, SEM) and energy dispersive X-ray spectroscopy (EDX) [266–268]. Isolated  $\text{Cu}^{2+}$  cations have also been proposed to interact with extraframework Al species, formed via dealumination, to generate inactive copper-aluminate domains in hydrothermally aged Cu-SSZ-13, evident in extended X-ray absorption fine structure (EXAFS) spectra that show decreased Cu–Cu scattering distances and increased Cu–Al scattering distances, and in  $\text{H}_2$  temperature programmed reduction (TPR) profiles that show decreased intensities of lower temperature ( $500$ – $670\text{ K}$ ) reduction features for isolated Cu cations with the concomitant appearance of higher temperature ( $790$ – $880\text{ K}$ ) reduction features attributed to copper-aluminates [269]. Additionally,  $^{27}\text{Al}$  MAS NMR spectra show decreased intensities for tetrahedral Al lines ( $\delta$  ca.  $60\text{ ppm}$ ) without concomitant increases in intensities for octahedral Al lines ( $\delta$  ca.  $0\text{ ppm}$ ), suggesting that interactions of Al with paramagnetic Cu render them invisible to NMR detection [93]. These results provide evidence for one possible deactivation mechanism of Cu-SSZ-13 through loss of isolated  $\text{Cu}^{2+}$  active sites during hydrothermal aging, but do not account for structural changes to active sites that may result from subsequent exposure to standard SCR reactants. Thus, identifying new zeolite topologies that retain SCR reactivity after hydrothermal aging treatments requires knowledge of how such treatments, and subsequent exposure to SCR reaction conditions, affect the structures of both Cu active sites and the zeolite framework.

Here, we investigate the effects of hydrothermal aging and subsequent exposure to standard SCR reactants at low temperatures ( $473\text{ K}$ ) on the structural and active site changes experienced by three different small-pore Cu-exchanged zeolites (Cu-CHA,

Cu-AEI, Cu-RTH). Bulk characterization techniques, including XRD patterns and micropore volumes, reveal only subtle differences between Cu-zeolites before and after hydrothermal aging, and after subsequent exposure to low temperature SCR reaction conditions, and are unable to provide direct insight into the decreases in SCR reactivity measured on hydrothermally aged, small-pore Cu-zeolites. We provide evidence that exposure of hydrothermally aged catalysts to SCR reaction conditions at low temperatures causes further structural changes to active Cu sites that are detectable by UV-visible spectroscopy, consistent with the formation of mixed copper-aluminate domains via reaction with extraframework Al species formed upon dealumination during hydrothermal aging. These findings demonstrate that active site and structural characterization of hydrothermally aged Cu-zeolites after exposure to SCR reactants at low temperatures provide more accurate inferences about their catalytic behavior.

## 5.2 Experimental Methods

### 5.2.1 Catalyst synthesis and treatment

A sample of CHA (SSZ-13) zeolite with a Si/Al ratio of 15 was made as reported elsewhere [109]. Briefly, 28.4 g of N,N,N-trimethyl-1-adamantylammonium hydroxide (TMAdaOH, Sachem, 25 wt%) were mixed with 71.4 g of deionized water (18.2 M $\Omega$ ), 0.87 g of aluminum hydroxide (SPI Pharma, 99.9 wt%, 0325 grade), and 34.6 g of 0.1 M sodium hydroxide (NaOH; Alfa Aesar), then stirred for 15 minutes at ambient conditions. 10 g of fumed silica (Cab-o-Sil M-5) were added to the mixture and stirred for 2 hours at ambient conditions. The final molar composition of the synthesis solution was 1 SiO<sub>2</sub>/ 0.033 Al<sub>2</sub>O<sub>3</sub>/ 0.20 TMAdaOH/ 0.02 NaOH/ 23.8 H<sub>2</sub>O. All reagents were used without further purification. The resulting solution was transferred to eight Teflon-lined Parr autoclaves (45 mL each) and held at 433 K for 10 days under rotation.

A sample of AEI (SSZ-39) zeolite with a Si/Al ratio of 9.5 was synthesized in a rotating oven at 413 K for 4 days as reported elsewhere [276], using cis-2,6-

dimethylpiperidinium hydroxide as the organic structure directing agent (OSDA). The molar composition of the synthesis mixture was 1 SiO<sub>2</sub>/ 0.017 Al<sub>2</sub>O<sub>3</sub>/ 0.07 OSDA/ 0.65 OH<sup>-</sup>/ 0.58 Na<sup>+</sup>/ 12.3 H<sub>2</sub>O, obtained by mixing (aqueous) OSDA, NaOH (1 M, RT Baker), double distilled water, sodium silicate (N type, PQ Corporation) and CBV500 (NH<sub>4</sub>-USY, Si/Al = 2.6, Zeolyst). A sample of RTH (SSZ-50) zeolite with a Si/Al ratio of 15 was made using the CBV720 synthesis protocol reported elsewhere [208, 210, 277].

As-synthesized zeolites were washed alternately with deionized water and acetone, recovered via centrifugation, and dried at 323 K for 24 hours. The dried samples were then treated to 873 K (0.0083 K s<sup>-1</sup>) in air (Commercial grade, Indiana Oxygen) for 6 hours before ion-exchanging in an aqueous 0.1 M NH<sub>4</sub>NO<sub>3</sub> solution (Sigma Aldrich; 1000 mL per g zeolite) at 353 K for 10 hours. NH<sub>4</sub>-exchanged zeolites were washed with deionized H<sub>2</sub>O, recovered via centrifugation, dried at 323 K for 24 hours, then treated at 823 K (0.0083 K s<sup>-1</sup>) in air for 6 hours to obtain H-form zeolites. Cu-exchanged CHA, AEI, and RTH zeolites were prepared via liquid phase ion-exchange of H-form zeolites using an aqueous 0.2 M Cu(NO<sub>3</sub>)<sub>2</sub> solution (99.999% trace metals basis, Sigma-Aldrich; 150 mL per g zeolite) at ambient temperature for 4 hours. The pH during the exchange was not controlled and the final pH of the solution was ca. 3.6.

Hydrothermal aging experiments were performed on Cu-zeolites in a three-zone horizontal tube furnace (Applied Test Systems Series 3210), in which each zone was equipped with independent temperature control (Watlow EZ-Zone PM Express). Once the furnace temperature reached 373 K, water was introduced via syringe pump (KD Scientific Legato 100) into a stream of flowing air (100 mL min<sup>-1</sup>, 99.999%, Indiana Oxygen), which was transferred to the furnace through stainless steel lines held at >373 K. Approximately 1 gram of catalyst was loaded into quartz boats held within the tube furnace and treated to 1073 K (0.033 K s<sup>-1</sup>) for 16 hours in flowing air (100 mL min<sup>-1</sup>, 99.999%, Indiana Oxygen) containing 10% (v/v) water. After treatment

for 16 hours at 1073 K, water was removed from the flowing air stream while the sample was cooled to ambient.

### 5.2.2 Catalyst structural characterization

Powder diffraction patterns were collected using a Rigaku SmartLab diffractometer with a Cu K $\alpha$  radiation source (1.76 kW), from 4 to 40° with a scan rate of 0.05° s<sup>-1</sup> and a step size of 0.01°. Diffraction patterns are normalized so that the maximum peak intensity in each pattern is unity. The diffraction patterns were compared to reference patterns to confirm the RTH, CHA and AEI topologies [1].

Ar adsorption isotherms were used to determine micropore volumes on zeolite samples (87 K) using a Micromeritics ASAP 2020 Surface Area and Porosity Analyzer. Micropore volumes were obtained by converting adsorbed gas volumes (cm<sup>3</sup> g<sub>cat</sub><sup>-1</sup> at STP) to liquid volumes assuming the liquid density of Ar at 87 K. Samples were pelleted and sieved to retain particles between 125–250  $\mu$ m in diameter. Samples (0.03–0.05 g) were degassed by heating to 393 K (0.167 K s<sup>-1</sup>) under high vacuum (ca. 5  $\mu$ m Hg) for 2 h, and then heating to 623 K (0.167 K s<sup>-1</sup>) under high vacuum (ca. 5  $\mu$ m Hg) and holding for 9 h. Micropore volumes (cm<sup>3</sup> g<sub>cat</sub><sup>-1</sup> at STP) were estimated from extrapolation of the linear volumetric uptake during the beginning of mesopore filling (ca. 0.08–0.30 P/P<sub>0</sub>) to zero relative pressure, which agreed with micropore volumes estimated from analyzing the semi-log derivative plot of the adsorption isotherm ( $\partial(V_{\text{ads}})/\partial(\ln(P/P_0))$  vs.  $\ln(P/P_0)$ ).

In order to quantify the fractions of framework and extraframework Al, <sup>27</sup>Al magic angle spinning nuclear magnetic resonance (MAS NMR) spectra were recorded on H-form and Cu-form CHA, AEI and RTH zeolite samples. NMR spectra were collected using a Chemagnetics CMX-Infinity 400 spectrometer in a wide-bore 9.4 Tesla magnet (Purdue Interdepartmental NMR Facility) and were acquired at ambient conditions using a 2.3  $\mu$ s pulse (equivalent to ca. 30 degrees), an acquisition time of 12.8 ms and a relaxation delay of 1 s, and were measured at 104.24 MHz and a MAS rate of 5 kHz. <sup>1</sup>H decoupling was used during acquisition, employing two-pulse phase



modulation (TPPM) scheme. Prior to packing in a 4 mm ZrO<sub>2</sub> rotor, zeolite samples were hydrated by holding for >48 h in a desiccator containing a saturated potassium chloride (KCl) solution. All <sup>27</sup>Al MAS NMR spectra are referenced to a static sample of AlCl<sub>3</sub> dissolved in D<sub>2</sub>O (0 ppm <sup>27</sup>Al line).

Diffuse reflectance UV-visible spectra were recorded under ambient conditions using a Varian UV-vis-NIR spectrophotometer (Cary 5000) with a diffuse reflectance accessory consisting of two ellipsoidal mirrors (Harrick Scientific Praying Mantis). Barium sulfate (BaSO<sub>4</sub>, 99.9%, Sigma-Aldrich) was used as the 100% reflectance standard. An *ex situ* sample holder was loaded with 0.1 g of sample, which was pelleted and sieved to retain particles between 125–250 μm in diameter. Spectra were collected from 7000 to 50 000 cm<sup>-1</sup> with a scan speed of 2000 cm<sup>-1</sup> min<sup>-1</sup>, and spectra of the H-form zeolite was subtracted from those for corresponding Cu-zeolites to correct for contributions of absorption from the framework.

### 5.2.3 Brønsted acid site quantification using NH<sub>3</sub> titration methods

The total number of Brønsted acid sites (H<sup>+</sup>) on H-form and Cu-exchanged zeolites was quantified by temperature programmed desorption (TPD) of NH<sub>3</sub> on a gas-phase plug flow reactor, as described by Bates et al. [78], using a procedure described elsewhere [171]. For H-form zeolites, NH<sub>3</sub> saturation was performed via aqueous-phase exchange with NH<sub>4</sub><sup>+</sup> cations, as reported elsewhere [78]. For Cu-exchanged zeolites, samples were saturated with 500 ppm NH<sub>3</sub> diluted with He (99.999%, UHP, Indiana Oxygen) at 433 K for 2 h with a total flow rate of 350 mL min<sup>-1</sup>. Following this NH<sub>3</sub> saturation step, the sample was flushed with 2.5–3.0% water in UHP He (wet purge) at 433 K for 8 h while maintaining the same total flow rate to desorb NH<sub>3</sub> bound to non-protonic sites. Following the wet purge step, samples were heated to 820 K (0.167 K s<sup>-1</sup>) under flowing He (UHP, 350 mL min<sup>-1</sup>). The total moles of NH<sub>3</sub> desorbed during the TPD experiment was measured using on-board calibrations in an MKS Multigas 2030 gas-phase FT-IR spectrometer [78].

#### 5.2.4 Kinetic measurements of standard SCR turnover rates

Standard selective catalytic reduction (SCR) kinetics were measured on a bench-top tubular glass reactor described elsewhere [37]. All samples were sieved to a nominal size of 125–250  $\mu\text{m}$  and diluted with silica gel to obtain a bed height of ca. 2.5 cm. Steady-state kinetic data were collected at NO conversions below 20% (differential); thus, the entire catalyst bed was exposed to approximately the same gas concentrations. Under standard SCR conditions, the reactant gas mixture comprised 300 ppm NO (3.6% NO/Ar, Praxair), 300 ppm  $\text{NH}_3$  (3.0%  $\text{NH}_3$ /Ar, Praxair), 7%  $\text{CO}_2$  (liquid, Indiana Oxygen), 10%  $\text{O}_2$  (99.5%, Indiana Oxygen), 2.5%  $\text{H}_2\text{O}$  (deionized, 18.2 M $\Omega$ , introduced through saturator), and balance  $\text{N}_2$  (99.999% UHP, Indiana Oxygen). For all kinetic measurements, the total gas stream was maintained at a flow rate of 1.5 L  $\text{min}^{-1}$  and at ambient pressure (ca. 101 kPa). Apparent reaction orders were measured by independently varying partial pressures of  $\text{NH}_3$  (0.02–0.05 kPa), NO (0.02–0.05 kPa) or  $\text{O}_2$  (5–15 kPa) in the reactant gas stream, and adjusting the balance  $\text{N}_2$  to maintain a constant total gas flow rate and pressure. Apparent activation energies were measured under standard SCR conditions by varying the temperature between 444–476 K. Outlet gas concentrations were analyzed using on-board gas calibrations on an MKS Multigas<sup>TM</sup> 2030 gas-phase Fourier transform infrared (FTIR) spectrometer and NO,  $\text{NO}_2$ ,  $\text{NH}_3$ ,  $\text{CO}_2$ , and  $\text{H}_2\text{O}$  concentration data was recorded every 0.95 s. Kinetic measurements were recorded after waiting for outlet gas concentrations to reach steady-state, which typically occurred after 2–4 hours. Reactant pressures and temperatures were then varied over the course of 18 hours, and finally returned to initial conditions to verify that catalytic rates returned to their initial steady-state values and that the catalyst had not undergone any deactivation.

## 5.3 Results and Discussion

### 5.3.1 Structural features of CHA, AEI and RTH topologies

The salient structural features of the three molecular sieve framework topologies studied here are summarized in Figure 5.1. The CHA framework [126] has three-dimensional micropore interconnectivity and is formed by the repetitive stacking of a hexagonal array of planar 6-membered rings (6-MR) connected in an AABBC-type stacking scheme that form hexagonal prisms (double 6-MR). These double 6-MR (D6R) units are ordered to form large chabazite cages that are ca. 0.73 nm in diameter, which are limited by symmetric 8-MR windows that are ca. 0.38 nm in diameter. The CHA framework contains only one crystallographically unique T-site and its unit cell contains 36 tetrahedrally-coordinated atoms (T-atoms) connected by 4-MR, 6-MR, and 8-MR units that are shared between adjacent cages.

The AEI framework [278] also has three-dimensional micropore interconnectivity and is constructed from a hexagonal array of 6-MR units similar to CHA, but neighboring D6R units are rotated  $180^\circ$  with respect to each other (Figure 5.1). The D6R units are ordered to form AEI cavities that are ca. 0.73 nm in diameter and are contained within 4-MR, 6-MR, and 8-MR units, with access into AEI cavities limited by symmetric 8-MR windows that are ca. 0.38 nm in diameter, as in the case of CHA. In contrast to the CHA unit cell, the AEI unit cell contains 48 T-atoms and three crystallographically-distinct T-sites.

The RTH framework [279] is unique among the three small-pore zeolites studied here because it does not contain D6R building units, but instead is formed by two sets of three 4-MR that are connected via 5-MR linkages. These chained 4-MR and 5-MR periodic building units are repeated with simple translations to form RTH cavities that are 0.81 nm in diameter, and are contained within 4-MR, 5-MR, 6-MR, and 8-MR units. Consequently, the RTH unit cell (32 T-atoms) contains both symmetric (0.38 nm x 0.41 nm) and asymmetric (0.25 nm x 0.56 nm) 8-MR windows that result in only two-dimensional pore interconnectivity. RTH contains four crystallographically-

distinct T-sites, three of which occupy positions accessible through either of the two 8-MR windows, and one that resides within the interconnected 4-MR chain and is inaccessible from the RTH cavity.

### 5.3.2 Synthesis and characterization of H-form and Cu-form zeolites before hydrothermal aging

Powder XRD patterns of H-form AEI, CHA, and RTH zeolites (Fig. 5.7, Supp. Info.) were consistent with reported diffraction patterns for these topologies [1] and did not show diffraction peaks for phase impurities. Ar adsorption isotherms (87 K) on H-form zeolites (Fig. 5.8, Supp. Info.) gave micropore volumes (Table 5.1) consistent with the AEI [278], CHA [109], and RTH [279] topologies.  $^{27}\text{Al}$  MAS NMR spectra of H-form zeolites (Fig. 5.9-5.11, Supp. Info.) show predominantly Al incorporated into tetrahedral framework positions ( $\text{Al}_f$ ,  $\delta$  ca. 60 ppm), with  $\text{Al}_f/\text{Al}_{\text{tot}}$  values quantified to be 0.85 for H-CHA, 0.85 for H-AEI, and 0.94 for H-RTH (Table 5.2). The number of protons per framework Al atom ( $\text{H}^+/\text{Al}_f$ , Table 5.2) measured by  $\text{NH}_3$  TPD (Fig. 5.2) on H-form zeolites was 0.95 and 0.85 for H-CHA and H-AEI, respectively, indicating that nearly every framework Al generated a proton. In contrast, the  $\text{H}^+/\text{Al}_f$  value was much lower on H-RTH (0.60, Table 5.2), suggesting either that some framework Al atoms generate  $\text{H}^+$  sites that are inaccessible to  $\text{NH}_3$ , or that not all Al atoms are associated with a corresponding proton site. In the RTH framework, it is plausible that some  $\text{H}^+$  sites are inaccessible to  $\text{NH}_3$ , which has a kinetic diameter (ca. 0.26 nm) [280] that is larger than one of the dimensions of the distorted RTH window (0.56 nm x 0.25 nm), and because one of the four T-sites in RTH is in a location that is inaccessible from the RTH cage. Infrared spectra collected after H-RTH was exposed to  $\text{NH}_3$  (433 K), however, showed complete disappearance of Brønsted acidic OH stretches (Fig. 5.13, Supp. Info.) indicating that all  $\text{H}^+$  sites are accessible to  $\text{NH}_3$ . Therefore, the  $\text{H}^+/\text{Al}_f$  value of 0.60 on H-RTH reflects the presence of distorted Al structures that do not generate  $\text{H}^+$  sites, but are otherwise detected as  $\text{Al}_f$  species in NMR spectra, as noted previously [78, 118, 281].

Powder XRD patterns of AEI, CHA, and RTH zeolites after Cu exchange do not show significant changes in structure compared to their respective H-form zeolites or the presence of bulk  $\text{Cu}_x\text{O}_y$  (Fig. 5.7, Supp. Info.). The micropore volume of each Cu-exchanged zeolite decreased slightly (Table 5.2; Fig. 5.8, Supp. Info.) due to the presence of extraframework Cu cations, which occupy a small, but detectable, fraction of the void volume. Gaseous  $\text{NH}_3$  titration [78, 171] of residual  $\text{H}^+$  sites on Cu-CHA ( $\text{Cu}/\text{Al} = 0.12$ ) shows that  $\text{H}^+$  sites are replaced with an exchange stoichiometry of two protons per Cu, reflecting the presence of only divalent  $\text{Cu}^{2+}$  cations (Table 5.2, Fig. 5.2). This result is consistent (within experimental error) with the sequential exchange of isolated  $\text{Cu}^{2+}$  at paired Al sites until saturation followed by subsequent exchange of monovalent  $[\text{CuOH}]^+$  at isolated Al sites [42, 79, 218]. Cu-RTH ( $\text{Cu}/\text{Al} = 0.11$ ) shows an  $\text{H}^+/\text{Cu}$  exchange stoichiometry of two that suggests only  $\text{Cu}^{2+}$  sites are present, while Cu-AEI ( $\text{Cu}/\text{Al} = 0.17$ ) shows an  $\text{H}^+/\text{Cu}$  exchange stoichiometry between 1 and 2 that suggests a mixture of  $\text{Cu}^{2+}$  and  $[\text{CuOH}]^+$  sites are present. UV-visible spectra of hydrated Cu-AEI, Cu-CHA, and Cu-RTH zeolites (Fig. 5.3) show absorption bands characteristic of d-d transitions for hydrated  $\text{Cu}^{2+}$  complexes (ca.  $12,500\text{ cm}^{-1}$ ) and broad bands for metal-ligand charge transfer ( $35,000\text{--}47,000\text{ cm}^{-1}$ ), which are convoluted by zeolitic framework metal-oxygen charge transfer ( $36,750$  and  $43,500\text{ cm}^{-1}$ ) and Cu-O charge transfer (ca.  $42,000\text{ cm}^{-1}$ ) [36, 282, 283]. An additional feature is present at ca.  $25,000\text{ cm}^{-1}$  in the UV-vis spectrum of Cu-RTH, but not in spectra of either Cu-AEI or Cu-CHA, and appears in a region attributed to Cu-O charge transfer in small Cu oxide clusters [36].

### 5.3.3 Standard SCR kinetics of Cu-zeolites before hydrothermal aging

Rates of NO consumption (473 K, per Cu) during standard SCR (equimolar NO and  $\text{NH}_3$ , with  $\text{O}_2$  as the oxidant) are shown in Table 5.3 and plotted in Fig. 5.4. The measured NO consumption rate (per Cu) was similar on Cu-AEI and Cu-CHA (within 1.3x), although direct quantitative comparison of these turnover rates is not rigorously justified since they appear to be measured in different kinetic regimes,

reflected in the different apparent  $\text{NH}_3$  reaction orders of -0.5 and -0.1 on Cu-CHA and Cu-AEI (Table 5.3), respectively. The measured NO consumption rate was lower (by 2.2–2.9x) on Cu-RTH than on either Cu-AEI or Cu-CHA (Table 5.3). At first glance, the similar turnover rates (per Cu) on Cu-CHA, Cu-AEI and Cu-RTH (within 3x, 473 K) seem reminiscent of standard SCR turnover rates (473 K) that have been reported to be insensitive to the zeolite topology (CHA, BEA, MFI), as a consequence of the solvation of Cu cations by  $\text{NH}_3$  during low temperature SCR conditions [79].

Apparent activation energies (Table 5.3) estimated from rate data collected between 444–476 K (Fig. 5.4) were similar on Cu-AEI ( $46 \pm 5 \text{ kJ mol}^{-1}$ ) and Cu-CHA ( $56 \pm 5 \text{ kJ mol}^{-1}$ ), and in a range previously reported for standard SCR activation energies on Cu-CHA (Si/Al = 35, Cu/Al = 0–0.31) [37,40]. Apparent activation energies were much lower on Cu-RTH ( $28 \pm 5 \text{ kJ mol}^{-1}$ ), however, and approximately half of the value measured on Cu-CHA, characteristic of severe intrazeolite mass transfer limitations. Both the CHA and AEI frameworks contain three-dimensional pore systems interconnected by symmetric 8-MR windows (0.38 nm diameter), but the RTH framework is a two-dimensional pore system with a limiting asymmetric 8-MR ring of size (0.25 nm) similar to the kinetic diameter of the SCR reactants (ca. 0.3 nm). In effect, the RTH framework appears to behave as a one-dimensional pore system for this reaction, in which reactants preferentially diffuse through the symmetric 8-MR window. Internal diffusion limitations have been proposed to account for the lower NO<sub>x</sub> conversions (423–573 K) in two-dimensional, small-pore LEV and DDR zeolites, when compared to three-dimensional small-pore CHA zeolites [250]. Thus, while small-pore zeolites show improved hydrothermal stability over medium and large-pore zeolites [93,253], considerations of pore connectivity and limiting aperture sizes are also critical in determining the reactivity of Cu sites located within them.

The number of residual  $\text{H}^+$  sites (per  $\text{Al}_{\text{tot}}$ ) on Cu-CHA before and after exposure to SCR gases was 0.72 and  $0.70 \pm 0.05$ , respectively. Similarly, the residual  $\text{H}^+/\text{Al}_{\text{f}}$  value on Cu-AEI and Cu-RTH changed only from 0.54 to  $0.50 \pm 0.05$  and from 0.38 to  $0.39 \pm 0.05$ , respectively (Table 5.3). Therefore, exposure to SCR gases did not

significantly change the number of residual  $H^+$  sites on Cu-AEI, Cu-CHA and Cu-RTH, indicating that framework Al remained largely intact on Cu-zeolites after NOx SCR catalysis. Ar micropore and mesopore volume measurements (87 K) on Cu-AEI, Cu-CHA and Cu-RTH before and after exposure to SCR gases were unchanged (Table 5.3, Fig. 5.6), with micropore volumes for both Cu-CHA and Cu-RTH of  $0.17 \text{ cm}^3 \text{ g}^{-1}$  and for Cu-AEI of  $0.18\text{--}0.19 \text{ cm}^3 \text{ g}^{-1}$  before and after exposure to SCR gases, respectively. Similarly, the mesopore volume for Cu-AEI, Cu-CHA and Cu-RTH zeolites before and after exposure to SCR gases were the same, within experimental error, between  $0.03\text{--}0.05 \text{ cm}^3 \text{ g}^{-1}$  (Table 5.3). Taken together, these characterization data of Cu-zeolites that have not been exposed to hydrothermal aging treatments indicate that minimal changes to  $H^+$  or Cu sites, or the zeolite framework, occur after exposure to low temperature standard SCR reaction conditions (473 K).

#### 5.3.4 Characterization of Cu-form zeolites before and after hydrothermal aging

Severe hydrothermal aging treatments of each Cu-exchanged zeolite, performed to reproduce the effects experienced during a 135,000 mile lifetime (1073 K, 10% (v/v)  $H_2O$ , 16 h) [268], did not result in detectable loss of long-range structure as inferred from powder XRD patterns (Fig. 5.5). After hydrothermal aging treatments, the Ar micropore volumes decreased by only ca. 10% on Cu-AEI and Cu-CHA, but remained constant on Cu-RTH (Table 5.3, Fig. 5.6).  $^{27}\text{Al}$  MAS NMR spectra of Cu-zeolites after hydrothermal aging (Fig. 5.1) show decreased intensities for tetrahedrally-coordinated Al lines ( $Al_f$ , ca. 60 ppm; Table 5.3) and increased intensities in octahedrally-coordinated Al lines ( $Al_{ex}$ , ca. 0 ppm; Fig. 5.1), indicating the formation of extraframework Al species from framework dealumination. Framework dealumination occurred to greater extents on Cu-RTH (ca. 25% loss in  $Al_f$ ) than on either Cu-AEI or Cu-CHA (ca. 7% loss in  $Al_f$ ), although we note that Al quantification from NMR spectra of Cu-zeolites will be affected by species that are not detected because of interactions with paramagnetic Cu [284]. Moreover, hydrothermal aging of Cu-RTH results in the appearance of a broad shoulder at ca. 40–50 ppm

reflecting penta-coordinated or distorted tetrahedral Al [123], which did not occur in either Cu-AEI or Cu-CHA. After hydrothermal aging treatments, XRD lines shifted to higher angles on Cu-CHA and Cu-AEI (Fig. 5.5) reflecting lattice contraction upon extraction of a small amount of framework Al (ca. 7% by  $^{27}\text{Al}$  NMR), while XRD lines shifted to lower angles on Cu-RTH (Fig. 5.5) reflecting lattice expansion that appears to arise from the more extensive dealumination that formed persistent partial-extraframework aluminum species in distorted coordination environments (ca. 40–50 ppm in  $^{27}\text{Al}$  NMR). After hydrothermal aging, each Cu-zeolite sample showed a ca. 70–80% decrease in the number of  $\text{H}^+$  sites measured by  $\text{NH}_3$  TPD (Table 5.3; Fig. 5.12, Supp. Info.), in spite of the only minor decreases in  $\text{Al}_f$  intensity observed in the  $^{27}\text{Al}$  MAS NMR spectra, which may reflect structural changes to extraframework Al species caused by the hydration treatments used prior to recording NMR spectra. These findings demonstrate that characterization of the bulk structure (e.g. XRD patterns, micropore volumes) or Al atoms ( $^{27}\text{Al}$  MAS NMR) are insufficient to describe the local site and structural changes caused by hydrothermal aging treatments [270], and serve as a reminder for the need to use techniques that probe and quantify active sites directly (e.g. base titration of proton sites) to accurately detect such structural changes [78, 281, 285].

In contrast to the dramatic changes observed for  $\text{H}^+$  sites on each Cu-zeolite after hydrothermal aging, the identity and coordination of Cu species appear to remain unchanged as inferred from UV-vis spectra (Fig. 5.3). UV-vis absorption bands for  $\text{Cu}^{2+}$  d–d transitions (ca.  $12,500\text{ cm}^{-1}$ ) appear identical for hydrated Cu-zeolites before and after hydrothermal aging, without any new features observed in the region for Cu oxide clusters (ca.  $25,000\text{ cm}^{-1}$ ). Slight changes in the intensities of absorbance bands characteristic of metal–ligand charge transfer ( $35,000\text{--}47,000\text{ cm}^{-1}$ ) are observed for each Cu-zeolite after hydrothermal aging, which may reflect changes in the zeolite structure caused by removal of framework aluminum atoms. Taken together, these results indicate that hydrothermal aging treatments of Cu-exchanged CHA, AEI and RTH zeolites cause framework dealumination and a decrease in the



numbers of corresponding  $\text{H}^+$  sites, but do not result in detectable changes to the exchanged Cu cations or to the long-range structural order in the zeolite framework.

### 5.3.5 Standard SCR kinetics of Cu-form zeolites before and after hydrothermal aging

The standard SCR rate (per Cu, 473 K) measured on hydrothermally aged Cu-AEI decreased by ca. 50% compared to the rate measured on Cu-AEI prior to aging (Table 5.3, Fig. 5.4). The standard SCR rate measured on hydrothermally aged Cu-CHA decreased by ca. 25% compared to the rate measured on Cu-CHA prior to aging (Table 5.3, Fig. 5.4). The standard SCR rate on Cu-RTH, however, was not measureable ( $<0.3 \times 10^{-3} \text{ mol NO (mol Cu)}^{-1} \text{ s}^{-1}$ ) after hydrothermal aging despite the presence of isolated, hydrated  $\text{Cu}^{2+}$  species detected in its UV-vis spectrum (Fig. 5.3). As a result, apparent activation energies and reaction orders could not be measured on Cu-RTH subjected to hydrothermal aging treatments. Although hydrothermally aged Cu-RTH shows undetectable SCR rates, XRD patterns and Ar micropore volumes indicate virtually no changes to Cu-RTH before and after aging. Thus, assessments of long-range structural features by XRD and micropore volume after Cu-zeolites have been hydrothermally aged cannot be used as accurate predictors of SCR catalytic behavior.

Hydrothermal aging treatments did not affect the apparent activation energies on either Cu-AEI (46–49  $\text{kJ mol}^{-1}$ ) or Cu-CHA (51–56  $\text{kJ mol}^{-1}$ ), nor the apparent NO (0.5),  $\text{O}_2$  (0.4) and  $\text{NH}_3$  (ca. 0) orders on Cu-AEI and the apparent NO (0.4–0.5) and  $\text{O}_2$  (0.4–0.6) orders on Cu-CHA (Table 5.3). The apparent  $\text{NH}_3$  order measured on Cu-CHA (-0.5) became less negative after hydrothermal aging (-0.1, Table 5.3); we surmise that structural changes caused by hydrothermal aging and exposure to SCR gases led to a change in operation to a new kinetic regime characterized by weaker  $\text{NH}_3$  inhibition. Turnover rates were similar between the hydrothermally-aged Cu-CHA and Cu-AEI samples ( $1.9\text{--}2.2 \times 10^{-3} \text{ mol NO (mol Cu)}^{-1} \text{ s}^{-1}$ ) and the apparent reaction orders and activation energies were identical for both samples (Table 5.3), providing evidence that these rate data were measured in equivalent kinetic regimes.

These data indicate that the Cu species that remain active on both CHA and AEI after hydrothermal aging behave catalytically similar, which may be linked to the nature of the  $\text{Cu}^{2+}$  exchange sites at the 6-MR windows of D6R composite building units that are found in both CHA and AEI.

### 5.3.6 Characterization of Cu-form zeolites before and after hydrothermal aging, and after exposure to NO<sub>x</sub> SCR

Ar adsorption isotherms (87 K) and micropore volumes (Fig. 5.6, Table 5.3) of Cu-zeolites after hydrothermal aging were indistinguishable before and after exposure to low temperature standard SCR reaction conditions (473 K). XRD patterns were also similar for hydrothermally-aged Cu-zeolites before and after exposure to standard SCR gases (Fig. 5.5). These characterization data indicate that further structural changes to the zeolite framework did not occur when aged Cu-zeolites were exposed to standard SCR gas mixtures. The number of  $\text{H}^+$  sites on hydrothermally-aged Cu-AEI and Cu-CHA zeolites were also similar before and after exposure to standard SCR gas mixtures (Table 5.3), but  $\text{H}^+$  sites were no longer detectable ( $<0.03 \text{ H}^+/\text{Al}$ , Table 5.3) on hydrothermally-aged Cu-RTH exposed to SCR gases. UV-vis spectra of hydrothermally-aged Cu-CHA and Cu-RTH zeolites after exposure to standard SCR reactants (Fig. 5.3) showed a reduction in  $\text{Cu}^{2+}$  d-d transition intensity (ca.  $12,500 \text{ cm}^{-1}$ ) and concomitant increases in intensity for broad absorption bands between  $20,000\text{--}40,000 \text{ cm}^{-1}$ . The spectra of Cu-AEI, however, retained similar d-d transition intensity after aging and exposure to SCR reactants, with an increase in intensity in the metal-ligand charge transfer region ( $35,000\text{--}47,000 \text{ cm}^{-1}$ ) that is also observed for Cu-CHA, but not for Cu-RTH.

The Cu structure in Cu-CHA, Cu-AEI and Cu-RTH, characterized by UV-vis spectra, showed hardly any changes after hydrothermal aging treatments, but showed noticeable decreases in  $\text{Cu}^{2+}$  intensity upon subsequent exposure to low temperature SCR reaction conditions. These findings provide evidence that hydrothermal aging causes removal of Al from framework to extraframework positions, and that further

structural changes continue to occur in the presence of SCR reactants at low temperatures (473 K) because  $\text{NH}_3$  facilitates the solvation and mobility of Cu cations [79]. We speculate that an inactive copper aluminate phase ( $\text{CuAl}_x\text{O}_y$ ) forms as a result of interactions of active Cu sites with extraframework Al(OH)<sub>3</sub> species, as proposed previously [93, 253, 269]. UV-vis spectra of hydrothermally-aged Cu-RTH reveal decreased intensities for hydrated  $\text{Cu}^{2+}$  d-d transitions along with increases in new charge transfer bands between 20,000–40,000  $\text{cm}^{-1}$  that may reflect  $\text{CuAl}_x\text{O}_y$  species and account for decreases in SCR rate. Interestingly, any remaining  $\text{H}^+$  sites in Cu-RTH upon hydrothermal aging and subsequent exposure to standard SCR reactants become inaccessible to  $\text{NH}_3$ , suggesting that Cu active sites in RTH, which appear to catalyze SCR in a diffusion-limited regime before hydrothermal aging, also become inaccessible to SCR reactants after hydrothermal aging.

#### 5.4 Conclusions

CHA and AEI zeolites are similar in structure, with three-dimensional micropore systems connected by symmetric 8-MR windows (0.38 nm diameter), while the RTH framework is a two-dimensional pore system with constrained, asymmetric 8-MR windows (0.56 nm x 0.25 nm) that limit access in one dimension and effectively causes the RTH framework to behave as a one-dimensional pore system for NO<sub>x</sub> SCR with  $\text{NH}_3$ . As a result, standard SCR turnover rates (per Cu, 473 K) and apparent activation energies are similar between Cu-CHA and Cu-AEI, but turnover rates are lower (by ca. 2–3x) and apparent activation energies are lower (by ca. 2x) on Cu-RTH. Hydrothermal aging causes dealumination of Cu-CHA, Cu-AEI and Cu-RTH, evident in a decrease in the fraction of  $\text{Al}_\text{f}$  determined from  $^{27}\text{Al}$  MAS NMR spectra and corresponding decreases in the number of  $\text{H}^+$  sites quantified by  $\text{NH}_3$  TPD, but does not cause noticeable changes in the bulk framework structure assessed by XRD and micropore volume or in the Cu structure by UV-vis spectroscopy. The number of active Cu sites, however, decreased after hydrothermally aged samples were subsequently exposed to low temperature standard SCR reactants, evident in changes

to UV-vis spectra and concomitant decreases in standard SCR turnover rates. Hydrothermal aging causes removal of Al from framework to extraframework positions, and further structural changes continue to occur in the presence of ammonia at low temperatures (473 K), which solvate and mobilize extraframework cations to facilitate the formation of inactive copper-aluminate phases ( $\text{CuAl}_x\text{O}_y$ ). These structural changes appear to occur more readily in Cu-RTH than either Cu-AEI or Cu-CHA, providing further evidence linking the presence of double six-membered rings (D6R) in small-pore molecular sieve frameworks to increased resistance to active site and framework structural changes upon hydrothermal aging.

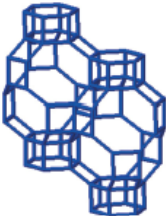
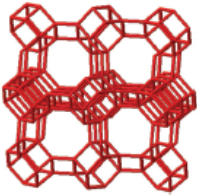
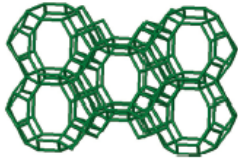
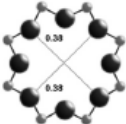
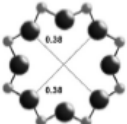
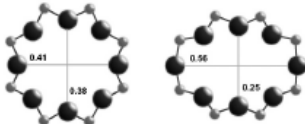
Bulk structural characterization of small-pore zeolites after hydrothermal aging treatments cannot be used to accurately infer catalytic behavior for low temperature NOx SCR with  $\text{NH}_3$ . This is evident in the case of hydrothermally-aged Cu-RTH, which deactivates completely upon exposure to standard SCR reactants but is characterized by similar bulk properties (XRD, micropore volume) before and after hydrothermal aging. Probes of Al structure (e.g.,  $^{27}\text{Al}$  MAS NMR) reveal that octahedrally-coordinated Al species are formed after hydrothermal aging of Cu-zeolites, but in amounts that are unable to account for the much larger disappearance in Brønsted acid sites titrated by  $\text{NH}_3$ , providing another reminder that methods to directly probe active sites are needed to assess their structural changes. We conclude that more accurate assessments of molecular sieve framework topologies that are viable for practical NOx SCR catalysis require quantification and characterization of Al and Cu site structures after hydrothermally aged samples are exposed to low temperature SCR reaction conditions. We expect that holistic approaches to active site characterization, especially of Al and Cu sites, in Cu-zeolites after hydrothermal aging and subsequent exposure to low temperature SCR reaction conditions will be able to provide more accurate guidance about molecular sieve topologies that are viable candidates for practical SCR technologies.

## 5.5 Acknowledgements

We acknowledge the financial support provided by the National Science Foundation GOALI program under award number 1258715-CBET. RG acknowledges the financial support from a Ralph E. Powe Junior Faculty Enhancement Award from the Oak Ridge Associated Universities (ORAU). MD acknowledges Research Foundation Flanders (FWO) for postdoctoral funding. We thank Dr. John Harwood (Purdue Interdepartmental NMR Facility) for assistance collecting the NMR spectra, and Dr. Atish A. Parekh for helpful technical discussions. We also thank Daniel Gonzalez (Universidad Nacional de Colombia), through the Undergraduate Research Experience Purdue-Colombia (UREP-C) program, for experimental assistance constructing the apparatus to perform hydrothermal aging treatments and performing some aging experiments on CHA zeolites. We also thank Sachem, Inc. for providing the organic structure-directing agent used to synthesize SSZ-13.

Additionally, I acknowledge the Royal Society of Chemistry for granting permission to reproduce this chapter of my thesis. Reproduced from *Reaction Chemistry & Engineering*, 2017, 2, 168-179 with permission from the Royal Society of Chemistry. The full article can be accessed here: [dx.doi.org/10.1039/C6RE00198J](https://doi.org/10.1039/C6RE00198J).

## 5.6 Figures and Tables

| Framework                             | CHA   | AEI  | RTH   |
|---------------------------------------|---|--|---|
| Crystal topology                      |  |  |  |
|                                       |  |   |  |
| Zeolite trade name                    | SSZ-13 (ref. 46)  | SSZ-39 (ref. 54)   | SSZ-50 (ref. 55)  |
| Space group                           | $R\bar{3}m$   | $Cmcm$   | $C2/m$  |
| Ring sizes (X-MR) <sup>a</sup>        | 8, 6, 4   | 8, 6, 4  | 8, 6, 5, 4  |
| Number of unique T-sites <sup>a</sup> | 1   | 3  | 4   |
| Connectivity <sup>a</sup>             | 3-D   | 3-D  | 2-D   |
| Window diameter <sup>b</sup> (nm)     | $0.38 \times 0.38$  | $0.38 \times 0.38$   | $0.54 \times 0.25$<br>$0.41 \times 0.38$  |
| Cage diameter <sup>c</sup> (nm)       | 0.73  | 0.73   | 0.81  |

<sup>a</sup> Structural information from the International Zeolite Association structural database.<sup>51</sup> <sup>b</sup> Window diameter taken as the maximum diameter of a sphere that can diffuse through the framework.<sup>68</sup> <sup>c</sup> Cage size taken as the maximum diameter of a sphere that be occluded within the framework.<sup>68</sup>

Table 5.1.

Structural properties of the 8-MR molecular sieve frameworks in this study (CHA, AEI, RTH).

Table 5.2.

Site and structural properties of H-form and Cu-form zeolites prior to hydrothermal aging

Table 2 Site and structural properties of H-form and Cu-form zeolites prior to hydrothermal aging

| Sample | Si/Al ratio <sup>a</sup> | Cu <sup>a</sup> wt% | Cu/Al ratio <sup>a</sup> | $V_{\text{ads,micro}}^b$ (cm <sup>3</sup> g <sup>-1</sup> ) | $V_{\text{ads,meso}}^b$ (cm <sup>3</sup> g <sup>-1</sup> ) | H <sup>+</sup> /Al ratio <sup>c</sup> | Al <sub>t</sub> /Al <sub>tot</sub> <sup>d</sup> | H <sup>+</sup> /Al <sub>t</sub> |
|--------|--------------------------|---------------------|--------------------------|---|--|---------------------------------------|---|---------------------------------|
| H-CHA  | 15                       | —                   | —                        | 0.18  | 0.04   | 0.95                                  | 0.85  | 1.10                            |
| Cu-CHA | 15                       | 0.7                 | 0.12                     | 0.17  | 0.05   | 0.72                                  | 0.90  | —                               |
| H-AEI  | 9.5                      | —                   | —                        | 0.20  | 0.01   | 0.85                                  | 0.85  | 1.00                            |
| Cu-AEI | 9.5                      | 1.7                 | 0.17                     | 0.19  | 0.01   | 0.54                                  | 0.91  | —                               |
| H-RTH  | 15                       | —                   | —                        | 0.20  | 0.05   | 0.60                                  | 0.94  | 0.61                            |
| Cu-RTH | 15                       | 0.7                 | 0.11                     | 0.17  | 0.04   | 0.38                                  | 0.98  | —                               |

<sup>a</sup> Elemental composition determined by atomic absorption spectroscopy (AAS). <sup>b</sup> Micropore and mesopore volumes determined from Ar adsorption isotherms (87 K) (Fig. S.2, ESI). <sup>c</sup> Number of H<sup>+</sup> sites quantified by selective NH<sub>3</sub> titration and temperature-programmed desorption.

<sup>d</sup> Fraction of tetrahedrally coordinated Al determined from <sup>27</sup>Al MAS NMR (Fig. S.3.1–S.3.3, ESI).

| Sample       | Exposure to<br>SCR gases | $V_{\text{ads,micro}}^a$<br>( $\text{cm}^3 \text{g}^{-1}$ ) | $V_{\text{ads,meso}}^a$<br>( $\text{cm}^3 \text{g}^{-1}$ ) | $\text{H}^+/\text{Al}_{\text{tot}}$<br>ratio <sup>b</sup> | $\text{Al}_\text{I}/\text{Al}_{\text{tot}}$ | Standard SCR rate<br>(per total Cu, 473 K) <sup>c</sup> | $E_{\text{app}}^d$<br>( $\text{kJ mol}^{-1}$ ) | NO<br>order <sup>e</sup> | O <sub>2</sub><br>order <sup>e</sup> | NH <sub>3</sub><br>order <sup>e</sup> |
|--------------|--------------------------|---|--|---|---|---|--|--------------------------|--------------------------------------|---------------------------------------|
| CHA          |                          |   |  |   |   |   |  |                          |                                      |                                       |
| H-Form       |                          | 0.18  | 0.04   | 0.95  | 0.85  |   |  |                          |                                      |                                       |
| Cu-Form      | Before                   | 0.17  | 0.05   | 0.72  | 0.90  |   |  |                          |                                      |                                       |
|              | After                    | 0.17  | 0.03   | 0.70  |   | 3.1   | $56 \pm 5$                                     | 0.4                      | 0.6                                  | -0.5                                  |
| Cu-Form aged | Before                   | 0.15  | 0.01   | 0.16  | 0.84  |   |  |                          |                                      |                                       |
|              | After                    | 0.15  | 0.07   | 0.14  |   | 2.2   | $51 \pm 5$                                     | 0.5                      | 0.4                                  | -0.1                                  |
| AEI          |                          |   |  |   |   |   |  |                          |                                      |                                       |
| H-Form       |                          | 0.20  | 0.01   | 0.85  | 0.85  |   |  |                          |                                      |                                       |
| Cu-Form      | Before                   | 0.19  | 0.01   | 0.54  | 0.91  |   |  |                          |                                      |                                       |
|              | After                    | 0.18  | 0.00   | 0.50  |   | 4.1   | $46 \pm 5$                                     | 0.5                      | 0.4                                  | -0.1                                  |
| Cu-Form aged | Before                   | 0.17  | 0.06   | 0.16  | 0.78  |   |  |                          |                                      |                                       |
|              | After                    | 0.16  | 0.02   | 0.15  |   | 1.9   | $49 \pm 5$                                     | 0.5                      | 0.4                                  | 0.0                                   |
| RTH          |                          |   |  |   |   |   |  |                          |                                      |                                       |
| H-Form       |                          | 0.20  | 0.05   | 0.60  | 0.94  |   |  |                          |                                      |                                       |
| Cu-Form      | Before                   | 0.17  | 0.04   | 0.38  | 0.98  |   |  |                          |                                      |                                       |
|              | After                    | 0.17  | 0.03   | 0.39  |   | 1.4   | $28 \pm 5$                                     | 0.4                      | 0.4                                  | -0.1                                  |
| Cu-form aged | Before                   | 0.17  | 0.10   | 0.07  | 0.72  |   |  |                          |                                      |                                       |
|              | After                    | 0.17  | 0.08   | 0.00  |   | n.d.*   | —  | —                        | —                                    | —                                     |

<sup>a</sup> Micropore and mesopore volumes determined from Ar adsorption isotherms (87 K) (Fig. 6). <sup>b</sup> Number of H<sup>+</sup> sites quantified by selective NH<sub>3</sub> titration and temperature-programmed desorption. <sup>c</sup> Units of  $10^{-3} \text{ mol NO (mol Cu)}^{-1} \text{ s}^{-1}$ . <sup>d</sup> Errors  $\pm 7 \text{ kJ mol}^{-1}$ . <sup>e</sup> Errors are  $\pm 0.1$ . \*n.d., not detectable ( $< 0.3 \times 10^{-3} \text{ mol NO (mol Cu)}^{-1} \text{ s}^{-1}$ ).

Table 5.3.

Site and structural properties of H-form zeolites, and of Cu-exchanged zeolites before and after hydrothermal aging, and before and after exposure to standard SCR gases. Standard SCR rates (473 K), apparent activation energies, and apparent reaction orders for Cu-form zeolites before and after hydrothermal aging treatments.

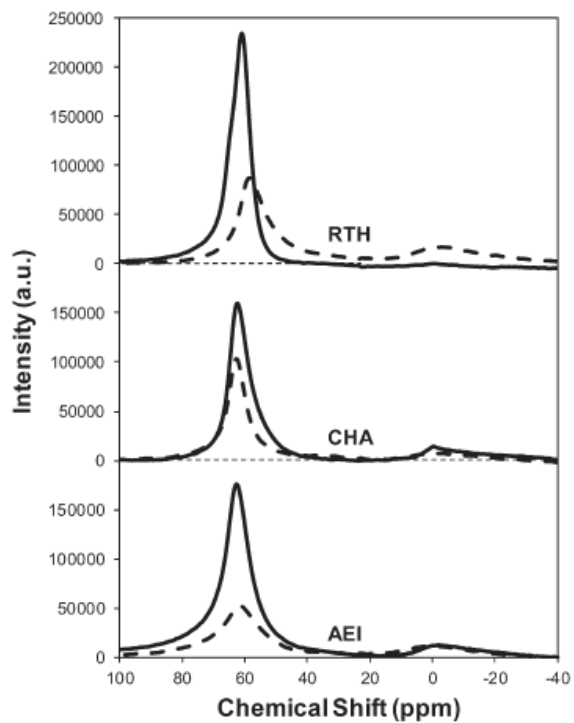


Figure 5.1.  $^{27}\text{Al}$  MAS NMR spectra of hydrated fresh (solid) and aged (dashed) Cu-form of RTH, CHA and AEI zeolites.



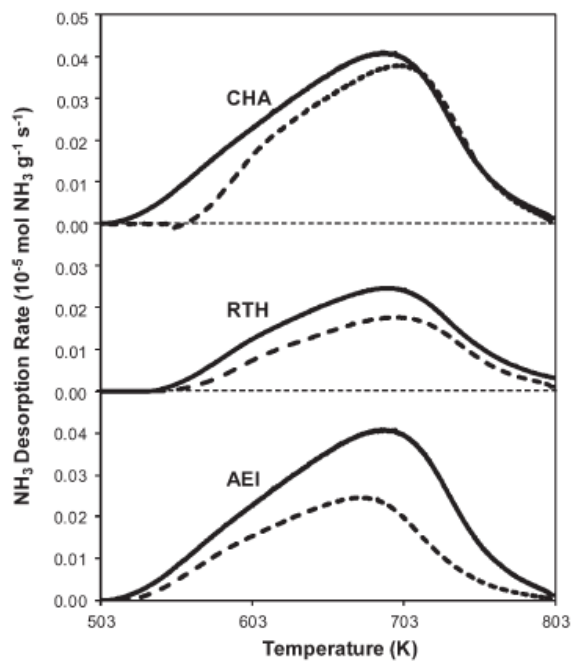


Figure 5.2.  $\text{NH}_3$  desorption rates as a function of temperature on H-form (solid) and fresh Cu-form (dashed) on AEI, CHA, and RTH zeolites.

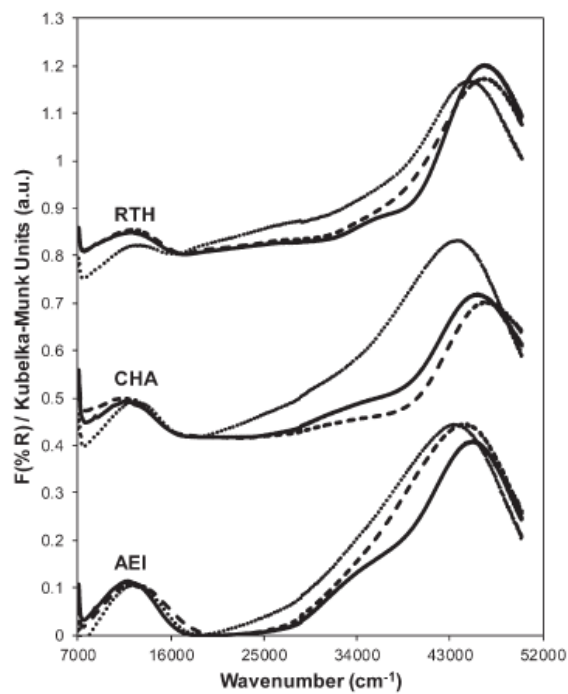


Figure 5.3. UV-vis spectra on hydrated fresh Cu-form before SCR (solid), aged Cu-form before SCR (dashed), and aged after SCR (dotted) on RTH, CHA and AEI zeolites. Spectra are offset for clarity (CHA: by 0.4 a.u., RTH: by 0.8 a.u.).

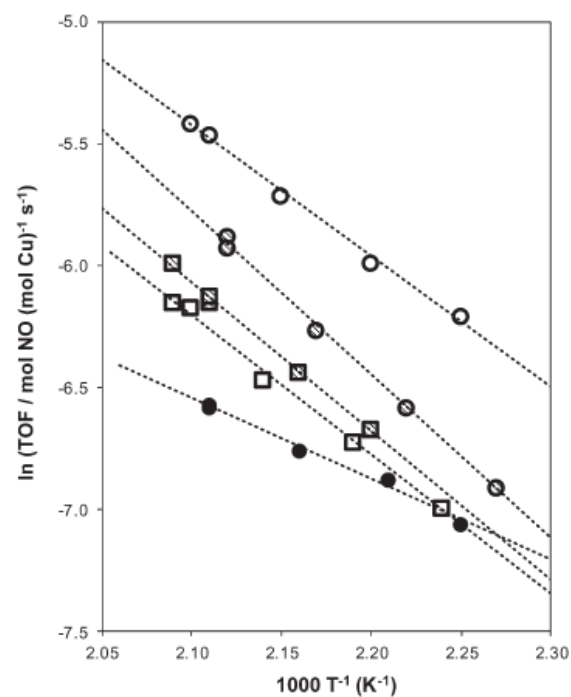


Figure 5.4. Dependence of standard SCR turnover rates (per Cu) on temperature for fresh (circles) and aged (squares) Cu-form AEI (hollow), CHA (cross hatched), and RTH (filled circles) zeolites.

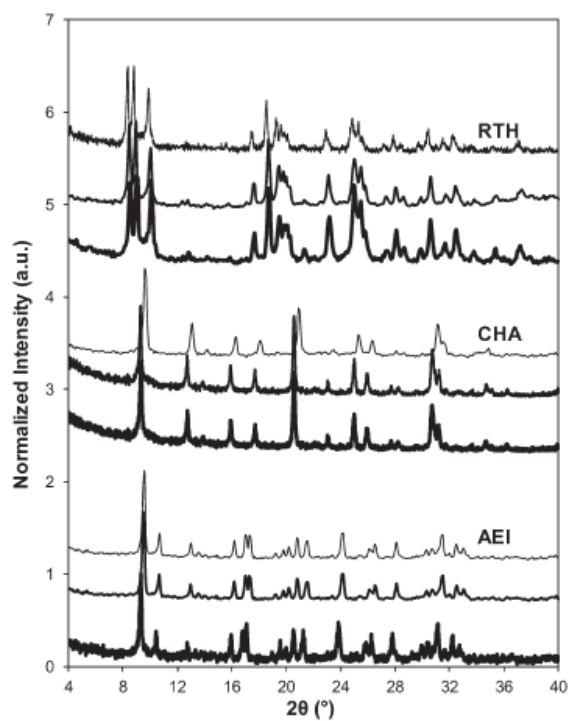


Figure 5.5. Powder XRD patterns of fresh Cu-form before SCR (dark), aged Cu-form before SCR (medium), and aged Cu-form after SCR (light) on AEI, CHA, and RTH zeolites. Diffraction patterns are normalized so that the maximum peak intensity in each pattern is unity, and offset for clarity.

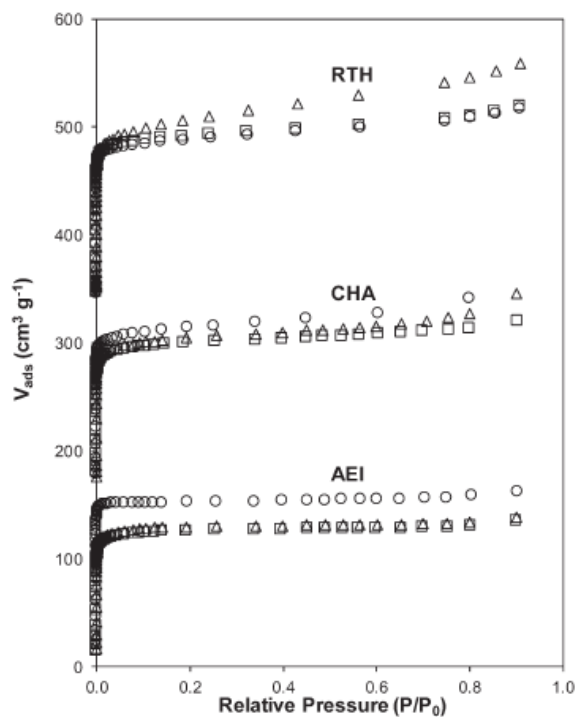


Figure 5.6. Ar adsorption isotherms (87 K) on fresh Cu-form before SCR (circles), aged Cu-form before SCR (triangles), aged Cu-form after SCR (squares) on AEI, CHA, and RTH zeolites. Isotherms are vertically offset for clarity (CHA: 160  $\text{cm}^3 \text{g}^{-1}$ , RTH: by 320  $\text{cm}^3 \text{g}^{-1}$ ).

## 5.7 Supporting Information

### 5.7.1 Powder X-ray diffraction patterns on H- and Cu-zeolites

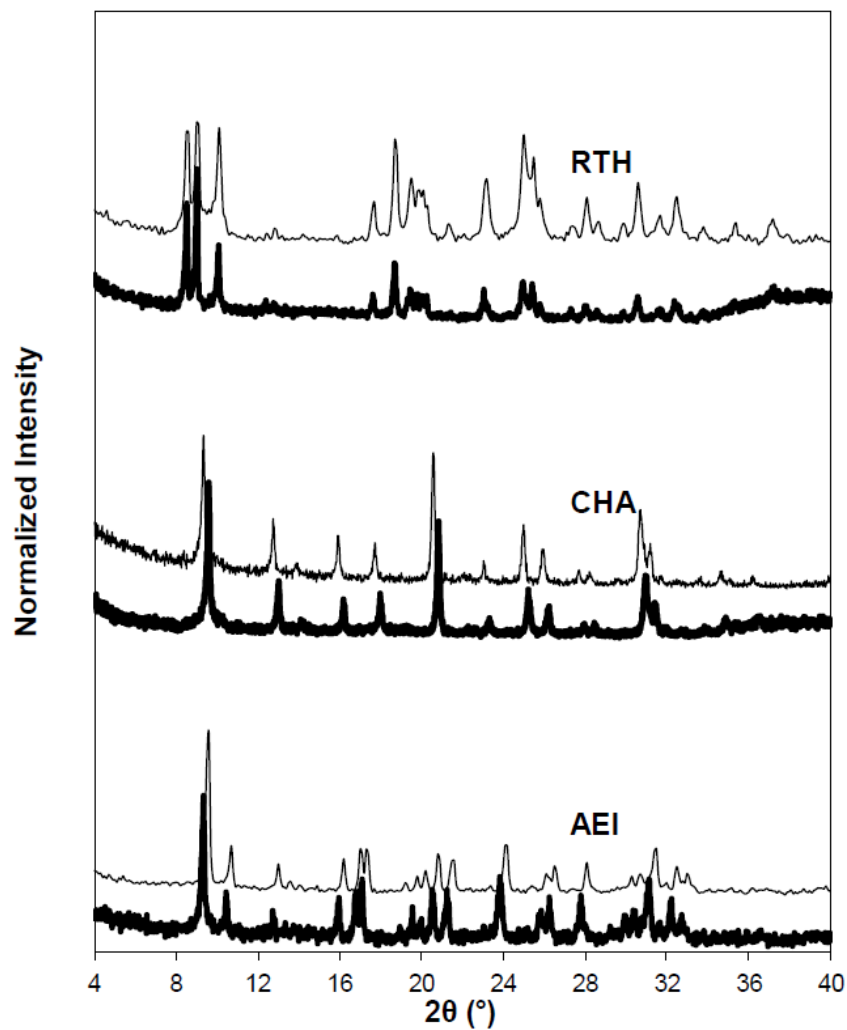


Figure 5.7. XRD patterns of H-form (dark) and Cu-form (light) AEI, CHA, and RTH zeolites. Diffraction patterns are normalized so that the maximum peak intensity in each pattern is unity.

### 5.7.2 Argon adsorption isotherms on H- and Cu-zeolites

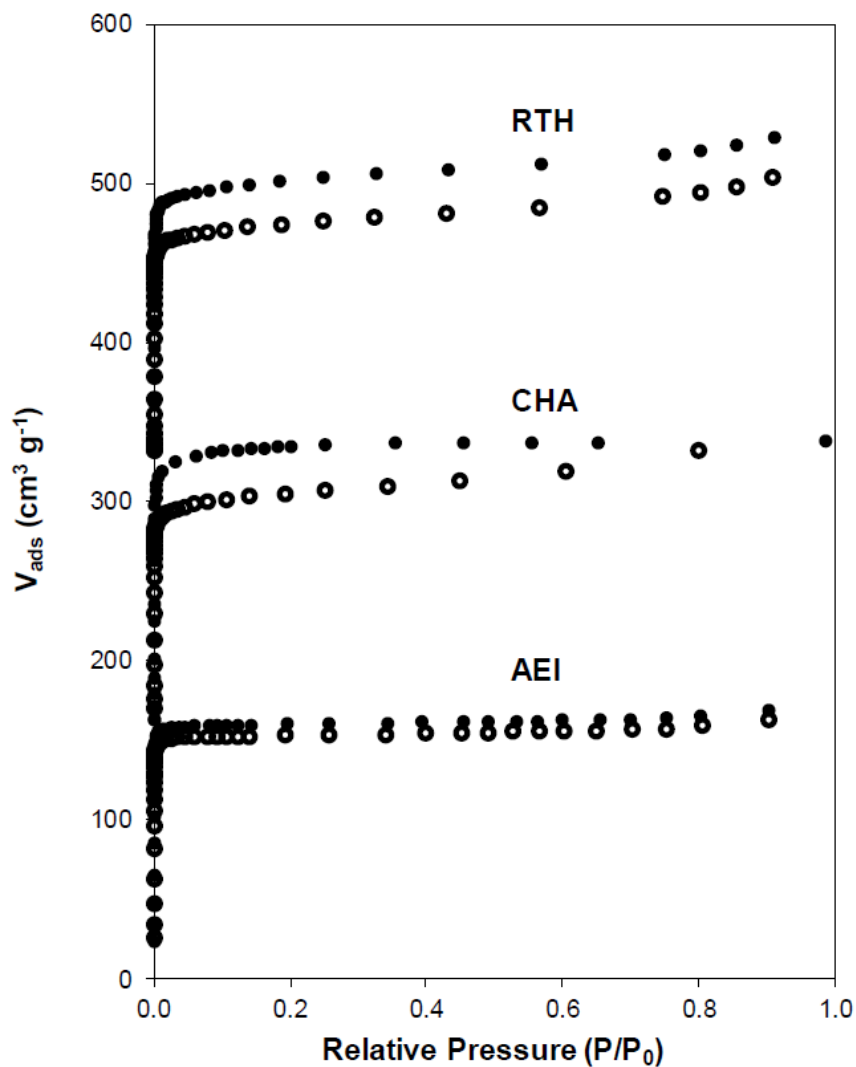


Figure 5.8. Ar adsorption isotherms (87 K) on H-form (filled) and Cu-form (open) RTH, CHA, and AEI zeolites. Adsorption isotherms are vertically offset (CHA:  $160 \text{ cm}^3 \text{ g}^{-1}$ , RTH:  $320 \text{ cm}^3 \text{ g}^{-1}$ ) for clarity.

### 5.7.3 $^{27}\text{Al}$ MAS NMR spectra on H- and Cu-zeolites

$^{27}\text{Al}$  MAS NMR spectra were measured on the H- and Cu-forms of the three zeolites in this study, AEI (Figure 5.9), CHA (Figure 5.10) and RTH (Figure 5.11),

in order to estimate the distribution of framework ( $\text{Al}_f$ ) and extra-framework ( $\text{Al}_{\text{ex}}$ ) Al species. NMR lines centered at 60 ppm were present for tetrahedral Al for RTH, and a small shoulder for penta-coordinated Al [286, 287] was present for CHA and AEI. The tetrahedral along with distorted tetrahedral and pentacoordinated Al NMR lines were integrated together to estimate the total number of  $\text{Al}_f$  species, although we recognize difficulties in quantifying  $\text{Al}_f$  content from NMR spectra, because some species can reversibly change between tetrahedral and octahedral coordination depending on the conditions of the measurement [118, 121, 122], and some extraframework alumina may also contain tetrahedrally-coordinated Al [118, 121, 122, 139, 286, 287]. The Al NMR lines centered at 0 ppm for octahedral Al were taken to reflect  $\text{Al}_{\text{ex}}$  species. Spectra of H- and Cu- form zeolites show Al incorporated predominantly into tetrahedral framework positions, with  $\text{Al}_f/\text{Al}_{\text{tot}}$  values given in Table 5.2 of the main text.



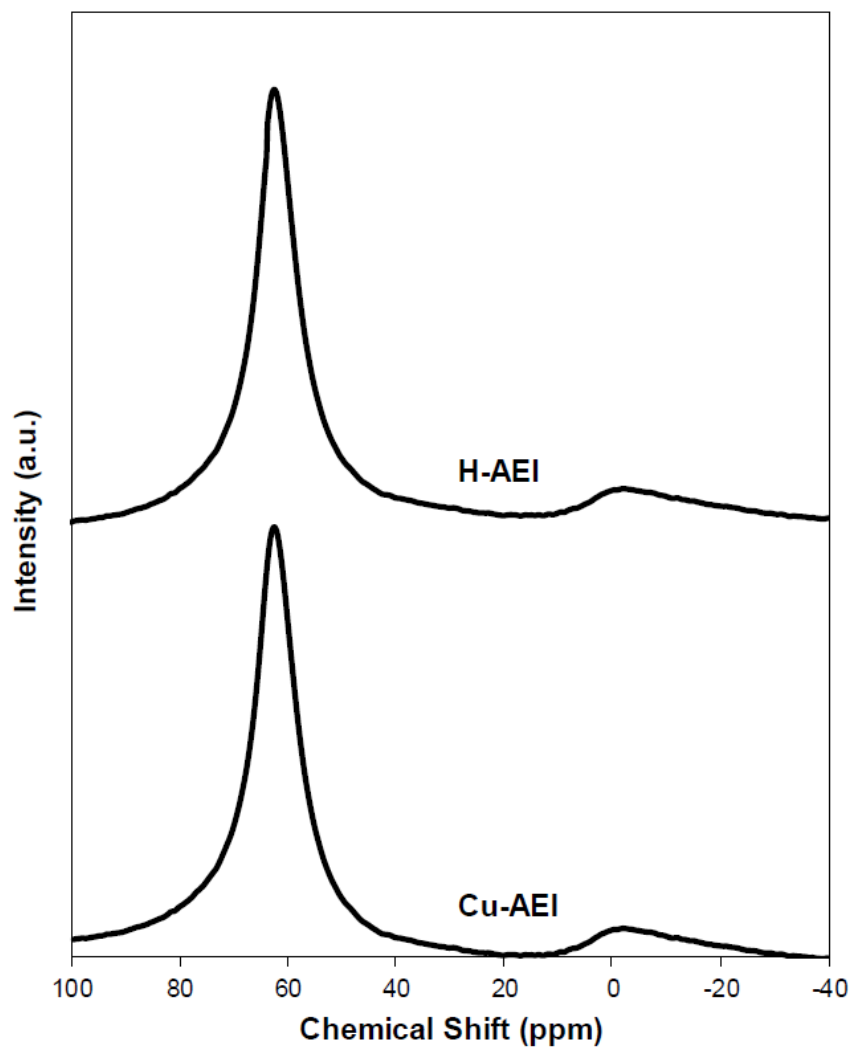


Figure 5.9.  $^{27}\text{Al}$  MAS NMR spectra of H-AEI and Cu-AEI.

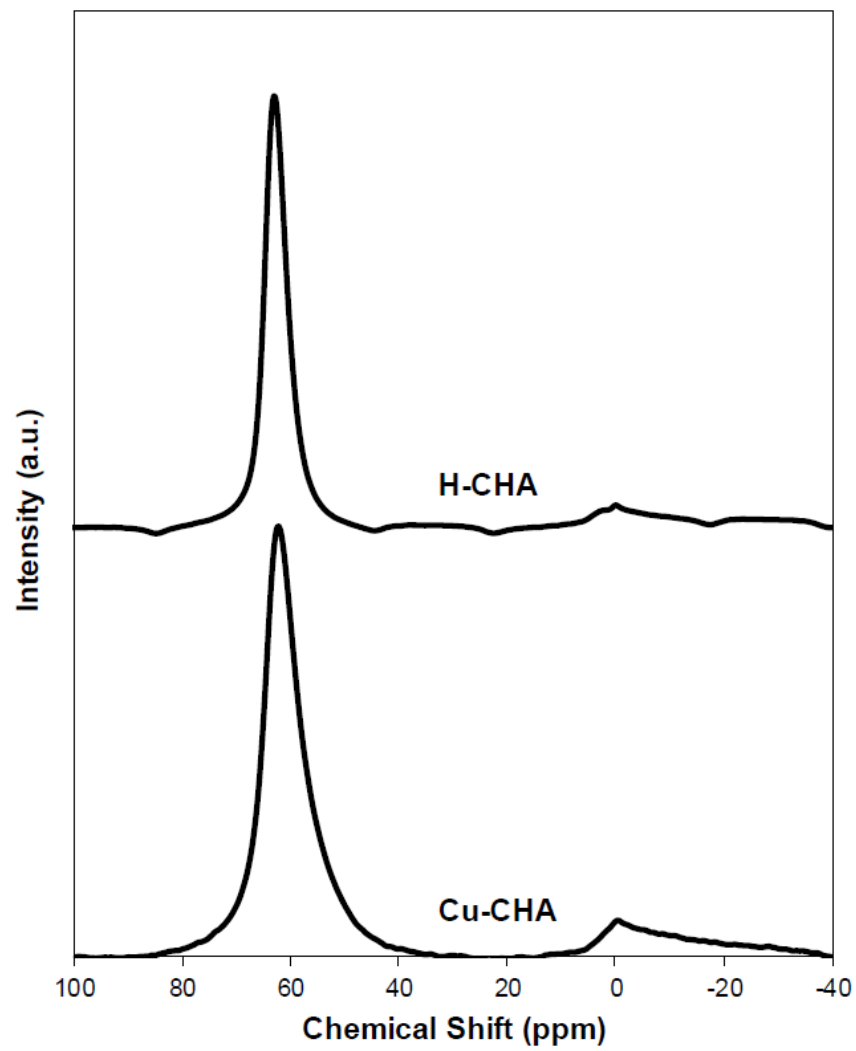


Figure 5.10.  $^{27}\text{Al}$  MAS NMR spectra of H-CHA and Cu-CHA.

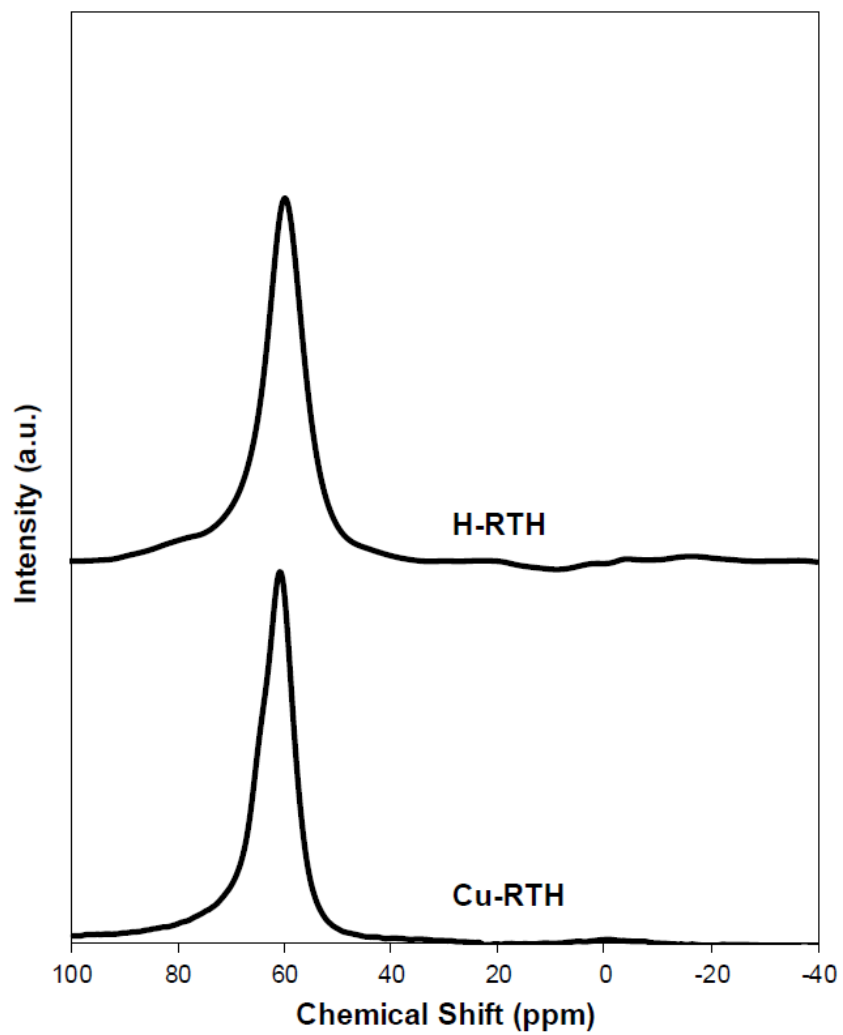


Figure 5.11.  $^{27}\text{Al}$  MAS NMR spectra of H-RTH and Cu-RTH.

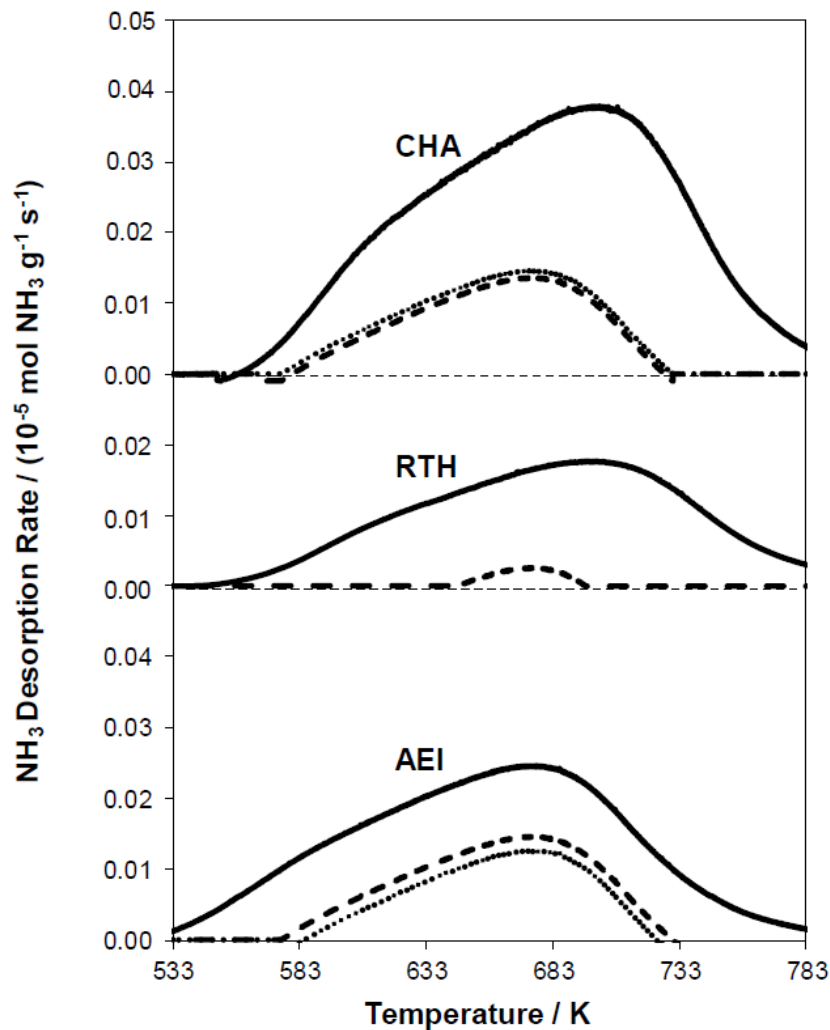
5.7.4 IR Spectra of H-RTH Before and After  $\text{NH}_3$  Exposure5.7.5  $\text{NH}_3$  TPD on Cu-zeolites

Figure 5.12.  $\text{NH}_3$  desorption rates as a function of temperature on fresh Cu-form after SCR (solid), aged Cu-form before SCR (dashed) and aged Cu-form after SCR (dotted) on CHA, RTH, and AEI zeolites.

*In situ* IR experiments were performed to monitor interactions of  $\text{H}^+$  sites in H-RTH (Si/Al = 15) with  $\text{NH}_3$ . H-RTH was pressed into a self-supporting wafer (ca. 0.40 g) and placed within an *operando* FTIR cell, using a procedure that has been

described elsewhere [288]. The sample was heated to 723 K and held for 2 h under  $50 \text{ cm}^3 \text{ min}^{-1}$  of 10%  $\text{O}_2$  (99.5%, Indiana Oxygen) and balance  $\text{N}_2$  (99.999% UHP, Indiana Oxygen), and then cooled to 433 K under flow (10%  $\text{O}_2$  and balance  $\text{N}_2$ ) to give the spectra (dark traces) in Figure 5.13 and reffig: Albarracin2016-SF7 (OH stretching region shown in Fig. 5.13, NH bending region shown in Fig. 5.14). The H-RTH wafer was then saturated in flowing  $\text{NH}_3$  (350 ppm, 3 h, 433 K), to give the spectra (light traces) in Figure 5.13. After  $\text{NH}_3$  saturation, Brønsted OH bands disappeared completely, and new IR bands for  $\text{NH}_4^+$  bending vibrations at  $1425 \text{ cm}^{-1}$  appeared concomitantly. These data indicate that all  $\text{H}^+$  sites in H-RTH were titrated by  $\text{NH}_3$ , and that the  $\text{H}^+/\text{Al}_f$  value of 0.61 measured in  $\text{NH}_3$  TPD experiments does not reflect a fraction of  $\text{H}^+$  sites that were inaccessible to  $\text{NH}_3$ .

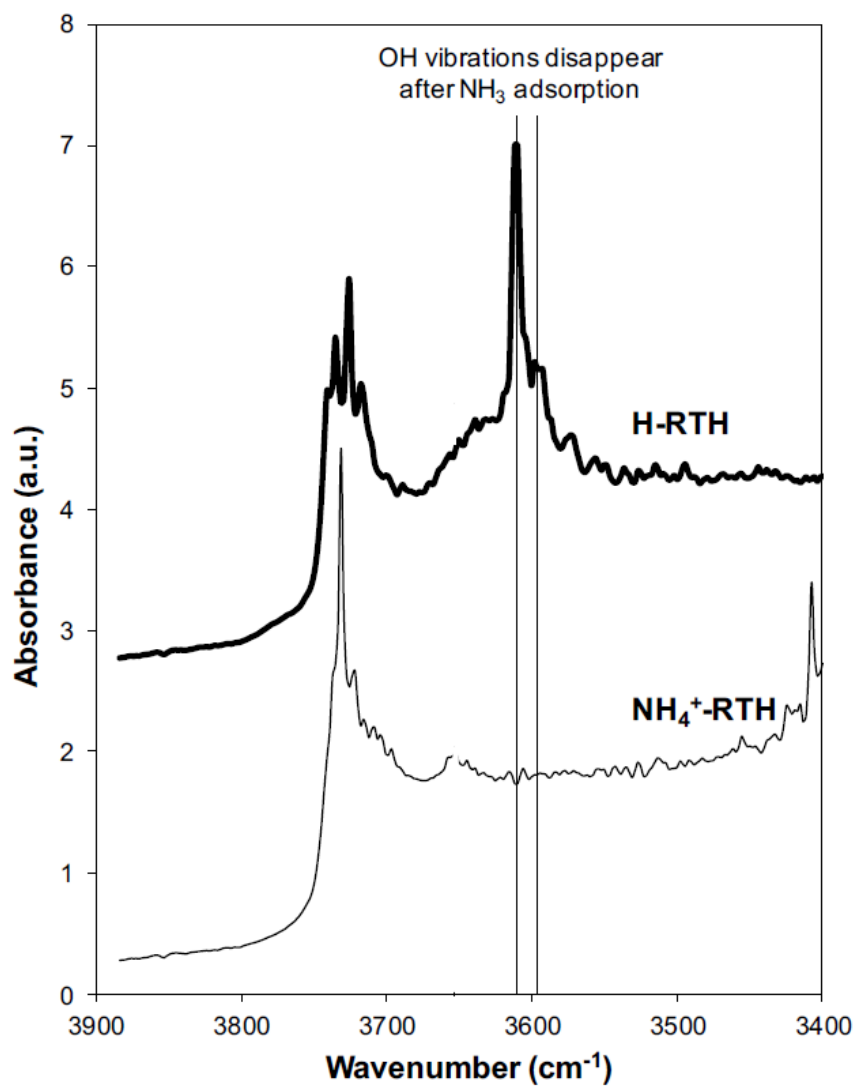


Figure 5.13. IR spectra (OH stretching region: 3400-3900 cm<sup>-1</sup>) of H-RTH at 433 K before (dark) and after (light) NH<sub>3</sub> saturation.

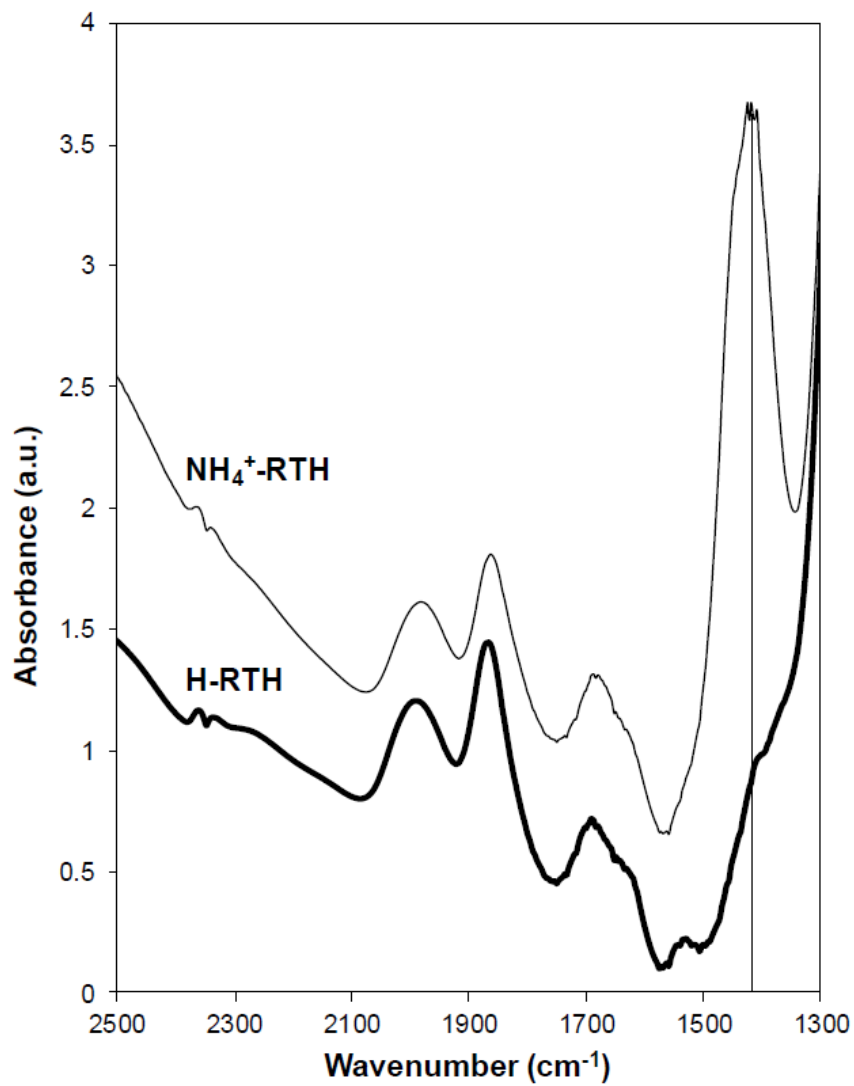


Figure 5.14. IR spectra (OH stretching region: 1300-2500  $\text{cm}^{-1}$ ) of H-RTH at 433 K before (dark) and after (light)  $\text{NH}_3$  saturation.





## 6. CATALYSIS IN A CAGE: CONDITION-DEPENDENT SPECIATION AND DYNAMICS OF EXCHANGED CU CATIONS IN SSZ-13 ZEOLITES

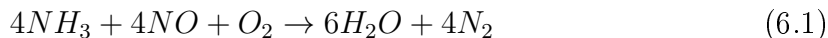
### 6.1 Introduction

In 1925 [289], Hugh Stott Taylor theorized that specific groups of atoms were responsible for the rate-enhancing capacity of heterogeneous catalyst surfaces, from which he coined the phrase “active site”. This concept has become ubiquitous in modern catalysis science and has proven indispensable to the emergence of rational catalyst design. Most catalytic solids, however, are structurally heterogeneous at the molecular scale. They contain a distribution of active sites of different catalytic reactivity [290–292] reflecting non-uniformities in active site coordination and local environment [293, 294], response to external stimuli [295, 296], and interactions with reacting molecules [297–300]. The integration of density functional theory (DFT) computational models and experimental spectroscopies measured *in operando* that interrogate active sites during catalysis can provide powerful insights into the coupling between active site composition, reaction environment, and reaction mechanism [301, 302]. In this work, we demonstrate how this approach enables the identification, quantification, and characterization of distinctly different active sites in a macro- and microscopically heterogeneous zeolite catalyst. We show through *operando* characterization that the composition and structure of active sites change dynamically during reaction, differ from their *ex situ* states, and that such reaction-environment-induced modifications are integral to observed catalytic performance.

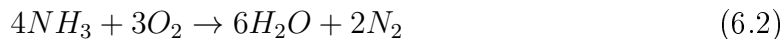
We demonstrate this capability in the context of Cu-exchanged zeolite catalysts. Zeolites are crystalline, nanoporous aluminosilicates constructed of corner-sharing  $\text{SiO}_4$  and  $\text{AlO}_4$  tetrahedra, or T-sites. Framework substitution of  $\text{Si}^{4+}$  by  $\text{Al}^{3+}$  introduces an anionic charge into the oxide lattice that must be charge-compensated

by extralattice cations. The Al sites are in general not ordered, so that at a given Si:Al ratio a zeolite presents a distribution of local Al environments [33, 303–306]. The common oxidation states of Cu are 1+ and 2+, and thus a single Cu ion can in principle charge-compensate one or two Al T-sites [307–314]. The exact form of this exchange and charge compensation can depend on Cu oxidation state, overall framework structure, and local Al siting. In addition, Cu is observed to form multi-nuclear oxo-complexes and oxide clusters that further enrich its exchange chemistry and catalysis [129, 315–319].

Cu-exchanged zeolites have been explored for a variety of hydrocarbon partial oxidations [317, 318, 320–330] and NOx reduction and decomposition chemistries [58, 331, 332]. Cu-zeolites have long been known to be active for the selective catalytic reduction (SCR) of NOx with NH<sub>3</sub> [92, 130, 133, 301, 333–338]. SCR catalysts promote the reduction of NOx by NH<sub>3</sub>:



over the competing and undesired oxidation of NH<sub>3</sub>:



Small pore Cu-exchanged SSZ-13, in particular, is able to satisfy all of the practical requirements of an SCR catalyst and is now in commercial use [89, 222, 249, 339]. However, the relationships between zeolite composition, reaction conditions, active site(s), and mechanism remain to be elucidated.

SSZ-13 has the chabazite topology. The single symmetry-distinct T-site organizes into four-, six-, and eight- membered rings (Figure 6.1, left) that form a cage ca. 0.8 nm in diameter [1]. SSZ-13 can be prepared in elemental compositions from highly enriched (Si:Al = 2) to infinitely dilute (Si:Al = ∞) in Al sites. The H-form (i.e., Al charge-compensated by H<sup>+</sup>) can be exchanged to various Cu:Al ratios, and the locations and forms of these exchanged Cu ions have received considerable attention [34, 36, 37, 39–41, 84, 91, 93, 129, 340–349]. X-ray absorption (XAS), UV-visible (UV-vis), and infrared spectra of zeolites [36, 37, 129, 328, 343, 349, 350] all

suggest exchanged Cu ions are present as hydrated and oxidized  $\text{Cu}^{\text{II}}(\text{H}_2\text{O})_6$  [351] at ambient conditions regardless of zeolite composition and topology.

The homogeneity of Cu sites under ambient conditions gives way to a rich variety of Cu species after high temperature and oxidative removal of  $\text{H}_2\text{O}$ . X-ray diffraction (XRD) reveals monomeric Cu ions in SSZ-13 that occupy either 6MR (A) sites [34,84], or both (A) and (B) sites [91,346] (Figure 6.1). We have reported that high Al content Cu-SSZ-13 zeolites ( $\text{Si}:\text{Al} = 5$ ) contain exclusively  $\text{Cu}^{\text{II}}$  in the (A) site under dry oxidizing conditions up to a  $\text{Cu}:\text{Al} = 0.20$  [37,85], as demonstrated through the 4-fold coordination of Cu with zeolitic oxygen in extended X-ray absorption fine structure spectra (EXAFS) and titrations of residual Brønsted acid sites that reveal a 2:1  $\text{H}^+:\text{Cu}^{2+}$  exchange stoichiometry. In contrast, Borfecchia et al. report 3-fold Cu coordination under similar conditions [39] on a  $\text{Si}:\text{Al} = 13$ ,  $\text{Cu}:\text{Al} = 0.44$  sample. Giordanino et al. report IR features attributable to Cu hydroxyl ( $[\text{Cu}^{\text{II}}\text{OH}]^+$ ) [36,39] on  $\text{Si}:\text{Al} = 13$ ,  $\text{Cu}:\text{Al} = 0.44$ , whereas Gao et al. only observe this band on a subset of  $\text{Si}:\text{Al} = 6$  samples [40]. DFT calculations generally indicate that isolated, unligated  $\text{Cu}^{\text{I}}$  and  $\text{Cu}^{\text{II}}$  ions prefer the A site (Figure 6.1, left) regardless of the location of Al [37,39,85,86,148,342,352–354].

$\text{H}_2$  temperature-programmed reduction (TPR) [40,248] experiments are consistent with the existence of at least two types of exchanged  $\text{Cu}^{\text{II}}$  with differing susceptibility to reduction. Borfecchia et al. similarly observe only a fraction of  $\text{Cu}^{\text{II}}$  ions to reduce in He at 673 K [39]. Chemical probes including NO,  $\text{NO}_2$ , and CO [41,248,355–359] will thus see a different mixture of Cu sites depending on sample history. For instance, NO adsorbs strongly on vacuum-reduced  $\text{Cu}^{\text{II}} \rightarrow \text{Cu}^{\text{I}}$  sites [248,355] but more weakly and dynamically on  $\text{Cu}^{\text{II}}$  sites [85,340]. The relevance of these *ex situ* probes to catalytic conditions has yet to be established.

Standard SCR is a redox reaction, as evidenced by the observation of both  $\text{Cu}^{\text{I}}$  and  $\text{Cu}^{\text{II}}$  in *operando* experiments [41,86,360], and thus the *ex situ* reducibility of catalysts might be expected to correlate with observed activity. However, catalysts with different *ex situ* properties exhibit similar SCR characteristics. Reactant cutoff

experiments demonstrate that both NO and NH<sub>3</sub> are necessary for the Cu<sup>II</sup> → Cu<sup>I</sup> reduction half-cycle across samples of various compositions [41,85]. Apparent activation energies are the same (ca. 70 kJ mol<sup>-1</sup>), and 473 K SCR turnover rates are linear in Cu content (Cu:Al = 0.08-0.20) on Si:Al = 5 samples [37,85,361]. Samples with compositions nearer to those studied by Borfecchia et al. present the same Cu<sup>I</sup>/Cu<sup>II</sup> fractions in *operando* XAS [41] and apparent activation energies [40] similar to those of the Si:Al = 5 samples but different susceptibilities to Cu reduction in H<sub>2</sub> TPR [40].

Thus, while there is general agreement that various isolated, exchanged Cu ions are present and contribute to the SCR catalysis, the precise nature, number, and reactivity of different cationic species, their dependence on zeolite composition (Si:Al and Cu:Al ratios) and framework topology, sample treatment history and environment, and their spectroscopic signatures under *ex situ* versus *in situ* conditions remain unknown. Here, we report a coordinated computational (stochastic simulation, ab initio dynamics, and free energy) and experimental (synthetic, spectroscopic, and titrimetric) analysis of Cu speciation under *ex situ* conditions and *in situ* and *operando* SCR conditions as a function of catalyst composition over a wide range of zeolite chemical composition space. We demonstrate that the types, numbers, and chemical characteristics of Cu sites depend on bulk composition of the zeolite, can be predicted through first-principles-based models, can be distinguished in the laboratory, and depend strongly on the environmental conditions. Environmental conditions have a profound impact on Cu ion siting, coordination, and mobility, resulting in SCR turnover rates (473 K) that are independent of the initial Cu cation site and the zeolite framework type. The results rationalize a large body of literature, resolve contradictory findings regarding the active sites for NO<sub>x</sub> SCR, and consolidate the understanding of Cu cation speciation in zeolites.

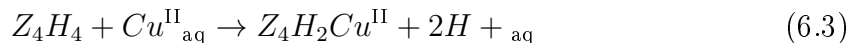
## 6.2 Results and Discussion

### 6.2.1 Cu Cation Speciation in Cu-SSZ-13.

#### First-Principles Speciation of Cationic Cu Complexes.

We first created molecular models for isolated Cu exchange sites in SSZ-13 and established their relative free energies under wet and oxidizing conditions relevant to Cu exchange and catalyst treatment; computational details can be found in section 6.5.3. We used a 12 T-site supercell [37,85,86] with a single Al framework. Charge-compensating  $\text{Cu}^I$  ions prefer to sit in the plane of the 6MR [37,85,86,352], and we label this structure as  $[\text{ZCu}^I]$  in Figure 6.1 to denote charge-compensation of a single Al (Z) by Cu. This notation also emphasizes the formal 1+ oxidation state of Cu, and this structure is used as the  $\text{Cu}^I$  reference in relating computed Bader charges to effective Cu oxidation states. An oxidized form of the Cu site compensating a single framework Al atom has been proposed [39,41,344] to be formed by addition of an extra-lattice OH ligand, which redirects the Cu into the 8MR according to the optimized  $[\text{ZCu}^{\text{II}}\text{OH}]$  structure shown in Figure 6.1.

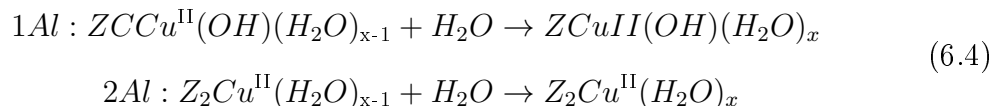
Similarly, two proximal framework Al atoms (2Al sites) can be charge compensated by a single  $\text{Cu}^{\text{II}}$  ion. The exchange energies of  $\text{Cu}^{\text{II}}$  at different potential 2Al sites were previously computed using a 2 x 1 x 1 24 T-site supercell containing 4 Al atoms distributed to place 2Al sites in each of the 4, 6, and 8MR [37]:



$\text{Cu}^{\text{II}}$  exchange at 2Al sites in the 6MR ring is 108 and 145 kJ mol<sup>-1</sup> more exothermic than exchange at 2Al sites in the 4MR and 8MR, respectively. We adopt a model with 2Al at third nearest-neighbor (3NN) positions in a 6MR for Cu near 2Al. Cu exchange at the 2NN Al 6MR is coordinatively similar and the exchange energy more endothermic by 22 kJ mol<sup>-1</sup>. The 3NN Al 6MR structure is labeled  $[\text{Z}_2\text{Cu}^{\text{II}}]$  in Figure 6.1 and is taken as the Bader charge standard for the  $\text{Cu}^{\text{II}}$  oxidation state. We previously found that this  $[\text{Z}_2\text{Cu}^{\text{II}}]$  site can be reduced by addition of H to an Al site proximal to Cu [85], which is the  $[\text{ZH}]/[\text{ZCu}^I]$  species shown in Figure 6.1.

The forward slash emphasizes that these two sites are proximal. Reduction to  $\text{Cu}^I$  decreases Cu coordination to the lattice but preserves Cu location within the 6MR.

Motivated by XAS [37,307,343] and molecular dynamics [362] evidence that exchanged  $\text{Cu}^{\text{II}}$  ions are hydrated under ambient conditions, we first explored  $\text{H}_2\text{O}$  coordination to the  $[\text{Z}_2\text{Cu}^{\text{II}}]$  and  $[\text{ZCu}^{\text{II}}\text{OH}]$  ions by computing the structures and successive adsorption energies of  $\text{H}_2\text{O}$  ligands ( $x = 1-6$ ):

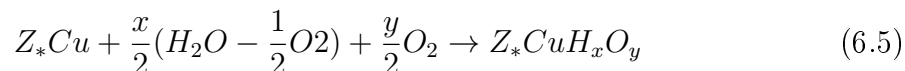


In each simulation, we started from the equilibrated ( $x - 1$ )  $\text{H}_2\text{O}$  structure, added another  $\text{H}_2\text{O}$  molecule, annealed for 150 ps at 473 K using NVT ab initio molecular dynamics (AIMD) at the GGA level, then subsequently optimized the geometry and evaluated the energy with the HSE06 functional including Tkatchenko Scheffler van der Waals (TSvdw) corrections (section E.2), and zero-point vibrational energies (ZPE) (Supporting Information 6.8.1). Energy and Cu coordination number (CN) results are summarized in Table 6.1, where CN is defined as the number of heavy atoms within 2.3 Å of Cu.  $\text{H}_2\text{O}$  adsorption energies are on the order of -70 to -90 kJ mol<sup>-1</sup> and are generally more exothermic on  $[\text{Z}_2\text{Cu}^{\text{II}}]$  than on  $[\text{ZCu}^{\text{II}}\text{OH}]$  sites. The computed Cu oxidation state is insensitive to added  $\text{H}_2\text{O}$ . On  $[\text{Z}_2\text{Cu}^{\text{II}}]$ , successive  $\text{H}_2\text{O}$  ligands generally displace framework oxygen ( $\text{O}_f$ ) from the first coordination sphere, until at  $x = 4$  the  $\text{Cu}^{\text{II}}$  ion is fully coordinated by  $\text{H}_2\text{O}$ ; additional  $\text{H}_2\text{O}$  molecules form a second coordination sphere through hydrogen bonds to first shell  $\text{H}_2\text{O}$ . With hydration, the Cu ion moves from within the 6MR (site A, Figure 6.1) to the 8MR (site B) to the cage center (site C). The final optimized  $x = 6$  structure is shown in Figure 6.1. The  $[\text{ZCu}^{\text{II}}\text{OH}]$  site behaves similarly with added  $\text{H}_2\text{O}$ ; the fully hydrated complex is shown in Figure 6.1.

Exchanged Cu may lose waters of hydration and acquire other ligands during synthesis and after oxidation or reduction treatments. We computed the structures and energies of various combinations of O, OH,  $\text{H}_2\text{O}$ , and  $\text{O}_2$  ligands on both the 1Al and the 2Al models in the nominally oxidized and reduced states. The list of candidate

structures was guided by chemical plausibility and includes proposed intermediate species reported elsewhere (e.g.,  $\text{Cu}^{\text{II}}\text{O}$ ,  $\text{Cu}^{\text{II}}(\text{OH})_2$ ) [86, 363]. Optimized structures, energies, and ZPEs of all 26 species are tabulated in Supporting Information 6.8.1.

We applied a first-principles thermodynamic analysis to rank the stability of this library of Cu-bound  $\text{H}_x\text{O}_y$  species as a function of temperature and hydrogen and oxygen potentials. We take  $\text{O}_2$  and  $\text{H}_2\text{O}$  as the oxygen and hydrogen references, respectively:



used the HSE06-TSvdw energies, and applied previously developed correlations [85] to estimate adsorbate entropies. The formation free energies ( $\Delta G_{\text{form}}$ ) are computed according to section E.2 and the  $\mu\text{H}_2\text{O}$  and  $\mu\text{O}_2$  related to T and P through the ideal gas relation. Results for an ambient condition (condition 1, 298 K, 2%  $\text{H}_2\text{O}$ , and 20%  $\text{O}_2$ ) representative of an air-exposed catalyst and an elevated temperature condition (condition 2, 673 K, 2%  $\text{H}_2\text{O}$ , and 20%  $\text{O}_2$ ) representative of an oxidation pretreatment are summarized in Figure 6.2. For clarity, species with  $\Delta G_{\text{form}} > +200$  kJ mol<sup>-1</sup> are not shown in condition 2. The relative energy alignment between Cu near 1Al and 2Al is described in section 6.2.1.

At the high temperatures (673 K) and high oxygen potentials (20%  $\text{O}_2$ ) of condition 2, the lowest free energy structure near the 2Al site is the isolated  $[\text{Z}_2\text{Cu}^{\text{II}}]$  ion. At these conditions, adsorption of a single  $\text{H}_2\text{O}$  ligand is endergonic by 15 kJ mol<sup>-1</sup>, and the reduced form of the Cu site ( $[\text{ZCu}^{\text{I}}]/[\text{ZH}]$ ) is endergonic by another 15 kJ mol<sup>-1</sup>. Other adsorbates on Cu sites near 2Al lead to complexes much higher in free energy, including adsorbed molecular  $\text{O}_2$ . Similarly, on Cu sites near 1Al, the lowest free energy structure is oxidized  $[\text{ZCu}^{\text{II}}\text{OH}]$  with normalized Bader charge (Supporting Information 6.8.1) of +1.8, slightly less than  $[\text{Z}_2\text{Cu}^{\text{II}}]$ . The reduced form of the site,  $[\text{ZCu}^{\text{I}}]$ , and its hydrated form,  $[\text{ZCu}^{\text{I}}(\text{H}_2\text{O})]$ , are very close in free energy to the oxidized  $[\text{ZCu}^{\text{II}}\text{OH}]$  state. Molecular  $\text{O}_2$  adsorption on the  $[\text{ZCu}^{\text{I}}]$  site is endergonic by 50 kJ mol<sup>-1</sup> relative to  $[\text{ZCu}^{\text{II}}\text{OH}]$ , and even higher in free energy are other oxidized forms, including  $[\text{ZCu}^{\text{II}}\text{O}]$  [363] and  $[\text{ZCu}^{\text{II}}(\text{OH})_2]$  [85]. The primary effect of

decreasing temperatures to ambient (condition 1) is a significant decrease in the free energies of all hydrated Cu states, which causes the most stable species to become the fully hydrated  $Z_2[Cu^{II}(H_2O)_4](H_2O)_2$  and  $Z[Cu^{II}(OH)(H_2O)_3](H_2O)_3$  complexes at 2Al and 1Al sites, respectively.

We generalize the analysis in Figure 6.2 to a range of temperatures and  $O_2$  pressures at fixed  $H_2O$  partial pressure (2%) and plot the lowest free energy species at each set of conditions in Figure 3 in the form of a phase diagram. For reference, conditions 1 and 2 of Figure 6.2 are labeled with red boxes on Figure 6.3. The phase diagrams are insensitive to the  $H_2O$  pressure over the range of experimental interest. For comparison, we report the corresponding T- $P_{H_2O}$  diagram in Supporting Information 6.8.2. As discussed below, these diagrams indicate that the stable Cu state (CN,  $O_f$ , and oxidation state) depends sensitively on the environmental conditions over ranges of experimental interest and that the lowest free energy species differ for Cu complexes that charge compensate 1Al or 2Al sites.

#### 1Al and 2Al Cu Exchange Populations.

To this point, we have treated the 1Al and 2Al sites independently. To place these two on a common energy scale, we computed the Cu exchange energy between the two sites:



We evaluated this energy in a large supercell containing separated  $Z_2$  and Z sites as well as in separate supercells constructed to conserve atomic numbers; results are in close agreement (+66 vs +69 kJ mol<sup>-1</sup>), and structures are given in Supporting Information 6.8.3. We used the +66 kJ mol<sup>-1</sup> result to offset the 0 K energies of  $[Z_2Cu^{II}H_2O]$  and  $[ZCu^{II}OH]$  and thus place the two site types on the same free energy y-axis shown in Figure 6.2. The zero of energy is defined as  $[ZCu^I]$ . The free energy associated with Cu near 2Al is substantially lower than that with Cu near 1Al at



both 298 K (-142 kJ mol<sup>-1</sup>) and 673 K (-55 kJ mol<sup>-1</sup>). These results indicate that Cu ions prefer to segregate to 6MR 2Al exchange sites over a wide range of conditions.

The relative density of Cu ions in 6MR 2Al sites and in 8MR 1Al sites will depend on the total Cu content and the number of such 2Al and 1Al sites present in a given SSZ-13 sample. We determined the Al distribution as a function of Si:Al ratio by numerical simulation [37,302] assuming random Al distribution subject to Lowenstein's rule [235], which prohibits 1NN Al pairs. We then assume that exchanged Cu ions populate all available 2NN and 3NN 2Al sites as [Z<sub>2</sub>Cu<sup>II</sup>] before occupying 1Al sites as [ZCu<sup>II</sup>OH]. Figure 6.4 reports the computed fraction of Cu present as [ZCu<sup>II</sup>OH] as a function of Si:Al and Cu:Al ratios. The region below the white line corresponds to a composition space containing exclusively Cu species near 2Al, while the region above the white line contains gradually increasing [ZCu<sup>II</sup>OH] fractions that become the dominant species in the upper right red area. To ensure 2Al 6MR stays charge compensated by a single Cu past the saturation point, we computed the energy of two [ZCu<sup>II</sup>OH] in a 6MR (Supporting Information 6.8.3):



Thus, these 6MR 2Al sites will remain populated by [Z<sub>2</sub>Cu<sup>II</sup>] as additional Cu is exchanged in the form of [ZCu<sup>II</sup>OH].

To test these model predictions, we prepared and analyzed a series of SSZ-13 catalysts of varying Si:Al and Cu:Al ratio (samples represented by white circles in Figure 6.4). An Al-rich SSZ-13 sample (Si:Al = 5) was synthesized using high Al FAU zeolite as the Al source [162] and characterized as reported previously [37,78,85,129,171] while lower Al content SSZ-13 samples (Si:Al = 15, 25) were synthesized using Al(OH)<sub>3</sub> as the Al source [84]. Powder XRD patterns (Supporting Information 6.8.4) and Ar adsorption isotherms (87 K, Supporting Information 6.8.26) were consistent with the CHA topology on all H-form SSZ-13 samples. The number of H<sup>+</sup> sites on each H-SSZ-13 sample was quantified from the NH<sub>3</sub> evolved during TPD of NH<sub>4</sub>-form samples, and were 0.65, 1.02, and 0.98 H<sup>+</sup>:Al for the Si:Al ratios of 5, 15, and 25, respectively. The high Al H-SSZ-13 sample (Si:Al = 5) contained fewer

H<sup>+</sup> sites than its number of framework Al atoms (H<sup>+</sup>:Al<sub>f</sub> = 0.76),<sup>102</sup> reflecting the imprecision with which *ex situ* methods such as <sup>27</sup>Al MAS NMR spectroscopy may characterize structural surrogates for H<sup>+</sup> sites. It also reflects the nonuniformity of SSZ-13 samples prepared using FAU to CHA interconversion methods [162], for which repeat synthesis experiments crystallized samples that contained H<sup>+</sup>:Al ratios that varied between 0.45 and 0.85 (Supporting Information 6.8.7).

Increasing amounts of Cu were exchanged into these three (Si:Al = 5, 15, 25) H-SSZ-13 samples from aqueous-phase Cu<sup>II</sup>(NO<sub>3</sub>)<sub>2</sub>. The number of residual H<sup>+</sup> sites was quantified using NH<sub>3</sub> TPD, which was performed after samples were saturated with gaseous NH<sub>3</sub> (433 K) and purged in wet helium (3% H<sub>2</sub>O, 433 K) to desorb Lewis acid-bound NH<sub>3</sub> and selectively retain NH<sub>4</sub><sup>+</sup> species [171], as illustrated by eq 6.8:

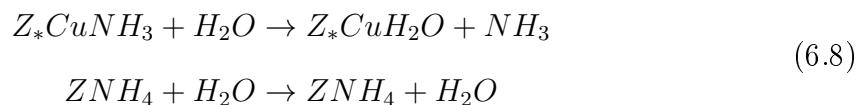
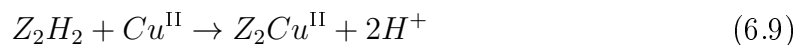
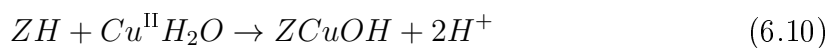


Figure 6.5 shows the number of residual H<sup>+</sup> sites present on each Cu-SSZ-13 sample after oxidative treatment in flowing air (773 K), normalized by the number of H<sup>+</sup> sites quantified on their respective H-SSZ-13 parent samples after the same oxidative treatment, as a function of Cu:Al ratio. The dashed lines in Figure 6.5 represent the number of residual H<sup>+</sup> sites as a function of Cu:Al ratio predicted from the simulation results in Figure 6.4. At a Si:Al ratio of 5, each exchanged Cu cation decreased the number of residual H<sup>+</sup> sites by two (on average) up to a Cu:Al ratio of 0.20 (Figure 6.5) [78, 171], consistent with the exchange stoichiometry:



On samples with Si:Al ratios of 15 and 25, each exchanged Cu exchanged two H<sup>+</sup> sites until Cu:Al ratios of 0.10 and 0.04, respectively, but only one additional H<sup>+</sup> site beyond this limit (Figure 6.5), consistent with the exchange reaction:



These Cu:H<sup>+</sup> exchange stoichiometries provide experimental evidence that cationic Cu species exchange sequentially as [Z<sub>2</sub>Cu<sup>II</sup>] sites until saturation and then as [ZCu<sup>II</sup>-OH] sites (Figure 6.2).

Figure 6.6 shows FTIR quantification of the disappearance of Brønsted ZH species and the appearance of [ZCu<sup>II</sup>OH] as a function of Cu density on the series of Cu-SSZ-13 samples with Si:Al = 15. The H-SSZ-13 spectrum includes four features in the O-H region, including modes at 3605 and 3580 cm<sup>-1</sup> [364, 365] from Brønsted sites, at 3732 cm<sup>-1</sup> from isolated silanols, and at 3700 cm<sup>-1</sup> from vicinal silanols [366]. The integrated area of the Brønsted ZH peaks of the Cu:Al 0.12 sample, taking that of the H-SSZ-13 sample as the baseline, decreased with a 2:1 H<sup>+</sup>:Cu ratio (Supporting Information 6.8.6), consistent with eq 6.9. A new, fifth feature appears at 3660 cm<sup>-1</sup> in Cu:Al > 0.21 samples, at a location consistent with previous assignment to [39] and the computed harmonic O-H stretch frequency of [ZCu<sup>II</sup>OH]. The integrated area of this 3660 cm<sup>-1</sup> band increases linearly across the range Cu:Al = 0.21-0.44 (Figure 6.6, inset), and the integrated areas of the Brønsted OH stretches decrease concurrently in a 1:1 H<sup>+</sup>:Cu ratio, consistent with eq 6.10. These vibrational data provide strong additional support for the sequential population of [Z<sub>2</sub>Cu<sup>II</sup>] followed by [ZCu<sup>II</sup>OH] sites.

Co<sup>II</sup> exchange provides a third independent enumeration of the number of 2Al 6MR sites on each sample, because Co<sup>II</sup> does not exchange at single Al sites as [ZCo<sup>II</sup>OH] at the exchange pH used here (pH ca. 3.2) [367]. Samples with Si:Al ratios 5, 15, and 25 were saturated with Co<sup>II</sup>, and the Co:Al contents were determined by atomic absorption (Supporting Information 6.8.5) to be 0.19, 0.10, and 0.04, respectively. These values agree quantitatively with the maximum number of 2Al 6MR sites predicted for each Si:Al ratio in Figure 6.4 for a random Al distribution in SSZ-13. Furthermore, the numbers of residual of H<sup>+</sup> sites on Co-saturated SSZ-13 samples were quantified by NH<sub>3</sub> titration and are plotted on Figure 6.5 as filled symbols, and agree quantitatively with the transition Cu:Al ratios between exchange of [Z<sub>2</sub>Cu<sup>II</sup>] and [ZCu<sup>II</sup>OH] species. These results indicate that isolated Co<sup>II</sup> and Cu<sup>II</sup> exhibit

identical preferences for 2Al 6MR sites and that both cations replace two Brønsted sites via eq 6.9 when exchanged at these sites.

The Cu:Al values that demarcate the transition between formation of  $[\text{Z}_2\text{Cu}^{\text{II}}]$  sites and  $[\text{ZCu}^{\text{II}}\text{OH}]$  sites are 0.20, 0.10, and 0.04 for the H-SSZ-13 samples with Si:Al ratios of 5, 15, and 25, respectively (Figure 6.5). These Cu:Al values are identical, within error, to the fraction of 2Al 6MR sites predicted from simulation of Al distribution in CHA frameworks at these Si:Al ratios (Figure 6.4). Taken together, these experimental and computational findings indicate that under the conditions of synthesis applied here [42], the concentration of 2Al 6MR sites is in agreement with a random Al distribution in SSZ-13 subject to Lowenstein’s rule, that 2Al 6MR are the preferred sites for  $\text{Cu}^{\text{II}}$  exchange, and that these sites saturate before remaining 1Al sites are populated with  $[\text{ZCu}^{\text{II}}\text{OH}]$ . This quantification allows us to identify and contrast the structures, properties, and catalytic performance under low-temperature (473 K) standard SCR conditions of samples that contain predominantly  $[\text{Z}_2\text{Cu}^{\text{II}}]$  or  $[\text{ZCu}^{\text{II}}\text{OH}]$  sites. We choose a sample with Si:Al = 5 and Cu:Al = 0.08 to represent a  $[\text{Z}_2\text{Cu}^{\text{II}}]$  site and a sample with Si:Al = 15 and Cu:Al = 0.44, similar in composition to that explored by others [36, 39, 41] to represent  $[\text{ZCu}^{\text{II}}\text{OH}]$ . We refer to these as the “2Al” and “1Al” samples, respectively. While the 1Al sample contains ca. 20%  $[\text{Z}_2\text{Cu}^{\text{II}}]$  sites, they are in the minority, and the bulk spectroscopic techniques applied here are primarily sensitive to the majority  $[\text{ZCu}^{\text{II}}\text{OH}]$  site.

### 6.2.2 Copper Cation Structure under *ex situ* Conditions.

We next combined XAS and AIMD simulations to explore the molecular and electronic structures of both model 1Al and 2Al samples as a function of the conditions represented in Figure 6.3. Results are summarized in Figures 6.7 and 6.8 and in Table 6.2. We expect the framework composition to be robust to the conditions studied here. Significant dealumination of SSZ-13 is observed only after several hours of exposure to 10%  $\text{H}_2\text{O}$  at ca. 1000 K [93, 222, 266, 271].

### Condition 1: Ambient Atmosphere (XAS/AIMD).

First, both 1Al and 2Al samples were subjected to high temperature oxidative treatments and then exposed to ambient atmosphere at 298 K, corresponding to condition 1 of Figure 6.3. The Cu K-edge X-ray absorption near edge spectra (XANES) collected on both samples were indistinguishable, as shown in Figure 6.7, left. A single edge at 8.988 keV corresponds to the  $1s \rightarrow 4p$  transitions of a  $\text{Cu}^{\text{II}}$  ion in a distorted square-planar or octahedral coordination [351]. EXAFS spectra of both samples from the same energy scan (Figure 6.7, middle) exhibited a high intensity first coordination shell peak at ca. 1.5 Å. The spectra were fitted using a  $\text{Cu}_2\text{O}(\text{s})$  experimental reference to estimate 4.0 Cu-O bonds (1.94 Å average distance) and 4.2 Cu-O bonds (1.93 Å average distance), respectively, on the 2Al and 1Al samples, which are identical within the  $\pm 5\%$  error of the fit (details in Supporting Information 6.8.9). Higher coordination shells beyond 2.0 Å appear with low intensity on both samples and indicate Cu-O bonds with extra-framework O species, as evidenced by the absence of scattering from Si or Al atoms bound to  $\text{O}_f$ . The XANES and EXAFS spectra are indistinguishable from each other and that of aqueous  $\text{Cu}^{\text{II}}$  complexes [351], which are also known to form a square-planar tetraaquo complex. These observations are in agreement with the phase diagram condition 1 predictions shown in Figure 6.3.

The EXAFS provides an ensemble average of the Cu coordination environment. To extract comparable information from simulation, we performed 298 K AIMD simulations (60 ps of equilibration followed by 90 ps of sampling) on the lowest free energy hydrated forms of  $[\text{Z}_2\text{Cu}^{\text{II}}]$  and  $[\text{ZCu}^{\text{II}}\text{OH}]$ . In both cases, Cu remained near the center of the cage (Figure 6.1) and was dynamic. Figure 6.8 superimposes the Cu positions relative to the zeolite cage during the 90 ps sampling. To quantify Cu mobility, we discretized the supercell into  $0.2 \times 0.2 \times 0.2$  Å cubes, counted the cubes visited at least once during the simulation, scaled by the cube volume, and normalized to the volume visited by  $\text{Z}_2[\text{Cu}^{\text{II}}(\text{H}_2\text{O})_4](\text{H}_2\text{O})_2$ . Results are summarized in Table 6.2 and further detailed in Supporting Information 6.8.10.  $\text{Z}[\text{Cu}^{\text{II}}\text{OH}(\text{H}_2\text{O})_3](\text{H}_2\text{O})_3$  is

estimated to be 1.38 times as mobile as  $[\text{Z}_2\text{Cu}^{\text{II}}(\text{H}_2\text{O})_4](\text{H}_2\text{O})_2$ , consistent with the weaker electrostatic attraction to a single Al as compared to two proximal Al atoms. Throughout the  $\text{Z}[\text{Cu}^{\text{II}}\text{OH}(\text{H}_2\text{O})_3](\text{H}_2\text{O})_3$  simulation, H atoms are observed to hop between nonframework O with a barrier of ca. 20 kJ mol<sup>-1</sup>, causing O bound to Cu to spend time as both OH and H<sub>2</sub>O.

The right panel of Figure 6.7 shows the computed radial distribution functions (RDFs) between Cu and all heavy atoms. Both RDFs show a prominent peak near 2 Å corresponding to the first coordination shell with peak area corresponding to four O atoms. These first RDF peaks correspond with the first EXAFS peak (the RDF and EXAFS are offset due to the difference between electron scattering and interatomic distances). The 1Al RDF is broadened in comparison to the 2Al due to the presence of both shorter Cu-OH and longer Cu-H<sub>2</sub>O bonds that are not resolvable by EXAFS. The RDFs are near-zero between 2.2 and 3.0 Å; structure appears beyond 3.0 Å. The results are consistent with the observation of only low intensity peaks beyond the first major one in the EXAFS and H<sub>2</sub>O solvated Cu complexes.

Condition 2: 20% O<sub>2</sub>, 673 K (XAS/AIMD).

Next, we collected XANES spectra at 298 K on both samples after 1 h treatment at 673 K in O<sub>2</sub>, corresponding to condition 2 in Figure 6.3. The vessels were sealed before cooling to prevent rehydration of Cu. Resultant XANES and EXAFS are shown in Figure 6.9. In addition to the 8.988 keV Cu<sup>II</sup> edge feature observed in Figure 6.7, an additional feature appears at 8.987 keV that reflects Cu<sup>II</sup> present in a lower than octahedral coordination environment [307]. Further, on the 1Al sample, a low intensity peak appears at 8.983 keV that we assign to 5% Cu<sup>I</sup> based on a fit using Cu<sup>I</sup> and Cu<sup>II</sup> references (Supporting Information 6.8.11).

The EXAFS (Figure 6.9, middle) exhibit high intensity peaks at ca. 1.5 Å that fit to 3.0 Cu-O bonds at 1.91 Å and to 3.8 Cu-O bonds at 1.94 Å on the 1Al and 2Al samples, respectively (Table 6.2). Consistent with the higher first-shell coordination and closer proximity to multiple Si/Al, the 2Al sample also exhibits a more distinct

second shell peak at ca. 2.4 Å than that on the 1Al sample. To ensure reversibility, we cycled samples between condition 1 and condition 2 and confirmed that XAS spectra were identical to those shown in Figure 6.7.

These EXAFS features are consistent with those expected for the  $[\text{Z}_2\text{Cu}^{\text{II}}]$  and  $[\text{ZCu}^{\text{II}}\text{OH}]$  species predicted to predominate at condition 2. Cu remains bound to multiple  $\text{O}_f$  for the duration of AIMD simulations on each, and each are computed to be about 8 times less mobile than the  $\text{Z}_2[\text{Cu}^{\text{II}}(\text{H}_2\text{O})_4](\text{H}_2\text{O})_2$  reference. The  $[\text{Z}_2\text{Cu}^{\text{II}}]$  site oscillates between three nearly isoenergetic minima (Supporting Information 6.8.12) that differ in the  $\text{O}_f$  nearest-neighbor to Cu. The first shell in the RDF (Figure 6.9, bottom right) convolutes these three and integrates to a CN 3.9. By deconvolution of the RDF, we assign the second feature at ca. 2.8 Å to one Al and one Si atom nearest Cu (Supporting Information 6.8.13). The AIMD CN is consistent with the EXAFS fit.

In contrast,  $[\text{ZCu}^{\text{II}}\text{OH}]$  only exhibits a “wagging” into and out of the 8MR plane during AIMD. The Cu- $\text{O}_f$  and Cu-OH pairs appear as sharp features in the RDF (Figure 6.9, top right). The integrated RDF and fitted CN are identical. The slightly broad second shell feature at ca. 2.75 Å arises from the Al nearest Cu (Figure 6.1). This second shell feature is at 0.25 Å shorter distance and one-half the integrated area of the  $[\text{Z}_2\text{Cu}^{\text{II}}]$  second shell, consistent with both the location and the magnitude of the EXAFS second shell features.

Condition 3: He, 673 K (XAS/AIMD).

As noted above, a small amount of  $\text{Cu}^{\text{I}}$  appears in the XANES of the calcined 1Al sample. This autoreduction feature [36, 39] becomes more prominent after treating the 1Al sample in flowing helium at 673 K for 1 h following the calcining treatment (Figure 6.9, left panel). From spectral deconvolution and EXAFS fitting, we infer 55% of the Cu to be present as  $\text{Cu}^{\text{I}}$  and the mean Cu-O coordination number to decrease to 2.4 (Table 6.2). In contrast, only 10%  $\text{Cu}^{\text{I}}$  is observed on the 2Al sample following the same He treatment, and the coordination number is unchanged.

The  $\text{Cu}^I$  feature becomes even more pronounced and the  $\text{Cu}^I$  fraction increases to 65% on the 1Al samples treated in 3%  $\text{H}_2$  at 523 K;<sup>76,77</sup> the 2Al sample is changed negligibly by  $\text{H}_2$  reduction. These observations of autoreduction in the 1Al but not 2Al samples are consistent with the predictions for condition 3 in Figure 6.3. That reduction is not complete on the 1Al sample suggests some kinetic as well as thermodynamic contribution to the autoreduction process, possibly associated with the mobility of the  $[\text{ZCu}^{\text{II}}\text{OH}]$ . Reoxidation of samples after the He purge or  $\text{H}_2$  treatment returns the XANES and EXAFS spectra to their post-calcination forms (additional details in Supporting Information 6.8.14), indicating that reduction and reoxidation are reversible.

To interpret the observed EXAFS, we used 298 K AIMD to compute the dynamics of the reduced  $[\text{ZCu}^I]$  site. The Cu ion stays within the 6MR and retains coordination to the same two  $\text{O}_f$  atoms; the computed RDF (Figure 6.9) is dominated by a Cu- $\text{O}_f$  feature at 1.93 Å that integrates to CN 2.1. The Cu mobility is enhanced by about 20% as compared to  $[\text{ZCu}^{\text{II}}\text{OH}]$  and  $[\text{Z}_2\text{Cu}^{\text{II}}]$ , but still roughly 8 times less than hydrated  $[\text{Z}_2\text{Cu}^{\text{II}}]$ . The second shell feature in EXAFS, spanning from roughly 2-3 Å, is echoed in the broad AIMD RDF past the first coordination shell, a consequence of  $[\text{ZCu}^I]$  mobility within the 6MR.

### 6.2.3 Copper Speciation at SCR Conditions.

The *ex situ* characterizations above show that Cu cations in the 1Al and 2Al samples are identical under ambient and hydrated conditions, exhibit different coordination after high-temperature oxidation, and respond differently to high-temperature reduction. We next explore the implications under catalytic conditions relevant to low-temperature NO<sub>x</sub> SCR.



### *operando* XAS Spectra and SCR Kinetics.

We used a custom-built reactor [87] designed to collect XAS spectra in *operando* to determine the Cu oxidation states of the 2Al and 1Al samples during steady-state SCR (300 ppm of NO, 300 ppm of NH<sub>3</sub>, 10% O<sub>2</sub>, 2% H<sub>2</sub>O) at 473 K under differential and plug-flow conditions (<20% NO conversion). Observed SCR turnover rates (TOR, mol NO s<sup>-1</sup> (mol Cu)<sup>-1</sup>), apparent NO, O<sub>2</sub>, and NH<sub>3</sub> reaction orders, and apparent activation energies (E<sub>app</sub>) (Table 6.3) were identical on the 2Al and 1Al samples, within experimental error, and identical to values measured on these samples in a different plug-flow reactor (section 5.5). *operando* XANES spectra for the two samples (Figure 6.10, left, black traces) indicate the presence of 50% and 55% Cu<sup>I</sup> (8.983 keV peak), respectively, that are identical within the fitting error (5%). Although the presence of both Cu<sup>II</sup> and Cu<sup>I</sup> species during standard SCR redox cycles is not surprising [41,85,86,130,360], the identical Cu<sup>I</sup> fractions and kinetic parameters (Table 6.3) are unexpected given the different structures, dynamics, and reducibility of [Z<sub>2</sub>Cu<sup>II</sup>] and [ZCu<sup>II</sup>OH] species in He and H<sub>2</sub>. These *operando* characterization results suggest that cationic copper sites are functionally equivalent during low-temperature standard SCR at 473 K.

### SCR Gas Species Binding Energies.

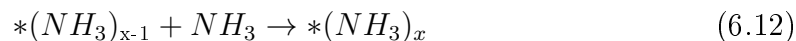
To understand Cu coordination in the SCR gas mixture (H<sub>2</sub>O, N<sub>2</sub>, NH<sub>3</sub>, NO, O<sub>2</sub>), we first computed adsorption energies of these species as well as NO<sub>2</sub>, which is often proposed as an SCR intermediate [41,356–359], on the oxidized and reduced forms of the 1Al and 2Al Cu sites using the same AIMD and HSE06-TSvdw optimization protocol. The computed NH<sub>3</sub> binding energy to the [ZH]/[ZCu<sup>I</sup>] Brønsted site is -151 kJ mol<sup>-1</sup>, quantitatively consistent with NH<sub>3</sub> differential heats observed via microcalorimetry on zeolitic H<sup>+</sup> sites [368–372]:



Thus, the  $\text{NH}_4^+$  form of this site prevails under SCR conditions, and we used the  $[\text{ZNH}_4]/[\text{ZCu}^I]$  structure shown in Figure 6.11 as the model for a reduced 2Al site.

Computed 1Al site binding energies are plotted against 2Al sites in Figure 6.11. Binding energies without the TSvdw correction are approximately 20 kJ mol<sup>-1</sup> more positive. Binding energies (Supporting Information 6.8.15) and structures on the  $[\text{Z}_2\text{Cu}^{\text{II}}]$  and  $[\text{ZCu}^{\text{II}}\text{OH}]$  sites are generally consistent with those for  $\text{H}_2\text{O}$ ,  $\text{NO}$ , and  $\text{NH}_3$  reported elsewhere [41, 341, 352–354], although the inclusion of hybrid exchange significantly decreases the  $\text{NO}$  binding relative to the GGA values [85, 341, 352–354]. The 1Al and 2Al binding energies are roughly linearly correlated, although deviations as large as 50 kJ mol<sup>-1</sup> are evident.  $\text{O}_2$  interacts weakly with all sites;  $\text{H}_2\text{O}$  and  $\text{NO}$  exhibit intermediate binding strengths.  $\text{NH}_3$  binds by -120 to -140 kJ mol<sup>-1</sup> on all four Cu adsorption sites and does not significantly alter the Cu oxidation state.  $\text{NO}_2$  binds strongly to reduced sites (oxidizing the Cu center to form a nitrite) but interacts weakly with oxidized Cu.  $\text{NO}$  is a notable outlier from the linear correlation: the HSE calculations predict  $\text{NO}$  to bind weakly to  $[\text{Z}_2\text{Cu}^{\text{II}}]$  (-25 kJ mol<sup>-1</sup>) but with intermediate strengths on  $[\text{ZCu}^{\text{II}}\text{OH}]$  (-75 kJ mol<sup>-1</sup>).  $\text{NO}$  locates near the OH ligand rather than Cu, similar to structures for this species reported elsewhere [341], but does not form a HONO-like structure.  $\text{N}_2$  more strongly adsorbs to  $[\text{ZCu}^I]$  than to other sites.

Because  $\text{NH}_3$  out-binds all other species and is similar in its coordination behavior to  $\text{H}_2\text{O}$ , we explored the sequential binding of additional  $\text{NH}_3$  on all four sites:



using an AIMD anneal at 473 K followed by HSE06-TSvdw optimization. Results are summarized in Table 6.4; structures and normalized Cu Bader charges are detailed in Supporting Information 6.8.1. Binding energies are roughly constant as  $\text{NH}_3$  displaces  $\text{O}_f$  from the Cu coordination sphere.  $\text{Cu}^I$  and  $\text{Cu}^{\text{II}}$  retain 2-fold and 4-fold coordination, respectively; additional  $\text{NH}_3$  beyond these limits are more weakly bound and not directly associated with Cu, instead forming hydrogen bonds with  $\text{NH}_3$  in the first coordination sphere. The only exception is  $\text{ZCu}^{\text{II}}\text{OH}(\text{NH}_3)_2$ ; this species adopts

a squareplanar conformation including a single  $O_f$  ligand at 0 K, but in the finite T dynamics adopts a trigonal planar form, free from  $O_f$ , for ca. 90% of the trajectory. Energy and entropy are evidently closely balanced between the two configurations.

### NH<sub>3</sub> Phase Diagrams.

We used a first-principles thermodynamic analysis to rank the free energies of the NH<sub>3</sub> species in Table 6.4 and  $H_xO_y$  structures from Figure 6.2, 42 species in total, taking O<sub>2</sub>, H<sub>2</sub>O, and NH<sub>3</sub> as oxygen, hydrogen, and nitrogen references, respectively:

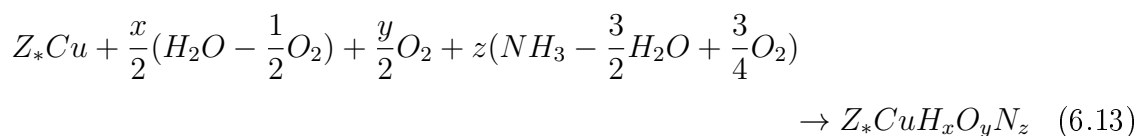


Figure 6.12 reports the lowest free energy 1Al and 2Al species as a function of T and O<sub>2</sub> partial pressure at H<sub>2</sub>O and NH<sub>3</sub> concentrations of 2%, and 300 ppm, respectively, representative of the experimental conditions shown in Figure 6.10. We chose O<sub>2</sub> pressure as an independent variable for direct comparison to the experimental results detailed in the proceeding section. The resultant phase diagrams are substantially different from the  $H_xO_y$  ones in Figure 6.3; NH<sub>3</sub>-containing species dominate the diagrams up to 773 K, and H<sub>2</sub>O is an unimportant adsorbate. The most prominent species in the 1Al and 2Al diagrams are reduced Cu<sup>I</sup> species and oxidized Cu<sup>II</sup> species, respectively, although both oxidized and reduced forms of Cu appear on both diagrams. Both sites are saturated with NH<sub>3</sub> at 473 K and successively lose NH<sub>3</sub> ligands with increasing temperature. At 473 K, the 2Al phase diagram (Figure 6.12, right) shows Cu preferring Cu<sup>I</sup>(NH<sub>3</sub>)<sub>2</sub> as the O<sub>2</sub> concentration decreases, and Cu<sup>II</sup>(NH<sub>3</sub>)<sub>4</sub> species as the O<sub>2</sub> concentration increases. The Cu<sup>I</sup>(NH<sub>3</sub>)<sub>2</sub> complex is the most stable 1 Al species over the entire O<sub>2</sub> range examined here.

Sidebars in Figure 6.12 rank the relative free energies of intermediates at the condition indicated by the chrome spheres in the phase diagrams (473 K and 10% O<sub>2</sub>), equivalent to those in Figure 6.10. Species with  $\Delta G_{\text{form}} > 0$  kJ mol<sup>-1</sup> are excluded for clarity; full results are tabulated in Supporting Information 6.8.16. The

analysis predicts a reduced and  $\text{NH}_3$ -saturated  $\text{Cu}^I$  to be the most stable 1Al species at these conditions.  $\text{Cu}^I$  complexes with one or three  $\text{NH}_3$  ligands are higher in free energy, and the first  $\text{Cu}^{\text{II}}$  species to appear is  $\text{Z}[\text{Cu}^{\text{II}}\text{OH}(\text{NH}_3)_3]$  at 50 kJ mol<sup>-1</sup> higher free energy than the most stable species. Thus, these two  $\text{NH}_3$ -saturated and  $\text{O}_f$ -liberated complexes are the most likely dominant forms of  $\text{Cu}^I$  and  $\text{Cu}^{\text{II}}$  under SCR conditions in the 1Al catalyst. The  $\text{Cu}^I/\text{Cu}^{\text{II}}$  ordering is reversed at the 2Al site, where the most stable complex is an oxidized and  $\text{NH}_3$ -saturated  $\text{Z}_2[\text{Cu}^{\text{II}}(\text{NH}_3)_4]$  at 16 kJ mol<sup>-1</sup> below the reduced and  $\text{NH}_3$ -saturated  $[\text{ZNH}_4]/\text{Z}[\text{Cu}^I(\text{NH}_3)_2]$ . The  $\text{Cu}^I/\text{Cu}^{\text{II}}$  fractions are the same in the *operando* XANES (Figure 6.10) on the 1Al and 2Al samples and likely kinetically rather than thermodynamically controlled. The thermodynamic screening identifies the species most relevant to catalysis and highlights the importance of  $\text{NH}_3$  coordination under SCR conditions.

XAS/AIMD for  $\text{Cu}^I/\text{Cu}^{\text{II}}$  with  $\text{NH}_3$ .

To explore Cu structure and dynamics under SCR conditions, we collected XAS and AIMD information on both 1Al and 2Al samples prepared with subsets of SCR gas mixtures that place them primarily in the  $\text{Cu}^I$  and  $\text{Cu}^{\text{II}}$  states.

Figure 6.10 shows the XANES and EXAFS at 473 K of 1Al and 2Al samples treated in 300 ppm of NO and  $\text{NH}_3$ . Consistent with previous reports [41, 85, 360], this treatment reduces Cu. In fact, the XANES and the EXAFS on both samples are indistinguishable, and the XANES fit to a  $\text{Cu}^I$  fraction of 100%. A prominent first shell peak at 1.88 Å in the EXAFS fits to 2.1 CN, which EXAFS cannot distinguish between O and N. The EXAFS is absent of longer-range structure.

These XAS results are consistent with the reduced Cu forms highlighted in Figure 6.12. We performed 473 K AIMD simulations on  $[\text{ZNH}_4]/\text{Z}[\text{Cu}^I(\text{NH}_3)_2]$  and  $\text{Z}[\text{Cu}^I(\text{NH}_3)_2]$  for the 2Al and 1Al sites, respectively. The linear  $\text{Cu}^I(\text{NH}_3)_2$  species are identical in structure and, as evidenced in the dynamics trajectory (Figure 6.13) and the volume visited (Table 6.2), highly mobile. Computed RDFs between Cu and other heavy atoms are shown in Figure 6.10. As in the EXAFS, the lone peak at

1.89 Å integrates to 2.0 CN; the Cu location is completely disordered with respect to the zeolite lattice. To probe the ability of this  $\text{NH}_3$ -mobilized  $\text{Cu}^I$  to diffuse between cages, we used the climbing image nudged elastic band (CINEB, Supporting Information 6.8.17) method to compute the energy to thread a  $\text{Cu}^I(\text{NH}_3)_2$  ion through the 8MR. The path starts with one  $\text{NH}_3$  in the plane of the 8MR, passes over a 37 kJ mol<sup>-1</sup> transition state in which the Cu is centered within the ring, and ends with the other  $\text{NH}_3$  in the 8MR. This modest barrier suggests rather facile transport of reduced Cu within the SSZ-13 lattice, as has been inferred from the  $\text{NH}_3$ -facilitated exchange of  $\text{Cu}^I$  [373].

Figure 6.10 similarly shows XAS spectra collected on the same samples during exposure to an oxidizing mixture of  $\text{NH}_3$  (300 ppm) and  $\text{O}_2$  (10%) at 473 K. The XANES are again similar to one another but markedly different from those at the reducing condition. Both samples exhibit a peak at 8.983 keV corresponding to a  $\text{Cu}^I$  species, 27% and 17% on the 1Al and 2Al samples, respectively, and a balance of  $\text{Cu}^{II}$  species. EXAFS shows prominent first coordination shells at 1.5 Å that fit to 3.2 and 3.5 O or N around Cu at 1.92 Å. Neither EXAFS exhibit second shell coordination in the 2.5-3.0 Å range. RDFs from AIMD performed at 473 K on  $\text{Z}[\text{Cu}^{II}(\text{OH})(\text{NH}_3)_3]$  and  $\text{Z}_2[\text{Cu}^{II}(\text{NH}_3)_4]$ , corresponding to the oxidized 1Al and 2Al species at SCR conditions, are also shown in Figure 6.10. As with  $\text{Cu}^I$ , both are free from framework oxygen and remain fully coordinated to  $\text{NH}_3$  through the course of the dynamics. RDFs integrate to ca. 3.9 CN; weighting the AIMD RDFs by the XANES-observed fractions of  $\text{Cu}^I$  and  $\text{Cu}^{II}$  recovers average coordination numbers of 3.2 and 3.6, close to the EXAFS-fitted values. These species were roughly 50% less mobile than their  $\text{Cu}^I(\text{NH}_3)_2$  counterparts (Table 6.2), and 30% more mobile than their hydrated forms (Table 6.2).

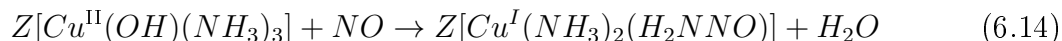
Finally, to confirm the transferability of EXAFS spectra collected under the non-catalytic  $\text{NO} + \text{NH}_3$  and  $\text{O}_2 + \text{NH}_3$  conditions to catalytic ones, we obtained 473 K SCR *operando* EXAFS on the recently enhanced APS Sector 10-ID beamline on a Si:Al = 25, Cu:Al = 0.42 sample similar to the 1Al catalyst (Figure 6.4); kinetic

details and spectra are provided in Supporting Information 6.8.18. This catalyst has a 60/40  $\text{Cu}^I/\text{Cu}^{\text{II}}$  ratio, a fit CN of 3.1, and no second shell structure. The CN is consistent with a 60/40 weighted average of 2CN  $\text{Cu}^I$  and 4CN  $\text{Cu}^{\text{II}}$ . The lack of second shell character demonstrates all Cu are  $\text{NH}_3$  solvated under *operando* conditions.

#### 6.2.4 SCR Mechansim

$\text{Cu}^{\text{II}} \rightarrow \text{Cu}^I$  Half-Cycle.

We previously proposed an NO-assisted  $\text{NH}_3$  dissociation to be responsible for the  $\text{Cu}^{\text{II}}$  to  $\text{Cu}^I$  reduction during SCR [85]. We report in Figure 6.14 and Supporting Information 6.8.19 the computed CI-NEB pathways for such a step starting from  $\text{NH}_3$ -saturated  $\text{Cu}^{\text{II}}$  identified in the XAS and DFT here. Both reactions proceed by attack of NO on a Cu-bound  $\text{NH}_3$  to form an N-N bond. In the process, a proton is transferred to an acceptor and an electron to Cu, leaving an  $\text{H}_2\text{NNO}$  intermediate that can decompose via proton transfers to  $\text{N}_2$  and  $\text{H}_2\text{O}$  [85,374]. In the 1Al case, the Cu-OH ligand acts as the proton acceptor, to form water:



In the 2Al case, an  $\text{O}_f$  plays the role of the acceptor, to form a new, proximal Brønsted site:



The first path is much more exothermic than the second (-267 vs -68  $\text{kJ mol}^{-1}$ ), reflecting the strong driving force for creating  $\text{H}_2\text{O}$ . Nonetheless, the computed barriers for these two paths are a similar 71 and 74  $\text{kJ mol}^{-1}$ , respectively, within the HSE06 model. These similarities reflect an early transition state dominated primarily by the partial desorption of  $\text{NH}_3$  from Cu to accommodate the attacking NO. The N-N separations at the transition states are over 2 Å, and the N-H bonds are only slightly elongated.

The key difference between the 1Al and 2Al paths is that  $\text{NH}_3/\text{NO}$  reduction of 2Al  $\text{Cu}^{\text{II}}$  should produce new Brønsted sites while 1Al  $\text{Cu}^{\text{II}}$  should not. The number

of  $\text{NH}_4^+$  species on samples treated in flowing NO and  $\text{NH}_3$  (473 K) were counted by TPD performed after purging physisorbed and  $\text{Cu}^I$  bound  $\text{NH}_3$  species in flowing wet helium (3%  $\text{H}_2\text{O}$ , 433 K) [171]. On all Cu-SSZ-13 samples, a larger number of  $\text{NH}_4^+$  species were present after reduction treatments than after oxidation treatments (Supporting Information 6.8.20). Figure 6.15 shows the number of additional  $\text{H}^+$  sites present after reduction of Cu sites to  $\text{Cu}^I$  as a function of the Cu:Al ratio on the Si:Al = 5 (blue), 15 (green), and 25 (orange) samples. The dashed lines indicate the excess  $\text{H}^+$  expected from the theoretical enumeration of 1Al and 2Al sites (Figure 6.4). In line with predictions, one additional  $\text{H}^+$  site is formed per Cu formed until all of the 2Al sites are filled, beyond which point no additional  $\text{H}^+$  sites were formed. Reoxidation in NO and  $\text{O}_2$  (Supporting Information 6.8.20) returns the samples to the state shown in Figure 6.5. The catalytic cycle can thus be closed on both 2Al and 1Al sites.

#### SCR Cycle Energies.

The results above highlight the importance of  $\text{NH}_3$  coordination during 473 K SCR. We previously proposed an SCR cycle on  $[\text{Z}_2\text{Cu}^{\text{II}}]$  sites that accounts for the observed Cu redox [85]. Figure 6.16 shows an elaboration of that cycle that incorporates  $\text{NH}_3$ -solvation inferred from the thermodynamic analysis and EXAFS on 1Al and 2Al sites. The mechanism includes five primary steps, starting from the 12 o'clock position: (1)  $\text{NH}_3$  adsorption on  $\text{Cu}^{\text{II}}$ ; (2) NO-assisted  $\text{NH}_3$  dissociation concurrent with  $\text{Cu}^{\text{II}}$  reduction to  $\text{Cu}^I$ ; (3)  $\text{N}_2$  and  $\text{H}_2\text{O}$  desorption from  $\text{Cu}^I$ ; (4)  $\text{Cu}^I$  reoxidation to  $\text{Cu}^{\text{II}}$  by NO and  $\text{O}_2$  (a non-elementary step); and (5) reaction of adsorbed  $\text{NO}_2$  with  $\text{NH}_3$  or  $\text{NH}_4^+$  to desorb  $\text{N}_2$  and  $\text{H}_2\text{O}$ . Figure 6.16 (right) compares the computed reaction energies for each step (details in Supporting Information 6.8.21). The similar energetics are consistent with the similar standard SCR turnover rates (473 K) measured on the two site types (Table 6.3).

### 6.2.5 SCR Rates on Other Cu-Zeolites.

All of the cationic Cu species in these cycles are  $\text{NH}_3$ -solvated and thus not sensitive to the location of charge-compensating framework Al. To test the generality of this observation, standard SCR rates were measured on synthesized and commercial Cu-ZSM-5 and Cu-BEA samples of compositions similar to the Si:Al = 15 SSZ-13 samples. Standard SCR rates (per g, 473 K) on Cu-exchanged MFI (Si:Al = 13), BEA (Si:Al = 13) (sample preparation and characterization described in Supporting Information 6.8.25, 6.8.26, and 6.8.4), and Cu-CHA (Si:Al = 5, 15) are shown in Figure 6.17 as a function of the Cu density (per g). The error was calculated by replicate experiments under the same conditions. These SCR rates were measured in a regime uncorrupted by mass or heat transfer artifacts (Koros-Nowak test [361] and in a kinetic regime characterized by similar apparent reaction orders and apparent activation energies (Supporting Information 6.8.22). Standard SCR rates (per g, 473 K) increased linearly with Cu density (per g) on the Cu-CHA samples of different Si:Al ratio (5, 15), as expected from the similar turnover rate measured for Cu at 1Al and at 2Al sites (section 6.2.3). Turnover rates for Cu-ZSM-5 and Cu-BEA samples are of the same magnitude and exhibit a similar dependence on Cu density. A linear fit to the entire data set has a correlation coefficient  $R^2 = 0.86$ . The Cu speciation was not determined on the Cu-ZSM-5 and Cu-BEA samples, and thus the observed scatter may have contributions from discrepancies between Cu wt% and isolated Cu ion density on these samples. These data suggest that both turnover rates and SCR mechanisms are independent of zeolite support at these conditions and in this kinetic regime. We surmise that this insensitivity to zeolite framework arises from  $\text{NH}_3$  solvation of both  $\text{Cu}^{\text{II}}$  and  $\text{Cu}^{\text{I}}$  species at 473 K, and that these  $\text{NH}_3$ -covered ions are responsible for observed SCR turnover.



## 6.3 Discussion

### 6.3.1 Al Distribution and Cu Speciation *ex situ*.

While the apparent macroscopic composition of a heterogeneous catalyst is typically simple to determine, relating that composition to the molecular-scale, functional composition of an active site remains a major challenge. The relevant macroscopic composition variables for the Cu-SSZ-13 materials are the Si:Al and Cu:Al ratios. As reported in Figure 6.4 and the supporting experimental results, two types of Cu sites are present over the composition ranges studied here, and the relative densities of each type of Cu site are a function of both composition variables. Figure 6.4 is based on two assumptions: first, that framework Al atoms are randomly sited during zeolite crystallization *modulo* Lowenstein’s rule, and second, that 6MR 2Al sites are populated by  $\text{Cu}^{\text{II}}$  cations to saturation before 1Al sites are populated with  $\text{Cu}^{\text{II}}\text{OH}$ . The close correspondence between these predictions and the experimental characterizations supports the model.

Synthesis conditions are well-known to influence Al siting in zeolites [32,42,48,56–58,65,70,74,147,172,173,305,306,375] and specifically in SSZ-13 [42], and thus the conclusions drawn from the synthetic conditions here cannot be extended to all Cu-zeolites or even to all Cu-SSZ-13 materials. We can, however, compare our findings to SSZ-13 zeolites prepared via procedures equivalent to those used here [34,37,109,162,168,250,376,377]. Fickel et al. [34] concluded, on the basis of XRD and EXAFS, that an SSZ-13 sample with Si:Al = 9 and Cu:Al = 0.18 contained predominantly Cu in the 6MR, in agreement with the models here that predict 80% of  $[\text{Z}_2\text{Cu}^{\text{II}}]$  in such sites. Gao et al. compared the  $\text{H}_2$  TPR of SSZ-13 zeolites with Si:Al = 6 and 12 and Cu:Al = 0.10–0.50 [40,347,348]. Samples we predict to contain  $[\text{Z}_2\text{Cu}^{\text{II}}]$  show only a 653 K TPR feature, while samples in the range expected to contain  $[\text{ZCu}^{\text{II}}\text{OH}]$  also exhibit a 503 K TPR feature, consistent with the readier reducibility of  $[\text{ZCu}^{\text{II}}\text{OH}]$  sites demonstrated here (Figures 6.3 and 6.9). FTIR similarly shows only a 895  $\text{cm}^{-1}$  Cu-perturbed T-O-T vibration in the composition range dominated by  $[\text{Z}_2\text{Cu}^{\text{II}}]$ ,

supplemented by a 940  $\text{cm}^{-1}$  feature in the range containing  $[\text{ZCu}^{\text{II}}\text{OH}]$  [348]. Davis and co-workers recently showed that these 2Al 6MR sites can be selectively protected against dealumination and deactivated for methanol-to-olefins (MTO) activity by preferential exchange of  $\text{Cu}^{\text{II}}$  ions [158, 270, 271], and Gao et al. used an analogous concept to exchange 2Al 6MR sites with alkaline earth cations [271].

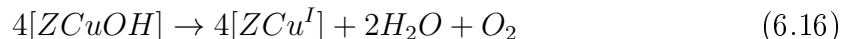
While this partitioning and counting of  $[\text{Z}_2\text{Cu}^{\text{II}}]$  and  $[\text{ZCu}^{\text{II}}\text{OH}]$  sites is successful, these sites themselves are not monolithic. A 6MR ring can have 2Al in 2NN or 3NN relative positions, and even for given positions, at finite temperature an exchanged ion is quite dynamic within the site, as illustrated by the AIMD simulations. Coordination numbers and bond distances from the HSE06 optimizations are similar to those extracted from the AIMD trajectories, but only the latter captures the contributions of dynamics to the EXAFS. For example, even for given Al positions within a 6MR,  $[\text{Z}_2\text{Cu}^{\text{II}}]$  samples several local minima (Supporting Information 6.8.13) during the AIMD, broadening the RDF (Figure 6.9) and reducing  $\text{CN} < 4$ . Thus, finite temperatures and Cu dynamics are important considerations in DFT models of these systems.

### 6.3.2 Cu Speciation *in situ*

Once microscopic sites are identified and enumerated, a second key challenge is to determine how they respond to environmental, *in situ* conditions. We find from the first-principles thermodynamics and spectroscopies that ambient conditions cause both the  $[\text{Z}_2\text{Cu}^{\text{II}}]$  and the  $[\text{ZCu}^{\text{II}}\text{OH}]$  species to exist as hydrated ions, liberated from coordination to zeolite framework oxygens, differing in composition by only a single proton, and differing only slightly in mobility (Figure 6.8). These observations are consistent with a large body of literature on Cu-zeolites. XAS and UV-vis spectroscopies of  $\text{Cu}^{\text{II}}$ -exchanged SSZ-13 [36, 87, 129, 350, 378], ZSM-5, and BEA zeolites under ambient conditions are identical to the corresponding spectra of aqueous  $\text{Cu}^{\text{II}}$  complexes, demonstrating the insensitivity of zeolite topology to solvated ions [36, 351]. Similarly, the perturbed T-O-T vibrations in IR spectra due to framework-bound  $\text{Cu}^{\text{II}}$

disappear upon hydration of  $\text{Cu}^{\text{II}}$  under ambient conditions [343]. Electron paramagnetic resonance (EPR) spectra at ambient observed for predominantly  $[\text{Z}_2\text{Cu}^{\text{II}}]$  samples have been taken as evidence of hydrated and mobile  $\text{Cu}^{\text{II}}$  [347]; broadening at 155 K is attributed to loss of that  $\text{Cu}^{\text{II}}$  ion mobility [272,311] and coalescence into a single sharp signal at 523 K to loss of the hydration sphere [349].

The first-principles thermodynamics and XAS spectroscopies are consistent with the loss of water ligands at high temperature in O<sub>2</sub>. Similarly, Borfecchia et al. [39] infer this loss from observed changes in EXAFS to a 3CN Cu species, the same behavior the Si:Al = 15, Cu:Al = 0.44 catalyst exhibits (Figure 6.9) after dehydration. We and Borfecchia et al. also observe the appearance of  $\text{Cu}^{\text{I}}$  under more reducing conditions. We assign this reduced fraction to  $[\text{ZCu}^{\text{II}}\text{OH}]$  species, based on the comparisons between the 1Al and 2Al samples. The autoreduction is not complete on any sample, suggesting some kinetic in addition to thermodynamic control of the reduction process. The nominal autoreduction stoichiometry:



implies a complicated, multistep process likely involving Cu dimer or higher-order intermediates [129,344,347] and thus a sensitivity to spatial Cu-Cu (and hence Al-Al) separations. Consistent with this inference, Gao et al. [40] report that the fraction of reducible  $[\text{ZCu}^{\text{II}}\text{OH}]$  at constant Cu:Al ratio decreases with increasing Si:Al ratio, or, equivalently, increasing mean  $[\text{ZCu}^{\text{II}}\text{OH}]$  separation.

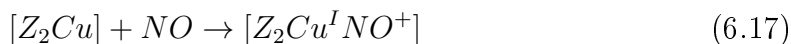
Under standard SCR conditions at 473 K,  $\text{Cu}^{\text{I}}$  and  $\text{Cu}^{\text{II}}$  ions near 1Al or 2Al are all predicted and observed to be fully solvated by  $\text{NH}_3$ , and further all Brønsted sites are present as  $\text{NH}_4^+$ . Both  $\text{NH}_4^+$  and Cu- $\text{NH}_3$  are observed in DRIFTS spectra at similar conditions [38,379,380] on Cu-SSZ-13 samples. In fact, both vibrational and XAS spectra of  $\text{NH}_3$  dosed to a number of Cu-exchanged zeolites are similar to those of aqueous  $\text{Cu}^{\text{I}}(\text{NH}_3)_2$  and  $\text{Cu}^{\text{II}}(\text{NH}_3)_4$  [37,41,87,379,381–385]. The standard SCR active sites at 473 K are  $\text{NH}_3$ -solvated Cu ions.

$\text{NH}_3$  solvation influences Cu mobility as well as structure, and this effect is insensitive to zeolite topology.  $\text{NH}_3$  is observed to promote the exchange of  $\text{Cu}^{\text{II}}$  from

CuO(s) into a number of zeolite frameworks, and this process is further promoted by *in situ* reduction of Cu<sup>II</sup> to Cu<sup>I</sup> by NH<sub>3</sub> and NO mixtures [373].

### 6.3.3 Mechanistic Implications for SCR.

The SCR reaction is well established to involve Cu<sup>I</sup> ↔ Cu<sup>II</sup> redox cycles [41, 85, 130, 360]. There has been some controversy regarding the species responsible for reduction [41, 85, 92, 355, 359]. Exposure to NO alone at 473 K does not reduce either the 1Al [ZCu<sup>II</sup>OH] (Supporting Information 6.8.24) or the 2Al ([Z<sub>2</sub>Cu<sup>II</sup>]) [85] samples, and the hybrid-exchange DFT results do not predict NO to strongly bind to or reduce either Cu<sup>II</sup> site. We thus find no evidence to support the elementary mechanistic steps:



or



Rather, NO and NH<sub>3</sub> together are necessary to reduce either of these sites. The reaction pathways and activation barriers for these reductions are computed to be similar on the [ZCu<sup>II</sup>OH] and [Z<sub>2</sub>Cu<sup>II</sup>] sites in the presence of solvating NH<sub>3</sub>. These barriers are also similar to the experimental apparent activation energies, although direct comparison of the experiment and computations is only possible through a kinetic model. The presence of both Cu oxidation states during standard SCR likely indicates that neither oxidation nor reduction alone is rate-limiting [85], and thus a satisfactory kinetic model would require kinetic details on both half-cycles. Reduction rates on the [ZCu<sup>II</sup>OH] and [Z<sub>2</sub>Cu<sup>II</sup>] may differ at temperatures at which NH<sub>3</sub> ligands are lost.

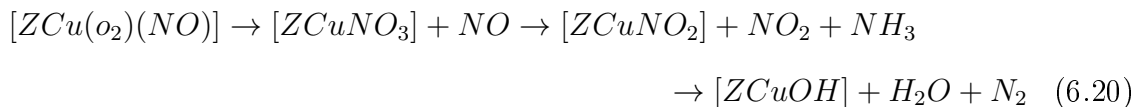
While NO and NH<sub>3</sub> are most effective at reducing Cu<sup>II</sup>, we and others [360, 386] also observe a partial reduction of Cu<sup>II</sup> → Cu<sup>I</sup> in flowing NH<sub>3</sub> and O<sub>2</sub>. DFT calculations identified an O<sub>2</sub> assisted NH<sub>3</sub> dissociation pathway that parallels but has a much

higher barrier than the NO-assisted  $\text{NH}_3$  dissociation reaction [85]. This pathway is unlikely to be catalytically relevant but could be responsible for this reduction.

The results presented here provide indirect mechanistic information about the SCR oxidation half-cycle. We find adsorbed  $\text{NO}_2$  to oxidize  $\text{Cu}^{\text{I}}$  to  $\text{Cu}^{\text{II}}$  as Cu-bound nitrite:



consistent with many proposals [41, 92, 356–359]. The source of  $\text{NO}_2$  and even its presence as a free intermediate during standard SCR is less clear. Janssens et al. [41] proposed NO oxidation to nitrite to occur on a single, reduced Cu site through the intermediacy of a nitrate with the initial step as rate-determining (RDS):



However, computed activation energies and the RDS assumption are inconsistent with experimental activation energies and the observed 50/50 mixture of  $\text{Cu}^{\text{I}}/\text{Cu}^{\text{II}}$  for SCR [37, 40, 85, 347]. Rather, as with autoreduction, NO oxidation may involve participation of more than one Cu species, facilitated by the solvation and high mobility of  $\text{Cu}^{\text{I}}(\text{NH}_3)_2$  and its low diffusion barrier between CHA cages. Solvated  $\text{Cu}^{\text{I}}$  ions are well-known to participate in dimeric Cu oxidation chemistries [307, 387–389] and a second-order dependence of SCR rate on Cu concentration has been observed on an Si:Al = 6 Cu-SSZ-13 catalyst at Cu:Al ratios <0.03 [349]. At higher temperatures, Cu is expected to desolvate (Figure 6.12), consistent with the FTIR findings of Giordanino et al. [38]. In sharp contrast to the 473 K spectra (Figure 6.10), EXAFS collected at 673 K in  $\text{NH}_3$  and  $\text{O}_2$  demonstrate similar second-shell character (Supporting Information 6.8.23) to the dry-oxidized framework bound Cu (Figure 6.9). Concurrent with this desolvation, apparent activation energies increase from 70 kJ mol<sup>-1</sup> at 473 K to 140 kJ mol<sup>-1</sup> [40] at 623 K, consistent with the dip in NO conversion observed [248] in non-differential measurements. Thus,  $\text{NH}_3$  (de)solvation likely has a large impact on SCR oxidation half-cycle rates.

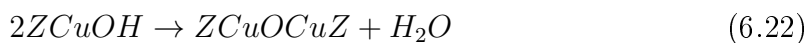
### 6.3.4 Implications for Partial Methane Oxidation.

The results and approach described here are useful for the interpretation of the recently observed [329] noncatalytic, stoichiometric partial oxidation of methane (PMO) on Cu-SSZ-13:



PMO is carried out in a three-step sequence [324–327,329] that can be understood in part through reference to Figure 6.3. In a first step, the Cu-SSZ-13 material is brought to ca. 673 K in  $O_2$  (ca. 20%) and balance inert, corresponding to condition 2 in the figure.  $O_2$  is then purged by inert, bringing the material to condition 3. We observe a subset of sites to reduce under these conditions, consistent with the participation of only a fraction of exchanged Cu in PMO [325]. Subsequent introduction of  $CH_4$  at 473 K results in the production of methanol, which is liberated by returning to percent level  $H_2O$  pressures, between conditions 1 and 2 of Figure 6.3.

Wulfers et al. demonstrated [329] PMO on Si:Al = 6 and 12, Cu:Al = 0.35 SSZ-13 materials. The Si:Al = 12 sample has roughly double (mol methanol per mol Cu) the performance of the Si:Al = 6 sample, in precise correlation with the predicted increase in  $[ZCu^{II}OH]$  sites (Figure 6.4). We conclude  $[ZCu^{II}OH]$  sites are likely precursors to  $ZCuOCuZ$  sites proposed to be responsible for PMO activity [318,321,322,326,328]:



and  $[Z_2Cu^{II}]$  sites are inactive.

## 6.4 Conclusions

While the macroscopic composition of a solid catalyst is generally straightforward to measure and control, the relationship between this apparent composition and the number and type of catalytically relevant active sites is generally difficult to infer. We illustrate here an example of a nontrivial catalytic system in which it is possible to determine through theory and experiment both the speciation and the number

density of active sites as a function of the relevant synthetic compositional variables. Further, we show that these distinct active sites can be tracked as they evolve under different exposure conditions, from ambient characterization, to dry and inert high temperature, to *operando* reaction conditions. This enumeration and tracking is enabled by site-sensitive spectroscopies that are able to interrogate the catalyst under working conditions and computational approaches that treat the catalyst in an “*operando*” fashion, incorporating reaction conditions and effective estimates of free energies avoiding the standard harmonic approximations into the predictions of site structure and composition.

We show that exchanged, atomically dispersed, and isolated Cu ions within the SSZ-13 cages populate two distinct types of sites, distinguished by the number of charge-compensating Al T-sites, and that the structure and dynamics of these two Cu types are strongly influenced by the environment they experience. H<sub>2</sub>O solvates both Cu types at ambient conditions, is lost at higher temperatures, and is replaced by NH<sub>3</sub> reactant at the 473 K SCR conditions. This NH<sub>3</sub> liberates Cu from the framework, greatly enhances Cu mobility, and masks some of the differences between the two site types. The sites remain distinct, however; while both Cu sites undergo similar redox cycles at similar rates under the conditions studied here, the mechanisms differ in detail, as illustrated by the intermediacy of transient Brønsted sites on one but not the other Cu site type (Figure 6.15).

These findings underscore the need for caution in extrapolating from *ex situ* characterizations to catalytic conditions. Reaction conditions can and in this example do have a substantial influence on active site structure and properties. These environment-induced modifications need not be limited to reactants. Surrogate “promoters” that modify active sites (e.g., by mobilizing at different conditions, or that modify redox properties) could provide an alternative to traditional catalytic material modifications for tuning catalytic activity.

## 6.5 Experimental Methods

### 6.5.1 DFT and AIMD Details

Plane-wave, supercell DFT supercell calculations employed a triclinic SSZ-13 supercell containing 12 T-sites [86] and Si:Al ratios of either 11:1 or 10:2. The first Brillouin zone was sampled at the  $\Gamma$  point only, as appropriate for this insulator. Many of the adsorbate structures considered here have multiple local minima. To identify representative structures for subsequent optimizations, initial structures were first annealed nonspin-polarized at 473 K in five independent simulations of 30 ps, each starting from different initial guess structures, for 150 ps total using the Car-Parrinello molecular dynamics software (CPMD; version 3.17.1) [390], the Perdew-Becke-Erzenhof [391] generalized gradient approximation (GGA) exchange-correlation functional, and ultrasoft pseudopotentials [392–394]. These Born-Oppenheimer molecular dynamics simulations were run in the NVT ensemble using a Nose-Hoover thermostat with a time step of 0.6 fs. RDFs from the final 90 of 150 ps simulations were constructed from the trajectories of a subset of these species for comparison to EXAFS results.

Low energy structures visited during the AIMD simulations were subsequently optimized using the Vienna Ab initio Simulation Package (VASP; version 5.3.5) [395]. Calculations were performed spin-polarized using the projector augmented wave (PAW) treatment of core-valence interactions [396,397] and a plane wave cutoff of 400 eV. For computational efficiency, structures were first relaxed within the GGA of Perdew et al. [391] and subsequently relaxed using the hybrid screened-exchange method of Heyd-Scuseria-Ernzerhof (HSE06) [398–401] and the Tkatchenko Scheffler method for van der Waals interactions (TSvdW) [402]. We converged self-consistent-field (SCF) electronic energies to  $10^{-6}$  eV and atomic forces to less than 0.03 eV/Å. Charge analysis was performed through the method of Bader [403–407]. Cu charges are reported normalized to  $\text{Cu}^{\text{II}}$  and  $\text{Cu}^{\text{I}}$  references ( $[\text{Z}_2\text{Cu}^{\text{II}}]$  and  $[\text{ZCu}^{\text{I}}]$ , respectively), then rounded to I or II reported as a superscript on Cu. Harmonic vibra-



tional frequencies of adsorbed species were calculated at the HSE06-TSvdW level by numerical differentiation of atomic forces with 0.01 Å displacements on the adsorbate atoms and used to compute zero-point vibrational energies (ZPE).

### 6.5.2 Ab Initio Free Energies

To relate DFT-computed energies to reaction conditions, we write the formation energies of adsorbed intermediates [408, 409] containing O and H relative to O<sub>2</sub> and H<sub>2</sub>O references:

$$\Delta G^{\text{form}}_{\text{x,y}}(T, \Delta\mu_{\text{O}_2}, \Delta\mu_{\text{H}_2\text{O}}) = \Delta E^{\text{form}}_{\text{x,y}} - T\Delta E^{\text{ST}}_{\text{x,y}}(T) - \frac{x}{2}(\Delta\mu_{\text{H}_2\text{O}} - \frac{1}{2}\Delta\mu_{\text{O}_2}) - \frac{y}{2}\Delta\mu_{\text{O}_2} \quad (6.23)$$

$$\Delta E^{\text{form}}_{\text{x,y}} = (E_{\text{ZCuHxOy}} - E_{\text{Z}^*\text{Cu}}) - \frac{x}{2}(E_{\text{H}_2\text{O}} - \frac{1}{2}E_{\text{O}_2}) - \frac{y}{2}E_{\text{O}_2} \quad (6.24)$$

The  $\Delta\mu$  are free parameters corresponding to the difference in chemical potential between 0 K and the conditions of interest. They can be related to corresponding temperatures and pressures through the ideal gas chemical potential relation.  $\Delta S^{\text{ST}}$  is the difference in entropy between a free and adsorbate-covered site. We have previously found that the harmonic oscillator approximation significantly underestimates actual entropies [85], consistent with observations made by others [340, 342, 410]. Comparisons with dynamics simulations suggest a simple heuristic in which the difference is approximated from the Sackur-Tetrode expression:

$$\Delta S^{\text{ST}}_{\text{x,y}} = (S_{\text{Z}^*\text{CuHxOy}} - S_{\text{Z}^*\text{Cu}}) \approx \frac{2}{3} \ln \left[ \left( \frac{2\pi M_{\text{x,y}} k_b T}{h^2} \right)^{3/2} \frac{V e^{5/2}}{N_A} \right] \quad (6.25)$$

where  $M_{\text{x,y}}$  is the total mass of the adsorbed species and  $V$  is the supercell volume. This model roughly treats adsorbed species as retaining 2/3 of their gas-phase translational entropy, similar to that discovered for adsorbates at surfaces [411].

It is straightforward to extend these expressions to ones appropriate in the presence of  $\text{NH}_3$ , conditions that present nitrogen as well as hydrogen and oxygen to the sites:

$$\begin{aligned} \Delta G^{\text{form}}_{x,y,z}(T, \Delta\mu_{\text{O}_2}, \Delta\mu_{\text{H}_2\text{O}}, \Delta\mu_{\text{NH}_3}) = \\ \Delta E^{\text{form}}_{x,y,z} - T\Delta E^{\text{ST}}_{x,y,z}(T) - \frac{x}{2}(\Delta\mu_{\text{H}_2\text{O}} - \frac{1}{2}\Delta\mu_{\text{O}_2}) \\ - \frac{y}{2}\Delta\mu_{\text{O}_2} - z(\Delta\mu_{\text{NH}_3} - \frac{3}{2}\Delta\mu_{\text{H}_2\text{O}} - \frac{3}{4}\Delta\mu_{\text{O}_2}) \quad (6.26) \end{aligned}$$

### 6.5.3 Zeolite Synthesis and Characterization.

Synthesis methods for all zeolites (SSZ-13, BEA, ZSM-5) can be found in Supporting Information 6.8.25. The crystal topologies of H-zeolites were confirmed from powder X-ray diffraction (XRD) patterns collected on a Rigaku SmartLab X-ray diffractometer equipped with a Cu  $K\alpha$  X-ray source (1.76 kW), and measured from  $4^\circ$  to  $40^\circ$  at a scan rate of  $0.00833^\circ \text{ s}^{-1}$  with a step size of  $0.01^\circ$  (Supporting Information 6.8.4). Micropore volumes of H-SSZ-13 zeolites were determined from Ar adsorption isotherms (87 K), and for H-BEA and H-ZSM-5 zeolites were determined from  $\text{N}_2$  adsorption isotherms (77 K), using a Micromeritics ASAP 2020 Surface Area and Porosity Analyzer, and were in reasonable agreement with the values expected for the CHA, BEA, and MFI frameworks and can be found in Supporting Information 6.8.26. Solid-state  $^{27}\text{Al}$  magic angle spinning nuclear magnetic resonance ( $^{27}\text{Al}$  MAS NMR) spectroscopy was used to estimate the fraction of framework and extraframework Al on H-form zeolites. SS NMR spectra were collected using a Chemmagetics CMX400 400 MHz spectrometer in a wide-bore 9.4 T magnet at ambient conditions from 456 scans with  $12.5 \mu\text{s}$  pulses and a 2 s delay and were measured at 104.24 MHz and MAS rate of 5 kHz. Prior to packing in a 4 mm  $\text{ZrO}_2$  rotor, zeolite samples were hydrated by holding for  $>48$  h in a desiccator containing a saturated potassium chloride (KCl) solution. All  $^{27}\text{Al}$  MAS NMR spectra are referenced to an aqueous 1.0 M  $\text{Al}(\text{NO}_3)_3$  solution. NMR spectra and quantification of extraframework Al for all H-zeolite samples can be found in Supporting Information 6.8.27.

Cu-zeolites were prepared by aqueous-phase Cu ion exchange of H-form zeolites with a  $\text{Cu}^{\text{II}}(\text{NO}_3)_2$  solution (0.001-0.1 M,  $100 \text{ cm}^3 \text{ g}^{-1}$ ; 99.999 wt%, Sigma-Aldrich) for 4 h and 300 rpm at ambient conditions, during which the pH was controlled to  $4.9 \pm 0.1$  through dropwise addition of a 1.0 M  $\text{NH}_4\text{OH}$  solution (Sigma-Aldrich). Co-SSZ-13 zeolites were prepared by ion exchange of HSSZ-13 with an aqueous 0.25 M  $\text{Co}^{\text{II}}(\text{NO}_3)_2$  solution ( $150 \text{ cm}^3 \text{ g}^{-1}$ ) for 4 h at ambient conditions, during which the pH was not controlled (pH stabilized between 3.2 and 3.6 after 4 h). Metal-exchanged zeolites were recovered by centrifugation and washed with deionized water six times ( $70 \text{ cm}^3 \text{ g}^{-1}$  per wash), dried at ambient temperature under flowing air, and then treated in flowing dry air ( $100 \text{ cm}^3 \text{ g}^{-1}$ ) to 773 K ( $0.0167 \text{ K s}^{-1}$ ) for 4 h. Elemental composition (Si, Al, Cu, Co) was determined using atomic absorption spectroscopy (AAS) on a PerkinElmer Analyst 300.

#### 6.5.4 $\text{NH}_3$ Temperature-Programmed Desorption.

Residual  $\text{H}^+$  sites on H-zeolites, on Cu- and Co-exchanged zeolites after oxidation treatments in air (20%  $\text{O}_2$ , balance  $\text{N}_2$ , 773 K, 4 h), and on Cu-zeolites after reduction treatments (500 ppm of  $\text{NO}$  + 500 ppm of  $\text{NH}_3$ , balance He, 473 K, 2 h) were titrated using the procedure described by Di Iorio et al. [171]. This titration method involves saturation of zeolites (ca. 0.03-0.05 g) with  $\text{NH}_3$  at 433 K (500 ppm, balance He, 2 h,  $350 \text{ cm}^3 \text{ min}^{-1}$ ), followed by removal of physisorbed and Cu-bound  $\text{NH}_3$  by treatment in wet helium (2.5-3.0%  $\text{H}_2\text{O}/\text{He}$ , 8 h,  $350 \text{ cm}^3 \text{ min}^{-1}$ ), to selectively retain surface  $\text{NH}_4^+$  species [78,105,171].  $\text{NH}_3$  was then evolved in a subsequent TPD in flowing He ( $350 \text{ cm}^3 \text{ min}^{-1}$ ) to 823 K ( $0.083 \text{ K s}^{-1}$ ), and quantified using on-board calibrations in a MKS MultiGas 2030 gas-phase FT-IR spectrometer. Further details can be found in Supporting Information 6.8.28.

### 6.5.5 Kinetics

Standard selective catalytic reduction (SCR) kinetics were measured on a bench-top tubular glass reactor described elsewhere [37]. All samples were sieved to a nominal size of 125-250  $\mu\text{m}$  and diluted with silica gel to obtain a bed height of ca. 2.5 cm. Steady-state kinetic data were collected at NO conversions below 20%, so that the entire bed was exposed to approximately the same gas concentrations, using a reactant gas mixture of 300 ppm of NO (3.6% NO/Ar, Praxair), 300 ppm of  $\text{NH}_3$  (3.0%  $\text{NH}_3$ /Ar, Praxair), 5%  $\text{CO}_2$  (liquid, Indiana Oxygen), 10%  $\text{O}_2$  (99.5%, Indiana Oxygen), 2.5%  $\text{H}_2\text{O}$  (deionized, 18.2 M $\Omega$ , introduced through saturator), and balance  $\text{N}_2$  (99.999% UHP, Indiana Oxygen) at 473 K and 1 atm. The total gas flow rate was maintained at 1.5 L min<sup>-1</sup>. Outlet gas concentrations were analyzed using on-board gas calibrations on an MKS MultiGas 2030 gas-phase Fourier transform infrared (FTIR) spectrometer, and NO,  $\text{NO}_2$ ,  $\text{NH}_3$ ,  $\text{CO}_2$ , and  $\text{H}_2\text{O}$  concentration data were recorded every 0.95 s.

### 6.5.6 Spectroscopic Methods (XAS, FTIR).

XAS experiments were carried out on the insertion device (ID) and bending magnet (BM) beamlines of the Materials Research Collaborative Access Team (MRCAT, Sector 10) at the Advanced Photon Source (APS) at Argonne National Laboratory. A cryogenically cooled double-crystal Si(111) monochromator was used with an uncoated glass mirror to minimize the presence of harmonics. Spectra were recorded in transmission mode with the ionization chambers optimized for the maximum current with linear response (ca.  $10^{10}$  photons s<sup>-1</sup>) using gas mixtures to give 10% absorption in the incident X-ray detector and 70% absorption in the transmission X-ray detector. A Cu metal foil spectrum was simultaneously collected while measuring sample spectra to calibrate the Cu K-edge to 8979 eV. *operando* experiments were performed at the 10-ID line in a special glassy carbon tube reactor described by Kispersky et al. [87], in which XAS spectra were collected simultaneously with steady-state stan-

dard SCR rate measurements to verify that rates were identical to those measured in separate differential plug-flow reactor experiments. XAS spectra were collected in an energy range between 8700 and 9890 eV for samples held under different gas conditions, and between 8700 and 9780 eV for *operando* experiments (additional details in Supporting Information 6.8.9). Multiple energy scans were taken to ensure the absence of time-dependent change or beam damage to the sample. Spectra were collected under isothermal conditions and normalized using a first-order polynomial in the pre-edge region and a third-order polynomial in the post-edge region. XANES spectra were fitted using a linear combination of  $\text{Cu}^{\text{I}}$  and  $\text{Cu}^{\text{II}}$  references [37,85,86] to determine the fractions of  $\text{Cu}^{\text{I}}$  and  $\text{Cu}^{\text{II}}$  in certain gas environments and under *operando* conditions. EXAFS data were fit from  $k = 2.7$  to ca.  $11 \text{ \AA}^{-1}$  (details of the fitting procedure in Supporting Information 6.8.9).

FTIR data were collected on zeolite samples using a Nicolet 6700 FTIR spectrometer equipped with a liquid nitrogen-cooled mercury cadmium telluride (MCT) detector. Catalyst samples (ca. 35-40 mg) were pressed into a self-supporting wafer (ca. 2 cm in diameter) and placed in a custom-built FTIR cell that has been described elsewhere [288]. Wafers were treated in flowing oxygen (10%  $\text{O}_2$ , balance He) to 673 K for 30 min and then cooled to 473 K, prior to collecting spectra. Spectra were collected with a resolution of  $4 \text{ cm}^{-1}$  and averaged over 1000 scans, baseline corrected, and normalized to the framework Si-O-Si combination/overtone band between 2100 and  $1750 \text{ cm}^{-1}$ . Additional details can be found in Supporting Information 6.8.6.

## 6.6 Acknowledgements

Financial support was provided by the National Science Foundation GOALI program under award number 1258715-CBET (Purdue) and 1258690-CBET (Notre Dame), and The Patrick and Jane Eilers Graduate Student Fellowship for Energy Related Research. Use of the Advanced Photon Source is supported by the U.S. Department of Energy, Office of Science, and Office of Basic Energy Sciences, under Contract no. DEAC02-06CH11357. We would like to thank Victor J. Cybulskis (Purdue) for his

help in performing XAS experiments at the APS. We thank Sachem, Inc., for providing the organic structure-directing agent used to synthesize SSZ-13. We thank the Center for Research Computing at Notre Dame, and EMSL, a DOE Office of Science User Facility sponsored by the Office of Biological and Environmental Research and located at Pacific Northwest National Laboratory, for support of computational resources.

Additionally, I acknowledge the American Chemical Society for granting permission to reproduce this chapter of my thesis. Adapted with permissions from The Journal of the American Chemical Society, 2016, 138, 6028-6048. Copyright (2016) American Chemical Society.

The full article can be accessed here: [dx.doi.org/10.1021/jacs.6b02651](https://doi.org/10.1021/jacs.6b02651).

## 6.7 Figures and Tables

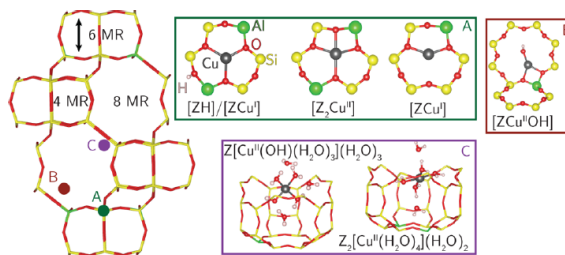


Figure 6.1. (left) Side view of the chabazite cage. (right) HSE06-optimized structures of (A,B) dehydrated oxidized and reduced Cu sites and (C) hydrated oxidized sites. Label indicates location of Cu ion within the chabazite cage.

Table 6.1.  
H<sub>2</sub>O Adsorption Energies ( $\Delta E_{\text{ads}}$ ) on Cu Sites Computed Using HSE06-TSvdw<sup>a</sup>

|                   | +xH <sub>2</sub> O                                 | 1   | 2   | 3    | 4   | 5   | 6   |
|-------------------|--|-----|-----|------|-----|-----|-----|
|                   | $\Delta E_{\text{ads}}$<br>(kJ mol <sup>-1</sup> ) | -84 | -94 | -108 | -84 | -90 | -73 |
| Z <sub>2</sub> Cu | cage location                                      | A   | A   | B    | C   | C   | C   |
|                   | O <sub>f</sub> /total CN                           | 3/4 | 3/4 | 2/4  | 0/4 | 0/4 | 0/4 |
|                   | $\Delta E_{\text{ads}}$<br>(kJ mol <sup>-1</sup> ) | -75 | -67 | -76  | -63 | -95 | -56 |
| ZCuOH             | cage location                                      | B   | C   | C    | C   | C   | C   |
|                   | O <sub>f</sub> /total CN                           | 2/4 | 0/3 | 0/3  | 0/4 | 0/4 | 0/4 |

<sup>a</sup>Cage location referenced to Figure 1. CN and O<sub>f</sub> indicate total Cu coordination number and number of close framework O contacts, respectively.

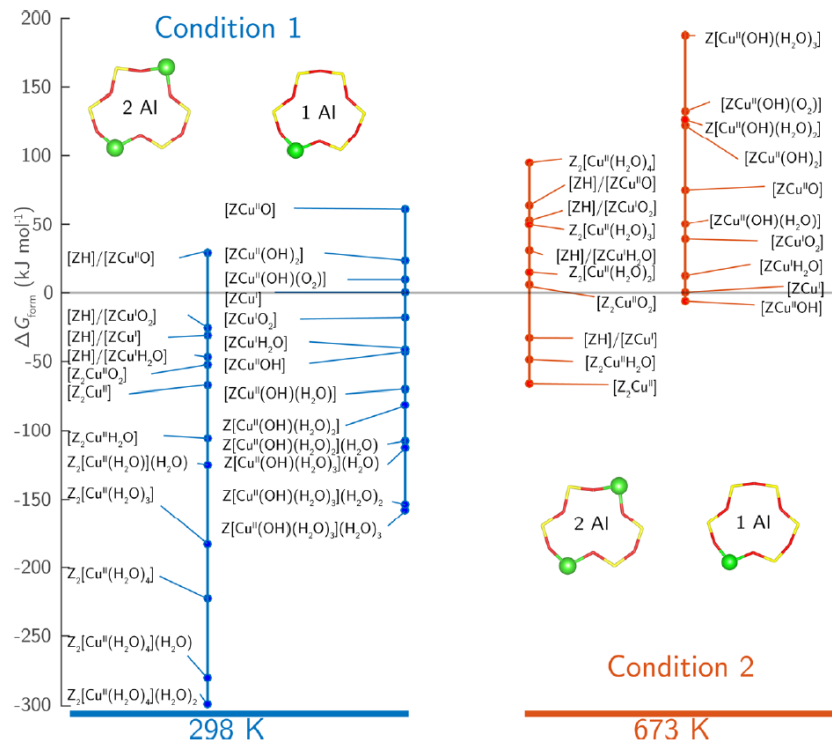


Figure 6.2. Formation free energies ( $\Delta G_{\text{form}}$ )  $\text{CuH}_x\text{O}_y$  species at (left) 298 K, 2%  $\text{H}_2\text{O}$ , 20%  $\text{O}_2$ , and at (right) 673 K, 2%  $\text{H}_2\text{O}$ , 20%  $\text{O}_2$  on the 2Al ( $\text{Z}_2\text{Cu}$ ) and 1Al ( $\text{ZCu}$ ) sites. Common energy reference set through eq 6.6.



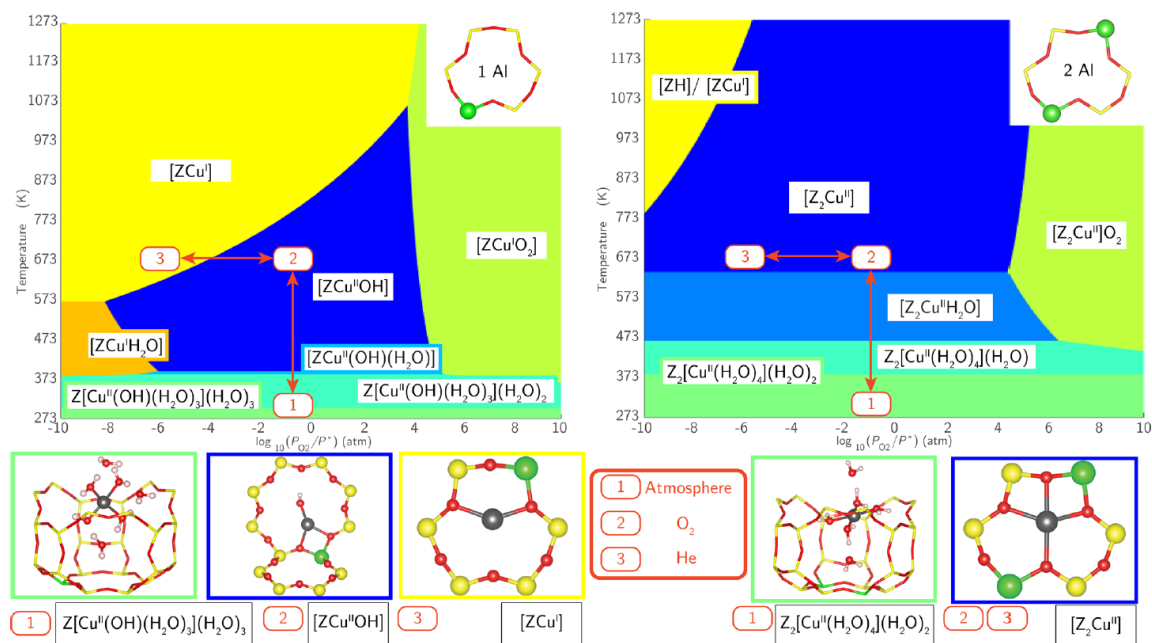


Figure 6.3. *ex situ* Cu speciation phase diagrams based on HSE06-TSvdw calculations on 1Al (left) and 2Al (right) Cu exchange sites. Regions indicate site composition that minimizes free energy at 2% H<sub>2</sub>O and given T and PO<sub>2</sub>. Labeled on the phase diagram and illustrated below are minimum free energy species at (1) ambient (298 K, 20% O<sub>2</sub>), (2) oxidizing (673 K, 20% O<sub>2</sub>), and (3) inert (673 K, 10<sup>-6</sup> atm O<sub>2</sub> in He).

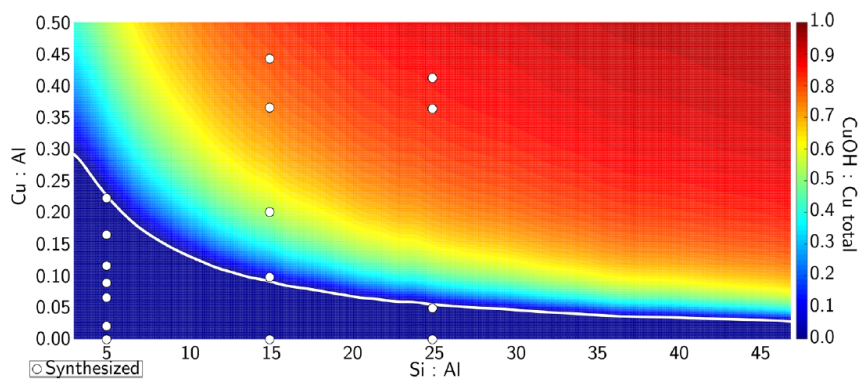


Figure 6.4. Predicted Cu site compositional phase diagram versus Si:Al and Cu:Al ratios. Color scale indicates predicted fraction of CuOH. White line demarcates transition from  $[Z_2Cu]$ -only region to mixed  $[Z_2Cu]/[ZCuOH]$  region. White circles indicated compositions of synthesized Cu-SSZ-13 samples.

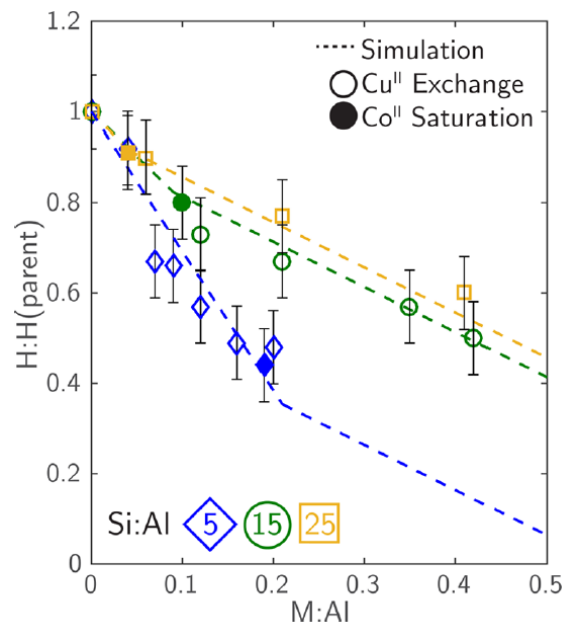


Figure 6.5. Residual  $H^+$  sites per parent sample  $H^+$  from  $\text{NH}_3$  titrations on oxidized M-SSZ-13 samples versus extent of M/Al exchange for Si:Al = 5 (blue), 15 (green), and 25 (orange). Open and filled symbols denote  $\text{Cu}^{2+}$  and saturated  $\text{Co}^{2+}$  exchange, respectively. Dashed lines are model predictions.

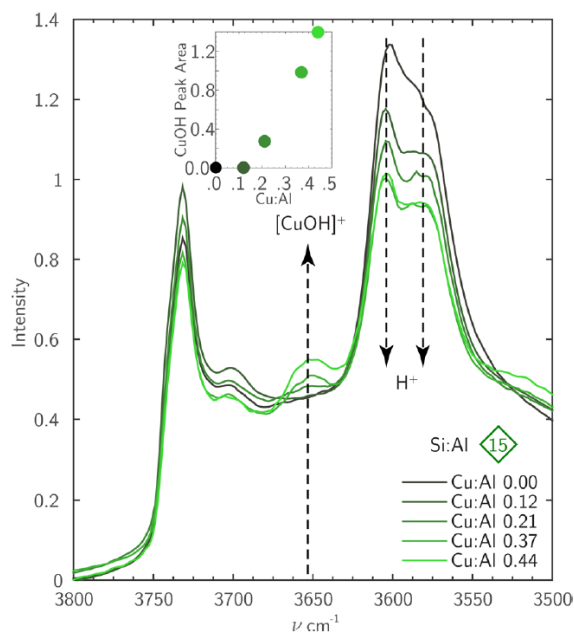


Figure 6.6. FTIR spectra of oxidized Cu-SSZ-13 samples (Cu:Al = 0-0.44, Si:Al = 15). Inset: Integrated 3660 cm<sup>-1</sup> CuO-H area as a function of Cu:Al ratio.

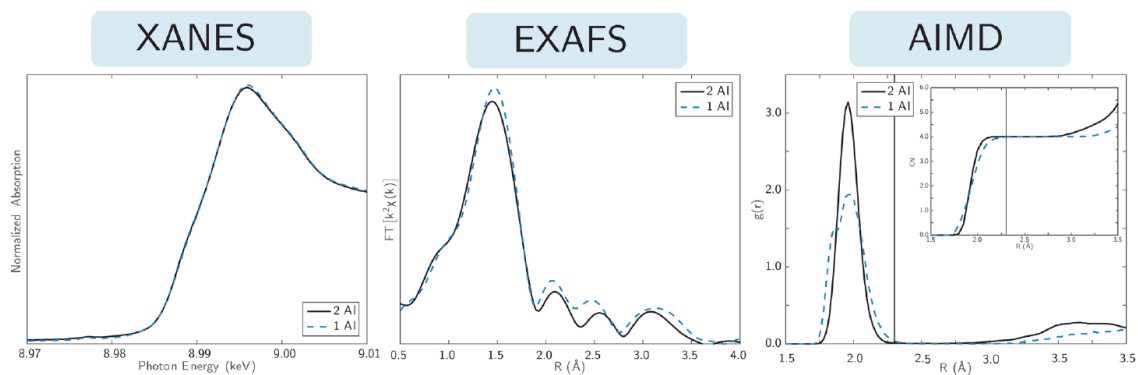


Figure 6.7. Left: XANES spectra collected on the 1Al (teal dashes) and 2Al (black lines) Cu-SSZ-13 samples under treatment in 2% H<sub>2</sub>O, 20% O<sub>2</sub> at 298 K. Middle: EXAFS spectra under the same conditions. Right: 298 K AIMD RDFs and integrated RDFs (inset).

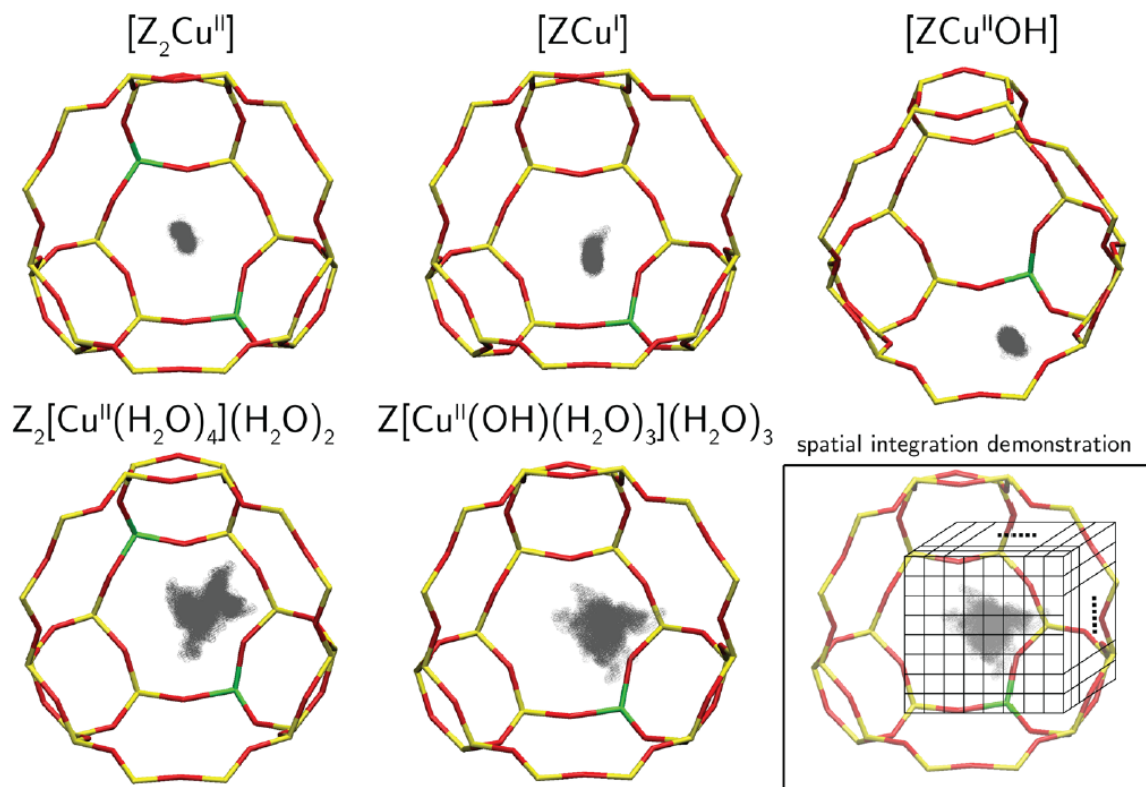


Figure 6.8. Cu positions (gray balls) visited during 90 ps of NVT AIMD at 298 K. Fixed zeolite framework shown for ease of visualization; framework was unconstrained during dynamics. Inset illustrates discretization used to compute relative Cu mobilities.

Table 6.2.

Comparison of AIMD (Left) and EXAFS (Right) Characterization of 2Al and 1Al Sites, Including Cu-X (X = O, N) Coordination Number (CN), Average Cu-X Distances, and Whether Second-Shell Features Appear.

| gas condition                            | sample | AIMD   EXAFS          |                         |              |                          |
|--|--------|-----------------------|-------------------------|--------------|--------------------------|
|  |        | CN                    | avg. bond dist.         | second shell | Cu mobility <sup>c</sup> |
| condition 1 (ambient)                    | 1Al    | 4.0 4.2               | 1.96 1.93               | N N          | 1.38                     |
|  | 2Al    | 4.0 4.0               | 1.96 1.94               | N N          | 1.00                     |
| condition 2 (O <sub>2</sub> )            | 1Al    | 3.0 3.0               | 1.89 1.91               | Y Y          | 0.11                     |
|  | 2Al    | 3.9 3.8               | 2.02 1.94               | Y Y          | 0.14                     |
| condition 3 (He)                         | 1Al    | 2.5 <sup>a</sup>  2.4 | 1.92 <sup>a</sup>  1.92 | Y Y          | 0.14 <sup>a</sup>        |
|  | 2Al    | 3.7 <sup>a</sup>  3.6 | 2.50 <sup>a</sup>  2.40 | Y Y          | 0.14 <sup>a</sup>        |
| NO + NH <sub>3</sub> , 473 K             | 1Al    | 2.0 2.2               | 1.89 1.88               | N N          | 3.26                     |
|  | 2Al    | 2.0 2.1               | 1.89 1.88               | N N          | 1.83                     |
| O <sub>2</sub> + NH <sub>3</sub> , 473 K | 1Al    | 3.3 <sup>b</sup>  3.2 | 1.97 <sup>b</sup>  1.92 | N N          | 2.21 <sup>b</sup>        |
|  | 2Al    | 3.6 <sup>b</sup>  3.5 | 2.00 <sup>b</sup>  1.92 | N N          | 1.31 <sup>b</sup>        |

<sup>a</sup>XANES weighted average of Cu<sup>I</sup> (ZCu<sup>I</sup>) and Cu<sup>II</sup> (Z<sub>2</sub>Cu and ZCuOH) structures obtained from AIMD. <sup>b</sup>XANES weighted average of Cu<sup>I</sup> (ZCu<sup>I</sup>(NH<sub>3</sub>)<sub>2</sub> and ZNH<sub>4</sub>/ZCu<sup>I</sup>(NH<sub>3</sub>)<sub>2</sub>) and Cu<sup>II</sup> (Z<sub>2</sub>Cu(NH<sub>3</sub>)<sub>4</sub> and ZCu(OH)(NH<sub>3</sub>)<sub>3</sub>) structures obtained from AIMD. <sup>c</sup>Volume visited by the minimum free energy forms of Cu<sup>I</sup> and Cu<sup>II</sup> (Figure 3) during 90 ps AIMD, normalized to the volume of hydrated Z<sub>2</sub>Cu (1.00).

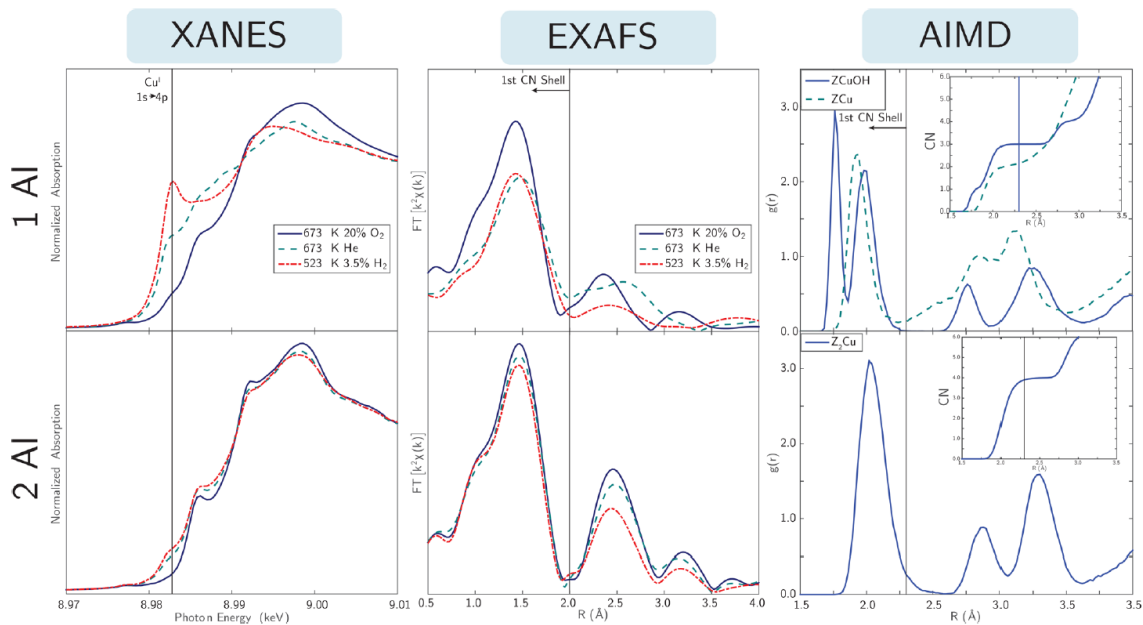


Figure 6.9. Left: XANES spectra collected on the 1Al (top) and 2Al (bottom) samples after treatment in 20%  $\text{O}_2$  at 673 K (solid blue lines), He at 673 K (dashed teal lines), and in 3%  $\text{H}_2$  at 523 K (dot-dash red lines). Middle: Corresponding EXAFS spectra. Right: AIMD Cu-Si/O/Al RDFs for ZCuOH and ZCu (top) and  $\text{Z}_2\text{Cu}$  (bottom). Insets show integrated RDFs.

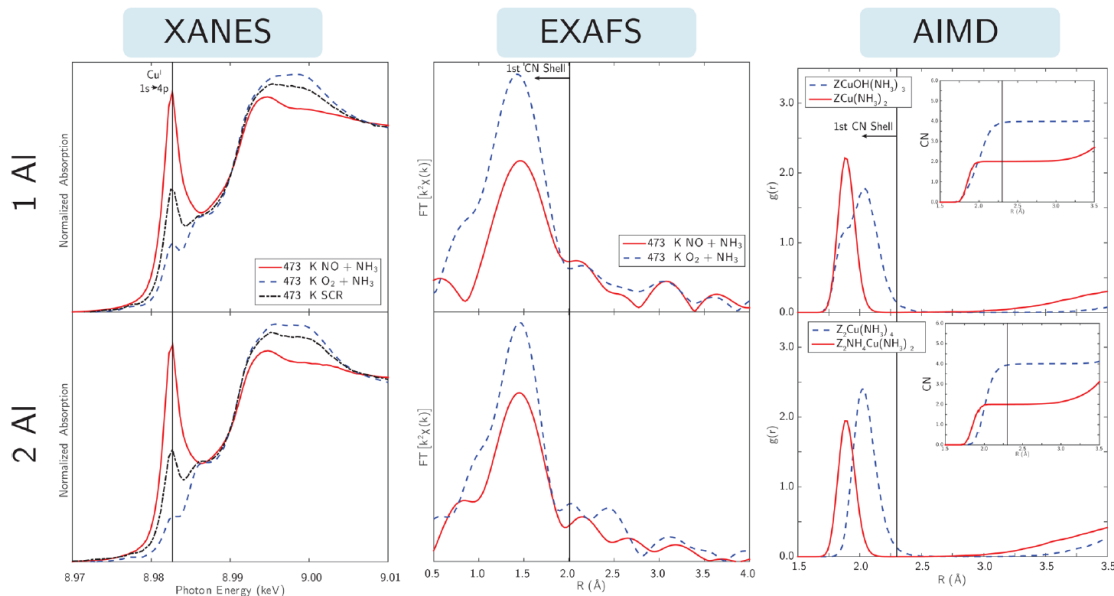


Figure 6.10. Left: XANES spectra of the 1 Al (top) and 2Al (bottom) Cu-SSZ-13 samples under treatment in 2% H<sub>2</sub>O, 10% O<sub>2</sub>, 300 ppm of NH<sub>3</sub> at 473 K (O<sub>2</sub> + NH<sub>3</sub>, blue traces), 2% H<sub>2</sub>O and 300 ppm of NO/NH<sub>3</sub> at 473 K (NO + NH<sub>3</sub>, red lines), and in 2% H<sub>2</sub>O, 10% O<sub>2</sub>, 300 ppm of NO/NH<sub>3</sub> at 473 K (black traces). Middle: EXAFS collected under same conditions. Right: AIMD Cu -Si/O/Al RDFs for the most stable Cu<sup>I</sup> (red lines) and Cu<sup>II</sup> (blue traces) species on the 1 and 2Al sites in the presence of NH<sub>3</sub>. Insets: Integrated RDFs.

Table 6.3.

Characterization of 2Al and 1Al Cu-SSZ-13 Catalysts during Low-Temperature (473 K) Standard SCR: XANES Cu<sup>I</sup>/Cu<sup>II</sup> Fraction, SCR Rates (per Cu and mol NO) in the *operando* Reactor/Plug-Flow Reactor, Apparent Activation Energies, and Apparent NO, O<sub>2</sub>, and NH<sub>3</sub> Orders.

|     | Cu <sup>I</sup> /Cu <sup>II</sup> | TOR <sup>a</sup> | E <sub>app</sub> (kJ mol <sup>-1</sup> ) | NO order              | O <sub>2</sub> order  | NH <sub>3</sub> order |
|-----|-----------------------------------|------------------|--|-----------------------|-----------------------|-----------------------|
| 2Al | 50/50 ± 5                         | 8.3/7.3          | 60 ± 10                                  | 0.8/0.8               | 0.3/0.3               | -0.2/-0.1             |
| 1Al | 55/45 ± 5                         | 9.9/8.0          | 74 ± 10                                  | n.m./0.7 <sup>b</sup> | n.m./0.3 <sup>b</sup> | n.m./0.0 <sup>b</sup> |

<sup>a</sup>(s<sup>-1</sup> mol Cu<sup>1-</sup> mol NO<sup>-1</sup>) × 10<sup>-3</sup>. <sup>b</sup>n.m. = not measured; 1Al orders were measured only in the PFR.



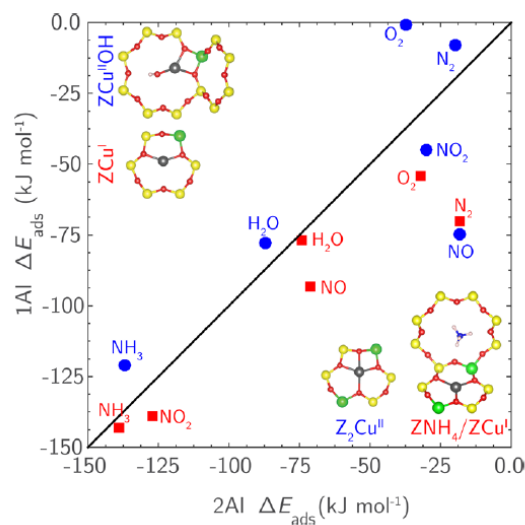


Figure 6.11. Parity plot of HSE06-TSvdw-computed binding energies of gaseous species relevant to SCR on 2Al oxidized ( $\text{Z}_2\text{Cu}$ , blue) and reduced ( $\text{ZNH}_4/\text{ZCu}$ , red) versus corresponding oxidized ( $\text{ZCuOH}$ , blue) and reduced ( $\text{ZCu}$ , red) 1Al sites.

Table 6.4.  
HSE06-TSvdw-Computed Sequential  $\text{NH}_3$  Adsorption Structures and Energies<sup>a</sup>.

|  | $+x\text{NH}_3$                                 | 1    | 2                     | 3    | 4    |
|--|---|------|-----------------------|------|------|
| $[\text{Z}_2\text{Cu}^{\text{II}}]$      | $\Delta E_{\text{ads}}$ (kJ mol <sup>-1</sup> ) | -132 | -136                  | -123 | -132 |
|  | cage location                                   | A    | A                     | B    | C    |
|  | $\text{O}_f/\text{total CN}$                    | 3/4  | 2/4                   | 1/4  | 0/4  |
| $[\text{ZNH}_4]/[\text{ZCu}^{\text{I}}]$ | $\Delta E_{\text{ads}}$ (kJ mol <sup>-1</sup> ) | -134 | -150                  | -72  | -73  |
|  | cage location                                   | B    | C                     | C    | C    |
|  | $\text{O}_f/\text{total CN}$                    | 1/2  | 0/2                   | 0/2  | 0/2  |
| $[\text{ZCu}^{\text{II}}\text{OH}]$      | $\Delta E_{\text{ads}}$ (kJ mol <sup>-1</sup> ) | -117 | -119                  | -116 | -47  |
|  | cage location                                   | B    | C, B <sup>b</sup>     | C    | C    |
|  | $\text{O}_f/\text{total CN}$                    | 2/4  | 0/3, 1/4 <sup>b</sup> | 0/4  | 0/4  |
| $[\text{ZCu}^{\text{I}}]$                | $\Delta E_{\text{ads}}$ (kJ mol <sup>-1</sup> ) | -137 | -151                  | -75  | -41  |
|  | cage location                                   | B    | C                     | C    | C    |
|  | $\text{O}_f/\text{total CN}$                    | 1/2  | 0/2                   | 0/2  | 0/2  |

<sup>a</sup>Cage location indicates optimized ion location referenced to Figure 1. CN and  $\text{O}_f$  indicate total Cu coordination number and number of close framework O contacts, respectively. <sup>b</sup>Trigonal planar, square planar values.

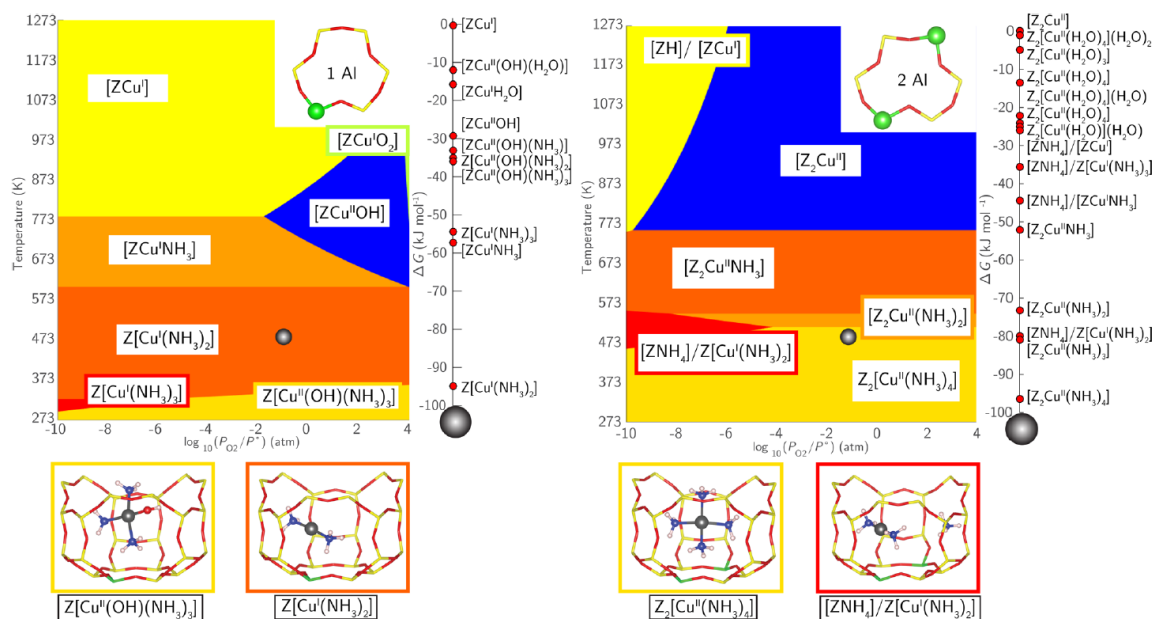


Figure 6.12. Phase diagrams for 1Al (left) and 2Al (right) sites with varying  $T$  and  $P_{O_2}$  at 300 ppm of  $NH_3$  and 2%  $H_2O$ . Relative rankings for all species  $\Delta G_{form} < 0$  at 473 K and 10%  $O_2$  (chrome spheres on the phase diagrams) are given to the right of each phase diagram. The structures shown on the bottom are the most stable  $Cu^I$  (red) and  $Cu^{II}$  (golden) under these conditions.

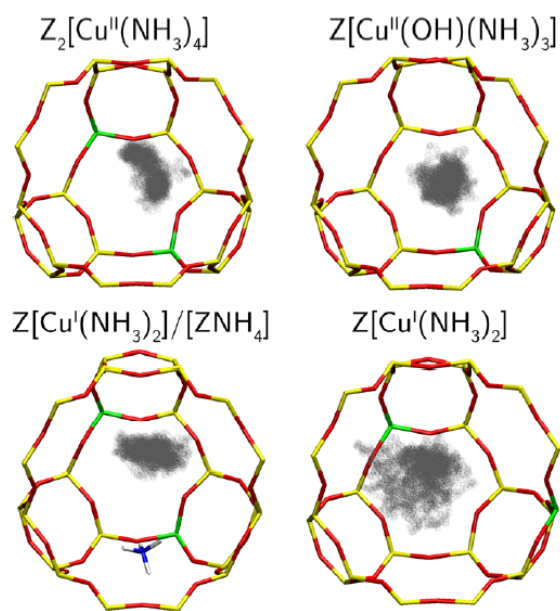


Figure 6.13. Cu positions (gray balls) sampled inside the zeolite cage during 90 ps of equilibrated NVT AIMD at 473 K for the most stable  $NH_3$  solvated  $Cu^I$  and  $Cu^{II}$  species.

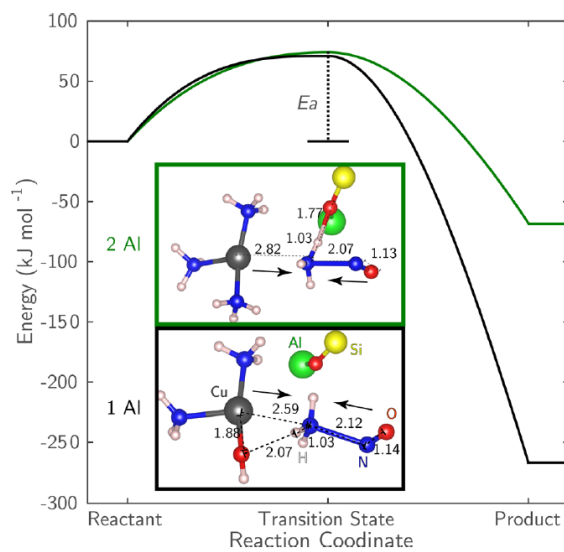


Figure 6.14. HSE06 CI-NEB calculated activation ( $E_a$ ) and reaction energies for NO-assisted reduction of  $\text{NH}_3$  solvated  $\text{Cu}^{\text{II}}$  1Al (black) and 2Al (green) sites. Transition state structures are shown boxed. For ease of visualization, most of the zeolite framework is hidden.

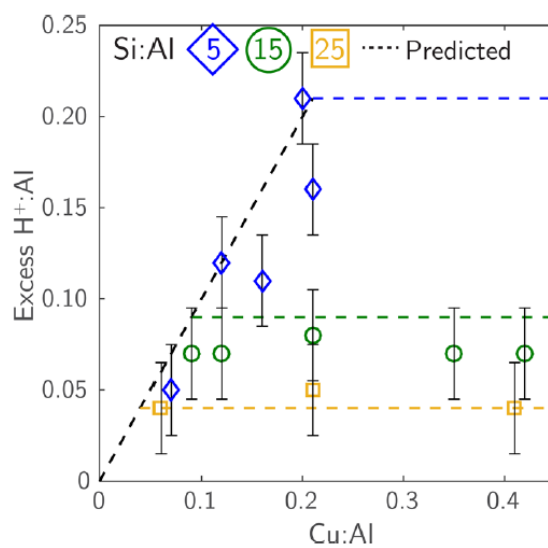


Figure 6.15. Number of extra H<sup>+</sup> sites (per Al) formed after reduction of Cu<sup>II</sup> to Cu<sup>I</sup> in flowing NO and NH<sub>3</sub> (473 K) as measured by NH<sub>3</sub> titration and TPD. Dashed lines represent the predicted number of H<sup>+</sup> formed on the basis of the assumption that reduction of only Cu<sup>II</sup> at 2Al sites forms a Cu<sup>I</sup>/H<sup>+</sup> site pair.

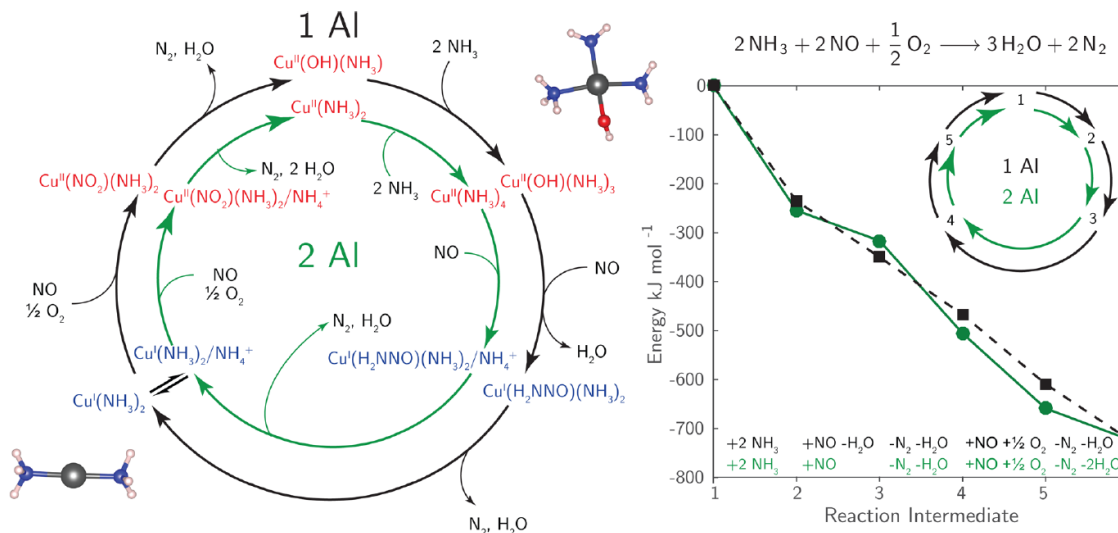


Figure 6.16. (Left) Proposed parallel standard SCR cycles for  $\text{NH}_3$ -solvated Cu ions near 1Al (black) or 2Al (green). (Right) HSE06-TSvdw computed reaction energies along each step of the proposed cycles. 1-5 correspond to the intermediates in the left panel. Listed are the molecules consumed (+) and generated (-) between each intermediate.

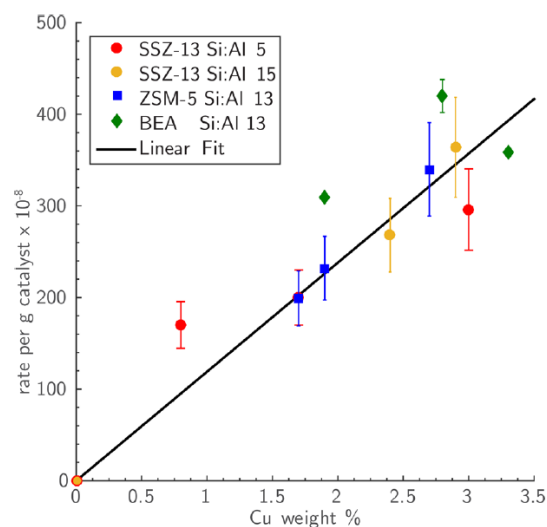


Figure 6.17. Standard SCR rates per g catalyst at 473 K on Cu-exchanged SSZ-13, ZSM-5, and BEA versus Cu weight percent.

## 6.8 Supporting Information

### 6.8.1 HSE06-TSvdw Values for Phase Diagram Species

Bader charges were normalized to  $Z\text{Cu}$  (1.00), and  $Z_2\text{Cu}$  (2.00).  $\Delta\text{ZPE}$  is defined as the ZPE difference between the adsorbate bound site and the bare site:

$$\Delta\text{ZPE}(Z_2\text{CuH}_2\text{O}) = \text{ZPE}(Z_2\text{CuH}_2\text{O}) - \text{ZPE}(Z_2\text{Cu}) \quad (6.27)$$

### 6.8.2 $\text{H}_2\text{O}$ Pressure Phase Diagrams

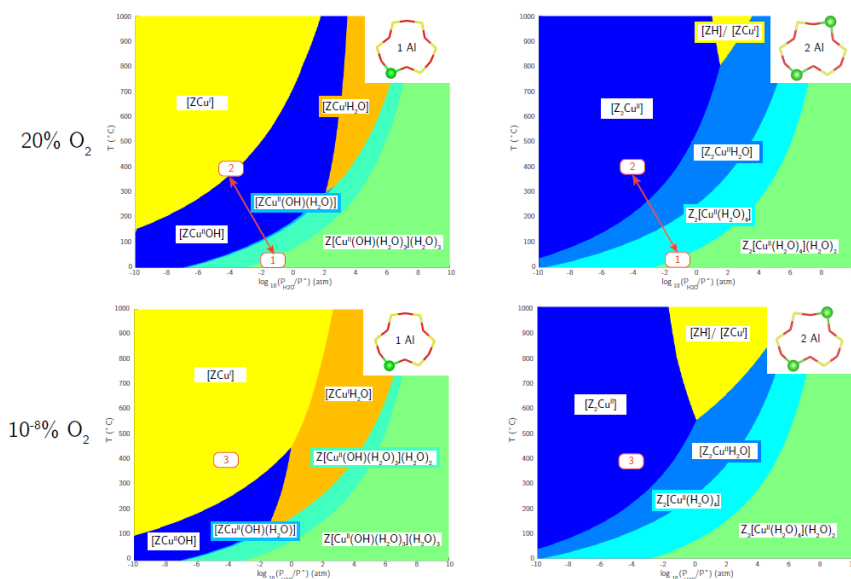


Figure 6.18.  $\text{H}_2\text{O}$  partial pressure phase diagrams at fixed  $\text{O}_2$  pressures.

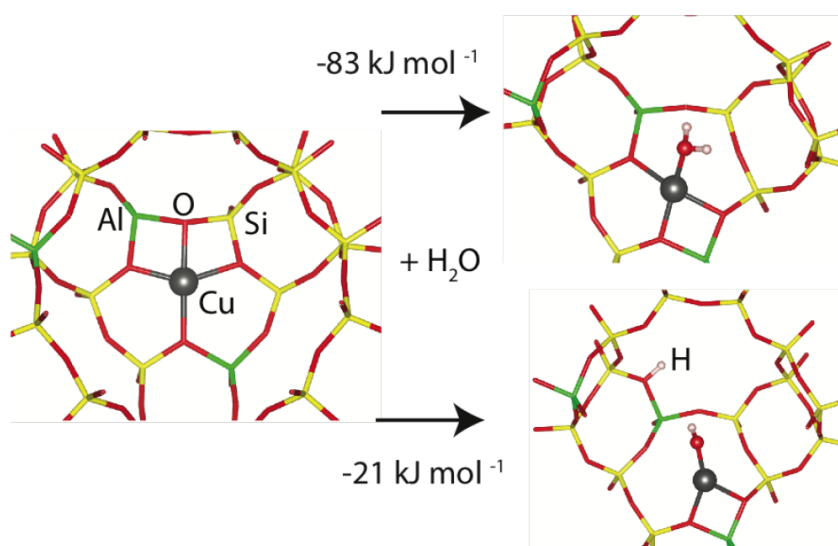
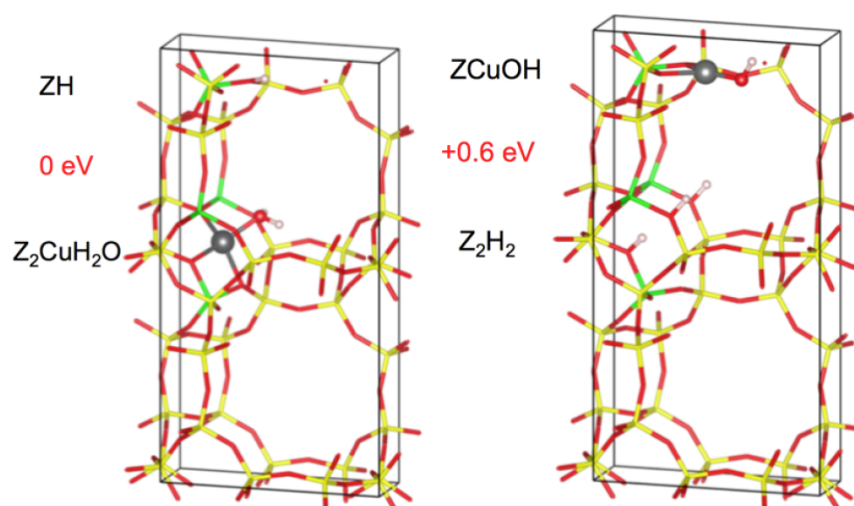


Table 6.5.  
Calculated total energies (kJ mol<sup>-1</sup>), ZPE's of adsorbed species, and normalized Bader charges for the 2Al system.

| Species   | Total Energy | $\Delta$ ZPE | Bader Charge |
|---|--------------|--------------|--------------|
| Z <sub>2</sub> Cu                                   | -351.11      | 0.00         | 2.00         |
| Z <sub>2</sub> CuH <sub>2</sub> O                   | -369.56      | 0.71         | 2.02         |
| Z <sub>2</sub> CuH <sub>2</sub> Ox2                 | -388.10      | 1.43         | 1.99         |
| Z <sub>2</sub> CuH <sub>2</sub> Ox3                 | -406.84      | 2.13         | 2.05         |
| Z <sub>2</sub> CuH <sub>2</sub> Ox4                 | -425.25      | 2.84         | 2.05         |
| Z <sub>2</sub> CuH <sub>2</sub> Ox5                 | -443.76      | 3.55         | 1.76         |
| Z <sub>2</sub> CuH <sub>2</sub> Ox6                 | -462.00      | 4.22         | 2.03         |
| Z <sub>2</sub> CuO2                                 | -365.30      | 0.11         | 1.70         |
| Z <sub>2</sub> HCu                                  | -355.98      | 0.32         | 1.05         |
| Z <sub>2</sub> HCuH <sub>2</sub> O                  | -374.17      | 1.01         | 1.06         |
| Z <sub>2</sub> HCuO                                 | -362.56      | 0.35         | 2.02         |
| Z <sub>2</sub> HCuO2                                | -370.45      | 0.44         | 1.70         |
| Z <sub>2</sub> HCu(OH)2                             | -378.17      | 1.00         | 2.07         |
| Z <sub>2</sub> CuNH <sub>3</sub>                    | -375.75      | 1.08         | 1.94         |
| Z <sub>2</sub> CuNH <sub>3</sub> x2                 | -400.41      | 2.15         | 1.87         |
| Z <sub>2</sub> CuNH <sub>3</sub> x3                 | -424.95      | 3.22         | 1.80         |
| Z <sub>2</sub> CuNH <sub>3</sub> x4                 | -449.59      | 4.31         | 1.72         |
| Z <sub>2</sub> CuNH <sub>4</sub>                    | -380.98      | 1.39         | 1.04         |
| Z <sub>2</sub> NH <sub>4</sub> CuNH <sub>3</sub>    | -405.62      | 2.46         | 0.96         |
| Z <sub>2</sub> NH <sub>4</sub> CuNH <sub>3</sub> x2 | -430.41      | 3.50         | 0.86         |
| Z <sub>2</sub> NH <sub>4</sub> CuNH <sub>3</sub> x3 | -454.32      | 4.47         | 0.84         |
| Z <sub>2</sub> NH <sub>4</sub> CuNH <sub>3</sub> x4 | -478.24      | 5.43         | 0.83         |

Table 6.6.  
Calculated total energies (kJ mol<sup>-1</sup>), ZPE's of adsorbed species, and normalized Bader charges for the 1Al system.

| Species                   | Total Energy | $\Delta$ ZPE | Bader Charge |
|---------------------------|--------------|--------------|--------------|
| ZCuOH                     | -366.87      | 0.35         | 1.80         |
| ZCuOH-H <sub>2</sub> O    | -385.20      | 1.03         | 1.92         |
| ZCuOH-H <sub>2</sub> Ox2  | -403.50      | 1.75         | 1.84         |
| ZCuOH-H <sub>2</sub> Ox3  | -421.82      | 2.44         | 1.65         |
| ZCuOH-H <sub>2</sub> Ox4  | -440.10      | 3.19         | 1.99         |
| ZCuOH-H <sub>2</sub> Ox5  | -458.67      | 3.90         | 2.04         |
| ZCuOH-H <sub>2</sub> Ox6  | -476.83      | 4.61         | 2.00         |
| ZCu(OH)O2                 | -380.90      | 0.48         | 1.84         |
| ZCu                       | -353.94      | 0.00         | 1.00         |
| ZCuH <sub>2</sub> O       | -372.25      | 0.68         | 1.05         |
| ZCuO                      | -360.31      | 0.04         | 1.73         |
| ZCuO2                     | -368.49      | 0.12         | 1.56         |
| ZCu(OH)2                  | -378.82      | 0.72         | 2.11         |
| ZCu(OH)NH <sub>3</sub>    | -391.35      | 1.42         | 1.80         |
| ZCu(OH)NH <sub>3</sub> x2 | -415.84      | 2.49         | 1.73         |
| ZCu(OH)NH <sub>3</sub> x3 | -440.29      | 3.55         | 1.70         |
| ZCu(OH)NH <sub>3</sub> x4 | -463.63      | 4.52         | 1.73         |
| ZCuNH <sub>3</sub>        | -378.61      | 1.06         | 0.95         |
| ZCuNH <sub>3</sub> x2     | -403.44      | 2.13         | 0.86         |
| ZCuNH <sub>3</sub> x3     | -427.37      | 3.10         | 0.85         |
| ZCuNH <sub>3</sub> x4     | -450.95      | 4.05         | 0.83         |

6.8.3  $Z_2Cu$  vs  $ZCuOH$  Exchange EnergeticsFigure 6.19.  $Z_2CuH_2O$  vs.  $ZH/ZCuOH$  energetics in a single supercell.Figure 6.20.  $Z_2CuH_2O$  vs.  $ZH/ZCuOH$  energetics in a  $2 \times 1 \times 1$  supercell.

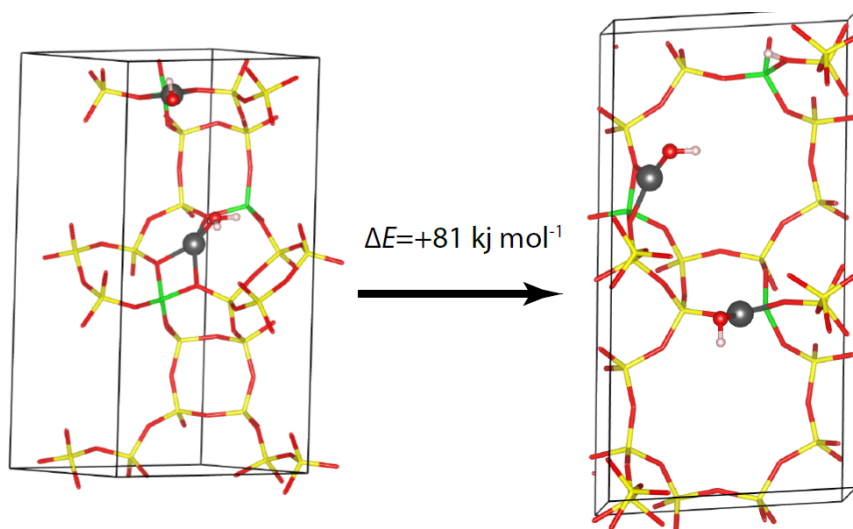


Figure 6.21.  $Z_2CuH_2O/ZCuOH$  vs.  $ZH/ZCuOHx2$  energetics in a  $2 \times 1 \times 1$  supercell.

#### 6.8.4 XRD Patterns

Powder X-ray diffraction (XRD) data were collected on a SmartLab Rigaku diffractometer using a  $Cu\ K\alpha$  source. Approximately 0.6 g of sample were loaded in a sample holder with a depth of 2 mm. Patterns were obtained from  $4$  to  $40^\circ\ 2\theta$  using a step size of  $0.01^\circ$  and scan rate  $0.05^\circ\ min^{-1}$  at ambient conditions.

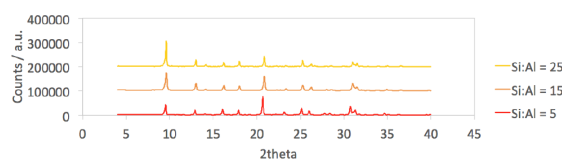


Figure 6.22. XRD spectra on the H-form of the Si:Al 5, 15, and 25 samples.

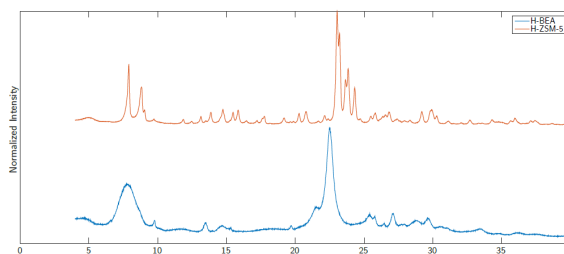


Figure 6.23. XRD spectra on the H-form of BEA and ZSM-5 samples.

### 6.8.5 Atomic absorption spectroscopy

Approximately 20 mg of sample were dissolved in 2 mL of HF, then diluted with between 50 to 120 mL deionized water (Millipore, Synergy UV Water Purification System,  $18.2 \text{ M}\Omega \text{ cm}^{-1}$  resistivity). Elemental analysis to measure the Si:Al, Co:Al, and Cu:Al of the dissolved sample was performed using atomic absorption spectroscopy (AAS) on a Perkin-Elmer AAnalyst 300. Na:Al and K:Al were measured also, but not detected within error.

### 6.8.6 FTIR Details

The IR data were collected using a Nicolet 6700 FTIR spectrometer equipped with a liquid nitrogen cooled MCT detector. Experiments were performed in a custom designed transmission FTIR cell, a detailed description of which can be found in our previous publication [288]. About 35-40 mg of each catalyst sample was loaded in the form of a self-supported wafer, 2 cm in diameter. All samples were treated with 10%  $\text{O}_2$  (UHP grade  $\text{O}_2$ , Indiana Oxygen diluted with UHP grade He, Indiana Oxygen) at 673 K for 30 min and then cooled down in the same gas flow to 473 K. All reported spectra were collected at 473 K with a resolution of  $4 \text{ cm}^{-1}$ , averaged over 1000 scans and baseline corrected for direct comparison. The IR spectrum of the H-form was subtracted from the corresponding spectrum for each Cu-SSZ-13 sample to obtain a

Table 6.7.  
AAS obtained Si:Al and Cu:Al values on all zeolite samples.

| Zeolite              | Si:Al | Cu:Al |
|----------------------|-------|-------|
| SSZ-13 (Synthesized) | 4.5   | 0.00  |
|                      |       | 0.02  |
|                      |       | 0.04  |
|                      |       | 0.09  |
|                      |       | 0.12  |
|                      |       | 0.16  |
|                      |       | 0.20  |
|                      | 14.8  | 0.00  |
|                      |       | 0.12  |
|                      |       | 0.21  |
|                      |       | 0.37  |
|                      |       | 0.44  |
|                      | 24.1  | 0.00  |
|                      |       | 0.06  |
|                      |       | 0.37  |
|                      |       | 0.41  |
| ZSM-5 (Commercial)   | 12.5  | 0.24  |
|                      |       | 0.27  |
|                      |       | 0.35  |
| BEA (Commercial)     | 13.0  | 0.25  |
|                      |       | 0.34  |
| BEA (Synthesized)    | 13.0  | 0.43  |

Table 6.8.  
AAS obtained Si:Al and Co:Al values after Co saturation.

| Zeolite              | Si:Al | Co:Al |
|----------------------|-------|-------|
| SSZ-13 (Synthesized) | 4.5   | 0.19  |
|                      | 14.8  | 0.10  |
|                      | 24.1  | 0.04  |

difference spectrum. The peak area for the CuOH species at  $3650\text{ cm}^{-1}$  [36,38] was quantified as a function of Cu loading.

All spectra were first normalized by their T-O-T vibrations between 2082 and  $1589\text{ cm}^{-1}$ . Difference spectra were obtained by subtracting the spectrum of H/SSZ-13 from each of the individual Cu/SSZ-13 sample spectra. This clearly showed the growth of the CuOH peak at  $3651\text{ cm}^{-1}$  with Cu loading, while the associated peak area was quantified by using a baseline between 3670 to  $3635\text{ cm}^{-1}$ . The corresponding Brønsted OH peak area was calculated by drawing a baseline between 3627 and  $3523\text{ cm}^{-1}$  for the difference spectra of each sample. Since both Brønsted hydroxyl peaks decreased with increasing Cu loading, the total Brønsted hydroxyl peak area was calculated rather than that for the individual peaks at 3580 or  $3605\text{ cm}^{-1}$ .

#### 6.8.7 Si:Al 5 repeat synthesis with H:Al ratios between 0.45-0.85

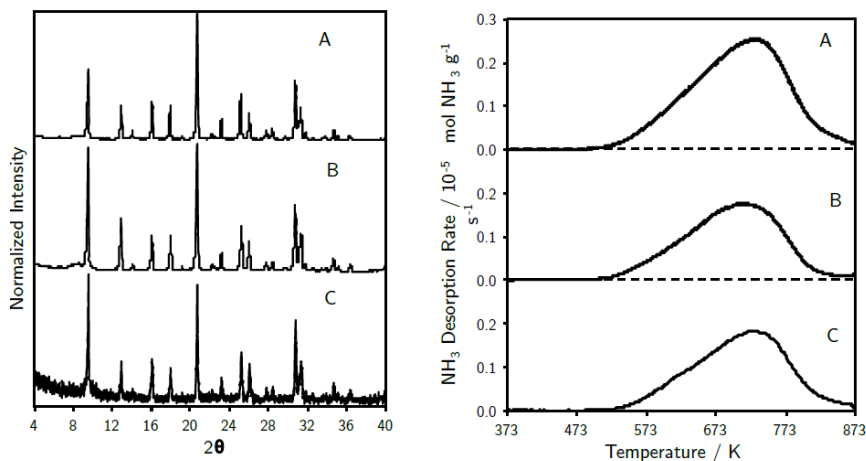


Figure 6.24. (left) XRD spectra for Si:Al 5 samples with H:Al ranging from 0.85(A) to 0.65(B) to 0.45(C) (right)  $\text{NH}_3$  TPDs following a purge of physisorbed  $\text{NH}_3$  to determine the number of H:Al.



## 6.8.8 Si:Al=5 Cu:Al=0.02 Data

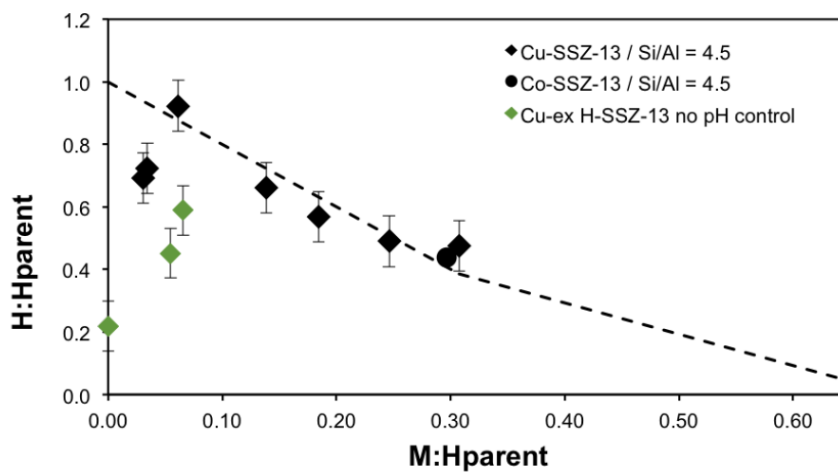


Figure 6.25. Residual  $\text{H}^+$  sites per parent sample  $\text{H}^+$  from  $\text{NH}_3$  titrations on oxidized M-SSZ-13 samples vs. extent of M/Al exchange for Si:Al = 5 at a pH=5 (black shapes) and no pH control (green shapes). Open and filled symbols denote  $\text{Cu}^{2+}$  and saturated  $\text{Co}^{2+}$  exchange, respectively. Dashed lines are model predictions.

When low concentrations of  $\text{Cu}^{\text{II}}$  and  $\text{NH}_4^+$  [78] are present during aqueous-phase Cu exchange of H-SSZ-13 (Si:Al=5) at ambient conditions, we observed a 40-80% decrease in the number of Brønsted acid sites relative to the parent SSZ-13 (Figure 6.25, green diamonds). These observations suggest that significant structural changes occur to framework Al atoms (e.g., dealumination) in high Al content H-SSZ-13 zeolites synthesized by the FAU-to-CHA conversion methods at low pH values and low concentrations of cations (80% loss in  $\text{H}^+$  sites when no Cu is present), consistent with reports that cations exchange  $\text{H}^+$  sites to stabilize framework Al against dealumination [270,271]. The addition of  $\text{NH}_4\text{OH}$  to maintain a pH of 5 during the exchange of low concentrations of Cu cations mitigated Al structural changes and only resulted in a decrease of 25% of the number of Brønsted acid sites (black diamonds). We have previously reported  $\text{NH}_3$  TPD data that quantified the loss of ca.0.25  $\text{H}^+/\text{Al}$  for

this SSZ-13 sample (Si:Al=5, Cu:Al=0.02) [78], which is much larger than expected from the  $\text{Cu}^{\text{II}}:\text{H}^+ 2:1$  exchange stoichiometry (0.04  $\text{H}^+:\text{Al}$  for a Cu:Al=0.02). In this manuscript, we have removed this data point from the correlation in Figure 6.5, in light of this new evidence for the simultaneous structural changes to zeolite exchange sites (framework Al) that occur during Cu exchange procedure to prepare this sample.

### 6.8.9 XAS Details

XAS experiments were carried out at Sector 10 of the Advanced Photon Source at Argonne National Laboratory. Spectra were collected at both beamlines, 10-ID and 10-BM. The high photon flux at the ID line (approximately 100 times higher than that at the BM line) was required to perform experiments in the *operando* reactor to get enough transmitted X-ray intensity through the catalyst bed. Cu metal foil spectrum was simultaneously collected while measuring sample spectra and its energy was calibrated to 8979 eV for the Cu K-edge. All spectra were collected under isothermal conditions and normalized using a 1st order polynomial in the pre-edge region and a 3rd order polynomial in the post-edge region. EXAFS data was fit from  $k = 2.7$  to 11 Å. Linear combination XANES fits to determine the Cu(I) and Cu(II) fractions under *operando* conditions were carried out using the appropriate references as explained in our previous publications [37,85,87]. 10-15 mg of each sample was loaded for *in situ* experiments. All spectra were collected in the step scan mode. Gas treatments were performed in the lab and the samples were transferred to the beamline and cooled down to room temperature before collecting spectra. The samples were oxidized in a 20%  $\text{O}_2/\text{He}$  (UHP grade, Airgas) flow, whereas the reducing treatments used either UHP He (Airgas) at 673 K, 3.5%  $\text{H}_2/\text{He}$  (UHP, Airgas) at 523 K or 1500 ppm  $\text{NH}_3$  (3%  $\text{NH}_3/\text{Ar}$ , Praxair) + 1500 ppm NO (0.3% NO/ $\text{N}_2$ , Airgas) at 673 K. The total flow rate in each case was 100 ml min<sup>-1</sup> and samples were exposed to the corresponding gas conditions for 45 min. A wide range of catalysts with varying Si/Al and Cu/Al ratios was used to sample the different Cu configurations and identify the

response of those species to the different gas treatments. The energy range for the data collected at the 10-BM line was 8700 eV to 9890 eV.

*operando* experiments were performed at the 10-ID line in a special glassy carbon tube reactor as described by Kispersky et al [87]. During these experiments XAS spectra were simultaneously collected while measuring the reaction rates for each sample to ensure that the standard SCR rate per mole Cu measured at APS matched with that measured in the lab. Typical standard SCR conditions used were 300 ppm NO, 300 ppm NH<sub>3</sub>, 10% O<sub>2</sub>, 2-2.5% H<sub>2</sub>O, 5% CO<sub>2</sub> with a total flow rate of 500 ml min<sup>-1</sup> at 458-463 K. 9-12 mg of each sample was loaded in the reactor to ensure differential conditions (< 20% conversion). Spectra under *operando* conditions were collected in the quick scan mode and averaged over 3-5 scans. The *in situ* experiments with 300 ppm NH<sub>3</sub>+10% O<sub>2</sub> were performed at the 10-ID line with 2.5-3% H<sub>2</sub>O and a total flow of 500 ml min<sup>-1</sup> at 673 K. The energy range for the data collected at the 10-ID line was 8700 eV to 9780 eV.

EXAFS data was fit from 2.7 to 10.5 Å range with DWF's of 0.001 at room temperature, 0.002 at 473 K and 0.0035 at 673 K. k<sup>2</sup> weighting was used to convert the data into R-space, and obtain the coordination numbers and bond distances under the various gas conditions.

#### 6.8.10 Mobility Calculation Details

Cu positions during the entire course of simulation are analyzed to find out its relative mobility when different ligands bind to Cu. Only Cu positions represented as 3D cartesian coordinates (x,y,z) after 60 ps of equilibration time are used for the study. To calculate the volume of space Cu traveled, the 3D cartesian space is discretized into 0.008 Å<sup>3</sup> cubes as illustrated in Figure 6.9. The number of cubes that Cu has visited at least once is counted and summed up to be the final volume. Absolute volumes Cu visited for different binding ligands are going to change according to the size of the cubes used, but relative ratio of this volume keeps the same for cube size 0.001 to 0.125 Å<sup>3</sup>.

### 6.8.11 XANES Fitting Details

Since XAS is a bulk technique, each sample spectrum is a linear combination of the corresponding oxidation states. A mixture of Cu(I) and Cu(II) are present under standard SCR conditions and therefore, a linear combination XANES fitting of the Cu(I) and Cu(II) references was used to obtain the relative amounts of each oxidation state under various conditions. Information about how the Cu(I) and Cu(II) references were generated is provided in our previous publication [85]. EXAFS data was fit from 2.7 to 10.5  $\text{\AA}^{-1}$  range with DWF's of 0.001 at room temperature, 0.002 at 473 K and 0.0035 at 673 K.  $k^2$  weighting was used to convert the data into R-space, and obtain the coordination numbers and bond distances under the various gas conditions.

### 6.8.12 $\text{Z}_2\text{Cu}$ Modes

The six oxygens in the 6MR are labeled from 1 through 6 clockwise to identify Cu-O coordination. The ring structures just adjacent to the 6MR are shown in Figure 6.26, where 4MR and 8MR alternates around the 6MR. In principle any four oxygens out of the six oxygens could be coordinated with Cu, however not all combinations are energetically stable at 0K. We found that at least two out of the four Cu-O bonds must come from the oxygen pair adjacent to the Al (i.e. O1/O6 pair, and O3/O4 pair). The rest of the two bonds must come from two other oxygens that's in the neighboring 4MR. Alternatively the two oxygen pairs can all be coordinated with Cu. This is because in a 6MR without Cu interaction, the TOT angle in the neighboring 4MR prefers to be  $<180^\circ$ , while the TOT angle in the neighboring 8MR prefers to be  $>180^\circ$ . When Cu is introduced in the 6MR and bonding with four of the oxygens, it is energetically more favorable to distort as less as TOT angles as possible. This can be illustrated in the three stable local minima that we found as detailed below.

In Figure 6.27, dashed lines show Cu-O coordination and the numbering of oxygens is consistent as in Figure 6.26. In modes 1 and 2 only one 8MR TOT angle is distorted

and in mode 3 two 8MR TOT angles are distorted. Distortion of three 8MR TOT angles are strongly unfavorable and thus create structures high in energy. The three stable mode structures are optimized with the same computational method described in section xx. Mode 1 is slightly higher in energy than 2 and 3. But we can conclude there three modes are almost isoenergetic. Cu-O coordination information as well as relative energetics data are summarized in Table 6.9.

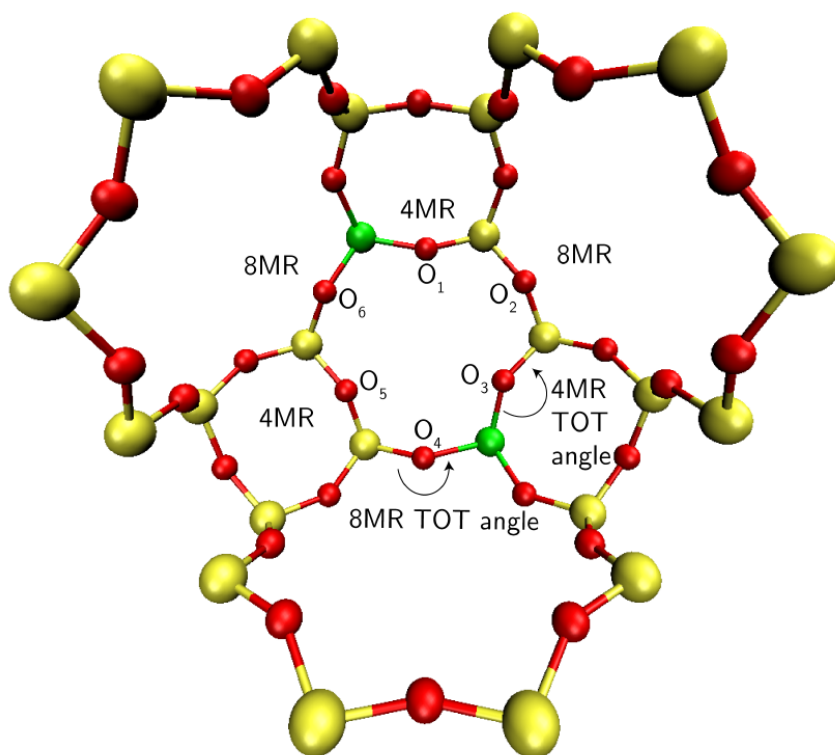
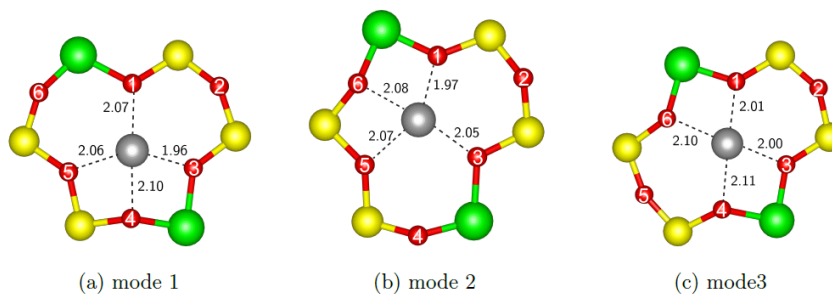


Figure 6.26. Ring structures surrounding the 6MR, shown in perspective view for clarity. 4MR and 8MR alternates around the 6MR.

Table 6.9.

Summary of Cu-O coordination in para  $Z_2Cu$  and relative energies for the three modes.

| Mode | Cu-O coordination |                |                |                | Relative energy [kJ/mol] | Avg Cu-O distance [Å] |
|------|-------------------|----------------|----------------|----------------|--------------------------|-----------------------|
| 1    | O <sub>1</sub>    | O <sub>3</sub> | O <sub>4</sub> | O <sub>5</sub> | 0                        | 2.08                  |
| 2    |                   |                | O <sub>5</sub> | O <sub>6</sub> | -4.6                     | 2.08                  |
| 3    |                   |                | O <sub>4</sub> | O <sub>6</sub> | -5.5                     | 2.09                  |

Figure 6.27. Pictures of  $Z_2Cu$  modes.

### 6.8.13 RDF Calculations

Pair-wise radial distribution function (RDF) ( $g(r)$ ) between Cu and other atoms (Si/Al/O/N) defines the average number of framework Si/Al/O/N atoms in a spherical shell of radius  $r$  distance away from the Cu:

$$dn(r) = \frac{N}{V} g(r) 4\pi r^2 dr \quad (6.28)$$

where  $R$  is the furthest distance away from the Cu we consider for the RDF;  $V$  is the volume of the model;  $N_{\text{total}}$  is the total number of atoms in a unit cell;  $dn(r)$  is the number of atoms in the shell volume averaged by number of MD trajectories. Hydrogens in the molecular structures are not considered in RDF calculation. To calculate the shell volume we use  $4\pi r^2 dr = V_{\text{shell}} = \frac{4}{3}[(r + dr)^3 - r^3]$ .  $V = 4/3\pi R^3$ ,

where we consider  $R$  up to 4.5 Å half of the supercell dimension, to avoid counting an atom in its periodic image. Substitute all into equation 6.28,

$$g(r) = \frac{dn(r)}{N * \frac{4}{3}\pi[(r + dr)^3 - r^3]/\frac{4}{3}\pi R^3} \quad (6.29)$$

We calculate  $g(r)$  for all atoms except H to obtain the overall RDF, we also calculate  $g(r)$  for each of the Cu-Si/Cu-Al/Cu-O/Cu-N combinations to obtain deconvoluted RDF's for each molecular structures (Figures 6.28 to 6.36).

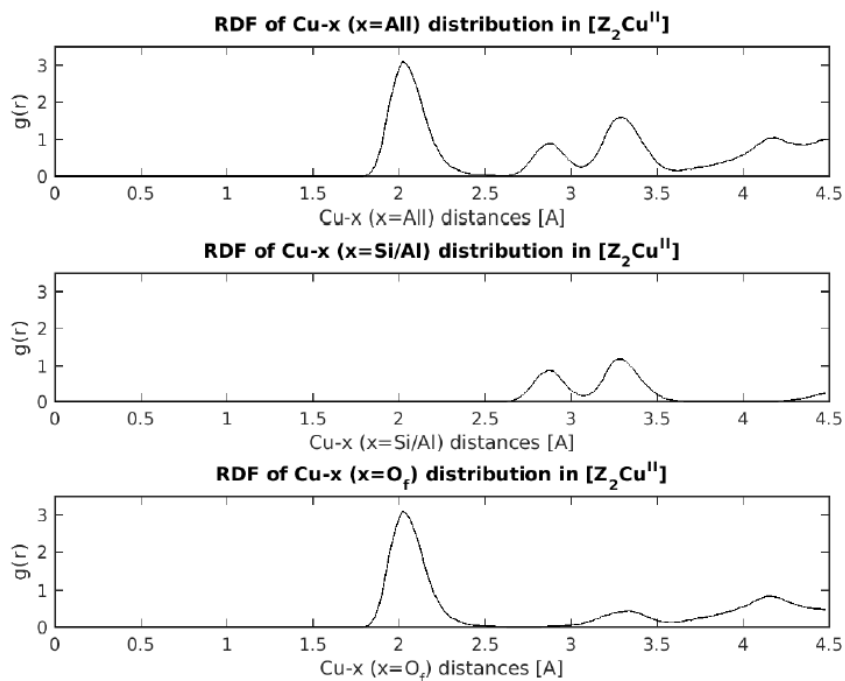


Figure 6.28. RDF of Cu-x (x=Si,Al,O) in  $[Z_2Cu^{II}]$ .

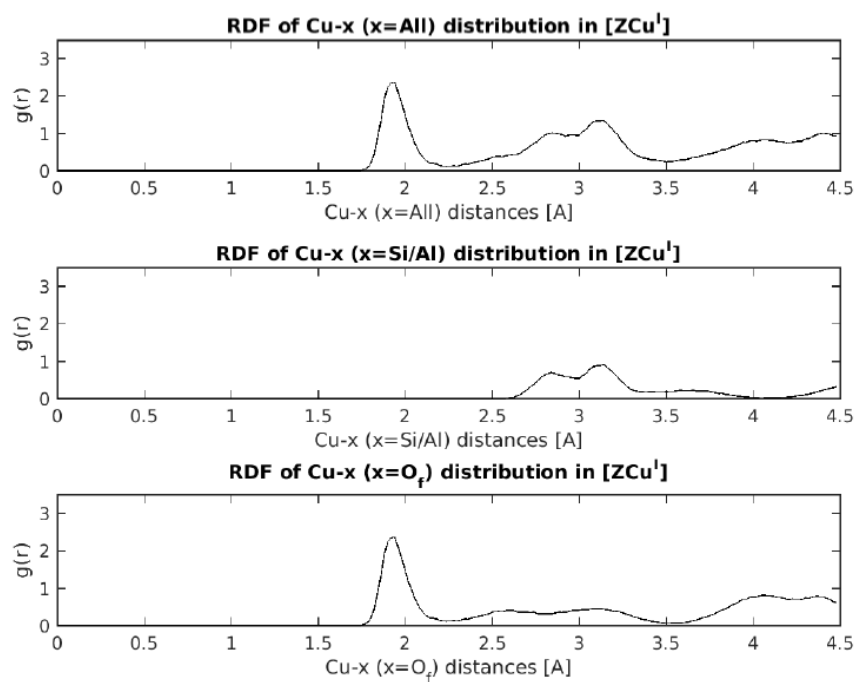


Figure 6.29. RDF of Cu-x (x=Si,Al,O) in [ZCu<sup>I</sup>].



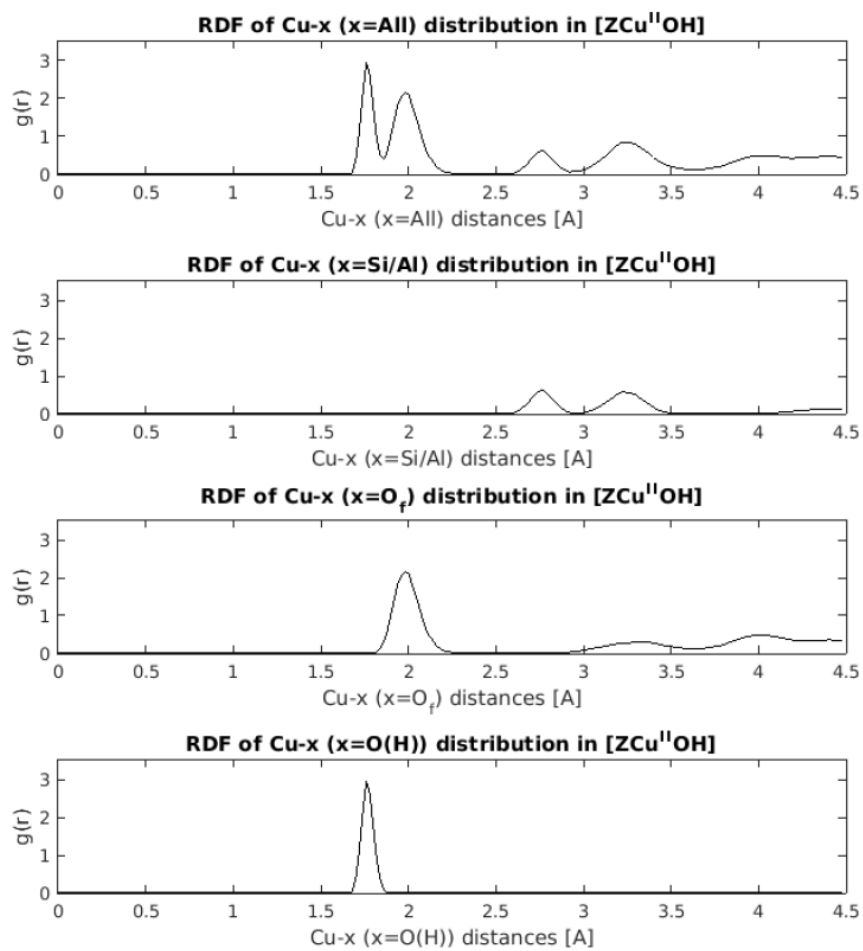


Figure 6.30. RDF of Cu-x (x=Si,Al,O) in [ZCu<sup>II</sup>OH].

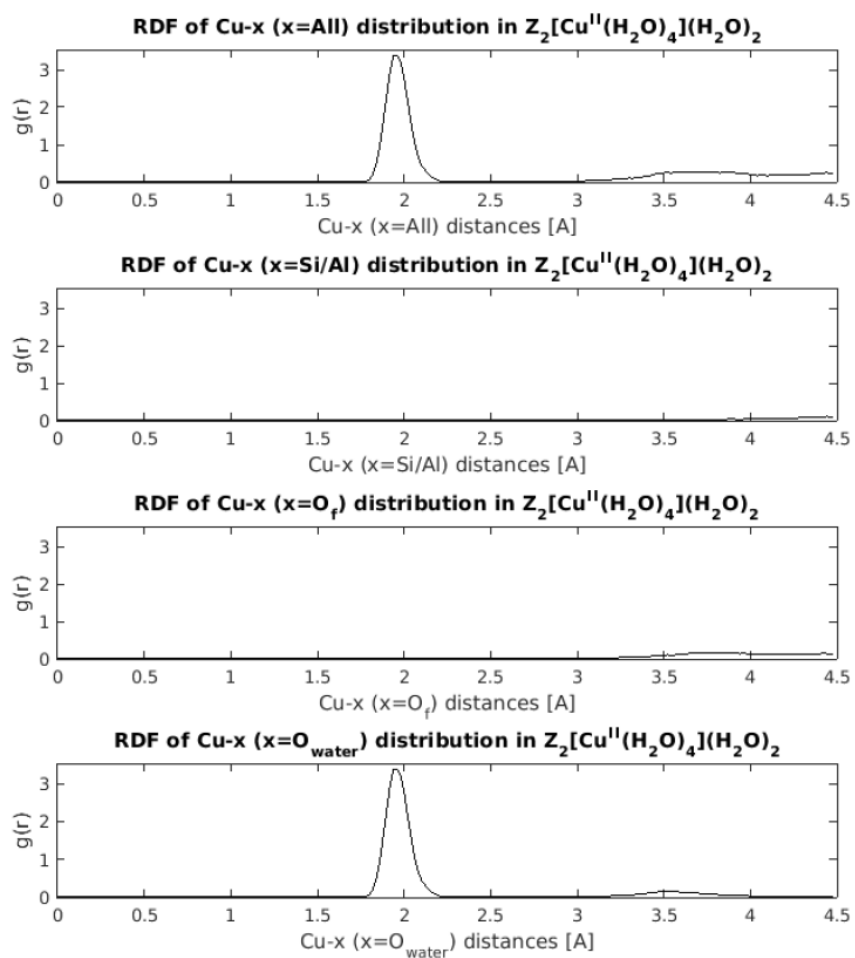


Figure 6.31. RDF of Cu-x (x=Si,Al,O) in  $Z_2[Cu^{II}(H_2O)_4](H_2O)_2$ .

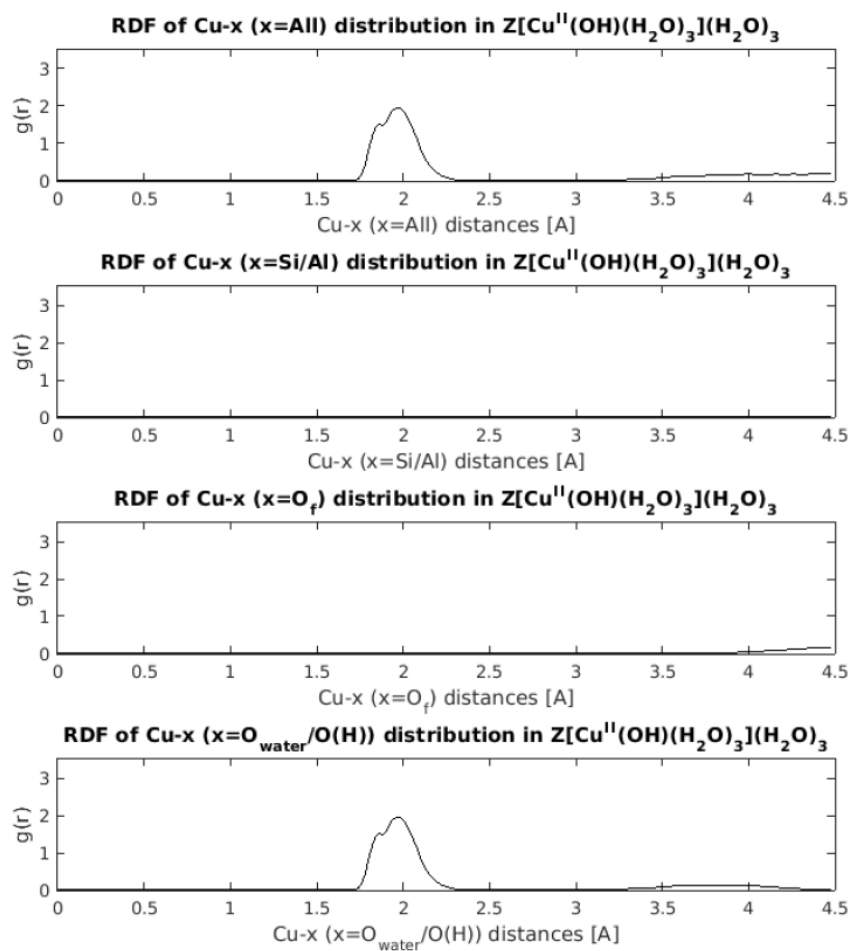


Figure 6.32. RDF of Cu-x (x=Si,Al,O) in  $Z_2[Cu^{II}(H_2O)_3](H_2O)_3$ .

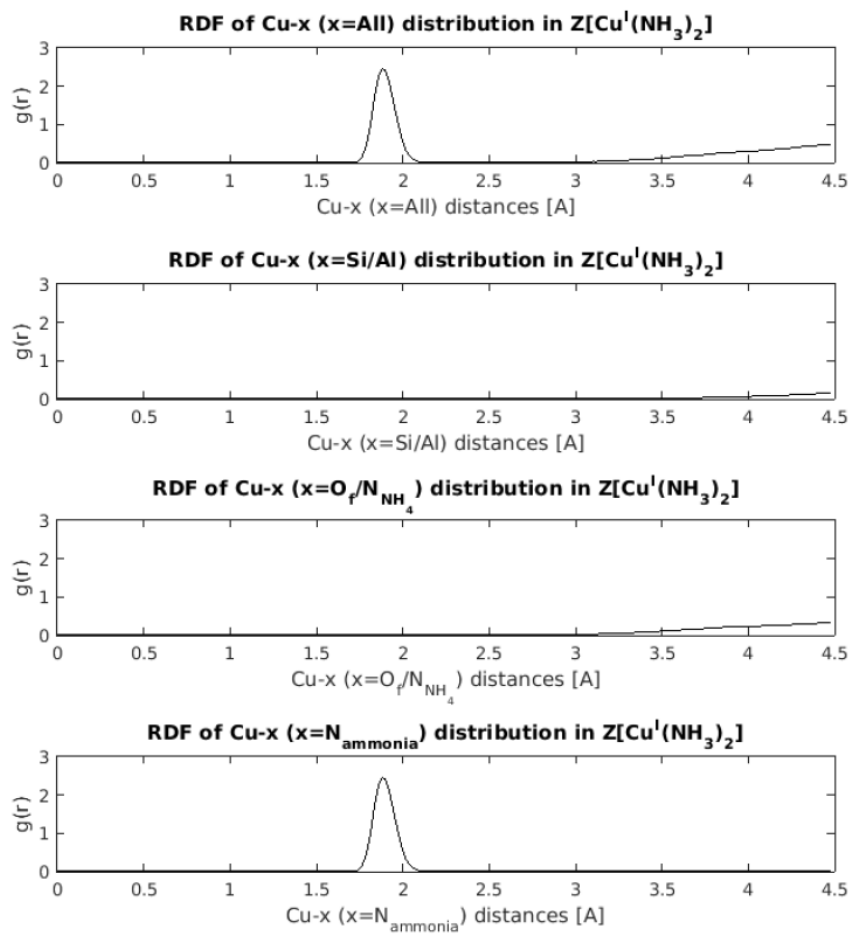


Figure 6.33. RDF of Cu-x (x=Si,Al,O,N) in  $Z[Cu^I(NH_3)_2]$ .

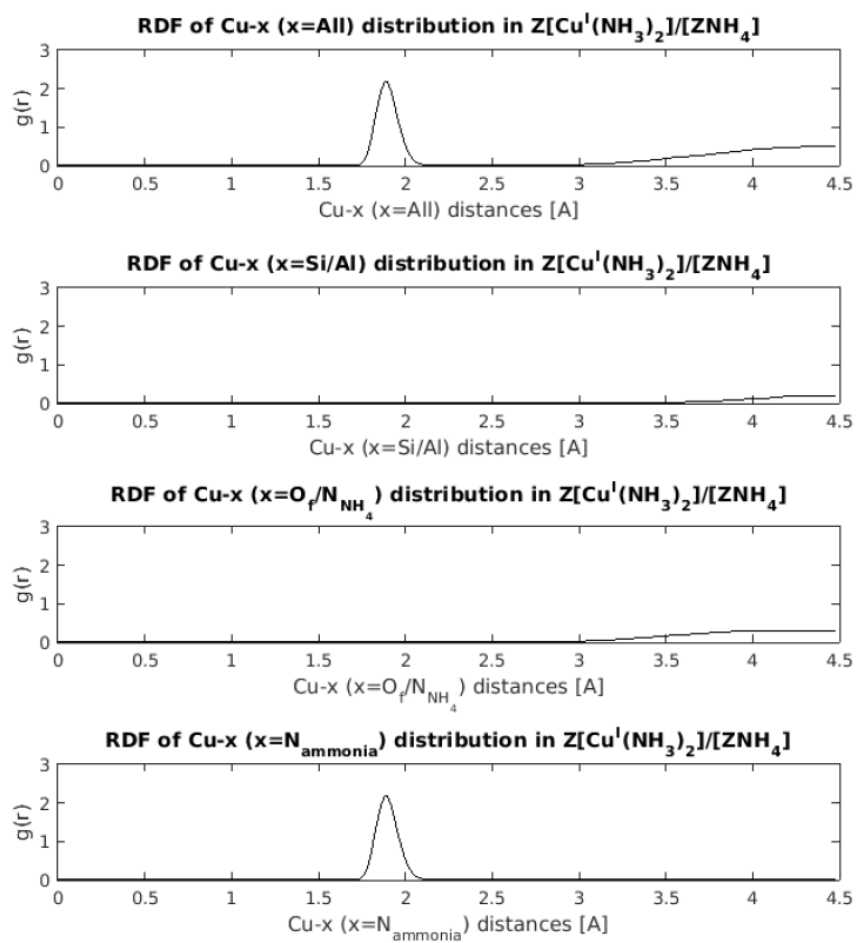


Figure 6.34. RDF of Cu-x ( $x=Si, Al, O, N$ ) in  $Z[Cu^I(NH_3)_2]/[ZNH_4]$ .

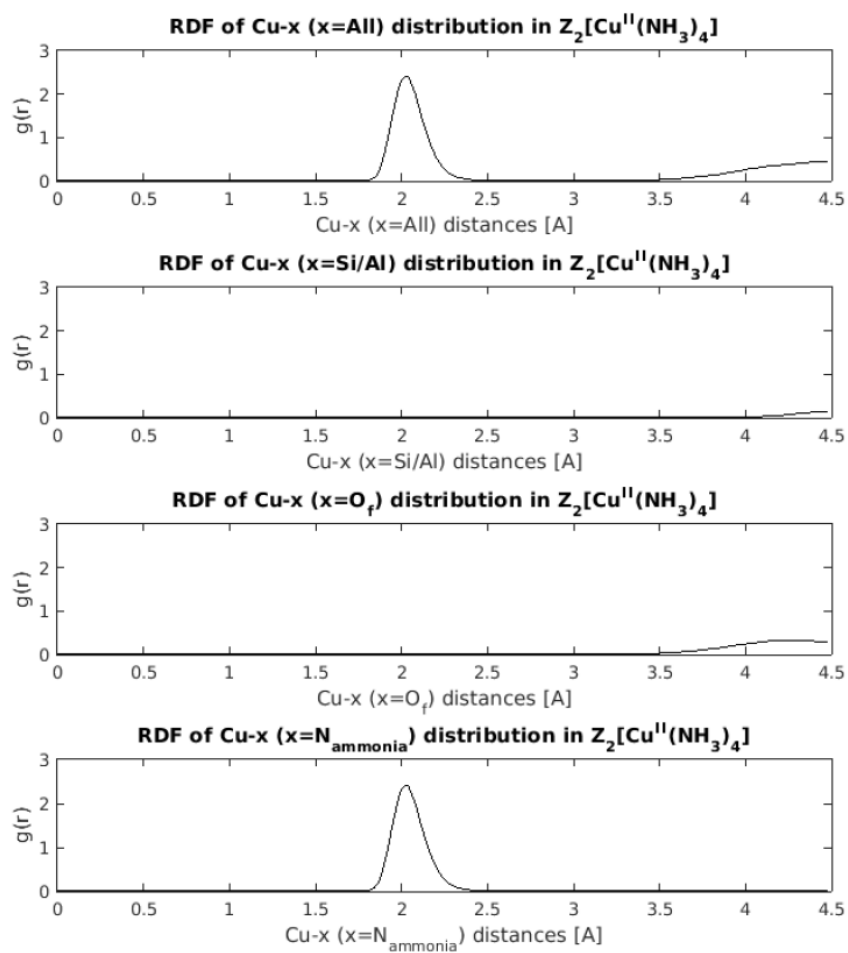


Figure 6.35. RDF of Cu-x (x=Si,Al,O,N) in  $Z_2[Cu^{II}(NH_3)_4]$ .

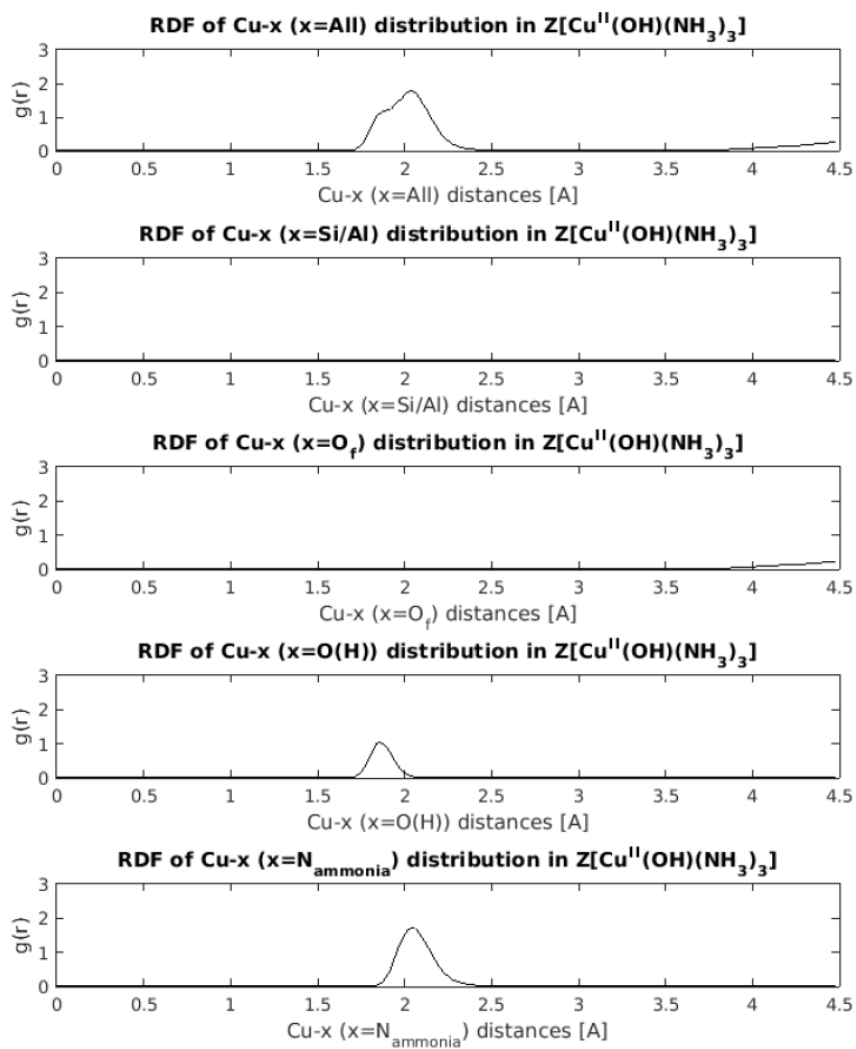


Figure 6.36. RDF of Cu-x ( $x=Si, Al, O, N$ ) in  $Z[Cu^{II}(OH)(NH_3)_3]$ .

## 6.8.14 XANES Reversibility Data

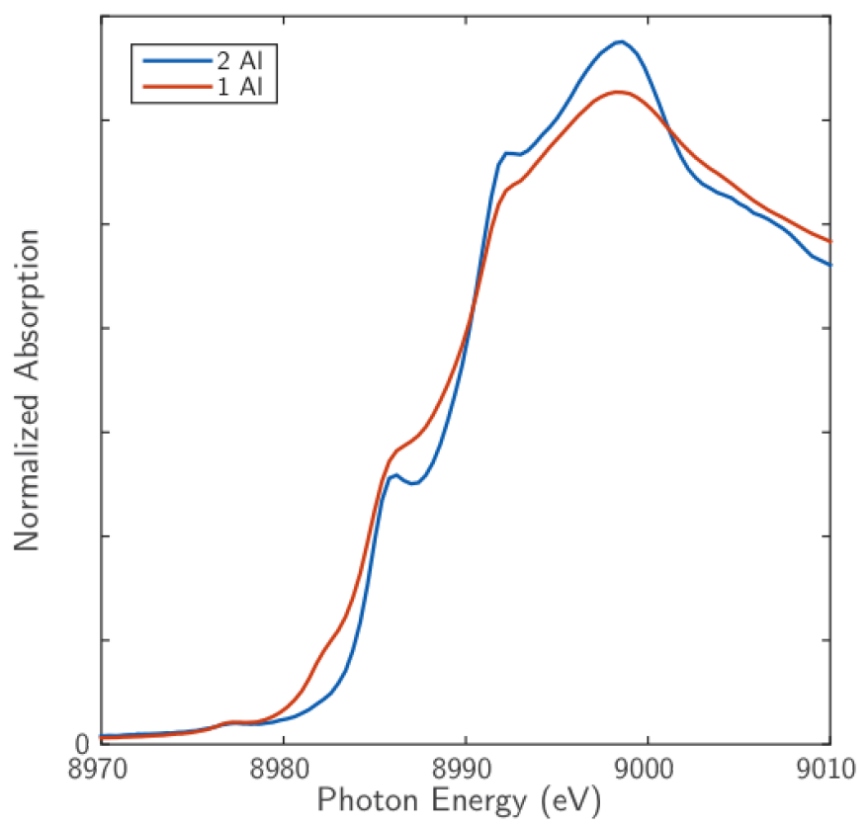


Figure 6.37. XANES spectra collected after exposing Si:Al 4.5 Cu:Al 0.08 (2Al) and Si:Al 15 Cu:Al 0.44 (1Al) to O<sub>2</sub> balance He at 673 K following pretreatment in He at 673 K.



Table 6.10.  
 Binding energies ( $\text{kJ mol}^{-1}$ ) for one of each of the SCR gas species on the  
 four different adsorption site models.

|                       | NH <sub>3</sub> | H <sub>2</sub> O | NO <sub>2</sub> | NO  | N <sub>2</sub> | O <sub>2</sub> |
|-----------------------|-----------------|------------------|-----------------|-----|----------------|----------------|
| Z <sub>2</sub> Cu     | -132            | -84              | -35             | -17 | -29            | -19            |
| ZCuOH                 | -117            | -75              | -44             | -73 | -8             | -1             |
| ZCu                   | -137            | -74              | -134            | -90 | -67            | -52            |
| ZNH <sub>4</sub> /ZCu | -134            | -71              | -122            | -69 | -17            | -31            |

Table 6.11.  
Full free energies of formation at SCR conditions for all  $\text{NH}_3$  2Al and 1Al  
phase diagram species.

| 2Al                                  | $\Delta G$ (kJ mol <sup>-1</sup> ) | 1Al                                 | $\Delta G$ (kJ mol <sup>-1</sup> ) |
|--------------------------------------|------------------------------------|-------------------------------------|------------------------------------|
| H/(OH) <sub>2</sub>                  | 391                                | OH-H <sub>2</sub> O <sub>x6</sub>   | 107                                |
| H/O                                  | 114                                | (OH) <sub>2</sub>                   | 73                                 |
| H/O <sub>2</sub>                     | 79                                 | O                                   | 72                                 |
| H/H <sub>2</sub> O                   | 59                                 | OH-H <sub>2</sub> O <sub>x5</sub>   | 67                                 |
| O <sub>2</sub>                       | 42                                 | OH-H <sub>2</sub> O <sub>x4</sub>   | 67                                 |
| H                                    | 36                                 | OH-O <sub>2</sub>                   | 67                                 |
| 2NH <sub>4</sub> CuNH <sub>3x4</sub> | 7                                  | OH-NH <sub>3x4</sub>                | 63                                 |
| Clean                                | 0                                  | OH-(H <sub>2</sub> O) <sub>x3</sub> | 36                                 |
| H <sub>2</sub> O <sub>x6</sub>       | -1                                 | NH <sub>3x4</sub>                   | 21                                 |
| H <sub>2</sub> O <sub>x3</sub>       | -5                                 | OH-H <sub>2</sub> O <sub>x2</sub>   | 16                                 |
| H <sub>2</sub> O <sub>x4</sub>       | -13                                | O <sub>2</sub>                      | 9                                  |
| Z <sub>2</sub> NH <sub>4</sub> Cu    | -20                                | Clean                               | 0                                  |
| H <sub>2</sub> O <sub>x5</sub>       | -22                                | OH/H <sub>2</sub> O                 | -12                                |
| H <sub>2</sub> O                     | -24                                | H <sub>2</sub> O                    | -15                                |
| H <sub>2</sub> O <sub>x2</sub>       | -25                                | OH                                  | -29                                |
| Z <sub>2</sub> NH <sub>4</sub> Cu    | -26                                | OH-NH <sub>3</sub>                  | -33                                |
| NH <sub>4</sub> /NH <sub>3x3</sub>   | -36                                | OH-NH <sub>3x2</sub>                | -35                                |
| NH <sub>4</sub> /NH <sub>3</sub>     | -44                                | OH-NH <sub>3x3</sub>                | -36                                |
| NH <sub>3</sub>                      | -52                                | NH <sub>3x3</sub>                   | -54                                |
| NH <sub>3x2</sub>                    | -73                                | NH <sub>3</sub>                     | -57                                |
| NH <sub>4</sub> /NH <sub>3x2</sub>   | -80                                | NH <sub>3x2</sub>                   | -94                                |
| NH <sub>3x3</sub>                    | -81                                |                                     |                                    |
| NH <sub>3x4</sub>                    | -96                                |                                     |                                    |

6.8.15 Four site Adsorbate Binding Energies

6.8.16  $\text{NH}_3$  phase diagram results at experimental SCR conditions

6.8.17 Cu diammine diffusion CI-NEB

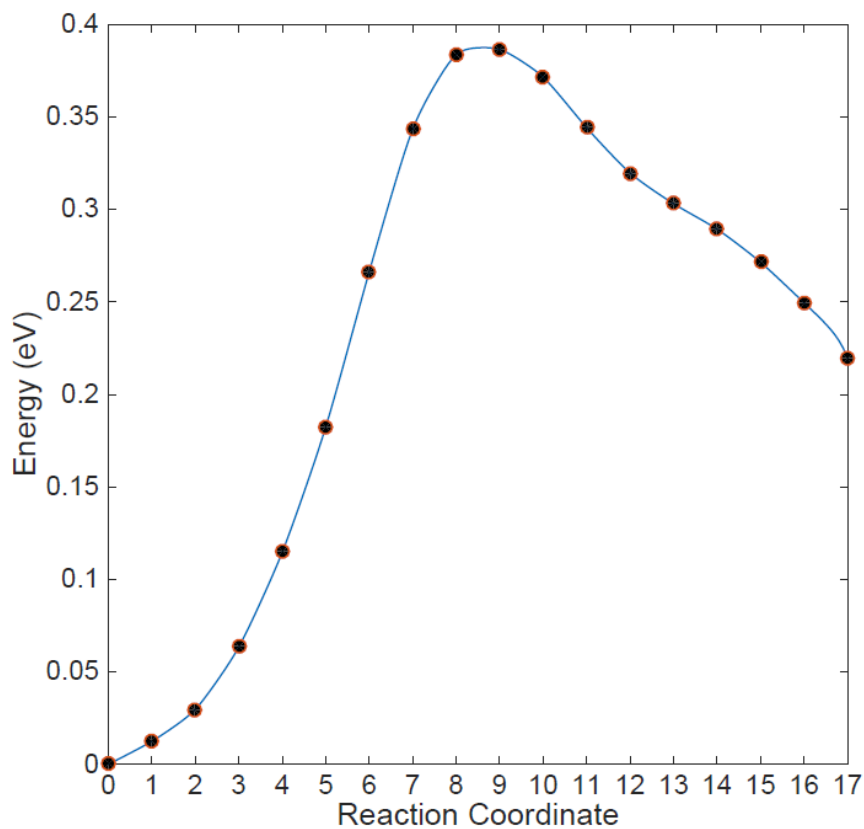


Figure 6.38. CI-NEB for Cu diammine to transverse the 8MR.

6.8.18 *operando* XAS

Conditions: 2%  $\text{H}_2\text{O}$ , 300 ppm  $\text{NH}_3$ , 10%  $\text{O}_2$ , 300 ppm  $\text{NO}$ ; Cu:Al = 0.41, Si:Al = 25, CN = 3.1 XANES: 60%  $\text{Cu}^I$ , 40%  $\text{Cu}^{II}$

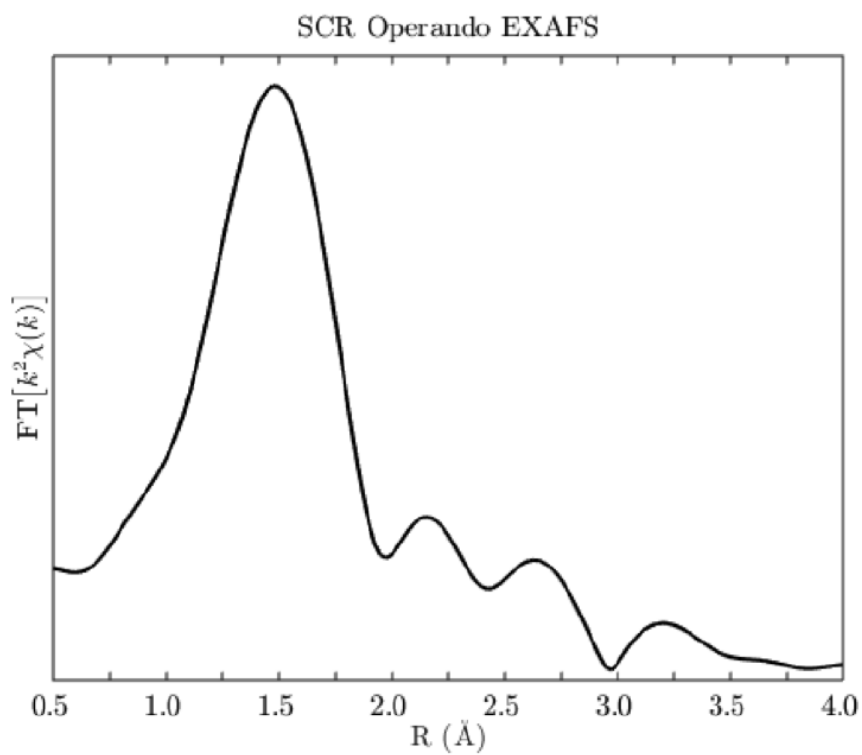


Figure 6.39. EXAFS spectrum collected at 473 K, 2% H<sub>2</sub>O, 300 ppm NH<sub>3</sub>, 10% O<sub>2</sub>, 300 ppm NO, on a Cu:Al = 0.41, Si:Al = 25 sample. Rate per gram catalyst is  $81 \times 10^{-8}$ .

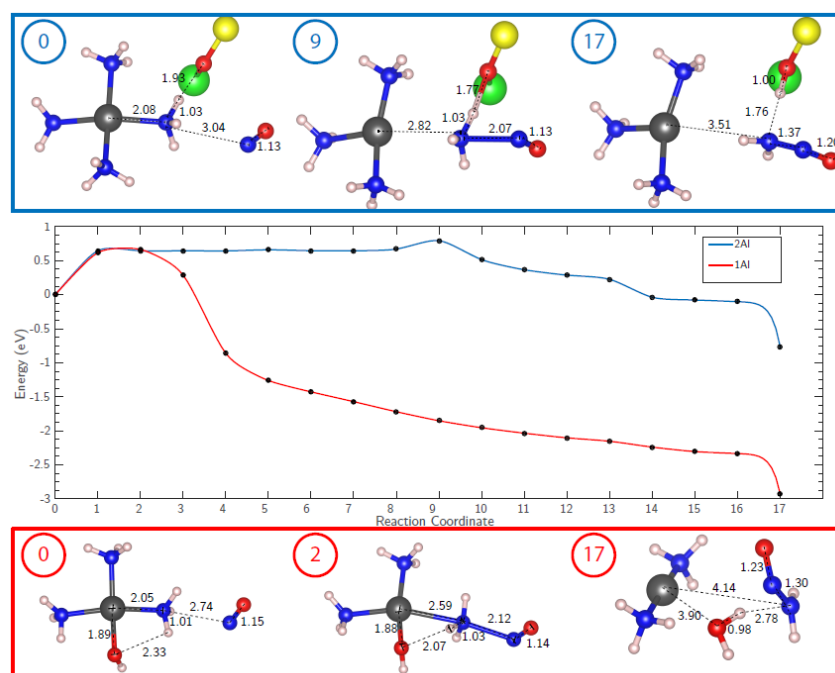
6.8.19 NO+NH<sub>3</sub> NEBS

Figure 6.40. XANES spectra collected after exposing Si:Al = 4.5, Cu:Al = 0.08 (2Al) and Si:Al = 15, Cu:Al = 0.44 (1Al) to O<sub>2</sub> balance He at 673 K following pretreatment in He at 673 K.

## 6.8.20 Disappearance of Proximal Sites Upon reoxidation

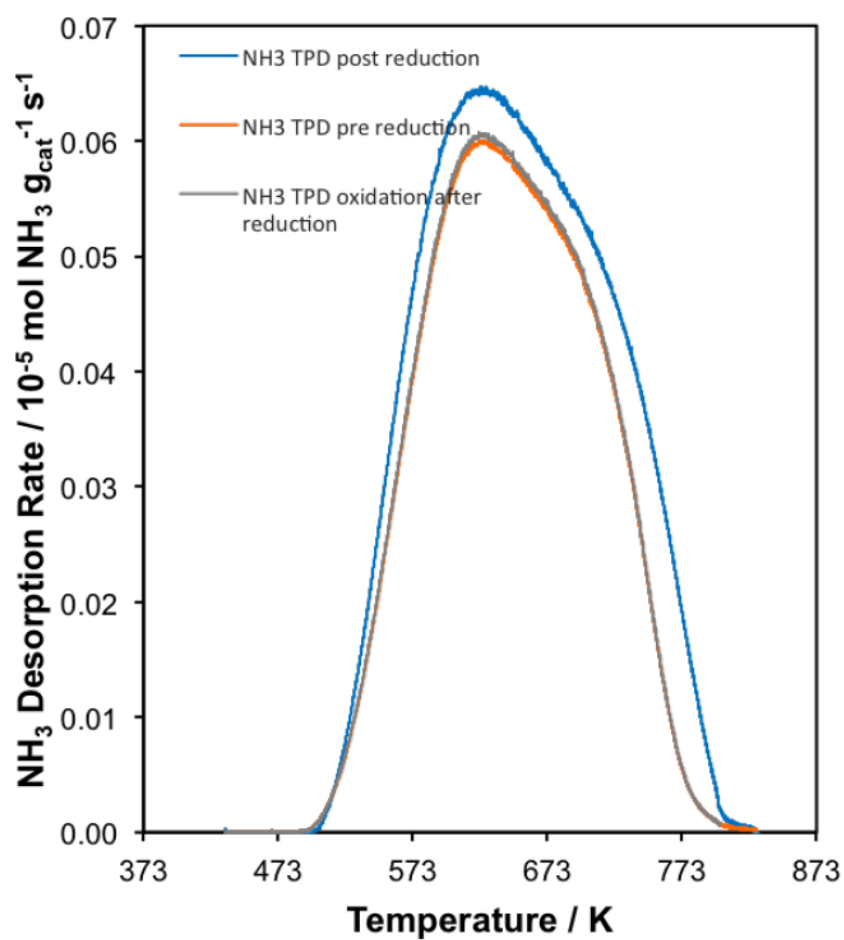


Figure 6.41. Titration of residual Brønsted sites on a Si:Al=5 Cu:Al=0.21 SSZ-13 sample, before reduction in NO+NH<sub>3</sub>, after reduction, and after reduction followed by oxidation.

Table 6.12.  
Mechanism Energies.

| Step | ZCu  | $\Delta E(\text{eV})$ |
|------|--|-----------------------|
| 1    | $\text{ZCuOH-NH}_3+2\text{NO}+2\text{NH}_3+1/2\text{O}_2$  | 0                     |
| 2    | $\text{ZCuOH-NH}_3\text{x}3+2\text{NO}+1/2\text{O}_2$  | -2.44                 |
| 3    | $\text{ZCuNH}_3\text{x}2\text{-H}_2\text{N}_2\text{O}+\text{NO}+1/2\text{O}_2$                         | -3.63                 |
| 4    | $\text{ZCuNH}_3\text{x}2+2\text{H}_2\text{O}+\text{N}_2+\text{NO}+1/2\text{O}_2$                       | -4.85                 |
| 5    | $\text{ZCuNO}_2\text{-NH}_3\text{x}2+2\text{H}_2\text{O}+\text{N}_2$                                   | -6.32                 |
| 6    | $\text{ZCuOH-NH}_3+3\text{H}_2\text{O}+2\text{N}_2$  | -7.49                 |
| Step | Z <sub>2</sub> Cu  | $\Delta E(\text{eV})$ |
| 1    | $\text{Z}_2\text{Cu-NH}_3\text{x}2+2\text{NO}+2\text{NH}_3+1/2\text{O}_2$                              | 0                     |
| 2    | $\text{Z}_2\text{Cu-NH}_3\text{x}4+2\text{NO}+1/2\text{O}_2$   | -2.64                 |
| 3    | $\text{Z}_2\text{Cu-NH}_3\text{x}2/\text{NH}_4/\text{N}_2\text{H}_2\text{O}$                           | -3.28                 |
| 4    | $\text{Z}_2\text{Cu-NH}_3\text{x}2/\text{NH}_4^+\text{H}_2\text{O}+\text{N}_2+\text{NO}+1/2\text{O}_2$ | -5.25                 |
| 5    | $\text{Z}_2\text{CuNO}_2\text{-NH}_3\text{x}2/\text{NH}_4^+\text{H}_2\text{O}+\text{N}_2$              | -6.84                 |
| 6    | $\text{Z}_2\text{Cu-NH}_3\text{x}2+3\text{H}_2\text{O}+2\text{N}_2$                                    | -7.49                 |

Table 6.13.

Rates, apparent orders, and apparent activation energies on BEA and ZSM-5 samples (only the rate was measured on the 3.3 Cu wt% BEA sample).

| ZSM-5 (Si/Al = 13) |       |                   |                               |          |                       |          |
|--------------------|-------|-------------------|-------------------------------|----------|-----------------------|----------|
| Cu wt%             | Cu:Al | Rate <sup>a</sup> | E <sub>app</sub> <sup>b</sup> | NO order | NH <sub>3</sub> order | O2 order |
| 1.7                | 0.24  | 199               | 61±10                         | 0.6      | -0.3                  | 0.5      |
| 1.9                | 0.27  | 232               | 64±10                         | 0.7      | -0.4                  | 0.4      |
| 2.7                | 0.36  | 340               | 77±10                         | 0.6      | -0.5                  | 0.4      |
| BEA (Si/Al = 13)   |       |                   |                               |          |                       |          |
| Cu wt%             | Cu:Al | Rate <sup>a</sup> | E <sub>app</sub> <sup>b</sup> | NO order | NH <sub>3</sub> order | O2 order |
| 1.9                | 0.25  | 314               | 48±15                         | 0.6      | 0.0                   | 0.3      |
| 2.6                | 0.34  | 438               | 58±15                         | 0.7      | -0.1                  | 0.3      |

<sup>a</sup> Rate per gram x 10<sup>-1</sup>

<sup>b</sup> kJ mol<sup>-1</sup>



6.8.21 Mechanism energies

6.8.22 Kinetic Data for BEA and ZSM-5

6.8.23  $\text{Z}_2\text{Cu}$  200 C vs 400 C EXAFS comparison

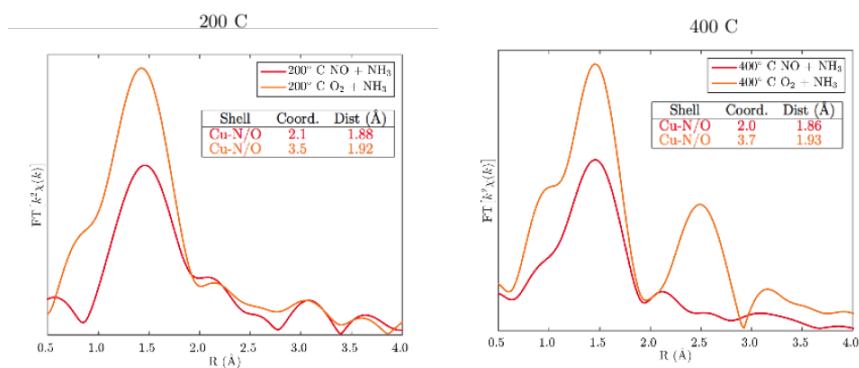


Figure 6.42. EXAFS spectra collected after exposing Si:Al 4.5 Cu:Al 0.08 (2Al) to either  $\text{NO} + \text{NH}_3$  (red) or  $\text{O}_2 + \text{NH}_3$  (orange), at (left) 200 C, and (right) 400 C.

## 6.8.24 200 C XANES, ZCuOH, NO only

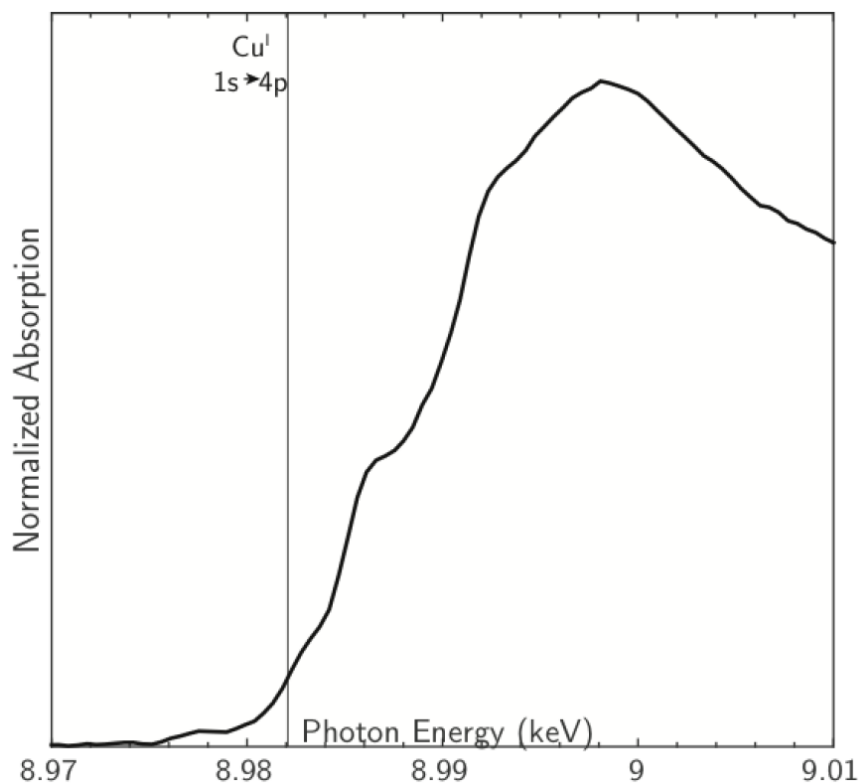


Figure 6.43. XANES spectra collected after exposing Si:Al 15 Cu:Al 0.44 to 300 ppm NO and balance He at 200 C until steady-state.

## 6.8.25 Synthesis details

CHA (SSZ-13) zeolites with a Si:Al ratio of 5 were synthesized as reported elsewhere [37,250], which was based on a method to convert FAU to CHA using N,N,N-trimethyl-1-adamantylammonium hydroxide (TMAdaOH) developed by Zones [109,162,376] and modified by Fickel et al. [34,250], with molar ratios of 1 SiO<sub>2</sub> / 0.033 or 0.017 Al<sub>2</sub>O<sub>3</sub> / 0.20 TMAdaOH / 0.17 Na<sub>2</sub>O / 26 H<sub>2</sub>O. A typical synthesis of SSZ-13 with Si:Al = 15 or 25 was performed by preparing an aqueous mixture of 28.4 g TMAdaOH (25 wt%, Sachem) with 77.4 g H<sub>2</sub>O (deionized; 18.2 MΩ) in a perfluoroalkoxy alkane (PFA) plastic vessel and stirring the solution for 15 minutes

under ambient conditions. 0.87 or 0.43 g (Si:Al = 15 or 25, respectively) of aluminum hydroxide (SPI Pharma) and 34.6 g of a 1M NaOH solution (Alfa Aesar) were added and the mixture was stirred for 15 minutes at ambient conditions to homogenize the contents. 10 g of fumed silica (Cab-o-Sil) were added and the mixture was stirred at ambient conditions for 2h to homogenize the mixture. The synthesis gel was loaded into four identical 45 cm<sup>3</sup> Teflon-lined stainless steel autoclaves (Parr Instruments) and heated under rotation at 433 K for 6 days at 60 RPM.

BEA (Beta) zeolites were synthesized with a Si:Al ratio of 13 following a modified procedure originally reported by Rubin [412]. A typical synthesis of BEA with Si:Al = 13 was prepared by dissolving 0.78 g of NaOH pellets (98%, Macron Fine Chemicals) in 92.1 g of an aqueous tetraethylammonium hydroxide (TEAOH) solution (35 wt%, Sachem) in a perfluoroalkoxy alkane (PFA) plastic vessel and stirring the solution for 15 minutes under ambient conditions. 139.0 g of colloidal silica (30 wt%, Ludox HS30, Sigma Aldrich) and 11.6 g of aluminum isopropoxide (98 wt%, Sigma Aldrich) were added to the mixture and stirred for 2h at ambient conditions to homogenize the contents. The synthesis gel was loaded into two 45 cm<sup>3</sup> and one 300 cm<sup>3</sup> Teflon-lined stainless steel autoclaves (Parr Instruments) and heated at 413 K for 8 days.

After synthesis of CHA and BEA zeolites, crystalline solid products were washed by alternating deionized water and acetone (99.9 wt%, Sigma Aldrich) rinses (50 cm<sup>3</sup> g solid<sup>-1</sup>) until the pH was constant between washes. Solids were recovered by centrifugation, dried under static air at 373 K for 24 h, and then treated in flowing dry air (100 cm<sup>3</sup> min<sup>-1</sup> g<sup>-1</sup>, 99.999% UHP, Indiana Oxygen) to 853 K (0.0167 K s<sup>-1</sup>) for 10 h. All zeolite samples were converted to the NH<sub>4</sub>-form by ion-exchange with a 1.0M aqueous NH<sub>4</sub>NO<sub>3</sub> (99.9 wt%, Sigma Aldrich) solution (100 cm<sup>3</sup> solution g<sup>-1</sup>) for 10 h at 353 K, followed by washing the solids six times with deionized water (50 cm<sup>3</sup> g<sup>-1</sup>), recovery via centrifugation, and drying the solids at 373 K for 24 h. NH<sub>4</sub>-form zeolites were converted to their H-form by treating the solids in flowing air (100 cm<sup>3</sup> min<sup>-1</sup> g<sup>-1</sup>, 99.999% UHP, Indiana Oxygen) at 773 K (0.0167 K s<sup>-1</sup>) for 4 h.

Cu-zeolites were prepared by aqueous-phase Cu ion exchange of H-form zeolites with a  $\text{Cu}^{\text{II}}(\text{NO}_3)_2$  solution ( $0.001\text{M}$ - $0.1\text{M}$ ,  $100\text{ cm}^3\text{ g}^{-1}$ ; 99.999 wt%, Sigma Aldrich) for 4 h and 300 RPM at ambient conditions, during which the pH was controlled to  $4.9 \pm 0.1$  through dropwise addition of a  $1.0\text{M}$   $\text{NH}_4\text{OH}$  solution (Sigma Aldrich). Co-SSZ-13 zeolites were prepared by ion exchange of H-SSZ-13 with an aqueous  $0.25\text{M}$   $\text{Co}^{\text{II}}(\text{NO}_3)_2$  solution ( $150\text{ cm}^3\text{ g}^{-1}$ ) for 4 h at ambient conditions, during which the pH was not controlled (pH stabilized between 3.2-3.6 after 4 h). Metal-exchanged zeolites were recovered by centrifugation and washed with deionized water six times ( $70\text{ cm}^3\text{ g}^{-1}$  per wash), dried at ambient temperature under flowing air, and then treated in flowing dry air ( $100\text{ cm}^3\text{ g}^{-1}$ ) to  $773\text{ K}$  ( $0.0167\text{ K s}^{-1}$ ) for 4h. Elemental composition (Si, Al, Cu, Co) was determined using atomic absorption spectroscopy (AAS) on a Perkin-Elmer AAnalyst 300.

Commercial BEA and ZSM-5 samples with  $\text{Si}:\text{Al} = 13$  were purchased from Zeolyst.

#### 6.8.26 Micropore volume

Zeolite samples were pelleted and sieved to obtain particles between  $180\text{-}250\text{ }\mu\text{m}$  in diameter, degassed by heating  $0.02\text{-}0.05\text{ g}$  of zeolite to  $393\text{ K}$  ( $0.167\text{ K s}^{-1}$ ) and holding under high vacuum (ca.  $5\text{ }\mu\text{mHg}$ ) for 2 h, and then further heating to  $623\text{ K}$  ( $0.167\text{ K s}^{-1}$ ) and holding high vacuum (ca.  $5\text{ }\mu\text{mHg}$ ) for 8 h. Micropore volumes ( $\text{cm}^3\text{ g}^{-1}$  at STP) were measured by extrapolating the linear volumetric gas adsorption during mesopore filling (ca.  $0.08\text{-}0.30\text{ P/P}_0$ ) to zero relative pressure. These estimates were in agreement with micropore volumes derived from analyzing the semi-log derivative plot of the adsorption isotherm ( $\partial V_{\text{ads}}/\partial \ln(\text{P/P}_0)$  vs.  $\ln(\text{P/P}_0)$ ). This analysis requires determining the first maximum of  $\partial V_{\text{ads}}/\partial \ln(\text{P/P}_0)$ , which corresponds to the relative pressure when micropore filling occurs, and then identifying the subsequent minimum that corresponds to the end of micropore filling [136, 137]. The micropore volumes were determined by converting adsorbed gas volumes (at STP) to liquid volumes

Table 6.14.  
Micropore volumes for H-SSZ-13, H-BEA, and H-ZSM-5.

| Zeolite  | Si/Al | Micropore Volume ( $\text{cm}^3 \text{ g}^{-1}$ ) |
|----------|-------|---|
| H-SSZ-13 | 5     | 0.16  |
|          | 15    | 0.18  |
|          | 25    | 0.20  |
| H-BEA    | 13    | 0.21  |
| H-ZSM-5  | 13    | 0.14  |

using a density conversion factor assuming the liquid density of  $\text{N}_2$ (77 K) or Ar (87 K) and can be found in Table 6.14.

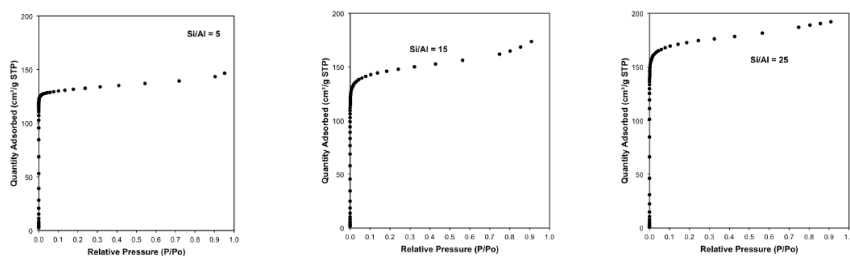


Figure 6.44. Micropore Ar adsorption isotherms on H-SSZ-13 5, 15, and 25 samples.

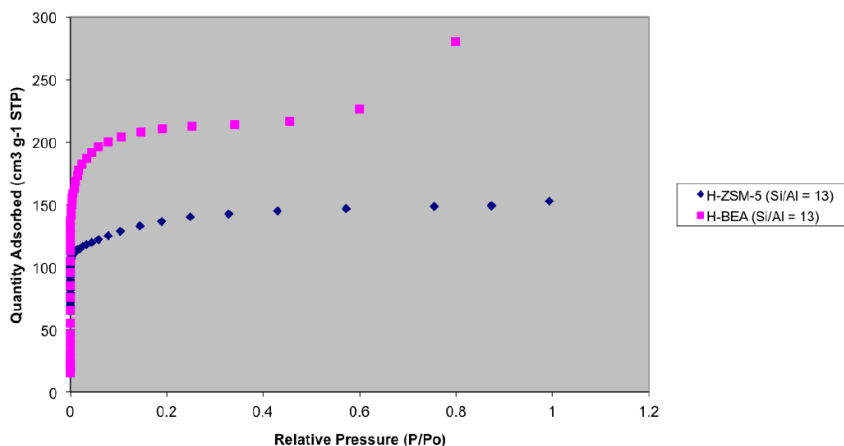


Figure 6.45. Micropore N<sub>2</sub> adsorption isotherms on H-BEA and H-ZSM-5.

#### 6.8.27 <sup>27</sup>Al NMR

Solid-state <sup>27</sup>Al magic angle spinning nuclear magnetic resonance (<sup>27</sup>Al MAS NMR) spectroscopy was used to estimate the fraction of framework and extraframework Al on H-form zeolites. SS NMR spectra were collected using a Chemagnetics CMX400 400 MHz spectrometer in a wide-bore 9.4 Tesla magnet at ambient conditions from 456 scans with 12.5 μs pulses and a 2 s delay and were measured at 104.24 MHz and MAS rate of 5 kHz. Prior to packing in a 4mm ZrO<sub>2</sub> rotor, zeolite samples were hydrated by holding for >48 h in a desiccator containing a saturated potassium chloride (KCl) solution. All <sup>27</sup>Al MAS NMR spectra are referenced to an aqueous 1.0M Al(NO<sub>3</sub>)<sub>3</sub> solution. NMR spectra and quantification of extraframework Al for all H-zeolite samples can be found in Table 6.15.

Table 6.15.  
 Fraction of extra-framework Al estimated from  $^{27}\text{Al}$  NMR.

| Si/Al | Fraction Tetrahedral | Fraction Octahedral |
|-------|----------------------|---------------------|
| 5     | 0.85                 | 0.15                |
| 15    | 0.95                 | 0.05                |
| 25    | 1.00                 | 0.00                |

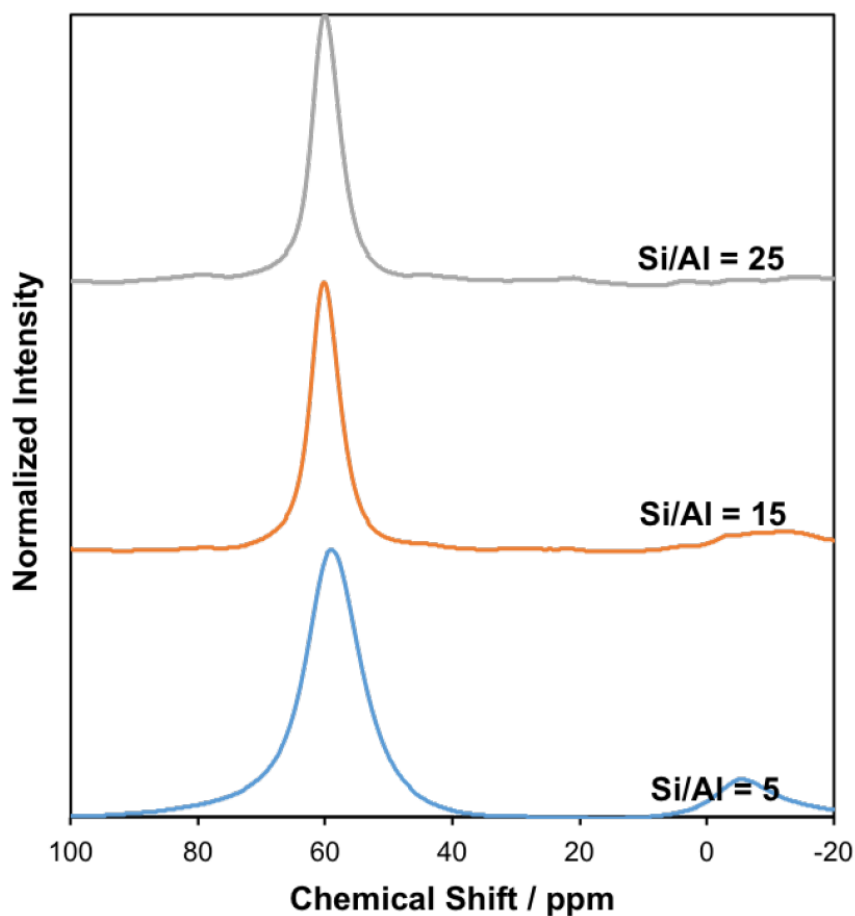


Figure 6.46.  $^{27}\text{Al}$  NMR spectra for SSZ-13 at Si:Al 5, 15, 25.

#### 6.8.28 $\text{NH}_3$ TPD

$\text{H}^+$  sites on H-SSZ-13, and oxidized and reduced forms of Cu-SSZ-13 samples were measured using the  $\text{NH}_3$  titration procedure described by Di Iorio et al. [171]. Oxidizing pre-treatment involved heating in synthetic air (commercial grade, Indiana Oxygen) at 773 K while the reducing pre-treatment involved flowing 500 ppm NO (from 3.6% NO/Ar, Praxair)+500 ppm  $\text{NH}_3$  (from 3%  $\text{NH}_3$  in Ar, Praxair) at 473 K for 2 hr. 30-50 mg of each sample, in either its oxidized or reduced forms, was saturated with 500 ppm  $\text{NH}_3$  diluted with UHP He (99.999% , Indiana Oxygen) at 433 K for 2 hr with a total flow rate of  $350 \text{ cm}^3 \text{ min}^{-1}$ . Following this  $\text{NH}_3$  saturation



step, the sample was flushed with 2.5-3.0% water in UHP He (wet purge) for 8 hours while still keeping the same total flow rate to desorb  $\text{NH}_3$  bound to non-protonic sites [171]. Wet purge was followed by a temperature programmed desorption (TPD) in UHP He from 433 K to 820 K at a ramp rate of  $0.167 \text{ K s}^{-1}$ .  $\text{NH}_3$  titration on the reduced form of Cu-SSZ-13 samples showed that  $\text{Cu}^{2+}$  sites balancing two Al atoms formed a  $\text{Cu}^+$  cation and a proximal  $\text{H}^+$  site upon reduction, while  $[\text{CuOH}]^+$  sites formed a  $\text{Cu}^+$  cation and  $\text{H}_2\text{O}$  without generating an additional  $\text{H}^+$  sites, as proposed in the reaction scheme shown above. Thus,  $\text{NH}_3$  titrations can be used *in situ* after oxidation and reduction treatments to distinguish between the  $\text{Z}_2\text{Cu}$  and  $[\text{CuOH}]^+$  sites by counting the total acid sites which are equal to the sum of residual acid sites on the oxidized form of the sample and the excess acid sites generated after reduction [85].

For Co-exchanged SSZ-13 samples, the number of  $\text{H}^+$  sites, after oxidative treatments in flowing air (773 K), were titrated *in situ* using a Micromeritics Autochem II 2920 Chemisorption analyzer and required the use of a lower gas flow rate than that of the H- and Cuexchanged SSZ-13 samples. The  $\text{NH}_3$  titration procedure involved saturating zeolite samples (30-50 mg) with 500 ppm  $\text{NH}_3$  (500 ppm  $\text{NH}_3/\text{He}$ , Indiana Oxygen) at 433 K for 5 h and a total flow rate of  $150 \text{ cm}^3 \text{ min}^{-1}$ . Subsequently,  $\text{NH}_3$ -saturated samples were wet purged at 433 K for 8 h prior to temperature programmed desorption (TPD) experiments. TPD experiments on H-SSZ-13 and Co-exchanged SSZ-13 were performed using a Micromeritics Autochem II 2920 Chemisorption analyzer equipped with an Agilent 5975C mass selective detector (MSD) to identify the gaseous species desorbing from the catalyst samples. Catalyst samples were supported between two quartz wool plugs inside a U-shaped quartz cell held within a clam-shell furnace, held in  $50 \text{ cm}^3 \text{ min}^{-1}$  flowing UHP He at ambient temperature for 1 h, and heated to 873 K ( $0.167 \text{ K s}^{-1}$ ). The effluent stream from the quartz cell passed through heated transfer lines held at 383 K to the MSD for analysis. The signal at  $m/z = 17$  was quantified by developing a calibration curve using four  $\text{NH}_4$ -exchanged ZSM-5 zeolites with varying Si/Al ratio ( $\text{Si/Al} = 17\text{-}89$ ) [78]. The total  $\text{NH}_3$  des-

orbed per gram of these zeolites were determined by performing TPD experiments on a gas-phase plug flow reactor, described in the subsequent paragraph. After each TPD experiment, a 0.5 cm<sup>3</sup> sample loop was filled with Ar (UHP, 99.999%, Indiana Oxygen) and injected into 50 cm<sup>3</sup> min<sup>-1</sup> UHP He flow. The area of this Ar pulse was used as an internal standard to correct for the instrumental drift between TPD experiments. The total NH<sub>3</sub> desorbed per gram of catalyst was quantified from the area under the  $m/z = 17$  signal, after subtracting the contribution from water at  $m/z = 17$  due to fragmentation.

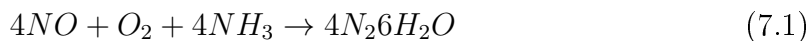
TPD experiments on Cu-exchanged samples were performed on a gas-phase plug flow reactor, as described by Bates et al [37]. The total moles of NH<sub>3</sub> desorbed during these TPD experiments were measured using on-board calibrations in a MKS Multigas 2030 gas-phase FT-IR spectrometer [78].

## 7. DYNAMIC MULTINUCLEAR SITES FORMED BY MOBILIZED COPPER IONS IN NOX SELECTIVE CATALYTIC REDUCTION

### 7.1 Introduction

Single-site heterogeneous catalysts promise to combine the attractive features of homogeneous and heterogeneous catalysts: active sites of regular and tunable architecture that provide precise catalytic function, integrated into a thermally stable, porous, solid host that facilitates access of substrates to those sites and separation of products from the catalyst [413]. In the conventional definition, a single-site catalyst contains functionally isolated active sites, such that reaction rates per active site are independent of their spatial proximity [15]. Single metal atoms incorporated into solid oxide supports are reported to follow this conventional single-site behavior in catalytic CO oxidation to CO<sub>2</sub> [302, 414, 415], selective hydrogenation [416, 417], and water-gas shift [418, 419]. Here we report that a nominally single-site catalyst [79] operates by dynamic, reversible, and density-dependent (non-mean field) interaction of multiple ionically tethered single sites, a behavior that lies outside the canonical definition of a single-site heterogeneous catalyst [420].

We discovered this phenomenon in the quest for a molecularly detailed model to unify the seemingly disparate observations of the catalytic function of copper-exchanged chabazite (Cu-CHA) zeolites, materials used in emissions control for the standard selective catalytic reduction (SCR) of nitrogen oxides (NO<sub>x</sub>,  $x = 1, 2$ ) with ammonia [218]:



Chabazite is a small-pore zeolite composed of cages (0.8 nm by 0.8 nm by 1.2 nm) interconnected by six-membered ring (6-MR) prisms and eight-membered ring (8-MR) windows (Fig. 7.1). Substitution of Si<sup>4+</sup> by Al<sup>3+</sup> within the framework introduces an

anionic charge that is balanced by extralattice cations. After Cu ion exchange and high-temperature oxidation treatment, two isolated Cu site motifs are present: discrete  $\text{Cu}^{II}$  ions that balance two proximal Al centers and  $[\text{Cu}^{II}\text{OH}]^+$  ions that balance single Al centers [35, 39, 79]. Under low-temperature ( $<523$  K) standard SCR conditions, ammonia coordinates to and liberates Cu ions from direct association with the zeolite support, and these solvated Cu ions act as the redox-active catalytic sites [85]. At typical Cu ion volumetric densities, standard SCR rates increase linearly with Cu density, as expected for a single-site catalyst. As shown here, however, experimental observations in the low-Cu density limit reveal a portion of the catalytic cycle in which  $\text{O}_2$  activation by transiently formed Cu pairs becomes rate limiting. These Cu pairs form from  $\text{NH}_3$ -solvated Cu ions with mobilities restricted by electrostatic attraction to charge-compensating framework Al centers, leading to catalytic function that is neither single site nor homogeneous.

Recognizing the intermediacy of this distinct catalytic state reconciles a number of controversies in Cu-zeolite SCR catalysis, including the role of the zeolite support in the catalytic mechanism, the sensitivity of SCR rates to Cu density under different conditions of observation, the extent to which standard and the closely related fast SCR cycles [41] are connected through common intermediates, the chemical processes that limit low-temperature  $\text{NO}_x$  SCR reactivity, and the origins of the apparent change in mechanism at elevated temperatures. These observations provide insight into the design of improved catalysts for SCR. More broadly, they reveal a distinct class of catalytic materials characterized by partially mobile ions that dynamically and reversibly form multinuclear active sites, a concept that may be exploited for a wide variety of reactions.

## 7.2 Turnover rates depend on the spatial density of single Cu sites

To assess the catalytic consequences of Cu ion density, we prepared a series of Cu-CHA samples with fixed framework Al composition ( $\text{Si}/\text{Al} = 15$ ) and Cu/Al content ranging from 0.04 to 0.44 [for synthesis methods and characterization data, see Supp.

Info. section 7.8.1, figs. 7.8 to 7.11, and tables 7.1 and 7.2, corresponding to Cu volumetric densities ( $\rho_{Cu}$ ) from  $(0.3 \text{ to } 4.2) \times 10^{-4} \text{ Cu A}^{-3}$ . We denote samples as Cu-CHA-X, where X indicates the mean Cu-Cu distance (in Å), assuming a homogeneous Cu distribution (table 7.2). Mean Cu-Cu distances vary from 40.7 to 16.6 Å from the least to most heavily Cu-exchanged samples, and the highest Cu loading corresponds to approximately one Cu ion per three chabazite cages (Fig. 7.1).

We observed that SCR rates increased linearly with Cu density at  $\rho_{Cu} > 1.9 \times 10^{-4} \text{ A}^{-3}$  (Fig. 7.1), as would be expected for a reaction catalyzed by isolated Cu sites. Turnover rates, apparent reaction orders, and apparent activation energies (table 7.3) are consistent with values reported for high-Cu density Cu-CHA samples [37, 349]. By contrast, standard SCR rates vary quadratically with Cu density below  $\rho_{Cu} < 1.13 \times 10^{-4} \text{ A}^{-3}$ . All kinetic quantities are consistent with those reported for Cu-dilute Cu-CHA samples [Si/Al = 4.5, Cu/Al < 0.02 [37]; Si/Al = 6, Cu/Al < 0.03 [349]]. We show that these two kinetic regimes, characterized by distinct kinetic parameters, reflect different rate-controlling elementary steps and prevalent reactive intermediates during steady-state NOx SCR.

To probe the mechanistic origins of this change in kinetic behavior, we used x-ray absorption near-edge structure (XANES) spectroscopy to quantify Cu oxidation state during steady-state standard SCR in *operando*. Figure 7.2 and table 7.4 report the steady-state  $\text{Cu}^I$  fraction obtained by XANES fitting (procedure detailed in Supp. Info. section 7.3) as a function of Cu density for three samples in Fig. 7.1 (Si/Al = 15) and seven other Cu-CHA zeolites (Si/Al = 4.5, 16, and 25; table 7.4). Consistent with prior observation, the site-isolated  $\text{Cu}^{II}$  ions observed *ex situ* evolve into a mixture of  $\text{Cu}^I$  and  $\text{Cu}^{II}$  ions during standard SCR catalysis, indicative of redox cycling between  $\text{Cu}^I$  and  $\text{Cu}^{II}$  oxidation states coupled with the SCR catalytic cycle [218]. The  $\text{Cu}^{II} \rightarrow \text{Cu}^I$  half-cycle (Fig. 7.2, inset) is accepted to occur on site-isolated  $\text{Cu}^{II}$ , to consume one equivalent of NO and  $\text{NH}_3$  per  $\text{Cu}^{II}$ , and to produce  $\text{N}_2$  and  $\text{H}_2\text{O}$  [41, 85].

The inverse relationship between steady-state  $\text{Cu}^I$  fraction and Cu volumetric density (Fig. 7.2) is inconsistent with the behavior expected of a single-site catalyst, for which the active-site oxidation state should depend only on the reaction conditions and temperature. The XANES data show that  $\text{Cu}^I$  is the minority oxidation state at the highest Cu density and smallest mean Cu-Cu separations ( $< 15$  Å) during steady-state catalytic operation but that its proportion increases with decreasing Cu density to the point that it becomes the majority oxidation state in the most dilute sample (mean Cu-Cu distance ca. 29 Å). In this dilute limit, the *operando* XANES and extended x-ray absorption fine structure (EXAFS) spectra become indistinguishable from those of a  $\text{Cu}^I$ -CHA sample reduced *in situ* or of  $\text{Cu}^I(\text{NH}_3)_2$  in aqueous solution (fig. 7.12 and table 7.4) [79]. This observation suggests that  $\text{Cu}^I \rightarrow \text{Cu}^{II}$  oxidation rates increase with Cu ion density and implies non-single site behavior in the oxidation half-cycle, a process that is not well understood mechanistically beyond the observation that it consumes  $\text{O}_2$  [218].

The coordination states of site-isolated  $\text{Cu}^I$  and  $\text{Cu}^{II}$  ions under standard SCR conditions at 473 K have been explored previously in detail [79]. X-ray absorption spectroscopy [85], x-ray emission spectroscopy [360,421], and density functional theory (DFT)-based models [79] (including *ab initio* thermodynamic phase diagrams in figs. 7.24 and 7.25) show that  $\text{NH}_3$  out-competes other gases present under standard SCR conditions, including  $\text{H}_2\text{O}$ , for binding at both  $\text{Cu}^I$  and  $\text{Cu}^{II}$  ions, which are respectively two- and four-fold coordinated. Consistent with these findings, the standard SCR reaction rate is zero order with respect to water pressure (1 to 10% atm; fig. 7.26). Schematic illustrations of the most probable coordination states of  $\text{Cu}^I$  and  $\text{Cu}^{II}$  ions under these conditions are shown in the inset of Fig. 7.2.

In the high-Cu density samples (Fig. 7.2, samples c to g), the first-shell Cu coordination number (CN) derived from *operando* EXAFS is three, consistent with the expectation for a nearly equimolar mixture of  $\text{Cu}^I$  and  $\text{Cu}^{II}$  [79], table 7.4. The CN decreases to two in the fully reduced (Fig. 7.2, samples a to b), lowest Cu density samples, consistent with site-isolated  $\text{Cu}^I(\text{NH}_3)_2$  as the most abundant

reactive intermediate present during steady-state standard SCR. In this limit, the SCR turnover rate is solely limited by the  $\text{Cu}^I \rightarrow \text{Cu}^{II}$  half-reaction. The increase in apparent  $\text{O}_2$  reaction order from 0.3 to 0.8 with decreasing Cu density reinforces the increasing kinetic relevance of the  $\text{Cu}^I \rightarrow \text{Cu}^{II}$  half-cycle as Cu becomes more dilute (Fig. 7.1). This change also corresponds with the transition from a first-order to a second-order dependence of SCR rate on Cu ion density [Fig. 7.1, [349]]. From these observations, we conclude that the kinetically relevant  $\text{O}_2$ -consuming step in the oxidation half-cycle is sensitive to Cu density.

### 7.3 $\text{Cu}^I$ site density requirements differ for oxidation with $\text{O}_2$ and $\text{NO}_2$

To probe the coupled roles of  $\text{O}_2$  and Cu density in the oxidation half-cycle, Cu-CHA-29, Cu-CHA-20, and Cu-CHA-15 (Fig. 7.2, labels a, c, and h, respectively) were first reduced to the  $\text{Cu}^I$  state in flowing NO and  $\text{NH}_3$  (details in Supp. Info. section 7.8.3, figs. 7.13 to 7.15) [79]. Then, samples were held under flowing  $\text{O}_2$ , and the transient evolution of the Cu oxidation state was monitored by using XANES. The  $\text{Cu}^I$  fraction decayed in the presence of  $\text{O}_2$  at different rates on the three samples (Fig. 7.3), and different fractions of  $\text{Cu}^I$  (0.05 to 0.30) persisted at steady state (table 7.6).

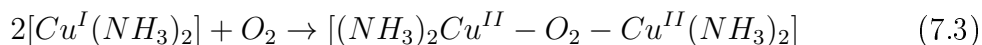
The dependence of the transient oxidation state response on Cu density suggests some underlying spatial requirements for  $\text{Cu}^I(\text{NH}_3)_2$  ions to react with  $\text{O}_2$ . After exploring various rate laws, we found that an expression that is second order in total  $\text{Cu}^I$  density  $[\text{Cu}^I]$  and offset by a recalcitrant fraction of  $\text{Cu}^I$ ,  $[\text{Cu}^I]_\infty$ , fits the data most satisfactorily [coefficient of determination ( $R^2$ ) = 0.99 (a), 0.98 (c), and 0.99 (h), Fig. 7.2; details in Supp. Info. section 7.8.4]. Normalizing to the initial  $\text{Cu}^I$  density,  $[\text{Cu}^I]_0$ , the integrated rate law becomes:

$$\text{Cu}^I \text{ Fraction} = \frac{[\text{Cu}^I](t)}{[\text{Cu}^I]_0} = \frac{1 - [\text{Cu}^I]_\infty/[\text{Cu}^I]_0}{1 + 2kt([\text{Cu}^I]_0 - [\text{Cu}^I]_\infty)} + \frac{[\text{Cu}^I]_\infty}{[\text{Cu}^I]_0} \quad (7.2)$$

where  $t$  is time and  $k$  is a pseudo-homogeneous second-order rate constant for disappearance of  $\text{Cu}^I$ . Solid lines in Fig. 7.3 denote best-fit regressions of the data to Eq.

7.2. Fitted  $k$  values of  $(1.0, 1.7, \text{ and } 8.2) \times 10^{-4} \text{ m}^3 \text{ mol Cu}^{-1} \text{ s}^{-1}$  for Cu-CHA-29, Cu-CHA-20 and Cu-CHA-15, respectively, increased systematically with Cu density. The variation in  $k$  demonstrates that all the reaction sites are not kinetically equivalent. Further analysis below suggests that the oxidation kinetics cannot be faithfully captured by a mean-field model.

This second-order Cu dependence suggests a pseudo-bimolecular reaction between two  $\text{Cu}^I(\text{NH}_3)_2$  ions and  $\text{O}_2$  during the transient experiment:



Oxygen-bridged Cu dimers are well known in Cu-zeolite chemistry [317,318,422] and find analogies in the biological chemistry of Cu that prevails at lower temperatures [316,388,423–426]. These dimers can adopt various oxygen-bridging configurations [389,424]. To probe the plausibility of this reaction between two caged  $\text{Cu}^I(\text{NH}_3)_2$  centers, we turned to DFT (computational details in Supp. Info. section 7.8.5).

We first considered the energy landscape for two  $\text{Cu}^I(\text{NH}_3)_2$  ions to occupy the same CHA cage. Starting from two  $\text{Cu}^I(\text{NH}_3)_2$  ions in adjacent cages that share an Al T-site vertex (Fig. 7.4, structure A), the computed barrier for one  $\text{Cu}^I(\text{NH}_3)_2$  to diffuse through an 8-MR window into the adjacent  $\text{Cu}^I(\text{NH}_3)_2$ -containing cage (structure B) is  $35 \text{ kJ mol}^{-1}$ , consistent with prior estimates of  $\text{Cu}^I(\text{NH}_3)_2$  diffusion barriers into an empty cage [79,427]. The net pairing cost is  $23 \text{ kJ mol}^{-1}$ . Thus, transport between adjacent Al-sharing cages is expected to be facile at temperatures of catalytic interest. Two  $\text{Cu}^I(\text{NH}_3)_2$  ions bind  $\text{O}_2$  more effectively ( $-59 \text{ kJ mol}^{-1}$ ) than does an isolated  $\text{Cu}^I(\text{NH}_3)_2$  ( $-26 \text{ kJ mol}^{-1}$ ) (table 7.10 and fig. 7.21), and the  $\text{O}_2$  binding energy more than offsets the energy cost for two  $\text{Cu}^I(\text{NH}_3)_2$  to cohabit the same cage. Initial reaction likely generates the end-on spin-triplet species shown in Fig. 7.4 (structure C), and further rearrangement and dissociation of  $\text{O}_2$  across two  $\text{Cu}^I$  centers ultimately leads to the di-oxo structure E, containing two four-fold coordinated  $\text{Cu}^{II}$  centers. Conversion of structure C into D is spin forbidden; the effective barrier in similar ligand environments is estimated to be  $20 \text{ kJ mol}^{-1}$  [423]. Subsequent conversion of structure D into E occurs with a modest barrier. The



rate-limiting process across this entire cascade (A to E, table 7.9) is the migration of  $\text{Cu}^I$  through the 8-MR; beyond that point, reaction energies are computed to be independent of the zeolite cage. Thus, the primary role of the zeolite support in this oxidation process is to regulate  $\text{Cu}^I$  mobility.

Structure E is consistent both with XANES observed  $\text{Cu}^{II}$  oxidation state and with the first and second-shell features extracted from EXAFS (Fig. 7.3, inset, and figs. 7.16 to 7.18) at the end of the transient  $\text{O}_2$  oxidation experiment. Thus, experiment and computation both reveal a second  $\text{Cu}^{II}$  state of the catalyst, distinct from framework-bound  $\text{Cu}^{II}$  observed after oxidative treatments and from  $\text{NH}_3$ -solvated  $\text{Cu}^{II}$  detected during low-temperature standard SCR [79,421]. Exposure of samples to  $\text{NO}$  and  $\text{NH}_3$  at 473 K after the transient  $\text{O}_2$  oxidation experiments reduces all sites to the original mononuclear  $\text{Cu}^I$  state, demonstrating that the SCR redox cycle can be closed through sequential stoichiometric reactions (SM section 7.8.6, fig. 7.19). Further, subsequent  $\text{O}_2$  treatment recovers the same transient response and the same fraction of  $\text{Cu}^I$  sites that are unresponsive to  $\text{O}_2$  exposure (table 7.7), indicating that  $\text{Cu}^I$  ions do not irreversibly aggregate during  $\text{O}_2$  exposure, but return to their original site isolated state after each reduction step.

To verify that the residual  $\text{Cu}^I$  fraction did not represent a physically inaccessible or chemically distinct site, transient  $\text{O}_2$  experiments were compared with an analogous transient  $\text{NO}_2$  experiment (details in Supp. Info. section 7.8.3) on reduced forms of the same three samples (figs. 7.13 to 7.15). After  $\text{NO}_2$  exposure at 473 K, the  $\text{Cu}^I$  fraction decayed with time as in the  $\text{O}_2$  experiment, but the  $\text{Cu}^I$  absorption edges disappeared completely after ca. 300 s. Further, the decrease in  $\text{Cu}^I$  fraction with time is best described [ $R^2 = 0.98$  (a), 0.98 (c), and 0.89 (h); details in Supp. Info. section 7.8.4 by a pseudo-first order rate expression with apparent rate constants ( $0.030 \text{ s}^{-1}$ ) that are independent of Cu density (SM section 7.8.4, fig. 7.20). Thus, all  $\text{Cu}^I$  sites are equivalently susceptible to oxidation by  $\text{NO}_2$ . We compute the reaction energy for  $\text{NO}_2$  binding to  $\text{Cu}^I(\text{NH}_3)_2$  to be  $-46 \text{ kJ mol}^{-1}$  and to generate a  $\text{Cu}^{II}$  center (SM section 7.8.5, fig. 7.21, and table 7.10).

We conclude that the spatial proximity of isolated  $\text{Cu}^I$  ions, and not the presence of minority dimeric Cu species at low Cu densities, is responsible for the transition in the standard SCR turnover rate from a quadratic to linear dependence on Cu ion density with increasing Cu density (Fig. 7.1). The steady-state and transient experiments and DFT models are consistent with a  $\text{Cu}^I \rightarrow \text{Cu}^{II}$  half-cycle that combines two  $\text{Cu}^I(\text{NH}_3)_2$  complexes with one  $\text{O}_2$  molecule to create a previously unobserved binuclear  $\text{Cu}^{II}$  intermediate (Eq. 7.3 and Fig. 7.4).

The available data exclude the possibility that  $\text{O}_2$  activation occurs on a persistent minority fraction of Cu ion pairs within single zeolite cages [428]. First, the fraction of isolated  $\text{Cu}^I(\text{NH}_3)_2$  complexes that could be reversibly oxidized with  $\text{O}_2$  (Fig. 7.3) exceeds by 10-fold the fraction of Cu pairs within a single cage if Cu were randomly dispersed on the zeolite support (SM section 7.8.7, fig. 7.22). Second, steady-state and transient rates of  $\text{Cu}^I$  oxidation with  $\text{O}_2$  would exhibit a first-order dependence on Cu density, as observed with  $\text{NO}_2$  as the oxidant. Rather, these results imply a pseudo-homogeneous reaction between equivalent site-isolated  $\text{Cu}^I$  ions with mobilities constrained in a manner that limits the total fraction of sites reactive toward  $\text{O}_2$ .

#### 7.4 Solvation by ammonia confers mobility to single Cu ions

To assess the mobility of  $\text{Cu}^I(\text{NH}_3)_2$  complexes over time scales inaccessible to conventional ab initio molecular dynamics, we turned to ab initio metadynamics (SM section 7.8.8), taking Cu-Al coordination distance as the collective variable, using a supercell with a minimum image distance of  $>10$  Å (SM section 7.8.8), and sampling at 473 K. Free energy was minimized at a Cu-Al distance of 4.7 Å and increased with Cu-Al separation until the Cu ion entered an 8-MR window separating two cages, at 8 Å (Fig. 7.5). Free energy decreased as the Cu ion moved into the adjacent cage, before increasing again as the Cu-Al distance exceeded 9 Å. Comparison with a point-charge model indicates that electrostatics dominate this distance-dependent free energy (SM section 7.8.9, Fig. 7.5). From the computed free-energy landscape,

we estimate the hopping rate for a  $\text{Cu}^I(\text{NH}_3)_2$  to leave its resting cage to be  $6 \times 10^6 \text{ s}^{-1}$  at 473 K, much faster than steady-state SCR turnover rates (table 7.3), and the equilibrium fraction of Cu ions outside their resting cage to be  $1.4 \times 10^{-5}$  at 473 K.

$\text{Cu}^I(\text{NH}_3)_2$  migration is thus rapid at 473 K but constrained by electrostatic tethering to charge-compensating framework Al sites. We next used this concept to predict the unoxidized fraction of  $\text{Cu}^I(\text{NH}_3)_2$  in the transient  $\text{O}_2$  experiments (Fig. 7.3), assuming that Cu ions are randomly associated with Al in the CHA lattice, that each Cu can access a limited diffusion volume, and that only  $\text{Cu}^I$  ions with overlapping diffusion volumes can form an  $\text{O}_2$ -bridged Cu pair (Fig. 7.4). To exercise the model, we distributed Al onto a periodic supercell of the CHA lattice following Loewenstein's rule [235], occupied sites with Cu following previously validated rules [79], counted the number of overlapping diffusion spheres at a given radius (Fig. 7.3,  $t = 0$ ) permitting each Cu to be counted only once, and repeated until the average unoxidized  $\text{Cu}^I$  fraction converged (SM section 7.8.10 and fig. 7.23). At the end of a single simulation, the unoxidized  $\text{Cu}^I$  fraction consisted of Cu ions that either were initially physically isolated from all other Cu (Iso) or were functionally isolated because they shared overlapping diffusion volumes with Cu ions that had more than one potential partner, the losers in a molecular game of musical chairs (MC). Representative initial and final simulation snapshots are shown in Fig. 7.3 for Cu densities corresponding to Cu-CHA-15, Cu-CHA-20, and Cu-CHA-29, and the predicted fraction of unoxidized  $\text{Cu}^I$  assuming a diffusion radius of 9 Å are plotted as solid horizontal bars in Fig. 7.3. Model results agree quantitatively with both experimental observation and the metadynamics observation of a ca. 9 Å maximum diffusion distance, implying that the Cu sites are neither conventionally heterogeneous (immobile) nor homogeneous (mobility governed by molecular diffusion) and demonstrating that the fraction of spectator  $[\text{Cu}^I]_\infty$  sites is a consequence of regulated and localized mobility due to electrostatic tethering.

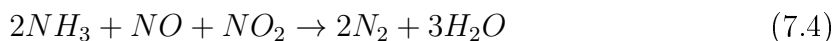
These observations resolve the outstanding issues regarding SCR catalysis raised in the introduction.  $\text{NH}_3$  solvates and mobilizes discrete Cu active sites under low-

temperature SCR conditions. When the activation of  $O_2$  is not rate controlling,  $NH_3$ -solvated Cu ions appear catalytically equivalent, such that rates increase linearly with their number density. In this regime, the zeolite framework itself has only a weak influence on the SCR turnover rate [79] because it functions primarily as an ionic host for homogeneous-like  $NH_3$ -ligated  $Cu^{II}$  complexes. Experiments performed on samples with low Cu density revealed, however, that a homogeneous picture of the SCR mechanism is incomplete.

Simulations reveal that  $NH_3$ -solvated  $Cu^I$  ions have sufficient mobility to travel through 8-MR CHA windows, visit adjacent cages, and form Cu site pairs that activate  $O_2$  via Eq. 7.3. Because of this requirement for dynamic Cu pairing, SCR rates scale approximately second order with Cu density under conditions in which the  $Cu^I \rightarrow Cu^{II}$  oxidation by  $O_2$  is rate determining, consistent with quantitative analysis of the transient oxidation of  $Cu^I$  with  $O_2$ . In contrast with previous assertions [429], binuclear  $Cu^{II}$  intermediates can be detected experimentally and are structurally distinct from the mononuclear  $NH_3$ -solvated  $Cu^{II}$  observed in *operando* [79, 421], and the number of such binuclear sites that can form on a given Cu-CHA sample can be quantitatively predicted. These results motivate a revision of previous mechanisms to incorporate this dynamic coupling of isolated Cu ions, as illustrated in Fig. 7.6. Isolated,  $NH_3$ -solvated  $Cu^{II}$  ions charge-compensating either one (left cycle) or two (right cycle) framework Al sites are reduced by NO and  $NH_3$  to produce  $N_2$ ,  $H_2O$ , and  $Cu^I(NH_3)_2$ . These two paths are distinguished only by the fate of the proton that is also generated [79]. Mobile  $Cu^I(NH_3)_2$  species can diffuse and combine in a reaction that consumes  $O_2$  and generates the  $Cu^{II}$  dimer intermediate observed here. We confirmed that this binuclear  $Cu^{II}$  complex reacts with two equivalents of NO per Cu (SM section 7.8.6, fig. 7.19) to regenerate  $Cu^I(NH_3)_2$  and close the SCR cycle.

A key aspect of our model is that Cu ions supported on the zeolite are neither mobile as prescribed by molecular diffusion processes, as in a homogeneous catalyst, nor segregated into separate ensembles of active and inactive sites, as in a heterogeneous catalyst. Rather, all Cu ions located within diffusion distances of other ions can

potentially form Cu pairs dynamically and reversibly during the SCR cycle, at rates influenced by the mobility and effective diffusion distances of Cu ions. Thus, rates of O<sub>2</sub>-assisted oxidations are sensitive to Cu proximity and could also be sensitive to the zeolite support composition and topology. By contrast, all NH<sub>3</sub>-solvated Cu<sup>I</sup> sites are equivalently susceptible to first-order oxidation by NO<sub>2</sub>, independent of Cu spatial density, and are subsequently reducible by NO and NH<sub>3</sub>. These observations demonstrate that fast SCR, in which oxidation capacity is provided by NO<sub>2</sub> rather than O<sub>2</sub>:



is not linked through a common intermediate to standard SCR under conditions in which Cu sites are solvated by NH<sub>3</sub> [41]. NO<sub>2</sub> oxidants accelerate SCR rates both by accelerating Cu<sup>I</sup> oxidation kinetics and by engaging a larger fraction of Cu sites in the catalyst.

At higher temperatures (>523 K), standard SCR rates are independent of Cu density [218,349], the apparent activation energy increases to 140 kJ mol<sup>-1</sup> [349], and Cu ions lose their NH<sub>3</sub> solvation shell [218], implicating the involvement of different O<sub>2</sub> activation steps that do not occur at the Cu ion pairs formed dynamically at lower temperatures (<523 K). Of greater practical importance to NO<sub>x</sub> emissions control is to increase SCR rates at even lower temperatures (<473 K) [218]. The results here imply that standard SCR onset ("light-off") temperatures, which are observed to depend on zeolite composition, topology, and Cu distribution [89], are sensitive to changes in rate-determining O<sub>2</sub> activation steps. Thus, optimization of Cu spatial distribution and promotion of Cu mobility are promising strategies for accelerating Cu<sup>I</sup> oxidation rates and improving low-temperature SCR catalysts.

## 7.5 Outlook

Our results point to a previously unrecognized catalytic mechanism that embodies salient features of homogeneous and heterogeneous catalysts. This mechanism

encompasses solvent mobilization of discrete active site precursors (e.g., single metal ions) and ionic bonds to the support that limit their mobility. The active site precursor has an effective diffusion distance and occupies a volumetric footprint that restricts its interactions only to other precursors within overlapping volumes; such catalytic behavior cannot be described by mean-field, Langmuir kinetics. The ionic tethering motif provides opportunities to confer catalytic benefits beyond immobilization strategies based on covalent anchors or tethers. This motif enables the *in situ* dynamic generation of multinuclear complexes implicated as active sites in O<sub>2</sub> activation and therefore could also apply to other reactions, such as the partial oxidation of methane to methanol on Cu-zeolites. We expect that design parameters to regulate the mobility of active sites and their precursors would include the structure, composition and electronic conductivity of the support, and the molecules that solvate such sites to promote their mobility. Manipulating these variables could open approaches to catalyst design for a wide variety of reactions by combining knowledge from homogeneous and heterogeneous catalysis.

## 7.6 Acknowledgements

Full details of experiments and computational models are provided in the supplementary information. Financial support was provided by the National Science Foundation GOALI program under award numbers 1258715-CBET (Purdue) and 1258690-CBET (Notre Dame), the National Science Foundation Faculty Early Career Development Program under award number 1552517-CBET (R.G.), Cummins, Inc. (I.K., A.J.S., A.A.P., J.D.A.-C.). and The Patrick and Jane Eilers Graduate Student Fellowship for Energy Related Research (C.P.). Use of the Advanced Photon Source is supported by the U.S. Department of Energy, Office of Science, and Office of Basic Energy Sciences, under Contract No. DE-AC02-06CH11357. We thank the Center for Research Computing at Notre Dame, and EMSL, a DOE Office of Science User Facility sponsored by the Office of Biological and Environmental Research and located at Pacific Northwest National Laboratory, for computational resources.

Additionally, I acknowledge the AAAS for granting permission to reproduce this chapter of my thesis. Adapted with permissions from Science, 2017, 357, 898-903. Reprinted with permission from AAAS.

The full article can be accessed here: [dx.doi.org/10.1126/science.aan5630](https://doi.org/10.1126/science.aan5630).

## 7.7 Figures and Tables

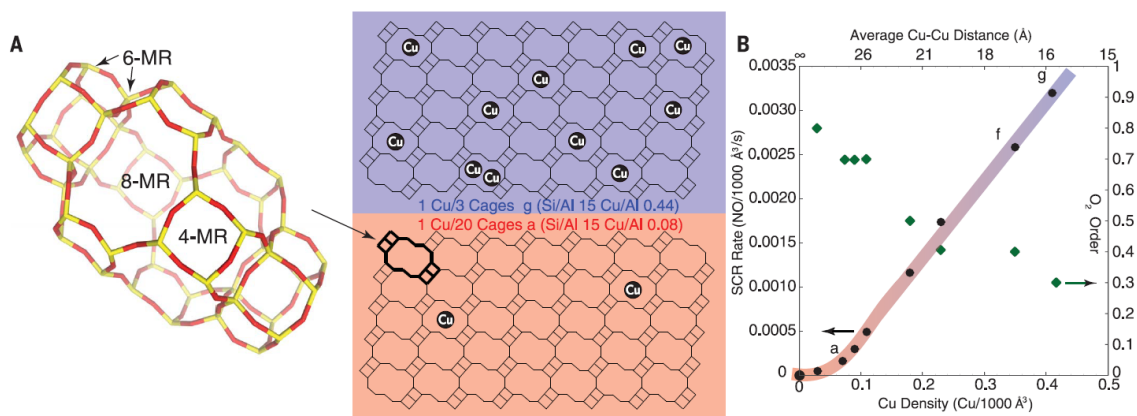


Figure 7.1. **Cu-density dependence of SCR rates.** (A) The CHA cage [1] and schematic representation of the Cu ion densities per CHA cage in samples a and g. (B) Standard NO<sub>x</sub> SCR rates (per volume catalyst; 473 K; measured in a differential reactor by using a gas mixture representative of practical low-temperature application, including 2.5% H<sub>2</sub>O; details in Supp. Info. section 7.8.2) and apparent O<sub>2</sub> orders measured on Cu-CHA-X samples (Si/Al = 15, table 7.3) of increasing Cu ion density. Colored line is a visual guide; regression fits to the quadratic ( $R^2 = 0.99$ ) and linear ( $R^2 = 0.99$ ) kinetic regimes are detailed in Supp. Info. section 7.8.2.



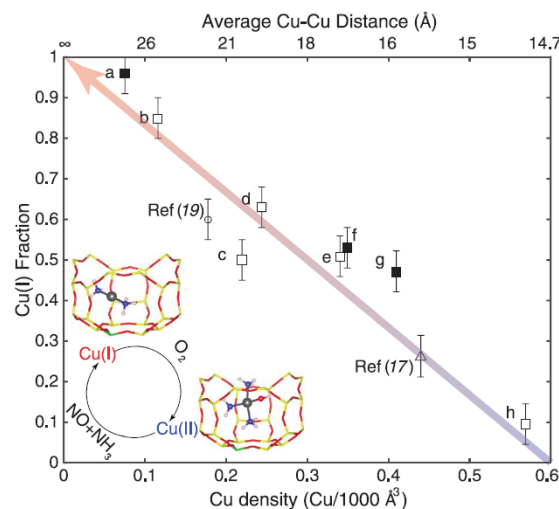


Figure 7.2. **Cu-density dependence of *operando* Cu oxidation state.** The dependence of Cu<sup>I</sup> fraction on Cu ion volumetric density during steady-state standard SCR at 473 K was measured by XANES (details in Supp. Info. section 7.8.3). Data points include samples a, f, and g shown in Fig. 7.1 (Si/Al = 15, filled squares), samples at Si/Al = 4.5 and Si/Al = 25 (open squares), and comparable literature data [open circle Ref [360], Si/Al = 16; open triangle Ref [41], Si/Al = 4.5]. Inset shows NH<sub>3</sub>-solvated, isolated Cu<sup>I</sup> and Cu<sup>II</sup> species previously observed and computed [79] to be present during standard SCR at 473 K. Gray, Cu; green, Al; yellow, Si; red, O; blue, N; and white, H. The colored arrow is a visual guide; error bars represent the absolute 5% uncertainty from linear combination XANES fitting (details in Supp. Info. section 7.8.3).

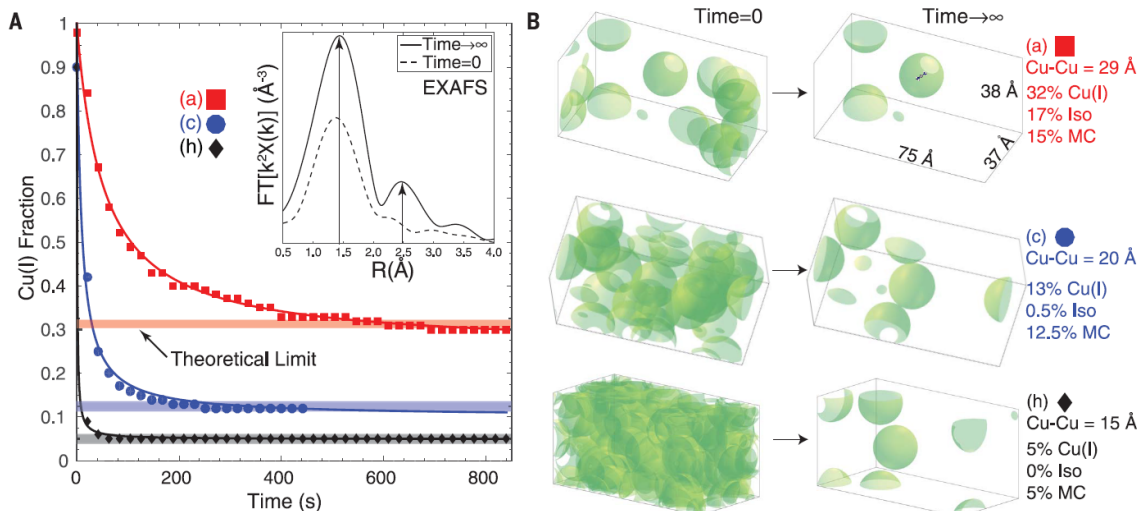


Figure 7.3. **Kinetics of Cu<sup>I</sup> oxidation by O<sub>2</sub>.** (A) Temporal evolution of the XANES-measured Cu<sup>I</sup> fraction is plotted for the Cu-CHA-29 (a, red), Cu-CHA-20 (c, blue), and Cu-CHA-15 (h, black) samples during transient oxidation in 10% O<sub>2</sub> at 473 K. Least-squares fit to Eq. 7.2 is shown by solid lines, and predicted recalcitrant Cu<sup>I</sup> fractions are shown as horizontal bars. [Cu<sup>I</sup>]<sub>∞</sub> was set by forcing the fit through the last (longest time) data point; [Cu<sup>I</sup>](0)/[Cu<sup>I</sup>]<sub>0</sub> was set to 1 (full details in Supp. Info. section 7.8.4). The Cu<sup>I</sup> fractions reported contain an absolute 5% error from linear combination XANES fits (details in Supp. Info. section 7.8.3). Inset, the Fourier transform of the k<sup>2</sup>-weighted EXAFS signal (FT[k<sup>2</sup>χ(k)]) in R-space (R) of Cu-CHA-15 collected before O<sub>2</sub> exposure and after the transient experiment. (B) Snapshots taken from simulated initial (time = 0) and final (time → ∞) Cu<sup>I</sup> spatial distributions corresponding to the three samples (a, c, and h) in (A). Cu<sup>I</sup> volumetric footprints are denoted by 9 Å-radius green spheres. Simulation results include decomposition of unoxidized Cu<sup>I</sup> fraction into physically isolated (Iso) and functionally isolated (MC) components.

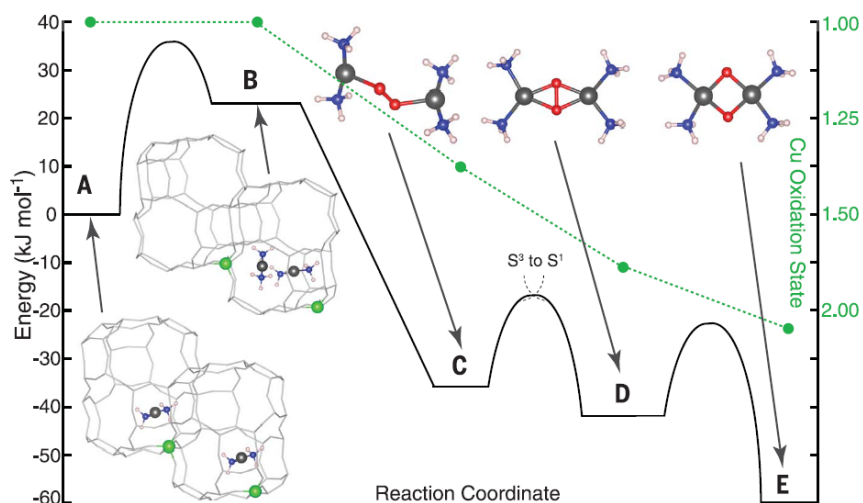


Figure 7.4. **Simulation of  $\text{O}_2$  adsorption and oxidation of two  $\text{Cu}^I(\text{NH}_3)_2$  equivalents.** DFT-computed energy landscape is shown for the diffusion of  $\text{Cu}^I(\text{NH}_3)_2$  through an 8-MR CHA window into an adjacent cage and subsequent bimolecular reaction with  $\text{O}_2$ . All minima and transition states were computed here, except C to D, which is taken from [423]. Gray, Cu; green, Al; red, O; blue, N; and white, H.

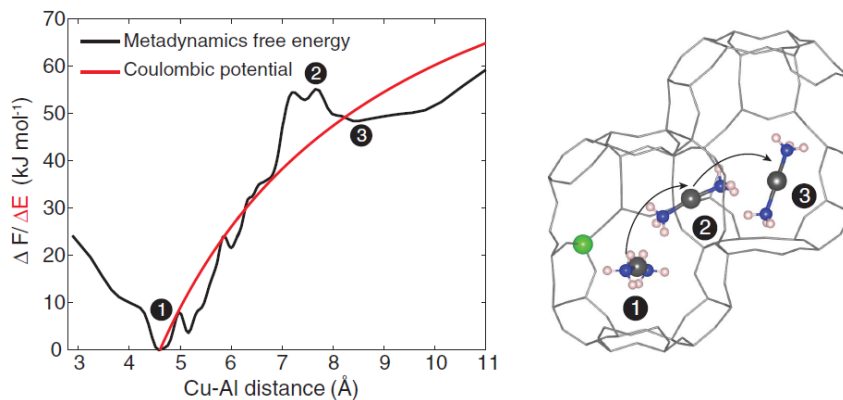


Figure 7.5. **Simulated  $\text{Cu}^I(\text{NH}_3)_2$  diffusion up to 11 Å from charge-compensating Al.** On left, the metadynamics-computed free energy at 473 K of  $\text{Cu}^I(\text{NH}_3)_2$  in the 72-T site CHA supercell versus Cu-Al distance. The red line is the energy profile predicted from a point-charge electrostatic model, described in Supp. Info. section 7.8.9. Labeled are reactant state (1) [ $\text{Cu}^I(\text{NH}_3)_2$  in the same cage as Al], transition state (2) [ $\text{Cu}^I(\text{NH}_3)_2$  diffusion through 8-MR], and product state (3) [ $\text{Cu}^I(\text{NH}_3)_2$  in the neighboring cage without Al]. Corresponding representative  $\text{Cu}^I(\text{NH}_3)_2$  configurations from the trajectories are shown on the right. Gray, Cu; green, Al; blue, N; and white, H.

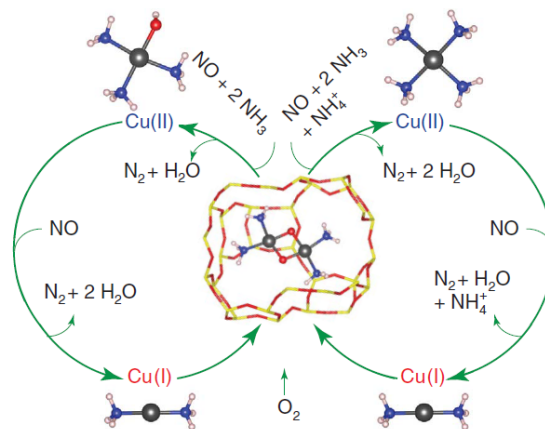


Figure 7.6. **Proposed low-temperature SCR catalytic cycle.** Reduction steps proceed on site-isolated Cu<sup>II</sup> ions residing near one (left-hand cycle) or two (right-hand cycle) framework Al centers with constrained diffusion of Cu<sup>I</sup> ions into single cages and oxidation by O<sub>2</sub> (inner step). NH<sub>4</sub><sup>+</sup> is formed and consumed in the right-hand cycle to maintain stoichiometry and charge balance. Gray, Cu; yellow, Si; red, O; blue, N; and white, H.

## 7.8 Supporting Information

### 7.8.1 Synthesis Methods and Characterization

#### Synthesis of SSZ-13 zeolites

Here, SSZ-13 is used to refer to materials of aluminosilicate composition and the chabazite (CHA) framework. High-aluminum SSZ-13 zeolites ( $\text{Si}/\text{Al} = 4.5$ ) were synthesized as previously reported [79]. A molar ratio of 1  $\text{SiO}_2$ / 0.031  $\text{Al}_2\text{O}_3$ / 0.017 TMAdaOH/ 0.770  $\text{Na}_2\text{O}$ / 12.1  $\text{H}_2\text{O}$  was used in the synthesis solution. Briefly, a 1M NaOH solution (3.3 wt% NaOH, Alfa Aesar) was added to deionized water (18.2 M $\Omega$ ) in a perfluoroalkoxy alkane (PFA) jar and stirred for 15 minutes at ambient conditions. Next, sodium silicate (10.6 wt%  $\text{Na}_2\text{O}$ , 25.6 wt%  $\text{SiO}_2$ ; Sigma Aldrich) was added to the NaOH solution and stirred for 15 minutes under ambient conditions. Then,  $\text{NH}_4$ -Y zeolite (Zeolyst CBV300,  $\text{Si}/\text{Al} = 2.6$ ) was added and the mixture was stirred for 30 minutes under ambient conditions. Finally, an aqueous TMAdaOH solution (25 wt%, Sachem) was added to the mixture and stirred for 30 minutes under ambient conditions. The synthesis mixture was then transferred to 45 mL Teflon-lined stainless steel autoclaves (Parr Instruments) and placed in a forced convection oven (Yamato DKN-402C) at 413 K and rotated at 60 RPM for 6 days.

Low aluminum SSZ-13 zeolites ( $\text{Si}/\text{Al} = 15$ -25) were synthesized in hydroxide media using a previously reported procedure [79]. A molar ratio of 1  $\text{SiO}_2$ / 0.0167-0.033  $\text{Al}_2\text{O}_3$ / 0.25 TMAdaOH/ 0.125  $\text{Na}_2\text{O}$ / 44  $\text{H}_2\text{O}$  was used to obtain  $\text{Na}^+/\text{TMAda}^+ = 1$  and  $\text{Si}/\text{Al} = 15$  or 25 in the synthesis solution. A typical synthesis involved adding an aqueous TMAdaOH solution to deionized  $\text{H}_2\text{O}$  in a PFA jar and stirring the solution under ambient conditions for 15 minutes. Next, aluminum hydroxide was added to the aqueous TMAdaOH solution. Then, a 5M NaOH solution (16.7 wt% NaOH in deionized water; NaOH pellets 98 wt%, Alfa Aesar) was added dropwise to the solution and stirred under ambient conditions for 15 minutes. Finally, colloidal silica was added and the mixture was stirred for 2 h under ambient conditions. All synthesis reagents were used without further purification. The synthesis solution was

then transferred to a 45 mL Teflon-lined stainless steel autoclave and placed in a forced convection oven at 433 K and rotated at 40 RPM for 6 days.

#### X-Ray diffraction of CHA zeolites

The CHA crystal framework was determined from powder X-ray diffraction (XRD) patterns measured on a Rigaku SmartLab X-ray diffractometer with a Cu K $\alpha$  radiation source ( $\lambda=0.154$  nm) operated at 1.76 kW. 0.01 g of zeolite powder were loaded onto a low-volume sample holder (Rigaku) and the diffraction pattern was recorded from 4-40°  $2\theta$  at a scan rate of 0.04° s<sup>-1</sup>. Powder XRD patterns for all synthesized materials were compared to diffraction patterns for CHA reported in the International Zeolite Association (IZA) structure database [1]. All XRD patterns reported here are normalized such that the maximum peak intensity in each pattern is unity. Diffraction patterns of CHA zeolites are shown in Fig. 7.8.

#### Adsorption isotherms to measure micropore volumes of CHA zeolites

Micropore volumes of CHA zeolites were determined from Ar adsorption isotherms measured at 87 K on a Micromeritics ASAP 2020 Surface Area and Porosity Analyzer. Typically, 0.03–0.05 g of pelleted and sieved sample (nominal diameter between 180-250  $\mu\text{m}$ ) were degassed by heating to 393 K (0.167 K s<sup>-1</sup>) under vacuum ( $<5$   $\mu\text{mHg}$ ) for 2 h, and then further heating to 623 K (0.167 K s<sup>-1</sup>) under vacuum ( $<5$   $\mu\text{mHg}$ ) and holding for 9 h. Volumetric gas adsorption within micropores (cm<sup>3</sup> g<sup>-1</sup> at STP) was estimated from analysis of semi-log derivative plots of the adsorption isotherm ( $\partial(V_{ads})/\partial(\ln(P/P_0))$  vs.  $\ln(P/P_0)$ ) to identify the micropore filling transition (first maximum) and then the end of micropore filling (subsequent minimum). Micropore volumes (cm<sup>3</sup> g<sup>-1</sup>) were obtained on SSZ-13 zeolites by converting standard gas adsorption volumes (cm<sup>3</sup> g<sub>cat</sub><sup>-1</sup> at STP) to liquid volumes using a density conversion factor assuming the liquid density of Ar at 87 K. Micropore volumes of

CHA zeolites are shown in Fig. 7.9. In each figure, adsorption isotherms are offset in increments of  $200 \text{ cm}^3 \text{ g}^{-1}$  for clarity.

#### Aqueous-phase Copper Ion-Exchange of H-SSZ-13

Cu-SSZ-13 zeolites were prepared by aqueous-phase Cu ion-exchange using  $\text{Cu}(\text{NO}_3)_2$  as the precursor. A pH meter (Mettler Toledo SevenEasy pH Meter S20) calibrated at pH values of 1.0 (Sigma Aldrich FLUKA 31044 Buffer solution pH 1.0 at 293 K), 4.0 (Hach Buffer Solution pH  $4.0 \pm 0.02$  at 298 K), and 7.0 (Hach Buffer Solution pH  $7.00 \pm 0.02$  at 298 K) was used to monitor the pH throughout the Cu ion-exchange process.

Typically, 1 to 2 g of H-SSZ-13 were added to 40 mL of deionized water (Millipore, Synergy UV Water Purification System,  $18.2 \text{ M}\Omega \text{ cm}^{-1}$  resistivity at 298 K) in a 250 mL borosilicate Erlenmeyer flask and stirred at 300 rpm using a magnetic stir bar for 30 minutes at 313 K. Depending on the Cu exchange level targeted, 20 to 100 mL of 0.001 M to 0.1M  $\text{Cu}(\text{NO}_3)_2$  solution (Sigma Aldrich, 99.999% trace metals basis) was added to the slurry. The pH was controlled to  $4.9 \pm 0.1$  by dropwise addition (ca. 2 drops per second) of 1.0 M  $\text{NH}_4\text{OH}$  (Sigma Aldrich, 28.0% Ammonium hydroxide solution, ACS reagent grade) immediately after addition of  $\text{Cu}(\text{NO}_3)_2$  and was maintained at  $4.9 \pm 0.1$  for 4 hours. Cu-exchanged SSZ-13 was recovered via centrifugation, and then washed with deionized water six times ( $70 \text{ mL H}_2\text{O g}^{-1}$  per wash). Cu-SSZ-13 catalysts were dried at 373 K in ambient air in a free convection oven for 12 hours, crushed with a mortar and pestle, then treated in flowing dry air ( $100 \text{ mL g}^{-1}$ , Indiana Oxygen, Zero grade air,  $< 1 \text{ ppm THC}$ ) to 773 K at a rate of  $1 \text{ K min}^{-1}$ .

#### Elemental Analysis using Atomic Absorption Spectroscopy

Typically, 0.02-0.05 g of dry sample (H-SSZ-13 or Cu-SSZ-13) were dissolved in approximately 2 mL of hydrofluoric acid (HF) (Mallinckrodt Baker, 48% HF, Baker Analyzed A.C.S. Reagent) in a 60 mL high density polyethylene (HDPE) bottle (2



oz., 60 mL Nalgene Wide-Mouth Amber HDPE bottles). A polyethylene pipet was used to transfer the HF. The sample was capped and left to dissolve for 12 hours then diluted with approximately 50 mL of deionized water (Millipore, Synergy UV Water Purification System,  $18.2 \text{ M}\Omega \text{ cm}^{-1}$  resistivity at 298 K).

Bulk elemental composition was determined using atomic absorption spectroscopy (AAS) on a Perkin Elmer AAnalyst 300. Silicon AAS standards were created by diluting a 1000 ppm silicon AAS standard solution (Sigma Aldrich, TraceCERT, 1000 mg/L Si in NaOH) to 15, 75, and 150 ppm. A linear calibration curve (ppm Si versus Si absorbance at 251.6 nm) was determined by plotting the absorbance of each silicon standard at 251.6 nm. Similar procedures were used for aluminum, copper and sodium on all reported SSZ-13 catalysts.

#### Cu site characterization and quantification

Cu K-edge X-ray absorption near edge spectroscopy (XANES) of samples under ambient conditions were indistinguishable from that of an aqueous  $\text{Cu}^{II}$  nitrate solution (Cu-CHA-20 and Cu-CHA-29 shown in Fig. 7.10) and did not show absorption characteristic of  $\text{Cu}^I$  (edge at ca. 8983 eV [381,430]) or of  $\text{Cu}^{II}$  within  $\text{Cu}_x\text{O}_y$  clusters [87,129]. Diffuse reflectance UV-Visible spectra collected on these samples under ambient, hydrated conditions are shown in Fig. 7.11. The peak at  $12500 \text{ cm}^{-1}$  is representative of hydrated isolated  $\text{Cu}^{II}$  ions. Peaks at ca.  $22500 \text{ cm}^{-1}$ , reported to be due to Cu-dimers in ZSM-5 [319], are not observed, indicating that predominantly isolated  $\text{Cu}^{II}$  species are present. The broad absorption features between  $30000 \text{ cm}^{-1}$  and  $50000 \text{ cm}^{-1}$  are due to contributions from the zeolite framework.

The enumeration of isolated  $\text{Cu}^{II}$  and  $\text{Cu}^{II}\text{OH}$  sites on each Cu-CHA zeolite was determined after oxidative treatment (20%  $\text{O}_2$ , 773 K) by quantifying the number of residual protons that remained after Cu exchange, given that  $\text{Cu}^{II}$  sites exchange two protons and  $\text{Cu}^{II}\text{OH}$  sites exchange one proton. The quantification was performed using methods that selectively titrate residual  $\text{H}^+$  sites in small-pore, metal-exchanged zeolites [171], in which  $\text{NH}_3$ -saturated samples are purged in flowing wet

helium (3% H<sub>2</sub>O in He, 433 K) to desorb Lewis acid-bound NH<sub>3</sub>, prior to temperature programmed desorption (Table 7.1). The Cu<sup>II</sup> and Cu<sup>II</sup>OH site quantities in the samples studied here are consistent with the thermodynamic preference for Cu<sup>II</sup> exchange at paired Al sites until saturation [79], followed by further exchange of Cu<sup>II</sup>OH sites at isolated Al. Taken together, the *ex situ* characterization of Cu sites by X-ray absorption, UV-Visible and quantification of residual H<sup>+</sup> sites by NH<sub>3</sub> titration, confirm that the Cu-CHA samples studied here contain only isolated Cu<sup>II</sup> cations, present either as Cu<sup>II</sup> at paired framework Al sites or as Cu<sup>II</sup>OH at isolated Al sites [79].

### 7.8.2 SCR Kinetics

Standard selective catalytic reduction (SCR) kinetic data were measured on a down-flow 3/8" ID tubular quartz reactor. All samples were pelletized (Specac 13mm Diameter Stainless Steel Evacuatable Pellet Die) under 10,000 psi pressure (Carver Laboratory Press), ground using a mortar and pestle, then sieved to retain 125 to 250  $\mu$ m particles (W.S. TYLER No. 60 and No. 120 all-stainless-steel). Typically, 0.015-0.050 g of sieved Cu-SSZ-13 catalyst were mixed with enough inert silica gel (Fisher Chemical Silica Gel (Davisil) Sorbent, Grade 923) to obtain a bed height of ca. 0.5 cm. Aluminum foil was wrapped around the quartz reactor to an outer diameter of ca. 2.54 cm, in order to enhance heat conduction and minimize any radial temperature gradients that may be present within the bed. The reactor was then placed within a clam-shell furnace (Applied Test Systems) and pressure-tested with helium (99.999%, Indiana Oxygen) at 5 psig for 20 minutes.

Steady state kinetic data were collected according to methods we have reported previously [37]. Briefly, rate data were measured at differential NO conversion below 20% (total gas flow rate was varied between 0.8 to 1.5 L min<sup>-1</sup>), to ensure the entire bed was exposed to approximately the same gas concentrations and temperatures using a gas mixture of 300 ppm NO (3.5% NO in Ar, Praxair), 300 ppm NH<sub>3</sub> (3.0% NH<sub>3</sub> in Ar, Praxair), 5% CO<sub>2</sub> (liquid, Indiana Oxygen), 10% O<sub>2</sub> (99.5%, Indiana Oxy-

gen), 2.5% H<sub>2</sub>O (deionized, introduced through 24" PermaPure MH Humidifier), and balance N<sub>2</sub> (boiloff liquid N<sub>2</sub>, Linde) at 473 K and 1 atm. The gas hourly space velocity (GHSV) was varied between 600,000 to 4,000,000 h<sup>-1</sup> for all kinetic experiments. NO, NO<sub>2</sub>, NH<sub>3</sub>, CO<sub>2</sub>, N<sub>2</sub>O, and H<sub>2</sub>O concentration data were recorded every 0.95 seconds using a MKS MultiGas 2030 gas-phase Fourier transform infrared (FTIR) spectrometer with on-board calibrations. Reaction temperatures were collected using two Omega K-type 1/16" OD thermocouples with one placed in contact with the top of the bed and the second placed in contact with the bottom of the bed. The temperature difference was always within 3 K during steady state SCR catalysis. Total gas flow rates were measured using a soap bubble flow meter.

In the limit of differential NO conversion, the gas concentrations and catalyst bed temperature can be assumed constant, allowing the NO consumption rate to be calculated using equation 7.5:

$$-r_{NO}[\text{mol NO}(\text{mol Cu s})^{-1}] = \frac{C_{NO,in} - C_{NO,out}}{10^6 \text{mol Cu}} \left( \frac{V_{total} P}{RT} \right) \quad (7.5)$$

where  $C_{NO,j}$  values are the concentrations of NO before and after the catalyst bed in ppm,  $V_{total}$  is the total volumetric flow rate, P is 1 atm, T is ambient temperature, and R is the gas constant. The rate of NO consumption can further be converted from rate per Cu (mol NO mol Cu<sup>-1</sup> s<sup>-1</sup> or NO Cu<sup>-1</sup> s<sup>-1</sup>) to rate per volume (molecules of NO consumed per 1000 Å<sup>-3</sup> s<sup>-1</sup>) using a multiplier for the number of Cu atoms per 1000 Å<sup>3</sup>.

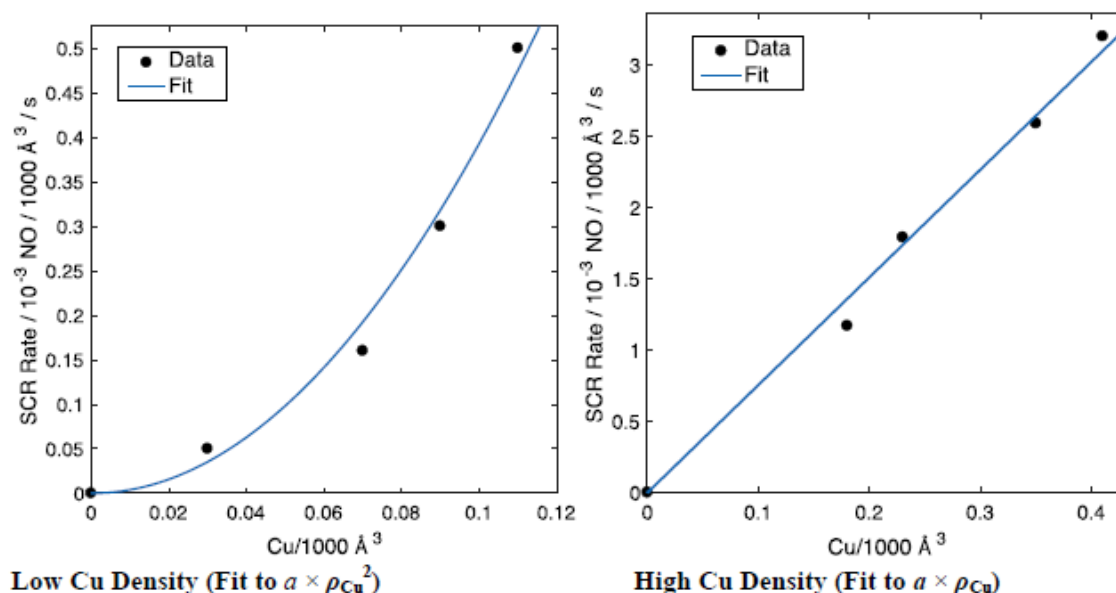
The experimental data are fitted to a power law rate expression where  $k_{app}$  is the apparent rate constant and  $\alpha$ ,  $\beta$ , and  $\gamma$  are the apparent reaction orders with respect to concentrations of NO, NH<sub>3</sub>, and O<sub>2</sub>, respectively.

$$-r_{NO} = k_{app} C_{NO}^{\alpha} C_{NH_3}^{\beta} C_{O_2}^{\gamma} \quad (7.6)$$

$$k_{app} = A e^{\frac{-E_{a,app}}{RT}} \quad (7.7)$$

SCR rates measured as a function of Cu density (Cu-CHA catalysts depicted in figure 7.1 and table 7.3) were fit to two different models, as shown below. The four

lowest Cu density samples were fit to  $\text{rate} = a \times \rho_{\text{Cu}}^2$  (best fit  $a = 39.3$ ,  $R^2=0.99$ ) and the four highest Cu density samples to  $\text{rate} = a \times \rho_{\text{Cu}}$  (best fit  $a = 7.56$ ,  $R^2=0.99$ ).



### 7.8.3 X-Ray Absorption Spectroscopy

X-ray absorption spectroscopy (XAS) experiments were performed at sector 10 MR-CAT (Materials Research Collaborative Access Team) of the Advanced Photon Source, Argonne National Laboratory. The insertion device beamline at sector 10 (10-ID) was used for the *operando* and *in situ* oxidation experiments due to the high photon flux available at that beamline. Incident and transmitted X-ray intensities were measured in ion chambers filled with 20% He in N<sub>2</sub> and 20% Ar in N<sub>2</sub>, respectively, to obtain approximately 10% and 70% absorption of the beam before and after the sample, respectively. A Cu metal foil reference spectrum (edge energy of 8979 eV) was measured simultaneously with each sample spectrum to calibrate the X-ray beam for spectral measurements at the Cu-K edge. All sample spectra were normalized using 1st and 3rd order polynomials for background subtraction of the pre- and post-edges, respectively.

The Cu K-edge XANES spectra consists of several distinct features indicative of the various electronic transitions for the  $\text{Cu}^I$  and  $\text{Cu}^{II}$  oxidation states [431, 432]. The peaks at 8977 eV and 8987 eV are representative of  $\text{Cu}^{II}$ . The peak centered at 8977 eV is due to the symmetry forbidden  $1s \rightarrow 3d$  transition, which becomes allowed due to mixing of the 3d and 4p orbitals and has been reported in several studies as a low intensity, pre-edge feature [36, 433–435]. The shoulder at 8987 eV is due to the  $1s \rightarrow 4p$  electronic transition [38, 436]. The presence of the sharp peak centered around 8983 eV is characteristic of the  $1s \rightarrow 4p$  transition for a two-coordinate  $\text{Cu}^I$  complex. This peak has previously been reported in the literature under a variety of environments including hydrocarbon SCR [437] and NO decomposition on Cu-ZSM-5 [438], thermal reduction of Cu-mordenite [439], Cu-Y [440], and two-coordinate  $\text{Cu}^I$  model compounds including copper(I) diamine complexes [381, 441, 442].

XAS is a bulk technique and each sample spectrum represents a mixture of oxidation states. Therefore, a linear combination XANES fitting of the  $\text{Cu}^I$  and  $\text{Cu}^{II}$  references was used to obtain the relative amounts of Cu in each oxidation state in a given spectrum. Information about how the  $\text{Cu}^I$  and  $\text{Cu}^{II}$  references were generated is provided in our previous publication [79]. An absolute error of 5% was used as a conservative estimate for the uncertainty in the linear combination XANES fitting. The largest source of uncertainty is the  $\text{Cu}^I$  reference used in the fitting, as there is no specific  $\text{Cu}^I$  reference spectrum, and the choice of reference may not exactly reproduce the  $\text{Cu}^I$  amine structure present in the sample. If the  $\text{Cu}^I$  reference used in the fitting is assumed to be an accurate representation of the  $\text{Cu}^I$  structure present, the uncertainty in the linear combination XANES fitting would decrease to 2-3%.

The Debye-Waller factor (DWF) was determined to be  $0.005 \text{ \AA}^2$  for gas conditions that included  $\text{NH}_3$ , and was  $0.003 \text{ \AA}^2$  for all other gas conditions. All extended X-ray absorption fine structure (EXAFS) fitting was performed with the DWF fixed at the appropriate value, and EXAFS fitting was only performed on the first coordination shell of Cu-O. The  $k^2$ -weighted data in R-space was fit by least-squares optimization to provide coordination numbers (CN) and interatomic bond distances. The EXAFS

data was fit over  $k = 2.7$  to  $8.5 \text{ \AA}^{-1}$ , incorporating as much data at high  $k$  values as possible.

### Operando XAS

Operando experiments were performed in a special glassy carbon tube reactor, and the details of the custom *operando* XAS reactor setup were described by Kispersky et al. [87]. During these experiments, XAS spectra were simultaneously collected while measuring the reaction rates for each sample to ensure that the standard SCR rate per mole Cu measured at APS were quantitatively the same, within error, to that measured in laboratory differential plug-flow reactors (PFR). Figure 7.27 shows standard SCR reaction rates measured on a representative sample (Cu-CHA-19) in the laboratory PFR and *operando* XAS reactor over a temperature range (450-480 K), indicating that rates are reproduced in the two reactor setups to within 10%. Table 7.5 shows that standard SCR reaction rates for catalyst samples in the *operando* reactor described above are within 10% of those measured in a separate plug flow reactor, thus establishing kinetic equivalence of the two reactors.

In *operando* experiments, 7-13 mg of Cu-CHA-15, 30 mg of Cu-CHA-20, or 25 mg of Cu-CHA samples (sieved to 125-250  $\mu\text{m}$ ) were loaded in the *operando* reactor to maintain differential conditions ( $< 20\%$  conversion). Gases were mixed and introduced into the reactor in a precise manner to avoid any side reactions. De-ionized  $\text{H}_2\text{O}$  was introduced into the feed stream by flowing He carrier gas through a heated shell type humidifier (Perma Pure MH-Series). All gas lines downstream of the humidifier were heated to above 373 K to prevent  $\text{H}_2\text{O}$  condensation. After introducing  $\text{H}_2\text{O}$ , NO (300 ppm in  $\text{N}_2$ , Matheson Tri-Gas) was introduced into the gas stream, followed by the introduction of  $\text{O}_2$  (20% in He, Airgas, Inc.). The reaction mixture was then preheated to 473 K. Ammonia (300 ppm in He, Airgas, Inc.) was introduced through a 1/16" stainless steel line that was located immediately upstream of the catalyst bed to minimize the possibility of gas-phase side reactions. Gas concentrations were measured using a MKS Multi-Gas 2030 gas analyzer FTIR with a cell temperature

of 464 K and based on factory provided calibration files. Standard SCR conditions of 300 ppm NO, 300 ppm NH<sub>3</sub>, 10% O<sub>2</sub>, 2% H<sub>2</sub>O, 5% CO<sub>2</sub>, a total flow rate of 1000-1200 mL min<sup>-1</sup> and a temperature of 463-473 K was used for all steady state experiments. Steady state spectra were collected in the quick scan mode with an edge step of 0.5 eV, a dwell time of 0.05 s at each step and an energy range between 8700 and 9700 eV, with each spectrum taking 2-3 min to acquire. Steady state data were averaged over 3-5 scans depending on the data quality obtained under different experimental conditions. Linear combination XANES fits to determine the Cu<sup>I</sup> and Cu<sup>II</sup> fractions under *operando* conditions were carried out using the appropriate references, as explained in our previous publications [37,85,87].

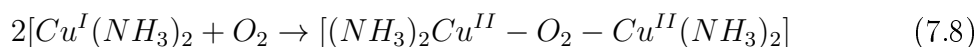
### Transient XAS

Transient O<sub>2</sub> and NO<sub>2</sub> oxidation experiments were carried out in the same flow reactor setup as used for *operando* experiments. Reduction with 300 ppm NO and 300 ppm NH<sub>3</sub> under a total flow of 1200 mL min<sup>-1</sup> at approximately 447 K gave 90±5, 90±5 and 98±5 % Cu<sup>I</sup>, for Cu-CHA-15, Cu-CHA-20, and Cu-CHA-29 samples, respectively. Following the reduction to Cu<sup>I</sup>, samples were exposed to either 10% O<sub>2</sub> or 100 ppm NO<sub>2</sub> at the same temperature in separate experiments. The Cu<sup>I</sup> and Cu<sup>II</sup> fractions during these transient experiments were followed by collecting XANES spectra (Figures 7.13-7.15) in quick scan mode from 8800 to 9400 eV. Each spectrum took 21 s to acquire with a step size of 0.5 eV and a dwell time of 0.03 s. Higher quality spectra were collected at the end of these transients by increasing the dwell time from 0.03 s to 0.05 s. Linear combination XANES fits to determine the Cu<sup>I</sup> and Cu<sup>II</sup> fractions from spectra collected during transient experiments were performed using the same procedure to fit spectra collected during *operando* XAS experiments. The fitted Cu<sup>I</sup> fraction before and at the end of O<sub>2</sub> and NO<sub>2</sub> oxidation transients are tabulated in Tables 7.6-7.8.

#### 7.8.4 Kinetic models for the transient oxidation experiments

##### O<sub>2</sub> oxidation of Cu<sup>I</sup>(NH<sub>3</sub>)<sub>2</sub>

The transient O<sub>2</sub> data in Figure 7.3 were fit to a modified pseudo-second-order rate law described below. The approximate second-order behavior can be rationalized by postulating that the following termolecular reaction describes the oxidation of two Cu<sup>I</sup> diamine complexes with O<sub>2</sub>:



If this step were elementary and all sites behaved identically, the following rate law would describe the rate of consumption of Cu<sup>I</sup> species:

$$\frac{d[\text{Cu}^I](t)}{dt} = -2k_a([\text{Cu}^I](t))^2[\text{O}_2] \quad (7.9)$$

Because O<sub>2</sub> is in stoichiometric excess during these transient experiments, its concentration can be subsumed into k<sub>a</sub> and the above expression can be rewritten as:

$$\frac{d[\text{Cu}^I](t)}{dt} = -2k([\text{Cu}^I](t))^2 \quad (7.10)$$

where k is a pseudo-second-order rate constant. To correct for the unoxidizable, recalcitrant fraction of Cu<sup>I</sup> (defined as [Cu<sup>I</sup>]<sub>∞</sub>) in the transient O<sub>2</sub> experiments (Figure 7.3), we introduce the transformation:

$$[\text{Cu}^I]_{\text{corr}}(t) = [\text{Cu}^I](t) - [\text{Cu}^I]_{\infty} \quad \frac{d[\text{Cu}^I]_{\text{corr}}(t)}{dt} = -2k([\text{Cu}^I]_{\text{corr}}(t))^2 \quad (7.11)$$

[Cu<sup>I</sup>]<sub>corr</sub>(t) is defined as the concentration of oxidizable Cu<sup>I</sup> (by O<sub>2</sub>) as a function of time during the transient O<sub>2</sub> experiment. Integrating from 0 to t and rearranging:

$$\text{Cu}^I \text{ Fraction} = \frac{[\text{Cu}^I](t)}{[\text{Cu}^I]_0} = \frac{1 - [\text{Cu}^I]_{\infty}/[\text{Cu}^I]_0}{1 + 2kt([\text{Cu}^I]_0 - [\text{Cu}^I]_{\infty})} + \frac{[\text{Cu}^I]_{\infty}}{[\text{Cu}^I]_0} \quad (7.12)$$

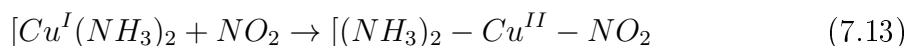
where Cu<sup>I</sup> Fraction is the time-dependent Cu<sup>I</sup> concentration divided by the initial Cu<sup>I</sup> concentration ([Cu<sup>I</sup>]<sub>0</sub>). The parameters in Eqn. 7.12 are k and [Cu<sup>I</sup>]<sub>∞</sub>. For each data series, we set [Cu<sup>I</sup>]<sub>∞</sub> to the last (longest time) Cu<sup>I</sup> Fraction data point, and used nonlinear least-squares regression to obtain the best-fit parameter of k. Results are summarized below:



|  | Cu-CHA-29 | Cu-CHA-20 | Cu-CHA-15 |
|--|-----------|-----------|-----------|
| $k [10^{-4} \text{ m}^3 (\text{mol Cu s})^{-1}]$ | 1.1       | 1.7       | 8.2       |
| $[\text{Cu}^I]_{\infty}/[\text{Cu}^I]_0$         | 0.26      | 0.10      | 0.05      |
| $R^2$  | 0.99      | 0.98      | 0.99      |

### NO<sub>2</sub> oxidation of Cu<sup>I</sup>(NH<sub>3</sub>)<sub>2</sub>

The transient NO<sub>2</sub> data in Figure 7.20 were fit to a pseudo-first-order rate law described below. The first-order behavior can be rationalized if we postulate that the observed oxidation kinetics are governed by the bimolecular reaction of a single Cu<sup>I</sup> diamine with NO<sub>2</sub>:



If this reaction is elementary, then the rate law that describes the rate of consumption of Cu<sup>I</sup> species is:

$$\frac{d[\text{Cu}^I](t)}{dt} = -k_a([\text{Cu}^I](t))[\text{NO}_2] \quad (7.14)$$

Because NO<sub>2</sub> is in stoichiometric excess during these transient experiments, its concentration can be subsumed into  $k_a$  and the above expression rewritten as:

$$\frac{d[\text{Cu}^I](t)}{dt} = -k([\text{Cu}^I](t)) \quad (7.15)$$

Upon integration and rearranging, the above expression becomes:

$$\text{Cu}^I \text{ Fraction} = \frac{[\text{Cu}^I](t)}{[\text{Cu}^I]_0} = e^{-kt} \quad (7.16)$$

where Cu<sup>I</sup> Fraction and [Cu<sup>I</sup>](t) and [Cu<sup>I</sup>]<sub>0</sub> are defined in the same way as reported in the previous subsection. The only unknown parameter in Eqn. 7.15 is k. Nonlinear least-squares regression was used to obtain the best-fit k value from the data in Figure 7.20. The results are summarized below:

|                              | Cu-CHA-29 | Cu-CHA-20 | Cu-CHA-15 |
|------------------------------|-----------|-----------|-----------|
| $k [10^{-2} \text{ s}^{-1}]$ | 2.6       | 2.8       | 3.0       |
| $R^2$                        | 0.98      | 0.98      | 0.89      |

### 7.8.5 DFT Methods

To construct the energy landscape for Cu diffusion through an 8-MR and reaction with  $\text{O}_2$  we calculated the energies of structures for A through E in Figure 7.4 using the following protocol.

Due to the dynamic and mobile nature of solvated Cu species in the zeolite cage, we used AIMD on all structures to seek low energy configurations. A 12 T-site supercell containing two Al atoms was used for Fig. 7.4 structures C and D, such that each Cu charge compensates 1Al. For Fig. 7.4 structure A, the 12 T-site supercell was doubled to create a 24 T-site supercell, so that each  $\text{Cu}^I(\text{NH}_3)_2$  can occupy one CHA cage. Multiple initial structures were guessed, and each geometry was sampled by Born-Oppenheimer molecular dynamics in the canonical ensemble (NVT) using the Car-Parrinello Molecular Dynamics (CPMD) software version 3.17.1 [443]. We used the Perdew-Becke-Erzenhof (PBE) [444] flavor of the generalized gradient approximation (GGA) exchange-correlation functionals and Vanderbilt ultrasoft pseudopotentials [392], and a plane wave cutoff of 30 Ry. The first Brillouin zone was sampled at the  $\Gamma$  point only for this insulator, and a Nose-Hoover thermostat was used to achieve the target temperature of 473 K. A 0.6 fs time step was used for a total sampling time of 150 ps, for each of structures A, C and D in Figure 7.4. Structures B and E came from guessing product structures for the Climbing Image Nudged Elastic Band (CI-NEB) calculations described below and were not sampled by AIMD.

Next, for structures A, C, and D, we selected several (3 to 4) low energy structures from the 150 ps of AIMD trajectories and performed electronic energy optimizations using the Vienna Ab initio Simulation Package (VASP) version 5.4.1 [395] and the same supercell. Periodic DFT calculations were performed using the projector aug-

mented wave (PAW) method with the PBE functional [444] and a 400 eV plane wave cutoff, and DFT-D2 [445] to calculate van der Waals dispersion energies. Electronic energies were converged self-consistently to less than  $10^{-8}$  eV, and forces to less than 0.01 eV/Å, on each atom. For the above calculations, PBE POTCARs for each atom were used. We performed spin-polarized calculations for Cu dimers to sample both the singlet and triplet state of the dimers. The lower energy structure was chosen and plotted on Figure 7.4 and reported in Table 7.10. Structures A, B, D and E are in singlet states and structure C is in triplet state.

Transition states (A to B, and D to E) were computed using the Climbing Image Nudged Elastic Band (CI-NEB) method [446] and the same functional and plane wave cutoff described above. Convergence criteria were tightened to less than  $10^{-8}$  eV for electronic energy and less than 0.01 eV/Å for force on each atom. The transition state from C to D is spin forbidden and was not computed here; we estimated the effective barrier from the literature as reported in Figure 7.4.

We followed a similar protocol for reactions of one  $\text{Cu}^I(\text{NH}_3)_2$  with  $\text{O}_2$  and  $\text{NO}_2$ . We first performed 150 ps of AIMD for  $\text{O}_2$  and  $\text{NO}_2$  adsorption on  $\text{Cu}^I(\text{NH}_3)_2$ , using a 12 T-site supercell with 1 Al, and with the CPMD software. Low energy structures were then selected and optimized (spin polarized) with both PBE/DFT-D2 and the hybrid screened-exchange Heyd-Scuseria-Ernzerhof (HSE06) functionals [400] with the Tkatchenko Scheffier method (TSvdW) [402] to correct for dispersion interactions. We performed these additional HSE06-TSvdw calculations because hybrid functionals have been shown to predict  $\text{NO}_x$  adsorption energies more accurately than GGA functionals [218]. Figure 7.19 and Table 7.10 reports the structures and adsorption energies.

### 7.8.6 NO titrations to probe reaction stoichiometry

The consumption of NO (per Cu) in sequential SCR reaction steps on Cu-CHA zeolites was measured and used to corroborate the reaction stoichiometry depicted in Figure 7.6. Typically, 10 to 20 mg of sample was loaded into the reactor system used

to measure steady-state SCR kinetics. The total gas flow rate used in the following procedure was 600 mL min<sup>-1</sup>. The samples in Figure 7.3 were first oxidized and dehydrated to their Cu<sup>II</sup> form [79] by treatment to 823 K (0.167 K s<sup>-1</sup>) in flowing 20% O<sub>2</sub> (99.5%, Indiana Oxygen) in balance He (99.999%, Indiana Oxygen), and then cooling to 473 K. The sample was then held flowing He for 30 minutes, and then fully reduced in a mixture of 300 ppm NO (3.5% NO in Ar, Praxair) and 300 ppm NH<sub>3</sub> (3.0% NH<sub>3</sub> in Ar, Praxair) in balance He. Following reduction of Cu sites to their Cu<sup>I</sup>(NH<sub>3</sub>)<sub>2</sub> states (corresponding to 6 o'clock positions in Figure 7.6), the samples were exposed to flowing 10% O<sub>2</sub> in balance He until steady-state was achieved (corresponding to the central position in Figure 7.6). The O<sub>2</sub> oxidized sample was then held in a flowing stream of 300 ppm of NO in balance He, until steady-state was achieved. Finally, 300 ppm NH<sub>3</sub> was introduced to the flow of NO in balance He, to reduce the sample back to Cu<sup>I</sup>(NH<sub>3</sub>)<sub>2</sub> (corresponding to 6 o'clock positions in Figure 7.6). Each of these sequential treatments was also performed in a blank reactor to measure a baseline signal in the FTIR spectrometer (MKS Multigas TM 2030) used to account for gas holdup and residence time in the reactor setup (NO conversion was not detected in the blank reactor), in order to calculate the NO consumption from the Cu-CHA catalyst during each treatment step (Figure 7.19).

Summarizing, after O<sub>2</sub> oxidation of Cu<sup>I</sup>(NH<sub>3</sub>)<sub>2</sub> to form a NH<sub>3</sub>-solvated Cu<sup>II</sup> dimer (central position in Figure 7.6), the two-step procedure described above exposes the catalyst to NO alone, and then to NO and NH<sub>3</sub> together. Exposure of NO in the step immediately following O<sub>2</sub>-assisted oxidation results in the consumption of one NO equivalent (NO:Cu = 0.98 ± 0.10) per Cu site. Once steady-state is achieved, the sequential addition of NH<sub>3</sub> to the flowing stream (already containing NO) consumes another equivalent of NO per Cu site (NO:Cu = 1.07 ± 0.11) and fully reduces the sample to Cu<sup>I</sup>(NH<sub>3</sub>)<sub>2</sub> (6 o'clock positions in Figure 7.6), which closes the catalytic cycle. The 2:1 NO:Cu consumption ratio is consistent with Figure 7.6. Starting from the Cu-oxo dimer in the center of the Figure 7.6, two NO molecules per Cu

are required to return to the 6 o'clock position in each cycle corresponding to the formation of  $\text{Cu}^I(\text{NH}_3)_2$  species.

### 7.8.7 Random Distribution of Cu per Cage

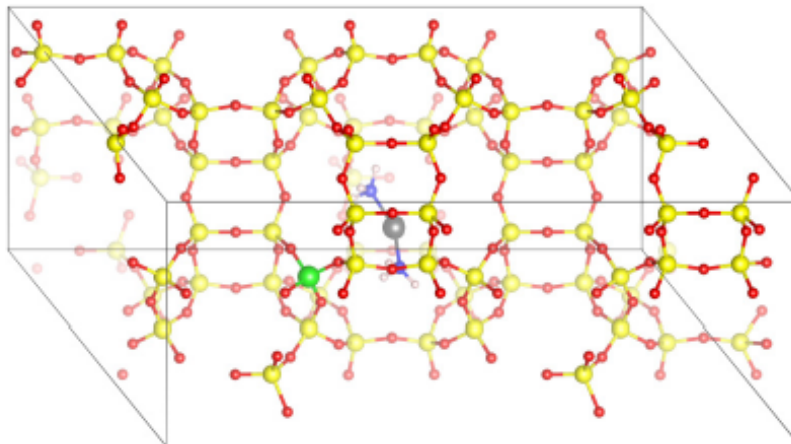
To eliminate the possibility that the oxidizable fraction of  $\text{Cu}^I$  corresponds to Cu pairs or larger aggregates that, by random chance, are present in the same cage and not from pairs formed from mobile  $\text{Cu}^I$  ions, we estimated the fraction of persistent pairs that would be present assuming that Cu are randomly distributed among cages. Results are compared with the observed fraction of oxidizable  $\text{Cu}^I$  in Figure 7.22. For Cu densities corresponding to the zeolites studied in Figure 7.3, this “immobile Cu dimer” model predicts values that are much smaller than the  $[\text{Cu}^I]_\infty$  values observed experimentally and predicted from the non-mean-field model described in 7.8.10:

$$\begin{aligned}
 \text{Cu} - \text{CHA} - 15 : \text{OxidizableCuFraction} &= 0.072; [\text{Cu}^I]_\infty / [\text{Cu}^I]_0 = 0.928 \\
 \text{Cu} - \text{CHA} - 20 : \text{OxidizableCuFraction} &= 0.012; [\text{Cu}^I]_\infty / [\text{Cu}^I]_0 = 0.988 \\
 \text{Cu} - \text{CHA} - 29 : \text{OxidizableCuFraction} &= 0.002; [\text{Cu}^I]_\infty / [\text{Cu}^I]_0 = 0.998 \quad (7.17)
 \end{aligned}$$

### 7.8.8 Metadynamics

We used metadynamics to compute the free energy landscape for a  $\text{Cu}^I(\text{NH}_3)_2$  to diffuse away from a charge-compensating Al center into an adjacent cage. To avoid interaction between periodic cells, a CHA supercell with 72 T-sites was adopted. The 72-T-site supercell (pictured below) was generated by propagating the 36 T-site CHA-silica supercell obtained from the database of zeolite structures [1] along one direction. A T-site silicon is replaced by aluminum and a  $\text{Cu}^I(\text{NH}_3)_2$  complex was inserted into a cage near the Al to create the initial  $\text{Cu}^I(\text{NH}_3)_2$  structure.

Figure 7.7. 72-T site supercell for metadynamics simulation. Color code for different elements in superimposed figure: gray=Cu, green=Al, yellow=Si, red=O, blue=N and white=H.



All calculations were performed in the CPMD program [443]. 6 ps of NVT molecular dynamics were run to pre-equilibrate the system. The NVT MD simulation was initiated by quenching the system to the non-spin-polarized Born-Oppenheimer potential surface with the Perdew-Becke-Erzenhof generalized gradient approximation (GGA) exchange-correlation functional [444] and ultrasoft pseudopotentials [392]. Plane waves were included up to 30 Rydberg and the Brillouin zone sampled at the  $\Gamma$  point. Self-consistent-field (SCF) electronic energies were converged to  $1 \times 10^{-7}$  Ha. The converged wavefunction was subsequently used to perform Car-Parrinello molecular dynamics [443] (CPMD) at 473 K with a time step of 0.12 fs. A Nose-Hoover thermostat was used for both ions and electrons. The electronic temperature was set to 0.02 K with frequency  $10000 \text{ cm}^{-1}$ . The fictitious electron mass was set to 400 atomic unit.

The pre-equilibrated structure, wavefunction, atomic velocities and thermostat were used for the subsequent metadynamics [447,448] simulation with a total simulation time of 12.5 ps. The time step and thermostat setting were the same as those in

the MD simulation. The collective variable was chosen to be the Cu-Al coordination number (CN), defined as:

$$CN = \frac{1 - (\frac{d_{ij}}{d_0})^p}{1 - (\frac{d_{ij}}{d_0})^{p+q}} \quad (7.18)$$

where  $d_{ij}$  is defined as distance between Al and Cu and  $p$  and  $q$  are arbitrary scaling constants. Values of other parameters are summarized in Table 7.11.  $d_0$  was chosen as largest Cu-Al separation distance observed in the regular NVT MD simulation at 473 K. The  $k$  and  $\mu$  were chosen such that the Lagrangian collective variable  $s$  and the physical collective variable  $S$  stay close, and that  $S$  fluctuates frequently at each position in the configuration space.

### 7.8.9 Electrostatics

We estimated the electrostatic interaction between a  $\text{Cu}^I$  ion and its charge-compensating Al center using Coulomb's Law. We assumed Cu and Al to be elementary positive and negative point charges, respectively, carrying the same electric charge as a proton,  $1.6 \times 10^{-19}$  C, and we used the computed dielectric constant of CHA-zeolite ( $\epsilon_r$ ), 2.7, reported by Rybicki and Sauer [449]. The equilibrium Cu-Al distance of 4.6 Å taken from the DFT-optimized  $\text{Cu}^I(\text{NH}_3)_2$  structure was used as the initial Cu-Al distance in the calculation. The energy of ionic separation of  $\text{Cu}^I$  and framework Al from 4.6 Å to  $r$  was calculated following Coulomb's law:

$$F = \frac{k_e q_{\text{Cu}} q_{\text{Al}}}{\epsilon_r r^2} \quad (7.19)$$

$$\Delta E = N_a \int_{4.6\text{\AA}}^r F dr^* \quad (7.20)$$

where  $k_e$  is the electric force constant in vacuum,  $N_a$  is the Avogadro constant,  $\epsilon_r$  is dielectric constant of CHA-zeolite,  $q_{\text{Cu}}$  and  $q_{\text{Al}}$  are Cu and Al charges, and  $r$  is the Cu-Al distance.

The computed Coulombic potential as a function of Cu-Al distance was plotted and compared with the metadynamics-computed free energy profile in Figure 7.5. The Coulombic potential and the computed free energy are similar up to 7 Å, consistent

with electrostatics dominating the interaction. The computed free energy is slightly more positive than the Coulombic potential for Cu-Al distance between 7 Å and 8 Å, highlighting the activation barrier for  $\text{Cu}^I(\text{NH}_3)_2$  to travel through an 8-member-ring window to a neighboring CHA cage, which is not captured by the Coulombic model. The computed free energy falls after  $\text{Cu}^I(\text{NH}_3)_2$  reaches the new cage and stays relatively invariant thereafter. The Coulombic potential continues to increase rapidly and surpasses the computed free energy above 8 Å. Such difference can be rationalized by many-body long range Coulombic interaction between  $\text{Cu}^I(\text{NH}_3)_2$  and framework Al in periodic images in the metadynamics simulation, which intrinsically lower the computed free energy compared to a two-point-charge Coulombic model.

#### 7.8.10 Stochastic Simulation

Here, we estimate the fraction of  $\text{Cu}^I$  able to form an oxo-bridged dimer (Figure 7.4), given a density of Cu and Al atoms in a CHA zeolite and a maximum distance that each Cu can diffuse from its charge compensating Al. Cu number densities between  $7 \times 10^{-4}$  and 0.99 Cu/1000 Å<sup>3</sup> and Cu-Al diffusion distances (represented by the green spheres in Figure 7.3) from 5-12.5 Å were modeled (Figure 7.23); procedural details are described below.

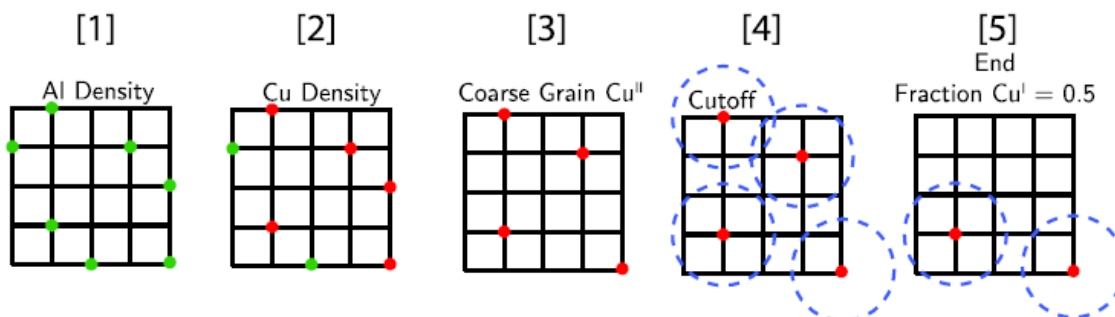
We use a 1536 T-site CHA periodic supercell [1] with a total volume of  $1.0172 \times 10^5$  Å<sup>3</sup>. The large cell size was used to avoid bias due to an even or odd number of exchanged Cu present at smaller cell sizes and long Cu diffusion distances. We performed stochastic simulations as a function of Si/Al (spanning 2 to 511), Cu/Al (0.0059 to 1), and a maximum Cu diffusion distance of 12.5 Å from the compensating framework Al atom.

A 2D schematic representation of the simulation scheme is shown below; the actual simulation was carried out on the 3D CHA lattice described above. In step [1], CHA T-sites were randomly populated with Al avoiding any Al-Al first-nearest-neighbors (Loewenstein's rule) [235]. In step [2], we associated Cu ions with these Al, obeying the previously validated rule [79] that 2Al 6MR sites first exchange  $\text{Cu}^{II}$



before remaining 1Al sites exchange  $\text{Cu}^{\text{II}}\text{OH}$ . Three types of Al exist at this point: those that are not associated with a Cu ion, those that compensate a  $\text{Cu}^{\text{II}}\text{OH}$ , and 2Al 6MR sites that share a  $\text{Cu}^{\text{II}}$ . In step [3], we delete from the lattice the Cu-free Al sites and one member of every Al pair that compensate a  $\text{Cu}^{\text{II}}$  ion. In step [4], we created an Al-Al neighbor list, including only neighbors that are within twice the prescribed Cu diffusion radius. In step [5], we then deleted overlapping pairs at random from the neighbor list, stopping when the number of available pairs vanishes. We recorded the number of remaining entries divided by the initial number of Cu as the  $\text{Cu}^{\text{I}}$  fraction. The simulation was then repeated until the average  $\text{Cu}^{\text{I}}$  fraction converged.

As we explored different Si/Al and Cu/Al ratios, we discovered that results were sensitive to total initial  $\text{Cu}^{\text{I}}$  density and insensitive to the underlying Si/Al and Cu/Al ratios. Results are shown in Figure 7.23, plotted as final  $\text{Cu}^{\text{I}}$  fraction vs initial  $\text{Cu}^{\text{I}}$  density, for a range of diffusion distances. Simulation results are of course discrete; for visual convenience we present the data using cubic spline interpolation. A diffusion distance of 9 Å, consistent with predictions from the metadynamics simulation (Figure 7.5), predicts final  $\text{Cu}^{\text{I}}$  fractions in close agreement with experimental observation (Figure 7.3).



To provide a visual representation of the simulation results, we took a snapshot of steps [3] and [5] for one simulation iteration at the initial Cu densities for the Cu-CHA zeolites represented in Figure 7.3. Cartesian coordinates of Al charge compensated by Cu were extracted from the stochastic simulations and green spheres 9 Å in radius

were plotted, representing the maximum diffusion length of each  $\text{Cu}^I(\text{NH}_3)_2$  (Figure 7.3,  $t=0$ ). Spheres are translucent so that overlapping spheres are easily visualized and periodic boundary conditions used to show the diffusion range of Cu across the supercell boundaries. Intersecting spheres around Cu coordinates were plotted both before step [3] and after step [5] pairing to show the geometrically isolated Cu (Iso) and statistically isolated “musical chairs” Cu (MC).

Figure 7.8. X-Ray diffraction patterns of H-SSZ-13 zeolites with Si/Al = 4.5 (blue), Si/Al = 15 (red), and Si/Al = 25 (black), measured using a Cu  $K\alpha$  source ( $\lambda = 0.154$  nm). Diffraction patterns are vertically offset for clarity. Cu-exchanged forms of these materials show equivalent XRD patterns [450].

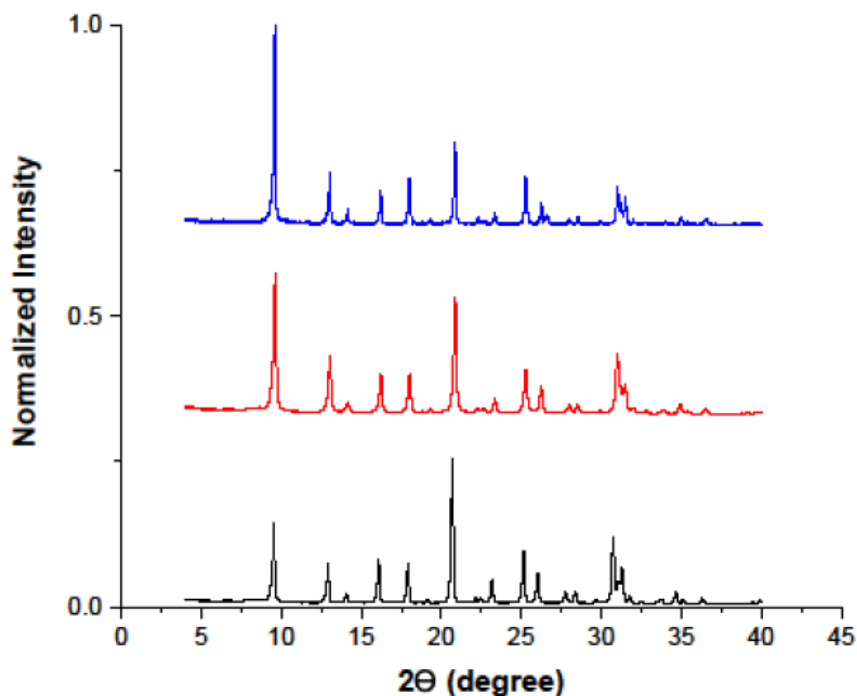


Figure 7.9. Ar adsorption isotherms on H-SSZ-13 with Si/Al = 4.5 (blue), Si/Al = 15 (red), and Si/Al = 25 (black). Isotherms are vertically offset for clarity (Si/Al=15: by 200 cm<sup>3</sup> g<sup>-1</sup>, Si/Al=25: by 400 cm<sup>3</sup> g<sup>-1</sup>). Cu-exchanged forms of these materials show similar adsorption isotherms, with slight decreases in micropore volumes caused by the presence of Cu [450].

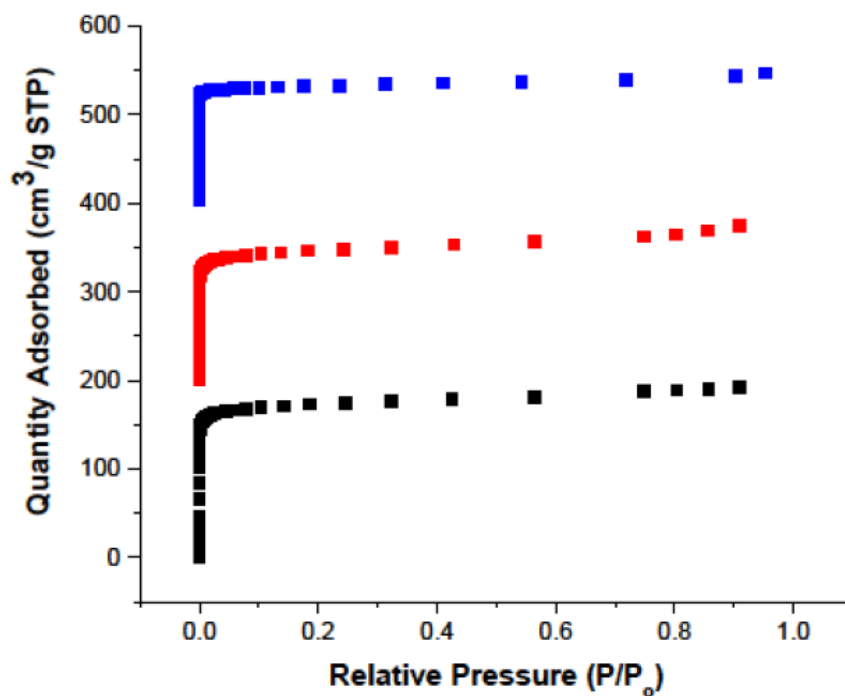


Figure 7.10. XANES spectra for Cu-CHA-20 (red) and Cu-CHA-29 (green) at ambient conditions, and for bulk Cu<sup>II</sup>O (pink).

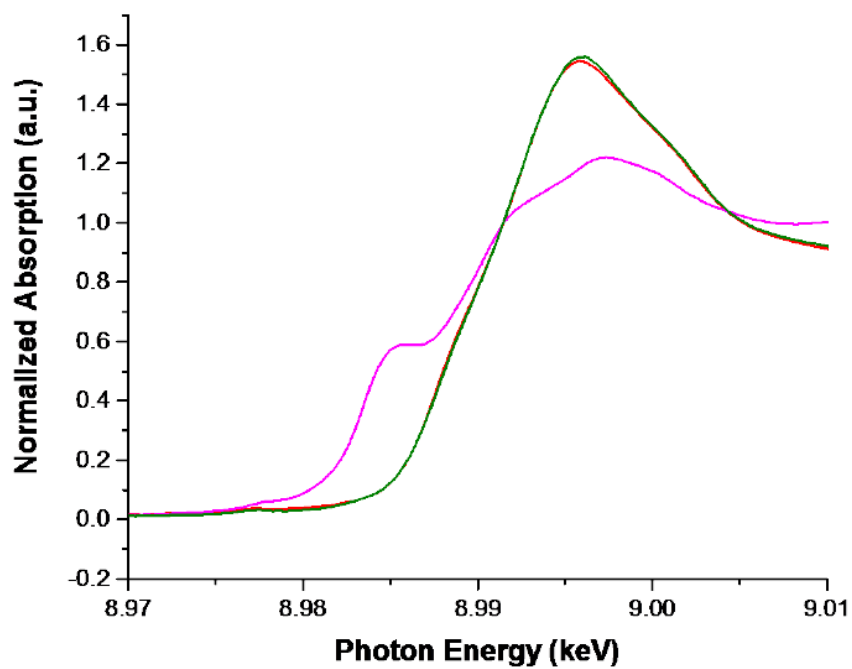


Figure 7.11. UV-Vis spectra for Cu-CHA-15 (blue), Cu-CHA-20 (black), and Cu-CHA-29 samples (red) recorded at ambient conditions.

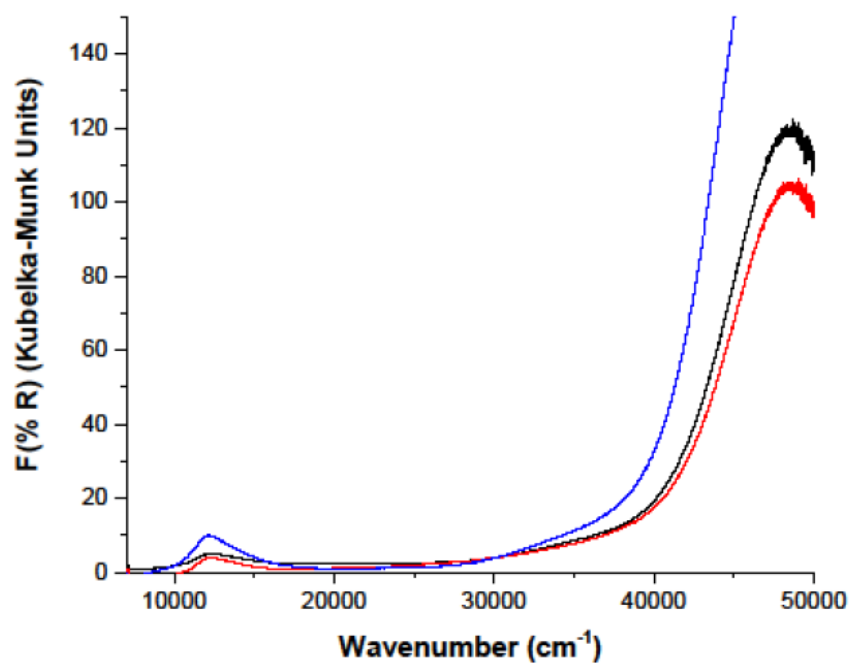


Figure 7.12. Operando XANES spectra of Cu-CHA-15 (red) and Cu-CHA-29 (dark blue) during steady-state standard SCR (300 ppm NO, 300 ppm NH<sub>3</sub>, 10% O<sub>2</sub>, 2% H<sub>2</sub>O, 5% CO<sub>2</sub>, 463-473 K). Reference spectra for aqueous Cu<sup>I</sup>(NH<sub>3</sub>)<sub>2</sub> (grey), isolated Cu<sup>I</sup> [79] (pink) and isolated Cu<sup>II</sup> (light blue) sites [79].

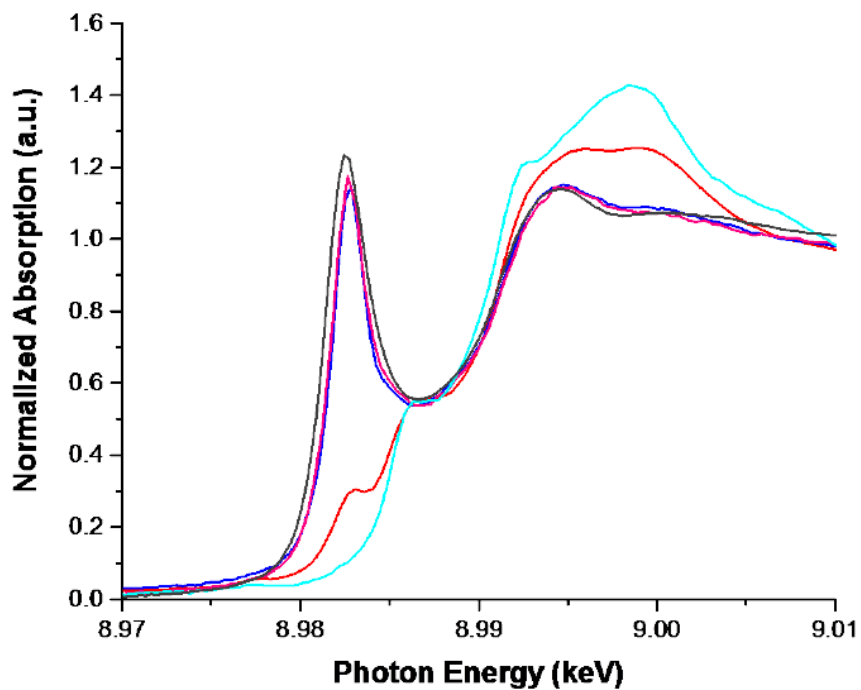


Figure 7.13. XANES spectra collected during transient oxidation of the reduced forms of Cu-CHA-29 sample with 10% O<sub>2</sub> (top) and 100 ppm NO<sub>2</sub> (bottom), as a function of time (labeled in figure).

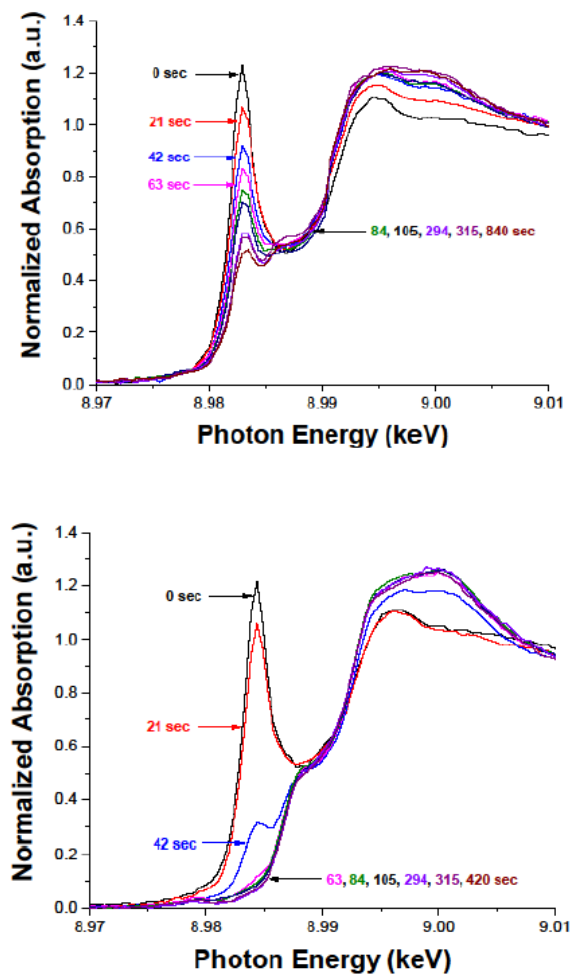


Figure 7.14. XANES spectra during transient oxidation of the reduced forms of Cu-CHA-20 sample with 10% O<sub>2</sub> (top) and 100 ppm NO<sub>2</sub> (bottom), as a function of time (labeled in figure).

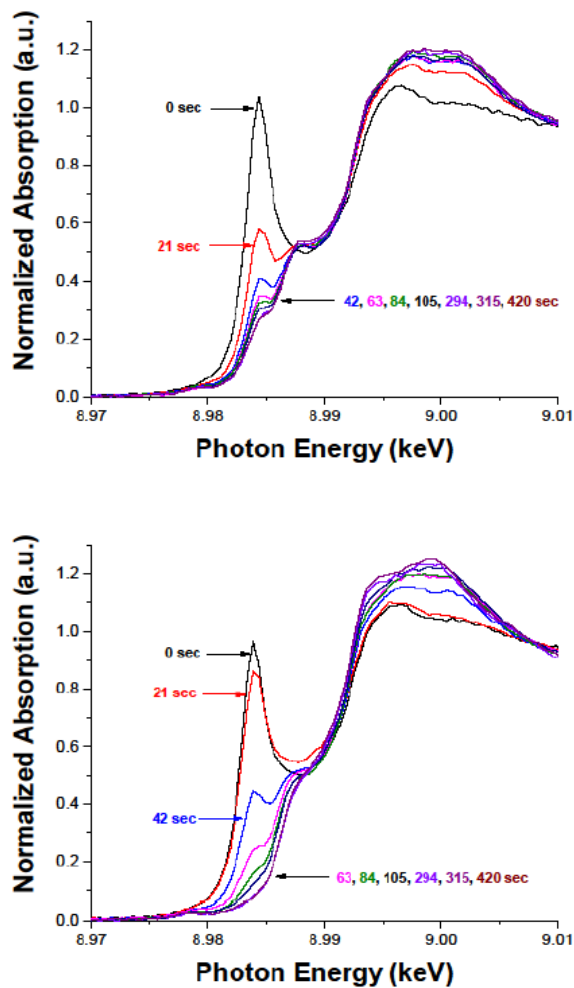




Figure 7.15. XANES spectra during transient oxidation of the reduced forms of Cu-CHA-15 sample with 10% O<sub>2</sub> (top) and 100 ppm NO<sub>2</sub> (bottom), as a function of time (labeled in figure).

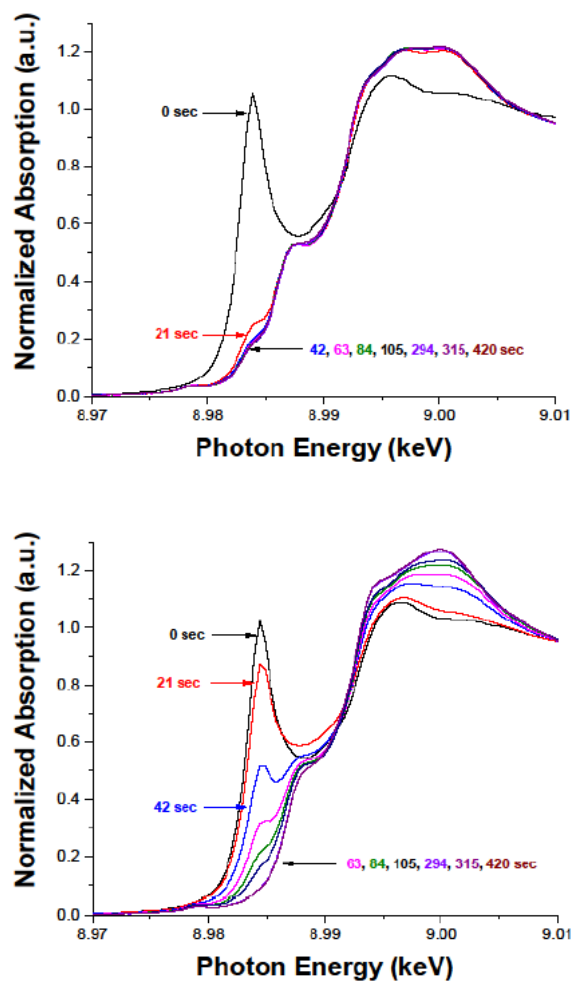


Figure 7.16. The  $k^2$  weighted Fourier transform (moduli and imaginary parts of FT on top left and top right, respectively) and raw EXAFS spectra (bottom) collected before (black) and after (red) oxidation with 10%  $O_2$  at 473 K, starting from the reduced  $Cu(I)(NH_3)_2$  state of Cu-CHA-29.

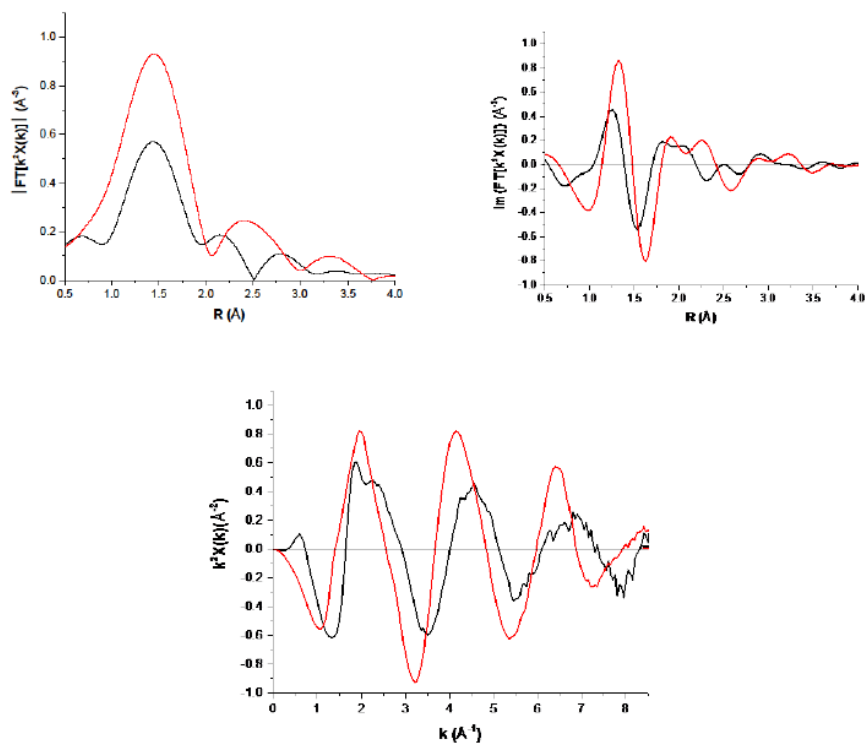


Figure 7.17. The  $k^2$  weighted Fourier transform (moduli and imaginary parts of FT on top left and top right, respectively) and raw EXAFS spectra (bottom) collected before (black) and after (red) oxidation with 10%  $O_2$  at 473 K, starting from the reduced  $Cu(I)(NH_3)_2$  state of Cu-CHA-20.

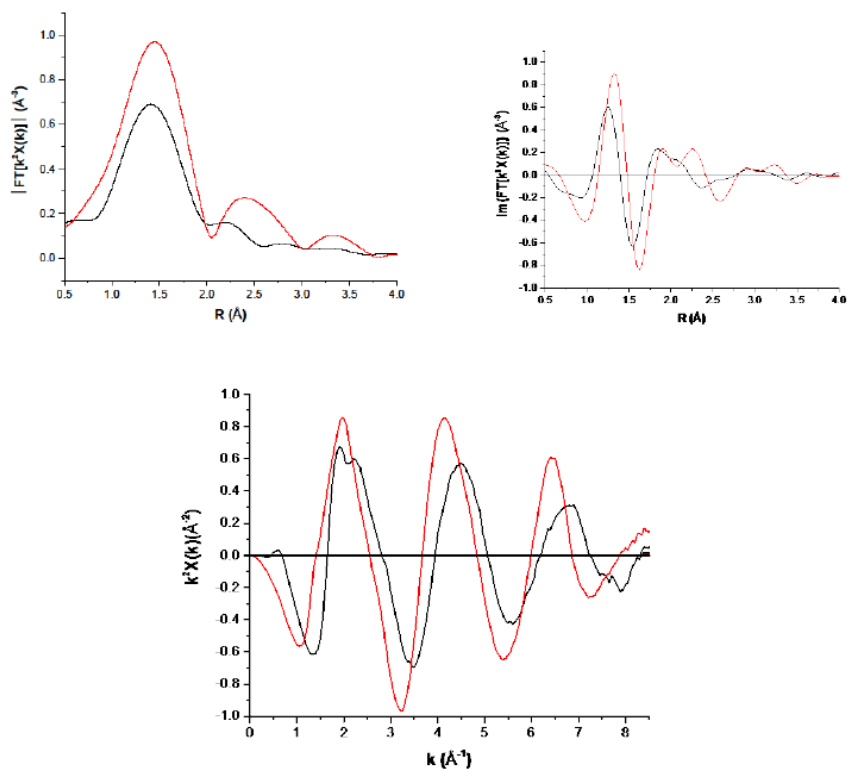


Figure 7.18. The  $k^2$  weighted Fourier transform (moduli and imaginary parts of FT on top left and top right, respectively) and raw EXAFS spectra (bottom) collected before (black) and after (red) oxidation with 10%  $O_2$  at 473 K, starting from the reduced  $Cu(I)(NH_3)_2$  state of Cu-CHA-15.

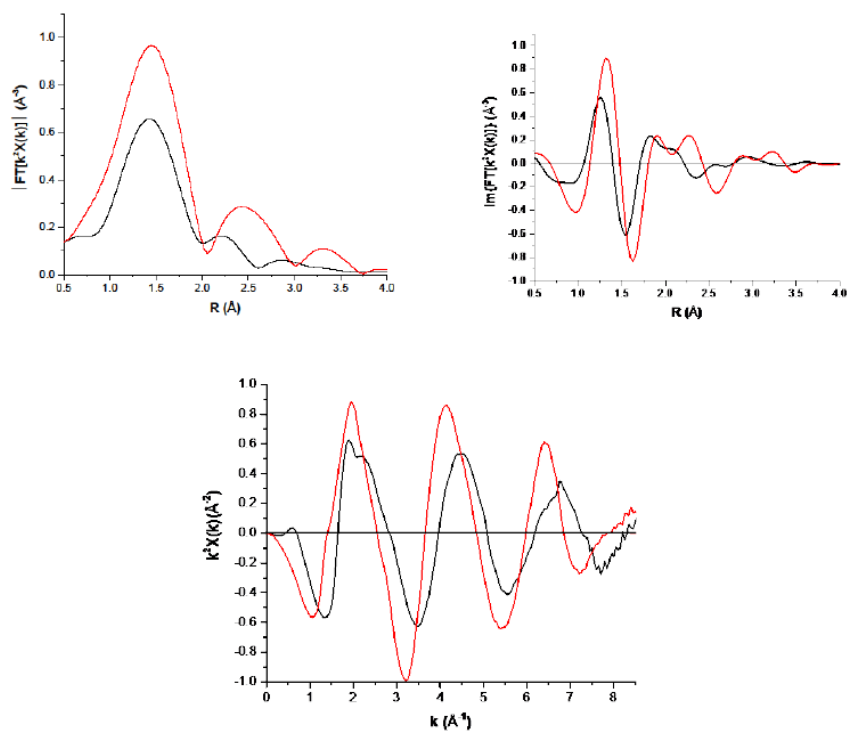


Figure 7.19. NO concentrations measured in the reactor effluent during five step-wise treatments of Cu-CHA-15, in order to quantify NO consumption (per Cu) in treatment steps 2, 4, and 5 above, which correspond to different steps in the proposed standard SCR cycle (Figure 6). Red and blue traces indicate experiments with the blank reactor and catalyst-loaded reactor, respectively.

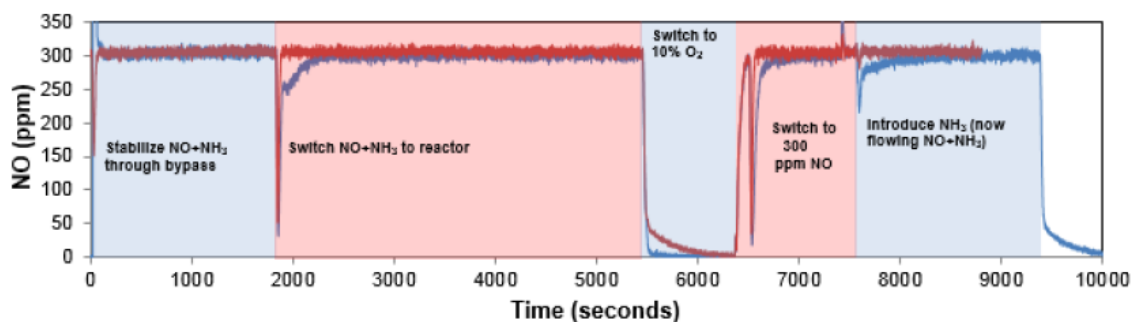


Figure 7.20. Temporal evolution of the XANES-measured  $\text{Cu}^I$  fraction in Cu-CHA-29 (A, red), Cu-CHA-20 (C, blue), and Cu-CHA-15 (H, black) during transient oxidation in 100 ppm  $\text{NO}_2$  at 473 K. Least-squares fit to Eq. 7.15 is shown by solid lines.

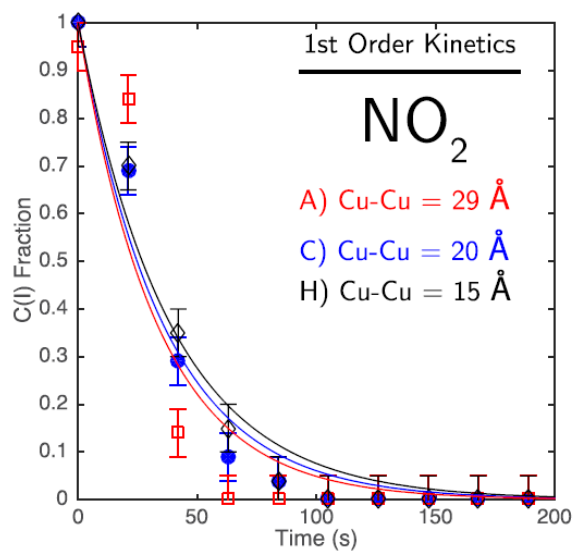


Figure 7.21. Structures for  $O_2$  configuration (A),  $O_2$  configuration (B) and  $NO_2$  (C) adsorbed on a single  $Cu^I(NH_3)_2$ . Calculations were performed in the CHA supercell described in 7.8.5, and the framework removed from this figure for clarity.

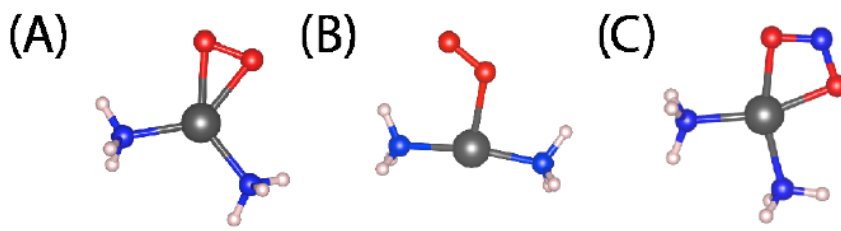


Figure 7.22. The fraction of lone Cu within zeolite cages randomly dispersed on the zeolite framework unable to oxidize compared with experimental measurements.

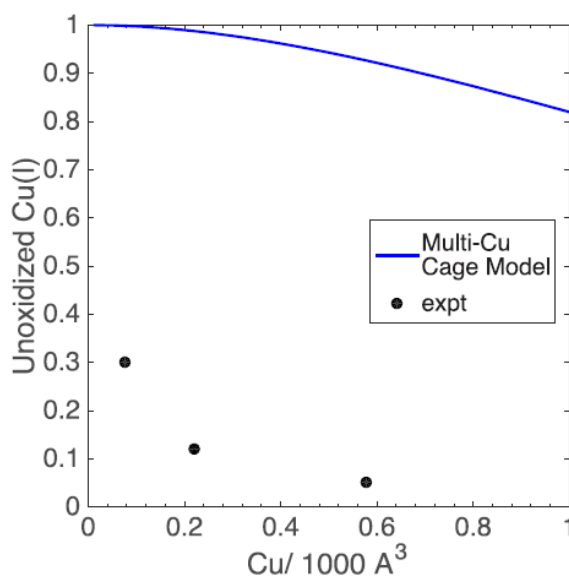


Figure 7.23. Fraction of unoxidizable  $\text{Cu}^I$  as a function of Cu density from simulation. Splines were drawn through the discrete simulations at each density to yield continuous curves in the figure. 9 Å (bold red line) represents the metadynamics-predicted maximum Cu diffusion distance. Black data points are experimental observations from Figure 7.3.

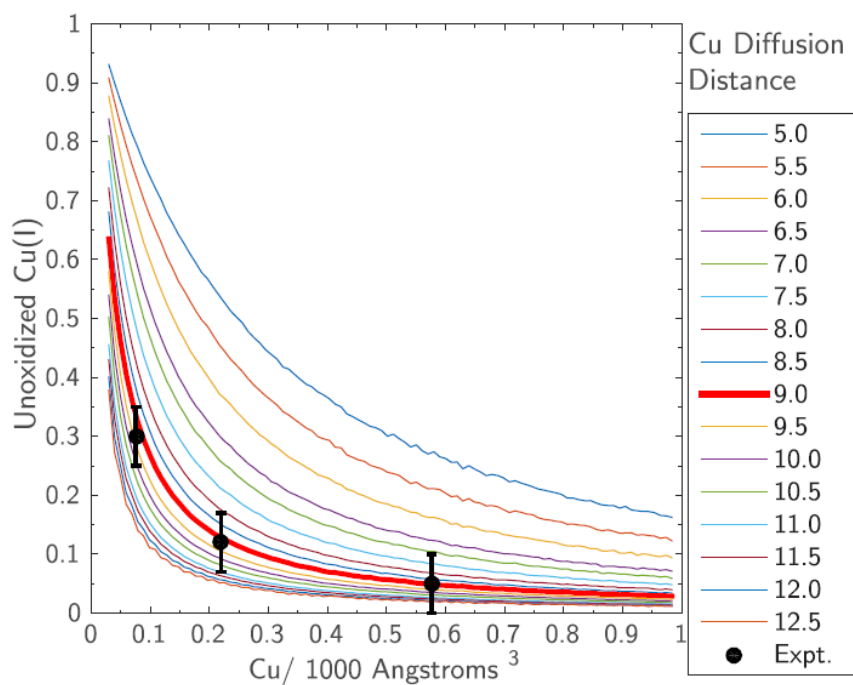


Figure 7.24. Phase diagrams for 2Al (“Z<sub>2</sub>”) exchanged Cu sites with varying  $P_{\text{NH}_3}$  and  $P_{\text{H}_2\text{O}}$  at 473 K and 10% O<sub>2</sub>. The chrome sphere demarcates  $\text{NH}_3$  and  $\text{H}_2\text{O}$  pressures equivalent to those used in the kinetic experiments reported in figure 7.1 and figure 7.2. All DFT-computed structures, energies, and methods used to generate this diagram can be found in Paolucci et al. [79].

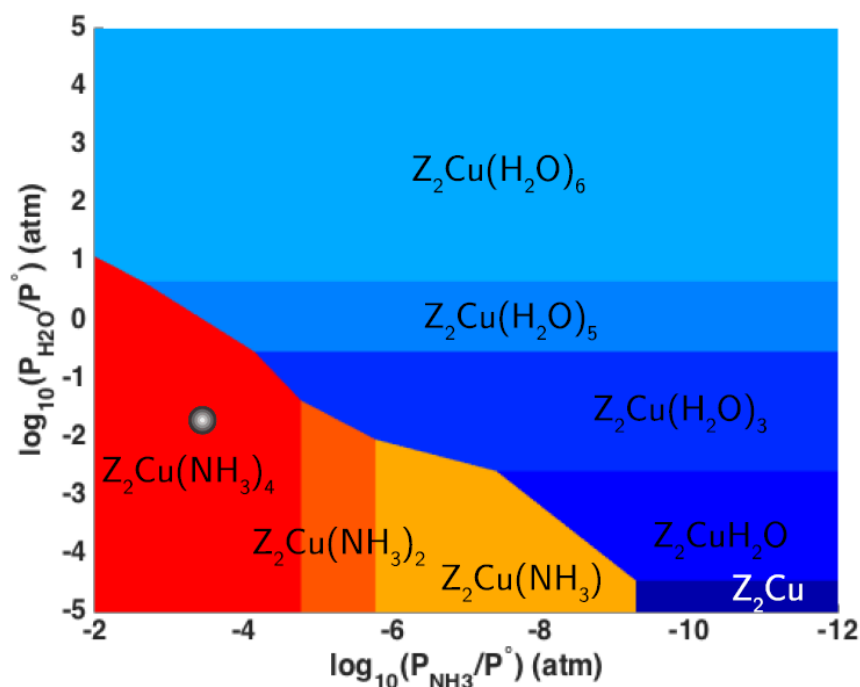




Figure 7.25. Phase diagrams for 1Al (“Z”) exchanged Cu sites with varying  $P_{\text{NH}_3}$  and  $P_{\text{H}_2\text{O}}$  at 473 K and 10%  $\text{O}_2$ . The chrome sphere demarcates  $\text{NH}_3$  and  $\text{H}_2\text{O}$  pressures equivalent to those used in the kinetic experiments reported in figure 7.1 and figure 7.2. All DFT-computed structures, energies, and methods used to generate this diagram can be found in Paolucci et al. [79].

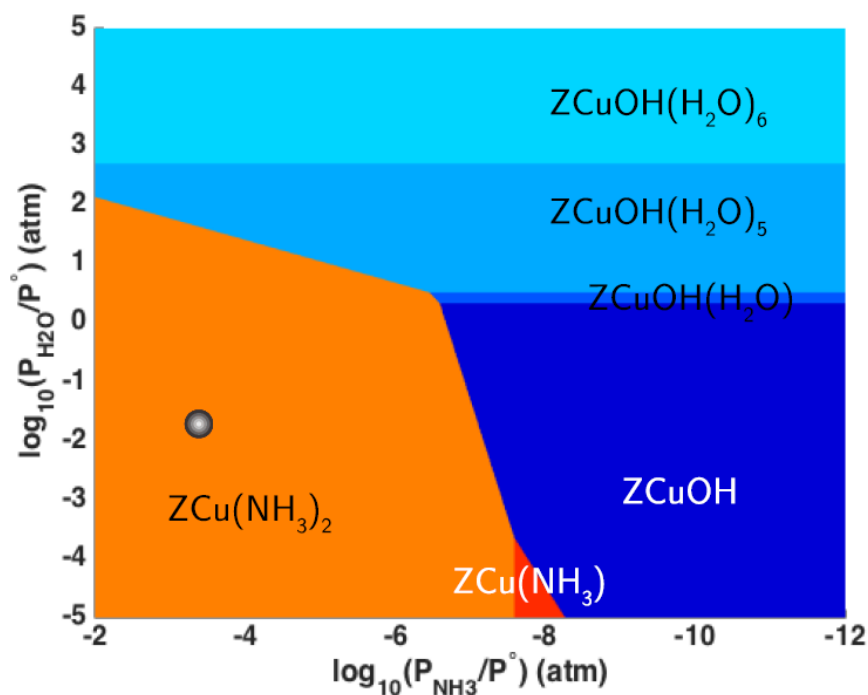


Figure 7.26. Dependence of SCR turnover rates (300 ppm NO, 300 ppm NH<sub>3</sub>, 10% O<sub>2</sub>, 7% CO<sub>2</sub>, 200-120000 ppm H<sub>2</sub>O and balance N<sub>2</sub> at 473 K) on H<sub>2</sub>O pressure on Cu-CHA-19. Line denotes regression of power rate law to measured rate data, with a best-fit slope of 0.03, corresponding to the apparent H<sub>2</sub>O reaction order.

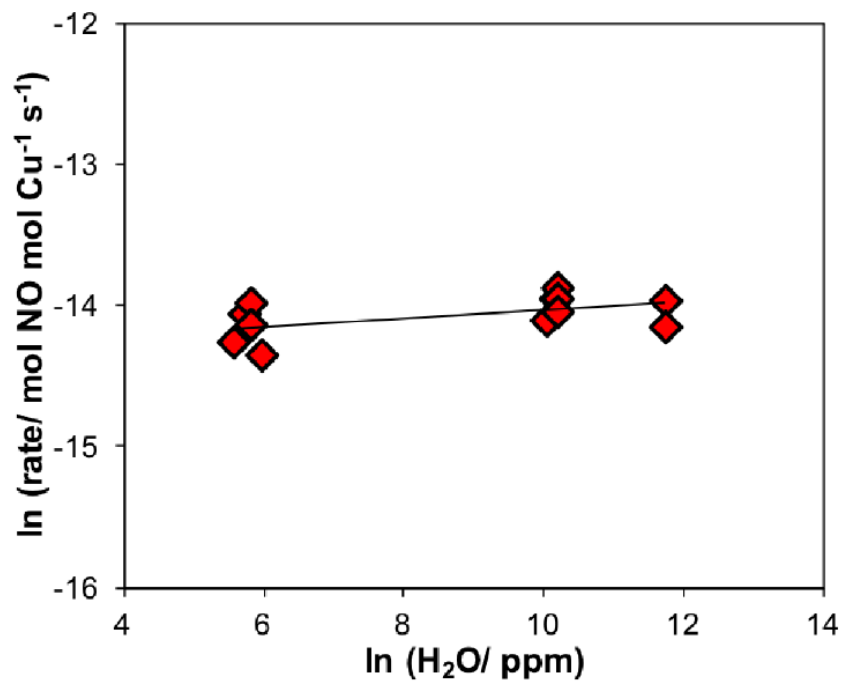


Figure 7.27. Standard SCR rates (300 ppm NO, 300 ppm NH<sub>3</sub>, 10% O<sub>2</sub>, 7% CO<sub>2</sub>, 3% H<sub>2</sub>O and balance N<sub>2</sub>) measured in the temperature range of 450–480 K on Cu-CHA-19 in the laboratory differential PFR (red squares) and in the *operando* XAS reactor (black triangle). Line denotes regression of an Arrhenius rate equation to the lab PFR rate data.

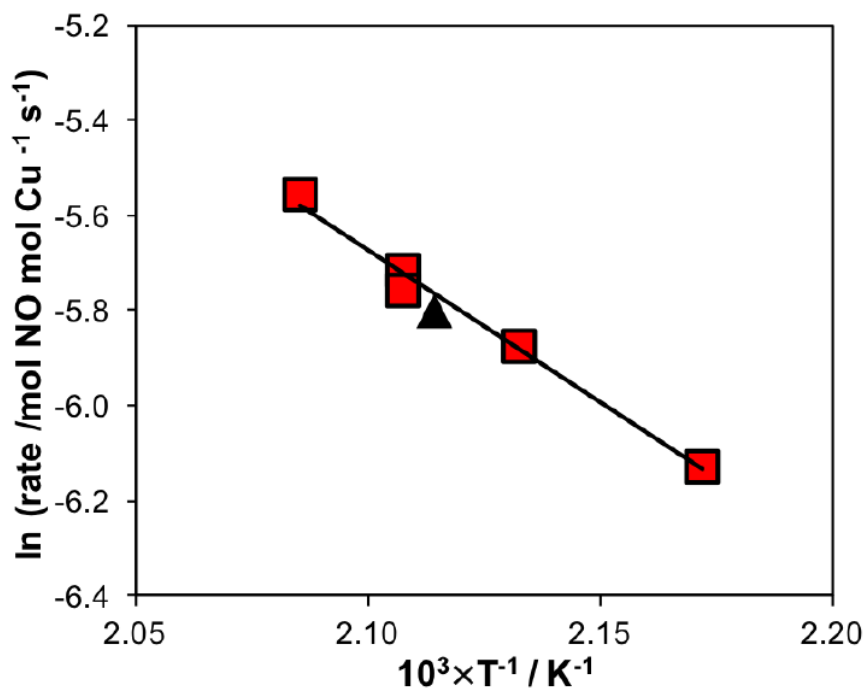


Table 7.1.

Bulk elemental analysis and fraction of isolated  $\text{Cu}^{II}$  and  $\text{Cu}^{II}(\text{OH})$  sites on a series of Cu-exchanged SSZ-13 samples with varying Si/Al (4.5-25) and Cu/Al (0.03-0.59); arranged by increasing Cu/Al for a fixed Si/Al ratio.

| Si/Al | Cu/Al | Cu wt% | $\text{H}^+/\text{Al}^a$ | $\text{H}^+/\text{Al}^b$ | $\text{Cu}^{II}\text{OH}^c/\text{Al}$ | $\text{Cu}^{II}/\text{Al}^c$ |
|-------|-------|--------|--------------------------|--------------------------|---------------------------------------|------------------------------|
| 4.5   | 0.08  | 1.4    | 0.46                     | 0.31                     | 0                                     | 0.08                         |
| 4.5   | 0.21  | 3.7    | 0.87                     | 0.42                     | 0                                     | 0.21                         |
| 15    | 0.03  | 0.3    | 0.98                     | 0.93                     | 0                                     | 0.03                         |
| 15    | 0.08  | 0.5    | 0.98                     | 0.81                     | 0                                     | 0.08                         |
| 15    | 0.10  | 0.7    | 0.98                     | 0.80                     | 0.01                                  | 0.09                         |
| 15    | 0.12  | 0.8    | 0.98                     | 0.73                     | 0.03                                  | 0.09                         |
| 15    | 0.19  | 1.3    | 0.98                     | 0.68                     | 0.10                                  | 0.09                         |
| 15    | 0.25  | 1.7    | 1.00                     | 0.64                     | 0.16                                  | 0.09                         |
| 15    | 0.37  | 2.4    | 0.98                     | 0.58                     | 0.28                                  | 0.09                         |
| 15    | 0.44  | 2.9    | 0.98                     | 0.51                     | 0.35                                  | 0.09                         |
| 25    | 0.21  | 0.8    | 0.98                     | 0.74                     | 0.17                                  | 0.04                         |
| 25    | 0.42  | 1.6    | 0.98                     | 0.58                     | 0.37                                  | 0.04                         |
| 25    | 0.59  | 2.4    | 0.98                     | 0.47                     | 0.55                                  | 0.04                         |

<sup>a</sup>  $\text{H}^+/\text{Al}$  measured on the H-form zeolite.

<sup>b</sup>  $\text{H}^+/\text{Al}$  measured on the Cu-exchanged zeolite.

<sup>c</sup> Determined from titration of residual  $\text{H}^+$  sites by  $\text{NH}_3$  and thermodynamic preferences for  $\text{Cu}^{II}$  and  $\text{Cu}^{II}\text{OH}$  siting [79].

Table 7.2.  
A series of Cu-exchanged SSZ-13 samples with varying Si/Al (4.5-25) and Cu/Al (0.03-0.44) (X = Mean Cu-Cu distance in A, rounded down, labels (a-h) correspond to those in Figure 7.2); arranged by increasing Cu/Al for a fixed Si/Al ratio.

| Cu Cation Density |       |                          | Mean Cu-Cu Distance  |             |      |               |
|-------------------|-------|--------------------------|--|-------------|------|---------------|
| Si/Al             | Cu/Al | / mol Cu m <sup>-3</sup> | / Cu atoms (10 <sup>3</sup> Å <sup>3</sup> ) <sup>-1</sup> | Cu per cage | / Å  | Cu-CHA-X      |
| 4.5               | 0.08  | 365                      | 0.22   | 0.17        | 20.6 | Cu-CHA-20 (c) |
| 4.5               | 0.21  | 958                      | 0.57   | 0.44        | 15.0 | Cu-CHA-15 (h) |
| 15                | 0.03  | 47                       | 0.03   | 0.02        | 40.7 | Cu-CHA-40     |
| 15                | 0.08  | 125                      | 0.07   | 0.05        | 29.4 | Cu-CHA-29 (a) |
| 15                | 0.10  | 157                      | 0.09   | 0.07        | 27.2 | Cu-CHA-27     |
| 15                | 0.12  | 188                      | 0.11   | 0.08        | 25.6 | Cu-CHA-25     |
| 15                | 0.19  | 298                      | 0.18   | 0.14        | 22.0 | Cu-CHA-22     |
| 15                | 0.25  | 395                      | 0.23   | 0.18        | 20.1 | Cu-CHA-20*    |
| 15                | 0.37  | 580                      | 0.35   | 0.27        | 17.6 | Cu-CHA-17 (f) |
| 15                | 0.44  | 689                      | 0.41   | 0.31        | 16.6 | Cu-CHA-16 (g) |
| 25                | 0.21  | 193                      | 0.11   | 0.08        | 25.4 | Cu-CHA-25 (b) |
| 25                | 0.42  | 395                      | 0.24   | 0.18        | 19.8 | Cu-CHA-19 (d) |
| 25                | 0.59  | 569                      | 0.34   | 0.26        | 17.7 | Cu-CHA-17*(e) |

\* Identifies the higher Si/Al density sample of two samples that share the same mean (rounded down) Cu-Cu distance.

Table 7.3.

Standard SCR kinetic parameters measured on a series of Cu-exchanged SSZ-13 samples with Si/Al = 15 and Cu/Al varying from 0.03-0.44; arranged by increasing Cu/Al. (X = Mean Cu-Cu distance in A, rounded down, labels (a, f, and g) correspond to those in Figure 7.2).

| Cu-CHA-X      | Cu Density   |  | Standard SCR Rate  |                                   | E <sub>app</sub>      |  |
|---------------|--|--|--|-----------------------------------|-----------------------|--|
|               | Cu atoms (10 <sup>3</sup> A <sup>3</sup> ) <sup>-1</sup> | / 10 <sup>-3</sup> mol NO (mol Cu s) <sup>-1</sup> | / 10 <sup>-3</sup> mol NO (10 <sup>3</sup> A <sup>3</sup> s) <sup>-1</sup> | O <sub>2</sub> Order <sup>a</sup> | kJ mol <sup>-1b</sup> |  |
| Cu-CHA-40 (a) | 0.03   | 1.8  | 0.05   | 0.8                               | 47                    |  |
| Cu-CHA-29     | 0.07   | 2.3  | 0.16   | 0.7                               | 50                    |  |
| Cu-CHA-27     | 0.09   | 3.3  | 0.30   | 0.7                               | 56                    |  |
| Cu-CHA-25     | 0.11   | 4.5  | 0.50   | 0.7                               | 56                    |  |
| Cu-CHA-22     | 0.18   | 6.5  | 1.17   | 0.5                               | 60                    |  |
| Cu-CHA-20*    | 0.23   | 7.8  | 1.79   | 0.4                               | 63                    |  |
| Cu-CHA-17 (f) | 0.35   | 7.4  | 2.59   | 0.4                               | 66                    |  |
| Cu-CHA-16 (g) | 0.41   | 7.8  | 3.20   | 0.3                               | 74                    |  |

<sup>a</sup> Errors in the apparent O<sub>2</sub> rate order are ± 0.1.

<sup>b</sup> Errors in the apparent activation energy (E<sub>app</sub>) are ± 7 kJ/mol. Consistent with prior reports [37, 349], E<sub>app</sub> increases systematically with increasing Cu density, reflecting the gradual transition from a kinetic regime in which O<sub>2</sub> activation is rate-determining (low Cu density) to one in which it is not (high Cu density).

\* Identifies the higher Si/Al density sample of two samples that share the same mean (rounded down) Cu-Cu distance.

Table 7.4.  
Operando steady state  $\text{Cu}^I$  fraction for a series of Cu-SSZ-13 samples with varying Cu density from 0.07-0.57 atom  $(10^3\text{\AA}^3)^{-1}$ . Feed conditions: 300 ppm NO, 300 ppm  $\text{NH}_3$ , 10%  $\text{O}_2$ , 5%  $\text{CO}_2$ , 2%  $\text{H}_2\text{O}$ , 473 K.

| Si/Al    | Cu/Al | Cu-CHA-X       | Cu Density |                           | Operando                            |  | EXAFS CN <sup>b</sup> |
|----------|-------|----------------|------------|---------------------------|-------------------------------------|--|-----------------------|
|          |       |                | Cu atoms   | $(10^3\text{\AA}^3)^{-1}$ | $\text{Cu}^I$ Fraction <sup>a</sup> |  |                       |
| 4.5      | 0.08  | Cu-CHA-20 (c)  | 0.22       |                           | 0.50                                |  | 3.4                   |
| 4.5      | 0.21  | Cu-CHA-15 (h)  | 0.57       |                           | 0.10                                |  | 3.9                   |
| 15       | 0.08  | Cu-CHA-29 (a)  | 0.07       |                           | 0.96                                |  | 2.1                   |
| 15       | 0.37  | Cu-CHA-17 (f)  | 0.35       |                           | 0.53                                |  | 3.2                   |
| 15       | 0.44  | Cu-CHA-16 (g)  | 0.41       |                           | 0.47                                |  | 3.3                   |
| 25       | 0.21  | Cu-CHA-25 (b)  | 0.11       |                           | 0.85                                |  | 2.4                   |
| 25       | 0.42  | Cu-CHA-19 (d)  | 0.24       |                           | 0.63                                |  | 2.8                   |
| 25       | 0.59  | Cu-CHA-17* (e) | 0.34       |                           | 0.51                                |  | 3.1                   |
| 16 [360] | 0.20  | -              | 0.18       |                           | 0.60                                |  | -                     |
| 4.5 [37] | 0.16  | -              | 0.44       |                           | 0.26                                |  | -                     |

\* Identifies the higher Si/Al density sample of two samples that share the same mean (rounded down) Cu-Cu distance.

<sup>a</sup>  $\text{Cu}^I$  Fraction measured during steady state catalysis. Errors are  $\pm 0.05$ .

<sup>b</sup> First-shell coordination number.

Table 7.5.

Operando steady state  $\text{Cu}^I$  fraction for a series of Cu-SSZ-13 samples with varying Cu density from 0.07-0.57 atom  $(10^3\text{\AA}^3)^{-1}$ . Feed conditions: 300 ppm NO, 300 ppm  $\text{NH}_3$ , 10%  $\text{O}_2$ , 5%  $\text{CO}_2$ , 2%  $\text{H}_2\text{O}$ , 473 K.

| Si/Al    | Cu/Al | Cu-CHA-X       | Cu Density<br>$(10^3\text{\AA}^3)^{-1}$ | Operando<br>$\text{Cu}^I$ Fraction <sup>a</sup> | CN <sup>b</sup> |
|----------|-------|----------------|---|---|-----------------|
| 4.5      | 0.08  | Cu-CHA-20 (c)  | 0.22                                    | 0.50  | 3.4             |
| 4.5      | 0.21  | Cu-CHA-15 (h)  | 0.57                                    | 0.10  | 3.9             |
| 15       | 0.08  | Cu-CHA-29 (a)  | 0.07                                    | 0.96  | 2.1             |
| 15       | 0.37  | Cu-CHA-17 (f)  | 0.35                                    | 0.53  | 3.2             |
| 15       | 0.44  | Cu-CHA-16 (g)  | 0.41                                    | 0.47  | 3.3             |
| 25       | 0.21  | Cu-CHA-25 (b)  | 0.11                                    | 0.85  | 2.4             |
| 25       | 0.42  | Cu-CHA-19 (d)  | 0.24                                    | 0.63  | 2.8             |
| 25       | 0.59  | Cu-CHA-17* (e) | 0.34                                    | 0.51  | 3.1             |
| 16 [360] | 0.20  | -              | 0.18                                    | 0.60  | -               |
| 4.5 [37] | 0.16  | -              | 0.44                                    | 0.26  | -               |

\* Identifies the higher Si/Al density sample of two samples that share the same mean (rounded down) Cu-Cu distance.

<sup>a</sup>  $\text{Cu}^I$  Fraction measured during steady state catalysis. Errors are  $\pm 0.05$ .

<sup>b</sup> First-shell coordination number.



Table 7.6.

Fitted  $\text{Cu}^I$  fraction before and after oxidation with 10%  $\text{O}_2$  at 473 K starting from  $\text{Cu}^I(\text{NH}_3)_2$  for Cu-CHA-20, Cu-CHA-15 and Cu-CHA-29.

| Cu-CHA-X  | $\text{Cu}^I$ Fraction Before <sup>a</sup> | $\text{Cu}^I$ Fraction After <sup>b</sup> |
|-----------|--|---|
| Cu-CHA-20 | 0.90                                       | 0.12                                      |
| Cu-CHA-15 | 0.90                                       | 0.05                                      |
| Cu-CHA-29 | 0.98                                       | 0.30                                      |

<sup>a</sup>  $\text{Cu}^I$  fraction measured before exposure to  $\text{O}_2$ . Errors are  $\pm 0.05$ .

<sup>b</sup>  $\text{Cu}^I$  fraction measured after exposure to  $\text{O}_2$ . Errors are  $\pm 0.05$ .

Table 7.7.

Fitted  $\text{Cu}^I$  fraction before and after repeated subsequent oxidation with 10%  $\text{O}_2$  at 473 K starting from  $\text{Cu}^I(\text{NH}_3)_2$  in each cycle for Cu-CHA-29.

| Cycle # | $\text{Cu}^I$ Fraction Before <sup>a</sup> | $\text{Cu}^I$ Fraction After <sup>b</sup> |
|---------|--|---|
| 1       | 0.98                                       | 0.30                                      |
| 2       | 0.95                                       | 0.32                                      |
| 3       | 0.98                                       | 0.31                                      |

<sup>a</sup>  $\text{Cu}^I$  Fraction measured before exposure to  $\text{O}_2$ . Errors are  $\pm 0.05$ .

<sup>b</sup>  $\text{Cu}^I$  Fraction measured after exposure to  $\text{O}_2$ . Errors are  $\pm 0.05$ .

Table 7.8.

Fitted  $\text{Cu}^I$  fraction before and after oxidation with 100 ppm  $\text{NO}_2$  at 473 K starting from  $\text{Cu}^I(\text{NH}_3)_2$  for Cu-CHA-20, Cu-CHA-15 and Cu-CHA-29.

| Cu-CHA-X  | $\text{Cu}^I$ Fraction Before <sup>a</sup> | $\text{Cu}^I$ Fraction After <sup>b</sup> |
|-----------|--|---|
| Cu-CHA-20 | 0.90                                       | 0.00                                      |
| Cu-CHA-15 | 0.90                                       | 0.00                                      |
| Cu-CHA-29 | 0.98                                       | 0.00                                      |

<sup>a</sup>  $\text{Cu}^I$  Fraction measured before exposure to  $\text{NO}_2$ . Errors are  $\pm 0.05$ .

<sup>b</sup>  $\text{Cu}^I$  Fraction measured after exposure to  $\text{NO}_2$ . Errors are  $\pm 0.05$ .

Table 7.9.

PBE+D2 DFT computed reaction energies (column 2), total energy differences along the reaction coordinate (column 3), and normalized Bader charge [79] derived Cu oxidation states for the product in each step (column 4) for all results reported in Figure 7.4.

| Reaction            | Reaction Energy<br>/ $\text{kJ mol}^{-1}$ | Energy<br>/ $\text{kJ mol}^{-1}$ | Cu Oxidation State |
|---------------------|---|----------------------------------|--------------------|
| A                   | -   | 0                                | 1.00               |
| A $\rightarrow$ TS1 | 35  | 35                               |                    |
| TS1 $\rightarrow$ B | 23  | 23                               | 1.00               |
| B $\rightarrow$ C   | -59                                       | -36                              | 1.39               |
| C $\rightarrow$ TS2 | 20 [423]                                  | -16                              |                    |
| TS2 $\rightarrow$ D | -26                                       | -42                              | 1.80               |
| D $\rightarrow$ TS3 | 19  | -23                              |                    |
| TS3 $\rightarrow$ E | -36                                       | -60                              | 2.10               |

Table 7.10.

Computed PBE+D2 and HSE06+TSvdw reaction energies for O<sub>2</sub> and NO<sub>2</sub> adsorption on a Cu<sup>I</sup>(NH<sub>3</sub>)<sub>2</sub> monomer. Rows 1 and 2 reference the two different (A, B) O<sub>2</sub> adsorption configurations in Figure 7.21. Columns 3 and 5 report the normalized Bader charge [79] derived Cu oxidation state.

|  | PBE+D2                 |           | HSE06+TSvdw            |           |
|--|------------------------|-----------|------------------------|-----------|
|  | / kJ mol <sup>-1</sup> | Ox. State | / kJ mol <sup>-1</sup> | Ox. State |
| Cu <sup>I</sup> (NH <sub>3</sub> ) <sub>2</sub> +O <sub>2</sub> (A)  | 2                      | 1.65      | 1                      | 1.47      |
| Cu <sup>I</sup> (NH <sub>3</sub> ) <sub>2</sub> +O <sub>2</sub> (B)  | -26                    | 1.32      | -11                    | 1.15      |
| Cu <sup>I</sup> (NH <sub>3</sub> ) <sub>2</sub> +NO <sub>2</sub> (C) | -46                    | 1.92      | -71                    | 2.27      |

Table 7.11.

Metadynamics parameters.

| Parameter   | CV     |
|---|--------|
| Harmonic spring constant, k (hartree)                                 | 5      |
| Mass of the fictitious particle, $\mu$ (hartree (a.u.) <sup>2</sup> ) | 100    |
| Gaussian height, W (hartree)  | 0.0005 |
| Gaussian width, s'  | 0.02   |
| Minimum Metadynamics time step, $\Delta t_{min}$ (a.u.)               | 100    |
| p   | 6      |
| q   | 6      |
| d <sub>0</sub> (Å)  | 6.2    |



## 8. INTRODUCING CATALYTIC DIVERSITY INTO SINGLE-SITE CHABAZITE ZEOLITES OF FIXED COMPOSITION VIA SYNTHETIC CONTROL OF ACTIVE SITE PROXIMITY

### 8.1 Introduction

In a landmark contribution to catalysis by aluminosilicate zeolites, Haag and co-workers reported that hexane cracking rates (per g, 811 K) increased linearly with total Al density (per g) in MFI, a low-symmetry framework containing 12 (orthorhombic) or 24 (monoclinic) unique tetrahedral sites (T-sites) [14]. This report suggested that MFI zeolites contained a single type of active Brønsted acid site ( $\text{H}^+$ ), whose catalytic behavior was independent of composition ( $\text{Si}/\text{Al} = 10\text{-}10000$ ) and topographic location, as would be expected for a single-site catalyst [15]. Turnover rates and selectivities of hydrocarbon reactions have since been recognized to depend on the location of  $\text{H}^+$  sites within a given zeolite framework, despite similarities in their acid strength described rigorously by deprotonation energy (DPE) [16], because the topology of microporous cavities influences the Gibbs free energies of confined intermediates and transition states through van der Waals interactions [143]. Efforts to deconvolute the catalytic behavior of active sites located within different voids of a given zeolite have required either preferential titration of protons within certain voids or acquisition of zeolites of different provenance, a viable strategy because Al incorporation within specific T-sites during crystallization is difficult to control, other than in a few emerging cases (FER [140], MFI [32]). The catalytic consequences of T-site location within such zeolites may be further convoluted by effects of site proximity, which is determined by atomic arrangements that are difficult to control systematically and independently of bulk composition [48].

Distinct ensembles of proton active sites in a zeolite arise from differences in the arrangement ( $\text{Al-O}(-\text{Si-O})_x\text{-Al}$ ) of framework Al atoms ( $\text{Al}_f$ ) between isolated ( $x > 2$ ) or paired configurations ( $x = 1, 2$ ) [48], with the latter identified functionally by their ability to exchange divalent cations. Proton proximity effects on catalysis have been studied in MFI zeolites by varying their bulk composition ( $\text{Si/Al}$ ) [61, 75, 76], and turnover rates (per  $\text{H}^+$ ) of hydrocarbon cracking are generally reported to increase with total Al content ( $\text{Al}_{\text{tot}}$ ) [61, 75]. Changes in bulk composition only influence Al proximity on average, however, given that framework Al arrangements show nuanced dependences on the conditions and reagent sources used during zeolite crystallization [48, 65, 74, 159]. As a result, the routes used to synthesize MFI zeolites influence framework Al arrangement, but in a manner that is neither randomly determined nor prescribed by any deterministic rules [48]. Thus, while the pairing of protons in MFI ( $\text{Si/Al} = 13\text{-}140$ ) has been proposed to increase alkene oligomerization [77] and alkane cracking [75] turnover rates, concomitant changes in Al distribution among different T-sites and void environments (i.e., straight and sinusoidal channels, and their intersections) [61] have precluded unambiguous kinetic assessments of proton proximity in MFI zeolites.

Here, we focus on the chabazite (CHA) topology, a high-symmetry framework containing a single crystallographically unique T-site. The CHA framework contains double six-membered ring building units that interconnect to form eight-membered ring windows (0.38 nm diam.), which limit diffusion into larger cavities (1.2 nm x 0.72 nm x 0.72 nm; 12 T atoms per CHA cage). The presence of a single T-site in the CHA framework promises to clarify how synthesis routes influence Al proximity independent of T-site location and, in turn, how proton proximity can influence Brønsted acid catalysis. First, we extend methods to synthesize CHA zeolites of effectively fixed composition ( $\text{Si/Al} = 14\text{-}17$ ), but with systematically varying framework Al arrangements that span the limit of site isolation (0% paired Al) to nearly half of the sites (44%) in paired configurations. Then, we use seven CHA samples with varying paired Al content to show that first-order and zero-order rate constants (per total

$\text{H}^+$ , 415 K) for the Brønsted acid-catalyzed methanol dehydration to dimethyl ether (DME) are nearly one order of magnitude larger on paired than on isolated protons. IR spectra measured during steady-state dehydration catalysis enable direct observation of surface methoxy species (ca.  $1457\text{ cm}^{-1}$ ) [451], providing evidence that paired protons in CHA zeolites can access alternate methanol dehydration pathways that do not propagate at isolated protons under these conditions. These results constitute a synthesis-structure-function relation for proton proximity effects in CHA zeolites, and they demonstrate that catalytic diversity can arise from differences in the atomic arrangement of active sites in single T-site zeolites of fixed composition.

## 8.2 Results and Discussion

### 8.2.1 Synthesis of CHA zeolites with different Al arrangements.

We recently reported that structure-directing agents (SDAs) of different cationic charge density can be used to systematically change the distribution of isolated and paired framework Al atoms in CHA zeolites (SSZ-13) [42]. Proximal protons that compensate paired Al sites were quantified by measuring  $\text{Co}^{2+}$  exchange isotherms, which were validated by (i) collecting UV-visible spectra that showed  $\text{Co}^{2+}$  d-d transitions (ca.  $19,500\text{ cm}^{-1}$ ) with undetectable cobalt oxide formation, (ii) quantifying residual  $\text{H}^+$  sites after  $\text{Co}^{2+}$  exchange using  $\text{NH}_3$  titration methods (2  $\text{H}^+$  replaced per  $\text{Co}^{2+}$ ), and (iii) quantifying paired Al sites with another divalent cation ( $\text{Cu}^{2+}$ ) [42,79] predicted by density functional theory to selectively titrate paired Al sites in CHA frameworks (i.e., arrangements of 2 Al in a 6-MR) [79]. The use of chemical titrants that directly probe the functional behavior of proximal protons, and directly quantify such sites, avoids inaccuracies in assessing the proximity of their structural surrogates. Although framework Al proximity in zeolites can be probed by NMR techniques, Al separated by one or two Si atoms in certain frameworks (e.g., MFI) can lead to protons stabilized within different voids [48], which do not function as proximal protons within the same void environment.

Here, we extend previously reported synthetic methods to prepare CHA zeolites of effectively fixed composition ( $\text{Si}/\text{Al}_f = 14\text{--}17$ ) with nearly half of their Al atoms (44%) in paired configurations. Unless otherwise specified, each zeolite contained nearly complete Al incorporation within framework locations ( $\text{Al}_f/\text{Al}_{tot} > 0.95$ ;  $^{27}\text{Al}$  MAS NMR, Section 8.7.2, Supporting Information), and compensating  $\text{H}^+$  sites present in similar amounts ( $\text{H}^+/\text{Al}_f > 0.95$  by  $\text{NH}_3$  titration, Table 8.1). Relevant characterization data for CHA zeolites are summarized in Table 8.1, with all characterization data and detailed methods provided in Section 8.7.2 of the Supporting Information.

CHA zeolites containing predominantly isolated Al atoms, which are unable to exchange divalent cations (e.g.,  $\text{Co}^{2+}$ ,  $\text{Cu}^{2+}$ ) but can quantitatively exchange monovalent cations (e.g.,  $\text{H}^+$ ,  $\text{Na}^+$ ,  $\text{NH}_4^+$ ), were crystallized at different compositions ( $\text{Si}/\text{Al} = 15\text{--}30$ ) in the presence of organic N,N,N-trimethyl-1-adamantylammonium cations ( $\text{TMAda}^+$ ) as the sole SDA and hydroxide as the counteranion [42]. The ability of  $\text{TMAda}^+$  cations to isolate framework Al atoms in CHA was verified by seven replicate crystallization experiments [42]. The adamantyl group (ca. 0.7 nm diam.) imposes steric constraints that limit occupation of each CHA cage (0.72 nm diam.) by only one  $\text{TMAda}^+$  molecule (Table 8.1, TGA experiments detailed in Section 8.7.2, Supporting Information) [162], while the single cationic charge at the quaternary ammonium center imposes electrostatic constraints that direct placement of one anionic framework Al center (Scheme 8.1) [200].

Despite the occlusion of a single  $\text{TMAda}^+$  molecule within each CHA cage, the bulk compositions of the crystallized zeolites do not reflect the incorporation of 1 Al atom per cage ( $\text{Si}/\text{Al} = 11$ ; 12 T atoms per cage), indicating that anionic lattice defects ( $\text{Si-O}^-$ ) form to compensate cationic charges of some  $\text{TMAda}^+$  molecules. CHA zeolites crystallized within a limited composition range ( $\text{Si}/\text{Al} = 15\text{--}30$ ) in hydroxide media, reflecting crystallization barriers imposed by a disparity in Coulombic interactions between occluded  $\text{TMAda}^+$  cations and the solid aluminosilicate polyanion [452].  $\text{TMAda}^+$  alone is unable to stabilize CHA frameworks with high Al density ( $\text{Si}/\text{Al}_f < 11$ ) because each cage (12 T atoms) contains one occluded  $\text{TMAda}^+$  cation [162].



TMAda<sup>+</sup> is also ineffective at stabilizing CHA frameworks with low Al density ( $\text{Si}/\text{Al}_f > 30$ ) because anionic lattice defects are required to form in order to balance excess cationic charges introduced by occluded cationic SDA molecules [225]. The electrostatic balance between occluded cations and anionic framework Al centers implies that using different mineralizers ( $\text{OH}^-$ ,  $\text{F}^-$ ), which facilitate reversible formation of Si-O and Al-O bonds during crystallization [453], should not influence framework Al arrangement within this composition range ( $\text{Si}/\text{Al} = 15\text{-}30$ ). This hypothesis was tested by preparing precursor solutions in fluoride media containing TMAda<sup>+</sup> as the sole SDA. These solutions crystallized CHA zeolites ( $\text{Si}/\text{Al} = 18$ ) that were also unable to exchange  $\text{Co}^{2+}$  (details in Section 8.7.2, Supp. Info.), demonstrating the ability of TMAda<sup>+</sup> cations to direct the incorporation of isolated framework Al atoms in CHA zeolites within this composition range ( $\text{Si}/\text{Al} = 15\text{-}30$ ), irrespective of the counteranion used as the mineralizer ( $\text{OH}^-$ ,  $\text{F}^-$ ).

CHA zeolites of fixed composition, but with systematically varying fractions of paired Al, were synthesized by varying the ratio of high ( $\text{Na}^+$ ) and low (TMAda<sup>+</sup>) charge density cations in the precursor solution, at fixed total cation content ( $(\text{Na}^+ + \text{TMAda}^+)/\text{Al}$ ) [42]. Our previous synthesis experiments used the same aluminum source ( $\text{Al}(\text{OH})_3$ ) and resulted in CHA zeolites ( $\text{Si}/\text{Al} = 14\text{-}16$ ) with varying percentages of paired Al (0-18%) that correlated linearly with the total amount of  $\text{Na}^+$  retained on the crystallized zeolite product (Figure 8.2).<sup>16</sup> This correlation suggests that a second anionic framework Al center, compensated by an extraframework  $\text{Na}^+$  cation, is incorporated proximal to a framework Al center compensating the ammonium group in a TMAda<sup>+</sup> cation occluded within a CHA cage, an assembly that preserves dispersive contacts between nonpolar siloxane portions of the zeolite framework and the hydrophobic adamantyl group of TMAda<sup>+</sup> (Scheme 8.1) [42]. Al precursors that differ in reactivity and dissolution rate [159] have been used to influence Al pairing in MFI zeolites crystallized from solutions containing TPA<sup>+</sup> cations, although without a discernible dependence on a single synthesis parameter and also often resulting in changes to bulk composition ( $\text{Si}/\text{Al} = 25\text{-}60$ ) [74]. Therefore, we attempted

to vary paired Al content further by crystallizing CHA using other Al sources ( $\text{AlCl}_3$ ,  $\text{Al}(\text{NO}_3)_3$ ,  $\text{NaAlO}_2$ ,  $\text{Al}_2\text{O}_3$ ,  $\text{Al}(\text{O-i-Pr})_3$ ) in hydroxide media with equimolar amounts of  $\text{Na}^+$  and  $\text{TMAda}^+$ , holding other synthesis parameters constant. Most samples contained proton fractions ( $\text{H}^+/\text{Al} < 0.6$ ) or micropore volumes ( $< 0.14 \text{ cm}^3 \text{ g}^{-1}$ ) that were abnormally low (data in Section 8.7.2, Supporting Information), except those synthesized using  $\text{Al}(\text{O-i-Pr})_3$  ( $\text{Si}/\text{Al}_f = 14$ ,  $0.16 \text{ cm}^3 \text{ g}^{-1}$ ,  $\text{H}^+/\text{Al}_f = 1.00$ , Table 8.1). This CHA zeolite contained more than twice the paired Al content (44%) as reported previously for CHA ( $\text{Si}/\text{Al} = 15$ ) synthesized using  $\text{Al}(\text{OH})_3$  [42], yet also incorporated a larger amount of  $\text{Na}^+$  during synthesis ( $\text{Na}^+/\text{Al}_{\text{tot}} = 0.26$ , Figure 8.2).

Taken together, these results suggest that the amount of  $\text{Na}^+$  retained on CHA zeolite products, when crystallized from mixtures of low charge density organic  $\text{TMAda}^+$  cations and high charge density inorganic  $\text{Na}^+$  cations, can serve as a predictive descriptor of the number of paired Al sites formed (Figure 8.2). This synthesis-structure relation is particularly useful given the stochastic nature of zeolite crystallization that can form nonuniform products upon replication of the same procedure. Indeed, two replicate crystallizations of CHA zeolites using  $\text{Al}(\text{OH})_3$  as the aluminum source ( $\text{Na}^+/\text{TMAda}^+ = 1$ ) led to detectable variations in paired Al content (18-30%), but which also correlated with the  $\text{Na}^+$  incorporated into the crystalline product (Figure 8.2). These findings support the hypothesis that  $\text{Na}^+$  becomes occluded in extraframework locations proximal to the cationic charge in  $\text{TMAda}^+$ , so as to direct the formation of paired framework Al [42]. They also indicate that the cationic charge density of occluded SDA molecules influences the anionic charge density introduced by  $\text{Al}^{3+}$  substitution within pure-silica zeolite lattices, concepts related to those proposed in charge density mismatch theory [192, 193, 452].

The methods to prepare this suite of CHA zeolites represent progress toward predictive synthetic control of active site arrangement, and the resulting materials can be used as model catalysts to facilitate connections between structure and function in zeolite catalysis. The CHA zeolites containing only isolated Al atoms at varying composition should behave as single-site catalysts, promising to clarify experimental

kinetic and spectroscopic assessments of proton active sites by experiment, which can be modeled more faithfully by theory. The CHA zeolites of fixed composition but varying paired Al content enable studying the catalytic consequences of proton proximity in zeolites, independent of structural heterogeneities arising from the multiplicity of T-sites. As discussed next, a structure-function relation is developed for isolated and paired protons in CHA zeolites using methanol dehydration to dimethyl ether (DME), a versatile probe reaction of the intrinsic acid strength and reactivity of solid Brønsted acids [82].

### 8.2.2 Methanol dehydration to dimethyl ether: a Brønsted acid probe reaction.

The dehydration of methanol to dimethyl ether can proceed through two different pathways on solid Brønsted acids, as reported in detail by Carr et al [82]. The associative dehydration pathway involves adsorption of gas-phase methanol at a  $H^+$  site to form a hydrogen-bonded methanol monomer (Step 1, Scheme 8.3). Adsorption of a second methanol forms a protonated methanol dimer, in which the proton is solvated away from the zeolite lattice and coordinated between the two nucleophilic oxygen atoms (Step 2, Scheme 8.3). Protonated dimers can rearrange to form an intermediate (Step 3, Scheme 8.3) that can decompose into water and an adsorbed dimethyl ether species (Step 4, Scheme 8.3), which desorbs to regenerate the  $H^+$  site (Step 5, Scheme 8.3). Methanol monomers and protonated dimers are the most abundant reactive intermediates (MARI) under experimental conditions investigated previously on medium-pore and large-pore zeolites (10-MR and larger) and polyoxometallate clusters (433 K, >0.2 kPa  $CH_3OH$ ) [82], resulting in the following rate expression (full derivation in Section 8.7.3, Supporting Information):

$$r_{DME,A} = \frac{k_{first,A} P_{CH_3OH}}{1 + \frac{k_{first,A}}{k_{zero,A}} P_{CH_3OH}} \quad (8.1)$$

In eq 8.1,  $k_{first,A}$  and  $k_{zero,A}$  are apparent first-order and zero-order rate constants, respectively, for the associative methanol dehydration pathway.

Alternatively, the dissociative dehydration pathway involves formation of methanol monomers (Step 1, Scheme 8.4), which initially eliminate water to form a surface methoxy group (Step 2, Scheme 8.4). Adsorption of a second methanol at an adjacent framework oxygen forms a surface methanol-methoxy pair (Step 3, Scheme 8.4). Addition of the surface methoxy to the nucleophilic oxygen atom of the coadsorbed methanol forms an adsorbed dimethyl ether species (Step 4, Scheme 8.4), which desorbs to regenerate the  $H^+$  site (Step 5, Scheme 8.4). An additional step involving formation of methanol dimers (Step 2, Scheme 8.4) inhibits the formation of surface methoxy groups that propagate the dissociative cycle.

The assumption of methanol monomers, protonated dimers, and surface methoxy-methanol pairs as MARI leads to the following rate expression, which predicts that rates become inhibited at high methanol pressures (full derivation in Section 8.7.3, Supporting Information):

$$r_{DME,D} = \frac{k_{first,D} P_{CH_3OH}}{1 + \frac{k_{first,D}}{k_{zero,D}} P_{CH_3OH} + \frac{k_{first,D}}{k_{inhibit,D}} P_{CH_3OH}^2} \quad (8.2)$$

In eq 8.2,  $k_{first,D}$  and  $k_{zero,D}$  are first-order and zero-order rate constants, respectively, for the dissociative dehydration pathway, and  $k_{inhibit,D}$  is an inhibition rate constant that reflects formation of an unreactive methanol dimer.

*in situ* IR spectra of H-MFI during steady-state methanol dehydration catalysis (433 K, 0.2-16 kPa  $CH_3OH$ ) do not show deformation modes for surface methoxy species (ca.  $1457\text{ cm}^{-1}$ ) involved in the dissociative pathway, yet show hydrogen-bonding modes for adsorbed  $CH_3OH$  monomers (ca.  $2380\text{ cm}^{-1}$ ) and protonated  $CH_3OH$  dimers (ca.  $2620\text{ cm}^{-1}$ ) involved in the associative pathway [451]. Further, periodic density functional theory (DFT) calculations indicate that DME formation proceeds with lower free energy barriers via the associative pathway on isolated  $H^+$  sites in MFI zeolites (by ca.  $50\text{ kJ mol}^{-1}$ , vdW-DF functional) [454]. Kinetic measurements were benchmarked in this study by comparing values for three commercially sourced H-MFI samples (Zeolyst) to literature reports (details in Section 8.7.3, Supporting Information) [83, 451]. Methanol dehydration rates on H-MFI (per  $H^+$ ,

415 K) increased linearly ( $<1$  kPa) and became invariant ( $>15$  kPa) with increasing methanol pressure, as predicted by the associative dehydration rate expression (eq 8.1). Moreover, first-order and zero-order rate constants (Figure 8.5) and apparent activation enthalpies and entropies (Section 8.7.3, Supporting Information) agreed quantitatively with literature values [451]. The equivalence of measured rate constants, and specifically activation enthalpies and entropies in both kinetic regimes, indicates that the dehydration turnover rates measured here on MFI zeolites (per  $\text{H}^+$ , 415 K) are measurements of equivalent catalytic phenomena reported by Jones et al [83, 451]. Such quantitative kinetic benchmarking, in turn, validates the direct comparison of dehydration rate data reported here for MFI and CHA zeolites (at 415 K) to literature precedent [455].

### 8.2.3 Methanol dehydration catalysis on CHA zeolites containing only isolated $\text{H}^+$ sites.

Methanol dehydration rates on H-CHA zeolites were measured under differential conversion, reflected in DME formation rates (per  $\text{H}^+$ ) that were invariant with space velocity at fixed methanol pressure (Section 8.7.5, Supporting Information). The presence of internal mass transport phenomena was investigated by performing a Koros-Nowak test [361] on CHA zeolites containing only isolated protons with varying framework Al composition ( $\text{Si}/\text{Al}_f = 14\text{-}27$ ). Zero-order rate constants (per  $\text{H}^+$ , 415 K) were similar (within 20%; Table 8.1) on CHA zeolites containing only isolated  $\text{H}^+$  sites but varying Al content ( $\text{Si}/\text{Al}_f = 14\text{-}27$ ), as expected for a kinetic regime in which active sites are saturated with reactant-derived intermediates and thus insensitive to intraparticle gradients in reactant concentration. In contrast, first-order rate constants (per  $\text{H}^+$ , 415 K) decreased with decreasing  $\text{H}^+$  site concentration (Table 8.1), behavior contrary to that predicted by the Koros-Nowak criterion for intraparticle reactant diffusion limitations [361]. These results suggest that intraparticle transport may become more restricted in CHA zeolites with lower Al content, which has been reported previously to lead to concomitant increases in crystallite size [168].

Indeed, SEM micrographs and dynamic light scattering measurements (Section 8.7.2, Supporting Information) indicate that crystallite sizes increase from 1.5 to 6  $\mu\text{m}$  (Table 8.1) with decreasing Al content ( $\text{Si}/\text{Al}_f = 14\text{--}27$ ) among the samples studied here. Figure 8.6 shows the intraparticle effectiveness factor ( $\eta$ ) for a first-order reaction in a spherical pellet as a function of the Thiele modulus ( $\phi$ ), with values estimated for these CHA zeolites (details and derivation of Thiele moduli and effectiveness factors in Section 8.7.5, Supporting Information). CHA zeolites with  $\text{Si}/\text{Al}_f = 14\text{--}18$  ( $\phi = 0.7\text{--}0.9$ ) are characterized by effectiveness factors near unity ( $\eta = 0.9\text{--}1.1$ ), indicating that intraparticle concentration gradients are absent and that rates measured on these samples are kinetic in origin. CHA zeolites with  $\text{Si}/\text{Al}_f = 27$  ( $\psi = 3.5$ ), however, are characterized by effectiveness factors below unity ( $\eta = 0.5$ ), indicating that intraparticle transport processes corrupt rates measured on this sample; thus, it was not studied further.

Methanol dehydration rates on isolated protons in H-CHA (per  $\text{H}^+$ , 415 K) increased linearly ( $<1$  kPa) before reaching a maximum and ultimately decreasing ( $>10$  kPa) with increasing methanol pressure (Figure 8.7 and Section 8.7.3, Supporting Information), in contrast with the behavior observed on HMF1. Reversible inhibition observed at high pressures ( $>10$  kPa) cannot be accounted for by the dissociative pathway, as isolated protons in H-CHA zeolites do not stabilize surface methoxy groups under these reaction conditions (415 K, 0.77 kPa; Figure 8.8) and thus catalyze methanol dehydration via the associative pathway. Competitive adsorption of product water with methanol at  $\text{H}^+$  sites is also unable to account for the apparent inhibition observed at high methanol pressures, both because measured dehydration rates were invariant with reactant space velocity, and because the rate inhibition measured from deliberate water cofeeding experiments is weaker than the observed inhibition (details in Section 8.7.6, Supporting Information). The kinetic inhibition observed at high methanol pressures occurs with the concomitant formation of methanol clusters (ca.  $3370\text{ cm}^{-1}$ ) [456] detected by *in situ* IR (Section 8.7.6, Supporting Information). Physisorbed methanol molecules contributing to larger clusters appear to be occluded

within CHA voids, but not within MFI voids under similar reaction conditions. Analogous inhibition of dehydration rates (per  $\text{H}^+$ , 415 K) at high methanol pressures is also observed on H-AEI zeolites (Section 8.7.6, Supporting Information), which is an eight-membered ring, window-cage framework of similar topology to CHA, suggesting that extraneous physisorbed methanol is stabilized within such cavities at these reaction conditions ( $>10$  kPa, 415 K) and inhibits DME formation rates. Therefore, turnover rates ( $r_{\text{DME}}$ ) on H-CHA zeolites were regressed to a modified rate expression (eq 8.3) that includes an ad-hoc correction ( $k_{\text{inhibit}}$ ) to account for the inhibition observed at higher methanol pressures in order to estimate first-order ( $k_{\text{first}}$ ) and zero-order ( $k_{\text{zero}}$ ) dehydration rate constants (derivation of rate law in Section 8.7.3, Supporting Information).

$$r_{\text{DME},A} = \frac{k_{\text{first},A} P_{\text{CH}_3\text{OH}}}{1 + \frac{k_{\text{first},A}}{k_{\text{zero},A}} P_{\text{CH}_3\text{OH}} + \frac{k_{\text{first},A}}{k_{\text{inhibit},A}} P_{\text{CH}_3\text{OH}}^2} \quad (8.3)$$

Zero-order rate constants for the associative pathway reflect free energy differences between DME formation transition states and protonated methanol dimer precursors of different cationic charge distribution but of similar size; thus, they are sensitive to differences in acid strength but are effectively insensitive to van der Waals interactions with confining environments [22, 82]. Zero-order rate constants for the associative pathway on isolated  $\text{H}^+$  sites in CHA are similar (within 25%, 415 K) to those in H-MFI (Figure 8.5), suggesting that isolated protons in CHA are similar in acid strength to those in MFI. These findings are consistent with DFT-predicted DPE values, a probe-independent measure of Brønsted acid strength, for  $\text{H}^+$  sites at isolated Al atoms in zeolites that become insensitive to T-site geometry and zeolite topology (DPE: 1185-1215  $\text{kJ mol}^{-1}$ ) [16] when rigorously ensemble-averaged among the different O atoms at each framework Al center. The insensitivity of acid strength to the location of Al atoms, when isolated within an insulating silica lattice, reflects the similar stabilities of conjugate anions formed upon deprotonation and their weak dependence on local geometry [16].

First-order rate constants for the associative pathway reflect free energy differences between DME formation transition states and hydrogen-bonded methanol monomer precursors of different cationic charge distribution and size; thus, they are sensitive to differences in both acid strength and confinement [22, 82]. First-order rate constants for the associative pathway were nearly an order of magnitude larger (415 K) on isolated  $\text{H}^+$  sites in H-CHA than in H-MFI (Figure 8.5), reflecting preferential stabilization of larger transition states over smaller methanol monomers within the more confining environments of CHA, given the similar acid strength of isolated protons in zeolitic frameworks. The dependence of methanol dehydration first-order rate constants reported for zeolites of widely varying pore size (0.5-1.2 nm free sphere diameter) [22] allows estimating the effective reaction volume in H-CHA from its first-order rate constant and suggests that methanol dehydration in CHA zeolites occurs within void sizes characteristic of 6-MR and 8-MR (Section 8.7.3, Supporting Information). Additionally, first-order and zero-order rate constants (per  $\text{H}^+$ , 415 K) on isolated  $\text{H}^+$  sites in CHA zeolites synthesized in fluoride media (Figure 8.5) are equivalent to those on CHA zeolites synthesized in hydroxide media, providing evidence that these samples contain only isolated framework Al atoms and protons of indistinguishable acid strength.

#### 8.2.4 Methanol dehydration catalysis on H-CHA zeolites containing paired protons.

Methanol dehydration rates are shown as a function of methanol pressure in Figure 8.7 for H-CHA zeolites of fixed composition ( $\text{Si}/\text{Al}_f = 14\text{-}17$ ), but with systematically increasing percentages of paired Al (0-44%). All rates were uncorrupted by intraparticle transport artifacts ( $\eta > 0.95$ ; Figure 8.6), and kinetic data for all samples can be found in Section 8.7.3 of the Supporting Information. Methanol dehydration rates on each H-CHA zeolite containing paired protons decreased at higher methanol pressures ( $>10$  kPa, Figure 8.7) concomitant with the formation of methanol clusters (ca.  $3370\text{ cm}^{-1}$ ; Section 8.7.4, Supporting Information) at high methanol pressures, as observed for H-CHA zeolites containing only isolated protons. Methanol dehydration turnover



rates on H-CHA (415 K), normalized per total proton, increased systematically with the fraction of protons compensating paired framework Al sites, over the entire range of methanol pressures studied.

Turnover rates measured on a given H-CHA zeolite were regressed to eq 8.3 in order to estimate first-order and zero-order rate constants, which are plotted in Figure 8.9 as a function of paired Al content. Rate constants were described using a weighted average of contributions (via eq 8.3) from isolated and paired protons on each sample, which allowed estimation of their individual first-order and zero-order rate constants (discussion in Section 8.7.3, Supporting Information); these are shown by the values extrapolated to 0% and 100% paired Al in Figure 8.9 and listed in Table 8.1. This kinetic treatment indicates that first-order and zero-order rate constants (per  $\text{H}^+$ , 415 K) in H-CHA are nearly an order of magnitude larger on paired protons than on isolated protons (Figure 8.9, Table 8.1).

Coincidentally, the crystallite sizes of CHA zeolites generally decreased with increasing paired Al content (Table 8.1). Possible contributions of ameliorated intraparticle transport restrictions to the turnover rate enhancements observed with increased paired Al content were further probed by synthesizing a CHA zeolite of similar composition ( $\text{Si}/\text{Al} = 16$ ;  $\text{TMAda}^+$  as the sole SDA), but with a smaller crystallite size using the hexadecyltrimethylammonium bromide (CTAB) surfactant to arrest crystal growth [457]. SEM micrographs of this CHA zeolite showed crystallites of ca. 800 nm diameter (Section 8.7.2, Supporting Information), which contained a small fraction of paired Al sites (6% paired Al) that presumably result from the presence of an additional quaternary amine (CTAB) during crystallization. Methanol dehydration rate constants (per  $\text{H}^+$ , 415 K) measured on this sample (Table 8.1, Figure 8.9) are equivalent to values expected from the correlation between dehydration rate constants and paired Al content measured on larger CHA crystallites (1–2  $\mu\text{m}$ ; Figure 8.9). Intraparticle concentration gradients are also predicted to be negligible within 800 nm diameter CHA crystallites ( $\eta > 0.95$ ; Figure 8.6). These results support the conclusion that methanol dehydration turnover rates measured here on CHA

zeolites of fixed composition ( $\text{Si}/\text{Al} = 15$ ;  $<2\ \mu\text{m}$  diam) are kinetic in origin, and that turnover rate enhancements reflect contributions from larger fractions of paired proton ensembles. The order-of-magnitude larger rate constants at paired protons may reflect lower apparent Gibbs free energy differences for the associative dehydration pathway, or the stabilization of intermediates that mediate dissociative dehydration pathways.

*in situ* IR spectra of H-CHA zeolites containing paired protons (Section 8.7.4, Supporting Information) showed formation of hydrogen-bonded methanol monomers at low pressures ( $<1\ \text{kPa}$ ) and protonated methanol dimers at higher pressures ( $>3\ \text{kPa}$ ), as observed for H-MFI and H-CHA zeolites containing only isolated protons. Yet, H-CHA zeolites containing paired protons also showed surface methoxy deformation modes (ca.  $1457\ \text{cm}^{-1}$ ) at low methanol pressures ( $<3\ \text{kPa}$ ; Figure 8.10), which appear as shoulders that overlap with deformation modes of gaseous methanol ( $1454\ \text{cm}^{-1}$ ) at higher pressures ( $>3\ \text{kPa}$ ). Integrated areas of surface methoxy deformation modes in CHA zeolites of similar total proton content, measured in the first-order kinetic regime at fixed  $\text{CH}_3\text{OH}$  pressure ( $0.77\ \text{kPa}$ ,  $415\ \text{K}$ ), increased linearly with paired Al content (Figure 8.10, inset), consistent with stabilization of surface methoxy species at paired protons. These quantitative spectral data provide direct evidence that the dissociative dehydration pathway can prevail on paired protons in H-CHA, which appears to accelerate observed dehydration turnovers by an order of magnitude ( $415\ \text{K}$ ) relative to those mediated by the associative pathway on isolated protons (Figure 8.9).

### 8.3 Conclusions

These data constitute a predictive synthesis-structure-function relation for the proximity of framework aluminum atoms, and of their charge-compensating extra-framework proton active sites, in single T-site CHA zeolite lattices. Synthesis and structure were connected by crystallizing CHA zeolites using low charge density organic  $\text{TMAda}^+$  cations and high charge density inorganic  $\text{Na}^+$  cations as cooperative

SDAs, in which the amount of  $\text{Na}^+$  retained within crystallized products correlated with the number of paired Al sites formed, which were quantified using validated  $\text{Co}^{2+}$  titration methods. Structure and catalytic function were connected by measuring kinetic rate constants of methanol dehydration to dimethyl ether on CHA zeolites of similar composition but varying paired Al content. Paired protons accelerate dehydration turnover rates by an order of magnitude (415 K) relative to isolated protons, because paired protons appear to stabilize surface methoxy species involved in an alternate dehydration mechanism. An order-of-magnitude difference in methanol dehydration rate constants, here reflecting the distinct catalytic behavior of isolated and paired protons in CHA zeolites, is quantitatively reminiscent of the difference in first-order dehydration rate constants conferred by the diverse confining voids of MFI intersections (ca. 0.7 nm diam.) and FAU supercages (ca. 1.3 nm diam.) [22].

Predictive synthetic control of the arrangement of framework Al atoms in zeolites of fixed composition, especially for those containing a single crystallographically unique T-site, provides opportunities to synthesize materials with tunable catalytic and structural properties, while maintaining a constant bulk density of active sites, if so desired. These synthetic protocols can be used to influence the speciation of extraframework Cu ions, which behave as active sites for the selective catalytic reduction (SCR) of nitrogen oxides with ammonia, because  $\text{Cu}^{2+}$  cations exchange preferentially at paired Al sites while  $[\text{CuOH}]^+$  species exchange at isolated Al sites in CHA zeolites [79]. Isolated framework Al atoms appear less susceptible to hydrothermal dealumination, according to  $^{29}\text{Si}$  NMR studies of steam-treated FAU zeolites that show preferential removal of Al atoms in next-nearest neighbor configurations  $((\text{Si-O})_2\text{-Si-(O-Al)}_2: \delta = -95 \text{ ppm})$  [150].<sup>34</sup> Moreover, the different  $\text{C}_1$  intermediates prevalent at distinct proton active site ensembles in CHA zeolites of similar composition, under identical operating conditions, may have implications for methanol conversion routes in small-pore zeolites, such as methanol-to-olefins (MTO) and methanol-to-hydrocarbons (MTH) catalysis. CHA molecular sieves (e.g., SAPO-34, SSZ-13) convert methanol selectively to ethene and propene,<sup>35,36</sup> but deactivate

upon formation of polycyclic aromatic species within CHA cages that hinder product diffusion [458,459]. The proximity of  $H^+$  sites within CHA zeolites, varied by changing bulk composition, has been proposed to influence the time-on-stream stability during MTO catalysis [158]. Surface methoxy groups have also been implicated as intermediates in hydride transfer reactions with adsorbed olefins [460,461] and in the initiation of C-C bond formation via carbonylation with carbon monoxide or formaldehyde present either as impurities in reactant feeds or formed *in situ* [462,463].

Within the context of aluminosilicate zeolites, these findings represent progress toward developing methods that may enable systematic and predictable control of the arrangement of matter at the atomic scale. The consequent and marked effects of active site proximity on methanol dehydration rate constants among high-symmetry (1 T-site) CHA zeolites of effectively fixed composition, at first glance, contrast the alpha test results of Haag and co-workers [14], in which hexane cracking rates appeared insensitive to the diverse active site ensembles likely present among low-symmetry (12 T-site) MFI zeolites of widely varying composition. This apparent discord can be reconciled by many possibilities, such as if the crystallization procedures of MFI samples studied led to similar Al arrangements, if the alpha test is insensitive to acid site proximity, or if acid site ensembles differ in catalytic function among different zeolite topologies. Nevertheless, the data reported here provide a provocative contrast to the landmark demonstration of Haag and co-workers. They demonstrate that catalytic diversity for the same reaction can be introduced into zeolites of fixed structure and composition, even for frameworks containing a single lattice T-site, through synthetic control of the atomic arrangement of matter.

## 8.4 Experimental Methods

### 8.4.1 Synthesis and preparation of MFI and CHA zeolites.

MFI zeolites (CBV8014, Si/Al = 43; CBV5524G, Si/Al = 30) were obtained from Zeolyst International in their  $NH_4$ -form and converted to their H-form accord-

ing to the procedures described below. CHA zeolites synthesized without  $\text{Na}^+$  in hydroxide media and Si-CHA were prepared by following previously reported procedures [42, 190]. Full details of synthetic procedures can be found in Section 8.7.1 of the Supporting Information.

CHA zeolites were prepared using different Al precursors by adapting procedures described by Deka et al. [84], which is a modified version of the original synthesis reported by Zones [109]. A synthesis molar ratio of  $1 \text{ SiO}_2 / 0.033 \text{ Al}_2\text{O}_3 / 0.25 \text{ TMAdaOH} / 0.125 \text{ Na}_2\text{O} / 44 \text{ H}_2\text{O}$  was used to obtain a  $\text{Si}/\text{Al} = 15$  and  $\text{Na}^+/\text{TMAda}^+ = 1$  in the synthesis solution. A typical synthesis involved adding an aqueous solution of TMAdaOH (25 wt%, Sachem) to deionized  $\text{H}_2\text{O}$  (18.2 M $\Omega$ ) in a perfluoroalkoxy alkane jar (PFA, Savillex Corp.) and stirring the solution under ambient conditions for 15 min. Next, either aluminum hydroxide ( $\text{Al}(\text{OH})_3$ , grade 0325, SPI Pharma), aluminum nitrate nonahydrate ( $\text{Al}(\text{NO}_3)_3$ , 98 wt%, Sigma-Aldrich), aluminum chloride ( $\text{AlCl}_3$ , 99 wt%, Sigma-Aldrich), alumina ( $\text{Al}_2\text{O}_3$ , 99.5 wt%, Alfa Aesar), sodium aluminate ( $\text{NaAlO}_2$ , technical grade, Alfa Aesar), or aluminum isopropoxide ( $\text{Al}(\text{O-i-Pr})_3$ , 98 wt%, Sigma-Aldrich) was added to the aqueous TMAdaOH solution. Then, a 5 M sodium hydroxide solution ( $\text{NaOH}$ : 16.7 wt%  $\text{NaOH}$  in deionized water;  $\text{NaOH}$  pellets 98 wt%, Alfa Aesar) was added dropwise to the synthesis mixture and stirred under ambient conditions for 15 min. Finally, colloidal silica (Ludox HS40, 40 wt%, Sigma-Aldrich) was added and the mixture was covered and stirred for 2 h under ambient conditions. All synthesis reagents were used without further purification. The synthesis solution was then transferred to a 45 mL Teflon-lined stainless steel autoclave (Parr Instruments) and placed in a forced convection oven (Yamato DKN-402C) at 433 K and rotated at 40 rpm for 6 days.

CHA zeolites were also synthesized in fluoride media using only  $\text{TMAda}^+$  as the SDA and without  $\text{Na}^+$  present following the procedure reported by Eilertsen et al. [168], using a molar ratio of  $1 \text{ SiO}_2 / 0.0167 \text{ Al}_2\text{O}_3 / 0.5 \text{ TMAdaOH} / 0.5 \text{ HF} / 3 \text{ H}_2\text{O}$ . In a typical synthesis,  $\text{Al}_2\text{O}_3$  was added to an aqueous TMAdaOH solution in a PFA jar and the mixture was stirred for 15 min under ambient conditions. Then,

tetraethylorthosilicate (TEOS, 98 wt%, Sigma-Aldrich) was added to the mixture, and the contents were covered and stirred for 2 h at ambient conditions until a homogeneous solution was obtained. Next, ethanol (200 proof, Koptec) was added to the synthesis solution and left uncovered to allow ethanol and excess water to evaporate in order to reach the target molar ratios. Once the synthesis solution had reached the desired  $\text{H}_2\text{O}/\text{SiO}_2$  ratio, concentrated hydrofluoric acid (HF; 48 wt%, Sigma-Aldrich) was added dropwise to the synthesis and homogenized for 15 min by hand. ***Caution: when working with hydrofluoric acid use appropriate personal protective equipment, ventilation, and other safety measures.*** Upon addition of HF, the solution immediately became a thick paste. The mixture was then left to sit uncovered under ambient conditions for 30 min to allow any residual HF to evaporate before transferring the solution to a 45 mL Teflon-lined stainless steel autoclave and heated in a forced convection at 423 K under rotation at 40 rpm for 6 days.

CHA zeolites were synthesized with 800 nm crystallite diameters following the procedure reported by Li et al. [457], but omitting the NaOH addition. First, a  $\text{Na}^+$ -free CHA synthesis solution was prepared (Section 8.7.1, Supporting Information), placed in a 45 mL Teflon-lined stainless steel autoclave and heated in a forced convection oven at 433 K while rotating at 40 rpm for 1 day. The autoclave was removed from the oven and quenched in a room temperature water bath for 4 h. After cooling to ambient conditions, hexadecyltrimethylammonium bromide (CTAB, 99 wt%, Sigma-Aldrich) was added to the synthesis mixture to act as a crystal growth inhibitor [457, 464]. The CTAB containing synthesis mixture was then returned to the autoclave and heated at 433 K and rotated at 40 rpm for 9 additional days.

Zeolite crystallization products were isolated via centrifugation and washed thoroughly with deionized water (18.2 M $\Omega$ ) and acetone (99.9 wt%, Sigma-Aldrich) in alternating steps (70 cm<sup>3</sup> solvent g<sup>-1</sup> per wash) until the pH of the supernatant remained constant between washes, followed by a final water wash to remove residual acetone. Solids were recovered via centrifugation, dried at 373 K under stagnant air for 24 h, and then treated in flowing dry air (1.67 cm<sup>3</sup> s<sup>-1</sup> g<sup>-1</sup>, 99.999% UHP, Indiana

Oxygen) at 853 K ( $0.0167 \text{ K s}^{-1}$ ) for 10 h. Residual  $\text{Na}^+$  was removed by converting to the  $\text{NH}_4$ -form via ion-exchange using  $150 \text{ cm}^3$  of an aqueous 1 M  $\text{NH}_4\text{NO}_3$  solution (8.0 wt% in  $\text{H}_2\text{O}$ ; 99.9 wt%, Sigma-Aldrich) per gram zeolite, and stirring for 24 h under ambient conditions. Solids were recovered via centrifugation and washed four times with deionized water ( $70 \text{ cm}^3 \text{ g}^{-1}$  per wash). Recovered  $\text{NH}_4$ -form zeolites were then dried at 373 K under stagnant air for 24 h, and converted to their H-form by treatment in flowing dry air ( $1.67 \text{ cm}^3 \text{ s}^{-1} \text{ g}^{-1}$ , 99.999% UHP, Indiana Oxygen) at 773 K ( $0.0167 \text{ K s}^{-1}$ ) for 4 h.

#### 8.4.2 Characterization of CHA and MFI zeolites.

Detailed experimental procedures and characterization data for all samples can be found in Section 8.7.2 of the Supporting Information. Error reported for elemental analysis of Al, Na, and Co, and  $\text{NH}_3$  TPD was determined for each data point by error propagation of experimentally measured variables to the calculated value.

CHA and MFI crystal topologies were measured using powder X-ray diffraction (XRD) and confirmed by comparison with an experimental reference and the CHA and MFI diffraction patterns reported in the International Zeolite Association (IZA) structure database [1]. Argon (87 K) and nitrogen (77 K) adsorption isotherms were used to estimate micropore volumes of CHA and MFI zeolites, respectively. Elemental composition (Al, Na, Co) of each zeolite was measured using atomic absorption spectroscopy (AAS). Thermogravimetric analysis (TGA) was used to measure the organic content of synthesized CHA zeolite products. The crystal sizes of all CHA zeolites were estimated from scanning electron microscopy (SEM) micrographs and averaged over a distribution of individual crystal sizes taken from different regions of the SEM sample stage. The number of  $\text{H}^+$  sites on CHA and MFI zeolites was quantified by temperature-programmed desorption (TPD) of samples after aqueous ion-exchange with  $\text{NH}_4^+$  cations, while the number of  $\text{H}^+$  sites remaining after Cu or Co-exchange of CHA zeolites was quantified from TPD of samples using gas-phase  $\text{NH}_3$  titrations with purging treatments to remove all non-Brønsted bound  $\text{NH}_3$  from

samples, as reported elsewhere [78, 171].  $^{27}\text{Al}$  magic angle spinning nuclear magnetic resonance (MAS NMR) spectra were recorded under ambient conditions on H-CHA zeolite samples to quantify their fraction of framework and extraframework Al.

$\text{Co}^{2+}$  titrations were performed on H-CHA zeolites via ion-exchange with  $150\text{ cm}^3$  of an aqueous  $0.25\text{ M Co}(\text{NO}_3)_2$  (4.6 wt%  $\text{Co}(\text{NO}_3)_2$ ; 99 wt%, Sigma-Aldrich) solution per gram of zeolite for 4 h at ambient conditions under stirring. The pH of the solution was not controlled and reached a stable value of ca. 3.3 after 4 h. After ion-exchange, the samples were recovered using centrifugation, washed four times with deionized water ( $70\text{ cm}^3$  per g solids per wash), and dried at 373 K under stagnant air for 24 h. Co-exchanged CHA zeolites were then treated in flowing dry air ( $1.67\text{ cm}^3\text{ s}^{-1}\text{ g}^{-1}$ , 99.999% UHP, Indiana Oxygen) at 773 K ( $0.0167\text{ K s}^{-1}$ ) for 4 h.

Samples in Table 8.1 are referred to according to the formula: [countercation]-[zeolite framework]-[mineralizing agent] ( $\text{Si}/\text{Al}_f$ , % paired Al). In this nomenclature, the countercation is the extraframework titrant introduced by the ion-exchange step immediately preceding analysis (e.g.,  $\text{NH}_4^+$  or  $\text{Co}^{2+}$ ) or after conversion to the H-form (e.g.,  $\text{H}^+$ ), while no countercation is used to describe zeolites in their directly synthesized form. The zeolite framework is either CHA or MFI, the mineralizing agent is either  $\text{OH}^-$  or  $\text{F}^-$ , the  $\text{Si}/\text{Al}_f$  ratio is determined from elemental analysis (AAS) and  $^{27}\text{Al}$  NMR, and the % paired Al is determined from  $\text{Co}^{2+}$  titration ( $100 \cdot 2 \cdot \text{Co}/\text{Al}$ ). For example, an H-form CHA zeolite synthesized in hydroxide media with a bulk composition of  $\text{Si}/\text{Al}_f = 15$  and 20% paired Al would have the sample name: H-CHA-OH(15,20%).

#### 8.4.3 Measurement of methanol dehydration rates and titration of Brønsted acid sites during catalysis.

Rates of methanol dehydration were measured at differential conversion ( $<10\%$ ) in a tubular packed-bed quartz reactor (7 mm inner diameter) with plug-flow hydrodynamics at 415 K. Catalyst samples were pelleted and sieved to retain particles between 180 and 250  $\mu\text{m}$ . The catalyst charged to the reactor was varied between



0.005 and 0.030 g to maintain differential conversions, and were diluted with Si-CHA (180-250  $\mu\text{m}$ ) to ensure a minimum of 0.025 g of total solids were charged to the reactor. The catalyst bed was supported in the reactor between two quartz wool plugs. Reactor temperatures were controlled using a resistively heated three-zone furnace (Series 3210, Applied Test Systems) and Watlow controllers (EZ-Zone Series). The temperature of the catalyst bed was measured with a K-type thermocouple in direct contact with the external surface of the quartz tube and positioned at the center of the catalyst bed. Methanol (99.9 wt%, Sigma-Aldrich) partial pressures were controlled using a syringe pump (Legato 100, KD Scientific) and injected into flowing He (UHP, Indiana Oxygen) and sent to the reactor through heated transfer lines maintained at  $>373$  K using resistive heating tape (BriskHeat Co.) and insulating wrap. Prior to contact with methanol, samples were treated in a 5%  $\text{O}_2/\text{He}$  flow ( $50\text{ cm}^3\text{ g}^{-1}\text{ s}^{-1}$ , 99.999%, Indiana Oxygen) by heating to 773 K ( $0.033\text{ K s}^{-1}$ ) and holding for 4 h. After cooling to reaction temperature (415 K), the gas stream was switched to He flow ( $150\text{ cm}^3\text{ g}^{-1}\text{ s}^{-1}$ ) while methanol, at a fixed partial pressure, was sent to a gas chromatograph (Agilent 6890GC) via heated transfer lines ( $>373$  K) for bypass calibration. Concentrations of reactants and products were measured using a gas chromatograph equipped with a flame ionization detector (HP Plot-Q KCl column, 0.53 mm ID x 30 m x 40  $\mu\text{m}$  film, Agilent). Only dimethyl ether and water were observed as products at all reaction conditions on all catalysts. Methane (25%  $\text{CH}_4/\text{Ar}$ , 99.999%, Indiana Oxygen) was introduced into the reactor effluent stream at a constant flow rate ( $0.083\text{ cm}^3\text{ s}^{-1}$ ) and used as an internal standard.

The total number of Brønsted acid sites in H-MFI zeolites was measured during steady state methanol dehydration catalysis using *in situ* titration with pyridine on the same reactor unit described above. Steady-state dehydration rates (3.5 kPa  $\text{CH}_3\text{OH}$ , 415 K) were achieved prior to the introduction of pyridine titrants. Pyridine (99.8 wt%, Sigma-Aldrich) was dissolved in methanol and evaporated into a flowing He stream ( $100\text{ cm}^3\text{ g}^{-1}\text{ s}^{-1}$ ) using a syringe pump to attain the desired concentration of reactant and titrant (3.5 kPa methanol, 0.5 Pa pyridine). The total number of

protons titrated was calculated by extrapolation of dehydration rates, measured as a function of the cumulative pyridine dosed to the bed, to values of zero and assuming a 1:1 pyridine:H<sup>+</sup> stoichiometry (Section 8.7.3, Supporting Information).

The internal reproducibility error on methanol dehydration rates for each sample and set of conditions was less than 10%. The uncertainties reported here for methanol dehydration rates on CHA and MFI zeolites were determined for each data point by propagation of error in each experimentally measured variable (e.g., temperature, methanol partial pressure, catalyst mass, proton site content) to calculated rates, in order to provide representative uncertainties for values that may be reproduced by an independent researcher. The uncertainties in first-order and zero-order rate constants were determined from error analysis of a least-squares regression to the measured rate data, accounting for uncertainties in rate measurements.

#### 8.4.4 Measurement of *in situ* IR spectra on CHA and MFI zeolites.

*in situ* IR spectra were collected on a Nicolet 4700 spectrometer with a HgCdTe detector (MCT, cooled to 77 K by liquid N<sub>2</sub>) by averaging 64 scans at a 2 cm<sup>-1</sup> resolution collected between 4000 and 400 cm<sup>-1</sup> range, taken relative to an empty cell background reference collected under dry He flow (0.33 cm<sup>3</sup> s<sup>-1</sup>, UHP, Indiana Oxygen) at 415 K. CHA catalysts were pressed into self-supporting wafers (0.01-0.02 g cm<sup>-2</sup>) and sealed within a custom-built quartz IR cell with CaF<sub>2</sub> windows; a detailed description of the IR cell design can be found elsewhere [465,466]. Wafer temperatures were measured within 2 mm of each side of the wafer by K-type thermocouples (Omega Engineering). The quartz IR cell was interfaced to a syringe pump (Legato 100, KD Scientific) via a stainless-steel transfer line (0.25 in. diameter) that was maintained >353 K using resistive heating tape (BriskHeat Co.) and insulating wrap, in order to deliver liquid reactants to the IR cell. Prior to each IR experiment, the catalyst wafer was treated in flowing dry air (13.3 cm<sup>3</sup> s<sup>-1</sup> g<sup>-1</sup>) purified by an FTIR purge gas generator (Parker Balston, < 1 ppm of CO<sub>2</sub>, 200 K H<sub>2</sub>O dew point) to 773 K (0.083 K s<sup>-1</sup>) for 4 h, and then cooled under flowing He (13.3 cm<sup>3</sup> s<sup>-1</sup> g<sup>-1</sup>) to 415

K. Methanol was introduced into the heated gas stream under steady-state flow, and methanol partial pressures were varied non-systematically between 0.1 and 22 kPa. IR spectra were recorded after equilibration of the surface was achieved (ca. 30 min) and peak intensities remained constant for 15 min. All IR spectra were baseline-corrected and normalized to combination and overtone zeolite T-O-T vibrational modes ( $1750\text{--}2100\text{ cm}^{-1}$ ) only when comparing between different parent CHA samples, because adsorption of methanol on the zeolite surface caused a systematic change to the T-O-T band area with changing methanol pressure 8.50-8.52. An IR spectrum of an empty IR cell under 2 kPa steady-state methanol pressure ( $13.3\text{ cm}^3\text{ s}^{-1}\text{ g}^{-1}\text{ He}$ ) was used as a reference for gas-phase methanol vibrational modes observed in spectra of catalyst wafers recorded under steady-state methanol pressure.

## 8.5 Acknowledgements

We acknowledge the financial support from the National Science Foundation under award number 1552517-CBET. We thank Sachem, Inc., for providing the organic structure-directing agent used to synthesize CHA zeolites, and Mark Davis (Caltech) and Michiel Dusselier (KU Leuven) for providing the AEI zeolite sample. We also thank John Harwood (Purdue Interdepartmental NMR Facility) for assistance collecting NMR spectra, Michael Cordon for assistance collecting SEM micrographs, and Hyun Chang Kim and You-Yeon Won (Purdue) for DLS measurements. Finally, we thank David Hibbitts (Florida), Juan Carlos Vega-Vila, and Jason Bates for technical discussions and feedback on this manuscript.

Additionally, I acknowledge the American Chemical Society for granting permission to reproduce this chapter of my thesis. Adapted with permissions from ACS Catalysis, 2017, 7, 6663-6674. Copyright (2017) American Chemical Society. The full article can be accessed here: [dx.doi.org/10.1021/acscatal.7b01273](https://doi.org/10.1021/acscatal.7b01273).

Table 8.1.  
Characterization Data and Methanol Dehydration Rate Constants for  
CHA Zeolites Synthesized at Different Compositions and with Different  
Fractions of Paired Al Sites in OH<sup>-</sup> and F<sup>-</sup> Media.

| Sample <sup>a</sup>           | Synthetic Details  |  |                                    |   | Al Arrangement   |   | Rate Constants (415 K)                             |                                 |                                |
|-------------------------------|--------------------|--|------------------------------------|---|--|---|--|---------------------------------|--------------------------------|
|                               | Si/Al <sub>f</sub> | H <sup>+</sup> /Al <sub>f</sub> <sup>b</sup> | Organic Content / wt% <sup>c</sup> | Crystal Size / $\mu\text{m}$ <sup>d</sup> | Occluded Na <sup>+</sup> /Al <sub>tot</sub> <sup>e</sup> | Al <sub>iso</sub> /Al <sub>tot</sub> <sup>f</sup> | Al <sub>pair</sub> /Al <sub>tot</sub> <sup>f</sup> | k <sub>first</sub> <sup>g</sup> | k <sub>zero</sub> <sup>h</sup> |
| CHA-OH(14,0%)                 | 14                 | 0.95   | 18.4                               | 2   | <0.01  | 1.00  | 0.00   | 22±4                            | 14±2                           |
| CHA-OH(17,0%)                 | 17                 | 1.00   | 22.5                               | 2   | <0.01  | 1.00  | 0.00   | 23±4                            | 12±2                           |
| CHA-OH(27,0%)                 | 27                 | 1.00   | 21.3                               | 6   | <0.01  | 1.00  | 0.00   | 9±2 <sup>i</sup>                | 11±2                           |
| CHA-F(18,0%)                  | 18                 | 1.02   | 22.9                               | 1   | <0.01  | 1.00  | 0.00   | 24±4                            | 13±2                           |
| CHA-OH(16,6%)                 | 16                 | 0.93   | n.m.*                              | 0.8                                       | n.m.*  | 0.94  | 0.06   | 22±3                            | 25±4                           |
| CHA-OH(15,18%)                | 15                 | 1.01   | 21.6                               | 1   | 0.05   | 0.82  | 0.18   | 36±7                            | 28±4                           |
| CHA-OH(16,24%)                | 16                 | 1.16 <sup>j</sup>                            | 20.1                               | 1   | n.m.*  | 0.76  | 0.24   | 32±8                            | 22±2                           |
| CHA-OH(17,30%)                | 17                 | 0.97   | 21.0                               | 1   | 0.25   | 0.70  | 0.30   | 40±8                            | 34±8                           |
| CHA-OH(14,44%)                | 14                 | 1.00   | 19.8                               | 0.3                                       | 0.26   | 0.56  | 0.44   | 85±17                           | 40±6                           |
| Isolated protons <sup>k</sup> | -                  | -  | -                                  | -   | -  | -   | -  | 18                              | 16                             |
| Paired protons <sup>l</sup>   | -                  | -  | -                                  | -   | -  | -   | -  | 130                             | 70                             |

<sup>a</sup> As explained in Section 4.2, samples are referred to by: [counter-cation]-[framework]-[mineralizing agent](Si/Al<sub>f</sub>, % paired Al).

<sup>b</sup> Error in H<sup>+</sup>/Al<sub>f</sub> from NH<sub>3</sub> TPD experiments is ±0.05.

<sup>c</sup> Expected organic content for one TMAda<sup>+</sup> per CHA cage: 22.7 wt%.

<sup>d</sup> Estimated from SEM micrographs. Error in crystal diameter is ±0.5  $\mu\text{m}$ .

<sup>e</sup> Na/Al<sub>tot</sub> retained on the synthesized zeolite product. Error in Na<sup>+</sup>/Al<sub>tot</sub> values is 12%.<sup>f</sup> Error in Al<sub>iso</sub>/Al<sub>tot</sub> and Al<sub>pair</sub>/Al<sub>tot</sub> is 10%.

<sup>g</sup> Units of k<sub>first</sub>: 10<sup>-3</sup> mol DME (mol H<sup>+</sup> s kPa)<sup>-1</sup>. Error determined from least-squares regression for each sample.

<sup>h</sup> Units of k<sub>zero</sub>: 10<sup>-3</sup> mol DME (mol H<sup>+</sup> s)<sup>-1</sup>. Error determined from least-squares regression for each sample.

<sup>i</sup> Values of k<sub>first</sub> for CHA-OH(27,0%) are corrupted by intraparticle mass transfer.

<sup>j</sup> H<sup>+</sup>/Al<sub>tot</sub> = 1.02 for CHA-OH(16,24%), suggestive of reversible Al structural changes upon hydration to acquire NMR spectra.

<sup>k,l</sup> First and zero-order rate constants on isolated and paired protons in CHA zeolites predicted from Figure 6.

\*n.m., not measured.

## 8.6 Figures and Tables

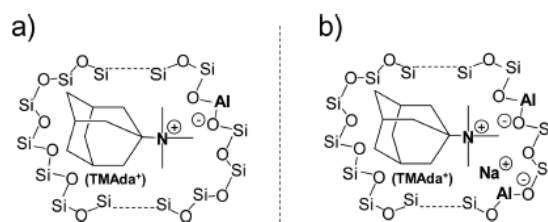


Figure 8.1. Schematic Representation of the Organization of Si and Al Atoms in the Crystallizing Polyanionic CHA Framework To Form (a) Isolated Al with Only TMAda<sup>+</sup> or (b) Paired Al in the Presence of TMAda<sup>+</sup> and Na<sup>+</sup> (adapted from Di Iorio et al [42]).

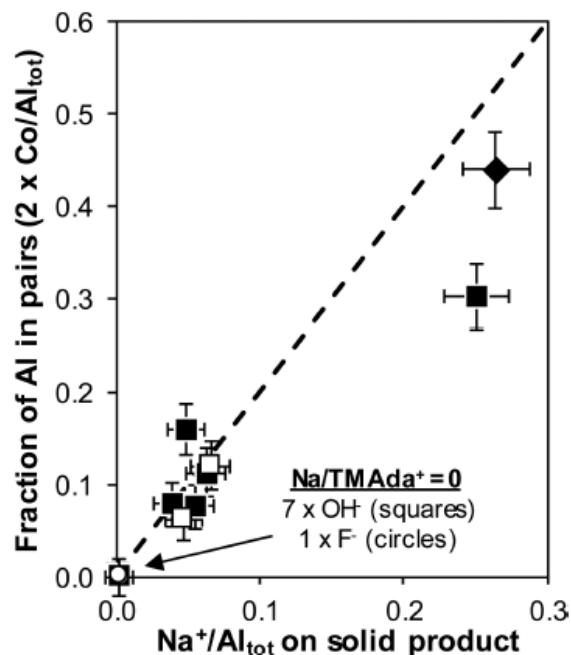


Figure 8.2. Fraction of Al in pairs as a function of Na<sup>+</sup> retained on CHA products of fixed composition ( $\text{Si}/\text{Al}_f = 14\text{--}18$ ) crystallized in OH<sup>-</sup> (squares) media with  $\text{Na}^+/\text{TMAda}^+ \leq 1$  (filled),  $\text{Na}^+/\text{TMAda}^+ > 1$  (open), and F<sup>-</sup> (open circle) media using Al(OH)<sub>3</sub> and Al(O-i-Pr)<sub>3</sub> (diamond) as aluminum sources. The dashed line represents the parity line (slope = 2) expected if each Na<sup>+</sup> cation formed a paired Al site. Eight independent CHA samples crystallized using only TMAda<sup>+</sup> are plotted at the origin.

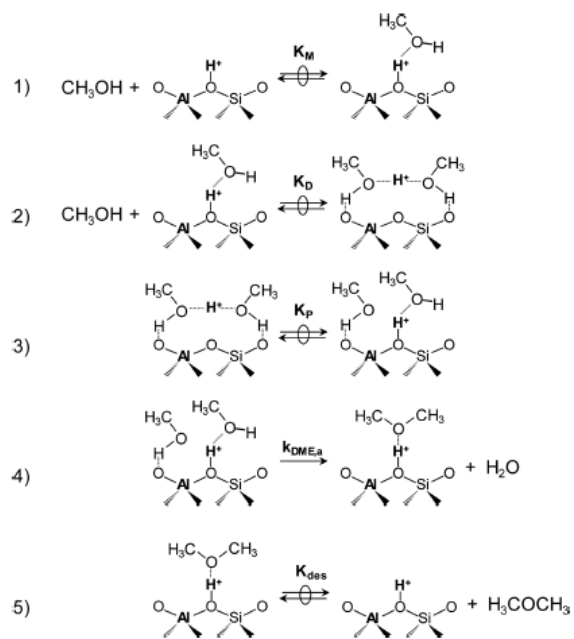


Figure 8.3. Elementary Steps in the Associative Methanol Dehydration Pathway (adapted from Carr et al [82]).

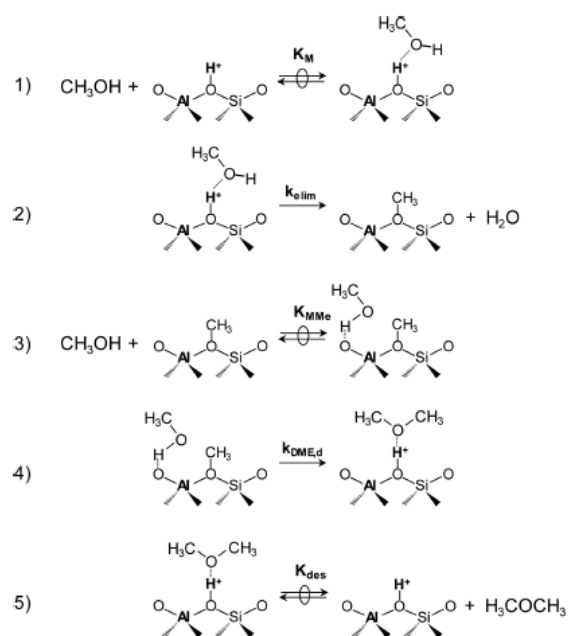


Figure 8.4. Elementary Steps in the Dissociative Methanol Dehydration Pathway (adapted from Carr et al [82]).



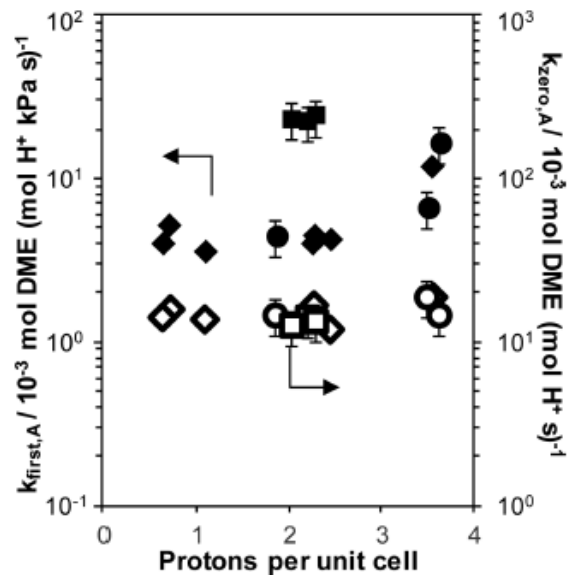


Figure 8.5. First-order (closed) and zero-order (open) associative methanol dehydration rate constants (per  $\text{H}^+$ ) as a function of  $\text{H}^+$  density (per unit cell) on H-zeolites. Data shown for H-CHA samples crystallized in  $\text{OH}^-$  and  $\text{F}^-$  media ( $\text{Si}/\text{Al} = 14\text{--}18$ ) to contain only isolated protons at 415 K, (squares), for commercial H-MFI samples ( $\text{Si}/\text{Al} = 17\text{--}43$ , Zeolyst) at 415 K (circles), and for H-MFI samples ( $\text{Si}/\text{Al} = 17\text{--}120$ , inclusive of commercial Zeolyst samples) reported by Jones et al. [83] at 433 K (diamonds).

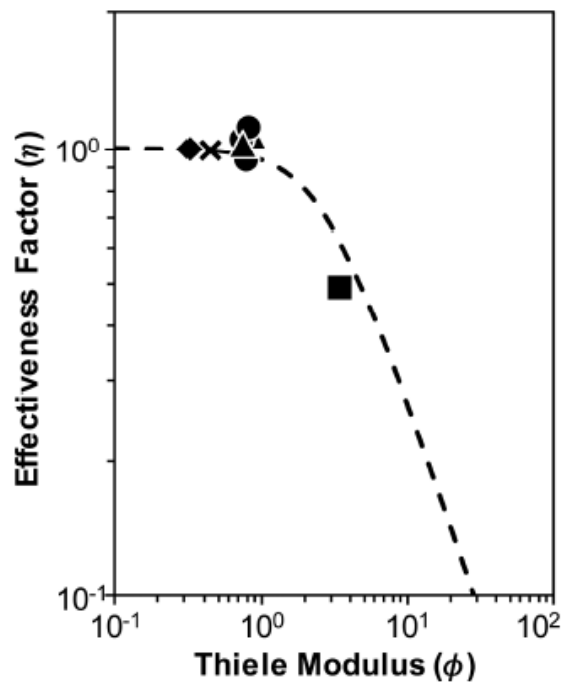


Figure 8.6. Dependence of the intraparticle effectiveness factor on the Thiele modulus for methanol dehydration on H-CHA zeolites with  $\text{Si}/\text{Al}_f = 14\text{-}18$  with 0% (circles), 18-30% (triangles), and 44% (diamond) paired Al. Data also shown for H-CHA with  $\text{Si}/\text{Al}_f = 27$  (square), and H-CHA synthesized with CTAB (cross). Dashed line is the effectiveness factor predicted for a first-order reaction in a spherical pellet (Section 8.7.5, Supporting Information).

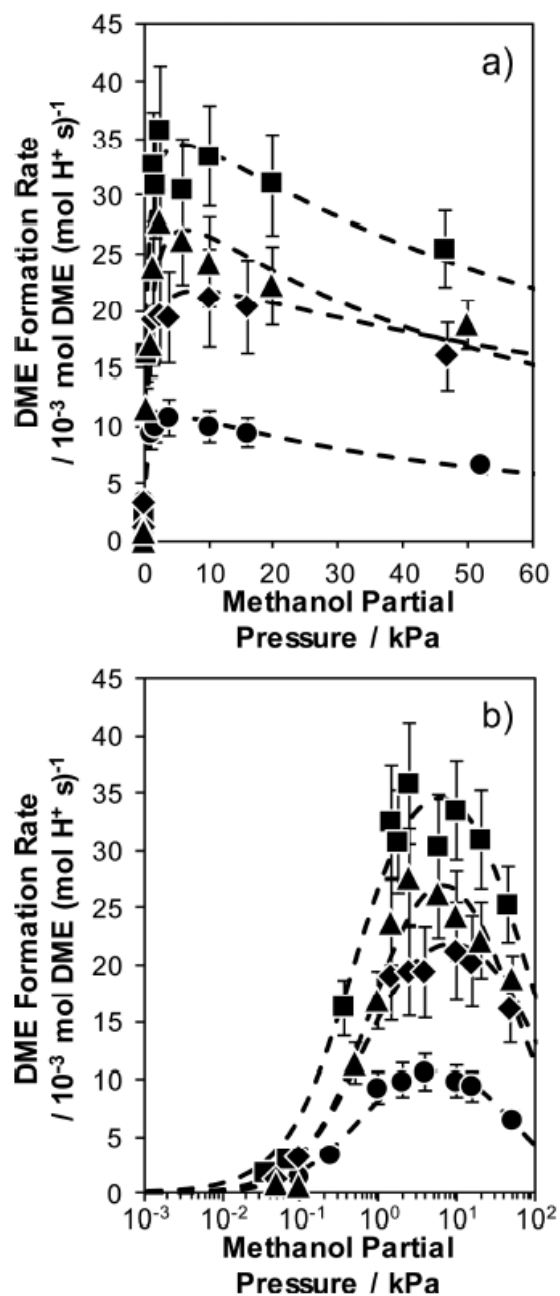


Figure 8.7. DME formation rates (per  $H^+$ , 415 K) as a function of methanol pressure on (a) linear and (b) logarithmic axes (for clarity) for H-CHA with 0% (circles), 18% (diamonds), 30% (triangles), and 44% (squares) paired Al. Dashed lines represent best fits of the methanol dehydration rate expression (eq 8.3) regressed to the data.

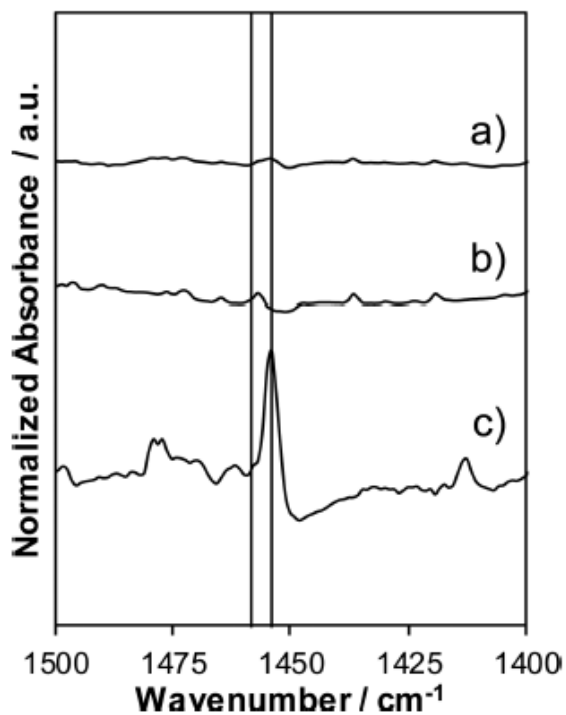


Figure 8.8. *in situ* IR spectra of (a) H-CHA ( $\text{Si}/\text{Al}_f = 14$ ) containing only isolated protons and (b) H-MFI ( $\text{Si}/\text{Al} = 43$ , Zeolyst) under 0.77 kPa  $\text{CH}_3\text{OH}$  at 415 K. Vertical dashed lines indicate the location of surface ( $1457\text{ cm}^{-1}$ ) and (c) gas-phase ( $1454\text{ cm}^{-1}$ ) methoxy deformation modes.

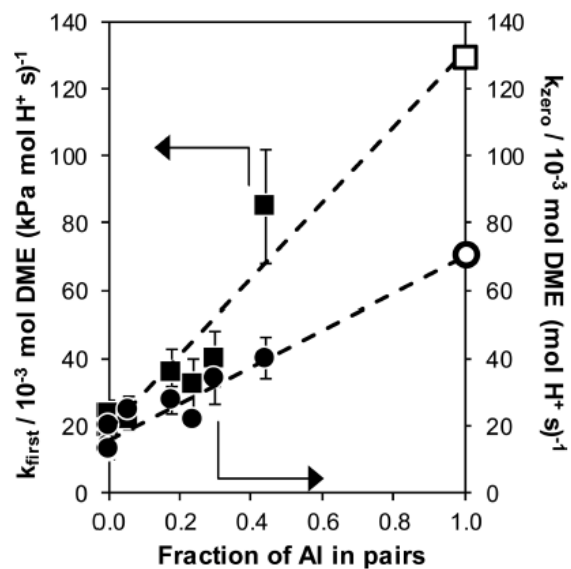


Figure 8.9. First-order (squares) and zero-order (circles) rate constants (415 K, per  $\text{H}^+$ ) on CHA zeolites ( $\text{Si}/\text{Al}_f = 14\text{--}18$ ) as a function of the fraction of Al in pairs. Dashed lines are linear regressions to the data points (solid). Extrapolated dehydration rate constants for paired protons are shown as open symbols.

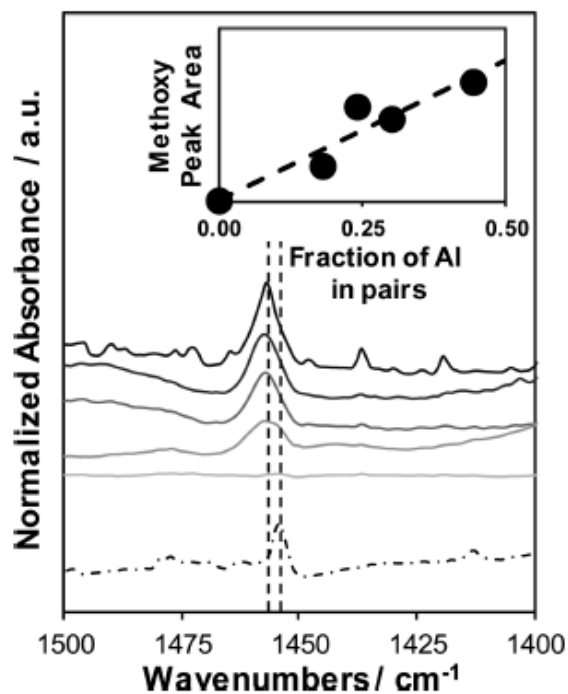


Figure 8.10. *in situ* IR spectra of H-CHA ( $\text{Si}/\text{Al}_f = 14\text{-}17$ ) containing 0-44% paired Al (light to dark) under 0.77 kPa  $\text{CH}_3\text{OH}$  (415 K). Dashed lines indicate the location of surface ( $1457\text{ cm}^{-1}$ ) and gas-phase ( $1454\text{ cm}^{-1}$ ; dash-dotted spectrum) methoxy deformation modes. The inset shows the integrated area of the surface methoxy peak as a function of the fraction of Al in pairs.

Table 8.2.

Weights (in grams) of synthesis reagents used in the crystallization of CHA zeolites with different Al precursors and equimolar amounts of  $\text{Na}^+$  and  $\text{TMAda}^+$  in  $\text{OH}^-$  media.

| Al precursor used            | Al source | Colloidal $\text{SiO}_2$ | 5M $\text{NaOH}$ | TMAdaOH | $\text{H}_2\text{O}$ |
|------------------------------|-----------|--------------------------|------------------|---------|----------------------|
| $\text{Al}(\text{OH})_3$     | 0.109 g   | 3.150 g                  | 1.284 g          | 4.432 g | 10.34 g              |
| $\text{Al}(\text{NO}_3)_3$   | 0.530 g   | 3.150 g                  | 1.284 g          | 4.432 g | 10.34 g              |
| $\text{AlCl}_3$              | 0.188 g   | 3.150 g                  | 1.284 g          | 4.432 g | 10.34 g              |
| $\text{Al}_2\text{O}_3$      | 0.114 g   | 3.150 g                  | 1.284 g          | 4.432 g | 10.34 g              |
| $\text{NaAlO}_2$             | 0.184 g   | 3.150 g                  | 1.154 g          | 4.432 g | 9.623 g              |
| $\text{Al}(\text{O-i-Pr})_3$ | 0.288 g   | 3.150 g                  | 1.284 g          | 4.432 g | 10.34 g              |

## 8.7 Supporting Information

### 8.7.1 Synthesis and ion-exchange of CHA and MFI zeolites

#### Synthesis of CHA zeolites with different Al precursors

The procedure for preparing CHA zeolites using various Al precursors is described in the main text. Table 8.2 shows the weights of various reagents used during crystallization.

#### Synthesis of $\text{Na}^+$ -free CHA zeolites in $\text{OH}^-$ media

$\text{Na}^+$ -free CHA zeolites were synthesized in hydroxide media at different compositions ( $\text{Si}/\text{Al} = 15\text{-}30$ ) following previously reported procedures [42]. Briefly, a molar ratio of  $1 \text{ SiO}_2 / X \text{ Al}_2\text{O}_3 / 0.5 \text{ TMAdaOH} / 44 \text{ H}_2\text{O}$  was used, where X is the desired Al content to reach a Si/Al molar ratio of 15 or 30. In a typical synthesis, an aqueous TMAdaOH solution was added to deionized water in a perfluoroalkoxy alkane (PFA) jar and stirred for 15 minutes under ambient conditions. Next,  $\text{Al}(\text{OH})_3$  was added to the TMAdaOH solution and the mixture was stirred for 15 minutes under

ambient conditions. Then, colloidal silica was added to the mixture and the contents were stirred for 2 h at ambient conditions until a homogeneous solution was obtained. All synthesis reagents were used without further purification. The synthesis solution was then transferred to a 45 ml Teflon-lined stainless steel autoclave and heated in a forced convection oven at 433 K and rotated at 40 RPM for 6 days.

#### Synthesis of Si-CHA zeolites in $F^-$ media

Pure  $SiO_2$  chabazite was synthesized following a previously reported procedures [42, 190] using a synthesis solution molar ratio of 1  $SiO_2$ / 0.5 TMAdaOH/ 0.5 HF/ 3  $H_2O$ . In a typical synthesis, TEOS was added to a PFA jar containing an aqueous TMAdaOH solution and stirred under ambient conditions. Ethanol, formed from the hydrolysis of TEOS, and excess water were then evaporated under ambient conditions to reach target molar ratios. Once the synthesis solution had reached the desired  $H_2O/SiO_2$  ratio, hydrofluoric acid (HF) was added dropwise to the synthesis and homogenized for 15 minutes. Caution: when working with HF acid, use appropriate personal protective equipment, ventilation, and other safety measures. The mixture was then left to sit uncovered under ambient conditions for 30 minutes to allow for any residual HF to evaporate before transferring the solution to a 45 ml Teflon-lined stainless steel autoclave and heated in a forced convection oven at 423 K under rotation at 40 RPM for 40 h.

#### 8.7.2 Characterization of CHA and MFI zeolites

##### Characterization data of all zeolites

Samples are labeled using the formula prescribed in the main text: [counter-cation]-[zeolite framework]-[mineralizing agent](Si/ $Al_f$ , % paired Al). Tables 8.3-8.6 contain characterization and kinetic data for CHA zeolites synthesized without  $Na^+$  in  $OH^-$  and  $F^-$  media (Table 8.3), with various Al precursors using equimolar amounts of  $Na^+$  and TMAda<sup>+</sup> (Table 8.4), with  $Al(OH)_3$  and equimolar amounts of  $Na^+$  and



Table 8.3.

Characterization data of CHA zeolites synthesized using  $\text{Al}(\text{OH})_3$  as the aluminum source, without  $\text{Na}^+$  in  $\text{OH}^-$  and  $\text{F}^-$  media.

| Sample        | Characterization and Site Distribution |                                 |  |                          |   | Kinetics                                     |                               |                              |
|---------------|--|---------------------------------|--|--------------------------|---|--|-------------------------------|------------------------------|
|               | Si/ $\text{Al}_\text{f}$               | $\text{H}^+/\text{Al}_\text{f}$ | Micropore Volume<br>/ $\text{cm}^3 \text{ g}^{-1}$ | Organic Content<br>/ wt% | $\text{Al}_{\text{iso}}/\text{Al}_\text{f}$ | $\text{Al}_{\text{pair}}/\text{Al}_\text{f}$ | $k_{\text{first}}^{\text{a}}$ | $k_{\text{zero}}^{\text{b}}$ |
| CHA-OH(14,0%) | 14                                     | 0.95                            | 0.18   | 18.4                     | 1   | 0  | 21.9                          | 13.9                         |
| CHA-OH(17,0%) | 17                                     | 1.00                            | 0.21   | 22.5                     | 1   | 0  | 22.6                          | 12.3                         |
| CHA-OH(27,0%) | 27                                     | 1.00                            | 0.17   | 21.3                     | 1   | 0  | 8.8                           | 11.1                         |
| CHA-F(17,0%)  | 17                                     | 0.55                            | 0.12   | 29.9                     | 1   | 0  | n.m.                          | n.m.                         |
| CHA-F(18,0%)  | 18                                     | 1.02                            | 0.21   | 22.9                     | 1   | 0  | 23.7                          | 13.1                         |

<sup>a</sup> Units of  $k_{\text{first}}$ :  $10^{-3} \text{ mol DME (mol H}^+ \text{ s kPa)}^{-1}$

<sup>b</sup> Units of  $k_{\text{zero}}$ :  $10^{-3} \text{ mol DME (mol H}^+ \text{ s)}^{-1}$

$\text{TMAda}^+$  and inclusion of hexadecyltrimethylammonium bromide (CTAB; Table 8.5), and for MFI zeolites (Table 8.6). Each table includes micropore volumes determined from adsorption isotherms (Section 8.7.2, bulk Si/Al ratio from atomic absorption spectroscopy (Section 8.7.2), organic content measured by thermogravimetric analysis (Section 8.7.2),  $\text{H}^+/\text{Al}$  values measured from  $\text{NH}_3$  temperature programmed desorption (Section 8.7.2), and the fraction of isolated ( $\text{Al}_{\text{iso}}/\text{Al}_{\text{tot}}$ ) and paired ( $\text{Al}_{\text{pair}}/\text{Al}_{\text{tot}}$ ) Al measured from  $\text{Co}^{2+}$  titration (procedure in main text). Also presented are first and zero-order rate constants (per  $\text{H}^+$ ) for the dehydration of methanol to dimethyl ether measured at 415 K (procedure in main text; Section 8.7.3).

#### X-Ray diffraction of MFI and CHA zeolites

Crystal topologies of H-form zeolites were assessed from powder X-ray diffraction (XRD) patterns measured on a Rigaku SmartLab X-ray diffractometer with a  $\text{Cu K}\alpha$  radiation source ( $\lambda=0.154 \text{ nm}$ ) operated at 1.76 kW. Typically, 0.50 g of zeolite powder were loaded onto a sample holder (Rigaku) and the diffraction pattern was

Table 8.4.

Characterization of CHA zeolites synthesized with various Al precursors with equimolar  $\text{Na}^+$  and  $\text{TMAda}^+$  in  $\text{OH}^-$  media.

| Synthesis                    |                          | Characterization and Site Distribution |   |                       |  |   | Kinetics                      |                              |
|------------------------------|--------------------------|--|---|-----------------------|--|---|-------------------------------|------------------------------|
| Al Precursor                 | Si/ $\text{Al}_\text{f}$ | $\text{H}^+/\text{Al}_\text{f}$        | Micropore Volume / $\text{cm}^3 \text{ g}^{-1}$ | Organic Content / wt% | $\text{A}_{\text{iso}}/\text{Al}_\text{f}$ | $\text{A}_{\text{pair}}/\text{Al}_\text{f}$ | $k_{\text{first}}^{\text{a}}$ | $k_{\text{zero}}^{\text{b}}$ |
| $\text{AlCl}_3$              | 11                       | 1.05                                   | 0.14  | n.m.                  | 0.80                                       | 0.20  | n.m.                          | n.m.                         |
| $\text{NaAlO}_2$             | 16                       | 1.42                                   | 0.02  | 19.5                  | 0.62                                       | 0.38  | n.m.                          | n.m.                         |
| $\text{Al}(\text{O-i-Pr})_3$ | 14                       | 1.00                                   | 0.16  | 19.8                  | 0.56                                       | 0.44  | 85.0                          | 40.1                         |
| $\text{Al}_2\text{O}_3$      | 18                       | 0.17                                   | 0.18  | 22.1                  | 1.00                                       | 0.00  | n.m.                          | n.m.                         |
| $\text{Al}(\text{NO}_3)_3$   | 19                       | 0.65                                   | 0.21  | 20.0                  | 0.80                                       | 0.10  | n.m.                          | n.m.                         |
| $\text{Al}(\text{OH})_3$     | 17                       | 0.97                                   | 0.16  | 21.0                  | 0.70                                       | 0.30  | 39.9                          | 34.2                         |

<sup>a</sup> Units of  $k_{\text{first}}$ :  $10^{-3} \text{ mol DME (mol H}^+ \text{ s kPa)}^{-1}$

<sup>b</sup> Units of  $k_{\text{zero}}$ :  $10^{-3} \text{ mol DME (mol H}^+ \text{ s)}^{-1}$

Table 8.5.

Characterization of CHA zeolites synthesized using  $\text{Al}(\text{OH})_3$  and equimolar  $\text{Na}^+$  and  $\text{TMAda}^+$  in  $\text{OH}^-$  media. Also included is CHA-OH(16,6%) zeolite, which was synthesized using  $\text{TMAda}^+$  and hexyldecyltrimethylammonium bromide (CTAB) in  $\text{OH}^-$  media.

| Sample         | Characterization and Site Distribution |                                 |   |                       |  |   | Kinetics                      |                              |
|----------------|--|---------------------------------|---|-----------------------|--|---|-------------------------------|------------------------------|
|                | Si/ $\text{Al}_\text{f}$               | $\text{H}^+/\text{Al}_\text{f}$ | Micropore Volume / $\text{cm}^3 \text{ g}^{-1}$ | Organic Content / wt% | $\text{A}_{\text{iso}}/\text{Al}_\text{f}$ | $\text{A}_{\text{pair}}/\text{Al}_\text{f}$ | $k_{\text{first}}^{\text{a}}$ | $k_{\text{zero}}^{\text{b}}$ |
| CHA-OH(15,18%) | 15                                     | 1.01                            | 0.17  | 21.6                  | 0.82                                       | 0.18  | 36.0                          | 27.5                         |
| CHA-OH(16,24%) | 16                                     | 1.16                            | 0.18  | 20.1                  | 0.76                                       | 0.24  | 32.1                          | 22.0                         |
| CHA-OH(17,30%) | 17                                     | 0.97                            | 0.16  | 21.0                  | 0.70                                       | 0.30  | 39.9                          | 34.2                         |
| CHA-OH(16,6%)  | 16 <sup>c</sup>                        | 0.93 <sup>c</sup>               | 0.18  | n.m.                  | 0.94                                       | 0.06  | 21.9                          | 24.7                         |

<sup>a</sup> Units of  $k_{\text{first}}$ :  $10^{-3} \text{ mol DME (mol H}^+ \text{ s kPa)}^{-1}$

<sup>b</sup> Units of  $k_{\text{zero}}$ :  $10^{-3} \text{ mol DME (mol H}^+ \text{ s)}^{-1}$

<sup>c</sup> Per total Al.  $^{27}\text{Al}$  NMR spectra not measured on CHA-OH(16,6%).

Table 8.6.  
 Characterization of commercial MFI zeolites (Si/Al = 30-43).

| Sample  | Characterization and Site Distribution |                                   |  |                             |                                     |                                      | Kinetics                        |                                |
|---------|--|-----------------------------------|--|-----------------------------|-------------------------------------|--------------------------------------|---------------------------------|--------------------------------|
|         | Si/Al <sub>tot</sub>                   | H <sup>+</sup> /Al <sub>tot</sub> | Micropore<br>Volume<br>/ cm <sup>3</sup> g <sup>-1</sup> | Organic<br>Content<br>/ wt% | A <sub>iso</sub> /Al <sub>tot</sub> | A <sub>psir</sub> /Al <sub>tot</sub> | k <sub>first</sub> <sup>a</sup> | k <sub>zero</sub> <sup>b</sup> |
| MFI(30) | 30                                     | 1.15                              | 0.14   | N/A                         | N/A                                 | N/A                                  | 3.9                             | 15.5                           |
| MFI(43) | 43                                     | 0.85                              | 0.16   | N/A                         | N/A                                 | N/A                                  | 4.4                             | 14.4                           |

<sup>a</sup> Units of k<sub>first</sub>: 10<sup>-3</sup> mol DME (mol H<sup>+</sup> s kPa)<sup>-1</sup>

<sup>b</sup> Units of k<sub>zero</sub>: 10<sup>-3</sup> mol DME (mol H<sup>+</sup> s)<sup>-1</sup>

recorded from  $4\text{-}40^\circ$   $2\theta$  at a scan rate of  $0.04^\circ \text{ s}^{-1}$ . Powder XRD patterns for all synthesized materials were compared to diffraction patterns for CHA (CHA) reported in the International Zeolite Association (IZA) structure database [1]. All XRD patterns reported here are normalized such that the maximum peak intensity in each pattern is set to unity. Diffraction patterns of CHA and MFI zeolites are shown in Figures 8.11-8.16.

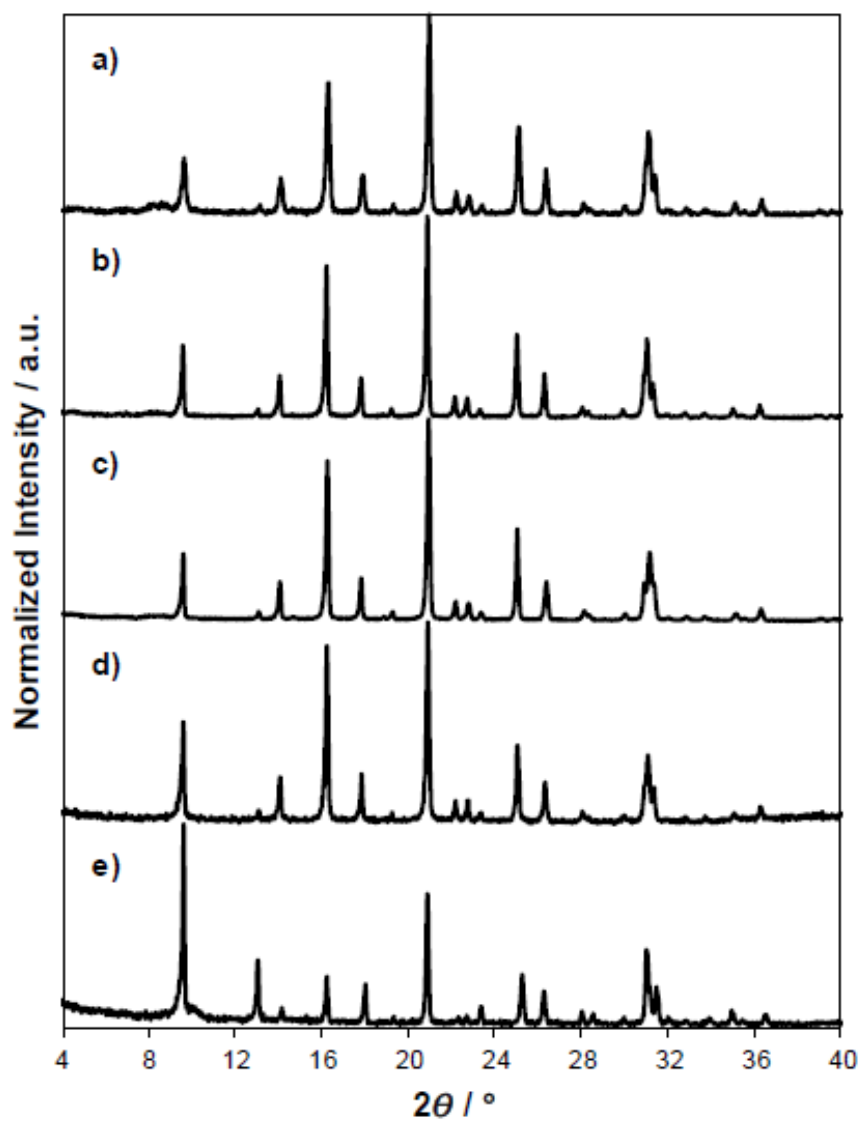


Figure 8.11. XRD patterns of a) CHA-F(18,0%), b) CHA-F(17,0%), c) CHA-OH(27,0%), d) CHA-OH(14,0%), and e) CHA-OH(17,0%) zeolites synthesized without Na<sup>+</sup>.

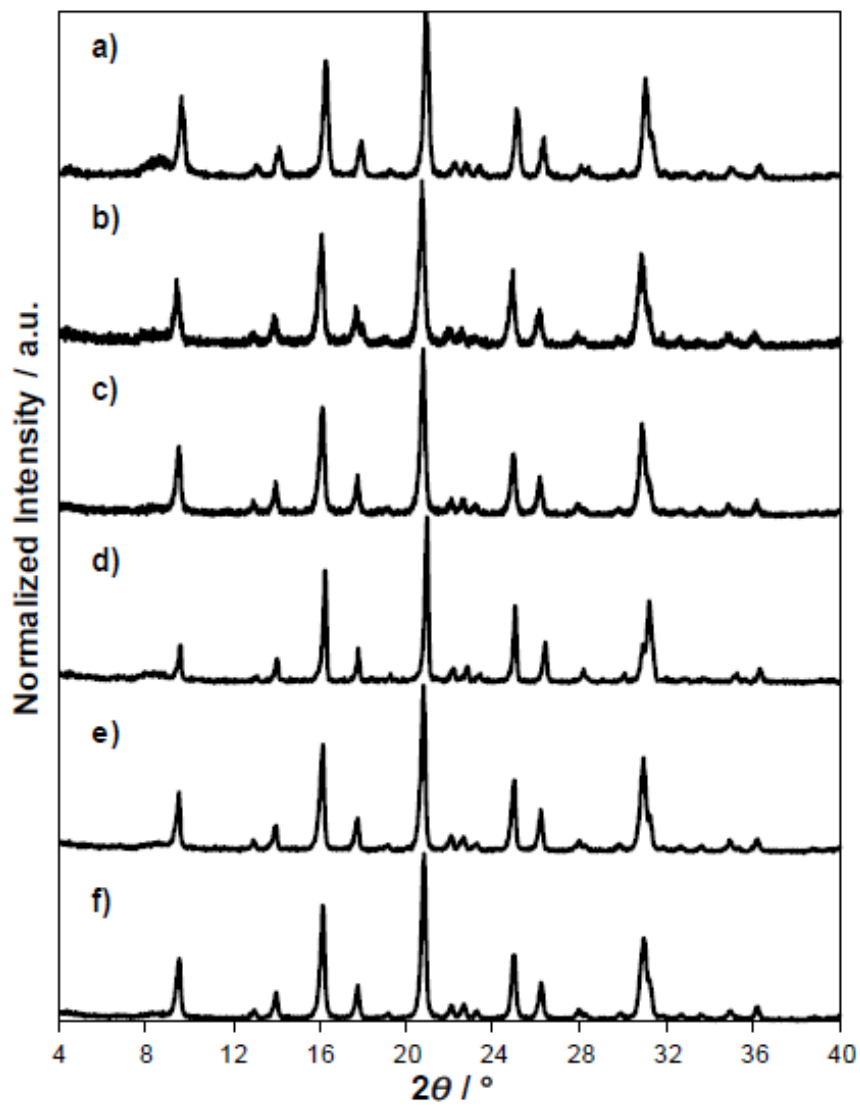


Figure 8.12. XRD patterns of CHA zeolites synthesized with a)  $\text{AlCl}_3$ , b)  $\text{NaAlO}_2$ , c)  $\text{Al}(\text{O-i-Pr})_3$ , d)  $\text{Al}_2\text{O}_3$ , e)  $\text{Al}(\text{NO}_3)_3$ , and f)  $\text{Al}(\text{OH})_3$  and equimolar  $\text{Na}^+$  and  $\text{TMAda}^+$  in  $\text{OH}^-$  media.

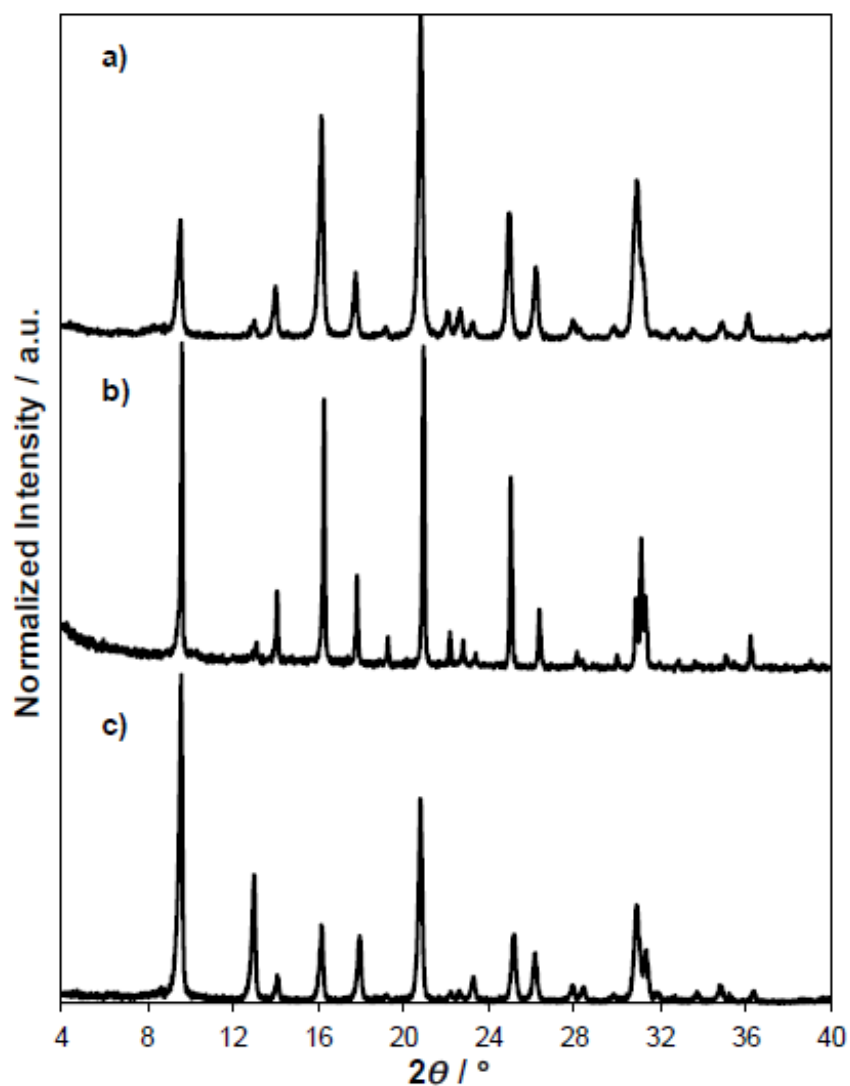


Figure 8.13. XRD patterns of a) CHA-OH(17,30%), b) CHA-OH(16,24%), and c) CHA-OH(15,18%) zeolites synthesized with  $\text{Al}(\text{OH})_3$  and equimolar  $\text{Na}^+$  and  $\text{TMAda}^+$  in  $\text{OH}^-$  media.

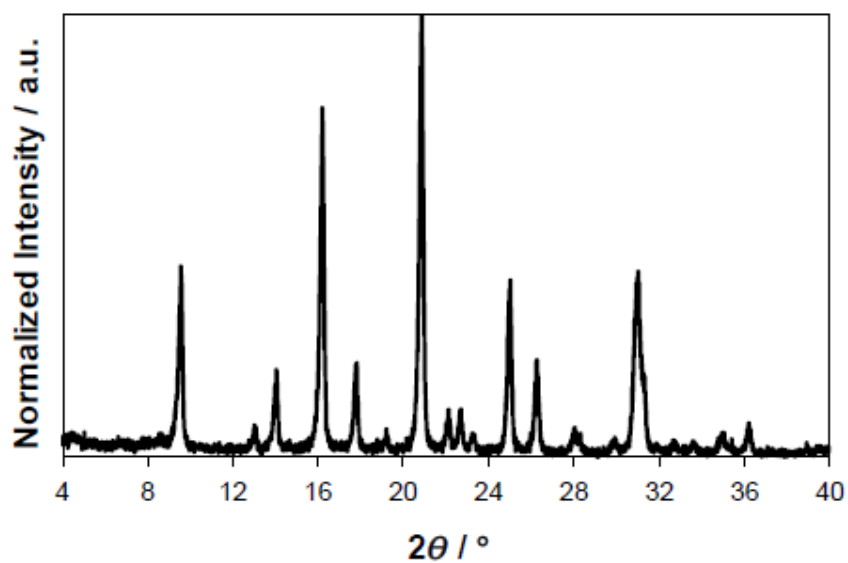


Figure 8.14. XRD patterns of  $\text{Na}^+$ -free CHA-OH(16,6%) zeolite synthesized with  $\text{Al}(\text{OH})_3$ ,  $\text{TMA}^+\text{da}^+$ , and CTAB in  $\text{OH}^-$  media.

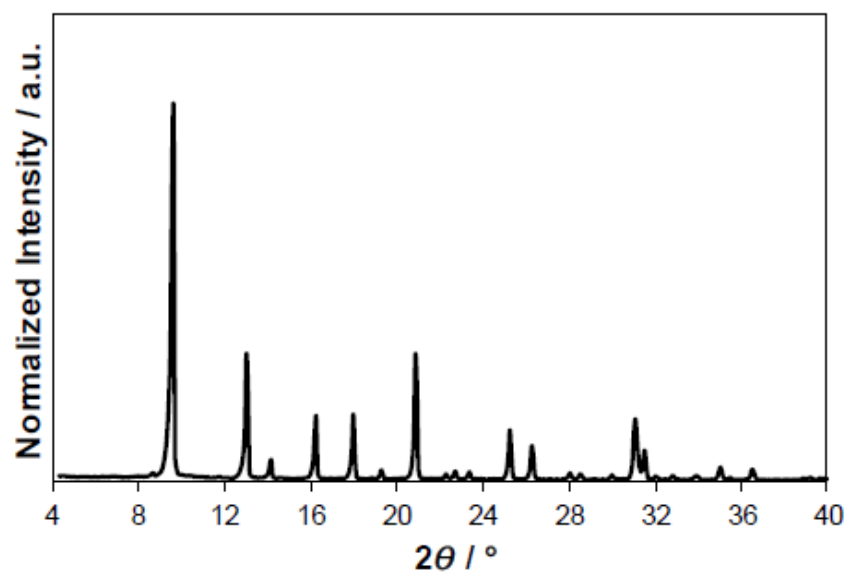


Figure 8.15. XRD pattern of Si-CHA synthesized with  $\text{TMA}^+\text{da}^+$  in  $\text{F}^-$  media.



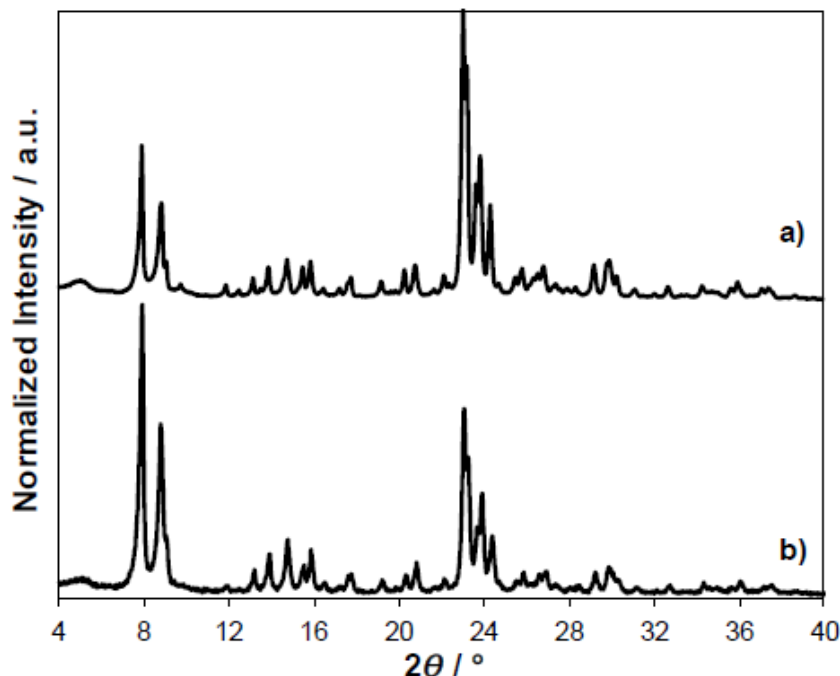


Figure 8.16. XRD patterns of a) H-MFI(30) and b) H-MFI(43) zeolites.

#### Adsorption isotherms to measure micropore volumes of CHA and MFI zeolites

Micropore volumes were determined on H-CHA zeolites from Ar adsorption isotherms measured at 87 K in a liquid Ar bath, and for H-MFI zeolites using N<sub>2</sub> adsorption isotherms held at 77 K in a liquid N<sub>2</sub> bath on a Micromeritics ASAP 2020 Surface Area and Porosity Analyzer. 0.03–0.05 g of sieved zeolite sample (nominal diameter between 180–250  $\mu\text{m}$ ) were degassed by heating to 393 K (0.167 K s<sup>-1</sup>) under vacuum (<5  $\mu\text{mHg}$ ) for 2 h, and then further heating to 623 K (0.167 K s<sup>-1</sup>) under vacuum (<5  $\mu\text{mHg}$ ) and holding for 9 h. Standardized gas volumes (cm<sup>3</sup> g<sub>cat</sub><sup>-1</sup> at STP) adsorbed were estimated from semi-log derivative plots of the adsorption isotherm ( $\partial(V_{\text{ads}})/\partial(\ln(P/P_0))$  vs.  $\ln(P/P_0)$ ). Micropore volumes (cm<sup>3</sup> g<sub>cat</sub><sup>-1</sup>) were obtained on CHA and MFI zeolites by converting standard gas adsorption volumes (cm<sup>3</sup> g<sub>cat</sub><sup>-1</sup> at STP) to liquid volumes using a density conversion factor assuming the liquid density of Ar at 87 K or N<sub>2</sub> at 77 K, respectively. Micropore volumes of CHA

and MFI zeolites are shown in Figures 8.17-8.22. In each figure, adsorption isotherms are offset in increments of  $200 \text{ cm}^3 \text{ g}_{\text{cat}}^{-1}$  for clarity.

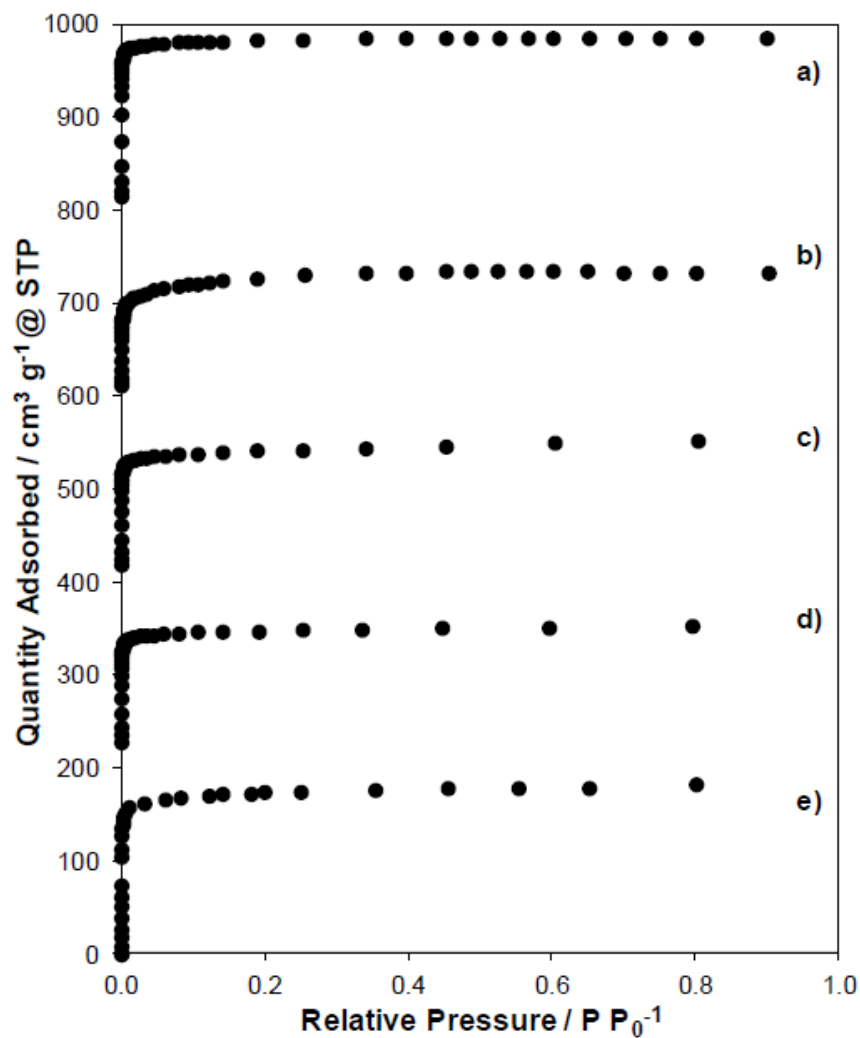


Figure 8.17. Ar adsorption isotherms (87 K) on a) CHA-F(18,0%), b) CHA-F(14,0%), c) CHA-OH(27,0%), d) CHA-OH(17,0%), and e) CHA-OH(18,0%) zeolites synthesized without  $\text{Na}^+$  using  $\text{OH}^-$  and  $\text{F}^-$  anions.

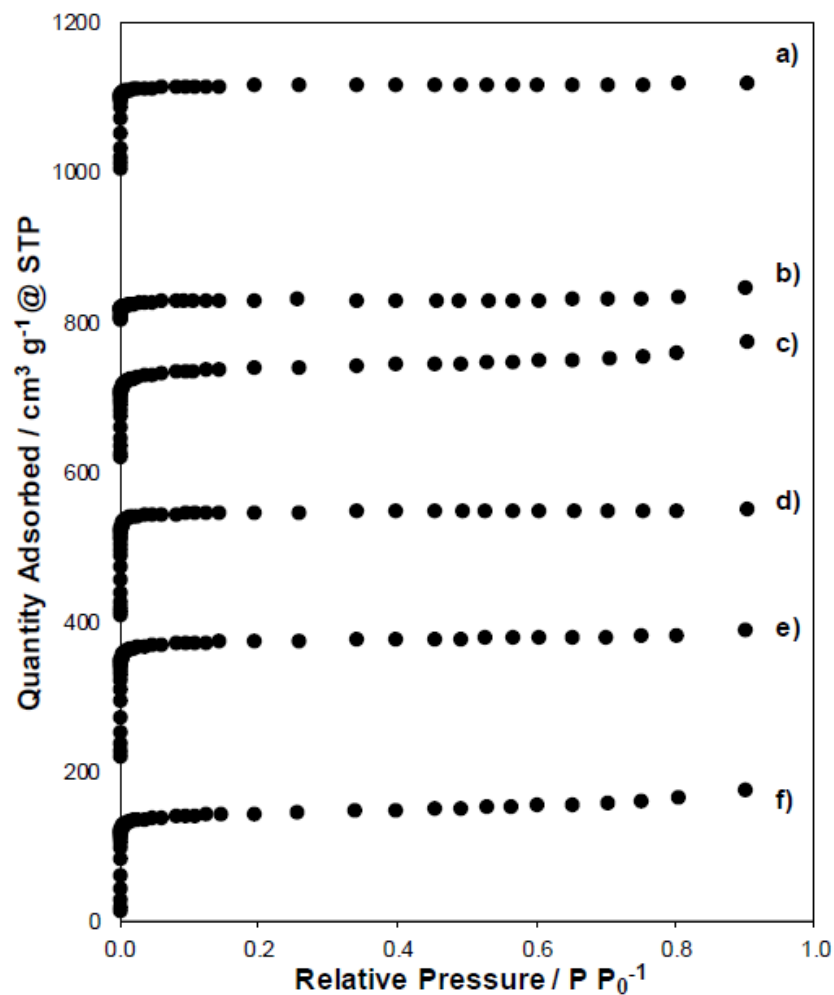


Figure 8.18. Ar adsorption isotherms (87 K) on CHA zeolites synthesized with a)  $\text{AlCl}_3$ , b)  $\text{NaAlO}_2$ , c)  $\text{Al}(\text{O-i-Pr})_3$ , d)  $\text{Al}_2\text{O}_3$ , e)  $\text{Al}(\text{NO}_3)_3$ , and f)  $\text{Al}(\text{OH})_3$  and equimolar  $\text{Na}^+$  and  $\text{TMAda}^+$  in  $\text{OH}^-$  media.

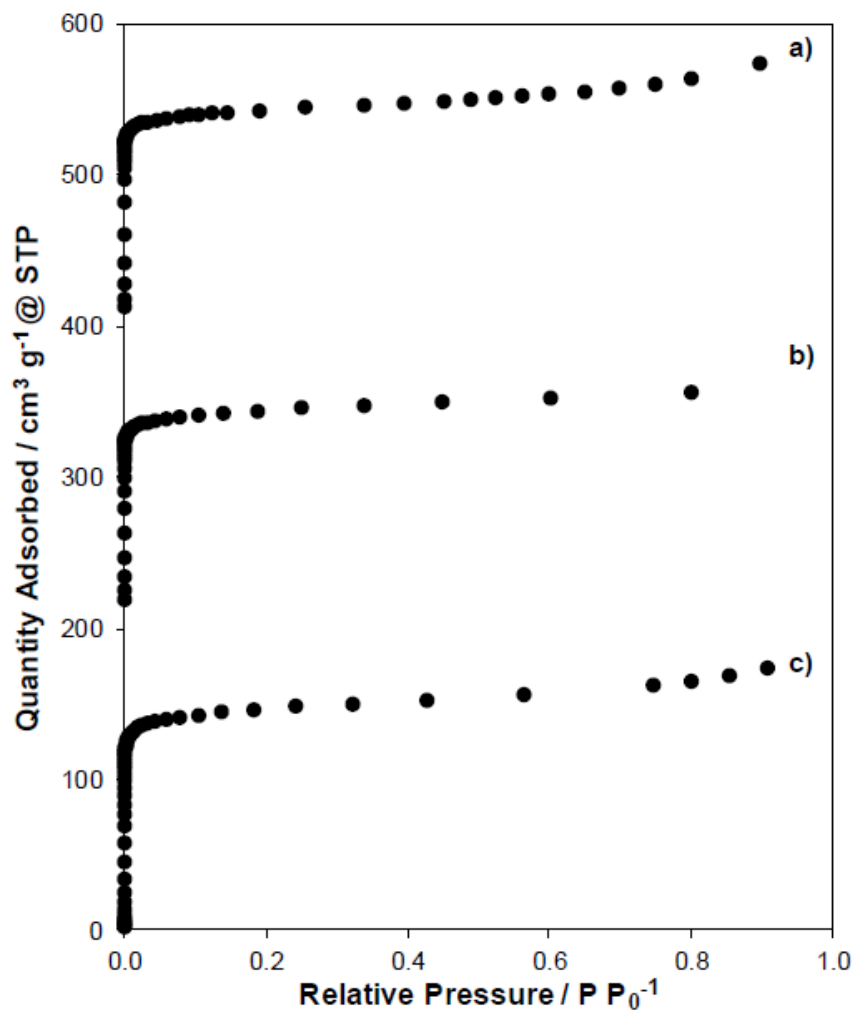


Figure 8.19. Ar adsorption isotherms (87 K) on a) CHA-OH(17,30%), b) CHA-OH(16,24%), and c) CHA-OH(15,18%) zeolites synthesized with  $\text{Al}(\text{OH})_3$  and equimolar  $\text{Na}^+$  and  $\text{TMAda}^+$  in  $\text{OH}^-$  media.

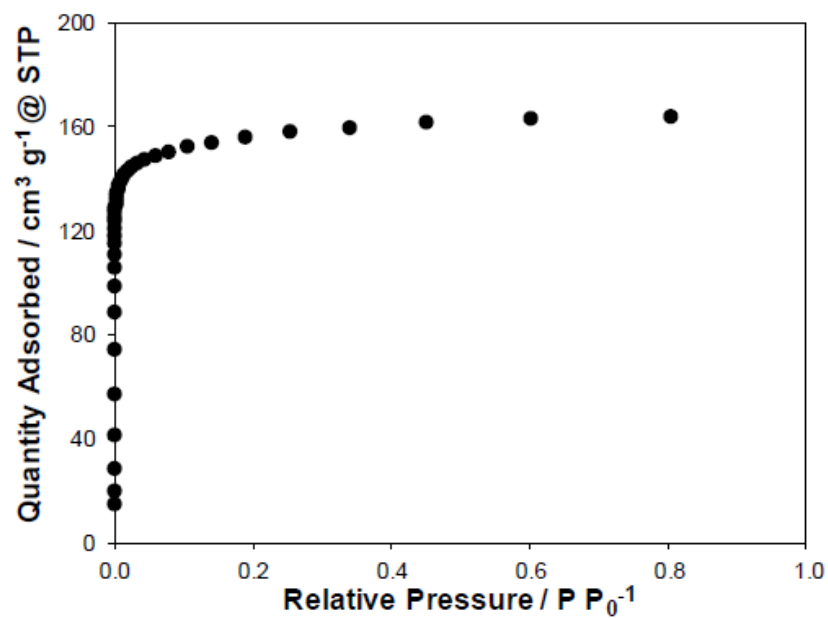


Figure 8.20. Ar adsorption isotherms (87 K) on Na<sup>+</sup>-free CHA-OH(16,6%) zeolite synthesized with Al(OH)<sub>3</sub>, TMAda<sup>+</sup>, and CTAB in OH<sup>-</sup> media.

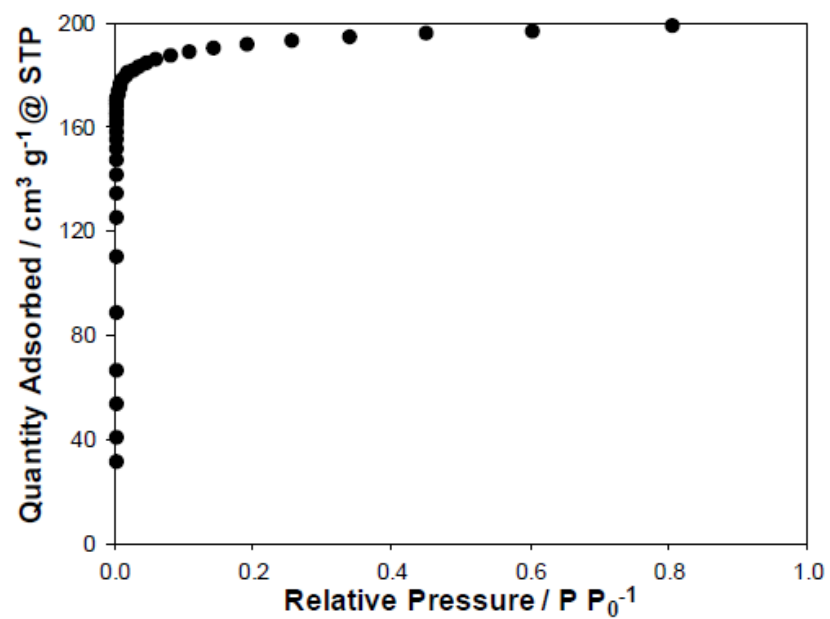


Figure 8.21. Ar adsorption isotherms (87 K) on Si-CHA zeolite synthesized with TMAda<sup>+</sup> in F<sup>-</sup> media.

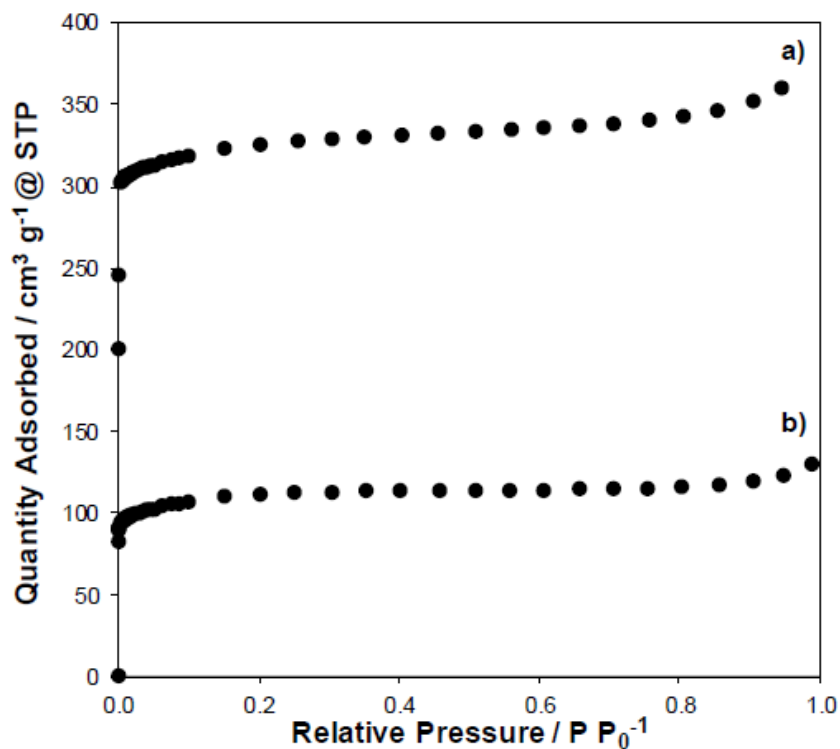


Figure 8.22.  $N_2$  adsorption isotherms (77 K) on a) H-MFI(30) and b) H-MFI(43) zeolites.

#### Elemental analysis of CHA and MFI zeolites

Atomic absorption spectroscopy (AAS) was used to quantify the total Al, Na, and Co elemental content of each sample using a Perkin Elmer AAnalyst 300 Atomic Absorption Spectrometer. AAS samples were prepared by dissolving 0.02 g of zeolite in 3 g of concentrated HF acid (48 wt%, Sigma Aldrich), letting the solution sit overnight (at least 8 hours), and then diluting with 50 g of deionized water (18.2 M $\Omega$ ). Caution: when working with HF acid, use appropriate personal protective equipment, ventilation, and other safety measures. Absorbances were measured using radiation sources at wavelengths of 309.3 nm for Al, in a reducing acetylene/nitrous oxide flame, and at 589.0 and 240.7 nm for Na and Co, respectively, in an oxidizing acetylene/air flame. Elemental compositions were determined from calibration curves derived from

standard solutions of known composition. Al and Na contents were determined after removal of organic content in zeolites by oxidative treatment (853 K, 10 h).

#### Quantification of organic content in as-synthesized CHA zeolites

Thermogravimetric analysis (TGA) experiments were performed on as-synthesized CHA zeolites using a TA Instruments SDT Q600 thermogravimetric analyzer and differential scanning calorimeter (TGA-DSC) by heating 0.02 g of as-synthesized CHA in  $83.3 \text{ cm}^3 \text{ s}^{-1} \text{ g}_{\text{cat}}^{-1}$  dry air (UHP, 99.999%, Indiana Oxygen) to 523 K ( $0.167 \text{ K s}^{-1}$ ) and holding for 0.5 h to remove physisorbed water before further heating to 1073 K ( $0.167 \text{ K s}^{-1}$ ). Removal of the occluded TMAda<sup>+</sup> molecule was characterized by a sharp exothermic heat flow centered around 773 K, which was accompanied by a sharp decrease in mass. All CHA zeolite samples exhibited a weight loss of about 20% due to combustion of one TMAda<sup>+</sup> molecule per CHA cage, consistent with reported organic weight loss of CHA zeolites synthesized with TMAda<sup>+</sup> [162,467].

#### Estimation of CHA crystal diameter using SEM and DLS

Scanning electron microscopy (SEM) micrographs of H-CHA zeolites were taken on a FEI Quanta 3D FEG Dual-beam SEM with an Everhart-Thornley attachment for high vacuum imaging and images were taken using the focused beam mode at 5 kV with a  $3 \mu\text{m}$  spot size. Crystal diameters of all CHA zeolites were estimated by averaging over a distribution of individual crystals (ca. 40-50) taken from multiple micrographs of different regions of the SEM slide. SEM micrographs shown in Figures 8.23-8.31 are representative images of each sample.

SEM images of CHA-OH(14-27,0%) (Figures 8.23-8.25) and CHA-F(18,0%) (Figure 8.26) show the presence of cubic crystal formations typical of CHA zeolites, but all images also contain smaller particles that appear to be under-developed crystals. Despite the non-uniformity of the crystal size distribution, XRD patterns show that CHA-OH(14-27,0%) zeolites are free of phase impurities. Images of CHA-OH(15,18%)



and CHA(16,24%) show a more uniform distribution of crystal sizes (Figures 8.27-8.28) than  $\text{Na}^+$ -free CHA zeolites, but there do appear to be aggregates of very small particles ( $<250$  nm) distributed throughout the sample. These small particles were not including in the average diameter of these CHA samples, which would result in an overestimation of the average crystal diameter and, due a larger estimated diffusion path length, would lead to a larger Thiele modulus (further discussion in Section 8.7.5). CHA-OH(17,30%) and CHA-OH(14,44%) appear to be completely composed of aggregates of smaller, crystalline CHA zeolites (Figures 8.29-8.30). Determination of the average crystal diameter was difficult due to the overlapping of crystal agglomerates and the diameter was conservatively estimated from intermediate sized aggregates consisting of a few smaller particles. CHA-OH(16,6%) zeolites synthesized from  $\text{TMAda}^+$  and CTAB contain smooth crystals and have a very uniform distribution of particle sizes (Figure 8.31).

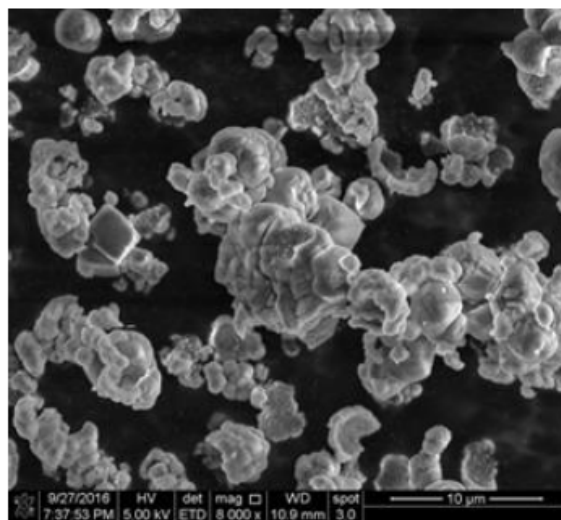


Figure 8.23. SEM image of the bulk sample of CHA-OH(14,0%).

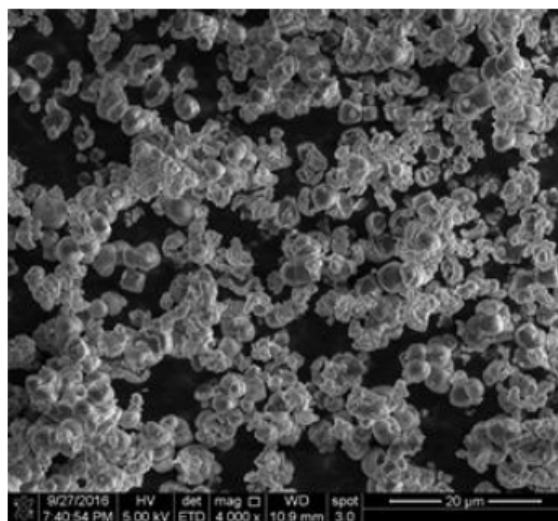


Figure 8.24. SEM image of the bulk sample of CHA-OH(17,0%).

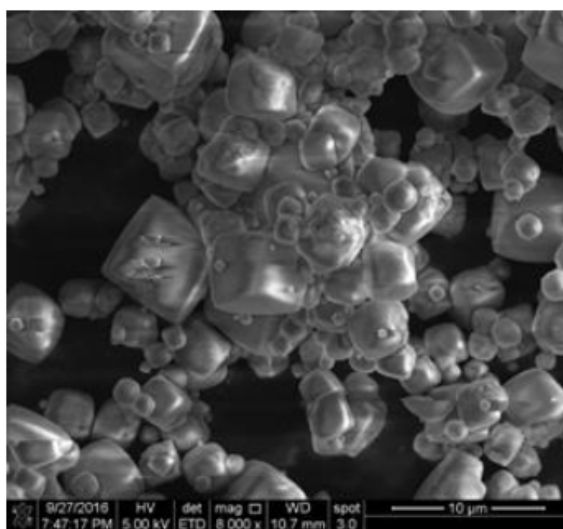


Figure 8.25. SEM image of the bulk sample of CHA-OH(27,0%).

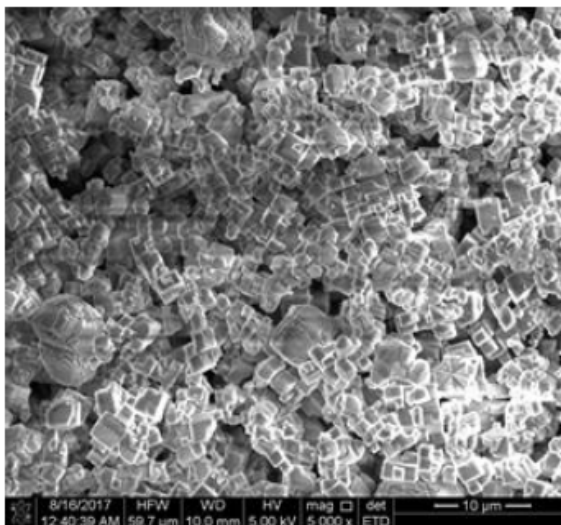


Figure 8.26. SEM image of the bulk sample of CHA-F(18,0%).

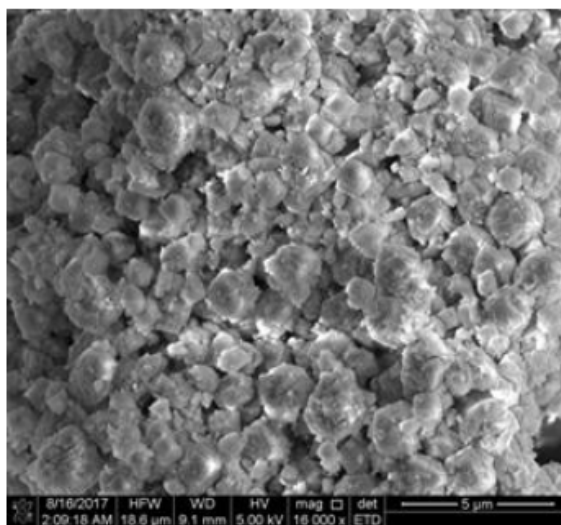


Figure 8.27. SEM image of the bulk sample of CHA-OH(15,18%).

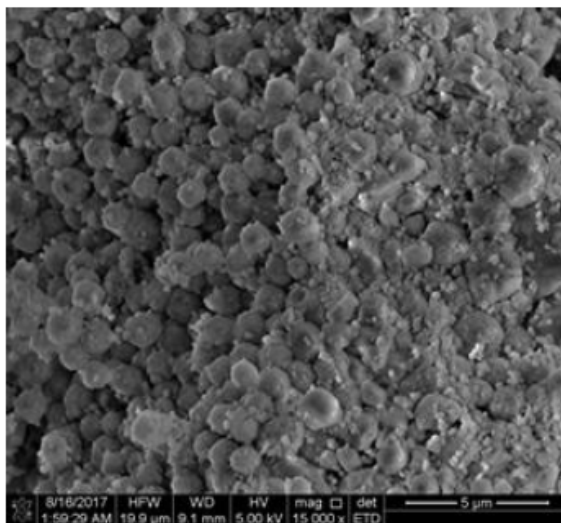


Figure 8.28. SEM image of the bulk sample of CHA-OH(16,24%).

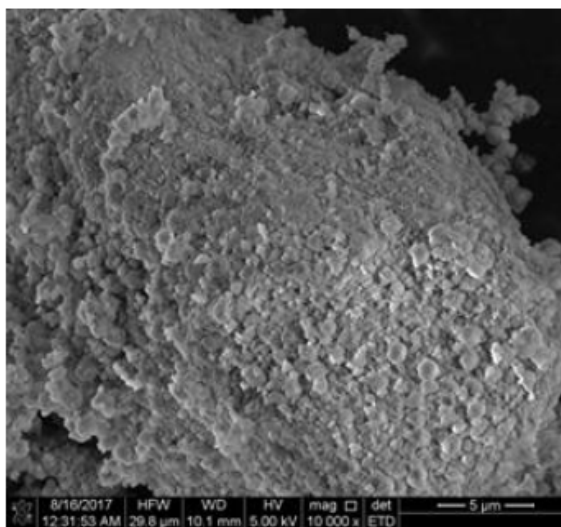


Figure 8.29. SEM image of the bulk sample of CHA-OH(17,30%).

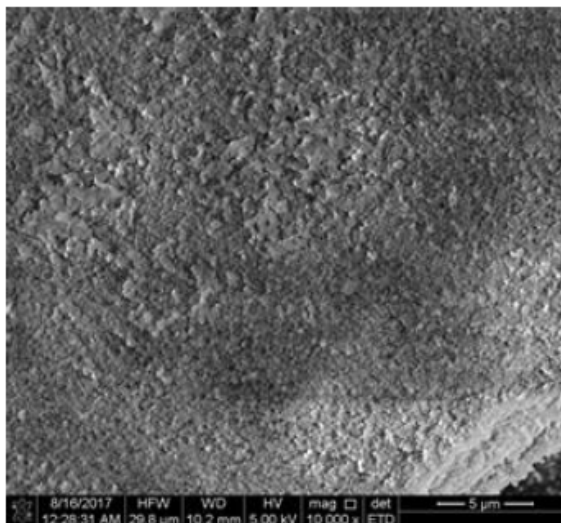


Figure 8.30. SEM image of the bulk sample of CHA-OH(14,44%).

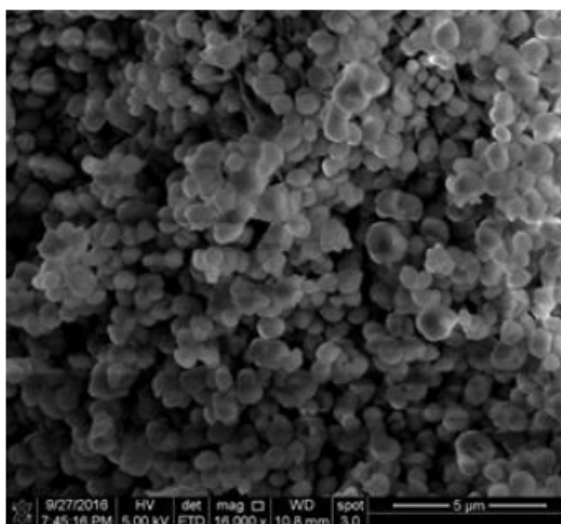


Figure 8.31. SEM image of the bulk sample of CHA-OH(16,6%).

Dynamic light scattering (DLS) was also used to estimate crystallite diameters and to corroborate particle size estimates from SEM micrographs. DLS measurements were performed on a Brookhaven ZetaPALS instrument at a wavelength of 659 nm at

Table 8.7.

Crystallite diameters ( $\mu\text{m}$ ) of CHA zeolites with different fractions of paired Al (Table 8.1, main text) estimated from DLS and SEM micrographs.

| Sample         | SEM / $\mu\text{m}$ | DLS / $\mu\text{m}$ |
|----------------|---------------------|---------------------|
| CHA-OH(14,0%)  | 2 $\pm$ 1           | 1.5 $\pm$ 0.3       |
| CHA-OH(17,0%)  | 2 $\pm$ 1           | n.m.                |
| CHA-OH(27,0%)  | 6 $\pm$ 1           | 4.6 $\pm$ 1.8       |
| CHA-F(18,0%)   | 1 $\pm$ 1           | n.m.                |
| CHA-OH(16,6%)  | 0.8 $\pm$ 1         | 0.8 $\pm$ 0.2       |
| CHA-OH(15,18%) | 1 $\pm$ 1           | 1.1 $\pm$ 0.3       |
| CHA-OH(16,24%) | 1 $\pm$ 1           | 1.6 $\pm$ 0.4       |
| CHA-OH(17,30%) | 1 $\pm$ 1           | 0.9 $\pm$ 0.4       |
| CHA-OH(14,44%) | 0.3 $\pm$ 1         | 0.7 $\pm$ 0.3       |

298 K using the Particle Sizing Software (version 3.60). Zeolite samples were diluted with water until a translucent suspension was obtained (typically 1 mg zeolite per 20  $\text{cm}^3$   $\text{H}_2\text{O}$ ), and suspended via agitation using a vortex mixer. Small aliquots (ca. 4.5  $\text{cm}^3$ ) of the zeolite suspension were placed within square acrylic cuvette cells prior to analysis. DLS measurements were recorded over a 10 minute period and averaged over three repeat measurements. Table 8.7 lists the crystallite diameters measured from DLS and from SEM micrographs for the samples listed in Table 8.1 of the main text.

#### Quantification of $\text{H}^+$ sites by $\text{NH}_3$ TPD

The number of  $\text{H}^+$  sites on H-zeolites was quantified by  $\text{NH}_3$  TPD after aqueous ion-exchange with  $\text{NH}_4^+$ , while the number of  $\text{H}^+$  sites remaining after Cu or Co-exchange of CHA zeolites was quantified using gas-phase  $\text{NH}_3$  titration and purge treatments shown to retain only  $\text{NH}_4^+$  species, as reported elsewhere [78,171]. Briefly,

gas-phase titrations were performed by saturating zeolite samples (0.03-0.05 g) in flowing gaseous  $\text{NH}_3$  (500 ppm  $\text{NH}_3$  in balance He, Matheson) at 433 K for 4 h and a total flow rate of  $20 \text{ cm}^3 \text{ s}^{-1} \text{ g}^{-1}$ .  $\text{NH}_3$ -saturated samples were then purged in wet, flowing He (ca. 3%  $\text{H}_2\text{O}$ ,  $20 \text{ cm}^3 \text{ s}^{-1} \text{ g}^{-1}$ ) at 433 K for 8 h prior to TPD. Data for each sample in Tables 8.3-8.6 ( $\text{H}^+$  per  $\text{Al}_f$ ) and in Tables 8.8-8.10 ( $\text{H}^+$  per  $\text{Al}_{\text{tot}}$ ).

#### $^{27}\text{Al}$ MAS NMR to characterization Al coordination environment

$^{27}\text{Al}$  magic angle spinning nuclear magnetic resonance (MAS NMR) spectra were recorded under ambient conditions on H-CHA zeolites to quantify framework and extraframework Al fractions. Spectra were recorded on a Chemagnetics CMX-Infinity 400 spectrometer in a wide-bore 9.4 Tesla magnet (Purdue Interdepartmental NMR Facility) and were acquired using a  $2.3 \mu\text{s}$  pulse (ca. 30 degrees), an acquisition time of 12.8ms and a relaxation delay of 1s, and were measured at 104.24 MHz and a MAS rate of 5 kHz.  $^1\text{H}$  decoupling was used during acquisition, employing a two-pulse phase modulation (TPPM) scheme. Samples were hydrated by storing for >48 h in a hydrator containing a saturated potassium chloride (KCl) solution prior to packing in a 4mm  $\text{ZrO}_2$  rotor. All  $^{27}\text{Al}$  MAS NMR spectra are referenced to a static sample of  $\text{AlCl}_3$  dissolved in  $\text{D}_2\text{O}$  (0 ppm  $^{27}\text{Al}$  line). Spectra are normalized so that the maximum intensity in each spectrum is set to unity and are shown in Figures 8.32-8.34. Fractions of framework ( $\text{Al}_f$ ) and extraframework Al ( $\text{Al}_{\text{ex}}$ ) per total Al are listed in Tables 8.8-8.10 and the error associated with each is  $\pm 0.05$ .

Table 8.8.

Fraction of framework Al atoms ( $\text{Al}_f/\text{Al}_{\text{tot}}$ ) from  $^{27}\text{Al}$  NMR and  $\text{H}^+/\text{Al}_f$  for each CHA zeolites synthesized without  $\text{Na}^+$  in  $\text{OH}^-$  and  $\text{F}^-$  media.

| Sample        | $\text{Si}/\text{Al}_{\text{tot}}$ | $\text{H}^+/\text{Al}_{\text{tot}}$ | $\text{Al}_f/\text{Al}_{\text{tot}}$ | $\text{Si}/\text{Al}_f$ | $\text{H}^+/\text{Al}_f$ |
|---------------|------------------------------------|-------------------------------------|--------------------------------------|-------------------------|--------------------------|
| CHA-OH(14,0%) | 14                                 | 0.95                                | 1.00                                 | 14                      | 0.95                     |
| CHA-OH(17,0%) | 16                                 | 0.96                                | 0.95                                 | 17                      | 1.00                     |
| CHA-OH(27,0%) | 26                                 | 0.97                                | 0.97                                 | 27                      | 1.00                     |
| CHA-F(17,0%)  | 14                                 | 0.44                                | 0.80                                 | 17                      | 0.55                     |
| CHA-F(18,0%)  | 18                                 | 1.02                                | 1.00                                 | 18                      | 1.02                     |

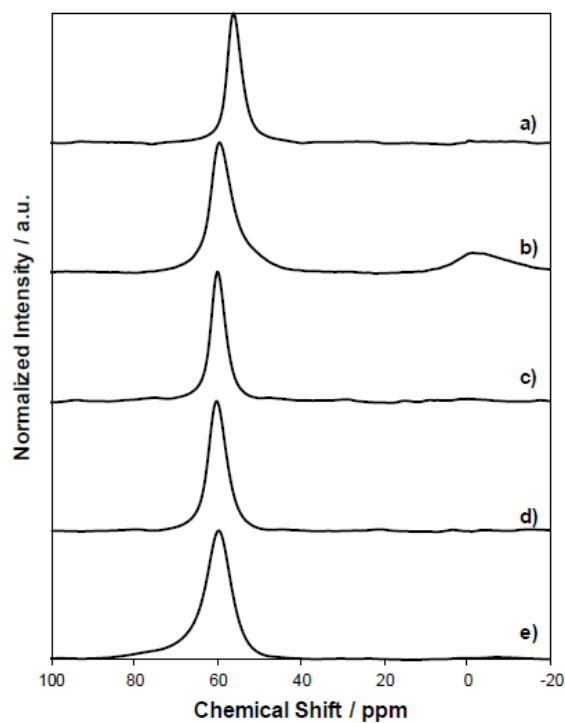


Figure 8.32.  $^{27}\text{Al}$  MAS NMR spectra of a) CHA-F (18,0%), b) CHA-F (17,0%), c) CHA-OH (27,0%), d) CHA-OH (14,0%), and e) CHA-OH (17,0%) zeolites synthesized without  $\text{Na}^+$  using  $\text{OH}^-$  and  $\text{F}^-$  anions.



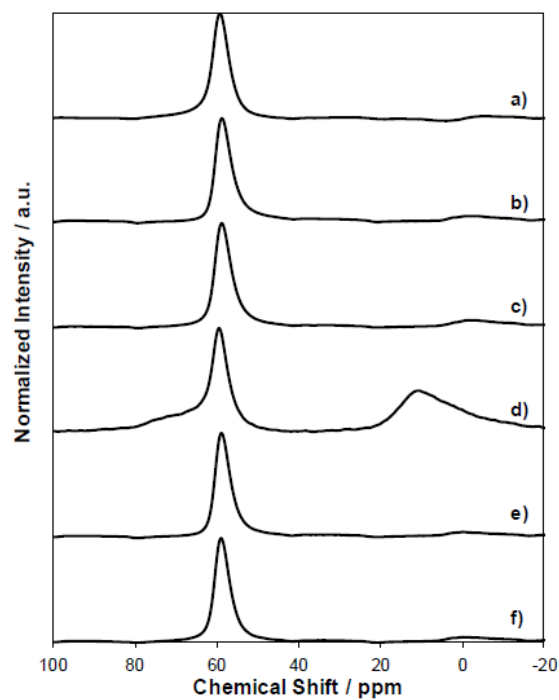


Figure 8.33.  $^{27}\text{Al}$  MAS NMR spectra of CHA zeolites synthesized with a)  $\text{AlCl}_3$ , b)  $\text{NaAlO}_2$ , c)  $\text{Al}(\text{O-i-Pr})_3$ , d)  $\text{Al}_2\text{O}_3$ , e)  $\text{Al}(\text{NO}_3)_3$ , and f)  $\text{Al}(\text{OH})_3$  and equimolar  $\text{Na}^+$  and  $\text{TMAda}^+$  in  $\text{OH}^-$  media.

Table 8.9.

Fraction of framework Al atoms ( $\text{Al}_f/\text{Al}_{\text{tot}}$ ) from  $^{27}\text{Al}$  NMR and  $\text{H}^+/\text{Al}_f$  for each CHA zeolite synthesized with various Al precursors and equimolar amounts of  $\text{Na}^+$  and  $\text{TMAda}^+$  in  $\text{OH}^-$  media.

| <b>Al Precursor</b>          | <b>Si/Al<sub>tot</sub></b> | <b>H<sup>+</sup>/Al<sub>tot</sub></b> | <b>Al<sub>f</sub>/Al<sub>tot</sub></b> | <b>Si/Al<sub>f</sub></b> | <b>H<sup>+</sup>/Al<sub>f</sub></b> |
|------------------------------|----------------------------|---------------------------------------|--|--------------------------|-------------------------------------|
| $\text{AlCl}_3$              | 11                         | 1.02                                  | 0.97                                   | 11                       | 1.05                                |
| $\text{NaAlO}_2$             | 13                         | 1.18                                  | 0.83                                   | 16                       | 1.42                                |
| $\text{Al}(\text{O-i-Pr})_3$ | 12                         | 0.83                                  | 0.83                                   | 14                       | 1.00                                |
| $\text{Al}_2\text{O}_3$      | 9                          | 0.09                                  | 0.52                                   | 18                       | 0.17                                |
| $\text{Al}(\text{NO}_3)_3$   | 16                         | 0.55                                  | 0.85                                   | 19                       | 0.65                                |
| $\text{Al}(\text{OH})_3$     | 15                         | 0.84                                  | 0.87                                   | 17                       | 0.97                                |

Table 8.10.

Fraction of framework Al atoms ( $\text{Al}_f/\text{Al}_{\text{tot}}$ ) from  $^{27}\text{Al}$  NMR and  $\text{H}^+/\text{Al}_f$  for different CHA zeolites synthesized with equimolar amounts of  $\text{Na}^+$  and  $\text{TMAda}^+$  in  $\text{OH}^-$  media.

| Sample         | Si/ $\text{Al}_{\text{tot}}$ | $\text{H}^+/\text{Al}_{\text{tot}}$ | $\text{Al}_f/\text{Al}_{\text{tot}}$ | Si/ $\text{Al}_f$ | $\text{H}^+/\text{Al}_f$ |
|----------------|------------------------------|-------------------------------------|--------------------------------------|-------------------|--------------------------|
| CHA-OH(15,18%) | 15                           | 0.99                                | 0.98                                 | 15                | 1.01                     |
| CHA-OH(16,24%) | 14                           | 1.02                                | 0.88                                 | 16                | 1.16                     |
| CHA-OH(17,30%) | 15                           | 0.84                                | 0.87                                 | 17                | 0.97                     |

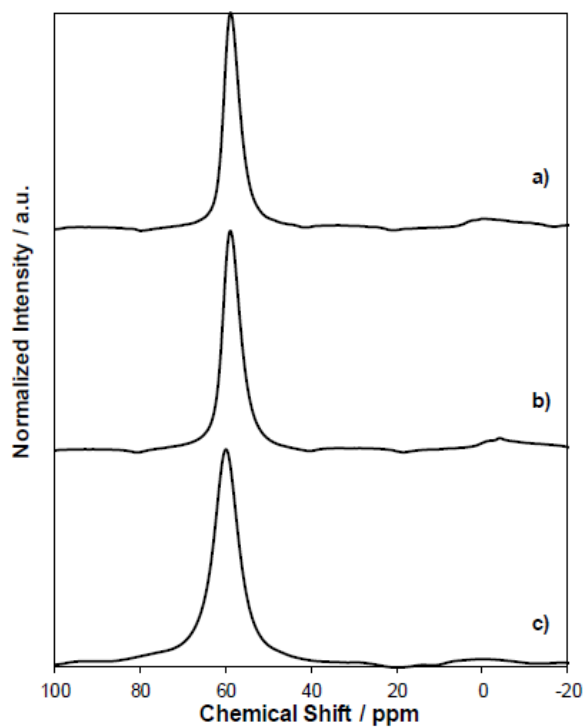


Figure 8.34.  $^{27}\text{Al}$  MAS NMR spectra of a) CHA-OH(17,30%), b) CHA-OH(16,24%), and c) CHA-OH(15,18%) zeolites synthesized with  $\text{Al}(\text{OH})_3$  and equimolar  $\text{Na}^+$  and  $\text{TMAda}^+$  in  $\text{OH}^-$  media.

## Validation of $\text{Co}^{2+}$ titration procedures on H-CHA-F zeolites

CHA zeolites crystallized with only  $\text{TMA}^+$  cations in  $\text{F}^-$  media at  $\text{Si}/\text{Al} < 15$  contained a large fraction of Al atoms unable to stabilize  $\text{NH}_4^+$  cations ( $\text{H}^+/\text{Al}_{\text{tot}} = 0.44$ ), consistent with previous observations suggesting that  $\text{TMA}^+$  cations alone are unable to stabilize CHA zeolites with  $\text{Si}/\text{Al} < 15$  [42]. CHA-F zeolites with  $\text{Si}/\text{Al} > 15$  contained nearly all of their Al atoms in the framework ( $\text{H}^+/\text{Al}_{\text{tot}} = 1.02$  from  $\text{NH}_3$  titrations; Table 8.3), yet were unable to exchange divalent  $\text{Co}^{2+}$  cations.  $\text{Co}^{2+}$  exchange isotherms (0.25-1M  $\text{Co}(\text{NO}_3)_2$ , 150  $\text{cm}^3$  solution  $\text{g}^{-1}$ , ambient temperature, no pH adjustment) were measured at different conditions ( $\text{Co}^{2+}$  molarity, repeat exchanges) to assess whether  $\text{Co}^{2+}$  exchange behavior was influenced by the hydrophobic nature of the framework resulting from fluoride-assisted crystallization [190]. Saturation  $\text{Co}^{2+}$  exchange capacities of zero, within experimental error, were measured for all H-CHA-F zeolites (Figure 8.35 and 8.36). To further demonstrate that H-CHA-F zeolites contain only isolated Al atoms,  $\text{Cu}^{2+}$  ion-exchanges were performed and the residual number of  $\text{H}^+$  sites, remaining after  $\text{Cu}^{2+}$ -exchange, were quantified with gas-phase  $\text{NH}_3$  titrations using previously reported procedures to determine the Cu-exchange stoichiometry (Table 8.11) [42]. Cu-exchange and subsequent  $\text{NH}_3$  titration data on CHA-OH(16,24%) [79] and CHA-OH(14,0%) [42] zeolites are included as references for CHA zeolites containing exclusively  $\text{Cu}^{2+}$  and  $[\text{CuOH}]^+$ , respectively. Both CHA-F zeolites ( $\text{Si}/\text{Al} = 17\text{-}18$ ) contain exclusively isolated  $[\text{CuOH}]^+$  cations, consistent with the 1  $\text{H}^+$  per  $\text{Cu}^{2+}$  exchange stoichiometry (Table 8.11, Figure 8.37), indicating that all framework Al is present as isolated sites. The possibility that  $[\text{CuOH}]^+$  preferentially exchanges before divalent  $\text{Cu}^{2+}$  cations is inconsistent with experimentally-measured  $\text{Cu}^{2+}$ -exchange isotherms (stoichiometry determined from  $\text{NH}_3$  titration), and DFT-calculated adsorption energies show that  $\text{Cu}^{2+}$  preferentially exchanges at paired Al sites before  $[\text{CuOH}]^+$  species exchange at isolated  $\text{H}^+$  sites [79].

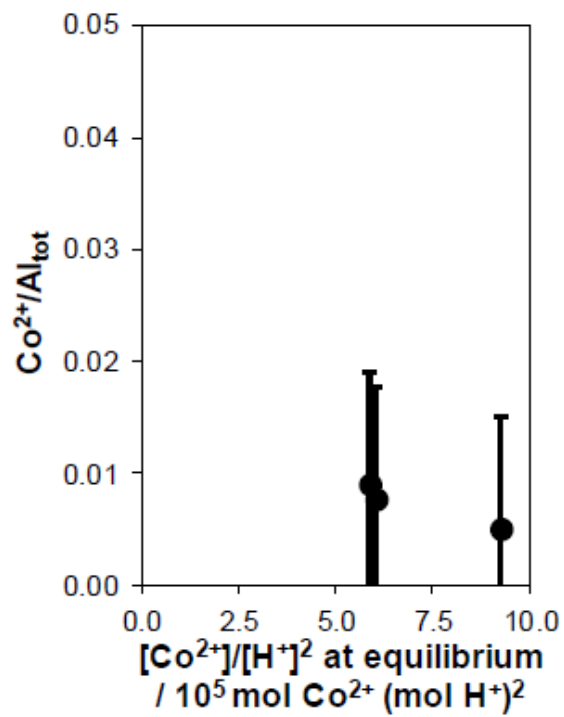


Figure 8.35. Amount of exchanged  $\text{Co}^{2+}$  retained on H-CHA-F(18,0%) as a function of the  $\text{Co}^{2+}$  concentration in solution at equilibrium.

Table 8.11.

Titration of residual  $\text{H}^+$  sites on CHA-OH(16,24%), CHA-OH(14,0%), CHA-F(17,0%), and CHA-F(18,0%) after  $\text{Cu}^{2+}$  ion-exchange.

| Sample         | Si/ $\text{Al}_{\text{tot}}$ | $\text{H}^+/\text{Al}_{\text{tot}}$<br>(on H-form) | Cu wt% | Cu/ $\text{Al}_{\text{tot}}$ | Measured<br>$\text{H}^+/\text{Al}_{\text{tot}}^{\text{a}}$ | $\text{H}^+/\text{Cu}$ |
|----------------|------------------------------|--|--------|------------------------------|--|------------------------|
| CHA-OH(16,24%) | 14                           | 1.02   | 0.2    | 0.03                         | 0.95   | 2.3                    |
| CHA-OH(14,0%)  | 14                           | 0.95   | 0.8    | 0.11                         | 0.82   | 1.2                    |
| CHA-F(17,0%)   | 14                           | 0.44   | 0.7    | 0.10                         | 0.36   | 0.8                    |
| CHA-F(18,0%)   | 17                           | 1.02   | 0.7    | 0.12                         | 0.93   | 0.8                    |

<sup>a</sup>  $\text{H}^+/\text{Al}_{\text{tot}}$  measured on Cu-exchanged CHA zeolites

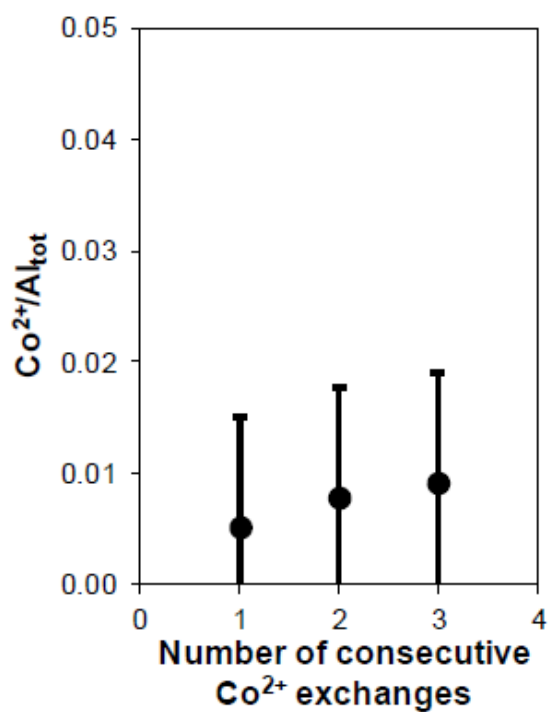


Figure 8.36. Amount of  $\text{Co}^{2+}$  retained on H-CHA-F(18,0%) as a function of successive  $\text{Co}^{2+}$  titrations with a 0.5M  $\text{Co}(\text{NO}_3)_2$  solution.

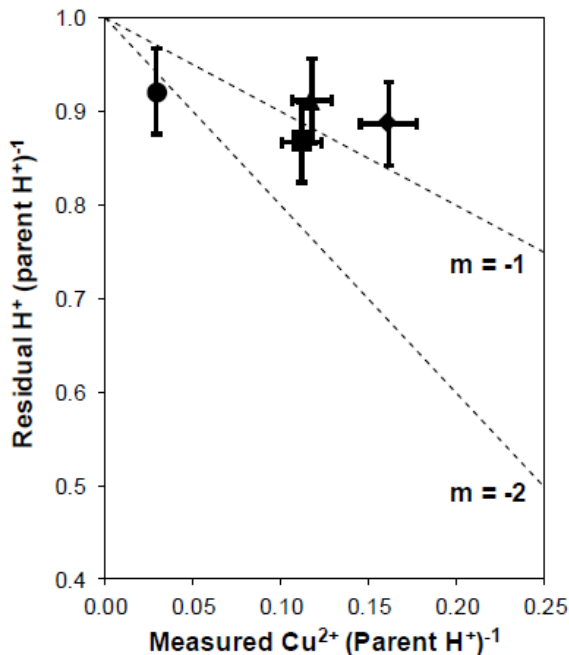


Figure 8.37. The number of residual  $\text{H}^+$  sites (per  $\text{H}^+$  site on the H-form parent zeolite) as a function of the Cu-loading (per  $\text{H}^+$  site on the H-form parent zeolite) for CHA-OH(16,24%) (circle), CHA-OH(14,0%) (square), CHA-F(17,0%) (diamond), and CHA-F(18,0%) (triangle) zeolites. Dashed lines represent the expected exchange stoichiometry for exclusively  $\text{Cu}^{2+}$  ( $m = -2$ ) or  $[\text{CuOH}]^+$  ( $m = -1$ ).

### 8.7.3 Methanol dehydration catalysis

#### Derivation of the associative methanol dehydration rate expression

A rate expression can be derived for the associative pathway using the pseudo-steady state hypothesis (PSSH) on reactive surface intermediates, and from assumptions about the irreversible or quasi-equilibrated nature of elementary steps. The concentrations of all surface intermediates (defined using square brackets), at steady-state, are described using PSSH:

$$\frac{d[C_{j*}]}{dt} \approx 0 \quad (8.4)$$

where  $[C_{j*}]$  is the concentration of surface species  $j$ . Density functional theory calculations show that the formation of dimethyl ether from the methanol-pair intermediate is irreversible and the rate-limiting elementary step for the associative dehydration pathway [82] and, as a result, the net rate of dimethyl ether formation from the associative pathway ( $r_{DME,A}$ ) can be expressed by the following expression:

$$r_{DME,A} = k_{DME,A}[P*] \quad (8.5)$$

Applying PSSH to the  $M^*$ ,  $D^*$ , and  $P^*$  intermediates, defined in the sequence of elementary steps in Scheme 8.12 (main text), yields the following expressions:

$$\frac{d[M*]}{dt} = k_M P_{CH_3OH}[*] + k_{-D}[D*] - k_{-M}[M*] - k_D P_{CH_3OH}[M*] \approx 0 \quad (8.6)$$

$$\frac{d[D*]}{dt} = k_D P_{CH_3OH}[M*] + k_{-P}[P*] - k_{-D}[D*] - k_P[D*] \approx 0 \quad (8.7)$$

$$\frac{d[P*]}{dt} = k_P[D*] - k_{-P}[P*] - k_{DME,A}[P*] \approx 0 \quad (8.8)$$

where  $k_j$  and  $k_{-j}$  are the forward and reverse rate constants for each elementary step, respectively, and  $P_{CH_3OH}$  is the gas phase methanol partial pressure. Assuming that methanol monomers and gas-phase methanol, methanol monomers and protonated dimers, and the intermediate methanol pairs and protonated dimers are all in quasi-equilibrium with each other, based on density functional theory calculations performed on unconfined, isolated  $H^+$  sites [82], steady-state surface concentrations are given by the representative equilibrium constants ( $K_j$ ):

$$[M*] = \frac{k_M}{k_{-M}} P_{CH_3OH}[*] = K_M P_{CH_3OH}[*] \quad (8.9)$$

$$[D*] = \frac{k_D}{k_{-D}} P_{CH_3OH}[M*] = K_D K_M P_{CH_3OH}^2[*] \quad (8.10)$$

$$[P*] = \frac{k_P}{k_{-P}} [D*] = K_P K_D K_M P_{CH_3OH}^2[*] \quad (8.11)$$

Substituting the expression for  $[P*]$  (Eq. 8.11) into Eq. 8.5, the rate expression become second-order in methanol partial pressure:

$$r_{DME,A} = k_{DME,A} K_P K_D K_M P_{CH_3OH}^2[*] \quad (8.12)$$



where the concentration of empty sites ( $[*]$ ) can be defined using a site balance to conserve the total number of sites involved in the reaction:

$$[L] = [*] + [M*] + [D*] + [P*] + [E*] \quad (8.13)$$

Here,  $[L]$  represents the total number of active sites (accessible to reactants) and can be quantified through direct titration by amine bases (e.g. *ex situ*  $\text{NH}_3$  titration, *in situ* pyridine titration). The total number of empty sites is assumed to be negligible because equilibrium between gas-phase methanol and vacant  $\text{H}^+$  sites and adsorbed methanol monomers (Step 1 in Scheme 8.12) favors the formation of methanol monomers adsorbed at  $\text{H}^+$  sites ( $K_M \gg 1$ ) [82], consistent with the observation that bridging OH vibrational bands are immediately and completely perturbed upon contact with gas-phase methanol during *in situ* IR experiments (Figure 8.49-8.51) [451]. The concentration of dimethyl ether ( $[E*]$ ) and methanol-pair intermediates ( $[P*]$ ) are also assumed to be negligible because equilibrium concentrations favor protonated methanol dimers and desorption of dimethyl ether into the gas-phase [82]. With these assumptions and substitution of Eqs. 8.9 and 8.10 into the site balance (Eq. 8.13), an expression for the concentration of empty sites can be obtained when methanol monomers and protonated dimers are the most abundant surface intermediates (MASI):

$$[*] = \frac{[L]}{K_M P_{\text{CH}_3\text{OH}} + K_D K_M P_{\text{CH}_3\text{OH}}^2} \quad (8.14)$$

Substitution of Eq. S118.14 into Eq. 8.12, yields a rate law in terms of only measurable quantities, equilibrium, and rate constants:

$$\frac{r_{\text{DME},A}}{[L]} = \frac{k_{\text{DME},A} K_P K_D P_{\text{CH}_3\text{OH}}}{1 + K_D P_{\text{CH}_3\text{OH}}} \quad (8.15)$$

This rate law can now be rearranged to yield an expression in terms of measurable first and zero-order apparent rate constants:

$$\frac{r_{\text{DME},A}}{[L]} = \frac{k_{\text{first}} P_{\text{CH}_3\text{OH}}}{1 + \frac{k_{\text{first}}}{k_{\text{zero}}} P_{\text{CH}_3\text{OH}}} \quad (8.16)$$

where  $k_{\text{first}}$  is the apparent first order rate constant and given by:

$$k_{\text{first}} = k_{\text{DME},A} K_P K_D \quad (8.17)$$

and  $k_{zero}$  is the apparent zero-order rate constant and given by:

$$k_{zero} = k_{DME,A}K_P \quad (8.18)$$

Derivation of the inhibited associative methanol dehydration rate expression

In order to account for the observed inhibition in the dimethyl ether formation rate (415 K, per  $H^+$ ) at high methanol partial pressures, an additional term involving an inhibitory methanol species ( $[I^*]$ ) needs to be added to the associative rate law. An additional methanol adsorption step involving methanol adsorbed at existing methanol dimers to form an inhibitory methanol trimer can be added to the existing set of elementary steps. The justification for including this step is described in detail in Section 8.7.6. This new adsorption step to form methanol clusters can be assumed to be in equilibrium with protonated methanol dimers and a gas-phase methanol species and an equilibrium constant can be defined to describe the concentration of these species on the surface:

$$[I^*] = \frac{k_I}{k_{-I}}[D^*]P_{CH_3OH} = K_I K_D K_M P_{CH_3OH}^3 [^*] \quad (8.19)$$

Including these methanol clusters as a MASI species, along with methanol monomers and protonated dimers, a new site balance can be derived:

$$[^*] = \frac{[L]}{K_M P_{CH_3OH} + K_D K_M P_{CH_3OH}^2 + K_P K_D K_M P_{CH_3OH}^3} \quad (8.20)$$

Substitution of Eq. 8.20 into Eq. 8.12, yields a new rate law in terms of only measurable quantities, and rate and equilibrium constants:

$$\frac{r_{DME,A}}{[L]} = \frac{k_{DME,A} K_P K_D P_{CH_3OH}}{1 + K_D P_{CH_3OH} + K_I K_D P_{CH_3OH}^2} \quad (8.21)$$

Derivation of the dissociative methanol dehydration rate expression

Rates of dimethyl ether formation via the dissociative pathway are governed by the rate at which methanol/methoxy pairs form dimethyl ether and, assuming this step to be irreversible, the rate expression becomes:

$$r_{DME,D} = k_{DME,D} [MMe^*] \quad (8.22)$$

The elimination of water from methanol monomers to form surface methoxy groups can be considered irreversible, because the equilibrated adsorption of methanol at surface methoxy species and the subsequent reaction to form dimethyl ether are considered to be much faster than the hydration of surface methoxy species to form methanol [82]. By applying PSSH to the  $M^*$ ,  $Me^*$ , and  $MMe^*$  intermediates, defined in Scheme 3 (main text), the following expressions are obtained:

$$\frac{d[M^*]}{dt} = k_M P_{CH_3OH}[*] + k_{-M}[M^*] - k_{elim}[M^*] \approx 0 \quad (8.23)$$

$$\frac{d[Me^*]}{dt} = k_{elim}[M^*] + k_{-MMe}[MMe^*] - k_{MMe}[Me^*] P_{CH_3OH} \approx 0 \quad (8.24)$$

$$\frac{d[P^*]}{dt} = k_{MMe}[Me^*] P_{CH_3OH} - k_{DME,D}[MMe^*] - k_{-MMe}[MMe^*] \approx 0 \quad (8.25)$$

where  $k_j$  and  $k_{-j}$  are the forward and reverse rate constants for each elementary step, respectively, and  $P_{CH_3OH}$  is the gas phase methanol partial pressure. Eqs. 8.23- 8.25 can be rearranged to solve for  $[M^*]$ ,  $[Me^*]$ , and  $[MMe^*]$ :

$$[M^*] = \frac{k_M P_{CH_3OH}[*]}{k_{-M} + k_{elim}} \quad (8.26)$$

$$[Me^*] = \frac{k_{elim}[M^*] + k_{-MMe}[MMe^*]}{k_{MMe} P_{CH_3OH}} \quad (8.27)$$

$$[P^*] = \frac{k_{MMe}[Me^*] P_{CH_3OH}}{k_{DME,D} + k_{-MMe}} \quad (8.28)$$

Substitution of Eqs. 8.26 and 8.28 into Eq. 8.27 yields an expression that can be explicitly solved for to find  $[Me^*]$ :

$$[Me^*] = \frac{k_{elim} \frac{k_M[*]}{k_{-M} + k_{elim}}}{k_{MMe}} \frac{k_{DME,D} + k_{-MMe}}{k_{DME,D}} \quad (8.29)$$

Further substitution of Eq. 8.29 back into Eq. 8.28 results in an expression that can be solved explicitly for  $[MMe^*]$ :

$$[MMe^*] = \frac{k_{elim}}{k_{DME,D}} \frac{k_M P_{CH_3OH}[*]}{k_{-M} + k_{elim}} \quad (8.30)$$

The adsorption of methanol to form methanol monomers, protonated dimers, and methanol/methoxy pairs can be considered quasi-equilibrated relative to the formation of dimethyl ether and surface methoxy groups and as a result  $k_M$ ,  $k_{-M}$ ,  $k_{MMe}$ , and  $k_{-MMe}$  are much greater than  $k_{elim}$  and  $k_{DME,D}$ . This allows Eqs. 8.26, 8.29,

and 8.30 to be written directly in terms of only forward rate constants, equilibrium constants, and measurable quantities:

$$[M*] = K_M P_{CH_3OH}[*] \quad (8.31)$$

$$[Me*] = \frac{k_{elim} K_M}{k_{DME,D} K_{MMe}} [*] \quad (8.32)$$

$$[MMe*] = \frac{k_{elim}}{k_{DME,D}} K_M P_{CH_3OH} [*] \quad (8.33)$$

The formation of protonated dimers can also be considered to be quasi-equilibrated and the surface concentration of such species can be expressed using Eq. 8.10. The rate of dimethyl ether formation can now be expressed in terms of quantifiable values by substitution of Eq. 8.33 into Eq. 8.22:

$$r_{DME,D} = k_{elim} K_M P_{CH_3OH} [*] \quad (8.34)$$

Considering methanol monomers, protonated dimers, and surface methoxy as MASI, the site balance for the dissociative pathway can be expressed as:

$$[L] = [M*] + [D*] + [Me*] \quad (8.35)$$

and the number of vacant sites can be solved for by substitution of Eqs. 8.10, 8.31, and 8.32 into Eq. 8.35:

$$[*] = \frac{[L]}{K_M P_{CH_3OH} + \frac{k_{elim} K_M}{k_{DME,D} K_{MMe}} + K_D K_M P_{CH_3OH}^2} \quad (8.36)$$

Substitution of Eq. 8.36 into 8.34 and dividing through by  $\frac{k_{elim} K_M}{k_{DME,D} K_{MMe}}$  yields a new rate expression in terms of only measurable quantities, rate constants, and equilibrium constants:

$$\frac{r_{DME,D}}{[L]} = \frac{k_{DME,D} K_{MMe} P_{CH_3OH}}{1 + \frac{k_{DME,D}}{k_{elim}} K_{MMe} P_{CH_3OH} + \frac{k_{DME,D}}{k_{elim}} K_{MMe} K_D P_{CH_3OH}^2} \quad (8.37)$$

Estimation of associative and dissociative first and zero-order rate constants using a generalized rate equation

Apparent first and zero-order rate constants can be predicted for both the dissociative and inhibited-associative dehydration pathways through a weighted-average

of both dehydration pathways using the relative fraction of paired and isolated  $H^+$  sites in each CHA zeolite:

$$\frac{r_{DME,D}}{[H^+]} = \gamma_{iso} \frac{k_A^{first} C_M}{1 + \frac{k_A^{first}}{k_A^{zero}} C_M + \frac{k_A^{first}}{k_A^{inverse}} C_M^2} + \gamma_{pair} \frac{k_D^{first} C_M}{1 + \frac{k_D^{first}}{k_D^{zero}} C_M + \frac{k_D^{first}}{k_D^{inverse}} C_M^2} \quad (8.38)$$

Here the subscript “A” refers to the associative pathway that occurs on the fraction of isolated  $H^+$  sites ( $\gamma_{iso}$ ) and the subscript “D” refers to the dissociative pathway that occurs on the fraction of paired  $H^+$  sites ( $\gamma_{pair}$ ).

### Elimination of background reaction artifacts

Several tests were performed to eliminate the contributions of background reactions from measured methanol dehydration rates. Rates of dimethyl ether formation were measured at 433 K and 3.5 kPa in an empty quartz reactor (per volume), over quartz wool (per gram), and over Si-CHA (per gram; pressed and sieved to a particle diameter of 180-250  $\mu\text{m}$  and held between two quartz wool plugs) after pretreatment to 773 K ( $0.033 \text{ K s}^{-1}$ ) in 5%  $O_2/He$  ( $0.83 \text{ cm}^3 \text{ s}^{-1}$ ; 99.999%, Indiana Oxygen) for 4 hours. For comparison, the dimethyl ether formation rate was also measured over an H-MFI catalyst (per gram; pelleted and sieved to a particle diameter of 180-250  $\mu\text{m}$  and held between two quartz wool plugs), in order to establish a baseline for comparison of the background reaction. Dimethyl ether formation rates were calculated by assuming differential conversions and validated by an observed linear increase in the methanol conversion with increasing reactor residence time. Contributions from quartz wool were subtracted from the reaction rate measured on Si-CHA and H-MFI. Measured rates of reaction of the blank reactor, quartz wool, Si-CHA, and H-MFI are presented in Table 8.12. Dimethyl ether formation rates (433 K, 3.5 kPa) in the gas-phase, on quartz wool, and on Si-CHA are more than six orders of magnitude lower than those measured on H-MFI (per gram). Thus, these background contributions were ignored when calculating rates of reaction on H-MFI and H-CHA catalysts.

Table 8.12.

Conversions and rates of DME formation (per gram) for various control materials measured at 433 K and 3.5 kPa CH<sub>3</sub>OH.

|                      | <b>CH<sub>3</sub>OH Conversion</b><br>/ % | <b>DME Formation Rate</b><br>/ mol DME (g <sub>cat</sub> s) <sup>-1</sup> | <b>DME Formation Rate</b><br>/ mol DME (L s) <sup>-1</sup> |
|----------------------|---|---|--|
| Blank Quartz Reactor | 3.9 x 10 <sup>-3</sup>                    | n.m.  | 2.1 x 10 <sup>-9</sup>                                     |
| Quartz Wool          | 1.1 x 10 <sup>-2</sup>                    | 1.4 x 10 <sup>-9</sup>  | n.m.   |
| Si-CHA               | 1.3 x 10 <sup>-2</sup>                    | 1.2 x 10 <sup>-9</sup>  | n.m.   |
| H-MFI(43)            | 12  | 4.8 x 10 <sup>-3</sup>  | n.m.   |

### Catalyst stability and time-on-stream deactivation

Deactivation of the catalyst was monitored by measuring methanol dehydration rate return points at a set of reference conditions (2.5 kPa  $\text{CH}_3\text{OH}$ , 415 K) at the beginning and end of every new catalyst loading (Figure 8.8 in main text and Figures 8.42-8.47) and no significant decrease in rate was observed as a function of time-on-stream for any of the catalysts reported here ( $<5\%$  after ca. 5 h time-on-stream; Figure 8.38).

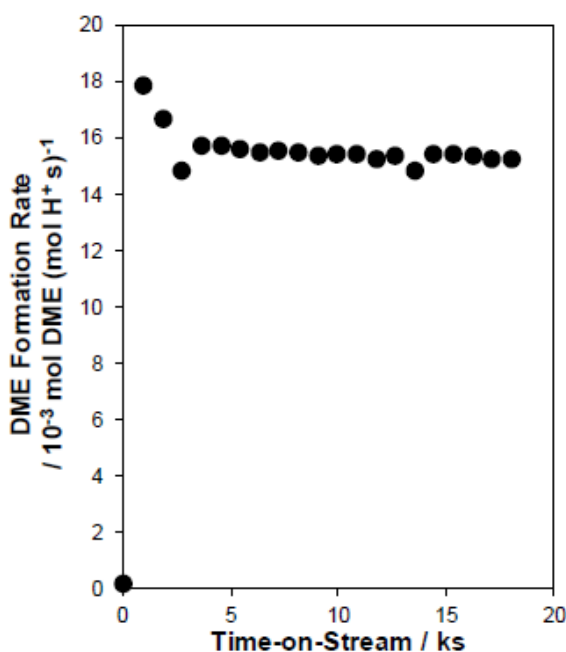


Figure 8.38. Methanol dehydration rates (per  $\text{H}^+$ , 415 K) on H-CHA-OH(14,0%) zeolites as a function of time-on-stream under 2.5 kPa  $\text{CH}_3\text{OH}$ .

### Elimination of approach to equilibrium artifacts

In addition to considering background artifacts contributing to the observed reaction rate, the proximity to the equilibrium conversion between methanol and dimethyl

ether must also be considered. Thermal equilibrium occurs when the ratio of the product and reactant thermodynamic activities are related by the equilibrium constant:

$$K = \frac{a_{DME}a_{H_2O}}{a_{CH_3OH}^2} \quad (8.39)$$

where the  $a_j$  terms are the thermodynamic activities of each species,  $j$ , and  $K$  is the equilibrium constant. These activities are related to the gas-phase concentrations and can be rewritten as:

$$a_j = \gamma_j RT C_j \quad (8.40)$$

Here,  $\gamma_j$  is the activity coefficient of species  $j$ ,  $R$  is the gas constant,  $T$  is the temperature, and  $C_j$  is the concentration of species  $j$ . Substituting Eq. 8.40 into Eq. 8.39, and assuming each species behaves ideally (i.e.  $\gamma_j = 1$ ), the equilibrium constant can now be rewritten in terms of the concentrations of each species:

$$K = \frac{C_{DME}C_{H_2O}}{C_{CH_3OH}^2} \quad (8.41)$$

Each of the concentration terms can now be written in terms of conversion to yield a final expression that describes the gas-phase equilibrium for methanol and dimethyl ether:

$$K = \frac{\frac{1}{4}X_{CH_3OH}^2}{(1 - X_{CH_3OH})^2} \quad (8.42)$$

The equilibrium constant can be expressed in terms of the free energies of reaction:

$$K = e^{\frac{-\Delta G_{RXN}^\circ}{RT}} \quad (8.43)$$

Where the free energy of reaction can be estimated from the standard free energies of formation for each species ( $\Delta G_j^\circ$ ) and the stoichiometric coefficient defined by the reaction chemistry ( $\nu_j$ ):

$$\Delta G_{RXN}^\circ = \sum \Delta G_j^\circ \frac{\nu_j}{\nu_{CH_3OH}} = \frac{1}{2} \Delta G_{H_2O}^\circ + \Delta G_{CH_3OH}^\circ = -9.65 \text{ kJ mol}^{-1} \quad (8.44)$$

The equilibrium constant can now be calculated at 433 K and gives  $K = 14.59$ , which can be used to calculate an equilibrium conversion of 0.88 (433 K). The approach to equilibrium was estimated to be  $<0.01$  at low conversions ( $<15\%$ ) and measured reaction rates should be uncorrupted by equilibrium.



## Benchmarking of measured reaction kinetics on H-MFI

In order to validate the measured kinetic data, methanol dehydration rates as a function of methanol partial pressure were measured on H-ZSM(30) and H-MFI(43) and compared with reported literature data at 433 K (Figure 8.39). Characterization data of H-MFI catalysts can be found in Table 8.6. DME formation rates (per  $\text{H}^+$ , 433 K) measured on both H-ZSM(30) and H-MFI(43) were nearly four times larger than those reported by Jones et al. under similar methanol partial pressures (0.1-20 kPa) and temperature (433 K) [83].

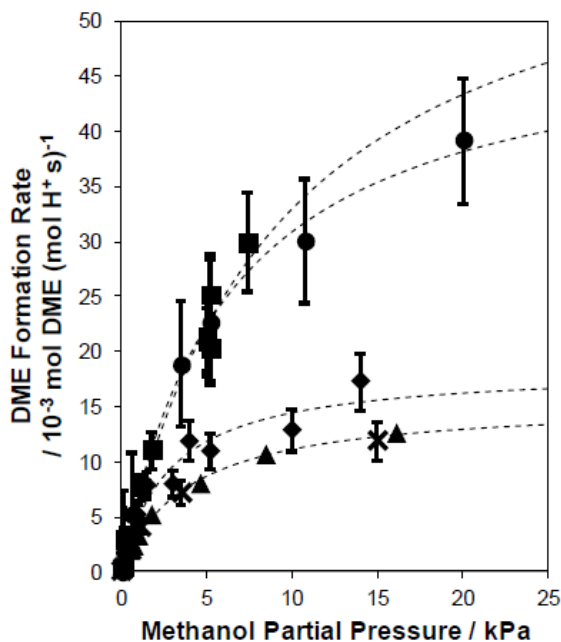


Figure 8.39. Methanol dehydration rates (per  $\text{H}^+$ ) on H-MFI(30) (squares) and H-MFI(43) (circles) at 433 K and on H-MFI(30) (diamonds) and H-MFI(43) (crosses) at 415 K. Triangle data points are methanol dehydration rates on H-MFI ( $\text{Si/Al} = 30$ ) at 433 K reported by Jones et al [83]. Dashed lines are regressions of the data to the associative pathway (Eq. 8.16).

In order to verify that this is not an error due to improper quantification of the number of Brønsted acid sites, *in situ* titration of  $\text{H}^+$  sites during steady state

methanol dehydration using pyridine was performed. Pyridine was chosen as the titrant because it is able to reversibly titrate available  $\text{H}^+$  sites within MFI and negligibly adsorbs on Lewis acid sites under steady state methanol dehydration conditions [83]. Methanol dehydration rates (433 K, per gram) decreased linearly with increasing amounts of pyridine dosed to the catalyst and were completely suppressed upon contact with sufficient amounts of pyridine (Figure 8.40).

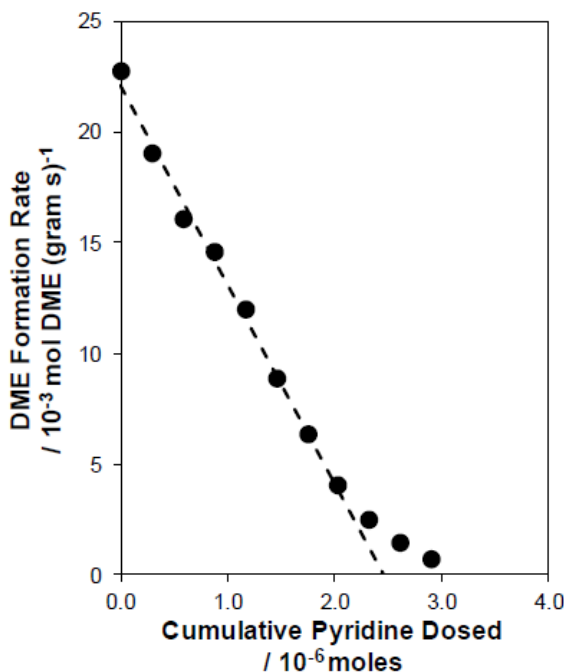


Figure 8.40. Methanol dehydration rates (per gram, 433 K) on H-MFI(43) zeolites as a function of cumulative moles of pyridine dosed. The dashed line is a linear regression to the data (last three points omitted).

Linear extrapolation of measured rates as a function of pyridine uptake to zero rate provides an estimate for the total number of catalytically active Brønsted acid sites and gives a  $\text{H}^+/\text{Al} = 0.87$ , in agreement with the number of protons measured by  $\text{NH}_3$  titration ( $\text{H}^+/\text{Al} = 0.85$  from  $\text{NH}_3$  TPD). Rates of DME formation (433 K) were fully recovered after treatment to 773 K ( $0.033 \text{ K s}^{-1}$ ) in 5%  $\text{O}_2/\text{He}$  ( $0.83 \text{ cm}^3 \text{ s}^{-1}$ ; 99.999%, Indiana Oxygen) for 4 hours, indicating that pyridine exclusively coordinates to  $\text{H}^+$

sites and that no structural changes occurred, leading to the observed decrease in the dehydration rate. These results indicate that the *ex situ*  $\text{NH}_3$  titrations are capable of quantifying  $\text{H}^+$  sites relevant for methanol dehydration chemistry in MFI zeolites and represent an accurate count of the number of active sites. Despite the confirmation that DME formation rates are properly normalized, the discrepancy between the measured and reported methanol dehydration rates persisted.

DME formation rates (per  $\text{H}^+$  from pyridine) were next measured as a function of temperature at various methanol pressures (0.1-20 kPa) until measured rates agreed with reported values from Jones et al [83]. Both first and zero-order rate constants (per  $\text{H}^+$  site from pyridine) on H-MFI(30) and H-MFI(43) were reproduced within 15% of the values reported by Jones et al. [83] at a temperature of 415 K (Figure 8.39). Additionally, activation parameters (405-433 K) in both the first and zero-order kinetic regimes agreed within 20% of those reported for methanol dehydration on MFI zeolites (Figure 8.41, Table 8.13), further indicating that first and zero order rate constants are being compared under the same catalytic conditions and that the difference in measured rates at 433 K is not due to a difference in surface coverages or apparent kinetic regimes. As both the first and zero-order rate constants (per  $\text{H}^+$  from pyridine) and apparent activation parameters were in agreement with those reported for MFI zeolites, the temperature of 415 K was chosen for all catalysts studied and the source of the discrepancy was not further investigated.

Table 8.13.

Activation parameters for associative rate first and zero order rate constants (per  $\text{H}^+$ ) on H-MFI(43) and an H-MFI ( $\text{Si}/\text{Al} = 30$ ) reported by Jones et al [451].

| Zeolite Sample                   | $\Delta H_{\text{zero}}$<br>/ $\text{kJ mol}^{-1}$ | $\Delta H_{\text{first}}$<br>/ $\text{kJ mol}^{-1}$ | $\Delta S_{\text{zero}}$<br>/ $\text{J mol}^{-1} \text{K}^{-1}$ | $\Delta S_{\text{first}}$<br>/ $\text{J mol}^{-1} \text{K}^{-1}$ | $\Delta G_{\text{zero}}$<br>/ $\text{kJ mol}^{-1}$ | $\Delta G_{\text{first}}$<br>/ $\text{kJ mol}^{-1}$ |
|----------------------------------|--|---|---|--|--|---|
| H-MFI<br>Si/Al = 43              | $93 \pm 5$   | $48 \pm 5$  | $-58 \pm 7$   | $-149 \pm 8$   | $119 \pm 10$                                       | $112 \pm 10$  |
| H-MFI<br>Si/Al = 30 <sup>a</sup> | $90 \pm 2$   | $42 \pm 2$  | $-75 \pm 2$   | $-160 \pm 10$  | $123 \pm 3$  | $111 \pm 9$   |

<sup>a</sup>Activation parameters reported by Jones et al.<sup>10</sup>

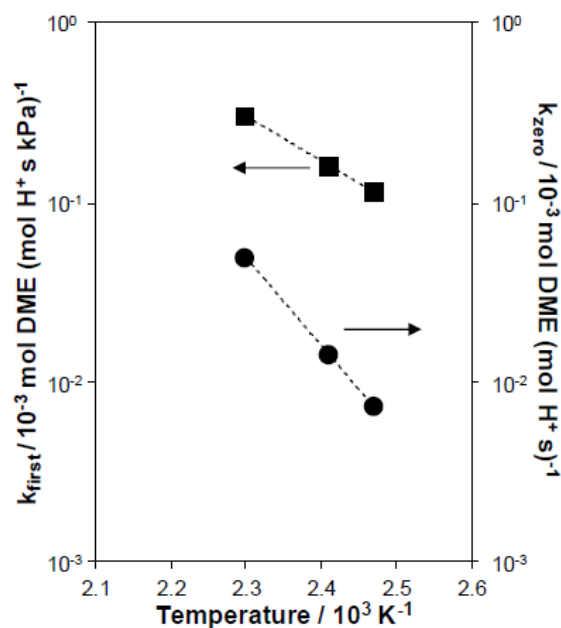


Figure 8.41. Associative rate first (squares) and zero (circles) order rate constants (per  $\text{H}^+$ ) on H-MFI(43) measured as a function of temperature (405-433 K).

DME formation rates (415 K) measured as a function of  $\text{CH}_3\text{OH}$  pressure

Rates of methanol dehydration (415 K, per  $\text{H}^+$ ) measured as a function of methanol partial pressure (0.05–50 kPa) are shown in Figure 8.8 of the main text for H-CHA-OH(14,0%), H-CHA-OH(15,18%), H-CHA-OH(16,24%), H-CHA-OH(17,30%), and H-CHA-OH(14,44%) zeolites. Figures 8.42–8.48 show methanol dehydration rates (per  $\text{H}^+$ , 415 K) as a function of methanol partial pressure for H-CHA-OH(16,0%), H-CHA-OH(26,0%), H-CHA-F(17,0%), H-CHA-OH(16,6%), H-MFI(17), H-MFI(30), and H-MFI(43), respectively.

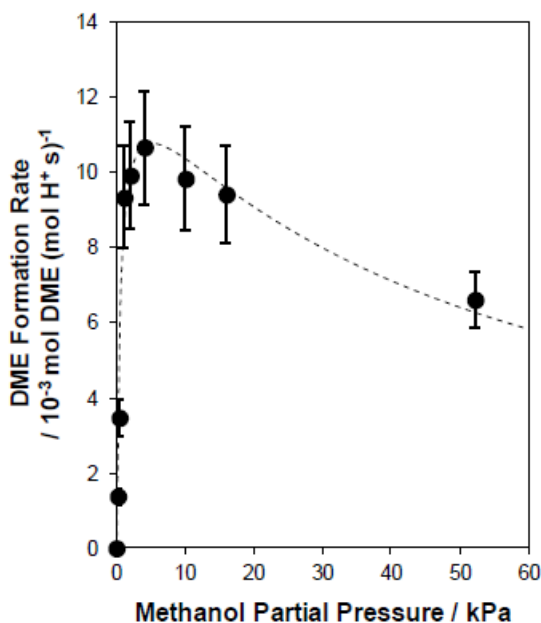


Figure 8.42. Methanol dehydration rates (per  $\text{H}^+$ , 415 K) on H-CHA-OH(16,0%) as a function of methanol partial pressure. Dashed line is a regression to the generalized rate expression (Eq. 8.38).

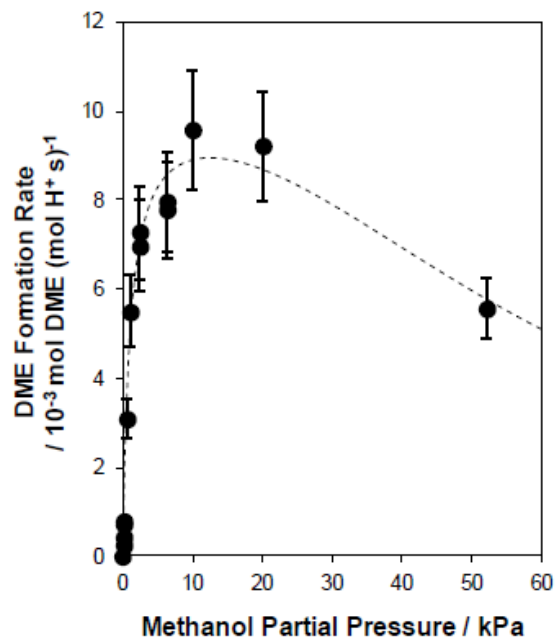


Figure 8.43. Methanol dehydration rates (per  $\text{H}^+$ , 415 K) on H-CHA-OH(26,0%) as a function of methanol partial pressure. Dashed line is a regression to the generalized rate expression (Eq. 8.38).

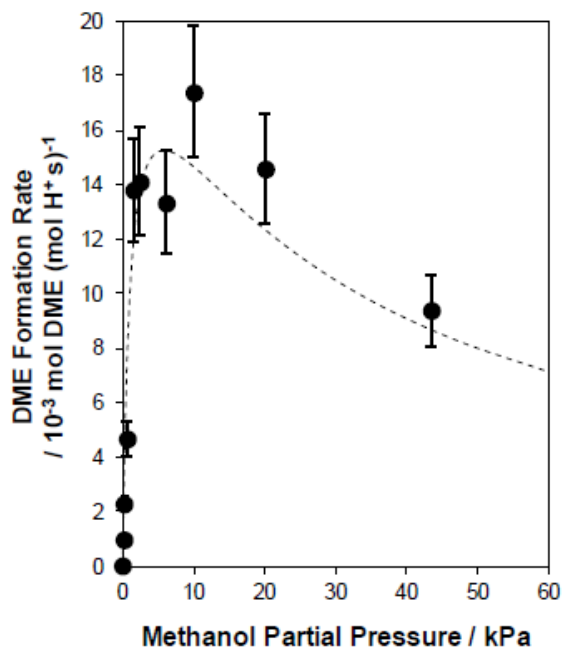


Figure 8.44. Methanol dehydration rates (per H<sup>+</sup>, 415 K) on H-CHA-F(17,0%) as a function of methanol partial pressure. Dashed line is a regression to the generalized rate expression (Eq. 8.38).

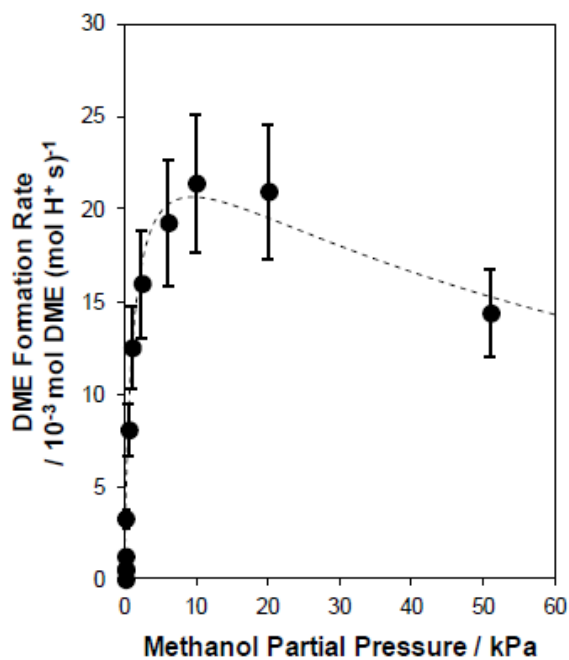


Figure 8.45. Methanol dehydration rates (per H<sup>+</sup>, 415 K) on H-CHA-OH(16,6%) as a function of methanol partial pressure. Dashed line is a regression to the generalized rate expression (Eq. 8.38).



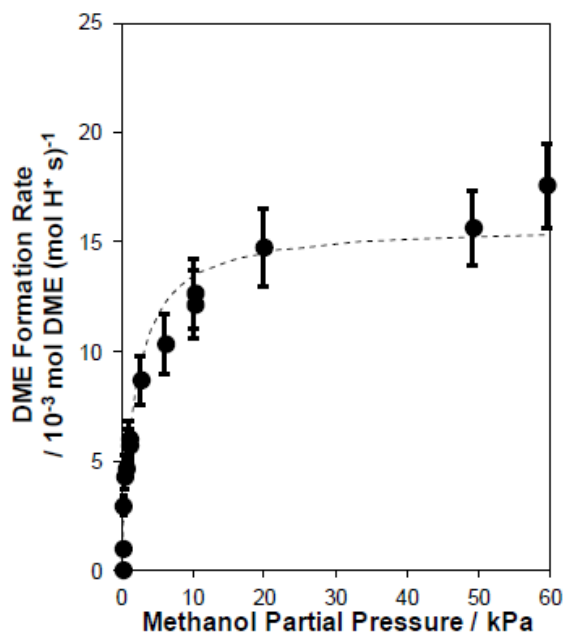


Figure 8.46. Methanol dehydration rates (per H<sup>+</sup>, 415 K) on H-MFI(17) as a function of methanol partial pressure. Dashed line is a regression to the associative rate expression (Eq. 8.16).

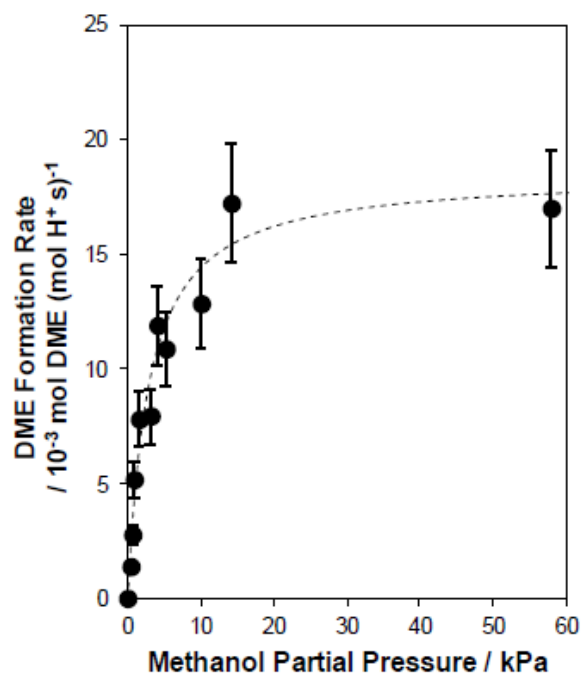


Figure 8.47. Methanol dehydration rates (per H<sup>+</sup>, 415 K) on H-MFI(30) as a function of methanol partial pressure. Dashed line is a regression to the associative rate expression (Eq. 8.16).

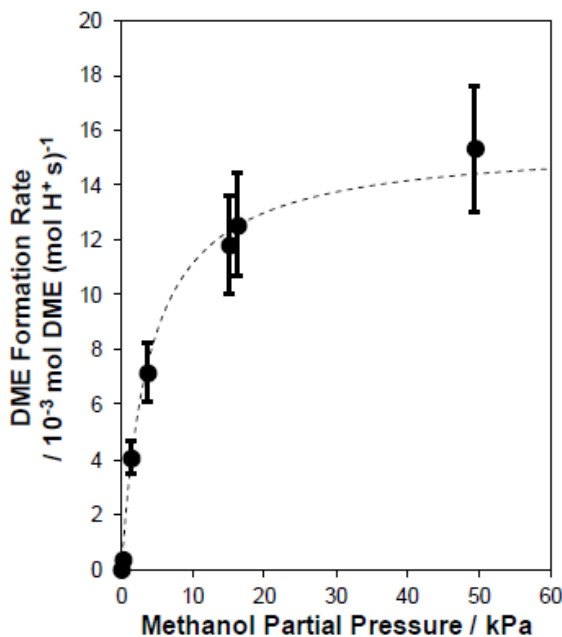


Figure 8.48. Methanol dehydration rates (per  $\text{H}^+$ , 415 K) on H-MFI(43) as a function of methanol partial pressure. Dashed line is a regression to the associative rate expression (Eq. 8.16).

Regression of reported associative first-order rate constants (433 K, per  $\text{H}^+$ ), measured on a wide range of zeolites with varying pore size (0.5-1.2 nm free sphere diameter) [22], allows for the estimation of first-order rate constants as a function of pore diameter and suggests that dehydration intermediates in CHA zeolites are confined in voids of size similar to that of the 6-MR and 8-MR apertures of the CHA framework (Figure 8.49).

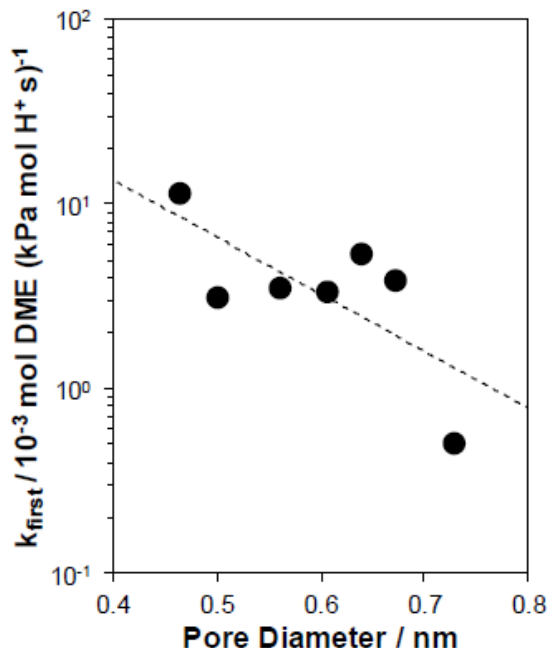


Figure 8.49. Associative first order rate constants (per  $\text{H}^+$ , 433 K) as a function of pore diameter in MFI, MTT, MTW, MOR, SFH, BEA, and FAU zeolites. Dashed line is an exponential regression to the data. All data is reproduced from Jones et al [22].

Estimation of dehydration rate constants on isolated and paired protons in CHA zeolites

Extraframework Al species, observed here on CHA zeolites containing  $\gg 30\%$  of Al in paired sites ( $^{27}\text{Al}$  NMR spectra in Section S.2, SI), do not contribute significantly to measured rates of methanol dehydration [83,118] and the presence of extra-lattice Al moieties, which have been shown to artificially decrease the void diameter surrounding reactive intermediates [118], is not responsible for the observed increase in both first and zero-order rate constants, because only first-order dehydration rate constants are sensitive to changes in void diameter [22]. Additionally, CHA-OH(15,18%) zeolites show first and zero-order rate constants larger than those measured on isolated protons in CHA, despite minimal amounts of extraframework Al (Figure 8.34), further indicating that extraframework Al species do not contribute to the observed

increase in apparent rate constants as a function of the fraction of Al atoms in pairs. Using the generalized dehydration rate expression (Eq. 8.38), the observed first and zero order rate constants (415 K, per  $\text{H}^+$ ) can be expressed as a function of the fraction of paired Al in each CHA catalyst. Extrapolation of the observed first and zero order rate constants to the limit of Al isolation (0% paired Al) allows for estimation of methanol dehydration rate constants for the associative pathway on isolated  $\text{H}^+$  sites. Additionally, extrapolation to the limit of complete pairing (100% paired Al) rate constants for the dissociative pathway on paired protons can be estimated and are nearly an order of magnitude larger than the associative rate constants (Figure 8.9 in main text).

#### 8.7.4 IR spectra under steady methanol dehydration

Measurement of *in situ* IR spectra on CHA and MFI zeolites

IR spectra recorded on H-CHA-OH(14,0%), H-CHA-OH(14,44%), and H-MFI(43) under various methanol pressures (0.15-22 kPa) are shown in Figures 8.50-8.52.

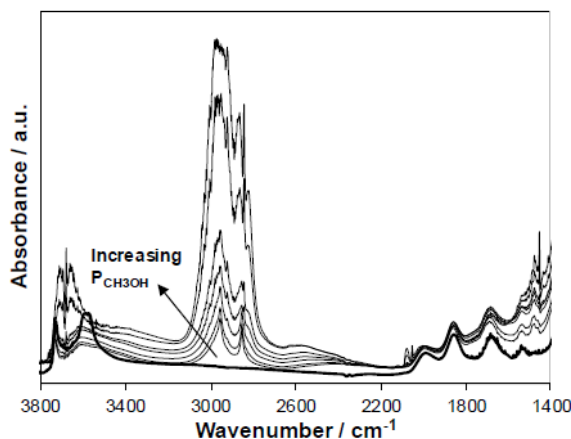


Figure 8.50. IR spectra of H-CHA-OH(14,0%) under 0 kPa  $\text{CH}_3\text{OH}$  (bold) and 0.15, 0.77, 1.5, 3.0, 5.9, 13.5, and 22 kPa  $\text{CH}_3\text{OH}$  (thin) at 415 K.

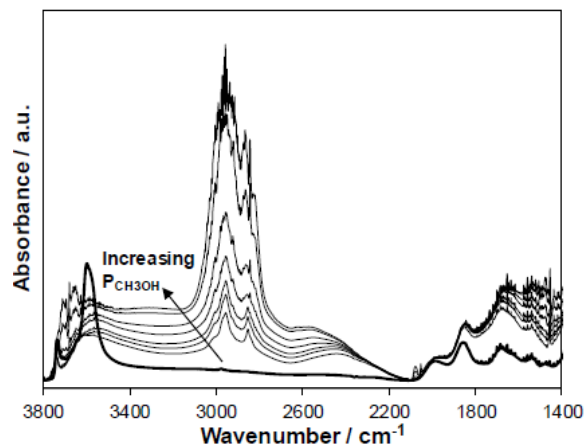


Figure 8.51. IR spectra of H-CHA-OH(14,44%) under 0 kPa CH<sub>3</sub>OH (bold) and 0.15, 0.77, 1.5, 3.0, 5.9, 13.5, and 22 kPa CH<sub>3</sub>OH (thin) at 415 K.

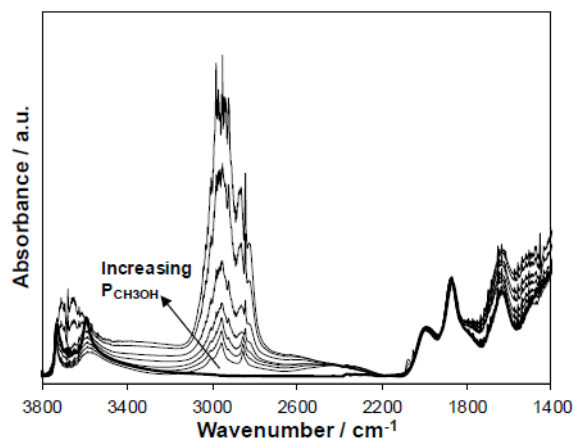


Figure 8.52. IR spectra of H-MFI(43) under 0 kPa CH<sub>3</sub>OH (bold) and 0.15, 0.77, 1.5, 3.0, 5.9, 13.5, and 22 kPa CH<sub>3</sub>OH (thin) at 415 K.

In order to establish an experimental reference for surface methoxy deformation modes, H-CHA-OH(14,0%), which was chosen because it contains a single type of active site (i.e., only isolated protons), was equilibrated under steady-state methanol pressure (0.15 kPa) and then purged in dry He ( $13.3 \text{ cm}^3 \text{ s}^{-1} \text{ g}^{-1}$ ) for 30 minutes

at 523 K until the spectra remained constant. Similar procedures have been used to isolated surface methoxy species observed during IR [451, 468, 469],  $^{13}\text{C}$  NMR [470], and neutron scattering [471] spectroscopic studies of methanol-to-olefins chemistry.

#### 8.7.5 Evaluation of mass transfer in CHA zeolites

##### Space velocity test to verify differential operation

Differential operation was confirmed by measuring the rate of methanol dehydration (per  $\text{H}^+$ , 415 K) as a function of inverse space velocity (i.e. residence time) at fixed methanol partial pressures on each MFI and CHA zeolite prior to kinetic analysis. Figure 8.53 shows a typical space velocity test performed at 1 kPa  $\text{CH}_3\text{OH}$ . On all catalysts tested, the  $\text{CH}_3\text{OH}$  conversion increased linearly with increasing residence time and DME formation rates (per  $\text{H}^+$ , 415 K) were invariant with residence time at fixed  $\text{CH}_3\text{OH}$  partial pressure. These results confirm that each catalyst is operating under differential conditions and rates are independent of reactor hydrodynamics.

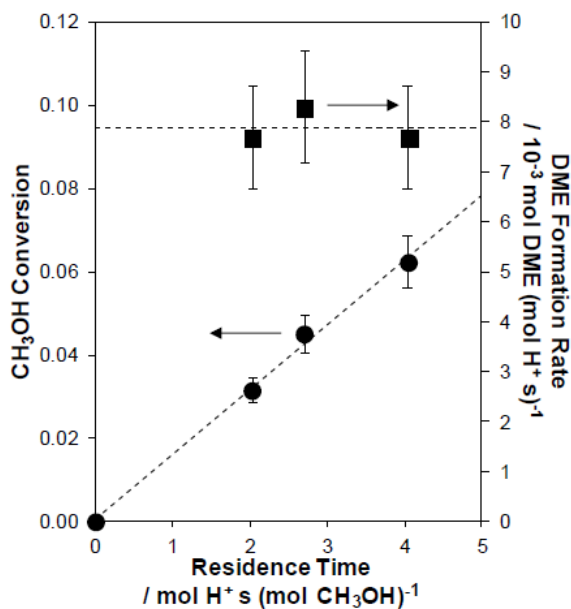


Figure 8.53. Methanol dehydration rates (squares; per  $\text{H}^+$ , 415 K, 1 kPa  $\text{CH}_3\text{OH}$ ) and conversion (circles) on H-CHA-OH(14,0%) as a function of residence time. Dashed lines represent a linear regression to conversion data and the average rate of DME formation.

Derivation of concentration gradients in spherical catalyst particles for coupled reaction and internal diffusion

When rates of internal mass transport become similar to or less than the rate of reaction, severe concentration gradients will exist within porous catalysts resulting in an inhomogeneous reaction rate and, in the process, corrupting measurements of reaction kinetics. The severity of these internal concentration gradients can be predicted through models of coupled reaction and transport phenomena and used to assess internal mass transport restrictions. For steady state reaction and diffusion within a spherical catalyst particle that is free of external mass transfer limitations (Section 8.7.5), the differential equation that describes the concentration of methanol as a function of particle radius is:

$$\frac{d^2 C_M}{dr^2} + \frac{2}{r} \frac{dC_M}{dr} - \frac{2\rho_s}{D_e} r'_{DME} = 0 \quad (8.45)$$



Here,  $C_M$  is the concentration of methanol ( $\text{mol m}^{-3}$ ),  $r$  is the distance from the center of the pellet (m),  $\rho_s$  is the proton density per volume ( $\text{mol H}^+ \text{m}^{-3}$ ),  $D_e$  is the effective self-diffusivity of methanol inside the pore ( $\text{m}^2 \text{s}^{-1}$ ), and  $r'_{DME}$  is the rate of DME formation ( $\text{mol DME (mol H}^+ \text{s)}^{-1}$ ). The factor of 2 accounts for the difference in stoichiometry between the product DME and methanol reactant ( $r_M = -2r_{DME}$ ). The self-diffusivity of methanol within CHA was estimated from reported molecular dynamics simulations of methanol diffusion within DDR zeolites ( $D_e(360 \text{ K}) = 7.5 \times 10^{-11} \text{ m}^2 \text{s}^{-1}$ ) [472], which is similar to CHA in both limiting pore diameter (8-MR, 0.37 nm) and pore connectivity (window-cage structure), and extrapolated to the relevant reaction temperature ( $D_e(415 \text{ K}) = 9.3 \times 10^{-11} \text{ m}^2 \text{s}^{-1}$ ) using Chapman-Enskog theory:

$$D_e(T_2) = D_e(T_1) \left( \frac{T_2}{T_1} \right)^{3/2} \quad (8.46)$$

The rate of DME formation (per  $\text{H}^+$ ) can be expressed using the generalized rate expression (Eq. 8.38) that weights the contribution from both the associative and dissociative pathways as a function of the relative population of isolated and paired Al sites, respectively and allows for Eq. 8.45 to be rewritten as:

$$\frac{d^2 C_M}{dr^2} + \frac{2}{r} \frac{dC_M}{dr} - \frac{2\rho_s}{D_e} \left[ \gamma_{iso} \frac{k_A^{first} C_M}{1 + \frac{k_A^{first}}{k_A^{zero}} C_M + \frac{k_A^{first}}{k_A^{inverse}} C_M^2} + \gamma_{pair} \frac{k_D^{first} C_M}{1 + \frac{k_D^{first}}{k_D^{zero}} C_M + \frac{k_D^{first}}{k_D^{inverse}} C_M^2} \right] = 0 \quad (8.47)$$

Figures 8.14-8.62 show concentration profiles as a function of particle radius and concentration at 415 K for each CHA zeolite studied here. Bulk-phase methanol concentrations were chosen to be similar to those used during methanol dehydration catalysis (0.05-52 kPa  $\text{CH}_3\text{OH}$ ). It is apparent that the low-aluminum CHA catalyst containing only isolated  $\text{H}^+$  sites ( $\text{Si/Al} = 30$ ) exhibits severe concentration gradients in the first-order kinetic regime ( $<1 \text{ kPa}$ ), in agreement with lower observed rates of DME formation (415 K, per  $\text{H}^+$ ) than on CHA with all isolated Al sites at higher Al content ( $\text{Si/Al} = 15$ ). These results are also in agreement with the measured crystallite size, which increases nearly four-fold from a particle diameter of  $1.5 \mu\text{m}$

(Si/Al = 15) to 6  $\mu\text{m}$  (Si/Al = 30). All other CHA zeolites examined at Si/Al = 15 (0-44% paired Al) contain crystallite sizes smaller than 1.5  $\mu\text{m}$  and show minimal internal concentration gradients despite rates of reaction that increased systematically with the fraction of paired Al (Figure 8.8 in main text).

There was, however, a general decrease in the crystallite size as a function of paired Al content and to eliminate this as a possible contributor to the increase in observed DME formation rates (415 K, per  $\text{H}^+$ ), a nano-sized CHA zeolite was synthesized using  $\text{TMAda}^+$  cations and the surfactant hexadecyl-trimethylammonium bromide (CTAB) in the absence of  $\text{Na}^+$  [457]. SEM micrographs show that the nano-sized CHA zeolite contains crystallites about 800 nm in diameter (Figure 8.31) and  $\text{Co}^{2+}$  titrations show that these zeolites contain a small fraction of paired Al sites ( $\text{Co}/\text{Al} = 0.03$ ), introduced by including an additional quaternary amine (i.e. CTAB). Methanol dehydration rates (415 K, per  $\text{H}^+$ ) on nano-sized CHA follow the same trend as seen for CHA zeolites prepared through conventional synthesis protocols, where both the first and zero order rate constants increase as a function of paired Al content (Figure 8.9 in main text; Tables 8.3-8.5). Predicted internal concentration gradients are also negligible on nano-sized CHA (Figure 8.58), in line with previous observations that CHA zeolite with crystallite sizes  $< 2 \mu\text{m}$  are free of internal concentration gradients. These results further demonstrate that the increase in DME formation rate (per  $\text{H}^+$ ) across CHA zeolites containing different amounts of paired Al (Si/Al = 15) is solely a function of the number of paired Al sites and not a crystal size effect.

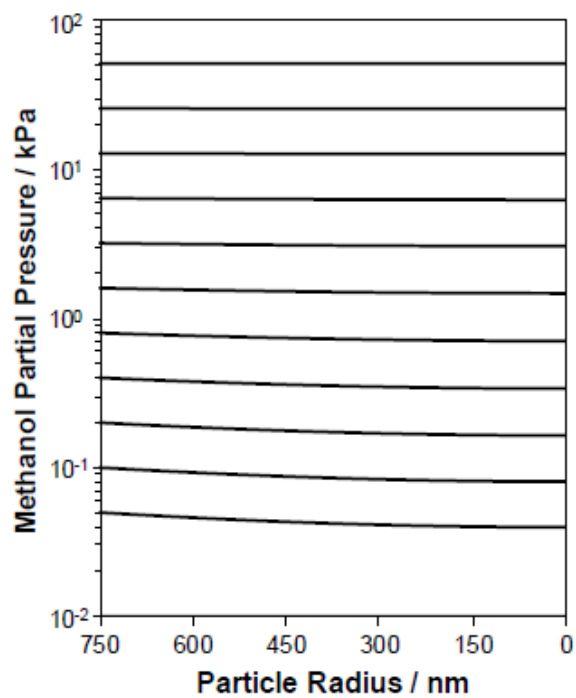


Figure 8.54. Methanol partial pressures in H-CHA-OH(14,0%) as a function of particle radius, where zero is the crystal center, for bulk  $\text{CH}_3\text{OH}$  pressures of 0.05, 0.1, 0.2, 0.4, 0.8, 1.6, 3.2, 6.4, 12.8, 25.6, and 51.2 kPa at 415 K.

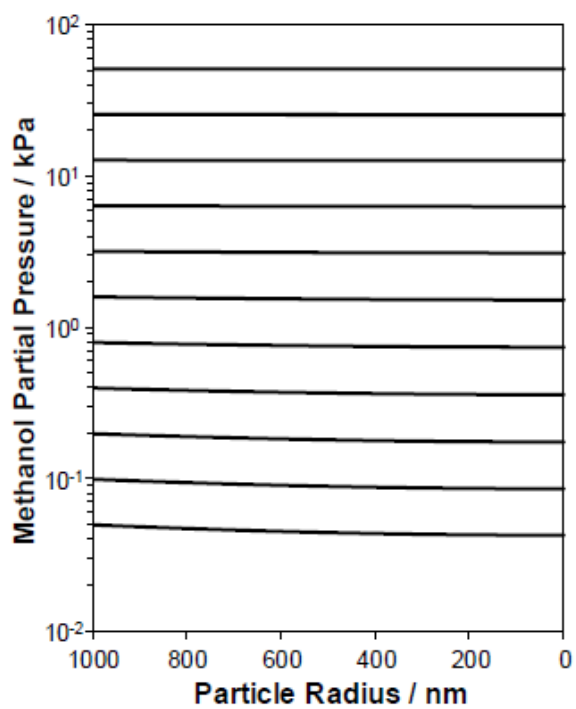


Figure 8.55. Methanol partial pressures in H-CHA-OH(17,0%) as a function of particle radius, where zero is the crystal center, for bulk  $\text{CH}_3\text{OH}$  pressures of 0.05, 0.1, 0.2, 0.4, 0.8, 1.6, 3.2, 6.4, 12.8, 25.6, and 51.2 kPa at 415 K.

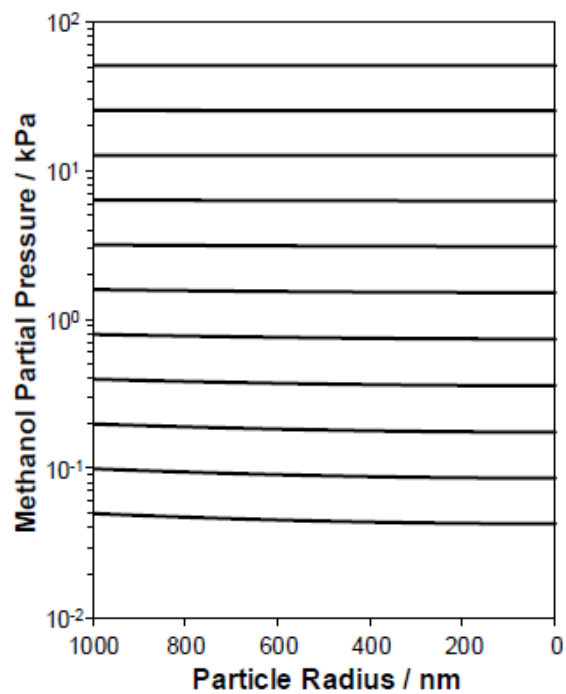


Figure 8.56. Methanol partial pressures in H-CHA-F(18,0%) as a function of particle radius, where zero is the crystal center, for bulk  $\text{CH}_3\text{OH}$  pressures of 0.05, 0.1, 0.2, 0.4, 0.8, 1.6, 3.2, 6.4, 12.8, 25.6, and 51.2 kPa at 415 K.

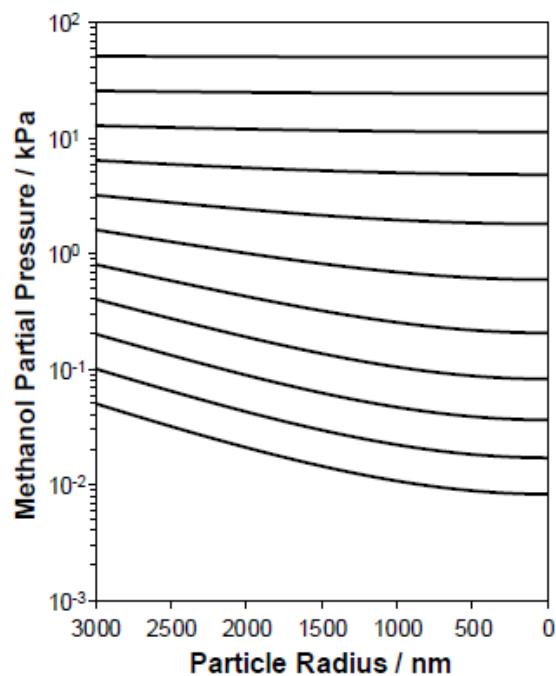


Figure 8.57. Methanol partial pressures in H-CHA-OH(27,0%) as a function of particle radius, where zero is the crystal center, for bulk  $\text{CH}_3\text{OH}$  pressures of 0.05, 0.1, 0.2, 0.4, 0.8, 1.6, 3.2, 6.4, 12.8, 25.6, and 51.2 kPa at 415 K.

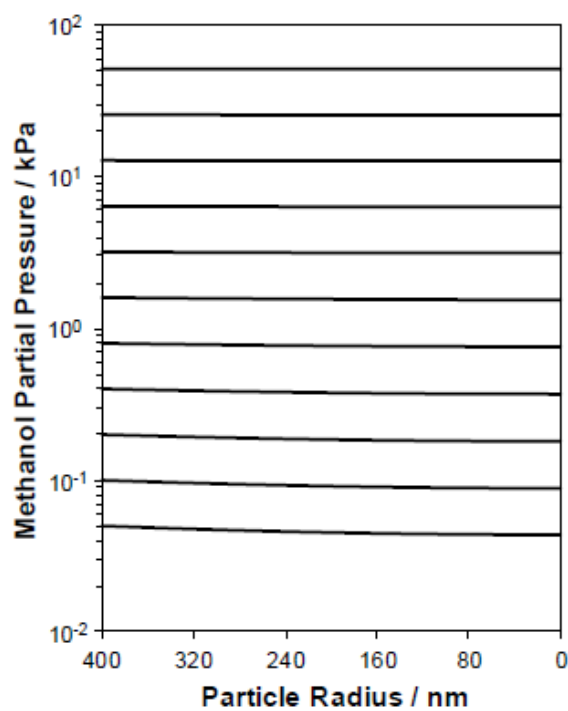


Figure 8.58. Methanol partial pressures in H-CHA-OH(16,6%) as a function of particle radius, where zero is the crystal center, for bulk  $\text{CH}_3\text{OH}$  pressures of 0.05, 0.1, 0.2, 0.4, 0.8, 1.6, 3.2, 6.4, 12.8, 25.6, and 51.2 kPa at 415 K.

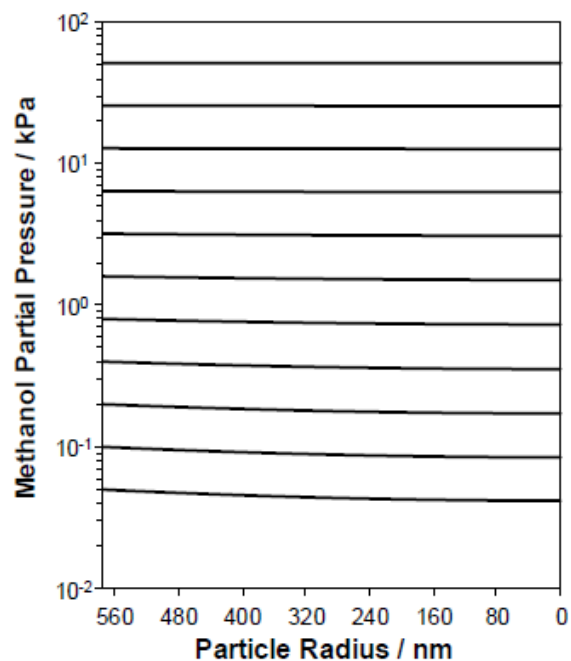


Figure 8.59. Methanol partial pressures in H-CHA-OH(15,18%) as a function of particle radius, where zero is the crystal center, for bulk  $\text{CH}_3\text{OH}$  pressures of 0.05, 0.1, 0.2, 0.4, 0.8, 1.6, 3.2, 6.4, 12.8, 25.6, and 51.2 kPa at 415 K.



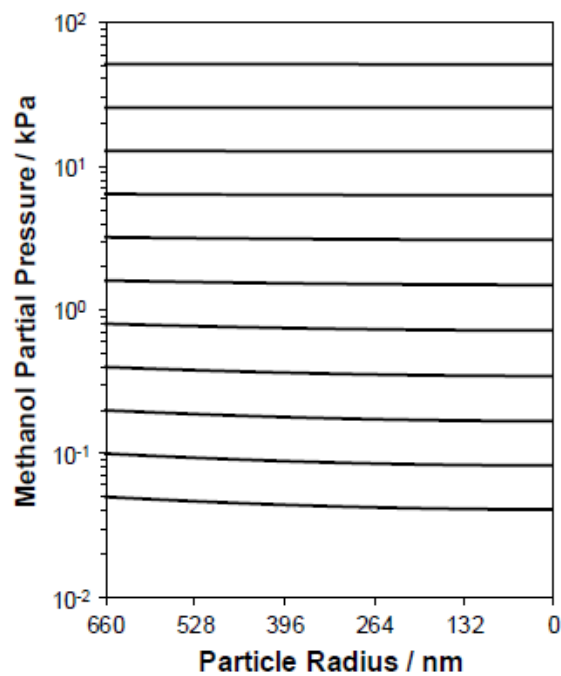


Figure 8.60. Methanol partial pressures in H-CHA-OH(16,24%) as a function of particle radius, where zero is the crystal center, for bulk  $\text{CH}_3\text{OH}$  pressures of 0.05, 0.1, 0.2, 0.4, 0.8, 1.6, 3.2, 6.4, 12.8, 25.6, and 51.2 kPa at 415 K.

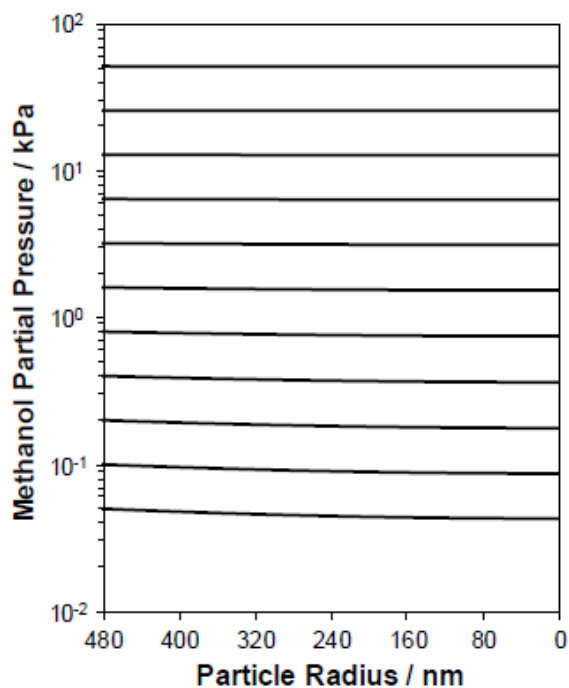


Figure 8.61. Methanol partial pressures in H-CHA-OH(17,30%) as a function of particle radius, where zero is the crystal center, for bulk  $\text{CH}_3\text{OH}$  pressures of 0.05, 0.1, 0.2, 0.4, 0.8, 1.6, 3.2, 6.4, 12.8, 25.6, and 51.2 kPa at 415 K.

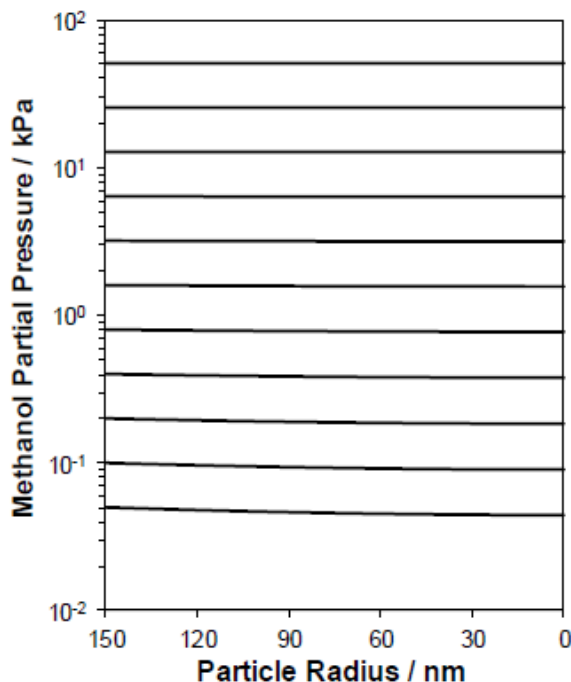


Figure 8.62. Methanol partial pressures in H-CHA-OH(14,44%) as a function of particle radius, where zero is the crystal center, for bulk  $\text{CH}_3\text{OH}$  pressures of 0.05, 0.1, 0.2, 0.4, 0.8, 1.6, 3.2, 6.4, 12.8, 25.6, and 51.2 kPa at 415 K.

#### Derivation of first and zero order effectiveness factors

A more quantitative evaluation of internal mass transfer can be evaluated by calculating the internal effectiveness factor as a function of the Thiele modulus for each CHA catalyst. For evaluation of the Thiele modulus, distinct first and zero order reaction rate laws were defined:

$$r'_{first} = (\gamma_{iso}k_A^{first} + \gamma_{pair}k_D^{first})C_M \quad (8.48)$$

$$r'_{zero} = \gamma_{iso}k_A^{zero} + \gamma_{pair}k_D^{zero} \quad (8.49)$$

The rate of reaction for each kinetic regime will be evaluated using a generalize rate expression (Eq. 8.38) that accounts for contributions from both relevant kinetic pathways that occur uniquely at isolated (e.g. associative) and paired protons (e.g.

dissociative). Additionally, all sites are assumed to be saturated with kinetically-relevant intermediates in the zero-order regime.

Eq. 8.45 can be non-dimensionalized by normalizing by the bulk fluid concentration ( $C_B$ ) and the particle radius ( $r_p$ ) to yield:

$$\frac{d^2\Psi}{d\lambda^2} + \frac{2}{\lambda} \frac{d\Psi}{d\lambda} - \frac{2\rho_s r_p^2}{C_B D_e} r'_{DME} = 0 \quad (8.50)$$

where,

$$\Psi = \frac{C_m(r)}{C_B} \quad (8.51)$$

$$\lambda = \frac{r}{r_p} \quad (8.52)$$

The different DME formation rates specific to each unique kinetic regime can further be rewritten using the non-dimensional concentration ( $\Psi$ ) to give:

$$r'_{first} = (\gamma_{iso} k_A^{first} + \gamma_{pair} k_D^{first}) \Psi C_B \quad (8.53)$$

$$r'_{zero} = \gamma_{iso} k_A^{zero} + \gamma_{pair} k_D^{zero} \quad (8.54)$$

Substitution of these rates into Eq. 8.50 yield the following differential equations that describe the concentration profile for each kinetic regime:

$$\frac{d^2\Psi}{d\lambda^2} + \frac{2}{\lambda} \frac{d\Psi}{d\lambda} - \frac{2\rho_s r_p^2 (\gamma_{iso} k_A^{first} + \gamma_{pair} k_D^{first})}{D_e} \Psi = 0 \quad (8.55)$$

$$\frac{d^2\Psi}{d\lambda^2} + \frac{2}{\lambda} \frac{d\Psi}{d\lambda} - \frac{2\rho_s r_p^2 (\gamma_{iso} k_A^{zero} + \gamma_{pair} k_D^{zero})}{C_B D_e} = 0 \quad (8.56)$$

A distinct Thiele Modulus ( $\phi_i$ ) can then be defined for each regime by the ratio of constants in the last term on the left-hand side as follows:

$$\phi_{first}^2 = \frac{2\rho_s r_p^2 (\gamma_{iso} k_A^{first} + \gamma_{pair} k_D^{first})}{D_e} \quad (8.57)$$

$$\phi_{first}^2 = \frac{2\rho_s r_p^2 (\gamma_{iso} k_A^{zero} + \gamma_{pair} k_D^{zero})}{C_B D_e} \quad (8.58)$$

Thiele moduli were estimated from the ratio of the reaction rate, evaluated independently for each sample using either experimentally measured first-order rate constants, or those calculated from the correlation between the apparent first-order rate constant as a function of the fraction of Al in pairs (Figure 8.9 in main text), to diffusion rate evaluated at the gas-phase concentration. The effectiveness factor can

then be expressed as the ratio of the observed reaction rate to the theoretical reaction rate evaluated at the bulk concentration:

$$\eta = \frac{r'_{DME}(C_m(r))}{r'_{DME}(C_B)} \quad (8.59)$$

Effectiveness factors were calculated from the ratio of the observed reaction rate, using apparent first-order rate constants, to the theoretical reaction rate evaluated at the gas-phase concentration, using first-order rate constants extracted from Figure 8.9 in the main text.

Equations 8.55 and 8.56 can be solved analytically for the concentration profile inside the catalyst pellet and substituted into Eqs. 8.53 and 8.54 to derive an expression for the actual rate of reaction as a function of particle radius for each unique kinetic regime. The effectiveness factor can then be evaluated as a function of the Thiele modulus for the first and zero order kinetic regimes:

$$\eta_{first} = \frac{3}{\phi_{first}^2} (\phi_{first} \coth(\phi_{first}) - 1) \quad (8.60)$$

$$\eta_{zero} = 1 \quad (8.61)$$

Figure 8.6 in main text shows the effectiveness factor for a first order reaction as a function of the Thiele modulus.

#### 8.7.6 Origin of kinetic inhibition in CHA zeolites

Unlike MFI, and other medium and large pore zeolites, CHA zeolites, across all composition and paired Al site concentrations, exhibit increasing inhibition of DME formation rates as methanol partial pressures increase >10 kPa (415 K, per H<sup>+</sup>; Figure 8.8 in main text; Figures 8.42-8.45). One potential source of the observed inhibition at high methanol pressures may be due to diffusion limitations of DME leaving the zeolite pores after desorption from the catalyst surface. Diffusion coefficients for DME were conservatively estimated as being one order of magnitude smaller than CH<sub>3</sub>OH diffusion coefficients in CHA zeolites (e.g. DME:  $D_e(T = 415 \text{ K}) = 7.5 \times 10^{-12} \text{ m}^2 \text{ s}^{-1}$ ). Experimentally measured DME self-diffusion coefficients ( $D_e(T = 293 \text{ K}) = 1.2 \times 10^{-9} \text{ m}^2 \text{ s}^{-1}$ ) [473] in MFI zeolites are only twice as large as methanol self-diffusion

coefficients in MFI derived from molecular dynamic simulations ( $D_e(T = 300 \text{ K}) = 2.5 \times 10^{-9} \text{ m}^2 \text{ s}^{-1}$ ) [472], suggesting that the estimate provided here for CHA zeolites is reasonable and a conservative estimate for the CHA framework. The ratio of the rate of DME formation (mol DME per unit time) and the transport rate of DME through the catalyst (mol DME per unit time) can be evaluated as a function of the internal concentration profile (Section 8.7.5) using Weisz-Prater criteria [474] to give an order of magnitude estimate for the presence of product diffusion and is expressed by:

$$\chi < \frac{r'_{DME} \rho_s \rho_B r_p^2}{D_e C_M} \quad (8.62)$$

Here,  $r'_{DME}$  is the rate of DME formation per  $\text{H}^+$  site (415 K),  $\rho_s$  is the density of  $\text{H}^+$  sites per gram,  $\rho_B$  is the bulk zeolite density (estimated to be  $2.2 \text{ g cm}^{-3}$ ),  $r_p$  is the particle radius,  $D_e$  is the effective diffusivity of DME, and  $C_M$  is the gas-phase concentration of methanol. At all points within each CHA zeolite, the value of  $\chi$  is  $< 10^{-2}$  indicating that the rate of DME formation is much slower than the rate at which DME is transported out of the catalyst and that product diffusion is not responsible for the observed inhibition of DME formation rates at high methanol pressures.

Alternatively, the presence of water formed through the dehydration process may be responsible for the inhibition at high methanol pressures, as water is known to inhibit alcohol dehydration reactions on solid acid catalysts [475]. The dependence of methanol dehydration rates in CHA zeolites on water partial pressure was investigated by co-feeding water during steady state catalysis (415 K) at various water to methanol ratios ( $P_{\text{H}_2\text{O}}/P_{\text{CH}_3\text{OH}} = 0.02\text{-}3.6$ ) and methanol pressures (0.05-50 kPa  $\text{CH}_3\text{OH}$ ) on H-CHA-OH(14,0%) and H-CHA-OH(14,44%) catalysts and are shown in Figures 8.63 and 8.64, respectively.

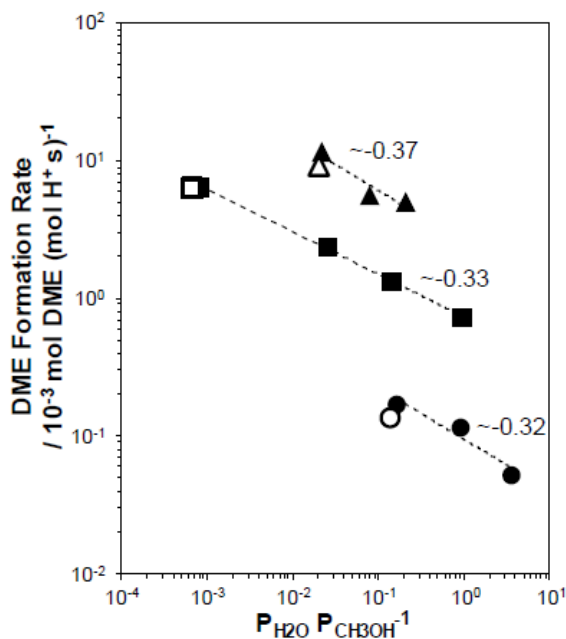


Figure 8.63. Methanol dehydration rates (per  $H^+$ , 415 K) on H-CHA-OH(14,0%) as a function of water pressure at 0.05 (circles), 2.5 (triangle), and 50 (squares) kPa  $CH_3OH$ . Open points from steady state rates (415 K), without co-feeding  $H_2O$ , and water pressures are from product formation. Labels indicate the water order under each set of conditions. Dashed lines are power law regressions to the data.

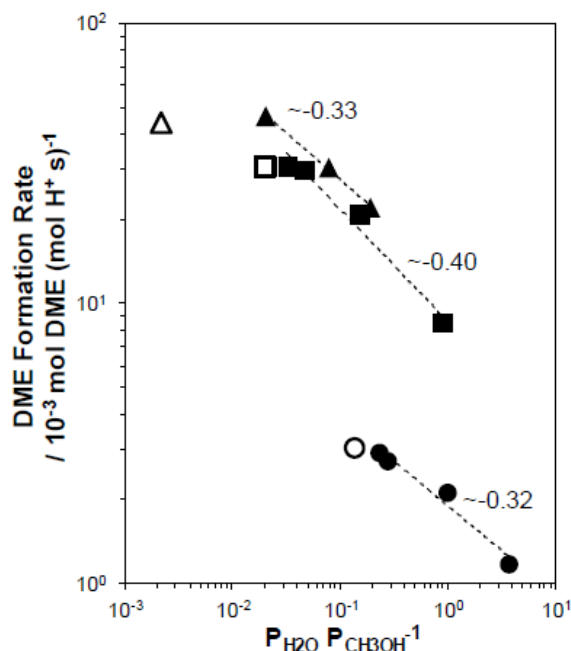


Figure 8.64. Methanol dehydration rates (per  $\text{H}^+$ , 415 K) on H-CHA-OH(14,44%) as a function of water pressure at 0.05 (circles), 2.5 (triangle), and 50 (squares) kPa  $\text{CH}_3\text{OH}$ . Open points from steady state rates (415 K), without co-feeding  $\text{H}_2\text{O}$ , and water pressures are from product formation. Labels indicate the water order under each set of conditions. Dashed lines are power law regressions to the data.

Figures 8.63 and 8.64 indicate that water inhibits the rate of DME formation at 415 K under all relevant methanol partial pressures (0.05–50 kPa) for both the associative (isolated  $\text{H}^+$  sites) and dissociative (paired  $\text{H}^+$  sites) pathways. The amount of water formed during methanol dehydration catalysis (415 K) when water is not intentionally co-fed (open points in Figures 8.63 and 8.64), however, is not enough to cause a measurable change in the rate of reaction, because of the low conversion in the differential regime. The origin of the approximately  $-1/3$  water order measured under every condition studied at 415 K likely reflects a fractional coverage of water on  $\text{H}^+$  sites and further analysis is beyond the scope of this work.

Another potential source of the inhibition observed in CHA zeolites at high methanol pressures may be due to clustering of methanol around  $\text{H}^+$  sites, which solvate the



proton away from the zeolite lattice [456]. Under steady-state methanol dehydration conditions (415 K,  $P_{CH_3OH} = 0.05\text{--}22$  kPa), IR spectra of H-CHA (0-44% paired Al) show a broad absorption band at ca.  $3370\text{ cm}^{-1}$  that increases with increasing  $CH_3OH$  pressure, which has been attributed to the formation of methanol clusters (Figures 8.50 and 8.51) [456]. Features for methanol clusters are also present in MFI zeolites at high methanol partial pressures ( $>5$  kPa  $CH_3OH$ ), but do not give rise to inhibited dehydration rates at high methanol pressures (Figures 8.46-8.48) [83], suggesting that certain structural features of the zeolite framework may stabilize the formation of these extended reactant structures within the pores.

The CHA framework is unique when compared to other zeolite frameworks studied for methanol dehydration (e.g. MFI, BEA, FAU, MOR, SFH, MTW, MTT) because it is a small-pore, window-cage framework that does not contain quasi-cylindrical pores. Instead, the CHA framework is comprised of 8-MR rings (0.38 nm in diameter) that limit diffusion of molecules into larger *chab*-cavities (0.73 x 1.2 nm), which may stabilize the formation of extended methanol structures under the reaction conditions studied. Methanol dehydration rates (per  $H^+$ , 415 K) were measured on H-AEI zeolites (AEI framework; synthesis and characterization reported elsewhere) [450], which is another small-pore, window-cage framework that consists of 8-MR (0.38 nm) that limit diffusion into *aei*-cavities (0.73 x 1.0 nm), to investigate if the zeolite framework is responsible for this inhibition. DME formation rates (415 K, per  $H^+$ ) measured on H-AEI zeolites (Figure 8.65) show similar inhibition at high methanol partial pressures as observed for all CHA zeolites, indicating that such inhibition may reflect formation of methanol clusters inside the cavities of small-pore window-cage frameworks (e.g. CHA, AEI).

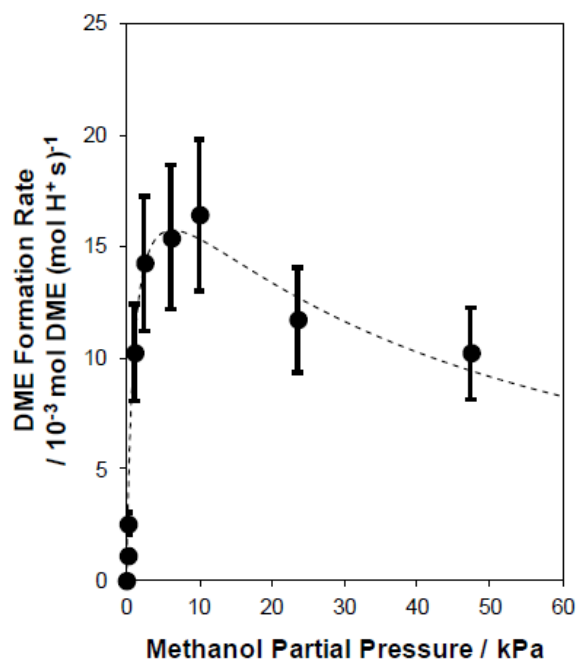


Figure 8.65. Methanol dehydration rates (per H<sup>+</sup>, 415 K) on H-AEI zeolite as a function of methanol partial pressure. Dashed line is a regression to the generalized rate expression (Eq. 8.38).

## REFERENCES

## REFERENCES

- [1] C. Baerlocher and L. B. McCusker. Database of zeolite structures, 2017.
- [2] Ramdas Pophale, Phillip A Cheeseman, and Michael W Deem. A database of new zeolite-like materials. *Physical Chemistry Chemical Physics*, 13(27):12407–12412, 2011.
- [3] Michael W Deem, Ramdas Pophale, Phillip A Cheeseman, and David J Earl. Computational discovery of new zeolite-like materials. *The Journal of Physical Chemistry C*, 113(51):21353–21360, 2009.
- [4] P Bernardo, E Drioli, and G Golemme. Membrane gas separation: a review/state of the art. *Industrial & Engineering Chemistry Research*, 48(10):4638–4663, 2009.
- [5] Jens Weitkamp and Lothar Puppe. *Catalysis and zeolites: fundamentals and applications*. Springer Science & Business Media, 2013.
- [6] Bert M Weckhuysen and Jihong Yu. Recent advances in zeolite chemistry and catalysis. *Chemical Society Reviews*, 44(20):7022–7024, 2015.
- [7] M. E. Davis. Ordered porous materials for emerging applications. *Nature*, 417(6891):813–821, 2002.
- [8] Thomas F Degnan. Applications of zeolites in petroleum refining. *Topics in Catalysis*, 13(4):349–356, 2000.
- [9] TF Degnan Jr. Recent progress in the development of zeolitic catalysts for the petroleum refining and petrochemical manufacturing industries. In *Studies in Surface Science and Catalysis*, volume 170, pages 54–65. Elsevier, 2007.
- [10] Sigmund M Csicsery. Shape-selective catalysis in zeolites. *Zeolites*, 4(3):202–213, 1984.
- [11] Thomas F Degnan. The implications of the fundamentals of shape selectivity for the development of catalysts for the petroleum and petrochemical industries. *Journal of Catalysis*, 216(1):32–46, 2003.
- [12] PB Weisz and VJ Frillette. Intracrystalline and molecular-shape-selective catalysis by zeolite salts. *The Journal of Physical Chemistry*, 64(3):382–382, 1960.
- [13] Po Bo Weisz, VJ Frillette, RW Maatman, and EB Mower. Catalysis by crystalline aluminosilicates ii. molecular-shape selective reactions. *Journal of Catalysis*, 1(4):307–312, 1962.
- [14] WO Haag, RM Lago, and PB Weisz. The active site of acidic aluminosilicate catalysts. *Nature*, 309:589–591, 1984.

- [15] M Boudart. Turnover rates in heterogeneous catalysis. *Chemical reviews*, 95(3):661–666, 1995.
- [16] Andrew J Jones and Enrique Iglesia. The strength of brønsted acid sites in microporous aluminosilicates. *ACS Catalysis*, 5(10):5741–5755, 2015.
- [17] Michele L Sarazen and Enrique Iglesia. Effects of charge, size, and shape of transition states, bound intermediates, and confining voids in reactions of alkenes on solid acids. *ChemCatChem*, 2018.
- [18] Gina Noh, Zhichen Shi, Stacey I Zones, and Enrique Iglesia. Isomerization and beta-scission reactions of alkanes on bifunctional metal-acid catalysts: Consequences of confinement and diffusional constraints on reactivity and selectivity. *Journal of Catalysis*, 2018.
- [19] Stanley Herrmann and Enrique Iglesia. Selective conversion of acetone to isobutene and acetic acid on aluminosilicates: Kinetic coupling between acid-catalyzed and radical-mediated pathways. *Journal of Catalysis*, 360:66–80, 2018.
- [20] Rajamani Gounder, Andrew J Jones, Robert T Carr, and Enrique Iglesia. Solvation and acid strength effects on catalysis by faujasite zeolites. *Journal of catalysis*, 286:214–223, 2012.
- [21] Rajamani Gounder and Enrique Iglesia. Catalytic consequences of spatial constraints and acid site location for monomolecular alkane activation on zeolites. *Journal of the American Chemical Society*, 131(5):1958–1971, 2009.
- [22] Andrew J Jones, Stacey I Zones, and Enrique Iglesia. Implications of transition state confinement within small voids for acid catalysis. *The Journal of Physical Chemistry C*, 118(31):17787–17800, 2014.
- [23] Aditya Bhan, Ayman D Allian, Glenn J Sunley, David J Law, and Enrique Iglesia. Specificity of sites within eight-membered ring zeolite channels for carbonylation of methyls to acetyls. *Journal of the American Chemical Society*, 129(16):4919–4924, 2007.
- [24] L. Gomez-Hortiguera, A. B. Pinar, F. Cora, and J. Perez-Pariente. Dopant-siting selectivity in nanoporous catalysts: control of proton accessibility in zeolite catalysts through the rational use of templates. *Chemical Communications*, 46(12):2073–5, 2010.
- [25] C. Marquez-Alvarez, A. B. Pinar, R. Garcia, M. Grande-Casas, and J. Perez-Pariente. Influence of al distribution and defects concentration of ferrierite catalysts synthesized from na-free gels in the skeletal isomerization of n-butene. *Topics in Catalysis*, 52(9):1281–1291, 2009.
- [26] A. B. Pinar, C. Marquez-Alvarez, M. Grande-Casas, and J. Perez-Pariente. Template-controlled acidity and catalytic activity of ferrierite crystals. *Journal of Catalysis*, 263(2):258–265, 2009.
- [27] Ana B. Pinar, Paul A. Wright, Luis Gomez-Hortiguera, and Joaquin Perez-Pariente. Synthesis of ferrierite zeolite with pyrrolidine as structure directing agent: A combined x-ray diffraction and computational study. *Microporous and Mesoporous Materials*, 129(1-2):164–172, 2010.

- [28] Yuriy Román-Leshkov and Mark E Davis. Activation of carbonyl-containing molecules with solid lewis acids in aqueous media. *Acs Catalysis*, 1(11):1566–1580, 2011.
- [29] Sungsik Park, Turgren Biligetu, Yong Wang, Toshiki Nishitoba, Junko N Kondo, and Toshiyuki Yokoi. Acidic and catalytic properties of zsm-5 zeolites with different al distributions. *Catalysis Today*, 303:64–70, 2018.
- [30] Turgren Biligetu, Yong Wang, Toshiki Nishitoba, Ryoichi Otomo, Sungsik Park, Hiroshi Mochizuki, Junko N Kondo, Takashi Tatsumi, and Toshiyuki Yokoi. Al distribution and catalytic performance of zsm-5 zeolites synthesized with various alcohols. *Journal of Catalysis*, 353:1–10, 2017.
- [31] Toshiyuki Yokoi, Hiroshi Mochizuki, Turgren Biligetu, Yong Wang, and Takashi Tatsumi. Unique al distribution in the mfi framework and its impact on catalytic properties. *Chemistry Letters*, 46, 2017.
- [32] Toshiyuki Yokoi, Hiroshi Mochizuki, Seitaro Namba, Junko N Kondo, and Takashi Tatsumi. Control of the al distribution in the framework of zsm-5 zeolite and its evaluation by solid-state nmr technique and catalytic properties. *The Journal of Physical Chemistry C*, 119(27):15303–15315, 2015.
- [33] BR Goodman, KC Hass, WF Schneider, and JB Adams. Statistical analysis of al distributions and metal ion pairing probabilities in zeolites. *Catalysis letters*, 68(1-2):85–93, 2000.
- [34] D. W. Fickel, J. M. Fedeyko, and R. F. Lobo. Copper coordination in cu-ssz-13 and cu-ssz-16 investigated by variable-temperature xrd. *Journal of Physical Chemistry C*, 114(3):1633–1640, 2010.
- [35] S. T. Korhonen, D. W. Fickel, R. F. Lobo, B. M. Weckhuysen, and A. M. Beale. Isolated cu<sup>2+</sup> ions: active sites for selective catalytic reduction of no. *Chemical Communications*, 47(2):800–802, 2011.
- [36] Filippo Giordanino, Peter NR Vennestrom, Lars F Lundegaard, Frederick N Stappen, Susanne Mossin, Pablo Beato, Silvia Bordiga, and Carlo Lamberti. Characterization of cu-exchanged ssz-13: a comparative ftir, uv-vis, and epr study with cu-zsm-5 and cu- $\beta$  with similar si/al and cu/al ratios. *Dalton Transactions*, 42(35):12741–12761, 2013.
- [37] Shane A Bates, Anuj A Verma, Christopher Paolucci, Atish A Parekh, Trunojoyo Anggara, Aleksey Yezerets, William F Schneider, Jeffrey T Miller, W Nicholas Delgass, and Fabio H Ribeiro. Identification of the active cu site in standard selective catalytic reduction with ammonia on cu-ssz-13. *Journal of Catalysis*, 312:87–97, 2014.
- [38] Filippo Giordanino, Elisa Borfecchia, Kirill A. Lomachenko, Andrea Lazzarini, Giovanni Agostini, Erik Gallo, Alexander V. Soldatov, Pablo Beato, Silvia Bordiga, and Carlo Lamberti. Interaction of nh<sub>3</sub> with cu-ssz-13 catalyst: A complementary ftir, xanes, and xes study. *Journal of Physical Chemistry Letters*, 5(9):1552–1559, 2014.
- [39] E Borfecchia, KA Lomachenko, F Giordanino, H Falsig, P Beato, AV Soldatov, S Bordiga, and C Lamberti. Revisiting the nature of cu sites in the activated cu-ssz-13 catalyst for scr reaction. *Chemical science*, 6(1):548–563, 2015.

- [40] Feng Gao, Nancy M Washton, Yilin Wang, Marton Kollar, Janos Szanyi, and Charles HF Peden. Effects of si/al ratio on cu/ssz-13 nh 3-scr catalysts: Implications for the active cu species and the roles of brønsted acidity. *Journal of Catalysis*, 331:25–38, 2015.
- [41] Ton VW Janssens, Hanne Falsig, Lars F Lundegaard, Peter NR Vennestrom, Søren B Rasmussen, Poul Georg Moses, Filippo Giordanino, Elisa Borfecchia, Kirill A Lomachenko, Carlo Lamberti, et al. A consistent reaction scheme for the selective catalytic reduction of nitrogen oxides with ammonia. *ACS Catalysis*, 5(5):2832–2845, 2015.
- [42] John R Di Iorio and Rajamani Gounder. Controlling the isolation and pairing of aluminum in chabazite zeolites using mixtures of organic and inorganic structure-directing agents. *Chemistry of Materials*, 28(7):2236–2247, 2016.
- [43] Hubert Koller and Mark Weisz. Solid state nmr of porous materials. *Solid State NMR*, 306(123):189–227, 2012.
- [44] J. Klinowski. Recent advances in solid-state nmr of zeolites. *Annual Review of Materials Science*, 18:189–218, 1988.
- [45] MT Melchior, DEW Vaughan, and AJ Jacobson. Characterization of the silicon-aluminum distribution in synthetic faujasites by high-resolution solid-state silicon-29 nmr. *Journal of the American Chemical Society*, 104(18):4859–4864, 1982.
- [46] Gunter Engelhardt, Endel Lippmaa, and Mart Magi. Ordering of silicon and aluminium ions in the framework of nax zeolites. a solid-state high-resolution 29 si nmr study. *Chemical Communications*, 14:712–713, 1981.
- [47] E Lippmaa, M Mägi, A Samoson, M Tarmak, and G Engelhardt. Investigation of the structure of zeolites by solid-state high-resolution silicon-29 nmr spectroscopy. *Journal of the American Chemical Society*, 103(17):4992–4996, 1981.
- [48] Jiri Dedecek, Z. Sobalika, and B. Wichterlova. Siting and distribution of framework aluminium atoms in silicon-rich zeolites and impact on catalysis. *Catalysis Reviews-Science and Engineering*, 54(2):135–223, 2012.
- [49] Zhiwu Yu, Anmin Zheng, Qiang Wang, Lei Chen, Jun Xu, Jean-Paul Amoureux, and Feng Deng. Insights into the dealumination of zeolite hy revealed by sensitivity-enhanced 27al dq-mas nmr spectroscopy at high field. *Angewandte Chemie International Edition*, 49(46):8657–8661, 2010.
- [50] Melinda J Duer. *Solid state NMR spectroscopy: principles and applications*. John Wiley & Sons, 2008.
- [51] Kenneth JD MacKenzie and Mark E Smith. *Multinuclear solid-state nuclear magnetic resonance of inorganic materials*, volume 6. Elsevier, 2002.
- [52] Ales Medek, John S Harwood, and Lucio Frydman. Multiple-quantum magic-angle spinning nmr: A new method for the study of quadrupolar nuclei in solids. *Journal of the American Chemical Society*, 117(51):12779–12787, 1995.

- [53] P J Kunkeler, B J Zuurdeeg, J C Van Der Waal, J A Van Bokhoven, D C Koningsberger, and H Van Bekkum. Zeolite beta: the relationship between calcination procedure, aluminum configuration, and lewis acidity. *Journal of catalysis*, 180(2):234–244, 1998.
- [54] Jan Kucera and Petr Nachtigall. A simple correlation between average t–o–t angles and 27 al nmr chemical shifts does not hold in high-silica zeolites. *Microporous and mesoporous materials*, 85(3):279–283, 2005.
- [55] Jiri Dedecek, Stepan Sklenak, Chengbin Li, Blanka Wichterlova, Vendula Gabova, Jiri Brus, Marek Sierka, and Joachim Sauer. Effect of al- si- al and al- si- si- al pairs in the zsm-5 zeolite framework on the 27al nmr spectra. a combined high-resolution 27al nmr and dft/mm study. *Journal of Physical Chemistry C*, 113(4):1447–1458, 2009.
- [56] Stepan Sklenak, Jiri Dedecek, Chengbin Li, Blanka Wichterlova, Vendula Gabova, Marek Sierka, and Joachim Sauer. Aluminium siting in the zsm-5 framework by combination of high resolution 27al nmr and dft/mm calculations. *Physical Chemistry Chemical Physics*, 11(8):1237–1247, 2009.
- [57] Stepan Sklenak, Jiri Dedecek, Chengbin Li, Blanka Wichterlova, Vendula Gabova, Marek Sierka, and Joachim Sauer. Aluminum siting in silicon-rich zeolite frameworks: A combined high-resolution 27al nmr spectroscopy and quantum mechanics/molecular mechanics study of zsm-5. *Angewandte Chemie International Edition*, 46(38):7286–7289, 2007.
- [58] J Dedecek, L Capek, P Sazama, Z Sobalik, and B Wichterlova. Control of metal ion species in zeolites by distribution of aluminium in the framework: From structural analysis to performance under real conditions of scr-nox and no, n2o decomposition. *Applied Catalysis A: General*, 391(1-2):244–253, 2011.
- [59] Petr Sazama, Edyta Tabor, Petr Klein, Blanka Wichterlova, Stepan Sklenak, Lukas Mokrzycki, Veronika Pashkkova, Masaru Ogura, and Jiri Dedecek. Al-rich beta zeolites. distribution of al atoms in the framework and related protonic and metal-ion species. *Journal of Catalysis*, 333:102–114, 2016.
- [60] Petr Sazama, Lukasz Mokrzycki, Blanka Wichterlova, Alena Vondrova, Radim Pilar, Jiri Dedecek, Stepan Sklenak, and Edyta Tabor. Unprecedented propane scr-nox activity over template-free synthesized al-rich co-bea zeolite. *Journal of Catalysis*, 332:201–211, 2015.
- [61] Amber Janda and Alexis T. Bell. Effects of si/al ratio on the distribution of framework al and on the rates of alkane monomolecular cracking and dehydrogenation in h-mfi. *Journal of the American Chemical Society*, 135(51):19193–19207, 2013.
- [62] P Sazama, J Dedecek, V Gabova, B Wichterlova, G Spoto, and S Bordiga. Effect of aluminium distribution in the framework of zsm-5 on hydrocarbon transformation. cracking of 1-butene. *Journal of Catalysis*, 254(2):180–189, 2008.
- [63] Zdenek Sobalik, Jiri Dedecek, Dalibor Kaucky, Blanka Wichterlova, Lucie Drozdova, and Roel Prins. Structure, distribution, and properties of co ions in fer revealed by ftir, uv–vis, and exafs. *Journal of Catalysis*, 194(2):330–342, 2000.



- [64] L Capek, J Dedecek, P Sazama, and B Wichterlova. The decisive role of the distribution of al in the framework of beta zeolites on the structure and activity of co ion species in propane-scr-nox in the presence of water vapour. *Journal of Catalysis*, 272(1):44–54, 2010.
- [65] Vendula Gabova, Jiri Dedecek, and Jiri Cejka. Control of al distribution in zsm-5 by conditions of zeolite synthesis. *Chemical Communications*, 0(10):1196–1197, 2003.
- [66] Lucie Drozdova, Roel Prins, Jiri Dedecek, Zdenek Sobalik, and Blanka Wichterlova. Bonding of co ions in zsm-5, ferrierite, and mordenite: An x-ray absorption, uv-vis, and ir study. *Journal of Physical Chemistry B*, 106(9):2240–2248, 2002.
- [67] Libor Capek, Jiri Dedecek, and Blanka Wichterlova. Co-beta zeolite highly active in propane-scr-no x in the presence of water vapor: effect of zeolite preparation and al distribution in the framework. *Journal of Catalysis*, 227(2):352–366, 2004.
- [68] J. Dedecek, D. Kaucky, and B. Wichterlova. Al distribution in zsm-5 zeolites: an experimental study. *Chemical Communications*, 11:970–971, 2001.
- [69] Jiri Dedecek and Blanka Wichterlova. Co<sub>2</sub><sup>+</sup> ion siting in pentasil-containing zeolites. i. co<sub>2</sub><sup>+</sup> ion sites and their occupation in mordenite. a vis-nir diffuse reflectance spectroscopy study. *The Journal of Physical Chemistry B*, 103(9):1462–1476, 1999.
- [70] Jiri Dedecek, Dalibor Kaucky, Blanka Wichterlova, and Olga Gonsiorova. Co<sub>2</sub><sup>+</sup> ions as probes of al distribution in the framework of zeolites. zsm-5 study. *Physical Chemistry Chemical Physics*, 4(21):5406–5413, 2002.
- [71] Dalibor Kaucky, Jiri Dedecek, and Blanka Wichterlova. Co<sub>2</sub><sup>+</sup> ion siting in pentasil-containing zeolites: li. co<sub>2</sub><sup>+</sup> ion sites and their occupation in ferrierite. a vis diffuse reflectance spectroscopy study. *Microporous and mesoporous materials*, 31(1):75–87, 1999.
- [72] Dalibor Kaucky, Alena Vondrova, Jiri Dedecek, and Blanka Wichterlova. Activity of co ion sites in zsm-5, ferrierite, and mordenite in selective catalytic reduction of no with methane. *Journal of Catalysis*, 194(2):318–329, 2000.
- [73] J. Dedecek, D. Kaucky, and B. Wichterlova. Co<sub>2</sub><sup>+</sup> ion siting in pentasil-containing zeolites, part 3.: Co<sub>2</sub><sup>+</sup> ion sites and their occupation in zsm-5: a vis diffuse reflectance spectroscopy study. *Microporous and Mesoporous Materials*, 35–36(0):483–494, 2000.
- [74] Veronika Pashkova, Petr Klein, Jiri Dedecek, Venceslava Tokarova, and Blanka Wichterlova. Incorporation of al at zsm-5 hydrothermal synthesis. tuning of al pairs in the framework. *Microporous and Mesoporous Materials*, 202:138–146, 2015.
- [75] Chenhai Song, Yueying Chu, Meng Wang, Hui Shi, Li Zhao, Xuefeng Guo, Weimin Yang, Jianyi Shen, Nianhua Xue, Luming Peng, and Weiping Ding. Cooperativity of adjacent brønsted acid sites in mfi zeolite channel leads to enhanced polarization and cracking of alkanes. *Journal of Catalysis*, 349:163–174, 2017.

- [76] Anton N. Mlinar, Paul M. Zimmerman, Fuat E. Celik, Martin Head-Gordon, and Alexis T. Bell. Effects of brønsted-acid site proximity on the oligomerization of propene in h-mfi. *Journal of Catalysis*, 288:65–73, 2012.
- [77] M Bernauer, E Tabor, V Pashkova, D Kaucký, Z Sobalík, B Wichterlová, and J Dedecek. Proton proximity—new key parameter controlling adsorption, desorption and activity in propene oligomerization over h-zsm-5 zeolites. *Journal of Catalysis*, 344:157–172, 2016.
- [78] Shane A. Bates, W. Nicholas Delgass, Fabio H. Ribeiro, Jeffrey T. Miller, and Rajamani Gounder. Methods for nh<sub>3</sub> titration of bronsted acid sites in cu-zeolites that catalyze the selective catalytic reduction of nox with nh<sub>3</sub>. *Journal of Catalysis*, 312:26–36, 2014.
- [79] Christopher Paolucci, Atish A Parekh, Ishant Khurana, John R Di Iorio, Hui Li, Jonatan D Albarracin Caballero, Arthur J Shih, Trunojoyo Anggara, W Nicholas Delgass, Jeffrey T Miller, Fabio H Ribeiro, Rajamani Gounder, and William F Schneider. Catalysis in a cage: condition-dependent speciation and dynamics of exchanged cu cations in ssz-13 zeolites. *Journal of the American Chemical Society*, 138(18):6028–6048, 2016.
- [80] R. F. Lobo, S. I. Zones, and M. E. Davis. Structure-direction in zeolite synthesis. *Journal of Inclusion Phenomena and Molecular Recognition in Chemistry*, 21(1-4):47–78, 1995.
- [81] Koki Muraoka, Watcharop Chaikittisilp, Yutaka Yanaba, Takeshi Yoshikawa, and Tatsuya Okubo. Directing aluminum atoms into energetically favorable tetrahedral sites in a zeolite framework by using organic structure-directing agents. *Angewandte Chemie International Edition*, 130(14):3804–3808, 2018.
- [82] Robert T Carr, Matthew Neurock, and Enrique Iglesia. Catalytic consequences of acid strength in the conversion of methanol to dimethyl ether. *Journal of Catalysis*, 278(1):78–93, 2011.
- [83] Andrew J Jones, Robert T Carr, Stacey I Zones, and Enrique Iglesia. Acid strength and solvation in catalysis by mfi zeolites and effects of the identity, concentration and location of framework heteroatoms. *Journal of Catalysis*, 312:58–68, 2014.
- [84] Upakul Deka, Amelie Juhin, Einar A Eilertsen, Hermann Emerich, Mark A Green, Satu T Korhonen, Bert M Weckhuysen, and Andrew M Beale. Confirmation of isolated cu<sup>2+</sup> ions in ssz-13 zeolite as active sites in nh<sub>3</sub>-selective catalytic reduction. *The Journal of Physical Chemistry C*, 116(7):4809–4818, 2012.
- [85] Christopher Paolucci, Anuj A Verma, Shane A Bates, Vincent F Kispersky, Jeffrey T Miller, Rajamani Gounder, W Nicholas Delgass, Fabio H Ribeiro, and William F Schneider. Isolation of the copper redox steps in the standard selective catalytic reduction on cu-ssz-13. *Angewandte Chemie International Edition*, 53(44):11828–11833, 2014.
- [86] J. S. McEwen, T. Anggara, W. F. Schneider, V. F. Kispersky, J. T. Miller, W. N. Delgass, and F. H. Ribeiro. Integrated operando x-ray absorption and dft characterization of cu-ssz-13 exchange sites during the selective catalytic reduction of nox with nh<sub>3</sub>. *Catalysis Today*, 184(1):129–144, 2012.

- [87] Vincent F Kispersky, A Jeremy Kropf, Fabio H Ribeiro, and Jeffrey T Miller. Low absorption vitreous carbon reactors for operando xas: a case study on cu/zeolites for selective catalytic reduction of no x by nh<sub>3</sub>. *Physical Chemistry Chemical Physics*, 14(7):2229–2238, 2012.
- [88] P.J. Andersen, J.E. Bailie, J.L. Casci, H.Y. Chen, J.M. Fedeyko, R.K.S. Foo, and R.R. Rajaram. Transition metal / zeolite scr catalysts, 2010.
- [89] Ja Hun Kwak, Russell G Tonkyn, Do Heui Kim, Janos Szanyi, and Charles HF Peden. Excellent activity and selectivity of cu-ssz-13 in the selective catalytic reduction of nox with nh<sub>3</sub>. *Journal of Catalysis*, 275(2):187–190, 2010.
- [90] I. Bull, G.S. Koermer, A. Moini, and S. Unverricht. Catalysts, systems and methods utilizing non-zeolitic metal-containing molecular sieves having the cha crystal structure, 2009.
- [91] Upakul Deka, Ines Lezcano-Gonzalez, Stewart J Warrender, A Lorena Picone, Paul A Wright, Bert M Weckhuysen, and Andrew M Beale. Changing active sites in cu-cha catalysts: denox selectivity as a function of the preparation method. *Microporous and Mesoporous Materials*, 166:144–152, 2013.
- [92] Sandro Brandenberger, Oliver Krocher, Arno Tissler, and Roderik Althoff. The state of the art in selective catalytic reduction of nox by ammonia using metal-exchanged zeolite catalysts. *Catalysis Reviews*, 50(4):492–531, 2008.
- [93] Ja Hun Kwak, Diana Tran, Sarah D Burton, Janos Szanyi, Jong H Lee, and Charles HF Peden. Effects of hydrothermal aging on nh<sub>3</sub>-scr reaction over cu/zeolites. *Journal of Catalysis*, 287:203–209, 2012.
- [94] H. Sjövall, L. Olsson, E. Fridell, and R. J. Blint. Selective catalytic reduction of nox with nh<sub>3</sub> over cu-zsm-5—the effect of changing the gas composition. *Applied Catalysis B: Environmental*, 64(3–4):180–188, 2006.
- [95] E.-Y. Choi, I.-S. Nam, and Y. G. Kim. Tpd study of mordenite-type zeolites for selective catalytic reduction of no by nh<sub>3</sub>. *Journal of Catalysis*, 161(2):597–604, 1996.
- [96] H. Y. Huang, R. Q. Long, and R. T. Yang. Kinetics of selective catalytic reduction of no with nh<sub>3</sub> on fe-zsm-5 catalyst. *Applied Catalysis A: General*, 235(1–2):241–251, 2002.
- [97] K. Rahkamaa-Tolonen, T. Maunula, M. Lomma, M. Huuhtanen, and R. L. Keiski. The effect of no<sub>2</sub> on the activity of fresh and aged zeolite catalysts in the nh<sub>3</sub>-scr reaction. *Catalysis Today*, 100(3–4):217–222, 2005.
- [98] P. S. Metkar, N. Salazar, R. Muncrief, V. Balakotaiah, and M. P. Harold. Selective catalytic reduction of no with nh<sub>3</sub> on iron zeolite monolithic catalysts: Steady-state and transient kinetics. *Applied Catalysis B: Environmental*, 104(1–2):110–126, 2011.
- [99] R. Q. Long and R. T. Yang. Catalytic performance of fe-zsm-5 catalysts for selective catalytic reduction of nitric oxide by ammonia. *Journal of Catalysis*, 188(2):332–339, 1999.

- [100] A. L. Kustov, T. W. Hansen, M. Kustova, and C. H. Christensen. Selective catalytic reduction of no by ammonia using mesoporous fe-containing hzsm-5 and hzsm-12 zeolite catalysts: An option for automotive applications. *Applied Catalysis B: Environmental*, 76(3-4):311-319, 2007.
- [101] J. A. Dumesic, N.Y. Topsøe, H. Topsøe, Y. Chen, and T. Slabiak. Kinetics of selective catalytic reduction of nitric oxide by ammonia over vanadia/titania. *Journal of Catalysis*, 163(2):409-417, 1996.
- [102] H. Schneider, S. Tschudin, M. Schneider, A. Wokaun, and A. Baiker. In situ diffuse reflectance ftir study of the selective catalytic reduction of no by nh<sub>3</sub> over vanadia-titania aerogels. *Journal of Catalysis*, 147(1):5-14, 1994.
- [103] S. Brandenberger, O. Krocher, A. Wokaun, A. Tissler, and R. Althoff. The role of bronsted acidity in the selective catalytic reduction of no with ammonia over fe-zsm-5. *Journal of Catalysis*, 268(2):297-306, 2009.
- [104] F. Gao, J. H. Kwak, J. Szanyi, and C. H F. Peden. Current understanding of cu-exchanged chabazite molecular sieves for use as commercial diesel engine denox catalysts. *Topics in Catalysis*, 56(15-17):1441-1459, 2013.
- [105] G. L. Woolery, G. H. Kuehl, H. C. Timken, A. W. Chester, and J. C. Vartuli. On the nature of framework bronsted and lewis acid sites in zsm-5. *Zeolites*, 19(4):288-296, 1997.
- [106] G. Bagnasco. Improving the selectivity of nh<sub>3</sub>tpd measurements. *Journal of Catalysis*, 159(1):249-252, 1996.
- [107] N. Y. Topsøe, H. Topsøe, and J. A. Dumesic. Vanadia-titania catalysts for selective catalytic reduction (scr) of nitric-oxide by ammonia combined temperature-programmed in-situ ftir and on-line mass-spectroscopy studies. *Journal of Catalysis*, 151:226-240, 1995.
- [108] N.Y. Topsøe, J. A. Dumesic, and H. Topsoe. Vanadia-titania catalysts for selective catalytic reduction of nitric-oxide by ammonia: I.i. studies of active sites and formulation of catalytic cycles. *Journal of Catalysis*, 151(1):241-252, 1995.
- [109] S. I. Zones. Zeolite ssz-13 and its method of preparation, 1985.
- [110] R. J. Gorte. What do we know about the acidity of solid acids? *Catalysis Letters*, 62:1-13, 1999.
- [111] J. Wang, T. Yu, X. Q. Wang, G. S. Qi, J. J. Xue, M. Q. Shen, and W. Li. The influence of silicon on the catalytic properties of cu/sapo-34 for nox reduction by ammonia-scr. *Applied Catalysis B-Environmental*, 127:137-147, 2012.
- [112] J. Datka, B. Gil, and A. Kubacka. Acid properties of nah-mordenites: Infrared spectroscopic studies of ammonia sorption. *Zeolites*, 15(6):501-506, 1995.
- [113] N. Katada and M. Niwa. Analysis of acidic properties of zeolitic and non-zeolitic solid acid catalysts using temperature-programmed desorption of ammonia. *Catalysis Surveys from Asia*, 8(3):161-170, 2004.

- [114] W. E. Farneth and R. J. Gorte. Methods for characterizing zeolite acidity. *Chemical Reviews*, 95(3):615–635, 1995.
- [115] O. Kresnawahjuesa, R. J. Gorte, D. de Oliveira, and L. Y. Lau. A simple, inexpensive, and reliable method for measuring bronsted-acid site densities in solid acids. *Catalysis Letters*, 82(3-4):155–160, 2002.
- [116] O. Kresnawahjuesa, R. Heussner, C.-C. Lee, G. Kühn, and R.J. Gorte. An examination of acid sites in h-lta zeolites. *Applied Catalysis A: General*, 199:53–60, 2000.
- [117] D. J. Parrillo, A. T. Adamo, G. T. Kokotailo, and R. J. Gorte. Amine adsorption in h-zsm-5. *Applied Catalysis*, 67(1):107–118, 1990.
- [118] R. Gounder, A. J. Jones, R. T. Carr, and E. Iglesia. Solvation and acid strength effects on catalysis by faujasite zeolites. *Journal of Catalysis*, 286:214–223, 2012.
- [119] A. I. Baiglow, D. J. Parrillo, G. T. Kokotailo, and R. J. Gorte. A study of dealuminated faujasites. *Journal of Catalysis*, 148:213–223, 1994.
- [120] B. Xu, F. Rotunno, S. Bordiga, R. Prins, and J. A. van Bokhoven. Reversibility of structural collapse in zeolite y: Alkane cracking and characterization. *Journal of Catalysis*, 241(1):66–73, 2006.
- [121] A. Omegna, R. Prins, and J. A. van Bokhoven. Effect of temperature on aluminum coordination in zeolites h-y and h-usy and amorphous silica-alumina: an in situ al k edge xanes study. *Journal of Physical Chemistry B*, 109(19):9280–9283, 2005.
- [122] A. Omegna, J. A. van Bokhoven, and R. Prins. Flexible aluminum coordination in aluminosilicates. structure of zeolite h-usy and amorphous silica-alumina. *Journal of Physical Chemistry B*, 107(34):8854–8860, 2003.
- [123] J. A. van Bokhoven, A. L. Roest, D. C. Koningsberger, J. T. Miller, G. H. Nachttegaal, and A. P. M. Kentgens. Changes in structural and electronic properties of the zeolite framework induced by extraframework al and la in h-usy and la(x)na: a  $^{29}\text{Si}$  and  $^{27}\text{Al}$  mas nmr and  $^{27}\text{Al}$  mq mas nmr study. *Journal of Physical Chemistry B*, 104(29):6743–6754, 2000.
- [124] M. Hunger, G. Engelhardt, and J. Weitkamp. Solid-state  $^{23}\text{Na}$ ,  $^{139}\text{La}$ ,  $^{27}\text{Al}$  and  $^{29}\text{Si}$  nuclear magnetic resonance spectroscopic investigations of cation location and migration in zeolites lanay. *Microporous Materials*, 3(4-5):497–510, 1995.
- [125] Zhenchao Zhao, Suochang Xu, Mary Y. Hu, Xinhe Bao, Charles H. F. Peden, and Jianzhi Hu. Investigation of aluminum site changes of dehydrated zeolite h-beta during a rehydration process by high-field solid-state nmr. *Journal of Physical Chemistry C*, 119(3):1410–1417, 2015.
- [126] L. S. Dent and J. V. Smith. Crystal structure of chabazite, a molecular sieve. *Nature*, 181(4626):1794–1796, 1958.
- [127] D. H. Olson, G. T. Kokotailo, S. L. Lawton, and W. M. Meier. Crystal structure and structure-related properties of zsm-5. *Journal of Physical Chemistry*, 85(15):2238–2243, 1981.

- [128] C. G. Pope. Amine adsorption study of the acid sites in hzsm-5. *Zeolites*, 10(1):28–31, 1990.
- [129] Anuj A Verma, Shane A Bates, Trunojoyo Anggara, Christopher Paolucci, Atish A Parekh, Krishna Kamasamudram, Aleksey Yezerets, Jeffrey T Miller, W Nicholas Delgass, William F Schneider, et al. No oxidation: A probe reaction on cu-ssz-13. *Journal of Catalysis*, 312:179–190, 2014.
- [130] Dmitry E Doronkin, Maria Casapu, Tobias Gunter, Oliver Muller, Ronald Frahm, and Jan-Dierk Grunwaldt. Operando spatially-and time-resolved xas study on zeolite catalysts for selective catalytic reduction of no x by nh3. *The Journal of Physical Chemistry C*, 118(19):10204–10212, 2014.
- [131] B. Moden, J. M. Donohue, W. E. Cormier, and H.-X. Li. The uses and challenges of zeolites in automotive applications. *Topics in Catalysis*, 53(19-20):1367–1373, 2010.
- [132] O. Mihai, C. R. Widyastuti, S. Andonova, K. Kamasamudram, J. Li, S. Y. Joshi, N. W. Currier, A. Yezerets, and L. Olsson. The effect of cu-loading on different reactions involved in nh3-scr over cu-bea catalysts. *Journal of Catalysis*, 311(0):170–181, 2014.
- [133] Krishna Kamasamudram, Neal W Currier, Xu Chen, and Aleksey Yezerets. Overview of the practically important behaviors of zeolite-based urea-scr catalysts, using compact experimental protocol. *Catalysis Today*, 151(3-4):212–222, 2010.
- [134] X. Auvray, W. P. Partridge, J.-S. Choi, J. A. Pihl, A. Yezerets, K. Kamasamudram, N. W. Currier, and L. Olsson. Local ammonia storage and ammonia inhibition in a monolithic copper-beta zeolite scr catalyst. *Applied Catalysis B: Environmental*, 126(0):144–152, 2012.
- [135] N. Y. Topsøe. Mechanism of the selective catalytic reduction of nitric oxide by ammonia elucidated by in situ on-line fourier transform infrared spectroscopy. *Science*, 265:1217–1219, 1994.
- [136] W. S. Borghard, P. T. Reischman, and E. W. Sheppard. Argon sorption in zsm-5. *Journal of Catalysis*, 139(1):19–23, 1993.
- [137] W. S. Borghard, E. W. Sheppard, and H. J. Schoennagel. An automated, high precision unit for low-pressure physisorption. *Review of Scientific Instruments*, 62(11):2801–2809, 1991.
- [138] H. Kraus, M. Müller, R. Prins, and A. P. M. Kentgens. Comments on the 27al nmr visibility of aluminas. *Journal of Physical Chemistry B*, 102(20):3862–3865, 1998.
- [139] Zeev Luz and Alexander J. Vega. Interaction of h-rho zeolite with water and methanol studied by multinuclear nmr spectroscopy. *Journal of Physical Chemistry*, 91(2):374–382, 1987.
- [140] Ana Belen Pinar, Luis Gomez-Hortiguera, and Joaquin Perez-Pariente. Cooperative structure directing role of the cage-forming tetramethylammonium cation and the bulkier benzylmethylpyrrolidinium in the synthesis of zeolite ferrierite. *Chemistry of Materials*, 19(23):5617–5626, 2007.

- [141] Ana B Pinar, Luis Gomez-Hortiguera, Lynne B McCusker, and Joaquin Perez-Pariente. Controlling the aluminum distribution in the zeolite ferrierite via the organic structure directing agent. *Chemistry of Materials*, 25(18):3654–3661, 2013.
- [142] Yuriy Román-Leshkov, Manuel Moliner, and Mark E Davis. Impact of controlling the site distribution of al atoms on catalytic properties in ferrierite-type zeolites†. *The Journal of Physical Chemistry C*, 115(4):1096–1102, 2010.
- [143] Rajamani Gounder and Enrique Iglesia. The catalytic diversity of zeolites: confinement and solvation effects within voids of molecular dimensions. *Chemical Communications*, 49(34):3491–3509, 2013.
- [144] Rajamani Gounder and Enrique Iglesia. The roles of entropy and enthalpy in stabilizing ion-pairs at transition states in zeolite acid catalysis. *Accounts of Chemical Research*, 45(2):229–238, 2012.
- [145] Aleksei Vjunov, Mirosław A. Derewinski, John L. Fulton, Donald M. Camaioni, and Johannes A. Lercher. Impact of zeolite aging in hot liquid water on activity for acid-catalyzed dehydration of alcohols. *Journal of the American Chemical Society*, 137(32):10374–10382, 2015.
- [146] Aleksei Vjunov, John L. Fulton, Donald M. Camaioni, Jian Z. Hu, Sarah D. Burton, Like Arslan, and Johannes A. Lercher. Impact of aqueous medium on zeolite framework integrity. *Chemistry of Materials*, 27(9):3533–3545, 2015.
- [147] Aleksei Vjunov, John L. Fulton, Thomas Huthwelker, Sonia Pin, Donghai Mei, Gregory K. Schenter, Niranjana Govind, Donald M. Camaioni, Jian Zhi Hu, and Johannes A. Lercher. Quantitatively probing the al distribution in zeolites. *Journal of the American Chemical Society*, 136(23):8296–8306, 2014.
- [148] Florian Goltl, Rosa E. Bulo, Jürgen Hafner, and Philippe Sautet. What makes copper-exchanged ssz-13 zeolite efficient at cleaning car exhaust gases? *Journal of Physical Chemistry Letters*, 4(14):2244–2249, 2013.
- [149] K. U. Gore, A. Abraham, S. G. Hegde, R. Kumar, J. P. Amoureux, and S. Ganapathy. Si-29 and al-27 mas/3q-mas nmr studies of high silica usy zeolites. *Journal of Physical Chemistry B*, 106(23):6115–6120, 2002.
- [150] J Klinowski, JM Thomas, CA Fyfe, and GC Gobbi. Monitoring of structural changes accompanying ultrastabilization of faujasitic zeolite catalysts. *Nature*, 296:533–536, 1982.
- [151] R. M. Lago, W. O. Haag, R. J. Mikovsky, D. H. Olson, S. D. Hellring, K. D. Schmitt, and G. T. Kerr. The nature of the catalytic sites in hzsm-5- activity enhancement. *Studies in Surface Science and Catalysis*, Volume 28:677–684, 1986.
- [152] Josef Macht, Michael J Janik, Matthew Neurock, and Enrique Iglesia. Mechanistic consequences of composition in acid catalysis by polyoxometalate keggins clusters. *Journal of the American Chemical Society*, 130(31):10369–10379, 2008.
- [153] MT Aronson, RJ Gorte, and W Eo Farneth. The influence of oxonium ion and carbenium ion stabilities on the alcohol/h-zsm-5 interaction. *Journal of Catalysis*, 98(2):434–443, 1986.

- [154] RA Van Santen and GJ Kramer. Reactivity theory of zeolitic broensted acidic sites. *Chemical Reviews*, 95(3):637–660, 1995.
- [155] Avelino Corma. Inorganic solid acids and their use in acid-catalyzed hydrocarbon reactions. *Chemical Reviews*, 95(3):559–614, 1995.
- [156] Marek Sierka, Uwe Eichler, Jerzy Datka, and Joachim Sauer. Heterogeneity of brønsted acidic sites in faujasite type zeolites due to aluminum content and framework structure. *The Journal of Physical Chemistry B*, 102(33):6397–6404, 1998.
- [157] Qingjun Zhu, Junko N. Kondo, Ryosuke Ohnuma, Yoshihiro Kubota, Masashi Yamaguchi, and Takashi Tatsumi. The study of methanol-to-olefin over proton type aluminosilicate cha zeolites. *Microporous and Mesoporous Materials*, 112(1-3):153–161, 2008.
- [158] Mark A. Deimund, Luke Harrison, Jonathan D. Lunn, Yu Liu, Andrzej Malek, Ramzy Shayib, and Mark E. Davis. Effect of heteroatom concentration in ssz-13 on the methanol-to-olefins reaction. *ACS Catalysis*, 6:542–550, 2016.
- [159] Jiri Dedecek, Vendula Balgova, Veronika Pashkova, Petr Klein, and Blanka Wichterlova. Synthesis of zsm-5 zeolites with defined distribution of al atoms in the framework and multinuclear mas nmr analysis of the control of al distribution. *Chemistry of Materials*, 24(16):3231–3239, 2012.
- [160] K.G. Strohmaier, S.C. Reyes, and D. Levin. High silica chabazite, its synthesis and its use in the conversion of oxygenates to olefins, 2008.
- [161] Yashodhan Bhawe, Manuel Moliner-Marin, Jonathan D. Lunn, Yu Liu, Andrzej Malek, and Mark Davis. Effect of cage size on the selective conversion of methanol to light olefins. *ACS Catalysis*, 2(12):2490–2495, 2012.
- [162] S. I. Zones. Conversion of faujasites to high-silica chabazite ssz-13 in the presence of n,n,n-trimethyl-1-adamantammonium iodide. *Journal of the Chemical Society, Faraday Transactions*, 87(22):3709–3716, 1991.
- [163] Nuria Martin, Manuel Moliner, and Avelino Corma. High yield synthesis of high-silica chabazite by combining the role of zeolite precursors and tetraethylammonium: Scr of nox. *Chemical Communications*, 51(49):9965–9968, 2015.
- [164] Masaya Itakura, Takayuki Inoue, Atsushi Takahashi, Tadahiro Fujitani, Yasunori Oumi, and Tsuneji Sano. Synthesis of high-silica cha zeolite from fau zeolite in the presence of benzyltrimethylammonium hydroxide. *Chemistry Letters*, 37(9):908–909, 2008.
- [165] Masaya Itakura, Ikuhiro Goto, Atsushi Takahashi, Tadahiro Fujitani, Yusuke Ide, Masahiro Sadakane, and Tsuneji Sano. Synthesis of high-silica cha type zeolite by interzeolite conversion of fau type zeolite in the presence of seed crystals. *Microporous and Mesoporous Materials*, 144(1-3):91–96, 2011.
- [166] Hiroyuki Imai, Nozomu Hayashida, Toshiyuki Yokoi, and Takashi Tatsumi. Direct crystallization of cha-type zeolite from amorphous aluminosilicate gel by seed-assisted method in the absence of organic-structure-directing agents. *Microporous and Mesoporous Materials*, 196:341–348, 2014.



- [167] Sarika Goel, Stacey I. Zones, and Enrique Iglesia. Synthesis of zeolites via interzeolite transformations without organic structure-directing agents. *Chemistry of Materials*, 27(6):2056–2066, 2015.
- [168] Einar A. Eilertsen, Bjornar Arstad, Stian Svelle, and Karl P. Lillerud. Single parameter synthesis of high silica chabazite from fluoride media. *Microporous and Mesoporous Materials*, 153:94–99, 2012.
- [169] Raquel Martinez-Franco, Manuel Moliner, Joakim R. Thøgersen, and Avelino Corma. Efficient one-pot preparation of Cu-SSZ-13 materials using cooperative OSDAs for their catalytic application in the SCR of NO<sub>x</sub>. *ChemCatChem*, 5(11):3316–3323, 2013.
- [170] M. J. Díaz-Cabañas, P. A. Barrett, and M. A. Camblor. Synthesis and structure of pure SiO<sub>2</sub> chabazite: the SiO<sub>2</sub> polymorph with the lowest framework density. *Chemical Communications*, 0(17):1881–1882, 1998.
- [171] John R. Di Iorio, Shane A. Bates, Anuj A. Verma, W. Nicholas Delgass, Fabio H. Ribeiro, Jeffrey T. Miller, and Rajamani Gounder. The dynamic nature of Brønsted acid sites in Cu-zeolites during NO<sub>x</sub> selective catalytic reduction: quantification by gas-phase ammonia titration. *Topics in Catalysis*, 58(7-9):424–434, 2015.
- [172] Subramanian Prasad and Maria Petrov. Mixed domain models for the distribution of aluminum in high silica zeolite SSZ-13. *Solid State Nuclear Magnetic Resonance*, 54:26–31, 2013.
- [173] D. E. Akporiaye, I. M. Dahl, H. B. Mostad, and R. Wendelbo. Aluminum distribution in chabazite: An experimental and computational study. *Journal of Physical Chemistry*, 100(10):4148–4153, 1996.
- [174] H. Praliaud and G. Coudurier. Optical spectroscopy of hydrated, dehydrated and ammoniated cobalt(II) exchanged zeolites X and Y. *Journal of the Chemical Society, Faraday Transactions*, 75:2601–2616, 1979.
- [175] H. Hoser, S. Krzyżanowski, and F. Trifiró. Optical spectra of Co-zeolites. *Journal of the Chemical Society, Faraday Transactions*, 71(3):665–669, 1975.
- [176] P. J. Dutta and J. H. Lunsford. Spectroscopic evidence for location of Co<sup>2+</sup> ions in zeolite-Y upon dehydration. *Journal of Chemical Physics*, 66(10):4716–4717, 1977.
- [177] A. A. Verberckmoes, B. M. Weckhuysen, and R. A. Schoonheydt. Spectroscopy and coordination chemistry of cobalt in molecular sieves. *Microporous and Mesoporous Materials*, 22(1-3):165–178, 1998.
- [178] K. Klier. Transition-metal ions in zeolites - the perfect surface sites. *Langmuir*, 4(1):13–25, 1988.
- [179] K. Klier, R. Kellerman, and P. J. Dutta. Spectra of synthetic zeolites containing transition-metal ions. 5.  $\pi$ -complexes of olefins and acetylene with Co(II) in a molecular-sieve. *Journal of Chemical Physics*, 61(10):4224–4234, 1974.
- [180] K. Klier. Stereospecific adsorption of nitrous oxide, cyclopropane, water, and ammonia on Co(II) in a synthetic zeolite. *Advances in Chemistry Series*, 101:480–489, 1971.

- [181] Tamás I. Korányi and János B. Nagy. Distribution of aluminum and boron in the periodical building units of boron-containing beta zeolites. *Journal of Physical Chemistry B*, 110(30):14728–14735, 2006.
- [182] M. Kato and T. Hattori. Ordered distribution of aluminum atoms in analcime. *Physics and Chemistry of Minerals*, 25(8):556–565, 1998.
- [183] Tamás I. Korányi and János B. Nagy. Distribution of aluminum in the periodical building units of faujasites. *Journal of Physical Chemistry C*, 111(6):2520–2524, 2007.
- [184] Tamás I. Korányi and János B. Nagy. Distribution of aluminum in different periodical building units of mor and bea zeolites. *Journal of Physical Chemistry B*, 109(33):15791–15797, 2005.
- [185] Tamás I. Korányi and János B. Nagy. Calculating the concentration of silical species in ferrierites by si-29 and al-27 nmr spectroscopy. *Journal of Physical Chemistry C*, 113(3):907–913, 2009.
- [186] D. Barthomeuf. Topology and maximum content of isolated species (al, ga, fe, b, si, ...) in a zeolitic framework - an approach to acid catalysis. *Journal of Physical Chemistry*, 97(39):10092–10096, 1993.
- [187] D. Barthomeuf. Zeolite acidity dependence on structure and chemical environment - correlations with catalysis. *Materials Chemistry and Physics*, 17(1-2):49–71, 1987.
- [188] S. Ramdas, J. M. Thomas, J. Klinowski, C. A. Fyfe, and J. S. Hartman. Ordering of aluminum and silicon in synthetic faujasites. *Nature*, 292(5820):228–230, 1981.
- [189] Edward Dempsey, G. H. Köhl, and David H. Olson. Variation of the lattice parameter with aluminum content in synthetic sodium faujasites. evidence for ordering of the framework ions. *Journal of Physical Chemistry*, 73(2):387–390, 1969.
- [190] M. A. Camblor, L. A. Villaescusa, and M. J. Díaz-Cabañas. Synthesis of all-silica and high-silica molecular sieves in fluoride media. *Topics in Catalysis*, 9(1-2):59–76, 1999.
- [191] Manuel Moliner. State of the art of lewis acid-containing zeolites: lessons from fine chemistry to new biomass transformation processes. *Dalton Transactions*, 43(11):4197–4208, 2014.
- [192] Min Bum Park, Yoorim Lee, Anmin Zheng, Feng-Shou Xiao, Christopher P. Nicholas, Gregory J. Lewis, and Suk Bong Hong. Formation pathway for lta zeolite crystals synthesized via a charge density mismatch approach. *Journal of the American Chemical Society*, 135(6):2248–2255, 2013.
- [193] G. J. Lewis, M. A. Miller, J. G. Moscoso, B. A. Wilson, L. M. Knight, and S. T. Wilson. Experimental charge density matching approach to zeolite synthesis. *Studies in Surface Science and Catalysis*, 154:364–372, 2004.
- [194] Seok Han Kim, Min Bum Park, Hyung-Ki Min, and Suk Bong Hong. Zeolite synthesis in the tetraethylammonium–tetramethylammonium mixed-organic additive system. *Microporous and Mesoporous Materials*, 123(1):160–168, 2009.

- [195] Mark A. Miller, Jaime G. Moscoso, Susan C. Koster, Michael G. Gatter, and Gregory J. Lewis. Synthesis and characterization of the 12-ring zeolites uzm-4 (bph) and uzm-22 (mei) via the charge density mismatch approach in the choline-li<sub>2</sub>o-sro-al<sub>2</sub>o<sub>3</sub>-sio<sub>2</sub> system. *Studies in Surface Science and Catalysis*, Volume 170:347–354, 2007.
- [196] C. Scott Blackwell, Robert W. Broach, Michael G. Gatter, Jennifer S. Holmgren, Deng-Yang Jan, Gregory J. Lewis, Beckay J. Mezza, Thomas M. Mezza, Mark A. Miller, Jaime G. Moscoso, R. Lyle Patton, Lisa M. Rohde, Michael W. Schoonover, Wharton Sinkler, Ben A. Wilson, and Stephen T. Wilson. Open-framework materials synthesized in the tma<sup>+</sup>/tea<sup>+</sup> mixed-template system: The new low si/al ratio zeolites uzm-4 and uzm-5. *Angewandte Chemie International Edition*, 42(15):1737–1740, 2003.
- [197] Joo Hyuck Lee, Min Bum Park, Jun Kyu Lee, Hyung-Ki Min, Mee Kyung Song, and Suk Bong Hong. Synthesis and characterization of eri-type uzm-12 zeolites and their methanol-to-olefin performance. *Journal of the American Chemical Society*, 132(37):12971–12982, 2010.
- [198] M. E. Davis and R. F. Lobo. Zeolite and molecular sieve synthesis. *Chemistry of Materials*, 4(4):756–768, 1992.
- [199] Avelino Corma, Fernando Rey, Jordi Rius, Maria J Sabater, and Susana Valencía. Supramolecular self-assembled molecules as organic directing agent for synthesis of zeolites. *Nature*, 431(7006):287, 2004.
- [200] Allen W Burton and Stacey I Zones. Organic molecules in zeolite synthesis: their preparation and structure-directing effects. *Studies in Surface Science and Catalysis*, 168:137–179, 2007.
- [201] Brandon C Knott, Claire T Nimlos, David J Robichaud, Mark R Nimlos, Seonah Kim, and Rajamani Gounder. Consideration of the aluminum distribution in zeolites in theoretical and experimental catalysis research. *ACS Catalysis*, 8(2):770–784, 2017.
- [202] Cecilia Bores, Scott M Auerbach, and Peter A Monson. Modeling the role of excluded volume in zeolite structure direction. *The journal of physical chemistry letters*, 2018.
- [203] Szu-Chia Chien, Scott M. Auerbach, and Peter A. Monson. Modeling the self-assembly of silica-templated nanoparticles in the initial stages of zeolite formation. *Langmuir*, 31(17):4940–4949, 2015.
- [204] Mohammad Navaid Khan, Scott M. Auerbach, and Peter A. Monson. Lattice monte carlo simulations in search of zeolite analogues: Effects of structure directing agents. *The Journal of Physical Chemistry C*, 119(50):28046–28054, 2015.
- [205] Ramdas Pophale, Frits Daeyaert, and Michael W Deem. Computational prediction of chemically synthesizable organic structure directing agents for zeolites. *Journal of Materials Chemistry A*, 1(23):6750–6760, 2013.
- [206] Yi Li, Hongxiao Cao, and Jihong Yu. Toward a new era of designed synthesis of nanoporous zeolitic materials. *ACS Nano*, 12(5):4096–4104, 2018.

- [207] Frits Daeyaert and Michael W. Deem. In silico design of chiral dimers to direct the synthesis of a chiral zeolite. *Molecular Physics*, 116(21-22):2836–2855, 2018.
- [208] Joel E Schmidt, Mark A Deimund, Dan Xie, and Mark E Davis. Synthesis of rth-type zeolites using a diverse library of imidazolium cations. *Chemistry of Materials*, 27(10):3756–3762, 2015.
- [209] Tracy M Davis, Albert Tianxiang Liu, Christopher M Lew, Dan Xie, Annabelle I Benin, Saleh Elomari, Stacey I Zones, and Michael W Deem. Computationally guided synthesis of ssz-52: a zeolite for engine exhaust clean-up. *Chemistry of Materials*, 28(3):708–711, 2016.
- [210] Joel E Schmidt, Michael W Deem, and Mark E Davis. Synthesis of a specified, silica molecular sieve by using computationally predicted organic structure-directing agents. *Angewandte Chemie International Edition*, 53(32):8372–8374, 2014.
- [211] Stephen K. Brand, Joel E. Schmidt, Michael W. Deem, Frits Daeyaert, Yanhang Ma, Osamu Terasaki, Marat Orazov, and Mark E. Davis. Enantiomerically enriched, polycrystalline molecular sieves. *Proceedings of the National Academy of Sciences*, 2017.
- [212] Eva Maria Gallego, M. Teresa Portilla, Cecilia Paris, Alejandro Leon-Escamilla, Mercedes Boronat, Manuel Moliner, and Avelino Corma. "ab initio" synthesis of zeolites for preestablished catalytic reactions. *Science*, 355(6329):1051, 2017.
- [213] Sichi Li, Hui Li, Rajamani Gounder, Anthony D. DeBellis, Imke B. Müller, Subramanian Prasad, Ahmad Moini, and William F. Schneider. First-principles comparison of proton and divalent copper cation exchange energy landscapes in ssz-13 zeolite. *The Journal of Physical Chemistry C*, 2018.
- [214] John R Di Iorio, Claire T Nimlos, and Rajamani Gounder. Introducing catalytic diversity into single-site chabazite zeolites of fixed composition via synthetic control of active site proximity. *ACS Catalysis*, 7(10):6663–6674, 2017.
- [215] Avelino Corma, EVA M GALLEGO, CHENGENG LI, CECILIA PARIS, NURIA GARCIA, JOAQUIN MARTINEZ, MERCEDES BORONAT, and MANUEL MOLINER. Making nanosized cha zeolite with controlled al distribution for optimizing mto performance. *Chemistry—A European Journal*, 2018.
- [216] Toshiki Nishitoba, Naohiro Yoshida, Junko N Kondo, and Toshiyuki Yokoi. Control of al distribution in the cha-type aluminosilicate zeolites and its impact on the hydrothermal stability and catalytic properties. *Industrial & Engineering Chemistry Research*, 57(11):3914–3922, 2018.
- [217] John M Findley, Peter I Ravikovitch, and David S Sholl. The effect of aluminum short-range ordering on carbon dioxide adsorption in zeolites. *The Journal of Physical Chemistry C*, 2018.
- [218] C Paolucci, JR Di Iorio, FH Ribeiro, R Gounder, and WF Schneider. Catalysis science of nox selective catalytic reduction with ammonia over cu-ssz-13 and cu-sapo-34. *Advances in Catalysis*, 59:1–107, 2016.

- [219] Dimitrios K. Pappas, Elisa Borfecchia, Michael Dyballa, Ilia A. Pankin, Kirill A. Lomachenko, Andrea Martini, Matteo Signorile, Shewangizaw Teketel, Bjørnar Arstad, Gloria Berlier, Carlo Lamberti, Silvia Bordiga, Unni Olsbye, Karl Petter Lillerud, Stian Svelle, and Pablo Beato. Methane to methanol: Structure–activity relationships for cu-cha. *Journal of the American Chemical Society*, 139(42):14961–14975, 2017.
- [220] Mark A. Newton, Amy J. Knorpp, Ana B. Pinar, Vitaly L. Sushkevich, Dennis Palagin, and Jeroen A. van Bokhoven. On the mechanism underlying the direct conversion of methane to methanol by copper hosted in zeolites; braiding cu k-edge xanes and reactivity studies. *Journal of the American Chemical Society*, 140(32):10090–10093, 2018.
- [221] Benjamin E. R. Snyder, Max L. Bols, Robert A. Schoonheydt, Bert F. Sels, and Edward I. Solomon. Iron and copper active sites in zeolites and their correlation to metalloenzymes. *Chemical Reviews*, 118(5):2718–2768, 2018.
- [222] HY Chen. *Urea-SCR technology for deNO<sub>x</sub> after treatment of diesel exhausts*. Springer, 2014.
- [223] Daniel F Shantz, Christian Fild, Hubert Koller, and Raul F Lobo. Guest-host interactions in as-made al-zsm-12: Implications for the synthesis of zeolite catalysts. *The Journal of Physical Chemistry B*, 103(49):10858–10865, 1999.
- [224] Allen W. Burton, Stacey I. Zones, and Saleh Elomari. The chemistry of phase selectivity in the synthesis of high-silica zeolites. *Current Opinion in Colloid & Interface Science*, 10(5–6):211–219, 2005.
- [225] Daniel F Shantz, Jörn Schmedt auf der Günne, Hubert Koller, and Raul F Lobo. Multiple-quantum 1h mas nmr studies of defect sites in as-made all-silica zsm-12 zeolite. *Journal of the American Chemical Society*, 122(28):6659–6663, 2000.
- [226] Allen W Burton, Greg S Lee, and Stacey I Zones. Phase selectivity in the syntheses of cage-based zeolite structures: An investigation of thermodynamic interactions between zeolite hosts and structure directing agents by molecular modeling. *Microporous and mesoporous materials*, 90(1-3):129–144, 2006.
- [227] Aseem Chawla, Rui Li, Rishabh Jain, R John Clark, James G Sutjianto, Jeremy C Palmer, and Jeffrey D Rimer. Cooperative effects of inorganic and organic structure-directing agents in zsm-5 crystallization. *Molecular Systems Design & Engineering*, 3(1):159–170, 2018.
- [228] Matthew D Oleksiak, Koki Muraoka, Ming-Feng Hsieh, Marlon T Conato, Atsushi Shimojima, Tatsuya Okubo, Watcharop Chaikittisilp, and Jeffrey D Rimer. Organic-free synthesis of a highly siliceous faujasite zeolite with spatially biased q4 (nal) si speciation. *Angewandte Chemie International Edition*, 56(43):13366–13371, 2017.
- [229] Min Bum Park, Donghui Jo, Him Chan Jeon, Christopher P Nicholas, Gregory J Lewis, and Suk Bong Hong. Zeolite synthesis from a charge density perspective: The charge density mismatch synthesis of uzm-5 and uzm-9. *Chemistry of Materials*, 26(23):6684–6694, 2014.

- [230] Chunyan Liu, Wenying Gu, Dejie Kong, and Hongchen Guo. The significant effects of the alkali-metal cations on zsm-5 zeolite synthesis: From mechanism to morphology. *Microporous and Mesoporous Materials*, 183:30–36, 2014.
- [231] Jin Shang, Gang Li, Ranjeet Singh, Penny Xiao, Jefferson Z Liu, and Paul A Webley. Potassium chabazite: a potential nanocontainer for gas encapsulation. *The Journal of Physical Chemistry C*, 114(50):22025–22031, 2010.
- [232] Yuewei Ji, Mark A Deimund, Yashodhan Bhawe, and Mark E Davis. Organic-free synthesis of cha-type zeolite catalysts for the methanol-to-olefins reaction. *ACS Catalysis*, 5(7):4456–4465, 2015.
- [233] Michel Bourgogne, Jean-Louis Guth, and Raymond Wey. Process for the preparation of synthetic zeolites, and zeolites obtained by said process, 1985.
- [234] Bo Liu, Yihong Zheng, Na Hu, Tian Gui, Yuqin Li, Fei Zhang, Rongfei Zhou, Xiangshu Chen, and Hidetoshi Kita. Synthesis of low-silica cha zeolite chabazite in fluoride media without organic structural directing agents and zeolites. *Microporous and Mesoporous Materials*, 196:270–276, 2014.
- [235] Walter Loewenstein. The distribution of aluminum in the tetrahedra of silicates and aluminates. *American Mineralogist: Journal of Earth and Planetary Materials*, 39(1-2):92–96, 1954.
- [236] Colin S Cundy and Paul A Cox. The hydrothermal synthesis of zeolites: history and development from the earliest days to the present time. *Chemical Reviews*, 103(3):663–702, 2003.
- [237] Christopher Paolucci, Ishant Khurana, Atish A Parekh, Sichi Li, Arthur J Shih, Hui Li, John R Di Iorio, Jonatan D Albarracin-Caballero, Aleksey Yezerets, and Jeffrey T Miller. Dynamic multinuclear sites formed by mobilized copper ions in nox selective catalytic reduction. *Science*, 357(6354):898–903, 2017.
- [238] Peter S Hammershoi, Yasser Jangjou, William S Epling, Anker D Jensen, and Ton VW Janssens. Reversible and irreversible deactivation of cu-cha nh3-scr catalysts by so2 and so3. *Applied Catalysis B: Environmental*, 226:38–45, 2018.
- [239] Yasser Jangjou, Quan Do, Yuntao Gu, Laura-Gaile Lim, Hong Sun, Di Wang, Ashok Kumar, Junhui Li, Lars C Grabow, and William S Epling. Nature of cu active centers in cu-ssz-13 and their responses to so2 exposure. *ACS Catalysis*, 8(2):1325–1337, 2018.
- [240] Feng Gao and Janos Szanyi. On the hydrothermal stability of cu/ssz-13 scr catalysts. *Applied Catalysis A: General*, 560:185–194, 2018.
- [241] Matthias Thommes. Physical adsorption characterization of nanoporous materials. *Chemie Ingenieur Technik*, 82(7):1059–1073, 2010.
- [242] Christopher GV Burgess, Douglas H Everett, and Stuart Nuttall. Adsorption hysteresis in porous materials. *Pure and Applied chemistry*, 61(11):1845–1852, 1989.

- [243] Takayuki Komatsu, Makoto Nunokawa, Il Shik Moon, Toshiya Takahara, Seitaro Namba, and Tatsuaki Yashima. Kinetic studies of reduction of nitric oxide with ammonia on  $\text{Cu}^{2+}$ -exchanged zeolites. *Journal of Catalysis*, 148(2):427–437, 1994.
- [244] Gérard Delahay, Stéphane Kieger, Nathalie Tanchoux, Philippe Trens, and Bernard Coq. Kinetics of the selective catalytic reduction of  $\text{NO}$  by  $\text{NH}_3$  on a  $\text{Cu}$ -faujasite catalyst. *Applied Catalysis B: Environmental*, 52(4):251–257, 2004.
- [245] Gérard Delahay, Enrique Ayala Villagomez, Jean-Marie Ducere, Dorothée Berthomieu, Annick Goursot, and Bernard Coq. Selective catalytic reduction of  $\text{NO}$  by  $\text{NH}_3$  on  $\text{Cu}$ -faujasite catalysts: an experimental and quantum chemical approach. *ChemPhysChem*, 3(8):686–692, 2002.
- [246] Joon Hyun Baik, Sung Dae Yim, In-Sik Nam, Young Sun Mok, Jong-Hwan Lee, Byong K Cho, and Se H Oh. Control of  $\text{NO}_x$  emissions from diesel engine by selective catalytic reduction (scr) with urea. *Topics in catalysis*, 30(1-4):37–41, 2004.
- [247] Joo-Hyoung Park, Hye Jun Park, Joon Hyun Baik, In-Sik Nam, Chae-Ho Shin, Jong-Hwan Lee, Byong K Cho, and Se H Oh. Hydrothermal stability of  $\text{CuZSM-5}$  catalyst in reducing  $\text{NO}$  by  $\text{NH}_3$  for the urea selective catalytic reduction process. *Journal of Catalysis*, 240(1):47–57, 2006.
- [248] Andrew M Beale, Feng Gao, Ines Lezcano-Gonzalez, Charles HF Peden, and Janos Szanyi. Recent advances in automotive catalysis for  $\text{NO}_x$  emission control by small-pore microporous materials. *Chemical Society Reviews*, 44(20):7371–7405, 2015.
- [249] Qing Ye, Lifeng Wang, and Ralph T Yang. Activity, propene poisoning resistance and hydrothermal stability of copper exchanged chabazite-like zeolite catalysts for scr of  $\text{NO}$  with ammonia in comparison to  $\text{Cu/ZSM-5}$ . *Applied Catalysis A: General*, 427:24–34, 2012.
- [250] D. W. Fickel, E. D’Addio, J. A. Lauterbach, and R. F. Lobo. The ammonia selective catalytic reduction activity of copper-exchanged small-pore zeolites. *Applied Catalysis B: Environmental*, 102(3-4):441–448, 2011.
- [251] K. C. C. Kharas, H. J. Robota, and D. J. Liu. Deactivation in  $\text{Cu-ZSM-5}$  lean-burn catalysts. *Applied Catalysis B: Environmental*, 2(2-3):225–237, 1993.
- [252] SA Gomez, A Campero, A Martinez-Hernandez, and GA Fuentes. Changes in  $\text{Cu}^{2+}$  environment upon wet deactivation of  $\text{Cu-ZSM-5}$  denox catalysts. *Applied Catalysis A: General*, 197(1):157–164, 2000.
- [253] Philip G Blakeman, Eric M Burkholder, Hai-Ying Chen, Jillian E Collier, Joseph M Fedeyko, Hoi Jobson, and Raj R Rajaram. The role of pore size on the thermal stability of zeolite supported  $\text{Cu}$  scr catalysts. *Catalysis Today*, 231:56–63, 2014.
- [254] Soran Shwan, Radka Nedyalkova, Jonas Jansson, John Korsgren, Louise Olsson, and Magnus Skoglundh. Hydrothermal stability of  $\text{Fe-BEA}$  as an  $\text{NH}_3$ -scr catalyst. *Industrial and Engineering Chemistry Research*, 51(39):12762–12772, 2012.

- [255] I. Bull, R. S. Boorse, W. M. Jaglowski, G. S. Koermer, A. Moini, J. A. Patchett, W.-M. Xue, P. Burk, J. C. Dettling, and M. T. Caudle. Copper cha zeolite cataysts, 2008.
- [256] Manuel Moliner, Cristina Franch, Eduardo Palomares, Marie Grill, and Avelino Corma. Cu-ssz-39, an active and hydrothermally stable catalyst for the selective catalytic reduction of no x. *Chemical Communications*, 48(66):8264–8266, 2012.
- [257] A Lorena Picone, Stewart J Warrender, Alexandra MZ Slawin, Daniel M Dawson, Sharon E Ashbrook, Paul A Wright, Stephen P Thompson, Lucia Gaberova, Philip L Llewellyn, Beatrice Moulin, et al. A co-templating route to the synthesis of cu sapo sta-7, giving an active catalyst for the selective catalytic reduction of no. *Microporous and Mesoporous Materials*, 146(1-3):36–47, 2011.
- [258] Dan Xie, Lynne B McCusker, Christian Baerlocher, Stacey I Zones, Wei Wan, and Xiaodong Zou. Ssz-52, a zeolite with an 18-layer aluminosilicate framework structure related to that of the denox catalyst cu-ssz-13. *Journal of the American Chemical Society*, 135(28):10519–10524, 2013.
- [259] Donghui Jo, Jong Bin Lim, Taekyung Ryu, In-Sik Nam, Miguel A Camblor, and Suk Bong Hong. Unseeded hydroxide-mediated synthesis and co 2 adsorption properties of an aluminosilicate zeolite with the rth topology. *Journal of Materials Chemistry A*, 3(38):19322–19329, 2015.
- [260] S Altwasser, J Jiao, S Steuernagel, J Weitkamp, and M Hunger. Elucidating the dealumination mechanism of zeolite hy by solid-state nmr spectroscopy. *Studies in Surface Science and Catalysis*, 154:3098–3105, 2004.
- [261] Malte Nielsen, Rasmus Yding Brogaard, Hanne Falsig, Pablo Beato, Ole Swang, and Stian Svelle. Kinetics of zeolite dealumination: insights from h-ssz-13. *ACS Catalysis*, 5(12):7131–7139, 2015.
- [262] K Ehrhardt, M Suckow, and W Lutz. Hydrothermal decomposition of aluminosilicate zeolites and prediction of their long-term stability. *Studies in Surface Science and Catalysis*, 94:179–186, 1995.
- [263] Lei Ma, Yisun Cheng, Giovanni Cavataio, Robert W McCabe, Lixin Fu, and Junhua Li. In situ drifts and temperature-programmed technology study on nh3-scr of nox over cu-ssz-13 and cu-sapo-34 catalysts. *Applied Catalysis B: Environmental*, 156:428–437, 2014.
- [264] M Valdez Lancinha Pereira, A Nicolle, and D Berthout. Hydrothermal aging effects on cu-zeolite nh3-scr catalyst. *Catalysis Today*, 258:424–431, 2015.
- [265] Luis R Aramburo, Lukasz Karwacki, Pablo Cubillas, Shunsuke Asahina, Matthijs de Winter, Martyn R Drury, Inge LC Buurmans, Eli Stavitski, Davide Mores, Marco Daturi, et al. The porosity, acidity, and reactivity of dealuminated zeolite zsm-5 at the single particle level: The influence of the zeolite architecture. *Chemistry—A European Journal*, 17(49):13773–13781, 2011.
- [266] Di Wang, Yasser Jangjou, Yong Liu, Munish K Sharma, Jinyong Luo, Junhui Li, Krishna Kamasamudram, and William S Epling. A comparison of hydrothermal aging effects on nh3-scr of nox over cu-ssz-13 and cu-sapo-34 catalysts. *Applied Catalysis B: Environmental*, 165:438–445, 2015.



- [267] Jiancheng Wang, Zhaoliang Peng, Hui Qiao, Lina Han, Weiren Bao, Liping Chang, Gang Feng, and Wei Liu. Influence of aging on in situ hydrothermally synthesized cu-ssz-13 catalyst for nh<sub>3</sub>-scr reaction. *Rsc Advances*, 4(80):42403–42411, 2014.
- [268] Steven J Schmieg, Se H Oh, Chang H Kim, David B Brown, Jong H Lee, Charles HF Peden, and Do Heui Kim. Thermal durability of cu-cha nh<sub>3</sub>-scr catalysts for diesel nox reduction. *Catalysis Today*, 184(1):252–261, 2012.
- [269] Wenkang Su, Zhenguo Li, Yue Peng, and Junhua Li. Correlation of the changes in the framework and active cu sites for typical cu/cha zeolites (ssz-13 and sapo-34) during hydrothermal aging. *Physical Chemistry Chemical Physics*, 17(43):29142–29149, 2015.
- [270] Michiel Dusselier, Mark A Deimund, Joel E Schmidt, and Mark E Davis. Methanol-to-olefins catalysis with hydrothermally treated zeolite ssz-39. *ACS Catalysis*, 5(10):6078–6085, 2015.
- [271] Feng Gao, Yilin Wang, Nancy M. Washton, Marton Kollar, Janos Szanyi, and Charles H. F. Peden. Effects of alkali and alkaline earth cocations on the activity and hydrothermal stability of cu/ssz-13 nh<sub>3</sub>-scr catalysts. *ACS Catalysis*, 5(11):6780–6791, 2015.
- [272] AV Kucherov and AA Slinkin. Introduction of transition metal ions in cationic positions of high-silica zeolites by a solid state reaction. interaction of copper compounds with h-mordenite or h-zsm-5. *Zeolites*, 6(3):175–180, 1986.
- [273] G. T. Kerr. Intracrystalline rearrangement of constitutive water in hydrogen zeolite y. *Journal of Physical Chemistry*, 71(12):4155–4156, 1967.
- [274] G. T. Kerr. Chemistry of crystalline aluminosilicates. vii. thermal decomposition products of ammonium zeolite y. *Journal of Catalysis*, 15(2):200–204, 1969.
- [275] Marius-Christian Silaghi, Celine Chizallet, Elena Petracovschi, Torsten Kerber, Joachim Sauer, and Pascal Raybaud. Regioselectivity of al–o bond hydrolysis during zeolites dealumination unified by brønsted–evans–polanyi relationship. *ACS Catalysis*, 5(1):11–15, 2014.
- [276] Michiel Dusselier, Joel E Schmidt, Roger Moulton, Barry Haymore, Mark Hellums, and Mark E Davis. Influence of organic structure directing agent isomer distribution on the synthesis of ssz-39. *Chemistry of Materials*, 27(7):2695–2702, 2015.
- [277] Joel E Schmidt, Mark A Deimund, and Mark E Davis. Facile preparation of aluminosilicate rth across a wide composition range using a new organic structure-directing agent. *Chemistry of Materials*, 26(24):7099–7105, 2014.
- [278] Stacey I Zones, Yumi Nakagawa, Susan T Evans, and Gregory S Lee. Zeolite ssz-39, 1999.
- [279] Gregory S Lee and Stacey I Zones. Zeolite ssz-50, 2003.
- [280] Gabriele Centi and Siglinda Perathoner. Nature of active species in copper-based catalysts and their chemistry of transformation of nitrogen oxides. *Applied Catalysis A: General*, 132(2):179–259, 1995.

- [281] Al Biaglow, DJ Parrillo, GT Kokotailo, and RJ Gorte. A study of dealuminated faujasites. *Journal of Catalysis*, 148(1):213–223, 1994.
- [282] J Texter, DH Strome, RG Herman, and K Klier. Chemical and spectroscopic properties of copper containing zeolites. *The Journal of Physical Chemistry*, 81(4):333–338, 1977.
- [283] Kyle L Fajdala, Ian J Drake, Alexis T Bell, and T Don Tilley. Atomic level control over surface species via a molecular precursor approach: Isolated cu (i) sites and cu nanoparticles supported on mesoporous silica. *Journal of the American Chemical Society*, 126(35):10864–10866, 2004.
- [284] Joseph Palamara, Karsten Seidel, Ahmad Moini, and Subramanian Prasad. Ion distribution in copper exchanged zeolites by using si-29 spin lattice relaxation analysis. *Journal of Magnetic Resonance*, 267:9–14, 2016.
- [285] Rajamani Gounder and Enrique Iglesia. The roles of entropy and enthalpy in stabilizing ion-pairs at transition states in zeolite acid catalysis. *Accounts of chemical research*, 45(2):229–238, 2011.
- [286] Jacek Klinowski. Nuclear magnetic resonance studies of zeolites. *Progress in nuclear magnetic resonance spectroscopy*, 16:237–309, 1984.
- [287] Ja Hun Kwak, Jian Zhi Hu, Do Heui Kim, Janos Szanyi, and Charles HF Peden. Penta-coordinated al<sup>3+</sup> ions as preferential nucleation sites for bao on  $\gamma$ -al<sub>2</sub>o<sub>3</sub>: An ultra-high-magnetic field 27al mas nmr study. *Journal of Catalysis*, 251(1):189–194, 2007.
- [288] Jun Wang, Vincent F Kispersky, W Nicholas Delgass, and Fabio H Ribeiro. Determination of the au active site and surface active species via operando transmission ftir and isotopic transient experiments on 2.3 wt.% au/tio<sub>2</sub> for the wgs reaction. *Journal of catalysis*, 289:171–178, 2012.
- [289] Hugh Stott Taylor. A theory of the catalytic surface. *Proc. R. Soc. Lond. A*, 108(745):105–111, 1925.
- [290] Malte Behrens, Felix Studt, Igor Kasatkin, Stefanie Kühn, Michael Hävecker, Frank Abild-Pedersen, Stefan Zander, Frank Girgsdies, Patrick Kurr, and Benjamin-Louis Knief. The active site of methanol synthesis over cu/zno/al<sub>2</sub>o<sub>3</sub> industrial catalysts. *Science*, 336(6083):893–897, 2012.
- [291] T Zambelli, J Wintterlin, J Trost, and G Ertl. Identification of the " active sites" of a surface-catalyzed reaction. *Science*, 273(5282):1688–1690, 1996.
- [292] Thomas F Jaramillo, Kristina P Jørgensen, Jacob Bonde, Jane H Nielsen, Sebastian Horch, and Ib Chorkendorff. Identification of active edge sites for electrochemical h<sub>2</sub> evolution from mos<sub>2</sub> nanocatalysts. *science*, 317(5834):100–102, 2007.
- [293] John Meurig Thomas. Design, synthesis, and in situ characterization of new solid catalysts. *Angewandte Chemie International Edition*, 38(24):3588–3628, 1999.

- [294] Young Dok Kim, Ari P Seitsonen, Stefan Wendt, Jinhai Wang, C Fan, Karl Jacobi, Herbert Over, and Gerhard Ertl. Characterization of various oxygen species on an oxide surface: RuO<sub>2</sub> (110). *The Journal of Physical Chemistry B*, 105(18):3752–3758, 2001.
- [295] Eric C Tyo, Chunrong Yin, Marcel Di Vece, Qiang Qian, Gihan Kwon, Sungsik Lee, Byeongdu Lee, Janae E DeBartolo, Sonke Seifert, Randall E Winans, et al. Oxidative dehydrogenation of cyclohexane on cobalt oxide (Co<sub>3</sub>O<sub>4</sub>) nanoparticles: The effect of particle size on activity and selectivity. *ACS Catalysis*, 2(11):2409–2423, 2012.
- [296] Taeho Hwang, Bryan R Goldsmith, Baron Peters, and Susannah L Scott. Water-catalyzed activation of H<sub>2</sub>O<sub>2</sub> by methyltrioxorhenium: A combined computational–experimental study. *Inorganic chemistry*, 52(24):13904–13917, 2013.
- [297] Andrew M Beale, Ad MJ van der Eerden, Kaisa Kervinen, Mark A Newton, and Bert M Weckhuysen. Adding a third dimension to operando spectroscopy: a combined uv-vis, raman and xafs setup to study heterogeneous catalysts under working conditions. *Chemical Communications*, 0(24):3015–3017, 2005.
- [298] Henrik Topsøe. Developments in operando studies and in situ characterization of heterogeneous catalysts. *Journal of Catalysis*, 216(1-2):155–164, 2003.
- [299] Bert M Weckhuysen. Determining the active site in a catalytic process: Operando spectroscopy is more than a buzzword. *Physical Chemistry Chemical Physics*, 5(20):4351–4360, 2003.
- [300] Isabel Xiaoye Green, Wenjie Tang, Matthew Neurock, and John T Yates. Spectroscopic observation of dual catalytic sites during oxidation of CO on a Au/TiO<sub>2</sub> catalyst. *Science*, 333(6043):736–739, 2011.
- [301] Alexey Boubnov, Hudson WP Carvalho, Dmitry E Doronkin, Tobias Gunter, Erik Gallo, Andrew J Atkins, Christoph R Jacob, and Jan-Dierk Grunwaldt. Selective catalytic reduction of NO over Fe-ZSM-5: mechanistic insights by operando HERFD-XANES and valence-to-core X-ray emission spectroscopy. *Journal of the American Chemical Society*, 136(37):13006–13015, 2014.
- [302] Eric J Peterson, Andrew T DeLaRiva, Sen Lin, Ryan S Johnson, Hua Guo, Jeffrey T Miller, Ja Hun Kwak, Charles HF Peden, Boris Kiefer, Lawrence F Allard, et al. Low-temperature carbon monoxide oxidation catalysed by regenerable atomically dispersed palladium on alumina. *Nature communications*, 5:4885, 2014.
- [303] Mark J Rice, Arup K Chakraborty, and Alexis T Bell. Site availability and competitive siting of divalent metal cations in ZSM-5. *Journal of Catalysis*, 194(2):278–285, 2000.
- [304] Mark J Rice, Arup K Chakraborty, and Alexis T Bell. Al next nearest neighbor, ring occupation, and proximity statistics in ZSM-5. *Journal of Catalysis*, 186(1):222–227, 1999.
- [305] Priit Sarv, Christian Fernandez, Jean-Paul Amoureux, and Kari Keskinen. Distribution of tetrahedral aluminium sites in ZSM-5 type zeolites: An <sup>27</sup>Al (multi-quantum) magic angle spinning NMR study. *The Journal of Physical Chemistry*, 100(50):19223–19226, 1996.

- [306] Daniel E Perea, Ilke Arslan, Jia Liu, Zoran Ristanović, Libor Kovarik, Bruce W Arey, Johannes A Lercher, Simon R Bare, and Bert M Weckhuysen. Determining the location and nearest neighbours of aluminium in zeolites with atom probe tomography. *Nature communications*, 6:7589, 2015.
- [307] Pieter Vanelderen, Julie Vancauwenbergh, Bert F Sels, and Robert A Schoonheydt. Coordination chemistry and reactivity of copper in zeolites. *Coordination Chemistry Reviews*, 257(2):483–494, 2013.
- [308] Mark J Rice, Arup K Chakraborty, and Alexis T Bell. Theoretical studies of the coordination and stability of divalent cations in zsm-5. *The Journal of Physical Chemistry B*, 104(43):9987–9992, 2000.
- [309] KC Hass and WF Schneider. Reliability of small cluster models for cu-exchanged zeolites. *The Journal of Physical Chemistry*, 100(22):9292–9301, 1996.
- [310] Bernhardt L Trout, Arup K Chakraborty, and Alexis T Bell. Local spin density functional theory study of copper ion-exchanged zsm-5. *The Journal of Physical Chemistry*, 100(10):4173–4179, 1996.
- [311] AV Kucherov, AA Slinkin, DA Kondrat'Ev, TN Bondarenko, AM Rubinstein, and Kh M Minachev. Cu<sup>2+</sup>-cation location and reactivity in mordenite and zsm-5: esr-study. *Zeolites*, 5(5):320–324, 1985.
- [312] G Spoto, A Zecchina, S Bordiga, G Ricchiardi, G Martra, G Leofanti, and G Petrini. Cu (i)-zsm-5 zeolites prepared by reaction of h-zsm-5 with gaseous cucl: spectroscopic characterization and reactivity towards carbon monoxide and nitric oxide. *Applied Catalysis B: Environmental*, 3(2-3):151–172, 1994.
- [313] Gemma Turnes Palomino, Paola Fiscaro, Silvia Bordiga, Adriano Zecchina, Elio Giamello, and Carlo Lamberti. Oxidation states of copper ions in zsm-5 zeolites. a multitechnique investigation. *The Journal of Physical Chemistry B*, 104(17):4064–4073, 2000.
- [314] Dana Nachtigallová, Petr Nachtigall, Marek Sierka, and Joachim Sauer. Coordination and siting of cu<sup>+</sup> ions in zsm-5: A combined quantum mechanics/interatomic potential function study. *Physical Chemistry Chemical Physics*, 1(8):2019–2026, 1999.
- [315] Patrick Da Costa, Björn Modén, George D Meitzner, Deuk Ki Lee, and Enrique Iglesia. Spectroscopic and chemical characterization of active and inactive cu species in no decomposition catalysts based on cu-zsm5. *Physical Chemistry Chemical Physics*, 4(18):4590–4601, 2002.
- [316] BR Goodman, KC Hass, WF Schneider, and JB Adams. Cluster model studies of oxygen-bridged cu pairs in cu- zsm-5 catalysts. *The Journal of Physical Chemistry B*, 103(47):10452–10460, 1999.
- [317] Pieter J Smeets, Ryan G Hadt, Julia S Woertink, Pieter Vanelderen, Robert A Schoonheydt, Bert F Sels, and Edward I Solomon. Oxygen precursor to the reactive intermediate in methanol synthesis by cu-zsm-5. *Journal of the American Chemical Society*, 132(42):14736–14738, 2010.

- [318] Julia S Woertink, Pieter J Smeets, Marijke H Groothaert, Michael A Vance, Bert F Sels, Robert A Schoonheydt, and Edward I Solomon. A [cu<sub>2</sub>o] 2+ core in cu-zsm-5, the active site in the oxidation of methane to methanol. *Proceedings of the National Academy of Sciences*, 106(45):18908–18913, 2009.
- [319] Marijke H Groothaert, Jeroen A van Bokhoven, Andrea A Battiston, Bert M Weckhuysen, and Robert A Schoonheydt. Bis ( $\mu$ -oxo) dicopper in cu-zsm-5 and its role in the decomposition of no: a combined in situ xafs, uv- vis- near-ir, and kinetic study. *Journal of the American Chemical Society*, 125(25):7629–7640, 2003.
- [320] Ramakrishnan Balasubramanian, Stephen M Smith, Swati Rawat, Liliya A Yatsunyk, Timothy L Stemmler, and Amy C Rosenzweig. Oxidation of methane by a biological dicopper centre. *Nature*, 465(7294):115, 2010.
- [321] Marijke H Groothaert, Pieter J Smeets, Bert F Sels, Pierre A Jacobs, and Robert A Schoonheydt. Selective oxidation of methane by the bis ( $\mu$ -oxo) dicopper core stabilized on zsm-5 and mordenite zeolites. *Journal of the American Chemical Society*, 127(5):1394–1395, 2005.
- [322] Pieter Vanelderen, Ryan G Hadt, Pieter J Smeets, Edward I Solomon, Robert A Schoonheydt, and Bert F Sels. Cu-zsm-5: A biomimetic inorganic model for methane oxidation. *Journal of catalysis*, 284(2):157–164, 2011.
- [323] Nadzeya V Beznis, Bert M Weckhuysen, and Johannes H Bitter. Cu-zsm-5 zeolites for the formation of methanol from methane and oxygen: Probing the active sites and spectator species. *Catalysis letters*, 138(1-2):14–22, 2010.
- [324] Evalyn Mae C Alayon, Maarten Nachtegaal, Andras Bodi, and Jeroen A van Bokhoven. Reaction conditions of methane-to-methanol conversion affect the structure of active copper sites. *ACS Catalysis*, 4(1):16–22, 2014.
- [325] Evalyn Mae C Alayon, Maarten Nachtegaal, Evgeny Kleymenov, and Jeroen A van Bokhoven. Determination of the electronic and geometric structure of cu sites during methane conversion over cu-mor with x- ray absorption spectroscopy. *Microporous and Mesoporous Materials*, 166:131–136, 2013.
- [326] Evalyn Mae C Alayon, Maarten Nachtegaal, Andras Bodi, Marco Ranocchiari, and Jeroen A van Bokhoven. Bis ( $\mu$ -oxo) versus mono ( $\mu$ -oxo) dicopper cores in a zeolite for converting methane to methanol: an in situ xas and dft investigation. *Physical Chemistry Chemical Physics*, 17(12):7681–7693, 2015.
- [327] Sebastian Grundner, Monica AC Markovits, Guanna Li, Moniek Tromp, Evgeny A Pidko, Emiel JM Hensen, Andreas Jentys, Maricruz Sanchez-Sanchez, and Johannes A Lercher. Single-site trinuclear copper oxygen clusters in mordenite for selective conversion of methane to methanol. *Nature communications*, 6:7546, 2015.
- [328] Pieter J Smeets, Marijke H Groothaert, and Robert A Schoonheydt. Cu based zeolites: A uv–vis study of the active site in the selective methane oxidation at low temperatures. *Catalysis today*, 110(3-4):303–309, 2005.
- [329] Matthew J Wulfers, Shewangizaw Teketel, Bahar Ipek, and Raul F Lobo. Conversion of methane to methanol on copper-containing small-pore zeolites and zeotypes. *Chemical Communications*, 51(21):4447–4450, 2015.

- [330] ST King. Reaction mechanism of oxidative carbonylation of methanol to dimethyl carbonate in cu- $\gamma$  zeolite. *Journal of Catalysis*, 161(2):530–538, 1996.
- [331] Pieter J Smeets, Bert F Sels, Robert M van Teeffelen, Hugo Leeman, Emiel JM Hensen, and Robert A Schoonheydt. The catalytic performance of cu-containing zeolites in n<sub>2</sub>o decomposition and the influence of o<sub>2</sub>, no and h<sub>2</sub>o on recombination of oxygen. *Journal of Catalysis*, 256(2):183–191, 2008.
- [332] Björn Modén, Patrick Da Costa, Benjamin Fonfé, Deuk Ki Lee, and Enrique Iglesia. Kinetics and mechanism of steady-state catalytic no decomposition reactions on cu-zsm5. *Journal of Catalysis*, 209(1):75–86, 2002.
- [333] Masakazu Iwamoto, Hiroshi Furukawa, Yoshihiro Mine, Fumihide Uemura, Shin-ichi Mikuriya, and Shuichi Kagawa. Copper (ii) ion-exchanged zsm-5 zeolites as highly active catalysts for direct and continuous decomposition of nitrogen monoxide. *Journal of the Chemical Society, Chemical Communications*, 0(16):1272–1273, 1986.
- [334] Antonio Grossale, Isabella Nova, Enrico Tronconi, Daniel Chatterjee, and Michel Weibel. The chemistry of the no/no<sub>2</sub>-nh<sub>3</sub> “fast” scr reaction over fe-zsm5 investigated by transient reaction analysis. *Journal of Catalysis*, 256(2):312–322, 2008.
- [335] Massimo Colombo, Isabella Nova, and Enrico Tronconi. A comparative study of the nh<sub>3</sub>-scr reactions over a cu-zeolite and a fe-zeolite catalyst. *Catalysis Today*, 151(3-4):223–230, 2010.
- [336] Alexander Shishkin, Hannes Kannisto, Per-Anders Carlsson, Hanna Härelind, and Magnus Skoglundh. Synthesis and functionalization of ssz-13 as an nh<sub>3</sub>-scr catalyst. *Catalysis Science & Technology*, 4(11):3917–3926, 2014.
- [337] Giovanni Cavataio, James Girard, Joseph Eli Patterson, Clifford Montreuil, Yisun Cheng, and Christine K Lambert. Laboratory testing of urea-scr formulations to meet tier 2 bin 5 emissions. Technical report, SAE Technical Paper, 2007.
- [338] Manfred Koebel, Martin Elsener, and Michael Kleemann. Urea-scr: a promising technique to reduce nox emissions from automotive diesel engines. *Catalysis today*, 59(3-4):335–345, 2000.
- [339] Jinyong Luo, Di Wang, Ashok Kumar, Junhui Li, Krishna Kamasamudram, Neal Currier, and Aleksey Yezerets. Identification of two types of cu sites in cu/ssz-13 and their unique responses to hydrothermal aging and sulfur poisoning. *Catalysis Today*, 267:3–9, 2016.
- [340] Florian Goltl, Philippe Sautet, and Ive Hermans. Can dynamics be responsible for the complex multipoint infrared spectra of no adsorbed to copper (ii) sites in zeolites? *Angewandte Chemie International Edition*, 54(27):7799–7804, 2015.
- [341] Renqin Zhang, Jean-Sabin McEwen, Marton Kollar, Feng Gao, Yilin Wang, Janos Szanyi, and Charles HF Peden. No chemisorption on cu/ssz-13: a comparative study from infrared spectroscopy and dft calculations. *Acs Catalysis*, 4(11):4093–4105, 2014.

- [342] Florian Goltl, Philippe Sautet, and Ive Hermans. The impact of finite temperature on the coordination of cu cations in the zeolite ssz-13. *Catalysis Today*, 267:41–46, 2016.
- [343] Ja Hun Kwak, Tamas Varga, Charles HF Peden, Feng Gao, Jonathan C Hanson, and Janos Szanyi. Following the movement of cu ions in a ssz-13 zeolite during dehydration, reduction and adsorption: A combined in situ tp-xrd, xanes/driftd study. *Journal of Catalysis*, 314:83–93, 2014.
- [344] Anita Godiksen, Frederick N Stappen, Peter NR Vennestrøm, Filippo Giordano, S øren Birk Rasmussen, Lars F Lundegaard, and Susanne Mossin. Coordination environment of copper sites in cu-cha zeolite investigated by electron paramagnetic resonance. *The Journal of Physical Chemistry C*, 118(40):23126–23138, 2014.
- [345] Peter NR Vennestrøm, Anna Katerinopoulou, Ramchandra R Tiruvalam, Arkady Kustov, Poul G Moses, Patricia Concepcion, and Avelino Corma. Migration of cu ions in sapo-34 and its impact on selective catalytic reduction of no x with nh<sub>3</sub>. *ACS Catalysis*, 3(9):2158–2161, 2013.
- [346] Casper Welzel Andersen, Martin Bremholm, Peter Nicolai Ravnborg Vennestrøm, Anders Bank Blichfeld, Lars Fahl Lundegaard, and Bo Brummerstedt Iversen. Location of cu<sup>2+</sup> in cha zeolite investigated by x-ray diffraction using the rietveld/maximum entropy method. *IUCrJ*, 1(6):382–386, 2014.
- [347] Feng Gao, Eric D Walter, Eric M Karp, Jinyong Luo, Russell G Tonkyn, Ja Hun Kwak, Janos Szanyi, and Charles HF Peden. Structure–activity relationships in nh<sub>3</sub>-scr over cu-ssz-13 as probed by reaction kinetics and epr studies. *Journal of catalysis*, 300:20–29, 2013.
- [348] Ja Hun Kwak, Haiyang Zhu, Jong H Lee, Charles HF Peden, and Janos Szanyi. Two different cationic positions in cu-ssz-13? *Chemical Communications*, 48(39):4758–4760, 2012.
- [349] Feng Gao, Eric D Walter, Marton Kollar, Yilin Wang, Janos Szanyi, and Charles HF Peden. Understanding ammonia selective catalytic reduction kinetics over cu/ssz-13 from motion of the cu ions. *Journal of Catalysis*, 319:1–14, 2014.
- [350] jiri Dedeczek and Blanka Wichterlova. Role of hydrated cu ion complexes and aluminum distribution in the framework on the cu ion siting in zsm-5. *The Journal of Physical Chemistry B*, 101(49):10233–10240, 1997.
- [351] John L Fulton, Markus M Hoffmann, John G Darab, Bruce J Palmer, and Edward A Stern. Copper (i) and copper (ii) coordination structure under hydrothermal conditions at 325 c: an x-ray absorption fine structure and molecular dynamics study. *The Journal of Physical Chemistry A*, 104(49):11651–11663, 2000.
- [352] Florian Goltl and Jurgen Hafner. Structure and properties of metal-exchanged zeolites studied using gradient-corrected and hybrid functionals. i. structure and energetics. *The Journal of chemical physics*, 136(6):064501, 2012.

- [353] Florian Goltl and Jurgen Hafner. Structure and properties of metal-exchanged zeolites studied using gradient-corrected and hybrid functionals. ii. electronic structure and photoluminescence spectra. *The Journal of chemical physics*, 136(6):064502, 2012.
- [354] Florian Goltl and Jurgen Hafner. Structure and properties of metal-exchanged zeolites studied using gradient-corrected and hybrid functionals. iii. energetics and vibrational spectroscopy of adsorbates. *The Journal of chemical physics*, 136(6):064503, 2012.
- [355] Ja Hun Kwak, Jong H Lee, Sarah D Burton, Andrew S Lipton, Charles HF Peden, and Janos Szanyi. A common intermediate for n<sub>2</sub> formation in enzymes and zeolites: Side-on cu–nitrosyl complexes. *Angewandte Chemie International Edition*, 52(38):9985–9989, 2013.
- [356] Pio Forzatti, Luca Lietti, Isabella Nova, and Enrico Tronconi. Diesel nox aftertreatment catalytic technologies: Analogies in lnt and scr catalytic chemistry. *Catalysis Today*, 151(3-4):202–211, 2010.
- [357] Massimo Colombo, Isabella Nova, and Enrico Tronconi. Detailed kinetic modeling of the nh<sub>3</sub>–no/no<sub>2</sub> scr reactions over a commercial cu-zeolite catalyst for diesel exhausts after treatment. *Catalysis Today*, 197(1):243–255, 2012.
- [358] Maria Pia Ruggeri, Tommaso Selleri, Massimo Colombo, Isabella Nova, and Enrico Tronconi. Identification of nitrites/hono as primary products of no oxidation over fe-zsm-5 and their role in the standard scr mechanism: A chemical trapping study. *Journal of Catalysis*, 311:266–270, 2014.
- [359] Maria Pia Ruggeri, Isabella Nova, Enrico Tronconi, Josh A Pihl, Todd J Toops, and William P Partridge. In-situ drifts measurements for the mechanistic study of no oxidation over a commercial cu-cha catalyst. *Applied Catalysis B: Environmental*, 166:181–192, 2015.
- [360] Tobias Gunter, Hudson WP Carvalho, Dmitry E Doronkin, Thomas Sheppard, Pieter Glatzel, Andrew J Atkins, Julian Rudolph, Christoph R Jacob, Maria Casapu, and Jan-Dierk Grunwaldt. Structural snapshots of the scr reaction mechanism on cu-ssz-13. *Chemical Communications*, 51(44):9227–9230, 2015.
- [361] RM Koros and EJ Nowak. A diagnostic test of the kinetic regime in a packed bed reactor. *Chemical Engineering Science*, 22(3):470, 1967.
- [362] George M Psofogiannakis, John F McCleerey, Eugenio Jaramillo, and Adri CT Van Duin. Reaxff reactive molecular dynamics simulation of the hydration of cu-ssz-13 zeolite and the formation of cu dimers. *The Journal of Physical Chemistry C*, 119(12):6678–6686, 2015.
- [363] AKS Clemens, Alexander Shishkin, PA Carlsson, Magnus Skoglundh, Martinez Casado, Zdenek Matej, Olivier Balmes, and H Harelind. Reaction-driven ion exchange of copper into zeolite ssz-13. *ACS Catalysis*, 5(10):6209–6218, 2015.
- [364] Marek Sierka and Joachim Sauer. Proton mobility in chabazite, faujasite, and zsm-5 zeolite catalysts. comparison based on ab initio calculations. *The Journal of Physical Chemistry B*, 105(8):1603–1613, 2001.



- [365] Luis J Smith, Anne Davidson, and Anthony K Cheetham. A neutron diffraction and infrared spectroscopy study of the acid form of the aluminosilicate zeolite, chabazite (h-ssz-13). *Catalysis letters*, 49(3-4):143–146, 1997.
- [366] Silvia Bordiga, Jenny G Vitillo, Gabriele Ricchiardi, Laura Regli, Donato Cocina, Adriano Zecchina, Bjørnar Arstad, Morten Bjørgen, Jasmina Hafizovic, and Karl Petter Lillerud. Interaction of hydrogen with mof-5. *The Journal of Physical Chemistry B*, 109(39):18237–18242, 2005.
- [367] CF Baes and RE Mesmer. The hydrolysis of cations, 489 p, 1976.
- [368] Aline Auroux, Vera Bolis, Piotr Wierzechowski, Pierre C Gravelle, and Jacques C Vedrine. Study of the acidity of zsm-5 zeolite by microcalorimetry and infrared spectroscopy. *Journal of the Chemical Society, Faraday Transactions 1: Physical Chemistry in Condensed Phases*, 75:2544–2555, 1979.
- [369] Aline Auroux. Calorimetry and thermal methods in catalysis. *Springer Series in Materials Science*, 154, 2013.
- [370] Sanjay B Sharma, Bernard L Meyers, Daniel T Chen, Jeffrey Miller, and James A Dumesic. Characterization of catalyst acidity by microcalorimetry and temperature-programmed desorption. *Applied Catalysis A: General*, 102(2):253–265, 1993.
- [371] C Lee, DJ Parrillo, RJ Gorte, and WE Farneth. Relationship between differential heats of adsorption and brønsted acid strengths of acidic zeolites: H-zsm-5 and h-mordenite. *Journal of the American Chemical Society*, 118(13):3262–3268, 1996.
- [372] Martin Brandle, Joachim Sauer, Roberto Dovesi, and Nicholas M Harrison. Comparison of a combined quantum mechanics/interatomic potential function approach with its periodic quantum-mechanical limit: Proton siting and ammonia adsorption in zeolite chabazite. *The Journal of chemical physics*, 109(23):10379–10389, 1998.
- [373] Soran Shwan, Magnus Skoglundh, Lars F Lundegaard, Ramchandra R Tirumala, Ton VW Janssens, Anna Carlsson, and Peter NR Vennestrom. Solid-state ion-exchange of copper into zeolites facilitated by ammonia at low temperature. *ACS Catalysis*, 5(1):16–19, 2014.
- [374] Donghai Sun, William F Schneider, James B Adams, and Debasis Sengupta. Molecular origins of selectivity in the reduction of no x by nh3. *The Journal of Physical Chemistry A*, 108(43):9365–9374, 2004.
- [375] Oc Hee Han, Chang-Sam Kim, and Suk Bong Hong. Direct evidence for the nonrandom nature of al substitution in zeolite zsm-5: An investigation by 27al mas and mq mas nmr. *Angewandte Chemie International Edition*, 41(3):469–472, 2002.
- [376] Stacey I Zones and Robert A Van Nordstrand. Novel zeolite transformations: the template-mediated conversion of cubic p zeolite to ssz-13. *Zeolites*, 8(3):166–174, 1988.

- [377] Chun-Chih Chang, Zhuopeng Wang, Paul Dornath, Hong Je Cho, and Wei Fan. Rapid synthesis of sn-beta for the isomerization of cellulosic sugars. *Rsc Advances*, 2(28):10475–10477, 2012.
- [378] MH Groothaert, K Lievens, Jeroen A van Bokhoven, AA Battiston, BM Weckhuysen, Kristine Pierloot, and RA Schoonheydt. Bis ( $\mu$ -oxo) dicopper as intermediate in the catalytic decomposition of no over cu-zsm-5. In *Studies in Surface Science and Catalysis*, volume 154, pages 2449–2457. Elsevier, 2004.
- [379] Haiyang Zhu, Ja Hun Kwak, Charles HF Peden, and Janos Szanyi. In situ drifts-ms studies on the oxidation of adsorbed nh<sub>3</sub> by no<sub>x</sub> over a cu-ssz-13 zeolite. *Catalysis today*, 205:16–23, 2013.
- [380] Janos Szanyi, Ja Hun Kwak, Haiyang Zhu, and Charles HF Peden. Characterization of cu-ssz-13 nh<sub>3</sub> scr catalysts: an in situ ftir study. *Physical Chemistry Chemical Physics*, 15(7):2368–2380, 2013.
- [381] Geraldine Lamble, Arild Moen, and David G Nicholson. Structure of the diamminecopper (i) ion in solution. an x-ray absorption spectroscopic study. *Journal of the Chemical Society, Faraday Transactions*, 90(15):2211–2213, 1994.
- [382] Di Wang, Li Zhang, Krishna Kamasamudram, and William S Epling. In situ-drifts study of selective catalytic reduction of no<sub>x</sub> by nh<sub>3</sub> over cu-exchanged sapo-34. *Acs Catalysis*, 3(5):871–881, 2013.
- [383] Hanna Sjoval, Erik Fridell, Richard J Blint, and Louise Olsson. Identification of adsorbed species on cu-zsm-5 under nh<sub>3</sub> scr conditions. *Topics in Catalysis*, 42(1-4):113–117, 2007.
- [384] Ines Lezcano-Gonzalez, Upakul Deka, Bjornar Arstad, A Van Yperen-De Deyne, Karen Hemelsoet, Michel Waroquier, Veronique Van Speybroeck, Bert M Weckhuysen, and Andrew M Beale. Determining the storage, availability and reactivity of nh<sub>3</sub> within cu-chabazite-based ammonia selective catalytic reduction systems. *Physical Chemistry Chemical Physics*, 16(4):1639–1650, 2014.
- [385] B Gomez-Lor, M Iglesias, C Cascales, E Gutierrez-Puebla, and MA Monge. A diamine copper (i) complex stabilized in situ within the ferrierite framework. catalytic properties. *Chemistry of materials*, 13(4):1364–1368, 2001.
- [386] Marta Moreno-Gonzalez, Beatriz Hueso, Mercedes Boronat, Teresa Blasco, and Avelino Corma. Ammonia-containing species formed in cu-chabazite as per in situ epr, solid-state nmr, and dft calculations. *The journal of physical chemistry letters*, 6(6):1011–1017, 2015.
- [387] Jessica M Hoover, Bradford L Ryland, and Shannon S Stahl. Mechanism of copper (i)/tempo-catalyzed aerobic alcohol oxidation. *Journal of the American Chemical Society*, 135(6):2357–2367, 2013.
- [388] Peng Chen and Edward I Solomon. O<sub>2</sub> activation by binuclear cu sites: noncoupled versus exchange coupled reaction mechanisms. *Proceedings of the National Academy of Sciences*, 101(36):13105–13110, 2004.
- [389] Edward I Solomon, David E Heppner, Esther M Johnston, Jake W Ginsbach, Jordi Cirera, Munzarin Qayyum, Matthew T Kieber-Emmons, Christian H Kjaergaard, Ryan G Hadt, and Li Tian. Copper active sites in biology. *Chemical reviews*, 114(7):3659–3853, 2014.

- [390] J Hutter, P Ballone, M Bernasconi, P Focher, E Fois, St Goedecker, M Parrinello, and M Tuckerman. Cpmc version 3.0. *MPI für Festkörperforschung and IBM Zurich Research Laboratory*, 1999, 1995.
- [391] John P Perdew and Yue Wang. Accurate and simple analytic representation of the electron-gas correlation energy. *Physical Review B*, 45(23):13244, 1992.
- [392] David Vanderbilt. Soft self-consistent pseudopotentials in a generalized eigenvalue formalism. *Physical Review B*, 41(11):7892, 1990.
- [393] Kari Laasonen, Roberto Car, Changyol Lee, and David Vanderbilt. Implementation of ultrasoft pseudopotentials in ab initio molecular dynamics. *Physical Review B*, 43(8):6796, 1991.
- [394] Kari Laasonen, Alfredo Pasquarello, Roberto Car, Changyol Lee, and David Vanderbilt. Car-parrinello molecular dynamics with vanderbilt ultrasoft pseudopotentials. *Physical Review B*, 47(16):10142, 1993.
- [395] Georg Kresse and Jürgen Furthmüller. Efficient iterative schemes for ab initio total-energy calculations using a plane-wave basis set. *Physical review B*, 54(16):11169, 1996.
- [396] Peter E Blöchl. Projector augmented-wave method. *Physical review B*, 50(24):17953, 1994.
- [397] Georg Kresse and D Joubert. From ultrasoft pseudopotentials to the projector augmented-wave method. *Physical Review B*, 59(3):1758, 1999.
- [398] Jochen Heyd, Gustavo E Scuseria, and Matthias Ernzerhof. Hybrid functionals based on a screened coulomb potential. *The Journal of chemical physics*, 118(18):8207–8215, 2003.
- [399] Jochen Heyd and Gustavo E Scuseria. Efficient hybrid density functional calculations in solids: Assessment of the heyd–scuseria–ernzerhof screened coulomb hybrid functional. *The Journal of chemical physics*, 121(3):1187–1192, 2004.
- [400] Jochen Heyd, Gustavo E Scuseria, and Matthias Ernzerhof. Hybrid functionals based on a screened coulomb potential. *J. Chem. Phys.*, 124:219906, 2006.
- [401] Aliaksandr V Krukau, Oleg A Vydrov, Artur F Izmaylov, and Gustavo E Scuseria. Influence of the exchange screening parameter on the performance of screened hybrid functionals. *The Journal of chemical physics*, 125(22):224106, 2006.
- [402] Alexandre Tkatchenko and Matthias Scheffler. Accurate molecular van der waals interactions from ground-state electron density and free-atom reference data. *Physical review letters*, 102(7):073005, 2009.
- [403] Richard FW Bader. Atoms in molecules: a quantum theory, vol 22, international series of monographs on chemistry, 1990.
- [404] W Tang, E Sanville, and G Henkelman. A grid-based bader analysis algorithm without lattice bias. *Journal of Physics: Condensed Matter*, 21(8):084204, 2009.

- [405] Edward Sanville, Steven D Kenny, Roger Smith, and Graeme Henkelman. Improved grid-based algorithm for bader charge allocation. *Journal of computational chemistry*, 28(5):899–908, 2007.
- [406] Graeme Henkelman, Andri Arnaldsson, and Hannes Jónsson. A fast and robust algorithm for bader decomposition of charge density. *Computational Materials Science*, 36(3):354–360, 2006.
- [407] Min Yu and Dallas R Trinkle. Accurate and efficient algorithm for bader charge integration. *The Journal of chemical physics*, 134(6):064111, 2011.
- [408] JM Bray and WF Schneider. First-principles thermodynamic models in heterogeneous catalysis. *Computational Catalysis*, 14:59, 2013.
- [409] Michael W Penninger, Chang Hwan Kim, Levi T Thompson, and William F Schneider. Dft analysis of no oxidation intermediates on undoped and doped lacoo<sub>3</sub> perovskite. *The Journal of Physical Chemistry C*, 119(35):20488–20494, 2015.
- [410] Giovanni Maria Piccini and Joachim Sauer. Effect of anharmonicity on adsorption thermodynamics. *Journal of chemical theory and computation*, 10(6):2479–2487, 2014.
- [411] Charles T Campbell and Jason RV Sellers. The entropies of adsorbed molecules. *Journal of the American Chemical Society*, 134(43):18109–18115, 2012.
- [412] Mae K Rubin. Synthesis of zeolite beta, 1992.
- [413] John Meurig Thomas. The societal significance of catalysis and the growing practical importance of single-site heterogeneous catalysts, 2012.
- [414] Kunlun Ding, Ahmet Gulec, Alexis M Johnson, Neil M Schweitzer, Galen D Stucky, Laurence D Marks, and Peter C Stair. Identification of active sites in co oxidation and water-gas shift over supported pt catalysts. *Science*, 350(6257):189–192, 2015.
- [415] John Jones, Haifeng Xiong, Andrew T DeLaRiva, Eric J Peterson, Hien Pham, Sivakumar R Challa, Gongshin Qi, Se Oh, Michelle H Wiebenga, Xavier Isidro Pereira Hernández, et al. Thermally stable single-atom platinum-on-ceria catalysts via atom trapping. *Science*, 353(6295):150–154, 2016.
- [416] Georgios Kyriakou, Matthew B Boucher, April D Jewell, Emily A Lewis, Timothy J Lawton, Ashleigh E Baber, Heather L Tierney, Maria Flytzani-Stephanopoulos, and E Charles H Sykes. Isolated metal atom geometries as a strategy for selective heterogeneous hydrogenations. *Science*, 335(6073):1209–1212, 2012.
- [417] Haisheng Wei, Xiaoyan Liu, Aiqin Wang, Leilei Zhang, Botao Qiao, Xiaofeng Yang, Yanqiang Huang, Shu Miao, Jingyue Liu, and Tao Zhang. Feo x-supported platinum single-atom and pseudo-single-atom catalysts for chemoselective hydrogenation of functionalized nitroarenes. *Nature communications*, 5:ncomms6634, 2014.

- [418] Ming Yang, Sha Li, Yuan Wang, Jeffrey A Herron, Ye Xu, Lawrence F Allard, Sungsik Lee, Jun Huang, Manos Mavrikakis, and Maria Flytzani-Stephanopoulos. Catalytically active  $\text{au-o (oh) x}$ -species stabilized by alkali ions on zeolites and mesoporous oxides. *Science*, 346(6216):1498–1501, 2014.
- [419] Ming Yang, Jilei Liu, Sungsik Lee, Branko Zugic, Jun Huang, Lawrence F Allard, and Maria Flytzani-Stephanopoulos. A common single-site  $\text{pt (ii)-o (oh) x}$ -species stabilized by sodium on “active” and “inert” supports catalyzes the water-gas shift reaction. *Journal of the American Chemical Society*, 137(10):3470–3473, 2015.
- [420] John Meurig Thomas, Robert Raja, and Dewi W Lewis. Single-site heterogeneous catalysts. *Angewandte Chemie International Edition*, 44(40):6456–6482, 2005.
- [421] Kirill A Lomachenko, Elisa Borfecchia, Chiara Negri, Gloria Berlier, Carlo Lamberti, Pablo Beato, Hanne Falsig, and Silvia Bordiga. The  $\text{cu-cha deno x}$  catalyst in action: Temperature-dependent  $\text{nh}_3$ -assisted selective catalytic reduction monitored by operando xas and xes. *Journal of the American Chemical Society*, 138(37):12025–12028, 2016.
- [422] Pieter Vanelderen, Benjamin ER Snyder, Ming-Li Tsai, Ryan G Hadt, Julie Vancauwenbergh, Olivier Coussens, Robert A Schoonheydt, Bert F Sels, and Edward I Solomon. Spectroscopic definition of the copper active sites in mordenite: Selective methane oxidation. *Journal of the American Chemical Society*, 137(19):6383–6392, 2015.
- [423] Markus Metz and Edward I Solomon. Dioxygen binding to deoxyhemocyanin: electronic structure and mechanism of the spin-forbidden two-electron reduction of  $\text{o}_2$ . *Journal of the American Chemical Society*, 123(21):4938–4950, 2001.
- [424] Liviu M Mirica, Xavier Ottenwaelde, and T Daniel P Stack. Structure and spectroscopy of copper- dioxygen complexes. *Chemical Reviews*, 104(2):1013–1046, 2004.
- [425] Liviu M Mirica, Michael Vance, Deanne Jackson Rudd, Britt Hedman, Keith O Hodgson, Edward I Solomon, and T Daniel P Stack. Tyrosinase reactivity in a model complex: an alternative hydroxylation mechanism. *Science*, 308(5730):1890–1892, 2005.
- [426] Scott D McCann and Shannon S Stahl. Copper-catalyzed aerobic oxidations of organic molecules: pathways for two-electron oxidation with a four-electron oxidant and a one-electron redox-active catalyst. *Accounts of chemical research*, 48(6):1756–1766, 2015.
- [427] Lin Chen, Jonas Jansson, Magnus Skoglundh, and Henrik Gronbeck. Mechanism for solid-state ion exchange of  $\text{cu}^+$  into zeolites. *The Journal of Physical Chemistry C*, 120(51):29182–29189, 2016.
- [428] Hanne Falsig, Peter NR Vennestrom, Poul Georg Moses, and Ton VW Janssens. Activation of oxygen and no in  $\text{nh}_3$ -scr over  $\text{cu-cha}$  catalysts evaluated by density functional theory. *Topics in Catalysis*, 59(10-12):861–865, 2016.

- [429] Feng Gao, Donghai Mei, Yilin Wang, Janos Szanyi, and Charles HF Peden. Selective catalytic reduction over cu/ssz-13: Linking homo-and heterogeneous catalysis. *Journal of the American Chemical Society*, 139(13):4935–4942, 2017.
- [430] Lung Shan Kau, Darlene J Spira-Solomon, James E Penner-Hahn, Keith O Hodgson, and Edward I Solomon. X-ray absorption edge determination of the oxidation state and coordination number of copper. application to the type 3 site in rhus vernicifera laccase and its reaction with oxygen. *Journal of the American Chemical Society*, 109(21):6433–6442, 1987.
- [431] Silvia Bordiga, Elena Groppo, Giovanni Agostini, Jeroen A van Bokhoven, and Carlo Lamberti. Reactivity of surface species in heterogeneous catalysts probed by in situ x-ray absorption techniques. *Chemical reviews*, 113(3):1736–1850, 2013.
- [432] Jeroen A Van Bokhoven and Carlo Lamberti. *X-ray absorption and X-ray emission spectroscopy: theory and applications*, volume 1. John Wiley & Sons, 2016.
- [433] C Lamberti, S Bordiga, F Bonino, C Prestipino, G Berlier, L Capello, F D’Acapito, FX Llabrés i Xamena, and A Zecchina. Determination of the oxidation and coordination state of copper on different cu-based catalysts by xanes spectroscopy in situ or in operando conditions. *Physical Chemistry Chemical Physics*, 5(20):4502–4509, 2003.
- [434] GR Shulman, Y Yafet, P Eisenberger, and WE Blumberg. Observations and interpretation of x-ray absorption edges in iron compounds and proteins. *Proceedings of the National Academy of Sciences*, 73(5):1384–1388, 1976.
- [435] James E Hahn, Robert A Scott, Keith O Hodgson, Sebastian Doniach, Sylvia R Desjardins, and Edward I Solomon. Observation of an electric quadrupole transition in the x-ray absorption spectrum of a cu (ii) complex. *Chemical Physics Letters*, 88(6):595–598, 1982.
- [436] Peter NR Vennestrøm, Ton VW Janssens, Arkady Kustov, Marie Grill, Anna Puig-Molina, Lars F Lundegaard, Ramchandra R Tiruvalam, Patricia Concepción, and Avelino Corma. Influence of lattice stability on hydrothermal deactivation of cu-zsm-5 and cu-im-5 zeolites for selective catalytic reduction of nox by nh<sub>3</sub>. *Journal of Catalysis*, 309:477–490, 2014.
- [437] Di-Jia Liu and Heinz J Robota. On the mechanism of no selective catalytic reduction by hydrocarbons over cu-zsm-5 via x-ray absorption spectroscopic study. *The Journal of Physical Chemistry B*, 103(14):2755–2765, 1999.
- [438] Di-Jia Liu and Heinz J Robota. In situ xanes characterization of the cu oxidation state in cu-zsm-5 during no decomposition catalysis. *Catalysis letters*, 21(3-4):291–301, 1993.
- [439] Yasushige Kuroda, Yuzo Yoshikawa, Shin-ichi Konno, Hideaki Hamano, Hironobu Maeda, Ryotaro Kumashiro, and Mahiko Nagao. Specific feature of copper ion-exchanged mordenite for dinitrogen adsorption at room temperature. *The Journal of Physical Chemistry*, 99(26):10621–10628, 1995.

- [440] C Lamberti, G Spoto, D Scarano, C Pazé, M Salvalaggio, S Bordiga, A Zecchina, G Turnes Palomino, and F D’Acapito. Cui-y and cuii-y zeolites: a xanes, exafs and visible-nir study. *Chemical physics letters*, 269(5-6):500–508, 1997.
- [441] Karina Mathisen, Michael Stockenhuber, and David G Nicholson. In situ xas and ir studies on cu: Sapo-5 and cu: Sapo-11: the contributory role of monomeric linear copper (i) species in the selective catalytic reduction of no x by propene. *Physical Chemistry Chemical Physics*, 11(26):5476–5488, 2009.
- [442] Arild Moen, David G Nicholson, and Magnus Rønning. Studies on the pre-edge region of the x-ray absorption spectra of copper (i) oxide and the diamminecopper (i) ion. *Journal of the Chemical Society, Faraday Transactions*, 91(18):3189–3194, 1995.
- [443] Richard Car and Mark Parrinello. Unified approach for molecular dynamics and density-functional theory. *Physical review letters*, 55(22):2471, 1985.
- [444] John P Perdew, Kieron Burke, and Matthias Ernzerhof. Generalized gradient approximation made simple. *Physical review letters*, 77(18):3865, 1996.
- [445] Stefan Grimme. Semiempirical gga-type density functional constructed with a long-range dispersion correction. *J. Comp. Chem.*, 27(15):1787–1799, 2006.
- [446] Graeme Henkelman, Blas P Uberuaga, and Hannes Jónsson. A climbing image nudged elastic band method for finding saddle points and minimum energy paths. *The Journal of chemical physics*, 113(22):9901–9904, 2000.
- [447] M. Parrinello M. Iannuzzi, A. Laio. Efficient exploration of reactive potential energy surfaces using car-parrinello molecular dynamics. *Physical review letters*, 90:238302, 2003.
- [448] M. Parrinello A. Barducci, M. Bonomi. Metadynamics. *Wiley Interdiscip. Rev. Comput. Mol. Sci.*, 1(5):826–843, 2011.
- [449] J. Sauer M. Rybicki. Acidity of two-dimensional zeolites. *Phys. Chem. Chem. Phys.*, 17:27873–27882, 2015.
- [450] Jonatan D. Albarracin-Caballero, Ishant Khurana, John R. Di Iorio, Arthur J. Shih, Joel E. Schmidt, Michiel Dusselier, Mark E. Davis, Aleksey Yezerets, Jeffrey T. Miller, Fabio H. Ribeiro, and Rajamani Gounder. Structural and kinetic changes to small-pore cu-zeolites after hydrothermal aging treatments and selective catalytic reduction of nox with ammonia. *Reaction Chemistry and Engineering*, 2:168–179, 2017.
- [451] Andrew J Jones and Enrique Iglesia. Kinetic, spectroscopic, and theoretical assessment of associative and dissociative methanol dehydration routes in zeolites. *Angewandte Chemie International Edition*, 53(45):12177–12181, 2014.
- [452] Min Bum Park, Sang Hyun Ahn, Christopher P. Nicholas, Gregory J. Lewis, and Suk Bong Hong. Charge density mismatch synthesis of zeolite beta in the presence of tetraethylammonium, tetramethylammonium, and sodium ions: Influence of tetraethylammonium decomposition. *Microporous and Mesoporous Materials*, 240:159–168, 2017.

- [453] Colin S. Cundy and Paul A. Cox. The hydrothermal synthesis of zeolites: Precursors, intermediates and reaction mechanism. *Microporous and Mesoporous Materials*, 82(1–2):1–78, 2005.
- [454] Arian Ghorbanpour, Jeffrey D Rimer, and Lars C Grabow. Computational assessment of the dominant factors governing the mechanism of methanol dehydration over h-zsm-5 with heterogeneous aluminum distribution. *ACS Catalysis*, 6(4):2287–2298, 2016.
- [455] Thomas Bligaard, R. Morris Bullock, Charles T. Campbell, Jingguang G. Chen, Bruce C. Gates, Raymond J. Gorte, Christopher W. Jones, William D. Jones, John R. Kitchin, and Susannah L. Scott. Toward benchmarking in catalysis science: Best practices, challenges, and opportunities. *ACS Catalysis*, 6(4):2590–2602, 2016.
- [456] Gabriele Mirth, Johannes A. Lercher, Michael W. Anderson, and Jacek Klinowski. Adsorption complexes of methanol on zeolite zsm-5. *Journal of the Chemical Society, Faraday Transactions*, 86(17):3039–3044, 1990.
- [457] Z. Li, M. T. Navarro, J. Martinez-Triguero, J. Yu, and A. Corma. Synthesis of nano-ssz-13 and its application in the reaction of methanol to olefins. *Catalysis Science and Technology*, 6(15):5856–5863, 2016.
- [458] James F Haw, Weiguo Song, David M Marcus, and John B Nicholas. The mechanism of methanol to hydrocarbon catalysis. *Accounts of chemical research*, 36(5):317–326, 2003.
- [459] Xiaochun Zhu, Jan P Hofmann, Brahim Mezari, Nikolay Kosinov, Leilei Wu, Qingyun Qian, Bert M Weckhuysen, Shunsuke Asahina, Javier Ruiz-Martinez, and Emiel JM Hensen. Trimodal porous hierarchical ssz-13 zeolite with improved catalytic performance in the methanol-to-olefins reaction. *ACS catalysis*, 6(4):2163–2177, 2016.
- [460] Andrew Hwang, Manjesh Kumar, Jeffrey D Rimer, and Aditya Bhan. Implications of methanol disproportionation on catalyst lifetime for methanol-to-olefins conversion by hssz-13. *Journal of Catalysis*, 346:154–160, 2017.
- [461] Sebastian Muller, Yue Liu, Felix M Kirchberger, Markus Tonigold, Maricruz Sanchez-Sanchez, and Johannes A Lercher. Hydrogen transfer pathways during zeolite catalyzed methanol conversion to hydrocarbons. *Journal of the American Chemical Society*, 138(49):15994–16003, 2016.
- [462] Yue Liu, Sebastian Muller, Daniel Berger, Jelena Jelic, Karsten Reuter, Markus Tonigold, Maricruz Sanchez-Sanchez, and Johannes A Lercher. Formation mechanism of the first carbon–carbon bond and the first olefin in the methanol conversion into hydrocarbons. *Angewandte Chemie International Edition*, 128(19):5817–5820, 2016.
- [463] Weiguo Song, David M Marcus, Hui Fu, Justin O Ehresmann, and James F Haw. An oft-studied reaction that may never have been: Direct catalytic conversion of methanol or dimethyl ether to hydrocarbons on the solid acids hzsm-5 or hsapo-34. *Journal of the American Chemical Society*, 124(15):3844–3845, 2002.



- [464] Yan Zhu, Zile Hua, Jian Zhou, Lijun Wang, Jinjin Zhao, Yun Gong, Wei Wu, Meiling Ruan, and Jianlin Shi. Hierarchical mesoporous zeolites: Direct self-assembly synthesis in a conventional surfactant solution by kinetic control over the zeolite seed formation. *Chemistry- A European Journal*, 17(51):14618–14627, 2011.
- [465] Viktor J. Cybulskis, James W. Harris, Yury Zvinevich, Fabio H. Ribeiro, and Rajamani Gounder. A transmission infrared cell design for temperature-controlled adsorption and reactivity studies on heterogeneous catalysts. *Review of Scientific Instruments*, 87(10):103101, 2016.
- [466] James W. Harris, Michael J. Cordon, John R. Di Iorio, Juan Carlos Vega-Vila, Fabio H. Ribeiro, and Rajamani Gounder. Titration and quantification of open and closed lewis acid sites in sn-beta zeolites that catalyze glucose isomerization. *Journal of Catalysis*, 335:141–154, 2016.
- [467] Mark A Deimund, Luke Harrison, Jonathan D Lunn, Yu Liu, Andrzej Malek, Ramzy Shayib, and Mark E Davis. Effect of heteroatom concentration in ssz-13 on the methanol-to-olefins reaction. *ACS Catalysis*, 6(2):542–550, 2015.
- [468] Pedro Salvador and W. Kladnig. Surface reactivity of zeolites type h-y and na-y with methanol. *Journal of the Chemical Society, Faraday Transactions 1: Physical Chemistry in Condensed Phases*, 73(0):1153–1168, 1977.
- [469] Hiroshi Yamazaki, Hisashi Shima, Hiroyuki Imai, Toshiyuki Yokoi, Takashi Tatsumi, and Junko N. Kondo. Evidence for a “carbene-like” intermediate during the reaction of methoxy species with light alkenes on h-zsm-5. *Angewandte Chemie International Edition*, 50(8):1853–1856, 2011.
- [470] Wei Wang, Andreas Buchholz, Michael Seiler, and Michael Hunger. Evidence for an initiation of the methanol-to-olefin process by reactive surface methoxy groups on acidic zeolite catalysts. *Journal of the American Chemical Society*, 125(49):15260–15267, 2003.
- [471] Alexander J. O’Malley, Stewart F. Parker, Arunabhiram Chutia, Matthew R. Farrow, Ian P. Silverwood, Victoria Garcia-Sakai, and C. Richard A. Catlow. Room temperature methoxylation in zeolites: insight into a key step of the methanol-to-hydrocarbons process. *Chemical Communications*, 52(14):2897–2900, 2016.
- [472] Rajamani Krishna and Jasper M van Baten. Hydrogen bonding effects in adsorption of water- alcohol mixtures in zeolites and the consequences for the characteristics of the maxwell- stefan diffusivities. *Langmuir*, 26(13):10854–10867, 2010.
- [473] C Herrmann, J Haas, and F Fetting. Effect of the crystal size on the activity of zsm-5 catalysts in various reactions. *Applied Catalysis*, 35(2):299–310, 1987.
- [474] PB Weisz and CD Prater. Interpretation of measurements in experimental catalysis. *Advances in Catalysis*, 6:143–196, 1954.
- [475] Joseph F. DeWilde, Hsu Chiang, Daniel A. Hickman, Christopher R. Ho, and Aditya Bhan. Kinetics and mechanism of ethanol dehydration on  $\gamma$ -al<sub>2</sub>o<sub>3</sub>: The critical role of dimer inhibition. *ACS Catalysis*, 3(4):798–807, 2013.

- [476] Jonatan D. Albarracin-Caballero, Ishant Khurana, John R. Di Iorio, Arthur J. Shih, Joel E. Schmidt, Michiel Dusselier, Mark E. Davis, Aleksey Yezerets, Jeffrey T. Miller, Fabio H. Ribeiro, and Rajamani Gounder. Structural and kinetic changes to small-pore cu-zeolites after hydrothermal aging treatments and selective catalytic reduction of nox with ammonia. *Reaction Chemistry & Engineering*, 2017.
- [477] Steven Nystrom, Alexander Hoffman, and David Hibbitts. Tuning brønsted acid strength by altering site proximity in cha framework zeolites. *ACS Catalysis*, 8(9):7842–7860, 2018.
- [478] Prashant Deshlahra, Robert T Carr, and Enrique Iglesia. Ionic and covalent stabilization of intermediates and transition states in catalysis by solid acids. *Journal of the American Chemical Society*, 136(43):15229–15247, 2014.
- [479] William Knaeble, Robert T Carr, and Enrique Iglesia. Mechanistic interpretation of the effects of acid strength on alkane isomerization turnover rates and selectivity. *Journal of Catalysis*, 319:283–296, 2014.
- [480] Zhenchao Zhao, Youdong Xing, Shihan Li, Xiangju Meng, Feng-shou Xiao, Robert McGuire, Andrei-Nicolae Parvulescu, Ulrich Muller, and Weiping Zhang. Mapping al distributions in ssz-13 zeolites from  $^{23}\text{Na}$  solid-state nmr spectroscopy and dft calculations. *The Journal of Physical Chemistry C*, 122(18):9973–9979, 2018.
- [481] Ya Guo, Tianjun Sun, Yiming Gu, Xiaowei Liu, Quanli Ke, Xiaoli Wei, and Shudong Wang. Rational synthesis of chabazite (cha) zeolites with controlled si/al ratio and their  $\text{CO}_2/\text{CH}_4/\text{N}_2$  adsorptive separation performances. *Chemistry – An Asian Journal*, 2018.
- [482] Angeles Pulido, Petr Nachtigall, Arnost Zukal, Irene Dominguez, and Jiri Cejka. Adsorption of  $\text{CO}_2$  on sodium-exchanged ferrierites: The bridged  $\text{CO}_2$  complexes formed between two extraframework cations. *The Journal of Physical Chemistry C*, 113(7):2928–2935, 2009.
- [483] Chi-Ta Yang, Amber Janda, Alexis T. Bell, and Li-Chiang Lin. Atomistic investigations of the effects of si/al ratio and al distribution on the adsorption selectivity of n-alkanes in brønsted-acid zeolites. *The Journal of Physical Chemistry C*, 122(17):9397–9410, 2018.
- [484] Eva M. Gallego, Chengeng Li, Cecilia Paris, Nuria Martin, Joaquín Martinez-Triguero, Mercedes Boronat, Manuel Moliner, and Avelino Corma. Making nanosized cha zeolites with controlled al distribution for optimizing methanol-to-olefin performance. *Chemistry – A European Journal*, 24(55):14631–14635, 2018.
- [485] Unni Olsbye, Stian Svelle, Morten Bjorgen, Pablo Beato, Ton V. W. Janssens, Finn Joensen, Silvia Bordiga, and Karl Petter Lillerud. Conversion of methanol to hydrocarbons: How zeolite cavity and pore size controls product selectivity. *Angewandte Chemie International Edition*, 51(24):5810–5831, 2012.
- [486] Ivar M Dahl and Stein Kolboe. On the reaction mechanism for hydrocarbon formation from methanol over sapo-34: I. isotopic labeling studies of the co-reaction of ethene and methanol. *Journal of Catalysis*, 149(2):458–464, 1994.

- [487] Ivar M Dahl and Stein Kolboe. On the reaction mechanism for hydrocarbon formation from methanol over sapo-34: 2. isotopic labeling studies of the co-reaction of propene and methanol. *Journal of Catalysis*, 161(1):304–309, 1996.
- [488] De Chen, Kjell Moljord, Terje Fuglerud, and Anders Holmen. The effect of crystal size of sapo-34 on the selectivity and deactivation of the mto reaction. *Microporous and Mesoporous Materials*, 29(1-2):191–203, 1999.
- [489] James Song, Yilin Wang, Eric D. Walter, Nancy M. Washton, Donghai Mei, Libor Kovarik, Mark H. Engelhard, Sebastian Proding, Yong Wang, Charles H. F. Peden, and Feng Gao. Toward rational design of cu/ssz-13 selective catalytic reduction catalysts: Implications from atomic-level understanding of hydrothermal stability. *ACS Catalysis*, 7(12):8214–8227, 2017.
- [490] A. Martini, E. Borfecchia, K. A. Lomachenko, I. A. Pankin, C. Negri, G. Berlier, P. Beato, H. Falsig, S. Bordiga, and C. Lamberti. Composition-driven copper speciation and reducibility in cu-cha zeolite catalysts: a multivariate xas/ftir approach to complexity. *Chemical Science*, 8(10):6836–6851, 2017.
- [491] Karthik Narsimhan, Kenta Iyoki, Kimberly Dinh, and Yuriy Roman-Leshkov. Catalytic oxidation of methane into methanol over copper-exchanged zeolites with oxygen at low temperature. *ACS Central Science*, 2(6):424–429, 2016.
- [492] Elisa Borfecchia, Dimitrios K. Pappas, Michael Dyballa, Kirill A. Lomachenko, Chiara Negri, Matteo Signorile, and Gloria Berlier. Evolution of active sites during selective oxidation of methane to methanol over cu-cha and cu-mor zeolites as monitored by operando xas. *Catalysis Today*, 2018.
- [493] Max L. Bols, Simon D. Hallaert, Benjamin E. R. Snyder, Julien Devos, Dieter Plessers, Hannah M. Rhoda, Michiel Dusselier, Robert A. Schoonheydt, Kristine Pierloot, Edward I. Solomon, and Bert F. Sels. Spectroscopic identification of the  $\alpha$ -fe/ $\alpha$ -o active site in fe-cha zeolite for the low-temperature activation of the methane c–h bond. *Journal of the American Chemical Society*, 140(38):12021–12032, 2018.
- [494] Sichi Li, Yujia Wang, Tong Wu, and William F. Schneider. First-principles analysis of site- and condition-dependent fe speciation in ssz-13 and implications for catalyst optimization. *ACS Catalysis*, pages 10119–10130, 2018.
- [495] R A Grieger and CA Eckert. Solvent effects on the activation volume of a diels-alder reaction. *Transactions of the Faraday Society*, 66:2579–2584, 1970.
- [496] Merdith G Evans and Michael Polanyi. Some applications of the transition state method to the calculation of reaction velocities, especially in solution. *Transactions of the Faraday Society*, 31:875–894, 1935.
- [497] R Van Eldik, T Asano, and WJ Le Noble. Activation and reaction volumes in solution. 2. *Chemical Reviews*, 89(3):549–688, 1989.
- [498] Rostam J Madon and Enrique Iglesia. Catalytic reaction rates in thermodynamically non-ideal systems. *Journal of Molecular Catalysis A: Chemical*, 163(1-2):189–204, 2000.

- [499] Jianwei Liu, David Hibbitts, and Enrique Iglesia. Dense co adlayers as enablers of co hydrogenation turnovers on ru surfaces. *Journal of the American Chemical Society*, 139(34):11789–11802, 2017.
- [500] Terrell L. Hill. Theory of physical adsorption. *Advances in Catalysis*, 4:211–258, 1952.
- [501] AL Myers and PA Monson. Adsorption in porous materials at high pressure: theory and experiment. *Langmuir*, 18(26):10261–10273, 2002.
- [502] PA Jacobs, Edith M Flanigen, JC Jansen, and Herman van Bekkum. *Introduction to zeolite science and practice*, volume 137. Elsevier, 2001.
- [503] Josiah Willard Gibbs. On the equilibrium of heterogeneous substances. *Transactions of the Connecticut Academy of Arts and Sciences*, 3:108–524, 1879.
- [504] Richard Maling Barrer and JA Davies. Sorption in decationated zeolites. i. gases in hydrogen-chabazite. *Proc. R. Soc. Lond. A*, 320(1542):289–308, 1970.
- [505] CA Eckert and M Boudart. On the use of fugacities in gas kinetics. *Chem. Eng. Sci.*, 18(2):144–147, 1963.
- [506] JM Prausnitz. Fugacities in high-pressure equilibria and in rate processes. *AIChE Journal*, 5(1):3–9, 1959.
- [507] Lovat V. C. Rees and Dongmin Shen. Adsorption of gases in zeolite molecular sieves. *Studies in Surface Science and Catalysis*, 137:579–631, 2001.
- [508] Ding-Yu Peng and Donald B Robinson. A new two-constant equation of state. *Industrial & Engineering Chemistry Fundamentals*, 15(1):59–64, 1976.
- [509] Schohn L Shannon and James G Goodwin Jr. Characterization of catalytic surfaces by isotopic-transient kinetics during steady-state reaction. *Chemical reviews*, 95(3):677–695, 1995.
- [510] Cristian Ledesma, Jia Yang, De Chen, and Anders Holmen. Recent approaches in mechanistic and kinetic studies of catalytic reactions using ssitka technique. *ACS Catalysis*, 4(12):4527–4547, 2014.
- [511] Takayuki Inoue, Masaya Itakura, Hery Jon, Yasunori Oumi, Atsushi Takahashi, Tadahiro Fujitani, and Tsuneji Sano. Synthesis of lev zeolite by interzeolite conversion method and its catalytic performance in ethanol to olefins reaction. *Microporous and Mesoporous Materials*, 122(1):149–154, 2009.
- [512] A.B. Barnes, G. De Paëpe, P.C.A. van der Wel, K.-N. Hu, C.-G. Joo, V.S. Bajaj, M.L. Mak-Jurkauskas, J.R. Sirigiri, J. Herzfeld, R.J. Temkin, and R.G. Griffin. High-Field Dynamic Nuclear Polarization for Solid and Solution Biological NMR. *Applied magnetic resonance*, 34(3-4):237–263, 2008.
- [513] Aaron J. Rossini, Alexandre Zagdoun, Moreno Lelli, Anne Lesage, Christophe Copéret, and Lyndon Emsley. Dynamic Nuclear Polarization Surface Enhanced NMR Spectroscopy. *Accounts of Chemical Research*, 46(9):1942–1951, 2013.
- [514] T. V. Can, Q. Z. Ni, and R. G. Griffin. Mechanisms of dynamic nuclear polarization in insulating solids. *Journal of Magnetic Resonance*, 253:23–35, 2015.

- [515] Takeshi Kobayashi, Olivier Lafon, Aany S. Lilly Thankamony, Igor I. Slowing, Kapil Kandel, Diego Carnevale, Veronika Vitzthum, Herve Vezin, Jean-Paul Amoureux, Geoffrey Bodenhausen, and Marek Pruski. Analysis of sensitivity enhancement by dynamic nuclear polarization in solid-state NMR: a case study of functionalized mesoporous materials. *Physical Chemistry Chemical Physics*, 15(15):5553–5562, 2013.
- [516] Olivier Lafon, Melanie Rosay, Fabien Aussenac, Xingyu Lu, Julien Trebosc, Odile Cristini, Christophe Kinowski, Nadia Touati, Herve Vezin, and Jean-Paul Amoureux. Beyond the Silica Surface by Direct Silicon-29 Dynamic Nuclear Polarization. *Angewandte Chemie International Edition*, 50(36):8367–8370, 2011.
- [517] C. A. Fyfe, K. C. Wong-Moon, Y. Huang, and H. Grondey. Inept experiments in solid-state nmr. *Journal of the American Chemical Society*, 117(41):10397–10398, 1995.
- [518] J. P. Amoureux, J. Trebosc, J. Wiench, and M. Pruski. Hmqc and refocused-inept experiments involving half-integer quadrupolar nuclei in solids. *Journal of Magnetic Resonance*, 184(1):1–14, 2007.
- [519] Lucio Frydman and John S. Harwood. Isotropic spectra of half-integer quadrupolar spins from bidimensional magic-angle spinning nmr. *Journal of the American Chemical Society*, 117(19):5367–5368, 1995.
- [520] Hubert Koller, Soumya Senapati, Jinjun Ren, Tobias Uesbeck, Vassilios Siozios, Michael Hunger, and Raul F. Lobo. Post-synthesis conversion of borosilicate zeolite beta to an aluminosilicate with isolated acid sites: A quantitative distance analysis by solid-state nmr. *The Journal of Physical Chemistry C*, 120(18):9811–9820, 2016.
- [521] Marc Baldus, David Rovnyak, and Robert G. Griffin. Radio-frequency-mediated dipolar recoupling among half-integer quadrupolar spins. *The Journal of Chemical Physics*, 112(13):5902–5909, 2000.
- [522] Q. Wang, B. Hu, O. Lafon, J. Trebosc, F. Deng, and J. P. Amoureux. Double-quantum homonuclear nmr correlation spectroscopy of quadrupolar nuclei subjected to magic-angle spinning and high magnetic field. *Journal of Magnetic Resonance*, 200(2):251–260, 2009.
- [523] Charlotte Martineau-Corcus, Jiri Dedecek, and Francis Taulelle. 27al-27al double-quantum single-quantum mas nmr: Applications to the structural characterization of microporous materials. *Solid State Nuclear Magnetic Resonance*, 84:65–72, 2017.
- [524] S. I. Zones, R. A. Van Nordstrand, D. S. Santilli, D. M. Wilson, L. Yuen, and L. D. Scampavia. Sequence of high silica zeolites found during synthesis experiments in the presence of a quaternary adamantammonium cation. *Studies in Surface Science and Catalysis*, 49:299–309, 1989.
- [525] N. E. Jacobsen. *Two-Dimensional NMR Spectroscopy: HETCOR, COSY, and TOCSY*. NMR Spectroscopy Explained: Simplified Theory, Applications and Examples for Organic Chemistry and Structural Biology. John Wiley & Sons, Inc., 2007.
- [526] Terry Gullion. *Rotational-echo, double-resonance NMR*. Springer, 2008.

- [527] Terry Gullion. Measurement of dipolar interactions between spin-12 and quadrupolar nuclei by rotational-echo, adiabatic-passage, double-resonance nmr. *Chemical Physics Letters*, 246(3):325–330, 1995.
- [528] B Notari. Titanium silicalites. *Catalysis Today*, 18(2):163–172, 1993.
- [529] Avelino Corma, Laszlo T Nemeth, Michael Renz, and Susana Valencia. Sn-zeolite beta as a heterogeneous chemoselective catalyst for baeyer–villiger oxidations. *Nature*, 412(6845):423, 2001.
- [530] JC Van der Waal, PJ Kunkeler, K Tan, and H Van Bekkum. Zeolite titanium beta: a selective catalyst for the gas-phase meerwein–ponndorf–verley, and oppenauer reactions. *Journal of Catalysis*, 173(1):74–83, 1998.
- [531] Avelino Corma and Hermenegildo Garcia. Lewis acids: from conventional homogeneous to green homogeneous and heterogeneous catalysis. *Chemical Reviews*, 103(11):4307–4366, 2003.
- [532] Jan C van der Waal, Keqin Tan, and Herman van Bekkum. Zeolite titanium beta: a selective and water resistant catalyst in meerwein–ponndorf–verley–oppenauer reactions. *Catalysis letters*, 41(1-2):63–67, 1996.
- [533] Rajamani Gounder. Hydrophobic microporous and mesoporous oxides as brønsted and lewis acid catalysts for biomass conversion in liquid water. *Catalysis Science & Technology*, 4(9):2877–2886, 2014.
- [534] Manuel Moliner, Yuriy Román-Leshkov, and Mark E Davis. Tin-containing zeolites are highly active catalysts for the isomerization of glucose in water. *Proceedings of the National Academy of Sciences*, 107(14):6164–6168, 2010.
- [535] Stavros Caratzoulas, Mark E Davis, Raymond J Gorte, Rajamani Gounder, Raul F Lobo, Vladimiro Nikolakis, Stanley I Sandler, Mark A Snyder, Michael Tsapatsis, and Dionisios G Vlachos. Challenges of and insights into acid-catalyzed transformations of sugars. *The Journal of Physical Chemistry C*, 118(40):22815–22833, 2014.
- [536] Jennifer D Lewis, Stijn Van de Vyver, Anthony J Crisci, William R Gunther, Vladimir K Michaelis, Robert G Griffin, and Yuriy Román-Leshkov. A continuous flow strategy for the coupled transfer hydrogenation and etherification of 5-(hydroxymethyl) furfural using lewis acid zeolites. *ChemSusChem*, 7(8):2255–2265, 2014.
- [537] Silvia Bordiga, Francesca Bonino, Alessandro Damin, and Carlo Lamberti. Reactivity of ti (iv) species hosted in ts-1 towards h<sub>2</sub> o<sub>2</sub>–h<sub>2</sub> o solutions investigated by ab initio cluster and periodic approaches combined with experimental xanes and exafs data: a review and new highlights. *Physical Chemistry Chemical Physics*, 9(35):4854–4878, 2007.
- [538] Susana Valencia Valencia and Avelino Corma Canos. Stannosilicate molecular sieves, 1999.
- [539] Chun-Chih Chang, Hong Je Cho, Zhuopeng Wang, Xuanting Wang, and Wei Fan. Fluoride-free synthesis of a sn-bea catalyst by dry gel conversion. *Green Chemistry*, 17(5):2943–2951, 2015.

- [540] Pierre Y Dapsens, Cecilia Mondelli, Jakub Jagielski, Roland Hauert, and Javier Pérez-Ramírez. Hierarchical sn-mfi zeolites prepared by facile top-down methods for sugar isomerisation. *Catalysis science & technology*, 4(8):2302–2311, 2014.
- [541] Pierre Y Dapsens, Cecilia Mondelli, and Javier Pérez-Ramírez. Design of lewis-acid centres in zeolitic matrices for the conversion of renewables. *Chemical Society Reviews*, 44(20):7025–7043, 2015.
- [542] Pei Li, Guanqi Liu, Haihong Wu, Yueming Liu, Jin-gang Jiang, and Peng Wu. Postsynthesis and selective oxidation properties of nanosized sn-beta zeolite. *The Journal of Physical Chemistry C*, 115(9):3663–3670, 2011.
- [543] Jan Dijkmans, Dries Gabriels, Michiel Dusselier, Filip de Clippel, Pieter Vanelderen, Kristof Houthoofd, Annelies Malfliet, Yiannis Pontikes, and Bert F Sels. Productive sugar isomerization with highly active sn in dealuminated  $\beta$  zeolites. *Green Chemistry*, 15(10):2777–2785, 2013.
- [544] Xiaoying Ouyang, Son-Jong Hwang, Dan Xie, Thomas Rea, Stacey I Zones, and Alexander Katz. Heteroatom-substituted delaminated zeolites as solid lewis acid catalysts. *ACS Catalysis*, 5(5):3108–3119, 2015.
- [545] William NP van der Graaff, Guanna Li, Brahim Mezari, Evgeny A Pidko, and Emiel JM Hensen. Synthesis of sn-beta with exclusive and high framework sn content. *ChemCatChem*, 7(7):1152–1160, 2015.
- [546] Jan Dijkmans, Jan Demol, Kristof Houthoofd, Shuigen Huang, Yiannis Pontikes, and Bert Sels. Post-synthesis sn $\beta$ : an exploration of synthesis parameters and catalysis. *Journal of Catalysis*, 330:545–557, 2015.
- [547] Patrick Wolf, Ceri Hammond, Sabrina Conrad, and Ive Hermans. Post-synthetic preparation of sn-, ti-and zr-beta: a facile route to water tolerant, highly active lewis acidic zeolites. *Dalton Transactions*, 43(11):4514–4519, 2014.
- [548] Bo Tang, Weili Dai, Guangjun Wu, Naijia Guan, Landong Li, and Michael Hunger. Improved postsynthesis strategy to sn-beta zeolites as lewis acid catalysts for the ring-opening hydration of epoxides. *ACS Catalysis*, 4(8):2801–2810, 2014.
- [549] Ceri Hammond, Daniele Padovan, Abbas Al-Nayili, Peter P Wells, Emma K Gibson, and Nikolaos Dimitratos. Identification of active and spectator sn sites in sn- $\beta$  following solid-state stannation, and consequences for lewis acid catalysis. *ChemCatChem*, 7(20):3322–3331, 2015.
- [550] Mercedes Boronat, Patricia Concepción, Avelino Corma, Michael Renz, and Susana Valencia. Determination of the catalytically active oxidation lewis acid sites in sn-beta zeolites, and their optimisation by the combination of theoretical and experimental studies. *Journal of Catalysis*, 234(1):111–118, 2005.
- [551] Ricardo Bermejo-Deval, Marat Orazov, Rajamani Gounder, Son-Jong Hwang, and Mark E Davis. Active sites in sn-beta for glucose isomerization to fructose and epimerization to mannose. *ACS Catalysis*, 4(7):2288–2297, 2014.

- [552] Christian M Osmundsen, Martin Spangsberg Holm, Søren Dahl, and Esben Taarning. Tin-containing silicates: structure–activity relations. *Proc. R. Soc. A*, 468(2143):2000–2016, 2012.
- [553] Bhakti S Kulkarni, Sailaja Krishnamurty, and Sourav Pal. Probing lewis acidity and reactivity of sn-and ti-beta zeolite using industrially important moieties: A periodic density functional study. *Journal of Molecular Catalysis A: Chemical*, 329(1-2):36–43, 2010.
- [554] Ricardo Bermejo-Deval, Rajeev S Assary, Eranda Nikolla, Manuel Moliner, Yuriy Román-Leshkov, Son-Jong Hwang, Arna Palsdottir, Dorothy Silverman, Raul F Lobo, Larry A Curtiss, et al. Metalloenzyme-like catalyzed isomerizations of sugars by lewis acid zeolites. *Proceedings of the National Academy of Sciences*, 109(25):9727–9732, 2012.
- [555] Neeraj Rai, Stavros Caratzoulas, and Dionisios G Vlachos. Role of silanol group in sn-beta zeolite for glucose isomerization and epimerization reactions. *ACS catalysis*, 3(10):2294–2298, 2013.
- [556] Yi-Pei Li, Martin Head-Gordon, and Alexis T Bell. Analysis of the reaction mechanism and catalytic activity of metal-substituted beta zeolite for the isomerization of glucose to fructose. *Acs Catalysis*, 4(5):1537–1545, 2014.
- [557] Li Li, Christophe Stroobants, Kaifeng Lin, Pierre A Jacobs, Bert F Sels, and Paolo P Pescarmona. Selective conversion of trioses to lactates over lewis acid heterogeneous catalysts. *Green chemistry*, 13(5):1175–1181, 2011.
- [558] E Escalona Platero, M Peñarroya Mentrut, C Otero Areán, and A Zecchina. Ftir studies on the acidity of sulfated zirconia prepared by thermolysis of zirconium sulfate. *Journal of Catalysis*, 162(2):268–276, 1996.
- [559] Gemma Turnes Palomino, Juan José Cuat Pascual, Montserrat Rodriguez Delgado, José Bernardo Parra, and Carlos Otero Areán. Ft-ir studies on the acidity of gallium-substituted mesoporous mcm-41 silica. *Materials chemistry and physics*, 85(1):145–150, 2004.
- [560] Michael R Basila, Theodore R Kantner, and Kee H Rhee. The nature of the acidic sites on a silica-alumina. characterization by infrared spectroscopic studies of trimethylamine and pyridine chemisorption1. *The Journal of Physical Chemistry*, 68(11):3197–3207, 1964.
- [561] Hong Je Cho, Paul Dornath, and Wei Fan. Synthesis of hierarchical sn-mfi as lewis acid catalysts for isomerization of cellulosic sugars. *Acs Catalysis*, 4(6):2029–2037, 2014.
- [562] Simon R Bare, Shelly D Kelly, Wharton Sinkler, John J Low, Frank S Modica, Susana Valencia, Avelino Corma, and Laszlo T Nemeth. Uniform catalytic site in sn- $\beta$ -zeolite determined using x-ray absorption fine structure. *Journal of the American Chemical Society*, 127(37):12924–12932, 2005.
- [563] Pierre Y Dapsens, Cecilia Mondelli, Bright T Kusema, René Verel, and Javier Pérez-Ramírez. A continuous process for glyoxal valorisation using tailored lewis-acid zeolite catalysts. *Green Chemistry*, 16(3):1176–1186, 2014.



- [564] Jan Dijkmans, Michiel Dusselier, Dries Gabriels, Kristof Houthoofd, Pieter CMM Magusin, Shuigen Huang, Yiannis Pontikes, Maarten Trekels, Andre Vantomme, Lars Giebeler, et al. Cooperative catalysis for multistep biomass conversion with sn/al beta zeolite. *ACS Catalysis*, 5(2):928–940, 2015.
- [565] Vitaly L Sushkevich, Alexandre Vimont, Arnaud Travert, and Irina I Ivanova. Spectroscopic evidence for open and closed lewis acid sites in zrbea zeolites. *The Journal of Physical Chemistry C*, 119(31):17633–17639, 2015.
- [566] Charles L Angell and Maria V Howell. Infrared spectroscopic investigation of zeolites and adsorbed molecules. iv. acetonitrile. *The Journal of Physical Chemistry*, 73(8):2551–2554, 1969.
- [567] Putcha Venkateswarlu. The rotation-vibration spectrum of methyl cyanide in the region  $1.6\ \mu$ — $20\ \mu$ . *The Journal of Chemical Physics*, 19(3):293–298, 1951.
- [568] Sounak Roy, Kevin Bakhmutsky, Eyas Mahmoud, Raul F Lobo, and Raymond J Gorte. Probing lewis acid sites in sn-beta zeolite. *Acs Catalysis*, 3(4):573–580, 2013.
- [569] J Barthel and R Deser. Ftir study of ion solvation and ion-pair formation in alkaline and alkaline earth metal salt solutions in acetonitrile. *Journal of solution chemistry*, 23(10):1133–1146, 1994.
- [570] Jochen Penzien, Anuji Abraham, Jeroen A van Bokhoven, Andreas Jentys, Thomas E Müller, Carsten Sievers, and Johannes A Lercher. Generation and characterization of well-defined zn<sup>2+</sup> lewis acid sites in ion exchanged zeolite bea. *The Journal of Physical Chemistry B*, 108(13):4116–4126, 2004.
- [571] B Wichterlova, Z Tvaruzkova, Z Sobalik, and P Sarv. Determination and properties of acid sites in h-ferrierite: A comparison of ferrierite and mfi structures. *Microporous and mesoporous materials*, 24(4-6):223–233, 1998.
- [572] Rafael van Grieken, Carmen Martos, Manuel Sánchez-Sánchez, David P Serano, Juan A Melero, José Iglesias, and Alvar G Cubero. Synthesis of sn-silicalite from hydrothermal conversion of sio<sub>2</sub>–sno<sub>2</sub> xerogels. *Microporous and Mesoporous Materials*, 119(1-3):176–185, 2009.
- [573] NY Chen. Hydrophobic properties of zeolites. *The Journal of Physical Chemistry*, 80(1):60–64, 1976.
- [574] CA Emeis. Determination of integrated molar extinction coefficients for infrared absorption bands of pyridine adsorbed on solid acid catalysts. *Journal of Catalysis*, 141(2):347–354, 1993.
- [575] Rajamani Gounder and Mark E Davis. Monosaccharide and disaccharide isomerization over lewis acid sites in hydrophobic and hydrophilic molecular sieves. *Journal of catalysis*, 308:176–188, 2013.
- [576] Rajamani Gounder and Mark E Davis. Beyond shape selective catalysis with zeolites: Hydrophobic void spaces in zeolites enable catalysis in liquid water. *AIChE Journal*, 59(9):3349–3358, 2013.
- [577] Nawal Kishor Mal and Arumugamangalam V Ramaswamy. Hydroxylation of phenol over sn-silicalite-1 molecular sieve: solvent effects. *Journal of Molecular Catalysis A: Chemical*, 105(3):149–158, 1996.

- [578] Ricardo Bermejo-Deval, Rajamani Gounder, and Mark E Davis. Framework and extraframework tin sites in zeolite beta react glucose differently. *ACS catalysis*, 2(12):2705–2713, 2012.
- [579] Mahesh Bhagwat, Pallavi Shah, and Veda Ramaswamy. Synthesis of nanocrystalline  $\text{SnO}_2$  powder by amorphous citrate route. *Materials Letters*, 57(9-10):1604–1611, 2003.
- [580] N Chiodini, A Paleari, D DiMartino, and G Spinolo.  $\text{SnO}_2$  nanocrystals in  $\text{SiO}_2$ : a wide-band-gap quantum-dot system. *Applied physics letters*, 81(9):1702–1704, 2002.
- [581] Feng Gu, Shu Fen Wang, Chun Feng Song, Meng Kai Lü, Yong Xin Qi, Guang Jun Zhou, Dong Xu, and Duo Rong Yuan. Synthesis and luminescence properties of  $\text{SnO}_2$  nanoparticles. *Chemical Physics Letters*, 372(3-4):451–454, 2003.
- [582] Guangsheng Pang, Siguang Chen, Yuri Koltypin, Arie Zaban, Shouhua Feng, and Aharon Gedanken. Controlling the particle size of calcined  $\text{SnO}_2$  nanocrystals. *Nano Letters*, 1(12):723–726, 2001.
- [583] EP Parry. An infrared study of pyridine adsorbed on acidic solids. characterization of surface acidity. *Journal of Catalysis*, 2(5):371–379, 1963.
- [584] E Selli and L Forni. Comparison between the surface acidity of solid catalysts determined by tpd and ftir analysis of pre-adsorbed pyridine. *Microporous and mesoporous materials*, 31(1-2):129–140, 1999.
- [585] NS Nesterenko, F Thibault-Starzyk, V Montouillout, VV Yushchenko, C Fernandez, J-P Gilson, F Fajula, and II Ivanova. The use of the consecutive adsorption of pyridine bases and carbon monoxide in the ir spectroscopic study of the accessibility of acid sites in microporous/mesoporous materials. *Kinetics and catalysis*, 47(1):40–48, 2006.
- [586] AI Biaglow, DJ Parrillo, and RJ Gorte. Characterization of h, na-y using amine desorption. *Journal of Catalysis*, 144(1):193–201, 1993.
- [587] Son-Jong Hwang, Rajamani Gounder, Yashodhan Bhawe, Marat Orazov, Ricardo Bermejo-Deval, and Mark E Davis. Solid state nmr characterization of sn-beta zeolites that catalyze glucose isomerization and epimerization. *Topics in Catalysis*, 58(7-9):435–440, 2015.
- [588] Sabrina Conrad, René Verel, Ceri Hammond, Patrick Wolf, Florian Göttl, and Ive Hermans. Silica-grafted sniv catalysts in hydrogen-transfer reactions. *ChemCatChem*, 7(20):3270–3278, 2015.
- [589] Nan-Yu Topsøe, Karsten Pedersen, and Eric G Derouane. Infrared and temperature-programmed desorption study of the acidic properties of zsm-5-type zeolites. *Journal of Catalysis*, 70(1):41–52, 1981.
- [590] Timothy D Courtney, Chun-Chih Chang, Raymond J Gorte, Raul F Lobo, Wei Fan, and Vladimiro Nikolakis. Effect of water treatment on sn-bea zeolite: Origin of 960  $\text{cm}^{-1}$  ftir peak. *Microporous and Mesoporous Materials*, 210:69–76, 2015.

- [591] Nafiseh Rajabbeigi, Ana I Torres, Christopher M Lew, Bahman Elyassi, Limin Ren, Zhuopeng Wang, Hong Je Cho, Wei Fan, Prodromos Daoutidis, and Michael Tsapatsis. On the kinetics of the isomerization of glucose to fructose using sn-beta. *Chemical Engineering Science*, 116:235–242, 2014.
- [592] T Blasco, MA Camblor, A Corma, P Esteve, JM Guil, A Martinez, JA Perdigon-Melon, and S Valencia. Direct synthesis and characterization of hydrophobic aluminum-free ti- beta zeolite. *The Journal of Physical Chemistry B*, 102(1):75–88, 1998.
- [593] Jeffrey R Christianson, Stavros Caratzoulas, and Dionisios G Vlachos. Computational insight into the effect of sn-beta na exchange and solvent on glucose isomerization and epimerization. *ACS Catalysis*, 5(9):5256–5263, 2015.
- [594] J Tauc, Radu Grigorovici, and Anina Vancu. Optical properties and electronic structure of amorphous germanium. *physica status solidi (b)*, 15(2):627–637, 1966.
- [595] Jan Tauc. Optical properties and electronic structure of amorphous ge and si. *Materials Research Bulletin*, 3(1):37–46, 1968.
- [596] EA Davis and NFf Mott. Conduction in non-crystalline systems v. conductivity, optical absorption and photoconductivity in amorphous semiconductors. *Philosophical Magazine*, 22(179):0903–0922, 1970.
- [597] J Datka, AM Turek, JM Jehng, and IE Wachs. Acidic properties of supported niobium oxide catalysts: an infrared spectroscopy investigation. *Journal of Catalysis*, 135(1):186–199, 1992.
- [598] Thomas Robert Hughes and Harry M White. A study of the surface structure of decationized y zeolite by quantitative infrared spectroscopy. *The Journal of Physical Chemistry*, 71(7):2192–2201, 1967.
- [599] Jérémie D. A. Pelletier and Jean-Marie Basset. Catalysis by Design: Well-Defined Single-Site Heterogeneous Catalysts. *Accounts of Chemical Research*, 49(4):664–677, 2016.
- [600] Christophe Copéret, Aleix Comas-Vives, Matthew P. Conley, Deven P. Estes, Alexey Fedorov, Victor Mougel, Haruki Nagae, Francisco Núñez-Zarur, and Pavel A. Zhizhko. Surface Organometallic and Coordination Chemistry toward Single-Site Heterogeneous Catalysts: Strategies, Methods, Structures, and Activities. *Chemical Reviews*, 116(2):323–421, 2016.
- [601] Javier Guzman and Bruce C. Gates. Supported molecular catalysts: metal complexes and clusters on oxides and zeolites. *Dalton Transactions*, 0(17):3303–3318, 2003.
- [602] Madelyn M. Stalzer, Massimiliano Delferro, and Tobin J. Marks. Supported Single-Site Organometallic Catalysts for the Synthesis of High-Performance Polyolefins. *Catalysis Letters*, 145(1):3–14, 2015.
- [603] Justin M. Notestein, Enrique Iglesia, and Alexander Katz. Grafted Metal-localixarenes as Single-Site Surface Organometallic Catalysts. *Journal of the American Chemical Society*, 126(50):16478–16486, 2004.

- [604] Staci L. Wegener, Tobin J. Marks, and Peter C. Stair. Design Strategies for the Molecular Level Synthesis of Supported Catalysts. *Accounts of Chemical Research*, 45(2):206–214, 2012.
- [605] Margherita Pucino, Victor Mougél, Roman Schowner, Alexey Fedorov, Michael R. Buchmeiser, and Christophe Copéret. Cationic Silica-Supported N-Heterocyclic Carbene Tungsten Oxo Alkylidene Sites: Highly Active and Stable Catalysts for Olefin Metathesis. *Angewandte Chemie International Edition*, 55(13):4300–4302, 2016.
- [606] Jelena Sepa, C. Lee, R. J. Gorte, David White, E. Kassab, E. M. Evleth, H. Jessri, and M. Allavena. Carbonyl  $^{13}\text{C}$  Shielding Tensors and Heats of Adsorption of Acetone Adsorbed in Silicalite and the 1:1 Stoichiometric Complex in H-ZSM-5. *The Journal of Physical Chemistry*, 100(47):18515–18523, 1996.
- [607] R. J Gorte and D White. Measuring sorption effects at zeolite acid sites: pursuing ideas from W.O. Haag. *Microporous and Mesoporous Materials*, 35–36:447–455, 2000.
- [608] Mark E Davis. New vistas in zeolite and molecular sieve catalysis. *Accounts of chemical research*, 26(3):111–115, 1993.
- [609] Avelino Corma, Marcelo E. Domine, Laszlo Nemeth, and Susana Valencia. Al-Free Sn-Beta Zeolite as a Catalyst for the Selective Reduction of Carbonyl Compounds (Meerwein-Ponndorf-Verley Reaction). *Journal of the American Chemical Society*, 124(13):3194–3195, 2002.
- [610] William R. Gunther, Vladimir K. Michaelis, Marc A. Caporini, Robert G. Griffin, and Yuriy Roman-Leshkov. Dynamic Nuclear Polarization NMR Enables the Analysis of Sn-Beta Zeolite Prepared with Natural Abundance  $^{119}\text{Sn}$  Precursors. *Journal of the American Chemical Society*, 136(17):6219–6222, 2014.
- [611] Patrick Wolf, Maxence Valla, Francisco Núñez Zarur, Aleix Comas-Vives, Aaron J. Rossini, Connor Firth, Hana Kallas, Anne Lesage, Lyndon Emsley, Christophe Copéret, and Ive Hermans. Correlating Synthetic Methods, Morphology, Atomic-Level Structure, and Catalytic Activity of Sn- $\beta$  Catalysts. *ACS Catalysis*, pages 4047–4063, 2016.
- [612] J. M. Newsam, M. M. J. Treacy, W. T. Koetsier, and C. B. De Gruyter. Structural Characterization of Zeolite Beta. *Proceedings of the Royal Society of London A: Mathematical, Physical and Engineering Sciences*, 420(1859):375–405, 1988.
- [613] S. Tolborg, A. Katerinopoulou, D. D. Falcone, I. Sádaba, C. M. Osmundsen, R. J. Davis, E. Taarning, P. Fristrup, and M. S. Holm. Incorporation of tin affects crystallization, morphology, and crystal composition of Sn-Beta. *Journal of Materials Chemistry A*, 2(47):20252–20262, 2014.
- [614] C. M. Zicovich-Wilson and R. Dovesi. Titanium-Containing Zeolites. A Periodic ab Initio Hartree-Fock Characterization. *The Journal of Physical Chemistry B*, 102(8):1411–1417, 1998.
- [615] Alessandro Damin, Silvia Bordiga, Adriano Zecchina, Klaus Doll, and Carlo Lamberti. Ti-chabazite as a model system of Ti(IV) in Ti-zeolites: A periodic approach. *The Journal of Chemical Physics*, 118(22):10183–10194, 2003.

- [616] Lina Han, Cui Wen, Zhiping Wu, Jiancheng Wang, Liping Chang, Gang Feng, Rongbin Zhang, Dejin Kong, and Jianwen Liu. Density functional theory investigations into the structures and acidity properties of Ti-doped SSZ-13 zeolite. *Microporous and Mesoporous Materials*, 237:132–139, 2017.
- [617] C. M. Zicovich-Wilson, R. Dovesi, and A. Corma. Interaction of Ti-Zeolites with Water. A Periodic ab Initio Study. *The Journal of Physical Chemistry B*, 103(6):988–994, 1999.
- [618] Cui Wen, Lu Geng, Lina Han, Jiancheng Wang, Liping Chang, Gang Feng, Dejin Kong, and Jianwen Liu. A comparative first principles study on trivalent ion incorporated SSZ-13 zeolites. *Physical Chemistry Chemical Physics*, 17(44):29586–29596, 2015.
- [619] Brandon C. Bukowski and Jeffrey Greeley. Scaling Relationships for Molecular Adsorption and Dissociation in Lewis Acid Zeolites. *The Journal of Physical Chemistry C*, 120(12):6714–6722, 2016.
- [620] Einar Andre Eilertsen, Silvia Bordiga, Carlo Lamberti, Alessandro Damin, Francesca Bonino, Bjornar Arstad, Stian Svelle, Unni Olsbye, and Karl Petter Lillerud. Synthesis of Titanium Chabazite: A New Shape Selective Oxidation Catalyst with Small Pore Openings and Application in the Production of Methyl Formate from Methanol. *ChemCatChem*, 3(12):1869–1871, 2011.
- [621] Ricardo Bermejo-Deval, Rajeev S. Assary, Eranda Nikolla, Manuel Moliner, Yuriy Román Leshkov, Son-Jong Hwang, Arna Palsdottir, Dorothy Silverman, Raul F. Lobo, Larry A. Curtiss, and Mark E. Davis. Metalloenzyme-like catalyzed isomerizations of sugars by Lewis acid zeolites. *Proceedings of the National Academy of Sciences*, 109(25):9727–9732, 2012.
- [622] Juan Carlos Vega-Vila, James W. Harris, and Rajamani Gounder. Controlled insertion of tin atoms into zeolite framework vacancies and consequences for glucose isomerization catalysis. *Journal of Catalysis*, 344:108–120, 2016.
- [623] Vitaly L. Sushkevich, Irina I. Ivanova, and Alexander V. Yakimov. Revisiting Acidity of SnBEA Catalysts by Combined Application of FTIR Spectroscopy of Different Probe Molecules. *The Journal of Physical Chemistry C*, 121:11437–11447, 2017.
- [624] Tyler R. Josephson, Glen R. Jenness, Dionisios G. Vlachos, and Stavros Caratzoulas. Distribution of open sites in Sn-Beta zeolite. *Microporous and Mesoporous Materials*, 245:45–50, 2017.
- [625] Alexander V. Yakimov, Yury G. Kolyagin, Søren Tolborg, Peter N. R. Vennestrom, and Irina I. Ivanova. Accelerated synthesis of Sn-BEA in fluoride media: effect of H<sub>2</sub>O content in the gel. *New Journal of Chemistry*, 40:4367–4374, 2016.
- [626] Helen Y. Luo, Daniel F. Consoli, William R. Gunther, and Yuriy Román-Leshkov. Investigation of the reaction kinetics of isolated Lewis acid sites in Beta zeolites for the Meerwein-Ponndorf-Verley reduction of methyl levulinate to  $\gamma$ -valerolactone. *Journal of Catalysis*, 320:198–207, 2014.

- [627] Revital Cohen, Christopher R. Graves, SonBinh T. Nguyen, Jan M. L. Martin, and Mark A. Ratner. The Mechanism of Aluminum-Catalyzed Meerwein-Schmidt-Ponndorf-Verley Reduction of Carbonyls to Alcohols. *Journal of the American Chemical Society*, 126(45):14796–14803, 2004.
- [628] Rajeev S. Assary, Larry A. Curtiss, and James A. Dumesic. Exploring Meerwein-Ponndorf-Verley Reduction Chemistry for Biomass Catalysis Using a First-Principles Approach. *ACS Catalysis*, 3(12):2694–2704, 2013.
- [629] Mercedes Boronat, Avelino Corma, and Michael Renz. Mechanism of the Meerwein-Ponndorf-Verley-Oppenauer (MPVO) Redox Equilibrium on Sn- and Zr-Beta Zeolite Catalysts. *The Journal of Physical Chemistry B*, 110(42):21168–21174, 2006.
- [630] Makoto Shibagaki, Kyoko Takahashi, and Hajime Matsushita. The Catalytic Reduction of Aldehydes and Ketones with 2-Propanol over Hydrous Zirconium Oxide. *Bulletin of the Chemical Society of Japan*, 61(9):3283–3288, 1988.
- [631] V. V. Ordonsky, V. L. Sushkevich, and I. I. Ivanova. Study of acetaldehyde condensation chemistry over magnesia and zirconia supported on silica. *Journal of Molecular Catalysis A: Chemical*, 333(1–2):85–93, 2010.
- [632] V. A. Ivanov, J. Bachelier, F. Audry, and J. C. Lavalley. Study of the Meerwein-Ponndorf-Verley reaction between ethanol and acetone on various metal oxides. *Journal of Molecular Catalysis*, 91(1):45–59, 1994.
- [633] Dennis Palagin, Vitaly L. Sushkevich, and Irina Igorevna Ivanova. C–C Coupling Catalyzed by Zeolites: is Enolization the Only Possible Pathway for Aldol Condensation? *The Journal of Physical Chemistry C*, 120(41):23566–23575, 2016.
- [634] Ivan Hung, Aaron J. Rossini, and Robert W. Schurko. Application of the Carr-Purcell Meiboom-Gill Pulse Sequence for the Acquisition of Solid-State NMR Spectra of Spin-1/2 Nuclei. *The Journal of Physical Chemistry A*, 108(34):7112–7120, 2004.
- [635] J. Herzfeld and Alan E. Berger. Sideband intensities in NMR spectra of samples spinning at the magic angle. *The Journal of Chemical Physics*, 73(12):6021–6030, 1980.
- [636] William Robert Gunther, Vladimir K. Michaelis, Robert G. Griffin, and Yuriy Román-Leshkov. Interrogating the Lewis Acidity of Metal Sites in Beta Zeolites With  $^{15}\text{N}$  Pyridine Adsorption Coupled With MAS NMR Spectroscopy. *The Journal of Physical Chemistry C*, 120(50):28533–28544, 2016.
- [637] M. J. Díaz-Cabañas, P. A. Barrett, and M. A. Camblor. Synthesis and structure of pure  $\text{SiO}_2$  chabazite: the  $\text{SiO}_2$  polymorph with the lowest framework density. *Chemical Communications*, 17:1881–1882, 1998.
- [638] Alexandre Zagdoun, Gilles Casano, Olivier Ouari, Martin Schwarzwaelder, Aaron J. Rossini, Fabien Aussenac, Maxim Yulikov, Gunnar Jeschke, Christophe Copéret, Anne Lesage, Paul Tordo, and Lyndon Emsley. Large Molecular Weight Nitroxide Biradicals Providing Efficient Dynamic Nuclear Polarization at Temperatures up to 200 K. *Journal of the American Chemical Society*, 135(34):12790–12797, 2013.

- [639] Alexandre Zagdoun, Aaron J. Rossini, David Gajan, Adrien Bourdolle, Olivier Ouari, Melanie Rosay, Werner E. Maas, Paul Tordo, Moreno Lelli, Lyndon Emsley, Anne Lesage, and Christophe Copéret. Non-aqueous solvents for DNP surface enhanced NMR spectroscopy. *Chemical Communications*, 48(5):654–656, 2011.
- [640] J. Z. Hu, D. W. Alderman, C. H. Ye, R. J. Pugmire, and D. M. Grant. An Isotropic Chemical Shift-Chemical Shift Anisotropy Magic-Angle Slow-Spinning 2d NMR Experiment. *Journal of Magnetic Resonance, Series A*, 105(1):82–87, 1993.
- [641] S. H. Vosko, L. Wilk, and M. Nusair. Accurate spin-dependent electron liquid correlation energies for local spin density calculations: a critical analysis. *Canadian Journal of Physics*, 58(8):1200–1211, 1980.
- [642] Chengteh Lee, Weitao Yang, and Robert G. Parr. Development of the Colle-Salvetti correlation-energy formula into a functional of the electron density. *Physical Review B*, 37(2):785–789, 1988.
- [643] Axel D. Becke. Density-functional thermochemistry. III. The role of exact exchange. *Journal of Chemical Physics*, 98(7):5648, 1993.
- [644] P. J. Stephens, F. J. Devlin, C. F. Chabalowski, and M. J. Frisch. Ab Initio Calculation of Vibrational Absorption and Circular Dichroism Spectra Using Density Functional Force Fields. *The Journal of Physical Chemistry*, 98(45):11623–11627, 1994.
- [645] Stefan Grimme. A consistent and accurate ab initio parametrization of density functional dispersion correction (DFT-D) for the 94 elements H-Pu. *The Journal of Chemical Physics*, 132(15):154104, 2010.
- [646] Stefan Grimme, Stephan Ehrlich, and Lars Goerigk. Effect of the damping function in dispersion corrected density functional theory. *Journal of Computational Chemistry*, 32(7):1456–1465, 2011.
- [647] M. J. Frisch, G. W. Trucks, H. B. Schlegel, G. E. Scuseria, M. A. Robb, J. R. Cheeseman, G. Scalmani, V. Barone, B. Mennucci, G. A. Petersson, and H. Nakatsuji. *Gaussian 09*. Gaussian Inc., 2009.
- [648] E. Cancès, B. Mennucci, and J. Tomasi. A new integral equation formalism for the polarizable continuum model: Theoretical background and applications to isotropic and anisotropic dielectrics. *The Journal of Chemical Physics*, 107(8):3032–3041, 1997.
- [649] Maurizio Cossi, Vincenzo Barone, Benedetta Mennucci, and Jacopo Tomasi. Ab initio study of ionic solutions by a polarizable continuum dielectric model. *Chemical Physics Letters*, 286(3–4):253–260, 1998.
- [650] Benedetta Mennucci and Jacopo Tomasi. Continuum solvation models: A new approach to the problem of solute’s charge distribution and cavity boundaries. *The Journal of Chemical Physics*, 106(12):5151–5158, 1997.
- [651] W. R. Wadt and P. J. Hay. Abinitio effective core potentials for molecular calculations - potentials for main group elements Na to Bi. *Journal of Chemical Physics*, 82(1):284–298, 1985.

- [652] P. Jeffrey Hay. Ab initio effective core potentials for molecular calculations. Potentials for K to Au including the outermost core orbitals. *The Journal of Chemical Physics*, 82(1):299–310, 1985.
- [653] Hay. Ab initio effective core potentials for molecular calculations. Potentials for the transition metal atoms Sc to Hg. *The Journal of Chemical Physics*, 82(1):270–283, 1985.
- [654] Georg Schreckenbach and Tom Ziegler. Calculation of NMR Shielding Tensors Using Gauge-Including Atomic Orbitals and Modern Density Functional Theory. *The Journal of Physical Chemistry*, 99(2):606–611, 1995.
- [655] Mykhaylo Krykunov, Tom Ziegler, and Erik van Lenthe. Hybrid density functional calculations of nuclear magnetic shieldings using Slater-type orbitals and the zeroth-order regular approximation. *International Journal of Quantum Chemistry*, 109(8):1676–1683, 2009.
- [656] G. te Velde, F. M. Bickelhaupt, E. J. Baerends, C. Fonseca Guerra, S. J. A. van Gisbergen, J. G. Snijders, and T. Ziegler. Chemistry with ADF. *Journal of Computational Chemistry*, 22(9):931–967, 2001.
- [657] E. Van Lenthe and E. J. Baerends. Optimized Slater-type basis sets for the elements 1–118. *Journal of Computational Chemistry*, 24(9):1142–1156, 2003.
- [658] Wolff. Calculation of DFT-GIAO NMR shifts with the inclusion of spin-orbit coupling. *The Journal of Chemical Physics*, 109(3):895–905, 1998.
- [659] Wolff. Density functional calculations of nuclear magnetic shieldings using the zeroth-order regular approximation (ZORA) for relativistic effects: ZORA nuclear magnetic resonance. *The Journal of Chemical Physics*, 110(16):7689–7698, 1999.
- [660] Matthew P. Conley, Aaron J. Rossini, Aleix Comas-Vives, Maxence Valla, Gilles Casano, Olivier Ouari, Paul Tordo, Anne Lesage, Lyndon Emsley, and Christophe Copéret. Silica-surface reorganization during organotin grafting evidenced by  $^{119}\text{Sn}$  DNP SENS: a tandem reaction of gem-silanols and strained siloxane bridges. *Physical Chemistry Chemical Physics*, 16(33):17822–17827, 2014.
- [661] Jan Dijkmans, Michiel Dusselier, Wout Janssens, Maarten Trekels, André Vantomme, Eric Breynaert, Christine Kirschhock, and Bert F. Sels. An Inner-/Outer-Sphere Stabilized Sn Active Site in bea-Zeolite: Spectroscopic Evidence and Kinetic Consequences. *ACS Catalysis*, 6(1):31–46, 2016.
- [662] American Institute of Chemical Engineers. AICHE DIPPr Database, 2016.



## APPENDICES



## A. A BRIEF REVIEW OF THE LITERATURE PERTAINING TO THE ROLE OF PAIRED AL SITES IN CHA FOR VARIOUS APPLICATIONS

### A.1 Introduction

The synthesis and characterization of CHA zeolites containing different arrangements of isolated and paired Al sites, at a fixed elemental composition, has enabled the preparation of model catalysts for investigating the role of active site structure and arrangement on both acid and redox catalysis. Control of the Al arrangement in CHA has enabled synthesis of Cu-containing zeolites with known distributions of divalent  $\text{Cu}^{2+}$  and monovalent  $[\text{CuOH}]^+$  cations (Chapter 6) [79]. This set of model Cu-CHA zeolites allowed us to assess the role of  $\text{Cu}^{2+}$  and  $[\text{CuOH}]^+$  site types and Cu ion spatial density on the kinetics and mechanisms of NOx SCR using a combination of kinetic, spectroscopic, and theoretical methods (Chapters 6 and 7) [79, 237], and to rationalize the seemingly disparate proposals in the literature regarding the SCR active site (Appendix B) [237, 476]. Moreover, this same set of model CHA zeolites, in their H-form, allowed us to investigate the role of proton proximity on methanol dehydration catalysis (Chapter 8 and Appendix C) [214]. Interrogating this set of catalysts revealed that methanol dehydration first- and zero-order rate constants (per  $\text{H}^+$ , 415 K) are nearly 10x larger at paired protons than at isolated protons, likely due to the ability of paired protons to stabilize the methoxy transition-state of the dissociative pathway. While our initial investigations have focused on two specific applications, the effects of Al proximity on adsorption and catalysis has begun to garner significant attention in the scientific literature for other applications. Here, some of the recent work investigating the role of framework Al arrangement in CHA on a variety of applications is briefly reviewed.

## A.2 Acid strength [477]

The deprotonation energy (DPE), a probe independent description of acid strength, of  $H^+$  sites has been shown to influence the rate of acid-catalyzed reactions that proceed through ion-pair intermediates and transition states [82,83,478,479]. In zeolites, the acid strength of protons can be altered by substitution of different trivalent heteroatoms (e.g.,  $Al^{3+}$ ,  $Ga^{3+}$ ,  $Fe^{3+}$ ) into the framework [83]. Recently, the proximity of framework Al atoms was reported to influence the acid strength of protons in aluminosilicate CHA zeolites [477]. The DPE of a proton when a second acid site is located in the same 6-membered ring is lower than an isolated proton, because the second acid site stabilizes the deprotonated lattice conjugate base across the 6-MR. Other Al pairs in the 8-MR do not lead to differences in DPE because residual protons do not orient within the 8-MR to stabilize the conjugate base. These effects are reversed when the cation at the second site is replaced with an ammonium, indicating that the preference of different cations to become confined within specific rings of CHA can alter the stability of the deprotonated site. These observations suggest that enhancement of methanol dehydration rates at paired protons in CHA may reflect an acid strength effect, but this is dependent on the coverage of the second site, which is still ongoing work.

## A.3 Characterization of Al arrangement [480]

Multi-quantum  $^{23}Na$  magic-angle spinning nuclear magnetic resonance ( $^{23}Na$  MQ MAS NMR) spectroscopic techniques have been reported, which can assess the correlation of  $Na^+$  nuclei in different coordination environments in CHA zeolites [480].  $^{23}Na$  MAS NMR spectra measured on a series of Na-exchanged high-silica CHA zeolites ( $Si/Al = 48$ ) show single Na coordination environment in the 6-MR. Increasing the total Al content leads to  $^{23}Na$  MQ NMR correlation between Na located in the 6-MR and an adjacent 8-MR, as observed from strong quadrupolar interactions between the two nuclei. These observations suggest that  $^{23}Na$  MQ NMR may be able to

distinguish different Al arrangements in CHA, but this technique may become limited if CHA zeolites contain moderate to high Al concentrations (approaching 1 Al per cage) with different arrangements.

#### A.4 CO<sub>2</sub> Adsorption [217,481]

The effect of Al arrangement in CHA zeolites has also been investigated for CO<sub>2</sub> adsorption. Kinetic Monte-Carlo CO<sub>2</sub> adsorption models have been developed for a series of CHA zeolites (and other zeolite frameworks) with different Si/Al ratios and degrees of Al clustering (i.e., Al proximity). These models indicate that CO<sub>2</sub> heats of adsorption are larger in Na-exchanged CHA at a fixed Si/Al = 11 with sparse Al distributions (isolated Al) than at clustered Al sites (i.e., paired Al). CO<sub>2</sub> adsorption, however, is also more favorable in zeolites with lower Si/Al. These models indicate, and support previous suggestions [482], that dual Na<sup>+</sup> sites in the 8-MR are the most favorable site for adsorbing CO<sub>2</sub>, which are formed in greater concentration in CHA zeolites with high Al concentrations, but sparse distributions [217]. These results are in reasonable agreement with experimental CO<sub>2</sub> gas-separation (from either CH<sub>4</sub> or N<sub>2</sub>) experiments performed on Na-CHA zeolites synthesized at various Si/Al ratios (4-50) [481], which showed greater selectivity for CO<sub>2</sub> at higher Al concentrations. The work of Guo et al. [481] does not attempt to manipulate the Al distribution at a fixed Si/Al ratio, so direct correlation between their observations and those of Findley et al. [217] are tentative. Moreover, proximal Al sites in MFI zeolites appear to be more selective for adsorbing linear alkanes at central C-C bonds than at terminal C-C bonds [483]. These results present an interesting application for CHA, and other, zeolites with tailored arrangements of framework Al atoms for gas separations, but also an additional characterization technique to probe the arrangement of Al atoms in CHA and other zeolites.

## A.5 MTO [216,484]

Small-pore CHA zeolites are selective in their conversion of methanol to light olefins (e.g., ethene, propene) instead of aromatics [485]. CHA zeolites containing different Al concentrations, and presumably different arrangements of Al, have previously been studied for MTO [158]. These previous results showed that low-silica CHA zeolites (i.e., likely containing paired protons) had increased initial propane selectivities, which is an indicator of hydrogen transfer events that facilitate deactivation [486, 487], and shorter catalyst lifetimes (time to <85% conversion) [158]. Additionally, the effects of Al arrangement on MTO have also been studied on CHA zeolites synthesized via FAU conversion with different arrangements of framework Al atoms, as inferred from  $^{29}\text{Si}$  NMR, but similar total Al concentrations ( $\text{Si}/\text{Al} = 10\text{--}13$ ) [216]. Nishitoba et al. found that CHA zeolites that contained larger amounts of  $\text{Q}_2$  sites (i.e.,  $\text{Si}(\text{OAl})_2(\text{OSi})_2$ ) had shorter MTO time-on-stream stability than CHA containing more isolated Al sites [216], consistent with the previous conclusion from Deimund et al [158]. Crystallite size and diffusion within microporous voids play a critical role in the time-on-stream stability of MTO catalysts [488]. Recently, Gallego et al. reported the synthesis of nano-crystalline CHA zeolites (60-80 nm in diameter) with different Al arrangements at similar bulk composition ( $\text{Si}/\text{Al} = 14$ ) and observed that nano-CHA containing higher amounts of isolated Al sites had longer time-on-stream stabilities than CHA zeolites of similar size, with higher fractions of paired Al [484]. Collectively, these results suggest that paired Al sites in CHA zeolites lead to shorter time-on-stream stability for MTO than isolated Al sites possibly due to their propensity to form propane at initial times. These results should be taken with hesitation as all transient MTO deactivation studied here begins from 100% conversion and does not provide a quantitative metric of catalyst lifetime or stability.

## A.6 Hydrothermal Stability and Sulfur Poisoning During NO<sub>x</sub> SCR [239,489]

The speciation of Cu cations in CHA zeolites between divalent Cu<sup>2+</sup> and monovalent [CuOH]<sup>+</sup> complexes depends on the underlying arrangement of framework Al atoms between isolated and paired sites [79]. Low-temperature NO<sub>x</sub> SCR rates (per Cu, <523 K) are indistinguishable on Cu-CHA catalysts containing either predominantly Cu<sup>2+</sup> or [CuOH]<sup>+</sup>, as long as catalysts operate in the reduction-limited regime (> ca. 2 wt% Cu) [79,237]. Cu-CHA catalysts do not show deactivation during steady-state SCR, but frequent sojourns to elevated temperatures (>800 K) in the presence of high water content (up to 10 wt%) during regeneration of up-stream particulate filters, and the presence of sulfur-containing compounds (e.g., SO<sub>2</sub> and SO<sub>3</sub>) in engine effluent lead to deactivation of Cu active sites. Song et al. have investigated the resistance of Cu-CHA zeolites to hydrothermal deactivation by preparing a series of Cu-exchange CHA zeolites at different Si/Al ratios (Si/Al = 6-35) to manipulate the Al arrangement, and, thus, the concentration of Cu<sup>2+</sup> or [CuOH]<sup>+</sup> active sites [489]. They conclude that Cu<sup>2+</sup> sites are more resistant to deactivation through Cu-oxide formation than [CuOH]<sup>+</sup>, and this formation of Cu-oxides clusters ultimately leads to the loss in SCR performance after hydrothermal aging. These results still leave lingering questions about the deactivating species (e.g., Cu-oxide or Cu-aluminate) during hydrothermal aging because prior work has demonstrated that Cu-oxide clusters are able to disperse into cationic Cu sites in the presence of SCR reaction gas mixtures [363]. In a similar approach, Cu-CHA zeolites of different Si/Al ratio (6 and 30) have been investigated for the resistance of different Cu sites to sulfur poisoning [239]. Jangjou et al. conclude that Cu<sup>2+</sup> cations are more resistant to sulfur poisoning by SO<sub>2</sub> than [CuOH]<sup>+</sup> and provide evidence that the hydroxide ligand promote the formation of highly stable bisulfate species [482]. Together, these results indicate that Cu<sup>2+</sup> is more resistant to both deactivation by hydrothermal aging and sulfur poisoning than [CuOH]<sup>+</sup>, suggesting that CHA zeolites containing high concentrations of Cu<sup>2+</sup> would lead to SCR catalysts with greater lifetimes.

## A.7 Partial methane oxidation to methanol [219,490–493]

Cu-exchanged zeolites have garnered further interest due to their ability to activate the C-H bond in methane in selective oxidation reactions that produce methanol [221]. Specifically in CHA zeolites,  $[\text{CuOH}]^+$  complexes that exchanged at isolated Al atoms have been proposed to be the precursor to the active site for partial methane oxidation (PMO) [219,492]. Pappas et al. observed that the total amount of methanol produced per Cu was lower on Cu-CHA zeolites that were expected to contain higher concentrations of  $\text{Cu}^{2+}$  cations than on samples synthesized to contain predominantly  $[\text{CuOH}]^+$  [219]. These reports do not systematically vary the Cu site identity at a fixed composition, however, which still leaves lingering questions about the role of Cu site density and speciation. Fe-containing zeolites have also been utilized for PMO [221] and recently paired Al sites in CHA were identified as the exchange site for extraframework  $\alpha$ -Fe active sites [493]. CHA zeolites synthesized through different procedures ( $\text{Si}/\text{Al} = 9$ ) were characterized by  $\text{Co}^{2+}$  titration to contain different fractions of paired Al sites, whose content correlated with the content of the proposed  $\alpha$ -Fe active site [493]. These observations are consistent with calculated phase-diagrams of Fe siting at different Al arrangements in CHA, which indicate that  $\alpha$ -Fe sites preferentially exchanged at paired Al in the 6-MR of CHA zeolites [494]. In both Cu- and Fe-exchanged CHA zeolites, the formation of the proposed active site (e.g.,  $[\text{CuOH}]^+$  or  $\alpha$ -Fe) depend directly on the underlying arrangement of framework Al atoms, indicating that different synthetic procedures can be used to control the formation of active sites for partial methane oxidation to methanol.



B. CATALYSIS SCIENCE OF NOX SELECTIVE CATALYTIC REDUCTION  
WITH AMMONIA OVER CU-SSZ-13 AND CU-SAPO-34

Due to copyright restrictions, this manuscript cannot be reproduced in full. The full text of Paolucci et al., *Adv. Catal.*, 2016, 59, 1-107 can be found at:

[dx.doi.org/10.1016/bs.acat.2016.10.002](https://doi.org/10.1016/bs.acat.2016.10.002).

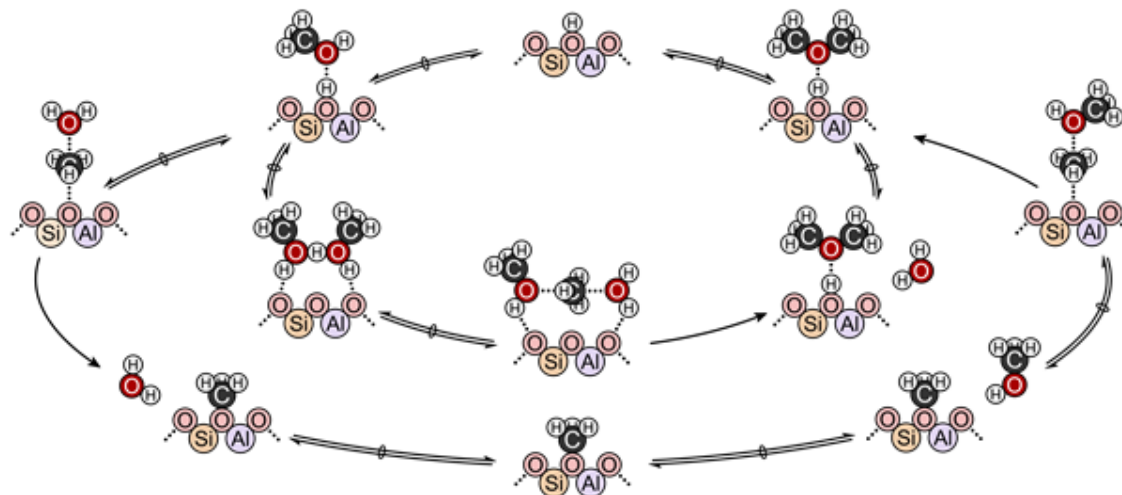


## C. EFFECTS OF ACID SITE PROXIMITY AND CONFINEMENT IN ZEOLITES ON PREVALENT REACTION MECHANISMS DURING METHANOL DEHYDRATION CATALYSIS

### C.1 Inhibition of methanol dehydration rates in CHA zeolites

Low-temperature ( $<453$  K) dehydration of methanol to dimethyl ether (DME) is a known probe of acid strength and confinement effects in zeolite catalysts and proceeds through two different mechanisms [21, 82]. The first step in both mechanisms is the quasi-equilibrated adsorption of gas-phase methanol at a proton. In the associative dehydration mechanism, DME and water are formed through the kinetically-relevant dehydration of protonated methanol dimers that form via quasi-equilibrated adsorption of a second methanol at a methanol monomer (Figure C.1, inner). While in the dissociative dehydration mechanism (Figure C.1, outer), methanol monomers are dehydrated to eliminate water and form a surface methoxy species. DME is then formed via a nucleophilic attack of a surface methoxy by a second methanol molecule that is in quasi-equilibrium with the bare surface methoxy. The dissociative mechanism is also inhibited by the formation of quasi-equilibrated methanol dimers that do not participate in DME formation.

Figure C.1. DFT calculated structures of intermediates and transition states for the associative (inner circle) and dissociative (outer circle) mechanisms.



Methanol dehydration proceeds via the associative dehydration mechanism on acidic polyoxometalate clusters [82] located on mesoporous supports, and on acid sites confined within medium- and large-pore zeolites [22], without inhibition at high methanol pressures. Associative methanol dehydration rates (per H<sup>+</sup>, 415 K) on small-pore CHA zeolites containing isolated protons, however, are inhibited at high methanol pressures, which has been previously accounted for by introducing an inhibitory surface intermediate to the list of elementary steps [214]. Adsorption within zeolites often deviates from ideality due to strong interactions between adsorbed species and the zeolite framework, particularly at high surface coverages (or adsorbate pressures). In turn, this can lead to rates of reaction that deviate from ideal rate laws due to adsorbate-adsorbate interactions and solvent crowding of the transition state [495–499]. These non-ideal interactions can be interpreted by deriving the associative dehydration rate law using non-ideal transition state theory treatments, which account for changes in rate due to differences in the activity coefficients of various adsorbed species.

### C.1.1 Estimation of methanol activity coefficients

Activity coefficients, which describe deviations from ideal solution behavior, of adsorbed species solvated within zeolites can be estimated by treating intrazeolite adsorption with solution thermodynamics [500–503] and by modeling adsorption using a Virial isotherm [504–506]:

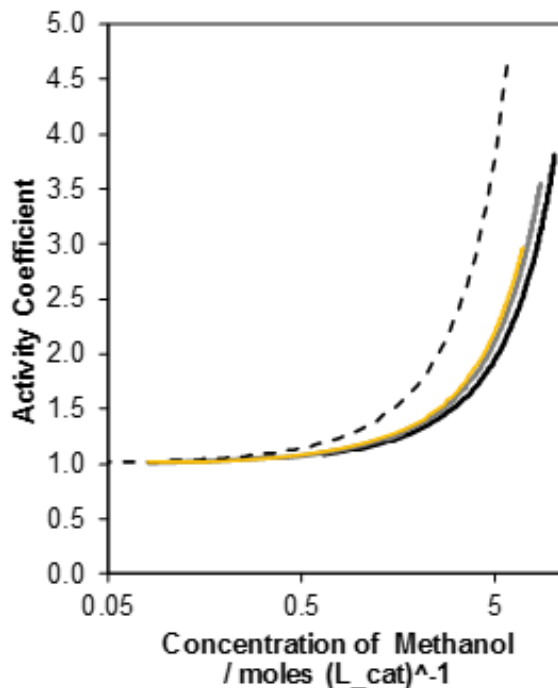
$$K = \frac{n}{p}\gamma \quad (\text{C.1})$$

$$\gamma = \exp(2A_1n + \frac{3}{2}A_2n^2 + \frac{4}{3}A_3n^3 + \dots) \quad (\text{C.2})$$

$$A_i = A_i^0(1 + a_iT) \quad (\text{C.3})$$

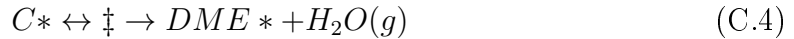
where  $K$  is the equilibrium constant,  $\gamma$  is the activity coefficient,  $n$  is the concentration (mole  $(L_{cat})^{-1}$ ) of adsorbed species in equilibrium with gas-phase pressure,  $p$  (atm), and the  $A_i$  terms are the  $i^{th}$  virial coefficients [504, 507]. Virial coefficients for various gases adsorbed in H-CHA (e.g.,  $O_2$ ,  $N_2$ , Ar, Kr) have been observed to vary linearly with temperature and depend on values of  $A_i^0$  and  $a_i$  [504]. Methanol adsorption isotherms measured on H-CHA zeolites (Si/Al = 15) as a function of temperature (288–308 K) were fit using Eq. C.1–C.3 to extract Virial coefficients and estimate activity coefficients of adsorbed methanol at reaction temperatures and pressures (415 K, <50 kPa).

Figure C.2. Methanol activity coefficient as a function of intrapore concentration on H-CHA (Si/Al = 15, 0% paired Al) at 293 K (black) and 308 K (grey), and extrapolated to 415 K (dashed), and on H-MFI (Si/Al = 43) at 293 K (yellow).



Activity coefficients are near unity at low intrapore concentrations of methanol, but increase with increasing adsorbed methanol concentration and with increasing temperature at constant intrapore concentration (Figure C.2), indicating that methanol is more loosely bound at high coverages and higher temperatures. The activity coefficients estimated in Figure C.2 represent bulk methanol activity coefficients and do not uniquely describe the activity coefficients of adsorbed methanol monomers, dimers, or the transition state. They do provide an initial estimate of how the activity coefficients deviate from ideality at high intrapore methanol concentrations and indicate the need to interpret methanol dehydration kinetics using non-ideal transition state theory formalisms [498, 505, 506].

The rate limiting step of the associative dehydration mechanism involves the concerted rearrangement and dehydration of a co-adsorbed methanol dimer ( $C^*$ ) to form the transition state ( $TS^\ddagger$ ) [82]:



where  $C^*$  and  $TS^\ddagger$  are quasi-equilibrated and the transition state irreversibly forms the products. A rate law can now be defined that is related to the concentration of the transition state and a barrier crossing coefficient,  $\nu_i$ :

$$\frac{r_{DME}}{[L]} = \nu_i \theta_{\ddagger} = \frac{k_b T}{h} \theta_{\ddagger} \quad (C.5)$$

where,  $k_b$  is the Boltzmann constant,  $T$  is the temperature, and  $h$  is the Planck constant. Here, the dehydration rate is normalized by the total number of  $H^+$  sites ( $[L]$ ), which allows writing the rate in terms of the coverage of various surface species ( $\theta_i$ ). The coverage of the activated complex can then be written in terms of reactive surface intermediates through quasi-equilibrium:

$$K_{\ddagger} = \frac{a_{\ddagger}}{a_{C^*}} = \frac{\theta_{\ddagger} \gamma_{\ddagger}}{\theta_{C^*} \gamma_{C^*}} \quad (C.6)$$

where  $a_i$  represents the thermodynamic activity of each species and  $\gamma_i$  are the activity coefficients. Substitution of Eq. C.6 into Eq. C.5 yields a rate law in terms of adsorbed surface intermediates:

$$\frac{r_{DME}}{[L]} = \frac{k_b T}{h} K_{\ddagger} \left( \frac{\gamma_C}{\gamma_{\ddagger}} \right) \theta_{C^*} \quad (C.7)$$

The concentration of co-adsorbed methanol dimers which are difficult to experimentally quantify, can then be related to the gas-phase methanol pressure via equilibrium relations involving the different reactive intermediates (Scheme C.1):

$$K_{C^*} = \frac{a_{C^*}}{a_{D^*}} = \frac{\theta_{C^*} \gamma_{C^*}}{\theta_{D^*} \gamma_{D^*}} \quad (C.8)$$

$$K_{D^*} = \frac{a_{D^*}}{a_{M^*} a_M} = \frac{\theta_{D^*} \gamma_{D^*}}{\theta_{M^*} \gamma_{M^*} \gamma_M} \left( \frac{P_0}{P_M} \right) \quad (C.9)$$

$$K_{M^*} = \frac{a_{M^*}}{a_* a_M} = \frac{\theta_{M^*} \gamma_{M^*}}{\theta_* \gamma_* P_M \gamma_M} \left( \frac{P_0}{P_M} \right) \quad (C.10)$$

where  $K_{C*}$ ,  $K_{D*}$ , and  $K_{M*}$  are equilibrium constants for co-adsorbed methanol dimers, protonated dimers, and methanol monomers, respectively, and  $P_0$  is a standard-state pressure of 1 bar. Sequential substitution of  $K_{C*}$ ,  $K_{D*}$ , and  $K_{M*}$  into Eq. C.7 yields:

$$\frac{r_{DME}}{[L]} = \frac{k_b T}{h} K_{\ddagger} K_{C*} K_{D*} K_{M*} \left( \frac{\gamma_M^2 \gamma_*}{\gamma_{\ddagger}} \right) \left( \frac{P_M}{P_0} \right)^2 \theta_* \quad (\text{C.11})$$

From Eq. C.11, the associative dehydration mechanism depends on the activity coefficients of two gas-phase methanol molecules, the transition state, an empty  $H^+$  site, methanol pressure, and the coverage of available  $H^+$  sites. During steady-state methanol dehydration catalysis (415 K, >0.05 kPa  $CH_3OH$ ),  $H^+$  sites within CHA zeolites are covered by methanol monomers, dimers, and methanol clusters [214]. The latter will not be considered as an inhibiting species here, so that the role of the activity coefficients can be investigated independently of reactant inhibition. Treating methanol monomers and protonated dimers as the most abundant reactive intermediates, results in the following site-balance:

$$1 = \theta_M + \theta_D \quad (\text{C.12})$$

Substitution of Eqs. C.9 and C.10 into Eq. C.12 gives:

$$\theta_* = \frac{1}{[K_M \left( \frac{\gamma_M \gamma_*}{\gamma_{M*}} \right) \left( \frac{P_M}{P_0} \right)] (1 + K_{D*} \left( \frac{\gamma_M \gamma_{M*}}{\gamma_{D*}} \right) \left( \frac{P_M}{P_0} \right))} \quad (\text{C.13})$$

Eq. C.11 can now be rewritten using Eq. C.13 to give:

$$\frac{r_{DME}}{[L]} = \frac{\frac{k_b T}{h} K_{\ddagger} K_{C*} K_{D*} \left( \frac{\gamma_M \gamma_{M*}}{\gamma_{\ddagger}} \right) \left( \frac{P_M}{P_0} \right)}{1 + K_{D*} \left( \frac{\gamma_M \gamma_{M*}}{\gamma_{D*}} \right) \left( \frac{P_M}{P_0} \right)} \quad (\text{C.14})$$

In the ideal case (i.e.,  $\gamma_i = 1$ ), Eq. C.14 reduces to:

$$\frac{r_{DME}}{[L]} = \frac{\frac{k_b T}{h} K_{\ddagger} K_{C*} K_{D*} \left( \frac{P_M}{P_0} \right)}{1 + K_{D*} \left( \frac{P_M}{P_0} \right)} \quad (\text{C.15})$$

Estimation of the fugacity of gas-phase methanol ( $\gamma_M$ ) at 415 K using the Peng-Robinson equation of state [508] gives activity coefficients near unity ( $\gamma_M > 0.98$ ), indicating that under the conditions studied here (415 K, 0.01-50 kPa  $CH_3OH$ ), gas-phase methanol behaves as an ideal gas. This allows Eq. C.14 to be simplified to:

$$\frac{r_{DME}}{[L]} = \frac{\frac{k_b T}{h} K_{\ddagger} K_{C*} K_{D*} \left( \frac{\gamma_{M*}}{\gamma_{\ddagger}} \right) \left( \frac{P_M}{P_0} \right)}{1 + K_{D*} \left( \frac{\gamma_{M*}}{\gamma_{D*}} \right) \left( \frac{P_M}{P_0} \right)} \quad (\text{C.16})$$



Allowing methanol pressure to approach zero reduces Eq. C.16 to the first-order limit:

$$\frac{r_{DME}}{[L]} = \frac{k_b T}{h} K_{\ddagger} K_{C*} K_{D*} \left( \frac{\gamma_{M*}}{\gamma_{\ddagger}} \right) \left( \frac{P_M}{P_0} \right) \quad (C.17)$$

The deviation from ideality of first-order dehydration kinetics ( $\eta_1$ ) can be defined as the ratio of the apparent dehydration rate constant to the rate constant under ideal conditions (i.e.,  $\gamma_i = 1$ ):

$$\eta_1 = \frac{k_{app}}{k_{ideal}} = \frac{\gamma_{M*}}{\gamma_{\ddagger}} \quad (C.18)$$

where  $k_{ideal}$  represents the rate constant for formation of the DME transition state under ideal conditions,

$$k_{ideal} = \frac{k_b T}{h} K_{\ddagger} K_{C*} K_{D*} \quad (C.19)$$

Changes in  $\eta_1$  as a function of methanol partial pressure, at constant temperature, arise from the dependence of  $\eta_1$  on the intrapore methanol pressure ( $\tau$ ):

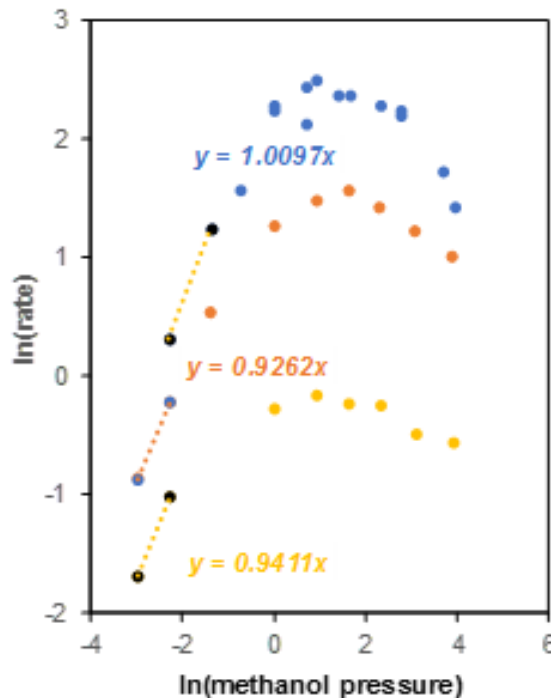
$$\left( \frac{\partial \ln(\eta_1)}{\partial P} \right)_T = \left( \frac{\partial \ln(\eta_1)}{\partial \tau} \right)_T \left( \frac{\partial \tau}{\partial P} \right)_T \quad (C.20)$$

which can be expressed in terms of activity coefficients by substitution of Eq. C.18 into Eq. C.20:

$$\left( \frac{\partial \ln(\eta_1)}{\partial P} \right)_T = \left[ \left( \frac{\partial \ln(\gamma_{M*})}{\partial \tau} \right)_T - \left( \frac{\partial \ln(\gamma_{\ddagger})}{\partial \tau} \right)_T \right] \left( \frac{\partial \tau}{\partial P} \right)_T \quad (C.21)$$

Apparent methanol activity coefficients asymptotically approach unity at low intrapore methanol concentrations (i.e., at low intrapore methanol pressures; Figure C.2), suggesting that any change in the methanol activity coefficients, under the low-pressure limit, will be small. As a result,  $\eta_1$  reflects deviation of the apparent reaction order from the ideal first-order limit caused by the dependence of the activity coefficients on methanol pressure. Analysis of the methanol dehydration reaction order on H-CHA containing only isolated protons (Si/Al = 15, 383-415 K) shows that orders are 0.9-1 at methanol pressures <0.2 kPa (Figure C.3), which indicates that under dilute intrapore methanol concentrations, first-order methanol dehydration kinetics are not influenced by changes in intrapore methanol pressures (i.e.,  $\gamma = 1$  at low pressures).

Figure C.3. Log-log analysis of the DME formation rate (per  $\text{H}^+$ ) as a function of methanol pressure (0.01-50 kPa) on H-CHA (Si/Al = 15, 0% paired Al) at 383 K (yellow), 403 K (orange), and 415 K (blue). Dashed lines are best-fit lines to extract reaction orders at low methanol pressures and corresponding reaction orders (i.e., slopes) are provided.



This is in agreement with activity coefficients predicted from methanol adsorption isotherms and extrapolated to 415 K (Figure C.2) and allows associative first-order methanol dehydration kinetics to be expressed without dependence on the activity coefficients:

$$\frac{r_{DME}}{[L]} = \frac{k_b T}{h} K_{\ddagger} K_{C*} K_{D*} \left( \frac{P_M}{P_0} \right) = k_{DME,a} K_C K_D \left( \frac{P_M}{P_0} \right) \quad (\text{C.22})$$

Without contributions arising from methanol activity coefficients, differences in apparent first-order associative dehydration rate constants (i.e.,  $k_{DME,a} K_C K_D$ ) reflect differences in Gibbs free energy between the associative dehydration transition state and a methanol monomer and gas-phase methanol molecule ( $\Delta G_{first} = \Delta G^{\ddagger} - \Delta G^{M*} - \Delta G^M$ ), and is sensitive to both the acid strength of  $\text{H}^+$  sites and confinement affects in zeolites [82].

Similarly, a zero-order rate law can be recovered at large methanol pressure:

$$\frac{r_{DME}}{[L]} = \frac{k_b T}{h} K_{\ddagger} K_{C^*} \left( \frac{\gamma_{D^*}}{\gamma_{\ddagger}} \right) \quad (C.23)$$

Again, the deviation from ideality of zero-order dehydration kinetics ( $\eta_0$ ) can be defined as the ratio of the apparent dehydration rate constant to the rate constant under ideal conditions:

$$\eta_0 = \frac{k_{app}}{k_{ideal}} = \frac{\gamma_{D^*}}{\gamma_{\ddagger}} \quad (C.24)$$

As with  $\eta_1$ , changes in  $\eta_0$  as a function of methanol partial pressure, at constant temperature, arise from the dependence of  $\eta_0$  on the intrapore methanol pressure ( $\tau$ ), and can be expressed in terms of activity coefficients:

$$\left( \frac{\partial \ln(\eta_0)}{\partial P} \right)_T = \left[ \left( \frac{\partial \ln(\gamma_{D^*})}{\partial \tau} \right)_T - \left( \frac{\partial \ln(\gamma_{\ddagger})}{\partial \tau} \right)_T \right] \left( \frac{\partial \tau}{\partial P} \right)_T \quad (C.25)$$

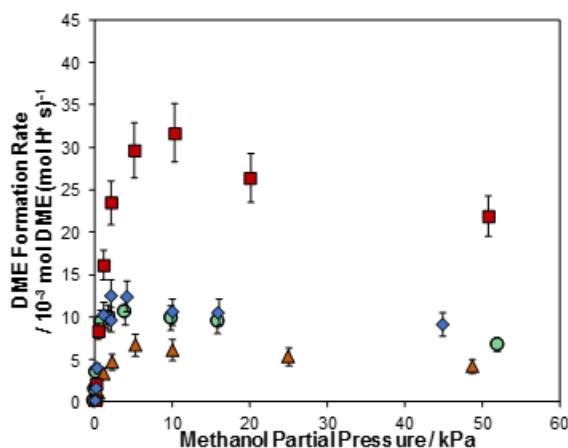
Rates of methanol dehydration on medium- and large-pore zeolites (e.g., MFI, BEA) reach a steady zero-order kinetic regime (415-433 K, >10 kPa CH<sub>3</sub>OH) [22], suggesting that the ratio of  $\frac{\gamma_{D^*}}{\gamma_{\ddagger}}$  does not vary with methanol pressure, under these conditions, in medium- and large-pore zeolites. This may reflect a similar dependence of both  $\gamma_{D^*}$  and  $\gamma_{\ddagger}$  on the intrapore methanol pressure, because these two charged complexes (i.e., methanol dimers and the transition state) are solvated to a similar extent by extraneous methanol and the zeolite framework [22], which would lead to rates that are independent of changes in the activity coefficients [498]. These observations suggest that the inhibition observed at high methanol pressures in CHA zeolites is likely not due to changes in activity coefficients that manifest at high intrapore methanol pressures because both  $\gamma_{D^*}$  and  $\gamma_{\ddagger}$  vary to a similar extent with methanol pressure.

### C.1.2 Inhibition in small-pore zeolites

Another possible explanation for the inhibition observed at high methanol pressures is slow diffusion of DME products out of the CHA pores. Inhibition at high methanol partial pressures is also been observed on other small-pore window-cage type zeolite frameworks (e.g., AEI [214], LEV, LTA; Figure C.4), suggesting that

the specific framework topology may be responsible for limited DME egress from the pores.

Figure C.4. DME formation rates (per total  $\text{H}^+$ ) measured at 415 K as a function of methanol partial pressure on a representative H-form CHA (green), LTA (orange), LEV (blue), and AEI (red) catalyst.

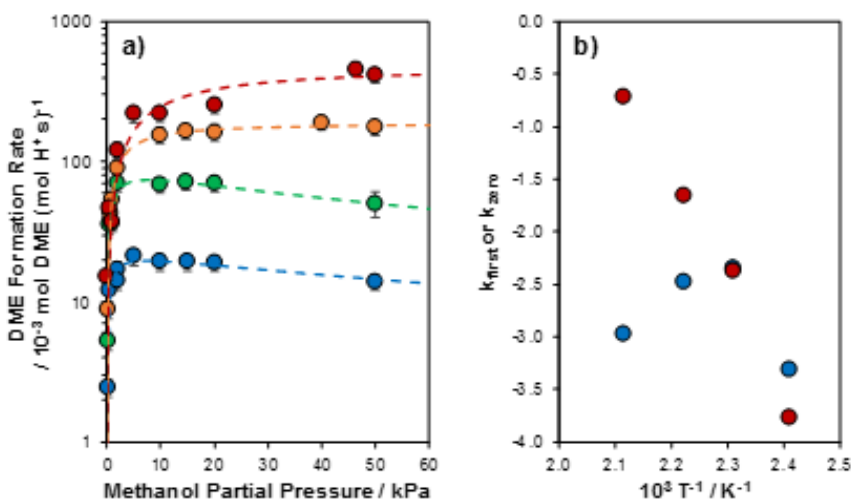


### C.1.3 Methanol dehydration rates at elevated temperatures

Inhibition of methanol dehydration rates (per  $\text{H}^+$ ) measured on CHA zeolites at high methanol partial pressures ( $>10$  kPa) appears to diminish as the temperature of reaction increases (415–473 K; Figure C.5). If the inhibition in CHA observed at 415 K were due to internal mass transport restrictions, then the observed inhibition would be expected to become more severe as the temperature of reaction increased, a behavior that is not observed here. Additionally, at elevated temperatures ( $>415$  K) the coverage of methanol would be expected to decrease with increasing temperature, which may suggest that adsorption of additional methanol at a protonated dimer may be responsible for inhibiting measured methanol dehydration rates in CHA at 415 K. At temperatures exceeding 450 K the formation of small olefins (e.g., ethene and propene) is observed at high methanol contact times (i.e., low methanol partial pressures) and decrease in concentration with decreasing methanol contact time (i.e., high methanol partial pressures) [485]. First-order rate constants (per  $\text{H}^+$ ) do not fol-

low an Arrhenius dependence on temperature (Figure C.5) likely because of the onset of severe internal mass transport limitations that arise at high temperatures, and the scavenging of methanol reactants to produce olefins under first-order methanol dehydration conditions ( $<1$  kPa). Zero-order rate constants (per  $H^+$ ), however, appear to still follow an Arrhenius dependence across this range of temperatures (415-473 K), suggesting that olefin formation is not significant at low methanol contact times in CHA [485]. These results suggest that methanol dehydration rates (per  $H^+$ ) are not inhibited by internal transport of DME out of the crystal, and support prior proposals of reactant inhibition [214].

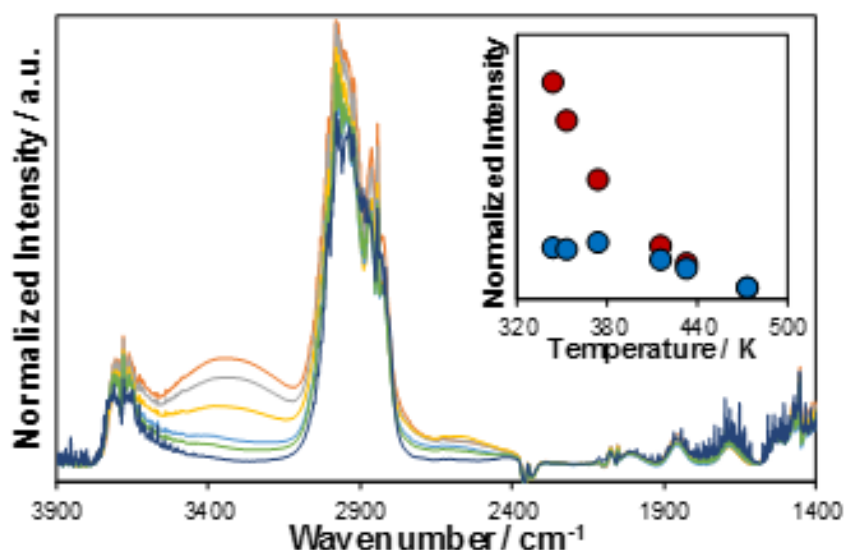
Figure C.5. (a) DME formation rates (per  $H^+$ ) measured at 415 K (blue), 433 K (green), 450 K (orange), and 473 K (red) and (b) first- (blue) and zero-order (red) rate constants (per  $H^+$ ) measured as a function of temperature (415-473 K) on a CHA zeolite containing 24% of Al in pairs.



Additionally, IR spectra measured during steady-state methanol dehydration at 10 kPa  $CH_3OH$  and various temperatures (343-473 K) on CHA zeolites containing 0% paired Al (Si/Al = 15) indicate that  $CH_3OH$  clusters (ca.  $3350\text{ cm}^{-1}$ ) [456] are a strong function of temperature (Figure C.6). The intensity of the adsorption band characteristic of methanol clusters [456] decreases at a greater rate than the intensity of the feature attributed to protonated methanol dimers ( $2620\text{ cm}^{-1}$ ; Figure C.6,

inset) [451] suggesting that methanol molecules in clusters (e.g., trimers or tetramers) [456] are more weakly adsorbed than protonated dimers. While these observations only qualitatively reflect methanol dimer and cluster formation, they do suggest that excess methanol adsorbs at dimers in CHA zeolites, which may lead to inhibition of methanol dehydration rates [214]. A direct comparison of these results with an MFI or \*BEA zeolite sample would help to further understand the role of methanol clusters in methanol dehydration catalysis.

Figure C.6. IR spectra of H-CHA (0% paired Al, Si/Al = 15) under 10 kPa CH<sub>3</sub>OH measured at 343 K (orange), 353 K (grey), 373 K (yellow), 415 K (light blue), 433 K (green), and 473 K (dark blue). Inset shows the intensity of the bands representative of methanol clusters (ca. 3350 cm<sup>-1</sup>; red) and protonated methanol dimers (ca. 2620 cm<sup>-1</sup>; blue) as a function of temperature.

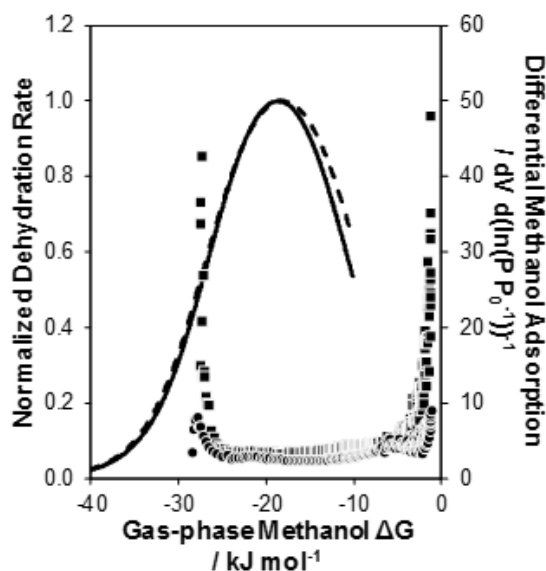


#### C.1.4 Methanol adsorption isotherms

Methanol adsorption isotherms (293 K) measured on H-CHA (Figure C.7) with both 0% and 44% paired Al indicate that methanol pore-fills in CHA at gas-phase free energies similar to those calculated at the maximum methanol dehydration rate (415 K, per H<sup>+</sup>). This apparent methanol micropore filling indicates that approximately

2 methanol molecules are adsorbed per proton when the maximum rate is reached, consistent with the onset of a zero-order regime.

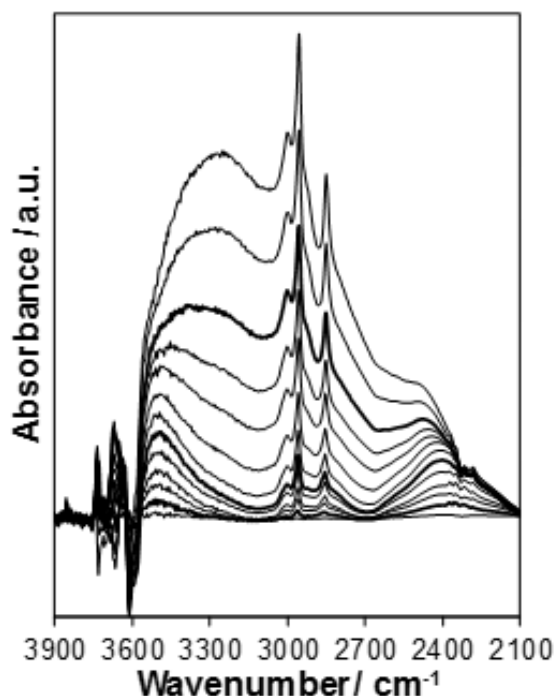
Figure C.7. Methanol dehydration rates (415 K, per proton) normalized to the maximum rate of H-CHA with 0% (solid) and 44% paired Al (dashed) and differential methanol adsorption data measured at 293 K on H-CHA with 0% (circles) and 44% paired Al (squares) as a function of the gas-phase methanol free-energy.



IR spectroscopy was used to support these observations by investigating different methanol surface intermediates that form during methanol adsorption isotherms (293 K). These spectra (Figure C.8) show that only methanol monomers form (ca.  $2380\text{ cm}^{-1}$ ) at low methanol coverages ( $\text{CH}_3\text{OH}/\text{H}^+ < 0.3$ ). Beyond a coverage of ca. 0.3  $\text{CH}_3\text{OH}$  per proton, the formation of protonated methanol dimers is observed (ca.  $2600\text{ cm}^{-1}$ ), whose band intensity increases until saturation at ca. 2.3  $\text{CH}_3\text{OH}$  per proton. At methanol coverages of  $\text{CH}_3\text{OH}$  per proton  $> 0.7$ , features characteristic of methanol clusters (ca.  $3300\text{ cm}^{-1}$ ) are observed and increase with increasing methanol adsorption (up to 3  $\text{CH}_3\text{OH}/\text{H}^+$ ). This set of adsorption experiments indicates that at the completion of micropore filling, protons in CHA zeolites are covered with ca. 2  $\text{CH}_3\text{OH}/\text{H}^+$  which coincides with the onset of inhibition in methanol dehydration

rates at similar gas-phase methanol free-energies (415 K, per  $\text{H}^+$ ). These results are also consistent with previous IR spectra measured during steady-state methanol dehydration catalysis that show the formation of methanol clusters at methanol pressures where rate inhibition begins to be observed ( $>5$  kPa) [214].

Figure C.8. Infrared spectra measured at 293 K on H-CHA with 0% paired Al as a function of methanol dosing (0.01-3  $\text{CH}_3\text{OH}/\text{H}^+$ ).



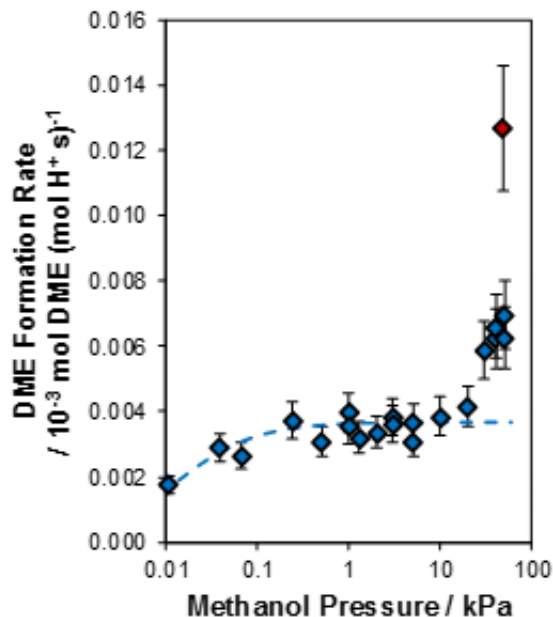
#### C.1.5 Inhibition at low temperatures (323 K)

Inhibition of methanol dehydration by adsorption of a single methanol at a protonated dimer should reach a -1 order regime at high enough methanol coverages. Methanol dehydration rates (per  $\text{H}^+$ ) were measured at 323 K in an attempt to force higher methanol coverages at high methanol pressures (Figure C.9). Under these conditions, DME formation rates (323 K, per  $\text{H}^+$ ) increase at high methanol pressures because the inlet reactant gas temperature is at a greater temperature than the catalyst bed. Rates begin to show an exponential increase with increasing methanol



pressure, suggesting their dependence on the inlet reactant gas temperature. Moreover, increasing the total flow rate of the system causes a further increase in rate at 50 kPa of methanol, further reinforcing the role of the reactant gas temperature. This is likely caused by an increase in thermal conductivity and heat capacity of the gas stream at high methanol partial pressures that causes the reactant gas to heat to temperatures greater than the reactor after passing through gas lines heated near 373 K. Unfortunately, without redesign of the experimental apparatus, these experiments were unable to reach conditions where -1 methanol order could be achieved.

Figure C.9. DME formation rates as a function of methanol pressure measured at 323 K and a total flow rate of  $25 \text{ cm}^3 \text{ min}^{-1}$  (blue) and  $100 \text{ cm}^3 \text{ min}^{-1}$  (50 kPa; red). Dashed line is a fit of the associative dehydration rate law, without inhibition, from Carr et al. [82] to rates measured below 10 kPa.

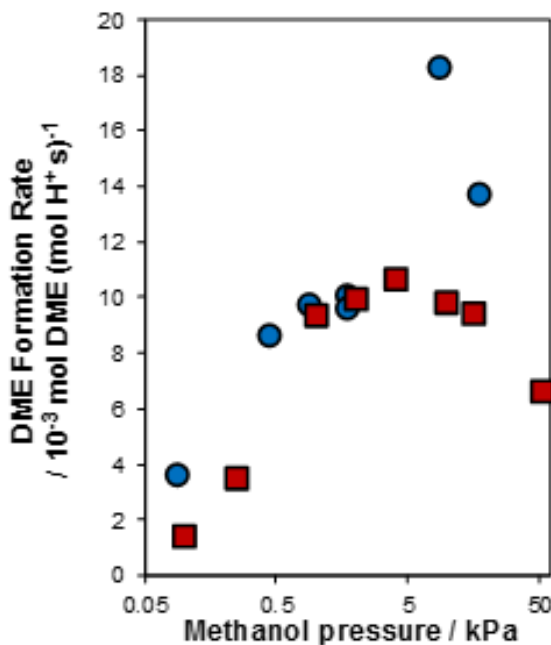


#### C.1.6 Steady-state isotopic transient kinetic analysis of methanol dehydration in CHA

The coverage of reactive intermediates can also be quantified during steady-state catalysis from transient isotopic reactant switches by monitoring the product response

using an online mass spectrometer [509]. Here, we perform a steady-state isotopic transient kinetic analysis (SSITKA) during methanol dehydration catalysis using a  $^{12}\text{CH}_3\text{OH}/^{13}\text{CH}_3\text{OH}$  switch on CHA zeolites containing 0% and 30% paired Al (Si/Al = 15) using a customer-built IR/MS reactor [465, 509]. Steady-state methanol dehydration rates (per  $\text{H}^+$ , 415 K) were measured between 0.1-25 kPa  $\text{CH}_3\text{OH}$  on CHA with 0% paired Al and were similar to those measured previously on the same sample in a plug-flow reactor (within 2x; Figure C.10) [214].

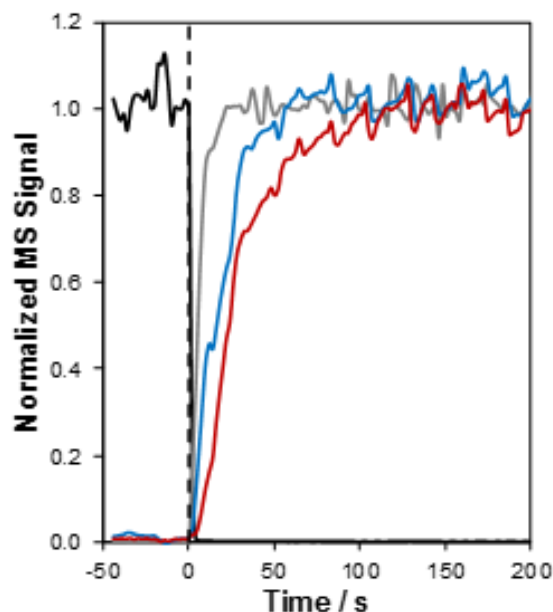
Figure C.10. DME formation rates (per  $\text{H}^+$ ) measured at 415 K as a function of pressure on a CHA zeolite with 0% paired Al on the SSITKA IR/MS (blue) and PFR (red) [214].



SSITKA experiments were performed by first establishing steady-state in an unlabeled  $\text{CH}_3\text{OH}$  flow (0.1-25 kPa) containing 2.5 kPa Ar as an inert tracer, then performing a switch to a second gas stream containing the same partial pressure of  $^{13}\text{CH}_3\text{OH}$  (0.1-25 kPa) and ca. 2.5 kPa of Kr as an inert tracer. The different inert tracer gases were used to monitor the gas holdup with the reactor and correct isotopic gas flows. After steady-state with the isotope was achieved, a second isotopic switch

was made back to the original unlabeled reactant stream. A representative isotopic transience is shown in Figure C.11.

Figure C.11. Steady-state isotopic switch from 12 kPa unlabeled  $\text{CH}_3\text{OH}$  to 12 kPa  $^{13}\text{CH}_3\text{OH}$  (blue). The  $^{13}\text{C}$ -DME response is shown in red. Ar (black) and Kr (grey) inert tracers are provided to show gas holdup.



Quantification of the number of surface intermediates that form DME ( $N_{DME}$ ) was done by integrating the difference between the final steady-state DME formation rate ( $\bar{r}_{DME}$ ) and the transient DME formation rate ( $r_{DME}(t)$ ) after switching [509]:

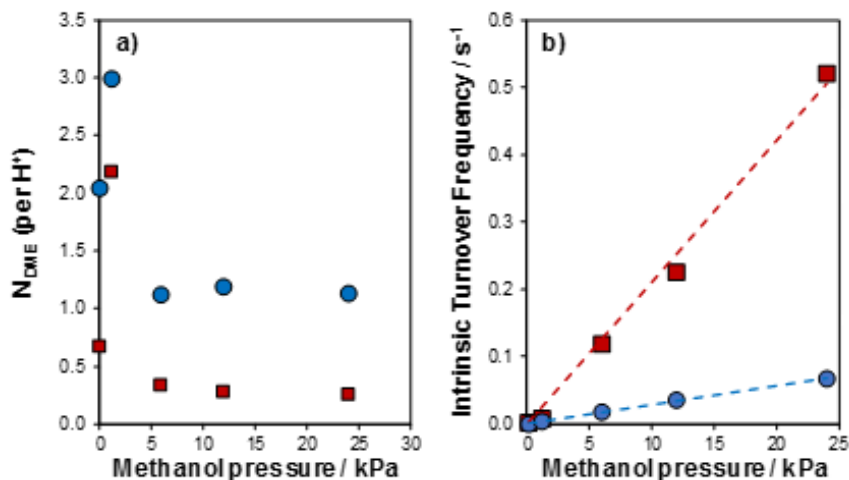
$$N_{DME} = \int_0^{\infty} (\bar{r}_{DME} - r_{DME}(t)) dt \quad (\text{C.26})$$

The intrinsic turnover frequency of the catalyst was calculated by taking the inverse of the mean surface residence ( $\tau_{DME}$ ) from the integral of the difference between the normalized inert tracer response ( $I^*(t)$ ) and the normalized transient DME formation rate ( $r_{DME}^*(t)$ ) [509]:

$$\tau_{DME} = \int_0^{\infty} (I^*(t) - r_{DME}^*(t)) dt \quad (\text{C.27})$$

The calculated values of  $N_{DME}$  and the intrinsic turnover frequency measured on CHA zeolites containing 0% and 30% paired Al sites ( $\text{Si}/\text{Al} = 15$ ) are shown in Figure C.12.

Figure C.12. (a)  $N_{DME}$  (per  $H^+$ ) and (b) the intrinsic turnover frequency (per  $H^+$ ) measured as a function of methanol pressure (0.1-25 kPa) at 415 K on CHA zeolites containing 0% (blue) and 30% (red) paired Al.



$N_{DME}$  increases at low methanol partial pressures ( $<1$  kPa) before sharply decreasing to steady values of 1.15 and 0.30 DME forming intermediates per  $H^+$  site on CHA with 0% and 30% paired protons. The values of  $N_{DME}$  measured at high methanol pressures ( $>5$  kPa) on CHA with 0% paired Al are consistent with each proton being equivalent and fully covered with DME forming intermediates. The lower value of  $N_{DME}$  (ca. 0.30) on CHA containing 30% paired Al indicating that either a subset of sites turnover at higher rates and control the transient DME formation rate (415 K) or that protons are not fully covered by methanol during steady-state catalysis. IR spectra measured during steady-state catalysis indicate that protons in CHA zeolites (0% or 30%) are fully covered by methanol during steady state dehydration catalysis (0.1-25 kPa) [214], suggesting that a fraction of the total sites are responsible for the transient DME response. The  $N_{DME}$  value of 0.30 is consistent with the total number of paired protons on CHA containing 30% paired Al, indicating that paired protons turnover at higher rates than isolated protons. This behavior is reflected in the measured intrinsic turnover frequencies (TOF) on CHA containing 0% and 30% paired protons (Figure C.12). Intrinsic TOFs (415 K) of both samples

increase linearly with methanol pressure (0.1-25 kPa), contrary to measured steady-state dehydration rates that become zero-order and inhibited at methanol pressures  $>5$  kPa [214], but are nearly an order of magnitude larger on CHA containing paired protons. These results are consistent with previous observations that both first- and zero-order methanol dehydration rate constants (per  $\text{H}^+$ , 415 K) are an order of magnitude larger at paired protons than at isolated protons in CHA zeolites [214].

The initial spike in coverage at low methanol pressures and the linear intrinsic TOF through 25 kPa  $\text{CH}_3\text{OH}$  on both CHA samples (Figure C.12), suggests that the transient values presented are likely not measured under the expected methanol pressures. Steady-state DME formation rates (per  $\text{H}^+$ , 415 K) are consistent with previously reported values (within 2x, Figure C.10) [214], but not with transiently measured intrinsic TOF. Together this suggests that methanol transport to the IR pellet surface is diffusion limited and that transient rates are measured under lower methanol pressures than expected of that chromatographic effects may be present across the catalyst pellet [510]. These SSITKA experiments were not performed in a true plug-flow reactor, so there is likely bypassing of the sample that also corrupts measured data. Variation of the methanol site contact time during these experiments could be performed to determine transient DME formation responses that are uncorrupted by external gas transport [510]. While these SSITKA experiments have produced exciting and encouraging data regarding the turnover of isolated and paired sites in CHA, there is still a large amount of work required in order to ensure that these experiments are performed under conditions that are free of concentration gradients.

## C.2 Interpretation of methanol dehydration activation parameters

Although more work is required to understand the mechanistic nature of the inhibition observed at high methanol pressures, these results collectively support prior proposals implicating adsorption of an additional methanol molecule as the source of inhibition in small-pore zeolites and we will use this assumption to model methanol

dehydration kinetics using a rate equation containing a trimeric inhibiting surface species. This results in both the associative and dissociative dehydration rate laws taking the same functional form and enables extraction of first- and zero-order rate constants for each pathway:

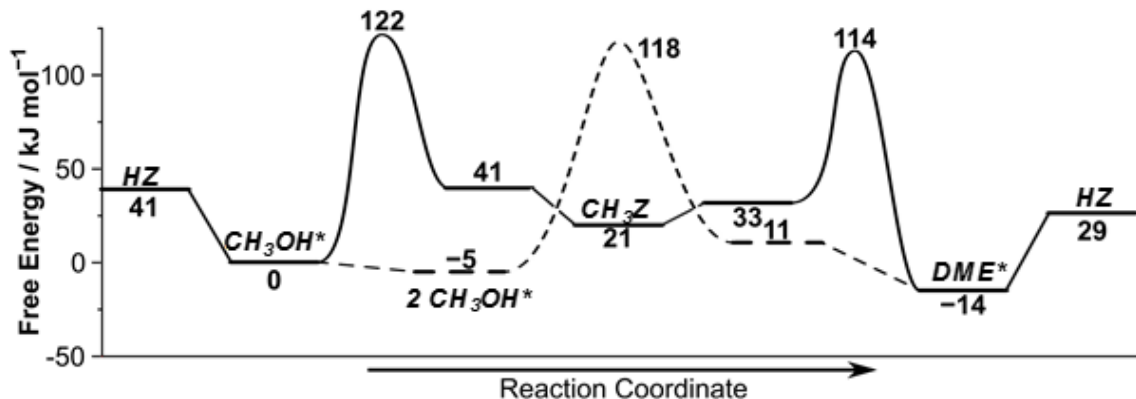
$$r_{DME,A} = \frac{k_{first,A} P_{CH_3OH}}{1 + \frac{k_{first,A}}{k_{zero,A}} P_{CH_3OH} + \frac{k_{first,A}}{k_{inhibit,A}} P_{CH_3OH}^2} \quad (C.28)$$

$$r_{DME,D} = \frac{k_{first,D} P_{CH_3OH}}{1 + \frac{k_{first,D}}{k_{zero,D}} P_{CH_3OH} + \frac{k_{first,D}}{k_{inhibit,D}} P_{CH_3OH}^2} \quad (C.29)$$

### C.2.1 Comparison of isolated protons in CHA and MFI

Methanol dehydration rates (415 K, per proton) measured on CHA zeolites (Chapter 8) containing predominantly isolated protons increase linearly at low methanol pressures, but approach a maximum and then decrease from inhibition at high methanol pressures (>10 kPa) [214]. IR spectra measured on CHA zeolites containing predominantly isolated protons under steady-state dehydration conditions (415 K, 0.1-22 kPa) do not show the formation of surface methoxy species, indicating that isolated protons in CHA zeolites dehydrate methanol via the associative mechanism. Additionally, density functional theory predicts a lower free energy activation barrier for DME formation via methanol monomers through protonated dimers (i.e., associative pathway) than dehydration of a methanol monomer to form a surface methoxy (i.e., dissociative pathway) on isolated protons in CHA (118 vs 122 kJ mol<sup>-1</sup>; Figure C.13). Associative dehydration zero-order rate constants (415 K, per H<sup>+</sup>) on CHA zeolites containing isolated protons are similar to those in MFI zeolites, indicating that isolated protons in CHA and protons in MFI are similar in acid strength [16, 83, 214]. First-order rate constants (415 K, per H<sup>+</sup>) on isolated protons in CHA are nearly 10x larger than in MFI, suggesting that this reaction occurs within a smaller void in CHA than in MFI [22]. This difference in first-order rate constant is similar to that expected from the difference in confinement between the 10-MR (ca. 0.56 nm) in MFI and the 8-MR (ca. 0.38 nm) window in CHA [214].

Figure C.13. DFT calculated free energies (433 K, 1 bar) for the associative (dashed) and dissociative (solid) methanol dehydration mechanisms on isolated protons in CHA.



First- and zero-order activation enthalpies ( $\Delta H$ ), entropies ( $\Delta S$ ), and Gibbs free energies ( $\Delta G$ ) were simultaneously estimated for isolated and paired protons in CHA by fitting DME formation rate data measured as a function of methanol pressure (0.05-50 kPa), temperature (383-423 K), and paired Al site content (0-44%) to equation C.30:

$$\frac{r_{DME}}{[H^+]} = \gamma \frac{k_{first}^p P_{CH_3OH}}{1 + \frac{k_{first}^p}{k_{zero}^p} P_{CH_3OH} + \frac{k_{first}^p}{k_{inverse}^p} P_{CH_3OH}^2} + (1 - \gamma) \frac{k_{first}^i P_{CH_3OH}}{1 + \frac{k_{first}^i}{k_{zero}^i} P_{CH_3OH} + \frac{k_{first}^i}{k_{inverse}^i} P_{CH_3OH}^2} \quad (C.30)$$

where  $\gamma$  is the fraction of protons in pairs,  $k_j^i$  are rate constants of isolated protons, and  $k_j^p$  are rate constants of paired protons. Apparent first, zero, and inhibiting rate constants were approximated using transition state theory:

$$k = \frac{k_b T}{h} e^{\frac{\Delta S}{R}} e^{\frac{-\Delta H}{RT}} (P_0 [\frac{100 kPa}{bar}])^{1-m} \quad (C.31)$$

where  $P_0$  is the standard state pressure of 1 bar to which the thermodynamic parameters are referred,  $m$  is the number of reactants that form the transition state,  $k_b$  is the Boltzmann constant,  $h$  is the Plank constant, and  $R$  is the ideal gas constant (8.314 J mol<sup>-1</sup> K<sup>-1</sup>). Apparent activation enthalpies and entropies for MFI were

obtained by fitting equation C.28 to a DME formation rate data (per  $\text{H}^+$ ) measured as a function of temperature (383-433 K) on two different MFI zeolites ( $\text{Si}/\text{Al} = 30, 43$ ). Activation parameters for protons in MFI and for isolated and paired protons in CHA are listed in Table C.1.

Table C.1.

Activation enthalpies, entropies, and free energies for first- and zero-order rate constants (415 K) at isolated and paired protons in CHA.

|                                | $\Delta H_{\text{zero}}$<br>/ $\text{kJ mol}^{-1}$ | $\Delta H_{\text{first}}$<br>/ $\text{kJ mol}^{-1}$ | $\Delta S_{\text{zero}}$<br>/ $\text{J mol}^{-1} \text{K}^{-1}$ | $\Delta S_{\text{first}}$<br>/ $\text{J mol}^{-1} \text{K}^{-1}$ | $\Delta G_{\text{zero}} (433 \text{ K})$<br>/ $\text{kJ mol}^{-1}$ | $\Delta G_{\text{first}} (433 \text{ K})$<br>/ $\text{kJ mol}^{-1}$ |
|--------------------------------|--|---|---|--|--|---|
| Jones <sup>a</sup>             | 90   | 42  | -75   | -160   | 123  | 111   |
| H-MFI                          |  |   |   |  |  |   |
| ( $\text{Si}/\text{Al} = 43$ ) | 92   | 37  | -61   | -165   | 118  | 108   |
| H-MFI                          |  |   |   |  |  |   |
| ( $\text{Si}/\text{Al} = 30$ ) | 91   | 46  | -62   | -143   | 117  | 108   |
| Isolated<br>CHA                | 115  | 60  | -7  | -98  | 117  | 101   |
| Paired CHA                     | 117  | 36  | 20  | -128   | 109  | 89  |

<sup>a</sup> Experimentally measured activation parameters on H-MFI ( $\text{Si}/\text{Al} = 30$ ) [Jones et al., *Angew.*, 2014]

First-order rate constants reflect differences in free energy between the same associative dehydration transition state and a methanol monomer and gas-phase methanol.  $\Delta G_{\text{first}}(433 \text{ K})$  are lower at isolated protons in CHA than at protons in MFI, consistent with larger first-order rate constants at isolated protons in CHA. As observed for associative zero-order rate constants,  $\Delta H_{\text{first}}$  is larger and  $\Delta S_{\text{first}}$  is lower at isolated protons in CHA than at protons in MFI. The higher  $\Delta H_{\text{first}}$  at isolated protons in CHA likely reflects the preferred stabilization of methanol monomers relative to the TS, while the lower  $\Delta S_{\text{first}}$  suggests that confinement of a gas-phase methanol to form the transition state is more entropically favorable in CHA than in MFI.



### C.2.2 Comparison of isolated and paired protons in CHA

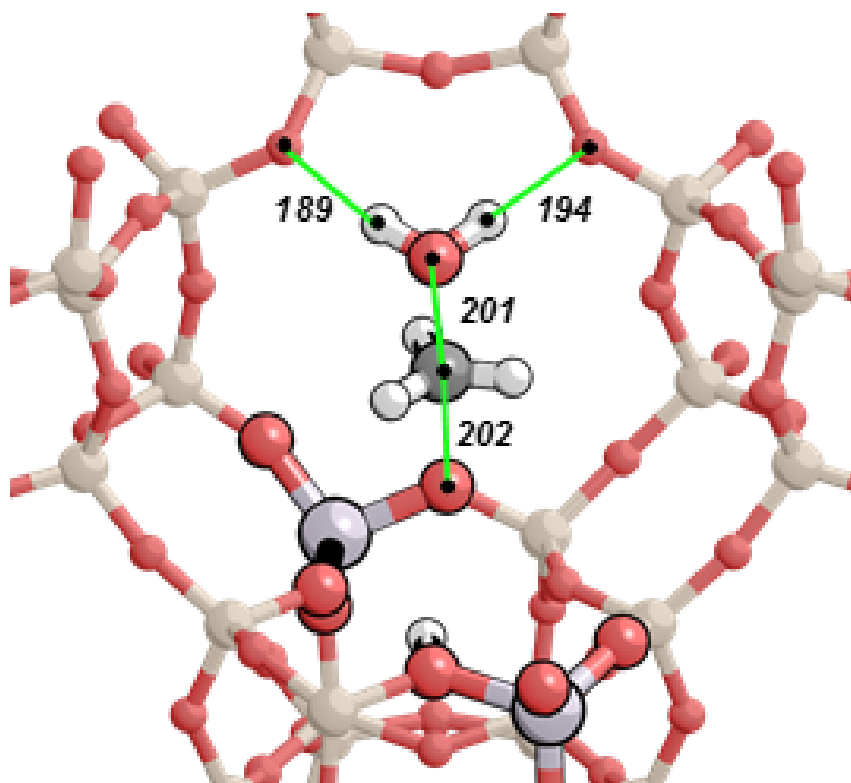
First- and zero-order methanol dehydration rate constants (415 K, per proton) are nearly 10x larger at paired protons than at isolated protons in CHA zeolites [214]. IR spectra measured under steady-state methanol dehydration conditions (415 K, 0.1-22 kPa) show the persistent presence of surface methoxy species on CHA zeolites containing paired Al sites. These results indicate that paired protons in CHA may allow methanol dehydration to proceed via the dissociative dehydration mechanism, which is inaccessible under equivalent operating conditions on isolated protons in CHA and protons in MFI zeolites (415 K, 0.1-22 kPa) [214]. Activation parameters estimated for paired protons in CHA (Table C.1) reflect those of the dissociative dehydration mechanism, which is assumed to occur only at paired protons, while those for isolated protons reflect the associative mechanism, assumed to occur only at isolated protons.

Differences in zero-order rate constants reflect differences in the free energy between the associative transition state and a protonated methanol dimer, and the dissociative transition state and a methoxy/methanol pair for isolated and paired protons, respectively.  $\Delta H_{zero}$  is similar for both the associative and dissociative pathways in CHA (Table C.1) reflecting similar stability between the two transition states and their respective intermediates.  $\Delta S_{zero}$ , however, is more positive at paired protons than at isolated protons. The small  $\Delta S_{zero}$  of the associative pathway likely reflects a transition state similar to the protonated dimer, but which loses some degrees of freedom of one of the methyl groups (Scheme C.1). In the dissociative pathway, the positive  $\Delta S_{zero}$  likely reflects the liberation of the strongly-adsorbed methoxy to form the transition state, assuming that both water and methanol have similar mobility in the gas-phase. Differences in first-order rate constants reflect differences in the free energy between the two different transition states and a methanol monomer and gas-phase methanol. Smaller  $\Delta H_{first}$  at paired protons reflects the difference in stability of the transition state and the methanol monomer, while gas-phase water and

methanol likely have similar gas-phase enthalpies. The larger  $\Delta H_{first}$  at isolated protons likely arise from adsorption of the second methanol at a methanol monomer to form the transition state (Scheme C.1).  $\Delta S_{first}$  is more negative at paired protons likely reflecting the large entropic penalty required to form a surface methoxy from a methanol monomer, despite the liberation of a gas-phase water molecule during methoxy formation. Negative  $\Delta S_{first}$  at isolated protons is likely reflective of adsorption and confinement of a gas-phase methanol required to form the transition state.

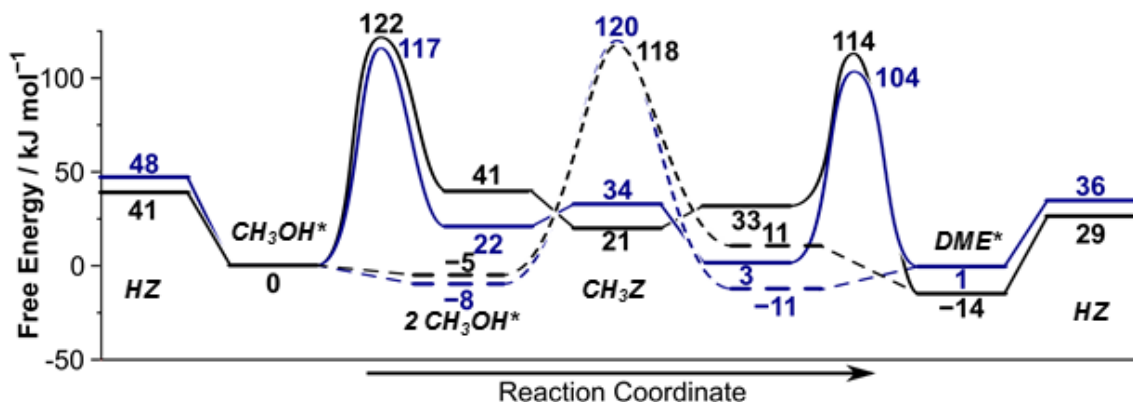
Experimentally derived activation parameters are able to provide some insight into the mechanistic underpinnings of methanol dehydration at paired and isolated sites, but are unable to rationalize this behavior with transition state structures or stabilities. Here, we turned to a preliminary DFT investigation to help shed light on why the dissociative pathway is favored at paired protons in CHA. The dissociative pathway proceeds through two distinct transition states to form water and a surface methoxy from a methanol monomer, and to form DME from a methoxy/methanol pair. Calculations at isolated protons showed that the barrier to form a surface methoxy is likely the rate-limiting barrier of the dissociative pathway (Figure C.13) and provide a starting point for this investigation. The stability of the methoxy transition state was probed by reorienting the bond angles between the four unique CHA framework oxygen atoms, methoxy, and water, which comprise the methoxy transition state, in order to determine the lowest energy structure. The methoxy transition state is preferentially stabilized in the 8-MR window adjacent to a paired proton (Figure C.14), because the size of the 8-MR (ca. 0.38 nm) allows the newly-formed water molecule to hydrogen bond with the adjacent oxygen atoms.

Figure C.14. Structure of the methoxy transition state at a paired proton in CHA. Values represent the distance between adjacent nuclei (green connectors) in pm.



Both the confinement of this transition state within the 8-MR and the stabilization of the conjugate anion by the second proton, result in a lower calculated free energy barrier for the dissociative pathway at a paired proton than for the associative pathway at either an isolated or paired site (Figure C.15). These results provide further evidence that methanol dehydration proceeds via the dissociative dehydration pathway at paired protons in CHA zeolites, and supports previous kinetic and spectroscopic evidence of methoxy formation and lower free energy barriers at paired protons in CHA.

Figure C.15. DFT calculated free energies (433 K, 1 bar) for the associative (dashed) and dissociative (solid) methanol dehydration mechanisms on isolated (black) and paired (blue) protons in CHA.

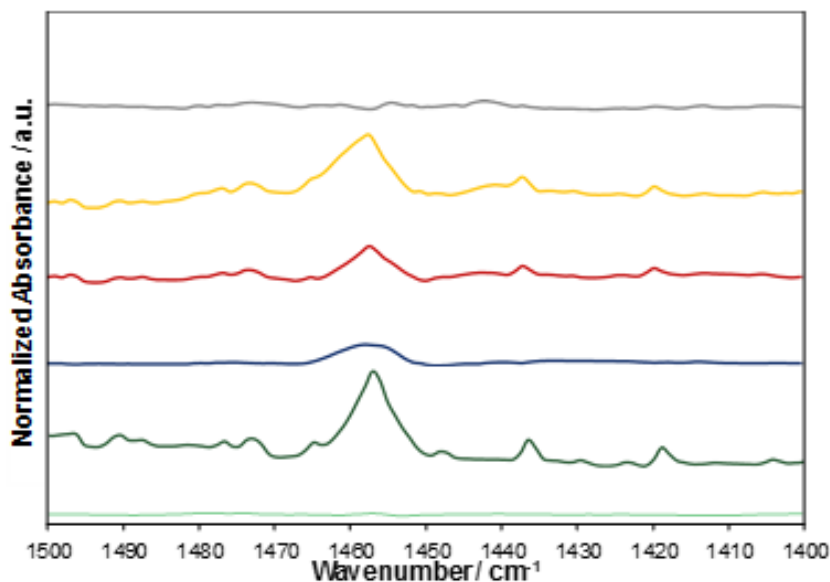


### C.3 Effect of paired protons in other zeolite frameworks

The observation made in CHA suggest that the presence of paired Al sites in a 6-MR adjacent to an 8-MR window are important for the stabilization of the methoxy transition state. Many other zeolite frameworks contain similar building structures to those found in CHA and provide a platform to further investigate methoxy formation in small-pore zeolites. CHA, LEV, AEI, and AFX zeolites are part of the AABBC zeolite family and contain double 6-MR adjacent to an 8-MR window, while RTH zeolites are built from chained 5-MR/4-MR building units and contain an 8-MR, but no adjacent 6-MR. LEV [511], AEI [270], AFX [34], and RTH [208] zeolites were synthesized according to reported procedures and all zeolites exchanged detectable amounts of Co<sup>2+</sup>, indicating the presence of paired Al sites. IR spectra measured on LEV, AEI, and AFX zeolites containing paired protons (12-34% paired Al) under steady-state methanol dehydration conditions (415 K, 0.77 kPa) reveal that surface methoxy species are present during methanol dehydration catalysis (Figure C.16). RTH zeolites, which were able to exchange Co<sup>2+</sup>, did not show the formation of surface methoxy under conditions where AEI, AFX, CHA, and LEV zeolites, which contained

paired protons, showed methoxy species (Figure C.16). These results further support the role of paired protons in the formation of surface methoxy species, but only when they are adjacent to an 8-MR window. This hypothesis still needs to be verified by measuring IR spectra on zeolites that contain 6-MR, but not double 6-MR, next to 8-MR (e.g., LTA) and on frameworks that contain paired Al in a double 6-MR, but no adjacent 8-MR (e.g., FAU). Additional experiments should be performed by synthesizing one of these alternative frameworks (e.g., AEI, AFX, LEV) with different fractions of paired Al sites to see if methoxy formation and methanol dehydration rates vary in the same way as observed in CHA [214].

Figure C.16. IR spectra of CHA containing 0% (light green) and 44% (dark green) paired Al, LEV (blue; Si/Al = 17, 12% paired Al), AEI (red; Si/Al = 16, 32% paired Al), AFX (yellow; Si/Al = 9, 34% paired Al), and RTH (grey; Si/Al = 15, 16% paired Al) under 0.77 kPa CH<sub>3</sub>OH at 415 K.





## D. SOLID-STATE NMR STRUCTURAL CHARACTERIZATION OF INORGANIC AND ORGANIC STRUCTURE DIRECTING AGENTS WITH FRAMEWORK AL ATOMS IN CHABAZITE ZEOLITES

### D.1 Introduction

Cationic structure-directing agents (SDA) direct the incorporation of Al into framework positions during zeolite crystallization [223, 224], but the interactions between mixtures of organic and inorganic SDAs with anionic Al centers are less well understood. Our initial investigation using a collaborative experimental and theoretical approach to probe different Al-Al arrangements in CHA zeolites synthesized using N,N,N-trimethyl-1-adamantyl ammonium (TMAda<sup>+</sup>) and different alkali (e.g., Na<sup>+</sup> or K<sup>+</sup>) cations is presented in Chapter 3. *Ab initio* molecular dynamics reveal that Al incorporation is directed by cationic structure directing agents and that bulky TMAda<sup>+</sup> molecules isolated framework Al atoms due to electrostatic interactions that prefer to separate like charges (e.g., anionic Al-Al in silica frameworks, or cationic N-N in quaternized nitrogen centers in SDAs) and minimize the distance between opposite charges (e.g., Al-N). Incorporation of different inorganic Na<sup>+</sup> cations disrupts the long-range ordering of Al and TMAda<sup>+</sup> and results in the stabilization of paired Al sites, relative to other Al-Al arrangements, because Na<sup>+</sup> cations prefer to locate and direct the placement of a second Al atom in the face of a six-membered ring in CHA. In this Appendix, we utilize solid-state magic angle spinning nuclear magnetic resonance (SS MAS NMR) techniques to probe the local coordination environment of TMAda<sup>+</sup> and Na<sup>+</sup> structure directing agents used in the crystallization of CHA zeolites that contain different amounts of paired and isolated Al sites.

## D.2 Sample Preparation

### D.2.1 Synthesis of CHA with different fractions of paired Al sites

CHA zeolites were synthesized using procedures reported in Chapters 3 and 8, and characterization data is provided in Table D.1.

| Sample               | Al Source                      | Na <sup>+</sup> /TMAda <sup>+</sup> <sup>a</sup> | Si/Al <sup>b</sup> | H <sup>+</sup> /Al <sup>c</sup> | Co/Al <sup>d</sup> | Na/Al <sup>b</sup> | TMAda <sup>+</sup> /Al <sup>e</sup> |
|----------------------|--------------------------------|--|--------------------|---------------------------------|--------------------|--------------------|-------------------------------------|
| A (OH <sup>-</sup> ) | Al(O-i-Pr) <sub>3</sub>        | 1  | 12                 | 0.85                            | 0.20               | 0.26               | 0.87                                |
| B (OH <sup>-</sup> ) | Al(OH) <sub>3</sub>            | 0  | 14                 | 0.95                            | 0.00               | <0.01              | 0.81                                |
| C (OH <sup>-</sup> ) | Al(OH) <sub>3</sub>            | 1  | 15                 | 1.01                            | 0.09               | 0.12               | 0.95                                |
| D (F <sup>-</sup> )  | Al <sub>2</sub> O <sub>3</sub> | 0  | 17                 | 1.02                            | 0.00               | <0.01              | 1.01                                |

<sup>a</sup> Na<sup>+</sup>/TMAda<sup>+</sup> molar ratio in synthesis solution

<sup>b</sup> Measured by atomic absorption spectroscopy; per total Al

<sup>c</sup> Measured by temperature programmed desorption of NH<sub>3</sub> after aqueous NH<sub>4</sub><sup>+</sup> ion-exchange

<sup>d</sup> Co<sup>2+</sup> ion-exchange on H-form zeolites; measured by AAS

<sup>e</sup> Determined by TGA weight loss after dehydration at 523 K

Table D.1.

Si/Al, H<sup>+</sup>/Al, Co/Al, Na<sup>+</sup>/Al, and TMAda<sup>+</sup>/Al data of CHA zeolites synthesized with different fractions of paired Al sites.

### D.2.2 Synthesis of N,N,N-trimethyl-d<sub>9</sub>-1-adamantylammonium hydroxide

The synthesis of N,N,N-trimethyl-d<sub>9</sub>-1-adamantylammonium iodide (TMAda-d<sub>9</sub>-I) was synthesized following the procedure reported by Zones for the unlabeled TMAdaI molecule<sup>Zones1985</sup>. A straight two-neck round-bottom flask (500 cm<sup>3</sup>) was connected to a reflux condenser and placed in an ice bath. 56.64 g of dimethyl formamide (99.7 wt%, Sigma-Aldrich) was added to the flask and stirred with an egg-shaped Teflon stir bar. 10 g of 1-adamantylamine (97 wt%, Sigma-Aldrich) was added to the flask and stirred until fully dissolved. 30 g of tributylamine (99 wt%, Sigma-Aldrich) was then added to the flask and the mixture was stirred for 5 minutes. A addition funnel (100 cm<sup>3</sup>) was attached to the second port of the flask and charged with 25 g of methyl-d<sub>3</sub> iodide (99.9%, Sigma-Aldrich) and added dropwise under stirring (ca. 1 drop per s).

**Caution: methyl iodide and tributylamine are extremely hazardous. Use**



*proper personal protective equipment and engineering controls to limit exposure.* The reaction mixture was allowed to slowly warm to room temperature and was stirred under an Ar purge for five days. Approximately 200 cm<sup>3</sup> of diethyl ether (99.9 wt%, Sigma-Aldrich) was added to the resulting slurry and stirred for 30 minutes to allow for further crystallization. The crystalline product was recovered through vacuum filtration using a porous glass frit (2-8  $\mu$ m pore size, Ace Glass) and resulted in a bronze colored slurry. This was then washed with 100 cm<sup>3</sup> of isopropyl alcohol (99.9 wt%, Sigma-Aldrich), resulting in pure white crystals. Residual isopropyl alcohol was evaporated overnight at room temperature leaving behind the TMAda-d<sub>9</sub>-I product (structure confirmed by <sup>1</sup>H and <sup>13</sup>C NMR in the results section).

TMAda-d<sub>9</sub>-I was converted to the OH- form via ion-exchange with Dowex Marathon A OH exchange resin. Approximately 5 grams of TMAda-d<sub>9</sub>-I was dissolved in ca. 10 g of deionized water (18.2 M $\Omega$  cm<sup>-1</sup>) and added to a 100 cm<sup>3</sup> burette packed with 50 cm<sup>3</sup> of hydrated resin. The TMAda-d<sub>9</sub> solution was allowed to pass through the resin at a rate of ca. 1 drop per second until all the solution had entered the packed bed. 25 cm<sup>3</sup> of deionized water was then added to the column and allowed to drain (ca. 1 drop per s) to flush the packed bed of any residual TMAda-d<sub>9</sub>-OH. The final purity and concentration was quantified by dropwise titration of the TMAda-d<sub>9</sub>-OH solution with 0.1 M HCl (38 wt% HCl, Macron Fine Chemicals) using phenolphthalein (ACS Reagent, Sigma-Aldrich) as an indicator. The final purity was measured to be >90% TMAda-d<sub>9</sub>-OH.

### D.2.3 Synthesis of CHA zeolites with TMAda-d<sub>9</sub>

CHA zeolites were synthesized with NaOH/TMAda-d<sub>9</sub>-I = 1 and without Na<sup>+</sup> using TMAda-d<sub>9</sub>-OH following previously reported procedures [42].

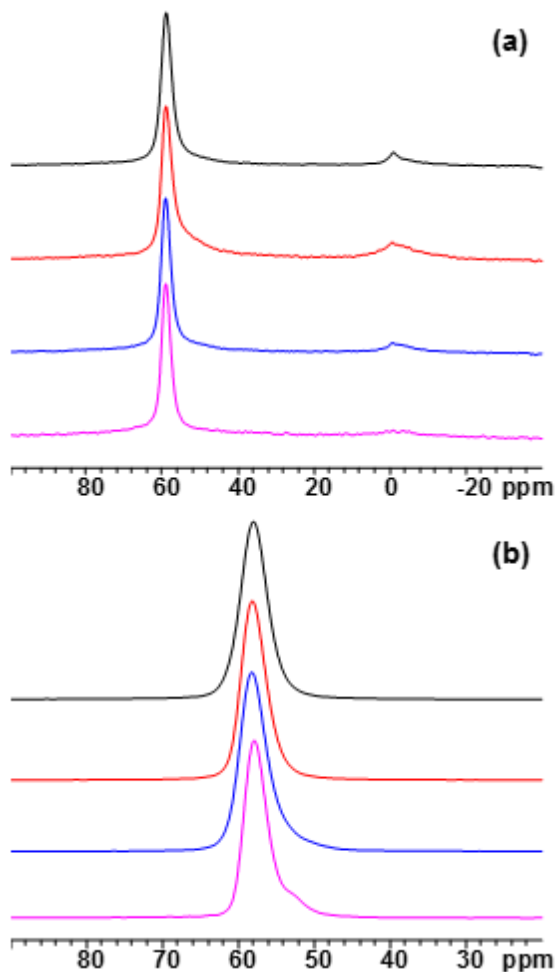
All samples were recovered from synthesis vessels via centrifugation and washed repeated with water and acetone to remove any residual synthesis media. Samples were then dried at 363 K for 24 hours and then the crystal structure was confirmed by X-ray diffraction (XRD). The total organic content was measured by thermal gravi-

metric analysis (TGA). Co-exchanged CHA zeolites were prepared following previously reported procedures [42]. Al, Na, and Co contents were measured by atomic absorption spectroscopy (AAS).  $\text{H}^+/\text{Al}$  values were measured using aqueous phase  $\text{NH}_3$  titrations described elsewhere [78,171].

### D.3 Results and Discussion

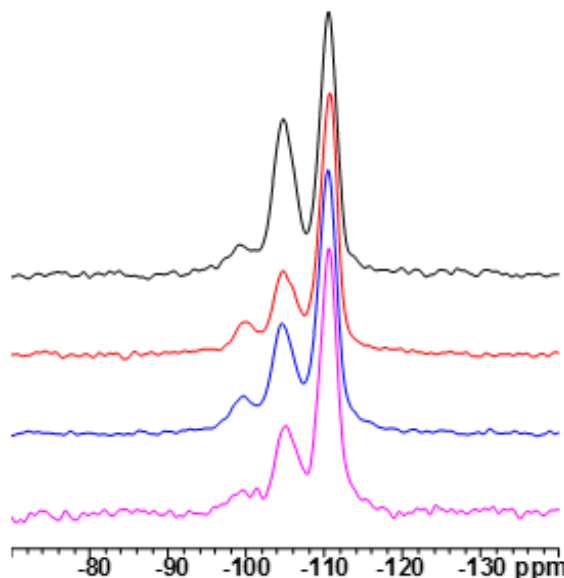
$^{27}\text{Al}$  SS MAS NMR spectra measured on as-synthesized CHA zeolites (Samples A-D) show predominantly tetrahedrally-coordinated Al atoms ( $\delta = 58$  ppm; Figure D.1) with a minority of octahedrally-coordinated Al ( $\delta = 0$  ppm; Figure D.1) in Samples A-C. Sample D showed an upfield shoulder ( $\delta = 52$  ppm) suggesting the presence of a secondary tetrahedral Al environment.

Figure D.1.  $^{27}\text{Al}$  SS MAS NMR spectra of Samples A (black), B (red), C (blue), and D (purple) over the whole range measured (a) and focused on the tetrahedral Al resonance (b).



$^{19}\text{F}$  SS MAS NMR did not show the presence of fluoride in as-synthesized Sample D, indicating that this shoulder is likely not due to pentahedrally-coordinated Al caused by coordination with fluoride anions present in the synthesis media.  $^{29}\text{Si}$  SS MAS NMR spectra revealed three different Si coordination environments (Figure D.2) with distinct chemical shifts corresponding to  $\text{Si}(\text{OSi})_4$  ( $\delta = -110$  ppm),  $\text{Si}(\text{OAl})(\text{OSi})_3$  ( $\delta = -105$  ppm), and either  $\text{Si}(\text{OAl})_2(\text{OSi})_2$  or  $\text{Si}(\text{OH})(\text{OSi})_3$  ( $\delta = -100$  ppm) connectivities.

Figure D.2.  $^{29}\text{Si}$  SS MAS NMR spectra of Samples A (black), B (red), C (blue), and D (purple).



Dynamic nuclear polarization NMR experiments were performed to try to enhance the signal-to-noise of both  $^{27}\text{Al}$  and  $^{29}\text{Si}$  MAS NMR spectra to resolve different coordination environments. DNP is used to enhance the sensitivity of NMR using microwave-promoted polarization transfer from unpaired electrons to nuclei, typically protons [512–514], whose hyperpolarization can be further transferred, via cross-polarization (CP), to the targeted heteroatom [515,516]. DNP enables acquisition of chemical shift anisotropy (CSA) parameters, which can then be compared to calculated values to discriminate local structure and location [513]. No enhancement of either  $^{29}\text{Si}$  or  $^{27}\text{Al}$  SS MAS NMR spectra were observed after microwave-promoted polarization of AMUPol-loaded CHA zeolites containing  $\text{TMAda}^+$ . We hypothesized that this was due to the presence of methyl groups on  $\text{TMAda}^+$  that inhibit hyperpolarization transfer from AMUPol radicals to protons inside the zeolite.  $\text{TMAda}^+$  was then synthesized from adamantylamine in the presence of deuterated methyl iodide ( $\text{CD}_3\text{I}$ ) to prepare  $\text{TMAda}^+ \text{-d-9-I}$  (Sample Prep). The presence of a quaternized N group with three  $\text{CD}_3$  groups was confirmed by the absence of methyl chemical

shifts in both  $^1\text{H}$  and  $^{13}\text{C}$  NMR spectra, and the presence of a  $^{13}\text{C}$  chemical shift of a C atom bound to a cationic N atom (Figure D.3). DNP-enhanced  $^{29}\text{Si}$  or  $^{27}\text{Al}$  MAS NMR spectra of CHA zeolites synthesized with TMAda+ $-d_9$  did not show improved signal-to-noise. Moreover, there was only minor enhancement of both  $^{29}\text{Si}$  or  $^{27}\text{Al}$  MAS NMR spectra on the hydrated H-form CHA (Figure D.4), suggesting that hyperpolarization transfer is inhibited in small-pore CHA zeolites.

Figure D.3.  $^{13}\text{C}$  NMR spectra of TMAda+ $-d_9$  dissolved in  $\text{D}_2\text{O}$  with an absent NMR line for methyl C ( $\delta = 48$  ppm). Inset shows the assignment of the different expected chemical shifts for TMAda+.

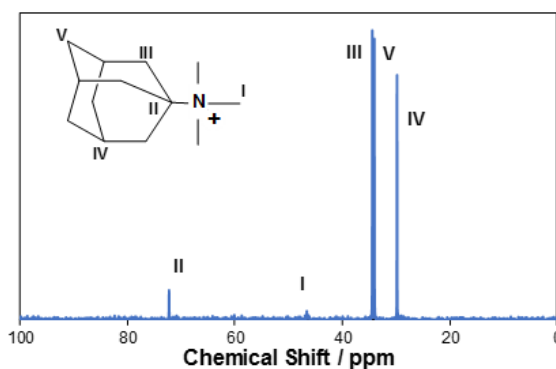
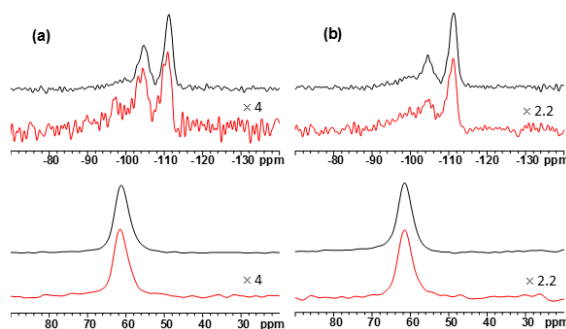


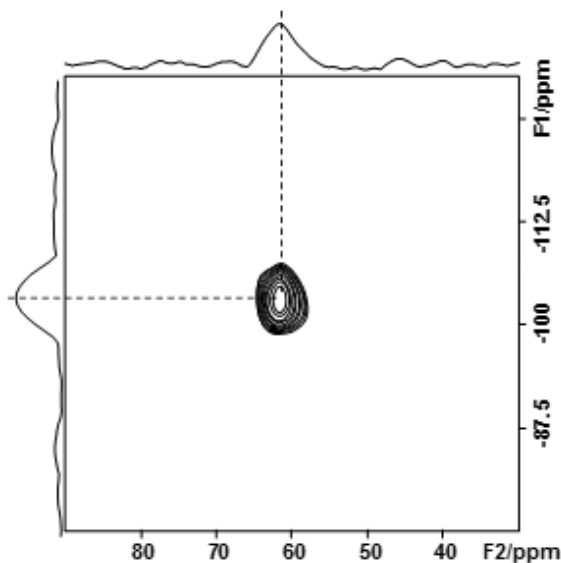
Figure D.4.  $^{29}\text{Si}$  (upper) and  $^{27}\text{Al}$  (lower) MAS DNP NMR spectra of Samples A (a) and C (b) without (black) and with (red) microwave-excitation.



$^{27}\text{Al}\{^{29}\text{Si}\}$  J-based insensitive nuclei enhanced by polarization transfer (INEPT) MAS NMR spectra (Figure D.5), which probe nuclear interactions through chemical bonds and are not affected by quadrupolar or dipole interactions [517, 518], revealed

a single cross-correlation between tetrahedrally-coordinated Al ( $^{27}\text{Al}$ ,  $\delta = 58$  ppm) and  $\text{Si}(\text{OAl})(\text{OSi})_3$  species ( $^{29}\text{Si}$ ,  $\delta = -105$  ppm), indicating that the  $^{29}\text{Si}$  feature at -100 ppm is due to silanol groups and that  $\text{Si}(\text{OAl})_2(\text{OSi})_2$  connectivities are absent in all samples studied, consistent with previous proposals [42].

Figure D.5.  $^{27}\text{Al}\{^{29}\text{Si}\}$  J-based INEPT MAS NMR spectrum of Sample A.



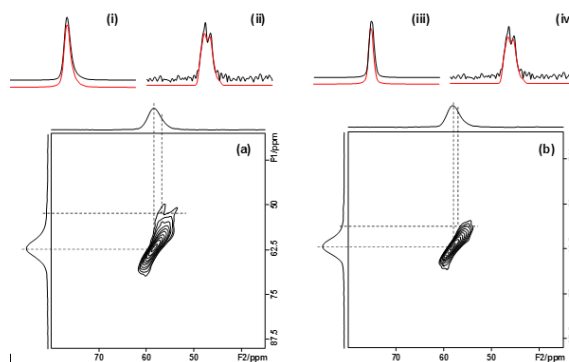
Triple quantum (3Q)  $^{27}\text{Al}$  SS MAS NMR experiments (Figure D.6), which minimize higher-order quadrupolar effects to resolve inequivalent sites and enable extraction of isotropic quadrupolar shifts [52,519], reveal two distinct Al environments with different quadrupolar coupling constants ( $C_Q$ ) and asymmetry parameters ( $\eta_Q$ ), but similar isotropic chemical shifts ( $\delta_{iso}$ ; Table D.2).

|                        | Sample C |        | Sample D |        |
|------------------------|----------|--------|----------|--------|
|                        | Site 1   | Site 2 | Site 1   | Site 2 |
| $C_Q$ / MHz            | 3.48     | 5.45   | 3.22     | 4.53   |
| $\eta_Q$ / <u>a.u.</u> | 0.51     | 0.44   | 0.53     | 0.30   |
| $\delta_{iso}$ / ppm   | 60       | 62     | 60       | 58     |

Table D.2.

Quadrupolar coupling constants ( $C_Q$ ), asymmetry parameters ( $\eta_Q$ ), and isotropic chemical shifts ( $\delta_{iso}$ ) for the two distinct sites observed on Samples C and D from 3Q 27Al SS MAS NMR spectra (Figure D.6).

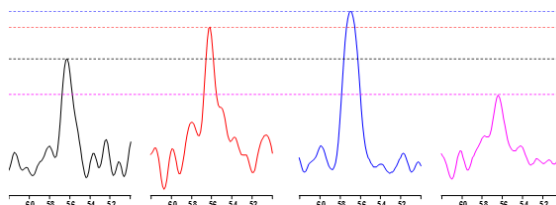
Figure D.6. 3Q 27Al SS MAS NMR spectra of Samples C (a) and D (b) and two distinct sites for Samples C ((i) and (ii)) and D ((iii) and (iv)).



CHA contains a single crystallographically-unique T-site, which should result in a single Al coordination environment. Moreover, these observations appear to be independent of interactions with extraframework cations, as Sample C is synthesized in the presence of both  $\text{Na}^+$  and  $\text{TMAda}^+$ , while only  $\text{TMAda}^+$  cations were used in the synthesis of Sample D. These multiple quantum spectra seem to reflect the presence of through-lattice interactions between adjacent framework Al centers [55,

520]. Homonuclear dipolar interactions between adjacent framework Al atoms were probed using  $^{27}\text{Al}$ - $^{27}\text{Al}$  single quantum-double quantum (SQ-DQ) MAS NMR [480, 521] and auto-correlation peaks between tetrahedrally-coordinated ( $^{27}\text{Al}$ ,  $\delta = 58$  ppm) framework Al atoms are shown in Figure D.7.

Figure D.7.  $^{27}\text{Al}$ - $^{27}\text{Al}$  SQ-DQ MAS NMR cross-correlation peaks of Samples A (black), B (red), C (blue), and D (purple). Dashed lines represent the magnitude of each cross-correlation peak for the corresponding samples (same color identities).



Auto-correlation peaks (i.e.,  $^{27}\text{Al}$ - $^{27}\text{Al}$  dipole interactions) were observed in each sample, indicating the presence of two Al atoms separated by less than ca. 6 Å [522]. Quantification of the distance between adjacent nuclei was not possible here, but could be achieved through calibration of SQ-DQ MAS NMR experiments using frameworks with precise Al-Al interatomic distances (e.g., AlPO frameworks). The magnitude of the Al-Al cross-correlation peak (Figure D.7) does not correlate with the total number of paired Al sites in Samples A-D, indicating that these samples contain additional Al-Al arrangements not limited to 2 Al atoms within the same six-membered ring (6-MR) of CHA. Furthermore, the presence of an auto-correlation peak in all samples indicates that 8-MR Al pairs, which may be separated by either two or three Si neighbors and are unable to exchange divalent  $\text{Co}^{2+}$  or  $\text{Cu}^{2+}$  cations [42, 79], contribute significantly to  $^{27}\text{Al}$ - $^{27}\text{Al}$  MQ spectra and convolute interpretation of these data sets into singular Al-Al arrangements, as has been previously suggested [523].

Next, we turn to probing the local environment of the extraframework SDA cations and their relationship with Al pairing.  $^{13}\text{C}$  SS MAS NMR spectra are similar for all as-synthesized CHA zeolites and are similar to  $^{13}\text{C}$  NMR spectra of TMAda+ in



solution [524], but do exhibit broadening of NMR lines consistent with confinement of the organic within CHA voids that limit free rotation (Figure D.8) [376,524].

Figure D.8.  $^{13}\text{C}$  SS MAS NMR spectra of as-synthesized CHA Samples A (black), B (red), C (blue), and D (purple). Inset shows the assignment of the five  $^{13}\text{C}$  NMR lines to the five unique C atoms of the TMA $^{+}$  molecule.

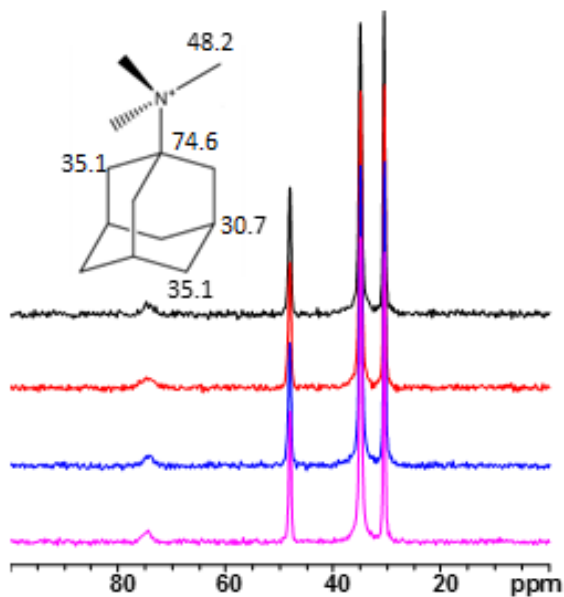
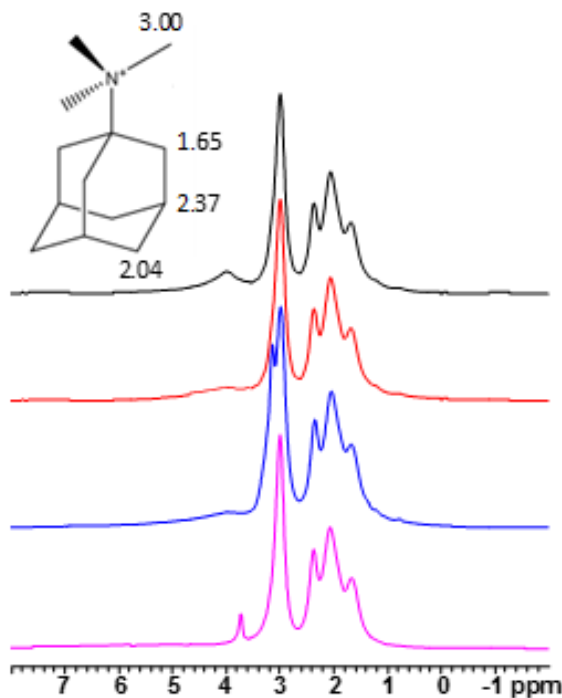
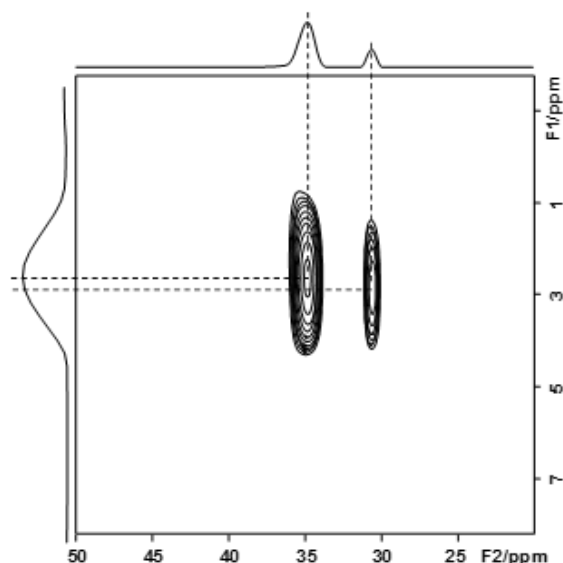


Figure D.9.  $^1\text{H}$  SS MAS NMR spectra of as-synthesized CHA Samples A (black), B (red), C (blue), and D (purple). Inset shows the assignment of the four unique H atoms of the TMAda<sup>+</sup> molecule.



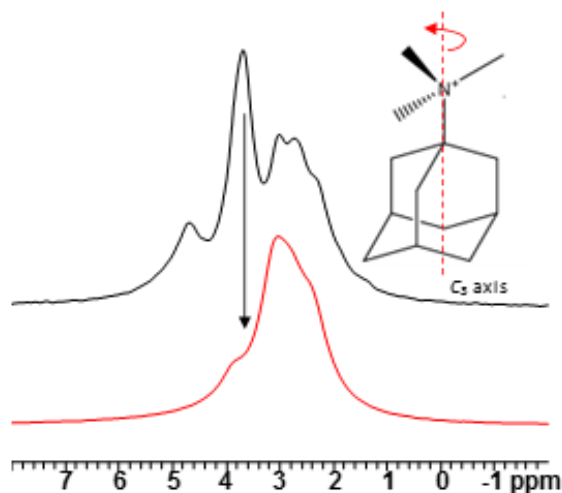
The presence of fully intact TMAda<sup>+</sup> was confirmed by  $^1\text{H}$  SS MAS NMR spectra (Figure D.9) and the assignment of the two  $^{13}\text{C}$  NMR lines at ca. 30.7 and ca. 35.1 ppm were confirmed using low-temperature (100 K)  $^1\text{H}$ - $^{13}\text{C}$  heteronuclear correlation (HETCOR) MAS NMR, which correlates two different nuclei chemically-bound together through spin-spin coupling (Figure D.10) [525].

Figure D.10.  $^1\text{H}$ - $^{13}\text{C}$  HETCOR SS MAS NMR spectra of as-synthesized Sample B measured at 100 K.



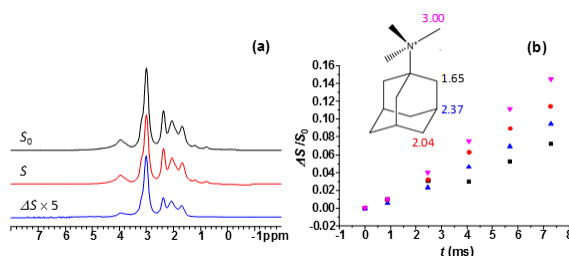
The dynamics of TMAda+ within the CHA cage was probed using variable-temperature  $^1\text{H}$  SS MAS NMR (293 K and 100 K) and show broadening of the methyl NMR line at 100 K, but not of other  $^1\text{H}$  NMR lines (adamantyl cage protons;  $\delta = 1.5\text{--}3$  ppm; Figure D.11). These results indicate that TMAda+ is free to rotate along its  $C_3$  axis, parallel to the  $c$ -axis of the CHA unit cell, but cannot rotate orthogonal to the  $c$ -axis of the CHA cage, consistent with *ab initio* molecular dynamics simulation presented in Chapter 4.

Figure D.11. Variable-temperature  $^1\text{H}$  SS MAS NMR spectra of Sample measured at 293 K (black) and 100 K (red). Black arrow is included to emphasize the broadening of the methyl  $^1\text{H}$  NMR line. Inset shows the  $\text{C}_3$ -axis of rotation of the TMAda+ molecule.



Cationic SDAs direct the placement of Al atoms into positions proximal to the quaternary N center during zeolite crystallization [80,200,223,224]. Rotational echo double resonance (REDOR) MAS NMR was used to probe the orientation of TMAda+ with respect to framework Al atoms by measuring the dipolar coupling between two heteronuclear nuclei (e.g.,  $^1\text{H}$  and  $^{27}\text{Al}$ ), which decays with distance ( $1/r^3$ ), and can be used as a probe of the distance separating the two interrogated nuclei [526].  $^1\text{H}\{^{27}\text{Al}\}$  REDOR MAS NMR was used to probe the distance between different H atoms on TMAda+ with framework Al atoms (magnitude of  $\Delta S/S_0$  reflects distance between nuclei; Figure 12) and indicated that Al atoms are located closest to methyl protons attached to the cationic end of TMAda+. It also appears that Al atoms are located near the back end of the adamantyl group, likely reflecting interactions of adamantyl protons with Al in an adjacent cage, and suggests that TMAda+ are oriented opposite to each other in adjacent cages.

Figure D.12.  $^1\text{H}\{^{27}\text{Al}\}$  REDOR MAS NMR spectra (a) without ( $S_0$ ) and with (S)  $^{27}\text{Al}$  dipolar dephasing of  $^1\text{H}$  spectra. (b) Shows the difference in dipolar dephasing of each unique proton in TMAda+ as a function of dephasing time.



Finally, the presence of  $^{23}\text{Na}$  was probed by MAS NMR and shows that Samples A-C contain  $\text{Na}^+$ , Sample D does not, likely reflecting a minor  $\text{Na}^+$  impurity in either the colloidal  $\text{SiO}_2$  source or  $\text{Al}(\text{OH})_3$  source used to synthesize Sample B. The concentration of  $\text{Na}^+$  in Sample B does appear to be in much lower quantities than Samples A or C (Figure D.13). After oxidative treatments to remove TMAda+, a sharpening of the  $^{23}\text{Na}$  MAS NMR lines is observed, indicating an increase in  $\text{Na}^+$  mobility, likely due to solvation by water (Figure D.13).

Figure D.13.  $^{23}\text{Na}$  MAS NMR of Samples A (black), B (red), and C (blue) before (a) and after (b) removal of TMAda+.

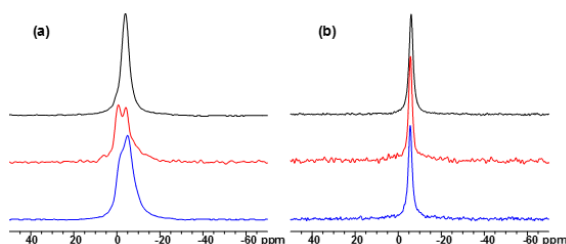
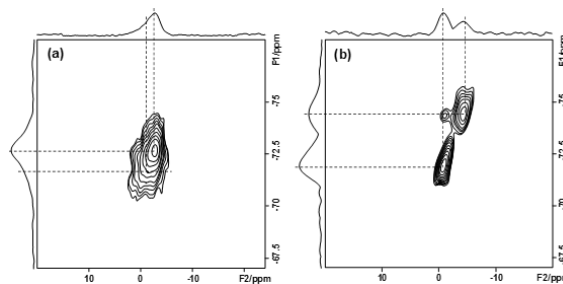
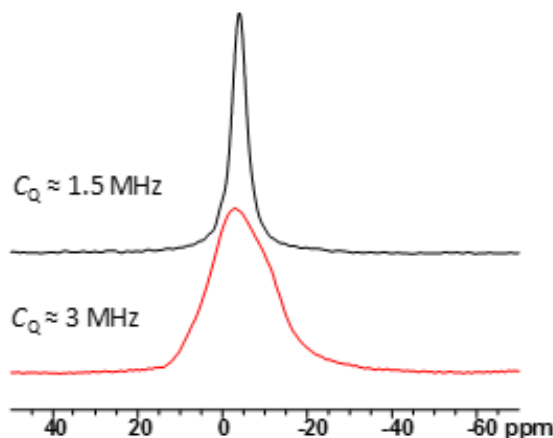


Figure D.14.  $^{23}\text{Na}$  3Q MAS NMR of Samples A (a) and C (b).

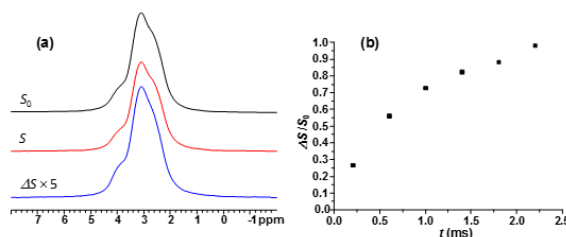
Two distinct  $\text{Na}^+$  environments were identified from  $^{23}\text{Na}$  triple-quantum (3Q) MAS NMR (Figure D.14) that likely reflect the incorporation of  $\text{Na}^+$  in different ring structures of CHA (e.g., 6-MR and 8-MR). Variable-temperature  $^{23}\text{Na}$  MAS NMR showed broadening of  $^{23}\text{Na}$  NMR lines and the emergence of a shoulder (Figure D.15), indicating the presence of multiple  $\text{Na}^+$  environments in as-synthesized CHA zeolites with different quadrupolar coupling constants ( $C_Q$ ), consistent with  $^{23}\text{Na}$  3Q MAS NMR spectra. These spectra suggest that at room temperature (ca. 293 K),  $\text{Na}^+$  cations are mobile even in the presence of TMAda+.

Figure D.15. Variable-temperature  $^{23}\text{Na}$  MAS NMR spectra taken at 293 K (black) and 100 K (red).

Finally, variable-temperature  $^1\text{H}\{^{23}\text{Na}\}$  REDOR MAS NMR showed no correlation between  $\text{Na}^+$  and the methyl protons on TMAda+ at room temperature, but a

strong correlation was observed at 100 K (Figure D.16), indicating that Na<sup>+</sup> cations are located near the quaternary N atom of TMAda<sup>+</sup>, but that Na<sup>+</sup> is free to move relative to TMAda<sup>+</sup>.

Figure D.16.  $^1\text{H}\{^{23}\text{Na}\}$  REDOR MAS NMR spectra (a) without ( $S_0$ , black) and with ( $S$ , red)  $^{23}\text{Na}$  dipolar dephasing of  $^1\text{H}$  spectra measured at 100 K. (b) Shows the difference in dipolar dephasing of methyl protons in TMAda<sup>+</sup> with  $^{23}\text{Na}$  as a function of dephasing time.



While this NMR analysis of the interactions of Na<sup>+</sup> and TMAda<sup>+</sup> with different Al arrangements in CHA is still incomplete, it does provide evidence that Na<sup>+</sup> atoms are incorporated near the quaternary N atom of TMAda<sup>+</sup> in CHA zeolites that contain paired Al sites. These results are consistent with previous proposals of Al siting in CHA [42] and DFT calculations of different Al-Al arrangements with Na<sup>+</sup> and TMAda<sup>+</sup> in CHA (Chapter ??). Selective titrimetric probes of Al-Al pairs in the 8-MR of CHA would provide complimentary evidence to  $^{27}\text{Al}$ - $^{27}\text{Al}$  auto-correlation in SQ-DQ MAS NMR spectra that indicate that even CHA zeolites that are unable to exchange  $\text{Co}^{2+}$  may still have two Al atoms located within the same ring (e.g., 8-MR). Furthermore,  $^1\text{H}$ - $^1\text{H}$  SQ-DQ MAS NMR experiments could be used to probe auto-correlation between Bronsted acid sites, which are not corrupted by quadrupolar broadening, to look for the presence of Al-Al pairs in H-form zeolites with higher sensitivity than  $^{27}\text{Al}$ - $^{27}\text{Al}$  SQ-DQ MAS NMR spectra. Resonant echo adiabatic passage double resonance (REAPDOR) MAS NMR, which allows for correlating dipole moments between spin-1/2 (e.g.,  $^{29}\text{Si}$ ) and quadrupolar nuclei (e.g.,  $^{23}\text{Na}$ ,  $^{27}\text{Al}$ ), something that is not possible in standard REDOR pulse-sequences [527], can also be used to identify interactions between  $^{23}\text{Na}$  and  $^{29}\text{Si}$  (e.g.,  $\text{Si}(\text{OAl})(\text{OSi})_3$ ),

at low-temperatures where Na<sup>+</sup> mobility is minimized. Low-temperature (100 K)  $^{23}\text{Na}\{^{27}\text{Al}\}$  and  $^{27}\text{Al}\{^{23}\text{Na}\}$  REAPDOR MAS NMR spectra may also be able to provide insight into the nature of the different Al and Na environments identified by multiple-quantum NMR spectra gathered here.



## E. TITRATION AND QUANTIFICATION OF OPEN AND CLOSED LEWIS ACID SITES IN TIN-BETA ZEOLITES THAT CATALYZE GLUCOSE ISOMERIZATION

### E.1 Introduction

Pure-silica molecular sieve frameworks containing Lewis acidic tetravalent heteroatoms (e.g.,  $\text{Sn}^{4+}$ ,  $\text{Ti}^{4+}$ ) catalyze a range of oxidation reactions [528–532], including the concerted Meerwein-Ponndorf-Verley carbonyl reduction (aldehyde, ketone) and Oppenauer alcohol oxidation via intramolecular or intermolecular cycles (MPVO), with recent attention focused on MPVO reactions of biomass-derived oxygenates containing carbonyl moieties [28, 191, 533–536]. Lewis acidic heteroatoms (M) can be tetrahedrally coordinated ( $\text{M}(\text{OSi})_4$ , “closed” site) or tri-coordinated ( $(\text{HO})\text{-M}(\text{OSi})_3$ ; “open” site) to the zeolite framework [537], each with its own strength and reactivity. Lewis acidic Sn-Beta zeolites have been prepared by direct hydrothermal crystallization (fluoride-assisted [529, 538], hydroxide-assisted [539] and by several indirect post-synthetic modifications, which first involve removing framework silicon atoms [540, 541] or heteroatoms (e.g., Zn, Al) [191] to form vacancy defects, followed by insertion of Lewis acidic heteroatoms (e.g., Sn, Ti) via vapor-phase deposition [542], via liquid-phase reflux or exchange [543–546], or via solid-state ion exchange [547–549]. Sn-Beta zeolites prepared by such diverse methods and treatments differ in their distribution of open and closed sites [550] and their density of other structures (e.g., Si-OH defects), requiring methods to quantify the number of open and closed sites in order to interpret turnover rate differences among samples of varying origin or treatment history.

Experimental and theoretical assessments of the strength of Lewis acid sites, inferred from their interactions with Lewis base probes, indicate that open sites are

stronger than closed sites in Sn-Beta. Deuterated acetonitrile ( $\text{CD}_3\text{CN}$ ) binding to framework Sn sites involves donation of electron density from the HOMO of  $\text{CD}_3\text{CN}$  (localized at the nitrogen atom) to the LUMO of the Sn site (a combination of the four antibonding  $\sigma^*(\text{Sn-O})$  orbitals) and concomitant lengthening of the four Sn-O bonds, which occurs to a greater extent in open Sn sites than in less flexible closed Sn sites according to theory (ONIOM and DFT) [550]. These findings are consistent with experiment, which has noted that infrared  $\nu(\text{C}\equiv\text{N})$  stretches for gas-phase  $\text{CD}_3\text{CN}$  ( $2265\text{ cm}^{-1}$ ) are more strongly perturbed when bound to open ( $2316\text{ cm}^{-1}$ ) than to closed Sn sites ( $2308\text{ cm}^{-1}$ ), and that IR peaks for  $\text{CD}_3\text{CN}$  bound to closed sites disappear preferentially upon evacuation of  $\text{CD}_3\text{CN}$ -saturated surfaces (298-433 K) [550-552]. Sn-Beta zeolites saturated with ammonia at 298 K and then evacuated at 393 K give rise to  $^{119}\text{Sn}$  NMR resonances for tetrahedrally-coordinated closed sites (ca. -443 ppm) but not for tetrahedrally-coordinated open sites (ca. -420 ppm), which instead appear as broad resonances characteristic of penta-coordinated Sn (-500 to -600 ppm; e.g.,  $(\text{NH}_3)(\text{HO})\text{-Sn-(OSi)}_3$ ) [551], indicating that  $\text{NH}_3$  binds more strongly at open Sn sites. Furthermore,  $\text{NH}_3$ -saturated Sn-Beta zeolites that are subsequently exposed to  $\text{CD}_3\text{CN}$  (308 K) show IR peaks at  $2308\text{ cm}^{-1}$  but not at  $2316\text{ cm}^{-1}$  [551], indicating that  $\text{NH}_3$  binds more strongly than  $\text{CD}_3\text{CN}$  to open Sn sites, as also predicted by DFT [553]. Taken together, these spectroscopic data and theoretical calculations provide evidence that open Sn sites bind Lewis bases more strongly than closed Sn sites in Sn-Beta. Experimental and theoretical assessments of catalytic oxidation reactivity also provide evidence that open sites are more reactive Lewis acid sites than closed sites in Sn-zeolites. Boronat et al. varied the distribution of open and closed sites in Sn-Beta by varying calcination conditions (e.g., humidity, bed depth) and observed that the initial rate of Baeyer-Villiger oxidation of adamantanone with aqueous  $\text{H}_2\text{O}_2$  (per g, 363 K, dioxane solvent) correlated linearly with IR peak areas for  $\text{CD}_3\text{CN}$  bound to open Sn sites, but not for  $\text{CD}_3\text{CN}$  bound to closed Sn sites [550]. Bermejo-Deval et al. exchanged sodium cations onto silanol groups proximal to open Sn sites in Sn-Beta and observed suppression of glucose-fructose

isomerization rates (per g, 353 K), concluding that open Sn sites were the dominant active site for this intramolecular MPVO reaction [551]. These experimental findings are consistent with activation enthalpies for intramolecular 1,2-hydride shift steps in glucose-fructose isomerization sequences that theory has predicted to be 5-10 kcal mol<sup>-1</sup> lower on open than on closed Sn sites [554–556]. Both theory and experiment indicate that open Sn sites are stronger Lewis acids and more reactive in oxidation reactions than closed sites, but these two types of sites have yet to be quantified precisely in Sn-zeolites, as required for rigorous normalization of catalytic turnover rates.

Pyridine is used as a base titrant of Lewis acid sites because it gives rise to IR peaks at 1455 cm<sup>-1</sup> and 1623 cm<sup>-1</sup> for perturbed gas-phase ring deformation modes (1439 cm<sup>-1</sup> and 1580 cm<sup>-1</sup>, respectively) when present in Lewis-bound adducts [557–560], but it does not distinguish between open and closed Lewis acid sites. As a result, pyridine titration of Sn-Beta zeolites has been used only to detect the presence of Lewis acidic Sn [377, 561], to infer the density of Lewis acidic Sn sites from integrated IR peak areas [542, 562], or to quantify the number of Lewis acidic Sn sites using integrated molar extinction coefficients ( $\mathcal{E}$ ) for Lewis acidic Al sites [545, 556, 563, 564]. Carbon monoxide has also been used as a base titrant to identify open (2185 cm<sup>-1</sup>) and closed (2176 cm<sup>-1</sup>) Lewis acidic Zr sites in Zr-Beta zeolites and to infer their density from integrated IR peak areas [565]. Deuterated acetonitrile, which is used to avoid Fermi resonance between the  $\nu(\text{C}\equiv\text{N})$  stretching mode and a combination of the symmetric  $\nu(\text{C}-\text{C})$  and deformation  $\nu(\text{CH}_3)$  modes in  $\text{CH}_3\text{CN}$  [566, 567], can distinguish between open (2316 cm<sup>-1</sup>) and closed (2308 cm<sup>-1</sup>) Lewis acid sites in Sn-Beta zeolites [547, 550–552]. These different IR vibrational stretching frequencies have been proposed to reflect supra-stoichiometric  $\text{CD}_3\text{CN}$  binding to Sn sites or the presence of additional  $\text{CD}_3\text{CN}$  within the immediate vicinity, based on temperature programmed desorption-thermogravimetric analysis (TPD-TGA) of  $\text{CD}_3\text{CN}$ -saturated Sn-Beta samples that evolved 1.6 mol  $\text{CD}_3\text{CN}$  per mol Sn [568] and reports of solvent-induced shifts in  $\text{CD}_3\text{CN}$  IR vibrations [569]. Yet, the distinct assignments of IR peaks to one  $\text{CD}_3\text{CN}$

bound at open ( $2316\text{ cm}^{-1}$ ) or closed ( $2308\text{ cm}^{-1}$ ) Sn sites are consistent with  $\nu(\text{C}\equiv\text{N})$  stretches predicted by density functional theory [550] and with their correlations to  $^{119}\text{Sn}$  NMR resonances for tetrahedral open (ca.  $-420\text{ ppm}$ ) and closed Sn sites (ca.  $-443\text{ ppm}$ ) in dehydrated Sn-Beta zeolites [554].  $\text{CD}_3\text{CN}$  has been used to infer the relative density of open and closed sites in Sn-Beta from integrated IR peak areas [550], and to quantify Lewis acidic Zn sites in Zn-exchanged Al-Beta using  $E$  values for  $\text{CD}_3\text{CN}$  bound to Lewis acidic Al sites [570, 571], but to our knowledge, it has not yet been used to quantify the number of open and closed Sn sites in Sn-zeolites. Here, for the first time, integrated molar extinction coefficients ( $\mathcal{E}$ ;  $\text{cm}\ \mu\text{mol}^{-1}$ ) are measured and reported for IR peaks of pyridine adsorbed on Lewis acidic Sn sites and of  $\text{CD}_3\text{CN}$  adsorbed on open and closed Sn sites in Sn-zeolites. We use these  $E$  values to quantify open and closed Sn sites on stannosilicates, focusing on Sn-Beta as a representative zeolite topology for which several different preparation strategies have been reported [191, 539, 541–547, 549, 563]. We demonstrate that the total number of Lewis acidic Sn sites on a given sample, taken as the number of open and closed Sn sites titrated by  $\text{CD}_3\text{CN}$  (1:1  $\text{CD}_3\text{CN}:\text{Sn}$ ) in IR experiments, agrees quantitatively with the number of Sn sites titrated by pyridine (1:1 pyridine:Sn) in IR experiments and by ammonia (1:1  $\text{NH}_3:\text{Sn}$ ) and n-propylamine (1:1 NPA:Sn) in TPD experiments. We also show that the number of active Sn sites in Sn-Beta can be estimated by partial poisoning with pyridine titrants prior to aqueous-phase glucose isomerization catalysis, which provides further evidence that the open Sn site is the predominant active site for glucose-fructose isomerization [551]. We use the number of open Sn sites to normalize initial turnover rates of glucose-fructose isomerization, chosen as a model intramolecular MPVO reaction for which mechanistic interpretation of rate data is tractable, prior to interpreting the catalytic consequences of structural heterogeneities prevalent among Sn-Beta zeolites prepared by different synthetic or post-synthetic methods.

## E.2 Experimental Methods

### E.2.1 Catalyst Synthesis

Sn-Beta samples were synthesized directly in fluoride media (Sn-Beta-F) at different Si/Sn ratios (Sn-Beta-F-X, X = Si/Sn) by adapting the method reported by Chang et al. [377], who prepared a seed solution comprising dealuminated Beta zeolites (filtered to retain particles <200 nm in diameter) dispersed in water via sonication. Here, dealuminated Beta zeolites (unfiltered) were used as seed material, and were prepared by adding 5 g of H-form Al-Beta (Zeolyst, CP814C, Si/Al=19) to 125 cm<sup>3</sup> of concentrated nitric acid (HNO<sub>3</sub>, Avantor, 69 wt%) and stirring for 16 h at 353 K. Dealuminated Beta solids were collected via centrifugation, washed thoroughly with deionized water (18.2 MΩ, 6 washes, 25 cm<sup>3</sup> (g zeolite)<sup>-1</sup> per wash), and then dried for 16 h at 373 K. The Sn-Beta synthesis gel was prepared by mixing 6.98 g of tetraethylorthosilicate (TEOS, Sigma Aldrich, >98 wt%) and 7.67 g of tetraethylammonium hydroxide (TEAOH, Sachem, 35 wt%) in a perfluoroalkoxy alkane (PFA) container (Savillex Corp.) and stirring for 1 h, followed by dropwise addition of a solution of 0.04-0.12 g of tin (IV) chloride pentahydrate (SnCl<sub>4</sub>·5H<sub>2</sub>O, Sigma-Aldrich, 98 wt%) in 0.64 g of deionized water. The resulting gel was stirred in a closed PFA container for 12 h, and then ethanol (6.04 g) and excess water (1.95 g) were allowed to evaporate. Next, 0.74 g of hydrofluoric acid (HF, Alfa Aesar, 48%) were added into the solution in a fume hood and stirred manually with a Teflon spatula for 300 s and residual HF allowed to evaporate for an additional 900 s. After homogenization, 0.579 cm<sup>3</sup> of water and 0.085 g of dealuminated Beta seeds (ca. 4.1 wt% of SiO<sub>2</sub>) were added and the gel was stirred manually with a Teflon spatula. The final molar composition of the gel was 1 SiO<sub>2</sub>/x SnCl<sub>4</sub>/0.56 TEAOH/0.54 HF/8.38 H<sub>2</sub>O, where x ranged between 0.003 and 0.01. This gel was transferred into a Teflon-lined stainless steel autoclave (45 cm<sup>3</sup>, Parr Instruments) and heated at 413 K in an isothermal oven (Yamato DKN-402C) with rotation (ca. 60 rpm) for either 6 days (Sn-Beta-F-105 and Sn-Beta-F-140) or 14 days (Sn-Beta-F-100, Sn-Beta-F-110, Sn-Beta-F-170, Sn-

Beta-F-220). The products were removed from the Teflon liner, washed thoroughly with water and acetone (Sigma Aldrich, >99.5 wt%, 5 washes each, ca. 25 cm<sup>3</sup> (g zeolite)<sup>-1</sup> per wash)), isolated by centrifugation, and dried for 16 h at 373 K. The dry zeolite powders were then treated in dry air (Ultra Zero Grade, Indiana Oxygen, 1.67 cm<sup>3</sup> s<sup>-1</sup> (g zeolite)<sup>-1</sup>) to 853 K (0.0167 K s<sup>-1</sup>) and held for 10 h in a muffle furnace (Nabertherm LE 6/11 equipped with a P300 controller). Two Sn-Beta samples were prepared via the post-synthetic reflux method reported by Dijkmans et al. (samples denoted Sn-Beta-OH) [543]. First, H-form Al-Beta zeolites (gel Si/Al molar ratios of 30 or 100) were synthesized by adapting the method reported by Chang et al. [377] without the aluminosilicate gel filtration step, followed by washing the crystalline solids thoroughly with water and acetone, recovering the solids by centrifugation, drying overnight at 373 K, and then treating in air (Ultra Zero Grade, Indiana Oxygen, 1.67 cm<sup>3</sup> s<sup>-1</sup> (g zeolite)<sup>-1</sup>) to 853 K (0.0167 K s<sup>-1</sup>) for 10 h in a muffle furnace. H-Beta zeolites with solid Si/Al ratios of 25 and 80 were dealuminated using the HNO<sub>3</sub> treatment described above (residual Si/Al >680 measured by AAS), and then used as the starting material to prepare Sn-Beta-OH-170 and Sn-Beta-OH-200, respectively. For Sn-Beta-OH-170, 2 g of dealuminated Beta was treated in air (Ultra Zero Grade, Indiana Oxygen, 1.67 cm<sup>3</sup> s<sup>-1</sup> g zeolite<sup>-1</sup>) to 853 K (0.0167 K s<sup>-1</sup>) for 10 h, and then 2 g were placed in a round bottom flask (500 cm<sup>3</sup>) and dried overnight at 423 K under rough vacuum (ca. 0.04 Torr, Oerlikon Trivac 140002E2) on a Schlenk line. For Sn-Beta-OH-200, the dealuminated Beta was not treated in air prior to the drying step under rough vacuum at 423 K. Next, isopropanol (Avantor, ChromAR HPLC Grade, >99.5 wt%) was dried over 3A molecular sieves (W. R. Grace, Type 3A, Grade 562, 4-8 mesh) for 72 h, and then transferred into the flask containing the dried dealuminated zeolite via air- and moisture-free cannula transfer. Separately, SnCl<sub>4</sub>·5H<sub>2</sub>O (0.027 or 0.081 mol Sn (g zeolite)<sup>-1</sup>) was added to a 50 cm<sup>3</sup> flask sealed with a septum (white rubber, Ace Glass), and dissolved in dry isopropanol transferred into the flask via gas-tight syringe. The isopropanolic SnCl<sub>4</sub>·5H<sub>2</sub>O solution was then transferred to the round bottom flask containing the dealuminated Beta,

and the contents were refluxed in argon (Indiana Oxygen, 99.999%) for 7 h. The solids were collected by centrifugation, washed 6 times (ca. 60 cm<sup>3</sup>) with isopropanol to prepare Sn-Beta-OH-170, or with methanol (Sigma Aldrich, >99.9%) to prepare Sn-Beta-OH-200, and then dried 16 h at 373 K. Washing the solids with methanol after the reflux procedure has been reported to remove residual SnCl<sub>4</sub> that leads to extraframework Sn upon air treatment at 823 K [545]. The dried solids were treated in air (Ultra Zero Grade, Indiana Oxygen, 1.67 cm<sup>3</sup> s<sup>-1</sup> (g zeolite)<sup>-1</sup>) at 473 K (0.05 K s<sup>-1</sup>) for 6 h, and then at 823 K (0.05 K s<sup>-1</sup>) for 6 h in a muffle furnace. Sn-xerogel was synthesized according to the procedure from van Grieken et al. [572]. 5.74 g of a 0.1 M HCl solution (Macron, 37%) were stirred with 52.0 g of TEOS and 67.6 g of deionized water for 2 h at ambient temperature. Then, 0.77 g of SnCl<sub>4</sub>·5H<sub>2</sub>O were added and the mixture stirred for 1 h. Finally, a 1 M NH<sub>4</sub>OH solution (Sigma Aldrich, 28%-30 wt% NH<sub>3</sub> basis) was added dropwise until the gel point was reached (ca. 12 cm<sup>3</sup>). The resulting clear gel was dried at 433 K for 12 h. The dried solids were then thoroughly washed with deionized water (5-10x, ca. 60 cm<sup>3</sup> per wash) until a stable pH was reached, dried at 433 K for 12 h, and then treated in air (Ultra Zero Grade, Indiana Oxygen, 1.67 cm<sup>3</sup> s<sup>-1</sup> (g zeolite)<sup>-1</sup>) to 853 K (0.0167 K s<sup>-1</sup>) for 10 h in a muffle furnace. A sample containing predominantly extraframework SnO<sub>2</sub> was prepared via incipient wetness impregnation of 1.12 g of a SnCl<sub>4</sub>·5H<sub>2</sub>O solution (0.60 M) on 1.82 g of as-made Si-Beta crystallized in fluoride medium [538] (sample denoted SnO<sub>2</sub>/Si-Beta). The impregnated solids were dried under rough vacuum at ambient temperature for 16 h, then treated in air (Ultra Zero Grade, Indiana Oxygen, 1.67 cm<sup>3</sup> s<sup>-1</sup> (g zeolite)<sup>-1</sup>) at 853 K (0.0167 K s<sup>-1</sup>) for 10 h in a muffle furnace.

### E.2.2 Catalyst Characterization

Bulk elemental compositions of samples were determined using atomic absorption spectroscopy (AAS) performed with a Perkin Elmer AAnalyst 300 Atomic Absorption Spectrometer. 1000 ppm AAS standards (Alfa Aesar, TraceCERT, +/- 4 ppm) for each metal were diluted to create calibration standards, and the instrument was cal-

ibrated for each element prior to collecting measurements. Zeolite samples (typically 0.02 g) were dissolved in 2 g of HF (48 wt%, Alfa Aesar) overnight and then further diluted with 30 g of deionized water. Absorbance values were measured at 396.2 nm and 284.0 nm in an acetylene/nitrous oxide flame for Al and Sn, respectively. Al and Sn weight fractions were used together with the unit cell formula for zeolite Beta to estimate Si/Al and Si/Sn ratios, respectively. Powder X-ray diffraction (XRD) patterns were collected on a Rigaku Smartlab X-ray diffractometer equipped with an ASC-6 automated sample changer and a Cu K $\alpha$  x-ray source (1.76 kW). Typically, 0.01 g of sample were packed within zero background, low dead volume sample holders (Rigaku) and diffraction patterns were measured from 4-40° at a scan rate of 0.00417° s<sup>-1</sup> with a step size of 0.02°. Scanning electron microscopy (SEM) and electron dispersive X-ray spectroscopy (EDS) were performed on a FEI Quanta 3D FEG Dual-beam SEM with an Everhart-Thornlev detector for high vacuum imaging. SEM micrographs were collected using the focused beam operating mode with a voltage of 5 kV and spot size of 4  $\mu$ m. EDS was performed using an Oxford INCA Xstrem-2 silicon drift detector with an Xmax80 window for supplemental elemental analysis. All analyses were performed at 20 kV at a spot size of 6  $\mu$ m at a magnification of 3000-6000x. N<sub>2</sub> (77 K) and H<sub>2</sub>O (293 K) adsorption isotherms were measured on samples (0.03 g, pelleted and sieved to retain 180-250  $\mu$ m diameter particles) using a Micromeritics ASAP2020 Surface Area and Porosity Analyzer. Prior to measurement of isotherms, samples were degassed by heating to 393 K (0.0167 K s<sup>-1</sup>) under vacuum (<0.005 Torr) for 2 h, then heating to 623 K (0.0167 K s<sup>-1</sup>) under vacuum for 8 h. Micropore volumes were determined from a semi-log derivative analysis of N<sub>2</sub> isotherms ( $\delta(V_{\text{ads}}/\text{g})/\delta(\log(P/P_0))$  vs.  $\log(P/P_0)$ ) to identify the completion of micropore filling (additional details in Section E.7.2). The hydrophobicity of each sample was assessed from the amount of water adsorbed at a relative pressure of 0.2, chosen elsewhere as a reference pressure corresponding to cyclohexane (298 K) filling of micropores in hydrophobic zeolites [573]. Diffuse reflectance UV-Vis (DRUV) spectra were collected on a Varian Cary 5000 UV-VIS-NIR equipped with a Harrick Praying



Mantis in-situ diffuse reflectance cell. Spectra were collected on samples: (i) first exposed to ambient conditions and held in flowing dry He ( $4.17 \text{ cm}^3 \text{ s}^{-1} (\text{g zeolite})^{-1}$ ) (“ambient” treatment); (ii) after subsequent treatment to 523 K ( $0.5 \text{ K s}^{-1}$ ) for 1800 s in flowing dry He ( $4.17 \text{ cm}^3 \text{ s}^{-1} (\text{g zeolite})^{-1}$ ) (“dehydration” treatment); and (iii) after subsequent exposure to a flowing wet He stream ( $4.17 \text{ cm}^3 \text{ s}^{-1} (\text{g zeolite})^{-1}$ , ca. 3% H<sub>2</sub>O, bubbled through a water saturator at ambient temperature) while cooling from 523 K to 303 K and holding for 300 s (“rehydration” treatment). Diffuse reflectance spectra were collected at a rate of  $10 \text{ nm s}^{-1}$ , using poly(tetrafluoroethylene) (PTFE, 1  $\mu\text{m}$  powder, Sigma-Aldrich) as the 100% reflectance standard, and then converted to an absorption spectrum using the Kubelka-Munk ( $F(R)$ ) function. Absorption edge energies were calculated from Tauc plots of  $[F(R)h\nu]^2$  vs.  $h\nu$  (additional details in Section E.7.3).

### E.2.3 Temperature Programmed Desorption

Temperature programmed desorption (TPD) experiments were performed using a Micromeritics Autochem II 2920 Chemisorption Analyzer interfaced with an Agilent 5793N mass selective detector (MSD) to quantify gaseous titrants evolved from the catalysts. Zeolite samples (0.03-0.05 g, sieved to 180-250  $\mu\text{m}$ ) were supported in a U-tube reactor between two quartz wool plugs inside of a clam-shell furnace. Zeolite samples were treated in air ( $25 \text{ cm}^3 \text{ s}^{-1} (\text{g zeolite})^{-1}$ , Indiana Oxygen, Ultra Zero Grade) to 673 K ( $0.167 \text{ K s}^{-1}$ ) for 4 h and then cooled to ambient temperature. For n-propylamine (NPA) titration experiments, samples were saturated in a flowing stream comprising NPA (1000 ppm certified concentration), 1% Ar and balance He ( $75 \text{ cm}^3 \text{ s}^{-1} (\text{g zeolite})^{-1}$ , Airgas, Certified Standard Grade) at 323 K for 4 h, and then purged in flowing He ( $25 \text{ cm}^3 \text{ s}^{-1} (\text{g zeolite})^{-1}$ ) at 338 K for 4 h to remove weakly-bound NPA (additional details in Section E.7.7). For NH<sub>3</sub> titration experiments, samples were saturated in flowing gaseous NH<sub>3</sub> (456 ppm certified concentration) in balance N<sub>2</sub> ( $25 \text{ cm}^3 \text{ s}^{-1} (\text{g zeolite})^{-1}$ , Indiana Oxygen, Certified Standard Grade) for 12 h, and then purged in flowing He ( $25 \text{ cm}^3 \text{ s}^{-1} (\text{g zeolite})^{-1}$ , Indiana Oxygen, 99.999%) for 8 h at 331

K to remove gaseous and physisorbed  $\text{NH}_3$  (additional details in Section E.7.8). After titrant saturation and purge treatments, TPD was performed in flowing He ( $25 \text{ cm}^3 \text{ s}^{-1} (\text{g zeolite})^{-1}$ ) to 873 K (at  $0.167 \text{ K s}^{-1}$ ), during which the U-tube reactor effluent was sent to the MSD via heated transfer lines held at 383 K. After each TPD experiment, a  $0.5 \text{ cm}^3$  sample loop was filled with argon (99.999% Indiana Oxygen) and injected by flowing He ( $25 \text{ cm}^3 \text{ s}^{-1}$ ) that was sent to the MSD in order to quantify the amount of  $\text{NH}_3$  or NPA desorbed from the integrated MSD signals and a calibrated response factor for  $\text{NH}_3$  or NPA relative to Ar.

#### E.2.4 Infrared Spectroscopy and Determination of Integrated Molar Extinction Coefficients

IR spectra were collected on a Nicolet 4700 spectrometer with a Hg-Cd-Te (MCT, cooled to 77 K by liquid  $\text{N}_2$ ) detector by averaging 64 scans at  $2 \text{ cm}^{-1}$  resolution in the 4000 to  $400 \text{ cm}^{-1}$  range and were taken relative to an empty cell background reference collected under dynamic vacuum (rotary vane rough pump, Alcatel 2008A,  $<0.1$  Torr) at either 303 K ( $\text{CD}_3\text{CN}$ ) or 423 K (pyridine). Self-supporting wafers ( $0.01\text{--}0.03 \text{ g cm}^{-1}$ ) were sealed within a custom-built quartz IR cell with  $\text{CaF}_2$  windows, equipped with a mineral-insulated resistive heating coil (ARi Industries) and encased in an alumina silicate ceramic chamber (Purdue Research Machining Services). Wafer temperatures were measured within 2 mm of each side of the wafer by K-type thermocouples (Omega). The quartz IR cell interfaced with a custom glass vacuum manifold that was used for sample pretreatment and exposure to controlled amounts of gaseous titrants. Prior to each IR experiment, wafers were treated in flowing dry air ( $6.66 \text{ cm}^3 \text{ s}^{-1} (\text{g zeolite})^{-1}$ ) purified by an FTIR purge gas generator (Parker Balston,  $<1$  ppm  $\text{CO}_2$ , 200 K  $\text{H}_2\text{O}$  dew point) to 823 K ( $0.083 \text{ K s}^{-1}$ ) for 1 h, and then held under dynamic vacuum (rotary vane rough pump, Alcatel 2008A,  $<0.1$  Torr) at 823 K for 1 h. The wafer was then cooled under dynamic vacuum to 303 K for adsorption experiments with  $\text{CD}_3\text{CN}$ , or to 423 K for adsorption experiments with pyridine. Titrants were purified via freeze-pump-thaw (3 cycles) and admitted

to the cell in sequential doses (ca.  $2.5 \times 10^{-7}$  mol). Equilibration of the sample with each dose was assumed when the final pressure in the cell and transfer line did not change for 180 s. For doses in which the final pressure was recorded as 0.0 Torr, as occurred during sub-saturation coverages, all of the titrant introduced to the cell was assumed to adsorb on the sample wafer. After dosing was complete, which occurred when samples reached equilibrium with a detectable gaseous titrant pressure (0.4-2.0 Torr), samples were exposed to dynamic vacuum (at 303 K for  $\text{CD}_3\text{CN}$  or at 423 K for pyridine) in order to remove gas-phase and weakly-bound species, which occurred when the pressure was recorded as 0.0 Torr. IR peaks for bound titrants did not change between spectra recorded after evacuation or after saturation, regardless of the titrant pressure used for saturation (Fig. E.39). Each wafer was also heated to 523 K ( $0.167 \text{ K s}^{-1}$ ) in dynamic vacuum to monitor the disappearance of IR peaks for bound titrant species.

IR spectra reported here were baseline-corrected and normalized to combination and overtone modes of zeolite Si-O-Si stretches ( $1750\text{-}2100 \text{ cm}^{-1}$ ). Integrated molar extinction coefficients ( $\mathcal{E}$ ,  $\text{cm } \mu\text{mol}^{-1}$ ) for pyridine adsorbed onto Lewis acid sites on three different Sn-Beta samples (Sn-Beta-F-100, Sn-Beta-F-140, and Sn-Beta-OH-170) were determined from the increase in integrated area for the IR peak at  $1450 \text{ cm}^{-1}$  with sequential doses of pyridine to the wafer, and multiplying by the cross-sectional area of the wafer ( $2.54 \text{ cm}^2$ ). This analysis assumed that pyridine selectively adsorbed on Lewis acid sites during titration, consistent with the absence of IR peaks for pyridine adsorbed to non-Lewis acidic sites and with the method proposed by Emeis [574] (details in Section E.7.6). IR peaks for  $\text{CD}_3\text{CN}$  species bound to open ( $2316 \text{ cm}^{-1}$ ) and closed ( $2308 \text{ cm}^{-1}$ ) Lewis acid sites, bound to Sn sites in highly-defective oxide surfaces ( $2287 \text{ cm}^{-1}$ ), hydrogen-bound to Si-OH sites ( $2275 \text{ cm}^{-1}$ ), and physisorbed or gas phase  $\text{CD}_3\text{CN}$  ( $2265 \text{ cm}^{-1}$ ) overlapped and required deconvolution into individual components (details in Section E.7.9). Integrated molar extinction coefficients for  $\text{CD}_3\text{CN}$  were determined for open Lewis acid sites ( $2316 \text{ cm}^{-1}$ ) and closed Lewis acid sites ( $2308 \text{ cm}^{-1}$ ) on Sn-Beta by using a non-linear least squares

regression of saturation peak areas on three Sn-Beta samples (Sn-Beta-F-100, Sn-Beta-F-105, Sn-Beta-OH-170), with the number of Lewis acid sites determined from pyridine chemisorption IR experiments. The number of sites titrated by pyridine or CD<sub>3</sub>CN on self-supporting sample wafers was estimated from integrated IR peak areas and values using the following equation:

$$Site\ density\ (\mu mol\ g^{-1}) = \frac{Integrated\ Peak\ Area\ (cm^{-1})}{\mathcal{E}(cm\ \mu mol^{-1})} * \frac{a_{CS}(cm^2)}{m(g)} \quad (E.1)$$

where  $a_{CS}$  and  $m$  are the cross-sectional area and mass of the wafer, respectively.

### E.2.5 Kinetic and Isotopic Tracer Studies of Glucose Reactions with Sn-Beta

Catalytic studies were performed in batch reactors using 1-10% (w/w) aqueous D-glucose (Sigma Aldrich, >99.5%) solutions with Sn-Beta samples. Reactant solutions were made with water (18.2 MΩ) adjusted to pH 5 (measured by Mettler Toledo Seven Compact pH Ion S220 probe) by addition of hydrochloric acid (Macron, 37% (w/w)) prior to glucose addition and filtration through 0.2 μm PTFE filters (VWR). Catalytic solids (ca. 0.01 g) were added to thick-walled glass reactors (10 cm<sup>3</sup>, VWR) sealed with crimp tops (PTFE/silicone septum, Agilent). Reactors and reactant solutions were heated separately for 600 s to 373 K atop a digital stirred hot plate (IKA RCT basic) prior to injecting the reactant solution (ca. 1 cm<sup>3</sup>) into the capped reactors. Reactors remained at 373 K while stirring at 750 rpm under autogenous pressure for various time intervals (300-14440 s) prior to quenching in an ice bath. Resulting product solutions were filtered through 0.2 μm PTFE filters, diluted to 1% (w/w) sugar concentration if necessary, and mixed with a 1% (w/w) aqueous D-mannitol (Sigma Aldrich, >98 wt%) solution as an internal standard. Component separation was performed using an Agilent 1260 high performance liquid chromatograph (HPLC) equipped with a Hi-Plex Ca column (7.7 x 300 mm, 8 μm particle size, Agilent) and an aqueous mobile phase (0.01 cm<sup>3</sup> s<sup>-1</sup>, 353 K), and quantification was performed using an evaporative light scattering detector (Agilent 1260 Infinity ELSD).

Initial rates of fructose formation were determined using a batch reactor model for a reversible first-order glucose-fructose isomerization reaction, which has been derived and discussed elsewhere [575]. Experimental batch reactor data were accurately described by this model and initial isomerization rates were determined by extrapolation of fructose product formation rates to zero reaction time. This extrapolation provides an estimate of initial reaction rates that are identical, within experimental error (15%), to reaction rates estimated using a differential (well-mixed) reactor model and data collected below 5% conversion (details in Section E.7.10).

Kinetic evaluation of pyridine-titrated Sn-Beta samples was performed by treating zeolite wafers in the IR cell in air to 723 K, as described in Section E.2.2. Samples were then exposed to controlled doses of pyridine at 423 K, typically between 0.03-0.40 moles of pyridine per Sn. An IR spectrum was collected to determine the moles of pyridine adsorbed on the sample, and then the titrated wafer was cooled to 333 K under dynamic vacuum, exposed to ambient conditions, removed from the cell, and crushed with a mortar and pestle. Powdered pyridine-titrated Sn-Beta samples were then transferred into a batch reactor and studied as described above.

Isotopic tracer studies were conducted using 1 cm<sup>3</sup> of a 5% (w/w) aqueous solution of D-glucose-D2 (Cambridge Isotope Laboratories, 2-D, 98%) adjusted to pH 5 and catalyst powders (ca. 0.01 g) at 373 K for 1-4 hours prior to quenching the reactors and filtering the product solutions with 0.2  $\mu$ m PTFE filters. Sugar separation was performed as described above, and the effluent was sent to an Agilent Infinity series fraction collector for solution collection. Liquid samples were frozen in liquid N<sub>2</sub> (77 K) prior to removal of water via a Labconco FreeZone lyophilizer. The recovered sugars were then dissolved in D2O (Cambridge Isotope Laboratories, 99.9%) and placed in a NMR tube (Wilmad LabGlass, 5 mm thin wall, 7 in., 400MHz) for NMR analysis. Solution <sup>1</sup>H NMR spectra were measured on a Bruker ARX400 spectrometer equipped with a 5 mm QNP probe at ambient temperature and were the average of 64 scans acquired at a rate of ca. 0.3 scans per second.

### E.3 Results and Discussion

#### E.3.1 Structural Characterization of Stannosilicates

Characterization data for the Sn-Beta samples used in this study are shown in Table E.1. Samples are denoted as Sn-Beta-X-Y, where X refers to the preparation method used (F = fluoride-assisted hydrothermal synthesis [377]; OH = post-synthetic Sn insertion into dealuminated Beta [543]) and Y is the Si/Sn ratio determined by atomic absorption spectroscopy. Powder XRD patterns for all zeolite samples (Fig. E.13) were consistent with the Beta topology and did not show diffraction peaks for bulk SnO<sub>2</sub> at 26.7° or 34° 2 $\theta$ . Diffraction peaks for bulk SnO<sub>2</sub> were also absent on a control sample prepared to contain SnO<sub>2</sub> supported on Si-Beta (SnO<sub>2</sub>/Si-Beta), indicating that any SnO<sub>2</sub> domains on this sample were small enough to be X-ray amorphous (<3 nm in diam.) [290]. N<sub>2</sub> adsorption isotherms measured at 77 K (Fig. E.14) indicated that micropore volumes were 0.21-0.24 cm<sup>3</sup> g<sup>-1</sup> for all Sn-Beta-F samples and 0.19-0.22 cm<sup>3</sup> g<sup>-1</sup> for all Sn-Beta-OH samples (Table E.1), also consistent with the Beta topology. H<sub>2</sub>O adsorption isotherms measured at 293 K (Fig. E.15 and E.16) showed H<sub>2</sub>O uptakes (at P/P<sub>0</sub> = 0.2) of 0.005-0.017 cm<sup>3</sup> g<sup>-1</sup> for Sn-Beta-F samples (Table E.1), consistent with the hydrophobic nature of low-defect zeolites crystallized in fluoride media [576], but showed higher H<sub>2</sub>O uptakes of 0.036-0.092 cm<sup>3</sup> g<sup>-1</sup> for Sn-Beta-OH samples (Table E.1), reflecting the more hydrophilic and defective nature of samples prepared via Sn insertion into framework vacancy defects of dealuminated zeolites.

Diffuse reflectance UV-visible (DRUV) spectroscopy has been used to probe Sn coordination and detect tetrahedrally-coordinated framework Sn centers, which have been assigned to bands centered at ca. 205 nm [534,577], yet such sites can coordinate water ligands to become penta- or hexa-coordinated [554] and give rise to bands centered at ca. 220 nm and ca. 255 nm, respectively [577]. DRUV bands for hexa-coordinated framework Sn centers at ca. 255 nm, however, also fall within a range characteristic of small SnO<sub>2</sub> domains, which give rise to DRUV bands centered at

lower wavelengths (ca. 240 nm) [568, 578] than for bulk  $\text{SnO}_2$  (ca. 280 nm) because of quantum confinement effects [579–582], precluding unambiguous characterization of Sn structure from DRUV spectra of Sn-zeolites exposed to ambient conditions. Thus, DRUV spectra were collected on each sample under ambient conditions, after dehydration treatments in flowing dry helium at 523 K, and after rehydration treatments while cooling to 303 K in flowing wet (3%  $\text{H}_2\text{O}$ ) helium (dehydrated spectra in Fig. E.17 and E.18). The positions of DRUV absorption ( $F(R)$ ) bands of maximum intensity, together with absorption edge energies (Tauc plots of  $[F(R) \cdot h\nu]^2$  vs.  $h\nu$  Fig. E.19 and E.20) are listed for each sample after dehydration treatments in Table E.1.

DRUV spectra of Sn-Beta-F-170 (Fig. E.3a) exposed to ambient conditions showed a broad band centered at ca. 250 nm, while spectra collected after dehydration showed a new band centered at ca. 207 nm with a shoulder centered at ca. 250 nm, which reverted to a band centered at ca. 250 nm after rehydration treatments. These spectral features are consistent with framework Sn centers that are octahedrally-coordinated under ambient conditions or upon exposure to water, but become tetrahedrally-coordinated in the absence of water [554]. DRUV spectra of Sn-Beta-OH-200 (Fig. E.3b) exposed to ambient conditions showed a band centered at ca. 230 nm, which shifted to ca. 190 nm upon dehydration and returned to ca. 230 nm after rehydration, similar to the spectral changes observed on Sn-Beta-F-170 (Fig. E.3a) and as expected from the reversible coordination of water ligands to framework Sn sites. These changes in DRUV spectra upon dehydration were observed to different extents among the different Sn-Beta samples in this study, for which bands did not always shift completely to ca. 210 nm upon dehydration, but did revert to a single band centered between ca. 230–250 nm upon rehydration. In sharp contrast, DRUV spectra of  $\text{SnO}_2/\text{Si-Beta}$  (Fig. E.3c) did not change after dehydration or rehydration treatments and remained centered at ca. 250 nm, indicating that Sn atoms within  $\text{SnO}_2$  domains did not change coordination in the presence of water. Absorption edge energies (Table E.1) on Sn-Beta-OH-170 (4.3 eV) and on Sn-xerogel

(4.4 eV) are characteristic of isolated Sn sites in silica [568] and higher than the edge energy on SnO<sub>2</sub>/Si-Beta (4.1 eV), which is characteristic of SnO<sub>2</sub> domains <3 nm in diameter (details in Section E.7.3) [581]. Absorption edge energies for nearly all Sn-Beta-F samples (4.2-4.3 eV; Table 1) fall within a range higher than reported for SnO<sub>2</sub> domains [579–582] and reflect the predominance of isolated framework Sn sites in these samples, while the lower absorption edge energy of 4.1 eV on Sn-Beta-F-100 (Table E.1) appears to reflect detectable amounts of small SnO<sub>2</sub> domains ( $\leq 3$  nm) on this sample.

We conclude that DRUV spectra collected on stannosilicates exposed to ambient conditions cannot unambiguously discern penta- or hexa-coordinated Sn atoms isolated within silica or stannic oxide domains [568,578], but changes to spectral features and absorption edge energies on dehydrated samples can distinguish between them because Sn centers isolated in silica (but not in stannic oxide) surfaces become tetrahedrally-coordinated [543,577]. The subtle, yet measurable, differences in DRUV absorption band maxima and edge energies among Sn-Beta-F and Sn-Beta-OH samples (Table E.1) may reflect different densities of framework Sn and extraframework SnO<sub>2</sub> sites, which catalyze glucose-fructose isomerization by Lewis acid-mediated and base-mediated mechanisms, respectively [578]. Isotopic tracer studies with glucose reactants deuterated at the second carbon (glucose-D2), performed in the aqueous phase under acidic conditions (pH=5) selectively formed fructose products that retained the deuterium label at the first carbon (fructose-D1) on all Sn-Beta samples in this study (additional details and NMR spectra in Section E.7.4), as expected from Lewis acid-mediated isomerization via intramolecular 1,2-hydride shift [142]. Therefore, the aqueous-phase glucose isomerization rates measured here reflect reactions catalyzed solely by Lewis acid sites on Sn-Beta samples prepared by different routes and that contain structural heterogeneities. Their effects on isomerization turnover rates can be interpreted only after normalization by numbers of active Lewis acidic sites, which require methods to quantify them.



### E.3.2 Quantification of Lewis acid sites: IR studies with pyridine

Infrared spectra were collected with increasing pyridine coverage on three Sn-Beta samples (Sn-Beta-F-100, Sn-Beta-F-140, Sn-Beta-OH-170) and are shown in Figure E.4. IR spectra showed two peaks centered at  $1450\text{ cm}^{-1}$  and  $1610\text{ cm}^{-1}$ , reflecting perturbed deformation modes of pyridine bound to Lewis acid sites [559], and a third peak centered at  $1490\text{ cm}^{-1}$  that reflects either ring stretches of pyridine coordinated to Lewis acid sites or pyridine protonated at Brønsted acid sites [559]. IR peaks centered at  $1550\text{ cm}^{-1}$  and  $1637\text{ cm}^{-1}$  characteristic only of protonated pyridine [558, 559, 583] were absent in all spectra (Fig. E.4), however, indicating that only Lewis acid sites were present on these Sn-Beta samples. Integrated areas of IR peaks for Lewis acid-bound pyridine ( $1450\text{ cm}^{-1}$ ) increased linearly with pyridine coverage on these three Sn-Beta samples with a slope of  $1.42 \pm 0.30\text{ cm } \mu\text{mol}^{-1}$  (Fig. E.5), which is the integrated molar extinction coefficient ( $\mathcal{E}$ ) for this IR peak. This  $\mathcal{E}(1450\text{ cm}^{-1}, \text{Sn})$  value, which is listed in Table E.2 together with literature values for reference, has not been reported previously and is ca.  $1.5\times$  lower than the widely-used  $\mathcal{E}(1455\text{ cm}^{-1}, \text{Al})$  value reported by Emeis for pyridine bound to Lewis acidic Al sites in crystalline and amorphous aluminosilicates ( $2.2 \pm 0.3\text{ cm } \mu\text{mol}^{-1}$ ) [574]. This single  $\mathcal{E}(1455\text{ cm}^{-1}, \text{Al})$  value was determined by simultaneously fitting data collected on different zeolite topologies (H-MOR, H-FAU, H-MFI), yet  $\mathcal{E}$  values among these different zeolites vary widely in the literature ( $>10\times$ ) [574, 584]. The  $\mathcal{E}(1455\text{ cm}^{-1}, \text{Al})$  value measured in our experimental apparatus on H-Y zeolite was  $1.45 \pm 0.10\text{ cm } \mu\text{mol}^{-1}$  (Section E.7.5) and within the range of values reported by Emeis and by Nesterenko et al. for dealuminated H-MOR zeolites ( $0.89\text{ cm } \mu\text{mol}^{-1}$ ) [585], suggesting that our apparatus provides reasonable estimates of  $\mathcal{E}$  values. Thus, we conclude that the generally-accepted literature  $\mathcal{E}(1455\text{ cm}^{-1}, \text{Al})$  value [574] does not accurately predict the number of Lewis acidic Sn sites in zeolites of the Beta topology, and use instead the  $\mathcal{E}(1450\text{ cm}^{-1}, \text{Sn})$  value of  $1.42 \pm 0.30\text{ cm } \mu\text{mol}^{-1}$  consistently measured here among Sn-Beta zeolites prepared by different routes.

Infrared spectra were collected after saturation of all Sn-Beta samples with pyridine and subsequent evacuation at 423 K to remove gaseous and weakly-bound species (additional details and spectra in Section E.7.6). Integrated IR peak ( $1450\text{ cm}^{-1}$ ) areas, together with the  $\mathcal{E}(1450\text{ cm}^{-1}, \text{Sn})$  value (Table E.2) determined from spectra collected at sub-saturation coverages (0.04-0.66 pyridine/Sn; Fig. E.5) that correspond to equimolar pyridine binding to Sn, were used to quantify the number of Lewis acidic Sn sites on each sample using Eq. E.1 and are reported in Table E.3. The fraction of Lewis acidic Sn sites (per total Sn) varied between 0.73-0.90 on seven of the eight Sn-Beta samples in this study (Table E.3), but was markedly lower on Sn-Beta-F-100 (0.49, Table E.3) that contained  $\text{SnO}_2$  detectable in DRUV spectral band centers and edge energies (Table E.1). The fraction of Lewis acidic Sn sites (per total Sn) was much lower, but measurable, on the  $\text{SnO}_2/\text{Si-Beta}$  control sample and Sn-xerogel (0.25 and 0.23, respectively Table E.3), suggesting that some tetrahedrally-coordinated Sn atoms (analogous to open and closed Sn sites in Sn-Beta) at their defective and undercoordinated surfaces are able to bind pyridine. On every Sn-Beta sample, pyridine titrates only a fraction of Sn sites at saturation coverages (Table E.3), either because of incomplete Sn incorporation within framework locations or incomplete accessibility of pyridine to framework Sn sites. Therefore, we next obtain independent estimates of the number of Lewis acid sites in these Sn-Beta samples using smaller base titrants that coordinate with Lewis acid sites and that can be quantified in temperature-programmed desorption (TPD) experiments.

### E.3.3 Quantification of Lewis acid sites: TPD studies with n-propylamine and ammonia

Reactive alkylamine titrants (e.g. n-propylamine, NPA) can distinguish between Lewis and Brønsted acid sites on a given surface because they coordinate to Lewis acid sites and desorb intact, but become protonated by Brønsted acid sites and decompose via Hoffman-type elimination reactions to form ammonia and the corresponding alkene (e.g., propene) [114, 116, 117, 586]. The saturation of Sn-Beta samples with

NPA and subsequent purging in flowing helium (338 K) led only to the desorption of NPA (TPD profiles in Section E.7.7) and not to any ammonia or propene, consistent with the undetectable levels of Brønsted acid sites in infrared spectra collected after pyridine saturation (Section E.3.2). The number of moles of NPA desorbed (per mol Sn) on each sample is listed in Table E.3, and is plotted against the number of moles of pyridine adsorbed at saturation in IR experiments (per mol Sn) in Figure E.6a for four Sn-Beta-F samples with high Sn content ( $\text{Si/Sn} < 150$ ). On these Sn-Beta samples, a similar number of NPA and pyridine molecules (within  $1.25\times$ ) were adsorbed at saturation coverages (Table E.3, Fig. E.6a), suggesting that NPA also binds to Sn with equimolar stoichiometry. On Sn-Beta samples with low Sn content (Sn-Beta-F-170, Sn-Beta-F-220) or with high defect density (Sn-Beta-OH-170, Sn-Beta-OH-200), however, a larger number (by  $1.6\text{--}2.5\times$ , Table E.3) of NPA desorbed during TPD than the number of pyridine adsorbed at saturation (Table E.3), reflecting the retention of NPA at residual defect silanol sites under the conditions studied here (control experiments performed on dealuminated Beta zeolites in Section E.7.7).

In contrast with reactive alkylamines, ammonia titrants desorb intact from both Lewis and Brønsted acid sites present on a given surface. The treatment of  $\text{NH}_3$ -saturated samples in flowing dry helium removes physisorbed  $\text{NH}_3$  species and enables the concurrent measurement of  $\text{NH}_3$  bound to Lewis and Brønsted sites during a TPD experiment, while treatment of  $\text{NH}_3$ -saturated samples in flowing wet helium has been shown to also desorb  $\text{NH}_3$  bound to Lewis acid sites (Al [105]; Cu [78, 171]) to enable quantifying  $\text{NH}_4^+$  species at Brønsted sites. The number of  $\text{NH}_3$  bound to Lewis acid sites on solid acids can be estimated from the difference between these two TPD methods, but on Sn-Beta zeolites devoid of protons were estimated after purging  $\text{NH}_3$ -saturated samples only in dry helium at 331 K ( $\text{NH}_3$  TPD profiles in Section E.7.8). The number of moles of  $\text{NH}_3$  desorbed (per mol Sn) in a subsequent TPD is listed in Table E.3 for each sample and was identical, within experimental error, to the number of Lewis acidic Sn sites titrated by pyridine on all samples except for Sn-Beta-F-105 and Sn-Beta-OH-170 (Table E.3, Fig. E.6b). These data suggest that  $\text{NH}_3$

binds to both open and closed Sn sites with equimolar stoichiometry, consistent with  $^{119}\text{Sn}$  MAS NMR spectra of  $\text{NH}_3$ -saturated Sn-Beta samples that show resonances attributed to penta-coordinated Sn (between -500 and -600 ppm) [551, 587]. Control experiments performed to saturate dealuminated Beta zeolites with  $\text{NH}_3$  and purge in dry helium did not evolve any  $\text{NH}_3$  in a subsequent TPD (details in Section E.7.8), in contrast to analogous control experiments performed with NPA. Thus, we conclude that the NPA and  $\text{NH}_3$  TPD techniques developed here can be used to accurately quantify the number of Lewis acidic Sn sites on Sn-Beta-F samples with high Sn contents ( $\text{Si/Sn} < 150$ ), but that NPA TPD overestimates the number of Lewis acid sites on samples containing dilute amounts of Sn ( $\text{Si/Sn} > 170$ ) or high defect densities (Sn-Beta-OH).

#### E.3.4 Quantification of open and closed Lewis acid sites: IR studies with deuterated acetonitrile

Infrared spectra were collected with increasing  $\text{CD}_3\text{CN}$  coverage (303 K) and are shown for one representative Sn-Beta sample (Sn-Beta-F-105) in Figure E.7a. Each IR spectrum was deconvoluted into principal component peaks (Fig. E.1, Fig. E.7b) centered at  $2316\text{ cm}^{-1}$ ,  $2308\text{ cm}^{-1}$ ,  $2287\text{ cm}^{-1}$ ,  $2275\text{ cm}^{-1}$  and  $2265\text{ cm}^{-1}$  (additional details in Section E.7.9), and the evolution of IR peak areas with increasing  $\text{CD}_3\text{CN}$  coverage is shown in Figure E.8. Initial  $\text{CD}_3\text{CN}$  doses led to the appearance of the  $2316\text{ cm}^{-1}$  peak, with a shoulder at  $2308\text{ cm}^{-1}$  and even smaller and broader peaks at  $2287\text{ cm}^{-1}$  and  $2275\text{ cm}^{-1}$ . Increasing  $\text{CD}_3\text{CN}$  coverages caused the  $2316\text{ cm}^{-1}$  peak to saturate, while the  $2308\text{ cm}^{-1}$ ,  $2287\text{ cm}^{-1}$ , and  $2275\text{ cm}^{-1}$  peaks continued to increase in area. At a coverage corresponding to  $\text{CD}_3\text{CN/Sn} = 1$ , the  $2316\text{ cm}^{-1}$  and  $2308\text{ cm}^{-1}$  peaks had already reached saturation, while the  $2287\text{ cm}^{-1}$  and  $2275\text{ cm}^{-1}$  peaks continued to increase in area. Finally, the  $2265\text{ cm}^{-1}$  peak for gas-phase  $\text{CD}_3\text{CN}$  appeared after saturation of all adsorption sites on the sample [571].

The IR peaks at ca.  $2316\text{ cm}^{-1}$  and ca.  $2308\text{ cm}^{-1}$  reflect  $\text{CD}_3\text{CN}$  bound to open and closed Lewis acidic Sn sites, respectively [550, 551], and have been correlated to

$^{119}\text{Sn}$  MAS NMR resonances at -423 ppm (open sites) and -443 ppm (closed sites) in dehydrated Sn-Beta (vacuum, 393 K) [551]. The ratio of open-to-closed site peak areas systematically decreases with increasing  $\text{CD}_3\text{CN}$  coverage (Fig. E.9), indicating that  $\text{CD}_3\text{CN}$  binds preferentially to open Sn sites, as also reported previously [550–553]. Open and closed Sn sites become saturated at a sub-stoichiometric  $\text{CD}_3\text{CN}/\text{Sn}$  coverage of 0.80 ( $4.14 \times 10^{-6}$  mol  $\text{CD}_3\text{CN}$ , Fig. E.8), which is similar to the number of total Sn sites titrated by pyridine (0.87, Table E.3) and provides evidence that  $\text{CD}_3\text{CN}$  also binds to Lewis acidic Sn sites with equimolar stoichiometry. We *speculate* that the IR peak at ca.  $2287\text{ cm}^{-1}$ , which appears prominently in IR spectra of Sn-xerogel samples at low  $\text{CD}_3\text{CN}$  coverages but is not prominent at any  $\text{CD}_3\text{CN}$  coverage for Si-xerogel or  $\text{SnO}_2/\text{Si}$ -Beta samples (spectra in Section E.7.9), reflects  $\text{CD}_3\text{CN}$  interacting with Sn of highly-defective coordination (e.g.,  $(\text{SiO})_2\text{Sn}(\text{OH})_2$ ). The existence of doubly-hydroxylated Sn sites has been proposed on Sn-Beta using  $^{119}\text{Sn}$  CPMAS NMR [536], and on grafted Sn- $\text{SiO}_2$  using in-situ DRIFTS [588]. The IR peak centered at ca.  $2275\text{ cm}^{-1}$  reflects  $\text{CD}_3\text{CN}$  bound to silanol groups [570, 571], and increases linearly in area with concomitant decreases in silanol OH stretching peak areas (ca.  $3740\text{ cm}^{-1}$ ) and concomitant increases in perturbed OH stretching peak areas (ca.  $3300\text{--}3600\text{ cm}^{-1}$ ) (Section E.7.9) [589].

Infrared spectra of Sn-Beta samples after saturation with  $\text{CD}_3\text{CN}$  and subsequent evacuation at 303 K retained four peaks in the  $\text{C}\equiv\text{N}$  stretching region (2316, 2308, 2287,  $2275\text{ cm}^{-1}$ , Fig. E.7b), whose areas were determined by deconvolution and were present in different proportions for each sample (Table E.9).

Integrated molar extinction coefficients were first determined for the  $2316\text{ cm}^{-1}$  and  $2308\text{ cm}^{-1}$  IR peaks from spectra of three Sn-Beta samples (Sn-Beta-F-100, Sn-Beta-F-105, Sn-Beta-OH-170), by non-linear least squares regression to minimize the error between the total number of Lewis acid sites counted by  $\text{CD}_3\text{CN}$  and pyridine (additional details in Section E.7.9). These  $\mathcal{E}(2316\text{ cm}^{-1}, \text{Sn})$  and  $\mathcal{E}(2308\text{ cm}^{-1}, \text{Sn})$  values were determined to be  $1.04 \pm 0.22$  and  $2.04 \pm 0.43\text{ cm}^2\text{ mol}^{-1}$  (Table E.2), respectively. Both  $\text{CD}_3\text{CN}$  and pyridine estimated the same number of Lewis acid

sites (to within  $1.25\times$ ) on five other Sn-Beta samples that were not used in estimating  $\mathcal{E}$  values for CD<sub>3</sub>CN (Sn-Beta-F-110, Sn-Beta-F-140, Sn-Beta-F-170, Sn-Beta-F-220, and Sn-Beta-OH-200), demonstrating that these  $\mathcal{E}$  values can accurately quantify Lewis acid sites on Sn-Beta zeolites. Next,  $\mathcal{E}$  values for the 2287 cm<sup>-1</sup> and 2275 cm<sup>-1</sup> peaks were estimated from non-linear least squares regression of IR peak areas with increasing CD<sub>3</sub>CN coverage on Sn-Beta-OH-170 (additional details in Section E.7.9), which was chosen because it showed the largest 2275 cm<sup>-1</sup> peak area of any Sn-Beta sample. These  $\mathcal{E}(2287\text{ cm}^{-1}, \text{Sn})$  and  $\mathcal{E}(2275\text{ cm}^{-1})$  values were determined to be  $2.13\pm0.45$  and  $0.74\pm0.16\text{ cm } \mu\text{mol}^{-1}$  (Table E.2), respectively. Increasing CD<sub>3</sub>CN coverage on dealuminated Beta led only to the appearance the 2275 cm<sup>-1</sup> peak, whose integrated areas were used to independently estimate an  $\mathcal{E}(2275\text{ cm}^{-1})$  value of  $0.89\pm0.09\text{ cm } \mu\text{mol}^{-1}$  (details in Section E.7.9), similar to the  $\mathcal{E}(2275\text{ cm}^{-1})$  value determined from least-squares regression of IR data collected on Sn-Beta-OH-170.

The numbers of open and closed Lewis acidic Sn sites on each Sn-Beta sample, determined from IR spectra collected after CD<sub>3</sub>CN saturation (303 K) and integrated molar extinction coefficients (Table E.2), are listed in Table E.3 and were calculated using Eq. E.1. The total number of Lewis acid sites quantified by CD<sub>3</sub>CN (per mol Sn) is plotted against the number of sites quantified by pyridine (per mol Sn) in Figure E.6c for each of the Sn-Beta-F and Sn-Beta-OH samples studied here. The total number of Lewis acid sites (open and closed) counted by CD<sub>3</sub>CN was identical, within experimental error, to the number of Lewis acid sites counted by pyridine titration in IR experiments on each of the Sn-Beta samples (Table E.3, Fig. E.6c), providing evidence that CD<sub>3</sub>CN also binds with equimolar stoichiometry to each Sn site and that either pyridine or CD<sub>3</sub>CN can accurately quantify the total number of Lewis acid sites in IR experiments. Among the Sn-Beta samples in this study, the fraction of Sn present as Lewis acid sites was almost always below unity (0.49-1.00, Table E.3), and the ratio of open-to-closed Lewis acid sites varied over a wide range (0.29-1.64, Table E.3). The consistent estimates of Lewis acidic Sn sites determined by more than one base titrant provides further evidence that the integrated molar

extinction coefficients in Table 2 apply generally to Sn-Beta zeolites prepared via different methods, in turn, enabling quantification of open (and closed) Sn sites to normalize turnover rates for glucose-fructose isomerization, as we discuss next.

### E.3.5 Glucose isomerization rate constants on hydrophobic and hydrophilic Sn-Beta zeolites

Aqueous-phase glucose-fructose isomerization on Lewis acid sites proceeds via quasi-equilibrated adsorption and ring-opening of glucose to form intermediates that coordinate to Sn sites through oxygen atoms at the C1 (aldehyde) and C2 (deprotonated OH) positions [554], subsequent kinetically-relevant intramolecular 1,2-hydride shift to form ring-opened fructose intermediates [142], and quasi-equilibrated ring-closing and desorption of fructose (Fig. E.2). Initial isomerization turnover rates are first-order in glucose concentration (0-10% (w/w), 373 K, Figure E.10) with measured H/D kinetic isotope values of 2.0-2.4 (373 K) for glucose deuterated at the second carbon, as expected for kinetically-relevant intramolecular 1,2-hydride shift in the absence of internal mass transfer limitations (details in Section E.7.10) [575]. The first-order dependence of isomerization rates on glucose concentration is consistent with dilute glucose coverages and with two coordinated water molecules as the most abundant surface intermediate (MASI) during reaction in liquid water, as expected from the saturation of framework Sn sites with water even in ambient atmosphere to give  $^{119}\text{Sn}$  MAS NMR resonances [554] and UV-Vis spectral features for octahedrally-coordinated Sn (Section E.3.1). These quasi-equilibrated reactions, elementary steps and mechanistic assumptions give a turnover rate equation that accurately describes aqueous-phase glucose-fructose isomerization on Sn-Beta zeolites (mechanistic details and derivation of rate expression in Section E.7.10) [575]:

$$r_{isom} = \alpha \frac{K_1 k_2}{K_4 K_5} C_G = k_{isom} C_G \quad (\text{E.2})$$

In this turnover rate equation,  $K_1$  is the adsorption equilibrium constant relating aqueous-phase glucose and ring-opened glucose intermediates bound to Sn sites,  $k_2$

is the rate constant for the intramolecular 1,2-hydride shift to form fructose,  $K_4$  and  $K_5$  are adsorption equilibrium constants for the sequential adsorption of two water molecules at Sn sites,  $C_G$  is the aqueous-phase glucose concentration,  $\alpha$  is a constant that contains the product of activity coefficients for reactants and intermediates in the mechanism (details in Section E.7.10), and  $k_{isom}$  is the effective first-order isomerization rate constant. The rate and equilibrium constants that comprise  $k_{isom}$  can be decomposed to show that measured first-order isomerization rate constants reflect the difference in free energy between the kinetically-relevant transition state (bound glucose-fructose isomerization transition states ( $\Delta G_{\ddagger,2*}^o$ ) and two aqueous-phase water molecules ( $2\Delta G_W^o$ )) and the most abundant surface intermediate (two bound water molecules ( $\Delta G_{2W*}^o$ ) and aqueous-phase glucose ( $\Delta G_G^o$ ); details in Section E.7.10) [576]:

$$k_{isom} = \alpha \frac{K_1 k_2}{K_4 K_5} = \alpha \frac{k_B T}{h} e^{-(\Delta G_{\ddagger,2*}^o + 2\Delta G_W^o) - (\Delta G_G^o + \Delta G_{2W*}^o)/RT} \quad (E.3)$$

Isomerization turnover rates (Eq. E.2) are rigorously normalized by the number of active Sn sites, demonstrated elsewhere to be open Sn sites based on selective  $\text{NH}_3$  pre-poisoning of open sites in Sn-Beta before glucose isomerization catalysis [551]. The number of Sn sites active for glucose isomerization was independently estimated here on two different Sn-Beta-F samples (Sn-Beta-F-110, Sn-Beta-F-170) from pyridine pre-poisoning studies, in which samples were pressed into self-supporting wafers and sealed in the IR cell, titrated with different amounts of pyridine (quantified from IR spectra and the E values in Table E.2), removed from the IR cell, and ground into a powder prior to measurement of isomerization rates. Initial isomerization turnover rates (per total Sn, 373 K) decreased with increasing pyridine coverage (per total Sn) for Sn-Beta-F-110 and Sn-Beta-F-170 (Fig. E.11), but not because of occlusion of intracrystalline void spaces or of pore openings at external crystallite surfaces, or because of restricted diffusion of glucose reactants within intracrystalline voids (details in Section E.7.10). Linear extrapolation of initial isomerization rates with increasing pyridine coverage (Fig. E.11) predicts full suppression of reactivity at pyridine



uptakes of  $0.49 \pm 0.10$  and  $0.15 \pm 0.03$  (per total Sn) for Sn-Beta-F-110 and Sn-Beta-F-170, respectively, which are similar to their fractions of open Sn sites counted ex-situ by  $\text{CD}_3\text{CN}$  ( $0.35 \pm 0.07$  and  $0.20 \pm 0.04$ , respectively). In contrast, pyridine uptakes required to fully suppress rates on Sn-Beta-F-110 and Sn-Beta-F-170 are not equivalent to their fractions of closed Sn sites ( $0.63 \pm 0.13$  and  $0.67 \pm 0.14$ , respectively), although closed Sn sites may be responsible for the residual isomerization reactivity observed at pyridine uptakes higher than predicted to fully suppress reactivity (Fig. E.11). The pyridine uptakes required to completely suppress the rates were also not equal to the value of unity expected if residual Sn sites on pyridine-titrated samples were equally reactive or undergo quasi-equilibrated structural changes during initial reaction times. These findings also suggest that pyridine preferentially titrates open Sn sites either in vacuum (423 K) or upon exposure to liquid water (373 K) and that pyridine desorption from Sn sites in Sn-Beta-F appears irreversible on the timescale of initial glucose isomerization rate measurements (373 K). Thus, we conclude that *initial* isomerization turnover rates are rigorously normalized by the number of open Sn sites present *initially* on Sn-Beta zeolites, which can be quantified from ex situ  $\text{CD}_3\text{CN}$  IR experiments (Table E.3). Turnover rates estimated at longer batch reaction times, or at steady-state in a flow reactor, may require different normalization to the extent that framework Sn sites change structure or coordination during exposure to liquid water at elevated temperatures (373 K) [590,591]. Values of  $k_{\text{isom}}$  (per open Sn, 373 K) are listed in Table E.10 for each Sn-Beta sample in this study, and are plotted against Sn content in Figure E.12. Values of  $k_{\text{isom}}$  were higher by ca. 50x (on average) on the six low-defect Sn-Beta-F samples synthesized in fluoride media than on the two highly-defective Sn-Beta-OH samples prepared by grafting of Sn atoms in dealuminated Beta zeolites (Fig. E.12). Values of  $k_{\text{isom}}$  reflect free energy differences between glucose isomerization transition states and two water molecules coordinated to active sites (Eq. E.3), and would decrease as adsorption equilibrium constants for coordinated water molecules ( $K_4$ ,  $K_5$ ) become larger (Eq. E.2), as proposed for hydrophilic zeolites with higher densities of defect silanol groups that hydrogen bond

with water bound at framework metal sites [592]. This mechanistic interpretation suggests that  $k_{isom}$  values are larger on hydrophobic Sn-Beta-F zeolites, *in part*, because of weaker kinetic inhibition of Sn sites by coordinated water molecules when such sites are confined within low-defect voids. These findings extend previous reports of  $k_{isom}$  values (per *total* Ti, 373 K) that were 10-30 $\times$  higher on hydrophobic than on hydrophilic Ti-Beta zeolites [576], and demonstrate that such differences persist after precise normalization by the number of active sites (open Sn) in Sn-Beta zeolites. We also note that the form of the kinetic rate equation in Eq. E.2, which is derived with the assumption of sequential, quasi-equilibrated adsorption of two water molecules, can instead be treated as one quasi-equilibrated step ( $K'=K_4 \cdot K_5$ ) [575] and is functionally equivalent to an equation derived for the case of only one water molecule as the MASI, as expected if framework Sn centers were penta-coordinated instead of tetrahedrally-coordinated [593]. Values of  $k_{isom}$  (373 K), after normalization by open Sn sites, varied among Sn-Beta-F samples of different crystallization time and Sn content by ca. 3x (Table E.10), reflecting residual heterogeneities in Sn active site structure or coordination or in the surrounding environments that influence free energy differences between glucose-fructose isomerization transition states and two water molecules bound at Sn centers (Eq. E.3). Total water uptakes measured from H<sub>2</sub>O adsorption isotherms (293 K) at a reduced pressure of 0.2, which corresponds to complete micropore filling with cyclohexane and has been used elsewhere as a descriptor of the hydrophobic properties of zeolites [573], differed by 3.5 $\times$  among these Sn-Beta-F samples (Table E.1). Although this water uptake reflects an integrated adsorption measurement on multiple binding sites, including framework Sn centers and defect silanol groups at intracrystalline and extracrystalline locations, the residual water uptake after accounting for binding on Sn (2 H<sub>2</sub>O/Sn) was directly proportional to the number of silanol groups titrated by CD<sub>3</sub>CN on the Sn-Beta-F samples studied here (Fig. E.49, Section E.7.10). Values of  $k_{isom}$  (per open Sn, 373 K) on Sn-Beta-F samples generally decreased with increasing silanol content (Fig. E.50, Section E.7.10), albeit with residual scatter in the correlation that seems reasonable

because  $k_{isom}$  values may only sense differences in the strength of water binding in the vicinity of active Sn sites. These findings and interpretations suggest that methods to insert Sn atoms into vacancy defects of Beta zeolites may benefit from further treatments to remove residual silanol defects to increase their hydrophobicity and, in turn, turnover rates for aqueous-phase glucose isomerization.

#### E.4 Conclusions

Titration and quantification procedures were developed for four different Lewis bases, two involving concurrent collection of infrared spectra (pyridine, deuterated acetonitrile) and two involving subsequent temperature programmed desorption (ammonia, n-propylamine), to quantify the number of Lewis acid sites in Sn-Beta zeolites prepared by hydrothermal and post-synthetic routes. On crystalline zeolites, integrated molar extinction coefficients ( $\mathcal{E}$ ) for IR peaks reflecting pyridine bound to Lewis acidic Sn sites ( $1450\text{ cm}^{-1}$ ) and  $\text{CD}_3\text{CN}$  bound to open ( $2316\text{ cm}^{-1}$ ) and closed ( $2308\text{ cm}^{-1}$ ) Sn sites were different from E values for Lewis acidic Al sites.  $\mathcal{E}$  values for Al sites are available in the literature, but quantify Sn sites imprecisely from IR spectra of Sn-Beta samples at saturation pyridine or  $\text{CD}_3\text{CN}$  coverages, while the  $\mathcal{E}$  values on Sn sites reported here estimate similar numbers of Lewis acid sites on the eight Sn-Beta samples in this study. Two additional TPD methods were also developed to selectively titrate and quantify Lewis acid sites in Sn-Beta zeolites with ammonia or n-propylamine, which are titrants used often to quantify Brønsted acid sites but seldom to quantify Lewis acid sites in solid acids.

Open Sn sites, which are partially hydrolyzed framework Sn centers with an OH ligand (Sn-OH) proximal to a silanol group (Si-OH), have been implicated as the dominant active site in Sn-Beta for glucose-fructose isomerization via intramolecular 1,2-hydride shift [551]. On two Sn-Beta samples, initial aqueous-phase glucose-fructose isomerization turnover rates (per total Sn, 373 K) decreased linearly with the number of pyridine titrants adsorbed prior to reaction, and become suppressed at pyridine uptakes similar to the number of open Sn sites counted ex-situ by  $\text{CD}_3\text{CN}$  (303 K).

These findings provide further evidence that open Sn sites are the dominant active site for glucose-fructose isomerization in Sn-Beta, and suggest that initial isomerization turnover rates should be normalized by the number of open Sn sites counted via  $\text{CD}_3\text{CN}$  titration, prior to interpretation of turnover rate differences among Sn-Beta zeolites of different preparation or treatment history.

Apparent first-order aqueous-phase isomerization rate constants (per open Sn site, 373 K) are ca. 50x higher, on average, on hydrophobic Sn-Beta zeolites crystallized in fluoride media (Sn-Beta-F) than on hydrophilic Sn-Beta zeolites (Sn-Beta-OH) prepared by post-synthetic insertion of Sn atoms into framework vacancy defects. These data are consistent with the stronger kinetic inhibition of Lewis acidic Sn sites confined within hydrophilic than within hydrophobic voids by coordinated water molecules, which are most abundant surface intermediates during isomerization in liquid water [576]. We expect that the titration methods developed here can be adapted to quantify Lewis sites on silicates containing other tetravalent Lewis acidic heteroatoms (e.g.,  $\text{Ti}^{4+}$ ,  $\text{Zr}^{4+}$ ,  $\text{Hf}^{4+}$ ). The approach described herein, which quantifies active Lewis acid sites ex-situ to normalize initial glucose-fructose isomerization turnover rates, provides the conceptual basis to rigorously assess how different synthetic and post-synthetic treatments of Sn-zeolites influence their density of open and closed Sn sites and, in turn, their catalytic behavior at initial reaction times. We expect that these methods can also be adapted to probe structural changes to framework Sn sites that occur during reaction or treatment in liquid media to cause different transient and steady-state catalytic behavior [536].

## E.5 Acknowledgements

We acknowledge the financial support provided by the Purdue Process Safety and Assurance Center (P2SAC), a 3M Non-Tenured Faculty Grant, and a Kirk Endowment Exploratory Research Recharge Grant. We thank Jason Bates for helpful discussions and comments on this manuscript and Viktor Cybulskis for developing the IR cell design. We also thank Dr. Yury Zvinevich for assistance in constructing a

custom-built active site titration unit, Cindy Tavera for experimental assistance with sample preparation, Jacklyn Hall for experimental assistance with isotopic tracer and liquid NMR experiments, and John Degenstein and Dr. Mike Detwiler for assistance with parameter estimation and spectral peak deconvolution. Finally, we thank Profs. John Morgan and Julie Liu for access to the lyophilizer, and Dr. John Harwood (Purdue Interdepartmental NMR Facility) for assistance with NMR.

Additionally, I acknowledge Elsevier for granting permission to reproduce this chapter of my thesis. Adapted with permissions from *Journal of Catalysis*, 2016, 335, 141-154. Copyright Elsevier. The full article can be accessed here: [dx.doi.org/10.1016/j.jcat.2015.12](https://doi.org/10.1016/j.jcat.2015.12)

## E.6 Figures and Tables

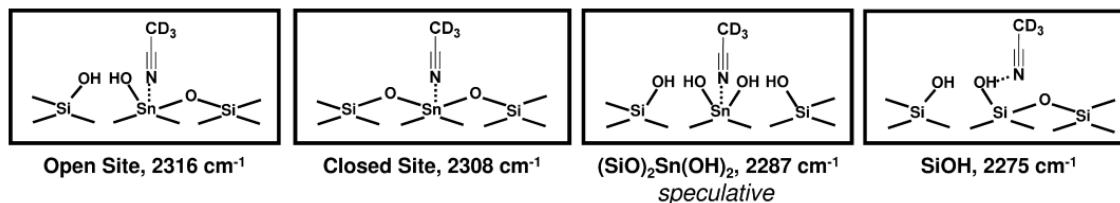


Figure E.1. Adsorption of  $\text{CD}_3\text{CN}$  on different sites in stannosilicates and corresponding  $\nu(\text{C}\equiv\text{N})$  infrared vibrational frequencies.

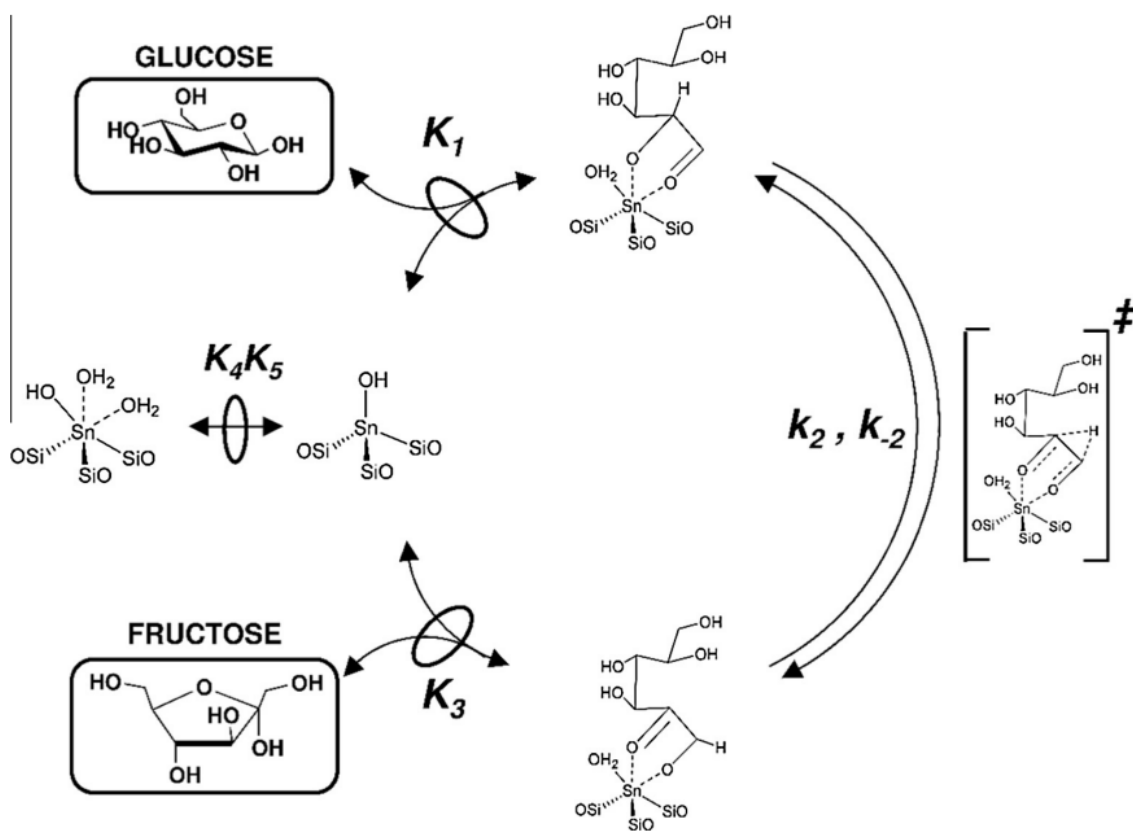


Figure E.2. Plausible reaction mechanism for glucose-fructose isomerization on open Sn sites in Sn-Beta involving kinetically-relevant 1,2-intramolecular hydride shift (Step 2). For clarity, kinetically-irrelevant steps are lumped as quasi-equilibrated reactions (Steps 1, 3-5).

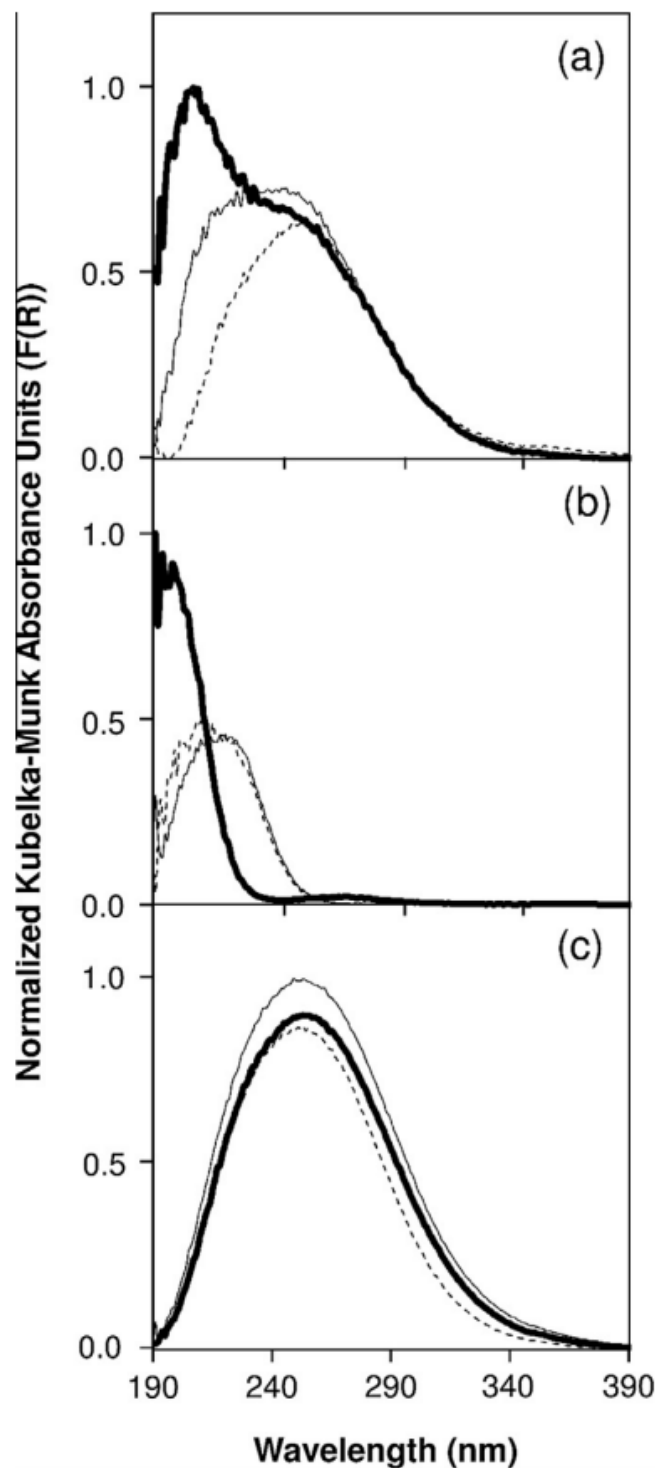


Figure E.3. Diffuse reflectance UV-Vis spectra in Kubelka-Munk units (normalized to the maximum  $F(R)$  intensity within each series) for (a) Sn-Beta-F-170, (b) Sn-Beta-OH-200, and (c) SnO<sub>2</sub>/Si-Beta collected under ambient conditions (thin solid line), after dehydration at 523 K (thick solid line), and after rehydration at 303 K (dashed line).

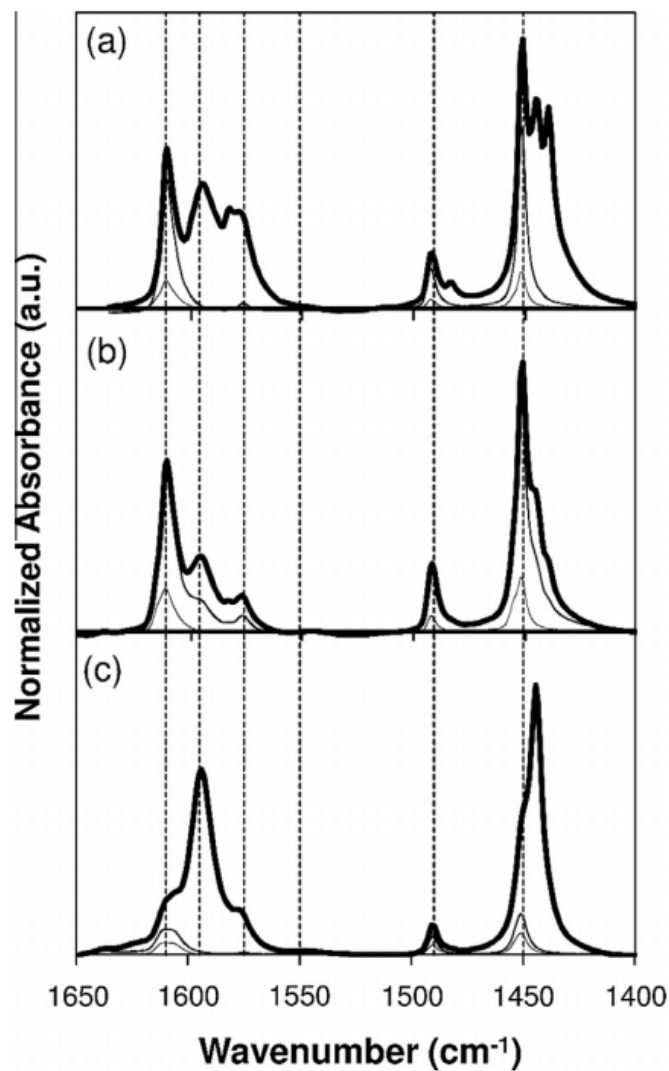


Figure E.4. IR spectra measured at low pyridine coverage (0.09-0.20 pyridine/Sn) and saturated spectra (thick lines) for (a) Sn-Beta-F-100, (b) Sn-Beta-F-140, and (c) Sn-Beta-OH-170. Dashed reference lines shown for Lewis acid sites ( $1615\text{ cm}^{-1}$ ,  $1450\text{ cm}^{-1}$ ), Lewis or Brønsted acid sites ( $1575\text{ cm}^{-1}$ ,  $1490\text{ cm}^{-1}$ ), Brønsted acid sites ( $1550\text{ cm}^{-1}$ ), and gas-phase pyridine ( $1595\text{ cm}^{-1}$ ).



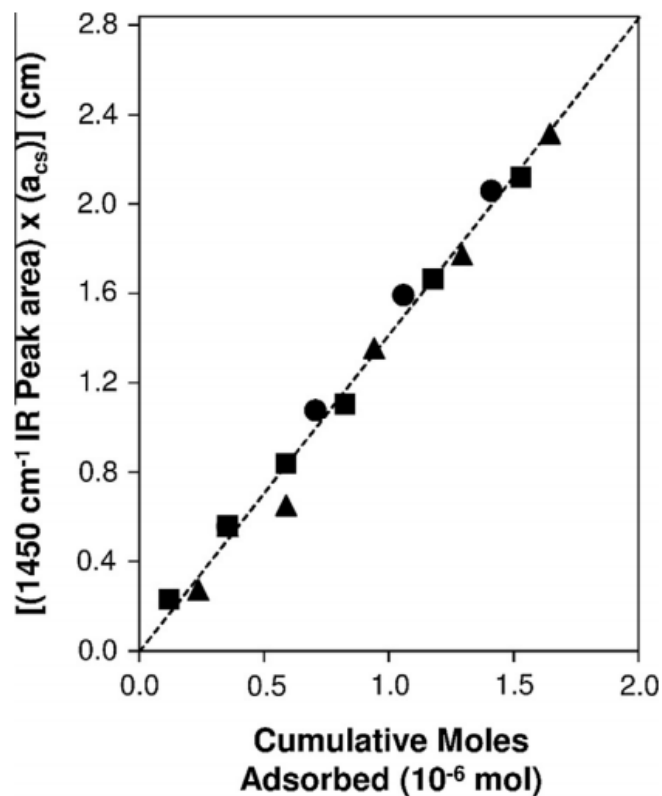


Figure E.5. Determination of the integrated molar extinction coefficient for pyridine adsorbed on Lewis acid sites ( $1450\text{ cm}^{-1}$ ) on Sn-Beta-OH-170 (black squares), Sn-Beta-F-140 (open triangles), Sn-Beta-F-100 (black circles), from IR peak areas corresponding to pyridine/Sn coverages between 0.04-0.66.

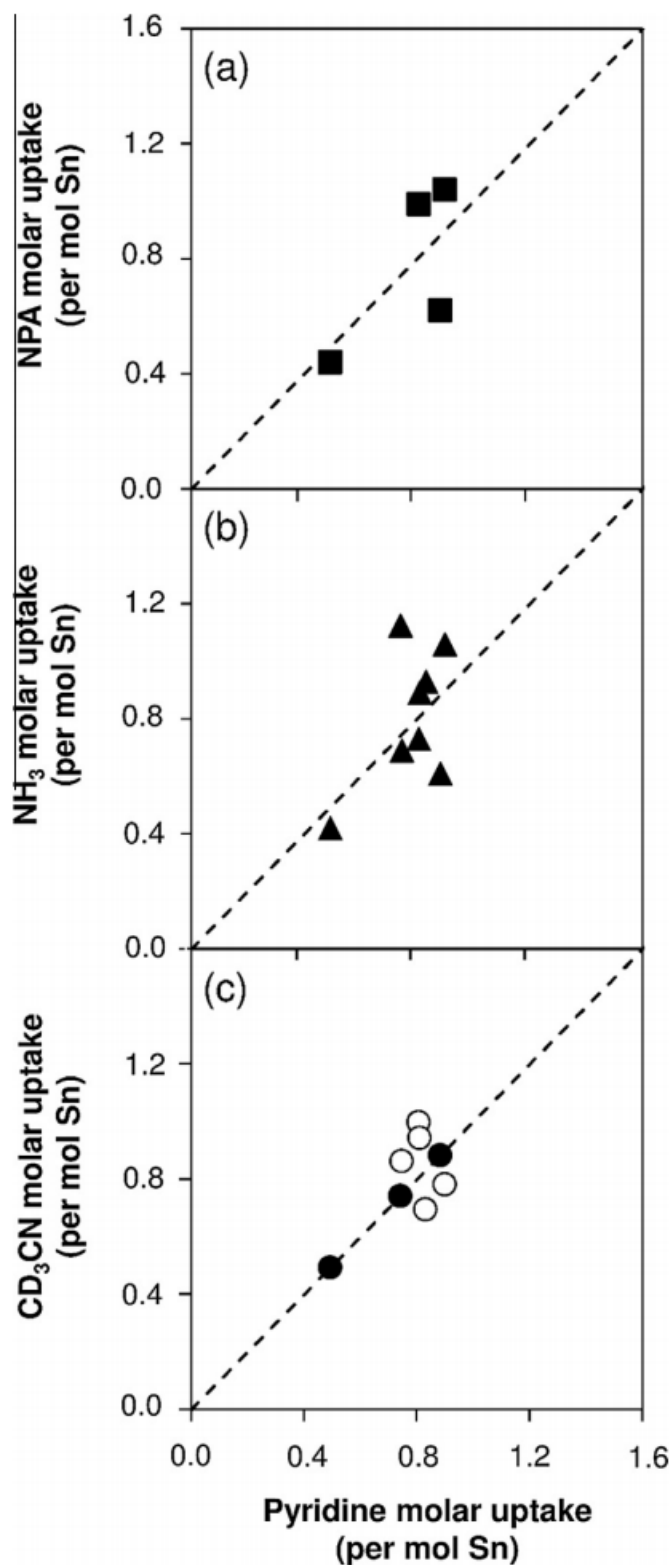


Figure E.6. Titrant molar uptakes (per Sn) compared to pyridine molar uptakes (per Sn) at saturation of Sn-Beta samples with (a) n-propylamine (NPA, black squares), (b) ammonia ( $\text{NH}_3$ , open triangles), and (c)  $\text{CD}_3\text{CN}$  (black circles were included and  $\circ$  were not included in fitting of  $\mathcal{E}$  values). Parity lines shown as dashed lines. NPA titration data not shown for samples denoted with an asterisk in Table 3E.3, for which TPD quantification includes binding to residual defect sites.

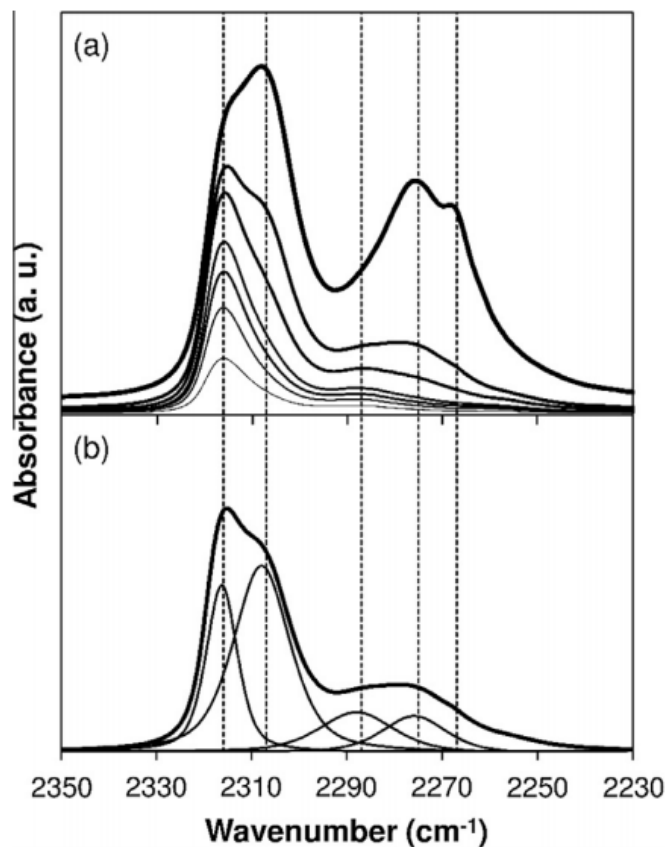


Figure E.7. FTIR difference spectra of Sn-Beta-F-105 (relative to the vacant surface) (a) with increasing CD<sub>3</sub>CN increasing coverage and (b) at a coverage of 0.65 CD<sub>3</sub>CN/Sn with deconvolution into component peaks. Dashed reference lines shown for open Sn sites (2316 cm<sup>-1</sup>), closed Sn sites (2308 cm<sup>-1</sup>), (SiO)<sub>2</sub>Sn(OH)<sub>2</sub> sites (*speculative assignment*, 2287 cm<sup>-1</sup>), silanol groups (2275 cm<sup>-1</sup>), and gas-phase CD<sub>3</sub>CN (2265 cm<sup>-1</sup>).

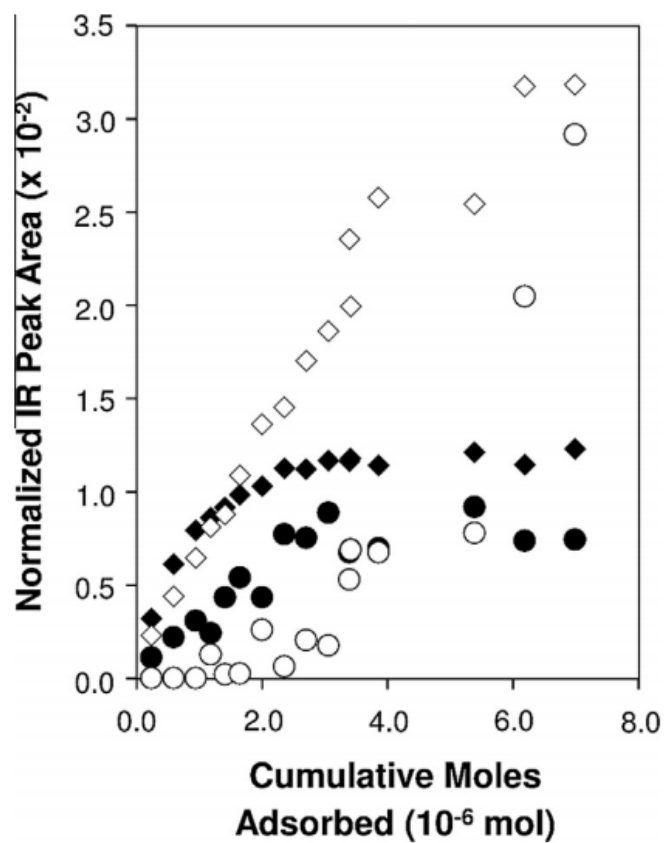


Figure E.8. Evolution of IR peak areas for  $2316\text{ cm}^{-1}$  (black triangles),  $2308\text{ cm}^{-1}$  (diamonds),  $2287\text{ cm}^{-1}$  (black circles), and  $2275\text{ cm}^{-1}$  (○) peaks with increasing  $\text{CD}_3\text{CN}$  coverage on Sn-Beta-F-105.

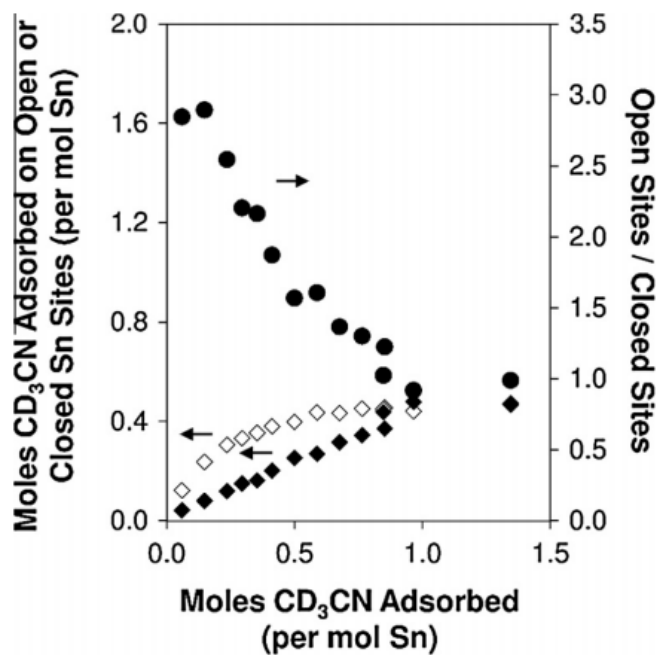


Figure E.9. Moles of  $\text{CD}_3\text{CN}$  adsorbed on open Sn sites (diamonds) and closed Sn sites (black triangles) on Sn-Beta-F-105, together with the ratio of open-to-closed Sn sites titrated (black circles), as a function of  $\text{CD}_3\text{CN}$  coverage.

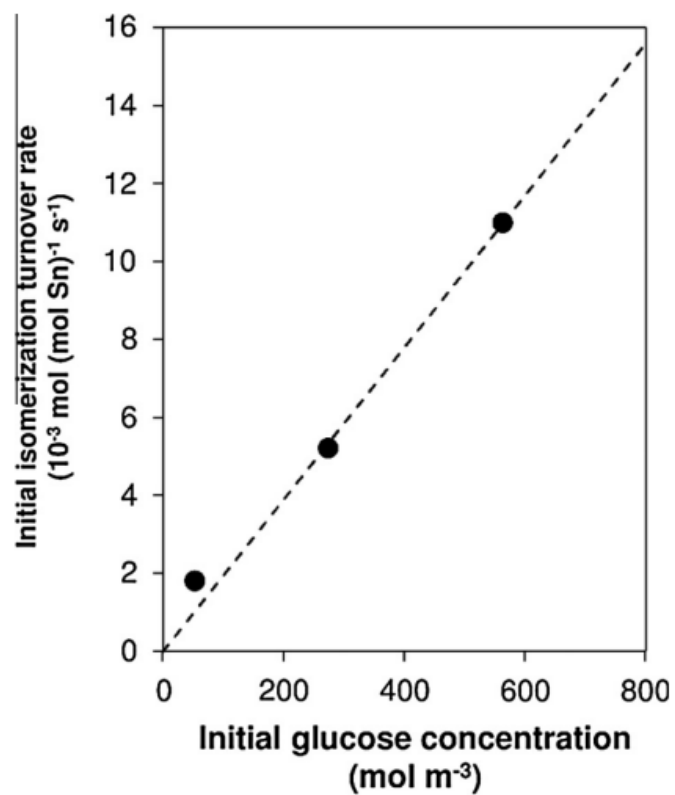


Figure E.10. Dependence of initial glucose-fructose isomerization turnover rate (per total Sn, 373 K) for Sn-Beta-F-220 on the initial aqueous-phase glucose concentration (1-10% (w/w)).

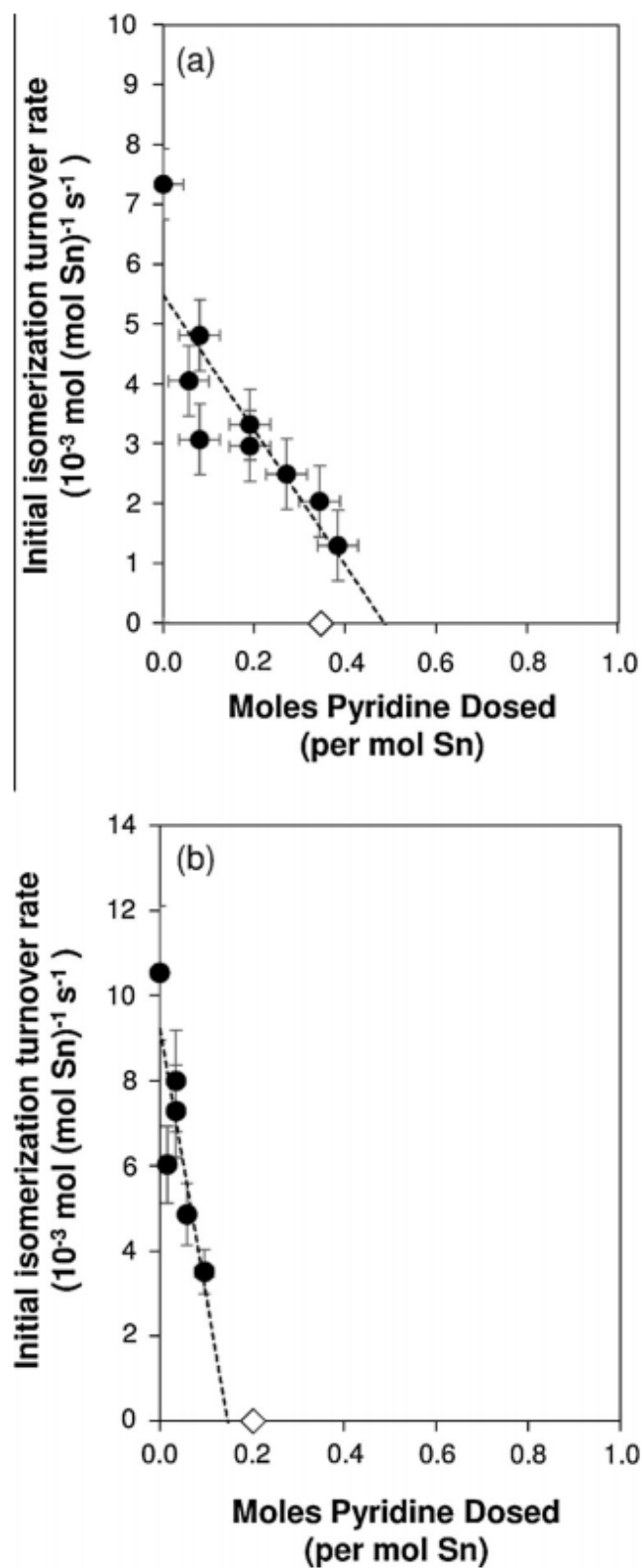


Figure E.11. Dependence of initial glucose-fructose isomerization turnover rates (per total Sn, 373 K, 1% (w/w) glucose) on pyridine coverage from titration before reaction on (a) Sn-Beta-F-110 and (b) Sn-Beta-F-170. The fraction of Sn open sites counted *ex situ* by  $\text{CD}_3\text{CN}$  are shown as open diamonds along the x-axes.

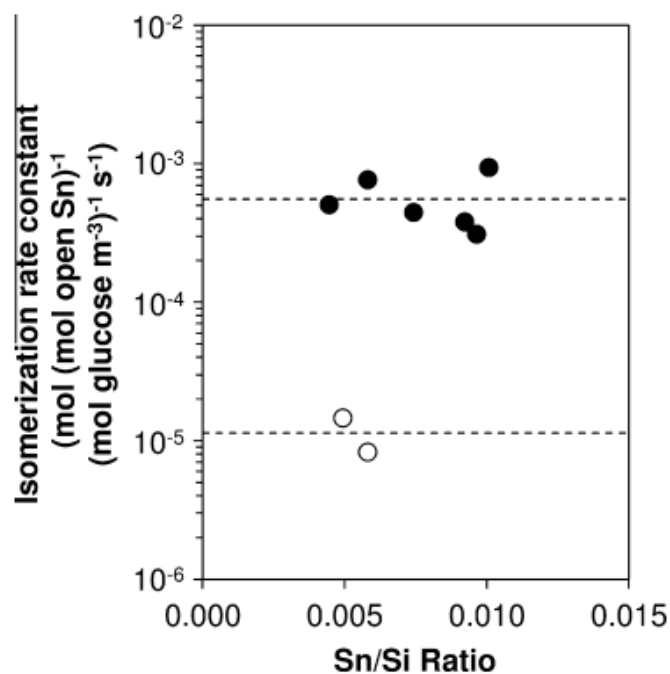


Figure E.12. First-order glucose-fructose isomerization rate constant (per open Sn site, 373 K) in water for hydrophobic Sn-Beta-F (black circles) and hydrophilic Sn-Beta-OH (○) samples as a function of Sn/Si ratio. Dashed lines indicate the averaged turnover rate within each series.



Table E.1.: Site and structural characterization data for the samples in this study.

| Sample                    | Crystallization Time | Si/Sn Ratio        | Si/Sn Ratio        | $V_{\text{ads}}$ ( $\text{N}_2$ , 77 K) | $V_{\text{ads}}$ ( $\text{cm}^3 \text{ g}^{-1}$ ) <sup>c</sup> | $V_{\text{ads}}$ ( $\text{H}_2\text{O}$ , 293 K) | DRUV Band         | DRUV Edge Energy  | Glucose-D2 Isotopic Tracer Studies <sup>f</sup> |
|---------------------------|----------------------|--------------------|--------------------|---|--|--|-------------------|-------------------|---|
|                           | (d)                  | (AAS) <sup>a</sup> | (EDS) <sup>b</sup> |   |  | ( $\text{cm}^3 \text{ g}^{-1}$ ) <sup>d</sup>    | (nm) <sup>e</sup> | (eV) <sup>e</sup> |   |
| Sn-Beta-F-100             | 14                   | 100                | 120                | 0.24                                    | 0.0069   | 0.0069   | 244               | 4.09              | Fructose-D1                                     |
| Sn-Beta-F-105             | 6                    | 105                | 140                | 0.22                                    | 0.015  | 0.015  | 216               | 4.17              | n.m.*   |
| Sn-Beta-F-110             | 14                   | 110                | 130                | 0.23                                    | 0.0095   | 0.0095   | 223               | 4.26              | Fructose-D1                                     |
| Sn-Beta-F-140             | 6                    | 140                | 105                | 0.22                                    | 0.017  | 0.017  | 238               | 4.19              | n.m.*   |
| Sn-Beta-F-170             | 14                   | 170                | 200                | 0.21                                    | 0.0073   | 0.0073   | 207               | 4.20              | Fructose-D1                                     |
| Sn-Beta-F-220             | 14                   | 220                | 300                | 0.22                                    | 0.0050   | 0.0050   | 197               | 4.29              | Fructose-D1                                     |
| Sn-Beta-OH-170            | -                    | 170                | 245                | 0.22                                    | 0.036  | 0.036  | 193               | 4.25              | Fructose-D1                                     |
| Sn-Beta-OH-200            | -                    | 200                | 280                | 0.19                                    | 0.092  | 0.092  | 195               | 4.69              | Fructose-D1                                     |
| SnO <sub>2</sub> /Si-Beta | -                    | 66                 | 63                 | 0.22                                    | 0.0052   | 0.0052   | 250               | 4.09              | No products**                                   |
| Sn-xerogel                | -                    | 110                | 130                | 0.02                                    | 0.024  | 0.024  | 245               | 4.37              | No products**                                   |

<sup>a</sup>Bulk composition determined by atomic absorption spectroscopy (AAS).

<sup>b</sup>Composition determined by energy dispersive X-ray spectroscopy (EDS).

<sup>c</sup>Micropore volume determined from total N<sub>2</sub> uptake at the end of micropore filling

in adsorption isotherms (77 K).

<sup>d</sup>H<sub>2</sub>O uptake at  $P/P_0 = 0.2$  (293 K) taken as a descriptor of hydrophobicity ( $P/P_0=0.2$  corresponds to full micropore filling with cyclohexane [573]).

<sup>e</sup>Diffuse reflectance UV-Vis spectra (band center at maximum F(R) intensity) and Tauc plots for samples after dehydration at 523 K (Section E.7.3).

<sup>f</sup>Fructose product formed from glucose-D2 reactants in water (373 K), <sup>1</sup>H NMR spectra shown in Figures E.21 and E.22 (Section E.7.4).

\*n. m., not measured

\*\*No products observed for SnO<sub>2</sub>/Si-Beta (0.01 g catalyst, 4 h) and Sn-xerogel (0.10 g catalyst, 5 h) in aqueous glucose (1% (w/w), 1 cm<sup>3</sup> solution, 373 K, pH = 5).

Table E.2.

Integrated molar extinction coefficients ( $\mathcal{E}$ ) for infrared peaks for pyridine and deuterated acetonitrile adsorbed to different sites on Sn-Beta and H-Y zeolites, determined assuming equimolar titrant binding to each type of site.

| Type of<br>Site                  | Peak<br>Center<br>( $\text{cm}^{-1}$ ) | $\mathcal{E}$ ,<br>literature<br>( $\text{cm}$<br>$\mu\text{mol}^{-1}$ ) | $\mathcal{E}$ , this<br>study<br>( $\text{cm}$<br>$\mu\text{mol}^{-1}$ ) |
|----------------------------------|--|--|--|
| <i>Pyridine</i>                  |  |  |  |
| Lewis acid, Al                   | 1455                                   | $2.20 \pm 0.30$ [574]  | $1.45 \pm 0.10$  |
| Brønsted acid, Al                | 1545                                   | $1.67 \pm 0.25$ [574]  | $1.95 \pm 0.13$  |
| Lewis Acid, Sn                   | 1450                                   | n.a.*  | $1.42 \pm 0.30$  |
| <i>Deuterated acetonitrile</i>   |  |  |  |
| Open Lewis acid, Sn              | 2316                                   | n.a.*  | $1.04 \pm 0.22$  |
| Closed Lewis acid, Sn            | 2308                                   | n.a.*  | $2.04 \pm 0.43$  |
| Sn(OH) <sub>2</sub> <sup>a</sup> | 2287                                   | n.a.*  | $2.13 \pm 0.45$  |
| Silanol, SiOH                    | 2275                                   | n.a.*  | $0.74 \pm 0.16$  |
| Lewis acid, Al                   | 2325, 2310                             | $3.6 \pm 0.2$ [571]  | n.m.**   |
| Brønsted acid, Al                | 2297                                   | $2.5 \pm 0.1$ [571]  | n.m.**   |

<sup>a</sup> speculative assignment.

\*n.a., not available

\*\*n.m., not measured

Table E.3.  
 Fraction of Lewis acidic Sn sites (per mol Sn) on each sample counted with  
 different base titrants. Binding stoichiometries of 1 per site for each titrant.

| Sample                    | Pyridine <sup>a</sup> | NH <sub>3</sub> <sup>b</sup> | NPA <sup>c</sup> | CD <sub>3</sub> CN <sup>d</sup> |             |               |                    |
|---------------------------|-----------------------|------------------------------|------------------|---------------------------------|-------------|---------------|--------------------|
|                           | <i>Total</i>          | <i>Total</i>                 | <i>Total</i>     | <i>Total</i>                    | <i>Open</i> | <i>Closed</i> | <i>Open/Closed</i> |
| Sn-Beta-F-100             | 0.49                  | 0.42                         | 0.44             | 0.49                            | 0.13        | 0.36          | 0.35               |
| Sn-Beta-F-105             | 0.88                  | 0.61                         | 0.62             | 0.88                            | 0.35        | 0.54          | 0.64               |
| Sn-Beta-F-110             | 0.81                  | 0.73                         | 0.99             | 1.00                            | 0.35        | 0.65          | 0.53               |
| Sn-Beta-F-140             | 0.90                  | 1.06                         | 1.04             | 0.78                            | 0.21        | 0.58          | 0.35               |
| Sn-Beta-F-170             | 0.75                  | 0.69                         | 1.24*            | 0.86                            | 0.20        | 0.67          | 0.29               |
| Sn-Beta-F-220             | 0.82                  | 0.89                         | 2.07*            | 0.94                            | 0.33        | 0.61          | 0.54               |
| Sn-Beta-OH-170            | 0.73                  | 1.12                         | 1.14*            | 0.73                            | 0.46        | 0.28          | 1.64               |
| Sn-Beta-OH-200            | 0.83                  | 0.93                         | 1.71*            | 0.69                            | 0.15        | 0.54          | 0.29               |
| SnO <sub>2</sub> /Si-Beta | 0.23                  | n.m.**                       | n.m.**           | 0.14                            | 0.03        | 0.11          | 0.26               |
| Sn-xerogel                | 0.25                  | n.m.**                       | n.m.**           | 0.10                            | 0.04        | 0.06          | 0.58               |

<sup>a</sup>Errors are  $\pm 20\%$ .

<sup>b</sup>Errors are  $\pm 5\%$ .

<sup>c</sup>Errors are  $\pm 10\%$ .

<sup>d</sup>Errors are  $\pm 15\%$ .

\*NPA binding on Sn-Beta-OH and Sn-Beta-F (with Si/Sn >150) overestimates  
 Sn Lewis acid sites (Section E.7.5).

\*\*n.m., not measured.

## E.7 Supporting Information

### E.7.1 X-ray diffractograms of stannosilicate samples.

See Figure E.13.

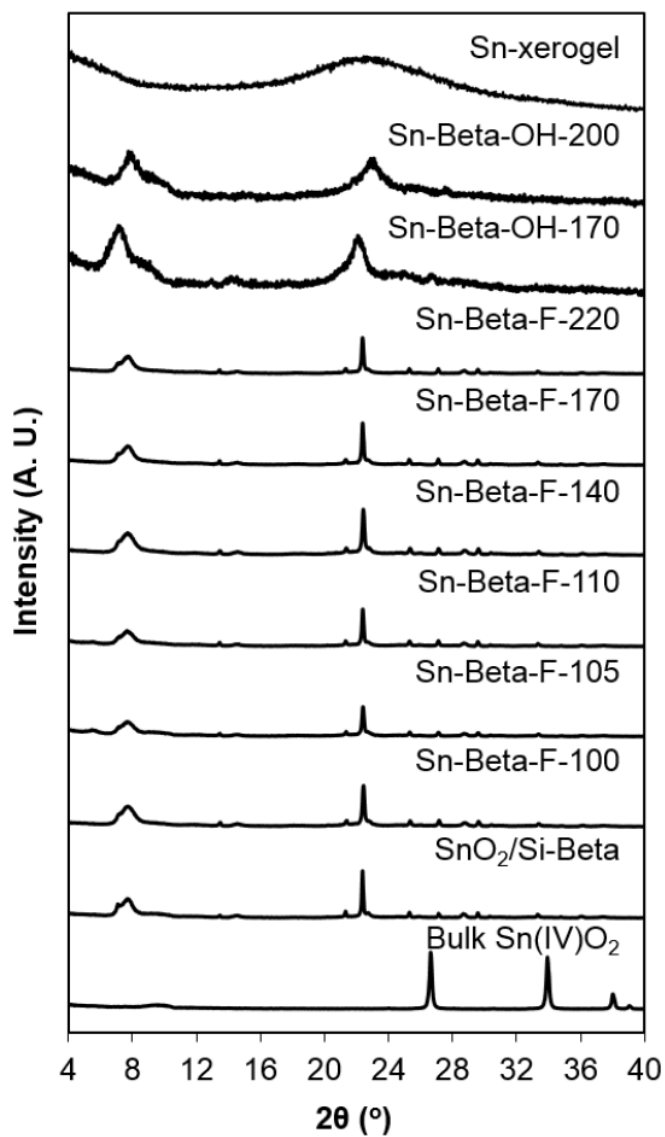


Figure E.13. Powder XRD patterns of the stannosilicate samples in this study. Patterns for Sn-Beta-OH-170 and Sn-Beta-OH-200 multiplied by 10 $\times$ , and Sn-xerogel multiplied by 5 $\times$ , for clarity.

### E.7.2 N<sub>2</sub> and H<sub>2</sub>O adsorption isotherms of zeolite samples.

N<sub>2</sub> adsorption isotherms (77 K) are shown for all Sn-Beta samples, SnO<sub>2</sub>/Si-Beta, and Sn-xerogel in Figure S.2. On each sample, the micropore volume was determined from a semi-log derivative analysis of the N<sub>2</sub> isotherms, by plotting  $\delta(V_{ads}/g)/\delta(\log(P/P_0))$  vs.  $\log(P/P_0)$  to identify the micropore filling transition (first maximum) and then the end of micropore filling (subsequent minimum) [136, 137]. The volume of adsorbed N<sub>2</sub> (at STP) at the end of micropore filling was converted to the volume of adsorbed liquid using the liquid N<sub>2</sub> molar density (0.029 mol cm<sup>-3</sup>). This method gave the micropore volumes listed in Table E.1.

H<sub>2</sub>O adsorption isotherms (293 K) are shown for Sn-Beta-F samples (Fig. E.15) and for Sn-Beta-OH, SnO<sub>2</sub>/Si-Beta, and Sn-xerogel samples (Fig. E.16). On each sample, the amount of water adsorbed at a relative pressure ( $P/P_0$ ) of 0.2 was used to assess hydrophobicity, as chosen originally by Chen [573] because cyclohexane (298 K) fills the pores of hydrophobic zeolites at  $P/P_0 = 0.2$ . The volume of adsorbed H<sub>2</sub>O (at STP) at  $P/P_0 = 0.2$  was converted to the volume of adsorbed liquid using the liquid H<sub>2</sub>O molar density (0.055 mol cm<sup>-3</sup>). This method gave the H<sub>2</sub>O uptake values listed in Table E.1.

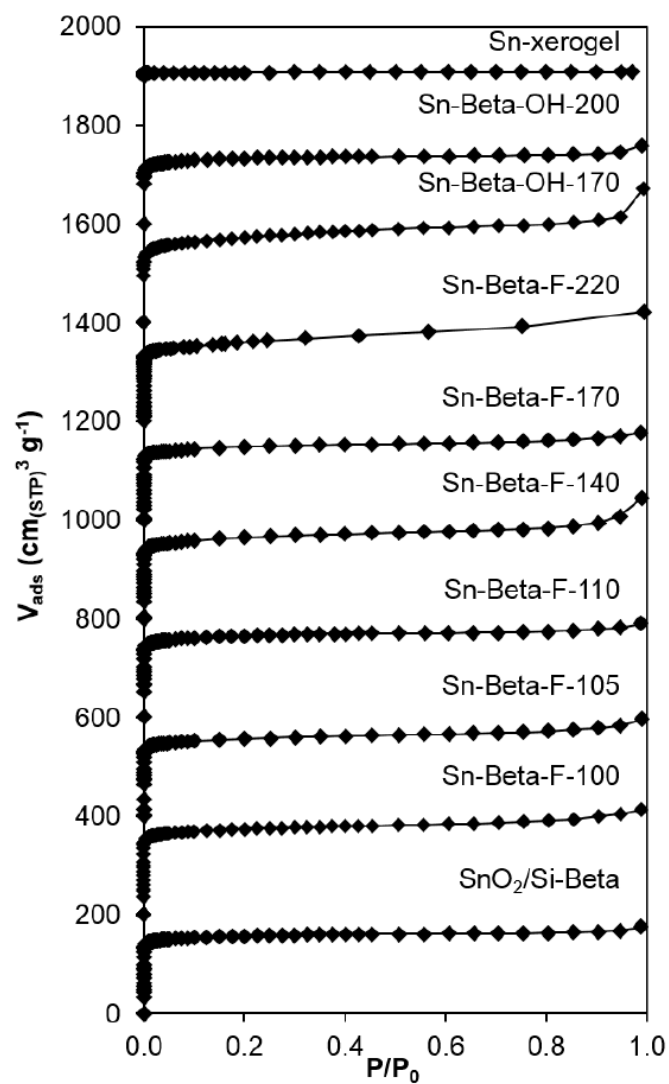


Figure E.14.  $N_2$  adsorption isotherms (77 K) for all samples used in this study. Isotherms offset by  $200 \text{ cm}^3 \text{ g}^{-1}$  for clarity.

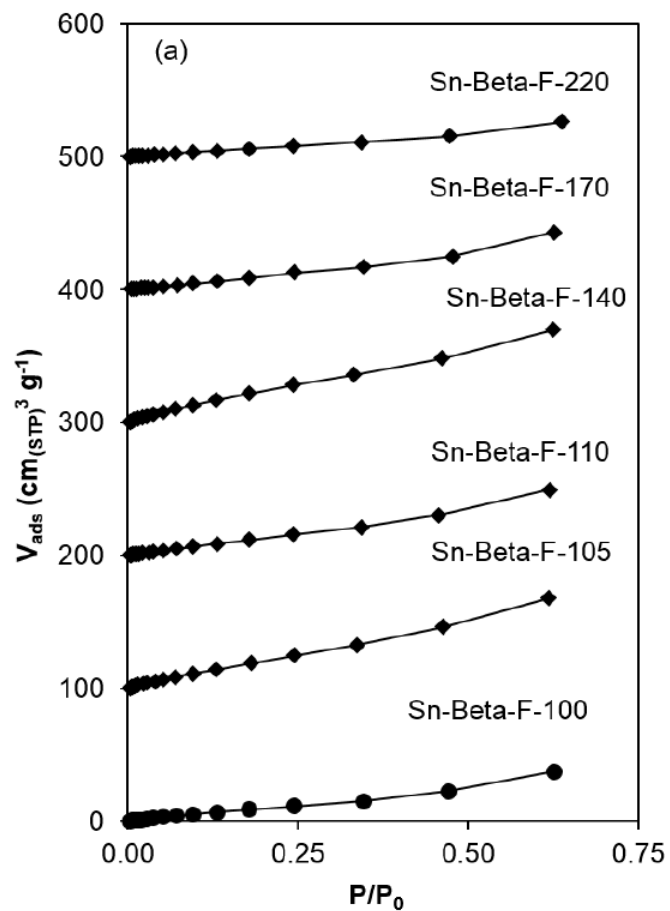


Figure E.15.  $\text{H}_2\text{O}$  adsorption isotherms (293 K) for Sn-Beta-F samples used in this study. Isotherms offset by  $100 \text{ cm}^3 \text{ g}^{-1}$  for clarity.



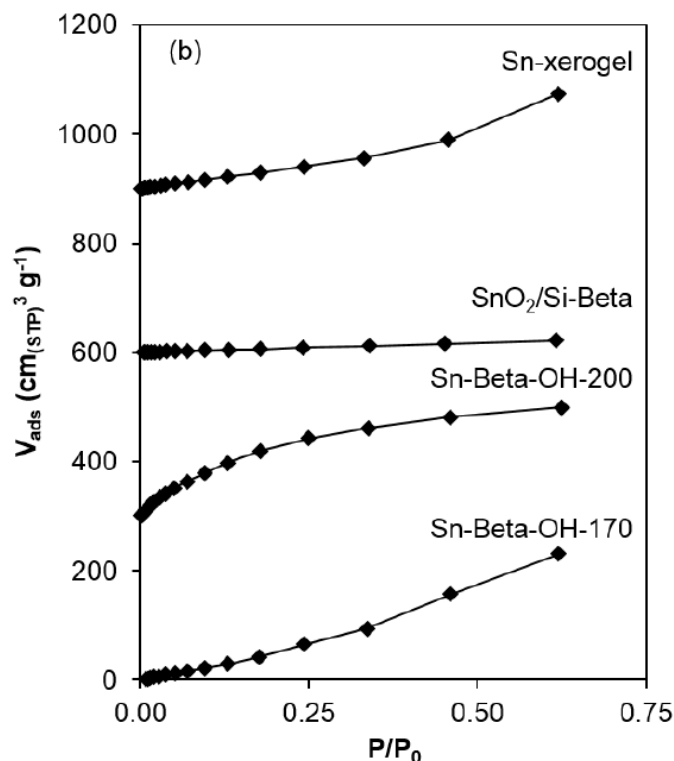


Figure E.16.  $\text{H}_2\text{O}$  adsorption isotherms (293 K) for Sn-Beta-OH samples,  $\text{SnO}_2/\text{Si-Beta-F}$ , and Sn-xerogel used in this study. Isotherms offset by  $300 \text{ cm}^3 \text{ g}^{-1}$  for clarity.

### E.7.3 Diffuse-reflectance UV-Visible spectra of zeolite samples.

DRUV spectra under ambient conditions, dehydrated conditions and rehydrated conditions (see Section E.2.2) are shown for  $\text{SnO}_2/\text{Si-Beta}$ , Sn-Beta-OH-200, and Sn-Beta-F-170 in Fig. E.3. All samples contain DRUV bands with maxima at ca. 240 nm under ambient conditions, characteristic of Sn in octahedral coordination [568, 578]. After dehydration treatments, DRUV bands for Sn-Beta-OH-200 and Sn-Beta-F-170 shift to ca. 210 nm characteristic of tetrahedral Sn [534, 577], while DRUV bands for the  $\text{SnO}_2/\text{Si-Beta}$  do not change because octahedrally-coordinated Sn atoms in  $\text{SnO}_2$  do not change coordination upon heating. Although under-coordinated Sn atoms near  $\text{SnO}_2$  surfaces may lose coordinated water upon dehydration, the fraction of such

Sn atoms appears small and noticeable changes to DRUV spectra after dehydration of  $\text{SnO}_2/\text{Si-Beta}$  are not observed.

DRUV spectra of all Sn-Beta-F samples, and for Sn-Beta-OH,  $\text{SnO}_2/\text{Si-Beta}$ , and Sn-xerogel after dehydration treatments at 523 K are shown in Figures E.17 and E.18, respectively. DRUV bands for Sn-Beta-F-100, Sn-Beta-F-105, and Sn-xerogel were centered at ca. 240 nm upon dehydration. DRUV bands for Sn-Beta-F-110, Sn-Beta-F-140, and Sn-Beta-F-170 were centered at ca. 210 nm, with a noticeable shoulder at ca. 255 nm. For each of these samples, the lack of a complete shift or remaining shoulder in DRUV spectra upon dehydration likely reflects some non-framework Sn species on these samples. DRUV bands for Sn-Beta-OH-170 at ca. 210 nm (ambient) may shift below 190 nm upon dehydration, while the shoulder present at ca. 250 nm remains after the thermal treatment, likely reflecting  $\text{SnO}_2$  nanoparticles larger than those that give rise to bands at ca. 230 nm due to quantum confinement effects [579–582].

Tauc plots are shown for all Sn-Beta-F samples, and for Sn-Beta-OH,  $\text{SnO}_2/\text{Si-Beta}$ , and Sn-xerogel in Figures E.19 and E.20, respectively. Linear regions in the low energy regime ( $< \text{ca. } 5 \text{ eV}$ ) of Tauc plots were extrapolated to determine the x-intercept values, which correspond to the band gap energies for the Sn species [594–596], which can be correlated to  $\text{SnO}_2$  particle size [579–582]. These values are summarized in Table E.4.

Table E.4.

Edge energies for all samples determined from x-intercepts of linear portions of Tauc plots (Figs. E.19 and E.20) DRUV band centers at maximum  $F(R)$  intensity are reported for spectra collected after dehydration treatments (Figs. E.17 and E.18), and parenthetical values are for second band observed in some DRUV spectra.

| Sample                    | Ambient<br>(eV) | Dehydrated<br>(eV) | Rehydrated<br>(eV) | Band<br>Maximum<br>(nm) |
|---------------------------|-----------------|--------------------|--------------------|-------------------------|
| Sn-Beta-F-100             | 4.20            | 4.09               | 4.19               | 244                     |
| Sn-Beta-F-110             | 4.34            | 4.26               | 4.34               | 223                     |
| Sn-Beta-F-170             | 4.27            | 4.20               | 4.20               | 207                     |
| Sn-Beta-F-220             | 4.09            | 4.29               | 4.25               | 197 (260)               |
| Sn-Beta-F-105             | 4.17            | 4.17               | 4.24               | 216                     |
| Sn-Beta-F-140             | 4.29            | 4.19               | 4.25               | 238                     |
| Sn-Beta-OH-170            | 4.02            | 4.25               | 4.10               | 267                     |
| Sn-Beta-OH-200            | 4.59            | 4.69               | 5.13               | 195                     |
| SnO <sub>2</sub> /Si-Beta | 4.06            | 4.09               | 4.16               | 250                     |
| Sn-xerogel                | 4.45            | 4.37               | 4.46               | 245                     |

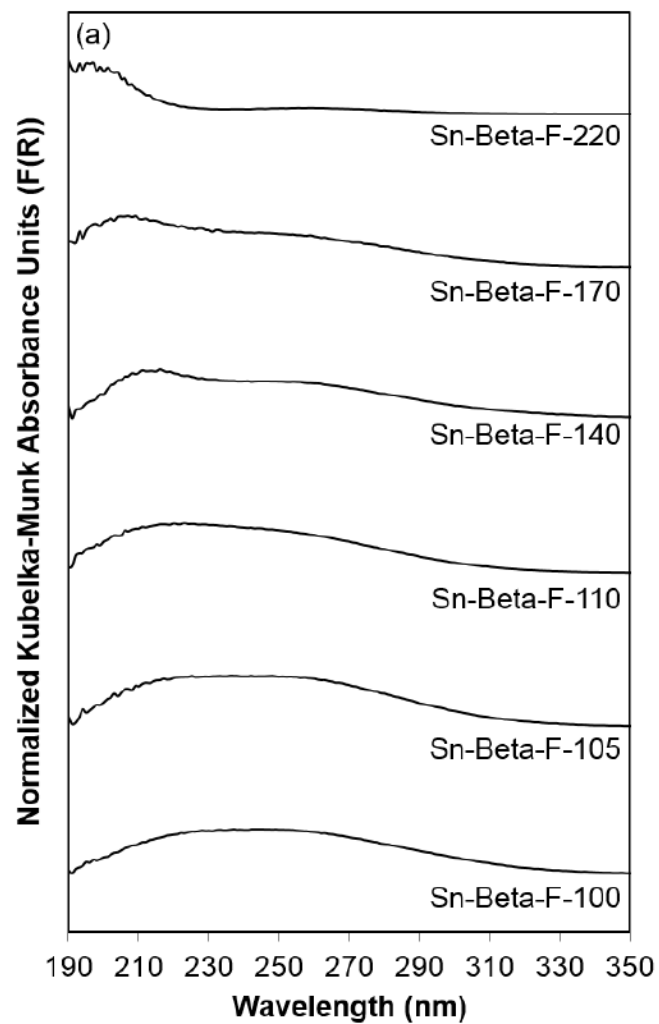


Figure E.17. DRUV spectra for Sn-zeolite samples collected after dehydration treatments (523 K). Spectra normalized to  $F(R)$  at the peak maximum and artificially offset for clarity.

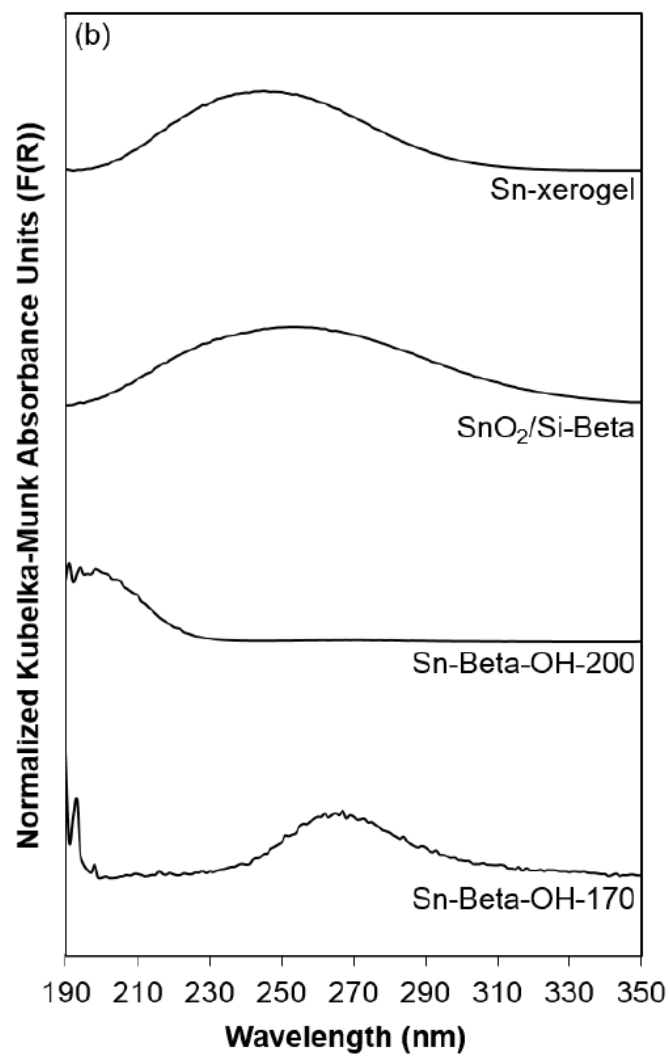


Figure E.18. DRUV spectra for Sn-zeolite samples collected after dehydration treatments (523 K). Spectra normalized to  $F(R)$  at the peak maximum and artificially offset for clarity.

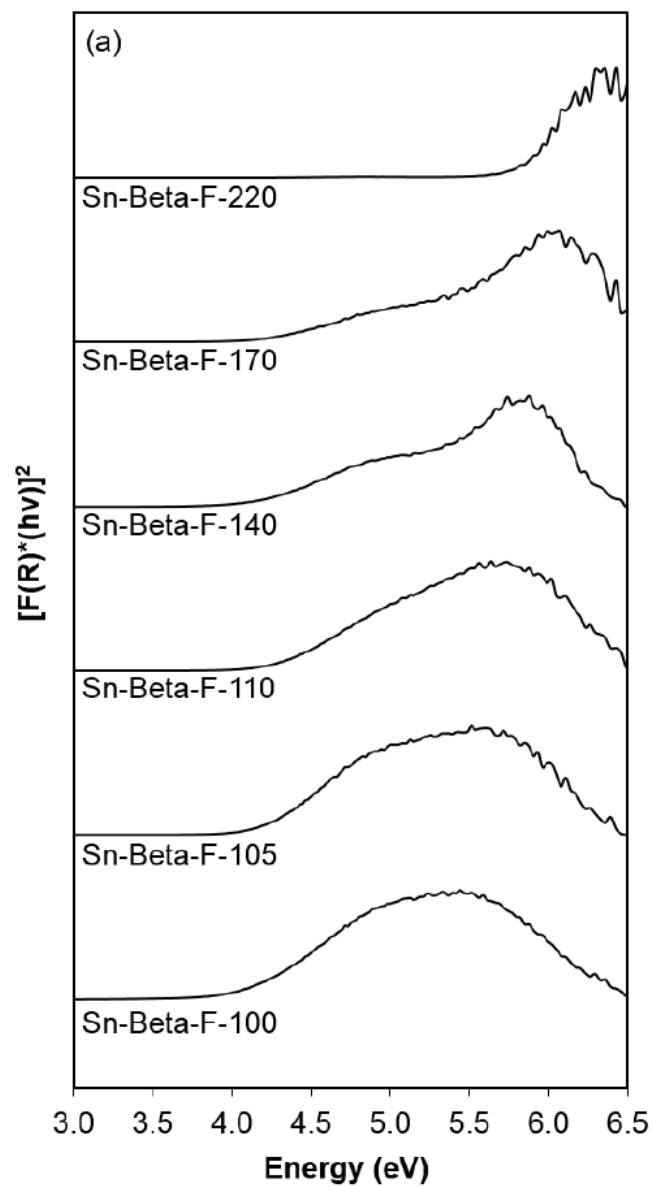


Figure E.19. Tauc plots for Sn-zeolite samples from DRUV spectra collected after dehydration treatments (523 K).

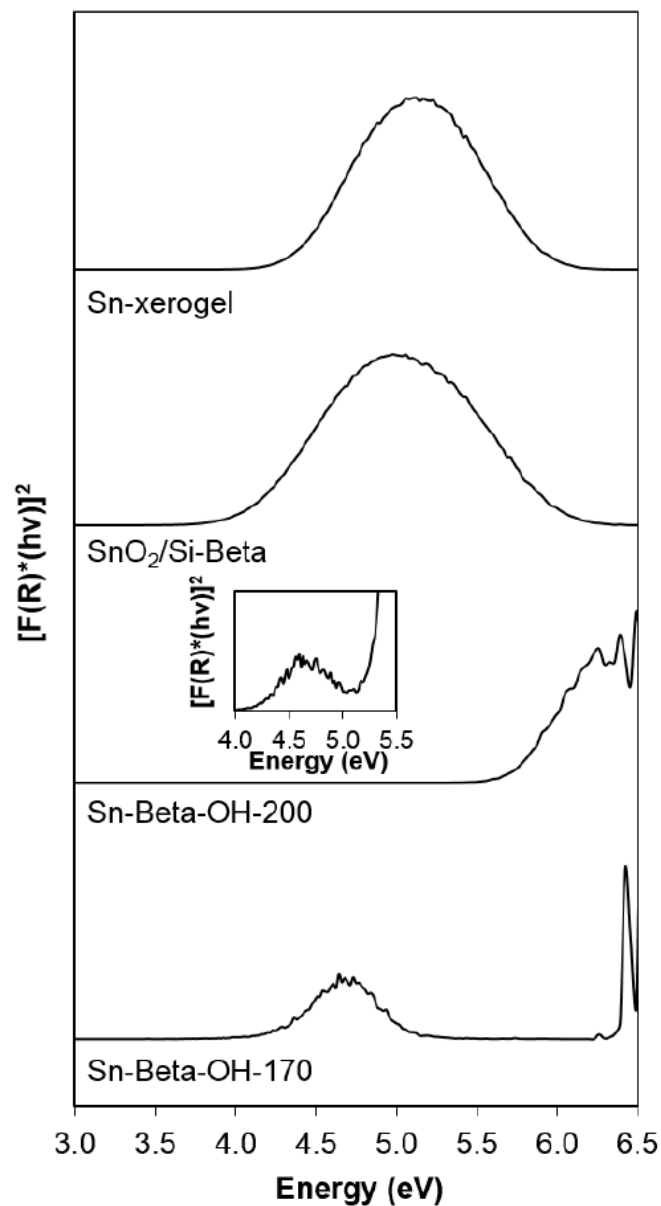


Figure E.20. Tauc plots for Sn-zeolite samples from DRUV spectra collected after dehydration treatments (523 K). Inset shows low-energy region for Sn-Beta-OH-200 that gives rise to the edge energy reported in Table E.1.

#### E.7.4 $^1\text{H}$ NMR spectra of sugars after reaction of glucose-D2 with zeolite samples in water.

$^1\text{H}$  NMR spectra of glucose fractions recovered after reaction show no change when compared to that of the labeled glucose-D2 reactant, which do not contain a resonance at  $\delta = 3.1$  ppm (Fig. E.21). The absence of this resonance corresponds to a deuterium atom bound to the  $\alpha$ -carbonyl carbon (C2 position) of glucose and indicates negligible H/D scrambling of glucose-D2 under the reaction conditions studied here [578].  $^1\text{H}$  NMR spectra of fructose fractions collected after reaction do not show a resonance at  $\delta = 3.45$  ppm, which indicates that deuterium rather than hydrogen is present at the fructose C1 position (Fig. E.22). This reflects fructose formation only via the Lewis acid-mediated intramolecular 1,2-hydride shift mechanism instead of the enolate-mediated mechanism catalyzed by bases [142]. Fructose formation was not observed with aqueous glucose solutions adjusted to pH=5 (with HCl) on  $\text{SnO}_2/\text{Si-Beta}$  or in reactors without catalyst present, further demonstrating that the fructose products formed with Sn-Beta samples solely reflect catalytic contributions of Lewis acidic Sn sites.



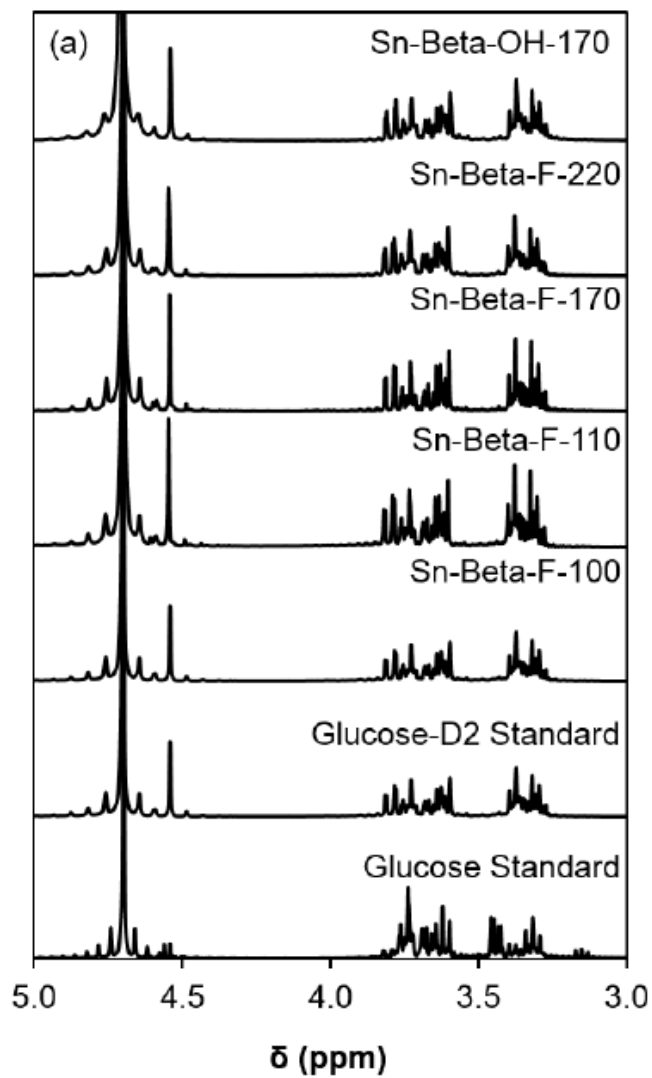


Figure E.21.  $^1\text{H}$  NMR spectra for glucose recovered after glucose isomerization catalysis with the Sn-Beta samples tested in this study. The resonating multiplet centered around  $\delta = 4.7$  ppm corresponds to residual water present after freeze drying the monosaccharide products

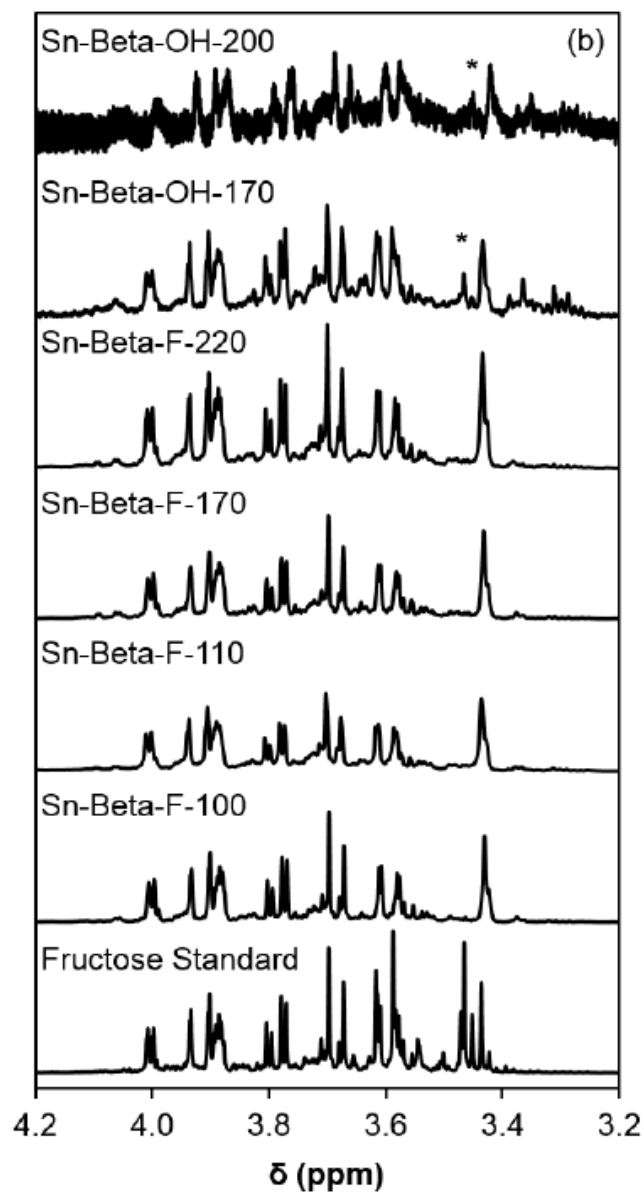


Figure E.22.  $^1\text{H}$  NMR spectra for the fructose recovered after glucose isomerization catalysis with the Sn-Beta samples tested in this study. A small resonance at  $\delta = 3.47$  ppm (denoted with an asterisk) is present in fructose products on Sn-Beta-OH-170 and Sn-Beta-OH-200, indicating a small contribution of the enolate mechanism by hydroxyl ions that becomes detectable at the longer reaction times ( $>4$  h) used to attain higher glucose conversion on these samples.

### E.7.5 Determination of integrated molar extinction coefficients for pyridine on H-Y zeolite.

NH<sub>4</sub>-Y (Zeolyst CBV300, Si/Al = 2.6) was treated at 823 K in flowing dry air ( $6.66 \text{ cm}^3 \text{ s}^{-1} (\text{g zeolite})^{-1}$ ) for 4 h to convert to the H-Y form. H-Y was pressed into a self-supporting wafer and treated under vacuum at 823 K in the IR cell for 1 h, before cooling to 423 K to perform pyridine titration experiments. As pyridine was successively dosed onto the wafer, IR spectra (Fig. E.23) showed bands for protonated pyridine ( $1630 \text{ cm}^{-1}$ ,  $1545 \text{ cm}^{-1}$ ) and for either protonated pyridine or pyridine bound to Lewis acidic Al sites ( $1490 \text{ cm}^{-1}$ ). Yet, no bands for pyridine bound to Lewis acidic Al sites ( $1610 \text{ cm}^{-1}$ ,  $1455 \text{ cm}^{-1}$ ) were observed (Fig. E.23). Deconvolution of IR spectra using the procedure described in Section S.9 was used to determine areas of individual IR peaks after each pyridine dose of known quantity. The  $\mathcal{E}$  value for the IR band at  $1540 \text{ cm}^{-1}$  (protonated pyridine), which was determined from the linear relationship between [integrated IR band area ( $\text{cm}^{-1}$ )\*wafer cross sectional area ( $\text{cm}^2$ )] and the total moles dosed ( $\mu\text{mol}$ , Fig. E.24), was  $1.95 \pm 0.13 \text{ cm } \mu\text{mol}^{-1}$ . This value is similar, within error, to the value reported by Emeis ( $1.67 \pm 0.25 \text{ cm } \mu\text{mol}^{-1}$ ) for pyridine adsorbed on Brønsted acid sites in Al-zeolites [574]. The error in the  $\mathcal{E}$  value was estimated by propagation of error in the moles of titrant adsorbed within each dose ( $\pm 0.05 \text{ Torr}$ ).

The H-Y wafer was then treated in flowing air at 953 K for 4 h, in dynamic vacuum (0.1 Torr) at 953 K for 1 h, and then cooled to 423 K for pyridine titration experiments. As pyridine was successively dosed onto the wafer, new IR bands at  $1610 \text{ cm}^{-1}$  and  $1455 \text{ cm}^{-1}$  characteristic of pyridine bound to Lewis acidic Al sites appeared (Fig E.23) [559]. Deconvolution of IR spectra using the same procedure as above was used to determine IR peak areas for each dose of known quantity. The  $\mathcal{E}$  value for the IR band at  $1455 \text{ cm}^{-1}$  (pyridine bound to Lewis acidic Al sites) was determined by first calculating the squared error between the number of moles dosed to the wafer and the estimated number of moles adsorbed for each dose, using the  $\mathcal{E}$  value of  $1.95 \text{ cm } \mu\text{mol}^{-1}$  for protonated pyridine at  $1540 \text{ cm}^{-1}$  and an initial guess

for the  $\mathcal{E}$  value for pyridine bound to Lewis acidic Al. The sum of squared errors was minimized in order to determine the best fit of E values for pyridine bound to Lewis acidic Al sites, which was  $1.45 \pm 0.10 \text{ cm } \mu\text{mol}^{-1}$ . This value is outside of the error of the E value for pyridine bound to Lewis acidic Al determined by Emeis on H-MOR, H-Y, and H-ZSM-5 zeolites and amorphous silica-alumina ( $2.20 \pm 0.33 \text{ cm } \mu\text{mol}^{-1}$  [574]), but falls within the range reported in the literature for pyridine bound to Lewis acidic Al sites in aluminosilicates ( $0.89\text{-}3.9 \text{ cm } \mu\text{mol}^{-1}$  [585, 597, 598]).

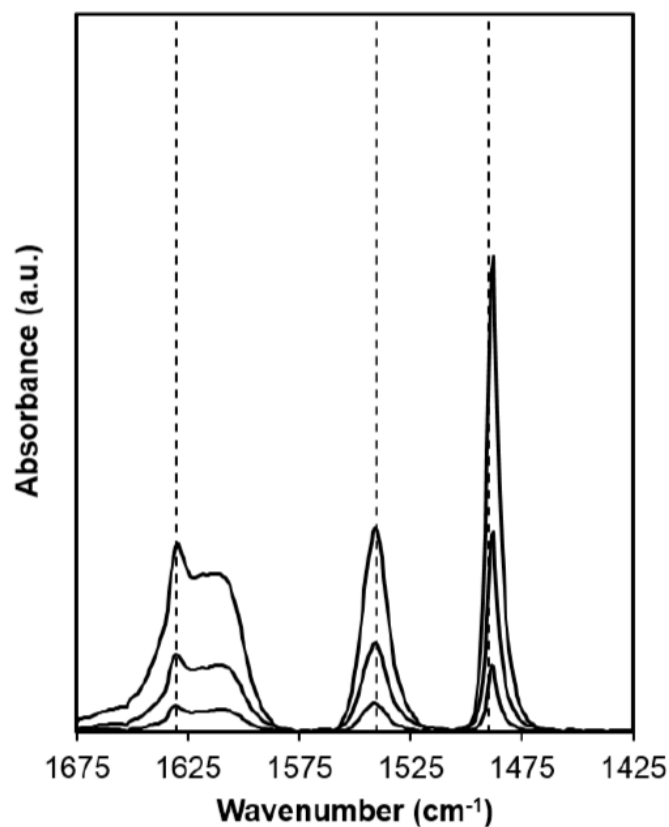


Figure E.23. IR spectra after progressive titration of pyridine on H-Y (Si/Al=2.6, Zeolyst) at 423 K (pyridine/Al = 0.005-0.040). Dashed lines at  $1630 \text{ cm}^{-1}$  (protonated pyridine),  $1545 \text{ cm}^{-1}$  (protonated pyridine), and  $1490 \text{ cm}^{-1}$  (protonated pyridine or pyridine bound to Lewis acidic Al sites).

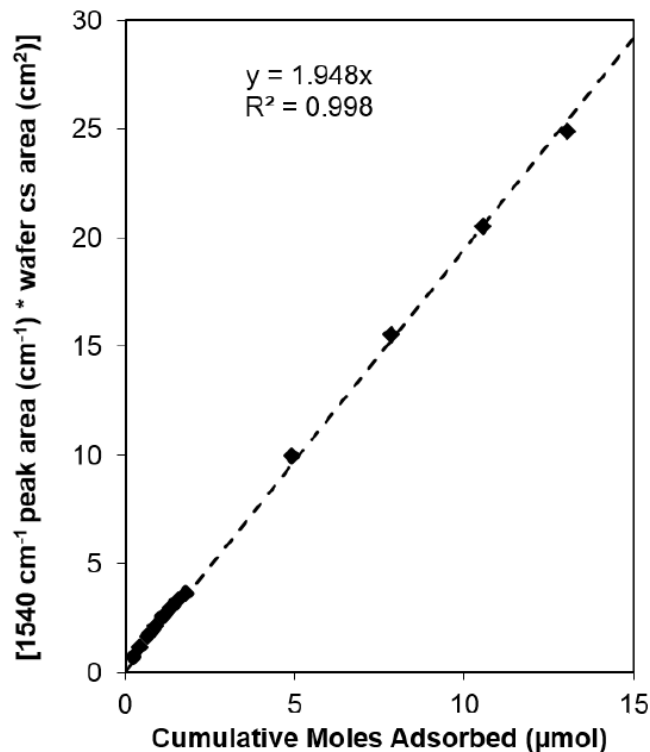


Figure E.24. Integrated area of  $1545\text{ cm}^{-1}$  IR peak multiplied by wafer cross-sectional area plotted against the amount of pyridine adsorbed on H-Y (Si/Al=2.6, Zeolyst) at 423 K.

#### E.7.6 Pyridine titration and infrared spectroscopy of zeolite samples.

IR spectra for each Sn-Beta sample after pyridine saturation and evacuation for 900 seconds under vacuum (0.1 Torr) at 423 K are shown in Figure E.26. This evacuation procedure was sufficient to remove gaseous pyridine and the majority of the weakly-bound physisorbed pyridine that convolutes the peak at  $1450\text{ cm}^{-1}$  (Fig E.27). IR spectra were baseline-corrected between  $1400\text{ cm}^{-1}$  to  $1650\text{ cm}^{-1}$  and deconvoluted in CasaXPS to determine the areas of IR peaks at  $1610\text{ cm}^{-1}$  and  $1450\text{ cm}^{-1}$ , which reflects pyridine bound to Lewis acidic Sn sites [559], using a combined Gauss-Lorentzian (SGL) lineshape with an 80% Lorentzian contribution. Additional bands at  $1439\text{ cm}^{-1}$ ,  $1445\text{ cm}^{-1}$ , and  $1490\text{ cm}^{-1}$  were included in the deconvolution

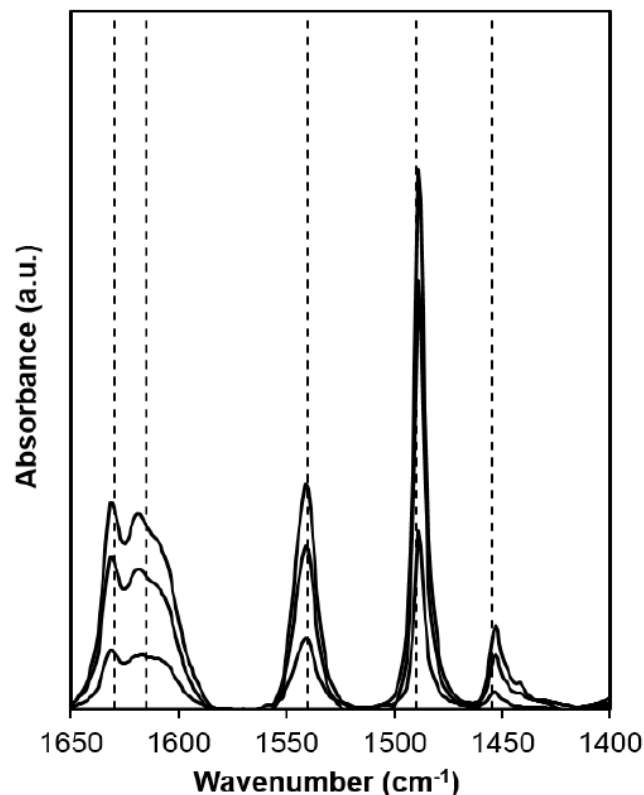


Figure E.25. IR spectra after progressive titration of pyridine on high temperature-treated H-Y (Si/Al=2.6, Zeolyst) at 423 K (pyridine/Al = 0.012-0.13). Dashed lines shown at 1630  $\text{cm}^{-1}$  (protonated pyridine), 1615  $\text{cm}^{-1}$  (pyridine bound to Lewis acidic Al sites), 1545  $\text{cm}^{-1}$  (protonated pyridine), 1490  $\text{cm}^{-1}$  (protonated pyridine or pyridine bound to Lewis acidic Al sites), and 1455  $\text{cm}^{-1}$  (pyridine bound to Lewis acidic Al sites).

and are representative of gas phase pyridine, physisorbed pyridine, and pyridine bound to Lewis acidic Sn sites or protonated pyridine [559]. Peak centers were allowed to vary within  $\pm 3 \text{ cm}^{-1}$  and full widths at half maximum peak height were constrained between  $5 \text{ cm}^{-1}$  and  $20 \text{ cm}^{-1}$ . The peak at  $1450 \text{ cm}^{-1}$  was virtually unchanged after exposure to dynamic vacuum at 423 K for 900 seconds (Fig E.28), and these IR spectra (Fig E.26) were used to determine the number of moles of Lewis acidic Sn sites present on each sample using Eq. E.1. The error in the  $\mathcal{E}$  value for pyridine bound to Lewis acidic Sn sites was estimated using the same procedure described in

Section E.7.5 . For Sn-Beta-OH-200, the peak area at  $1445\text{ cm}^{-1}$  was ca.  $4\times$  that of the peak at  $1450\text{ cm}^{-1}$  after saturation and exposure to dynamic vacuum for 900 s (while this was  $\leq$  ca.  $1\times$  on all other samples), leading to inaccurate deconvolution of the  $1450$  and  $1445\text{ cm}^{-1}$  peaks. In order to determine the saturation coverage of pyridine on Lewis acid sites in Sn-Beta-OH-200, the integrated absorbance at  $1450\text{ cm}^{-1}$  was estimated from the spectrum of a dose after the saturation of the peak for pyridine to Sn Lewis acid sites, but before complete saturation of the surface defect sites.

#### E.7.7 n-Propylamine temperature programmed desorption (TPD) experiments on zeolites.

A response factor for n-propylamine (NPA,  $m/z = 59$ ) was developed by filling a sample loop (1 or  $5\text{ cm}^3$ ) with a mixture of 1000 ppm NPA and 1% Ar in balance He (certified gas mixture, Airgas), and then injecting the loop contents into flowing He ( $1.66\text{ cm}^3\text{ s}^{-1}$ ). This stream was transferred via heated gas lines ( $383\text{ K}$ ) to an expansion volume ( $150\text{ cm}^3$ ) and then into a mass selective detector (MSD). An additional data point was collected by flowing  $20\text{ cm}^3\text{ min}^{-1}$  of 1000 ppm NPA to the MSD for 20 s. Afterwards, a  $0.5\text{ cm}^3$  sample loop was filled with Ar (99.999%, Indiana Oxygen) and injected into flowing He ( $1.66\text{ cm}^3\text{ s}^{-1}$ ) and sent to the MSD. Integrated area ratios for NPA and Ar MSD traces and the molar ratios of each component are plotted in Figure E.29 to obtain the response factor of NPA (relative to Ar), enabling quantification of NPA MSD traces when using an Ar standard to account for signal drift.

NPA TPD profiles are shown for all Sn-Beta samples in Figure S.14. Each sample was saturated with NPA for 4 h at  $323\text{ K}$  ( $75\text{ cm}^3\text{ s}^{-1}\text{ g}^{-1}$ ), purged in flowing dry He for 4 or 8 h at  $338\text{ K}$  ( $25\text{ cm}^3\text{ s}^{-1}\text{ g}^{-1}$ ), and then held in flowing He ( $25\text{ cm}^3\text{ s}^{-1}\text{ g}^{-1}$ ) from 338 to  $773\text{ K}$  ( $0.167\text{ K s}^{-1}$ ). After each TPD experiment, a  $0.5\text{ cm}^3$  sample loop was filled with Ar and pulsed into flowing He and sent to the MSD to quantify the NPA evolved in the TPD (Tables E.5 and E.6).

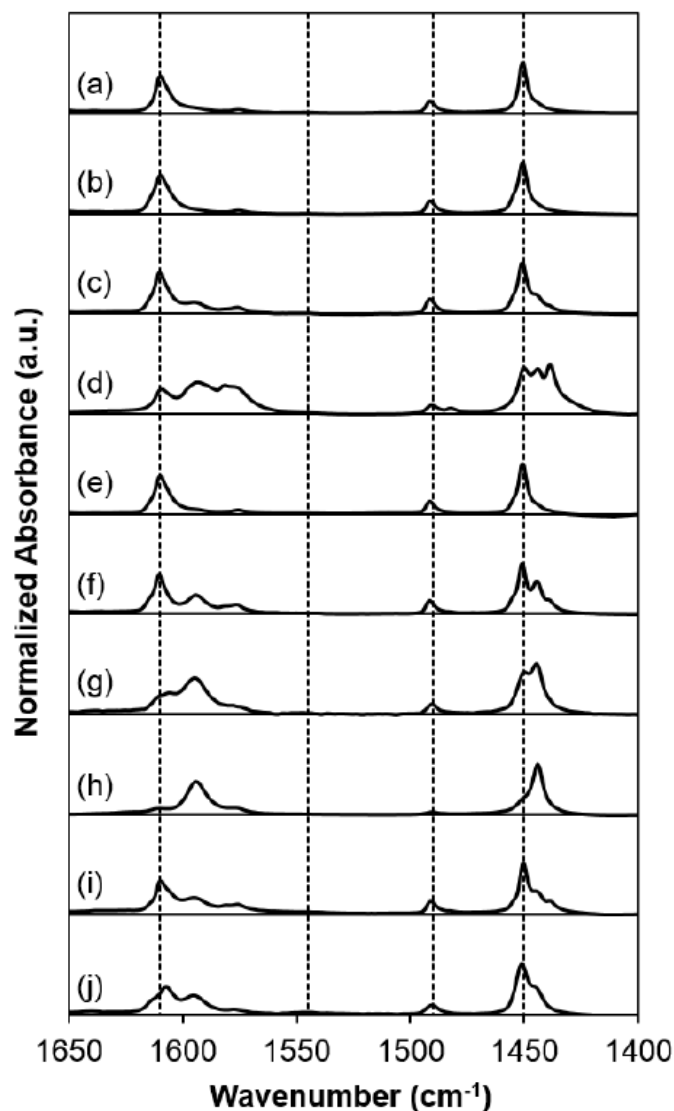


Figure E.26. IR difference spectra for pyridine saturated Sn-Beta samples after evacuation at 423 K for 900 s for (a) Sn-Beta-F-100, (b) Sn-Beta-F-105, (c) Sn-Beta-F-110, (d) Sn-Beta-F-140, (e) Sn-Beta-F-170, (f) Sn-Beta-F-220, (g) Sn-Beta-OH-170, (h) Sn-Beta-OH-200, (i) SnO<sub>2</sub>/Si-Beta, and (j) Sn-xerogel. All spectra normalized to the overtone and combination modes of Si-O-Si stretches (1750-2100 cm<sup>-1</sup>) and to the maximum peak intensity for clarity. Dashed lines shown at 1610 cm<sup>-1</sup> (pyridine bound to Lewis acidic Sn sites), 1540 cm<sup>-1</sup> (protonated pyridine), 1490 cm<sup>-1</sup> (protonated pyridine or pyridine bound to Lewis acidic Sn sites), and 1450 cm<sup>-1</sup> (pyridine bound to Lewis acidic Sn sites).



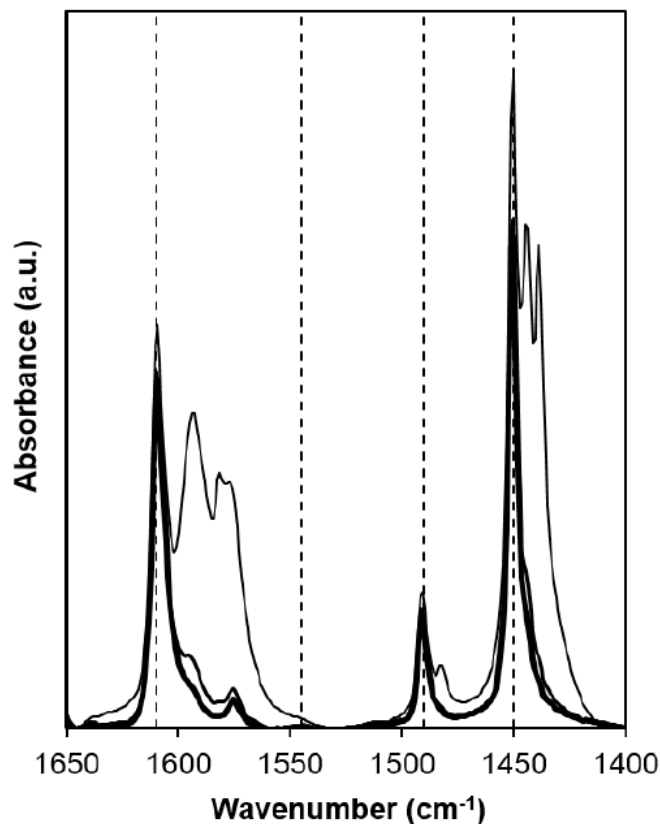


Figure E.27. IR spectra for pyridine-saturated Sn-Beta-F-100 during exposure to dynamic vacuum at 423 K for 0 s, 300 s, and 900 s (thin to thick traces) after saturation with pyridine. Dashed lines shown at  $1610\text{ cm}^{-1}$  (pyridine bound to Lewis acidic Sn sites),  $1545\text{ cm}^{-1}$  (protonated pyridine),  $1490\text{ cm}^{-1}$  (protonated pyridine or pyridine bound to Lewis acidic Sn sites), and  $1450\text{ cm}^{-1}$  (pyridine bound to Lewis acidic Sn sites).

Table E.5.

Molecules of NPA desorbed per Sn after saturation with 1000 ppm NPA for 4 h at 323 K followed by purging for 4 h and 8 h.

| Sample        | NPA/Sn<br>(4 hr<br>purge) | NPA/Sn<br>(4 hr<br>purge) |
|---------------|---------------------------|---------------------------|
| Sn-Beta-F-100 | $0.48 \pm 0.07$           | $0.44 \pm 0.06$           |
| Sn-Beta-F-105 | $0.59 \pm 0.09$           | $0.62 \pm 0.09$           |
| Sn-Beta-F-110 | $1.07 \pm 0.15$           | $0.99 \pm 0.13$           |
| Sn-Beta-F-140 | $1.18 \pm 0.16$           | $1.04 \pm 0.1$            |
| Sn-Beta-F-170 | $1.30 \pm 0.17$           | $1.24 \pm 0.17$           |
| Sn-Beta-F-220 | $2.02 \pm 0.27$           | $2.07 \pm 0.28$           |

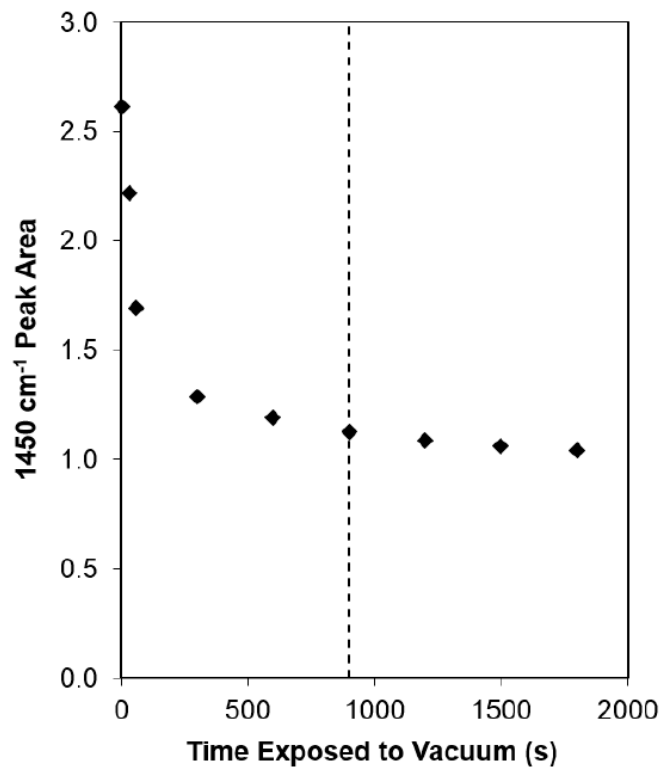


Figure E.28. Integrated area of the IR peak at  $1450\text{ cm}^{-1}$  as a function of time exposed to dynamic vacuum at 423 K for pyridine-saturated Sn-Beta-F-100. Dashed line at 900 seconds added for reference.

Table E.6.

Moles of NPA desorbed per g zeolite after saturation with 1000 ppm NPA for 4 h at 323 K followed by purging for 8 h.

| Sample            | NPA/g<br>( $\times 10^4$ ) |
|-------------------|----------------------------|
| Sn-Beta-F-100     | .719                       |
| Sn-Beta-F-105     | .971                       |
| Sn-Beta-F-110     | 1.48                       |
| Sn-Beta-F-140     | 1.26                       |
| Sn-Beta-F-170     | 1.18                       |
| Sn-Beta-F-220     | 1.52                       |
| Sn-Beta-OH-170    | 1.09                       |
| Sn-Beta-OH-200    | 1.39                       |
| Si-Beta-F         | 0.031                      |
| Dealuminated Beta | 1.59                       |

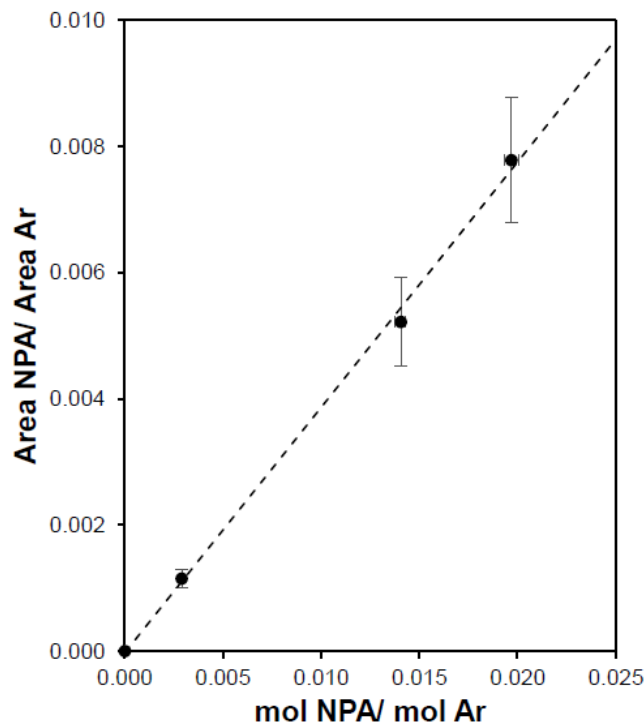


Figure E.29. NPA ( $m/z = 59$ ) response factor calibration curve of the mass spectrometer area ratio of NPA/Ar as a function of the molar ratio of NPA/Ar.

The appropriate saturation and purge length were determined by varying the purge duration (4 h, 8 h, 12 h, 16 h) at a given saturation condition (4 h at 323 K in  $25 \text{ cm}^3 \text{ s}^{-1} \text{ g}^{-1}$ , Figs. E.31 and E.32). A purge performed at 323 K after the same saturation conditions was taken as the 0 h purge length reference for the higher temperature (338 K) purge treatments. The low temperature purge (323 K) resulted in an NPA signal that is a convolution of two separate features, but purging at 338 K removed the low temperature feature and resulted in a symmetric and single TPD feature. For purges 4 h or longer, the number of NPA molecules evolved during TPD was constant, within experimental error, at 1.03 NPA/Sn for Sn-Beta-F-140 and 1.30 NPA/Sn for Sn-Beta-F-170 (Fig. E.32). In order to verify that increased saturation time did not influence the quantification, the saturation time was varied as the purge

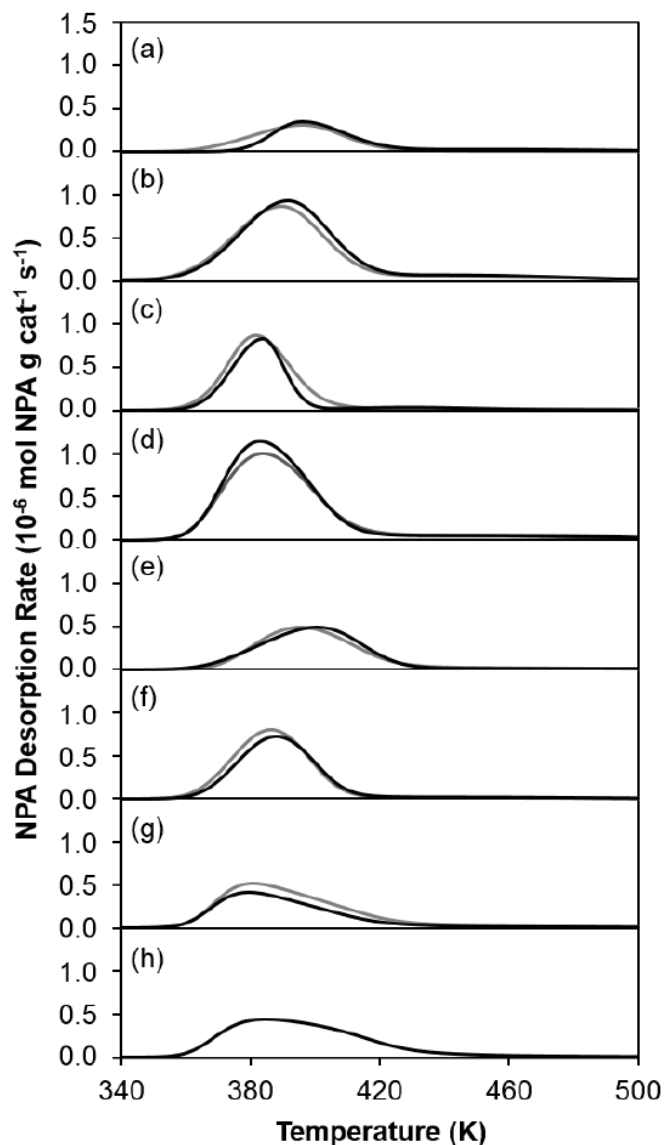


Figure E.30. NPA TPD profiles after saturation with 1000 ppm NPA for 4 h at 323 K followed by purging for 4 h (grey trace) and 8 h (black trace) at 338 K in  $25 \text{ cm}^3 \text{ s}^{-1} \text{ g}^{-1}$  UHP He on (a) Sn-Beta-F-100, (b) Sn-Beta-F-105, (c) Sn-Beta-F-110, (d) Sn-Beta-F-140, (e) Sn-Beta-F-170, (f) Sn-Beta-F-220, and (g) Sn-Beta-OH-170 and (h) Sn-Beta-OH-200.

conditions were kept constant (8 h, 338 K, He flow =  $0.83 \text{ cm}^3 \text{ g zeolite}^{-1} \text{ s}^{-1}$ ). The number of NPA molecules evolved during the TPD was constant, within experimental error, at 1.02 NPA/Sn for Sn-Beta-F-140 (Fig. E.33).

The number of NPA molecules (per Sn) evolved on Sn-Beta-F samples with low Sn content (Sn-Beta-F-170, Sn-Beta-F-220) and on highly-defective Sn-Beta-OH samples (Sn-Beta-OH-170, Sn-Beta-OH-200) were much larger than unity (Table E.5). These findings suggest that the saturation and purge treatments used here may not be sufficient to remove NPA at other binding sites on zeolite samples. Control experiments performed on purely-siliceous Beta zeolites (Si-Beta-F) did not evolve a significant amount of NPA in TPD experiments (Table E.6), but those performed on dealuminated Beta zeolites (parent Si/Al = 15) evolved as much or more NPA (per g) as the low Sn content Sn-Beta-F and the highly-defective Sn-Beta-OH samples (Table E.6). These findings suggest that the saturation and purge conditions used in this study causes NPA retention on residual defect sites in zeolite samples, which may lead to inaccurate quantification of Lewis acidic Sn sites by NPA TPD for samples with low Sn content and high defect densities.

#### E.7.8 Ammonia temperature programmed desorption experiments on zeolite samples.

A response factor for ammonia ( $\text{NH}_3$ ,  $m/z = 17$ ) was developed by performing  $\text{NH}_3$  TPD experiments on four  $\text{NH}_4$ -ZSM-5 zeolites (Si/Al = 17–89, Zeolyst). The moles of  $\text{NH}_3$  desorbed from each material was measured in independent TPD experiments performed in a gas-phase plug-flow reactor connected to a MKS Multigas 2030 gas-phase FTIR spectrometer with an on-board  $\text{NH}_3$  calibration as described elsewhere [78]. After each  $\text{NH}_3$  TPD experiment, a  $0.5 \text{ cm}^3$  loop was filled with Ar and injected into flowing He ( $0.83 \text{ cm}^3 \text{ s}^{-1}$ ). The total  $\text{NH}_3$  desorbed was quantified from the  $m/z = 17$  MSD trace after subtracting the contributing fractionation products of water ( $m/z = 17$ ), which appears in constant proportion to the  $m/z = 18$  signal for its parent ion. The ratio of integrated areas for  $\text{NH}_3$  and Ar are plotted as a function of their molar ratio (Figure E.34) to give a response factor of  $\text{NH}_3$  (relative to Ar) in the MSD, which enables the quantification of  $\text{NH}_3$  MSD traces when using an Ar standard to account for signal drift.

NH<sub>3</sub> TPD profiles are shown for all Sn-Beta samples in Fig. E.35. Each sample was saturated with NH<sub>3</sub> for 5 h at 323 K (75 cm<sup>3</sup> s<sup>-1</sup> g<sup>-1</sup>), purged in flowing dry He for 8 h at 331 K (25 cm<sup>3</sup> s<sup>-1</sup> g<sup>-1</sup>) to remove any physisorbed NH<sub>3</sub>, then kept in flowing He (25 cm<sup>3</sup> s<sup>-1</sup> g<sup>-1</sup>) as the temperature increased to 773 K (0.167 K s<sup>-1</sup>). After each TPD experiment, a 0.5 cm<sup>3</sup> loop (383 K) was filled with Ar and pulsed into flowing He sent to the MSD to correct for instrument drift. The number of molecules of NH<sub>3</sub> desorbed (per Sn) are given in Tables E.7 and E.7.

Table E.7.  
Molecules of NH<sub>3</sub> desorbed (per Sn) after saturation with 500 ppm NH<sub>3</sub> for 5 h at 323 K, followed by purging for 8 h.

| Sample         | NH <sub>3</sub> /Sn<br>(8 hr<br>purge) |
|----------------|--|
| Sn-Beta-F-100  | 0.42±0.02                              |
| Sn-Beta-F-105  | 0.61± 0.04                             |
| Sn-Beta-F-110  | 0.73± 0.04                             |
| Sn-Beta-F-140  | 1.06± 0.05                             |
| Sn-Beta-F-170  | 0.69± 0.03                             |
| Sn-Beta-F-220  | 0.89± 0.04                             |
| Sn-Beta-OH-170 | 1.12± 0.06                             |
| Sn-Beta-OH-200 | 0.93±0.05                              |

Table E.8.  
Moles of  $\text{NH}_3$  desorbed (per g) after saturation with 500 ppm  $\text{NH}_3$  for 5 h at 323 K followed by purging for 8 h.

| Sample            | $\text{NH}_3/\text{g}$<br>( $\times 10^4$ ) |
|-------------------|---|
| Sn-Beta-F-100     | 0.686                                       |
| Sn-Beta-F-105     | 0.956                                       |
| Sn-Beta-F-110     | 1.09  |
| Sn-Beta-F-140     | 1.29  |
| Sn-Beta-F-170     | 0.657                                       |
| Sn-Beta-F-220     | 0.652                                       |
| Sn-Beta-OH-170    | 1.08  |
| Sn-Beta-OH-200    | 0.754                                       |
| Si-Beta-F         | 0.003                                       |
| Dealuminated Beta | 0.157                                       |

Appropriate saturation and purge durations were determined by varying the purge length (0, 4, 8, 12 h) at a fixed saturation conditions (5 h, 323 K, flowing 500 ppm  $\text{NH}_3$  at  $75 \text{ cm}^3 \text{ s}^{-1} \text{ g}^{-1}$ ). For purges of 4 h and longer, the number of  $\text{NH}_3$  molecules evolved per Sn during the TPD was constant, within experimental error, at  $0.43 \text{ NH}_3/\text{Sn}$  for Sn-Beta-F-100 (Fig. E.36). In order to verify that saturation times did not influence the quantification, the saturation time was varied at fixed purge conditions (8 h, 331 K, flowing He at  $25 \text{ cm}^3 \text{ s}^{-1} \text{ g}^{-1}$ ) and the moles of  $\text{NH}_3$  evolved during TPD was constant, within experimental error, at  $0.44 \text{ NH}_3/\text{Sn}$  for Sn-Beta-F-100 (Fig. E.37).

#### E.7.9 Deuterated acetonitrile titration and infrared spectroscopy of zeolites.

Sn-Beta samples were saturated with  $\text{CD}_3\text{CN}$  by exposure to a gaseous pressure sufficient to give rise to an IR peak at  $2265 \text{ cm}^{-1}$  for gaseous  $\text{CD}_3\text{CN}$ . IR spectra corresponding to samples saturated with  $\text{CD}_3\text{CN}$  were collected after subsequent exposure

to ca. 30 seconds of dynamic vacuum (ca. 0.1 Torr) at 303 K, which did not noticeably decrease the IR peaks for closed Sn sites at  $2308\text{ cm}^{-1}$  but did remove gaseous  $\text{CD}_3\text{CN}$  present in the cell (Fig. E.38). The IR peak areas for  $\text{CD}_3\text{CN}$ -saturated samples after evacuation at 303 K were not a function of the initial saturation pressure (and number of moles) of  $\text{CD}_3\text{CN}$  used (Fig. E.39)



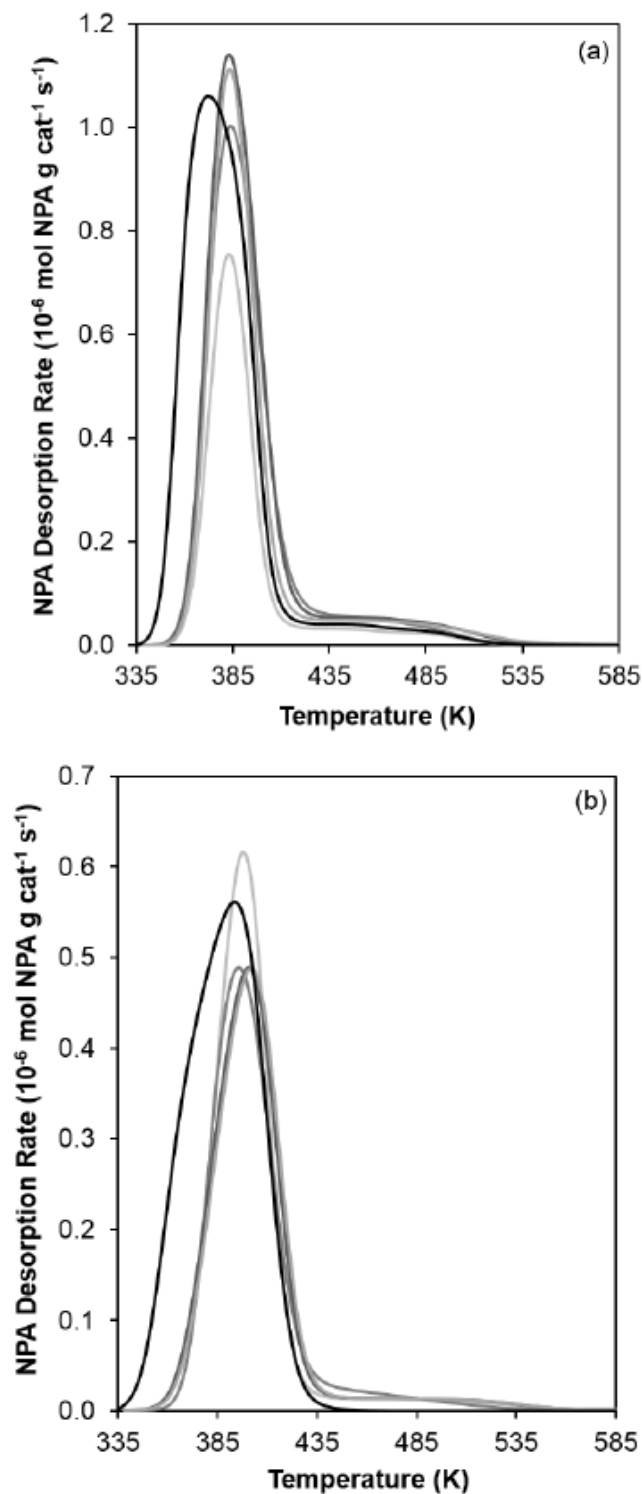


Figure E.31. NPA TPD profiles on (a) Sn-Beta-F-140 and (b) Sn-Beta-F-170 after saturation in 1000 ppm NPA for 4 h followed by purging at 338 K in 25 cm<sup>3</sup> s<sup>-1</sup> g<sup>-1</sup> He for 4 h (dark grey trace), 8 h (grey trace), 12 h (light grey trace), and 16 h (faint grey trace). A purge performed at 323 K for 8 h in 25 cm<sup>3</sup> s<sup>-1</sup> g<sup>-1</sup> He is used to represent a 0 h purge at 338 K (black trace).

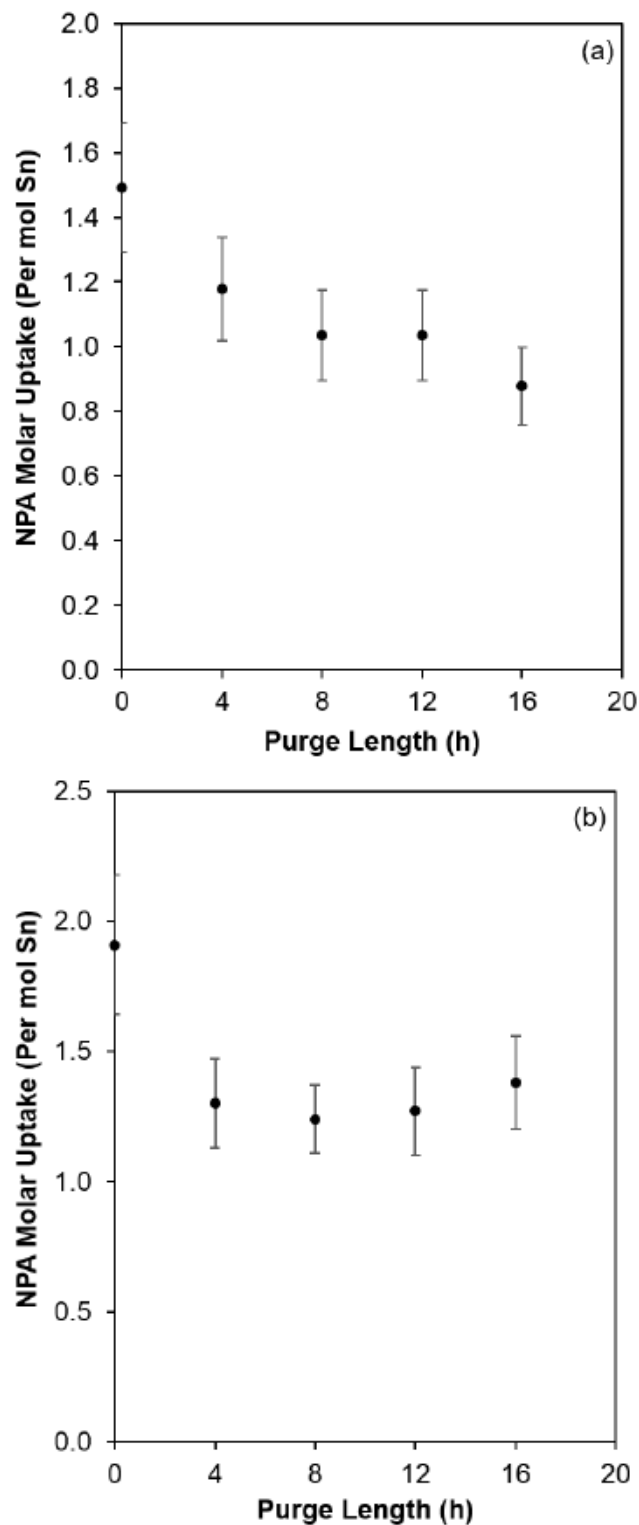


Figure E.32. Molecules of NPA desorbed per molecule of Sn as a function of the purge length on (a) Sn-Beta-F-140 and (b) Sn-Beta-F-170 after saturation in 1000 ppm NPA for 4 h followed by purging at 338 K in  $25 \text{ cm}^3 \text{ s}^{-1} \text{ g}^{-1} \text{ He}$ . A purge performed at 323 K for 8 h in  $25 \text{ cm}^3 \text{ s}^{-1} \text{ g}^{-1} \text{ He}$  is used as a representation for a 0 h purge at 338 K.

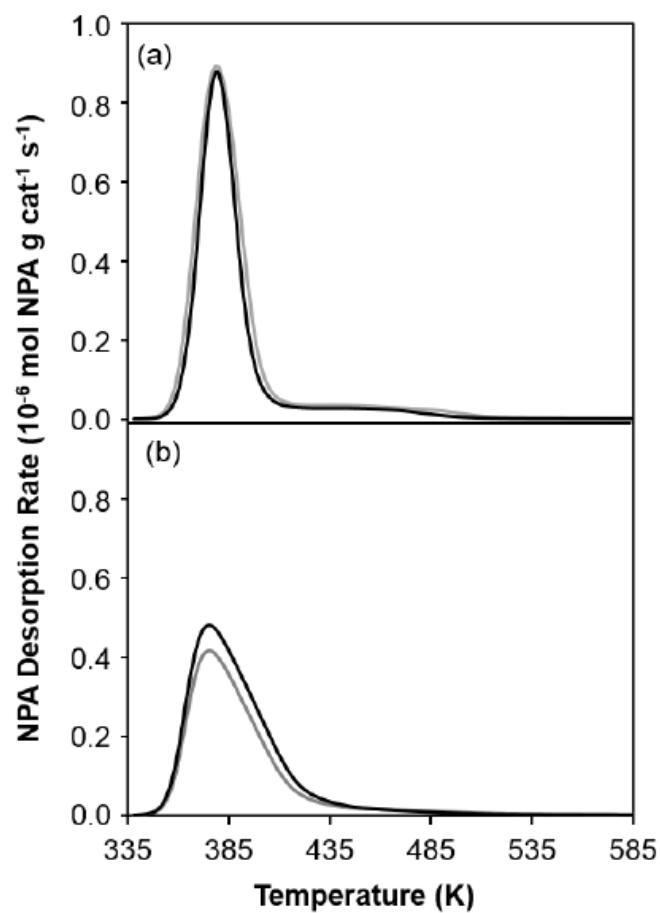


Figure E.33. NPA desorption rate on (a) Sn-Beta-F-140 and( b) Sn-Beta-OH-170 after saturation in 1000 ppm NPA for 4 h (grey trace) and 16 h (black trace) followed by an 8 h purge at 338 K in  $25 \text{ cm}^3 \text{ s}^{-1} \text{ g}^{-1}$  He.

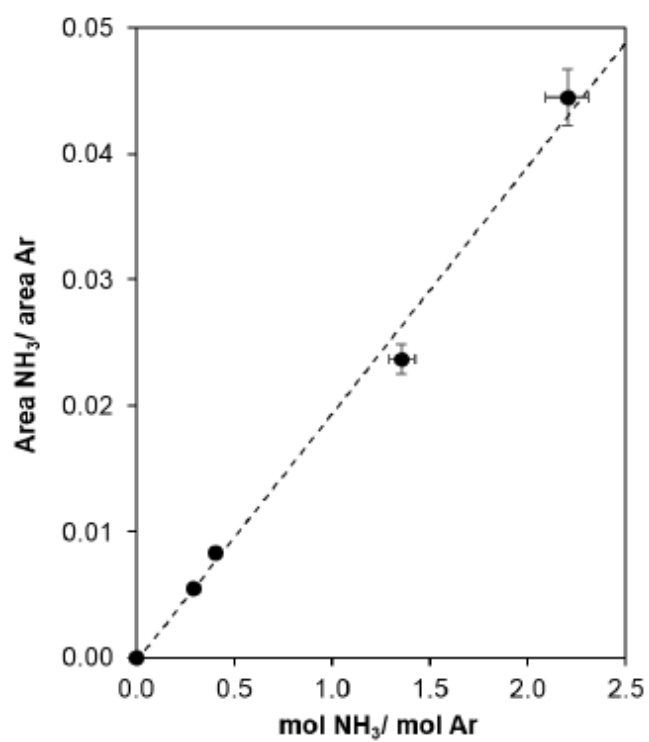


Figure E.34. NH<sub>3</sub> ( $m/z = 17$ ) calibration curve of the mass spectrometer area ratio of NH<sub>3</sub>/Ar as a function of the molar ratio of NH<sub>3</sub>/Ar.

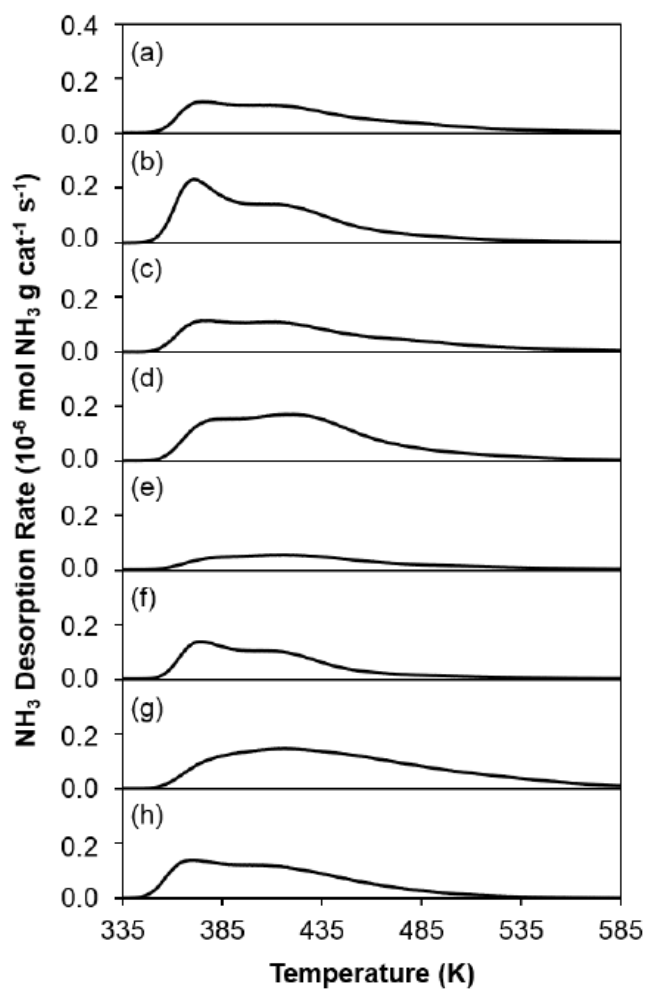


Figure E.35.  $\text{NH}_3$  TPD profiles after saturation in  $75 \text{ cm}^3 \text{ s}^{-1} \text{ g}^{-1}$  500 ppm  $\text{NH}_3/\text{He}$  at 323 K for 5 h followed by purging in dry He ( $25 \text{ cm}^3 \text{ s}^{-1} \text{ g}^{-1}$ ) at 331 K for 8 h on (a) Sn-Beta-F-100, (b) Sn-Beta-F-105, (c) Sn-Beta-F-110 (d) Sn-Beta-F-140, (e) Sn-Beta-F-170, (f) Sn-Beta-F-200, (g) Sn-BEA-OH-170, (h) Sn-Beta-OH-200.

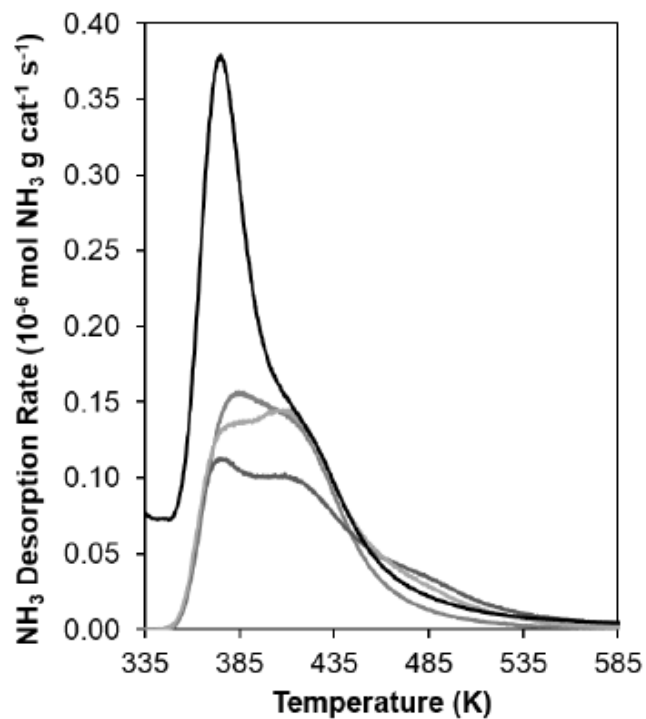


Figure E.36. NH<sub>3</sub> TPD profiles after saturation of Sn-Beta-F-100 for 5 h in 75 cm<sup>3</sup> s<sup>-1</sup> g<sup>-1</sup> 500 ppm NH<sub>3</sub>/He at 323 K followed by purging in dry He (25 cm<sup>3</sup> s<sup>-1</sup> g<sup>-1</sup>) at 331 K for 0 h (black trace), 4 h (dark grey trace), 8 h (grey trace), and 12 h (light grey trace).

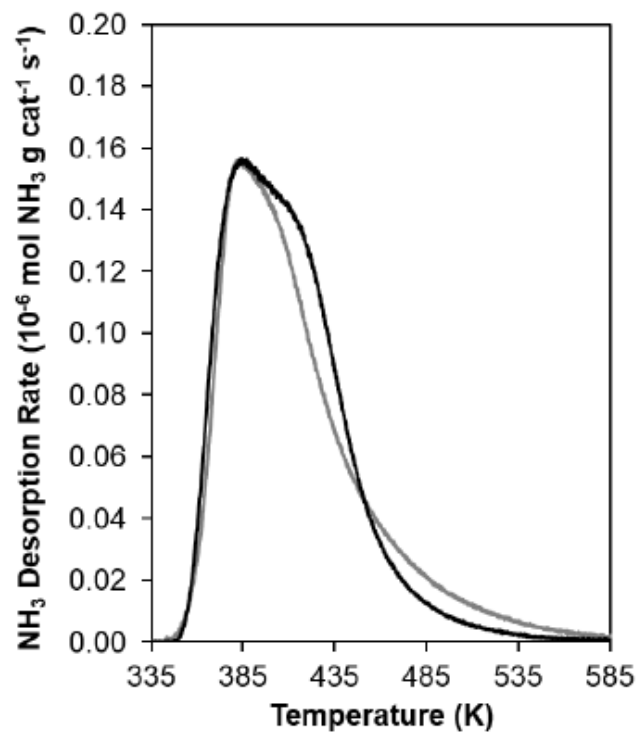


Figure E.37. NH<sub>3</sub> TPD profiles after saturation of Sn-Beta-F-100 for 5 h (black trace) or 16 h (grey trace) in 75 cm<sup>3</sup> s<sup>-1</sup> g<sup>-1</sup> 500 ppm NH<sub>3</sub>/He at 323 K followed by purging in dry He (25 cm<sup>3</sup> s<sup>-1</sup> g<sup>-1</sup>) at 331 K for 8 h.

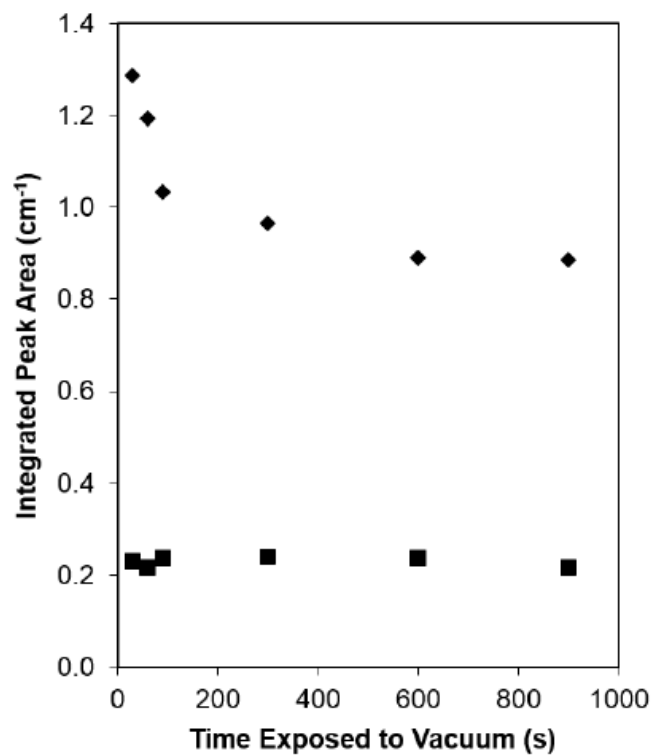


Figure E.38. IR peak areas for Sn-BEA-F-100 after saturation and exposure to dynamic vacuum for open Sn sites (squares) and closed Sn sites (diamonds) as a function of time exposed to dynamic vacuum.



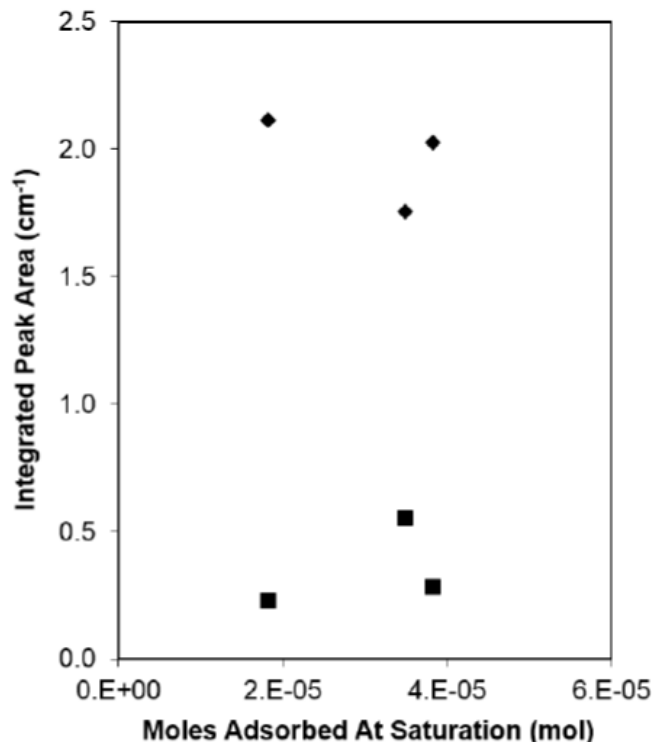


Figure E.39. IR peak areas for Sn-BEA-F-140 after saturation for open Sn sites (squares) and closed Sn sites (diamonds) as a function of moles adsorbed at saturation

Deconvolution of IR spectral features, after subtraction of IR spectra for CD<sub>3</sub>CN-free wafers, was performed in CasaXPS. Individual components for IR peaks at 2316 cm<sup>-1</sup>, 2308 cm<sup>-1</sup>, 2287 cm<sup>-1</sup>, 2275 cm<sup>-1</sup>, and 2265 cm<sup>-1</sup> were used to determine areas within each CD<sub>3</sub>CN dose that correspond to open Sn sites, closed Sn sites, (SiO)<sub>2</sub>Sn(SiOH)<sub>2</sub> sites (speculative assignment), SiOH sites, and gas phase CD<sub>3</sub>CN, respectively (Table E.9). IR peak centers were fixed within  $\pm 5$  cm<sup>-1</sup>, and the full widths at half maxima were constrained to be between 5 cm<sup>-1</sup> and 20 cm<sup>-1</sup>. The sum of Gauss-Lorentzian (SGL) line shapes were used for each component, with a 50% Lorentzian correction to a normally distributed Gaussian line shape (SGL(50)), as was used previously for deconvolution of IR spectra obtained after CD<sub>3</sub>CN adsorption to Zn exchanged Al-Beta [570].

The relationship between the number of moles of CD<sub>3</sub>CN dosed, the number of moles adsorbed to each type of site (resulting in a band area, BA, for each site), and the value of the integrated molar extinction coefficient (IMEC, or  $\mathcal{E}$  for short) is given by:

$$\begin{aligned} \text{Cumulative Moles Adsorbed} = & \frac{2316 \text{ cm}^{-1} BA}{2316 \text{ cm}^{-1} IMEC} + \frac{2308 \text{ cm}^{-1} BA}{2308 \text{ cm}^{-1} IMEC} + \\ & \frac{2287 \text{ cm}^{-1} BA}{2287 \text{ cm}^{-1} IMEC} + \frac{(2275 \text{ cm}^{-1} BA)}{2275 \text{ cm}^{-1} IMEC} \quad (\text{E.4}) \end{aligned}$$

$\mathcal{E}$  values were determined for CD<sub>3</sub>CN bound to Lewis acidic Sn sites in Sn-Beta by minimizing the squared error between the moles of pyridine bound to Lewis acidic Sn sites (using the  $\mathcal{E}$  value measured for Sn-Beta:  $1.42 \pm 0.30 \text{ cm } \mu\text{mol}^{-1}$ , Section E.7.6). This was achieved by varying the  $\mathcal{E}$  values for CD<sub>3</sub>CN bound to open and closed Sn sites using the Excel Solver function with multistart, in order to avoid finding initial guess-dependent local minima. This procedure led to values of  $\mathcal{E}(2316 \text{ cm}^{-1})$  and  $\mathcal{E}(2308 \text{ cm}^{-1})$  of  $1.04 \pm 0.22 \text{ cm } \mu\text{mol}^{-1}$  and  $2.04 \pm 0.43 \text{ cm } \mu\text{mol}^{-1}$ , and agreement with the total number of moles of Lewis acidic Sn sites counted by pyridine (Fig. E.6). Then,  $\mathcal{E}$  values for the  $2287 \text{ cm}^{-1}$  and  $2275 \text{ cm}^{-1}$  peaks were determined from a series of spectra collected with increasing CD<sub>3</sub>CN coverage on Sn-Beta-OH-170, which showed an intense  $2275 \text{ cm}^{-1}$  peak for all CD<sub>3</sub>CN doses and an IR peak at  $2287 \text{ cm}^{-1}$  of similar intensity to the rest of the samples in this study. The  $\mathcal{E}$  values for  $2316 \text{ cm}^{-1}$  and  $2308 \text{ cm}^{-1}$  were fixed from the previous fitting, and only the initial doses were used for which there was no detectable IR peak at  $2265 \text{ cm}^{-1}$  for gas phase or physisorbed CD<sub>3</sub>CN. The  $\mathcal{E}$  values that minimized the sum of squared errors for all CD<sub>3</sub>CN doses on Sn-Beta-OH-170 were  $2.13 \pm 0.45 \text{ cm } \mu\text{mol}^{-1}$  and  $0.74 \pm 0.16 \text{ cm } \mu\text{mol}^{-1}$  for the IR peaks at  $2287 \text{ cm}^{-1}$  and  $2275 \text{ cm}^{-1}$ , respectively. The four  $\mathcal{E}$  values can be used to quantify the numbers of each type of site using integrated peak areas determined after saturation of Sn-Beta samples using Eq. E.1. The error in the  $\mathcal{E}$  value for CD<sub>3</sub>CN bound to each of the sites (open Sn sites, closed Sn

sites,  $(\text{SiO})_2\text{Sn}(\text{SiOH})_2$  sites, and SiOH sites) was estimated using the same procedure described in Section E.7.5. The assignment of the  $2275\text{ cm}^{-1}$  peak to  $\text{CD}_3\text{CN}$  bound to SiOH groups is supported by the correlation between the integrated areas for perturbed SiOH groups (Fig. E.40), which give rise to a broad absorption between  $3000\text{--}3600\text{ cm}^{-1}$ , that increased linearly with  $2275\text{ cm}^{-1}$  peak areas. Furthermore, the integrated areas for terminal SiOH groups (Fig. E.41), which give rise to IR peaks at  $3740\text{ cm}^{-1}$ , decreased linearly with an increase in  $2275\text{ cm}^{-1}$  peak areas.  $\text{CD}_3\text{CN}$  adsorption experiments performed on a dealuminated Beta sample gave rise to IR spectra that showed a small peak at  $2300\text{ cm}^{-1}$  that saturated quickly, while the IR  $2275\text{ cm}^{-1}$  peak grew continuously with increasing  $\text{CD}_3\text{CN}$  coverage (Fig. E.42). These IR data were used to independently estimate the  $\mathcal{E}$  value for the  $2275\text{ cm}^{-1}$  peak to be  $0.89 \pm 0.09\text{ cm } \mu\text{mol}^{-1}$  (Fig. E.43). A sample prepared to have framework Sn in an amorphous silica network (Sn-xerogel), gave rise primarily to a peak at  $2287\text{ cm}^{-1}$  at low  $\text{CD}_3\text{CN}$  coverages (Fig. E.44,  $\text{CD}_3\text{CN}/\text{Sn} < 0.2$ ), prior to the appearance of the peak at  $2275\text{ cm}^{-1}$  for  $\text{CD}_3\text{CN}$  hydrogen bound to SiOH groups (Fig. E.45). The peak at  $2287\text{ cm}^{-1}$  was also observed at low  $\text{CD}_3\text{CN}$  coverages for all Sn-Beta samples. This peak was not observed to a significant degree for  $\text{SnO}_2/\text{Si-Beta}$ , a sample with small extraframework octahedral  $\text{SnO}_2$  domains (Fig. E.46), nor on bulk  $\text{SnO}_2$  or a metal-free silica sample (Si-xerogel). Thus, we speculate this peak may be a highly defective framework Sn site, such as an  $(\text{SiO}_2)\text{Sn}(\text{OH})_2$  site. No clear correlation with any band in the  $\nu(\text{OH})$  region is observed for this  $2287\text{ cm}^{-1}$  peak, as in the case of the  $2275\text{ cm}^{-1}$  peak. The peak at  $2287\text{ cm}^{-1}$  was included in deconvolution of the spectra for the Sn-Beta samples, which may contain these defective framework Sn sites.

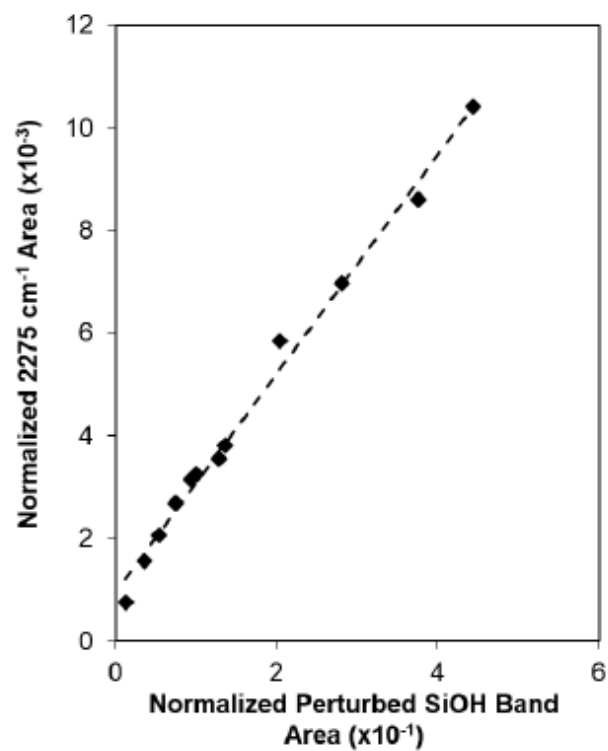


Figure E.40. 2275 cm<sup>-1</sup> peak area versus perturbed OH peak area (3000-3600 cm<sup>-1</sup>).

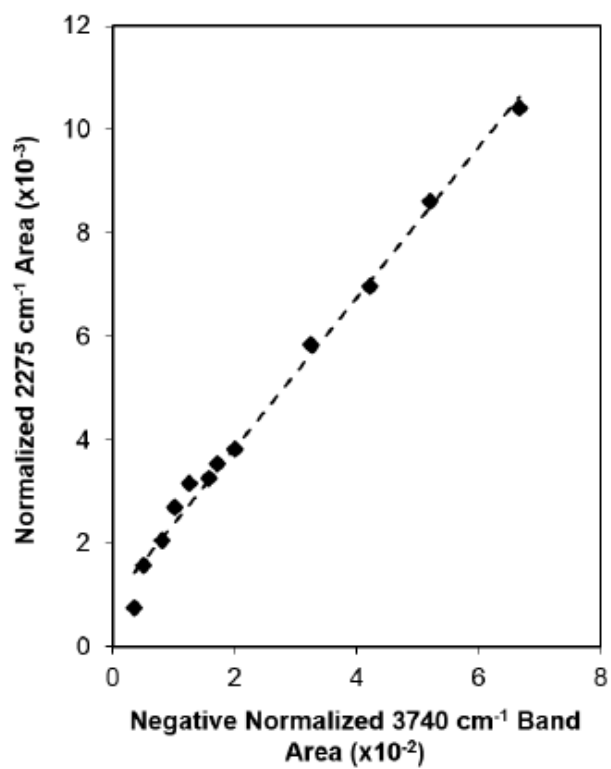


Figure E.41. 2275 cm<sup>-1</sup> band area versus negative SiOH band area (ca. 3740 cm<sup>-1</sup>).

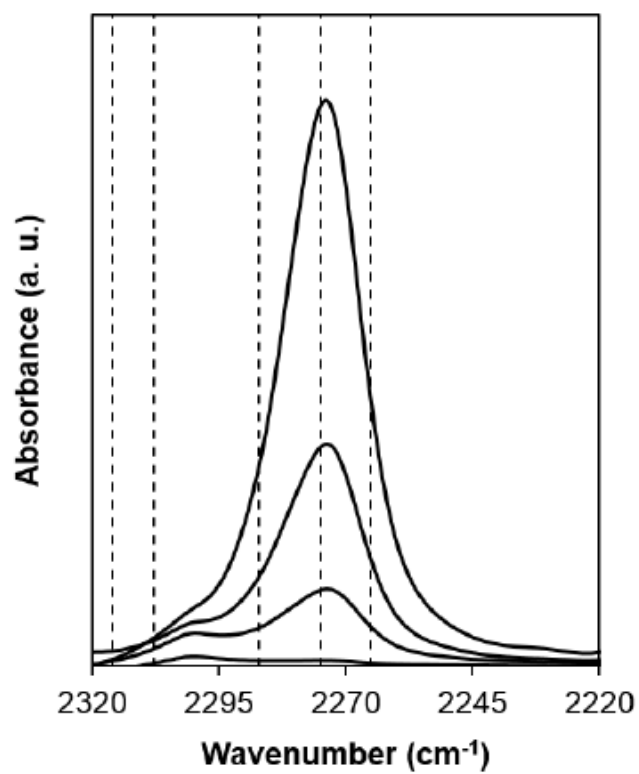


Figure E.42. FTIR spectra of a dealuminated Beta zeolite after sequential doses of CD<sub>3</sub>CN. Dashed lines shown at 2316 cm<sup>-1</sup>, 2308 cm<sup>-1</sup>, 2287 cm<sup>-1</sup>, 2275 cm<sup>-1</sup>, and 2265 cm<sup>-1</sup>.

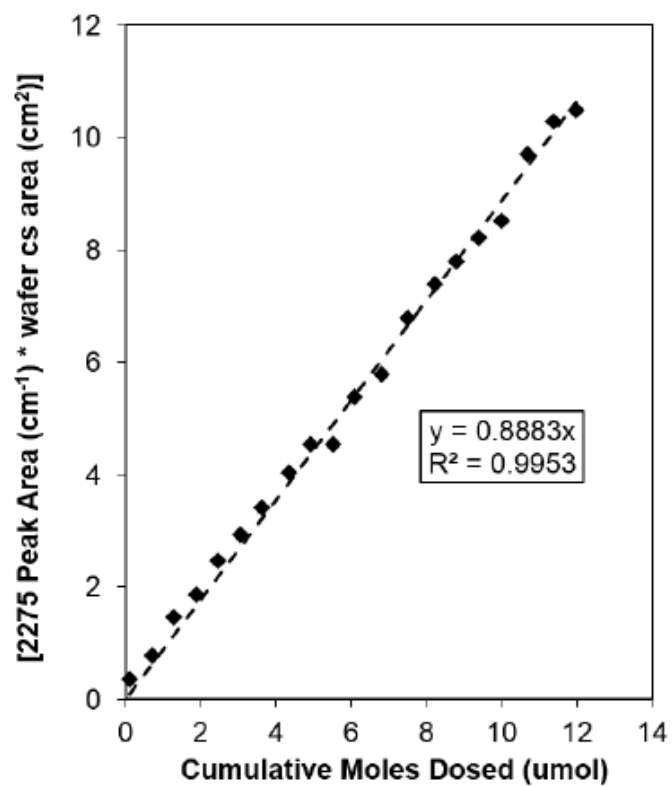


Figure E.43. IR band area for the  $2275\text{ cm}^{-1}$  peak on dealuminated Beta as a function of moles  $\text{CD}_3\text{CN}$  adsorbed. The slope of this line is the  $\mathcal{E}$  value estimated for the  $2275\text{ cm}^{-1}$  site.

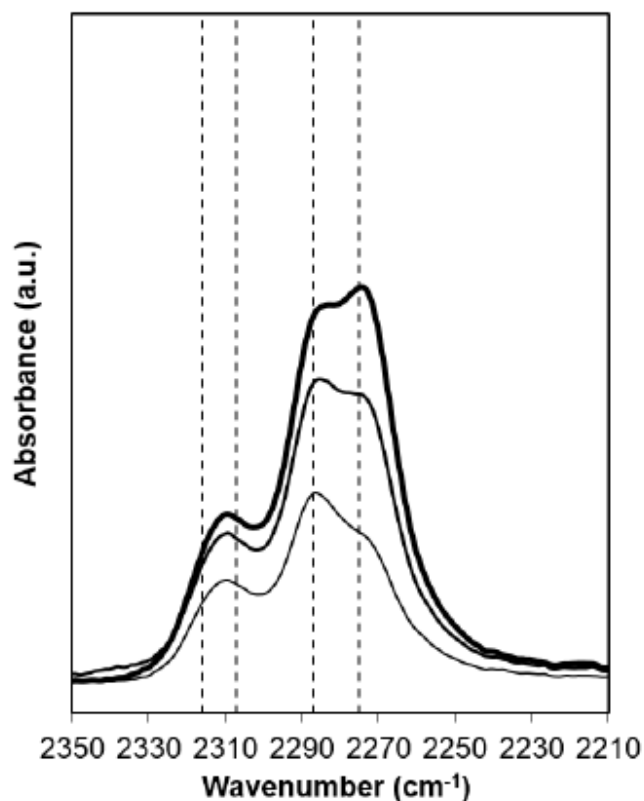


Figure E.44. IR spectra of  $\text{CD}_3\text{CN}$  three sequential doses (0.05 mol  $\text{CD}_3\text{CN}/\text{Sn}$  per dose) on Sn-xerogel. Dashed lines shown at  $2316\text{ cm}^{-1}$ ,  $2308\text{ cm}^{-1}$ ,  $2287\text{ cm}^{-1}$ , and  $2275\text{ cm}^{-1}$ .

Table E.9.

Peak areas at saturation for the  $2316\text{ cm}^{-1}$ ,  $2308\text{ cm}^{-1}$ ,  $2287\text{ cm}^{-1}$ ,  $2275\text{ cm}^{-1}$  and  $2265\text{ cm}^{-1}$  peaks for all Sn samples in this study.

| Sample         | 2316<br>$\text{cm}^{-1}\text{Area}$<br>$\text{cm}^{-1}$ | 2308<br>$\text{cm}^{-1}\text{Area}$<br>$\text{cm}^{-1}$ | 2287<br>$\text{cm}^{-1}\text{Area}$<br>$\text{cm}^{-1}$ | 2275<br>$\text{cm}^{-1}\text{Area}$<br>$\text{cm}^{-1}$ | Moles<br>$2287\text{ cm}^{-1}$<br>sites (per<br>Sn) |
|----------------|---|---|---|---|---|
| Sn-Beta-F-100  | 0.22  | 1.19  | 0.27  | 0.43  | 0.078   |
| Sn-Beta-F-105  | 0.36  | 1.96  | 0.33  | 2.24  | 0.079   |
| Sn-Beta-F-110  | 0.92  | 3.36  | 1.26  | 1.17  | 0.23  |
| Sn-Beta-F-140  | 0.73  | 2.22  | 0.34  | 3.24  | 0.094   |
| Sn-Beta-F-170  | 0.37  | 2.47  | 0.37  | 1.39  | 0.096   |
| Sn-Beta-F-220  | 0.50  | 1.81  | 1.26  | 1.17  | 0.41  |
| Sn-Beta-OH-170 | 0.74  | 0.88  | 0.17  | 12.4  | 0.052   |
| Sn-Beta-OH-200 | 0.88  | 2.02  | 0.27  | 24.5  | 0.010   |



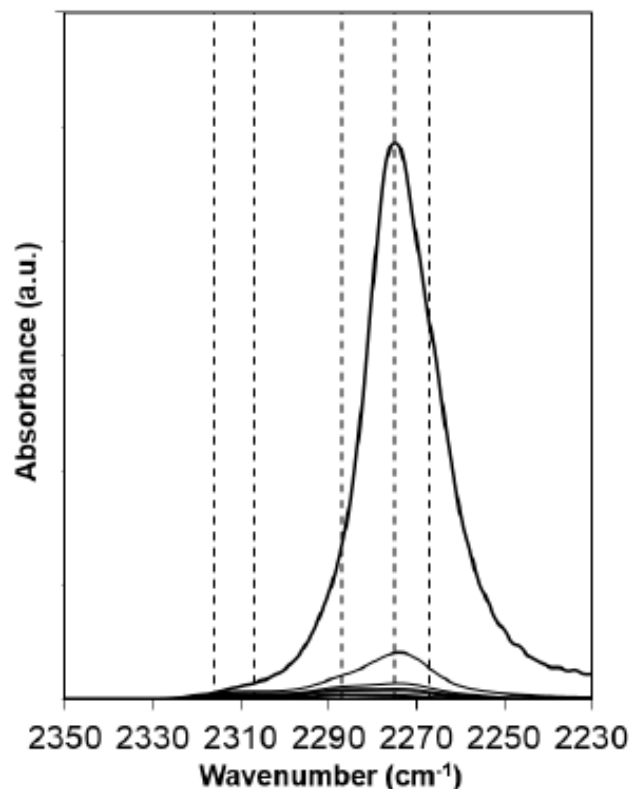


Figure E.45. IR spectra of  $\text{CD}_3\text{CN}$  dosed on Sn-xerogel to saturation. Dashed lines shown at  $2316\text{ cm}^{-1}$ ,  $2308\text{ cm}^{-1}$ ,  $2287\text{ cm}^{-1}$ , and  $2275\text{ cm}^{-1}$ .

#### E.7.10 Kinetic measurements of glucose isomerization on zeolite samples.

A more detailed kinetic and mechanistic study of glucose-fructose isomerization on Lewis acids has been previously reported [575]; here, we include an abridged discussion to supplement the data and analysis in this manuscript. Aqueous-phase glucose (G) adsorbs onto vacant Sn sites (\*) and forms ring-opened intermediates on Sn sites ( $\text{G}^*$ ) in a quasi-equilibrated step (Step 1, Fig. E.2), followed by kinetically-relevant intramolecular 1,2-hydride shift to form ring-opened fructose intermediates ( $\text{F}^*$ ) (Step 2, Fig. E.2) that undergo quasi-equilibrated ring-closing and desorption into the aqueous phase (Step 3, Fig. E.2). Two water molecules sequentially adsorb onto Sn sites ( $\text{W}^*$ ,  $2\text{W}^*$ ) in quasi-equilibrated steps (Steps 4-5, Fig. E.2), and  $2\text{W}^*$  is assumed

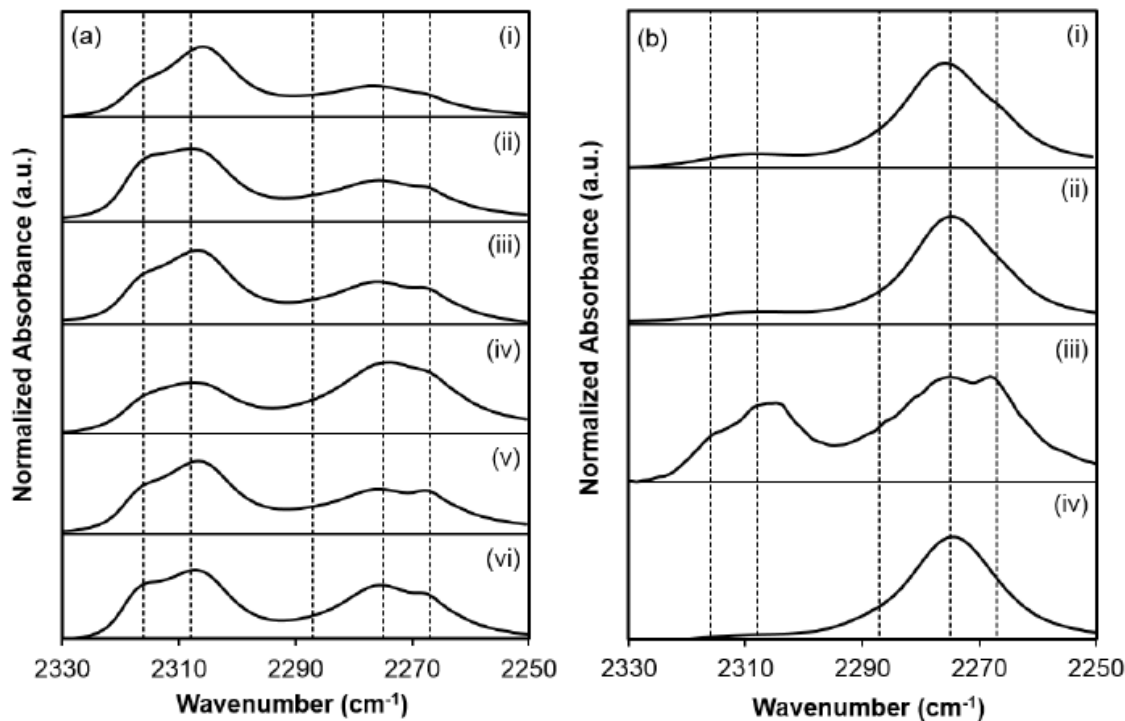


Figure E.46. IR difference spectra at  $\text{CD}_3\text{CN}$  saturation coverages (relative to the  $\text{CD}_3\text{CN}$ -free wafers and normalized to the maximum intensity of each spectra for clarity). (a) Spectra for (i) Sn-Beta-F-100, (ii) Sn-Beta-F-105, (iii) Sn-Beta-F-110, (iv) Sn-Beta-F-140, (v) Sn-Beta-F-170, (vi) Sn-Beta-F-220. (b) Spectra for (i) Sn-Beta-OH-170, (ii) Sn-Beta-OH-200, (iii)  $\text{SnO}_2/\text{Si-Beta}$ , (iv) Sn-xerogel. Dashed lines shown at  $2316\text{ cm}^{-1}$ ,  $2308\text{ cm}^{-1}$ ,  $2287\text{ cm}^{-1}$ ,  $2275\text{ cm}^{-1}$  and  $2265\text{ cm}^{-1}$ .

to be the most abundant surface intermediate (MASI) during catalysis in liquid water [575]. These mechanistic assumptions lead to glucose-fructose isomerization turnover rates ( $\eta \ll 1$ ) per total number of active Sn sites ( $[L]$ ) given by [575]:

$$\frac{r_{isom}}{[L]} = \frac{\gamma_{2W*}\gamma_G\gamma_*}{\gamma_W^2 c_W^2 \gamma_*} \frac{k_2 K_1}{K_4 K_5} c_G = k_{isom} c_G \quad (\text{E.5})$$

In this equation,  $\gamma_j$  are activity coefficients for species  $j$ ,  $c_W$  is the water concentration,  $c_G$  is the glucose concentration,  $K_j$  is the equilibrium coefficient for a given step, and  $k_2$  is the isomerization rate constant for the kinetically-relevant hydride

shift step. This turnover rate equation gives a first-order dependence in aqueous glucose concentration, and an effective first order isomerization rate constant that can be decomposed to give the following dependence on Gibbs free energies of reactive intermediates and transition states in the mechanism, where  $\alpha$  is a constant that contains the product of the activity coefficients for reactants and intermediates as shown in equation E.5 [575]:

$$k_{isom} = \alpha \frac{K_1 k_2}{K_4 K_5} = \alpha \frac{k_B T}{h} e^{-((\Delta G_{\ddagger, 2*}^o + 2\Delta G_W^o) - (\Delta G_G^o + \Delta G_{2W*}^o))/RT} \quad (\text{E.6})$$

Initial glucose isomerization turnover rates (per mol Sn, 373 K) were measured on Sn-Beta samples in batch reactors under autogenous pressure according to methods reported previously and described in the main text [575]. Initial rates were measured by fitting a reversible, first-order rate expression integrated in a batch reactor model to the temporal evolution of measured monosaccharide concentrations, and extrapolated to initial times using the model derived previously [575]. Initial rates calculated from data collected under differential conditions (<5% conversion) and a differential reactor model (with corrections for approach-to-equilibrium) give the same value, within experimental error, as the initial rates calculated by extrapolating batch reactor data to initial time using the batch reactor model.

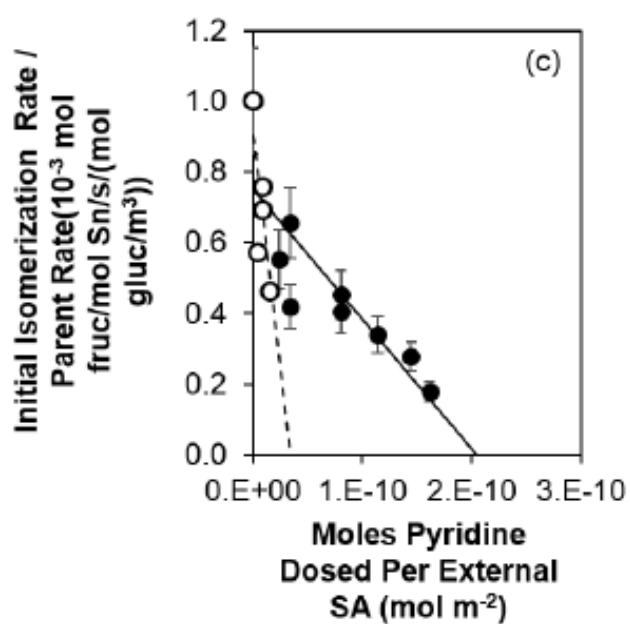
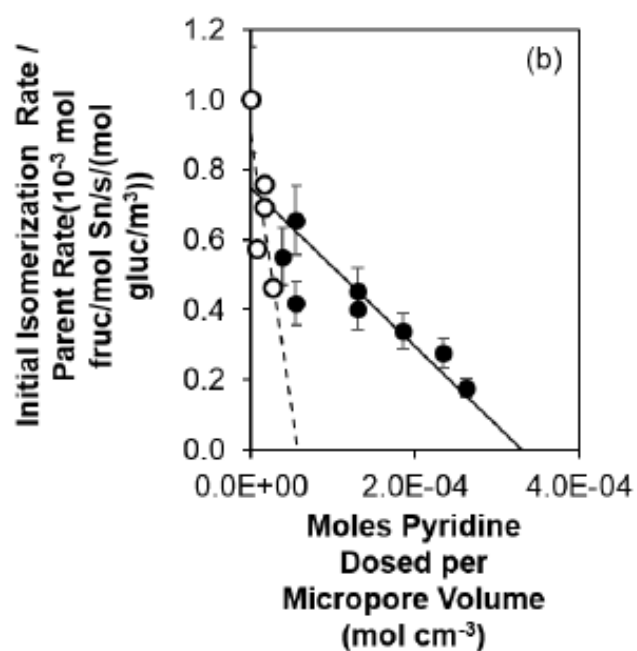
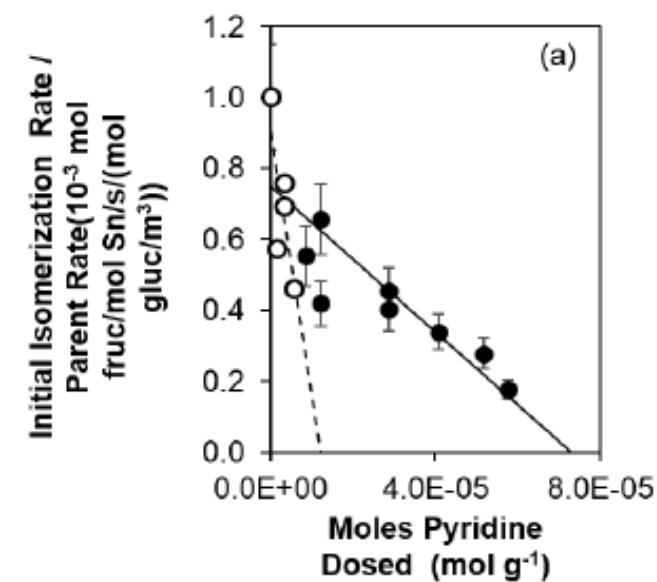
Here, we focus on measurements of initial rates of glucose-fructose isomerization. At initial times, high fructose to mannose (F/M) selectivities are expected for Sn-Beta samples containing predominantly framework Sn sites, as mannose is formed only as a series product via reverse hydride shift from fructose, instead of via direct 1,2-carbon shift from glucose in parallel [551]. After 600 s of reaction time, mannose formation was undetectable on all samples in this study, indicating that initial mannose formation rates are negligible and can be neglected from initial rate calculations. Therefore, initial rates of fructose formation are indistinguishable (within 10%) from initial rates of glucose consumption for all samples in this study.

The H/D kinetic isotope effect (KIE) was measured with glucose-D2 reactants, and is predicted to be 2.1 (at 373 K) if the intramolecular 1,2-hydride shift is kinetically-

relevant (C-H scissoring frequency of 1500  $\text{cm}^{-1}$ ) [578]. In the presence of strong internal reactant mass transfer limitations, the observed H/D KIE value would be equivalent to the square root of the kinetically-relevant value (ca. 1.4 at 373 K) [575]. Measured H/D KIE values were between 2.0-2.4 for all Sn-Beta samples tested in this study, consistent with the absence of internal mass transfer limitations [575].

The H/D KIE value was also measured on a Sn-Beta-F-170 pre-poisoned with pyridine to be  $2.3 \pm 0.2$ , as expected for kinetically-limited isomerization rates, suggesting the decrease in observed isomerization rates with increasing amounts of pyridine pre-titration (Fig. E.11) does not reflect the introduction of diffusion limitations for glucose reactants. Initial isomerization turnover rates (373 K, normalized to rates on untitrated samples) are plotted in Figure E.47 against the moles of pyridine adsorbed per gram, per micropore volume, and per surface area of Sn-Beta-F-110 and Sn-Beta-F-170. If occlusion of micropore volume were the mechanism by which pyridine titration suppressed catalytic reactivity, then the amount of pyridine titrants adsorbed onto Sn-Beta-F-110 and Sn-Beta-F-170 (nearly identical  $\text{N}_2$  micropore volumes of 0.22 and 0.21  $\text{cm}^3 \text{g}^{-1}$ , respectively) should be similar on a per gram or per micropore volume basis. Analogously, if occlusion of pore mouths at external crystallite surfaces by adsorbed pyridine were responsible for the decrease in isomerization rates, then the amount of pyridine required to fully suppress rates would be similar on an external surface area basis, which can be estimated from crystallite sizes (approximating the Beta crystallites as spheres) derived from SEM images (Fig. E.48). The amount of pyridine required to fully suppress rates on both Sn-Beta samples does not agree with any of these properties, suggesting that occlusion of external pore mouths or internal void spaces cannot account for the decrease in reactivity with increasing pyridine coverage.





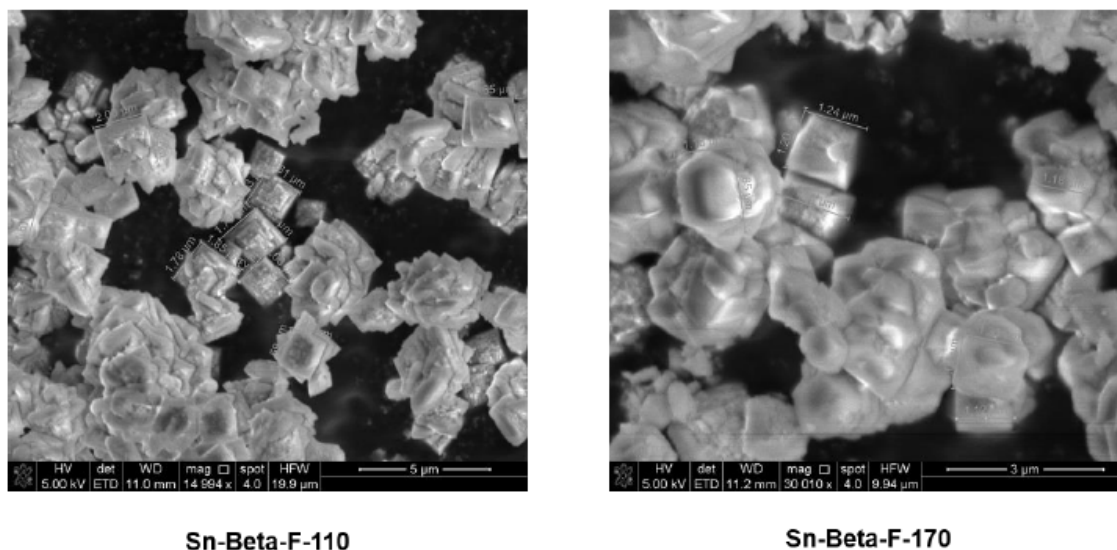


Figure E.48. Scanning electron microscope images of Sn-Beta-F-110 and Sn-Beta-F-170.

Measurements of water adsorption isotherms on Sn-Beta zeolites and subsequent calculations of the volume of water adsorbed at a relative pressure of 0.2, a reference pressure reflecting complete micropore filling of hydrophobic zeolites with cyclohexane, were used to estimate the hydrophobicity of the zeolites in this study. The volume of water adsorbed within low-defect, Sn-Beta-F samples was ca. 6x smaller, on average, than that adsorbed within post-synthetically prepared Sn-Beta-OH samples. The volume of water adsorbed among Sn-Beta-F samples, however, varied by  $3.4\times$  ( $0.005\text{--}0.017\text{ cm}^3\text{ g}^{-1}$ ). Glucose isomerization rate constants (per open Sn site, 373 K) generally decreased with increasing silanol content among Sn-Beta-F samples (Fig. E.50), although significant scatter is observed in the correlations shown in Fig. E.50 suggesting other structural heterogeneities among the Sn-Beta-F samples may influence isomerization rates. The silanol densities ( $\text{mol g}^{-1}$ ) measured from IR peaks at  $2275\text{ cm}^{-1}$  in spectra of  $\text{CD}_3\text{CN}$ -saturated samples and their E value ( $0.74\text{ cm } \mu\text{mol}^{-1}$ , Section E.7.9) was directly proportional to the molar water uptake at  $P/P_0 = 0.2$  after accounting for water bound to all Sn sites (Fig. E.49(a)) or to Lewis

acidic Sn sites (Fig. E.49(b)), assuming 2:1 H<sub>2</sub>O:Sn binding stoichiometry (<sup>119</sup>Sn NMR evidence [554]).



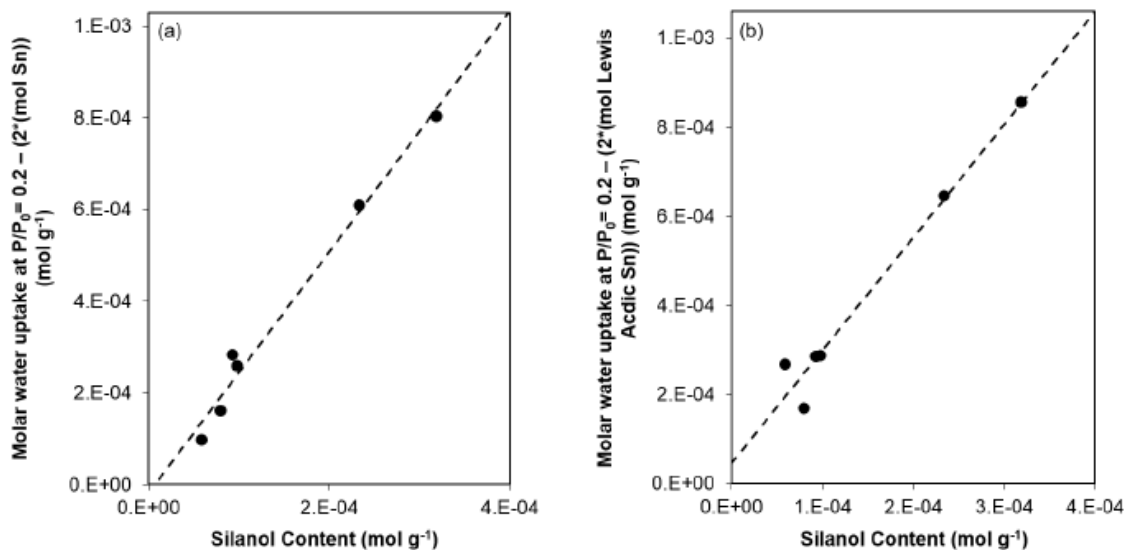


Figure E.49. Molar water uptake measured at  $P/P_0=0.2$ , after subtracting the contribution from (a) total Sn (estimated by AAS) or (b) Lewis acidic Sn assuming 2:1 H<sub>2</sub>O:Sn binding stoichiometry, plotted as a function of the silanol content.

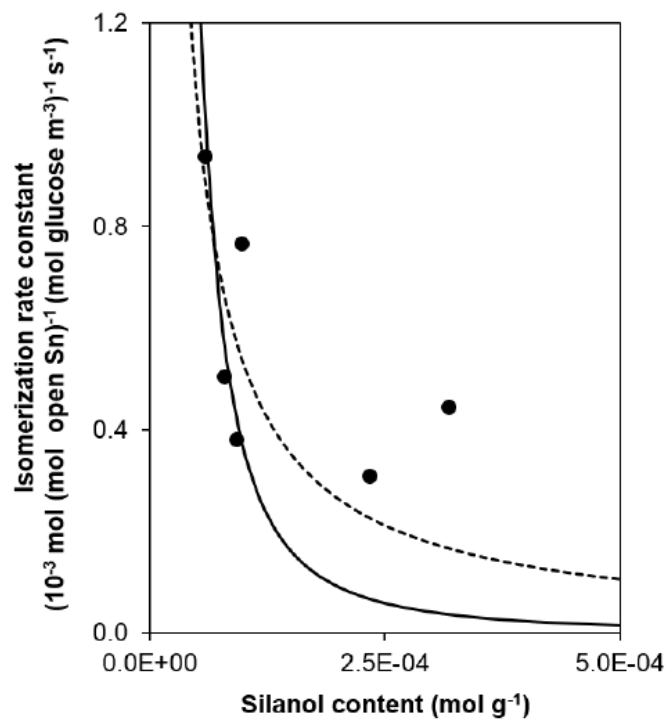


Figure E.50. Rate constants per open Sn sites for all Sn-Beta-F samples as a function of the silanol content measured using the E value for the peak for CD<sub>3</sub>CN bound to silanol sites centered at 2275 cm<sup>-1</sup>. Trendlines show correlation of rate constant with 1/(mol SiOH g<sup>-1</sup>) (dashed line) and 1/(mol SiOH g<sup>-1</sup>)<sup>2</sup> (solid line) determined by linear regression.

Table E.10.  
Site and structural characterization data for the samples in this study.

| Sample         | $V_{ads}$ at<br>$P/P_0 =$<br>$0.2^a$ | Rate Constant Per<br>Open Sn Sites<br>$10^3$ mol fructose (mol<br>open $\text{Sn}^{-1}$<br>$(\text{mol glucose m}^{-3})^{-1}$<br>$\text{s}^{-1b}$ |
|----------------|--------------------------------------|---|
| Sn-Beta-F-100  | 0.0069                               | 0.94  |
| Sn-Beta-F-105  | 0.015                                | 0.31  |
| Sn-Beta-F-110  | 0.0095                               | 0.38  |
| Sn-Beta-F-140  | 0.017                                | 0.44  |
| Sn-Beta-F-170  | 0.0073                               | 0.77  |
| Sn-Beta-F-220  | 0.0048                               | 0.50  |
| Sn-Beta-OH-170 | 0.036                                | 0.0083  |
| Sn-Beta-OH-200 | 0.092                                | 0.015   |

<sup>a</sup>Errors are  $\pm 5\%$ .

<sup>b</sup>Errors are  $\pm 15\%$ .



## F. MOLECULAR STRUCTURE AND CONFINING ENVIRONMENT OF TIN SITES IN SINGLE-SITE ZEOLITES

### F.1 Introduction

Single-site heterogeneous catalysts contain active sites that behave uniformly as a result of site isolation and well-defined structures. Their catalytic behavior depends on their local coordination, defined by the bonding of sites to the support and to ancillary ligands [413, 599–602], which provides a primary environment that influences the electronic properties of the active sites [599, 600, 603–605]. Their catalytic behavior also depends on their secondary environments, which can result from organic ligands [599, 600, 603–605], or from confinement of sites within an inorganic cavity that provides enthalpic and entropic stabilization of bound reactive intermediates through van der Waals and electrostatic interactions [23, 143, 606, 607]. As a result, accurate descriptions of catalytic active sites require precise definitions of both the local structure and the secondary environments of the binding sites, in turn, requiring spectroscopic and kinetic probes sensitive to both environments.

Zeolites belong to one of the most widely used and studied classes of heterogeneous catalysts [155, 608] for which primary and secondary environments influence catalytic reactivity. The substitution of some silicon atoms in the crystalline zeolite lattice with heteroatoms provides a route to prepare single-site catalysts that contain isolated metal atoms with well-defined local structures and confining environments. Among siliceous frameworks containing tetravalent heteroatoms ( $M^{4+} = \text{Sn, Ti, Zr, Hf}$ ), Sn-Beta zeolites have received considerable attention because of their ability to catalyze a broad range of reactions including the Baeyer-Villiger oxidation of ketones [529], the intermolecular Meerwein-Ponndorf-Verley oxidation of alcohols and Oppenauer reduction of aldehydes (MPVO) [609], and the related

intramolecular MPVO cycle of glucose-fructose isomerization [534]. Different four-coordinate Sn local structures have been proposed, including “closed” sites with four framework bonds  $[\text{Sn}-(\text{OSi}\equiv)_4]$  and “open” sites with three framework bonds and an OH ligand  $[(\text{HO})-\text{Sn}-(\text{OSi}\equiv)_3]$ , which exist as either “hydrolyzed-open” (adjacent  $\equiv\text{Si}-\text{OH}$ ) or “defect” sites (adjacent to a framework Si vacancy) (Fig. F.1). Closed and open Sn sites have been identified using IR and  $^{119}\text{Sn}$  solid-state NMR spectroscopy together with density functional theory (DFT) calculations [550, 551] and their detailed local structures in Sn-Beta zeolites have been refined by the combined use of dynamic nuclear polarization enhanced solid-state NMR (DNP NMR) and DFT calculations. DNP is used to significantly enhance the NMR sensitivity utilizing microwave-promoted polarization transfer from unpaired electrons to nuclei, typically protons [512–514], whose hyperpolarization can be transferred to the targeted heteroatoms (e.g.,  $^{119}\text{Sn}$ ) [515, 516, 547, 610] through cross-polarization (CP). DNP enables acquiring  $^{119}\text{Sn}$  chemical shift anisotropy (CSA) parameters at natural abundance, which can be compared to values calculated from DFT to discriminate local Sn structure and location [611]. In the case of Sn-Beta zeolites, however, precise structural assignments are complicated by the presence of different metal-framework coordination modes, multiple tetrahedral-site (T-site) locations [562, 611] and crystal polymorph [612], and the inhomogeneous spatial distribution of Sn throughout crystallites [613]. In contrast to most molecular sieves, chabazite (CHA) is a high-symmetry framework containing only one crystallographically unique T-site, which promises to clarify interpretations of experimental characterization data and to provide model structures that can be described more accurately by theory. Periodic DFT studies of metal-substituted zeolites have estimated Ti heteroatom stability in CHA [614], and compared adsorbate (water, ammonia, pyridine) binding energies at various heteroatom sites in CHA [615–618]. Such studies have also estimated ammonia binding energies [267], and developed linear scaling relationships for O- and S-containing compounds [619], bound at different heteroatoms in CHA. Theoretical

studies of metal-substituted CHA frameworks continue to proliferate, despite commensurate experimental progress to prepare and characterize such model catalysts.

Here, we report the direct hydrothermal synthesis of Sn-CHA zeolites, their catalytic function as solid Lewis acids for substrates of varying size, and the detailed structural characterization of Sn active sites that distinguishes their primary and secondary environments. The single T-site nature of Sn-CHA allows more accurate theoretical modeling, and the use of  $\text{CD}_3\text{CN}$  titrants enables quantifying different Lewis acidic Sn structures detected by bulk spectroscopic techniques. We provide evidence that Sn-CHA catalyzes the MPVO reaction of propionaldehyde and ethanol, yet is essentially unreactive for glucose isomerization. The ability to complement DNP NMR with DFT calculations enables identifying different local Sn structures (closed vs. open vs. defect), while the combination of IR and DNP NMR with pyridine titrants, unable to traverse eight-membered ring CHA micropore apertures, enables probing different secondary confining environments in CHA (microporous vs. mesoporous voids) and establishing a structure-reactivity relationship that highlights the critical role of microporous confining environments around Sn sites for aqueous-phase glucose-fructose isomerization.

## F.2 Results and Discussion

### F.2.1 Synthesis of Sn-CHA and Bulk Structural Characterization of Stannosilicates

Hydrothermal synthesis routes to prepare CHA molecular sieves containing framework Sn heteroatoms have not been reported previously to our knowledge; therefore, syntheses were performed by adapting reported procedures for the fluoride-assisted hydrothermal synthesis of Ti-CHA [620] (details in Section F.6.2). Generally, synthetic routes for Sn-CHA involved first homogenizing the silicon precursor (tetraethylorthosilicate) and the tin precursor (an ethanolic solution of stannic chloride pentahydrate) in an aqueous hydrogen peroxide solution, and then adding the organic structure-directing agent (aqueous N,N,N-trimethyl-1-adamantylammonium hydrox-

ide). After a reaction and homogenization period (24 h), ethanol and excess water were evaporated from this solution to obtain the low water contents typical of fluoride-assisted zeolite crystallization ( $\text{H}_2\text{O}/\text{SiO}_2 = 3$ ), which required performing one intermediate rehydration ( $\text{H}_2\text{O}/\text{SiO}_2 = 40$ ) and dehydration cycle; attempts to crystallize Sn-CHA without this rehydration cycle were unsuccessful (10 days, 423 K). Finally, aqueous hydrofluoric acid was added as the mineralizing agent to form a powder, which crystallized Sn-CHA (2 days, 423 K).

Structural characterization data are listed in Table F.1 for all samples in this study. Stannosilicate molecular sieves are labeled Sn-X-Y-Z, where X is the framework type (CHA or Beta), Y is the mineralizing agent used (-F: fluoride, -OH: hydroxide), and Z is the silicon-to-tin molar ratio determined from atomic absorption spectroscopy. Powder XRD patterns were used to confirm the intended crystal topologies (Section F.6.3, Fig. F.6) and that samples did not contain extracrystal-line  $\text{SnO}_2$  domains larger than 3 nm in diameter [290]. Argon (CHA) and nitrogen (Beta, xerogel) adsorption isotherms (Section F.6.4, Fig. F.7) were used to determine the micropore volumes reported in Table F.1, which were consistent with previous reports for each sample topology [42,467,621], except those measured for Sn-CHA-F-60 and Sn-CHA-F-70, which were lower ( $0.15\text{-}0.16\text{ cm}^3\text{ g}^{-1}$ ) than those measured for Si-CHA-F and Al-CHA ( $0.20\text{-}0.23\text{ cm}^3\text{ g}^{-1}$ ) [42,467]. Non-local density functional theory (NLDFT) treatments of Ar adsorption isotherms used to determine pore size distributions (Section F.6.4, Figs. F.8 and F.9) provide evidence for mesoporous voids (5-10 nm diam.) in Sn-CHA-F samples, but not Si-CHA-F, evident in the  $\sim 5\times$  larger volumes of adsorbed Ar at reduced pressures characteristic of mesopore filling ( $0.05\text{-}0.8\text{ P/P}_0$ ) for Sn-CHA-F than for Si-CHA-F. Replicate synthesis of Sn-CHA resulted in samples with different Sn content ( $\text{Si}/\text{Sn} = 60$  and  $70$ ) but otherwise indistinguishable bulk structural characteristics, while the Sn-Beta-F-116 sample studied here is representative of a larger suite of Sn-Beta-F samples ( $>20$ ) we have studied previously [466,622].

Diffuse-reflectance UV-visible (DRUV) spectra of Sn-CHA-F-70, Sn-Beta-F-116, and Sn-xerogel (Section F.6.5, Figure F.10) were collected after dehydration treat-



ments (523 K), in order to avoid the ambiguity of interpreting overlapping absorption bands (220-250 nm) for hexacoordinate framework Sn centers with coordinated ligands (e.g., water) [577] and for any Sn located within nanometer-sized non-framework SnO<sub>2</sub> domains [579–582]. DRUV spectra showed dominant absorption bands for isolated tetrahedral Sn in Sn-CHA-F-70 (ca. 220 nm) and Sn-Beta-F-116 (ca. 210 nm) [534, 577], but also showed broad bands (ca. 250 nm) characteristic of hexacoordinate Sn, reflecting either the presence of minority SnO<sub>2</sub> or incomplete dehydration at 623 K (Fig. F.11; TGA analysis in Section F.6.6). Absorption edge energies (F.1) extracted from Tauc plots (Fig. F.12) were characteristic of isolated, tetrahedral Sn in zeolitic frameworks ( $\geq 4.1$  eV) [568, 581] for both Sn-CHA samples (4.12-4.33 eV) and for Sn-Beta-F-116 (4.23 eV), and higher than for SnO<sub>2</sub> domains (ca. 3 nm) supported on Si-Beta (4.09 eV) [466]. Sn K-edge X-ray absorption spectra (XAS) for Sn-CHA-F-70, Sn-Beta-F-116, and Sn-xerogel (Section F.6.7 indicated average Sn coordination numbers of six ( $5.7\text{--}5.8 \pm 0.6$ ) under ambient conditions and four ( $3.8\text{--}4.0 \pm 0.4$ ) after dehydration, the behavior expected of framework Sn centers. The average Sn-O bond length in Sn-CHA-F-70 derived from EXAFS ( $1.96 \pm 0.02$  Å) was longer than expected from density functional theory (DFT) predictions for closed and defect Sn sites (1.88 Å, Section F.2.5), perhaps indicating the presence of residual water in Sn-CHA-F-70 at 523 K. These bulk characterization techniques indicate that the Sn-CHA and Sn-Beta samples studied here contain predominantly Sn atoms isolated within framework positions. We next use site-sensitive characterization techniques that provide increasing resolution into the molecular-level details of local Sn coordination and geometry.

### F.2.2 Quantifying Lewis acidic Sn sites using d<sub>3</sub>-acetonitrile and pyridine titration and IR spectroscopy

Infrared (IR) spectra of Sn-CHA samples saturated with CD<sub>3</sub>CN are shown in Figure F.2, and used to quantify their number of Lewis acidic Sn sites. Sn-Beta zeolites show  $\nu(\text{C}\equiv\text{N})$  vibrations characteristic of CD<sub>3</sub>CN bound to open ( $2316\text{ cm}^{-1}$ )

and closed ( $2308\text{ cm}^{-1}$ ) Sn sites (Section F.6.8, Fig. S.10) [550], which were quantified using integrated molar extinction coefficients ( $\mathcal{E}$ ;  $\text{cm } \mu\text{mol}^{-1}$ ) measured previously for these sites [466]. On Sn-CHA zeolites,  $\nu(\text{C}\equiv\text{N})$  vibrations for  $\text{CD}_3\text{CN}$  bound to Lewis acidic Sn sites ( $2310\text{ cm}^{-1}$ ), to ex-tracrystalline Sn [623] or to Si-OH groups next to open Sn sites [624] ( $2287\text{ cm}^{-1}$ ; dominant features in an amorphous xerogel [466]), and to silanol groups ( $2275\text{ cm}^{-1}$ ) increased simultaneously with  $\text{CD}_3\text{CN}$  coverage (Fig. F.2a) [466]. One convoluted peak at  $2310\text{ cm}^{-1}$  for  $\text{CD}_3\text{CN}$  bound to open and closed Lewis acidic Sn sites was observed for Sn-CHA-F with increasing  $\text{CD}_3\text{CN}$  coverage (Fig. F.2a), as also observed on high-defect Sn-Beta zeolites (Sn-Beta-OH) [622]. In contrast, low-defect Sn-Beta-F zeolites show two distinct peaks at  $2316\text{ cm}^{-1}$  and  $2308\text{ cm}^{-1}$  at different  $\text{CD}_3\text{CN}$  coverages (Fig. F.15) [466,622]. Lewis acidic Sn sites were quantified (Table F.2) after deconvolution of IR spectra at saturation  $\text{CD}_3\text{CN}$  coverages [466,622] to extract contributions from component peaks for open and closed Sn sites and silanol groups (deconvoluted spectra for Sn-CHA-F-60 in Fig. F.2b). The concentrations of silanol groups on Sn-CHA-F-60 and Sn-CHA-F-70 were  $2\text{--}12\times$  higher than on Sn-Beta-F zeolites [466]. These data are consistent with larger  $\text{H}_2\text{O}$  uptakes measured on Sn-CHA-F ( $0.12\text{--}0.15\text{ cm}^3\text{ g}^{-1}$  at  $P/P_0 = 0.2$ ; Fig. F.7b) than on Si-CHA-F (by  $7\times$ ) and on Sn-Beta-F zeolites (by  $13\times$ , on average).

The fraction of Lewis acidic Sn sites (per total Sn) titrated by  $\text{CD}_3\text{CN}$  was unity within experimental error ( $\pm 20\%$ ) in Sn-CHA-F-60 (1.18) and Sn-CHA-F-70 (1.14), consistent with bulk characterization methods reflecting the predominance of framework Sn sites. This quantification assumed equimolar  $\text{CD}_3\text{CN}$  binding to each Sn site, consistent with saturation of Lewis acidic Sn sites below monolayer  $\text{CD}_3\text{CN}$  coverages (per total Sn) during sequential dosing experiments on Sn-Beta zeolites [466]. Equimolar  $\text{CD}_3\text{CN}$  binding stoichiometry to each Sn site is also consistent with the absence of hexacoordinate Sn resonances in  $^{119}\text{Sn}$  NMR spectra of Sn-Beta saturated with acetonitrile [625], and with quantitative titration of Lewis acid sites using pyridine, n-propylamine, and ammonia [466], the adsorption of which leads to penta-coordinate  $^{119}\text{Sn}$  resonances in NMR spectra.<sup>18</sup> Equivalent fractions of Lewis acid

sites in Sn-CHA-F-60 (1.08, Table F.2) and Sn-CHA-F-70 (1.20, Table F.2) were also quantified by ammonia titration and temperature programmed desorption methods developed previously on Sn-Beta zeolites (Section F.6.9) [466]. These titration data indicate that the Sn-CHA samples studied here contain predominantly Lewis acidic Sn sites incorporated within framework locations, and that integrated molar extinction coefficients for IR vibrations of  $\text{CD}_3\text{CN}$  bound at Sn sites in Beta zeolites can also be used to quantify Sn sites in CHA zeolites.

Framework Sn sites may be confined within either microporous or mesoporous voids, both of which are detected in Ar adsorption isotherms, of Sn-CHA. The location of Sn within different confining environments was probed using pyridine as a probe molecule (ca. 0.6 nm), which cannot access microporous voids in CHA that are limited by eight-membered ring window apertures (ca. 0.4 nm). Any vibrations observed for pyridine bound to Lewis acidic Sn sites thus reflect Sn atoms located at external crystallite surfaces or within mesoporous voids, similar to previous reports for  $\text{H}^+$  sites located in partially-mesoporous Al-CHA zeolites synthesized in fluoride media [459]. IR spectra measured after pyridine saturation (423 K) of Sn-CHA-F (Section F.6.8, Fig. F.16) showed prominent peaks at  $1450\text{ cm}^{-1}$  and  $1610\text{ cm}^{-1}$  reflecting deformation modes of pyridine coordinated to Lewis acid sites [559], and a minor peak for protonated pyridine at  $1545\text{ cm}^{-1}$  ( $20\times$  smaller area than  $1450\text{ cm}^{-1}$  peak) as observed previously for post-synthetically prepared Sn-Beta-OH zeolites [622]. The fraction of Sn sites accessible to pyridine was 0.20 (per total Sn) for both Sn-CHA-F-60 and Sn-CHA-F-70 (Table F.2, using  $E(1450\text{ cm}^{-1})$  values measured previously for Sn-Beta-F zeolites [466]. The accessibility of 20% of the Sn sites in Sn-CHA to pyridine is consistent with a uniform distribution of Sn throughout Sn-CHA crystallites, which show lower than expected micropore volumes (by 20-25%) and the presence of mesoporous voids.

### F.2.3 Catalytic interrogation of the confining environment around Sn sites in Sn-CHA

#### Intermolecular propionaldehyde-ethanol MPVO reactions

The Lewis acidic behavior of framework Sn sites of Sn-CHA-F-60 was probed using intermolecular MPVO reactions of ethanol and propionaldehyde, chosen because both molecules ( $<0.4$  nm) can traverse 8-MR CHA windows. Intermolecular MPVO reactions proceed via coordination of an alcohol and an aldehyde (or ketone) to a Lewis acid site, subsequent deprotonation of the alcohol, and kinetically-relevant hydride transfer from the alcohol carbon to the carbonyl carbon in a six-membered transition state, as demonstrated experimentally for Lewis acidic Beta zeolites [626] and by theoretical simulations for aluminum alkoxide complexes [627] and Beta zeolites [628,629]. Intermolecular MPVO rates (333 K) were measured using dilute propionaldehyde solutions in ethanol solvent (0.6 M propionaldehyde), and a representative transient reaction profile is shown in Figure F.17 (Section F.6.10). 1-propanol formation rates increased with reaction time and reached 2.75 turnovers (per mol Sn) after 6 h, demonstrating the catalytic nature of Sn sites in Sn-CHA-F-60 (Fig. F.18a). 1,1-diethoxy propane, a condensation product of two ethanol molecules and one propionaldehyde molecule, was also detected and is consistent with intermolecular MPVO reactions of ethanol and acetone (discussion in Section F.6.10) in the presence of solid Lewis acids (e.g.,  $\text{ZrO}_2$ ), which catalyze aldol condensation reactions of acetaldehyde products [630–633] with primary alcohols to form acetals [630]. The total formation of 1-propanol and 1,1-diethoxy propane was nearly equal to the consumption of propionaldehyde (Fig. F.18b), resulting in carbon balance closure for  $\text{C}_3$  compounds in the ethanol-propionaldehyde reaction on Sn-CHA-F-60. Ethanol conversions were  $\leq 7\%$  in all cases (Fig. F.18b), and the total concentrations of acetaldehyde, ethanol, and twice the 1,1-diethoxy propane concentration resulted in carbon balance closure for  $\text{C}_3$  compounds. Closure of both  $\text{C}_2$  and  $\text{C}_3$  carbon balances demonstrates that further byproduct formation, other than 1,1-diethoxy propane, was not observed over Sn-

CHA during intermolecular MPVO reactions of ethanol and propionaldehyde under the conditions studied here.

The initial 1-propanol formation rate measured on Sn-CHA-F-60 (Table F.3) was  $40\times$  lower than that measured on Sn-Beta, but  $60\times$  higher than on Sn-xerogel. Rates are  $90\times$  higher on Sn-Beta-F-116 than on Sn-CHA-F-60 when normalized by the number of Sn sites in open coordination, which is the more reactive site in Sn-Beta predicted by theory [628,629] and identified by experiment for glucose isomerization mediated by an analogous intramolecular hydride shift [466]. The higher intermolecular MPVO reaction rates on Sn-Beta may reflect transport limitations in Sn-CHA, differences in prevalent coverages of reactive intermediates, or differences in transition state stability between the different frameworks. Isotopic tracer experiments using  $C_2D_5OH$  reactants were performed to confirm that 1-propanol products were formed over Sn-CHA-F-60 via a Lewis-acid mediated intermolecular hydride shift mechanism. The 1-propanol formed from reaction showed mass spectra with a one-unit increase in fragments for  $CH_3CH_2CHDOH$  ( $m/z = 60$ ) and  $CHDOH$  ( $m/z = 32$ ), as expected for deuterium incorporation within propionaldehyde (Section F.6.10, Fig. F.20).

#### Glucose-fructose isomerization via intramolecular MPVO cycles

Intramolecular MPVO cycles isomerize glucose into fructose via mechanisms whose details are generally accepted on Lewis acid sites incorporated within Beta zeolites, and were used to probe the reactivity of pyridine-accessible Sn sites in Sn-CHA. The catalytic cycle involves quasi-equilibrated adsorption, ring-opening and deprotonation of glucose at framework Sn sites, followed by a kinetically-relevant intramolecular 1,2-hydride shift step, and then by quasi-equilibrated fructose ring-closure and desorption.<sup>64,65</sup> First-order rate constants, measured in a kinetic regime in which adsorbed water molecules at framework metal centers are most abundant surface intermediates, are  $10\text{--}50\times$  higher (at 373 K) among low-defect than among high-defect Ti-Beta (per Ti site) and Sn-Beta (per open Sn site) zeolites.<sup>43,66</sup> The higher first-order rate constants on low-defect M-Beta-F than high-defect M-Beta-OH zeolites reflect

lower apparent free energies of activation, which measure the difference in stability between kinetically-relevant isomerization transition states and two water molecules bound at active metal sites.<sup>43,66</sup> As a result, glucose isomerization turnover rates and rate constants, measured in the first-order kinetic regime, provide a quantitative kinetic probe of the reactivity of Lewis acidic Sn sites, and can be used to assess the catalytic consequences of their primary local environment and secondary confining environment.

Glucose-fructose isomerization turnover rates (398 K, 1% (w/w) glucose; Table F.3) on Sn-CHA-F-60, normalized by the number of pyridine-accessible Sn sites, were four orders-of-magnitude lower than turnover rates on Sn-Beta-F-116. Isomerization turnover rates were also four orders-of-magnitude lower on an amorphous Sn-xerogel, which contains only unconfined Sn sites, than on Sn-Beta-F-116 (Table F.3). Isomerization turnover rates measured on Sn-xerogel and on Sn-CHA-F-60 were similar (within  $2\times$ ), which is within the residual variation in turnover rates (within  $2\text{--}3\times$ ) measured previously among Sn-Beta-F ( $>6$  samples) or among Sn-Beta-OH ( $>16$  samples) of varying Sn content.<sup>43,44</sup> The similar glucose-fructose isomerization turnover rates measured on Sn-xerogel and Sn-CHA, upon normalization by the number of pyridine-accessible sites, provides quantitative kinetic evidence supporting the presence of approximately 20% of the framework Sn sites located within mesoporous voids of Sn-CHA. These data highlight the crucial role of confining microporous environments in aqueous-phase glucose isomerization, and indicate that rates measured on Sn-Beta zeolites reflect reactions occurring at Sn sites confined within their 12-MR microporous voids, and not at any unconfined Sn sites that may be located at external crystallite surfaces. We conclude from these catalytic intramolecular and intermolecular MPVO probe reactions, together with the IR spectra collected after  $\text{CD}_3\text{CN}$  and pyridine titration, that Sn-CHA zeolites contain framework Sn sites that function as Lewis acids and are located within both microporous and mesoporous voids.

### F.2.4 Probing local Sn structure using $^{119}\text{Sn}$ DNP NMR spectroscopy

DNP enhanced  $^{119}\text{Sn}\{^1\text{H}\}$  CPMAS NMR characterization of Sn-CHA-F-70 was performed in its hydrated and dehydrated states. An asymmetric peak characteristic of hexa-coordinated Sn (ca. -720 ppm) was detected in the hydrated state (Fig. F.22a), while a broad peak characteristic of tetra-coordinated Sn (ca. -430 ppm) was detected after dehydration (Fig. F.22b), with asymmetric broadening and a wider distribution of resonances reflecting the greater inhomogeneity or asymmetry of Sn sites after dehydration. The  $^{119}\text{Sn}\{^1\text{H}\}$  CPMAS NMR sensitivity was considerably higher on the hydrated sample (ca. 1800 s signal averaging time for a spectrum with a signal-to-noise ratio = 35, Fig. F.22a), reflecting the protonrich environment present within microporous voids, than on the dehydrated sample (ca. 21 h signal averaging time using Carr-Purcell Meiboom-Gill (CPMG) [634] echo trains for a spectrum with a signal-to-noise ratio = 15, Fig. F.22b), suggesting inefficient CP from  $^1\text{H}$  to  $^{119}\text{Sn}$  resulting from the absence of water (and perhaps TCE molecules from the biradical solution) within zeolitic pores. These changes in Sn coordination upon dehydration are consistent with XAS data (Section F.2.1), and the behavior expected of framework Sn sites.

The increased NMR sensitivity afforded by DNP enables performing 2D  $^{119}\text{Sn}\{^1\text{H}\}$  CP magic-angle turning (CPMAT) experiments, which can separate the chemical shift anisotropy (CSA) for each isotropic  $^{119}\text{Sn}$  site that contributes to the broadened  $^{119}\text{Sn}$  NMR resonance observed in the 1D spectra [611]. CSA is a second rank tensor defined by three principal components ( $\delta_{11}$ ,  $\delta_{22}$ , and  $\delta_{33}$ ), and can also be described using the Herzfeld-Berger convention [635] by the isotropic chemical shift ( $\delta_{iso}$ ), span ( $\Omega$ ), and skew ( $\kappa$ ) (Eqs. F.1-F.3):

$$\delta_{iso} = \frac{\delta_{11} + \delta_{22} + \delta_{33}}{3} \quad (\text{F.1})$$

$$\Omega = \delta_{11} - \delta_{33} \quad (\text{F.2})$$

$$\kappa = \frac{3(\delta_{22} - \delta_{iso})}{\Omega} \quad (\text{F.3})$$

CSA is very sensitive to the neighboring electronic environment of the observed nuclei, and is thus an effective probe to elucidate Sn site structures at the molecular level. The 2D  $^{119}\text{Sn}\{^1\text{H}\}$  CPMAT NMR spectrum of the hydrated Sn-CHA-F-70 sample, which is shown in Figure F.3, contained a single asymmetrically broadened peak on the isotropic dimension ( $\delta_{iso} = -713$  ppm) and did not contain a sharp feature for extraframework  $\text{SnO}_2$  (-605 ppm) [621]. The corresponding projection (at  $\delta_{iso}$ ) on the isotropic dimension was extracted and fit to acquire the experimental CSA parameters listed in Table F.4. Two components with the same isotropic chemical shift, but different span ( $\Omega$ ) and skew ( $\kappa$ ), were required to fit the experimental data, a surprising result considering the single T-site in the CHA framework (Figs. F.3a and F.22c). This two-component fitting suggests at least two similar Sn sites are present, with slightly different coordination environments or local geometries, but coincidentally at the same isotropic chemical shift. These CSA components do not reflect contributions of Sn sites incorporated in minority amorphous stannosilicate domains, which are characterized by different isotropic chemical shifts ( $\delta_{iso} = -600$ , -626, and -690 ppm, Fig. F.23). 2D  $^{119}\text{Sn}\{^1\text{H}\}$  CPMAT experiments performed with varying DNP build-up time (1-20 s recycle delays), did not affect the relative areas of the two component peaks used in the CSA fitting (Section F.6.11, Table F.9), indicating that both sites are distributed evenly within the sample and unaffected by  $^1\text{H}$ - $^1\text{H}$  spin diffusion on the time scale studied. Overall, these data suggest that these two components represent Sn sites of different local structure incorporated within the CHA framework and evenly distributed among mesoporous and microporous voids.

The 2D  $^{119}\text{Sn}\{^1\text{H}\}$  CPMAT NMR spectrum of dehydrated Sn-CHA-F-70 showed two asymmetrically broadened resonances on the isotropic dimension ( $\delta_{iso} = -437$  and -480 ppm, fit from the 1D DNP enhanced CP-Total Sideband Suppression spectrum), which were analyzed to acquire experimental CSA parameters (Section F.6.11, Fig. F.24). The resonance at -480 ppm appears between the range of chemical shifts



characteristic of tetracoordinated (ca. -430 ppm) and pentacoordinated Sn (ca. -550 ppm), but was too low in intensity to estimate CSA parameters (Table F.4). The Sn site at -480 ppm may represent a minor fraction of Sn that is not completely dehydrated in Sn-CHA-F-70 despite vacuum treatment (773 K), which might reflect strongly adsorbed water molecules bound at silanol and stannanol groups in defect Sn sites (Fig. F.1). The CSA parameters for the resonance at -437 ppm are similar to those reported previously for dehydrated Sn-Beta, although the larger span for Sn-CHA (159 ppm) than for Sn-Beta (ca. 100 ppm) [611] may reflect more distorted local Sn environments in CHA (Table F.4).

Dehydrated Sn-CHA-F-70 was saturated with  $^{15}\text{N}$ -pyridine at ambient temperature and characterized by  $^{15}\text{N}$  and  $^{119}\text{Sn}$  DNP NMR to further probe the structure of Sn sites that bind pyridine. The 1D  $^{119}\text{Sn}\{^1\text{H}\}$ CPMAS NMR spectrum of  $^{15}\text{N}$ -pyridine-saturated Sn-CHA-F-70 (Fig. F.28) shows a broad distribution of resonances ranging from -400 to -750 ppm, while the 2D  $^{119}\text{Sn}\{^1\text{H}\}$  CPMAT NMR spectrum (Fig. F.29) shows two peaks in the isotropic dimension characteristic of pentacoordinated (ca. -596 ppm) and hexacoordinated Sn (ca. -694 ppm), whose corresponding CSA parameters are listed in Table F.5. The pentacoordinated Sn resonance was expected from the equimolar binding of pyridine to Sn [466], while the hexacoordinated Sn resonance implies that some Sn sites can bind a second pyridine molecule. The binding of two pyridine molecules at a single Sn site, which was not observed by IR spectroscopy (423 K), likely resulted from the excess  $^{15}\text{N}$  pyridine used to saturate Sn-CHA at ambient temperature prior to NMR experiments.

Two isotropic peaks were observed in the 1D DNP enhanced  $^{15}\text{N}\{^1\text{H}\}$  CPMAS NMR spectrum of  $^{15}\text{N}$ -pyridine saturated Sn-CHA-F-70 (Fig. F.30), and the 2D  $^{15}\text{N}$  CPMAT NMR is shown in Figure F.4, with the associated CSA parameters given in Table F.5. The resonance at 262 ppm reflects pyridine bound to Lewis acidic Sn sites, similar to that observed for stannosilicate materials with pores large enough to accommodate pyridine (MFI, MCM-41, Beta, xerogel, Fig. F.31) [636]. The resonance centered at 289 ppm reflects pyridine interacting with silanol groups

[636], an assignment corroborated by the  $^{15}\text{N}\{^1\text{H}\}$  CPMAS NMR spectrum of  $^{15}\text{N}$ -pyridine saturated Si-CHA-F ( $\delta_{iso} = 286$  ppm, Section F.6.12, Fig. F.32). Among the metallosilicates studied by Gunther et al., only high-defect zeolites synthesized in alkaline media showed a  $^{15}\text{N}$  resonance for pyridine bound to SiOH groups [636]. Thus, the observation of this resonance in Sn-CHA-F-70 reflects the presence of a considerable concentration of silanol defects, consistent with  $\text{H}_2\text{O}$  adsorption isotherms that quantified  $12\times$  higher  $\text{H}_2\text{O}$  uptake in Sn-CHA-F-70 than in Sn-Beta-F [466], and with  $\text{CD}_3\text{CN}$  titration that quantified  $2\text{--}12\times$  higher SiOH concentrations in Sn-CHA than in Sn-Beta-F (Table F.2) [466]. The presence of these defects is also consistent with the high percentage of (HO)-Si-(OSi) $_3$  ( $\text{Q}_3$ ) sites (21%) quantified by direct-polarized  $^{29}\text{Si}$  solid-state NMR spectrum (Fig. F.27). Taken together, the IR and NMR data for pyridine-saturated Sn-CHA zeolites indicate that ca. 20% of its framework Sn sites are located within mesoporous voids that also contain a high concentration of SiOH defects.

#### F.2.5 DFT calculations of $^{119}\text{Sn}$ DNP NMR chemical shifts, spans, and CSA parameters

The different local structures of Sn sites proposed to be present in zeolitic frameworks, which are closed, hydrolyzed-open, and defect sites (Figure F.1), were investigated by DFT calculations, with optimized structures for Sn-CHA shown in Figure F.5. The hydrated states of Sn sites (pseudo-octahedral geometry) were modeled with two water molecules bound to Sn for closed and defect sites, and one water molecule bound to Sn for hydrolyzed-open site given its additional bond to the proximal silanol group. Two additional water molecules outside the Sn coordination sphere and implicit water ( $\epsilon = 80.4$ ) were also included in the model (Fig. F.5). DFT-optimized structures of hydrated closed and defect Sn sites have average Sn-O distances of 2.04 Å, and the hydrolyzed-open Sn site has an average Sn-O distance of 2.02 Å. All values are similar to the average Sn-O bond distances for hydrated Sn-CHA measured by XAS ( $2.01 \pm 0.02$  Å, Section F.6.7). Calculated  $^{119}\text{Sn}$  NMR CSA parameters for hy-

hydrated defect and hydrolyzed-open sites (Section F.6.13, Table F.10) provided closest agreement to the two sets of CSA parameters required to fit the experimental data. Given the peak width of the NMR resonances (6 ppm) and the error between calculated and experimental values ( $\pm 10$  ppm), it is not possible to distinguish hydrolyzed-open and defect sites from the isotropic peak. Moreover, the difference between the DFT calculated spans for hydrated hydrolyzed-open and defect Sn sites (74 ppm) resembles the difference in the spans of the two components required to fit the experimental  $^{119}\text{Sn}$  DNP NMR data for hydrated Sn-CHA (ca. 83 ppm). Therefore, we conclude that the two components identified in 2D  $^{119}\text{Sn}\{^1\text{H}\}$  CPMAT NMR spectra reflect hydrated hydrolyzed-open and defect framework Sn sites. We note, however, that experimental DNP NMR measurements may enhance contributions from  $^{119}\text{Sn}$  sites in close proximity with protons due to more efficient polarization transfer, as observed in the increased sensitivity to  $(\text{HO})_2\text{Si}(\text{OSi})_2$  ( $\text{Q}_2$ ) and  $\text{Q}_3$  silanol groups in  $^{29}\text{Si}$  DNP NMR (Figs. F.25-F.26) compared to direct-excitation  $^{29}\text{Si}$  NMR (Fig. F.27).

DFT-optimized structures of dehydrated hydrolyzed-open Sn sites showed average Sn-O distances of 1.98 Å, similar to the average Sn-O bond distance measured for dehydrated Sn-CHA by XAS ( $1.96 \pm 0.02$  Å, Section F.6.7). The DFT-optimized structure was a pentacoordinate Sn site, while the average coordination number from XAS was four. Furthermore, the calculated  $^{119}\text{Sn}$  NMR parameters for hydrolyzed-open Sn sites (-566 ppm, Table F.10) did not agree with those measured experimentally (-437 and -480 ppm). Closed and defect Sn sites showed average Sn-O distances of 1.88 Å, which are significantly lower than the Sn-O bond distance in dehydrated Sn-CHA measured by XAS and may reflect incomplete dehydration of Sn-CHA prior to XAS measurements. Calculated  $^{119}\text{Sn}$  NMR parameters of dehydrated defect Sn sites were indistinguishable from dehydrated closed Sn sites (Fig. F.5; Table F.10), in contrast to calculated  $^{119}\text{Sn}$  NMR chemical shifts of Sn-Beta [611] which are separated by ca. 20 ppm for defect and closed sites. The similar isotropic chemical shifts for both sites appear to reflect strong hydrogen bonding between SiOH and SnOH groups in

defect Sn sites that are present in close proximity in the CHA framework. Calculated NMR parameters for pyridine-saturated Sn-CHA ( $^{119}\text{Sn}$  and  $^{15}\text{N}$ ) suggest that the pentacoordinate Sn sites observed experimentally reflect one pyridine molecule coordinated to closed Sn sites, while two pyridine molecules most likely coordinate to defect Sn sites and result in hexacoordinated Sn (Fig. F.5; Table F.11). These structural assignments of the different pyridine binding modes to Sn sites are also consistent with the calculated pyridine adsorption energies (Table F.12), which further indicate that closed and defect Sn sites favor binding of one and two pyridine molecules, respectively, at 298 K.

In summary, comparison of the experimental and calculated  $^{119}\text{Sn}$  NMR parameters suggests that the Sn sites observed in hydrated Sn-CHA are predominantly defect and hydrolyzed-open Sn sites, whose signals may be preferentially enhanced by DNP due to their proton-rich environment, while those observed in dehydrated Sn-CHA are predominantly defect and closed Sn sites, which cannot be distinguished by NMR. The high ratio of Si Q<sub>3</sub> sites in direct-polarized  $^{29}\text{Si}$  NMR (21%, Fig. F.27) also suggests that silanol defects are present in large concentrations on Sn-CHA-F zeolites prepared using the methods here, and likely located within mesoporous voids. In pyridine-titrated dehydrated Sn-CHA, polarization transfer from protons within coordinated pyridine can enhance the  $^{119}\text{Sn}$  NMR signal, and the different binding stoichiometry of pyridine molecules (one or two) results in Sn sites with different coordination numbers (five or six, respectively), such that both closed and defect sites can be detected and distinguished. These assignments also suggest that closed sites present after sample dehydration under vacuum can undergo reversible structural changes to form hydrolyzed-open sites upon hydration.

### F.3 Conclusions

Chabazite molecular sieves containing isomorphously substituted framework tin heteroatoms (Sn-CHA) were prepared via direct fluoride-mediated hydrothermal synthesis routes. Lewis acidic Sn sites in Sn-CHA were titrated in equimolar stoichiometry

etry by ammonia and  $d_3$ -acetonitrile, providing values identical within experimental error to the total Sn content. These data indicate that integrated molar extinction coefficients for IR vibrations of  $CD_3CN$  bound at Sn sites in Sn-Beta can be used to quantify such sites in Sn-CHA. IR spectra of Sn-CHA zeolites titrated by pyridine, a molecule too large to traverse eight-membered ring CHA windows, indicated that 20% of the framework Sn sites were located within mesoporous voids.

Sn-CHA zeolites catalyze intermolecular MPVO and subsequent condensation reactions of ethanol and propionaldehyde, confirming that framework Sn sites confined within CHA micropores function as Lewis acid centers capable of mediating hydride shift steps. In contrast, aqueous-phase glucose-fructose isomerization at Sn sites located within mesoporous voids of Sn-CHA and amorphous silica matrices proceeds at turnover rates that are four orders-of-magnitude lower than Sn sites confined within Sn-Beta zeolites. These data provide evidence that unconfined Sn sites in stannosilicates are effectively unreactive for aqueous-phase glucose isomerization.

DNP NMR characterizations of Sn-CHA zeolites show that Sn sites were incorporated into framework lattice positions, consistent with UV-Visible and X-ray absorption spectra that detect tetracoordinated Sn centers upon sample dehydration. The NMR signal enhancements enabled by DNP allow resolving two distinct Sn sites characterized by identical isotropic chemical shift but different chemical shift anisotropy. Comparison of experimentally measured  $^{119}Sn$  NMR CSA parameters with those calculated from DFT supports the presence of framework Sn sites with (defect) and without (closed) neighboring framework Si vacancy defects in dehydrated Sn-CHA, which form hydrated defect and hydrolyzed-open sites upon exposure to ambient conditions or aqueous solution. Such assignments to Sn sites in different local coordination environments (e.g., defect, hydrolyzed-open, closed) were made possible by the structural simplicity of the CHA framework, which contains one lattice T-site and facilitates more accurate theoretical modeling of experimental spectra.

Overall, integrating the controlled synthesis of a model crystalline catalyst containing isolated metal centers, the detection of specific spectroscopic signatures sensitive

to their primary coordination and secondary confining environments, and the computation of plausible active site structures, was essential to resolve the local structure of metal binding sites and to demonstrate the role of secondary confining voids in catalysis.

#### F.4 Acknowledgements

Purdue researchers acknowledge the financial support provided by the Purdue Process Safety and Assurance Center (P2SAC) and a 3M Non-Tenured Faculty Grant. At Purdue, we thank Juan Carlos Vega-Vila for assistance with glucose isomerization reactions, Evan Wegener and Dr. Jeffrey T. Miller for XAS measurements and data analysis, Jason Bates for measurement of H<sub>2</sub>O adsorption isotherms, and Michael Cordon for assistance with SEM imaging. We also thank Sachem, Inc. for supplying the organic structure directing agent used in synthesis of CHA molecular sieves. The work of WCL and ACV is supported by Swiss National Foundation (200020-149704 and Ambizione project PZ00P2-148059, respectively). ACV also acknowledges the Holcim Stiftung for financial support. WCL thanks Mr. Erwin Lam for the help and discussion about DFT calculations. We thank Dr. David Gajan and Dr. Anne Lesage at CRMN Lyon for assisting with measurements on the 400 MHz DNP spectrometer and for fruitful discussions. We thank Prof. Lyndon Emsley and the group members at EPFL for fruitful discussions. We also thank ScopeM (ETH Z'urich) for use of their electron microscopy facilities and Dr. Frank Krumeich for recording TEM images.

Additionally, I acknowledge the American Chemical Society for granting permission to reproduce this chapter of my thesis. Adapted with permissions from Chemistry of Materials, 2017, 29, 8824-8837. Copyright (2017) American Chemical Society. The full article can be accessed here: [dx.doi.org/10.1021/acs.chemmater.7b03209](https://doi.org/10.1021/acs.chemmater.7b03209).

## F.5 Figures and Tables

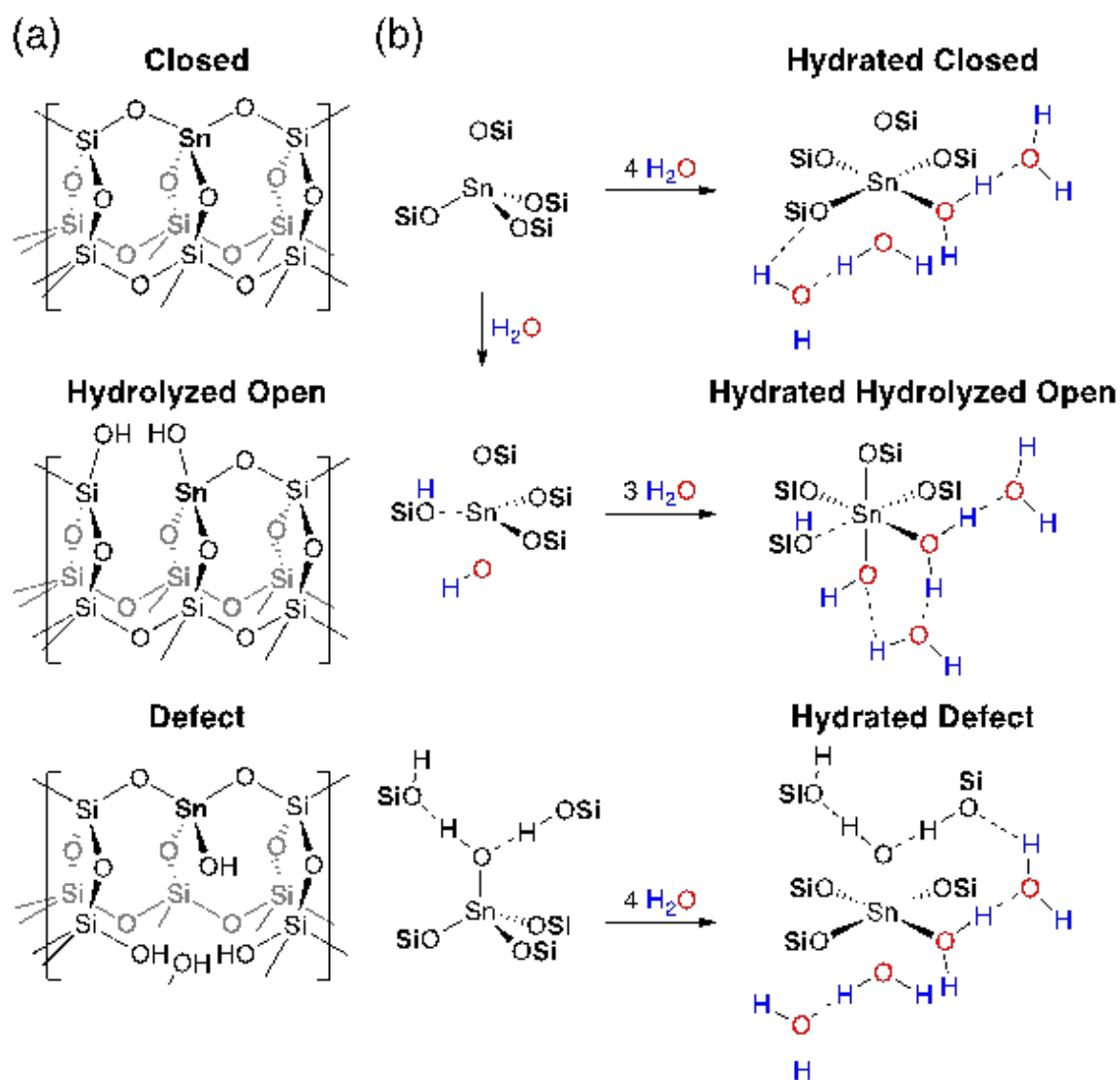


Figure F.1. Depictions of (a) framework Sn structures (closed, hydrolyzed-open, and defect) that may be present in Sn zeolites, and (b) the proposed molecular structures of Sn sites under dehydrated and hydrated conditions.

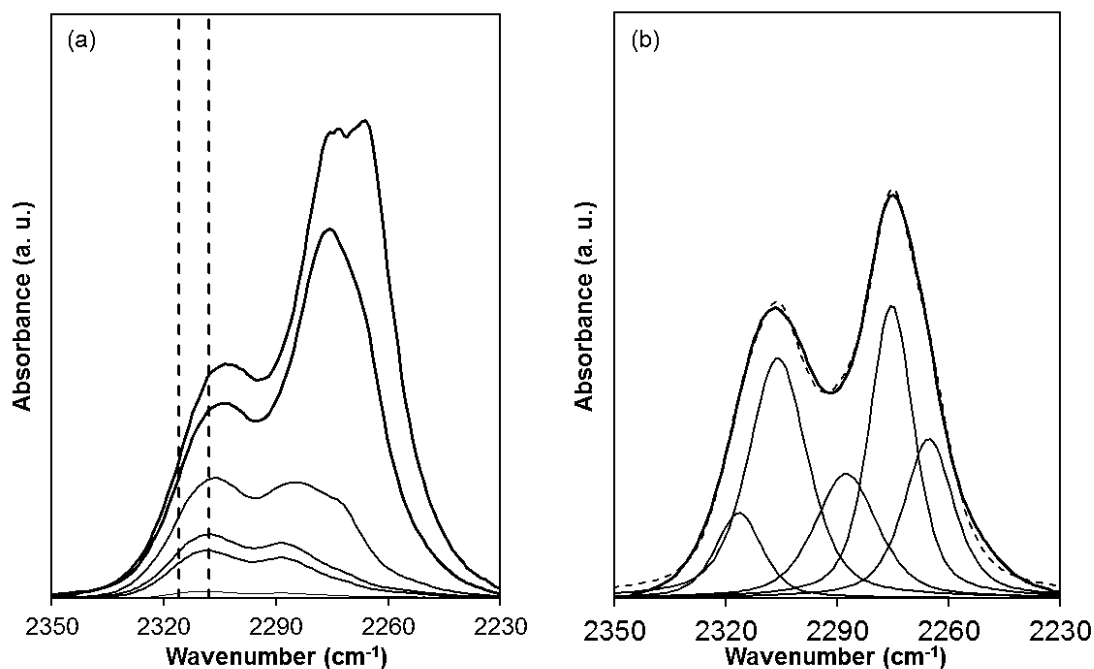


Figure F.2. (a) IR difference spectra (relative to zero coverage) of Sn-CHA-F-70 upon sequential dosing of CD<sub>3</sub>CN to saturation coverages. Vertical dashed lines are shown for open (2316 cm<sup>-1</sup>) and closed (2308 cm<sup>-1</sup>) Sn sites. (b) IR spectra of CD<sub>3</sub>CN-saturated Sn-CHA-F-60, with thin dotted curve representing the sum of the component peaks, shown as thin solid lines for CD<sub>3</sub>CN bound to open (2316 cm<sup>-1</sup>) and closed Sn sites (2308 cm<sup>-1</sup>), Sn sites within high defect surfaces (2287 cm<sup>-1</sup>), hydrogen bound to SiOH groups (2275 cm<sup>-1</sup>), and gas phase or physisorbed CD<sub>3</sub>CN (2265 cm<sup>-1</sup>).



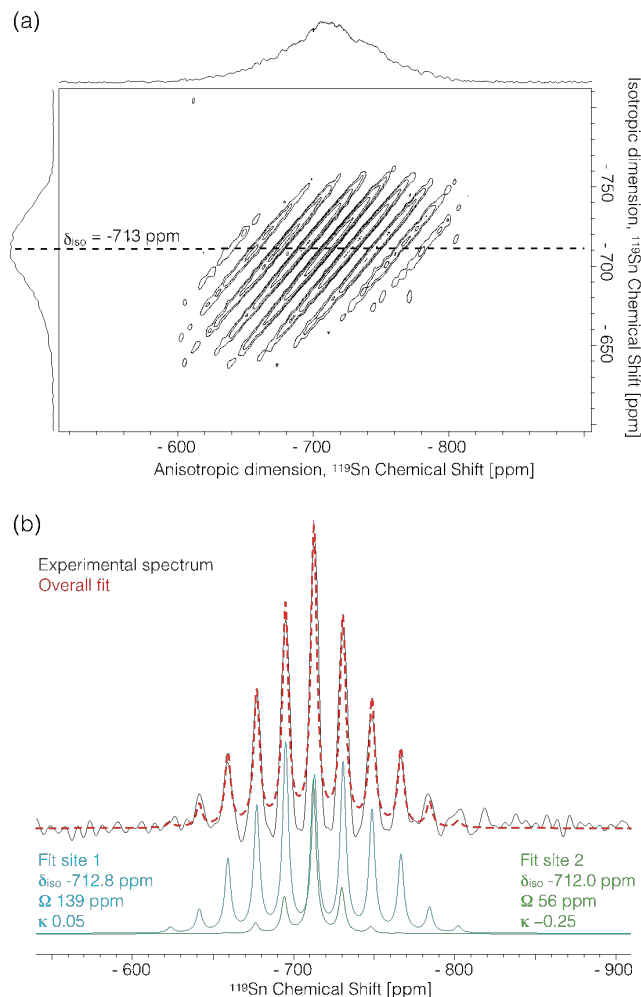


Figure F.3. (a) 2D  $^{119}\text{Sn}$  CPMAT spectrum of hydrated Sn-CHA-F-70 and (b) extracted 1D  $^{119}\text{Sn}$  NMR spectrum for Sn-CHA-F-70 (blue trace) fit with two sets of CSA parameters (light blue and green traces) and their combination (red trace) resulting in better description of the experimental spectrum. The spectrum was acquired on Bruker 600 MHz (14.1 T) DNP NMR spectrometer. MAS = 4 kHz; CP contact time = 1.5 ms; recycle delay = 3.5 s; 256 scans per  $t1$  increment, and 85  $t1$  increments were acquired. The CSA fit was done using solid lineshape feature in Bruker's Topspin program.

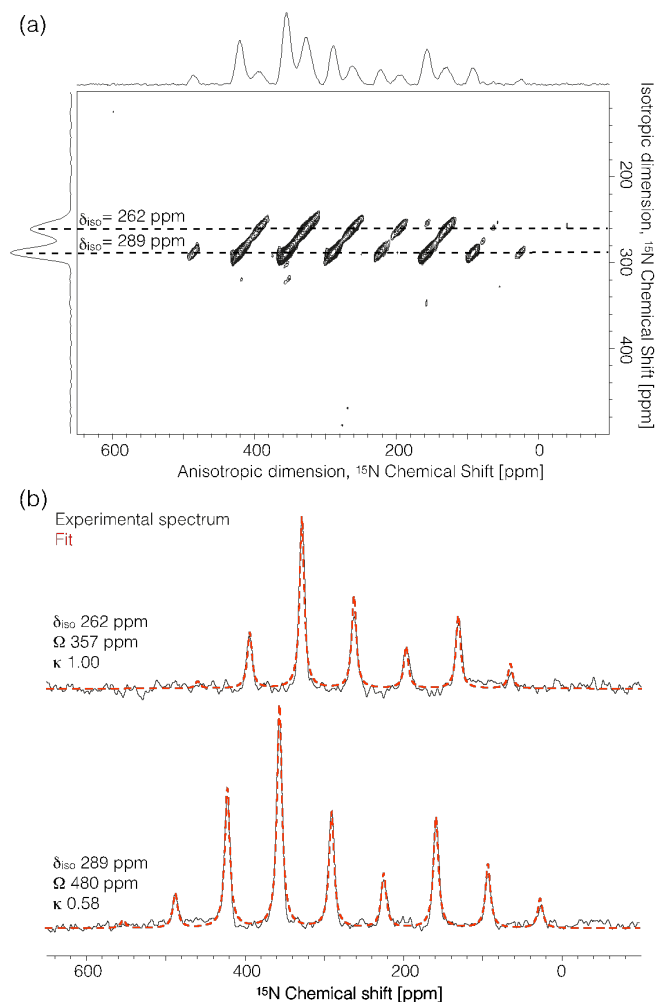


Figure F.4. (a) 2D  $^{15}\text{N}\{^1\text{H}\}$  CPMAT NMR spectrum and (b) extracted 1D  $^{15}\text{N}$  NMR spectra and corresponding CSA fit for pyridine-saturated Sn-CHA-F-70. The spectrum was acquired on Bruker 600 MHz (14.1 T) DNP NMR spectrometer. MAS= 4 kHz; CP contact time= 8.0 ms; recycle delay = 4.5 s; 112 scans per  $t_1$  increment, and 112  $t_1$  increments were acquired. The CSA fit was performed using the solid lineshape feature in Bruker's Topspin program.

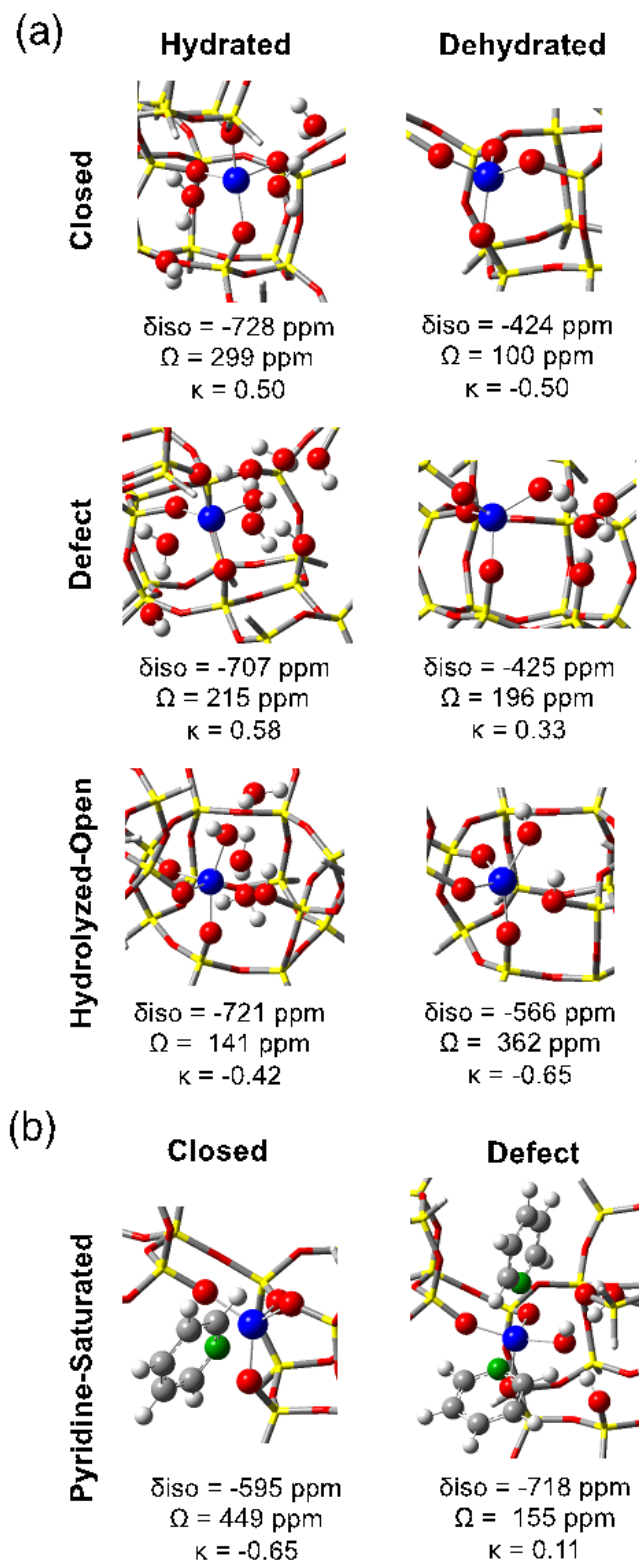


Figure F.5. DFT optimized structures for (a) hydrated closed Sn sites, defect-open Sn sites, and hydrolyzed-open Sn sites, for dehydrated closed Sn sites, defect Sn sites, and hydrolyzed-open Sn sites, and (b) for pyridine saturated closed Sn, and defect Sn sites. Calculated isotropic chemical shifts ( $\delta_{iso}$ ), span ( $\Omega$ ), and skew ( $\kappa$ ) are shown for each site. Details of DFT calculations are in Section F.6.13.

Table F.1.  
Site and structural characterization data for the samples in this study.

| Sample        | Si/Sn<br>Ratio<br>(AAS) <sup>a</sup> | Si/Sn<br>Ratio<br>(EDS) <sup>b</sup> | V <sub>ads, micro</sub><br>(cm <sup>3</sup><br>g <sup>-1</sup> ) | DRUV<br>Band<br>Center<br>(nm) <sup>e</sup> | DRUV<br>Edge<br>Energy<br>(eV) <sup>e</sup> |
|---------------|--------------------------------------|--------------------------------------|--|---|---|
| Sn-CHA-F-60   | 59                                   | 65                                   | 0.16 <sup>c</sup>  | 219   | 4.33  |
| Sn-CHA-F-70   | 70                                   | 65                                   | 0.15 <sup>c</sup>  | 223   | 4.12  |
| Sn-Beta-F-116 | 116                                  | 122                                  | 0.23 <sup>d</sup>  | 222   | 4.23  |
| Sn-xerogel    | 110                                  | 130                                  | 0.02 <sup>c</sup>  | 245   | 4.37  |
| Si-CHA-F      | n.m.*                                | n.m.*                                | 0.23 <sup>c</sup>  | n.m.*                                       | n.m.*                                       |

<sup>a</sup>Bulk composition determined by atomic absorption spectroscopy (AAS).

<sup>b</sup>Composition determined by energy dispersive X-ray spectroscopy (EDS).

<sup>c</sup>Micropore volume determined from Ar adsorption isotherms (87 K).

<sup>d</sup>Micropore volume determined from N<sub>2</sub> adsorption isotherms (77 K).

<sup>e</sup>Diffuse reflectance UV-Vis spectra (band center at maximum F(R) intensity) and Tauc plots for samples after dehydration at 523 K(Section F.6.5).).

\*n. m., not measured.

Table F.2.  
Lewis acid site and silanol group concentrations determined using pyridine and acetonitrile IR and ammonia TPD for the samples in this study..

| Sample        | Pyridine <sup>a</sup> | CD <sub>3</sub> CN <sup>b</sup> |             |               |                       | NH <sub>3</sub> <sup>c</sup> |
|---------------|-----------------------|---------------------------------|-------------|---------------|-----------------------|------------------------------|
|               | <i>Total</i>          | <i>Total</i>                    | <i>Open</i> | <i>Closed</i> | <i>SiOH</i>           | <i>Total</i>                 |
| Sn-CHA-F-60   | 0.21                  | 1.18                            | 0.42        | 0.76          | 5.26*10 <sup>-4</sup> | 1.08                         |
| Sn-CHA-F-70   | 0.20                  | 1.14                            | 0.36        | 0.78          | 8.46*10 <sup>-4</sup> | 1.20                         |
| Sn-Beta-F-116 | 0.71                  | 1.07                            | 0.45        | 0.76          | 5.71*10 <sup>-4</sup> | 0.77                         |

<sup>a</sup>Errors are  $\pm 20\%$ .

<sup>b</sup>Errors are  $\pm 20\%$ .

<sup>c</sup>Errors are  $\pm 5\%$ .

Table F.3.  
Intramolecular and intermolecular MPVO reaction rates measured on the  
samples in this study.

| Catalyst      | Glucose isom. rate<br>(per total Sn) <sup>a</sup> | Glucose isom. rate<br>(per pyridine<br>accessible Sn) <sup>b</sup> | Ethanol-<br>propionaldehyde MPVO<br>rate<br>(per total Sn) <sup>c</sup> |
|---------------|---|--|---|
| Sn-CHA-F-60   | 3.62*10 <sup>-6</sup>                             | 1.72*10 <sup>-5</sup>  | 1.96*10 <sup>-4</sup>   |
| Sn-Beta-F-116 | 2.90*10 <sup>-1</sup>                             | 2.90*10 <sup>-1</sup>  | 8.24*10 <sup>-3</sup>   |
| Sn-xerogel    | 7.45*10 <sup>-6</sup>                             | 7.45*10 <sup>-6</sup>  | 3.48*10 <sup>-6</sup>   |
| Si-CHA-F      | n.p.*   | n.p.*  | n.p.*   |

<sup>a</sup>398 K, 1% w/w glucose in water, Errors are  $\pm 15\%$ .

<sup>b</sup>398 K, 1% w/w glucose in water, Errors are  $\pm 15\%$ .

All Sn sites in Sn-Beta-F-116 and Sn-xerogel assumed  
to be pyridine accessible.

<sup>c</sup>333 K, 0.6 M propionaldehyde in ethanol solvent,

1-propanol formation rate, Errors are  $\pm 15\%$ .

\*n. p., no products observed.

Table F.4.  
Chemical shift anisotropy (CSA) parameters for the two different Sn sites identified in the hydrated and dehydrated states of Sn-CHA-F-70.

| Catalyst          | CSA<br>Param-<br>eters         |                          |                  |
|-------------------|--------------------------------|--------------------------|------------------|
|                   | Chemical Shift                 | Span                     | Skew             |
|                   | $(\delta_{iso}, \text{ppm})^a$ | $(\Omega, \text{ppm})^b$ | $(\kappa)^c$     |
| Hydrated Sn-CHA   |                                |                          |                  |
| Site1             | $-713 \pm 3$                   | $139 \pm 4$              | $0.05 \pm 0.06$  |
| Site2             | $-712 \pm 3$                   | $56 \pm 4$               | $-0.25 \pm 0.25$ |
| Dehydrated Sn-CHA |                                |                          |                  |
| Site3             | $-442 \pm 9$                   | $159 \pm 12$             | $0.24 \pm 0.08$  |
| Site4             | $-484 \pm 3$                   | $139 \pm 14$             | $0.16 \pm 0.1$   |

<sup>a</sup>Errors are determined by peak width.

<sup>b</sup>Errors are the results of error propagation calculations.

Table F.5.  
Chemical shift anisotropy (CSA) parameters for the two different Sn sites identified in the hydrated and dehydrated states of Sn-CHA-F-70.

| Catalyst              | Detected<br>Nuclei | CSA<br>Param-<br>eters  |                   |              |
|-----------------------|--------------------|-------------------------|-------------------|--------------|
|                       |                    | Chemical Shift          | Span              | Skew         |
|                       |                    | ( $\delta_{iso}$ , ppm) | ( $\Omega$ , ppm) | ( $\kappa$ ) |
| Sn-CHA-F-70           |                    |                         |                   |              |
| Lewis acidic Sn sites | $^{15}\text{N}$    | 262±5                   | 357±7             | 1.00±0.06    |
| <i>One pyridine</i>   | $^{119}\text{Sn}$  | -596±5                  | 331±7             | -0.32±0.06   |
| <i>Two pyridine</i>   | $^{119}\text{Sn}$  | -694±6                  | 132±8             | 0.18±0.18    |
| <i>SiOH groups</i>    | $^{15}\text{N}$    | 289±5                   | 480±7             | 0.58±0.04    |
| Si-CHA-F              | $^{15}\text{N}$    | 286±10                  | –                 | –            |



## F.6 Supporting Information

### F.6.1 Statement of author contributions

JWH is a graduate student who wrote the manuscript, analyzed experimental data, synthesized Sn-xerogel and Sn-Beta, and performed characterization and catalytic reactivity experiments of all samples. JRD is a graduate student who synthesized Si-CHA-F and Sn-CHA and assisted with characterization of Sn-CHA. AMH is an undergraduate student who measured DRUV spectra and intermolecular MPVO reactivity. WCL is a graduate student who performed all NMR measurements and DFT calculations, and assisted with writing sections of the manuscript. TCO is a research fellow who assisted with NMR measurements and DFT calculations. ACV is a research fellow who guided and assisted the DFT calculations. CC and RG are senior investigators who guided research efforts, assisted with data analysis and interpretation, and manuscript writing.

### F.6.2 Experimental and theoretical methods

#### Catalyst Synthesis

Sn-CHA molecular sieves were synthesized by adapting the procedure reported for the synthesis of Ti-CHA by Eilertsen et al. [620]. In a typical synthesis, 40 g of ethanol (200 proof, Koptec) were added to a perfluoroalkoxy alkane (PFA, Savillex Corp.) container, followed by addition of 25 g of tetraethylorthosilicate (TEOS, 98 wt%, Sigma Aldrich) and then stirring for 300 s under ambient conditions. Next, a solution containing 0.601 g of  $\text{Sn(IV)Cl}_4(\text{H}_2\text{O})_5$  (98 wt%, Sigma Aldrich) dissolved in 10 g of ethanol was added dropwise to the mixture comprised of TEOS and ethanol, and then stirred for 300 s under ambient conditions. After this period of homogenization, 0.577 g of hydrogen peroxide ( $\text{H}_2\text{O}_2$ , 30 wt%, Alfa Aesar) were added dropwise and the solution was stirred for 900 s under ambient conditions. Next, 42.329 g of an aqueous N,N,N-trimethyl-1-adamantylammonium hydroxide solution (TMAdaOH, 25 wt%, Sachem), the structure directing agent for CHA, were added dropwise to the

Sn-containing solution under constant stirring. The solution gelatinized after approximately 15-20 g of TMAdaOH were added, and was hydrated with 49.920 g of deionized water (18.2 M $\Omega$ ) and manually stirred with a Teflon spatula until a uniform solution was obtained. The remaining TMAdaOH was added dropwise and no further gelatinization occurred. The resulting solution was covered and stirred at ambient temperature for 24 h. In each of the synthesis procedures reported in this section, reagents were used without further purification.

After this period of time, the solution was uncovered and ethanol (61.65 g, including that generated by hydrolysis of TEOS) and excess water (77.78 g) were allowed to evaporate to reach the target weight and desired H<sub>2</sub>O/SiO<sub>2</sub> ratio of 3. This resulted in a dry powder that was rehydrated with approximately 80 g of water (18.2 M $\Omega$ ), stirred for 24 hours to obtain a homogeneous solution, and dehydrated again to reach the desired H<sub>2</sub>O/SiO<sub>2</sub> ratio of 3. Attempts to crystallize Sn-CHA without this intermediate rehydration step resulted in amorphous products, even after extended periods of time in the synthesis oven (up to 10 days at 423 K). Next, 2.69 g of hydrofluoric acid (HF, 48 wt%, Alfa Aesar) were added dropwise to the synthesis powder and stirred manually with a Teflon spatula for 300 s and residual HF allowed to evaporate for an additional 900 s. Caution: when working with hydrofluoric acid use appropriate personal protective equipment, ventilation, and other safety measures. The final molar composition of the synthesis powder was 1 SiO<sub>2</sub>/ 0.014 SnO<sub>2</sub>/ 0.43 TMAdaOH/ 0.38 HF/ 3 H<sub>2</sub>O. The powder was transferred to four Teflon-lined stainless steel autoclaves (45 cm<sup>3</sup>, Parr Instruments) and heated at 423 K in an isothermal oven (Yamato DKN-402C) with rotation (ca. 60 rpm) for 48 hours.

Pure silica chabazite was synthesized following the procedure reported by Dázquez-Cabañas et al. [637]. In a typical synthesis, 13 g of TEOS were added to a PFA jar containing 25.849 g of an aqueous TMAdaOH solution and stirred under ambient conditions for 300 s. The vessel was left uncovered and ethanol, formed from the hydrolysis of TEOS, and excess water were evaporated to reach a target H<sub>2</sub>O/SiO<sub>2</sub> ratio of 3. This resulted in a dry powder, at which point an additional 10 g of water

were added to ensure complete hydrolysis of TEOS and to allow additional time for residual ethanol to completely evaporate. This rehydration procedure was performed twice. Once the synthesis solution had reached the desired  $\text{H}_2\text{O}/\text{SiO}_2$  ratio of 3, 1.28 g of HF (48 wt%, Sigma Aldrich) were added dropwise to the synthesis and homogenized for 300 s using a Teflon spatula. Upon addition of HF to the powdered synthesis mixture, the powder immediately became a thick paste that liquefied slightly under stirring. The solution was left uncovered under ambient conditions for 900 s to allow for any residual HF to evaporate before transferring the solution to two Teflon-lined stainless steel autoclaves ( $45\text{ cm}^3$ , Parr Instruments) and heating in a forced convection oven (Yamato DKN-402C) at 423 K under rotation at 40 RPM for 48 h.

Sn-Beta was prepared in fluoride media by modification of a previously reported method [529] using Si-Beta zeolites as seed material. Sn-Beta zeolites were synthesized using the same procedure as Si-Beta, except that dropwise addition of a solution of 0.30 g of tin (IV) chloride pentahydrate ( $\text{SnCl}_4 \cdot 5\text{H}_2\text{O}$ , Sigma-Aldrich, 98 wt%) in 1.95 g of deionized water was performed prior to evaporation of ethanol and water, such that the synthesis gel had a molar  $\text{SiO}_2/\text{SnO}_2$  ratio of 130. After the HF addition step and addition of the Sn-Beta synthesis gel to the Teflon liner, 1.73 g of water and 0.254 g of as-made Si-Beta seeds (ca. 4.2 wt% of total  $\text{SiO}_2$ ) were added directly to the liner and the mixture was stirred manually using a Teflon spatula prior to heating in an isothermal oven held at 413 K for 21 days with rotation at 60 RPM.

The solids obtained from all zeolite syntheses were removed from their Teflon liners, washed thoroughly with water and acetone (Sigma Aldrich, >99.5 wt%, 5 washes each, ca.  $25\text{ cm}^3\text{ (g zeolite)}^{-1}$  each wash)), isolated by centrifugation, and dried at 373 K for 16 h. The dry zeolite powders were then treated in dry air (Ultra Zero Grade, Indiana Oxygen,  $1.67\text{ cm}^3\text{ s}^{-1}\text{ (g zeolite)}^{-1}$ ) to 853 K ( $0.0167\text{ K s}^{-1}$ ) and held for 10 h in a muffle furnace (Nabertherm LE 6/11 equipped with a P300 controller).

Amorphous Sn-xerogel was synthesized using the procedure reported by van Grieken et al. [572]. 5.74 g of a 0.1 M HCl solution (Macron, 37%) were added to a mixture of

52.0 g of TEOS and 67.6 g of deionized water and stirred for 2 h at ambient temperature. Then, 0.77 g of  $\text{SnCl}_4 \cdot 5\text{H}_2\text{O}$  were added and the mixture stirred for 1 h. Next, a 1 M  $\text{NH}_4\text{OH}$  solution prepared from concentrated  $\text{NH}_4\text{OH}$  (Sigma Aldrich, 28%-30 wt%  $\text{NH}_3$  basis) was added dropwise until the gel point was reached (ca.  $12 \text{ cm}^3$ ). The resulting clear gel was dried for 12 h at 433 K. The dried solids were washed with deionized water (5-10 washes, ca.  $60 \text{ cm}^3$  per wash) until a constant pH was reached, dried for 12 h at 433 K, and then treated in air (Ultra Zero Grade, Indiana Oxygen,  $1.67 \text{ cm}^3 \text{ s}^{-1} (\text{g zeolite})^{-1}$ ) to 853 K ( $0.0167 \text{ K s}^{-1}$ ) for 10 h in a muffle furnace.

### Zeolite Structural Characterization

The bulk Sn content of each sample in this study was determined using atomic absorption spectroscopy (AAS) performed with a Perkin Elmer AAnalyst 300 Atomic Absorption Spectrometer. A 1000 ppm Sn standard (Alfa Aesar, TraceCERT,  $\pm 4$  ppm) was diluted to create calibration standards, and the instrument was calibrated each day before collecting measurements. Sn absorbance values were measured at 284.0 nm in an acetylene/nitrous oxide flame. Catalyst samples (ca. 0.02 g) were dissolved in 2 g of HF (48 wt%, Alfa Aesar) overnight and then further diluted with 30 g of deionized water, prior to elemental analysis. The Sn weight fractions were used together with the unit cell formula for Beta zeolite to estimate the Si/Sn ratio in each sample.

Powder X-ray diffraction (XRD) patterns were collected on a Rigaku Smartlab X-ray diffractometer with an ASC-6 automated sample changer and a  $\text{Cu K}\alpha$  x-ray source (1.76 kW). Samples (ca. 0.01 g) were packed within zero background, low dead volume sample holders (Rigaku) and diffraction patterns were measured from  $4$ - $40^\circ$  at a scan rate of  $0.0417^\circ \text{ s}^{-1}$  with a step size of  $0.02^\circ$ .

Scanning electron microscopy (SEM) and electron dispersive X-ray spectroscopy (EDS) were performed on a FEI Quanta 3D FEG Dual-beam SEM with an Everhart-Thornley detector for high vacuum imaging. SEM micrographs were collected in the focused beam operating mode with a voltage of 5 kV and spot size of  $4 \mu\text{m}$  for samples

after high temperature oxidative treatment, but without additional preparation (e.g., sputtering with a metal coating to avoid charging of the metal oxide surface). EDS was performed using an Oxford INCA Xstrem-2 silicon drift detector equipped with an Xmax80 window for supplemental elemental analysis. EDS analyses were performed at 20 kV with a 6  $\mu\text{m}$  spot size at a magnification of 3000-6000 $\times$ .

Ar (87 K) and N<sub>2</sub> (77 K), and H<sub>2</sub>O (293 K) adsorption isotherms were measured using a Micromeritics ASAP2020 Surface Area and Porosity Analyzer. Samples (ca. 0.03 g) were pelleted and sieved to retain 180-250  $\mu\text{m}$  diameter particles prior to analysis. Samples were degassed by heating to 393 K (0.0167 K s<sup>-1</sup>) under vacuum (<0.005 Torr) for 2 h, then heating to 623 K (0.0167 K s<sup>-1</sup>) under vacuum for 8 h prior to measurement of adsorption isotherms. Micropore volumes were determined from a semi-log derivative analysis of Ar and N<sub>2</sub> isotherms ( $\delta(V_{ads}/g)/\delta(\log(P/P_0))$  vs.  $\log(P/P_0)$ ) to identify the completion of micropore filling. Reported pore volumes were converted from volumes adsorbed at STP to the number of moles adsorbed and then converted to liquid volumes using the liquid molar densities at their respective adsorption temperatures (Ar: 87 K, 0.0350 mol cm<sup>-3</sup>, N<sub>2</sub>: 77 K, 0.0288 mol cm<sup>-3</sup>, H<sub>2</sub>O: 293 K, 0.0554 mol cm<sup>-3</sup>).

## Sn Active Site Characterization

**Diffuse Reflectance UV-Visible Spectroscopy** Diffuse reflectance UV-Visible (DRUV) spectra were collected on a Varian Cary 5000 UV-VIS-NIR using a Harrick Praying Mantis in-situ diffuse reflectance cell. The following spectra were collected on each sample: (i) after exposure to ambient conditions and held in dry He flow (4.17 cm<sup>3</sup> s<sup>-1</sup> (g zeolite)<sup>-1</sup>) (“ambient”); (ii) after subsequent treatment to 523 K (ca. 0.5 K s<sup>-1</sup>) for 1.8 ks in dry He flow (4.17 cm<sup>3</sup> s<sup>-1</sup> (g zeolite)<sup>-1</sup>) (“dehydrated”); and (iii) after subsequent exposure to a wet He stream (4.17 cm<sup>3</sup> s<sup>-1</sup> (g zeolite)<sup>-1</sup>, ca. 3% H<sub>2</sub>O, bubbled through a glass saturator containing water at ambient temperature) while cooling to 303 K and holding for 300 s (“rehydrated”). DRUV spectra were collected at a resolution of 10 nm s<sup>-1</sup>, using poly(tetrafluoroethylene) (PTFE, 1  $\mu\text{m}$  powder,

Sigma-Aldrich) as the 100% reflectance standard, and were converted to an absorption spectrum using the Kubelka-Munk ( $F(R)$ ) function. Tauc plots of  $[F(R)h\nu]^2$  vs.  $h\nu$  were used to calculate absorption edge energies (additional details in Section F.6.6).

**Infrared Spectroscopy** IR spectra were collected on a Nicolet 4700 spectrometer equipped with a Hg-Cd-Te (MCT, cooled to 77 K by liquid N<sub>2</sub>) detector by averaging 64 scans at 2 cm<sup>-1</sup> resolution in the 4000 to 400 cm<sup>-1</sup> range, and were taken relative to an empty cell background reference collected under dynamic vacuum (rotary vane rough pump, Alcatel 2008A, <0.1 Torr) at either 423 K (pyridine) or 303 K (CD<sub>3</sub>CN). Self-supporting wafers (0.01-0.03 g cm<sup>-2</sup>) were sealed within a custom-built quartz IR cell with CaF<sub>2</sub> windows, equipped with resistive heating cartridges (Chromalox) held in a conductive brass block that is encased in an alumina silicate insulating chamber (Purdue Research Machining Services), as described elsewhere. [465] Wafer temperatures were measured within 2 mm of each side of the wafer by K-type thermocouples (Omega). The quartz IR cell was connected to a custom glass vacuum manifold used for sample pretreatment and exposure to controlled amounts of gaseous titrants.

Prior to each IR experiment, sample wafers were treated in flowing dry air (6.66 cm<sup>3</sup> s<sup>-1</sup> (g zeolite)<sup>-1</sup>) purified by a purge gas generator (Parker Balston, <1 ppm CO<sub>2</sub>, 200 K H<sub>2</sub>O dew point) to 823 K (0.083 K s<sup>-1</sup>) for 1 h, and then held under dynamic vacuum (rotary vane rough pump, Alcatel 2008A, <0.1 Torr) at 823 K for 1 h. Next, the sample wafer was cooled under dynamic vacuum to 303 K for adsorption experiments with CD<sub>3</sub>CN, or to 423 K for adsorption experiments with pyridine. Each titrant was purified via freeze-pump-thaw (3 cycles) and introduced to the sample in sequential doses (ca. 2.5 x 10<sup>-7</sup> mol). Equilibration of the sample with each titrant dose was assumed when the final pressure in the cell remained constant for 180 s. After samples reached equilibrium with a detectable gaseous titrant pressure (0.4-2.0 Torr) dosing was considered complete, and samples were exposed to dynamic vacuum (60 s at 303 K for CD<sub>3</sub>CN or 900 s at 423 K for pyridine) to remove gas-phase and weakly-bound species.

IR spectra reported were baseline-corrected and normalized to combination and overtone modes of zeolite Si-O-Si stretches ( $1750\text{--}2100\text{ cm}^{-1}$ ). IR peaks for  $\text{CD}_3\text{CN}$  species bound to open ( $2316\text{ cm}^{-1}$ ) and closed ( $2308\text{ cm}^{-1}$ ) Lewis acidic Sn sites, bound to Sn sites in highly-defective oxide surfaces ( $2287\text{ cm}^{-1}$ ), hydrogen-bound to Si-OH sites ( $2275\text{ cm}^{-1}$ ), and physisorbed or gas phase  $\text{CD}_3\text{CN}$  ( $2265\text{ cm}^{-1}$ ) overlapped and required deconvolution into individual components [466]. Similarly, those for pyridine adsorbed at Lewis acidic Sn sites ( $1450\text{ cm}^{-1}$ ) and at SiOH groups ( $1445\text{ cm}^{-1}$ ) required deconvolution prior to quantification. The number of sites titrated by pyridine or  $\text{CD}_3\text{CN}$  on self-supporting sample wafers was estimated from integrated IR peak areas and values using the following equation:

$$\text{Site density}(\mu\text{mol g}^{-1}) = \frac{\text{Integrated Peak Area}(\text{cm}^{-1})}{\mathcal{E}(\text{cm } \mu\text{mol}^{-1})} * \frac{a_{CS}(\text{cm}^2)}{m(\text{g})} \quad (\text{F.4})$$

where  $a_{CS}$  and  $m$  are the cross-sectional area and mass of the wafer, respectively.

**Ammonia Temperature Programmed Desorption** Ammonia temperature programmed desorption (TPD) was performed using a Micromeritics Autochem II 2920 Chemisorption Analyzer connected to an Agilent 5793N mass selective detector (MSD) to quantify the number of moles of ammonia desorbed from Sn-CHA. Sn-CHA (ca. 0.03 g, sieved to  $180\text{--}250\text{ }\mu\text{m}$ ) was supported in between two plugs of quartz wool in a quartz U-tube reactor, which was held inside a clam-shell furnace. The catalyst was treated in air ( $25\text{ cm}^3\text{ s}^{-1}$  (g zeolite) $^{-1}$ , Indiana Oxygen, Ultra Zero Grade) to 673 K ( $0.167\text{ K s}^{-1}$ ) for 4 h and then cooled to ambient temperature. The sample was then saturated in flowing  $\text{NH}_3$  in balance helium ( $25\text{ cm}^3\text{ s}^{-1}$  (g zeolite) $^{-1}$ , 500 ppm gravimetric mixture, Indiana Oxygen) for 12 h, and then weakly bound and physisorbed  $\text{NH}_3$  were removed by purging the sample in flowing He ( $25\text{ cm}^3\text{ s}^{-1}$  (g zeolite) $^{-1}$ , Indiana Oxygen, 99.999%) for 8 h at 331 K. After the saturation and purge treatment, which was used previously to accurately quantify the number of Lewis acidic Sn sites in Sn-Beta zeolites [466], TPD was performed in flowing He ( $25\text{ cm}^3\text{ s}^{-1}$  (g zeolite) $^{-1}$ ), with the reactor effluent transported to the MSD via heated lines held at

383 K. After the experiment, a 0.5 cm<sup>3</sup> sample loop was filled with argon (Indiana Oxygen, 99.999%) and injected via flowing He (0.83 cm<sup>3</sup> s<sup>-1</sup>) to the MSD to quantify the amount of NH<sub>3</sub> desorbed from integrated MSD signals and a calibrated response factor for NH<sub>3</sub> relative to Ar, as reported previously.<sup>7</sup>

**DNP NMR Spectroscopy** Hydrated Sn-CHA was prepared by high temperature oxidative treatment at 853 K (described in Section F.6.2) and exposure of the resulting solids to ambient conditions. Dehydrated Sn-CHA was prepared by treatment of the hydrated sample under high vacuum ( $1.0 \times 10^{-4}$  Torr) to 773 K (0.067 K s<sup>-1</sup>) overnight. After dehydration, the sample was transferred into an argon-filled glovebox, where all DNP sample preparations were performed. Dehydrated Sn-CHA was treated with <sup>15</sup>N pyridine by adding 50  $\mu$ L of <sup>15</sup>N-labeled pyridine (99% isotopic enrichment, Cortecnet Inc.) into a suspension of dehydrated Sn-CHA (0.10 g) in anhydrous pentane (ca. 1 cm<sup>3</sup>). The mixture was stirred at ambient temperature for 600 s, removed from the argon-filled glovebox under inert conditions, and then exposed to high vacuum ( $1.0 \times 10^{-4}$  Torr) at ambient temperature for 900 s to remove solvent and excess pyridine. The <sup>15</sup>N-labeled pyridine-treated Sn-CHA sample was then reintroduced into an argon-filled glovebox, where subsequent DNP sample preparation was conducted. All DNP samples were prepared by impregnating the solids with a 16 mM TEKPol [638] solution in 1,1,2,2-tetrachloroethane (TCE) [639]. Each impregnated solid was then packed in its own 3.2 mm sapphire rotor. A Teflon spacer was added within each rotor to contain the impregnated solid, and the rotors were then closed with zirconia drive caps.

The DNP NMR measurements were performed either using a Bruker 400 MHz (9.4 T) or a Bruker 600 MHz (14.1 T) DNP spectrometer coupled with corresponding gyrotron microwaves emitting at 263 and 395 GHz located at CRMN Lyon and ETH Z'urich, respectively. All experiments were performed using 3.2 mm HXY or HX low temperature magic-angle spinning (LTMAS) probes operating at 100 K. Cross-polarization (CP) MAS experiments with <sup>1</sup>H ramped spin-lock pulse were used to



transfer the DNP hyperpolarization from  $^1\text{H}$  to heteronuclei ( $^{15}\text{N}$ ,  $^{29}\text{Si}$ , and  $^{119}\text{Sn}$ ). The spin-lock pulses were optimized matching the Hartmann-Hahn condition under MAS with minor adjustment to maximize the CP efficiency experimentally. The  $^1\text{H}$   $90^\circ$  excitation and decoupling pulses were optimized and set to 100 kHz. DNP polarization build-up time constant ( $T_{\text{DNP}}$ ) was measured using saturation-recovery experiments with microwaves on, and the recycle delays of all measurements were set to  $1.3 \times T_{\text{DNP}}$ . For variant DNP build-up time experiments, the recycle delay were chosen as 1,  $1.3 \times T_{\text{DNP}}$ , 10, and, 20 seconds. 2D CP magic-angle turning (MAT) spectra were acquired with the  $5\text{-}\pi$  pulse sequence of Grant and co-workers. [640] Extractions of NMR spectra at the corresponding isotropic chemical shift in the isotropic dimensions were fit using the solid lineshape analysis (SOLA) feature in Bruker's Topspin program in order to determine CSA parameters.

### Density Functional Theory Calculations

The structures of the Sn-CHA cluster and their corresponding hydrated and pyridine-coordinated structures were fully optimized with B3LYP [641–644] including D3 empirical dispersion corrections and Becke-Johnson damping [645,646] using the Gaussian 09 code [647]. Solvent (water) effects were included for the hydrated systems optimizing by means of the Polarizable Continuum Model (PCM) method [648–650]. A combination of different basis sets was used to obtain the ground-state geometries and energies. Sn was described by the LanL2DZ effective core pseudopotential (ECP) [651–653] augmented with a d polarization function; the O and N atoms directly bonded to Sn were described by a 6-31+G(d) basis set, while Si, C, H, and the remaining O atoms were described by the 6-31G(d,p) basis set. In the optimization, only Si and O atoms forming part of the rings containing the Sn atom were allowed to relax.

Calculations of the NMR parameters [654,655] were carried out at the B3LYP-D3 level as implemented in the ADF code (2012) [656]. The all-electron TZP basis set [657] was used for all atoms in the NMR parameter calculations. Relativistic

effects and spin-orbit couplings were taken into account through the ZORA method [658,659] for the calculations of the isotropic chemical shift ( $\delta_{iso}$ ) and the principal components ( $\delta_{11}$ ,  $\delta_{22}$ , and  $\delta_{33}$ ) of all considered species. For the calculations of  $\delta_{iso}$ , the chemical shieldings of  $\text{Sn}(\text{CH}_3)_4$  and  $\text{CH}_3\text{NO}_3$  were used as references for  $^{119}\text{Sn}$  and  $^{15}\text{N}$ , respectively. This methodology has been previously tested for molecular and surface Sn species and showed excellent agreement with experiments within 10-15 ppm for  $^{119}\text{Sn}$  NMR [660].

### Kinetic Studies of MPVO Reactions with Sn-CHA

**Intramolecular MPVO with glucose** Intramolecular MPVO reactions were performed in batch reactors using 1% (w/w) D-glucose (Sigma Aldrich,  $\geq 99.5\%$ ) solutions prepared in Millipore water (18.2 M $\Omega$ ) with the pH controlled to 2 with hydrochloric acid (Macron, 37% (w/w)) to suppress background reactions. Catalysts (Sn-CHA and Sn-xerogel: ca. 0.1 g; Sn-Beta: 0.01 g, diluted 1:9 in Si-CHA-F) were added to glass reactors (10 cm<sup>3</sup>, VWR) and sealed with crimp-tops (PTFE/silicone septum, Agilent) before heating to 398 K atop a digital stirred hotplate (IKA RCT basic). Reactant solutions (ca. 2 cm<sup>3</sup>) were pre-heated separately (600 s) and then injected to the capped, preheated reactors, and stirred at 750 rpm under autogenous pressure for either 600 s (Sn-Beta) or 6 h (Sn-CHA, Sn-xerogel) prior to quenching in an ice bath. The obtained solutions were filtered with 0.2  $\mu\text{m}$  PTFE filters and mixed with a 1% (w/w) aqueous D-mannitol solution (Sigma-Aldrich  $\geq 98\%$ ) used as an internal standard. Product analysis was performed using an Agilent 1260 high performance liquid chromatograph (HPLC) with a Hi-Plex Ca column (7.7 x 300 mm, 8  $\mu\text{m}$  particle size, Agilent) an aqueous mobile phase (0.01 cm<sup>3</sup> s<sup>-1</sup>, 353 K), and an evaporative light scattering detector (Agilent 1260 Infinity ELSD).

**Intramolecular MPVO with glucose** Intermolecular MPVO reactions were performed in batch reactors using solutions of 0.05-0.2 M acetone (Sigma-Aldrich,  $\geq 99.9\%$ ) and propionaldehyde (Alfa Aesar, 97%) in ethanol (Sigma-Aldrich,  $\geq 99.5\%$ ) as the

solvent. Control experiments were performed using solutions of acetaldehyde (Sigma-Aldrich,  $\geq 99.5\%$ ), isopropanol (Sigma-Aldrich,  $\geq 99.5\%$ ), acetone, propionaldehyde, and ethanol. All chemicals were used as received without further purification. Catalytic solids (ca. 0.02 g) were added to thick-walled glass reactors followed by addition of reactant solutions (2–5 cm<sup>3</sup>). Crimp-top sealed reactors were heated at 333 K atop a digital stirred hotplate while stirring at 750 rpm under autogenous pressure for various time intervals (0.25 – 6 h) prior to quenching in an ice bath. Resulting product solutions were filtered through 0.2  $\mu\text{m}$  PTFE filters, and mixed with ca. 30  $\mu\text{L}$  of a 5% (w/w) solution of either 2-butanol (Sigma-Aldrich,  $\geq 99.5\%$ , acetone-ethanol reactions) or n-pentanol (Sigma-Aldrich,  $>99\%$ , propionaldehyde-ethanol reactions) diluted in ethanol as internal standards. Product analysis was performed using an Agilent 7890 gas chromatograph (GC) equipped with a DB-Wax column (J&W Scientific, 60 m x 530  $\mu\text{m}$  x 1.00  $\mu\text{m}$ ) and an Agilent 7693 autosampler. Isotopic labeling studies were performed using propionaldehyde and d<sub>5</sub>-ethanol (C<sub>2</sub>D<sub>5</sub>OH, Cambridge Isotopes, 98%). Product analysis was performed using an Agilent 7890A GC equipped with a DB-Wax column (J&W Scientific, 60 m x 530  $\mu\text{m}$  x 1.00  $\mu\text{m}$ ), an Agilent 7693 autosampler, and an Agilent 5975C mass spectrometer. Calibration curves for ethanol, acetone, isopropanol, propionaldehyde, n-propanol, and acetaldehyde were created using standards of known concentration relative to known concentrations of 2-butanol or n-pentanol. Initial rates of product formation were determined by extrapolating to zero time using batch reactions under differential acetone or propionaldehyde conversion ( $<5\%$ , ca. 900 s).

### F.6.3 X-ray diffraction patterns

The XRD patterns for samples in this study are shown in Figure F.6. XRD patterns for Si-CHA-F, Sn-CHA-F-60 and Sn-CHA-F-70 contain prominent peaks at  $16.2^\circ$  and  $20.9^\circ$   $2\theta$  as expected for CHA zeolites [467]. The XRD pattern for Sn-Beta-F-116 contains a broad peak at  $7.5^\circ$   $2\theta$  and a prominent peak at  $22.4^\circ$   $2\theta$  characteristic of the Beta topology [621]. The XRD patterns for Sn-CHA-F-60, Sn-CHA-F-70, Sn-Beta-F-116, and Sn-xerogel do not contain peaks at  $26.7^\circ$  and  $34^\circ$   $2\theta$  that would appear if  $\text{SnO}_2$  domains greater than 3 nm in size were present [290].

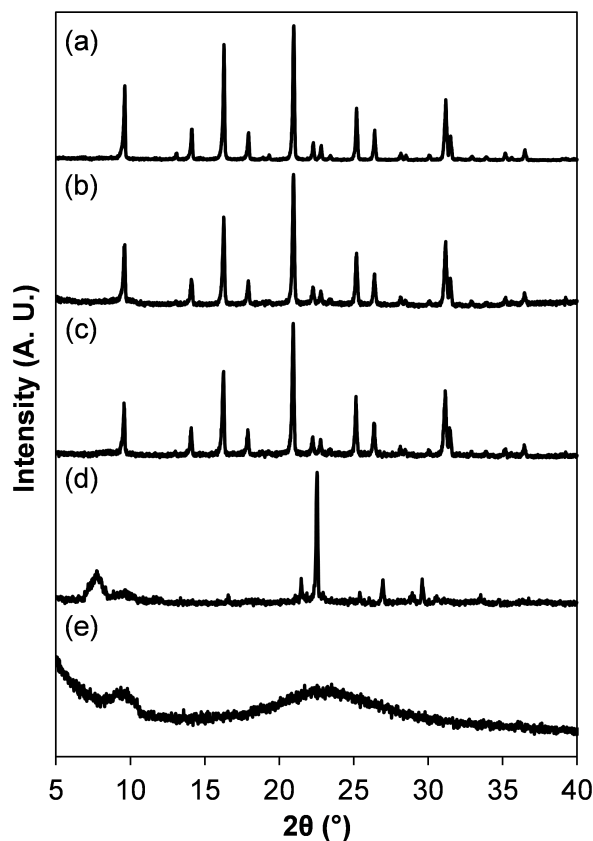


Figure F.6. XRD patterns for (a) Si-CHA-F (b) Sn-CHA-F-60 (c) Sn-CHA-F-70 (d) Sn-Beta-F-116 and (e) Sn-xerogel. Patterns are normalized to their maximum intensity and offset vertically for clarity.

### F.6.4 Adsorption isotherms and pore size distributions

Pore volume and architectures were characterized by measuring adsorption isotherms for CHA zeolites using argon (87 K), and for Beta zeolites and xerogels using N<sub>2</sub> (77 K). Adsorption isotherms are shown in Figure F.7, with micropore volumes reported in Table F.1. Non-local density functional theory (NLDFT) treatments of Ar adsorption isotherms to determine pore size distributions are shown for Sn-CHA-F samples in Figure F.8, and for Sn-Beta and Sn-xerogel in Figure F.9.

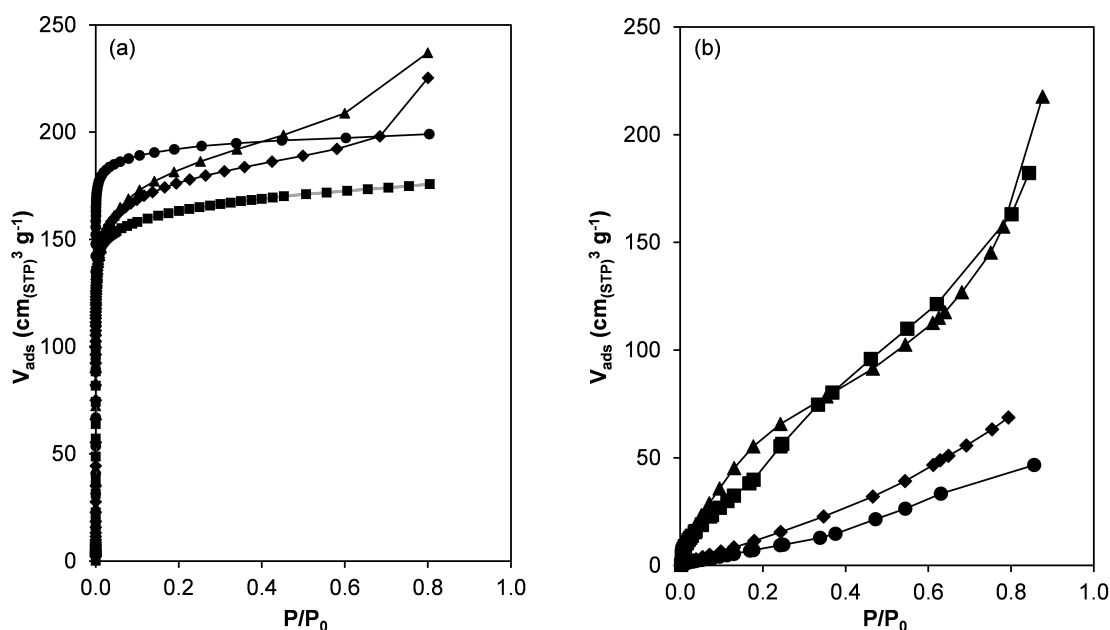


Figure F.7. (a) Ar adsorption isotherms for Si-CHA-F (circles) Sn-CHA-F-60 (diamonds), Sn-CHA-F-70 (triangles) and N<sub>2</sub> adsorption for Sn-Beta-F-116 (squares). Micropore volumes are reported in Table F.1. (b) water adsorption isotherms on Sn-CHA-F-60 (squares), Sn-CHA-F-70 (triangles), Sn-Beta-F-116 (diamonds), and Si-CHA (circles).

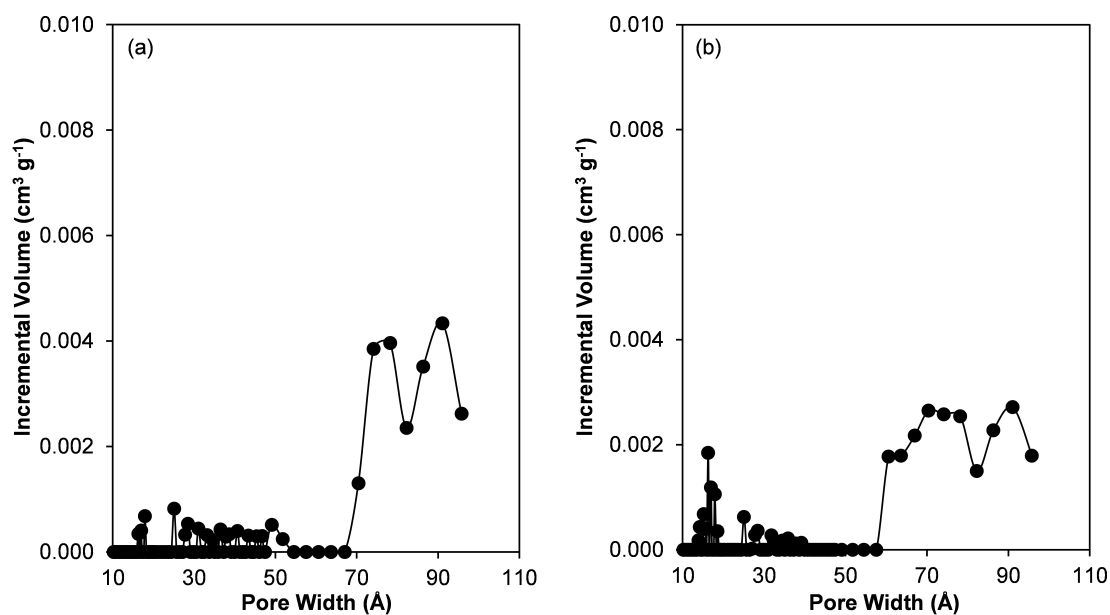


Figure F.8. Pore size distribution of (a) Sn-CHA-F-60 and (b) Sn-CHA-F-70 from NLDT analysis of Ar adsorption isotherm (87 K). Solid lines included to guide the eye.

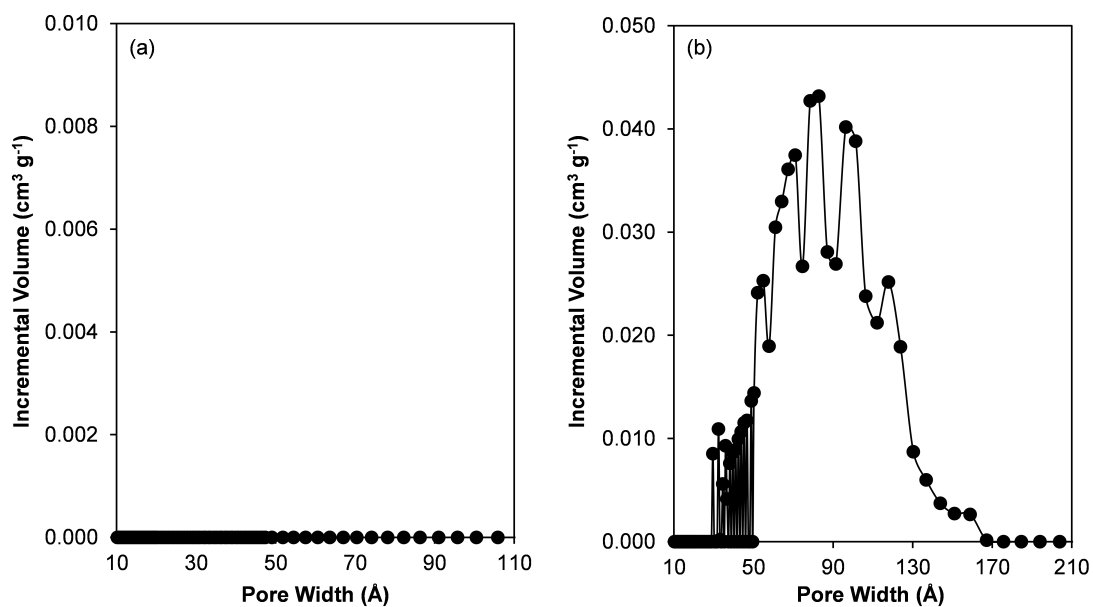


Figure F.9. Pore size distribution of (a) Si-CHA-F and (b) Sn-xerogel from NLDFT analysis of Ar adsorption isotherm (87 K). Solid lines included to guide the eye.

## F.6.5 Diffuse reflectance UV-visible spectra and Tauc plots

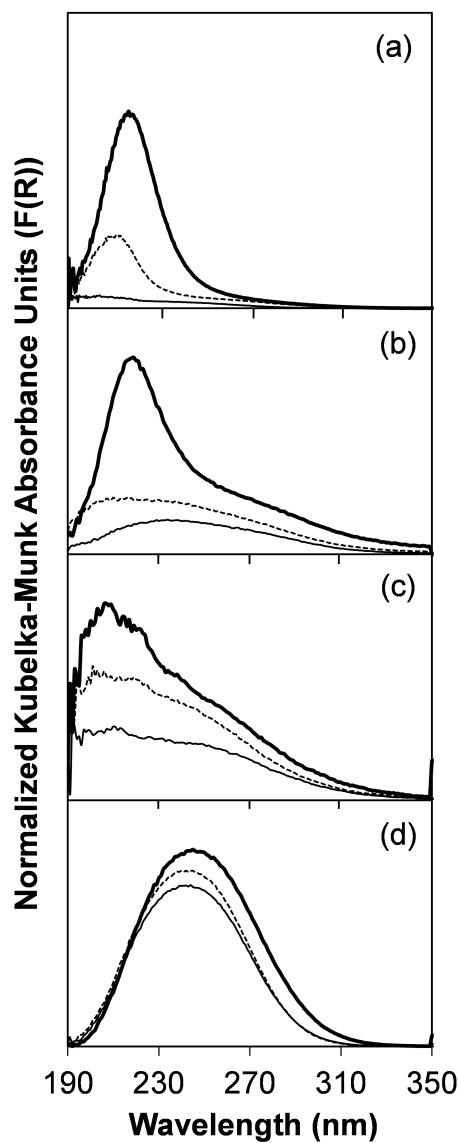


Figure F.10. DRUV spectra in Kubelka-Munk units (normalized to the maximum  $F(R)$  intensity) for (a) Sn-CHA-F-60 (b) Sn-CHA-F-70, (c) Sn-Beta-F-116, and (d) Sn-xerogel collected (i) under ambient conditions (thin solid line), (ii) after dehydration at 523 K (thick solid line), and (iii) after rehydration at 303 K (dashed line).



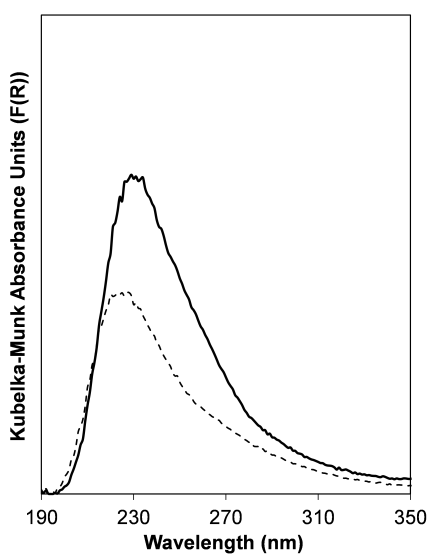


Figure F.11. DRUV spectra for Sn-CHA-70 after dehydration in flowing He at 523 K (dotted line) and 623 K (solid line).

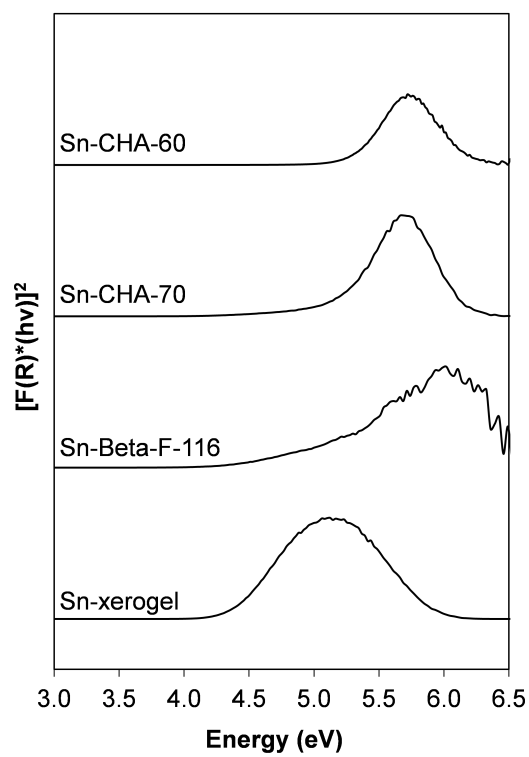


Figure F.12. Tauc plots for the samples in this study.

### F.6.6 Thermogravimetric analysis

Thermogravimetric analysis was performed on Sn-CHA-F-70 using a  $0.167\text{ K s}^{-1}$  temperature ramp to 523 K, followed by an 1800 s isothermal step at 523 K in order to recreate the conditions used in DRUV and XAS measurements. After the isothermal step, the temperature was increased to 873 K with an  $0.167\text{ K s}^{-1}$  ramp rate. The TGA profile for Sn-CHA-F-70 includes 0.8% weight loss above 623 K, which was the maximum temperature tested for DRUV. The DRUV spectra for Sn-CHA-F-70 did not change between 523 K and 623 K (Figure F.12), though the weight loss above 623 K amounts to more than one mole water per mol Sn (Figure F.14b). Assuming all of the weight lost results from desorption of bound water ligands, the TGA profile suggests Sn-CHA-F-70 may not be completely dehydrated at 623 K, in contrast to Si-CHA-F and Sn-Beta-F-116, which do not change mass above 523 K (Figure F.15a). This weight loss is endothermic based on the differential scanning calorimetry (DSC) profile, which presumably excludes condensation of silanols as a possible cause of the high temperature water evolution on Sn-CHA-F-70 during TGA (Figure F.15b).

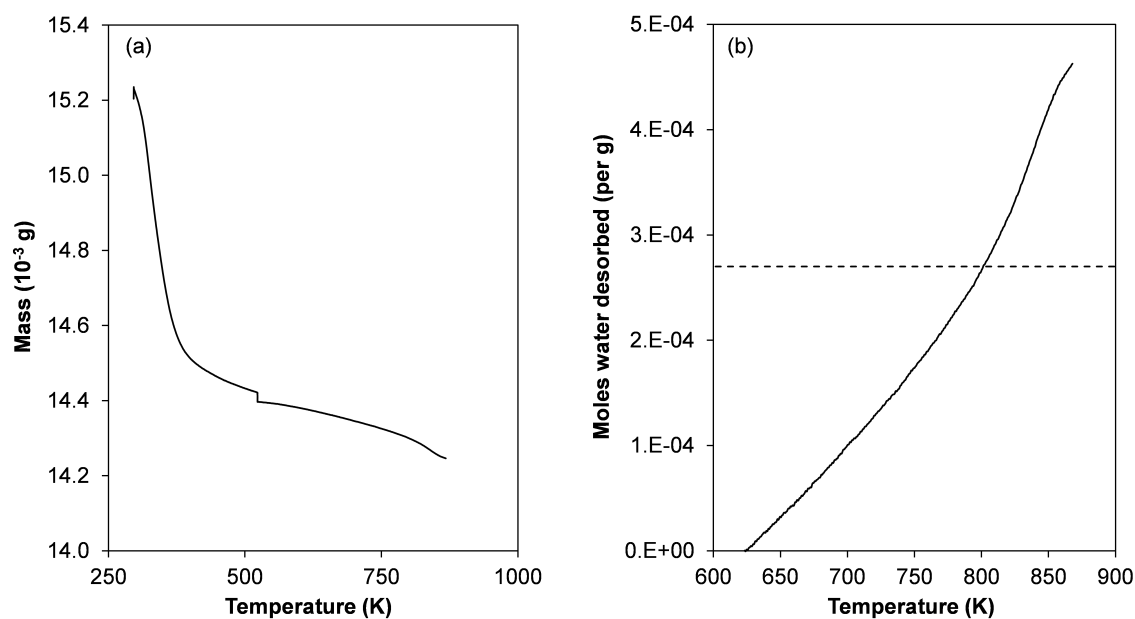


Figure F.13. (a) TGA profile for Sn-CHA-70 and (b) moles of water desorbed (per g zeolite) above 623 K (solid line) compared to the moles of Sn present in Sn-CHA-F-70 (dotted line).

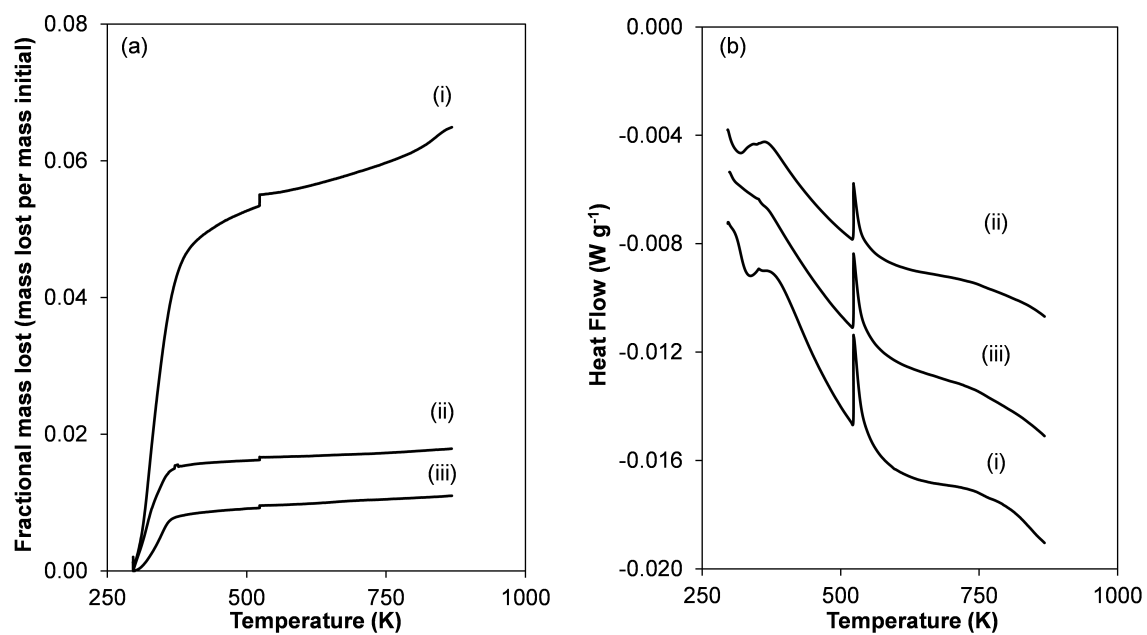


Figure F.14. (a) Fractional mass lost and (b) heat flow (per g zeolite) as functions of temperature for (i) Sn-CHA-F-70 (ii) Si-CHA-F and (iii) Sn-Beta-F-116.

### F.6.7 X-ray absorption spectroscopy

XAS measurements were performed at the Sn K edge (29.200 keV) on the bending magnet beamline of the Materials Research Collaborative Access Team (MRCAT) at the Advanced Photon Source (APS), Argonne National Laboratory. The APS X-ray ring has a current of 102 mA and the beamline has a flux of  $5 \times 10^{10}$  photons  $\text{s}^{-1}$ . Photon energies were selected using a water-cooled, double-crystal Si(111) monochromator, which was detuned by approximately 50% to reduce harmonic reflections. Measurements were conducted in step-scan transmission mode and data points were collected in three separate regions: a pre-edge region (-250 to -50 eV, step size = 10 eV, dwell time = 0.25 s), the XANES region (-50 to -30 eV, step size = 5 eV, dwell time 0.25 s and -30 to 30 eV, step size 0.5 eV, dwell time = 0.5 s), and the EXAFS region (0 to 6  $\text{\AA}^{-1}$ , step size = 0.05  $\text{\AA}^{-1}$ , dwell time = 0.5 s and 6 to 15  $\text{\AA}^{-1}$ , step size = 0.05  $\text{\AA}^{-1}$ , dwell time 1 s). The ionization chambers were optimized for the maximum current with linear response (ca.  $10^{10}$  photons detected  $\text{s}^{-1}$ ) with 10% absorption in the incident ion chamber and 70% absorption in the transmission detector. During each measurement, a third detector in series collected a Sn foil reference spectrum for energy calibration.

Samples were pressed into self-supporting wafers in a cylindrical stainless-steel holder containing six wells. The amount of sample was adjusted to obtain an absorbance ( $\mu\text{x}$ ) approximately equal to 1.0. The sample holder was placed in a quartz reactor tube (1 in. OD, 10 in. length) and sealed by two Ultra-Torr fittings with Kapton windows through which gas could be flowed. Measurements were performed on samples under ambient conditions. Samples were then heated to 523 K (0.167 K  $\text{s}^{-1}$ ) in flowing He (1.67  $\text{cm}^3 \text{s}^{-1}$ , Airgas, Built-In Purifier Grade, 99.9997%) and held for 1800 s to remove adsorbed water. The dehydrated samples were cooled to room temperature in He and measurements performed at room temperature in He.

XAS spectra were analyzed using WinXAS 3.2 software. Data was normalized with linear and cubic fits of the pre-edge and post-edge regions, respectively. The

oxidation state of each sample was determined by comparing the XANES energy to that of Sn foil, SnO, and SnO<sub>2</sub> reference compounds. The EXAFS was extracted by performing as cubic spline fit of the normalized absorption spectrum with 5 nodes from 2.0 to 14 Å<sup>-1</sup>. Coordination parameters were obtained through a least-squares fit in R-space of the magnitude and imaginary parts of the Fourier transform of the k<sup>2</sup>-weighted EXAFS from 2.55 to 10.0 Å. Experimental phase shift and back scattering amplitude fitting functions for Sn-O scattering pairs were determined from SnO<sub>2</sub> (6 Sn-O bonds at 2.05 Å).

X-ray absorption spectroscopy (XAS) is a synchrotron based technique used to provide bulk characterization of oxidation states (near edge region, XANES) and coordination numbers and bond distances (fine structure region, EXAFS). XAS spectra measured on select samples from this study are reported in Table F.6. The Sn K edge energy for materials studied here was 29.2025 keV, in agreement with a Sn(IV)O<sub>2</sub> reference, demonstrating that the incorporated Sn is tetravalent. The coordination number and average bond lengths determined from analysis of the EXAFS region of SnO<sub>2</sub> were six Sn-O bonds at 2.05 Å. The spectral intensity in the EXAFS region for stannosilicate samples under ambient and dehydrated conditions (523 K, flowing He) was compared to determine the number of Sn-O bonds present under both condition for Sn-Beta, Sn-CHA, and Sn-xerogel, confirming the presence of six Sn-O bonds at ambient conditions and four Sn-O bonds after dehydration in each sample.

For Sn-CHA-F-70 and Sn-Beta-F-116, the bond distance decreased from 2.01 Å and 2.00 Å to ca. 1.96 Å and 1.92 Å, respectively, upon dehydration. The difference spectra (hydrated – dehydrated) in Sn-CHA-F-70 results in two Sn-O bonds, presumably due to removal of coordinated water ligands, at a bond distance of 2.14 Å, which agrees with the Sn-O distance for bound water ligands estimated from DFT for Sn-CHA (Section F.2.5). For Sn-xerogel, the bond distance decreased slightly from 2.03 Å to 2.00 Å, suggesting that this amorphous material has longer Sn-O bond distances than the crystalline materials. Bare et al. performed EXAFS analysis on bulk SnO<sub>2</sub> (cassiterite) and hydrothermally synthesized Sn-Beta, and found the Sn-O

distances to be 2.05 Å and 1.91 Å, respectively, after pre-treatment at 798 K in flowing dry air and cooling to ambient temperature [562]. EXAFS analysis performed by Dijkmans et al. found that dehydrated Sn-Beta (823 K, N<sub>2</sub>) had three Sn-O bonds at 1.92 Å, with a fourth bond elongated to 2.13 Å, with 1.3 second-shell Si atoms located at 2.96 Å and 2.7 Si atoms located at 3.17 Å [661]. Han et al. calculated Ti-O bond lengths of ca. 1.82 Å for Ti-CHA [616], bond distances similar to those found in Ti-Beta dehydrated at 623 K for 1 h (1.80 Å) [592]. By extension, Sn-O bond lengths in Sn-CHA may be expected to be similar to those found in Sn-Beta (ca. 1.92 Å). Considering the ca. 0.02 Å error in bond distances in EXAFS, the dehydrated Sn-O distances measured for Sn-CHA and in literature for Sn-Beta are approximately equivalent, though the dehydrated Sn-O distances measured for Sn-CHA are longer than those expected from our calculations (ca. 1.89 Å), outside of the error of the measurement.



Table F.6.  
Summary of XAS studies on stannosilicate materials.

| Sample                     | Edge<br>Energy,<br>keV | Oxidation<br>State | Scatter | N <sup>a</sup> | R, Å <sup>b</sup> | $\Delta \sigma^2$<br>(*10 <sup>3</sup> ) <sup>c</sup> | $\Delta E_o$ ,<br>eV <sup>d</sup> |
|----------------------------|------------------------|--------------------|---------|----------------|-------------------|---|-----------------------------------|
| Sn Foil                    | 29.2000                | 0                  |         |                |                   |   |                                   |
| SnO                        | 29.004                 | II                 |         |                |                   |   |                                   |
| SnO <sub>2</sub>           | 29.2028                | IV                 | Sn-O    | 6.0            | 2.05              | 0.0   | 0.2                               |
| Sn-Beta,<br>ambient        | 29.2030                | IV                 | Sn-O    | 5.7            | 2.00              | 3.0   | -0.4                              |
| Sn-Beta,<br>dehydrated     | 29.2025                | IV                 | Sn-O    | 3.8            | 1.92              | 3.0   | -0.9                              |
| Sn-CHA-F-70,<br>ambient    | 29.2013                | IV                 | Sn-O    | 4.8            | 2.01              | 4.0   | -1.5                              |
| Sn-CHA-F-70,<br>dehydrated | 29.2013                | IV                 | Sn-O    | 4.0            | 1.96              | 3.0   | -1.6                              |
| Sn-xerogel,<br>ambient     | 29.2026                | IV                 | Sn-O    | 5.8            | 2.03              | 3.0   | 0.4                               |
| Sn-xerogel,<br>dehydrated  | 29.2024                | IV                 | Sn-O    | 4.0            | 2.00              | 3.0   | 1.2                               |

<sup>a</sup>Coordination number, Errors are  $\pm 10\%$

<sup>b</sup>Sn-O bond distance, Errors are  $\pm 0.02$  Å

<sup>c</sup>Relative Debye-Waller factor

<sup>d</sup>Relative edge energy

## F.6.8 Supplementary infrared spectra

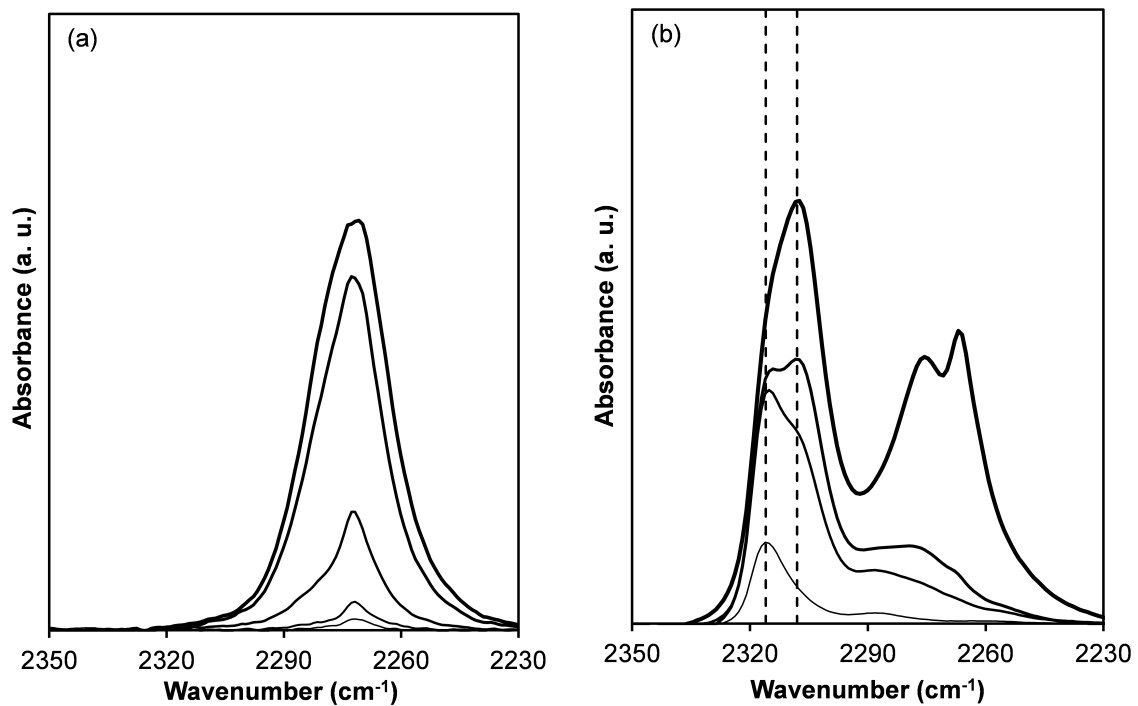


Figure F.15. IR difference spectra (relative to zero coverage) of (a) Si-CHA-F and (b) Sn-Beta-F-116 upon sequential dosing of CD<sub>3</sub>CN to saturation coverages; dashed lines are shown at 2316 cm<sup>-1</sup> and 2308 cm<sup>-1</sup> for open and closed Sn sites, respectively.

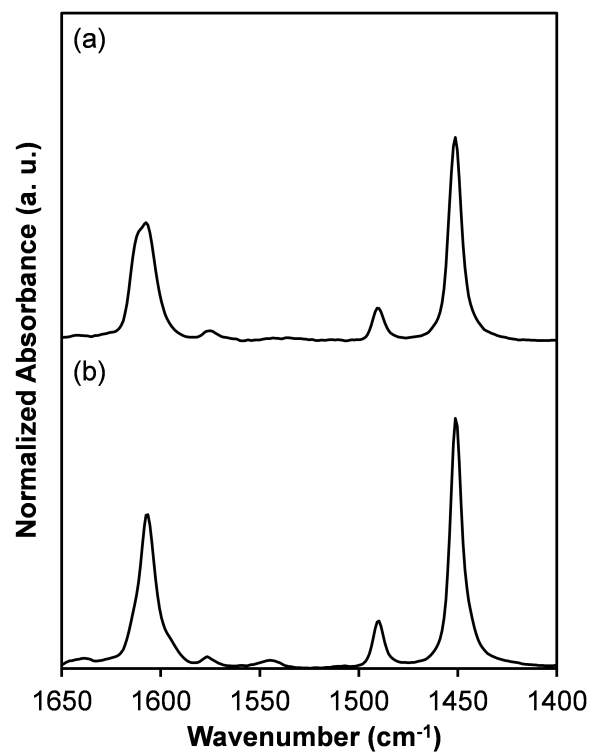


Figure F.16. IR difference spectra (relative to zero coverage) for (a) Sn-CHA-F-60 and (b) Sn-CHA-F-70 saturated with pyridine and then exposed to dynamic vacuum ( $10^{-1}$  Torr, 900 s). Spectra are offset vertically for clarity.

### F.6.9 Ammonia temperature programmed desorption

Ammonia titration of Lewis acid sites on Sn-CHA-F was performed to corroborate the quantification obtained from  $\text{CD}_3\text{CN}$  titration. Saturation of Sn-CHA-F-60 and Sn-CHA-F-70 with ammonia followed by a purge step (331 K, 8 h, He) and subsequent TPD, a procedure used previously to quantify Lewis acid sites in Sn-Beta [466], led to desorption of 1.07 and 1.20 mol  $\text{NH}_3$  (mol Sn) $^{-1}$ , respectively, (quantification in Table F.2; desorption profiles in Figure F.17), equivalent to the number of sites quantified by  $\text{CD}_3\text{CN}$  for both samples. While  $\text{NH}_3$  desorption from SiOH nest defects in highly-defective dealuminated Beta zeolites was observed previously using this procedure [466], the quantity of  $\text{NH}_3$  desorbed from dealuminated Beta ( $1.57 \times 10^{-5}$  mol  $\text{NH}_3$  per g) was ca. 6% of that desorbed from Sn-CHA-F-70 (per g), suggesting the desorption from Sn-CHA-F-70 arises primarily from desorption from Sn sites and not from SiOH groups.

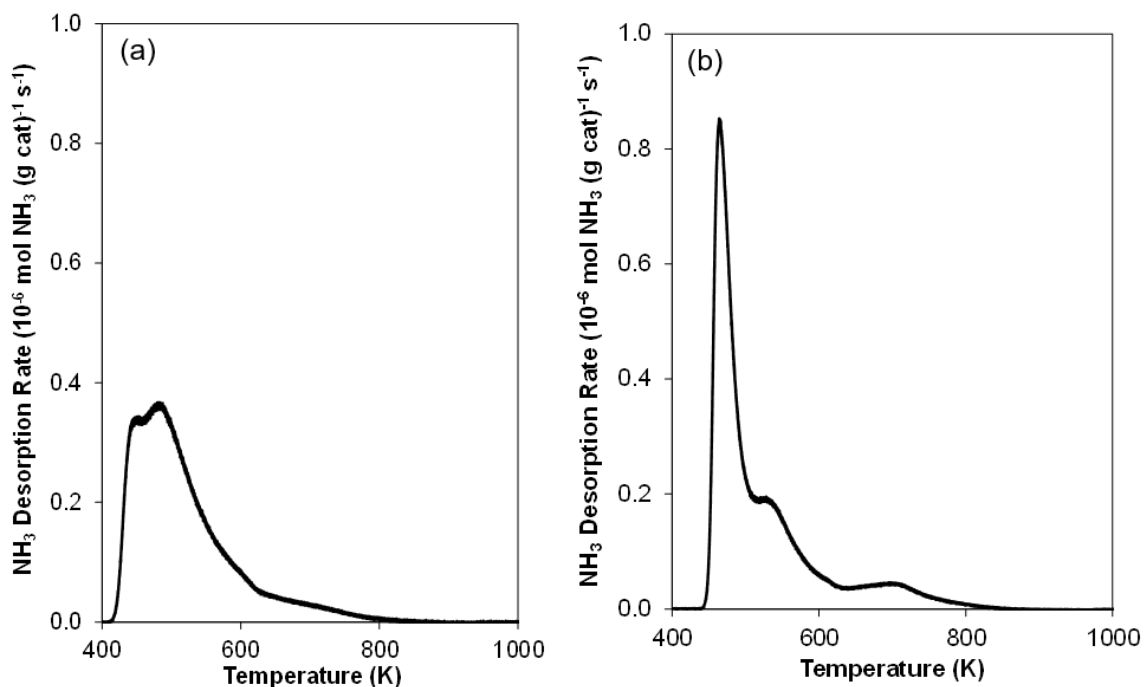


Figure F.17. Temperature programmed desorption profile for  $\text{NH}_3$ -saturated (a) Sn-CHA-F-60 and (b) Sn-CHA-F-70.

#### F.6.10 Intermolecular MPVO reactions

Intermolecular MPVO reactions were performed between ethanol and acetone, in order to avoid known condensation reactions of terminal aldehydes and their MPV product alcohols. Initial acetaldehyde formation rates (313 K), measured under differential acetone conversions (<10%) in ethanol solvent and far from the equilibrium acetone conversion (ca. 60%, Fig. F.18), were  $3.20 \times 10^{-2}$  and  $3.80 \times 10^{-3}$  mol (mol Sn) $^{-1}$  s $^{-1}$  for Sn-Beta-F-116 and Sn-CHA-F-60, respectively (Table F.7). The ethanol-acetone MPVO rate for Sn-Beta-F-116 per open Sn site is  $10\times$  greater than that for Sn-CHA-F-60 (per Sn site). Open sites are the most reactive sites in Sn-Beta-F zeolites based on theoretical calculations [628,629] and previous experimental studies of the glucose isomerization reaction that is mediated by an analogous kinetically-relevant intramolecular hydride shift [466]. The lower reaction rate on Sn-CHA-F-60 may reflect diffusion limitations in Sn-CHA-F-60, or differences in transition state stability or prevalent surface coverages in Sn-CHA-F-60.

Due to poor separation between ethanol and isopropanol in GC chromatograms when ethanol solvent was used, determination of isopropanol formation rates was not possible for these reactions and precluded confirmation that acetaldehyde was formed via a MPVO reaction. This complication was avoided by performing reactions with ethanol diluted in acetone solvent. Under these conditions (0.2 M ethanol, 333 K), the isopropanol formation rate over Sn-Beta-F-116 was  $2.2 \times 10^{-3}$  mol (mol Sn) $^{-1}$  s $^{-1}$ , and the isopropanol:acetaldehyde ratio was ca. 2:1, as would be expected if acetaldehyde underwent subsequent condensation reactions to a greater extent than isopropanol. In acetone solvent, Sn-CHA-F-60 produced acetaldehyde at a rate of  $7.0 \times 10^{-5}$  mol (mol Sn) $^{-1}$  s $^{-1}$ , ca.  $15\times$  lower than the acetaldehyde production rate observed for Sn-Beta-F-116, similar to the  $10\times$  lower acetaldehyde production rate observed over Sn-CHA-F-60 for ethanol-acetone MPVO in ethanol solvent. However, the isopropanol:acetaldehyde ratio over Sn-CHA-F-60 was only 0.05, suggesting severe diffusion limitations for isopropanol formed in Sn-CHA pores. The ratio of

initial isopropanol formation rates between Sn-Beta-F-116 and Sn-CHA-F-60 in the ethanol-acetone reaction in acetone solvent was ca.  $260\times$ , while the initial 1-propanol formation rates (Section F.2.3) were  $40\times$  higher for Sn-Beta-F-116 than Sn-CHA-F-60. The amount of acetaldehyde formed over Sn-CHA-F-60 was only 0.25 moles (mol Sn)<sup>-1</sup>, potentially due to blockage of pores preventing completion of multiple catalytic turnovers over intrapore Sn sites in Sn-CHA-F-60.

Acetaldehyde and isopropanol are produced in equimolar selectivity via the desired MPVO pathway, however, under the conditions studied here, the acetaldehyde-to-isopropanol selectivity was less than unity over Sn-Beta-F-116. Ivanov et al. studied the ethanol-acetone MPVO reaction over amorphous alumina and zirconia catalysts in the gas phase (413 K), and found that i) water was a reaction product and ii) the isopropanol production rate was always greater than the acetaldehyde production rate, two results which were proposed to be due to acetaldehyde condensation or alcohol dehydration [632]. Shibagaki et al. found that only secondary alcohols were able to reduce hexanal over hydrous ZrO<sub>2</sub>, and that reduction of hexanal by ethanol resulted primarily in formation of 1,1-diethoxy ethane with 91% yield [630]. Ordonsky et al. studied acetaldehyde condensation over Lewis acidic ZrO<sub>2</sub>/SiO<sub>2</sub> catalysts, with selectivity to crotonaldehyde of >85% (gas-phase, 403 K) [631], while Palagin et al. recently demonstrated that Sn-Beta catalyzes gas-phase acetaldehyde condensation reactions (473 K) [633]. Consistent with these observations, GC-MS analysis suggests a major secondary product in this reaction over Sn-Beta-F-116 and Sn-CHA-F-60 was 1,1-diethoxy ethane, which forms from condensation of an acetaldehyde molecule with two ethanol molecules, and is not formed by co-reaction of isopropanol and acetaldehyde or by reaction of ethanol alone (Table F.8).

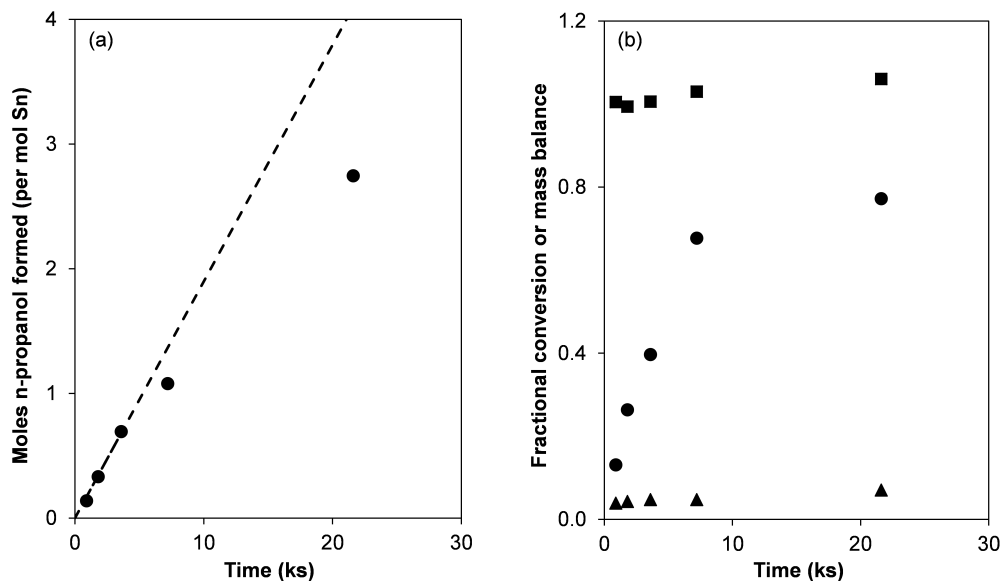


Figure F.18. (a) Transient reaction profile for the reaction of ethanol and propionaldehyde over Sn-CHA (333K, 0.6 M propionaldehyde diluted in ethanol solvent). Linear fit to first four data points (dotted line) demonstrates that determination of initial rate by extrapolation to initial time is accurate for data within the first 3600s of reaction time. (b) Propionaldehyde conversion (circles), ethanol conversion (triangles), and C<sub>3</sub> mass balance ((propionaldehyde + n-propanol + 1,1-diethoxy propane)/(moles propionaldehyde converted)) (squares) as a function of time.

Table F.7.

Reaction rates over Sn-CHA-F-60, Sn-Beta-F-116, Si-CHA-F, and Sn-xerogel, for the intermolecular MPVO reaction of ethanol and acetone.

| Catalyst      | Ethanol, 0.2 M<br>acetone rate<br>(per Sn) <sup>a</sup> | 0.2 M Ethanol,<br>acetone rate<br>(per Sn) <sup>b</sup> |
|---------------|---|---|
| Sn-CHA-F-60   | $3.80 \cdot 10^{-3}$                                    | $7.0 \cdot 10^{-5}$                                     |
| Sn-Beta-F-116 | $3.20 \cdot 10^{-2}$                                    | $2.2 \cdot 10^{-3}$                                     |
| Sn-xerogel    | n.m.*   | $1.6 \cdot 10^{-4}$                                     |
| Si-CHA-F      | n.p.**  | n.p.**  |

<sup>a</sup>313 K, 0.2 M acetone in ethanol solvent, acetaldehyde formation rate

Errors are  $\pm 15\%$ .

<sup>b</sup>333 K, 0.2 M ethanol in acetone solvent, acetaldehyde formation rate

Errors are  $\pm 15\%$ .

\*n.m., not measured.

\*\*n. p., no products observed.

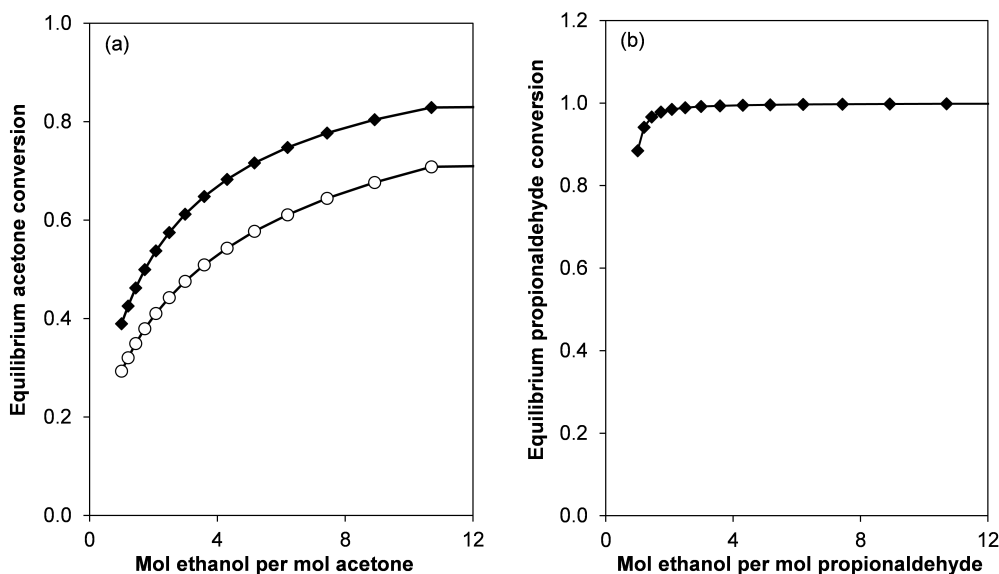


Figure F.19. Equilibrium conversion of (a) acetone as a function of initial ethanol:acetone ratio (diamonds, 333 K; circles, 313 K) and (b) propionaldehyde as a function of initial ethanol:propionaldehyde ratio (333 K). Determined using AIChE DIPPR database [662].



Table F.8.

Control experiments performed using Sn-CHA-F-60, Sn-Beta, Si-CHA-F, and Sn-xerogel, as well as those performed in empty reactors.

| Reactants                  | Catalyst     |                      |   |   |   |
|----------------------------|--------------|----------------------|---|---|---|
|                            | <i>Blank</i> | <i>Si-Cha-F</i>      | <i>Sn-CHA-F-60</i>                                    | <i>Sn-Beta-F-116</i>                                  | <i>Sn-xerogel</i>                                     |
| Ethanol + Acetone          | n.p.*        | n.p.*                | CH <sub>3</sub> CHO, isopropanol, 1,1-diethoxy ethane | CH <sub>3</sub> CHO, isopropanol, 1,1-diethoxy ethane | CH <sub>3</sub> CHO, isopropanol, 1,1-diethoxy ethane |
| Ethanol + Propionaldehyde  | n.p.*        | 1,1-diethoxy propane | CH <sub>3</sub> CHO, 1-propanol, 1,1-diethoxy propane | CH <sub>3</sub> CHO, 1-propanol, 1,1-diethoxy propane | CH <sub>3</sub> CHO, 1-propanol                       |
| Ethanol                    | n.m.**       | n.m.**               | n.p.*   | n.m.**  | n.m.**  |
| Ethanol + Acetaldehyde     | n.m.**       | n.p.*                | 1,1-diethoxy ethane                                   | n.m.**  | n.m.**  |
| Isopropanol + Acetaldehyde | n.m.**       | n.p.*                | n.p.*   | n.m.**  | n.m.**  |
| Acetaldehyde               | n.m.**       | n.p.*                | 2,4,6-Trimethyl-1,3,5-trioxane                        | n.m.**  | n.m.**  |

\*n. p., no products observed.

\*\*n.m., not measured.

Isotopic labeling experiments with  $\text{C}_2\text{D}_5\text{OH}$ .

The major fragments in the mass spectra for 1-propanol formed during the reaction of  $\text{C}_2\text{D}_5\text{OH}$  and propionaldehyde over Sn-CHA-F-60 shifted to higher mass by  $m/z = 1$  (Figure F.20), suggesting 1-propanol is formed via an intermolecular hydride shift over Sn-CHA. Due to the presence of trace 1-propanol in the reactant solution itself, there are some small intensity fragments that remain unshifted from the unlabeled product. Mass spectra for the reaction of  $\text{C}_2\text{D}_5\text{OH}$  with propionaldehyde over Sn-Beta-F-116 are shown in Figure F.21, and are comparable to that shown in Figure F.21a for Sn-CHA-F-60.

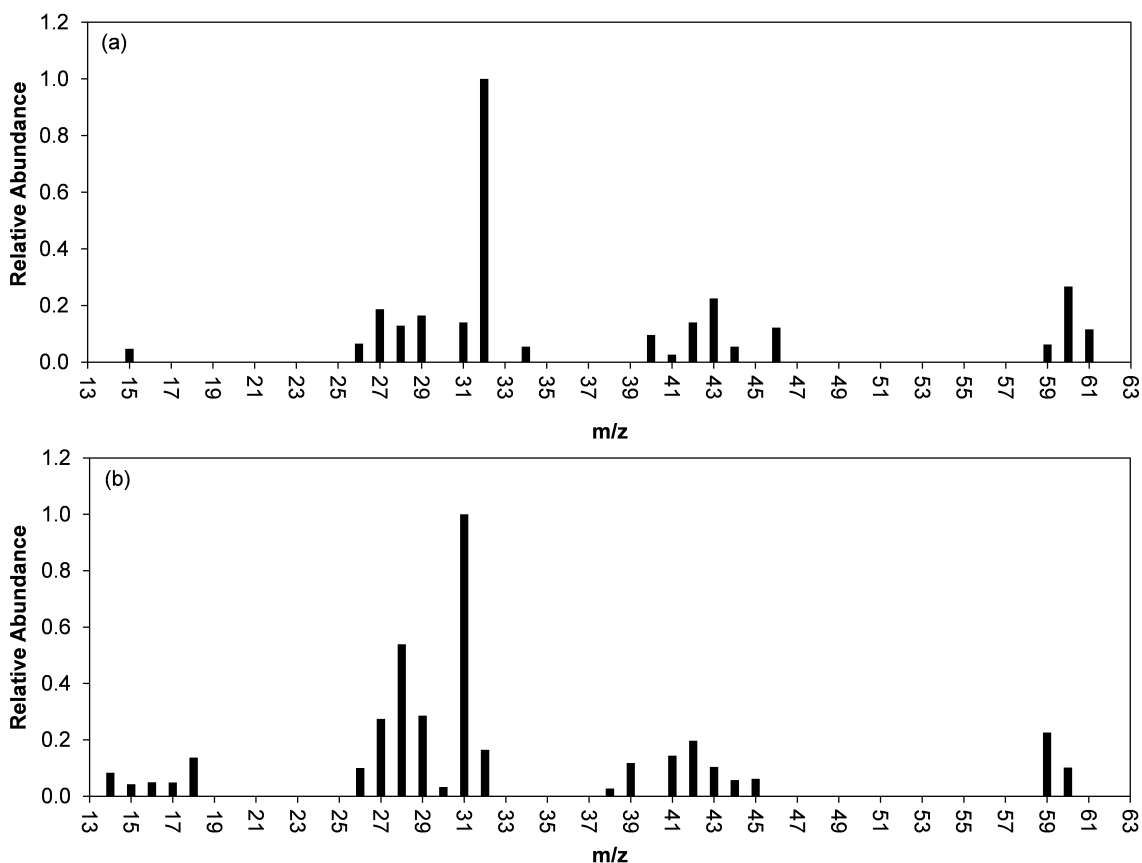


Figure F.20.  $m/z$  spectra for n-propanol formed over Sn-CHA-F-60 from reactions in (a)  $\text{C}_2\text{D}_5\text{OH}$  and (b)  $\text{C}_2\text{H}_5\text{OH}$  solvent.

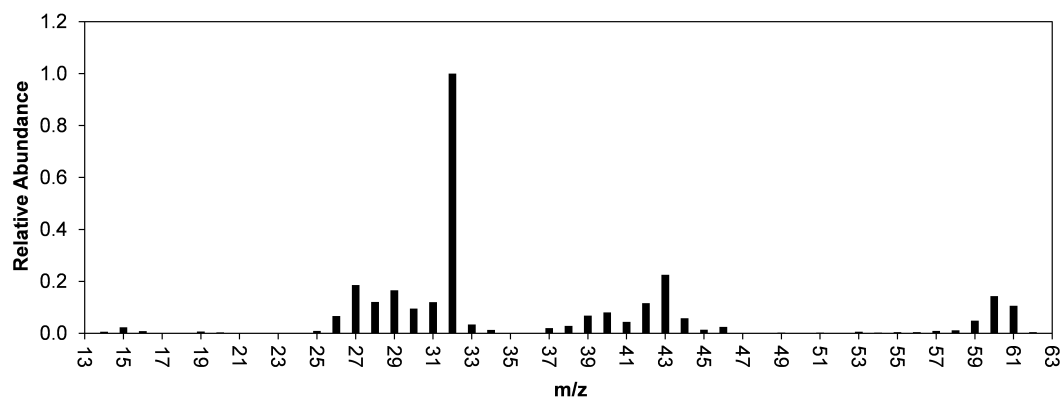


Figure F.21.  $m/z$  spectra for n-propanol formed over Sn-Beta-F-116 from reaction of  $C_2D_5OH$  and propionaldehyde in  $C_2D_5OH$  solvent.

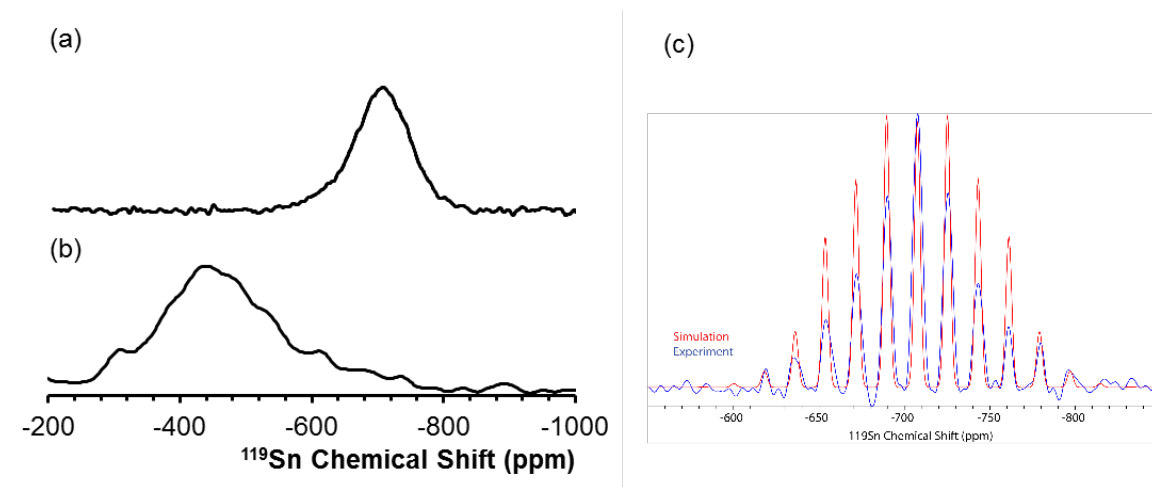
F.6.11 Additional details for  $^{119}\text{Sn}$ , and  $^{29}\text{Si}$  NMR spectra for Sn-CHA-F

Figure F.22. (a) 1D  $^{119}\text{Sn}$  DNP enhanced CP spin-echo MAS spectrum for hydrated Sn-CHA-F-70 (MAS = 4 kHz, CP contact time = 1.5 ms, recycle delay = 3.5 s, 512 scans). (b) Reconstructed 1D  $^{119}\text{Sn}$  DNP enhanced CP-CPMG spectrum for dehydrated Sn-CHA-F-70 after dehydration under vacuum ( $1 \times 10^{-4}$  Torr) at 773 K (MAS = 10 kHz, CP contact time = 1.5 ms, recycle delay = 3.0 s, 24636 scans). 20 echoes were acquired, and 17 echoes were used to reconstruct the full-echo spectrum. Both were measured on a Bruker 600 MHz (14.1 T) DNP spectrometer. (c) extracted 1D  $^{119}\text{Sn}$  NMR spectrum for Sn-CHA-F-70 (blue trace) fit with one set of CSA parameters (red trace). The spectrum was acquired on Bruker 600 MHz (14.1 T) DNP NMR spectrometer. MAS = 4 kHz; CP contact time = 1.5 ms; recycle delay = 3.5 s; 256 scans per  $t_1$  increment, and 85  $t_1$  increments were acquired. The CSA fit was done using solid lineshape feature in Bruker's Topspin program2D.

$^{119}\text{Sn}$  DNP enhanced CPMAT experiments of hydrated Sn-CHA-F-70 were performed with varying recycle delays (1-20 seconds). The recycle delay did not affect the relative areas of the two components in the CSA fitting (Table F.9). It is plausible that the proton-rich environment in the hydrated sample facilitated  $^1\text{H}$ - $^1\text{H}$  spin diffusion to transfer the hyperpolarization to Sn sites within both micropores and mesopores of Sn-CHA on this time scale, or that the slightly-different Sn sites leading

to the two CSA fit are distributed similarly between the microporous and mesoporous portions of the Sn-CHA.

Table F.9.  
Reaction rates over Sn-CHA-F-60, Sn-Beta-F-116, Si-CHA-F, and Sn-xerogel, for the intermolecular MPVO reaction of ethanol and acetone.

| Recycle delay (s) | Site 1 <sup>a</sup> | Site 2 <sup>a</sup> |
|-------------------|---------------------|---------------------|
| 1.0               | 85%                 | 15%                 |
| 4.1               | 87%                 | 13%                 |
| 10                | 85%                 | 15%                 |
| 20                | 86%                 | 14%                 |

<sup>a</sup>Errors are  $\pm 9\%$ ,

calculated by the signal-to-noise ratio of the spectrum.

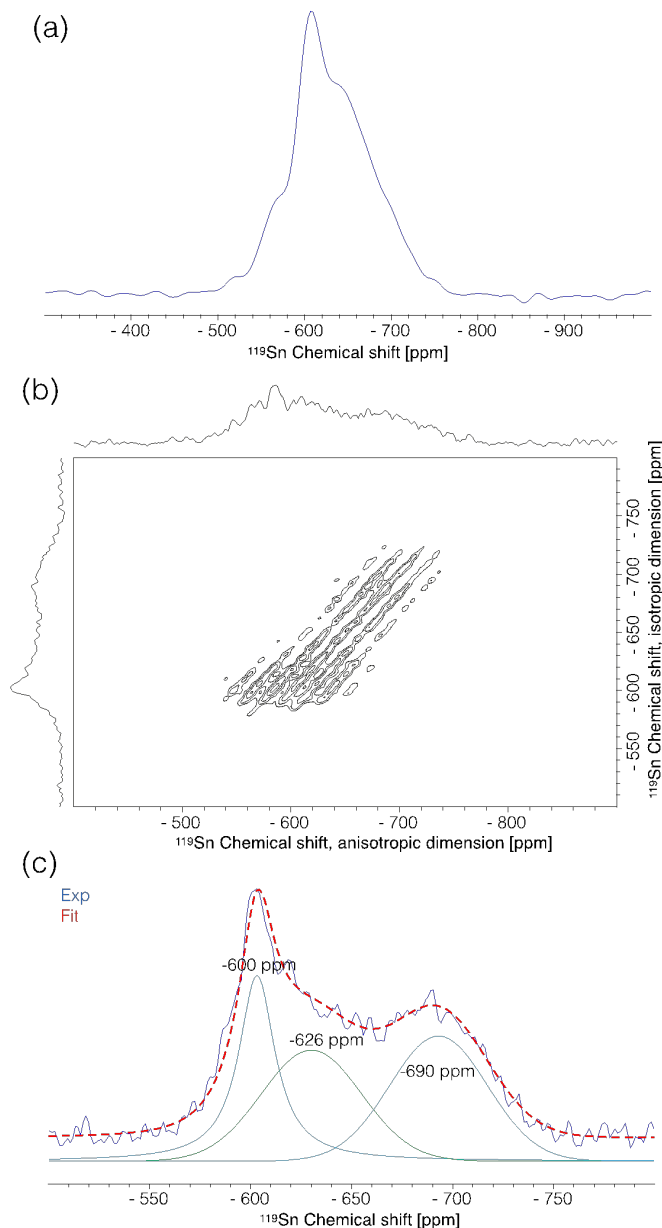


Figure F.23. (a) 1D DNP-enhanced reconstructed CP-CPMG spectrum of hydrated Sn-xerogel. MAS = 10 kHz. Number of scans = 512. Recycle delay = 3.9 s. 20 echoes were collected, and 19 echoes were used to reconstruct the single full-echo spectrum. (b) 2D DNP-enhanced CPMAT spectrum of hydrated Sn-xerogel. MAS = 4 kHz. Recycle delay = 3.9 s. Number of scans = 224 per  $t_1$  increment. 91  $t_1$  increments were collected and used. Both spectra were measured on Bruker 600 MHz (14.1 T) DNP spectrometer. (c) The sum of the positive projection of the f1 (isotropic) dimension of the 2D CPMAT spectrum (blue trace), and the corresponding peak deconvolution (red trace) using the solid lineshape feature implemented in Bruker Topspin software.

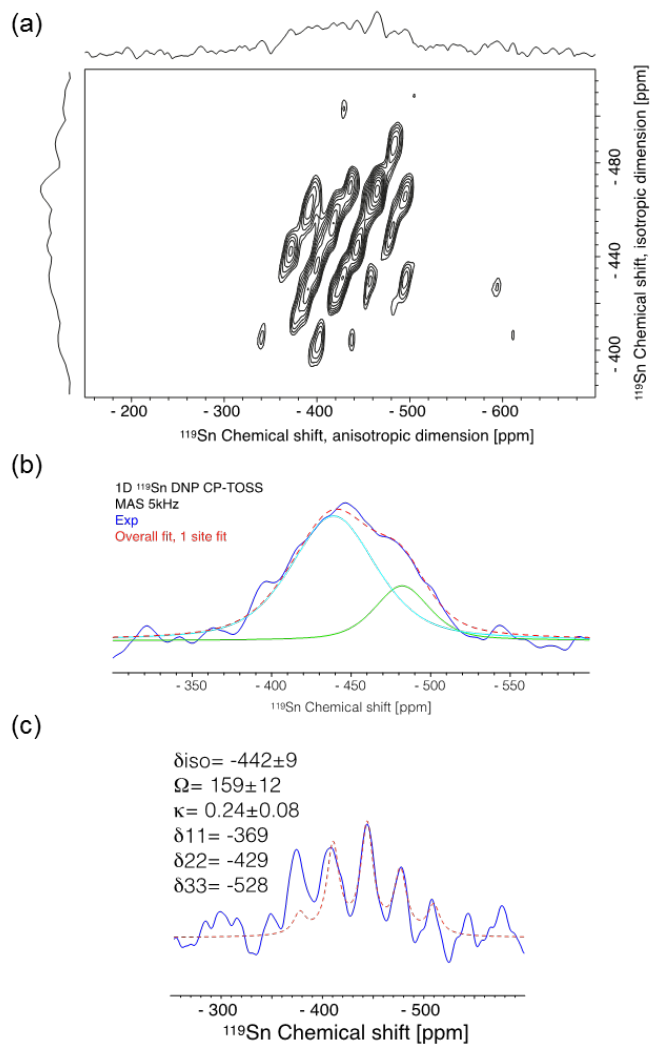


Figure F.24. (a) 2D DNP enhanced CPMAT spectrum of dehydrated Sn-CHA-F-70, measured on Bruker 400 MHz (9.4 T) DNP spectrometer. MAS = 5 kHz. Recycle delay = 6.2 s. CP contact time = 4.0 ms. 896 scans were acquired for each  $t1$  increment, and 16  $t1$  increments were collected. (b) 1D DNP enhanced CP-Total Sideband Suppression (CP-TOSS) spectrum of dehydrated Sn-CHA-F-70, measured on Bruker 400 MHz (9.4 T) DNP spectrometer, and the corresponding fit of isotropic sites (-437 and -480 ppm). (c) Fit values of CSA parameters of the isotropic site extracted at -437 ppm on the isotropic dimension of the 2D CPMAT spectrum for dehydrated Sn-CHA-F-70. CSA fit was done using the solid lineshape feature in Bruker Topspin software

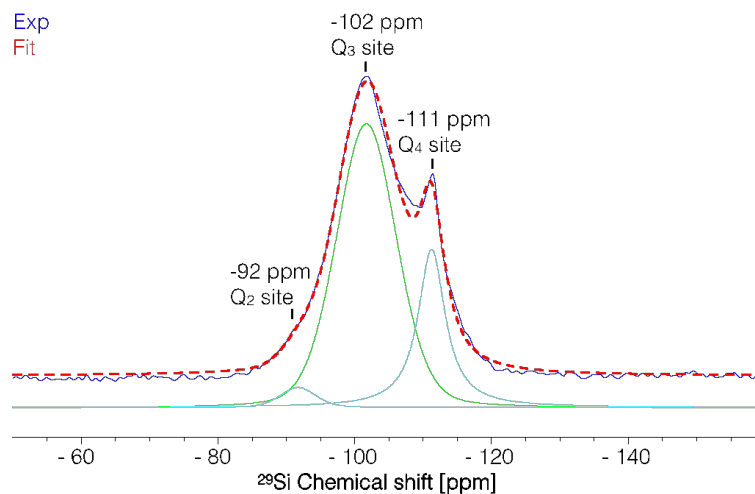


Figure F.25.  $^{29}\text{Si}$  DNP enhanced CPMAS NMR spectra for hydrated Sn-CHA-F-70, measured on Bruker 600 MHz (14.1 T) DNP spectrometer. The corresponding peak deconvolution (envelope: red trace) using solid lineshape feature implemented in Bruker Topspin software.



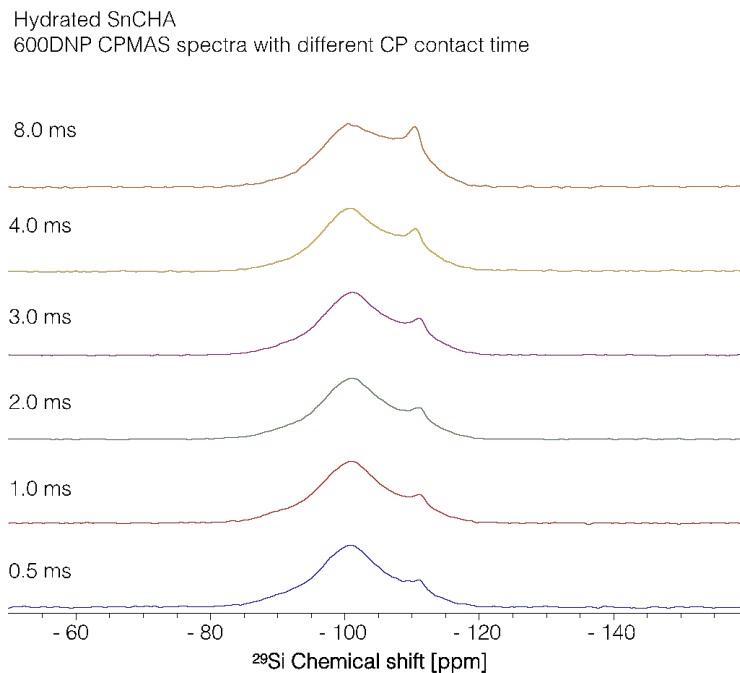


Figure F.26.  $^{29}\text{Si}$  DNP enhanced CPMAS NMR spectra for hydrated Sn-CHA-F-70 with varying CP contact time, measured on Bruker 600 MHz (14.1) DNP spectrometer. MAS = 10kHz. Recycle delay = 5 s. 32 to 128 scans were acquired to have spectra with a high signal-to-noise ratio.

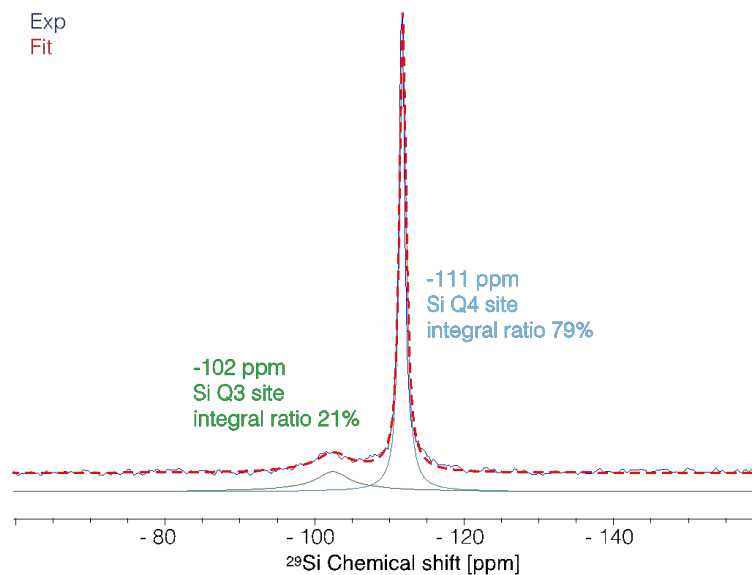


Figure F.27.  $^{29}\text{Si}$  NMR direct-excitation spectra for hydrated Sn-CHA-F-60 measured on 700 MHz (16.4 T) NMR spectrometer. The experimental spectrum (blue trace) was fit (red trace) with the solid lineshape feature in Bruker Topspin software. MAS = 10 kHz. Number of scans = 40. Recycle delay = 3600 s to make sure of full relaxation of NMR signals. The ratio of two sites ( $\text{Q}_4$  vs.  $\text{Q}_3$ ) was estimated by integrating the area of each peak.

F.6.12 2D  $^{119}\text{Sn}$  and 2D  $^{15}\text{N}$  CPMAT spectra of pyridine saturated Sn-CHA-F-70 and  $^{15}\text{N}$  NMR spectra of pyridine saturated Si-CHA-F.

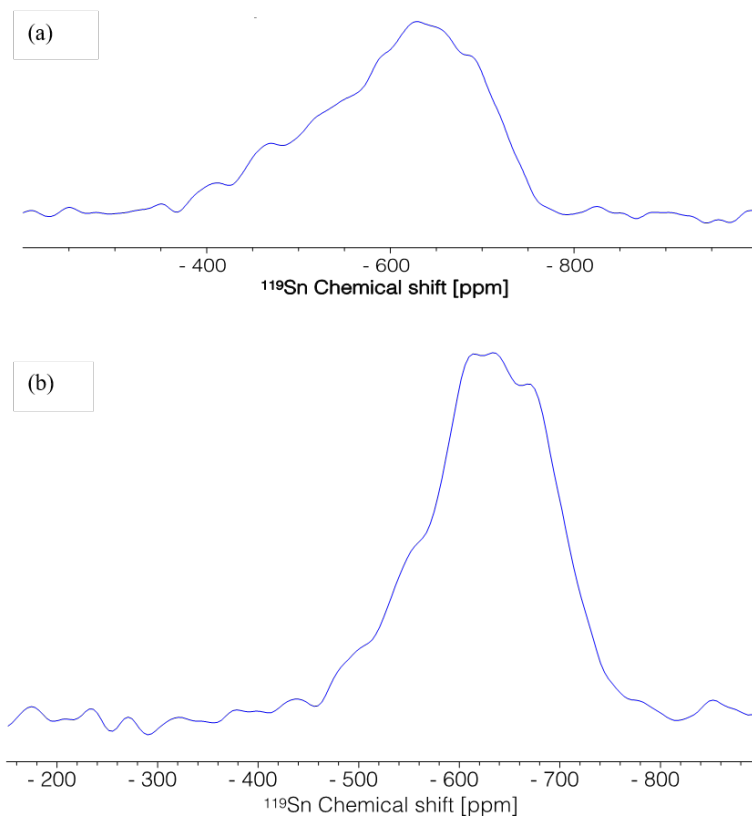


Figure F.28. 1D  $^{119}\text{Sn}$  DNP enhanced reconstructed CP-CPMG spectrum for pyridine saturated, dehydrated (a) Sn-CHA-F-70 and (b) Sn-xerogel. MAS= 10 kHz. Recycle delay= (a) 3.0 s and (b) 6.2 s. CP contact time= (a) 4.0 ms and (b) 1.5 ms. (a) 520 and (b) 1024 scans were acquired. 20 echoes were acquired, and (a) 19 echoes and (b) 6 echoes were used to reconstruct the single full-echo spectra. Both spectra were acquired on Bruker 600 MHz (14.1 T) DNP NMR spectrometer.

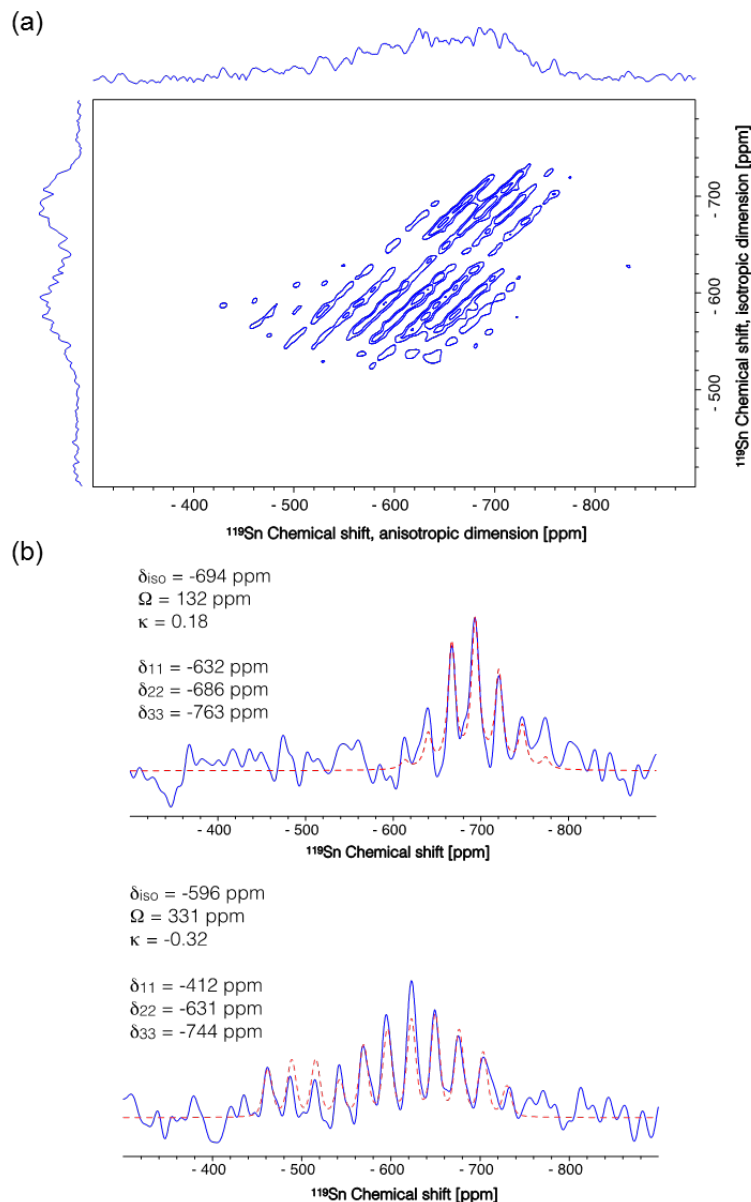


Figure F.29. (a) 2D  $^{119}\text{Sn}$  CPMAT NMR spectra for pyridine-saturated Sn-CHA-F-70 and (b) extracted 1D  $^{119}\text{Sn}$  NMR spectra for pyridine-saturated Sn-CHA-F-70 for the two resonances observed in the isotropic dimension. The spectrum was acquired on Bruker 600 MHz (14.1 T) DNP NMR spectrometer. MAS= 6 kHz; CP contact time= 4.0 ms; recycle delay = 3.0 s; 448 scans per  $t1$  increment, and 107  $t1$  increments were acquired. The CSA fit was done using the solid lineshape feature in Bruker's Topspin program.

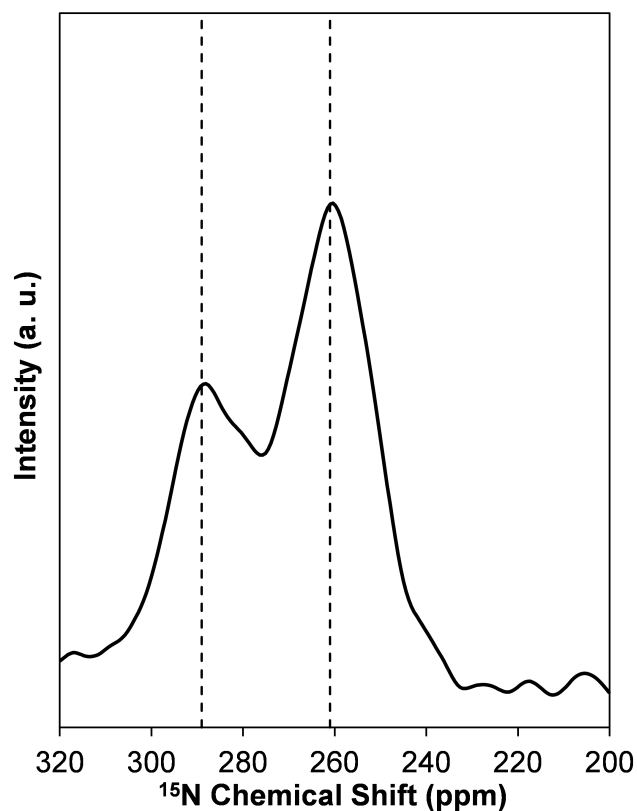


Figure F.30. 1D  $^{15}\text{N}$  NMR spectra for pyridine saturated, dehydrated Sn-CHA-F-70 (dotted lines are shown at 289 ppm and 262 ppm for pyridine hydrogen bound to SiOH groups and pyridine bound to Lewis acidic Sn sites, respectively). The spectrum was acquired on Bruker 600 MHz (14.1 T) DNP NMR spectrometer. MAS= 10 kHz; CP contact time= 8.0 ms; recycle delay = 4.5 s; 512 scans were acquired.

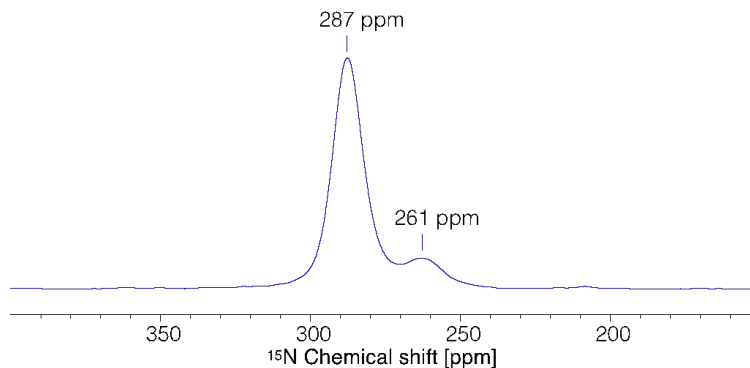


Figure F.31. DNP-enhanced  $^{15}\text{N}$  CPMAS spectrum of  $^{15}\text{N}$  pyridine treated dehydrated Sn-xerogel (MAS = 11.5 kHz, Recycle delay = 6.8 s, number of scans = 64). The spectrum was acquired on Bruker 600 MHz (14.1 T) DNP NMR spectrometer.

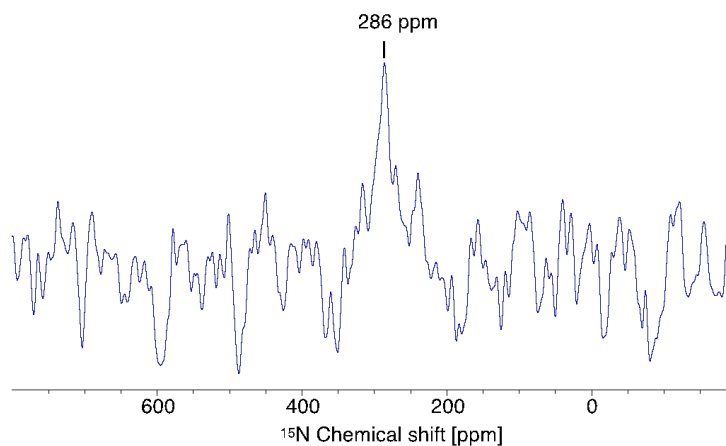


Figure F.32. DNP-enhanced  $^{15}\text{N}$  CPMAS spectrum of  $^{15}\text{N}$  pyridine treated dehydrated Si-CHA-F. The spectrum was acquired on Bruker 600 MHz (14.1 T) DNP NMR spectrometer. MAS= 10 kHz; CP contact time= 8.0 ms; recycle delay = 6.0 s; 7136 scans were acquired.

## F.6.13 DFT Calculations

Table F.10.

NMR CSA parameters calculated from DFT for hydrated (two water molecules bound to each Sn site, two second shell waters, and implicit water) and dehydrated Sn-CHA.

| Sn Site                | $^{119}\text{Sn } \delta_{iso}$<br>(ppm) | Span<br>( $\Omega$ , ppm) | Skew<br>( $\kappa$ ) |
|------------------------|--|---------------------------|----------------------|
| Hydrated               |  |                           |                      |
| <i>closed</i>          | -728                                     | 299                       | 0.50                 |
| <i>hydrolyzed-open</i> | -721                                     | 141                       | -0.42                |
| <i>defect</i>          | -707                                     | 215                       | 0.58                 |
| Dehydrated             |  |                           |                      |
| <i>closed</i>          | -424                                     | 100                       | 0.50                 |
| <i>hydrolyzed-open</i> | -566                                     | 392                       | -0.65                |
| <i>defect</i>          | -425                                     | 196                       | 0.33                 |

Table F.11.

NMR CSA parameters calculated with DFT for pyridine saturated Sn-CHA-F and Si-CHA-F.

| Site             | One Bound Pyridine Molecule     |                   |              | Two Bound Pyridine Molecules    |                   |              |
|------------------|---------------------------------|-------------------|--------------|---------------------------------|-------------------|--------------|
|                  | $^{119}\text{Sn } \delta_{iso}$ | Span              | Skew         | $^{119}\text{Sn } \delta_{iso}$ | Span              | Skew         |
|                  | (ppm)                           | ( $\Omega$ , ppm) | ( $\kappa$ ) | (ppm)                           | ( $\Omega$ , ppm) | ( $\kappa$ ) |
| Sn-CHA-F         |                                 |                   |              |                                 |                   |              |
| <i>defect Sn</i> | -623                            | 421               | -0.36        | -718                            | 132               | 0.18         |
| <i>closed Sn</i> | -595                            | 449               | -0.65        | -728                            | 221               | 0.77         |
| Si-CHA-F         |                                 |                   |              |                                 |                   |              |
| <i>SiOH</i>      | 300                             | 606               | 0.49         |                                 |                   |              |

Table F.12.

DFT calculated pyridine adsorption free energies (calculated at 298 K) with respect to each site and the corresponding isolated pyridine molecules ( $\Delta G$ , kcal mol<sup>-1</sup>). The optimized structures were calculated at the lower level of theory described in the computational details section (Section F.6.2). The energies correspond to single-point calculations performed with the M06, and Sn was described by the LanL2DZ effective core pseudopotential (ECP) augmented with a d polarization function; the rest of atoms directly were described by a 6-311+G(d, p) basis set. The thermal correction terms were included and taken from the calculations at the lower level of theory described in the computational details section (Section F.6.2).

| One pyridine binding |        |
|----------------------|--------|
| <i>closed</i>        | -12.86 |
| <i>defect</i>        | -15.55 |
| Two pyridine binding |        |
| <i>closed</i>        | -11.59 |
| <i>defect</i>        | -17.85 |

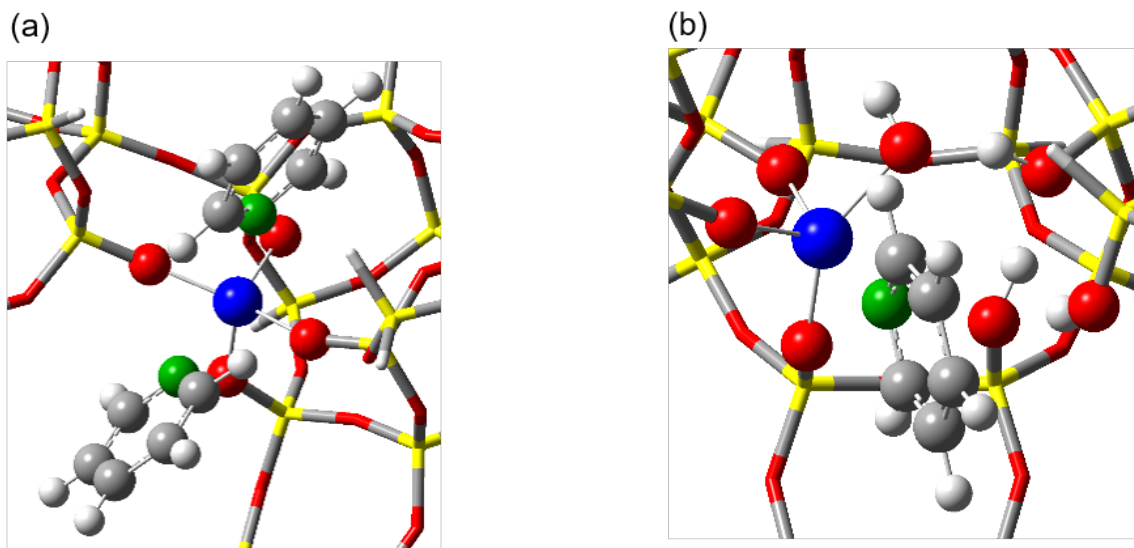


Figure F.33. DFT optimized (B3LYP-D3) structures for pyridine saturated (a) closed Sn with 2 bound pyridine and (b) defect Sn sites with one bound pyridine. Atoms that were not bound directly to Sn were treated with the 6-31G(d,p) basis set (Si: yellow, O: red, C: gray, H: white)), while O and N atoms bonded to Sn were treated with the 6-31+G(d) basis set (N: green, O: red) and Sn (blue) was treated with the LanL2DZ effective core pseudopotential augmented with a d polarization function.



VITA

## VITA

John Di Iorio was born in Kirkland, WA and was raised in Redmond, WA. The son of a pediatrics nurse and a medical coding specialist, John attended elementary school at Horace Mann Elementary School (not Horseman, as many first-graders once thought) and Redmond Junior High School (now Redmond Middle School), before attending Redmond High School. John grew up riding bikes and trailblazing through the backwoods of the Nike and Hartman park forests. As an avid soccer player, he was a part of the Redmond High School soccer team and local rec league team. John joined the high school cross-country team and earned a spot on the 4th-place state varsity roster his senior year. He and his family would routinely travel to the Oregon coast for summer vacations and this still remains one of his favorite travel destinations.

After graduating from Redmond High, John attended The University of Washington where he majored in Chemical Engineering. During his time at UW, John discovered ultimate frisbee and spent many Friday evenings playing ultimate well into the night. He spent two years as a Resident Advisor for the engineering residence hall community and worked closely with the UW College of Engineering to organize and plan engagement events. Many of these activities focused on developing simple demonstrations of various scientific principles that members of the engineering community could participate in (including rocketry, non-Newtonian fluids, aerodynamics, structural design, and chemistry). John also spent three years working as an undergrad research assistant for Graham Allan working the conversion of biomass and plastics to fuels and chemicals using supercritical water. Through this research, John was able to spend his summers working as a intern at a local start-up company,

Xtrudx based in Auburn, WA, assisting in the design and construction of a continuous supercritical water reactor.

John decided to continue his education by attending graduate school at Purdue University where he became a member of the inaugural Gounder Group. He worked endlessly with Michael Cordon and Ravi Joshi to build, design, construct, leak test, calibrate, install, and manage the birth of an academic lab space. Perhaps the greatest accomplishment of our time is the installation of a He line to the ASAP 2020 free space port that, with the meticulous help of Ravi, will most likely retain pressure until well after Raj has left Purdue. After leaving Purdue, John will begin a post-doctoral appointment at the MIT working with Prof. Yuriy Roman-Leshkov.